The 9th
US-Japan Seminar
on
Dielectric &
Piezoelectric Ceramics

November 2-5, 1999

Rizzan Sea-Park Hotel
Tanch-Bay, Okinawa, JAPAN

Traditional Crafts of Okinawa

Shi-sa (Tsuboyayaki ware)

Shi-sa conveyed to Okinawa in 13th century through Chinese Silk Road from the Orient in ancient times. Root of Shi-sa is the lion, symbol of power, courage, and pride. Craftwork of lion became "Sphinx" in Egypt, beast to guard palace in China, and became shi-sa in Okinawa to protect peoples' houses. Shi-sa is still loved by Okinawan people as talisman for protecting their houses from disaster and inviting good luck.

Bingata (Dyed Fabrics)

Bingata displays Okinawa's sense of beauty characterized by vivid colors and smooth patterns. Dying methods consist of katazome dyed with stencils and tsutsuzome dyed with cylinders. Bingata is often compared to yuzen dye of Kyoto, but the Okinawan fabrics do not incorporate embroidery or tie-dyes. Bingata is indispensable for Ryukyu dance performances.

REPORT DOCUMENTATION PAGE

Form Approved
OMB No. 0704-0188

The public reporting burden for this collection of information is estimated to average 1 hour per response, including the time for reviewing instructions, searching existing data sources, gathering and maintaining the data needed, and completing and reviewing the collection of information. Send comments regarding this burden estimate or any other aspect of this collection of information, including suggestions for reducing the burden, to Department of Defense, Washington Headquarters Services, Directorate for Information Operations and Reports (0704-0188), 1215 Jefferson Davis Highway, Suite 1204, Arlington, VA 22202-4302. Respondents should be aware that notwithstanding any other provision of law, no person shall be subject to any penalty for failing to comply with a collection of information if it does not display a currently valid OMB control number.
PLEASE DO NOT RETURN YOUR FORM TO THE ABOVE ADDRESS.

1. REPORT DATE *(DD-MM-YYYY)*	2. REPORT TYPE	3. DATES COVERED *(From - To)*
14-12-1999	Conference Proceedings	2-5 November 1999

4. TITLE AND SUBTITLE

9th US-Japan Seminar on Dielectric and Piezoelectric Ceramics

5a. CONTRACT NUMBER
F6256299M9152

5b. GRANT NUMBER

5c. PROGRAM ELEMENT NUMBER

6. AUTHOR(S)

Conference Committee

5d. PROJECT NUMBER

5e. TASK NUMBER

5f. WORK UNIT NUMBER

7. PERFORMING ORGANIZATION NAME(S) AND ADDRESS(ES)
Science University of Tokyo
Faculty of Science and Technology

Noda 278-8510
Japan

8. PERFORMING ORGANIZATION REPORT NUMBER

N/A

9. SPONSORING/MONITORING AGENCY NAME(S) AND ADDRESS(ES)

AOARD
UNIT 45002
APO AP 96337-5002

10. SPONSOR/MONITOR'S ACRONYM(S)

AOARD

11. SPONSOR/MONITOR'S REPORT NUMBER(S)
CSP-981028

12. DISTRIBUTUION/AVAILABILITY STATEMENT

Approved for public release; distribution is unlimited.

13 SUPPLEMENTARY NOTES

14. ABSTRACT
Proceedings from the 9th US-Japan Seminar on Dielectric & Piezoelectric Ceramics, held 2-4 Nov 99, in Okinawa, Japan, includes contributed papers pertaining to:
Basic Science
Piezoelectric Materials and Devices
Thin Film Dielectrics
Multilayer Ceramic Capacitors
Advanced Processing and Packaging

19991220 111

15. SUBJECT TERMS

Active Control, Electronic Ceramic, Electronic Devices, Electronics

16. SECURITY CLASSIFICATION OF:			17. LIMITATION OF ABSTRACT	18. NUMBE OF PAGES	19a. NAME OF RESPONSIBLE PERSON
a. REPORT	b. ABSTRACT	c. THIS PAGE			Joanne H. Maurice
U	U	U	UU	456	**19b. TELEPHONE NUMBER** *(Include area code)* +81-3-5410-4409

Standard Form 298 (Rev. 8/98)
Prescribed by ANSI Std. Z39.18

The 9th US-Japan Seminar on
Dielectric and Piezoelectric Ceramics

PROGRAM SUMMARY
and
EXTENDED ABSTRACT

General Chairmen: Tadashi Takenaka, Science University of Tokyo, Japan
                    Thomas R. Shrout, The Pennsylvania State University, USA

Program Chairmen: Takaaki Tsurumi, Tokyo Institute of Technology, Japan
                    Shoko Yoshikawa, Active Control eXperts, Inc., USA

Financial Committee: Kazuo Miyabe, TDK Corp., Japan

Administration: Michiko Fukutomi, Tokyo Institute of Technology, Japan

November 2-5, 1999
Rizzan Sea Park Hotel, Tancha Bay, Okinawa, Japan

The 9th US-Japan Seminar on
Dielectric and Piezoelectric Ceramics
November 1999

SCHEDULE SUMMARY

	Morning	*Afternoon*	*Evening*
Tuesday November 2			18:00 Registration & Welcome Reception
Wednesday November 3	8:45-9:00 Opening Remarks --- **Session I** 9:00-10:00 Plenary Lectures 10:00-12:30 Oral & Poster	**Session II** 14:00-15:00 Plenary Lectures 15:00-18:00 Oral & Poster	
Thursday November 4	**Session III** 8:30-9:30 Plenary Lectures 9:30-12:30 Oral & Poster	**Session IV** 14:00-15:00 Plenary Lectures 15:00-18:00 Oral & Poster	19:00-21:00 Banquet
Friday November 5	**Session V** 8:30-9:30 Plenary Lectures 9:30-12:00 Oral & Poster	12:00-13:30 Farewell Party (Lunch) 13:30- Optional Excursion	

Preface

This "Extended Abstract" book comprises the contributions to the *9th US-JAPAN SEMINAR ON DIELECTRIC AND PIEZOELECTRIC CERAMICS* which will be held in Rizzan Sea Park Hotel Tancha Bay, Okinawa, Japan from November 3 to 5, 1999. This Seminar followed eight previous seminars which were held approximately every two years since 1982. The Seminar covered recent advances in the broad and rapidly progressing field of dielectrics, piezoelectrics and ferroelectrics including their ceramics, thin films and single crystals. The Seminar consists five sessions such as "Basic Science", "Piezoelectric Materials and Devices", "Thin Film Dielectrics", "Multilayer Ceramic Capacitors" and "Advanced Processing and Packaging". Each session has two plenary talks from one Japanese side and one US side and 15-25 contributed papers. All contributed papers will be discussed at 5 poster sessions followed each oral presentation without discussion within 4 minute for Japanese speakers or 3 minute for US speakers. This presentation style is the traditional way for our recent US-Japan Seminar. The attendants will come from mainly Japan and USA and from a few other countries. We would like to thank all speakers, contributors, session chairs and paper authors for their effort in making the Okinawa Seminar a hugely successful one.

September 30, 1999

General chairman for Japanese side
Tadashi Takenaka

Program chairman for Japanese side
Takaaki Tsurumi,

PROGRAM

TUESDAY, NOVEMBER 2

    18:00   *Registration and Welcome Reception*

WEDNESDAY, NOVEMBER 3

    8:45–9:00   Opening Remarks: T. Takenaka *(Science University of Tokyo, Japan)*

        Session I —Basic Science

    Session Chair: Susan Trolier-McKinstry, The Pennsylvania State University
                        Takashi Yamamoto, National Defense Academy

    9:00–10:00   ***Plenary Lectures***   **Page**

    10:00–10:30   ***Break***

    10:30–11:20   ***Contributed Papers***

11:20–12:30   **Poster View**

12:30–14:00   _**Lunch**_

| _**Session II —Piezoelectric Materials and Devices**_ |

Session Chair: Ahmad Safari, Rutgers University
                    Akira Ando, Murata Manufacturing Co., Ltd.

14:00–15:00   _**Plenary Lectures**_   **Page**

15:00–16:30 *Contributed Papers*

16:30–18:00   Poster View, Discussion and Break

THURSDAY, NOVEMBER 4

Session III — Thin Film Dielectrics

Session Chair: Angus Kingon, North Carolina State University
Tadashi Shiosaki, Nara Institute of Science and Technology

8:30–9:30 *Plenary Lectures*

9:30–11:00 *Contributed papers*

11:00–12:30   *Poster View, Discussion and Break*

12:30–14:00   *Lunch*

Session IV — Multilayer Ceramic Capacitors

Session Chair: Donald M. Smyth, Lehigh University
Hirosi Kishi, Taiyo Yuden Co., Ltd.

14:00–15:00   *Plenary Lectures*   **Page**

15:00–16:30   *Contributed papers*

FRIDAY, NOVEMBER 5

Session V — Advanced Processing and Packaging

  Session Chair: Robert Pohanka, Office of Naval Research
        Tadashi Takenaka, Science University of Tokyo

10:40–12:00   *Poster View, Discussion and Break*

12:00–13:30   *Farewell Party (Lunch)*

13:30   *Optional Excursion (NOT free of charge)*

Session I —Basic Science

Plenary Lectures

Contributed Papers

MLCs Technologies of Today and Future

Yukio Sakabe
Murata Manufacturing Co., Ltd.
Yasu　Yasu-gun Shiga 520-2393 Japan
Fax: +81-77-587-1923, e-mail: sakabe@murata.co.jp

Abstract: Development of $BaTiO_3$-based dielectric materials for nickel electrode MLCs has significantly progressed due to the steep increase of Pd market price and expanding the needs for capacitors of large capacitance. Ultra-fine $BaTiO_3$ powder was synthesized and evaluated its dielectric behavior with particle size. Hydrolysis methods provide a suitable $BaTiO_3$ powder for preparing a smooth and defect free ultra- thin layer of few micron meters. $BaTiO_3$ ceramics composed of grains of 150nm in diameter has still ferroelectric characteristics and provided MLC with high dielectric constant of 1560. Performance of the MLCs changed severely with thickness of dielectrics and electrode layer due to the increase of voltage and mechanical stress.

The maximum capacitance of MLC has reached to 100μF that has been in the territory of Tantalum and Aluminum electrolytic capacitors. MOCVD was applied to form the thinner layer than that by conventional slurry coating method. ($Ba_{1-x}Sr_x$)TiO_3 dielectrics of 200nm thick were multi-stacked with Pt electrode on MgO substrate to prepare the MLC of high volumetric efficiency. This feasibility study showed one direction of the developments for future styles of the ceramic capacitors.

1. INTRODUCTION

With the advent of advanced electronic devices such as handy-phone and personal computer, the demand for surface mountable chip components continues to increase. Under these circumstances, the principal developments in the multilayer ceramic capacitors (MLCs) industry are miniaturization, improvement of volumetric efficiency, cost reduction, improvement in reliability and the design of new products with high performance.

In Japan, the MLC production unit has grown by 22.4% in fast quarter of this year. The MLC of large capacitance has become comparable performance to tantalum electrolytic capacitors. Aluminum electrolytic capacitor has lost 6.5% in the same time period. Today, the production unit volume difference between these two capacitors has expanding. This trend will continue from now on, because the MLC has higher volumetric efficiency, lower ESR and lower ESL at high frequency. These advantages meet the all needs from today's telecommunication equipment and personal computer.

The other hand, the price of MLCs is steadily decreasing at a rate of more than 10% a year. Since dramatic increase of palladium price in 1996, significant advances have been achieved in reduction of dielectric thickness to increase the volumetric efficiency and reduce the material cost of MLCs. Advanced technologies for ultra-fine powder synthesis, thin green sheet preparation, and stacking of high layer count (>350) have let to MLCs of large capacitance comparable to tantalum electrolytic capacitors.

Base metal electrode MLCs expanded the product line up utilizing the nickel compatible X7R dielectrics, fine Ni and Cu electrode powder. In this report, the recent developments of MLC technologies and a new challenge for future are overviewed.

2. BaTiO₃ FOR ULTRA-THIN DIELECTRIC LAYER

Miniaturization is one of the key technologies in the capacitors industry. By incorporating thinner dielectric layers with nickel compatible dielectrics and nickel electrode, large capacitance MLCs comparable to tantalum electrolytic capacitors has been developed. To reduce the dielectric thickness less than 3μm, further development of ultra-fine grain $BaTiO_3$ of high dielectric constant has been required.

Extensive works on the particle size effects of $BaTiO_3$ have been made, and several models for critical size of ferroelectricity have been proposed [1-14]. Arlt et al. reported that there was an optimal value of grain size at about 0.8μm for the maximum dielectric constant [4]. Results from our reliability study claimed that dielectric layer should be pore-free ceramics with grain of smaller in sized, and at least 5 grains are required for the ceramic layer. To design the capacitor of large capacitance par unit volume, the dielectrics is expected to have large dielectric constant with smaller grain in size. To realize the ideal $BaTiO_3$ powder of fine and good crystallinity, we synthesized the $BaTiO_3$ powder of 70nm in size by hydrolysis method [15,16]. Dense dielectric ceramics of grain size ranging from 150nm to 900nm were prepared with calcined $BaTiO_3$ powder doping the grain growth inhibitors and glass powder as sintering agent. MLC test samples were prepared with 1.6μm thick green sheet and Ni paste for inner electrode. The chip capacitors of size 2.0mm × 1.25 mm were fired in a reducing atmosphere at various temperature ranging from 1000℃ to 1250℃ for 2 h. Ferroelectric domain structure was still observed in these 0.15 μm sized grains as shown in Fig. 1. Grain boundary layer of 1 nm thick was recognized for the doped $BaTiO_3$ ceramics. It was confirmed by TEM analysis that Si, Mg, Ti and Ba ions located in the boundary layer and triple point of the grains.

Grain size dependence of dielectric constant is shown in Fig.2. Dielectric constant at room temperature decreased with grain size at a region smaller than 0.8μm. The doped $BaTiO_3$ has smaller dielectric constant than the pure $BaTiO_3$, because of the formation of the heterogeneous grain boundary layer. The doped $BaTiO_3$, however, provided relatively high dielectric constant of 1000 even with small grain of 100nm.

Fig.1. TEM image of the doped BaTiO₃ ceramics of grain size 150nm.
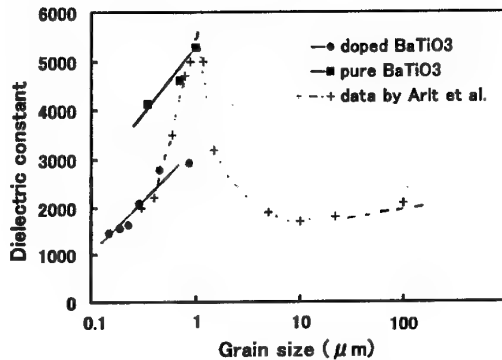
Fig.2. Grain size dependence of dielectric constant.

Temperature dependence of dielectric constant is shown in Fig. 3. Dielectric constant of doped specimens decreased with grain size, resulting in stable temperature dependence. Curie temperature was plotted against the reciprocal of the grain size in Fig.4. Curie temperature was linearly related to the reciprocal of the grain size, accordingly, Curie temperature decreased with grain size. D-E hysteresis curve of the pure and doped BaTiO₃ ceramics was measured. Non-linear D-E curve was still observed at doped BaTiO₃ ceramics with grain size of 150nm.
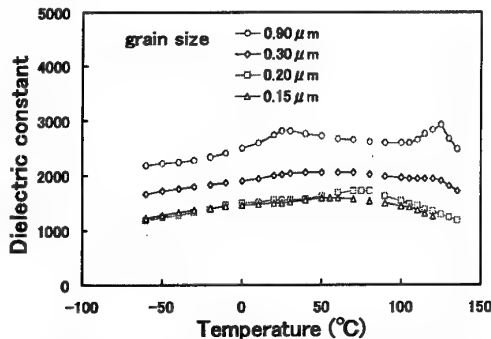
.Fig.3. Temperature dependence of dielectric constant of ultra-fine grained BaTiO₃
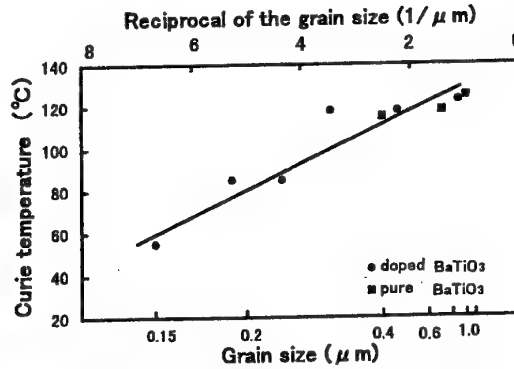
Fig.4. Dependence of Curie temperature on grain size.

Electrical properties of the MLC with dielectric layer of 1μm thick are shown in Table I . High dielectric constant ceramics with stable characteristics under high AC and DC voltage stress are indispensable for designing the MLC with thinner layers. The ultra-fine BaTiO₃ was rather stable under voltage stress than conventional dielectrics. This is a big advantage for high volumetric capacitors designing with thinner layer. It was supposed that the high surface tension in the ultra-fine grain provided the small voltage dependence.

Table I   Electrical properties of MLC with ultra-fine grain BaTiO₃ ceramics (average grain size of 150nm)

Chip size (mm)	2.0×1.25×0.4
Dielectric thickness (μm)	1.0
Active layer's number	5
Inner electrode	Ni
Firing temperature (℃)	1150
Capacitance (nF) at 1kHz/1Vrms	89
Dielectric constant	1560
Dissipation factor (%)	2.1
Resistivity (Ω- cm) logR at 10V	12.5
Break down voltage(kV/mm)	115

One of the most critical processing parameter is the degree of homogeneous mixing of additives and binder in the slurry. High density and defect free layer is realized by preparing the homogeneous slurry for sheet casting. The surface roughness is becoming more serious problem with thinning the dielectric sheet. The roughness of 3μm thick sheet must be controlled to less than 0.3μm to insure a smooth surface contact with the inner nickel electrode. This is also very important factor to avoid the concentration of electric field at aspirates, where the charge emission from the inner electrode is accelerated, resulting in short failure.

For the same reason, the nickel metal powder for the electrode paste must also be very fine, typically less than 0.5μm, and well dispersed in the paste. Very fine Ni powder (<0.4μm) prepared by CVD and/or chemical synthesis has been supplied. The powder provides MLCs with higher capacitance because of the higher coverage of the electrode at the ceramic interface. Fig.5 shows that Ni electrode with 0.2μm powder has higher coverage than that with 0.5μm powder.
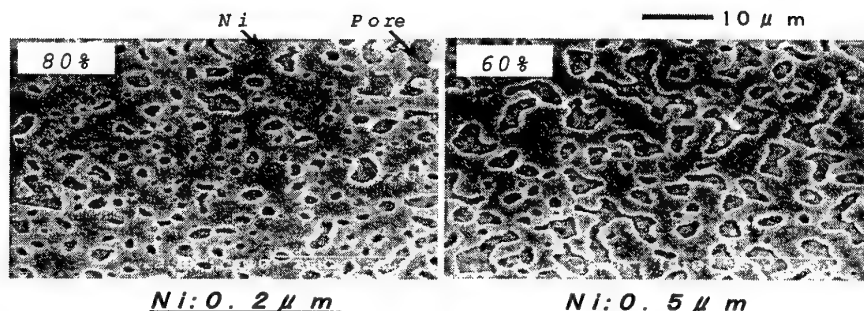
Fig.5. SEM photographs of inner-electrode of MLCs with fine Ni powder. Percentage shows coverage rate.

3. PERFORMANCE CHANGE WITH THINNING LAYER

Voltage stress increases with thinning the dielectric layer, resulting in the serious changes in capacitance and dissipation factor of $BaTiO_3$ ceramics. This tendency is remarkable for the dielectrics having higher dielectric constant. Fig.6 shows temperature dependence of dielectric constant of X7R material of various thickness [17]. Applied AC voltage was 0.5Vrms at 1kHz. Dielectric constant of ferroelectric phase increase with decreasing thickness of the layer, resulting in the clockwise rotation in the TC curve. New dielectric materials, which provide high dielectric constant and stable characteristics under high voltage stress, are required to realize the large capacitance MLCs with thinner layer and higher layer count.

The thickness of the inner electrode also effects on the temperature dependence of dielectric constant as shown in Fig.7. Dielectric constant increases due to an increase of horizontal compression from the thick metal electrode layer.

4. DEVELOPMENT OF BME-MLCs TECHNOLOGIES

Since 1996, the market price of palladium has steeply increased from $140/oz in 1996 to $178/oz in 1997, $284/oz in 1998 and $350/oz in this year. The MLC manufactures had extreme pressure to reduce the electrode cost, and accelerated the expansion of MLCs production to substitute palladium with base metal such as nickel and copper. Further miniaturization with thinner dielectric layer and electrode laydown also affected the cost reduction of the MLCs. We estimate the fabrication of nickel paste reached 80% in weigh of inner electrode paste consumption in Japan. Worldwide statistics shows the consumption of palladium in electronics sector fell by 480k oz to 2070k oz in 1998. Over the next few years, the usage in electronics is likely to fall as nickel electrode MLC technology has so much improved to be adopted for higher specific products of large capacitance with X7R materials. Till 3 years ago, NPO materials have been used only to design the MLCs of relatively small capacitance capacitors, because the electrode cost of the large capacitance NPO capacitors with Pd were too high to compete with other capacitors. Highly reliable nickel compatible NPO dielectrics were developed for large capacitance MLCs that can replace film capacitors of capacitance less than 0.01µF.
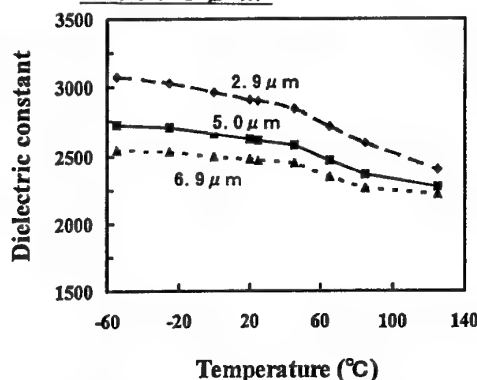
Fig.6 Thickness dependence of dielectric constant at 0.5Vrms 1kHz.
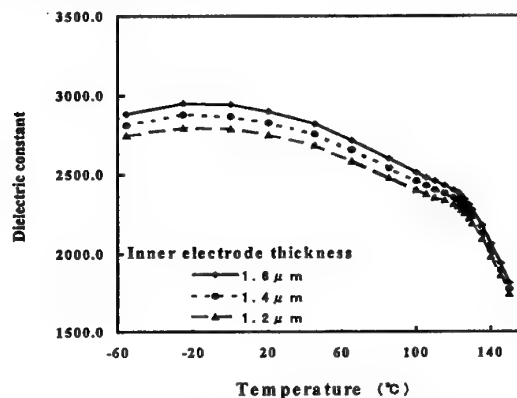
Fig.7 Dielectric constant changes with thickness of the electrode. Dielectric thickness was 2.9mm. Applied voltage was 0.5Vrms 1kHz.

Copper is an another ideal electrode material of MLCs because of its high conductivity and low price. High-Q MLC with low-fire and reduction-resistant dielectrics was developed for microwave applications. Copper electrode yielded lower ESR than conventional Pd electrode at high frequency as shown in Fig. 8.

Foster reported an alternative to the BME [18]. The system use pure Ag and/or high silver Ag/Pd electrode with low-fire dielectrics which densify at temperature less than 1000℃. The high dielectric constant materials of NPO and X7R, which were comparable to the conventional formulations, were developed. Advantage of this system is that the process equipment for conventional MLCs can be used.

1005type 4.5pF

ESR(mohm) vs Frequency(MHz) — Cu, Pd

1005type 4.5pF

Q vs Frequency(MHz) — Cu, Pd
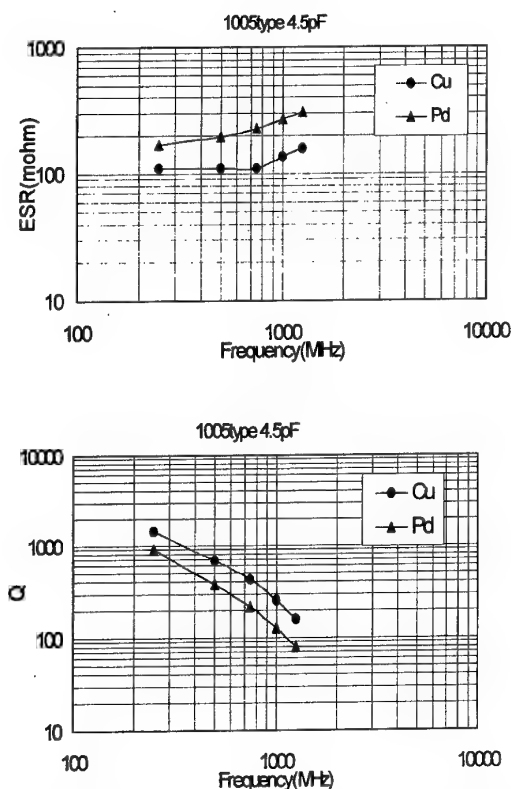
Fig.8. Frequency dependence of ESR and Q value of MLCs with copper and Pd electrode. Sample:1005 size 4.5pF.

5. PERFORMANCE OF MLCs of X5R-100μF

Ceramic chip capacitor of 100μF was developed with nickel electrode system to meet the condition of decouping capacitors for VLSI and switching mode power supply. The fundamental characteristics of the newly developed X5R 100μF MLC are shown in Table II. Large volumetric efficiency of $1.17\mu F/mm^3$ was achieved by chip size of $5.7 \times 5.0 \times 3.0$ mm and 3.3μm thick dielectrics of 525 layers. Used X5R dielectrics had

Table II. Characteristics of MLC of X5R-100μF - 6.3V

Chip size	$5.7 \times 5.0 \times 3.0$ (mm)
Dielectric thickness,	3.3μm
Inner electrode	Ni
Active layer number	525
Capacitance (1kHz 0.5Vrms)	108μF
Dissipation factor (1kHz 0.5Vrms)	3.3%
TCC	X5R
Insulation resistance	$1.0 \times 10^7 \Omega$
BDV	$197V_{DC}$

dielectric constant of 3900. Frequency response of the MLC was excellent for the applications due to the low ESR and low ESL characteristics as shown in Fig.9.

The large capacitance MLCs have been realized by reliable Ni compatible dielectrics and established technologies of manufacturing process, handling the thinner sheets and firing in a low $P(O_2)$ atmosphere.

The capacitors have large potential to replace Ta and Al electrolytic capacitors in the range from 10 to 100μF. The major technical advantages over Ta and Al capacitors are higher breakdown voltage, higher reliability and lower ESR at high frequency.
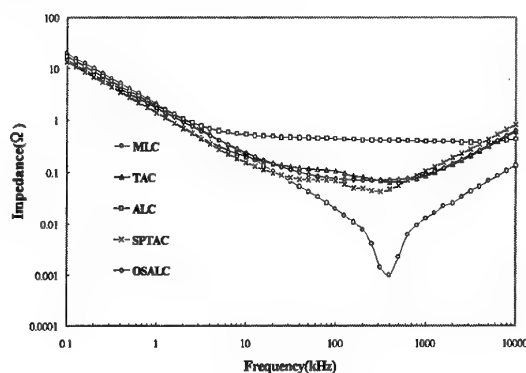
.Fig.9. Frequency dependence of impedance of the several capacitors of 100μF

6. MLCs WITH MOCVD METHOD

Thinner dielectric layer of MLC less than few micron meters is formed by sheet casting machines such as reverse roll coater, lip coater and die coater with homogeneous mixture of fine ceramic powder, additives and binder. We believe that these conventional sheet methods have technical limits of the dielectric thickness of around 1μm. Therefore, new techniques are required to prepared the dielectric layer of sub-micron thick for higher volumetric efficiency. We have investigated the microstructure and dielectric properties of $(BaSr)TiO_3$ thin films prepared by metalorganic chemical vapor deposition (MOCVD), and designed the MLCs to demonstrate the new technologies for next generation of capacitor manufacturing [19,20].

A schematic diagram of the MOCVD system used to deposit the BST layers is shown in Fig.10. $(Ba(C_{11}H_{19}O_2)_2(C_8H_{23}N_5)_2)$, $(Sr(C_{11}H_{19}O_2)_2(C_8H_{23}N_5)_2)$ or $(Sr(C_{11}H_{19}O_2)_2(C_6H_{18}N_4)_2)$, and $(Ti(i\text{-}OC_3H_7)_4)$ were used as Ba, Sr, and Ti sources respectively. Oxygen was used as an oxidant, and argon as a carrier gas. The deposition conditions for the BST layers are summarized in Table III. The structure of the MLC with BST thin layers is schematically shown in Fig. 11. MgO single crystal was used as a substrates and Pt as the electrode of the MLC with BST thin layers. RF magnetron sputtering formed the Pt electrode at temperature lower than 100°C.

SEM image of the cross sectional view of the MLC with $(Ba_{0.7},Sr_{0.3})TiO_3$ thin layers is shown in Fig.12. The capacitor was constructed with fifteen BST dielectric layers and sixteen Pt electrode layers. The average thickness of dielectric and electrode were 0.22 and 0.23 μm respectively, giving a total thickness of 7.0 μm. The MLC of 0.4×0.4mm in size yielded capacitance of 34 nF and dissipation factor (tanδ) of 2.6% at 1 kHz and 100 mV. Capacitance per unit volume was 30 $\mu F/mm^3$ that was 10 times larger than MLCs of today.
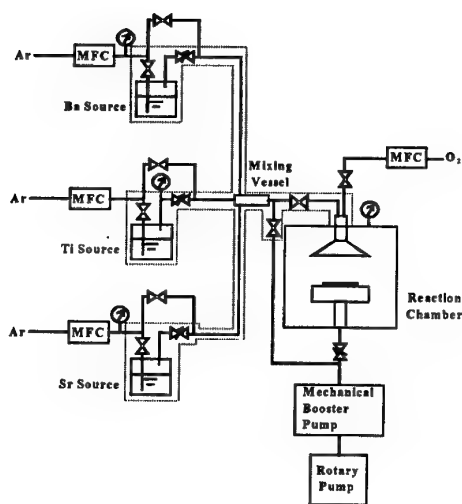
Fig.10. Schematic diagram of the MOCVD apparatus for BST thin films.
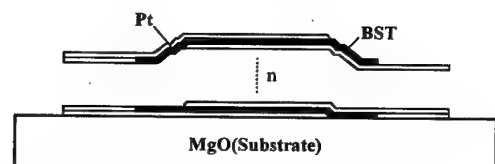
Fig.11. Structure of the MLC on MgO substrate

Table III. Deposition conditions of BST layers

Source temperature	
Ba source	130-158°C
Sr source	107-128°C
Ti source	40°C
Substrate temperature	650°C
Chamber pressure	13.3kPa
Deposition time	65-120min
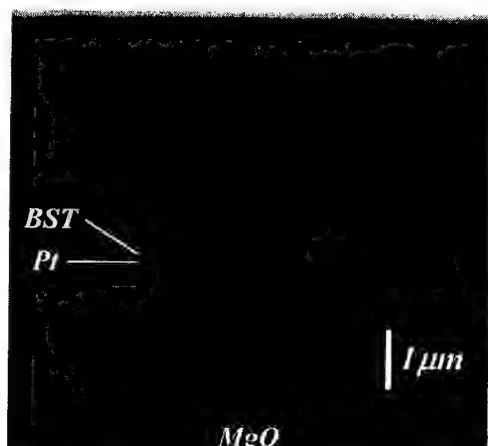
Fig.12. Cross sectional SEM image of multilayer capacitor with fifteen $(Ba_{0.7},Sr_{0.3})TiO_3$ dielectric layers.

The dielectric constant was evaluated about 350 that was comparable to that of the other worker's [21]. Figure 13 shows the temperature dependence of the single-layer and multilayer capacitor with $(Ba_{0.7},Sr_{0.3})TiO_3$ dielectrics. The maximum capacitance value was obtained at -10°C and -30°C, respectively.
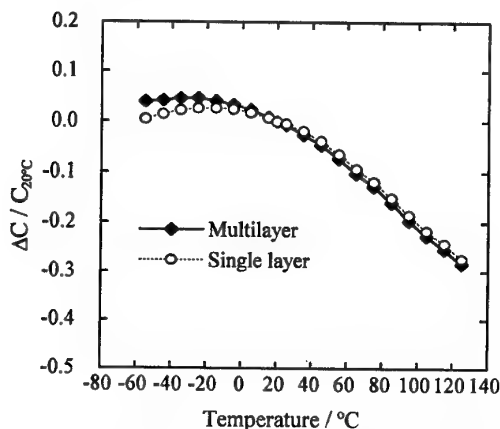
Fig.13. Capacitance change of MLC with $(Ba_{0.7},Sr_{0.3})TiO_3$ dielectric layer by MOCVD.

The capacitance of this capacitor changes considerably with DC biasing field. It decreased 27% and 34% under DC biasing voltage of 1.5 V and 2.0 V, respectively. This is one of the important subjects in future works. The leakage current at 1V was about 0.2nA, and the breakdown voltage was about 6V. The acceptable CR product of 121MΩ·µF was obtained. But short failure rate was still high, around 50%, which may due to the inhomogeneity of the deposited ceramic layer. As show in Fig.14, surface of the single BST film was homogenous and smooth. With increasing the layer count, however, the surface morphology had change to the rather poor structure. Further development on multi-stacking technologies of the homogenous dielectrics of nano meters thick with base metal electrode is expected for next century.

1µm
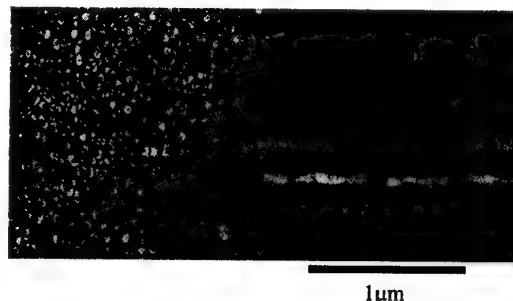
Fig.14. SEM images of the surface and fractured face of the single BST film.

7. SUMMARY

1. Significant progress has been done in the BME-MLCs study and manufacturing since 1996 because of the dramatic increase of the palladium price. Reliability of nickel compatible X7R dielectrics was so much improved by employing the rare-earth elements. To

form the thinner dielectric layer, ultra-fine $BaTiO_3$ powder was studied and applied to the MLCs of dielectric layers few micron meters thick. With this technology, large capacitance MLCs comparable to Ta and Al electrolytic capacitors was realized. MLC of 100µF has superior frequency performance than electrolytic capacitors.

2. The technologies of BME have been developed to the NPO materials, and realized the large capacitance NPO capacitors which can replace the film capacitors. Copper electrode provided high frequency capacitors with low ESR and high-Q value.

3. MLCs on MgO substrate with MOCVD was prepared to demonstrate the feasibility of a new manufacturing process of the capacitors. Fifteen dielectric layer of $(BaSr)TiO_3$ 200nm in thick yielded 30µF/mm^3 that was 10 times higher volumetric efficiency than conventional ceramic capacitors.

REFERENCES

[1] H. Kniepkamp and W. Heywang, Z. Angew, Phys. **6**,385 (1954)

[2] W. R. Bussen, L.E. Cross, and A. Goswami, J. Am. Ceram. Soc. **49**,33 (1966)

[3] A. Yamaji, E. Enomoto, K. Kinosita and T. Murakami, J. Am. Ceram. Soc., **60**, 97-101, (1977)

[4] G. Arlt, D. Hennings and G. de With, J. Appl. Phys.**58**, 1619 (1985)

[5] K. Uchino, E. Sadanaga and T. Hirose, J. Am. Ceram. Soc., **72**, [8] 1555, (1989)

[6] K. Uchino, E. Sadanaga, K. Oohashi, T. Morohasi and H. Yamamura, Ceram. Trans.**8** , 107, (1989)

[7] M. H. Frey and D. A. Payne, Appl. Phys. Lett. **63**,2753 (1993).

[8] S. Wada, T. Suzuki and T. Noma, J. Ceram. Soc,.**104** [5],383 (1996)

[9]H. Hsiang and F. Yen, J. Am. Soc,.79 [4],1053 (1996).

[10]M. H. Frey and D. A. Payne, Phys. Rev.B, **54** 3125(1996).

[11] X. Li and W. Shih, J. Am. Ceram. Soc,. **80**[11] 2844, (1997)

[12] R. N. Viswanath and S. Ramasamy, Nano Stractured Materials **8**, [2] 155, (1997)

[13] W. L. Zhong, Y. G. Wang, P. L. Zhang and B. D. Qu, Phys. Rev.B,**50**, 698 (1994).

[14] M. H. Frey and D. A. Payne, Phys.Rev,B, **54**, 3153,(1996)

[15] Y. Sakabe, N. Wada and Y. Hamaji, J. Korean. Phys.Soc,. ,**32**, 260, (1998)

[16] Y. Sakabe, N. Wada and Y. Hamaji, Proceedings, **11**[th]. IEEE, ISAF 565 (1998).

[17] Y. Yoneda, T. Hosokawa, N. Ohmori and S. Takeuchi, *CARTS-EUROPE' 96*, 11 (1996)

[18] B.C. Foster, *CARTS-EUROPE' 98*, (1998).

[19] Y. Takesima, K. Shiratuyu, H. Takagi and Y. Sakabe, J.J.Appl. Phys. 36, [9B],5870, (1997).

[20] Y. Sakabe, Y. Takesima and K. Tanaka, J. Electroceramics 3:2, 115, (1999)

[21] M.M. Watt, P. Woo, T. Rywak, L. McNeil, A. Kassam, V. Joshi, J.D. Cuchiaro and B.M. Melnick, Proceedings, **11**[th]. IEEE, ISAF 11 (1998).

Scientific and Engineering Issues of the State-of-the-Art and Future Multilayer Capacitors

C.A. Randall, Y. Tsur, and J. Van Tassel

Center for Dielectric Studies, Materials Research Laboratory
The Pennsylvania State University, University Park, PA 16802 U.S.A.
Fax: (814) 865-2326; e-mail: car4@psu.edu

ABSTRACT

BaTiO$_3$-based multilayer capacitors are rich with the science of crystal chemistry, defect chemistry, phase transition theory, ferroelectricity, and processing. State-of-the-art multilayer capacitors are fabricated with base metals, submicron grains and have thickness of layers approaching one micron. There are, however, needs to keep improving the volumetric efficiency of capacitance, improve reliability in thin layers, and increase the number of active layers. This paper summarizes and reviews some of the studies our group is performing to scientifically aid progress in this fast moving field. Specifically, we will review size effect issues, the role of rare-earth doping in improving degradation resistance, and the potential of electrophoretic deposition to produce multilayer structures with nanopowders.

I. FUNDAMENTAL SIZE LIMITATIONS OF FERROELECTRIC BASED CAPACITORS

In a traditional multilayer capacitor (MLC) made from BaTiO$_3$, there are a number of factors in which to consider the influence of size and the ultimate dilution of high dielectric permittivity characteristics. In the grain size range of 0.7 μm, the room temperature permittivities are maximized through the internal stress that develops via the spontaneous strain at the cubic-tetragonal phase transition. This stress then raises the permittivity of the Curie-Weiss tetragonal–orthorhombic phase transition. This interplay of stress and dielectric permittivity through electrostrictive coupling is accounted for semi-quantitatively in the Phenomenological Devonshire theory, Buessem et al.[1] More recently, Frey and Payne demonstrated that for much smaller grain sizes 80 nm to 0.1 μm, the dielectric permittivity is systematically diluted by a thin grain boundary phase that increases its relative volume fraction as grain size decreases.[2]

At crystallite sizes below 40 nm, the ferroelectric phase transition shows evidence of a size effect instability. In a systematic glass–ceramic study, Randall et al. and Tanaka et al. have both demonstrated that the BaTiO$_3$ ferroelectric transition temperature begins to drop with crystallite size.[3,4] This is very difficult to show in bulk materials, where there is the competition between densification and grain growth.

Various annealing studies were performed and produced samples with different size distributions in a BaTiO$_3$ glass ceramic. Dielectric characterization demonstrated size effects consistent with the theoretical predictions of Binder for finite sized ferroelectrics, namely:

(i) A shift to lower temperatures of the phase transition temperature.

(ii) Broadening of the thermodynamic anomalies at the phase transition region.

(iii) Reduction of the magnitude of the dielectric permittivity at the phase transition.[6]

These trends are compared to the Binder scaling laws in Figure 1.

A phenomenological model by Zeks and Tilley was applied to the phase transition temperature data and crystallite statistical median.[7] This demonstrated that the critical size effect under this boundary condition ~ 13 nm, with no significant shifting of the Curie temperature with crystal sizes down to 40 nm. The theoretical model is also compared to other authors' data and demonstrates good agreement with the trend, Figure 2.[3,4,8,9] The governing phenomenological equation is given by:

$$\tan\left(\frac{L\tau^{\frac{1}{2}}}{2\zeta(0)}\right) = \frac{\zeta(0)}{\delta\tau^{\frac{1}{2}}} \qquad (1)$$

where $\zeta^2(T) = -\kappa/\alpha\,(T-T_c)$, and $\tau = \left(1 - \frac{T_c}{T_{C\infty}}\right)$,

and L is the crystallite size, $T_{c\infty}$ is bulk temperature phase transition temperature, T_c is the transition at a finite crystal

size, κ is the Ginsburg coefficient, α_o is the Landau inverse Curie constant, $\zeta(T)$ is coherence length at any temperature, and δ is the polarization gradient region $\cong 5$ nm (this is the only adjustable variable). The sizes predicted in this study are close to the typical correlation lengths expected for displacive ferroelectric phase transitions in bulk crystals. In addition, the ratio of the Curie constant and Ginsburg coefficient are in excellent agreement with earlier data.

The size data in $BaTiO_3$ has often been estimated to be $\cong 100$ nm. Frequently, x-ray techniques were used, and where unable to deconvolute the tetragonal spontaneous strain, over the line broadening and residual strain in powders. The spontaneous strain is more effectively resolved with accurate line broadening x-ray studies as a function of temperature. This then shows ferroelectric behavior in crystallites much smaller than 100 nm.

In the case of thin film ferroelectrics, the dielectric properties are not only influenced by the dimensions of the active layer, or the grain size, but also the coherent crystal size. This has been very nicely demonstrated in epitaxial films by both Ahn et al. and Maria et al.[11,12] In a PMN:PT epitaxial films, large shifts of the phase transition temperature were noted with coherent x-ray size of 30 nm, whereas 100 nm crystal coherency showed approximately bulk transition temperature. Likewise, very thin 10 nm films with almost perfect coherency in all 3–D demonstrate bulk transition temperatures. These important results illustrate size effect phenomena is dependent on the dimensionality of a coherent ferroelectric crystal.

In multilayer capacitors with materials as $BaTiO_3$, the doping is important to control the temperature coefficient of capacitance. In 100 nm grain size X7R materials the dielectric permittivity approaches $\cong 1500$, with $\tan\delta \approx 0.02$.[13] Between 0.2 μm (present X7R grain size) and 0.04 μm there is very little problem with the intrinsic size effect as discussed above. However, there is a consideration with the dilution of the dielectric constant with low K grain boundaries. Assuming the dilution of dielectric permittivity with a low grain boundary phase, similar to Frey et al., there will be a continued advantage in miniaturization in the capacitance volumetric efficiency figure of merit in the foreseeable future. A more significant problem is the control of the temperature coefficient of capacitance for X7R applications and the ability to miniaturize both the grain structure and the dielectric layer thickness. Utilizing chemical coating of powders gives some advantages to the formation of the required core-shell structures for X7R. Figure 3(a) shows the development of an X7R dielectric characteristics with sintering temperature, and (b) the corresponding chemical

variations determined from EDS studies in a transmission electron microscope, (c) the core-shell microstructure.[12–15.] This may not be so controllable on a production scale for grain sizes approaching 0.05 μm without better understanding of core-shell formation, particle size control, and the role of each dopant.

(a)

(b)

(c)
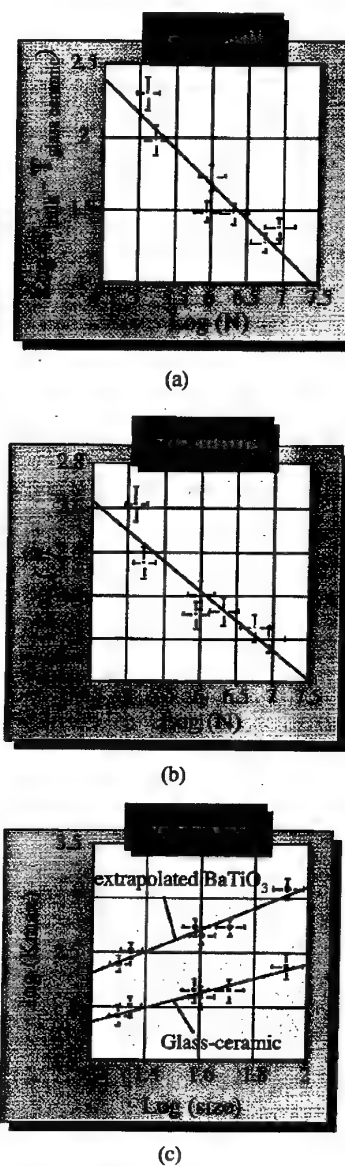
Figure 1. Evidence for fundamental size effect behavior in $BaTiO_3$ glass-ceramics: (a) shifting of transition temperature, (b) broadening or rounding of phase transition behavior, (c) peak dielectric constant versus crystal size L, or N (no. of formula unit cells).
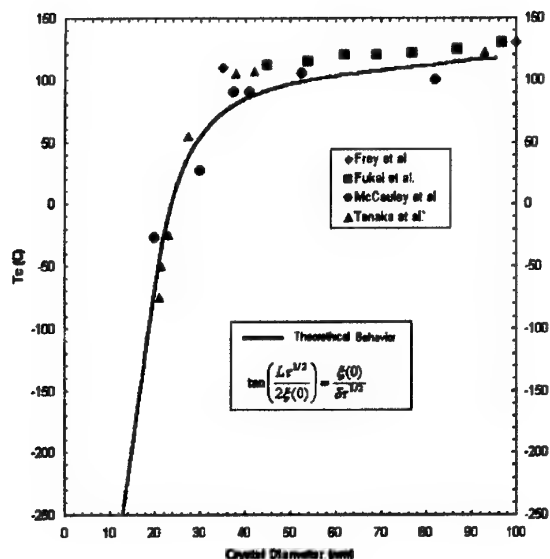
Figure 2. Transition temperature versus crystallite size from a number of recent studies, Zeks-Tilley phenomenological model is fitted to the data.

II. BASE-METAL—RARE EARTH OCCUPANCY

One of the most important advances in multilayer capacitor materials is the development of X7R and Y5V capacitors cofired with nickel electrodes.[17-20] The success of the development of such capacitors hinges on the use of rare earth and Y-based doping to enhance the degradation resistance of the material. This is particularly important as the degradation process is controlled by the electro-migration of oxygen vacancies. Sintering at low partial pressures of oxygen ($\cong 10^{-10}$ atm) creates additional oxygen vacancies, and therefore both their concentration and effective mobilities have to be reduced to render high degradation resistant dielectrics.

The basic mechanism by which this is obtained is not well understood at this time. We have recently extended the defect chemistry of BaTiO$_3$ to demonstrate the interplay of Ba-stoichiometry, partial pressure of oxygen and rare-earth dopants site occupancy at the sintering temperature.

We have demonstrated that the following equation (2) is general for both single and two phase regions of BaTiO$_3$ phase field.

$$R_{Ba}^{\bullet} + V_{Ti}^{''''} \rightleftarrows R_{Ti}^{'} + V_{Ba}^{''} \tag{2}$$

(a)

(b)

(c)
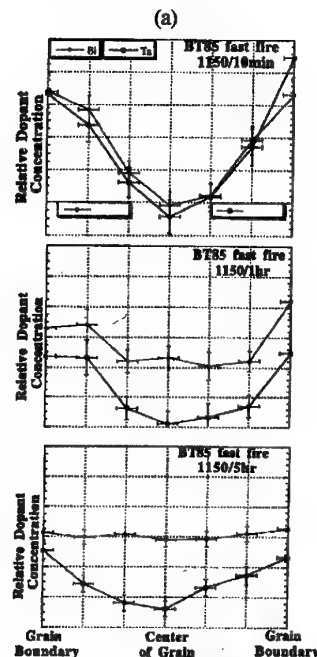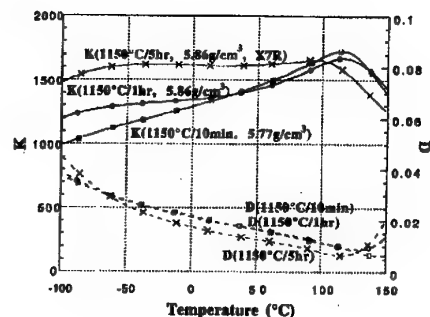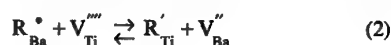
Figure 3. (a) Dielectric temperature dependence of ceramics fired at different conditions to obtain high densities, X7R behavior, and 0.15 μm grains, (b) dopant spatial variation for these materials towards the development of X7R behavior, (c) core-shell structure in submicron BaTiO$_3$.

— 9 —

The symbols are consistent with the classical Kroger-Vink notation.[19] This equation can be re-expressed as its corresponding mass-action relation:

$$\frac{\left[R^{\bullet}_{Ba}\right]}{\left[R^{'}_{Ti}\right]} = K(R,T)\frac{\left[V^{''}_{Ba}\right]}{\left[V^{'}_{Ti}\right]} \qquad (3)$$

These equations only hold at high temperatures, where all these species are mobile, from previous diffusion studies we anticipate T≥1100°C. From equation (3), it shows that a Ba-rich phase drives the ratio towards B-site and vice versa for Ti-rich. This equation is only a concentration proportionality, and the relative concentrations depend on the constant K for each dopant species to be considered.

Further, at high temperatures, the Schottky reaction is important, and therefore we need to consider its mass action relation, namely:

$$\left[V^{''}_{Ba}\right]\left[V^{''''}_{Ti}\right]\left[V^{\bullet\bullet}_{o}\right]^3 = K_s \cdot \qquad (4)$$

For both Ba and Ti-rich stoichiometries, the chemical potential are fixed from the adjacent phases, it can be readily shown that the concentrations of the metal vacancies are proportional to the oxygen vacancy concentrations, viz

$$\frac{\left[V^{''}_{Ba}\right]}{\left[V^{''''}_{Ti}\right]}\alpha\left[V^{\bullet\bullet}_{o}\right] \qquad (5)$$

So we can generalize at high temperatures; (T≥1100°C):

$$\frac{\left[R^{\bullet}_{Ba}\right]}{\left[R^{'}_{Ti}\right]}\alpha\frac{\left[V^{''}_{Ba}\right]}{\left[V^{''''}_{Ti}\right]}\alpha\left[V^{\bullet\bullet}_{o}\right] \qquad (6)$$

Recently, precise x-ray studies have verified this interrelationship. Figure 4 shows the influence of lattice parameter on idealized 1% rare earth doped barium titanate, with Ba –rich samples made with Ba/Ti=1.01 and Ti-rich Ba/Ti=0.99, with samples fired in reducing atmosphere, $PO_2 \sim 10^{-10}$ atm. The ionic radius is the octahedral coordinated radii, in accordance to the revised tables of Shannon.[20] We can identify three regimes of behavior in Figure 4:

Regime (I): Small cations, such as Yb and Lu, occupy the B –site and are compensated via oxygen vacancies.

Regime (II): This ionic radii range of rare-earth dopants and Y are amphoteric, since they are either acceptors or donors. For the Ba –rich case all the dopants expand the lattice owing to the B-site occupancy, as acceptors. The Ti-rich samples have less probability of occupancy on the B-site and therefore has a smaller unit cell volume.

Regime (III): Large cations, La, Nd, occupy the A-site. The compensation mechanism is dependent on Ba-rich or Ti-rich stoichiometery, consistent with earlier studies of Chan et al.[23]

Note that all the "magic" dopants used by the BME capacitor manufacturers that aid degradation resistance are amphoteric![16–18]

In the case of the site occupancy dependence on oxygen partial pressure, we considered the difference of sintering in air versus 10^{-10} atm for Ba-rich and Ti-rich compositions with Er-doping. Table I shows the volumes in cubic angstroms with the errors (as determined by maximum likelihood method).[25] Higher partial pressure causes a lower concentration of oxygen vacancies during the firing. This alters the metal vacancy ratio towards more Ti-vacancies and the site occupancy toward more $\left[R^{'}_{Ti}\right]$, so the air fired samples have larger volumes. So a question that has still to be answered is: "What is the atomistic advantage of amphoteric B-site occupancy in BME dielectrics?" We earlier have hypothesized that the ionic radii ≈ 0.90Å is an optimum in degradation resistance, as it balances maximum solubiilty on B-site with maximum local strain. The B-site occupancy developed a local pinning site that limits the oxygen vacancy mobility.[22] The above results in Figure 4 are consistent with this picture, in that the average lattice is expanded for the Ba-rich case. However, we have recently become aware of work in the ionic conductor literature, where 2-phase segregation leads to higher mobility of defect species.[26] If this is appropriate for the BaTiO₃ BME materials, the amphoteric dopants can buffer or expand the single phase region at low P(O₂) firings, and thereby limit the mobility of the oxygen vacancy in a more homogeneous phase. We are further investigating the atomistic mechanism that provides high degradation resistance.
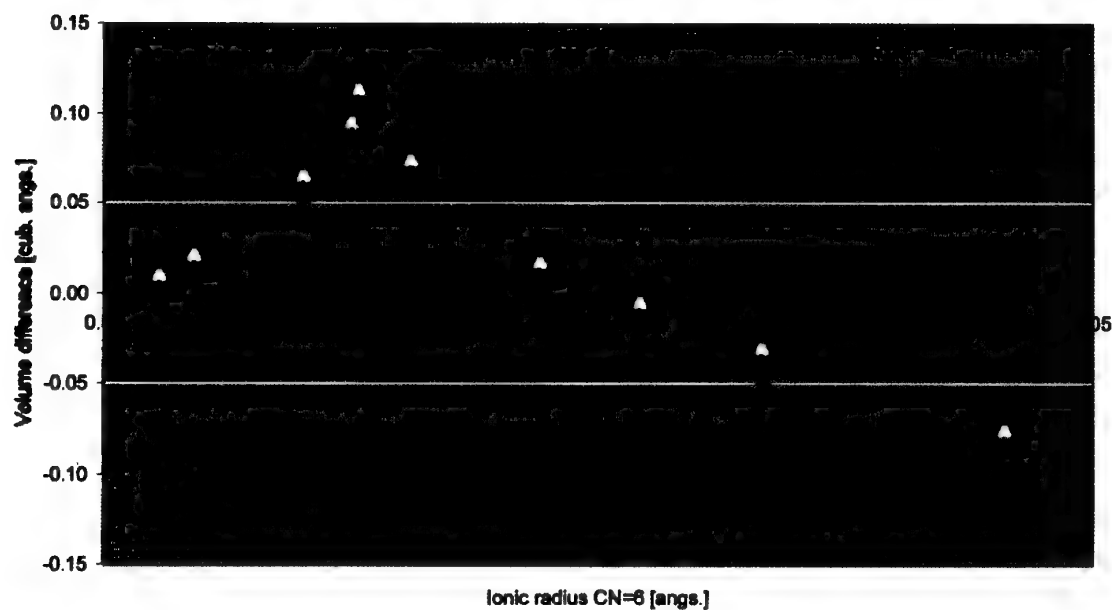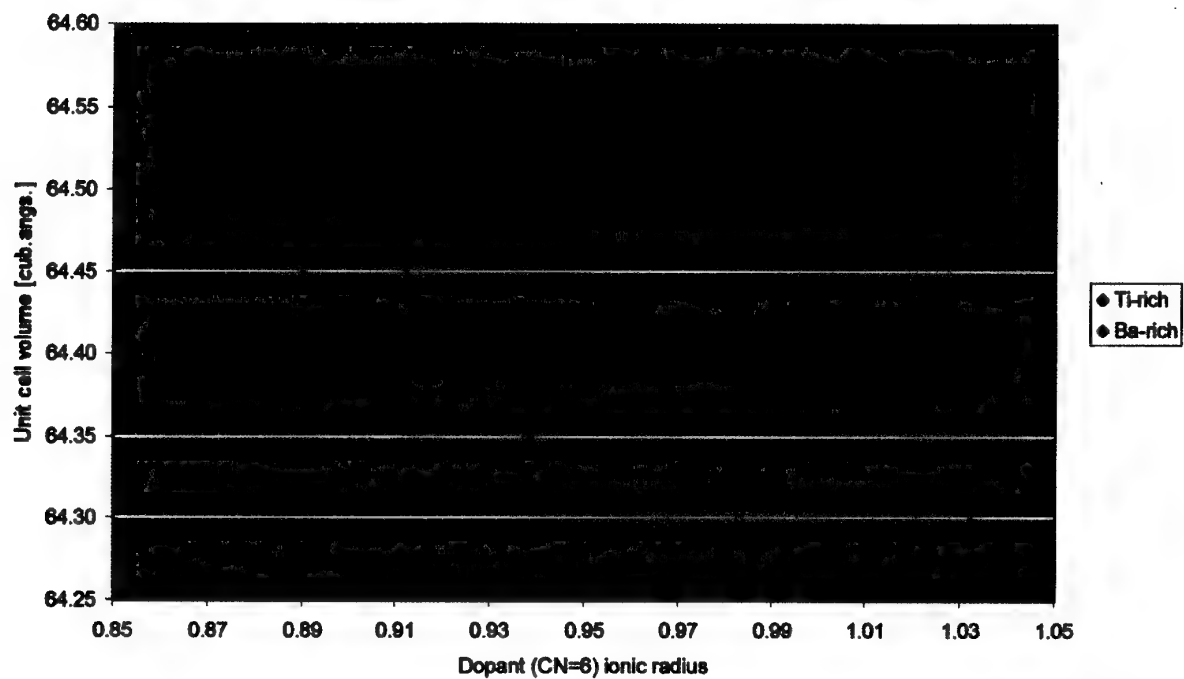
Figure 4. (a) Room temperature unit cell volume for rare-earth doped $BaTiO_3$ with Ba and Ti excess, fired at low PO_2's, (b) unit cell volume difference between Ba- and Ti-excess compositions fired at low PO_2's.

Table 1.   Er-doped BaTiO$_3$ unit cell volume under various firing conditions, volumes in cubic Angstroms.

Fired at	Ba-rich	Ti-rich	Difference
10^{-10} atm.	64.453(12)	64.4533(11)	0.67(33)
air	64.556(15)	64.523(12)	0.033(37)

In terms of the miniaturization of BME multilayers, it is not only the compositional development that is important, but also the control of reoxidation step. In BME materials, the sintering is at a $P(O_2)$'s $\cong$ 10^{-10} atm and above and temperatures 1130 to 1350°C. The reoxidation annealing steps is typically at higher $PO_2 \cong$ 10^{-7} atm for times $\cong$ 2 hours and temperatures ~ 900°C. There are two electrode-ceramic interfacial reactions that have to be limited: first, the oxidation of the nickel electrodes, and second, the interdiffusion of nickel into the dielectrics. As the active layer dimensions reduce in future BME-MLCs, the control of the reoxidation anneal process becomes more critical, and more complex annealing profiles may be required.

III. HOW TO FABRICATE FUTURE SUBMICRON MULTILAYER CAPACITORS?

The advancement of colloidal science, enabling optimum dispersions and controlling of incongruent dissolution and the mass-product ion of submicron powders by a variety of chemical methods has evolved tape casting and similar technologies to produce fired tapes ~ 1.0 µm. A number of leading capacitor companies have suggested that 1.0 µm may be the limit of traditional tape casting or similar techniques. There have been some preliminary investigations for alternative methods to fabricate multilayer capacitors with electrochemical-hydrothermal synthesis, metal-organic chemical vapor deposition, sol-gel, and electrophoretic deposition.

Traditional and state-of-the-art production processes use mechanical devices to manipulate particulate slurries or inks; a doctor blade in tape casting or a squeegee and patterned screen in screen printing. In contrast, electrophoretic deposition (EPD) uses electric fields to act directly on particles, moving them to the desired location independent of the suspending solution. EPD has been the focus of our efforts in miniaturization of electroceramic devices with particulate materials. We believe that for off–chip surface mount passive devices, there are advantages in processing with EPD in terms of high density packing, applicable to nanosized powders, self-regulation of thickness in deposition, and relatively rapid deposition rates.

To fabricate multilayer structures, we are developing a hybrid technology combining EPD with traditional tape casting and a lamination process. For those unfamiliar with EPD, there are two excellent reviews to consider published by Sarkar and Nicholson, and Gani.[27,28] In principle, there are two basic steps to the powder consolidation by EPD. First, the development of a charged-stable-non-aqueous suspension of particles. Particles have to be primary particles to optimize the particle packing field. In the second step, an electric field is applied across the suspension, causing charged particles to migrate to the electrode of opposite charge. The particles accumulate at the electrode, and a voltage gradient has to overcome the interparticle repulsion. Once in contact, strong, short-range Van der Waals forces hold the particles in a solid deposit.

With present day state-of-the-art MLCs the tape casting technology has out-paced the scaling down of the electrode materials. In the modern MLC devices, the thickness of electrodes approaches the dielectric layer thickness. This leads to a number of problems with cosintering stresses between the dielectric material and the electrode. There is, therefore, a need to reduce the electrode thickness before reducing the active layer thickness to below one micron.

Given this short-term need to reduce the electrode thickness, our EPD studies have focused on electrode materials in multilayer structures. As a model demonstration, we have used silver-palladium powders, 0.3 µm diameter. The silver-palladium powder was deposited onto film with a sputtered platinum layer on the deposition side. To deposit the particles in an acetic acid suspension, an electric field of 300 V/cm was applied. For the thinnest depositions, the field was pulsed on and off to allow electro-convective circulation to dissipate. This was done to maximize the thickness uniformity. The current density is approximately 30 µA/cm^2 and remains constant through the deposition period.[29]

The BaTiO$_3$ layers were laminated in a heated uniaxial press at 40 MPa and 70°C. The silver-palladium deposition was placed face down onto the BaTiO$_3$ layer and pressed. Under these conditions, there was enough binder diffusion to adhere the two layers, and the metal powder transfer printed completely to the stack. This process was continued to produce alternative layers of dielectric and electrode. Figure 5 (a) shows a fractured green cross-section of the Ag-Pd powder layer and the dielectric layers, (b) shows a sintered cross-section with 1.2 µm thick electrodes, and (c) 0.6 µm thick electrodes. The continuity and the thickness control is excellent compared to rival processing technologies.

The concept of combining EPD tape formation and lamination has a lot of potential for future generation multilayer devices. We are working on techniques to develop multicomponent tapes as shown in Figure 6. If this

technology is to be developed, further advances have to be made in dispersion of nanoparticles and impregnation of binder molecules into nanopowder compacts.

IV. SUMMARY AND CONCLUSIONS

In this paper we touched upon some of the basic science that underpins the modern and future base-metal multilayer capacitors. We first considered the size limitations and indicated that there is no major intrinsic influence of the phase transition until grain sizes reduce below 40 nm in ferroelectric dielectrics. There is, however, a systematic dilution of the dielectric permittivity owing to a low dielectric constant grain boundary region. The volume efficiency is still improved for high K dielectrics into submicron layers. The ability to control core-shell microstructure and X7R properties will continue to be a challenge if grain sizes reduce to 0.05 μm in 0.3 μm active layers, for example.

Nakano, et al., have demonstrated that the ability to control the degradation resistance to thinner layers requires better control of processing.[31,32] In attempting to understand the role of Y and rare earths, we have developed a proportionality concentration that is valid at high temperatures. In model compositional systems, these trends have all proven to be consistent with:

$$\frac{\left[R^{\bullet}_{Ba}\right]}{\left[R^{'}_{Ti}\right]} \, \alpha \, \frac{\left[V^{''}_{Ba}\right]}{\left[V^{''''}_{Ti}\right]} \, \alpha \, \left[V^{\cdot\cdot}_{o}\right]$$

This concentration ratio demonstrates the relative trends on Ba-stoichiometry and PO_2 in controlling the site occupancy. The so-called magic dopants Dy, Ho, and Y are strongly amphoteric, able to change between the twelve-fold coordinate site and the octahedral site, to become a donor or acceptor respectively. The role of these amphoteric dopants is still not solved in terms of the control of degradation resistance. As size continues to reduce the ability to control degradation and electrode-ceramic interface effects becomes more vital.

The continued miniaturization of multilayer capacitors may require new methods to control ultra-thin tapes. Electrophoretic deposition methods are being explored to fabricate such submicron layers. To address the immediate short-term needs, we are fabricating thin electrodes and laminating them into multilayer stacks. Future studies will involve both metal and dielectric layer tapes.
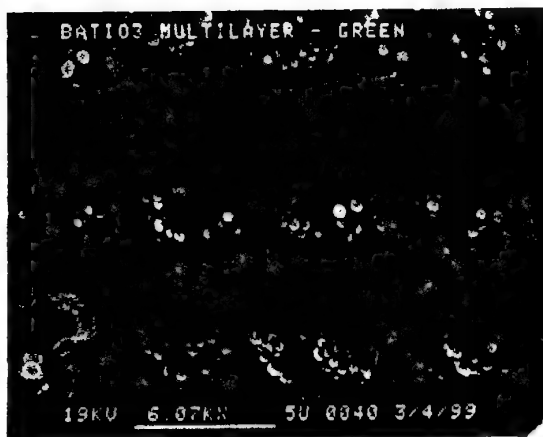
(a)

(b)
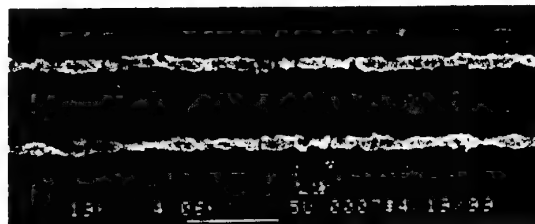
(c)

Figure 5. Multilayer structure developed from EPD-tape technology (a) fractured green body (large particles are Ag-Pd), (b) fired multilayers with 1.2 μm electrodes, and (c) 0.6 μm thick electrodes.
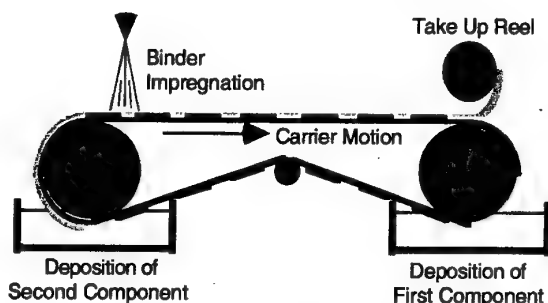
Figure 6. Schematic of a possible method to co-deposit local capacitor and electrode materials.

V. ACKNOWLEDGMENTS

VI. REFERENCES

1. W.R. Buessem, L.E. Cross, and A.K. Goswami, *J. Am. Ceram. Soc.* **49** [1] 33–36 (1966).

2. M.H. Frey, Z. Xu, P. Han, and D. Payne, *Ferroelectrics* **206–207**, 337–353 (1998).

3. C.A. Randall, D. McCauley, and D. Cann, *Ferroelectrics*, **206–207** 325–335 (1998).

4. M. Tanaka and J. Makino, *Ferroelectric Letts.* **24** 13–23 (1998).

5. M.H. Frey and D. Payne, *Phys. Rev. B* **54** [5] 3158–65 (1996).

6. K. Binder, *Ferroelectrics* **73** 43-67 (1987).

7. B. Zeks and D.R. Tilley, *Solid State Communications* **49** 823 (1984).

8. D.L. McCauley, R.E. Newnham, and C.A. Randall, *J. Am. Ceram. Soc.* **81** [4] 979–87 (1998).

9. Y. Fukai, S. Izamisawa, T. Atake, A. Hamano, T. Shirakami, and H. Ikawa, *Ferroelectrics* **203** [1-4] 227–239 (1997).

10. C. Ahn, *ISAF 13*, Montreux, Switzerland (1998).

11. J.P. Maria, W. Hackenberger, S. Trolier-McKinstry, *J. Appl. Phys.* **84** [9] 5147–5154 (1998).

12. Y. Sakabe, S. Wada, J. Ikeda, Y. Hanaji, Proc. Eleventh IEEE Int. Symp. of Ferroelectrics, IEEE Cat. 98CH36245, 565–569 (1999).

13. X. Liu, C.A. Randall, S. Cheng, Proc. Int. Soc. for Hybrid Microelectronics, Philadelphia, Pennsylvania, 356–361 (1997).

14. S.A. Bruno and I. Burn, U.S. Patent #5,155,072 (1992).

15. J. Beeson, L. Mann, S. Venigalla, and S. Costantino, *Proceedings of the Eighth US–Japan Seminar on Dielectric and Piezoelectric Ceramics*, 180–183 (1997).

16. T. Nomura, A. Sato, and Y. Nakano, J. Soc. Mat. Eng. Res. Jap. 5 44 (1992).

17. S. Sumita, M. Ikeda, Y. Nakano, K. Nishiyama, T. Nomura, *J. Am. Ceram. Soc.* **74** 2739 (1991).

18. H. Kishi, Y. Okino, and N. Yamaoka, *Proceedings of Seventh US–Japan Seminar on Dielectric and Piezoelectric Ceramics*, 255–260 (1995).

19. T.A. Kroger and H.J. Vink, *Solid State Physics* **3** 307 (1956).

20. R.D. Shannon, *Acta Cryst.* **A32** 751–767 (1976).

21. H. Chan, M.P. Harmer, and D. Smyth, *J. Am. Ceram. Soc.* **69** [6] 507–510 (1986).

22. A. Hitomi, X. Liu, T.R. Shrout, and C.A. Randall, *Proceedings of the Eighth US–Japan Seminar on Dielectric and Piezoelectric Ceramics*, 144–147 (1997).

23. K. Takada, E. Chang, and D.M. Smyth, *Adv. Ceram.* **19** 147–152 (1987).

24. D. Hennings and P. Groen, *Annual Meeting of Am. Ceram. Soc.,* Indianapolis (1999).

25. Y. Tsur and C.A. Randall, submitted *to J. Am. Ceram. Soc.*

26. J. Maier, Prog. *Solid St. Chem.* **23** 171–263 (1995).

27. P. Sarkar and P.S. Nicholson, *J. Am. Ceram. Soc.* **79** [8] 1987–2002 (1996).

28. M.S.J. Gani, *Industrial Ceramics* **14** [4] 163–174 (1994).

29. J. Van Tassel, A. Daga, C.A. Randall, *Proceedings of IMAPS '99 Conference*, Chicago (1999).

30. J. Van Tassel and C.A. Randall, *J. Europ. Ceram. Soc.* **19** 955–958 (1999).

31. Y. Nakano, A. Sato, A. Hitomi, and T. Nomura, Ceram. Trans. 32 119–128 (1993).

32. S. Sato and T. Nomura, "Tape Casting Thin Layers for Fabrication of Multilayer Ceramic Capacitors," Electroceramic Device Manufacturing Workshop, Penn State (1997).

Phenomenology of the Elasto-Dielectric Response in the Field Forced Ferroelectric Phases of Lead Zinc Niobate : Lead Titanate (PZN:PT) Relaxor Ferroelectrics

L. Eric Cross and Petr Hana

Materials Research Laboratory, The Pennsylvania State University, University Park, PA 16802
Fax: (814) 863-7846, email: lec3@psu.edu

In the relaxor ferroelectric phases of the perovskite structure dielectrics it is clearly not possible to apply simple Landau:Ginsburg:Devonshire phenomenology as below the Vogel:Fulcher freezing temperature the system is in a metastable frozen state. In single crystals of PZN:PT solid solution at compositions close to the morphotropic boundary (MPB) however, the most interesting and useful properties occur in the field forced ferroelectric phase, where the dielectric response is not dispersive at low frequency. For the 001 oriented electric field poled rhombohedral state which exhibits the most exciting piezoelectric properties it is shown that the high field deformation can be described by a field forced monoclinic phase and that the intrinsic shape change calculated for the single domain states is more than adequate to account for the exceptionally high strain behavior. The capability to field force a strongly monoclinic phase was unexpected, however very recent precise x-ray studies using the synchrotron source at Brookhaven appear to confirm a stable monoclinic phase in PZT at compositions close to the morphotropic phase boundary.

From the induced spontaneous electric polarization as a function of temperature in the 111 field poled single crystal it appears that the PZN:4.5% PT composition in the rhombohedral ferroelectric phase is very close to tricritical behavior, as may be expected from the close approach in free energy of rhombohedral and tetragonal states. These and aspects of the proposed phenomenology will be briefly discussed.

1. INTRODUCTION

Earlier studies[1,2] have suggested that the high initial anhysteritic strain of 001 oriented electric fields in rhombohedral phase PZN:PT with compositions which are not too close to the morphotropic phase boundary (MPB) may be associated with a field driven phase change from rhombohedral to monoclinic (3m $\Rightarrow$ m) symmetry. Since the 3m $\Rightarrow$ m ferroelectric phase change in the perovskite can be second order (continuous) even large intrinsic domain shape changes could be reversible and anhysteritic. For field forced phase changes in the relaxor, dispersion is very largely lost and the properties are stabel with time, so that it is not outrageous to expect that reversible thermodynamics may be applied to derive estimates of the elasto-dielectric responses. In this brief report Landau:Ginsburgh:Devonshire phenomenology is applied to demonstrate for 95.5 PZN:4.5 PT:

(a) That the intrinsic shape change of the rhombohedral domain induced in the 3m $\Rightarrow$ m phase change which is consistent with the observed polarization change is more than adequate to account for the observed quasi-linear strain induced by the 001 oriented field.

(b) The observed P^4 vs T dependence of the polarization in the ferroelectric rhombohedral phase suggests a tricritical behavior which may be expected in a system derived from the m3m prototype where the orthorhombohic phase is suppressed.

(c) The dielectric behavior below, and well above the relaxation range is consistent with the proposed simple phenomenology.

2. THERMODYNAMIC PHENOMENOLOGY

For the perovskite ferroelectrics stemming from the prototype m3m symmetry the Gibbs Free Frequence AG takes the form.

The coefficienta α_i, α_{ij}, α_{ikj} are the dielectric stiffness and higher order stiffness at constant and zero stress, s_{ij} the elastic compliances at constant polarization and Q_{ij} the electrostrictive coupling constants in polarization notation. The function contains all permitted stiffness coefficients up to sixth order, but only first order elastic and electrostrictive constants.

$$\Delta G \quad = \alpha_1\left[P_1^2+P_2^2+P_3^2\right]+\alpha_{11}\left[P_1^4+P_2^4+P_3^4\right]$$
$$+\alpha_{12}\left[P_1^2P_2^2+P_2^2P_3^2+P_3^2P_1^2\right]$$
$$+\alpha_{111}\left[P_1^6+P_2^6+P_3^6\right]$$
$$+\alpha_{112}\left[P_1^4\left(P_2^2+P_3^2\right)+P_2^4\left(P_1^2+P_3^2\right)+P_3^4\left(P_1^2+P_2^2\right)\right]$$

$$+\alpha_{123}P_1^2P_2^2P_3^2$$
$$-\frac{1}{2}S_{11}\left[X_1^2+X_2^2+X_3^2\right]$$
$$-S_{12}\left[X_1X_2+X_2X_3+X_3X_1\right]$$
$$-\frac{1}{2}S_{44}\left[X_4^2+X_5^2+X_6^2\right]$$
$$-Q_{11}\left[X_1P_1^2+X_2P_2^2+X_3P_3^2\right]$$
$$-Q_{12}\left[X_1\left(P_2^2+P_3^2\right)+X_2\left(P_1^2+P_3^2\right)+X_3\left(P_1^2+P_2^2\right)\right]$$
$$-Q_{44}\left[X_4P_2P_3+X_5P_1P_3+X_6P_1P_2\right] \quad (1)$$

From equation (1) relations may be simply derived for the polarization states, the relative free energies and the dielectric stiffness from which the susceptibility (permittivity) may also be derived.

Since the deformation of the prototype is purely electrostrictive the shape change for any ferroelectric phase including monoclinic and triclinic can be derived from equation (1). These relations are given in Table I. It is also interesting to note that the volume change s_v into each phase is of the same form, Table II and depends only on the total polarization.

3. APPLICATION TO 95.5 PZN:4/5 PT

For 001 poling field rhombohedral PZN:PT may be driven to single domain tetragonal state where measurements of longitudinal strain change Δs_3 and transverse strain change Δs_1, between 50 kV/cm and 65 kV/cm compared to total polarization P_3 yield values of $Q_n = +0.094 \text{ m}^4/\text{c}^2$ and $Q_{12} = -0.047 \text{ m}^4/\text{c}^2$. Measurements of ΔV_s over the field range up to 40 kV/cm suggest ΔV_s is small and that P_T does not change much. Assuming P_T is constant P_1 and P_2 can be calculated over the field range 0 to 40 kV/cm and the tilt angle from 001 direction evaluated from the induced monoclinic phase (Table III)

Table I
Possible Electrostrictive Spontaneous Deformation
in Perovskite Ferroelectrics

Cubic Prototype
$P_1 = P_2 = P_3 = 0$
$s_1 = s_2 = s_3 = 0 \quad s_4 = s_5 = s_6 = 0$

Tetragonal
$P_1 = P_2 = 0 \quad P_3^2 = 0$
$s_1 = s_2 = Q_{12}P_3^2 \quad s_3 = Q_{11}P_3^2$
$s_4 = s_5 = s_6 = 0$

Orthorhombic
$P_1 = 0 \quad P_2^2 = P_3^2 = 0$
$s_1 = 2Q_{12}P_3^2$
$s_2 = s_3 = \left(Q_{11}+Q_{12}\right)P_3^2 \quad s_4 = Q_{44}P_3^2$
$s_5 = s_6 = 0$

Rhombohedral
$P_1^2 = P_2^2 = P_3^2 = 0$
$s_1 = s_2 = s_3 = \left(Q_{11}+2Q_{12}\right)P_3^2$
$s_4 = s_5 = s_6 = Q_{44}P_3^2$

Monoclinic (1)
$P_1^2 = P_2^2 \neq 0 \quad P_3^2 \neq 0 \quad P_1^2 \neq P_3^2$
$s_1\left(Q_{11}+Q_{12}\right)P_1^2+Q_{12}P_3^2$
$s_2 = \left(Q_{11}+Q_{12}\right)P_1^2+Q_{12}P_3^2$
$s_3 = Q_{11}P_3^2+\left(Q_{11}+Q_{12}\right)P_1^2$
$s_4 = Q_{44}P_1P_3$
$s_5 = Q_{44}P_1P_3$
$s_6 = Q_{44}P_1^2$

Monoclinic (2)
$P_1^2 \neq 0 \quad P_2^2 \neq 0 \quad P_1^2 \neq P_2^2 \quad P_3^2 = 0$
$s_1 = Q_{11}\left(P_1^2+Q_{12}P_1^2\right)$
$s_2 = Q_{12}P_1^2+Q_{11}P_1^2$
$s_3 = Q_{12}\left(P_1^2+P_2^2\right)$
$s_4 = 0 \quad s_5 = 0 \quad s_6 = Q_{44}P_1P_2$

Triclinic
$P_1^2 = 0 \quad P_2^2 = 0 \quad P_3^2 = 0$
$P_1^2 = P_2^2 = P_3^2$
$s_1 = Q_{11}P_1^2+Q_{12}\left(P_2^2+P_3^2\right)$
$s_2 = Q_{11}P_2^2+Q_{12}\left(P_1^2+P_3^2\right)$
$s_3 = Q_{11}P_3^2+Q_{12}\left(P_1^2+P_2^2\right)$
$s_4 = Q_{44}P_2P_3 \quad s_5 = Q_{44}P_1P_3$
$s_6 = Q_{44}P_1P_2$

Table II
Volume Strain s_v as a Function of
Total Polarization PT in All Possible Phases

Volume Change	
Cubic	$s_v = 0$
Tetragonal	$s_v = (Q_{11} + 2Q_{12})P_3^2$
Orthorhombic	$s_v = 2(Q_{11} + 2Q_{12})P_3^2$
	$= (Q_{11} + 2Q_{12})P_{Total}^2$
Rhombohedral	$s_v = 3(Q_{11} + 2Q_{12})P_3^2$
	$= (Q_{11} + 2Q_{12})P_{Total}^2$
Monoclinic (1)	$s_v = 2(Q_{11} + 2Q_{12})P_1^2 + (Q_{11} + 2Q_{12})P_3^2$
	$= (Q_{11} + 2Q_{12})P_{Total}^2$
Monoclinic (2)	$s_v = (Q_{11} + 2Q_{12})P_1^2 + (Q_{11} + 2Q_{12})P_2^2$
	$= (Q_{11} + 2Q_{12})P_{Total}^2$
Triclinic	$s_v = (Q_{11} + 2Q_{12})(P_1^2 + P_2^2 + P_3^2)$
	$= (Q_{11} + 2Q_{12})P_{Total}^2$

Table III
Calculated Polarization and Tilt Angle for PZN:PT
95.5/4.5 Under High DC E_3 Field

Field	Polarization P_3		Polarization P_1
kV/cm	$\mu c/cm^2$	Angle θ	$\mu c/cm^2$
5	27.8	50.1	23.47
10	29.8	46.5	22.21
15	31.4	43.4	21.04
20	33	40.34	19.82
25	34.3	37.5	18.64
30	35.6	34.6	17.42
35	36.75	31.9	16.19
40	37.85	29.1	14.87

From P_3 and P_1 in Table III, s_1 and s_3 can be determined and shown to be larger than the measured values (figure 1). Thus the calculated intrinsic change is more than adequate to describe the total shape change in this field region.
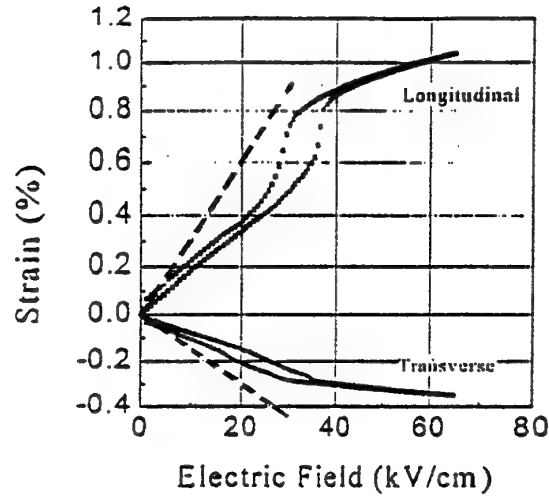
Fig. 1   Field Induced Strain s_3 and s_1 for 001 E-field
on 95.5 PZN:4.5PT.
— Measured Values.
---- Intrinsic Calculated Strains.

Examination of P_3 vs T shows a behavior close to $P^4 \propto T$ suggesting tricritical behavior and very small values of α_{11} and α_{12}. In this case the sixth order terms will dictate phase stability and it is easy to see why the orthorhombic phase may be suppressed.

Measurements of the dielectric permittivity for the <111> poled single domain state give linear relations for $1/\varepsilon$ vs T with Curie constant $C \sim 3.10^5$ similar to the value measured in the paraelectric phase above 220°C where $C \sim 2.8.10^5$.

In connection with the proposed monoclinic phase in PZN:PT it is interesting to note that recent studies at Brookhaven[3] have confirmed a stable monoclinic phase in PZT at lower temperature in compositions close to the MPB, and the induction of a monoclinic phase at room temperature on poling the ceramics.[4]

4.   FUTURE DEVELOPMENTS
Work is in progress to determine the magnitude and temperature dependence of the α_{ij} for a sequence of composition in the PZN:PT family including both rhombohedral 3m and tetragonal 4mm ferroelectric phases.

5. REFERENCES

1. Park, S.E. and T. R. Shrout, "Relaxor Based Ferroelectric Single Crystals for Electro Mechanical Actuators," Mat. Res. Innov. **1**, 20-25 (1997).

2. Park, S.E. and T.R. Shrout, "Characteristics of Relaxor Based Piezoelectric Single Crystals for Ultrasonic Transducers, IEEE Trans. UFFC **44** (5), 1140-1147 (1997).

3. Noheda, B., D.E. Cox, G. Shirane, J. Gonzalo, L.E. Cross, and S.E. Park, "A Monoclinic Ferroelectric Phase in the $Pb(Zr_{1-x}Ti_x)O_3$ Solid Solution," Applied Physics Letters **74**(14), 2059-2061 (1999).

4. G. Shirane, Private Communication (1999).

Domain Structure of PbTiO$_3$ Single Crystals
by Kelvin Force Microscope

Takashi Yamamoto, Shinobu Omika, Junichi Sakamoto and Eiji Matuzaki
Department of Electrical Engineering
National Defense Academy, Yokosuka 239-8686, Japan

Abstract – 90 ° a-c, 90 ° a-a, 180 ° a-a, 180 ° c-c domain and these connected domain structures of PbTiO$_3$ single crystals have been investigated by Kelvin force microscope. A new discrimination method for classifying these domain structures was proposed by combining among surface gradient, surface electrical potential and etching rate. Two kinds of c domain, where +c domain and −c domain was called, could be measured separately.

1. Introduction

Ferroelectric (FE) integrated devices have received much attention for their potential applications in non-volatile FE random access memory (FRAM) and micro-actuator/sensor devices. However, fatigue of polarization still remains as a serious problem for such usage, which domain structure closely relates to the polarization arrangement and domain switching was the domain reversal phenomena by electrical field. Over the past year, numerous observation techniques such as polarizing light microscopy (birefringence)[1], scanning electron microscopy (SEM) with etching[2] and decoration[3], and transmission electron microscopy (TEM)[4] have been developed to study the domain structure in FE materials. Using these methods, four kinds of domain ; i.e. 90 ° a-c, 90 ° a-a, 180 ° a-a, 180 ° c-c domain in tetragonal FE crystal structure have been reported in FT materials such as BaTiO$_3$,[5] PbTiO$_3$ and Pb(Zr$_1$.Ti$_x$)O$_3$ (x > 0.465). Compared with these traditional methods for domain structure observation, atomic force microscopy (AFM) has several merits, which the surface roughness can be measured in a wide range of the X-Y direction, a high measurement resolution of the Z-direction. Moreover, Kelvin force microscopy (KFM) could be simultaneously measured on surface electric potential and surface roughness with a high resolution in the same measurement area as by the AFM.

In this paper, pure PbTiO$_3$, 0.5 and 1 mole % Mn-doped PbTiO$_3$ single crystals were prepared by the flux method with excess PbO. Morphologies on grown surface of single crystal were measured by KFM.

2. Experimental Procedure

Pure and Mn-doped PbTiO$_3$ single crystals were grown by the flux technique in air. 99.9%-pure TiO$_2$, 99.99%-pure PbO and 99.6% pure MnCO$_3$ were mixed at a mole ratio of 0.3(PbTiO$_3$) - 0.7(PbO) for pure-PT and 0.3(PbTiO$_3$ + 0.5 mole % or 1.0mol%MnO) – (0.7)PbO for Mn-doped PT. The single crystal was synthesized in platinum (Pt) crucible. The temperature increases at a rate of 200℃/h up to 1200℃. The soaking time for melting the pure-PT and Mn-doped PT was 3 h at 1200℃. It is then cooled slowly at the rate of 2℃/h, to a temperature between 1200℃ and 800℃ where pure-PT, Mn-doped PT single crystal were grown in the excess PbO flux. The crystals are then cooled to room temperature at the rate of the rate of 100℃/h. The plate-shape single
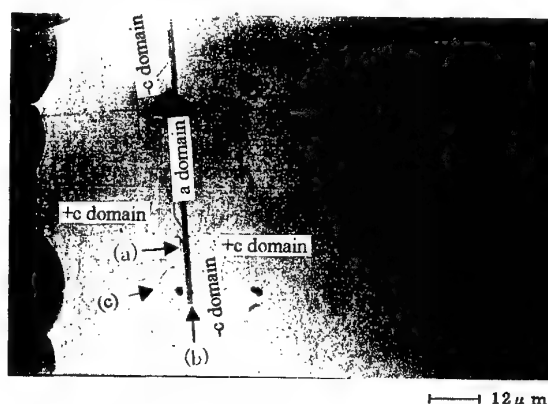
Fig.1 Optical micro-graph of 90 ° a-(+c) domain and 90 ° a-(-c) domain and 180 +c - -c domain of 1.0 mole % Mn-doped PT.
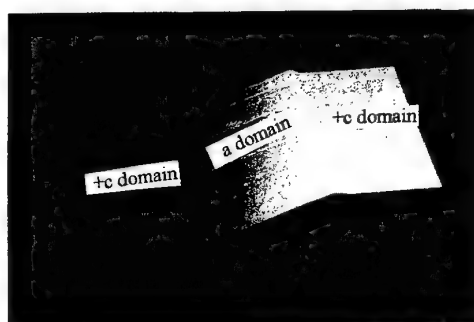
Fig. 2(a) Bird's-eye view image of surface roughness and its cross section of 90 ° a – (+c) domain shown by arrow (a) in Fig.1
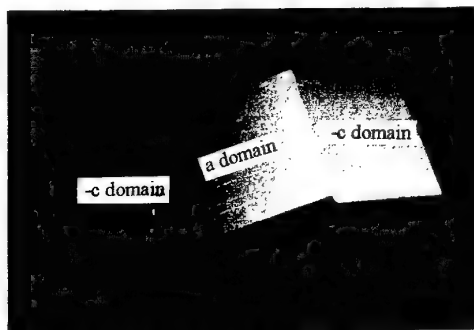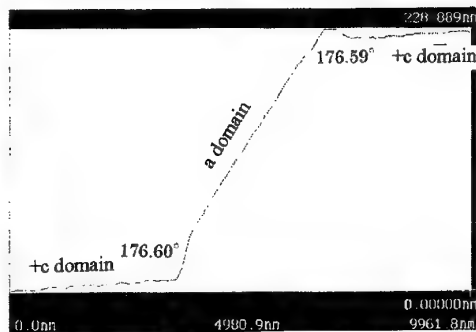
Fig. 2(b) Bird's-eye view image of surface roughness and its cross section of 90 ° a – (-c) domain shown by arrow (b) in Fig.1
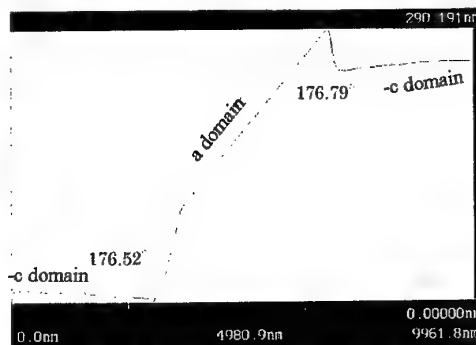
crystals are grown at the center and on the sides of the crucible. After that, excess PbO was removed in a hot thin HNO_3 water solution. Surface roughness with a high resolution of 0.1 nm in the Z-direction and 30 nm in the X-Y direction and surface electrical potential with a high resolution of 3mV and a space resolution of 0.1 μ m have been measured by the tapping mode by Kelvin force microscopy (KFM) using a commercially available apparatus (Seiko Electronics Co., SPI 3700).

3. Results and Discussion
3.1 90 ° a-c domain (surface gradient)

Figure 1 shows the optical micro-graph of as-grown (001) surface in 1.0 mol% Mn-doped PT. Straight dark stripe is a-domain and surrounding area are +c domain and –c domain. Figure 2(a) shows the bird's-eye view image of surface roughness and its cross section in the area (10 μ m x 10 μ m) shown by arrow (a) in Fig.1. The angles of the gradient are 3.41 ° to 3.40 ° ,where the measured value is 176.59 ° and 176.60 ° . Also, Figure 2(b) shows the bird's-eye view image of surface roughness and its cross section in the area (10 μ m x 10 μ m) shown by arrow (b) in Fig.1. The angles of the

gradient are 3.21 ° to 3.48 ° . The angles of surface gradient were the same within the error. As well known, the surface gradient of 90 ° a-c domain was controlled by the following equation, θ (deg.) = $2\tan^{-1}(c/a) - 90$, where c/a is crystal tetragonality[6]. These values coincided with experimental values[7].

3.2 90 ° a-c domain (etching rate)

As-grown crystal in this experiment was washed in the thin hot HNO_3 water solution for removing the crucible after growing. During this process, each surfaces were etched by the different speed depended on each surface. Right portions in Figs 2(a) and 2(b) show the different etching rate in the same c domain. The surface of c domain (called -c domain) in Fig.2(b) was largely etched than that (called +c domain) in Fig.2(a). Such difference caused by the difference of etching rate between +c domain and –c domain, which H^+ ion in thin hot HNO_3 water solution was drown to the negative electrical potential in the surface of –c domain than +c domain and attacked the surface of –c domain.

3.3 90 ° a-c domain (surface electrical potential)

Figures 3(a) and 3(b) show the bird's-eye
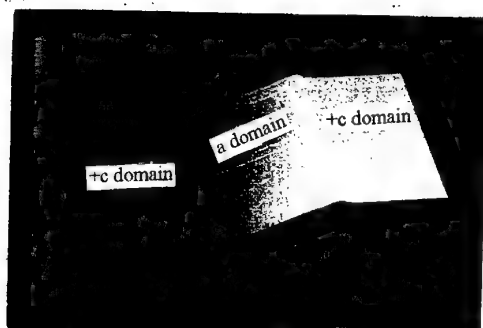
Fig. 3(a) Bird's-eye view image of surface roughness and its electrical potential of 90° a − (-c) domain shown by arrow (a) in Fig.1
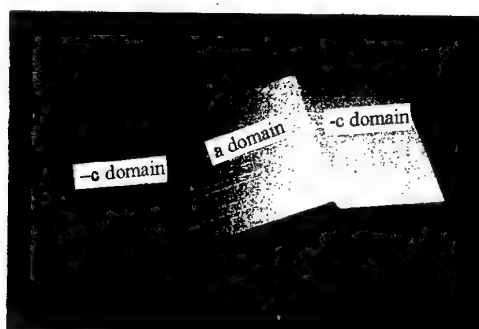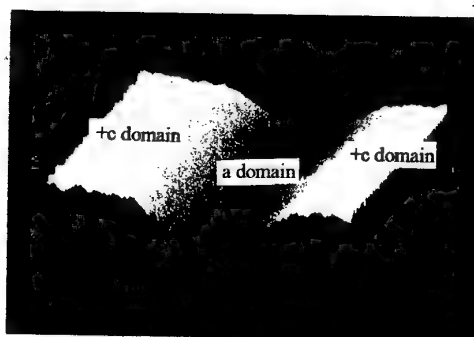
Fig. 3(b) Bird's-eye view image of surface roughness and its electrical potential of 90° a − (-c) domain shown by arrow (b) in Fig.1
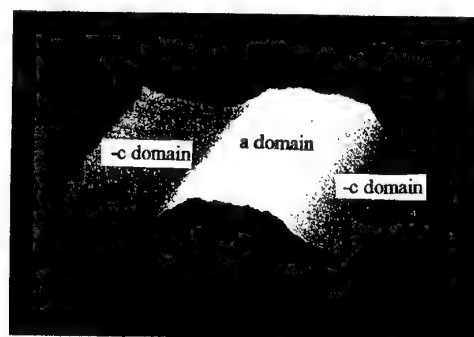
view images of surface roughness and surface electrical potential in the area shown by arrows (a) and (b) of Figs. 1. As discussed in 3.1 and 3.2 sections, this area is typical 90° a-c domain, where c domain/a domain/c domain. Considering +c and –c domains in the same c domain and a domain as the standard level of electrical potential, the relative level in electrical potential of +c domain, a domain, -c domain were higher in turn of +c domain > a domain > -c domain. From these considerations, the area shown by arrow (a) was recognized as 90° +c domain/a domain/ +c domain boundary. Similarly, the area shown by arrow (b) was recognized as 90° –c domain/a domain/ -c domain boundary.

3.4 180° c-c domain

In general, 180° c-c domain boundary could not be observed by optical micro-graph and transmission electron micro-graph, because crystal anisotropy along c-axis between +c and -c domain was zero. However, 180° c-c domain boundary becomes possible to visualize when that boundary was etched. Curved line shown by arrow (c) in Fig. 1 is 180° c-c domain boundary. Figure 4(a) shows the bird's-eye view image of surface roughness and its

cross. The surface was very smooth and the step between top and bottom flat area was 0.1 μ m, where this height depend on etching time. Figure 4(b) shows the bird's-eye view image of surface roughness and its cross. The electrical potential of top was higher than that of bottom. The difference of such a height was caused by the difference of etching in +c domain and –c domain. Moreover, the boundary of 180° c-c domain was freely curved for lack of structure anisotropy in crystal. On the other hand, 90° a-c domain boundary was rigidly straight for satisfying lattice anisotropy of c-axis and a-axis in crystal.

3.4 New determination method of domain structure using KFM

KFM method with a simultaneous measurement of surface roughness and surface electrical potential was powerful tool to study the domain structure of FE material. As well known, types of domain structure with a tetragonal crystal structure were 90° a-c domain, 90° a-a domain, 180° c-c domain and 180° a-a domain. Firstly, the angle of surface gradient in 90° a-c domain boundary was strictly determined and could be classified either 90° a-c domain or the other domain by
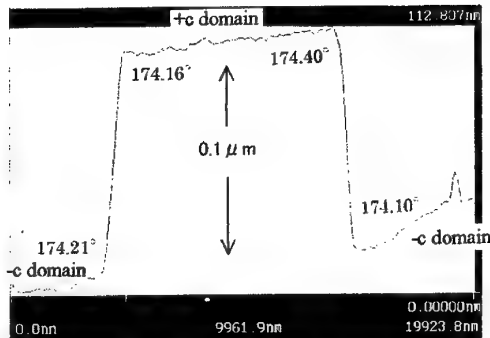
Fig. 4(a) Bird's-eye view image of surface roughness and its cross section of 180° +c – (-c) domain shown by arrow (c) in Fig.1
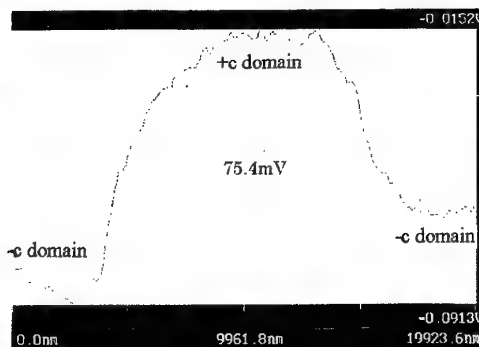
Fig. 4(b) Bird's-eye view image of surface electrical potential and its cross section of 180° +c – (-c) domain shown by arrow (c) in Fig.1

measuring the angle at the boundary. Secondly, if the absolute values of surface electrical potential on surfaces of domain could be measured, all domain structures should be readily determined. However, the measured electrical potential in this experiment was relative because the domain structure was not uniform from the surface to the bottom. Therefore, the domain structure between +c domain/ a domain / -c domain and a domain/ -c domain/ a domain as one example could not be classified. Thirdly, the etching rate among +c domain, -c domain and a domain was different and the steps caused by etching was precisely measured by KFM (including AFM). Therefore, comparing with the steps made by etching in the same sample, above-mentioned domain structure between +c domain/ a domain / -c domain and a domain/ -c domain/ a domain could be classified. From these results, a new determination method for domain structure was proposed using Kelvin force microscope.

4. Conclusion

The relations among 90° a-c, domain, 90° a-a domain, 180° c-c, domain, 180° a-a

domain structures have been investigated in pure, Mn-doped PT using a Kelvin force microscope. By classifying +c and –c domain, all domain structures could be determined.

References

[1] F. Gilleta : Phys. Status Solid 11 (1972) 721.
[2] A. Sawada and R. Abe : Jpn. J. Appl. Phys. 6 (1967) 699.
[3] V. P. Konstantinova, N. A. Tichomirova and M. Glogarova, Ferroelectrics 20 (1978) 259.
[4] M. Tanaka and G. Honjo : J. Phys. Soc. Jpn. 19 (1964) 654.
[5] T. Mitsu, T. Tatsuzaki amnd E. Nakamura, Ferroelectrics (Maki Book Co., Tokyo, (1969) 307 (in Japanese).
[6] F.Jona and G.Shirane, Ferroelectrics Crystals (Pergamon Press., London, (1962) 162.
[7] T. Yamamoto, K. Kawano, M. Saito and S. Omika,: Jpn. J. Appl. Phys. 36 (1997)6145.

SHG Microscope: Principle and Its Application to Nondestructive Observation of 180° Domain Structure and Domain Reversal Process in Ferroelectrics

Haruyuki Mohri, Sunao Kurimura* and Yoshiaki Uesu

Department of Physics, Waseda University

3-4-1 Okubo, Shinjuku-ku, Tokyo 169-8555

Fax: 81-3202-4962, e-mail:uesu93@mn.waseda.ac.jp

*Laser Research Center, Institute for Molecular Science, Okazaki-shi 444-8585

The SHG microscope is a kind of the interference microscope, where the 2D images are constructed by the second harmonic(SH) waves produced in a specimen. In particular, the interference between the SH waves from the specimen and the standard plate enables us to observe the ferroelectric 180° domain structures nondestructively. The observation principle and its application to the domain reversal process in MgO:LiNbO$_3$ under the electric field are described.

1. INTRODUCTION

Several methods have been proposed for observing ferroelectric 180° domain structures. However some methods exploit special material properties of the specimen[1,2], and others require extremely thin sample[3], or provide only knowledge of the surface state[4]. Usual optical microscopes cannot be applied to this problem, as the optical properties are same for up and down polarization states. Our motivation of the study was to invent a simple and general method for observing 180° domain structure of bulk sample as well as of thin film and we finally reached an idea of utilizing the properties of the polar 3rd-rank tensor of ferroelectrics: The 3rd-rank tensor has an opposite sign for up and down polarization state. In nonlinear optics, the second harmonic(SH) waves are produced via the SHG tensor which is the third rank and the phase difference between SH waves from up and down domains are π. This phenomenon cannot produce the intensity contrast but if the SH waves from both domains interfere with those produced in a homogeneous standard plate, up and down domain states can be distinguished by the intensity contrast. Based upon the idea, we constructed a nonlinear optical microscope, which is termed SHG microscope[5], and successfully applied it to the observation of domain structures of BaTiO$_3$, and periodically inverted domain structures of LiTaO$_3$ quasi-phase matching devices[6]. In this paper, the further improvement of the SHG microscope in order to obtain high intensity contrast and the observation of the domain reversal process in MgO:LiNbO$_3$ are reported.

2. PRINCIPLE OF OBSERVATION AND OPTICAL SYSTEM

The highest intensity can be obtained when the amplitudes and the phases of SH wave from one of the domains and the standard plate are same as

shown in Fig.1. The amplitude of the standard plate can be varied by rotating it to change the effective path length.*
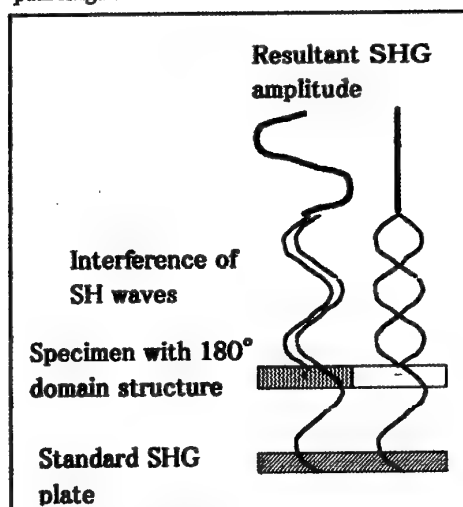
Fig.1 The interference of SH waves from the sample and the standard plate which produces the intensity contrast.

The phase is adjusted by rotating a glass plate located between the standard plate and the sample. The optical system of the SHG microscope is illustrated in Fig.2. A pulse Nd:YAG laser with the wavelength of 1.064μm, the repetition frequency of 10kHz, power 300mW is used as a light source. The fundamental wave passes through a half-wave plate, a polarizer, a lens, the standard plate which is made of MgO doped LiNbO$_3$(MgO:LN), a glass phase plate and a specimen. The fundamental wave is eliminated by a filter located in front of an objective and the SH wave passing through a 532 filter is finally detected by a CCD camera which is synchronized with the laser oscillation. Prior to the observation of real domain structures, we checked the function of the microscope using a sample made of one up and one down domains: A monodomain Y-cut Mg:LN was cut into two part which were placed making the polarization

direction opposite as shown in Fig.3(a). By adjusting the amplitude and the phase, we obtained the intensity contrast as shown in (b) and the contrast was reversed by rotating the phase plate(c).
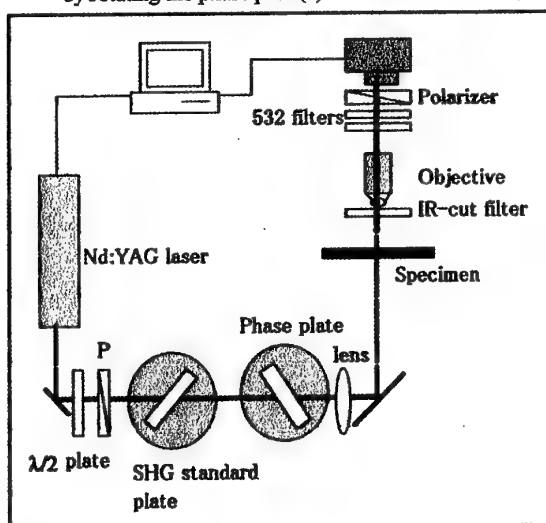
.Fig.2 Optical system of SHG microscope
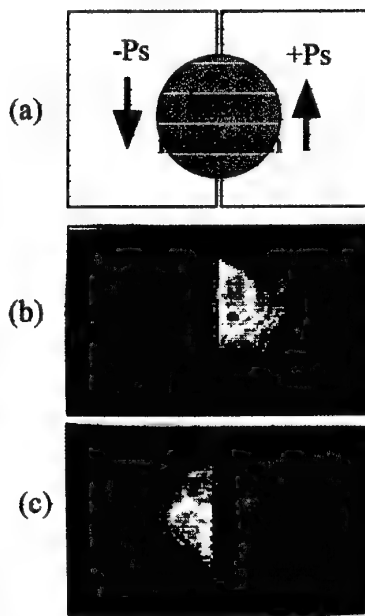
Fig.3 The SHG images of the sample consisting of one up and one down polarization domains. (a) shows sample illustration, (b) an image with maximum contrast, (c) same image as (b) but with reversed contrast.
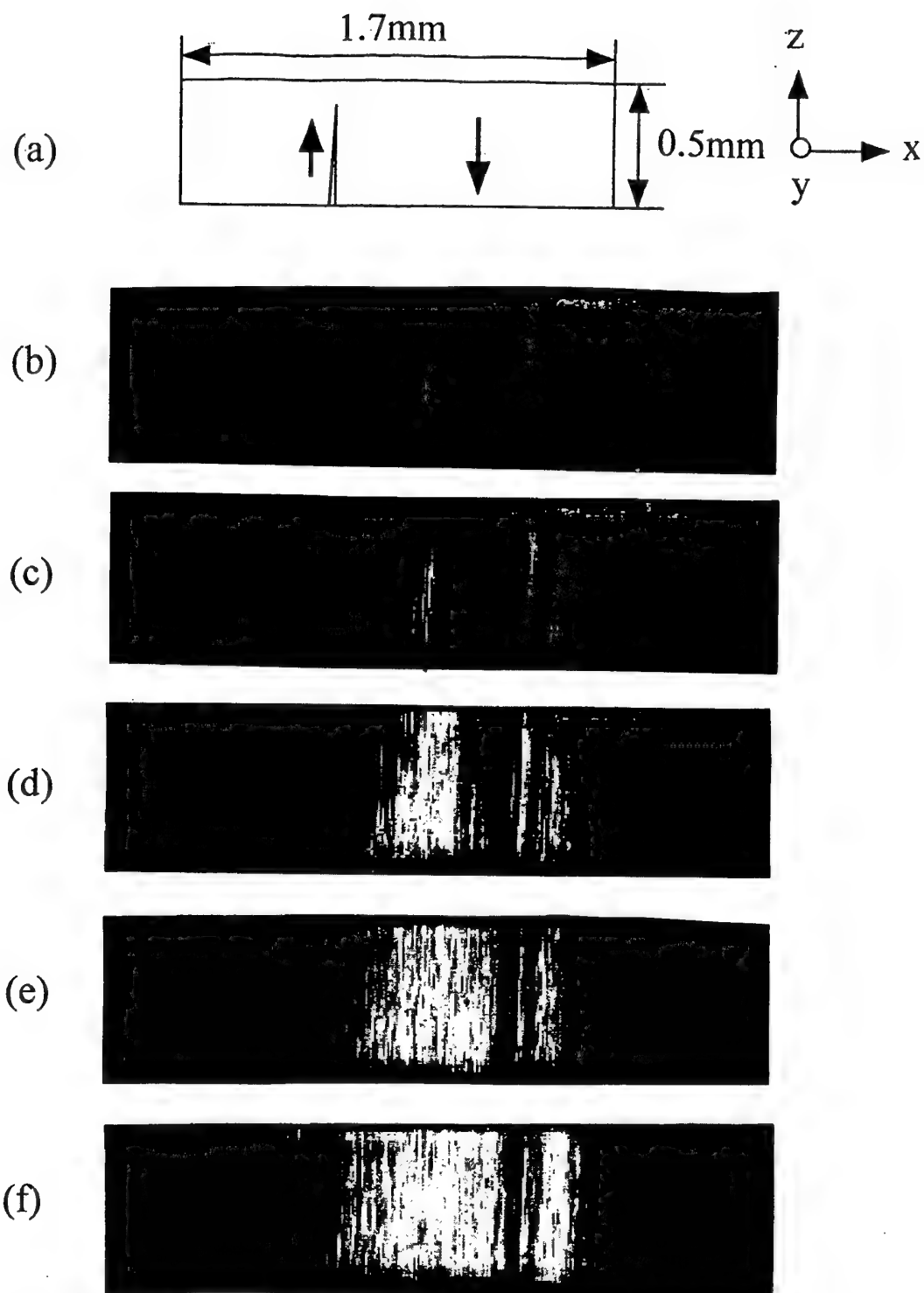
Fig.4 SHG microscopic observations of the domain reversal process in MgO:LiNbO₃ under pulsed electric field.
(a) denotes sample orientation and dimensions, (b) SHG image taken after 5 shots of pulsed electric field of 8kv/mm,
(c)after further 5 shots of pulsed electric field of 4kv/mm, (d)after further 10 shots of 4kv/mm, (e)after further 10 shots
of 4kv/mm, (f)after further 10 shots of 4kV/mm.

The Rotation angle agrees well with the calculated value. The fact means that ferroelectric 180° domain structure can be observed by our microscope.

3. OBSERVATION OF DOMAIN REVERSAL PROCESS IN MgO:LiNbO$_3$

Using the SHG microscope, we observed the domain reversal process in MgO:LN under the pulsed electric field. The domain reversal of this crystal has been first reported by the etching technique[7]. As this method is destructive, several samples have been prepared and the domain reversal process was observed at each pulse shot with different samples. The SHG microscope enables us to observe the process using one sample.

A sample was cut from a Y-cut MgO:LN crystal. The dimension and orientation of the sample is illustrated in Fig.4(a). Electrodes were prepared with Ag paste on the z surfaces. The pulse electric field between 4 and 8 kV/mm was applied to the sample immersed in silicon oil. All experiments were performed at room temperature.

The results are shown in Fig.4(b)-(f). The observation starts with monodomain sample which provides a dark image by adjusting the phase plate. Then 5 shots of pulsed electric field of 8kv/mm are applied to the sample. Several spike-like regions with the reversed polarization (white region in the figure) develop from the + electrode((b)). 5 pulses of 4 kV/mm induce nucleation of spike-like domains as well as domain growth to the front direction.(c). Nucleation and growth in both front and side directions are observed by further applications of pulsed electric field of same amplitude and same shot ((d) to (f)) and almost single domain state with opposite polarity to the

initial state is obtained ((f)). In this procedure, the domain motion stopped at each stage of the pulse-application.

The spatial resolution of the SHGM is limited to a few μm due to optical noises, which will be reduced if we choose carefully the optical elements. In principle, the spatial resolution of the SHG image is expected to be better than the ordinary microscope, as the SH amplitude is proportional to the square of the incident electric field. It should be also pointed out that the characterization of polar thin films such as ferroelectric thin film is easily achieved by our SHGM[8]. We have also successfully applied the microscopy to the observation of monolayer molecules at the air-water interface[9]. The maximum time resolution is now sub-second, which is mainly limited by the transfer velocity of the image to the computer.

References

1. J.P.Dougherty, E.Sawaguchi and L.E.Cross, Appl. Phys. Lett. 20, 364(1972)

2. V.Grubsky, S.MacCormack and J.Feinberg, Opt.Lett. 21, 6(1996).

3. M.Tanaka and G.Honjo: J.Phys.Soc.Jpn, 19,954 (1964)

4. R.LeBihan and M.Maussion, Ferroelectrics, 7,307(1994)

5. Y.Uesu, S.Kurimura and Y.Yamamoto, Appl.Phys.Lett. 66, 2165(1995)

6. S.Kurimura and Y.Uesu, J.Appl.Phys. 81,369(1997)

7.A.Kuroda, S.Kurimura and Y.Uesu, Appl.Phys.Lett. 69,1565(1996)

8. Y.Uesu and N.Kato, Phys.Solid State, 41,688(1999)

9. N.Kato, K.Saito and Y.Uesu, Thin Solid Films, 338, 5(1999)

(Ba,Sr)TiO$_3$ Dielectrics: Relationship between Bulk and Thin Film Properties

Angus I Kingon, Stephen K Streiffer*, Charles B Parker, and Susanne Stemmer**

Department of Materials Science and Engineering, NCSU, Raleigh. NC 27695-7919
Fax: (919) 515 3419, Email: angus_kingon@ncsu.edu
*Argonne National Laboratory, Materials Science Division, Argonne, Il 60439- 4838
Email: streiffer@anl.gov
**University of Illinois at Chicago, Chicago, Il 60607-7059
Email: stemmer@uic.edu

Thin films of complex perovskites have a number of potentially important applications. Of major scientific and practical concern is the scaling of properties as film dimensions are reduced. This paper describes a satisfactory relationship between bulk and thin film dielectric properties of (Ba,Sr)TiO$_3$. Relative contributions of strain, A:B cation stoichiometry, and interface are separated to explain temperature dependent dielectric behavior.

1. INTRODUCTION

(Ba,Sr)TiO$_3$ (BST) thin films represent an important dielectric system for application in high density DRAMs, as well as for backend capacitors integrated onto the Si chip. There has been significant development over the past six years, such that incorporation into 4Gb DRAM appears likely.[1]

One of the disappointments regarding BST films has been the very substantial lowering of the dielectric constants of thin films relative to their bulk analogues. An example of experimental thin film dielectric permittivity versus temperature data, in comparison with polycrystalline bulk data of the same Ba/Sr ratio is shown in Fig. 1. This behavior is of concern, as it may limit the extendability of BST through future generations. There has been scattered speculation regarding the origin of the lowered dielectric constant. The effect has been linked to film strain, intrinsic ferroelectric size effects through grain size or film thickness scaling, and extrinsic interface effects. No satisfactory description of the dielectric behavior of the perovskite films has been presented, nor have relative contributions of different phenomena to the dielectric function been discerned.

As a result, we have investigated the dielectric response of a series of {100} fiber-textured (Ba$_x$Sr$_{1-x}$)Ti$_{1+y}$O$_{3+z}$ samples deposited by liquid-source metal-organic chemical vapor deposition onto Pt/SiO$_2$/Si, as a function of the two most commonly varied microstructural parameters, *viz* film thickness and Ti nonstoichiometry (y). The thickness dependent data allows us to extrapolate to obtain the thickness independent dielectric susceptibility, and thus examine directly the effect of composition (ie y, the Ti non-stoichiometry) on the "bulk" film properties. Thereafter, we discuss the effect of biaxial strain originating from the thermal mismatch with the silicon substrate on the temperature-dependent dielectric susceptibility. The approach allows us to examine the relative contributions to the lowering of the dielectric permittivity.
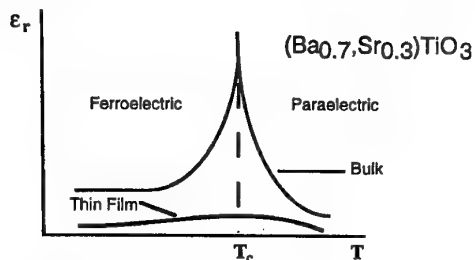
Figure 1: Typical permittivity versus temperature dependence for a BST thin film[2] compared to a bulk ceramic sample with the same Ba/Sr ratio[3].

2. EXPERIMENTAL

All films were BST with Ba/Sr=70/30 deposited by liquid source MOCVD under the auspices of the US DRAM Consortium. Experimental procedures have been described previously[4,5].

3. RESULTS AND DISCUSSION

3.1 Empirical Description of the Dielectric Data

It has been shown in earlier work that the field dependence of the dielectric response of these BST thin

films is well described by the familiar free energy expansion[6]:

$$E_{app} = 2\alpha'_3 P_3 + 4\alpha'_{33} P_3^3 \qquad (1)$$

where E_{app} is the apparent field applied to the dielectric in the thickness direction, the α's are the empirical dielectric stiffnesses, and P refers to the polarization. It has also been demonstrated[6] that the dielectric stiffness α'_3 in the first order term carries almost all the temperature and thickness dependence. This term can therefore be decomposed into:

$$\alpha'_3 \approx \frac{\beta}{t} + \gamma(T) \qquad (2)$$

where β is the thickness dependent and γ the thickness independent portions of the dielectric stiffness.

The experimental dielectric data for several thicknesses and compositions have also been examined in Curie - Weiss form, with typical data for y=0.04 (ie 51%Ti) shown in Fig 2. Besides the thickness dependence, it can be seen that the films fit Curie-Weiss behavior above a temperature of about 380K. Below this temperature, for all film thicknesses and compositions, there is a deviation from the classical behavior. By utilizing only the data above this temperature, an effective Curie-Weiss constant (C') and extrapolated Curie temperature can be obtained. The Curie constant is almost thickness independent, but strongly stoichiometry dependent. The composition closest to stoichiometry is closest to the bulk value. The apparent thickness dependence of the Curie-Weiss temperature (see Fig 2) can be described as a shift of the curves along the temperature axis. This is possibly best deduced by rearranging equations (1), (2) and the Curie-Weiss expression, to yield[5]:

$$T_3(t) = \theta - \frac{2\varepsilon_0 C' \beta}{t} \qquad (3)$$

where T_3 is an extrapolated intercept (effective Curie temperature) for a given thickness.

3.2 Removing the Thickness Dependence: Ti Stoichiometry

The dielectric properties can be stripped of their thickness dependence by fitting the data to Equation (2), for all temperatures. This yields the dielectric stiffness or the susceptibility of the bulk of

the films as a function of temperature, as well as the parameter β of Eqn 2. The data is plotted in Fig 3, for two different compositions. Notice again the deviation from Curie-Weiss behavior at about 380K, as well as the strong dependence upon the Ti content. Fig 4 shows the data plotted as relative dielectric constant for the "bulk" of the films at 300K as a function of Ti stoichiometry.
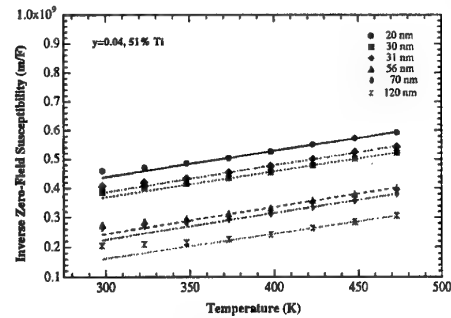
Fig 2: Inverse susceptibility versus temperature for BST films of different thickness, and one Ti stoichiometry.
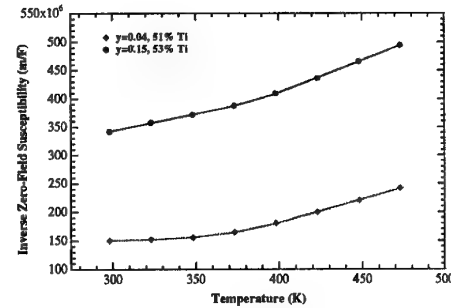
Fig 3: Inverse susceptibility versus temperature, stripped of film thickness dependence, ie described by $2\gamma(T)$ in Eqn 2.
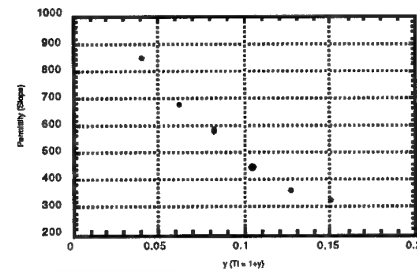
Fig 4: Effective relative permittivity values calculated from the experimental data, as a function of the Ti stoichiometry (y).

There is an important difference between the thin films and bulk BST which should be noted. The

solid solubility limit for Ti over-stoichiometry of bulk BST is known to be small, ie less than y=0.001[7]. In contrast, the solubility limit for excess Ti in these thin films is dramatically larger, around y=0.1[8]. Excess Ti is accomodated in the grain interiors. At Ti excesses as large as y=0.15 (Ba+Sr/Ti=46.5/53.5), Ti can be observed at the grain boundaries, probably in the form of amorphous TiOx[8]. Other properties such as dielectric loss and degradation correlate strongly with the excess titanium.[9]

3.3 Temperature and Stress Dependent Landau-Ginzberg-Devonshire Description

We have recently undertaken an analysis of the effect of biaxial stress, due to the thermal mismatch of the BST film and silicon substrate, on the dielectric properties[2,5]. The approach extends the thermodynamic analysis undertaken by Pertsev and coworkers[10] and Desu et al[11]. The symmetry-breaking imposed by the biaxial strain implies that one must consider different orientations of the spontaneous polarization with respect to the plane as separate "phases". The strain modifies the thermodynamic stability and thus the Curie-Weiss temperatures of these phases[10]. We have added the temperature dependence of the mismatch strain, allowing us to calculate the temperatures corresponding to the transition from the prototype phase to the phases with the polarization in the plane θ_1, and normal to the plane θ_3, respectively. The apparent modifications to the bulk Curie constants can also be calculated. It is clear from the analysis (consistent with intuition) that the biaxial strain in this case increases the stability of the phase with in-plane polarization, and decreases the stability of the phase with polarization normal to the plane. In addition, as long as one includes the appropriate coupling terms between the in-plane and out-of-plane polarization, one can calculate the full temperature dependence of the dielectric stiffness (inverse susceptibility), over the entire temperature range. Similarly, the temperature-dependent values of the spontaneous polarizations can be calculated. The solid lines in Fig 3 are the calculated values of dielectric susceptibility (with the thickness dependence stripped out). The values of strain which were utilized were those experimentally measured by x-ray diffraction. The agreement to the experimental data is excellent although the presence of several adjustable parameters must be noted. The agreement has been shown to extend to far lower temperatures[5].

The analysis has several important implications, which are worth emphasizing. Firstly, it provides strong evidence for the role of stress in modifying the temperature dependent permittivity. The calculated results also emulate the shape or rounding of the inverse susceptibility versus temperature curve. In addition, the analysis is consistent with a phase transition from the prototype phase to a ferroelectric phase with in-plane polarization at θ_1, of 390K, yielding an explanation for the measured deviation from Curie-Weiss behavior observed in all samples. It should be noted that no hysteresis was observed in the P-E loops at temperatures between θ_1 and θ_3. However, this is expected, as the polarization is confined to the film plane, and would therefore not be observable in the capacitor configuration utilized.

3.4 Origins of the Thickness Dependence

The thickness dependence is treated empirically in this work. It has several possible origins which could yield the observed series or interfacial capacitance. These include:

- extrinsic interface effects, particularly atmospheric contamination
- compositional changes in the BST adjacent to the interface, driven by film nucleation effects or by segregation under thermodynamic equilibrium
- microstructural changes adjacent to the growth interface
- incomplete polarization screening by the metal electrodes, or built-in fields due to Fermi level pinning and charge transfer
- suppression of the soft mode near the interface, ie the so-called "dead layer" theory[12]

We have recently presented a discussion of these various possibilities[5], concluding that the last mechanism has attractive features for description of the available data. Other mechanisms are not excluded, however. This topic will be discussed in greater detail at the Workshop.

4. CONCLUSIONS AND IMPLICATIONS

We find that the overall behavior of these samples is adequately described by mean-field, Landau-Ginzburg-Devonshire theory as for bulk ferroelectrics. We have quantified the impact of three separable factors for these films that greatly alter the permittivity as a function of temperature, compared to that found for bulk ceramic samples at the same Ba/Sr ratio of 70/30: i) Ti nonstoichiometry; ii) the apparent "interface" effect which results in a reduction of the dielectric constant with decreasing thickness; and iii) plane equibiaxial stress resulting from thermal expansion mismatch with the Si substrate. When properly considered, these three factors yield a satisfactory description of the relationship between the temperature-dependent dielectric properties of the thin films and the bulk. The results form a strong basis for making decisions regarding BST capacitor development.

4. ACKNOWLEDGEMENTS
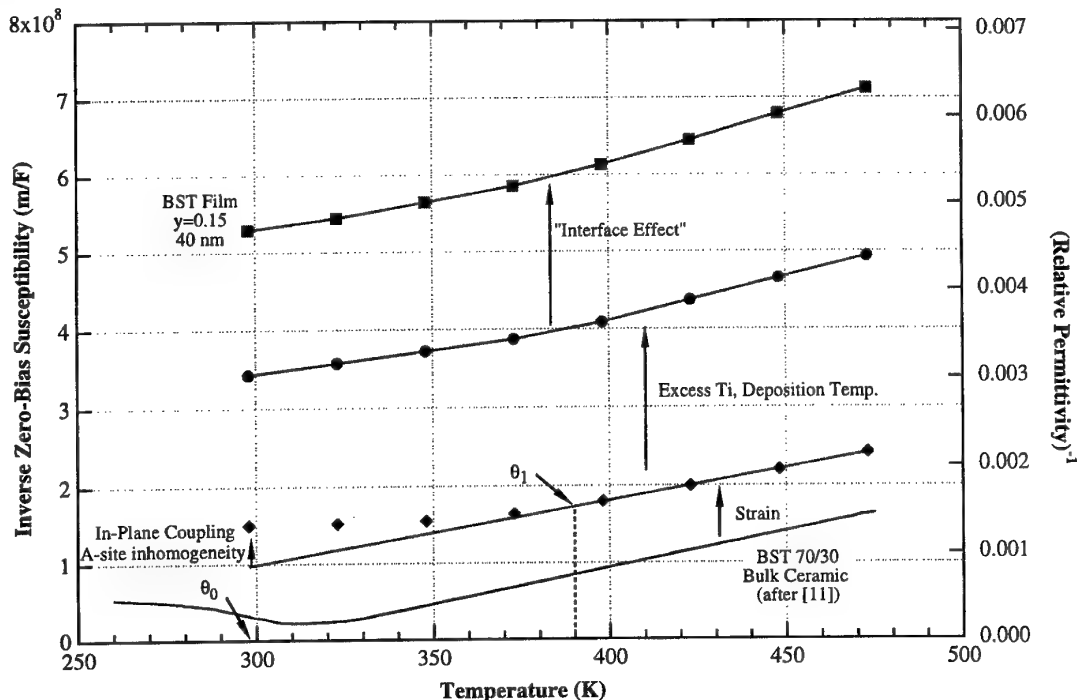
Fig 5: Summary showing the relative contributions to the dielectric behavior of BST films, with the data referring to a typical film with y=0.15 (Ba+Sr/Ti=46.5/53.5) and thickness of 40nm. θ_1 is the predicted Curie-Weiss temperature for a transition from a paraelectric phase to a ferroelectric phase with the polarization in the plane of the film.

REFERENCES

[1] A.I. Kingon, S.K. Streiffer, C. Basceri, and S.R. Summerfelt, MRS Bull. **21**, 46 (1996)

[2] Streiffer S K, Basceri C, Parker C B, Lash S E, Christman J, Maiwa H, and Kingon A I, Proc. of the International Symposium on the Applications of Ferroelectrics, IEEE, 31, 1999.

[3] A.D. Hilton and B.W. Rickers, J. Phys. D: Appl. Phys. **29**, 1321 (1996).

[4] P.C. van Buskirk, J.F. Roeder, C. Basceri, S.E. Lash, C.B. Parker, S.K. Streiffer, and A.I. Kingon, J. Korean Phys. Soc. **32**, S1591 (1998).

[5] S.K. Streiffer, C. Basceri, C.B. Parker, S.E. Lash and A.I. Kingon, to be published in J. Appl. Phys., October 15, 1999.

[6] Cem Basceri, S.K. Streiffer, Angus I. Kingon, and R. Waser, J. Appl. Phys. **82**, 2497 (1997).

[7] R.K. Sharma, N.-H. Chan, and D.M. Smyth, J. Am. Ceram. Soc. **64**, 448, (1981).

[8] S. Stemmer, S.K. Streiffer, N.D. Browning, and A.I. Kingon, Appl. Phys. Lett. **74**, 2432 (1999).

[9] C. Basceri, Ph.D. Thesis, North Carolina State University, 1997.

[10] N.A. Pertsev, A.G. Zembilgotov, and A.K. Tagantsev, Phys. Rev. Lett. **80**, 1988 (1998).

[11] S.B. Desu, V. P. Dudkevich, P.V. Dudkevich, I.N. Zakharchenko, and G.L. Kushlyan, Mat. Res. Soc. Symp. Proc. **401**, 195 (1996).

[12] C Zhou and D.M. Newns, J. Appl. Phys. **82**, 3081 (1997).

Quantum Paraelectricity in Epitaxial Titanate Perovskites

R.M.V. Rao[1], K. Shimada[2], M. Lippmaa[2], M. Kawasaki[2], Y. Inaguma[3], M. Itoh[3], H. Munekata[1], and H. Koinuma[3]

[1] Imaging Science and Engineering Laboratory, Tokyo Institute of Technology, 4259 Nagatsuta, Midori-ku, Yokohama 226, Japan

[2] Department of Innovative & Engineered Materials, Tokyo Institute of Technology, 4259 Nagatsuta, Midori-ku, Yokohama 226, Japan

[3] Materials Structures Laboratory, Tokyo Institute of Technology, 4259 Nagatsuta, Midori-ku, Yokohama 226, Japan

Fax: 81-45-924 5399, e-mail: radhika@oxide.rlem.titech.ac.jp

Thin films of $La_{1/2}Na_{1/2}TiO_3$ (LNTO) fabricated by pulsed laser deposition show interesting dielectric properties exhibiting temperature-insensitive dielectric constant below 50 K. This onset temperature is significantly higher than those observed in known quantum paraelectric materials like $SrTiO_3$ which shows the onset temperature below 10 K. Also, unlike STO the dielectric properties of LNTO do not vary when electric field is applied. The dielectric constant of LNTO is very stable under electric bias. The dissimilar nature of these materials are explored and discussed.

INTRODUCTION

Quantum paraelectric materials pertain to a special group of ferroelectric materials that exhibit increase in dielectric constant as the temperature decreases. At low temperatures, the quantum fluctuations dominate the ferroelectric displacement fluctuations, thereby stabilizing the paraelectric phase and resulting in temperature-invariable dielectric constant below a certain temperature. $SrTiO_3$ (STO) and $KTaO_3$ are well-known quantum paraelectric materials which show such behavior below 10K [1-3]. These are also known to switch to ferroelectric state under applied bias voltage or pressure. These features are quite advantageous for the tunable microwave devices [4-6].

Thin films of STO are known to exhibit ferroelectric-type dielectric maxima at low temperatures. Also, the values of dielectric constant obtained in thin films are much lower than those of single crystals [7, 8]. This poses a limitation while seeking applications in microwave and capacitor devices. However, recently it was shown that the step-flow growth during pulsed laser deposition (PLD) of STO dramatically improved the dielectric properties. The dielectric constant of these films was very high exceeding 10^4 [9].

$La_{1/2}Na_{1/2}TiO_3$ (LNTO) is relatively newer member of this group of quantum paraelectric materials. LNTO and related materials have been identified to be prospective materials for microwave device applications owing to their good high frequency dielectric properties [10, 11]. Recently, Inaguma *et al* have reported high temperature

quantum paraelectricity in LNTO ceramics [12]. In this material, dielectric constant was seen to increase as the temperature is lowered, but saturated at around 50 K and remained constant below 50 K. Also the study of series of compositions in the system, $Ln_{1/2}Na_{1/2}TiO_3$, with many rare earth cations substituting for La has been reported. Many of these compositions show similar behavior with dielectric constant becoming temperature-invariable at as high temperatures as 70 K [13].

Materials having dielectric properties that do not vary much with temperature are very useful for many applications. LNTO is particularly attractive as intrinsically its dielectric constant can be maintained temperature-insensitive over a wide temperature range. Also, it could be easily coupled with high temperature superconductors for various applications of operation temperature set at 60 K, cooled by a refrigerator.

In this work, we report the fabrication of epitaxial perovskite titanate (STO and LNTO) thin films by pulsed laser deposition and characterization of their dielectric properties to discuss the phase stability between ferroelectricity and quantum paraelectricity.

EXPERIMENTAL

The ceramic LNTO targets were prepared by solid state reaction of the starting materials, La_2O_3, Na_2CO_3 and TiO_2, all of analytical grade reagents. Stoichiometric (La:Na:Ti=1:1:2) and Na-rich compositions (1:1.5:2 and 1:1.75:2) to

compensate for sodium volatility were prepared. LNTO films were deposited on (001) LaAlO₃, sapphire (0001) and conducting 0.5 wt% Nb-doped SrTiO₃ (001) substrates by pulsed laser deposition (PLD). A 248 nm KrF excimer laser with laser fluence of 5 J/cm^2 and a repetition rate of 5 Hz was used. The substrate temperature was varied from 470 to 650°C and was measured using an infrared pyrometer. The target-to-substrate distance was 3 cm. The ablation was carried out in oxygen atmosphere of 0.001 torr. The films were then annealed at a temperature of 800°C for 12 hours in flowing oxygen atmosphere.

Step-flow growth of STO was fabricated in a special ultrahigh vacuum PLD chamber [14]. The substrate was heated to typically 1200°C in 10^{-6} Torr of oxygen. KrF excimer laser pulses were focussed on a rotating single crystal of STO target with a fluence of 5 J/cm^2. The reflection high energy electron diffraction (RHEED) specular spot intensity was monitored in situ to check the growth process. At temperatures below 900°C, the STO film growth proceeded in a layer-by-layer mode and at 1200°C, film growth was found to proceed in step-flow mode.

RESULTS AND DISCUSSION

The composition of the LNTO films was determined by electron probe microanalysis (EPMA). The ratio of Na/(La+Ti+Na) estimated for the films deposited at various substrate temperatures is shown in Fig. 1. Due to sodium evaporation, its content decreased as the deposition temperature was elevated. Ideal stoichiometry could not be obtained using stoichiometric targets even at low substrate temperatures (400-550°C). The film composition could be stoichiometric at around 500°C and 600°C for Na/La=1.5 and 1.75 targets respectively. Since the latter case showed better crystallinity, the characterization results hereafter are focussed on the films deposited at 600°C from Na/La=1.75 target.
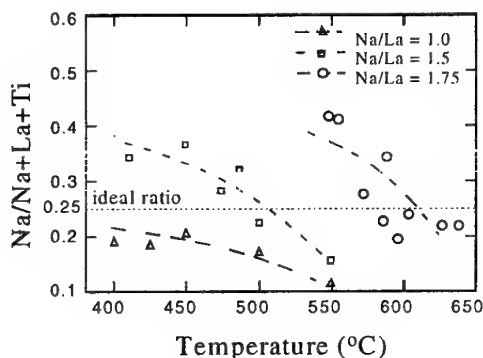
Fig. 1 Na-content in LNTO films represented by Na/(La+Na+Ti) ratio obtained by EPMA as a function of substrate temperature. The triangle symbols indicate films fabricated by stoichiometric target, the square La:Na:Ti=1:1.5:2 and the circle by La:Na:Ti=1:1.75:2 targets.

Fig. 2 (a) and (b) shows the XRD patterns of as deposited and annealed films deposited on the LaAlO₃ substrate. The Na-content did not vary after annealing. The films are epitaxial in nature with c-axis orientation. The increase in the intensity of (002) peak after annealing indicates the improved crystallinity of the film during annealing. This can be clearly seen in Fig. 2(c) which compares the (002) peaks for the substrate and the film.

The LNTO and STO films on conducting SrTiO₃ (Nb-doped) substrates were used for the dielectric measurements. The top contact electrodes of 0.5-1 mm diameter were formed using a stencil mask by metal deposition of aluminum or platinum. The capacitance and the loss tangent, tanδ were measured by employing HP4284A precision LCR meter. The dielectric constant was calculated assuming parallel plate configuration.

A 320 nm STO film grown at 800°C in the layer-by-layer mode showed a relatively modest dielectric constant as shown in Fig. 3(a). The variation in the dielectric constant value was less than 10% during a bias scan in the ±1V range. A 380 nm STO film grown at 1200°C in step-flow mode showed a very different behavior as shown in Fig. 3(b) and (c). A bias scan performed at 4.2 K (Fig. 3, inset) indicated that the maximum value of capacitance was attained at bias of +0.8 V. Corresponding dielectric constant values are similar to those of unstrained single crystals.
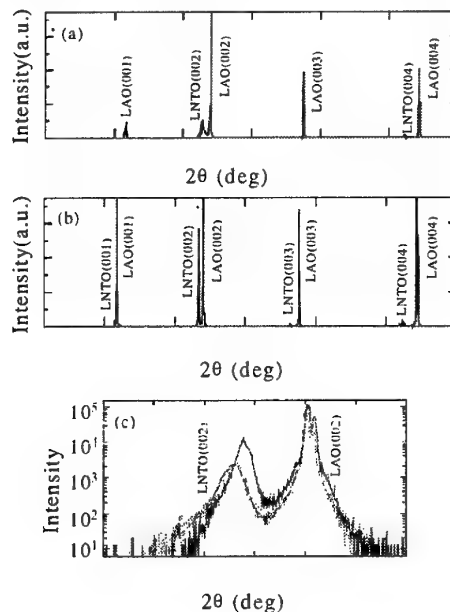
Fig. 2 X-ray diffraction patterns of (a) as-deposited and (b) annealed LNTO/LaAlO₃ films. The improvement in crystallinity after annealing is shown in (c) which shows a slow scan of (002) reflection of LNTO.
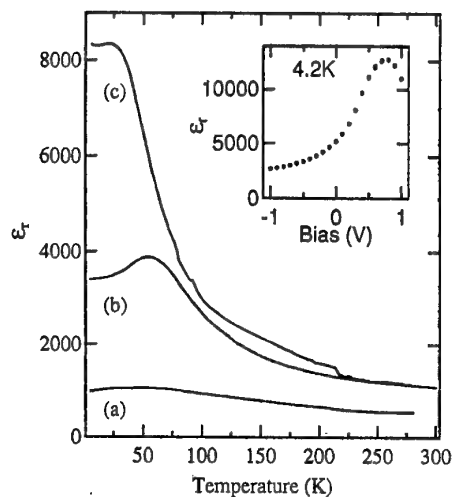
Fig. 3 Temperature dependence of the dielectric constant, ε_r of a film grown at 800°C in the layer-by-layer mode, (a). Dielectric constant of a step-flow film grown at 1200°C, measured during cooling (b) and during heating at a +0.8 V dc bias (c). The bias dependence of dielectric constant at 4.2 K is shown in the inset. The measurement frequency was 500 kHz.
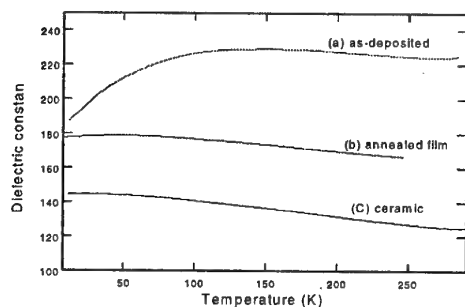
Fig. 4 Temperature dependence of dielectric constant of LNTO measured at 200 kHz for (a) as-deposited film, (b) annealed film and (c) ceramic.
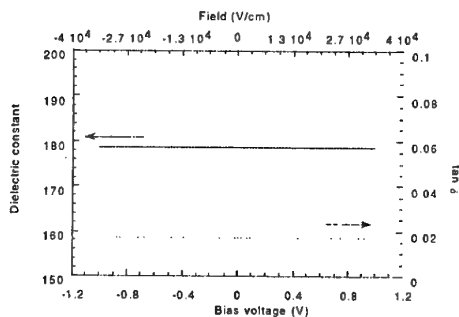
Fig. 5 Bias dependence of dielectric constant and tanδ of LNTO films at 7 K at a measuring frequency of 200 kHz.

Very high values of dielectric constant of STO films grown by step-flow mode especially at low temperatures could be the result of stabilization of quantum paraelectric phase. If the crystal quality is low, local distortions can easily stabilize the ferroelectric state. Also, the large voltage tunability of dielectric constant observed could be attributed to the competition between the para- and ferroelectric states at low temperatures.

The variation of dielectric constant with temperature for ceramic LNTO as well as for the LNTO films as deposited and annealed at 800°C are shown in Fig. 4. The thickness of LNTO films was of the order of 300 nm. Though the ceramics show a flat region below 50 K, the as-deposited thin films do not exhibit such behavior. However, the temperature variation of dielectric constant for annealed LNTO films is similar to that of the ceramic LNTO. Therefore, the improvement of crystallinity is critical to stabilize quantum paraelectric nature of LNTO as well. The annealed films show an increase in dielectric constant as the temperature is lowered till about 50 K, below which it remains constant.
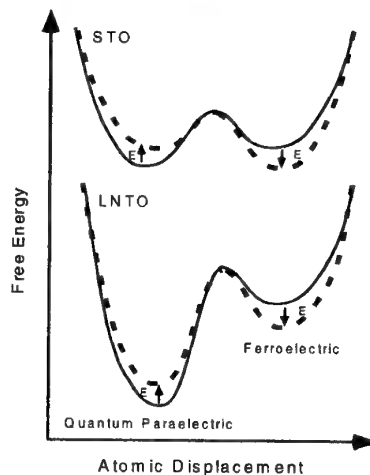
Fig. 6 Schematic of effect of bias voltage (dashed line) on potential energy wells of quantum paraelectric and ferroelectric states for (a) STO and (b) LNTO.

The phase control from quantum paraelectricity to ferroelectricity can be done by the application of electric field in case of STO as shown in Fig. 3. The dielectric properties were measured for the LNTO thin films under application of dc bias field. No dependence of bias voltage on dielectric constant of LNTO was observed at any temperature. Fig. 5 shows that the dielectric constant of LNTO films are very stable even under electric field in contrast to other known quantum paraelectric materials.

This fact indicates that the quantum paraelectric state in LNTO is very stabilized. Fig. 6

schematically illustrates the difference in the stability of paraelectric and ferroelectric states for STO and LNTO materials. A small lattice distortion and/or application of electric field destabilizes the ferroelectric state in STO. Whereas in the case of LNTO, the application of electric filed in the range of $\pm 4 \times 10^4 Vcm^{-1}$ has no effect in destabilizing the deep potential well of paraelectric state. In order to switch LNTO to a ferroelectric state, much large bias should be applied, which however, exceeds the breakdown voltage.

Inaguma *et al* have explained the appearance of ferroelectricity and quantum paraelectricity in perovskite titanates in terms of Ti-O bond length, electron configuration of certain cations and mass inequality [15]. For larger perovskites which are ferroelectrics like $BaTiO_3$, the increase in the volume of the $[TiO_6]$- octahedra results in reducing the repulsive forces. In case of smaller perovskites, for example, $Ln_{1/2}Na_{1/2}TiO_3$ (Ln =lanthanides), the repulsive forces increase resulting in the rotation of the $[TiO_6]$- octahedra to compensate this force. This prevents ferroelectricity resulting in quantum paraelectricity at low temperatures. $SrTiO_3$ has an ideal perovskite size without any $[TiO_6]$- octahedra tilting and thus its dielectric properties can be manipulated by applying electric field or pressure.

CONCLUSIONS

Highly stable quantum paraelectric $La_{1/2}Na_{1/2}TiO_3$ and highly tunable $SrTiO_3$ films were fabricated. The $SrTiO_3$ films grown by step-flow mode exhibit very high dielectric constant especially at low temperature which can be tuned to ferroelectric, resulting in a large tunability of dielectric constant. The $La_{1/2}Na_{1/2}TiO_3$ films exhibit, on the other hand, voltage-independent and temperature-independent dielectric constant at low temperatures. The contrasting nature of these two quantum paraelectric materials is brought into picture.

REFERENCES

1. K.A. Muller and H. Burkard, *Phys. Rev. B* **19** (7) 3593, 1979.
2. E. Sawaguchi, A. Kikuchi and Y. Kodera, *J. Phys. Soc. Jpn.* **17** 1666, 1962.
3. U.T. Hochli, H.E. Weibel and L.A. Boatner, *Phys. Rev. Lett.* **39** (18) 1158, 1977.
4. J. Hemberger, P. Lunkenheimer, R. Viana, R. Bohmer and A. Loidl, "Electric field-dependent dielectric constant and nonlinear susceptibility in $SrTiO_3$," *Phys. Rev. B* **52** (18) 13159, 1995.
5. H. Vogt and H. Uwe, *Phys. Rev. B* **29** (2) 1030, 1984.
6. Yu A. Bokov, Z.G. Ivanov, A.L. Vasiliev, E. Olsson and T. Claeson, *Supercond. Sci. Technol.* **9** 178, 1996.
7. H.C. Li, W. Si, A.D. West, and X.X. Xi, *Appl. Phys. Lett.* **73** 190, 1998.
8. A.T. Findikoglu, C. Doughty, S.M. Anlage, Q. Li, X.X. Xi and T. Venkatesan, *Appl. Phys. Lett.* **63** 3215, 1993.
9. M. Lippmaa, N. Nakagawa, M. Kawasaki, S. Ohashi, Y. Inaguma, M. Itoh and H. Koinuma, *Appl. Phys. Lett.* **74** 3543, 1999.
10. M.G. Jenkins, *Int. J. Fract.* **34** 281, 1987.
11. H. Kim, S. Kucheiko, S.J. Yoon and H.J. Jung, *J. Am. Ceram. Soc.* **80** 1316, 1997.
12. Y. Inaguma, J. Sohn, I. Kim, M. Itoh and T. Nakamura, *J. Phys. Soc. Jpn.* **61** (10) 3831, 1992.
13. P. Sun, T. Nakamura, Y. Shan, Y. Inaguma and M. Itoh, *Ferroelectrics* **200** 93, 1997.
14. S. Ohashi, M. Lippmaa, N. Nakagawa, H. Nagasawa, H. Koinuma and M. Kawasaki, *Rev. Sci. Instrum.* **70** 178, 1999.
15. Y. Inaguma, M. Itoh, Y-J. Shan and T. Nakamura, Proc. Second symposium on Atomic-scale surface and interface Dynamics, Tokyo, p233, 1998.

Charge Transport and Fatigue Resistance in $SrBi_2Ta_2O_9$

A. C. Palanduz[+] and D. M. Smyth

Lehigh University, Materials Research Center, 5 E. Packer Ave., Bethlehem, PA 18015, U.S.A.
Fax: (610) 758-3526, e-mail: dms4@Lehigh.edu
[+]Crystal Physics and Electroceramics Laboratory, Department of Materials Science and Engineering, Massachusetts Institute of Technology, Cambridge, MA 02139, U.S.A.

$SrBi_2Ta_2O_9$ is a ferroelectric oxide that is highly resistant to polarization fatigue. It is proposed that this results from self-doping due to extensive cation place exchange between the Sr^{+2} and Bi^{+3} cations. Rather than being completely self-compensating, this results in separate defect chemistries and transport properties in the two distinctly different structural layers of the compound. The $Bi_2O_2^{+2}$ layers are acceptor-doped by replacement of Bi^{+3} by Sr^{+2} and exhibit a high level of oxygen ion transport. However, this ionic transport is isolated from the major ferroelectric response that resides in the $SrTa_2O_7^{-2}$ perovskite-like layers. The latter layers are donor-doped by replacement of Sr^{+2} by Bi^{+3}. The compensating defects are most likely cation vacancies that are immobile. Electrons are also present at smaller concentrations but have extremely low mobilities. Thus in the region of ferroelectric response there are no mobile charges that could migrate to domain walls and pin their motion.

INTRODUCTION

There is increasing interest in the use of ferroelectric thin films as nonvolatile memory elements in Si-based microcircuitry. The physical dimensions, switching voltages, switching times, and amount of switchable charge are all highly compatible with existing technology. However, the original ferroelectric of choice, $Pb(Zr_{1-x}Ti_x)O_3$ (PZT) suffers from polarization fatigue, i.e. after having been switched of the order of 10^8 times, the amount of switchable charge gradually decays until the distinction between a switching event and a nonswitching event is lost. While this problem has been somewhat reduced by the use of donor-doping and conducting oxide electrodes, a more stable material is desirable. It has since been determined that the remanent polarization of the Bi-layer ferroelectrics, particularly $SrBi_2Ta_2O_9$ (SBT), remains stable for at least 10^{12} cycles. Even though its initial polarization is less than that of PZT, the long-term stability is a desirable feature.

PROPOSED MODEL FOR FATIGUE RESISTANCE

It is of obvious interest to determine the reasons for the resistance of SBT to polarization fatigue. For that purpose, we have undertaken an investigation of the defect chemistry and charge transport properties of SBT and related materials. We propose that the stability of SBT is directly related to its layered structure. SBT consists of fluorite-like $Bi_2O_2^{+2}$ layers alternating with perovskite-like $SrTa_2O_7^{-2}$ layers. Careful structural analyses of both SBT (1) and the isostructural SBN (2), its niobium-containing analog, indicate that there is substantial place exchange between the Sr^{+2} and Bi^{+3} ions. This helps to reduce the charge imbalance between the two layers. The amount of exchange was found to vary from a few percent to more than ten percent. In a non-layered structure such place exchange would be expected to be self-compensating, i. e. there would be equal numbers of acceptor and donor centers and no other compensating defects would be necessary. However, in the layered structures of SBT and its relatives, it appears that self-compensation is imperfect, and that there is some local compensation within the layers by lattice and/or electronic defects. Our studies indicate that this results in defect concentrations of the order of 1% in both layers. Thus the $Bi_2O_2^{+2}$ layer behaves as a 1% acceptor-doped material, with the excess

$Sr_{Bi}{}'$ compensated by oxygen vacancies that support a substantial ionic conductivity. The perovskite-like layer acts as a 1% donor-doped material with the excess $Bi_{Sr}{}^{\cdot}$ compensated by strontium vacancies at high oxygen activities and by electrons under reducing conditions. In undoped SBT, the conductivity under equilibrium conditions (550-750°C) is dominated by the ionic conductivity in the Bi-layers, while in undoped SBN n-type conductivity prevails.

It would be expected that a high oxygen vacancy conductivity would be extremely detrimental to polarization fatigue. However, in SBT the ionic conductivity is confined to the Bi-layers, while most of the ferroelectric response lies in the perovskite-like layers. The oxygen vacancies cannot enter the perovskite-like layers because they contain an excess of donor centers. The electronic conductivity in the perovskite-like layers is very temperature dependent, with an activation energy near 2 eV, consistent with a highly activated electron mobility. Polarization fatigue is attributed to the migration of charged species, e.g. electrons, holes, or oxygen vacancies, to domain boundaries where they hinder polarization reversal by pinning the domain walls. In SBT it appears that there are no mobile charged species in the perovskite-like layers where most of the ferroelectric polarization occurs. The following section summarizes the experimental evidence that supports the above model. The experimental data are depicted in (3) and (4).

THE EXPERIMENTAL EVIDENCE

Tantalum and niobium have very similar chemical behavior. They have the same dominant oxidation state, +5, and due to the Lanthanide Contraction have virtually identical ionic radii. The major difference is that Ta^{+5} is more difficult to reduce than Nb^{+5} as is expected for the heavier member of the pair. Thus we expect the properties of the isostructural SBT and SBN to be very similar. However, their equilibrium electrical conductivities, measured as a function of oxygen activity at temperatures between 550 and 750°C, are very

different. For undoped SBT there is a broad plateau where the conductivity is independent of oxygen activity, with slight up-turns at both ends. This is typical of acceptor-doped oxides with predominantly oxygen ion conductivity with some contributions at each end due to holes created by oxidation and electrons due to reduction, e.g. Y-doped ZrO_2 or Ca-doped CeO_2. Transport number measurements confirm that the broad plateau is due to ionic conduction. On the other hand, in SBN the conductivity rises with reduction from pure oxygen with a log-log slope of -1/4, indicative of an increase in the electron concentration due to reduction in a region where excess donors are compensated by ionic defects, most likely strontium vacancies. At lower oxygen activities the conductivity becomes independent of oxygen activity indicating that electrons have taken over the task of charge compensation. Thermopower measurements confirm that the conduction is n-type.

The addition of 1% acceptors to SBT enhances its acceptor-doped behavior, while the addition of 1% donors substantially reduces it, without changing the general shape of the conductivity profiles. This indicates that the addition of 1% donors is insufficient to overpower the acceptor-doped behavior of SBT. Similarly, the addition of 1% acceptors and donors to SBN changes the levels of the conductivity profiles without changing their shape. But when 3% donors are added to SBT, the conductivity profile becomes similar to that of undoped SBN, while the addition of 3% acceptors to SBN changes its conductivity profile to the shape seen for undoped SBT. The intrinsic doping levels in the undoped oxides appear to be about 1.5% excess acceptors in SBT, and 1.5% excess donors in SBN. This is far in excess of any reasonable level of accidental impurities, or of compositional error. Thus the apparent dopant concentrations in the nominally undoped oxides are attributed to the misplaced cations not being entirely self-

compensating. The two oxides actually have very similar behaviors but are displaced laterally along the doping line. In undoped SBT the ionic conductivity in the Bi-layers is dominant, while in undoped SBN the n-type electronic conductivity in the perovskite-like layers prevails. This is not entirely unexpected. Since Ta^{+5} is less easily reduced than Nb^{+5}, Ta compounds are expected to have larger band gaps than Nb compounds, and trapping levels are thus expected to be deeper in Ta compounds. This is seen to be the case in Ta_2O_5 as compared to Nb_2O_5.

If there were little temperature dependence to the electron mobility then the conductivity in the region of compensation of donors by electrons should be independent of temperature. However, it is observed that the conductivity is highly thermally activated in this region with an activation energy of near 2 eV in SBN. This seems most likely to reflect a very low, thermally activated electron mobility. Extrapolation down to device application temperatures leads to incredibly low levels of n-type conductivity. With the ionic conductivity confined to the Bi-layers, and the electrons being extremely immobile in the perovskite-like layers where most of the ferroelectric response resides, there are no mobile species that can migrate to domain walls and trap their motion, which would lead to polarization fatigue.

REFERENCES
1. A. D. Rae, J. G. Thompson and R. L. Withers, *Acta Crystallogr.*, Section B, 48, 418-28 (1992).
2. S. M. Blake, M. J. Falconer, M. McCreedy and P. Lightfoot, *J. Mater. Chem.*, 7 [8], 1609-13 (1997).
3. A. C. Palanduz and D. M. Smyth, *J. Europ. Ceram. Soc.*, 19, 731-35 (1999).
4. A. C. Palanduz and D. M. Smyth, submitted to *J. Electroceram.*

Structure and Ferroelectric Properties of Bismuth-Layer-Structured Ferroelectric Single Crystals

Hiroshi Irie, Masaru Miyayama[*] and Tetsuichi Kudo[*]

Research Center for Advanced Science and Technology (RCAST), The University of Tokyo, 4-6-1 Komaba, Meguro-ku, Tokyo 153-8904, Japan
Fax: 81-3-5452-5300, e-mail: irie-hrs@imat.chem.t.u-tokyo.ac.jp
Department of Applied Chemistry, School of Engineering, The University of Tokyo, 7-3-1 Hongo, Bunkyo-ku, Tokyo 113-8656, Japan
Fax: 81-3-3818-0284, e-mail: tmiyaya@hongo.ecc.u-tokyo.ac.jp, kudo@iis.u-tokyo.ac.jp

Ferroelectric properties along the a(b)-axis and the c-axis in single crystals of various bismuth-layer-structured ferroelectrics (BLSFs) were investigated. By measuring P-E hysteresis curves of BLSFs, values of the saturated remanent polarization and the coercive electric field were found to be related with the Curie temperature and the number of RO_6 octahedra (m) between bismuth layers, respectively. The saturated remanent polarization was larger in the BLSF with a high Curie temperature. This is attributed to a large atomic displacement with a high Curie temperature. In contrast, the saturated coercive electric field was smaller in the BLSF with a large number of m. This phenomenon is assumed to be caused by the decrease in the strain energy of the octahedra from the bismuth layer, which leads to easy movement of the octahedral cations in the direction of an applied external electric field.

1. INTRODUCTION

Bismuth-layer-structured ferroelectrics (BLSFs) have a crystal structure in which bismuth oxide layers ($(Bi_2O_2)^{2+}$ layers) are interleaved with pseudo-perovskite blocks along the c-axis, as shown in Fig. 1. The pseudo-perovskite blocks have a formula of $(Me_{m-1}R_mO_{3m+1})^{2-}$, where Me is mono-, di-, or trivalent ions; R is tetra-, penta-, or hexavalent ions, such as Ti^{4+}, Nb^{5+}, and Ta^{5+}; and m is the number of RO_6 octahedra in the pseudo-perovskite block (m = 1, 2, 3, 4, and 5).

Single crystals of $PbBi_2Nb_2O_9$ (PBN), $Bi_4Ti_3O_{12}$ (BIT), $PbBi_4Ti_4O_{15}$ (PBT), $BaBi_4Ti_4O_{15}$ (BBT), $Pb_2Bi_4Ti_5O_{18}$ (P2BT) were grown and their electrical properties measured by Newnham et.al.[2-5], Kim et.al.[6-8], and Yi et.al.[9,10]. Their electrical anisotropy originating from the two-dimensional layer structure have likewise been reported. According to these reports, ferroelectricity in the BLSF arises from the RO_6 octahedra in the perovskite block, and spontaneous polarization takes place mainly in the direction parallel to the bismuth layer (the a- or b-axis).

The authors measured the polarization reversal velocity as a function of electric field along the a(b)-axis in the BLSF single crystals, such as PBN, BIT, PBT, BBT, P2BT, and B2BT, and reported[11] that the polarization reversal velocity decreased with increasing the number of RO_6 octahedra (m) in the BLSFs because of the decrease in the strain energy of the RO_6 octahedra from the bismuth layer. The polarization reversal velocity is the index of an easiness of the polarization reversal, that is, the index of a coercive field, which is one of the most important properties in the ferroelectrics. Therefore, in the present study, the saturated P-E hysteresis curves were measured along the a(b)-axis and the c-axis separately in various BLSF single crystals, as mentioned above, and the relationship between their ferroelectric properties (the coercive field and the remanent polarization) and their structures or Curie temperatures was investigated.
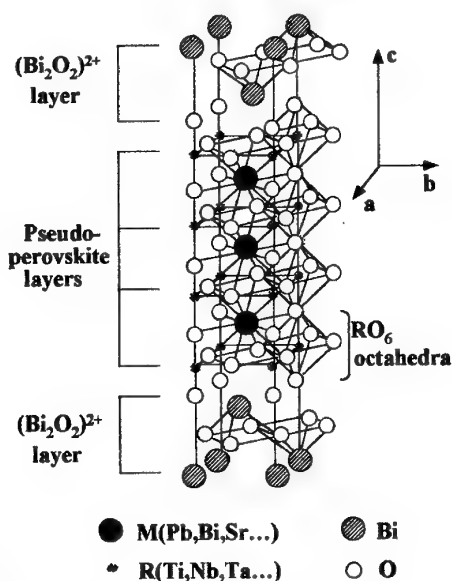
Fig. 1 Schematic illustration showing the crystal structure of BLSF (m=4). One half of the pseudo-tetragonal unit cell.

2. EXPERIMENTAL

2.1 Single-crystal growth

Various single crystals of BLSF as listed in Table I were chosen as samples. Among them, only the BIT single crystal was grown by a flux growth method using Bi_2O_3 as a flux, as it has an incongruent melting point at 1220℃. The other crystals, namely PBN, PBT, BBT, P2BT and B2BT, were grown by a melting-slow cooling method, as these have congruent melting points at 1195, 1200, 1170, 1190 and 1150℃, respectively. Reagent-grade (purity > 99.9%) oxides of component atoms except $BaCO_3$ as starting materials were ball-milled for 16 h with ZrO_2 balls as a milling medium in a polyethylene bottle, and packed into a double platinum crucible to prevent volatilization of Bi_2O_3 and PbO components. In order to obtain a vertical temperature gradient as suggested by Morrison[12], the crucible was set in a vertical tube furnace, the temperature of which was monitored with two thermocouples positioned at the upper and lower parts of the crucible. The samples were heated to 1250℃ at approximately 300℃/h, maintained at that temperature for 4 h, and cooled at a rate of 4℃/h to 950℃, keeping the vertical temperature gradient of 2-3℃/mm. Single crystals obtained by these methods were plate like thin sheets (~ 0.2 mm).[2-10]

Table I   BLSF samples used in the present study

m	Compound	Abbreviation	Curie temperature/℃
2	$PbBi_2Nb_2O_9$	PBN	560
3	$Bi_4Ti_3O_{12}$	BIT	676
4	$PbBi_4Ti_4O_{15}$	PBT	570
	$BaBi_4Ti_4O_{15}$	BBT	395
5	$Pb_2Bi_4Ti_5O_{18}$	P2BT	310
	$Ba_2Bi_4Ti_5O_{18}$	B2BT	325

2.2 Characterization of single crystal

Phase identification of the single crystals was performed using an X-ray diffractometer (Model PW-1729, Philips) after pulverizing the single crystals. Characterization of single crystals was performed by a Laue camera.

2.3 P-E hysteresis curve measurement

Samples for measuring P-E hysteresis curves were obtained by the following processes. The desired segment was cut from the obtained plate-like single crystals by scribing and breaking or by means of an abrasive wire saw. Ag conductive resin was applied to the segment on the a(b)-c plane when measuring the P-E hysteresis curve along the a(b)-axis or on the a-b plane along the c-axis.

The P-E hysteresis curves were measured by an RT6000HVS (Radiant Technologies, Inc.) in a silicone oil bath at room temperature and 110℃.

3. RESULTS

3.1 Characterization of single crystal

Each powders prepared by pulverizing of as-grown single crystals was identified to have a single phase using an X-ray diffractometer. A back-reflection Laue pattern, the symmetry and the spread of diffraction spots, taken by the incident beam perpendicular to the plate surface revealed that the plate surface corresponded to the c-axis.[6-10]

3.2 P-E hysteresis curve measurements

Figures 2(a), 2(b), 2(c), and 2(d) show the saturated hysteresis curves along the a(b)-axis at room temperature for the BIT, BBT, B2BT, and P2BT single crystals, respectively. However, the saturated ones in the PBN and PBT single crystals were failed to measure because of the structural matter discussed later or of the deficiencies caused by Pb volatilization during crystal growth. Figure 3(a) shows the saturated hysteresis curves along the c-axis at room temperature for the BIT, B2BT, and P2BT single crystals. Compared with the a(b)-axis, these remanent polarizations and coercive fields are smaller. Figure 3(b) shows the hysteresis curves along the c-axis at room temperature for the PBN, PBT, and BBT single crystals. The P-E relations showed linearity, which means there are no polarizations along the c-axis in these compounds.
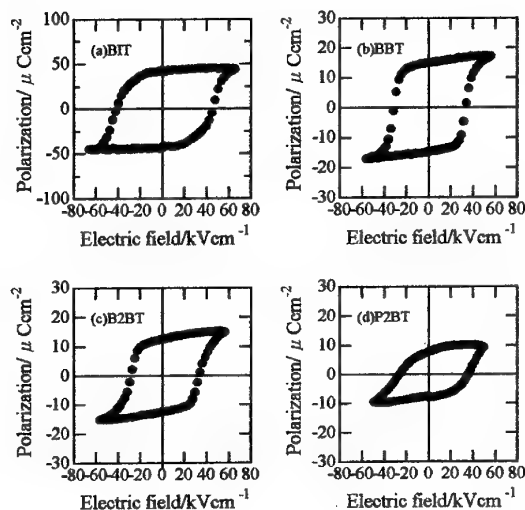
Fig. 2 P-E hysteresis curves for (a) BIT, (b) BBT, (c) B2BT, and (d) P2BT single crystals at room temperature along the a(b)-axis.

4. DISCUSSION

According to Cummins et.al.[13], the spontaneous polarization vector in BIT lies in the orthorhombic a-c plane at an angle of less than 5° from the a-b plane. Therefore, the remanent polarization and the coercive field along the c-axis are smaller than those along the a(b)-axis because polarization reversal takes place by 'rocking' up to approximately 10° of the spontaneous polarization vector. This theory can be applied to the other BLSFs. Therefore, in BLSFs, the remanent polarizations and the coercive fields along the c-axis were smaller than those along the a(b)-axis.

According to Newnham et. al.[2], there is no spontaneous polarization in the direction perpendicular to the bismuth layer (the c-axis) in compounds having the perovskite block with an even number of RO_6 octahedra, due to mirror symmetry; however, a small degree of spontaneous polarization could be observed in compounds having the perovskite block with an odd number of RO_6 octahedra below the Curie temperature. Results in Figs. 3(a) and 3(b) coincided with this theory, that is, there were small degree of the remanent polarizations in the BIT, B2BT, and P2BT single crystals, whereas, there were no remanent polarizations in the PBN, BBT, and PBT single crystals.

Figures 4(a) and 4(b) show the relationship between the ferroelectric properties and the temperature difference between the Curie temperature and the measuring temperature along the a(b)-axis, where Pm, Pr, Em, and Ec are given in Fig. 5. A plot in Fig. 5 is an example of a saturated hysteresis curve. Pr and Pm were larger in BLSFs with a high Curie temperature, as shown in Fig. 4(a). It is assumed to be caused by that ferroelectrics with a high Curie temperature have a large atomic displacement which leads to a large spontaneous polarization. According to Fig. 4(b), Em and Ec were larger in BLSFs
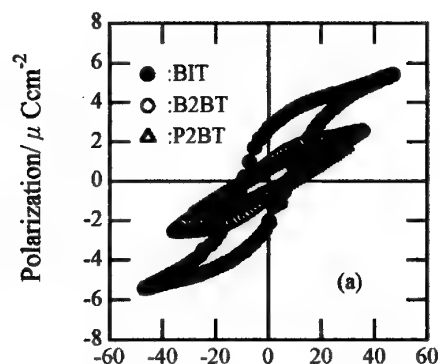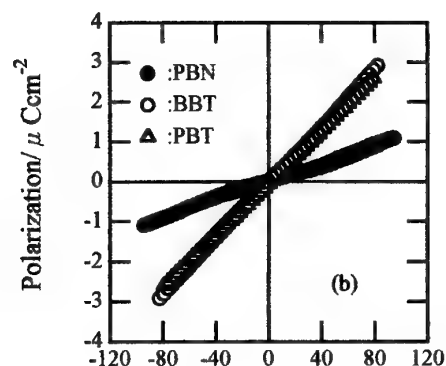
Fig. 3 P-E hysteresis curves for (a) BIT, B2BT, and P2BT, and (b) PBN, BBT, and PBT single crystals at room temperature along the c-axis.
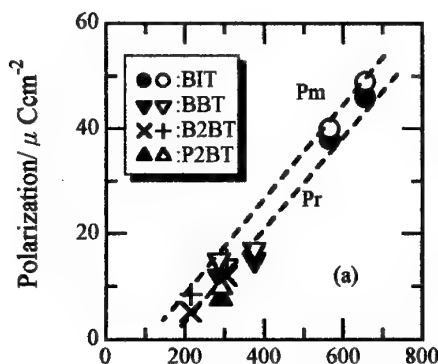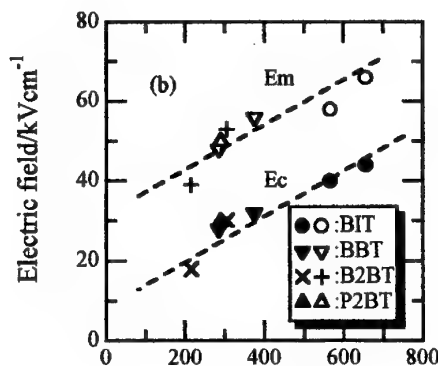
Fig. 4 Relationships (a) between Pm, Pr and Tc-T and (b) between Em, Ec and Tc-T along the a(b)-axis.
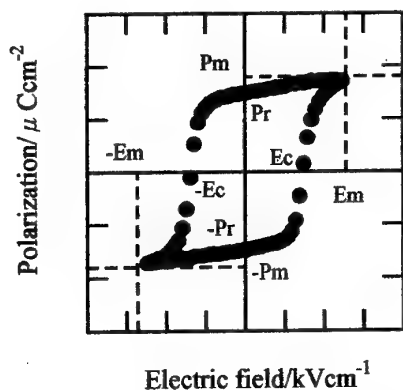
Fig. 5 Locations of Pm, Pr, Em, and Ec.

Fig. 6 Relationship between Em, Ec and m along the a(b)-axis.

with a high Curie temperature, however, this relationship holds true in the BLSFs, for which the saturated hysteresis curves could be measured, such as BIT, BBT, B2BT, and P2BT single crystals. The plots of PBN single crystal, for example, were not on the broken lines in Fig. 4(b). The PBN, whose Curie temperature is 560°C, has more than 80 kV/cm of Em, and the saturated hysteresis curve could not be measured at room temperature. Figure 6 shows the relationship between the electric field (Em and Ec) and the number of RO_6 octahedra (m) along the a(b)-axis at the room temperature. Em and Ec were smaller in BLSFs with the large number of RO_6 octahedra. This would be attributed to that the strain energy of the RO_6 octahedra from the bismuth layer decreases with increasing m and the octahedral cations, which are considered to be the origin of ferroelectricity, can easily move toward the direction of the applied electric field. Consequently, it was found that the number of m contributed to the saturated coercive field.

As mentioned above, it was unable to measure the saturated hysteresis curve along the a(b)-axis for PBN and PBT. This may be due to Pb volatilization during crystal growth or a small number of m (m=2 for PBN). The remanent polarization and the coercive field at room temperature along the a(b)-axis in the PBT (m=4) single crystals were 4 μ C/cm^2 and 50 kV/cm, respectively, under applied electric field of 70 kV/cm, while those in the PBN (m=2) single crystals were 1.1 μ C/cm^2 and 3.5 kV/cm under 70 kV/cm. The Em of the PBN single crystal was more than 80 kV/cm. These results approximately agreed with the tendency observed in Fig. 6.

Along the c-axis, the BLSFs with an odd number of RO_6 octahedra have the same relationships, that is, Pr and Pm were larger in BLSFs with the high Curie temperature, and Em and Ec were smaller with the large number of m.

5. CONCLUSIONS

By measuring the P-E hysteresis curves in various BLSFs, it is concluded that the saturated remanent polarizations was larger in BLSFs with a high Curie temperature because of a large atomic displacement in BLSFs with a high Curie temperature. It is also concluded that the saturated coercive electric field was smaller in BLSFs with a large number of m. This phenomenon is assumed to be caused by the decrease in the strain energy of the RO_6 octahedra from the bismuth layer, which leads to easy movement of the octahedral cations in the direction of an applied external electric field.
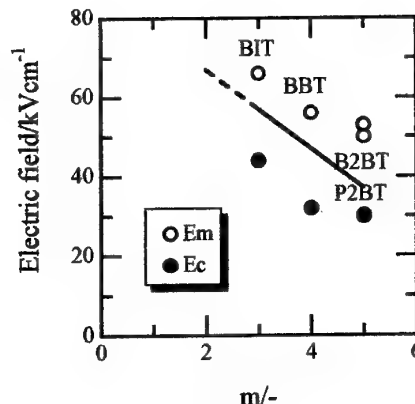
REFERENCES

1) B. Aurivillius, *Arkiv Kemi*, 1, 463-512 (1949).
2) R. E. Newnham, R. W. Wolfe and J. F. Dorrian, *Mater. Res. Bull.*, 6, 1029-1040 (1971).
3) R. E. Newnham, R. W. Wolfe, R. S. Horsey, F. A. Diazz-Colon and M. I. Kay, *Mater. Res. Bull.*, 8, 1183-1196 (1973).
4) J. F. Dorrian, R. E. Newnham and D. K. Smith, *Ferroelectrics*, 3, 17-27 (1971).
5) R. A. Armstrong and R. E. Newnham, *Mater. Res. Bull.*, 7, 1025-1034 (1972).
6) S. K. Kim, M. Miyayama and H. Yanagida, *J. Ceram. Soc. Jpn.*, 102, 722-726 (1994).
7) S. K. Kim, M. Miyayama and H. Yanagida, *J. Ceram. Soc. Jpn.*, 103, 315-318 (1995).
8) S. K. Kim, M. Miyayama and H.Y anagida, *Mater. Res. Bull.* 31, 121-131 (1996).
9) I. S. Yi and M. Miyayama, *Jpn. J. Appl. Phys.*, 36, 1321-1324 (1997).
10) I. S. Yi and M. Miyayama, *J. Ceram. Soc. Jpn*, 106, 285-289 (1998).
11) H. Irie, M. Miyayama and T.Kudo, *Jpn. J. Appl. Phys.* (in press)
12) A. D. Morrison, *Ferroelectrics*, 1, 75-78 (1970)
13) S. E. Cummins and L. E. Cross, *J. Appl. Phys.*, 39, 2268-2274 (1968).

Commonalities of the influence of lower valent substitutents on PZT

Dwight Viehland

Naval Sea Command, Code 2132, Newport, RI 02841
Fax: 401-832-6401; e-mail: ViehlandD@Npt.NUWC.Navy.Mil

Abstract

Studies of the structure-property relations of lead zirconate titanate (PZT) modified with lower valent substitutions on the A- and B-sites have been performed as a function of dopant concentration. These investigations have yielded common changes induced by these substitutions on ferroelectric phases. The commonalities are the presence of fine domains and polarization pinning effects.

I. Introduction

Piezoelectric resonators and transducers are one of the most important applications of lead zirconate titanate (PZT) ceramics. One of the unique physical characteristics which makes PZT an excellent material for these applications is that it can be made electrically "hard" to polarization switching by appropriate compositional modifications. In addition, "hard" PZTs have high mechanical quality factors. An interaction between impurities and domain boundaries is believed to be the origin of the "hard" switching characteristics.

The effect of various impurities on the mechanical quality factor have previously been studied[1-4]. It is believed that variations of domain mobility due to impurity correlated vacancies are the cause of "hard" PZT behavior. Domain boundary pinning effects have been studied by Postnikov et al[5] using internal friction methods and by Carl and Hardtl[6] using dielectric methods. Furthermore, in recent years, multilayer devices based on morphotropic phase boundary (MPB) compositions of "hard" PZT ceramics have received special attention because of their excellent electromechanical behavior[7-9]. For these multilayer structures, the configuration and interaction of domains with impurities and internal stresses have been reported to significantly influence their electromechanical performance. All of these previous investigations have demonstrated that an interaction between impurities and/or associated vacancies required for charge neutrality with domains is important to the development of "hard" PZT characteristics. However, only limited information concerning the influence of impurities and defects on the structure-property relationships of hard PZT ceramics has been published.

II. Experimental

The PZT compositions studied in this investigation were the rhombohedral-ferroelectric $Pb(Zr_{0.65}Ti_{0.35})O_3$. The substitution of A-site Pb^{2+} ions by K^{1+} and Cs^{1+}, and B-site Zr^{4+}/Ti^{4+} ions by Fe^{3+} were made according to the formulae $Pb_{1-y/2}K_y(Zr_{0.65}Ti_{0.35})_{1-y/4}O_3$ and $Pb(Zr_{0.65}Ti_{0.35})_{1-y}Fe_yO_3$, respectively.

The abbreviations of the modified PZT specimens which will be used in this paper are PMZT 100y/100x/100(1-x), where M represents K, Cs, Fe, La respectively. All starting materials were powders of greater than 99.9% purity. Details of powder processing can be found in a previous publication[13]. Dense ceramic pellets were formed by hot pressing at 1100~1150°C for 2 hours at a pressure of 60 MPa, which was followed by an annealing at 1300°C for 2 hours in a PbO excess environment.

Transmission electron microscopy (TEM) specimens were prepared by ultrasonically drilling 3-mm discs which were mechanically polished to ~100 μm. The center portions of these discs were then further ground by a dimpler to ~10 μm, and argon ion-milled to perforation using a liquid nitrogen cooling stage to minimize induced damage. TEM studies were done on a Phillips EM-420 microscope operating at an accelerating voltage of 120 kV. The P-E behavior was characterized with a computer-controlled, modified Sawyer-Tower circuit using a measurement frequency of 50 Hz.

III. Results

III.1 Dependence of P-E curves on lower valent A-site modification

Figure 1(a) shows the P-E loops for PZT compostions with K^{1+} concentrations of 1 at.% and with various Zr/Ti ratios. Data are shown for PKZT compositions of 1/40/60, 1/52/48, 1/65/35, and 1/95/5. Double-loop-like characteristics are evident in Figures 1(a)-(c) for the tetragonal- and rhombohedral-structured ferroelectric compositions. Double-loop-like characteristics have previously been reported in aged ferroelectric ceramics[10-12], which suggests that the defects required for charge compensation upon K^{1+} modification may pin domain walls and prevent nucleation and growth of domains in the direction favored by an applied electric field. Comparisons of the data in these two figures demonstrates that the coercive field decreases with increasing Zr/Ti ratio. The trends in the double-loop-like characteristics of the P-E data shown in Figure 1(a) suggest that significant changes in domain stability occur in PKZT with changing Zr/Ti ratio.

III.2 Dependence of ferroelectric domain morphology upon lower valent A-site modification

Typical domain morphologies of the rhombohedral-structure PKZT compositional sequence 100y/65/35 are given in Figure 1(b)-(d). Figures 1(b)-(d) show the room temperature bright-field images for the PKZT compositions 0/65/35, 1/65/35 and 4/65/35, respectively. Significant changes in the domain structures can be seen with increasing K-content. For 0/65/35

(Figure 1(b)), normal micron-sized 180° domains can readily be seen, which are typical of a long-range ordered ferroelectric state. The domains are several microns in length and ~0.5 m in width. However, with the addition of only 1 at.% K^{1+}, significant changes in the domain morphology were observed. In Figure 1(c), the size of the domain structures can be seen to be decreased dramatically for 1/65/35, relative to that for 0/65/35. The length of the domains was less than 1 μm and their widths were less than 0.1 μm. In addition, the domain boundaries can be seen to be significantly more "wavy", relative to the nearly straight boundaries found for the lower K-content specimen. With increment in the K-content, the changes in the domain patterns were found to become more pronounced. For 4/65/35, a further decrease in the domain size was observed, as can be seen in Figure 1(d). The lengths of the domains were less than 0.5 μm and their widths were approximately several hundred angstroms. In addition, the degree of "wavy" character in the domain patterns was significantly increased with increasing K^{1+}.

In fact, the waviness was the dominant morphological characteristic of the patterns for 4/65/35. However, it should also be noticed that the domains maintained a significant degree of preferred orientation along a family of crystallographically equivalent polar directions. The waviness in the morphology was due to continuous bending of the domain orientation between various equivalent directions on a length scale of ~0. m. The pinning and bending of domain boundaries can be taken as the reason for the enhancement of electrical switching and the decrease of mechanical loss[13].

The influence of lower valent A-site modifications is further illustrated in Figure 2. This figure demonstrates the influence of Cs^{1+} on the domain structure and P-E behavior. For PCZT 3/65/35, the domain structure can be seen to be highly irregular. The morphologies were "wavy" in character. However, they were larger in size than those for the PKZT composition 4/65/35. large fragmented (indicated by an F) and "wavy" (indicated by a W) domains can be
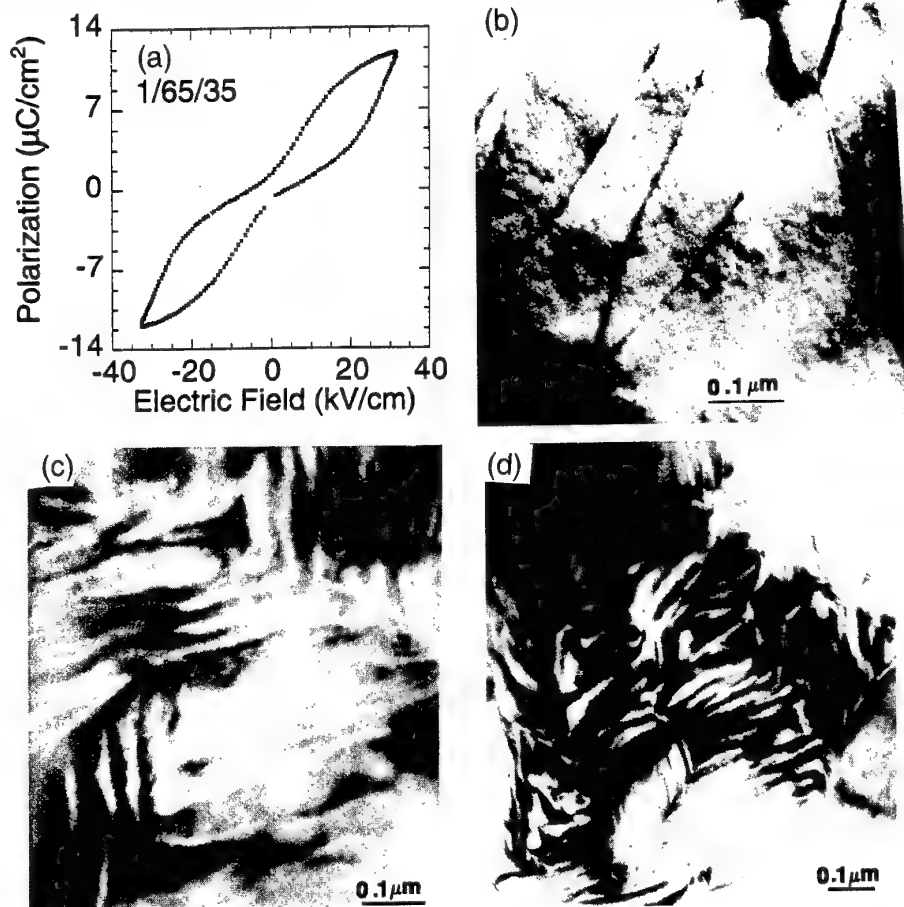
Figure 1   Room-temperature P-E curves and bright-field TEM images for various PKZT compositions. (a) P-E curve for 1/65/35, (b) bright-field image for 0/65/35, (c) bright-field image for 1/65/35, and (d) bright-field image for 8/65/35.
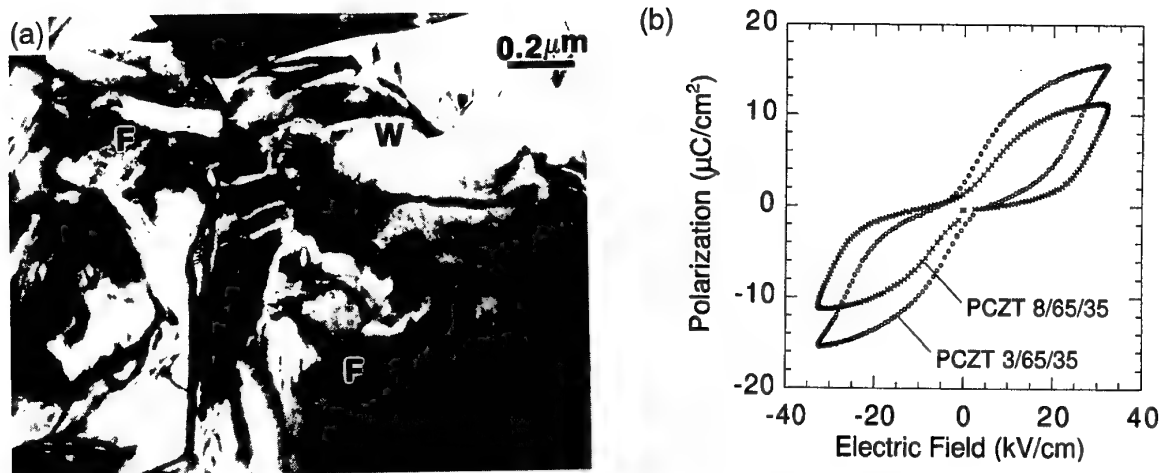
Figure 2   Structure-property relations for cesium modified PZT 65/35 containing 3 at% Cs. (a) Bright-field image, and (b) P-E characteristics.
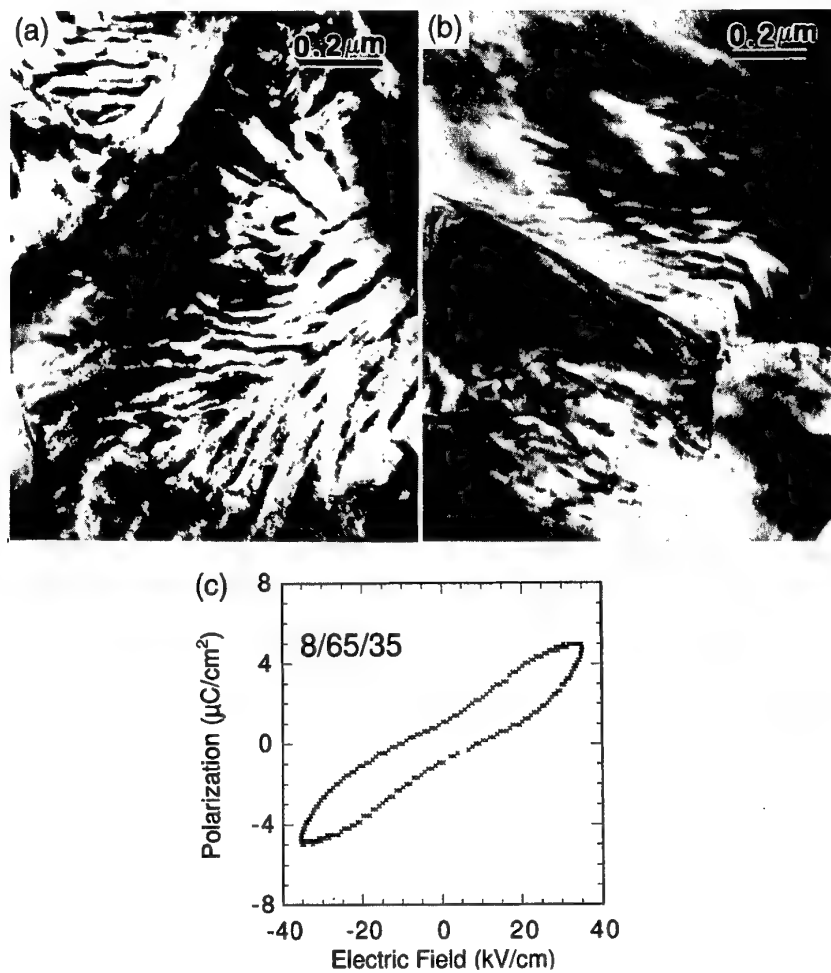
Figure 3   Bright-field TEM images for iron modified PZT 65/35 with various iron concentrations. (a) 3 and (b) 8 at.%

seen to coexist, as shown in Figure 2(a). The domain size and morphology was similar to that observed for PKZT 1/65/35 (see Figure 1(c)). P-E curves for PCZT 3/65/35 and 8/65/35 are shown in Figure 2(b). Double-loop-like characteristics are present, indicating polarization pinning. The degree of double-loop-like characteristics and the coercive field for polarization switching were both increased with increasing Cs^{1+} concentration, however the switchable polarization was decreased. These results indicate that the influence of lower valent A-site modifications is similar for various types of dopants.

II.3 Dependence of ferroelectric domain morphology upon lower valent B-site modification

The effect of lower valent substitutions on the B-site were investigated as a function of Fe^{3+} concentration for PFZT y/65/35. Figures 3(a) and (b) shows bright field images of the domain structures for PFZT 3/65/35 and 8/65/35. Similar "wavy" morphologies can be seen in the domain structures, as for PKZT. However, the decrease in the size of the domains and the increase of the degree of "wavy" character was slower with increasing Fe^{3+} concentration, relative to increasing K^{1+}. Similar double-loop-like P-E curves were also observed, as shown in Figure 3(c) for PFZT 8/65/35.

The changes induced in the domain patterns and P-E behavior with increasing concentrations of lower valent substitutions are similar for substitutions which occur on the A-sites and B-sites. This indicates that generic structure-property changes result in hard PZT behavior. The physical mechanism for this generic behavior is associated with the mobility of oxygen vacancies, which can diffuse to domain boundaries, resulting in polarization pinning.[13,14]

IV. Conclusion

The stability of domains and the polarization behavior have been studied for lower valent modified PZT ceramics as a function of dopant concentration by TEM and modified Sawyer-Tower polarization methods. The modifications investigated were K^{1+} on the A-site, Cs^{1+} on the A-site, and Fe^{3+} on the B-site. Common changes were observed in "hard" PZTs including: (i) the presence of fine domains, and (ii) double-loop like P-E characteristics.

Acknowledgement

References

1. F. Kulcsar,"Electromechanical properties of lead zirconate titanate ceramics with lead partially replaced by calcium or strontium", J. Am. Ceram. Soc., 42, 49 (1059).
2. F. Kulcsar,"Electromechanical properties of lead zirconate titanate ceramics modified with certain three- or five- Valent additions", ibid., 343.
3. S. Takahashi and M. Takahashi, "Efects of impurities on the mechanical quality factor of lead zirconanate titanate ceramics", Jpn J. Appl. Phys. 11, 31 (1972).
4. V.S.Postnikov, V.S.Pavlov and S.K.Turkov, "Internal Friction in Ferroelectrics due to interaction of domain boundaries and point defects", J. Phys. Chem. solids, 31, 1785 (1970).
5. H. Thomann, "Stabilization Effects in Piezoelectric Lead Zirconate Titanate Ceramics", Ferroelectrics 4, 141 (1972).
6. K. Carl and K. Hardt, Ferroelectrics 17, 473 (1978).
7. G. Hartling, "Chemically Reduced PLZT Ceramics for Ultra-High-Displcaement Actuators", Bull. Am. Ceram. Soc., 73, 93 (1994).
8. K. Uchino, "Piezoelectric ceramics in smart actuators and systems", Proc. 1st European Conf. on Smart Structures and Materials, Glassgow, 1992.
9. L.E.Cross, "Boundary Conditions for Shape Memory in Ceramic Material Systems", Journal of Intelligent Materials Systems and Structures 6, 55 (1995).
10. C. R. Griffiths and R. Russell, J. Am. Cer. Soc. 55,110 (1972).
11. G. H. Johker, J. Am. Cer. Soc. 55, 53 (1972).
12. H. Dederichs and G. Arlt, Ferroelectrics 68, 281 (1986).
13. Q. Tan and Dwight Viehland, Influence of lower valent A-site modifications on the structure-property relations of lead zirconate titanate", submitted, (1996).
14. Q. Tan, Z.K.Xu, J.F.Li and D.Viehland, "Influence of lower valent A-site modifications on the structure-property relations of lead zirconate titanate", J. Appl.Phys.81, 532 (1996).

Domain Switching and Rotation
in Soft and Hard PZT Ceramics

Toshio Ogawa
Shizuoka Institute of Science and Technology, 2200-2 Toyosawa, Fukuroi, 437-8555, Japan
Fax: 81-538-45-0154, e-mail: ogawa@ee.sist.ac.jp

Domain switching and rotation in soft lead zirconate titanate (PZT) ceramics were investigated in comparison with those in hard PZT ceramics by measuring the poling field dependence of the dielectric and piezoelectric properties. The minimum dielectric constant (ε r) and maximum frequency constant (fcp) were observed at the coercive fields, which correspond to the poling fields required to obtain the minimum planar coupling factor. These phenomena were due to the $180°$ domain clamping at these fields. The fields of $90°$ ($71°$ or $109°$) domain rotation were estimated using the relationships between the maximum ε r and minimum fcp. While minimum ε r and maximum fcp due to domain clamping were observed in the compositions of tetragonal and rhombohedral soft PZT ceramics, domain rotations which caused maximum ε r and minimum fcp were mainly observed in rhombohedral hard PZT ceramics. It was thought that the reason why domain rotations which caused maximum ε r and minimum fcp were not obtained in soft PZT was the mechanical softness of the ceramics.

1. INTRODUCTION

The degradation of lead zirconate titanate (PZT) thin films due to domain switching and rotation needs to be reduced for their application to ferroelectric random access memory (FRAM) devices. Through the processes employed to develop the materials for FRAM devices, the evaluation and control of domain structures were recognized to be significant. Previously, we had reported on how to evaluate and control the domain structures of PZT ceramics [1-7]. Subsequent to this, we proposed a new concept for domain-controlled ferroelectric ceramics and their devices [8,9]. It was thought that PZT ceramics with different domain structures could be fabricated even when the ceramics had identical compositions. Domain switching and rotation in PZT ceramics can be caused by both mechanical stress and an electric field, because the ceramics possess ferroelastic and ferroelectric properties. Since an electric field affects the dielectric and piezoelectric properties of PZT ceramics by switching and rotating domains, we measured the dependence of these properties on the poling field. In this pursuit, we confirmed, for the first time, that domain clamping affected the dielectric constant and frequency constant in the entire range of compositions of soft PZT ceramics studied. Furthermore, we discuss the difference in the effect of domain switching and rotation on the dielectric and piezoelectric properties between soft and hard PZT ceramics.

2. EXPERIMENTAL

We prepared two kinds of ferroelectric ceramics, namely, soft and hard PZT ceramics. The soft PZT ceramics were composed of $0.05Pb(Sn_{1/2}Sb_{1/2})O_3$-$yPbTiO_3$-$zPbZrO_3$, where y=0.62, z=0.33; y=0.50, z=0.45; y=0.47, z=0.48; y=29, z=0.66 and y=0.20, z=0.75. The hard PZT ceramics consisted of the soft PZT ceramics modified by the addition of 0.4wt% MnO_2 [10], and were investigated in comparison with the soft ceramics. The powders were uniaxially pressed at a pressure of 150MPa, and fired at 1240°C for 2h. The sample disks after firing were 14mm in diameter and 1mm thick. Poling was conducted at 80°C for 30min while varying the poling field (E) from $0 \rightarrow +0.25 \rightarrow +0.5 \rightarrow +0.75 \rightarrow +1.0 \rightarrow \cdots +3.0 \rightarrow 0 \rightarrow -3.0 \rightarrow 0$ to +3.0kV/mm. After poling, the dielectric and piezoelectric properties were measured at room temperature using an LCR meter (HP4263A) and an impedance/gain-phase analyzer (HP4194A).

3. RESULTS AND DISCUSSION

3.1 Dielectric and Piezoelectric Properties

Figures 1 (a)~(c) illustrate the relationships among the composition (z), planar coupling factor (kp), dielectric constant (ε r) and frequency constant (fcp) in soft ($\bigcirc$) and hard ($\bullet$) PZT ceramics, respectively. In this case, the poling was conducted at 80°C for 30min by applying E of +3.0kV/mm. The mechanical quality factors (Qmp) were 70-250 in soft PZT ceramics and 1160-6000 in hard PZT ceramics within the composition range studied. The crystalline phases are tetragonal at z=0.33, 0.45, 0.48 for soft PZT and at z=0.33, 0.45 for hard PZT, and rhombohedral at z=0.66, 0.75 for soft PZT and at z=0.48, 0.66, 0.75 for hard PZT, as evident from Figs. 1 (b) and (c) and the results of X-ray diffraction analyses. The morphotropic phase boundary (M.P.B.) in soft PZT shifted to the lead titanate ($PbTiO_3$) side when MnO_2 was added to form hard PZT. There was a great difference in kp, ε r and fcp between soft and hard rhombohedral PZT in comparison with those of tetragonal PZT.

3.2 Poling Field Dependence

Figures 2 ~ 4 show the effect of E on kp, ε r and fcp at various compositions of z when E was varied from 0 to $\pm$ 3.0kV/mm. In the figures, the open ($\bigcirc$) and closed ($\bullet$) circles correspond to soft and hard PZT ceramics, respectively. From the plot of kp vs E, the fields at which kp was minimum were determined to be coercive fields (Ec).
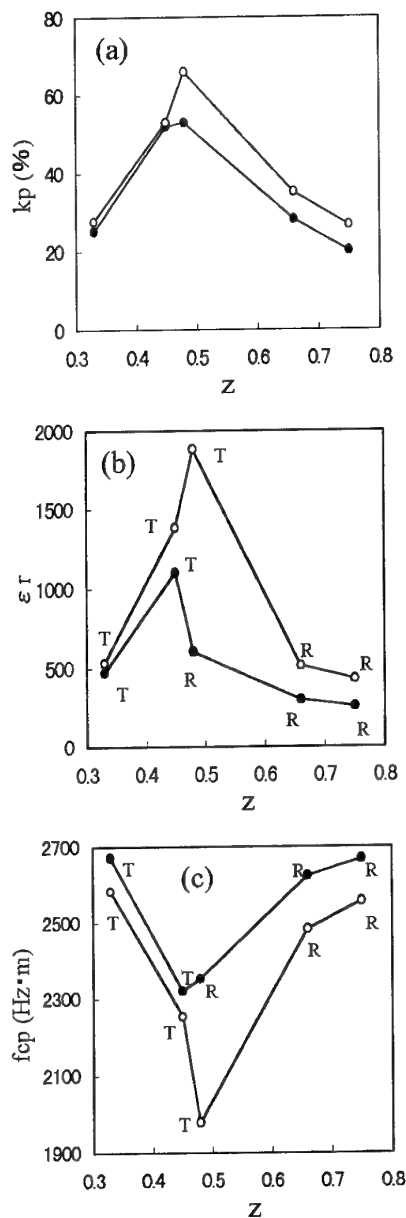
Fig. 1 Composition (z) dependence of (a) kp, (b) ε r and (c) fcp in soft ($\bigcirc$) and hard ($\bullet$) PZT ceramics. T: tetragonal, R: rhombohedral.

Fig. 2 Poling field (E) dependence of (a) kp, (b) ε r and (c) fcp in soft ($\bigcirc$) and hard ($\bullet$) PZT ceramics at z=0.33.

Although kp was minimum at Ec, the poling field dependence of crystal orientations with domains aligned by 90° (71° or 109°) rotation was almost constant near Ec [1,2,5-7]. Therefore, after having fully poled the virgin (as-fired) ceramics, 180° switching was the dominant factor affecting kp for both soft and hard PZT. We believe that the minimum kp owing to electrical domain clamping, such as ↑↓, occurred at the coercive fields. From the plot of E dependence of ε r, ε r was found to be minimum at Ec for all compositions (z=0.33, 0.45, 0.48, 0.66, 0.75) in soft PZT ceramics and in tetragonal (z=0.33, 0.45) compositions in hard PZT ceramics. We observed, for

the first time, that ε r for the entire compositions in soft PZT ceramics was minimal at Ec because of electrical domain clamping. In hard PZT ceramics, while ε r decreased with increasing E (initial poling), it became maximum at E=±0.5kV/mm in rhombohedral phases (z=0.48, 0.66, 0.75). It is thought that the field corresponding to the ε r peak is the threshold field of 71° or 109° domain rotation. From the plot of fcp vs E, fcp was found to be maximum at Ec for all compositions of soft PZT ceramics, and tetragonal (z=0.33, 0.45) and rhombohedral (z=0.48, 0.66) compositions of hard PZT ceramics. That is, when domain clamping (↑↓) occurred at Ec, fcp

(half the bulk wave velocity) increased because the ceramics became mechanically hard. While fcp at these compositions (z=0.33, 0.45, 0.48 ,0.66 on hard PZT) exhibited a peak at Ec, it became minimum at E=± 0.5kV/mm (z=0.75) and at E=± 0.5, -1.75 & +1.5kV/mm (z=0.66) in hard PZT ceramics, as shown in Fig. 4 (c). These fields of minimum fcp were lower and higher than Ec, respectively. Since the decrease in fcp means that the ceramics have become mechanically soft, it was thought that the 71° or 109° domain rotation occurred at the E corresponding to the minimum fcp. From Fig. 4 (c), we could estimate that the poling fields of ± 0.5, ± 1.0 and -1.75 & +1.5

kV/mm corresponded to the first 71° (109°) domain rotation, 180° domain switching and the second 71° (109°) rotation, respectively [5-7].

Figure 5 shows bird's-eyes views regarding E vs ε r vs Z in soft (a) and hard (b) PZT ceramics. While two valleys along Ec were clearly observed in tetragonal and rhombohedral soft PZT ceramics, there were two valleys along Ec in tetragonal hard PZT ceramics. The hills between ± Ec corresponded to the first rotation of 90° and 71° (109°) domains. From the bird's-eyes views, the relationships between poling field, dielectric and piezoelectric properties and composition were clarified.
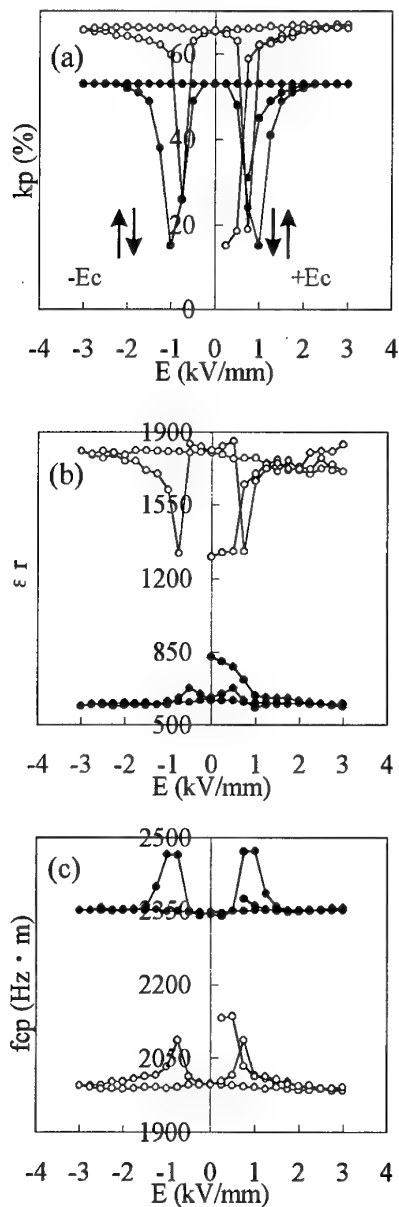
Fig. 3   Poling field (E) dependence of (a) kp, (b) ε r and (c) fcp in soft (○) and hard (●) PZT ceramics at z=0.48.
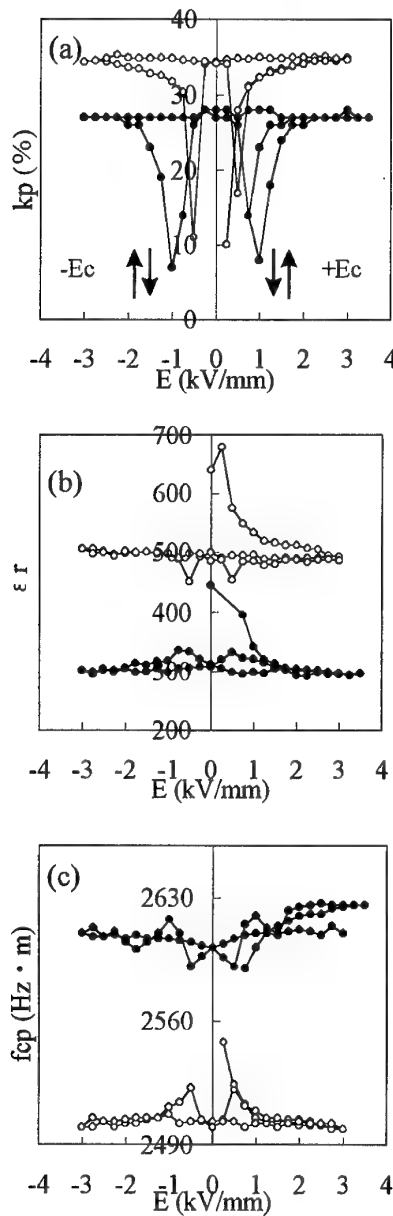
Fig. 4   Poling field (E) dependence of (a) kp, (b) ε r and (c) fcp in soft (○) and hard (●) PZT ceramics at z=0.66.

(a)

ε r

☒ 0-100   ■ 100-200
☐ 200-300   ☒ 300-400
■ 400-500   ☒ 500-600
☒ 600-700   ☒ 700-800
■ 800-900   ☒ 900-1000
☒ 1000-1100 ☒ 1100-1200
■ 1200-1300 ■ 1300-1400
☒ 1400-1500 ■ 1500-1600
☒ 1600-1700 ☒ 1700-1800
☒ 1800-1900 ☐ 1900-2000

$E\ (kV/mm)$

(b)

$E\ (kV/mm)$
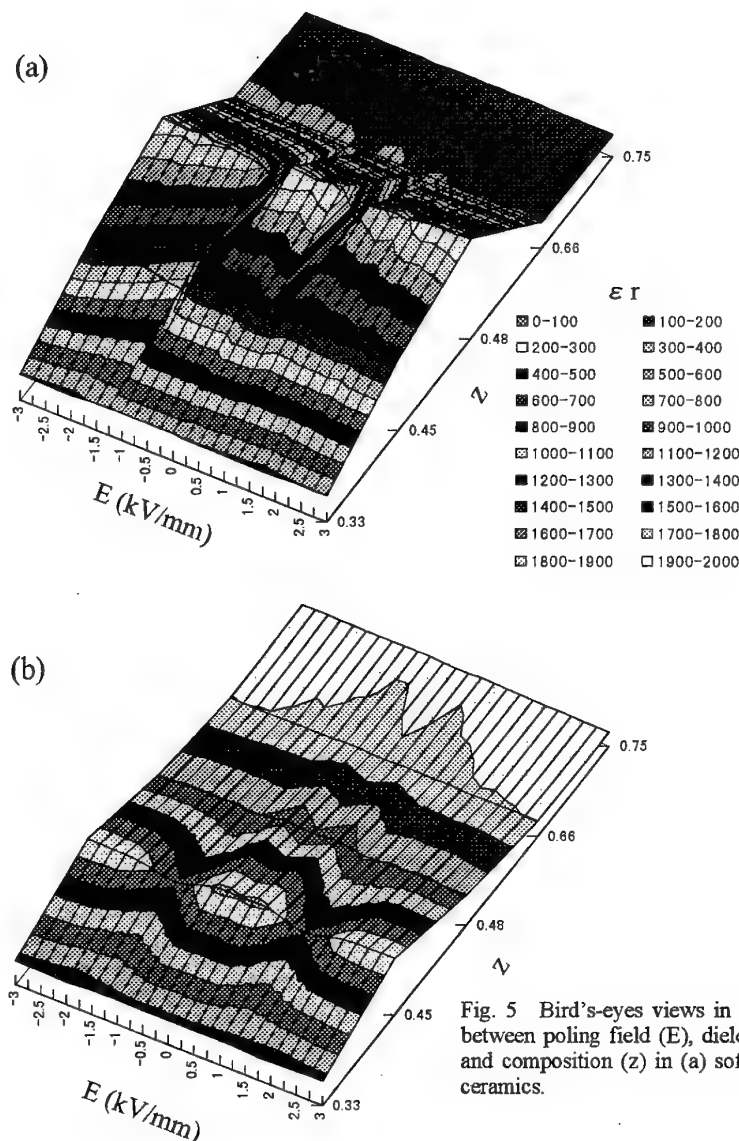
Fig. 5 Bird's-eyes views in case of relationship between poling field (E), dielectric constant (ε r) and composition (z) in (a) soft and (b) hard PZT ceramics.

4. SUMMARY

Poling field dependence of dielectric and piezoelectric properties was investigated in soft PZT ceramics in comparison with those in hard PZT ceramics. The relationships between 180° domain switching, 180° domain clamping, 90° (71° or 109°) domain rotation and dielectric and piezoelectric properties were evaluated.

References

1. T. Ogawa, Y. Takeshita, T. Miyamoto and D.I. Chun, Ferroelectrics, **186**, 119-122 (1996).
2. A. Yamada, Y. K. Chung, M. Takahashi and T. Ogawa, Jpn. J. Appl. Phys., **35**, 5232-5235 (1996).
3. A. Yamada, T. Ogawa, M. Takahashi and Y. K. Chung, Trans. Mater. Res. Soc. Jpn., **20**, 603-606 (1996).
4. A. Yamada, T. Ogawa and Y. K. Chung, Jpn. J. Appl. Phys., **36**, 5958-5962 (1997).
5. T. Ogawa, A. Yamada, Y. K. Chung and D. I. Chun, J. Korean Phys. Soc., **32**, S724-S726 (1998).
6. T. Ogawa and K. Nakamura, Jpn. J. Appl. Phys., **37**, 5241-5245 (1998).
7. T. Ogawa, "9th Cimtec-World Ceramics Congress: Getting into the 2000's", Ed. by P. Vincenzini, Techna Srl, Italy (1999) **Part E**, pp.193-203.
8. T. Ogawa, Ferroelectrics, **169**, 55-62 (1995).
9. T. Ogawa and A. Yamada, "Electroceramics in Japan I", Ed. by N. Mizutani et al., Trans Tech Publications, Switzerland (1998) **Vol. 1**, pp.81-87.
10. T. Ogawa, Ceram. Bull., **70**, 1042-1049 (1991).

Ferroelectricity-Evoking Mass-Inequality Factor
for Perovskite Titanates $ATiO_3$

Tetsuro Nakamura, Yue Jin Shan, Mitsuru Itoh* and Yoshiyuki Inaguma**

Department of Applied Chemistry, Faculty of Engineering, Utsunomiya University,

7-1-2 Yoto, Utsunomiya 321 - 8585, Japan

Fax: 81-28-689-6009, e-mail: shan@cc.utsunomiya-u.ac.jp

*Materials and Structure Laboratory, Tokyo Institute of Technology 4259 Nagatsuta, Yokohama 226 - 8503, Japan

Fax: 81-45-924-5354, e-mail: itoh1@rlem.titech. ac.jp

**Department of Chemistry, Faculty of Science, Gakushuin University,

1-5-1 Mejiro, Toshima-ku, Tokyo 171- 8588, Japan

Fax: 81-3-5992-1029, e-mail: yoshiyuki.inaguma@gakushuin. ac.jp

Physical origin of the displacive type ferroelectricity in perovskite oxides ABO_3 is proposed as mass-inequalities in the TO-modes. Through the analysis of an isolated two-particle harmonic oscillator with the counter masses M and m, we found an additional increase δ in the amplitude of the lighter particle for the case $M > m$, relative to the case $M = m$. Such an additional increase in the amplitude caused by the mass-inequality $M > m$ in a TO-mode must be a driving factor of a displacive type ferroelectric phase transition! Defining a dimensionless mass-inequality factor $f(M/m) = (M-m)\{M(M+m)\}^{-1/2}$ for TO-modes in perovskite titanates $ATiO_3$, we have evaluated this factor for each TO-mode, f_L for Last's mode, f_S for Slater's mode, and f_O for oxygen-octahedron deformation mode. Then, these factors are averaged as overall ferroelectricity-evoking factor F, together with a statistical weights w_L, w_S, and w_O ($w_L + w_S + w_O = 1$), $F = w_L f_L + w_S f_S + w_O f_O$. Finally, some tentative relations T_c versus F are shown for ferroelectric $PbTiO_3$, $BaTiO_3$, and $SrTiO_3^*$.

1. INTRODUCTION

Infrared active TO-modes (transverse optic modes) of a cubic perovskite oxide ABO_3 can be divided into the three component-modes: ① Last's mode (A-BO_3), ② Slater's mode (B-O_3), and ③ Oxygen-octahedron deformation mode (O_I-$2O_{II}$)[1]. It is predicted that a pertinent amount of mass-inequality in the TO-mode gives a so called structural instability, resulting in a displacive type ferroelectric phase transition.

Most theory of the displacive type structural phase transition at least contain the two following assumptions[2, 3]: the one is an imaginary bare soft mode frequency ($\omega_b^2 < 0$) for the TO-mode in question to account for the presence of a structural instability to undergo a ferroelectric phase transition, and the other is a quartic anharmonic couplings with the other modes for giving a temperature dependence to the soft mode frequency ω_{TO}, through the elaborating mathematical expressions.

However, no substantial physical origins of these terms "structural instability" and "quartic anharmonic interactions" have ever been interpreted. Thus, we could not know how to design chemically and synthesize a preovskite oxide having a structural instability with a quartic anharmonicity.

In this paper we will propose that the physical origin of the instability and the softening of the relevant TO-mode comes from its mass-inequality. To show this we will discuss the mass-inequality effect in an isolated classical two particle harmonic oscillator model[4, 5], in stead of discussing it in the multi-coupled oscillator models in the solid state, because it is quite difficult to clarity the effect of mass-inequality on the amplitude of a single TO-mode in the solid state where there are so many couplings among the different modes with different mass-inequalities.

2. MASS-INEQUALITY V.S. AMPLITUDE IN A HARMONIC OSCILLATOR

2.1 Single-particle Harmonic Oscillator Model

For any TO-mode in ABO_3 between the counter masses M and m, its one-dimensional Newtonian equation is given by

$$\mu \frac{d^2\chi}{dt^2} = -C\chi, \qquad (1)$$

where $\chi = \chi_m - \chi_M$ is the relative coordinate, $\mu = Mm$

$/(M+m)$ the reduced mass and C the harmonic constant. Requiring a sinusoidal solution with the angular frequency ω for Eq.(1),

$$\chi = \chi^0 \cos \omega t , \qquad (2)$$

we obtain $\quad C = \mu \omega^2 = \dfrac{Mm}{M+m} \omega^2 . \qquad (3)$

The amplitude of the TO-mode in question χ^0 can be obtained from the equipartition of thermal energy $kT/2$ to each freedom, and a boundary condition (kinetic energy) = 0. This follows that

$$\chi^0 = \sqrt{\frac{2kT}{C}} = \sqrt{\frac{2kT}{\omega^2}} \sqrt{\frac{1}{M} + \frac{1}{m}} \quad . \qquad (4)$$

The amplitude χ^0 has a mass-dependence as indicated in Eq.(4). If the harmonic constant C in Eq.(4) is exactly kept at a constant value, χ^0 is independent of the masses M and m. Then, χ^0 does not change at all as M/m changes. Under this condition, however, if we consider the individual displacements of the oscillating counter masses χ_M and χ_m from their center of gravity, together with their amplitudes χ_M^0 and χ_m^0, we will find an additional increment in the amplitude of the lighter particle χ_m^0 for the case $M > m$ relative to that for the case $M = m$. This is shown in the following section.

2.2 Two-particle Harmonic Oscillator Model[4, 5]

In order to get the correlations of the relative coordinate χ of the two-particles with their individual displacements χ_m and χ_M from their center of gravity, we describe the motions of the two particles with the separate Newtonian equations:

$$m \frac{d^2 \chi_m}{dt^2} = f = -C_m \chi_m , \qquad (5)$$

$$M \frac{d^2 \chi_M}{dt^2} = F = -C_M \chi_M . \qquad (6)$$

where C_m and C_M are harmonic constants. To keep the steady oscillation of the two particles, we put the condition to the forces, $\quad f = -F . \qquad (7)$

Then, we require the solutions of the sinusoidal forms with the opposite phase and the same angular frequency ω for Eqs.(5) and (6):

$$\chi_m = \chi_m^0 \cos \omega t , \qquad (8)$$

$$\chi_M = -\chi_M^0 \cos \omega t . \qquad (9)$$

If follows from Eqs.(5), (6), (7), (8) and (9) that

$$-m \omega^2 \chi_m = f = -C_m \chi_m , \qquad (10)$$

$$-M \omega^2 \chi_M = -f = -C_M \chi_M . \qquad (11)$$

Now, dividing the first and second terms in Eq.(10) by those in Eq.(11), we obtain an important relationship

$$\frac{\chi_m}{\chi_M} = -\frac{M}{m} . \qquad (12)$$

This means that the displacement of the lighter particle χ_m is wider than that of the heavier one χ_M for $M > m$, and their directions are always in the opposite.

From the definitions of χ, χ_m and χ_M, together with Eq.(12), we obtain the relations among the amplitudes:

$$\chi = \chi_m - \chi_M = (\chi_m^0 + \chi_M^0) \cos \omega t = \chi^0 \cos \omega t ,$$

$$\chi^0 = \sqrt{\frac{2kT}{C}} = \chi_m^0 + \chi_M^0 = (1 + \frac{m}{M}) \chi_m^0 = (1 + \frac{M}{m}) \chi_M^0 . \quad (13)$$

Thus, it follows from Eq.(13) that

$$\chi_m^0 = \frac{M}{M+m} \sqrt{\frac{2kT}{C}} , \qquad (14)$$

$$\chi_M^0 = \frac{m}{M+m} \sqrt{\frac{2kT}{C}} . \qquad (15)$$

The amplitudes of the individual particles χ_m^0 and χ_M^0, respectively, show clearly the mass-dependence for a constant C. Figure 1 shows χ_m^0 and χ_M^0 as a function of the mass ratio M/m. χ_m^0 increases from $\chi_m^0 = \chi^0/2$ for $M/m = 1$ up to $\chi_m^0 = \chi^0 = \sqrt{\dfrac{2KT}{C}}$ for $M/m = \infty$, while χ_M^0 decreases from $\chi_M^0 = \chi^0/2$ for $M/m = 1$ down to $\chi_M^0 = 0$ for $M/m = \infty$. Figure 2 shows the individual displacements χ_m and χ_M of the two particles Eq.(8) and Eq.(9), respectively, as a function of time t for both cases $M = m$ and $M > m$. Comparing the case $M > m$ in Fig. 2b with the case $M = m$ in Fig. 2a, we find an additional effective increase in the displacement of the lighter particle χ_m toward the outer space (the shadowed parts in
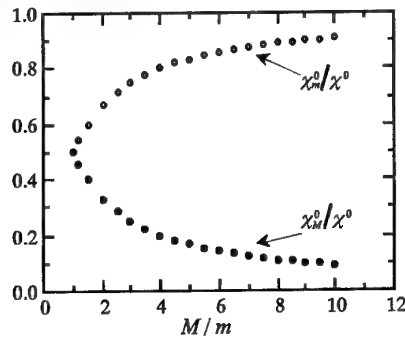
Fig. 1 χ_m^0 vs. M/m and χ_M^0 vs. M/m

Fig. 2b), at the expense of a decrease in that of the heavier particle χ_M, even so we assumed a strict constant C. The additional, effective increase δ in the displacement of the lighter particle χ_m is evaluated from Eq.(14) as follows:

$$\delta = \chi_m^0 (M > m) - \chi_m^0 (M = m)$$

$$= \frac{M}{M+m} \chi^0 - \frac{1}{2} \chi^0 = \frac{\chi^0}{2} \cdot \frac{M-m}{M+m} = \sqrt{\frac{kT}{2C}} \cdot \frac{M-m}{M+m} . (16)$$

The value of $\delta/\chi_-^0 = \frac{1}{2} \cdot \frac{M-m}{M+m}$ is indicated in Fig. 1 as a function of M/m.
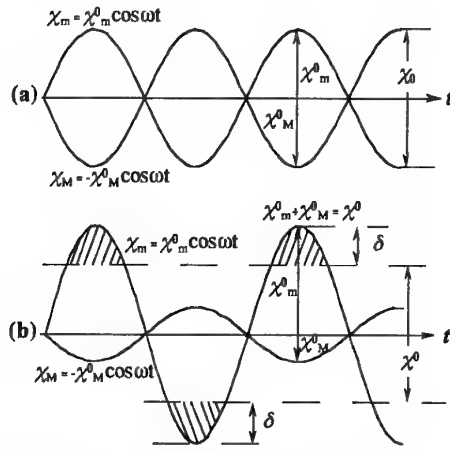
Fig. 2 The effect of mass-inequality on the two-particle harmonic oscillator for (a) the case of equal masses $M = m$. (b) the case of different masses $M > m$. The lighter particle needs a wider space (shadowed area) in oscillation for the case (b) $M > m$, compared with the case of (a) $M = m$.

3. FERROELECTRICITY-EVOKING FACTOR IN PEROVSKITE OXIDE

As is shown in the preceding section, a mass-inequality in an isolated two-particle harmonic oscillator produces an additional increase δ in the amplitude of the lighter particle χ_m. Now, we consider that the above situation is applicable to a ferroelectric TO-mode ($k=0$) in the perovskite oxide ABO_3, although an expected amount of δ in the two-particle harmonic oscillator would be appreciably depressed in the TO-mode of the real solid ABO_3. This depressed amount of δ in the solid state ABO_3 must be preserved as a kind of internal energy with various anharmonic terms in the lattice, contributing to a structural instability or a mode instability in ABO_3. Thus, we consider that the δ caused by mass-inequality in Eq.(16) is the main physical origin of the so called structural instability which can cause to a ferroelectric phase transition.

We have obtained δ in Eq.(16) upon the assumption that C is independent of the masses. However, C has a mass-dependence in Eq.(3). Therefore, we have to correct the mass-dependence of δ. It follows from Eqs.(16) and (3) that

$$\delta = \sqrt{\frac{kT}{2m\omega^2}} \cdot \frac{M-m}{\sqrt{M(M+m)}} \equiv \delta^0 \cdot f(M/m). \quad (17)$$

Here, m is the mass of the lighter particle in the two-particle harmonic oscillator, ω is the angular frequency of the oscillator and δ^0 is the absolute value of the additional

displacement. Now, we define a nondimensional mass-inequality factor,

$$f(M/m) = \frac{M-m}{\sqrt{M(M+m)}} \quad . \quad (18)$$

which can be called as ferroelectricity-evoking factor in occasion of application to the TO-mode in ABO_3.

We will restrict the discussions, hereafter, within the perovskite titanate $ATiO_3$ because it contains several ferroelectric compounds. Table I shows a tentative calculation of the ferroelectricity-evoking mass-inequality factor in Eq.(18) for the component modes of the TO-modes in $PbTiO_3$, $BaTiO_3$, $SrTiO_3$ and $SrTiO_3^*$ where 90% of natural oxygen atoms ^{16}O were replaced by ^{18}O [6]. Since it is supposed that the infrared active TO-modes in $ATiO_3$ are intimately mixed together in the crystal, the overall ferroelectricity-evoking factor F for $ATiO_3$ would be averaged over the three component-modes f_i (i = L, S, O) with an adequit statistical weight w_i:

$$F = \sum_{i=L,S,O} w_i f_i = w_L f_L + w_S f_S + w_O f_O, \quad (19)$$

where $w_L + w_S + w_O = 1$. The statistical weight will be given by

$$w_i = w_i^0 \exp(-E_i/kT), \quad (20)$$

where w_i^0 will be the total mass or the reduced mass of the i-th mode and E_i is the excitation energy of the i-th mode. The values of w_i in Table I were obtained by use of the total mass of the component mode.

Table I. Mass-inequality factor $f(M/m)$ for Last's mode f_L, for Slater's mode f_S, and oxygen-octahedron deformation mode f_O, and their weight factors w_L, w_S, and w_O, respectively in perovskite titanate $ATiO_3$. Here, O* means that 90% of the natural oxygen atoms ^{16}O are replaced by ^{18}O, therefore O* = 17.8 a.u., while O = 15.999 a.u.

$ATiO_3$	$PbTiO_3$	$BaTiO_3$	$SrTiO_3^*$	$SrTiO_3$
T_c / K	763	403	23	—
f_L	0.44429	0.23169	0.09867	0.06217
w_L	0.67811	0.61846	0.54980	0.56052
f_S	0.00193	0.00193	0.07524	0.00193
w_S	0.21450	0.25425	0.29476	0.29285
f_O	0.40825	0.40825	0.40825	0.40825
w_O	0.10710	0.12730	0.15543	0.14663
$F_1 = \sum_i w_i f_i$ Putting $f_L < 0$ for $SrTiO_3$	0.34542	0.19575	0.03138	0.02558
$F_2 = \sum_i w_i f_i$ Putting $f_O < 0$ for all $ATiO_3$	0.25797	0.09185	0.01297	-0.02445

Table I indicates the two kinds of overall ferroelectricity-evoking factors F_1 and F_2. F_1 was obtained by putting f_L

< 0 for Sr-compounds because of their tendency of tilts harmful to the ferroelectric collinear displacements. F_2 was obtained by putting $f_O < 0$ for all $ATiO_3$. Since f_O is a common factor for the perovskite oxides ABO_3, no essential change from the setting $f_L, f_S, f_O > 0$ is expected by this setting.

Figure 3 shows the Tc vs. F_1 and F_2 for ferroelectric
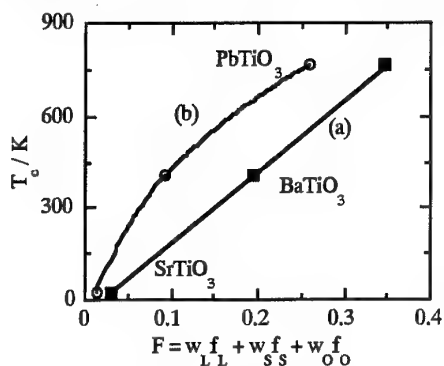
Fig. 3 Curie temperature T_c versus ferroelectricity-evoking factor F for PbTiO$_3$, BaTiO$_3$ and SrTiO$_3$*. (a) T_c vs. F_1, (b) T_c vs. F_2

PbTiO$_3$, BaTiO$_3$ and SrTiO$_3$*. Now, we are searching for the suitable setting of F factor which is consistent with the experimental evidences. In any case, it is among the neighboring [TiO$_6$]-octahedra, which is emphasized that the mass-inequality factor $f(M/m)$ in Eq.(18) is the basic origin of a spontaneous displacement for a TO-mode, and may be applicable to accounting for the displacive type ferroelectric phenomena through a method in Eq.(19) etc.

4. References

1) T. Nakamura, T. Sakudo, Y. Ishibashi and Y. Tominaga, "Ferroelectricity involved in Structural Phase Transition" (in Japanese), Shokabo, Tokyo (1988) p77.
2) M. Tokunaga, K. Fujii and T. Matsubara, *J. Phys. Soc. Jpn.*, **58**[7], 2430-2433 (1989).
3) E. Pytte, "structural Phase Transition and Soft Modes", Ed. by E. J. Samuelsen, E. A. Andersen and J. Feder (Universitetsforlaget, Oslo, 1971) p.133.
4) T. Nakamura, Y-J. Shan, P-H. Sun, Y. Inaguma and M. Itoh, *Ferroelectrics*, **219**, 71-81 (1998).
5) T. Nakamura, Y-J. Shan, M. Miyata, K. Kobayashi, Y. Inaguma and M. Itoh, *Korean J. Ceramics*, **5**[1], 82-86 (1999).
6) M. Itoh, R. Wang, Y. Inaguma, Y-J. Shan and T. Nakamura, *Phys.Rew. Lett*, **82**, 3540 - 3543 (1999).

Dielectric Properties and Depoling Characteristics of $Pb(Zr_{0.05}Ti_{0.05})O_3$ Based Ceramics: Near-Critical Grain Size Behavior

B. A. Tuttle, J. A. Voigt, T. W. Scofield, P. Yang, D. H. Zeuch and M. A. Rodriguez

Sandia National Laboratories, Albuquerque, NM 87185
Fax: 505 844-2974, email: batuttl@sandia.gov

ABSTRACT

Chemically prepared $Pb(Zr_{0.051}Ti_{0.949})_{0.982}Nb_{0.018}O_3$ ceramics were fabricated that were greater than 95% dense for sintering temperatures as low as 925°C. Achieving high density at low firing temperatures permitted isolation of the effects of grain size, from those due to porosity, on both dielectric and pressure induced transformation properties. Specifically, two samples of similar high density, but with grain sizes of 0.7 μm and 6.7 μm, respectively, were characterized. The hydrostatic ferroelectric (FE) to antiferroelectric (AFE) transformation pressure was substantially less (150 MPa) for the lower grain size material than for the larger grain size material. In addition, the dielectric constant increased and the Curie temperature decreased for the sample with lower grain size. All three properties: dielectric constant magnitude, Curie point shift, and FE to AFE phase transformation pressure were shown to be semi-quantitatively consistent with internal stress levels on the order of 100 MPa.

1. INTRODUCTION

Chemical preparation techniques [1] have been developed to fabricate PZT 95/5 ceramics with more uniform and repeatable dielectric properties than ceramics processed using conventional mixed oxide techniques. While a number of authors [2-7] have investigated the properties of PZT 95/5 ceramics, unlike our work, systematic investigation of microstructural effects was not the major purpose of these previous studies. Fritz and Keck [2] have demonstrated that a hydrostatic pressure of approximately 300 MPa is required to transform coarse grain PZT 95/5 based ceramics from the poled ferroelectric (FE) state to the antiferroelectric (AFE) state. The overall decrease in unit cell volume after transformation of approximately 0.7% to 1% for coarse grain mixed oxide ceramics is consistent with the measurements of our study for the chemically

prepared materials. Rietveld analyses of the rhombohedral, ferroelectric phase of coarse grain, chem-prep ceramics similar to those in this study resulted in the following measured lattice parameters: $a = 4.148$Å and $\alpha = 89.74°$. Similar analyses indicated that the lattice parameters for the orthorhombic, antiferroelectric phase of the same composition were: $a = 5.865$Å, $b = 11.746$Å and $c = 8.198$Å. These lattice parameters yield FE and AFE unit cell volumes of 71.32 Å^3 and 70.59 Å^3 or a 1.02% decrease in volume upon transformation. The AFE phase was obtained by grinding the surface of the FE specimen with 600 grit SiC; thus, transforming some rhombohedral ferroelectric phase to antiferroelectric phase of the same Zr to Ti stoichiometry. The AFE unit cell volume was in good agreement with that measured for unstressed, AFE, PZT 98/2 chem-prep ceramics, making appropriate adjustments for the Zr content.

The transformation temperature from the ferroelectric to paraelectric state (Curie point) for these materials is on the order of 225°C. PZT 95/5 based FE materials also exhibit a transformation from a low temperature rhombohedral phase of space group R3c at 25°C to a high temperature rhombohedral ferroelectric phase of space group R3m in the temperature range of 45°C to 70°C, as shown by Dai, Xu and Viehland [6]. El-Harrad and coworkers [7] have investigated phase transformations of La and Nb doped PZT 95/5 materials as a function of temperature using Raman spectroscopy and dielectric property measurements.

2. EXPERIMENTAL PROCEDURE

PZT powders used in this study [1] were synthesized from lead acetate, titanium isopropoxide, and Zr-n-butoxide and niobium butoxide precursors. Agglomeration of the resultant powders was minimized by use of a precipitating solution of oxalic acid and propanol. The easily filterable powders of related batches exhibited a very uniform particle size after calcination with mean particle size of

1.5 μm and crystallite sizes on the order of 60 nm. The powders in this study contained 6 mol% excess Pb and were calcined at the relatively low temperature of 775°C for 8 hours to enhance densification at low firing temperatures (below 1100°C). Powder compacts were formed by uniaxial pressing at 2.75 MPa followed by iso-pressing at 200 MPa resulting in green densities of approximately 58%. Firing conditions of 925°C and 1200°C for a 1.5 hour soak time, using PZT 95/5 atmosphere control powder, were used to densify the two different samples to densities of 97.4% and 96.0%, respectively. While the 925°C sample had 2.7 weight percent excess PbO compared to the expected stoichiometric level, the sample fired at 1200°C was within 0.5 weight percent of the expected stoichiometry.

A JSM-6400XV SEM was used to determine grain size from both polished and fractured specimens. Fracture specimens of both the 925°C and 1200°C sample were investigated. For the 1200°C ceramic, a polished specimen was fabricated by sequential polishing with a final 0.05 μm alumina abrasive treatment. The sample was then annealed at 950°C for 1 hour and then subjected to a 10 second etch using 600:11:1 deionized water:HCl :HF etchant. The difference in the measured grain size of the fractured surface versus the polished surface was less than 20%. Dielectric test samples were surface polished to 3 μm diamond finish and then sputter deposited with 20 nm Cr// 100 nm Au electrodes to the edge of the samples. Dielectric hysteresis measurements were made with a Radiant Technologies RT6000HVS ferroelectric test system at 2 Hz frequency using a single cycle waveform. Hydrostatic depoling measurements were made with a stress application rate of 10.3 MPa/sec using Isobar H fluid as the pressure transmission medium. Integration of charge released from the poled ferroelectric sample during the application of pressure was obtained using a large value capacitor (roughly 20 μF) in series with the test specimen. Samples were poled at 30 kV/cm for 10 seconds at 25°C and then subjected to a single shot dielectric hysteresis measurement using a 0.03 Hz field before hydrostatic depoling.

3. RESULTS AND DISCUSSION

The dielectric hysteresis loops of the 925°C and 1200°C samples measured at 2 Hz are shown in Fig. 1. Remanent polarizations of 28 μC/cm^2 and 14 μC/cm^2 were obtained for the two samples. The decrease in polarization and the increase in coercive field of the fine grain sample are both consistent with inhibited switching of ferroelectric domains in ceramics with grain size that are near that of the critical grain size. Our previous studies [8] using transmission electron microscopy analyses indicate a critical grain size for 71° and 109° domain formation on the order of 0.3 μm for these chemically prepared PZT 95/5 materials. The decrease in remanent polarization leads to a decrease in the piezoelectric d$_{33}$ coefficient from 70 pC/Nt down to 31 pC/Nt.
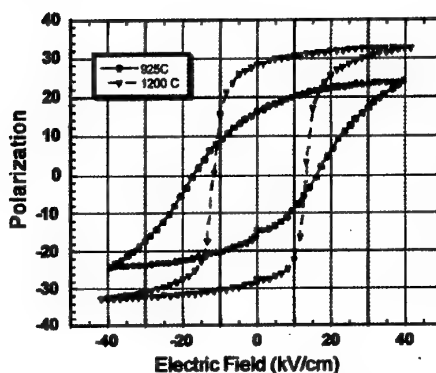
Fig. 1. Dielectric hysteresis characteristics of 925°C and 1200°C samples

Interestingly, the dielectric constant measured at 1 kHz is substantially higher for the small grain size sample; $K_{33} = 511$ compared to $K_{33} = 335$ for the sample fired at 1200°C. This intriguing result strongly suggests that the higher volume fraction of PbO-rich second phase in the fine grain sample is not having a significant dilution effect on dielectric properties. We attribute this increase in dielectric constant to the enhancement of internal stress in the fine grain material, similar to that observed by Buessem, Cross and Goswami [9] for barium titanate. The enhanced internal stress was proposed to minimize the spontaneous deformation, effectively leading to compression along the polar c-axis and tension along the a-axes of the average crystallite. Devonshire theory was used to demonstrate that such stress effects could explain the enhancement of the dielectric constant from 2,000 for 10 μm grain size samples to 5,000 for 0.7 μm grain size samples. Similar values of internal stress, 35 MPa to 76 MPa (5000 to 11,000 psi), have been proposed

by Pohanka, Rice and Walker [10] in barium titanate based materials to explain the roughly 62 MPa decrease in strength measured above and below the Curie point.

Hydrostatic depoling curves are shown in Fig. 2 for the small and large grain size samples. Hydrostatic depoling curves exhibit, with increasing hydrostatic pressure, 4 distinct regions: (1) a linear region for which charge released with increased pressure is proportional to the piezoelectric coefficient, (2) a slightly nonlinear region, (3) a highly nonlinear region for which there is rapid transformation from the FE to AFE phase and (4) another slightly nonlinear region that diminishes as grain size becomes smaller over the 900 to 1275°C firing temperature range. The second region is almost nonexistent for the large grain sample compared to the small grain size sample. If the nonlinearity were due to substantial ferroelectric domain rearrangement, we would expect that domain motion would be facilitated in large grain specimens. Thus, large grain specimens would have a more significant nonlinearity in region 2 than small grain specimens. The opposite phenomena has occurred for our data, with the small grain size sample having the slightly nonlinear region 2 extending over a far greater pressure range. The diffuseness of the transformation in this region is consistent with a greater distribution of internal stress within the fine grain specimen. Specifically, localized regions of the FE sample that are under larger effective compressive stress in the polar direction will transform to the AFE phase at lower external applied pressures.
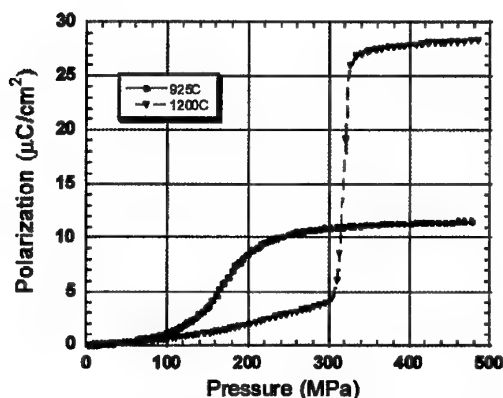
Two other substantial property differences of the two samples are the lower released polarization and the lower transformation pressure of the fine grain sample compared to the large grain sample. As expected, the released polarization values are in reasonable agreement with the remanent polarization values of the two specimens. We have defined the transformation pressure as that hydrostatic pressure for which half of the polarization is released. A substantial decrease in hydrostatic transformation pressure, from 314 MPa to 165 MPa, was observed for the fine grain sample with respect to the large grain sample. We postulate that this decrease is due to enhanced magnitude of internal stress within the samples, similar to the previously described work [9] of the dielectric constant enhancement of fine grained barium titanate ceramics.

Dielectric transformation behavior was characterized to determine if the calculated sign and magnitude of internal stress that could account for the change in Curie point with grain size was consistent with the change in hydrostatic pressure required for FE to AFE transformation. The change in dielectric constant versus temperature behavior in the vicinity of the Curie point is shown in Fig. 3. Data was taken on cooling at a rate of 1°C/min. The smaller grain size material has a significantly lower peak dielectric constant value (8,990 compared to 17,300) and a lower transformation temperature (218.3°C compared to 222.4°C). The width in the transformation peak is consistent with enhanced micro-strain in the finer grain size material. X-ray diffraction profile analysis of the (200) peak of the large and fine grain size samples indicates that beta, which includes effects of crystallite broadening as well as microstrain, has increased from .023 for the large grain sample to 0.073 for the fine grain sample.

Fig. 2. Hydrostatic depoling curves for samples fired at 925°C and 1200°C
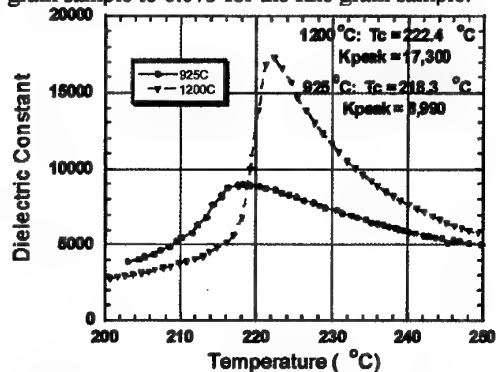
Fig. 3. Dielectric transformation behavior of 1200°C and 925°C samples.

Changes of the Curie point with stress in PZT based materials have been analyzed by Krueger and coworkers [11], Tuttle and Payne [12,13] and Yang [14]. The differential Gibbs free energy under constant electric field conditions is given by

$$dG = - (S_{PE} - S_{FE})\ dT + (V_{PE} - V_{FE})d\pi. \qquad (1)$$

where dG is the change in free energy, S_{PE}, S_{FE} are the entropy of the paraelectric and ferroelectric state, respectively, V_{PE}, V_{FE} are the unit cell volumes of the paraelectric and ferroelectric phases, and $d\pi$ is the change in hydrostatic stress. The change in Curie point with hydrostatic stress, $dT_c / d\pi$ is then given by

$$dT_c / d\pi = (V_{PE} - V_{FE}) / (S_{PE} - S_{FE}). \qquad (2)$$

Thus, as internal stress increases, it is expected that there will be a decrease in the Curie point, since the volume change at the transformation temperature is negative and the entropy change is positive. A value of 0.0683°C / MPa has been measured [14] for PZST 75/20/5 ceramics, for which S corresponds to Sn substitution in the perovskite lattice. Using this difference value of Curie point change with pressure, a decrease in transformation temperature of 10.3°C is calculated; whereas, a decrease of 3.1°C is calculated using the difference value for BaTiO₃. For our samples, an intermediary temperature decrease of 4.1°C in Curie point was measured. Use of the hydrostatic pressure difference of 150 MPa obtained from the depoling measurements is admittedly a rough estimate of the effective internal stress. Considering the complexities of the above factors, our measured change in Curie Point is in order of magnitude agreement with the hypothesis that internal stress phenomena responsible for the decrease in FE to AFE transformation pressure are consistent with the change in Curie point of our chem-prep PZT materials. Experiments to provide more accurate Curie point – hydrostatic stress difference values for our PZT 95/5 ceramics will be undertaken shortly.

4. SUMMARY

We have shown that for PZT 95/5 based ceramics as grain size decreased the changes in three distinct properties were consistent with an enhancement of internal stress. Specifically, the FE to AFE hydrostatic transformation pressure decreased by roughly 150 MPa and the low field dielectric constant increased by more than 50%, as grain size decreased from 6.7 μm to 0.7 μm. Further, the measured Curie point was 4.1°C less for the 0.7 μm grain size sample than for the sample of 6.7 μm grain size. Rough calculation of the change in dielectric transformation temperature with grain size indicated internal stress magnitudes on the order of 70 to 170 MPa in approximate agreement with the 150 MPa difference measured for the hydrostatic transformation pressure.

References

1. J. A. Voigt, D.L. Sipola, B.A. Tuttle, and M. Anderson, U.S. Patent No. 5,908,802, issued June 1, 1999.
2. I. Fritz and J. Keck, *J. Phys. Chem. Solids*, **39**, pp. 1163-67, (1978).
3. D.H. Zeuch, S.T. Montgomery and J.D. Keck, *J.Mater. Res.*, **9** 1322-27 (1994).
4. D.H. Zeuch, S.T. Montgomery and D.J. Holcomb, *J. Mater. Res.*, **14**, 1814-27 (1999).
5. R.H. Dungan and L.J. Storz, *J. Amer. Ceram. Soc.*, **68**, pp. 530-33 (1985).
6. X. Dai, Z. Xu and D. Viehland, *J. Amer. Ceram. Soc'* **8**, pp. 2815-23 (1995).
7. I. El-Harrod, P. Becker, C. Carabatos-Nedelec, J. Handerek, Z.Ujima, and D. Dmytrow, *J. Appl. Phys.*, **78** (9) 5581-91 (1995).
8. B.A. Tuttle, T.J. Headley, C.Drewien, J. Michael, J.A.Voigt and T.J. Garino, *Ferroelectrics*, **222**, 209-18 (1999).
9. W.R. Buessem, L.E. Cross, and A.K..Goswami,, *J. Amer. Ceram. Soc.*, **49** pp. 33-6 (1966).
10. R. C. Pohanka, R.W. Rice and B.E. Walker, Jr, *J. Amer. Ceram. Soc.*, **59** pp. 71-74 (1976).
11. D. Berlincourt, H. Krueger and B. Jaffe, *J. Phys. Chem. Solids*, **25**, 659-74 (1964).
12. B.A. Tuttle and D.A. Payne, *Ferroelectrics*, **37**, 1436-8 (1981).
13. B.A. Tuttle, Ph.D. Thesis, University of Illinois at Urbana-Champaign, 124-8 (1981).
14. P. Yang, Ph.D. Thesis, University of Illinois at Urbana-Champaign, (1992).

Ferroelectricity in SrTi($^{16}O_{1-x}^{18}O_x)_3$

Mitsuru Itoh* and Ruiping Wang

Materials & Structures Laboratory, Tokyo Institute of Technology
4259 Nagatsuta, Midori, Yokohama 226-8503, Japan
Fax: 81-45-924-5354, e-mail: m.itoh@rlem.titech.ac.jp

Quantum ferroelectric SrTi$^{18}O_3$ with $T_c \cong$ 23 K, discovered by present authors, shows interesting dielectric properties in the cryogenic temperature range. Recently, we have succeeded in finding out the existence of a critical composition in partially oxygen-isotope exchanged samples, SrTi($^{16}O_{1-x}^{18}O_x)_3$. The sample with the critical composition shows a dielectric constant of 170000 at ~0K. Dielectric constant of all the samples prepared in the present study, especially sample near the critical composition, show strong dependence on amplitude of ac test signal, which is considered to be correlated to the depinning of the ferroelectric domain walls by the applied ac field.

1. INTRODUCTION

SrTiO$_3$ is one of the most widely studied materials in solid state physics and chemistry. It undergoes a zone boundary phase transition at around 105K [1] and becomes quantum paraelectric [2] at low temperatures. Its dielectric constant perpendicular to c axis increases to about 30000 upon cooling and then remains temperature independent below 3K because of quantum fluctuations. Ferroelectricity can be induced by A-site doping [3,4] or by applying electric field [5], uniaxial stress [6]. Recently, a dielectric constant peak around 23K was found by our group in a 93% oxygen-isotope exchanged SrTiO$_3$ (STO18). Below the peak temperature, a hysteresis loop in D vs E and the splitting of peak below 20 cm^{-1} in Raman spectra was clearly observed, supporting that the dielectric peak corresponds to evolution of ferroelectricity in STO18 [7]. The heat anomaly at 42 K, which was observed by heat capacity measurement for STO18, was conjectured corresponding to a phase transition, leading to the lowering of the crystal symmetry from tetragonal to a lower one. However, the significant difference between the dielectric peak temperature and the heat anomaly temperature is puzzling. The effects of oxygen-isotope exchange on the dielectric behavior of SrTiO$_3$, thus, require to be studied in more detail.

In this paper, we report dielectric behavior of a series partially oxygen-isotope exchanged samples SrTi($^{16}O_{1-x}^{18}O_x)_3$. The existence of a critical concentration was successfully confirmed and the dielectric peak temperature was found to follow the quantum ferroelectric relation well. A dependence of dielectric constant on the amplitude of test signal was observed for all the samples in the present study, which was considered to be correlated to the depinning of the ferroelectric domain walls.

2. EXPERIMENTAL

Single crystal plates of SrTiO$_3$, with edges parallel to pseudocubic [100] directions, were cut from a single crystal lump. They were then polished to optical quality with sizes of about $3 \times 3 \times 0.7$ mm^3. Early experiment has proved that, for dielectric constant measurements, it is necessary to remove the surface stress layers of about 150 μm thickness [8]. To do this, crystals were etched in boiling orthophosphoric acid for about 3 hours to yield crystals with dimensions approximately $2.5 \times 2.5 \times 0.4$ mm^3. Oxygen-isotope exchange was carried out by heating the crystals at 1273 K in $^{18}O_2$ gas (Isotech, Co.). Duration of heating varied from 3 hours to about three weeks according to expected exchange rate x. The final exchange rates were determined from weight increment of the crystals. To ensure homogeneity of the isotope exchange, all the samples (except pure SrTiO$_3$) were vacuum-sealed in quartz tubes and annealed at 1273 K. In this way, seven samples with exchange rate 0%(STO16), 26%(STO18-26), 37%(STO18-37), 45%(STO18-45), 57%(STO18-57), 72%(STO18-72), and 93%(STO18), respectively, were obtained.

Electrodes of gold were prepared by vacuum deposition onto the large faces. The dielectric constant was measured at temperatures 2.2 K $< T <$ 300 K using an HP4284A LCR meter. Raman spectra were recorded by a Jobin-Yvon microscopic laser Raman spectrometer with an Ar coherent light of λ = 514.53 nm at 0.01mw power by means of back scattering. The laser beam size was about 2 μm.

3. RESULTS AND DISCUSSION

Figure 1(a) shows the dielectric constant (ε) vs temperature (T) data measured within 2.2 K < T < 50 K at frequency f = 10 kHz. Amplitude (E_0) of the test signal is 0.04 kV/m. ε of STO16 increases monotonically in a well-known manner [2] down to 4 K and is almost a constant for T < 4 K. The observed value $\varepsilon \cong$ 30000 near 2 K is in well agreement with the early report [2]. When fitting ε vs T data within 20 K < T < 70 K using Barrett-type quantum paraelectric law [9]

$$\varepsilon(T) = A/[(T_1/2)\coth(T_1/2T)-T_0] \qquad (1)$$

best-fit parameters A = 1.29×10^5 K, T_1 = 82 K and T_0 = 32 K are got, which are consistent with A = 9.0×10^4 K, T_1 = 84 K and T_0 = 38 K in previous reaearch [10], indicating the good quality of the sample. Similar to STO16, no ε peak is observed down to the lowest T measured for STO18-26. However, on further increasing exchange rate, ε peaks. The peaks are round for STO18-37, STO18-45 and become sharper for STO18-57, STO18-72, and STO18. The peak temperature T_m shifts to higher T with x in a non-linear manner (Fig. 2(a)), which is very similar to the impurity-concentration-dependence of ferroelectric transition temperature T_c in Ca-substituted SrTiO$_3$

FIG. 2. Variation of dielectric constant peak temperature (a), critical exponential γ (b) versus oxygen isotope exchange rate x. Solid line in (a) is the best fitting line to quantum ferroelectric relation. Solid lines in (b) are the guides to eyes and broken lines show our conjecture (see text).

[3]. Indeed, the T_m follows the law of quantum ferroelectrics [11]

$$T_m = A\,(x-x_c)^{1/2} \qquad (2)$$

well (Fig. 2(a)), with the critical composition x_c = 0.33. The critical exponent γ, which is obtained by fitting ε data on the high T side of T_m to formula

$$\varepsilon = C(T-T_m)^\gamma \qquad (3)$$

is shown in Fig. 2(b). For STO18-72 and STO18, γ is around 1.2. While x_c is approached, either from lower or higher x, γ shows a strong increase. Theoretically it is predicted that, γ equals 2 at the critical point x_c. We consider the strong increase of γ near x_c corresponding to the prediction, as shown in broken lines. It thus seems that we are observing quantum ferroelectric behavior for SrTi(^{16}O$_{1-x}$^{18}O$_x$)$_3$ samples with x > 0.33.

Keeping in mind that a ferroelectric phase transition is commonly accompanied by a structural phase transition, Raman spectrum was investigated from 4 K to room T. In Fig. 3(a), Raman spectra for STO16 and STO18 at 4 K, 10 K and 50 K are shown comparatively. Two intense modes below 20cm^{-1},

FIG. 1. Temperature dependence of dielectric constant ε for SrTi(^{16}O$_{1-x}$^{18}O$_x$)$_3$ with amplitude E_0 of the test signal 0.04 kV/m (a) and 2.3~3.2 kV/m (b), respectively.
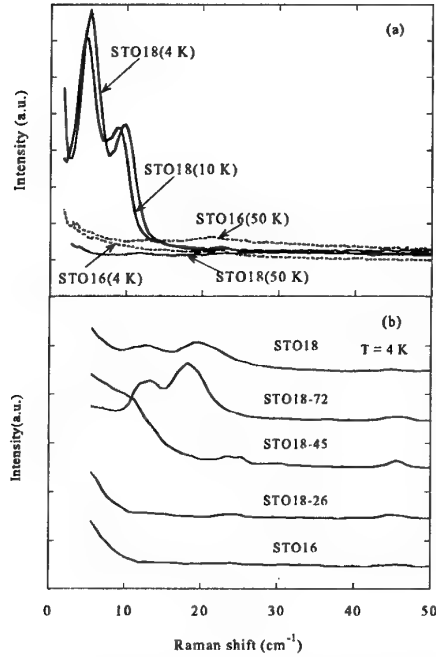
FIG. 3. (a) Raman spectra for $SrTi(^{16}O_{1-x}{}^{18}O_x)_3$ samples at 4 K. (b) Raman spectra for STO16 and STO18 at 4, 10, and 50 K.

FIG. 4. Time dependence of the normalized polarization of STO16, STO18-37 and STO18 after FC (poling field E = 10 kV/m). Measurements were carried out at 5 K (STO16), 6 K (STO18-37), and 21 K (STO18) respectively.

probably correspondent to TO_1 phonon, are clearly observed for STO18, signifying the decrease in crystal symmetry. This decrease in symmetry in the ferroelectric Ca-substituted system has been confirmed by Raman scattering [12]. The two modes are softened with decreasing temperature and disappear at 50 K. In Fig. 3(b), Raman spectra for $SrTi(^{16}O_{1-x}{}^{18}O_x)_3$ samples at 4 K are shown. In contrast to STO16 and STO18-26, whose spectra show almost no structure, the two intense modes are observed in STO18-72. As for STO18-45, though no obvious peaks are detected, via comparing to STO16, change in spectrum is unambiguous. We gauss that, similar to STO18-72 and STO18, TO_1 phonon exists in STO18-45, too. However, the modes are so softened (probably because $T = 4$ K is too near $T_c = 7.8$ K), that they are partly beyond our measurement limit, so the modes could not been observed clearly. Therefore, consistent with the dielectric constant results, Raman scattering supports the evolution of ferroelectricity in $SrTi(^{16}O_{1-x}{}^{18}O_x)_3$ samples with $x > 0.33$. Measurements of D vs E loop and pyroelectricity [13] give the same results.

Fitting ε vs T data of STO18 at the high T range of the peak to formula (1) yields A = 1.2886 $\times 10^5$ K, $T_1 = 87$ K and $T_0 = 44$ K. These parameters are similar to those of STO16, with the subtle difference that the ^{18}O substitution makes $T_1 - 2T_0$

negative, an indicator of ferroelectricity. For other samples, $T_1 - 2T_0$ value decreases with increasing x, yet remains positive. It thus seems that the behavior in intermediately oxygen-isotope exchanged samples is rather complex. To gain a deeper understanding of the nature of the low-T state in partially oxygen-isotope exchanged samples, variation of polarization (P) with time (t) was investigated. After slow cooling the samples in an electric field $E = 10$ kV/m to below T_c, P was measured in zero external field for times up to $t = 10^4$ s at a fixed temperature. The results are shown in Fig. 4. No time dependence of P of STO16 is viewed. However, a long-time exponential relaxation is observed for STO18-37 and STO18, which is typical of glass-like behavior. P decreases by ~20% for STO18-37 and ~14% for STO18 in the time interval of 10^3 s.

It is interesting to notice that, in the T range of several kelvin higher than T_m to the lowest T investigated, ε of the samples depend on the amplitude E_0 of the ac test signal strongly. In Fig. 1(b), ε, measured under $E_0 = 2.3 \sim 3.2$ kV/m, is shown in the same vertical scale as that of Fig. 1(a). Comparing the two figures, several differences are noticed: (1) ε is significantly enhanced by higher E_0. For STO18-37 ε increases from ~ 110000 to ~ 170000 with increasing E_0 from 0.04 kV/m to 2.5 kV/m at around 2 K. (2) T_m, measured under higher E_0, is $2 \sim 3$ K lower than that measured under lower E_0. (3) ε peaks are smeared by higher E_0.

The dependence of ε on E_0 has been reported for the Ca-substituted $SrTiO_3$ with $x = 0.007$ [14]. The domain-wall pinning at spatial fluctuations of the random fields, caused by randomly distributed Ca^{2+}-V_0 centers substituting Ti^{4+}-O^{2-} ion pairs, is

said to suppress the critical divergence of ε at T_c. The depinning of the domain-walls is suggested to be at the origin of the E_0-enhanced ε. Viewing the similarity of the $\varepsilon \sim E_0$ behavior exhibited by the $SrTi(^{16}O_{1-x}{}^{18}O_x)_3$ samples to that by the Ca-substituted $SrTiO_3$, we consider that the E_0-enhanced ε (Fig. 1) correlates to the depinning of the domain-walls, too. However, despite of the similarity of the two systems, the substantial differences between the two systems are worth mentioning: (1) In contrast to the dilute impurity concentration in the Ca-substituted $SrTiO_3$ ($x = 0.007$), the exchange rates in the $SrTi(^{16}O_{1-x}{}^{18}O_x)_3$ samples are rather high in the present study ($x \geq 0.26$). (2) Unlike the Ca-substitution, ^{18}O-isotope-exchange is not expected to give any vacancies and cause random fields. Therefore, the mechanism for the domain-wall-pinning in the $SrTi(^{16}O_{1-x}{}^{18}O_x)_3$ samples is an open question and requires further research.

4. SUMMARY

Measurements of the temperature dependence of the dielectric constant ε showed the existence of an ε peak for $SrTi(^{16}O_{1-x}{}^{18}O_x)_3$ samples with $x > 0.26$. The peak temperature was found varying with ^{18}O composition in a non-linear way, indicating that the ε peaks were caused by a fairly cooperative mechanism rather by impurity effect. Fitting the peak temperature to the quantum ferroelectric relation (formula (2)) yielded a critical concentration $x_c = 0.33$.

Two intense modes were observed by low-temperature Raman spectrum measurement for $SrTi(^{16}O_{1-x}{}^{18}O_x)_3$ samples with $x > 0.26$, further supporting the evolution of ferroelectricity by ^{18}O-isotope exchange at $x > x_c$.

The long-time exponential relaxation reveals a glass-like behavior in the samples, leading us to come to the conclusion that, similar in the case of intermediately doped $KTaO_3$ [15], the low-temperature state in the $SrTi(^{16}O_{1-x}{}^{18}O_x)_3$ samples is probably both ferroelectric and glass-like.

Similar to the Ca-substituted $SrTiO_3$, strong

dependence of ε on amplitude of ac test signal was detected at low temperatures, which is considered to be correlated to the depinning of the ferroelectric domain walls by the applied ac field.

6. REFERENCES

[1] F. W. Lytle, J. Appl. Phys. **35**, 2212 (1964).
[2] K. A. Müller, H. Burkard, Phys. Rev. **B 19**, 3593 (1979).
[3] J. G. Bednorz and K. A. Müller, Phys. Rev. Lett. **52**, 2289 (1984).
[4] C. Ang, Z. Yu, P. M. Vilarinho, and J. L. Baptista, Phys. Rev. **B 57**, 7403 (1998).
[5] P. A. Fleury, J. F. Scott, and J. M. Worlock, Phys. Rev. Lett. **21**, 16 (1968).
[6] H. Uwe and T. Sakudo, Phys. Rev. **B 13**, 271 (1976).
[7] M. Itoh, R. Wang, Y. Inaguma, Y-J, Shan and T. Nakamura, Phys. Rev. Lett. **82**, 3540 (1999).
[8] K. Aso, Jpn. J. Appl. Phys. **15**, 1243 (1976).
[9] J. H. Barrett, Phys. Rev. **86**, 118 (1952).
[10] E. Sawaguchi, A. Kikuchi and Y. Kodera, J. Phys. Soc. Jpn. **17**, 1666 (1962).
[11] T. Schneider, H. Beck, and E. Stoll, Phys. Rev. **B** 13, 1123 (1976); R. Morf, T. Schneider, and E. Stoll, *ibid* **16**, 462 (1977).
[12] U. Bianchi, W. Kleemann and J. G. Bednorz, J. Phys.: Condens. Matter **6**, 1229 (1994).
[13] M. Itoh *et al*, unpublished.
[14] U. Bianchi, J. Dec, W. Kleemann, and J. G. Bednorz, Phys. Rev. **B 51**, 8737 (1995).
[15] W. Kleemann, Inter. J. Mod. Phys. **B 7**, 2469 (1993)

Diffusion of Oxide Ions in Zinc Oxide Ceramics and Thin Films

Hajime HANEDA, Isao SAKAGUCHI, Akio WATANABE, Manabu KOMATSU,
Tsuyoshi OGINO*, Tadashi TAKENAKA**, and Naoki OHASHI***
National Institute for Research in Inorganic Materials, 1-1 Namiki, Tsukuba, IBARAKI 305-0044 JAPAN.
Fax: 81-298-55-1196, e-mail: haneda@nirim.go.jp
*Kyushu University, 6-1 Kasugakoen, Kasuga, Fukuoka 816-8580
e-mail: ogino9@asem.kyushu-u.ac.jp
**Science University of Tokyo, 2641 Yamazaki, Noda, Chiba 278-0022
Fax: 81-23-0856, e-mail: takata@voscc.nagaokaut.ac.jp
***Tokyo Institute of Technology, 2-12-1 Ookayam, Meguroku, Tokyo 152-0033
e-mail: nohashi@ceram.titech.ac.jp

The diffusion characteristics of oxide ions in ZnO were studied to revealed the relationship between the electric properties and defect characteristics. Non-doped single crystals were grown by evaporation. ZnO based ceramics prepared by a hot-isostatic-pressing were used for oxygen diffusion experiment. The thin films, prepared with a RF sputtering method, were also used. The diffusion coefficient was determined by solid-gas exchange, using ^{18}O as tracers. The values of the lattice diffusion coefficients with higher valence dopants compared with zinc ions are greater than lower valence dopant such as lithium ions. Using the data at deeper depth, the grain boundary diffusivities of oxide ions were also evaluated. Although the lattice diffusion coefficients varied by two orders of magnitude, the products of grain boundary width and grain boundary diffusion coefficient were less sensitive to the type of dopants. Thin films had a lot of meta-stable oxygen defects. The characteristics of the sub-grain boundary diffusion were influenced by the Al-donor concentration. The Al 0.3at.% doped-thin films had no preferential diffusion along sub-grain boundaries.

1. INTRODUCTION

Metal-oxide varistors used in surge arresters are ZnO-based ceramic semiconductor devices with highly nonlinear current-voltage characteristics similar to back-to-back Zener diodes, but with much greater current-, voltage, and energy-handling capabilities[1-2]. Such materials are characterized by non-uniform grain size, porosity, second phase distribution, impurity segregation and grain-grain disorientation. The electric properties of ZnO varistors are, furthermore, known to be greatly influenced by the defect chemistry of ceramics.

The intrinsic stoichiometric deviation exists with lattice defects in ZnO. In the case of zinc excess these point defects can be zinc interstitials or oxygen vacancies. In general, diffusion coefficients, and their temperature and dopant dependence permit conclusions with respect to the transport mechanism and thus to the kind of defect structure. If the oxygen vacancy is the dominant defects in zinc excess ZnO, the oxygen diffuses through the oxygen vacancy. In this paper, we focus our attention on attempts to investigate diffusion of oxygen ions in various ZnO-based ceramics. Furthermore, we also examined the oxygen diffusivity along grain boundaries.

2. EXPERIMENTAL PROCEDURE

ZnO based ceramics prepared by a hot-isostatic-pressing technique were used for oxygen diffusion experiment[3]. Precursor powders were 4N-grade(Hakusui Chem. Co. LTD). To clarify the doping effect on the oxygen diffusion, Co-, Mn-, Al- and Li-doped samples were used. The doping amounts were fixed to 0.3 at.%. These powdered were pressed at 30MPa in to discs 12mm in diameter and 6 mm in thickness, and then CIPed at 160MPa. Thereafter they

were presintered in O_2 for 5h at 1250° C. Pores in samples were closed after presintering. These discs were HIPed at 1250° C under a pressure of 130MPa in Ar atmosphere without any capsule because of no open pore, and then annealed in O_2 at 1000° C for 5h. After hipping and annealing, all samples have the porosity under 0.2%, and no-doped sample has a transparent characteristic, which is very favorable to eliminate effects of pore during diffusion experiments. Samples were cut from ceramics into disks shape. One side of the large faces was polished to optical flatness with diamond paste of decreasing particle size (10, 3, 1, 0.5mm).

The depositions of zinc oxides were carried out using a radio frequency magnetron sputtering system with a horizontal substrate holder 3cm away from a sputtering target. The sputtering targets of zinc oxides were fabricated from ZnO powder and Al-nitrate, with some doping levels of aluminum ions, by a conventional ceramic powder processing. The powder mixtures were calcined, and pressed, and then sintered at 1200°C for 24h in air and finally shaping in 7.5cm-diameter. Commercial available polished $Al_2O_3(0001)$ wafers were used as substrates. To get high quality films, we adopted a reverse sputter etching process before deposition. When the chamber was evacuated below 10^{-4} Pa, the substrate was heated to the required temperature. Argon gas was then introduced to a pressure of 1 Pa with desired concentration of oxygen. Film thickness was measured by Dektak 3030 profiler.

Diffusion coefficient was determined by a solid-gas exchange technique[4]. After being cleaned with water, ethanol, acetone, and ethanol, the samples were placed inside a platinum crucible with platinum susceptor in a vessel of a RF furnace. The system was evacuated, and the ^{18}O-enriched oxygen gas with 5kPa

pressure was introduced into vessel that was closed from the gas line. The sample crucible was first heated at 800°C for 15 minutes to maintain the constant concentration at sample surface, and then the temperature was elevated to a desired temperature for isotope exchange. The temperature was monitored by an optical pyrometer. Although the temperature accuracy of pyrometer is in 10K, the temperature variation among samples in a same experimental cycle is believed to be less than few degrees. After isotopic exchange of oxygen between the gaseous phase and the samples during a given time, the furnace was cooled down by switching off the power and ^{18}O-enriched gas was re absorbed back into zeolite storage flask by sold trapping with liquid nitrogen.

The ^{18}O diffusion profiles (concentration versus depth) were measured using a Cameca magnetic sector secondary ion mass spectrometer (SIMS, MS-4f) with ^{133}Cs$^+$ as the primary ions, an accelerating voltage 10kV, and beam current of 5 to 20nA. The samples were coated with Au films of 20nm thickness to maintain the sample surface at constant potential during the SIMS analysis. An electron gun was used as a supplemental neutralizing source. The primary beam scanned at 100μm area, and signals of secondary ions were detected at 40% central square of a sputtered crater. Intensities for the negative ions ^{16}O and ^{18}O were measured as a function of time. The crater depths were measured using a Dektak 3000 profilometer. After a predetermined time of sputtering to eliminate locally the Au film, the concentrations of ^{18}O are converted as a function of depth.

The concentration (c(x,t)) of ^{18}O at any sample depth was determined from the ion intensities:

$$c(x,t) = \frac{I(^{18}O)}{I(^{18}O) + I(^{16}O)} \qquad (1)$$

If the surface is maintained at a constant concentration of ^{18}O, C$_g$, which is the same concentration as in the gaseous phase, and if the concentration in the solid is initially uniform (C(x,0)=C0, natural abundance, 0.204%), the following relation can be used to calculate the diffusion coefficients, D [5]:

$$\frac{c(x,t) - c_0}{c_g - c_0} = \text{erfc}\left(\frac{x}{2\sqrt{Dt}}\right) \qquad (2)$$

Where x is the penetration, t the duration of diffusion annealing, and erfc=1-erf (erf the Gaussian error function).

In the polycrystalline samples, the tracer diffuses deeper inside than expected from the volume diffusion. This is due to the effect of grain boundary diffusion. Le Claire(4) have proposed the relation between the grain boundary diffusion coefficient and concentration at large depth, which is useful in present case. The value of (Dt)$^{1/2}$ was smaller than the grain size, so a product of oxygen grain boundary coefficient, D' and grain boundary width, δ, is evaluated as follows [6]:

$$D' \cdot \delta = 0.66 \ (4D/t)^{1/2}\left[- \frac{\partial \log (c(x))}{\partial x^{6/5}}\right]^{-5/3} \qquad (3)$$

3. RESULTS and DISCUSSION
3.1 Lattice diffusion in polycrystalline samples.

Figure 1 shows a typical depth profile of ^{18}O in a ZnO sample. Lattice diffusion coefficients were obtained, using data near surface(<1000nm) with the Eq.(2). The profile had a long tail. The long tail at deeper depth was not due to the lattice diffusion but might be caused by the diffusion along grain boundaries, seen in Fig.2.

The lattice diffusion coefficients of oxygen ions depended on dopants. The lattice diffusion coefficients were greater in Al-doped samples than in the Li-doped. According to this fact it might be believed that the oxygen ions diffuse with an interstitialcy mechanism as follows,

Interstitialcy model:

$$Li_2O + O_i'' \rightarrow 2Li_{Zn}' + 2O_i^x \qquad (4)$$
$$Al_2O_3 \rightarrow 2Al_{Zn}^· + 2O_0^x + O_i''$$
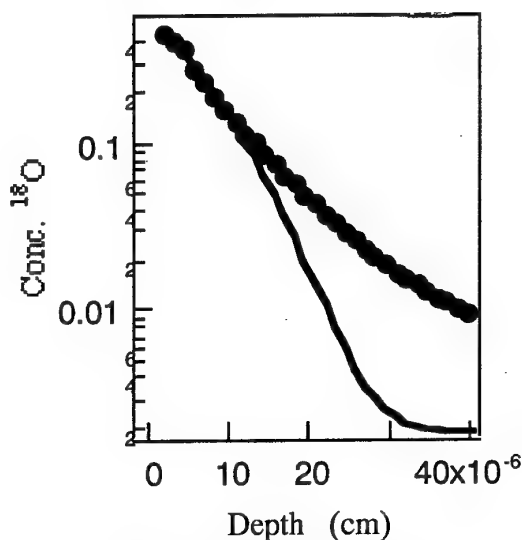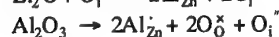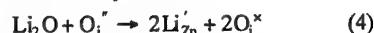
Fig.1. Typical depth profiles ^{18}O in Co-doped ZnO (1330K,3120s). D=1.3x10^{-14} cm^{2}s^{-1}

The activation energies of oxide ion diffusion took about 200kJ/mol of mean value in polycrystalline samples. On the contrary the diffusion coefficients had been lower in single crystal than that of present studies, and the activation energies had been 571kJ/mol[7]. The difference of mechanism caused the discrepancy, and the oxide ions are believed to diffuse through the oxygen vacancy. The mechanism depends on the condition of samples in this temperature range.

3.2 Grainboudary diffusion in polycrystl samples.

As seen in figure 2 of ^{18}O ion image at 2μm depth, the grain boundary network could be observed in pure ZnO. It is considered to be an evidence of contribution of grain boundary diffusion to the long

tail of diffusion profiles. Same high diffusivities paths along grain boundary were appeared in all samples. Using the date at tail parts, one can calculate the products of D' δ with Eq.(3). The range of D' δ is shown in Fig.3., including the range of the volume diffusion coefficients. The variation range of the grain boundary diffusion coefficients was narrower than that for the lattice diffusion, which indicates that the structure of grain boundaries and mechanism for grain boundary diffusion of oxygen ions little depend on the characteristics of the dopants, suggesting that the grain boundary diffusion is mainly controlled by the structure of grain boundaries.
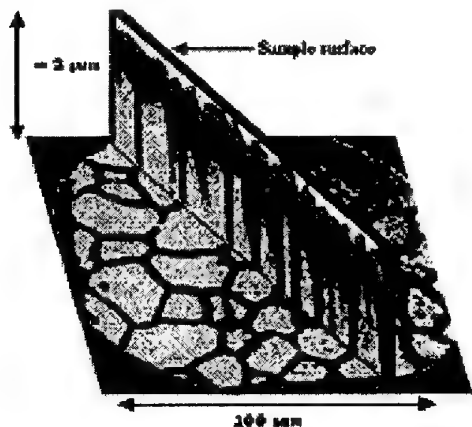
Fig.2. Oxygen 18 3-D distribution in non-doped ZnO after oxygen diffusion annealing at 1243K for 5h.
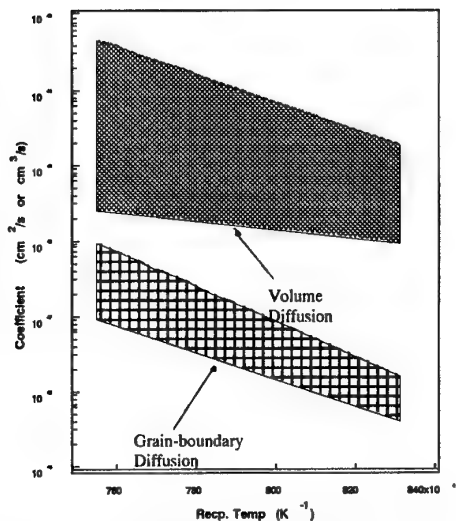
Fig.3. Temperature dependences of grain boundary diffusion coefficients and the volume diffusion coefficients.
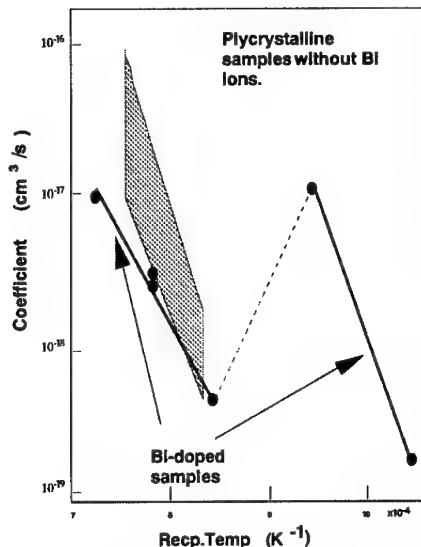
Fig.4. Comparison between the grain boundary diffusion in the samples without Bi ions and that with Bi ions.

3.3 Bi-doping effect.
    The varistor characteristics are very sensitive to the type of dopant, and then is believed to be related with the preferential oxidation at grain boundary. Bi-dopant is well known to give a high non-linearity of V-I characteristics[8], which is caused by the existence of some excess oxygen ions. In the present study, the grain boundary diffusivity drastically changed at a temperature above which the electrical non-linearity was lost. We concluded that the grain boundary structure change to a state without grain boundary electric state above this temperature and the grain boundary diffusion drastically decreased. We believe that this phenomenon is an evidence of structural transition at grain boundaries.
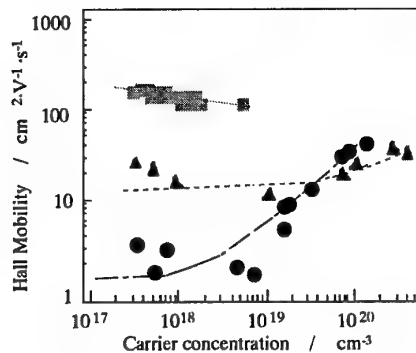
Fig.5. Hall mobilities vs. carrier concentrations in zinc oxide thin films. Rectangulars, single crystals. Closed circles, non-doped thin films. Triangles, Al-doped.

3.4 Diffusivities in thin films.
    The hall mobilities and carrier concentration were evaluated in zinc oxide thin films. Seen in Fig.5., in pure thin films, the mobility was increasing with

increasing carrier concentration, i.e. the sub-grainboundaries were believed to play a role of the scattering centers for electron, i.e. same as the varistor characteristics. However aluminum ions reduced the effect. If the analogy of ceramic varistor could be applied to the case of thin films, the grainboundary diffusivity should be less in Al-doped thin films than non-doped thin films. Fig.. shows a depth profile in non-doped and Al 0.3%-doped thin films. The long tail was observed at deeper region of the non-doped thin films, i.e., the sub-grain boundaries were short circuit of diffusion of oxide ions. On the contrary, the depth profiles were fitted only by contribution of the lattice diffusion in Al-doped thin films. Hence, it is concluded that the sub-grainboundary diffusion coefficients were larger in non-doped thin films than Al-doped.
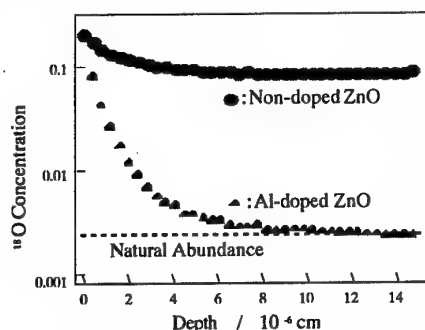
Fig.6. Oxygen 18 depth profiles in Non-doped ZnO and Al-doped(0.3%) ZnO

REFERENCES

[1]   G.D.Mahan, L.M.Levinson, and H.R.Philipp, Appl.Phys.Lett., 33, 80 (1978).

[2] T.K.Gupta, J.Am.Cerm.Soc., 73, 1817 (1990).

[3]   A.Watanabe, H.Haneda, T.Ikegami, J.Tanaka, Y.Moriyoshi, S.Shirasaki, and T.Yamamoto, in "Hot isostatic pressing: theory and applicatons,' ed. by M.Koizumi (Els.Sci.Pub. Essex, 1992), p.105.

[4] Y.Oishi and W.D.Kingery, J.Chem.Phys., 33, 905 (1960).

[5]   J. Crank, in "THE MATHEMATICS OF DIFFUSION,"(Oxford University Press, London, 1957) P.30.

[6] A.D.Le Claire, Brit. J. Appl. Phys., 14, 351-6 (1963).

[7] H. HANEDA, I. SAKAGUCHI, A. WATANABE and J. TANAKA, Diffusion and Defect Forum, 143-147, 1219-24 (1997).

[8] K.Kostic, O.Milosevic, and D.Uskokovic, Sinter' 85 (1985) p.301.

Advance Processing Technology For Piezoelectric Ceramics

Kazuo Miyabe, Kazushi Tachimoto, Kenji Horino, Masakazu Hirose
, Mahoko Takada, Takeo Tsukada, Tomohisa Azuma, Junichi Yamazaki

TDK Corporation, Materials Research Center

570-2, Aza-Matsugashita, Minami-Hatori, Narita-shi, 286, Japan

Abstract-   The demand for the ceramic resonators, which are a key component in many electronic devices, has been increasing every year. Many efforts are being made for miniaturization and improvement of various parameters of the resonators, including high reliability. Generally research and development in this area focuses on the materials improvement, but during these investigations new knowledge of processing technology, like fabrication and lapping etc., can been achieved that brings us close to the good results without coming back the material development. This paper addresses following areas of the processing techniques:

1) Improvement of anti-heat resistant properties of PZT by high temperature poling treatment

2) Improvement of Q_m of PT by N_2 heat treatment. We confirmed that Enhancement of piezoelectric properties are related to the existence of the domain and it's rotation.

3) It is widely believed that the pours and non-homogeneity of the composition in wafers causes a non-uniform charge distribution in the wafers during poling causing spurious mode generation. We have found that the spurious mode occurrence is largely due to minor thickness variations in the substrate.

It is believed that there is still room for improvement in these processing techniques as the further understanding in their relationship to the properties of piezoelectric ceramics is required.

Introduction

At present, many products utilize components made by the piezoelectric ceramics. Most of the products have been around since 1960-70's and are improving continuously. Thanks to the materials research, advance processing technology, and design techniques. The trend is towards miniaturization and operation at higher frequencies.

Researchers have relentlessly investigated the effects of small amount of additives in the ceramic materials in order to improve their piezoelectric properties. Some reports suggested improvement of properties due to sintering and poling conditions such as sintering in O_2, N_2, PbO-atmospheres and HIP. It has been found, as a result of these processes, that the piezoelectric properties increase with the heat treatment in low pressure partial oxygen atmosphere.

With the emergence of new processing technologies, the existing materials and devices are improving and finding new applications in a variety of areas.

In case of resonators, a couple of decades ago, quartz resonators were widely in use, but have now been replaced by ceramic resonators in most applications. Ceramic resonators have dominated the field in the frequencies ranging from 400kHz to 60MHz.

Also, the shapes required by appliance manufacturers have changed from discrete-type to chip-type products. It is important for the chip-type components to maintain high level of temperature stability. Frequency shift due to soldering and heat-shock test cycles are undesirable. It is required that the piezoelectric properties remain unchanged in a wide temperature range.

Until recently PZT resonators were in use but these resonators have a frequency limit as they resonate on their natural (first harmonic) frequency. PT ($PbTiO_3$) resonators have overcome this problem because designed to operate at the 3rd harmonic over-tone mode, which , in turn, makes them useful for high frequency applications.

We have been studying the relationship between ceramic fabrication process and the piezoelectric properties in the modified PZT and PT. We have come to recognize the importance of the processing technology on the piezoelectric properties.

Spurious modes occurrence is one of the significant problems of these resonators. One of the reasons of occurrence of the spurious mode could be due to the pours and non-homogeneity of the composition in the wafers, that causes non uniform charge distribution during poling. Resonator surface vibration contour measurements suggest a clue to this problem. Until about a decade ago precise measurement techniques of vibration in the resonators were not available. The optical fiber interferometric sensing system developed by Dr. Yasuo Hirose is capable of making these tiny vibration measurements with high precision. The main cause of the spurious mode was largely due to minor thickness variations in the substrate.

The aim of this paper is to present details about the processing technology that has significant effect on the piezoelectric materials applications.

1. The development of anti-heat resistance piezoelectric properties in soldering process by

high poling temperature treatment in PZT

The composition of the specimens used in this study was $Pb[(Mg_{1/3}Nb_{2/3})_{0.05}Ti_{0.47}Zr_{0.48}]O_3+CoO$ (0.2wt%)+ $MnCO_3$ (0.2wt%). As shown in Fig.1, the illustration shows poling conditions. Normal poling was carried out by applying a dc field of 3KV/mm for 30min in a silicon oil bath.

High temperature poling was performed under constant current of 2.5mA during cooling from 600 °C to 120 °C.

Table.1 shows the effect of poling condition on the initial characteristics. Kt of both poling conditions was nearly equivalent. Nt is a product of Fr and thickness. But the permittivity and Nt, of the high temperature poling were slightly smaller.

The relationship between the heat test temperature and Kt is shown in Fig 2.

In the case of normal poling, Kt at 180 °C was degraded to half that of the initial state, and it disappeared above 250 °C.

On the contrary, in the case of high temperature poling, Kt did not show major degradation until Curie temperature. Furthermore, Kt remained visible above Curie temperature.

This Fig.3 shows the temperature dependence of f_{90} change. Values of f_{90}, representing the ratio of change of the 90°domain structure, were measured with high-temperature X-ray diffraction from room temperature to 400 °C. f_{90} under normal poling changed –10% at 250 °C. On the other hand, f_{90} under high temperature poling only changed –5% at 360 °C.

This Fig.4 shows the relationship between dc bias field and Kt. The polarity of normal poling was reversed in a field of 2KV/mm. However, that of high temperature poling was reversed in 3KV/mm.

These results indicate that the high temperature poling results in superior heat resisting properties to the normal poling. And domain structure of the high temperature poling is more stable than that of the normal poling after the heat test.

SEM images of the specimens are shown in Photo.4 and 5 which show the initial and post –heat test states, respectively. a) and b) in both photographs correspond to normal and high poling conditions, respectively

In the initial state, there are few clear domain structures within the normal poling sample. However, distinct domain structures are observed in almost all the grains in the case of high temperature poling.

After the heat test, in the case of normal poling, domain structures disappeared. On the contrary, in the case of high temperature poling, domain structures did not show any major changes after test.

The high temperature poling were generally performed in fabrication of single crystals. Also, The degradation of Kt in $BaTiO_3$ ceramics had investigated in past years. But It had never good informations . It is considered the composition of materials. It is efficient to get the stable properties about many composition of PZT.
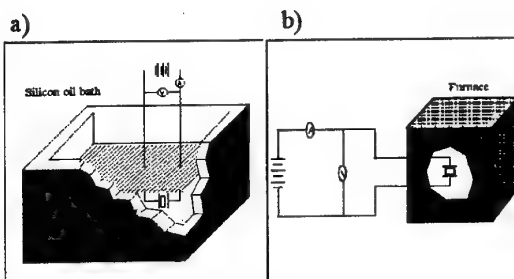
FIG. 1. Poling condition:
   a)Normal poling and b)High poling

	k_t (%)	$\varepsilon_{33}^T/\varepsilon_0$	N_t (Hz m)
Normal poling	43.7	1190	2120
High poling	43.2	1170	2015

Table.1 Summary of initial characteristics of normal and high poling samples

Composition:

$Pb[(Mg_{1/3}Nb_{2/3})_{0.05}Ti_{0.47}Zr_{0.48}]O_3$
$+CoO$ (0.2wt%)+ $MnCO_3$ (0.2wt%)
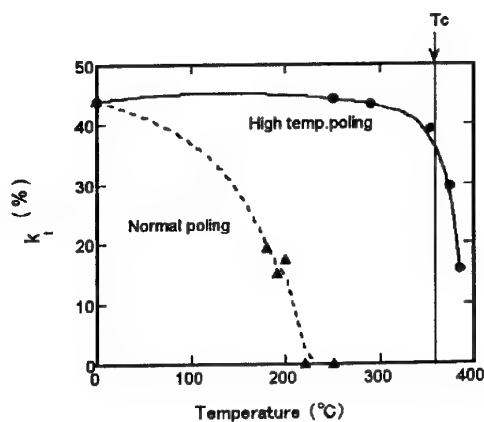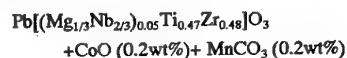
FIG.2. Relationship between the temperature of heat test and Kt.
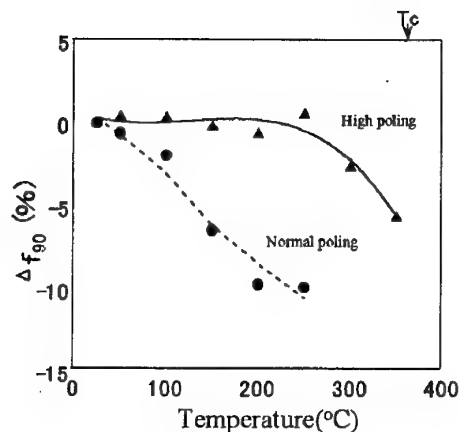
FIG.3. Temperature dependence of f_{90} examined with high poling temperature X-ray diffraction.
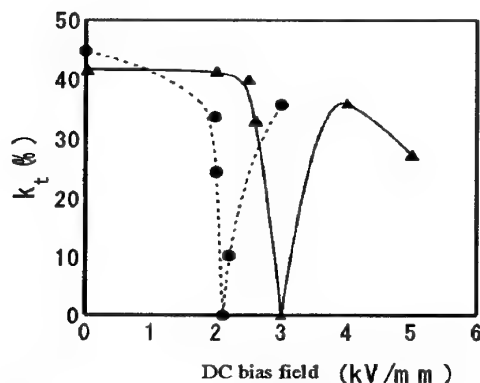
FIG. 4. Relationship between dc bias field and Kt.

a)   b)
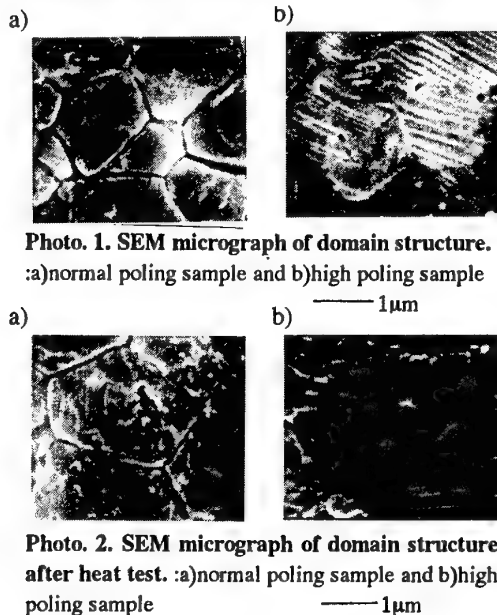
Photo. 1. SEM micrograph of domain structure. :a)normal poling sample and b)high poling sample
—— 1μm

a)   b)

Photo. 2. SEM micrograph of domain structure after heat test. :a)normal poling sample and b)high poling sample   —— 1μm

2. Enhancement of piezoelectric properties by N₂ treatment in PT ceramics.

The composition of the specimens used in this study was $0.69PbTiO_3+0.3SrTiO_3+0.01Bi_{2/3}TiO_3$ with Mn 0.1atm% and Nb 0.1atm%.

The sintered bodies were cut into square of $7 \times 7.5 \times 0.25$ ($10^{-9}m^3$). The specimens were heated at 600~1100 °C for 1 hour in tubular furnace with flowing gases. (The flow rate is 2 l/min for air, N_2, O_2, and mixed gases).

After heat treatment in various environments, the poling was carried out by applying DC field of 5kV/mm for 30min in the silicon oil bath at 120°C. Mechanical factor Q_m, coupling factor and frequency constant were then calculated. Especially the calculation of coupling factor was made by the values of the 3rd overtone resonance and anti resonance frequency at the thickness extensional trapped energy mode.

The relationship between mechanical quality factor (Q_m) and annealing temperature by varying the partial oxygen pressure (PO₂) in nitrogen gas is shown in Fig 5.

In the case of pure nitrogen-annealing (PO₂=10^{-5}), it can be seen that Q_m has maximum value at 750°C and the falls above 950°C. Also, the maximum point of Q_m tends to shift to high temperature region as PO₂ increases. Qm decreases in the air annealing (PO₂=2x10^{-1}) with the increase in annealing temperature. The oxygen concentration during N₂ annealing is shown in Fg.6. It is obvious that the oxygen releases from these specimen during annealing in low partial oxygen pressure atmosphere.
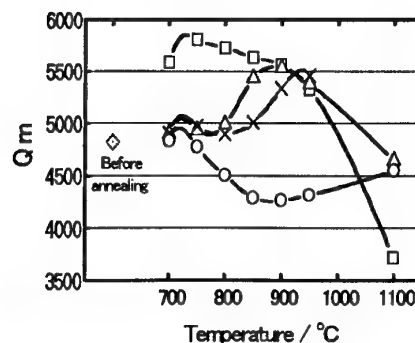
FIG. 5. Annealing temperature dependence of with varying Po₂ atmosphere.
◇;before annealing, □;Po₂ =10^{-5}, △;Po₂= 10^{-4}, ×;Po₂=10^{-3} , ○;Po₂= 2 ×10^{-1}

Amount of Mn^{3+} and Mn^{2+} of annealing specimens, which was measured by ESR and potentiometric titration , are listed in Table 1. The amounts of Mn^{3+} and Mn^{2+} hardly changed during annealing in N_2 atmosphere, but there is a small change in O_2 atmosphere.

This Photo.3,4 shows scanning electron microscope images. The domain structure of the N_2-annealed specimen was clearly observed with the SEM.

The typical of specimen's hysteresis is shown in Fig.7. Hysteresis for the atmosphere annealed specimens before poling was measured. It was observed that the polarization curve raises suddenly over about 8MV/m. Accordingly, we defined two kinds of slopes $((\Delta P/\Delta E)_1$ and $(\Delta P/\Delta E)_2)$ in Fig.8

The results of above estimation are shown in Fig.9, 10. High Q_m specimens have high $(\Delta P/\Delta E)_2$ and low $(\Delta P/\Delta E)_1$, while low Q_m specimens exhibit high $(\Delta P/\Delta E)_2$ and low $(\Delta P/\Delta E)_1$. From the result of analysis of P-E hysteresis curve, it can be said the decrease of Ei means N_2-annealing makes switching of domains easier at the lower fields. As compared with the two kinds of slopes for high Q_m specimens, it is hard to occur domain rotation in low external field but a considerable rotation occurs in the high external field.

It can be said that the rotation occurs at $180°$ domains at lower electric field and $90°$ domain rotation takes place at higher electric field. The improvement of Q_m in this experiment could be caused by the difference of rotational mechanism of domains in each condition.

It is said that heat treatments at non-air atmosphere was degraded piezoelectric properties. But It is considered the composition of materials. We have found that It is efficient to get the stable properties about a composition of PT.

a)   b)
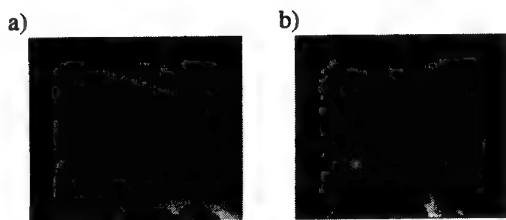
Photo. 3. SEM micrograph of domain structure. :a) without heat treatment sample and b) with heat treatment sample (850°C-1hr, N_2 flow)

——— 1µm
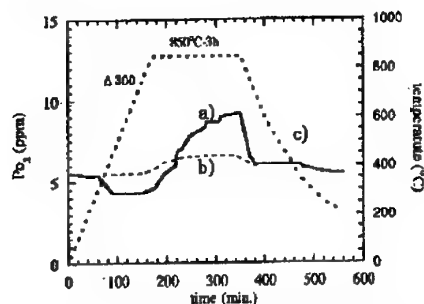
FIG. 6. Chang in O_2 partial pressure during the N2 annealing process in the furnace.
(Samples:600g N_2 Flow: 1.6l/min 150mmΦ tublar furnace) a)PO_2 with sample b) PO_2 without sample c)temperature

	Mn^{3+}	Mn^{2+}
Before annealing	0.17	0.37
$PO_2=10^{-5}$ (N_2)	0.17	0.38
$PO_2=1$ (O_2)	0.2	0.43
Measurement error	±0.01	±0.05

(wt %)

Table2. Amount of Mn^{3+} and Mn^{2+} of N_2-and O_2-annealing specimens.
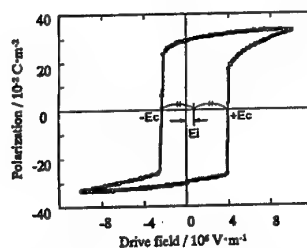
FIG. 7. Interal bias field (Ei) and coercive field(Ec) of PT-based ceramics.
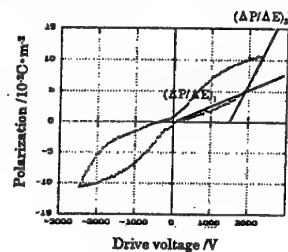
FIG. 8. DE-hysterisis curve of non-poling PT-based ceramics (the definition of $(\Delta P/\Delta E)_1$ and $(\Delta P/\Delta E)_2$.)
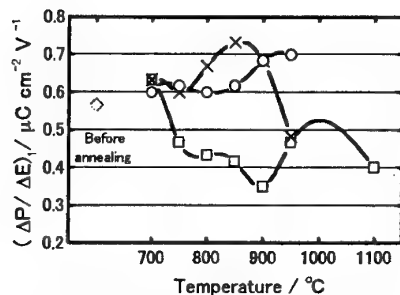
FIG. 9. Annealing temperature dependence of $(\Delta P/\Delta E)_1$ with varying Po_2 atmosphere.
◇:before annealing, □;$Po_2 = 10^{-5}$, ×; $Po_2 = 10^{-3}$, O;$Po_2 = 2 \times 10$
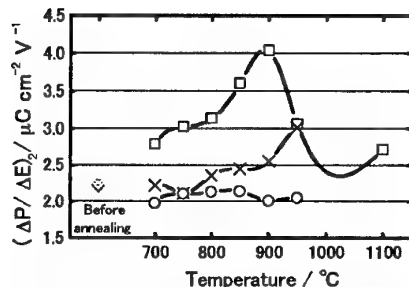
FIG. 10. Annealing temperature dependence of $(\Delta P/\Delta E)_2$ with varying Po_2 atmosphere.
◇:before annealing, □;$Po_2 = 10^{-5}$, ×;$Po_2 = 10^{-3}$, O;$Po_2 = 2 \times 10$

3. The spurious mode occurrence is largely due to minor thickness variation in the substrate using optical fiber interferometric sensing

The optical fiber interferometric sensing system developed by Yasuo Hirose is capable of making such measurements.
The spurious mode occurs close to the TE3 mode in $PbTiO_3$ based piezoelectric ceramic resonators. Measurement by the optical fiber interferometric sensing system revealed that the vibration amplitude contours at spurious mode were twin peaks.

Fig. 11 shows the optical path configuration for vertical vibration measurements. The sensitivity of the system is of 0.01 angstrom order for vertical vibration amplitudes and the frequency range is from 10 kHz up to a hundred MHz. Fig. 12 shows the occurrence of the spurious mode in the ceramic resonators. Fig.13 shows an impedance waveform free of spurious mode. There are similarities in the amplitude contours between both resonators at the TE3 mode resonance frequency and at the inharmonic mode. The difference is that the spurious mode occurs close to the anti-resonance frequency of the TE3. Measurements at the spurious mode revealed that the contour has twin peaks. Location of the single peak contour, just before (Fig.12 B) and after (Fig.12 C) the spurious mode, is respective to that of the twin spurious peaks.
Chips obtained from the same wafer had both types of samples, i.e. spurious free and those with the spurious mode. It was experimentally confirmed that the spurious contours always occur at the same location on the both sides of a chip..
It can be said that electrode thickness taper also causes the spurious mode. But in the actual practice such an electrode taper does not occur with regular evaporation process.
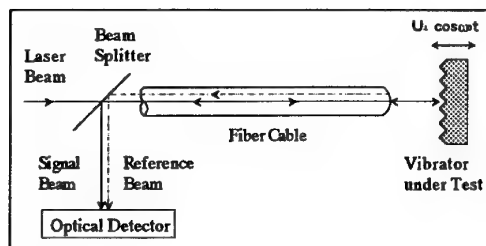
FIG. 11. Optical path configuration for the vertical vibration measurement

It is shown in Fig. 14 that the spurious that occurs in the sample chips is similar to one that occurs in the

thickness taper model. Dislocation of the vibration contour from the center of the circular electrode and the taper direction in thickness of the chips correlated to each other. The vibration contour, before spurious mode, occurred in the area where the chip is thick. Contour after spurious mode occurred in the relatively thinner area.

the regular lapping process. As a result of the experiments, it can be said the dislocation of the contours was due to the thickness taper of the chips
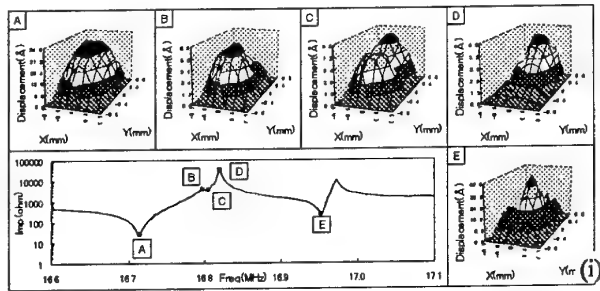
FIG. 12. Occurrence of spurious mode in the ceramic resonators and their vibration amplitude contours
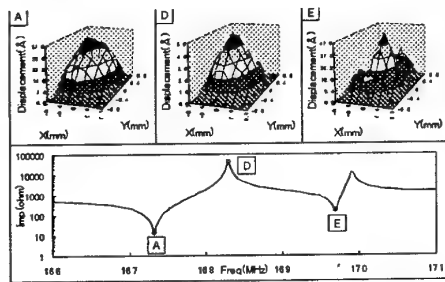
FIG. 13. Spurious-free ceramic resonators and their contours.

A	Resonance frequency of TE3
B	Frequency just before the spurious mode
C	Resonance frequency of the spurious mode
D	Anti-resonance frequency of TE3
E	Resonance frequency of the inharmonic mode
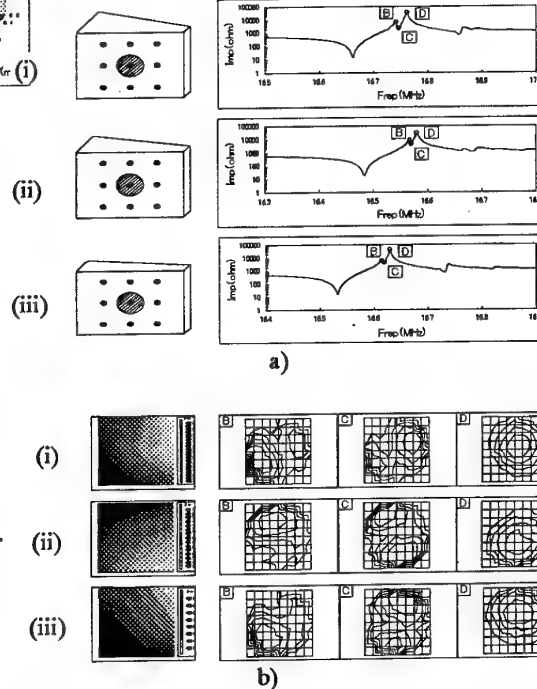
FIG. 14. (i) R=2.0μm. (ii) R=1.4μm . (iii) R=0.7μm (where R is the maximum thickness difference in a chip). (a)left: thickness   taper   models,   right: impedance waveform (b)left: thickness contours in a chip (One gradation is 0.1μm deference), right: vibration contours.

As mentioned before, the lapping process leaves thickness taper in the wafers. Before cutting the wafer into smaller chips it was necessary to confirm the location of each chip to avoid any confusion. Fig.14 confirms that the spurious mode occurs due to the un-symmetry in the chip's thickness.

Fig. 15 shows the relationship between the chip's thickness difference and occurrence of the spurious mode in the impedance dynamic range is linear. The graph shows that the data of the thickness taper models is a continuation of the data from the chips prepared by
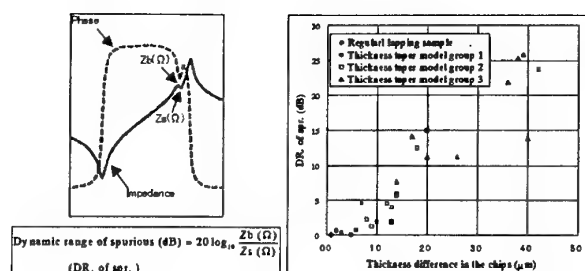
FIG.15. Spurious mode dynamic range and difference of chip thickness.

Acknowledgment

Concluding Remarks

This Paper focuses on the processing technology of the piezoelectric ceramics. Piezoelectric ceramics are now among the high functional materials, and their utilization is expected to grow in the future.

Processing methods described here can be applied to design various piezoelectric devices. Like it may be possible to reduce extro-thermal energy of high power devices, such as the piezoelectric transformers and the ultrasonic motors using high temperature poling.

For overall enhancement of the piezoelectric devices, it is important to understand domain control in the microstructure and to get a precise flat surface fabrication. Especially, it is necessary to have a through understanding of the domain structure and its rotation mechanism.

References

[1]M.Hirose, M.Takada, H.Oka, K.Miyabe:
   Jpn.J.Appl.Phys.33 (1994) 5345.

[2]K. Tachimoto, K. Horino, M. Takada, K.Miyabe:
14th Ferroelectric Materials Application
   Meeting .Japan

[3] S.L.Fu, S.Y.Cheng and C.C.Wei,
   IMC 1986, Proceeding,Kobe, (1986) 273

[4] T.Yamamoto, Y.Shimizu and M.Watanabe,
Nippon   Seramikkusu   Kyokai   Gakujutsu
Rombunshi,(in Japanese) 98 (1990) 781

[5] T.Yamakawa, M.Kataoka, T.Ezaki, S.Takahashi
and Y.Inoue,
   J.Japan. Soc. Powder and Powder Metallurgy, 43
(1996) 1132

[6] N D.Patel and P S.Nicholson,
Am.Ceram.Soc.Bull.,65 (1986) 783

[7]K.Tachimoto, K.Horino, M.Takada and K,Miyabe,
The 14th Kyouyuu
   dentai ouyou kaigi yokoushuu, (in Japanese) 125
(1997)

[8]T.Kamiya, T.Suzuki, T.Tsurumi and M.Daimon,
Japan.J.Appl.Phys.,31 (1992) 3058

[9]S.Takahashi, Ferroelectrics., 41 (1982) 143

[10] Y. Hirose, T. Abe, H. Komai and Y. Tsuzuki,
   Trans. IEICE,E70, 3 (1987), p.195

[11]Y. Hirose, T. Abe, H. Komai and Y. Tsuzuki,
   Trans. IEICE,E70, 3 (1987), p.195

[12]Y. Hirose, M. Kitajima and Y. Tsuzuki, JJAP, **28**,
   Suppl.28-1 (1989), p.91

[13]Y. Hirose and Y. Tsuzuki, Proc. 43rd Annual Symp.
   on Freq. Control (1989), p.360Y. Hirose, T. Abe, H.
   Komai and Y. Tsuzuki, Trans. IEICE,E70, 3 (1987),
   p.195

[14]Y. Hirose, M. Kitajima and Y. Tsuzuki, JJAP, **28**,
   Suppl.28-1 (1989), p.91

[15]Y. Hirose and Y. Tsuzuki, Proc. 43rd Annual Symp.
   on Freq. Control (1989), p.360Y. Hirose, M.
   Kitajima and Y. Tsuzuki, JJAP, **28**, Suppl.28-1
   (1989), p.91

[16]Y. Hirose and Y. Tsuzuki, Proc. 43rd Annual
Symp. on Freq. Control (1989), p.360

Growth and Characterization of Alkaline Bismuth Titanate Single Crystal Piezoelectrics

Y.-M. Chiang, G.W. Farrey, A.N. Soukhojak, and S.A. Sheets

Department of Materials Science and Engineering
Massachusetts Institute of Technology
Cambridge, MA 02139 USA
Fax: 617-253-6471, e-mail: ychiang@mit.edu

Single crystals in the $Na_{1/2}Bi_{1/2}TiO_3$-$BaTiO_3$ system have been grown and characterized. The phase stability diagram has been established. A variety of actuation characteristics are observed depending on composition and phase. In the rhombohedral ferroelectric phase, low-hysteresis <001> actuation with d_{33} values as high as 650 pC/N is found, while in near-MPB compositions, a field-forced AFE-FE transition with actuation strain reaching 0.45% at 30 kV/cm is observed at room temperature and low measurement frequency. In tetragonal phase ferroelectric crystals, <001> actuation is hysteretic, with low-field d_{33} values reaching 550 pC/N, k_t reaching 0.57, and field-induced strains as high as 0.4% being obtained at 30 kV/cm. A tetragonal phase crystal with a highly cation-nonstoichiometric composition (nearly 25% A-site deficiency) reached much higher strain of 0.85% at 40 kV/cm, suggesting the deliberate introduction of cation nonstoichiometry as a route to property engineering. In all of these crystals, growth defects and variations in domain microstructure due to compositional variations appear to still limit the piezoelectric properties, indicating that improved crystal quality will lead to better properties. An electromechanically active single crystal NBT-BT fiber has been grown using Edge-defined Film-fed Growth (EFG), demonstrating that continuous growth of single crystal piezoelectric fibers is possible in this system.

1. INTRODUCTION

The advent of single crystal perovskite piezoelectrics exhibiting unprecedented high values of actuation strain (ε>1.5%), piezoelectric strain coefficients (d_{33}>1500 pC/N), and electromechanical coupling factors (k_{33}>90%), exemplified by the lead-relaxor compounds $Pb(Mg,Nb,Ti)O_3$ (PMNT) and $Pb(Zn,Nb,Ti)O_3$ (PZNT) [1,2] has raised the possibility that alternative single crystal piezoelectric systems of high performance, particularly lead-free alternatives, may exist. We have recently grown and characterized single crystals of lead free perovskites, e.g., doped $(Na_{1/2}Bi_{1/2})TiO_3$ [3,4]. Aside from reduced toxicity in processing and use, these perovskites have higher elastic moduli, lower density, higher strength, and higher fracture toughness than the lead perovskites, which is advantageous for mechanical reliability and certain weight-based figures of merit (e.g., actuation energy density). Recent results have shown promising electromechanical properties in the rhombohedral ferroelectric, rhombohedral antiferroelectric, and tetragonal ferroelectric phases. While specific properties depend on the crystal phase, poling procedures, and measurement frequency, d_{33} values of 650 pC/N, peak strains routinely greater than 0.4% and as high as 0.85%, and thickness-mode coupling coefficients k_t=57% have been obtained. These results indicate that high piezoelectric performance may be obtainable in a broad range of single crystal perovskite compounds outside of the lead-relaxor systems. However, much work remains to be done to discover and optimize specific compositions.

In this paper, we present recent results for the model system $Na_{1/2}Bi_{1/2}TiO_3$-$BaTiO_3$. It is found that compositional engineering, especially of the cation nonstoichi- ometry, can have important effects on the piezoelectric response of single crystals. Compositional uniformity, influencing the microstructure of flux-grown crystals, is also found to be critical to properties. The phase diagram for single crystal NBT-BT has been determined from dielectric measurements and is compared to previously published results for polycrystalline materials. Finally, growth of single-crystal fibers of NBT-BT using the Edge-defined Film-fed Growth method (EFG) is described.

2. FLUX-GROWN SINGLE CRYSTALS
2.1 Growth Method and Experimental Procedures

A self-flux method was used, in which powders (>99% purity) of Na_2CO_3, Bi_2O_3, TiO_2, and $BaCO_3$ were mixed with an excess of Na_2CO_3 and Bi_2O_3. After calcining for 2h at 800°C, the powders were loaded into covered platinum crucibles, which in turn were placed inside a covered alumina crucible. No additional sealing of crucibles was necessary, and weight losses during growth did not exceed 1 wt%. A typical growth run consisted of a 5h homogenization of the melt at 1350°C, followed by cooling at 5°C/h to 800°C, which is below the solidus temperature of the system. Subsequent experiments have shown that depending on BT composition and the amount of excess flux, the temperature range of growth can be substantially narrowed. The crystals appear to grow from a simple two-phase solid-liquid equilibrium, although at lower temperatures the flux crystallizes to Na_2O and Bi_2O_3. This procedure typically resulted in 20-50 spontaneously nucleated crystals of varying sizes from a 100g batch, the largest being ~2cm. The growth morphology of well-separated crystals was cubic. Impinged crystals usually showed at least one {001}

face of the cubic phase, which facilitated orientation of the crystals for cutting and testing.

The majority of crystals were sectioned using a wire saw into plates of 0.3-1.0 mm thickness (Fig. 1), or rectangular bars of 1.0 x 1.0 x 3.0 mm. Faces were polished with diamond abrasive film to a final grit size of 0.5 μm. A tripod polisher was used to maintain flat and parallel faces. Gold electrodes of ~1 μm thickness were applied by sputtering. Capacitance, dissipation factor, and resonance measurements were conducted using an HP 4192A impedance analyzer. Electric-field induced strain measurements were conducted using a laser-interferometer apparatus with automated data collection. Polarization was determined by integrating the current during actuation and dividing by electrode area. The piezoelectric strain coefficient d_{33} was measured directly from the slope of the strain vs. field behavior.
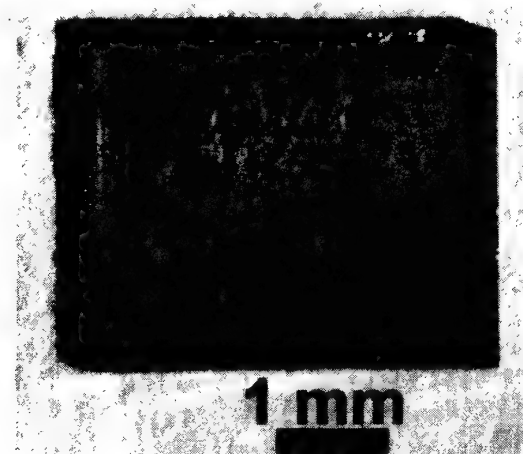
Figure 1: Cut and polished single crystal plate.

2.2 Compositional Analyses

Crystal compositions were analyzed by electron probe microanalysis (EPMA) using a JEOL JXA-733 instrument (JEOL Corp., Peabody, MA). The cation compositions were determined using the following standards: TiO_2, $NaAlSi_3O_8$, $Bi_4Ge_3O_{12}$, and $BaSO_4$. In computing crystal compositions from the raw data, we have assumed that Ti^{4+} cannot substitute on the perovskite A-site, and that Na^{1+}, Bi^{3+}, and Ba^{2+} cannot substitute on the B-site. This is consistent with the behavior of these cations in perovskite oxides in general. We have assumed that the cation valences are fixed at the values given, since growth was conducted in air, and determined the oxygen concentration by imposing the condition of overall electrical neutrality. Vacancies on the A, B, and O sites were allowed. To accommodate for nonstoichiometry, when an excess of A or B cations existed it was assumed that this respective sublattice was fully occupied, with the cation deficiency appearing on the other sublattice, and oxygen vacancies appearing if necessary for charge neutrality. Thus the overall composition of the crystals can be described as: $(Na,Bi,Ba)_{1-x}Ti_{1-y}O_{3-\delta}$. Consideration of counting statistics indicates that the Ti, Na, Bi, and O concentrations given are accurate to 1-2% of the absolute value, whereas the Ba concentration is accurate to ~5% of the absolute value.

Almost all of the analyzed crystals showed significant nonstoichiometry. Out of 57 crystals, 48 were found to contain an A-site deficiency, 9 a B-site deficiency, and 56 some oxygen deficiency. Table I lists compositions for a limited number of these crystals. Certain crystals exhibited unusually high nonstoichiometry, such as crystal 42 in Table I which has ~25% A-site deficiency. This crystal was confirmed to be a single-phase perovskite using single-crystal X-ray diffraction, despite the unusually high nonstoichiometry. As shown later, unusual piezoelectric response accompanies such high levels of nonstoichiometry. The phase of the analyzed crystals, determined by X-ray diffraction and given in Table I, could also be correlated with the Ba concentration and the extent of cation nonstoichiometry based on a tolerance-factor approach, although detailed discussion is beyond the scope of this paper. It was found that the present flux-growth method typically results in a variation of Ba doping levels between individual crystals about a mean value that is close to the nominal composition. This proved to be advantageous: it allowed characterization of a range of compositions using fewer growth runs.

Table I: Electron Microprobe Analysis of Flux-Grown

$(Na, Bi, Ba)_{1-x}Ti_{1-y}O_{3-\delta}$ Crystals

Sample	Na	Bi	Ba	Ti	O	A:B	Phase*
1	0.536	0.443	0.000	1.000	2.935	0.979	R
4	0.524	0.444	0.032	0.990	2.940	1.010	R
17	0.501	0.448	0.051	0.993	2.958	1.007	R
18	0.454	0.434	0.054	1.000	2.930	0.942	R
19	0.487	0.457	0.056	0.984	2.953	1.016	R
23	0.468	0.464	0.026	1.000	2.956	0.958	R
39	0.484	0.446	0.054	1.000	2.964	0.984	AFE
40	0.500	0.445	0.055	0.991	2.955	1.009	AFE
41	0.435	0.435	0.056	1.000	2.927	0.926	AFE
42	0.273	0.418	0.053	1.000	2.817	0.744	T
44	0.465	0.437	0.066	1.000	2.956	0.968	T
46	0.390	0.432	0.088	1.000	2.933	0.910	T
47	0.426	0.418	0.089	1.000	2.703	0.933	T
48	0.469	0.426	0.091	1.000	2.964	0.986	T
50	0.385	0.415	0.128	1.000	2.944	0.928	T

*R = rhombohedral phase; T = tetragonal phase; AFE = antiferroelectric rhombohedral phase

2.3 Dielectric Measurements and the $Na_{1/2}Bi_{1/2}TiO_3$-$BaTiO_3$ Phase Diagram

Five single crystals of nearly cation-stoichiometric composition, but varying in Ba doping level, were used to establish the NBT-BT phase stability diagram as a function of composition and temperature. The crystals contained 0%, 3.2%, 5.4%, 6.6%, and 8.8% BT respectively, and XRD had shown that the first three were of rhombohedral phase and the last two of tetragonal phase at room temperature. Measurements were made of unpoled crystals upon heating at 200°C/h between room temperature and 600°C, at frequencies of 1 kHz, 10 kHz, and 100 kHz. Local maxima and inflections in the relative dielectric constant ε_r were used to identify the phase boundaries. Figures 2a-2c show ε_r and dissipation factor tan δ vs. temperature for the undoped, 3.2% BT, and 6.6% BT crystals respectively. Each shows two local maxima/inflections between room

temperature and 400°C, and tan δ that increases with increasing temperature. The latter behavior is attributed to increasing conductivity, possibly due to the oxygen nonstoichiometry (vacancies) that is present in all of these crystals. This feature has not been seen in polycrystalline NBTs [5,6], which may be due to differences in defect chemistry, or may be a result of blocking grain boundaries in the polycrystalline materials. From these results we have constructed the phase diagram shown in Figure 3. Also plotted for comparison is the phase stability diagram determined by Takenaka et al. [7] on polycrystalline NBT-BT samples, at unspecified measurement frequencies. At room temperature, XRD of our crystals confirms that the morphotropic phase boundary between rhombohedral ferroelectric and tetragonal ferroelectric phase fields is located at about 5.9% BT. This result is consistent with Takenaka et al. [7]. The phase boundaries between the rhombohedral ferroelectric (R-FE) and antiferroelectric (AFE) phase fields, and that between the AFE and paraelectric (PE) fields, are also in close agreement between our two studies. An interesting new result, however, is that the phase boundary between the tetragonal ferroelectric (T-FE) and AFE phase fields is strongly frequency-dependent, decreasing in temperature as frequency is lowered. This implies relaxor behavior, and is also discussed later with respect to the frequency-dependence of piezoelectric actuation in this system. Note that for near-MPB compositions, the AFE phase field may extend nearly to room temperature at low frequencies. This supports the possibility of field-forced AFE-FE single crystal actuation.
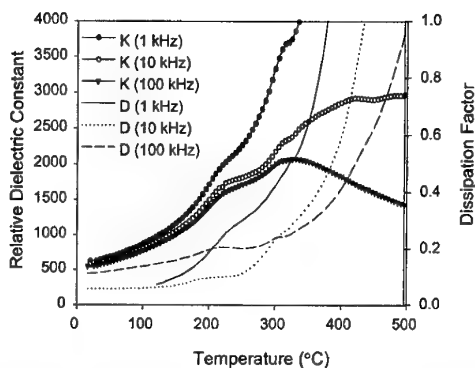
Figure 2a: Relative dielectric constant and dissipation factor vs. temperature and frequency for undoped NBT (sample 1 in Table 1)
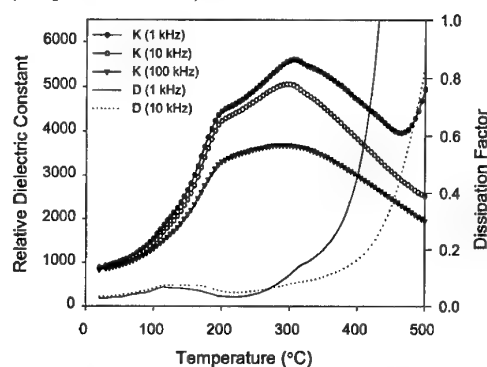
Figure 2b: Relative dielectric constant and dissipation factor vs. temperature and frequency for rhombohedral NBT-3.2% BT (sample 4 in Table 1).
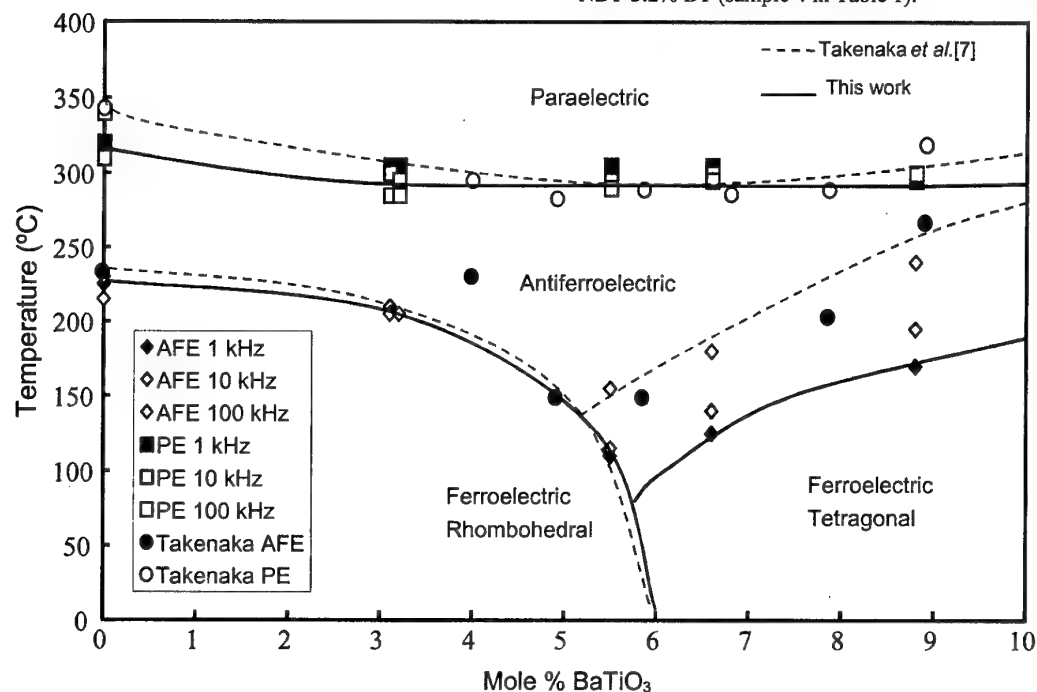
Figure 3: NBT-BT phase diagram based on dielectric measurements.
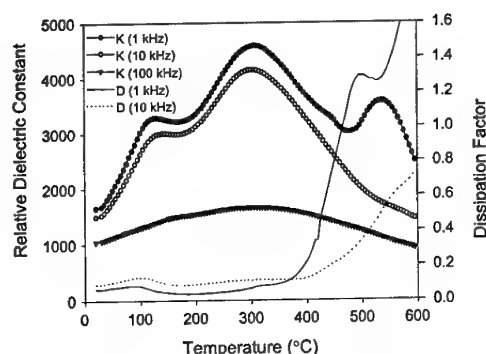
Figure 2c: Relative dielectric constant and dissipation factor vs. temperature and frequency for tetragonal phase NBT-6.6% BT (sample 44 in Table 1).

The ε_r and tan δ values of a number of crystals were also measured before and after poling at twice their coercive field for 5 min. at 60°C. The change in dielectric constant upon poling varied widely, suggesting that individual crystals differed substantially in the ease of poling, which we attribute to variations in crystal quality. Typical 1 kHz values for ε_r after poling ranged from 500 in undoped NBT, increasing with BT concentration across the R-FE field to 2000 near the MPB. In the tetragonal phase field, values of ε_r were in the range 1500-1800 after poling. Corresponding dissipation factors for poled samples increased with BT concentration from 0.028 to 0.050 across the R-FE field, and decreased with BT concentration from 0.065 to 0.048 from the MPB to ~9% BT within the T-FE field. Given that virtually all of the present crystals exhibit measurable oxygen deficiency, it is possible that these relatively high values of tan δ can be decreased by doping or changing growth conditions in order to alter the defect chemistry.

2.4 Electromechanical Characterization

As the phase diagram was not fully understood at the outset of this study, the optimal poling procedure for crystals in this system was not clear. The dielectric constant measurements showed that individual crystals of similar composition could vary widely in the extent of poling despite identical procedures. This is believed to reflect variations in individual crystal quality and homogeneity. Most crystals were poled by applying an electric field of twice the apparent coercive field for 5 min at an elevated temperature of 50-100°C, and strain tested under a 1 Hz ac field. For most crystals this meant that poling was conducted within an FE field, although for the near-MPB compositions these temperatures are within the AFE field.

Within the rhombohedral phase field, the strain vs. field relationship measured along the cubic <001> was relatively linear with little hysteresis (Fig. 4). Certain crystals, such as NBT-3.2%BT crystal in Fig. 4, exhibited particularly low hysteresis. This suggests that the proposed model for lead-relaxor crystals [1] whereby poling introduces a four-fold symmetric, static domain configuration applies to these crystals as well. We observed that d_{33} generally increased near the MPB,

as shown in Fig. 5. However, the highest d_{33} to date of 650 pC/N was measured in an NBT-2.6%BT crystal, falling well within the R-FE phase field. Microscopic examination of the crystals indicated that variations in crystal quality dominate the observed properties. Fig. 6 shows a single crystal plate of undoped NBT, viewed with incident light from the direction indicated. Regions of anisotropic opalescence are separated from regions of transparency within the same crystal, revealing variations in domain microstructure that are probably the result of grown-in compositional nonuniformity. Even the sample exhibiting d_{33} = 650 pC/N was microstructurally nonuniform in its domain structure under optical microscopy. It is therefore likely that the d_{33} values intrinsically possible in these compositions have not yet been achieved in the present crystals. Thickness- and bar-mode coupling coefficients k_t and k_{33} were measured using the resonance-antiresonance method in those crystals which satisfied the necessary geometric requirements. Within the R-FE field, the higher k_t values ranged from 0.32 to 0.39, and the highest k_{33} measured was 0.55 for a crystal with 3.2% BT. (The sample exhibiting the highest d_{33} was not measured due to geometric limitations.) These fall well below the maximum values of 0.94 measured in rhombohedral phase PMNT crystals [ref.], but it is not yet clear to what extent they are influenced by crystal quality.

Measured at 1 Hz
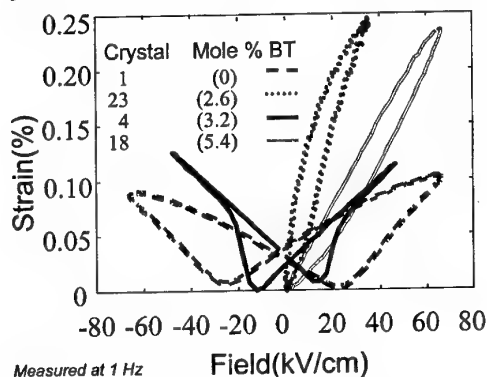
Figure 4: Strain vs. applied field at room temperature for rhombohedral phase single crystals actuated along <001> directions under a 1 Hz ac field. Crystal 23 was tested with a 17 kV/cm dc bias. Crystal 18 was tested with a 30 kV/cm dc bias.
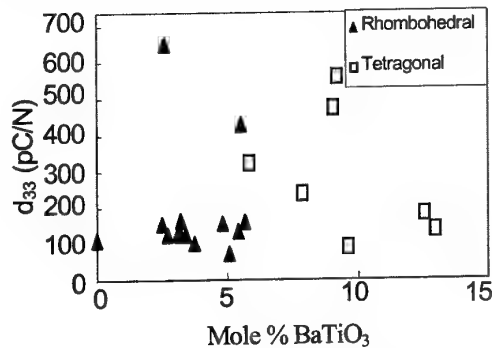
Figure 5: Piezoelectric strain coefficient vs. mole % BT.

Figure 6: Optical image of NBT (001) with glancing light. Note opalescent and clear regions.

Crystals within the tetragonal phase showed higher hysteresis as expected from domain rotation when actuated along the cubic <001>. Several crystals reached maximum strains near 0.4% at 30 kV/cm (Fig. 7). The low-field d_{33} values measured after poling varied widely, presumably due to crystal quality, with the highest measured value being 550 pC/N. A single crystal with exceptionally high A-site deficiency, sample 42 in Table I, also showed an unusually high strain of 0.85% (Fig. 7). (In comparison, the lower-strain sample in Fig. 7 is sample 48, and is nearly cation-stoichiometric.) Clearly, cation nonstoichiometry in the present system has a major influence on the actuation characteristics. The mechanism(s) of this behavior remain to be understood. Thickness-mode coupling coefficients were measured in several tetragonal phase samples. The highest values of k_t = 0.56 and 0.57 were measured in two crystals with ~9% Ba concentration. These values are only slightly less than the highest k_t values of 0.64 measured in PZNT single crystals [8].
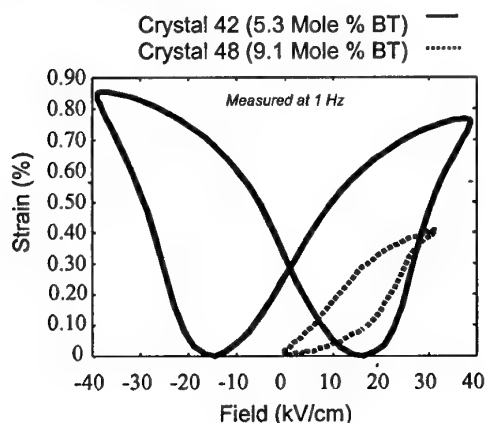
Figure 7: Strain vs. applied field at room temperature for tetragonal phase crystals actuated along <001> directions under a 1 Hz ac field. Crystal 48 was actuated under a 15±15 kV/cm field.

A crystal of near-MPB composition, sample 39 in Table I, exhibited a sharp onset in the actuation strain at 30 kV/cm, reaching 0.45% strain (Fig. 8), suggesting a field-forced AFE-FE phase transition, as is known for systems such as (Pb,La)(Sn,Zr,Ti)O₃ [9]. (Three plates cut from the same crystal showed similar behavior.) The corresponding polarization-field loop showed "double loops" supporting this interpretation, as does the fact that similar behavior has been observed in polycrystalline NBT-BT of near MPB composition at higher temperatures [7]. Referring to the phase diagram in Fig. 3, it is apparent that at 1 kHz frequency, the AFE phase field extends to about 100°C at the MPB between R-FE and T-FE phase fields. Since the results in Fig. 8 were obtained at an even lower measurement frequency of 1 Hz, it is possible that the AFE field under these conditions does extend to room temperature.
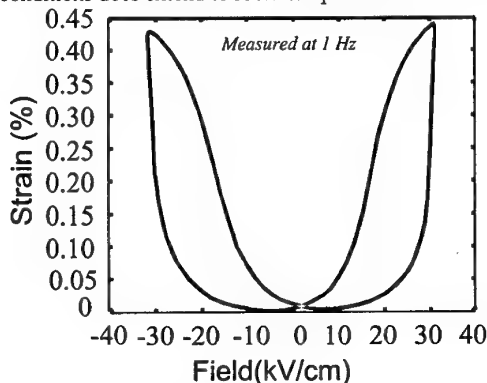
Figure 8: Strain vs. applied field for crystal 39 (5.4 mole % BT) actuated at room temperature along <001> under a 1 Hz ac field.

2.5 Electrorheological behavior

In virtually all samples the electromechanical response exhibited significant frequency dependence, e.g. Fig. 9. In some samples the polarization significantly lagged the sinusoidal ac electric field due to FE/AFE switching and/or dielectric relaxation. In several samples the electrostrictive strain noticeably lagged dielectric polarization (Fig. 10). The latter phenomenon has not been previously identified in the literature. In the NBT-BT system, the effect is pronounced and is worth detailed investigation.
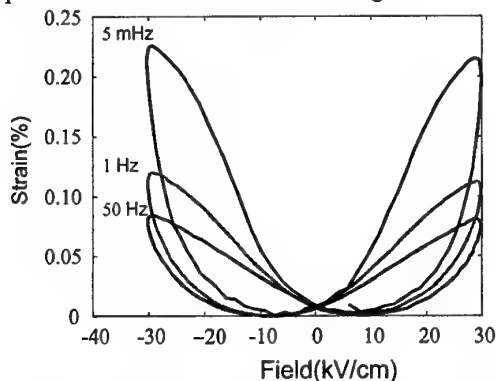
Figure 9: Crystal 47. Longitudinal strain along <100> vs. applied ac field of different frequencies at room temperature.
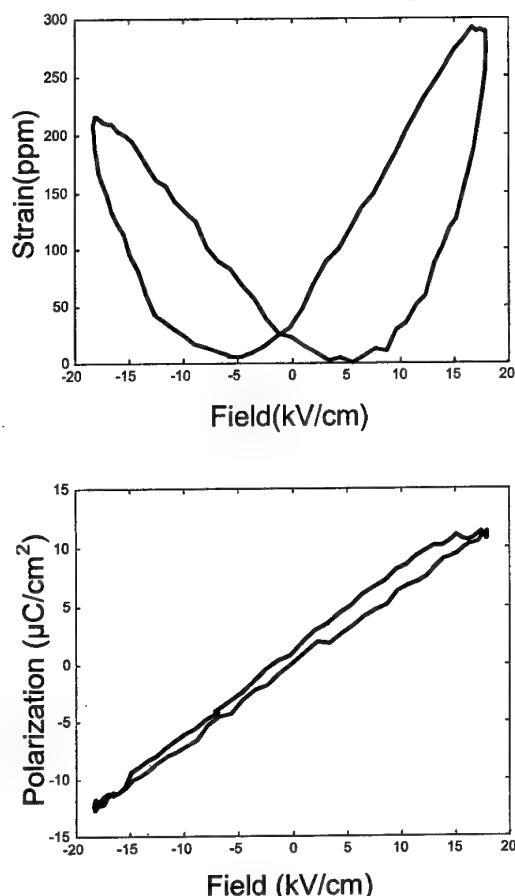
The observed delays in dielectric and mechanical responses to ac electric field and the frequency dependence of the latter can be accounted for by separate relaxation phenomena in *electrical* and *elastic* subsystems of the same material, which represent systems of mobile charges and attracting/repulsing atoms respectively.

Electro-relaxation phenomena have been extensively experimentally and theoretically studied in liquid crystals, including ferroelectric ones [10]. As a result, electrorheology appeared as a study of flow under an applied electric field.

The kinetics of ferroelectric switching has been previously modeled [11]. However, to our knowledge, electrorheology has not been applied to describe the electromechanical response of ceramic piezo-electric/electrostrictive materials. Our observations of NBT-BT system showing relaxation phenomena in electric and elastic subsystems suggest that electro-rheology is a useful concept for describing frequency dependent electromechanical behavior.

To model the frequency dependent electrome-chanical behavior of the NBT-BT system we assumed that 1) FE/AFE switching, 2) dielectric polarization, and 3) electrostrictive strain response to dielectric polarization are not instantaneous and have three corresponding time constants. These time constants enter the electrorheological kinetic linear differential equations for the rates of the respective parameters of the general form:

$$\frac{dx}{dt} = \frac{1}{\tau}(x_e - x),$$

where x is a changing parameter, x_e is its equilibrium value at the current conditions, t is time, and τ is the respective time constant. The equilibrium value x_e is given by the appropriate static phenomenological law. The physical meaning of the time constants is similar to

Figure 10: Crystal 42. Longitudinal strain and polarization along <100> vs. applied 1 Hz ac field at room temperature.
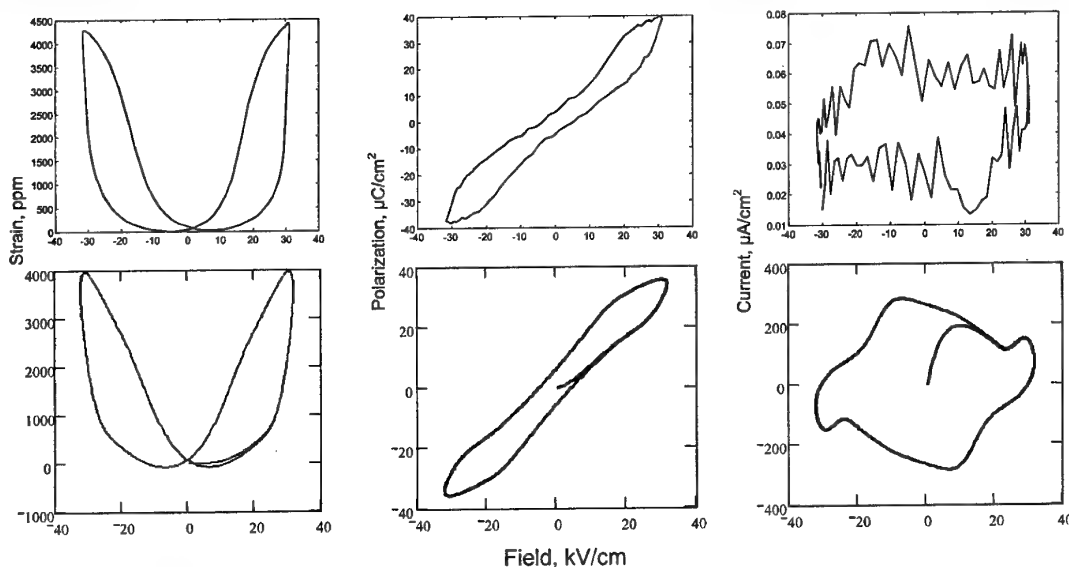
Fig. 11: Crystal 39. Longitudinal strain, polarization and current along <100> vs. applied 1 Hz ac field at room temperature. Top: measured, bottom: simulated.

viscosity, which describes change of material spatial coordinates in time under an applied stress.

Results of electromechanical behavior simulations using electrorheological approach show that the latter is qualitatively and quantitatively adequate to describe the experimental data (Fig. 11). We were able to model any electromechanical response we observed in the NBT-BT system at different frequencies: pure and mixed cases of FE, FE/AFE and electrostrictive behavior with or without relaxation in the electrical and elastic sub-systems. The simulated frequency dependence of electromechanical response was somewhat exaggerated. A possible explanation is the use of a single time constant instead of a more realistic continuous spectrum of time constants characteristic of the relaxor behavior. The values of time constants we identified for different samples were in the range of 1-60 ms—remarkably large magnitudes for an electromechanical response of a ceramic material.

We envision the tilting of oxygen octahedra in the perovskite structure as a possible mechanism of relaxation in the elastic subsystem of the NBT-BT crystals. We observed superlattice reflections in electron diffraction pattern of the NBT-BT crystals compatible with the octahedral tilt [4].

3. EDGE-DEFINED FILM-FED GROWTH OF POLY- AND SINGLE-CRYSTAL FIBERS

In order to implement single crystal piezoelectrics in technological applications, suitable and economical processing and fabrication methods must be developed. High quality crystals of precisely controlled orientation are necessary (to date, the pseudocubic <001> is preferred). For the particular class of applications known as "active-fiber composites" [12], it is clear that single crystal piezoelectric fibers exhibiting properties similar to those measured in bulk crystals would provide a quantum leap in performance. For the growth of single crystal fibers, the technique known as Edge-defined Film-fed Growth [13] is a highly promising approach for the following reasons:

- High growth rate, up to 60 mm/hr (faster than Czochralski growth)
- Possibility for simultaneous growth of many fibers
- Fiber cross-sectional shape control
- Diameters from 100 μm to several millimeters possible
- Better control over composition than in Czochralski growth

There are several requirements that materials systems to be grown by the EFG method must satisfy [13]. The most important of these is that the compound melts congruently, or that the rapid crystallization inherent in EFG allows non-equilibrium growth of the desired crystal through a multiple phase field. We conducted phase equilibrium studies on NBT-BT compositions containing between 5.5% and 10% BaTiO$_3$ and found that they do melt congruently. This composition range spans those in which the flux-grown single crystals have shown promising actuation. EFG experiments were conducted using a modified BCG 365 Crystal Grower (T.E. Brown (Barrington) & Co., Cambridge, England) equipped with B-100 RF generator (Lindberg, Chicago, IL). Temperature was measured by automatic pyrometer and controlled by a digital controller/programmer (Type 818, Eurotherm Corp., Reston, VA). Porous ceramic insulation was used to reduce heat loss and control temperature gradients. A platinum crucible and die were used, designed to limit vaporization from the melt by minimizing the exposed liquid surface area, and the growth was conducted in air.

Initially, a short polycrystalline fiber was grown in the following experiment. Several flux-grown single crystals (~3 g) of composition 0.94Na$_{1/2}$Bi$_{1/2}$TiO$_3$– 0.06BaTiO$_3$ were melted at ~1330°C, and a 0.3 mm diameter platinum wire was lowered to touch the melt and form a liquid meniscus at the die tip, also of 0.3 mm diameter. The crystal was then pulled at a rate of 18 mm/hr. The resulting sample (Fig. 12, top) were ~0.3 mm in diameter and ~4 mm long. Microscopic examination of the sample revealed a random faceting of the surface consistent with a polycrystalline nature. Growth was terminated when the liquid meniscus collapsed due to inadvertent variation. Longer crystals of this diameter are believed to be possible with improved temperature control.
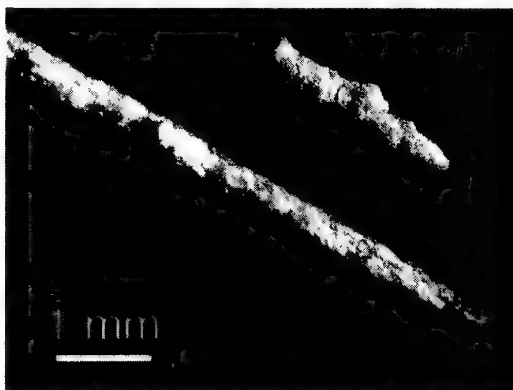
Figure 12: NBT-BT fibers obtained by EFG. Top: polycrystal, bottom: single crystal.
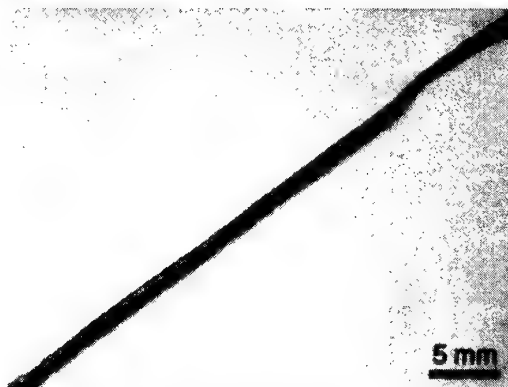
Figure 13: NBT-BT single crystal fiber obtained by EFG. Diameter 0.8-0.9 mm, length 60 mm.

Single crystal EFG growth was then carried out using a platinum die having a 0.5 mm diameter tip. A single crystal from the same flux grown batch as the source material was attached to a platinum wire as a seed. A pulling rate of 25 mm/hr was used. All other

conditions were the same as for the polycrystalline growth. The resulting crystal (Fig. 12, bottom, and Fig. 13) was 0.8-0.9 mm in diameter and ~60 mm long, with growth terminating only when contact with the die was lost as the melt supply was depleted. The color of the grown filament was identical to that of the source crystals. Microscopic examination of a polished cross-section of this sample revealed ferroelectric domains, some inclusions, and other growth defects, but no grain boundaries, thereby showing that it is a single crystal fiber.

In order to identify the phase of the single crystal fiber, a portion was ground and examined by X-ray diffraction. Fig. 14 shows that the fiber consists of single-phase rhombohedral perovskite, the same as the starting NBT-BT crystal from which it was grown. EPMA showed the fiber to be cation-stoichiometric but lower in Ba concentration than the starting crystals, having 2.4% BT. Electrodes were applied to short sections (2-3 mm) of this fiber, and the field-induced strain was measured in the same apparatus as described earlier. The actuation characteristics (Fig. 15) under symmetric and dc-biased ac field show clearly that the fiber is electromechanically active, although the properties fall far short of those in flux-grown single crystals of the same nominal composition [3]. This we attribute to the grown-in defects in the single crystal fiber, visible in optical microscopy. Further refinement of the growth process is expected to improve the properties of these EFG fibers.
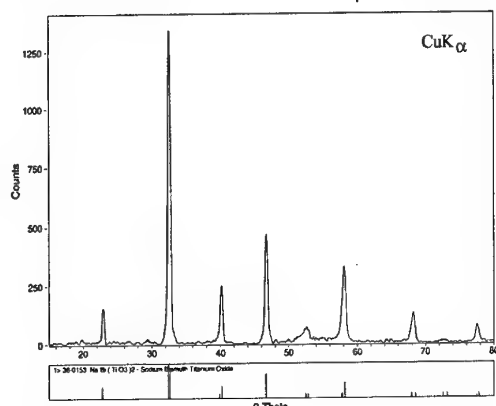
Figure 14: Powder XRD pattern of NBT-BT single crystal fiber obtained by EFG.
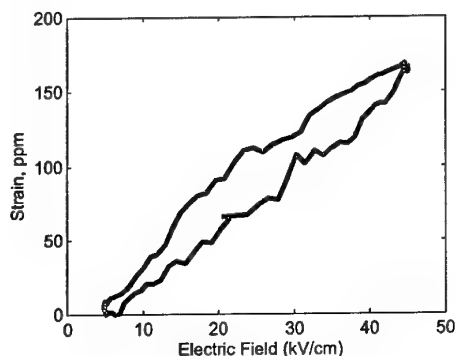
Figure 15: NBT-BT Single crystal fiber. Longitudinal strain along <100> vs. applied dc-biased ac field at room temperature.

4. CONCLUSIONS

Composition-structure-property relationships have been studied in flux-grown $Na_{1/2}Bi_{1/2}TiO_3$-$BaTiO_3$ single crystals. A rich variety of actuation characteristics are observed depending on composition and phase. Rhombohedral ferroelectric and tetragonal ferroelectric phases exhibit actuation characteristics similar to those in lead-relaxor single crystals, although the piezoelectric constants (d_{33} = 650 pC/N, k_{33} = 0.55, k_t=0.57) do not yet reach the level of the lead relaxors. Crystal quality appears to limit the present samples such that the ultimate performance possible in this composition system has not yet been determined. In near-MPB compositions, single-crystal AFE-FE field forced actuation has been demonstrated at room temperature, and yields significant actuation strain (0.45% at 30 kV/cm). Cation nonstoichiometry has been found to have a significant influence, with grown-in A-site deficiencies of 25% being observed, and resulting in actuation strain of 0.85% in a tetragonal ferroelectric crystal. The EFG growth of single crystal fibers has been demonstrated.

REFERENCES

1. S. –E. Park and T. R. Shrout, *J. Appl. Phys.*, **84** [4] 1804-11 (1997).
2. J. Kuwata et al., *Jpn. J. Appl. Phys.*, **21**, 1298-1302 (1982).
3. Y. –M. Chiang et al., *Appl. Phys. Lett.*, **73**, [25], 3683-5 (1998).
4. A.N. Soukhojak *et al.* To appear in *J. Phys. Chem. Solids* (1999).
5. S. Kuharuangrong and W. Schulze, *J. Am. Ceram. Soc.*, **79** [5], 1273-80 (1996).
6. O. Elkechai and J.P. Mercurio, *Proc. of Ninth IEEE ISAF '94*, 253-6 (1994).
7. T. Takenaka *et al.*, *Jpn. J. Appl. Phys.*, **30** [9b], 2236-9 (1991).
8. S. –E. Park and T. R. Shrout, *Proc. – IEEE Ultrason. Symp.*, **2**, 935-942 (1996).
9. D. Berlincourt *et al.*, *J. Phys. Chem. Solids*, **25**, 659-74 (1964).
10. D. Wei and G.N. Patey, *Phys. Rev. E*, **47** [4] 2954-7 (1993).
11. P.J. Chen and S.T. Montgomery, *Ferroelectrics*, **23** 199-208 (1980).
12. A.A. Bent and N. W. Hagood. SPIE Paper No. 2441-50, *Proc. 1995 North Amer. Conf. Smart Struct. and Mater.*, San Diego, CA (1995).
13. B. Chalmers, H.E. LaBelle and A.I. Mlavsky, *Mat. Res. Bull.* **6** 681-90 (1971).

High Piezoelectric Performance of Barium Titanate Single Crystals with Engineered Domain Configurations

Satoshi Wada, Shingo Suzuki, Tatsuo Noma, Takeyuki Suzuki, Minoru Osada[1], Masato Kakihana[2], Seung-Eek Park[3], L. Eric Cross[3] and Thomas R. Shrout[3]

Tokyo University of Agriculture & Technology, 24-16 Nakamachi 2-chome, Koganei, Tokyo 184-8588, Japan
Fax: 81-42-388-7040, e-mail: swada@cc.tuat.ac.jp
[1]Institute of Physical & Chemical Research, 2-1 Hirosawa, Wako, Saitama 351-0198, Japan
Fax: 81-48-462-4623, e-mail: mosada@postman.riken.go.jp
[2]Tokyo Institute of Technology, 4259 Nagatsuta-cho, Midori-ku, Yokohama 226-8502, Japan
Fax: 81-45-924-5309, e-mail: kakihana@rlem.titech.ac.jp
[3]Materials Research Laboratory, Pennsylvania State University, University Park, PA 16802-4801, U.S.A.
Fax: 1-814-865-2326, e-mail: sxp37@psu.edu

In barium titanate single crystals, piezoelectric properties were investigated at room temperature as a function of crystallographic orientation. When unipolar electric-field was applied along [001] direction, its strain *vs* electric-field curve showed a large hysteresis, and finally barium titanate crystal became to single-domain state with d_{33} of 125pC/N over 20kV/cm. On the other hand, electric-field exposure below 5kV/cm along [111] direction resulted in high d_{33} of 203pC/N and hysteresis free strain *vs* electric-field behavior, which suggested formation of engineered domain configuration in tetragonal barium titanate crystal. Moreover, as electric-field over 6kV/cm applied along [111] direction, two discontinuous changes were observed in its strain *vs* electric-field curve. In-situ domain observation and Raman measurement under electric-field revealed an electric-field induced phase transition from tetragonal to monoclinic around 10kV/cm, and that from monoclinic to rhombohedral around 30kV/cm. Moreover, in monoclinic barium titanate crystal, electric-field exposure along [111] direction resulted in formation of another new engineered domain configuration with d_{33} of 295pC/N.

1. INTRODUCTION

Recently, in [001] oriented rhombohedral $Pb(Zn_{1/3}Nb_{2/3})O_3$-$PbTiO_3$ (PZN-PT) single crystals, ultrahigh piezoelectric activities were found by Park and Shrout[1-4], with strain over 1.7 %, d_{33} over 2500pC/N, k_{33} over 90 % and hysteresis-free strain *vs* electric-field behavior. (1-*x*)PZN-*x*PT crystals with *x*<0.09 have rhombohedral *3m* symmetry at room temperature, and their polar directions are <111>.[5,6] However, unipolar electric-field exposure along the [111] direction showed a large hysteretic strain *vs* electric-field behavior and a low d_{33} below 100pC/N. On the other hand, unipolar electric-field exposure along the [001] direction exhibited non-hysteretic strain *vs* electric-field behavior and d_{33} over 2500pC/N in 0.92PZN-0.08PT crystals. To explain the above strong anisotropy in piezoelectric properties, *in situ* domain observation was done using [111] and [001] oriented 0.92PZN-0.08PT single crystals.[7,8] As a result, when electric field was applied along the [001] direction, a very stable domain structure appeared under 0.2kV/cm, and domain wall motion was undetectable under DC-bias of up to 20kV/cm, resulting in hysteresis-minimized strain *vs* electric-field behavior.

Figure 1 shows a schematic domain configuration for [001] poled rhombohedral *3m* crystals. [001] poled *3m* crystals must have four domains with four equivalent polar vectors along [111], [$\bar{1}$11], [1$\bar{1}$1] and [$\bar{1}\bar{1}$1] directions. Therefore, the component of each polar vector along the [001] direction is completely equal each other, so that each domain wall cannot move under electric-field exposure along the [001] direction owing to the equivalent domain wall energies.[3,4] This suggests the possibility of controlling domain configuration in
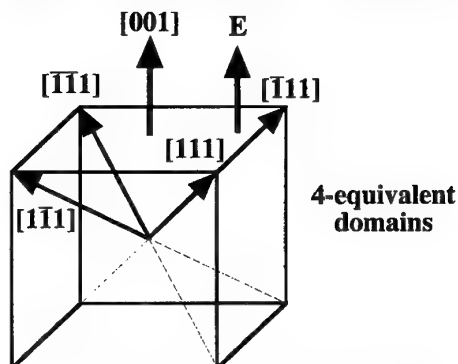
Fig. 1   Schematic domain configuration for [001] poled rhombohedral *3m* crystal.

single crystals using crystallographic orientation, and the appearance of a new technology in domain engineering field, as well as a conventional constraint of domain wall motion by acceptor dopants, *i.e.*, "Hard" PZT. Thus, this special domain structure in single crystals (Fig. 1) using crystallographic orientation was called an engineered domain configuration.[2,4,7,8]

The engineered domain configuration is expected to possess the following three features for piezoelectric performance: (1) hysteresis-free strain *vs* electric-field behavior, (2) higher piezoelectric constant and (3) change of macroscopic symmetry.[7,8] Therefore, if the concept of the engineered domain configuration can be applied to other ferroelectric single crystals, enhanced piezoelectric properties are expected. In this study, a barium titanate ($BaTiO_3$) single crystal was chosen for the first step in the application of the engineered domain configuration. This is because $BaTiO_3$ crystal is one of

the well-studied ferroelectrics, a non-lead ferroelectric, and a perovskite-type structure similar to PZN-PT.

In this study, the piezoelectric properties of BaTiO₃ crystals were investigated at room temperature as a function of crystallographic orientation. Their domain configurations were also observed as a function of electric field and crystallographic orientation. The behavior of domain wall motion will be discussed in relation to the observed strain *vs* electric-field behavior. Moreover, *in situ* Raman measurement was done to study changes in crystal symmetry as a function of electric field and crystallographic orientation.

2. EXPERIMENTAL

BaTiO₃ single crystals were prepared by a top-seeded solution growth (TSSG) method at Fujikura, Ltd. In TSSG-grown BaTiO₃ crystals, the concentration of most impurities was below 2-3ppm.[9] The details of preparation of BaTiO₃ single crystals and their characterization were described elsewhere.[9] These crystals were oriented along [001] and [111] directions using the back-reflection Laue method. All characterizations and treatments were done at Fujikura.

For electrical measurement, samples were prepared by polishing to achieve flat and parallel surfaces onto which gold electrodes were sputtered. Prior to piezoelectric measurements, dielectric properties were measured with a LCR meter at room temperature, and their dielectric loss was below 0.1 % at 100Hz. High electric field measurements included polarization and strain using a modified Sawyer-Tower circuit and a linear variable differential transducer. Electric fields were applied using an amplified triangular waveform at 0.1Hz.

For *in situ* domain observation and *in situ* Raman measurement under DC-bias, samples were prepared by polishing to an optimum size of 0.2x0.5x4mm³. Their top and bottom surfaces (0.5x4mm²) were mirror-polished. Gold electrodes were sputtered on both sides (0.2x4mm²), and the width between electrodes was around 0.5mm along the [001] or [111] direction. The details were described elsewhere.[7,8, 10] Domain configuration was always observed under crossed-nicols using a polarizing microscope. DC-bias exposure was done along the [001] or [111] direction, being normal to the incident polarized light. Raman spectra under DC-bias were measured in the backward scattering geometry using a Raman scattering spectrometer with a triple monochromator. DC-bias exposure was done in the same way as that in domain observation. The top surface (0.5x4mm²) was excited by unpolarized Ar ion laser with a wavelength of 514.5nm and power below 20W/cm². The details are described elsewhere.[11]

3. RESULTS AND DISCUSSION

3.1 [001] oriented BaTiO₃ single crystals

Figure 2 shows a strain *vs* electric-field curve of a [001] oriented BaTiO₃ crystal measured using a unipolar electric field. It should be noted that this curve was not obtained at the 1st cycle of electric-field exposure, but after the 2nd cycle of electric-field exposure, *i.e.*, this strain behavior means that after poling. The strain
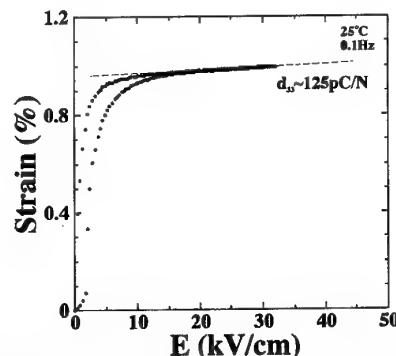
Fig. 2   Strain *vs* electric-field curve for [001] oriented BaTiO₃ crystal under unipolar electric field below 35kV/cm.

behavior exhibits a large strain of around 1 % and a remarkable hysteresis. Such a large strain of around 1% can be caused by tetragonality of BaTiO₃, c/a~1.011, which suggests that domain reorientation can contribute significantly to strain behavior. Moreover, at high electric field above 20kV/cm, the apparent d_{33} was directly estimated at 125pC/N. This value was close to d_{33}~90pC/N in the single-domain BaTiO₃ crystal reported by Zgonik *et al.*,[12] which indicated that over 20kV/cm, BaTiO₃ crystal might be single-domain state. Therefore, Fig. 2 suggests that domain wall motion can affect largely strain behavior.

In situ domain observation was done under DC-bias below 22.1kV/cm.[13] Under no bias, systematic domain configuration with 90° W₁ domain walls of {101} planes was observed. Domain wall motion was observed below 1kV/cm, and finally at around 22.1kV/cm, an almost single-domain state was achieved. On the other hand, with decreasing electric field from 22.1kV/cm, new domains appeared and domain wall density increased. However, domain wall density at decrease of electric field was less than that at increase of electric field, even if the electric fields had the same values. This revealed that a difference in the domain wall density at increasing and decreasing electric fields caused the large hysteresis in the strain *vs* electric-field curve (Fig. 2).

3.2 [111] oriented BaTiO₃ single crystals

Strain *vs* electric-field behaviors in [111] oriented BaTiO₃ crystals were very complicated. All curves were also obtained after the 2nd cycle of electric-field exposure. To simplify the complicated phenomena, these behaviors were separated into four regions: (1) low electric field under 5kV/cm, (2) middle electric field from 5 to 16kV/cm, (3) high electric field from 16 to 26kV/cm and (4) ultrahigh electric field above 26kV/cm, and each behavior is discussed.

3.2.1 Low electric-field region: In the low electric-field region as shown in Fig.3, strain was almost proportional to electric field without hysteresis. Domain wall motion in [001] oriented BaTiO₃ crystals was observed below 1kV/cm. Thus, the strain behavior in Fig. 3 suggested that the engineered domain configuration, as shown in Fig. 4, was induced in [111] poled tetragonal BaTiO₃ crystals. Moreover, the apparent d_{33} obtained directly was 203pC/N, which was almost 1.6 times higher than
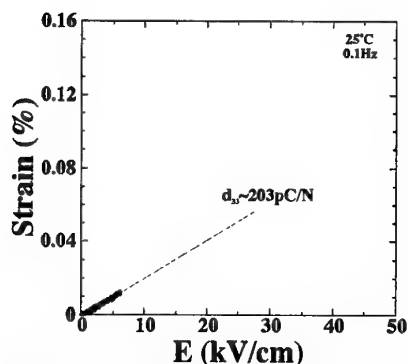
Fig. 3   Strain *vs* electric-field curve for [111] oriented BaTiO₃ crystal under unipolar electric field below 5kV/cm.
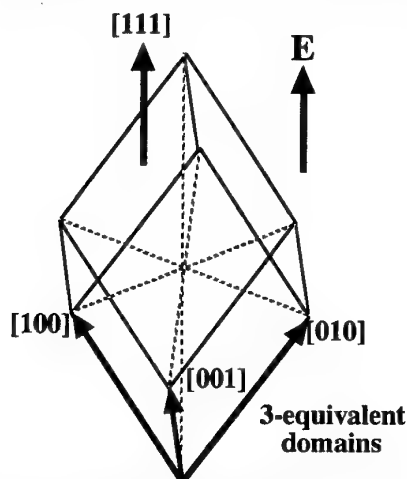
Fig. 4   Schematic engineered domain configuration for [111] poled tetragonal *4mm* BaTiO₃ crystal.

that in a [001] poled single-domain BaTiO₃ crystal.

To confirm the formation of the engineered domain configuration, *in situ* domain observation was done below 4kV/cm.[13] The domain structure under no DC-bias was highly systematic, and three ferroelectric domains with polar directions of [100], [010] and [001] were observed. Although the electric field increased to 4kV/cm, the domain structure did not change. This domain configuration was almost the same as the expected one in Fig. 4. Thus, we confirmed the formation of the engineered domain configuration in [111] poled tetragonal BaTiO₃ crystals.

The above results indicate that application of the engineered domain configuration to tetragonal BaTiO₃ crystals resulted in enhanced piezoelectric activities, *i.e.*, higher d_{33} and non-hysteretic strain *vs* electric-field behavior. Therefore, we believe that the concept of the engineered domain configuration is universal, and can apply to all perovskite-type ferroelectric crystals.

3.2.2 Middle electric-field region: From 5 to 16kV/cm, a large hysteresis was observed in Fig. 5. In general, a hysteresis in the strain *vs* electric-field curve suggests the occurrence of domain wall motion or electric-field-induced phase transition. Thus, *in situ* domain observation and *in situ* Raman observation were done in this electric-field region. As a result, with increasing electric field from 6 to 10kV/cm, domain wall density
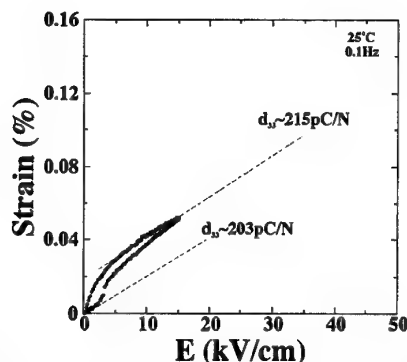
Fig. 5   Strain *vs* electric-field curve for [111] oriented BaTiO₃ crystal under unipolar electric field below 26kV/cm.

increased, while from 10 to 16kV/cm, domain wall density decreased, and partially single-domain region appeared. Measurement of the extinction position in the single-domain region revealed that the regions were assigned to ones with polar directions of <110>. This suggests the formation of monoclinic (=orthorhombic) *m* phase in tetragonal BaTiO₃ crystals. The details are described elsewhere.[11]   Moreover, *in situ* Raman measurement was also done in the same electric-field region. As a result, it was found that in electric-field region from 6 to 16kV/cm, two phases, tetragonal *4mm* and monoclinic *m*, coexisted, and at 16kV/cm, all regions became to monoclinic *m* phase. The details are also described elsewhere.[11] The above results suggested that from 6 to 16kV/cm, an electric-field-induced phase transition occurred from *4mm* to *m*, which is accompanied by the large hysteresis in Fig. 5, but more work may be needed.

3.2.3 High electric-field region: From 16 to 26kV/cm, strain was almost proportional to electric field with a non-hysteretic behavior, as shown in Fig. 6. This strain behavior suggested that another engineered domain configuration such as that shown in Fig. 7 can be induced in [111] poled monoclinic BaTiO₃ crystals. Moreover, the apparent d_{33} obtained directly from Fig. 6 was 295pC/N, which was almost 2.4 times higher than that in a [001] poled single-domain BaTiO₃ crystal. *In situ* Raman measurement in this region revealed that its symmetry was still monoclinic *m*.[11] To confirm the existence of this new engineered domain configuration, *in situ* domain observation in the same electric-field was
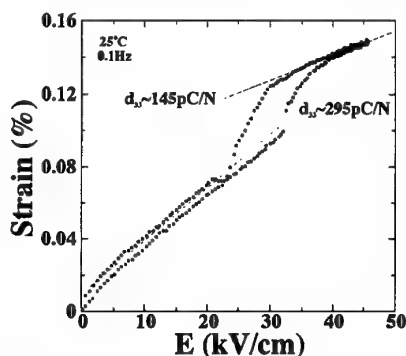
Fig. 6   Strain *vs* electric-field curve for [111] oriented BaTiO₃ crystal under unipolar electric field below 45kV/cm.
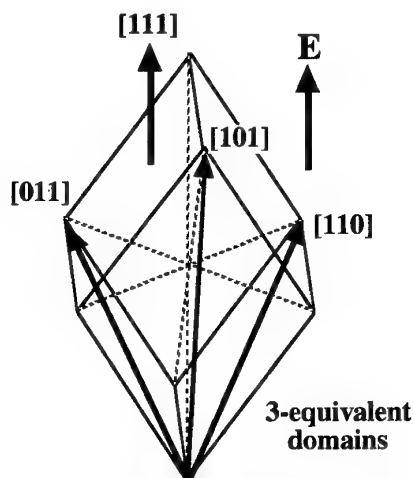
Fig. 7   Schematic engineered domain configuration for [111] poled monoclinic *m* BaTiO₃ crystal.

also done.[13] Even if the electric field increased from 16.3 to 24.5kV/cm, the domain structure did not change. This domain configuration was almost the same as the expected one in Fig. 7. Thus, we confirmed a formation of another new engineered domain configuration in [111] poled monoclinic BaTiO₃ crystals and its enhanced piezoelectric property.

3.2.4 Ultrahigh electric-field region: Above 26kV/cm, a large hysteresis was observed in Fig. 6. To clarify the origin of this change, *in situ* domain observation was done under electric fields from 25 to 30kV/cm.[13] As a result, at 29kV/cm, small cracks occurred near the electrodes, and the cracks grew with increasing electric field. At 30kV/cm, some regions with the extinction position along the [111] direction appeared partially, and then the crystal broke. This indicates the appearance of regions with polar direction of [111] at 30kV/cm, *i.e.*, the formation of rhombohedral *3m* phase in monoclinic *m* BaTiO₃ crystals. Details on this are also described elsewhere.[11] Above 40kV/cm, there is no hysteresis, which suggests the formation of single-domain state in rhombohedral BaTiO₃ crystals. Therefore, we consider that from 30 to 40kV/cm, two phases, *m* and *3m*, coexisted, and above 40kV/cm, all of regions became to *3m*. The above results reveal that above 30kV/cm, an electric-field-induced phase transition occurred from *m* to *3m*. Moreover, in single-domain rhombohedral BaTiO₃ crystals over 40kV/cm, the apparent d_{33} was around 145pC/N, which was 1.2 times larger than that in [001] poled single-domain tetragonal BaTiO₃ crystals.

4. CONCLUSION

In BaTiO₃ single crystals, when a unipolar electric field was applied along the [001] direction, the strain *vs* electric-field curve showed a large hysteresis, and finally BaTiO₃ crystal became to single-domain state with d_{33} of 125pC/N over 20kV/cm. *In situ* domain observation revealed that this large hysteresis is caused by a difference in domain wall density at increase and decrease of electric fields. On the other hand, the strain *vs* electric-field curve in [111] oriented BaTiO₃ single crystals exhibited a very complicated strain behavior.

An electric-field exposure below 5kV/cm resulted in a high d_{33} of 203pC/N and a non-hysteretic strain *vs* electric-field behavior, which suggested the formation of the engineered domain configuration in a tetragonal BaTiO₃ crystal. Therefore, it was confirmed that application of the engineered domain configuration to tetragonal BaTiO₃ crystals caused more enhanced piezoelectric activities compared with single-domain BaTiO₃ crystals. Moreover, *in situ* domain observation and *in situ* Raman measurement under electric fields suggested that the discontinuous change around 10kV/cm can be assigned to the electric-field-induced phase transition from *4mm* to *m* while the discontinuous change around 30kV/cm was assigned to the electric-field-induced phase transition from *m* to *3m*. Moreover, in monoclinic BaTiO₃ crystal, an electric-field exposure from 16 to 26kV/cm gave a high d_{33} of 295pC/N and a hysteresis-free strain *vs* electric-field behavior, which revealed the formation of another new engineered domain configuration in a monoclinic BaTiO₃ crystal. In this study, we found two engineered domain configurations in the [111] poled *4mm* and *m* BaTiO₃ single crystals and their enhanced piezoelectric properties. The difference in d_{33} between tetragonal and monoclinic phases with different engineered domain configurations will be discussed on the basis of crystallography elsewhere.[11] On the basis of the above results, we believe that the concept of the engineered domain configuration is universal and can be applied to all perovskite-type ferroelectric crystals, and improved piezoelectric activity can be achieved.

References
[1]S.-E. Park, M. L. Mulvihill, P. D. Lopath, M. Zipparo and T. R. Shrout, *Proc. 10th IEEE Int. Sympo. Applications of Ferroelectrics* Vol. **1**, 79-82 (1996).
[2]S.-E. Park and T. R. Shrout, *IEEE Trans. Ultrasonics, Ferroelectrics and Frequency Control*, **44** ,1140-47 (1997).
[3]S.-E. Park and T. R. Shrout, *Mater. Res. Innovat.*, **1**, 20-25 (1997).
[4]S.-E. Park and T. R. Shrout, *J. Appl. Phys.*, **82**, 1804-11 (1997).
[5]J. Kuwata, K. Uchino and S. Nomura, *Ferroelectrics*, **37**, 579-82 (1981).
[6]J. Kuwata, K. Uchino and S. Nomura, *Jpn. J. Appl. Phys.*, **21**, 1298-302 (1982).
[7]S. Wada, S.-E. Park, L. E. Cross and T. R. Shrout, *J. Korean Phys. Soc.*, **32**, S1290-93 (1998).
[8]S. Wada, S.-E. Park, L. E. Cross and T. R. Shrout, *Ferroelectrics*, **221**, 147-55 (1999).
[9]S. Ajimura, K. Tomomatu, O. Nakao, A. Kurosaka, H. Tominaga and O. Fukuda, *J. Opt. Soc. Am. B*, **9**, 1609-13 (1992).
[10]D.-S. Paik, S.-E. Park, S. Wada, S.-F. Liu and T. R. Shrout, *J. Appl. Phys.*, **85**, 1080-83 (1999).
[11]S. Wada, S. Suzuki, T. Noma, T. Suzuki, M. Osada, M. Kakihana, S.-E. Park, L. E. Cross and T. R. Shrout, submitted to *J. Appl. Phys.*
[12]M. Zgonik, P. Bernasconi, M. Duelli, R. Schlesser, P. Gunter, M. H. Garrett, D. Rytz, Y. Zhu and X. Wu, *Phys. Rev. B*, **50**, 5941-49 (1994).
[13]S. Wada, S. Suzuki, T. Noma, T. Suzuki, M. Osada, M. Kakihana, S.-E. Park, L. E. Cross and T. R. Shrout, *Jpn. J. Appl. Phys.*, (1999) in press.

CRYSTALLOGRAPHICALLY ENGINEERED SINGLE CRYSTALS FOR HIGH PERFORMANCE PIEZOELECTRICS

Seung-Eek Park, Satoshi Wada*, Paul W. Rehrig, Shi-Fang Liu,
L. Eric Cross, and Thomas R. Shrout

Materials Research Laboratory, The Pennsylvania State University, University Park,PA16802, USA

Fax: 814-865-2326, email: sxp37@psu.edu

* Tokyo University of Agriculture & Technology, Tokyo 184-8588, Japan

Crystallographic engineering, a concept to utilize crystal anisotropy as well as an engineered domain configuration, resulted in significant enhancement in piezoelectric activity not only for relaxor ferroelectric crystal but for normal ferroelectric $BaTiO_3$ crystals. Electromechanical couplings (k_{33}) ~ 85% and piezoelectric coefficients (d_{33}) as high as 500 pC/N, higher or comparable to those of lead based ceramics such as PZT and significantly larger than those of tetragonal $BaTiO_3$ crystals (k_{33} ~ 65%, d_{33} ~ 130 pC/N), were detected from crystallographically engineered orthorhombic $BaTiO_3$ crystals.

1. INTRODUCTION

Recently, crystallographically engineered relaxor ferroelectric single crystals of $Pb(Zn_{1/3}Nb_{2/3})O_3$ (PZN), $Pb(Mg_{1/3}Nb_{2/3})O_3$ (PMN) and their solid solutions with the normal ferroelectric $PbTiO_3$ (PT) revealed piezoelectric properties much superior to morphotropic phase boundary (MPB) ceramics such as $Pb(Zr,Ti)O_3$ (PZT).[1-4] Ultrahigh piezoelectric properties (k_{33} ~ 94%, d_{33} ~ 2500 pC/N), hysteresis minimized strain values as high as 0.6%, and large E-field induced strain values (1.7%) were reported. Actuator performance of these crystals was also found to be superior to polycrystalline ceramics, i.e. the strain energy density ~ 66400 J/m^3 was delivered at 20kV/cm for PZN-4.5%PT crystals, 5 times higher than hard PZT.[5] These ultrahigh properties could be achievable from rhombohedral crystals oriented along their non-polar <001> axis, a key concept of crystallographic engineering. In contrast, rhombohedral crystals poled along their polar direction <111> exhibited significantly inferior properties, i.e. k_{33} < 50% and d_{33} ~ 100 pC/N.

In addition to the ultrahigh piezoelectric performance, hysteresis minimized strain vs. E-field behavior was another important characteristic of crystallographically engineered relaxor ferroelectric single crystals. This behavior indicates minimal domain motion under bias, a phenomenon not expected for crystals of multi-domain state. The stable domain configuration resulted in highly reliable materials for actuation, i.e. no material degradation was detected for more than 10^7 unipolar driving cycles at high fields (>50 kV/cm, 1kHz).[5]

Based on the concept of crystallographic engineering used for high performance relaxor ferroelectric single crystals, single crystals or epitaxial form of any known ferroelectric materials may exhibit significant enhancement in electromechanical performance. It was the objective of this paper to review and apply the concept to other ferroelectric crystals such as $BaTiO_3$, in order to evaluate the possibility of piezoelectric performance enhancement. Strain vs. E-field behavior of engineered crystals will be discussed with respect to crystal structure and domain configuration.

2. ENGINEERED DOMAIN CONFIGURATION AND MACROSCOPIC SYMMETRY

In ref. [6], macroscopic symmetry 4mm out of local 3m symmetry was suggested assuming that each type of <111> domain distributed equivalently for <001> oriented crystals to exhibit a static domain configuration under bias. The stable domain configuration was evidenced by in-situ domain observation [7] and hysteresis minimized strain vs. E-field behavior. This type of behavior was found in other <001> oriented rhombohedral crystals such as (1-x)PZN-xPT (x=0-0.09), or (1-y)PMN-yPT (y=0.2-0.35), or (1-z) PSN-zPT (z=0.25-0.45). There is another way for domain configuration to be static under dc bias, domains of <111> and <-1-11> and of <-111> and <1-11> being equally distributed but distribution of two pairs not equal resulting in lower macroscopic symmetry 2mm. Recent investigation on elastic properties of these crystallographically engineered relaxor-PT crystals revealed that symmetry 2mm is more probable,[8] the detail of which will be reported else where.

It is believed that crystallographic engineering is key to acquire ultrahigh piezoelectric property in relaxor ferroelectric single crystals. Here, the question arises, will similar piezoelectric property enhancement be observed for normal ferroelectric perovskite crystals? - the topic of the following section.

3. CRYSTALLOGRAPHICALLY ENGINEERED $BaTiO_3$ BASED SINGLE CRYSTALS

3.1 $BaTiO_3$ crystals with high piezoelectric performance

As considered in the phenomenological theory by Devonshire,[9] the unit cell symmetry dictates the direction of polar shift, i.e. orthogonal (4mm), face diagonal (mm2), and body diagonal (3m) based on the primitive perovskite cell. Also in orthorhombic crystals, four polarization directions (<101>, <011>, <-101>, <0-11>) are energetically equivalent and analogous
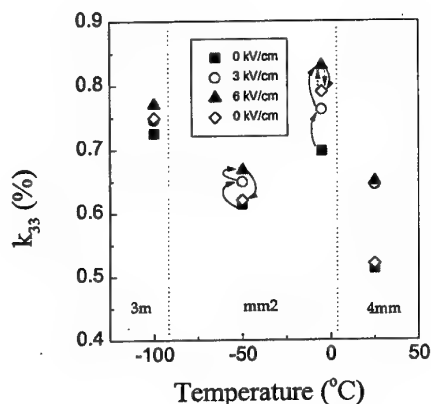
Fig. 1 k_{33} as a function of temperature for <001> poled BaTiO$_3$ crystals under various dc-bias. (solid arrows : first cycle, dashed arrows: second cycle)

crystallographic engineering is expected when E-field is applied along <001>.

Figure 1 presents longitudinal electromechanical coupling (k_{33}) as a function of temperature for <001> poled BaTiO$_3$ crystals, under dc-bias. Samples for measuring dielectric and piezoelectric properties were prepared using commercially available BaTiO$_3$ single crystals (optical grade, Fujikura Ltd.), grown by top seeded solution growth (TSSG) technique. At room temperature, the increase of k_{33} value from ~0.53 (0 kV/cm) to 0.65 (6kV/cm) was the result of domain reorientation, which had been partially depoled due to domain instability in the tetragonal crystal poled along its polar direction <001>. Note that a similar behavior was found for rhombohedral PZN crystals poled along its polar <111> direction.   It is also noted that k_{33} ~ 0.53 (0 kV/cm), a value from partially depoled crystals in this work, corresponds to values reported earlier, i.e. ~0.56 [10] and ~0.55 [11] for tetragonal BaTiO$_3$ crystals.
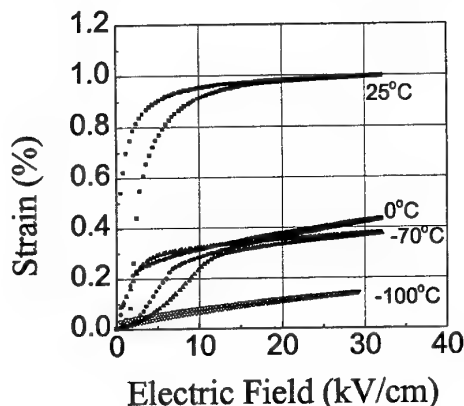
Fig. 2 Strain vs. unipolar E-field behaviors of <001> Oriented BaTiO$_3$ crystal

At lower temperatures, k_{33} was also found to be dependent on dc-bias due to crystal depoling as a result of phase transitions as well as domain instability. For an orthorhombic crystal at -5°C, k_{33} ~ 0.7 initially detected at 0 kV/cm increased with increasing bias, followed by k_{33} as high as 0.83 at 6 kV/cm. After E-field exposure, the unbiased k_{33} value was as high as 0.79, being a starting point of second cycle (dashed arrows in fig. 1). The initial lower value of electromechanical coupling for the first cycle (solid arrows in fig. 1) must be a consequence of depoling caused by the tetragonal-orthorhombic phase transition. Note that a k_{33} ~ 0.83 for non-lead BaTiO$_3$ crystals is significantly larger than room temperature k_{33} values of Pb-based polycrystalline PZT's (0.5 to 0.75), the current piezoelectric material of choice.

Fig. 2 presents strain vs. unipolar E-field behavior for <001> poled BaTiO$_3$ crystals at various temperatures. Room temperature strain values as high as 1% is a consequence of depoling and domain reorientation. This significant c-a domain switching may be ascribed to the pointed load by LVDT probe. Note that total strain as high as 1.07% strain is involved with a full ferroelectric strain curve of BaTiO$_3$ crystals, but practically unusable. Single domain state tetragonal crystals, reflected by the non-hysteretic strain vs. E-field behavior, could be achieved at E-fields > ~10 kV/cm at room temperature as shown in fig. 2. Piezoelectric coefficient d_{33} ~ 128pC/N, similar to that theoretically simulated by Devonshire,[9] was calculated from the non-hysteretic portion of strain vs. E-field behavior at 20 kV/cm.

The hysteresis found in the orthorhombic crystal (0°C, -70°C at E<10kV/cm in fig.2) was also ascribed to domain instability. In contrast, the engineered domain state of the rhombohedral crystal (-100°C) was found to be stable as can be seen in fig. 2, resulting in the crystal retaining macro-symmetry 4mm (or 2mm) for the overall range of applied E-field. Note relaxor based single crystals with stable engineered domain states are also rhombohedral. Although further study is required to clarify the relationship between crystal structure and engineered domain state, it is suggested that lattice symmetry should determine the (in)stability of the engineered domain state and that rhombic lattice distortion be critical to stabilize the domain state in <001> poled ferroelectric crystals.

For comparison of piezoelectric activity, only non-hysteretic portion of the strain vs. E-field (E>10 kV/cm) curves are presented in fig. 3 and apparent d_{33}'s calculated from fig. 3 are plotted in fig. 4. As plotted, crystallographic engineering results in BaTiO$_3$ crystals with significantly enhanced piezoelectric activity such as d_{33} ~ 500 pC/N. This value is comparable to room temperature d_{33} values of PZT's. The rhombohedral BaTiO$_3$ crystal at -100°C exhibited d_{33} as high as 350 pC/N, also larger than that of polycrystalline PZT's at the same temperature.[12] Here another question arises, - can orthorhombic or rhombohedral BaTiO$_3$ be stabilized at room temperature? Piezoelectric properties of orthorhombic Ba(Zr,Ti)O$_3$ crystals is the topic of the following section.
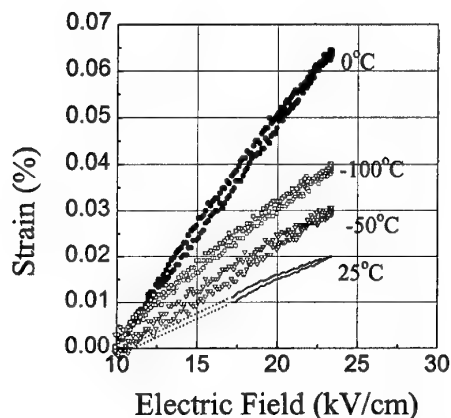
Fig. 3 Strain vs. E-field behavior as a function of temperature for <001> oriented BaTiO₃ crystals (non-hysteretic portion).

3.2 Crystallographically Engineered Ba(Zr,Ti)O₃ Single Crystals

It is well known that the phase transition temperatures in BaTiO₃ can be altered by doping with either A or B-site substitutions.[10] Zirconium is one element that pinches the transition temperatures so that the rhombohedral-orthorhombic and orthorhombic-tetragonal phase transition temperatures are raised while the Curie temperature is lowered. By varying the amount of dopant it is possible to stabilize either rhombohedral or orthorhombic phase at room temperature. A templated grain growth (TGG) was used to produce crystals with Zr concentrations between 4.5 and 8.5 mol% for rapid assessment of crystals of varying composition. Details in the crystal growth procedure can be found elsewhere.[13]
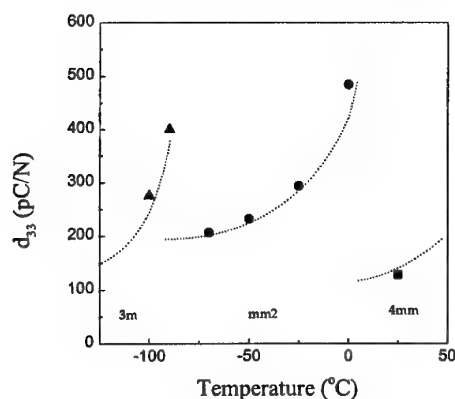
Fig. 4 d_{33} as a function of temperature for <001> oriented BaTiO₃ crystals.
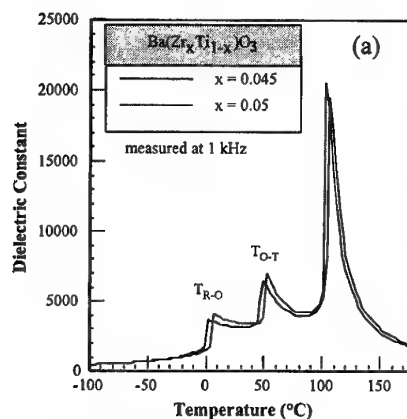
Fig. 5 Dielectric constant as a function of temperature at 1kHz for TGG grown Ba(Zr$_x$Ti$_{1-x}$)O₃ single crystals

Fig. 5 shows the dielectric constant (k_3^T) as a function of temperature and mol% zirconium. As seen in polycrystalline Zr-doped BaTiO₃, the transition temperatures are pinched with increasing mol% zirconium.[13,14] The 4.5 (BZT-4.5) and 5.0 (BZT-5.0) mol% Zr samples show distinct transition temperatures with both the rhombohedral-orthorhombic and orthorhombic-tetragonal transition temperatures shifted up by approximately 80°C (T$_{R-O}$ = 0°C) and 45°C (T$_{O-T}$ = 50°C), respectively. The result of this shift is that the orthorhombic phase is stabilized at room temperature.

Fig. 6 shows the unipolar strain behavior at room temperature for BZT-4.5 and BZT-5.0 crystals poled and excited along the pseudocubic ⟨001⟩ as a function of electric field. Both crystals show maximum strain levels of approximately 0.48% at a maximum field of ~60 kV/cm, which includes ~0.35% strain associated with domain reorientation.
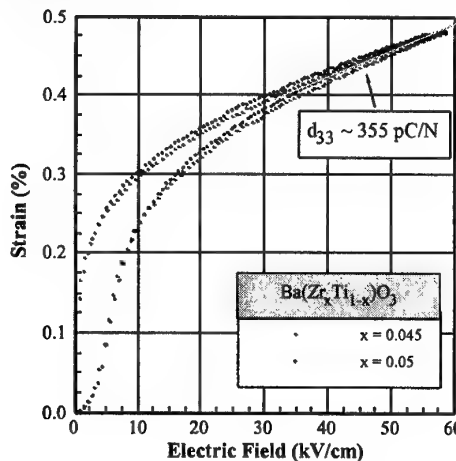
Fig. 6 Strain vs. unipolar E-field behaviors for TGG grown Ba(Zr$_x$Ti$_{1-x}$)O₃ single crystals, where x = 0.045 and 0.05.
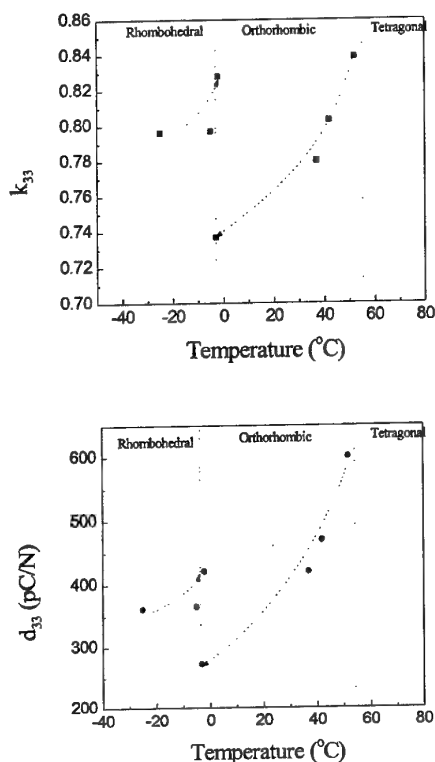
Fig. 7 k_{33} and d_{33} of <001> Ba(Zr$_{0.05}$Ti$_{0.95}$)O$_7$ crystal.

It is noted that this partial depoling at lower field was also detected for orthorhombic BaTiO$_3$ crystals in the previous section. After saturation, the strain

behavior from 30-60 kV/cm corresponds to a d_{33} of 355 and 340 pC/N for BZT-4.5 and BZT-5.0, respectively. Using the IEEE standard technique,[16] k_{33} and d_{33} values of 0.74 and 340 pC/N, respectively, were also determined for 4.5 mol% Zr-doped orthorhombic BaTiO$_3$ single crystal (BZT-4.5), under 5 kV/cm.

Similar to undoped BaTiO$_3$, maximum electromechanical coupling and piezoelectric coefficients could be found at temperature range close to phase boundary, as shown in fig. 7. For Ba(Zr$_{0.05}$Ti$_{0.95}$)O$_3$, k_{33}~85% and d_{33}~600pC/N were detected under 5kV/cm at 50°C. Authors effort to optimize the composition to achieve maximum room temperature piezoelectric activity is ongoing.

4. CONCLUSIONS

Crystallographic engineering resulted in ferroelectric perovskite single crystals with significantly enhanced piezoelectric properties. Crystallographic engineering of BaTiO$_3$ crystals resulted in orthorhombic crystals (0°C) with k_{33} ~ 85% and d_{33} ~ 500 pC/N, better or comparable to those of PZT's. At -90°C, rhombohedral BaTiO$_3$

crystals with k_{33} ~ 79% and d_{33} ~ 400 pC/N were found to be superior to PZT's at the same temperature. Although analogous macro-symmetry, rhombohedral (3m) crystals (-100°C) exhibited a stable domain configuration whereas the adjacent orthorhombic crystal (-70°C) were depoled. Single crystals of room temperature orthorhombic Ba(Zr,Ti)O$_3$ prepared using templated grain growth technique exhibit k_{33} and d_{33} values up to 0.85 and 600 pC/N, respectively, also by utilizing crystallographic engineering.

5. REFERENCES

1. J. Kuwata, K. Uchino, and S. Nomura, *Jap. J. Appl. Phys.*, **21** [9], 1298-1302, 1982.
2. S.-E. Park and T. R. Shrout, *J. Appl. Phys.*, **82** [4], 1804-1811, 1997.
3. S.-E. Park and T. R. Shrout, *IEEE Trans. on Ultras., Ferro. Freq. Cont. on Ultras. Trans..*, **44** [5], 1140-1147, 1997.
4. S.-F. Liu, S.-E. Park, T. R. Shrout, and L. E. Cross, *J. Appl. Phys.*, 85 [5], 2810-2814, 1999.
5. S.-E. Park, V. Vedula, M.-J. Pan, W. S. Hackenberger, P. Pertsch, and T. R. Shrout, *Proceedings on SPIE's 5th Annual International Symmposium on Smart Structures and Materials*, San Diego, CA, March 1998.
6. S.-E. Park and T. R. Shrout, *Proceedings on 8th US-Japan Seminar on Dielectric and Piezoelectric Ceramic Thin Films*, 235-241, Plymouth, MA, October 1997.
7. S. Wada, S.-E. Park, L. E. Cross, and T. R. Shrout, *J. Korean Phys. Soc.*, 32, 1290-1293, 1998.
8. J. Yin and W. Cao, Private Communication.
9. A. F. Devonshire, *Philosophical Magazine*, **42**, pp. 1065-1079, 1951.
10. B. Jaffe, W. R. Cook and H. L. Jaffe, *Piezoelectric Ceramics*, Academic Press Ltd., New York, 1971.
11. M. Zgonik, P. Bernasconi, M. Duelli, R. Schlesser, and P. Gunter, Phys. Rev. B, **50** [9], pp. 5941-5948, 1994.
12. X. L. Zhang, Z. X. Chen, L. E. Cross, W. A. Schulze, J. Mat. Science, **18**, pp. 968-972, 1983.
13. P. Rehrig, "Templated grain growth of BaTiO$_3$ based perovskite single crystals," Ph. D. Thesis, The Pennsylvania State University, 1999.
14. D. Hennings and A. Schnell, *J. Am. Ceram. Soc.*, **65** [11], 539-544, 1982.
15. R. C. Kell and N. J. Hellicar, *Acustica*, **6** , 235-238, 1956.
16. IEEE Standard on Piezoelectricity, American National Standards Institue, 1976.

Non-180° Domain Contribution to the Properties of PZN-PT Single Crystals

Takaaki Tsurumi, Keishiro Okamoto, Naoki Ohashi and Yohachi Yamashita*

Department of Metallurgy and Ceramics Science, Graduate School of Science and Engineering,
Tokyo Institute of Technology,
Fax: 81-3-5734-2514, e-mail: ttsurumi@ceram.titech.ac.jp
*Materials and Devices Research Lab., Toshiba Corp.
Fax: 81-44-520-5893, e-mail: yohachi.yamashita@toshiba.co.jp

In order to elucidate the non-180° domain contribution to the properties of $0.91Pb(Zn_{1/3}Nb_{2/3})O_3$-$0.9PbTiO_3$ (PZN-PT) single crystals, [001] crystal plates with uniform domain structures, 110° (010) type domains and 70° type (011) domains, were cut from a large wafer, and electric and piezoelectric properties were measured for these crystal plates. The experimental results of dielectric constants, P-E hysteresis curves, electric-field-induced strains and their frequency dependence indicated that the domain contribution to these properties is larger in the 70° domains than in the 110° domains. This difference in the domain contribution of the two domain structures was considered by the relation between the directions of spontaneous polarization and domain walls and possibility of the domain reversal by electric field.

1. INTRODUCTION

A giant piezoelectric effect (k_{33}=0.92 and d_{33}=1500pC/N) of $Pb(Zn_{1/3}Nb_{2/3})O_3$-$PbTiO_3$ (PZN-PT) single crystals was first discovered by Kuwata et al.[1]. Park and Shrout [2-4] recently found that [001] oriented rhombohedral PZN-PT single crystals showed an electric-field-induced strain of 1.7% at 120kV/cm, d_{33} over 2500pC/N and hysteresis-free strain vs. electric field behavior. They pointed out that a very stable domain structure was formed in [001] wafer of PZN-PT crystal under DC-bias and the domain wall motion was not detectable up to 20kV/cm. The large and hysteresis-minimized strain of PZN-PT crystals was due to this domain situation, called engineered domains.

However, the relation between the domain structures and electric or piezoelectric properties is still ambiguous in PZN-PT crystals because of the lack of experimental results on the dependence of these properties on the domain structures. Yamashita et al. [5-6] have been trying to make large PZN-PT crystals, and recently they have grown crystal ingots with 40mmφ by Bridgeman method. Wafers with 20 - 40mmφ can be obtained from the ingots, which enable us to select crystal plates with a uniform domain structure. In this study, we have measured electric and piezoelectric properties of PZN-PT crystals with specified domain structures and found a marked dependence of properties on domain structures.

2. EXPERIMENTAL PROCEDURE

[001] wafers of PZN-PT crystals with the composition of 0.91PZN-0.9PT were provided from Toshiba Corp. Domain structures in the wafers were identified with an optical microscope. Crystal plates (2x2mm²) with uniform domain structures were cut from the wafer and used for the following measurements.

Dielectric constants of the crystal plates were measured by an impedance analyzer (hp4192A) as a function of frequency. P-E hysteresis curves were measured by a ferroelectric test system (Radiant Tech. RT66A) at 5Hz.

The electric-field-induced strains of PZN-PT crystal plates were measured by a laser-fiber type non-contact dilatometer (resolution: 0.025μm) and a Mach-Zehnder type laser interferometer shown in Fig.1 [7]. In this system, He-Ne laser beam is sprit into two directions (beam1 and beam2) by a polarized beam splitter. The beam1 is a reference beam. The beam2 is reflected by the two mirrors attached on the surfaces of a PZN-PT crystal plate. The beam1 and beam2 are joined at a half mirror to make interference fringes. The piezoelectric displacement of the crystal moves the fringes, which can be detected as a change of light intensity. The signal of the photo-detector is amplified and stored in a digital oscilloscope with the signal applied to the crystal. The displacement of the crystal can be calculated from the change in the signal of photo-detector.
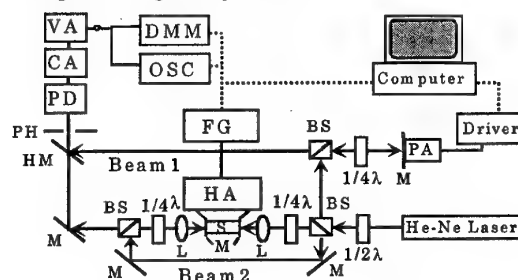
VA:Voltage amp., OSC:Storage oscilloscope,
HA:High voltage amp., M:Mirror, L:Lens,
HM:Harf mirror, BS:Beam splitter,
PH:Pin hole, DMM:Digital multi meter,
FG:Function generator,PD:Photo diode,
CA:Current amp., PA:piezo-actuator, S:Sample

Fig.1 Schematic diagram of Mach-Zehnder interferometer

3. RESULTS AND DISCUSSION

3.1 Identification of Domain Structure

A photograph of a wafer of PZN-PT crystal is shown in Fig.2. This wafer was not homogeneous and consisted of

four kinds of different regions. Inclusions of PbO were observed in one region. Three different domain structures, two with stripe domain walls and one with randomly oriented domains, were observed in other regions.

5mm

Fig.2 Photograph of a wafer

Optical micrographs of two kinds of domain structures with stripe domain walls were shown in Fig.3. Crossed nicols observation in polarizing microscope indicated that the domain walls were vertical to the crystal plates and the extinction positions of neighboring domains were approximately identical for both domain structures. By considering these information and the relation between extinction positions and the direction of domain walls, the domain structures (A) and (B) in Fig.3 were identified as $110°$ (010) type domains (Fig.4(A)) and $70°$ (011) type domains (Fig.4(B)) in rhombohedral phase. For electric measurements, Pt-sputtered electrodes were made on the surfaces with gray color in Fig.4.

(A) 10 μm   (B) 2 μm
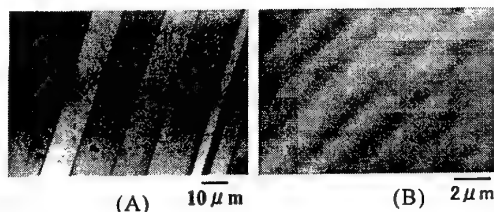
Fig.3 Two domain structures observed in PZN-PT crystals

Direction of electric field

(A)   (B)
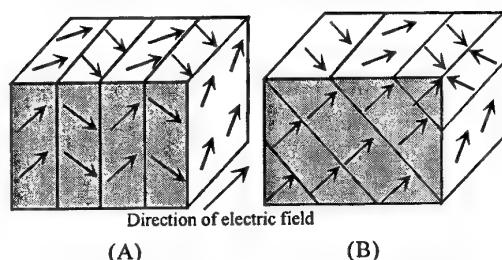
Fig.4 Two domain structures corresponding to the optical micrographs in Fig.3(A) and Fig.3 (B).
(A) $110°$ (010) type domains and
(B) $70°$ (011) type domains.
Arrows denote projections of the polarization vector into the corresponding plane.

3.2 Electric Properties
Figure 5 shows the frequency dependence of relative dielectric constant of the crystal plates with the domain structures in Fig.4 (A) and (B). Dielectric constants decrease with increasing frequency for both crystals. It

is important that the dielectric constant of $70°$ domains is larger that that of $110°$ domains. Arlt et al.[8] pointed out that the non-$180°$ domain wall motion increased the dielectric constant. The non-$180°$ domain contribution to the dielectric constant was also observed in PT single crystals [9]. The results in Fig.5 indicate that the non-$180°$ domains affects the dielectric constants in PZN-PT crystals, and the domain contribution of $70°$ domains are larger than that of $110°$ domains if the electric field is applied to the direction shown in Fig.4.
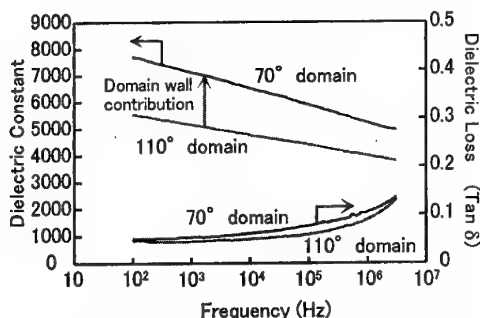
Fig.5 Dielectric properties of PZN-PT crystals with different domain structures.

Figure 6 shows the P-E hysteresis curves of PZN-PT crystals with different domain structures. Spontaneous polarization of the $70°$ domain crystal is about $28\mu C/cm^2$ and that of $110°$ domain crystal is about $22\mu C/cm^2$. Coercive field of the two crystals is about 650V/mm and independent of domain structure. It should be noted that the shape of the P-E hysteresis curves depends on the domain structures, i.e.: the $110°$ domain crystal shows a hysteresis curve with a rectangular shape, indicating the digital domain switching mainly due to the $180°$ domain reversal. The gradual polarization reversal in the $70°$ domain crystal shows the contribution of non-$180°$ domains. The P-E hysteresis curves indicate that the contribution of $70°$ domains is larger than that of $110°$ domains.
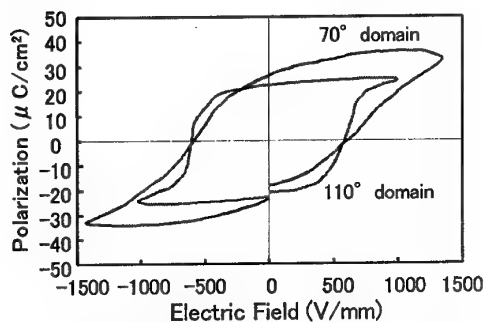
Fig.6 P-E hysteresis curves of PZN-PT crystals with different domain structures.

3.3 Electric-Field-Induced Strains
Figure 7 shows the electric-field-induced strain vs. electric field curve of PZN-PT crystals measured by the laser-fiber type dilatometer. The frequency was about 0.02Hz. Before the

measurements, the poling procedure was carried out at 1.5kV/mm for 30 min at room temperature. It was found that the strain vs. electric field curve changes markedly with the domain structures.

In the 70° domain crystal, a large hysteresis is observed in the strain curve. This hysteresis is due to the contribution of domain wall motion in 70° domain structure. The strain of the 70° domain crystal is larger than that of the 110° domain crystal. In the first measurement of the 110° domain crystal, a large residual strain was observed (dotted line in Fig.7) but the residual strain was reduced in the successive measurements. This seems to indicate that the poling of the crystal is proceeded during the first measurement. After the full poling, the residual strain and hysteresis were not observed in the 110° domain crystal, showing that the non-180° domain contribution is small [7]. The results in Fig.7 indicates that the domain contribution to the electric-field-induced strain is larger in the 70° domain crystal than in the 110° domain crystals.
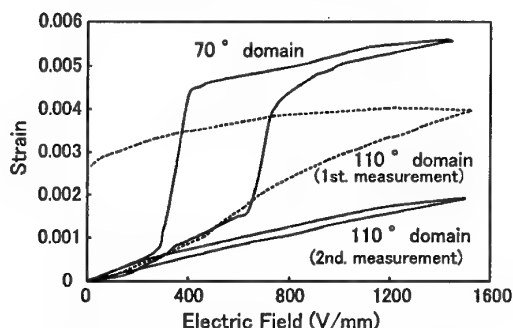
Fig.7 Electric-field-strain vs. electric field curves of PZN-PT crystals.

The apparent piezoelectric constants, determined from the slope of the strain vs. electric curve, are shown in Fig.8 as a function of frequency. The strains at high frequencies were measured by the interferometer shown in Fig.1. Large dispersion of piezoelectric constant is observed in the 70° domain crystal. The similar dispersion was observed in PZT ceramics [7] but the relaxation frequency of PZT ceramics (100- 400Hz) was much higher than PZN-PT crystals (~0.1Hz). The dispersion of piezoelectric constant is caused by the non-180° domain wall motion (extrinsic piezoelectric effect)
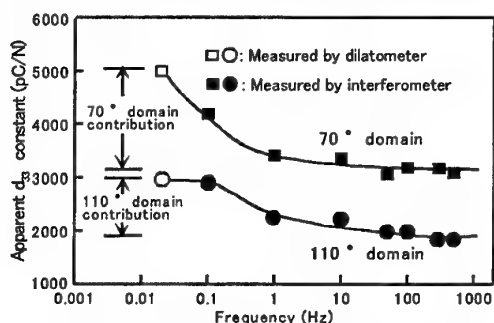
Fig.8 Apparent piezoelectric constant of PZN-PT crystals as a function of frequency.

because the velocity of the ferroelastic domain wall motion is restricted in the crystal. In the 110° domain crystal, the dispersion of piezoelectric constant is also observed but its degree is less than the 70° domain crystal. This result also indicates that the domain contribution to the apparent piezoelectric constants is larger in the 70° domain crystal than in the 110° domain crystal.

The apparent piezoelectric constants of the two crystals asymptotically approach to certain values with increasing frequency (Fig.8). The piezoelectric constant at high frequencies can be regarded as an intrinsic piezoelectric effect without the domain contribution. However, it is important that the piezoelectric constants at high frequencies are different in the two domain structures. This means that the domain contribution still exists in the piezoelectric constants at high frequencies because the averaged crystallographic orientation is the same in the two crystals. We have not understand the origin of the non-180° domain contribution to the piezoelectric constant at higher frequencies than the observed relaxation, but it may be a vibration of domain walls rather than the shift of domain wall which contributes to the electric-field-strain at low frequencies. The variation of the piezoelectric properties in the crystal plates cut from the same wafer is a serious problem for practical applications such as ultrasonic transducers. In order to understand the domain contribution in piezoelectric property, it seems to be necessary to measure the piezoelectric dispersion in a wide frequency region.

3.4. 70° and 100° Domains and Their Contributions to the Properties

All experimental results mentioned above indicated that the contribution to the properties was larger in the 70° domains than in the 110° domains. The reason was considered as follow.

Figure 9 shows the directions of spontaneous polarization and the domain walls in 70° (010) type domains and 110° (011) type domains. From the consistency of spontaneous strains in neighboring domains, the following equation should be satisfied [10]:

$$\left(S_{ij} - S'_{ij}\right)x_i x_j = 0 \qquad (1)$$

where S_{ij}, S'_{ij} are spontaneous strains in neighboring domains, and x_i, x_j are coordinates on the domain wall between two neighboring domains. In the 110° (010) type domain, the directions of spontaneous polarization in the neighboring domains (a1 and a2) are 3 and 2 (Fig.9(A)) and the equation of domain wall becomes $y = 0$ to satisfy the eq.(1). In the 70° (011) type domain, the directions of spontaneous polarization in the neighboring domains (b1 and b2) are 1 and 3 (Fig.9(B)) and the equation of domain wall becomes $y = -z$.

The electric field was applied along the [100] direction in this study as shown in Fig.9. In the 110° domains, the spontaneous polarization along the 2-direction (a2 domain) has to switch to the 4'-direction by the electric field. However, this switching does not likely to occur because it requires the change in direction of domain walls. After switching, the equation

of domain wall separating the neighboring domains with the polarization direction of 3 and 4' is $y = -x$, therefore, the switching of spontaneous polarization from 2 to 4' direction in the a2 domain requires the rotation of whole domain walls. On the other hand, the spontaneous polarization in the $70°$ domains easily change its direction by the electric field (1 to 3 direction in b1 domain in Fig.9(B)) without the change of the equation of domain wall. This mean the shift of domain walls easily occurs in the $70°$ domains by the application of electric field along [100]. We think this difference in the $110°$ and $70°$ domains give the differences in the domain contribution to the properties observed for the two domain structures.

(A) 110° (010) type domain
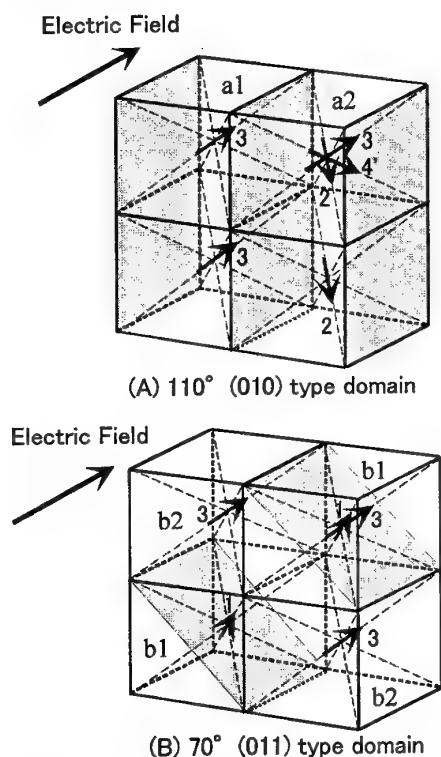
(B) 70° (011) type domain

Fig.9 Directions of spontaneous polarization and domain walls in (A) 110° domain and (B)70° domain structures in rhombohedral phase.

4. SUMMARY

PZN-PT crystal plates with uniform domain structures, $110°$ (010) type domains and $70°$ (001) type domains, were cut from a [001] wafer, and electric and piezoelectric properties were measured for the crystal plates with the two domain structures. All experimental results indicated that the domain contribution to the properties was larger in $70°$ domains than in $110°$ domains. The reason of this difference was considered by the relation between the directions of spontaneous polarization and domain walls in the two domain structures.

References
[1] J.Kuwata, K.Uchino and S.Nomura,Jpn.J.Appl.Phys., 21, 1298 (1982).
[2] S.-E.Park, M.L.Mulvihill, P.D.Lopath, M.Zipparo and T.R.Shrout, Proc.10th IEEE Int. Sumpo. Applications of Ferroelectrics, Vol.1, 79 (1996).
[3] S.-E.Park, and T.R.Shrout, IEEE Trams. Ultrasonics, Ferroelectrics and Frequency Control, 44, 1140 (1997).
[4] S.-E.Park and T.R.Shrout, J.Appl.Phys., 82, 1804 (1997).
[5] T.Kobayashi, S.Shimanuki, S.Saitoh and Y.Yamashita, Jpn.J.Appl.Phys., 36, 6035 (1997).
[6] K.Harada, S.Shimanuki, T.Kobayashi, S.Saitoh and Y.Yamashita, J.Am.Ceram.Soc., 81, 2785 (1998).
[7] T.Tsurumi, N.Ikeda and N.Ohashi, J.Ceram.Soc.Jpn., 106,1062-66 (1998).
[8] G.Arlt, H.Dederichs and R.Herbiet, Ferroelctrics, 74, 37 (1987).
[9] K.Kakuta, T.Tsurumi and O.Fukunaga, Jpn.J.Appl.Phys., 34, 5341-45 (1995).
[10] J.Sapriel, Phys.Rev., B12, 5128 (1975).

Effective Material Properties of Multi-domain Ferroelectric Crystals

Wenwu Cao and Jiří Erhart[*]

Materials Research Laboratory, The Pennsylvania State University, University Park, PA 16802
Fax: 01-814-865-2326, e-mail: cao@math.psu.edu

There are three distinct groups of crystalline materials: single domain single crystals, multi-domain single crystals and ceramics. They form a three level hierarchical structure with the single domain single crystals as the fundamental base. The properties of single domain single crystals are well defined and dictated by the symmetry of the crystal. However, relationship between properties of single domain single crystals and the other two higher level groups is still not well established. A simple volume percentage weighting scheme plus an orientational average is insufficient for complex systems. Moreover, the recently developed PZN-PT and PMN-PT multi-domain single crystal systems have only limited number of domains in each sample, which do not justify the use of statistical average. On the other hand, the well defined orientational relationship among those limited number of domains in a multi-domain single crystal system makes it possible to directly calculate the effective material properties. This paper presents a calculation scheme for the effective material properties of a twined ferroelectric system. Numerical application was performed on a twin structure consisting two domains of tetragonal $BaTiO_3$ crystal with their polarization vectors in [100] and [010] and a domain wall orientated in [110].

I. INTRODUCTION

The macroscopic properties of a multi-domain ferroelectric system are the collective contribution of many differently oriented domains. Generally speaking, the macroscopic symmetry of a multi-domain system is different from the microscopic symmetry of the crystal. The symmetry operations here refer to the spatial relationship among the building blocks, i.e., the domains, rather than the atomic arrangements. The multi-domain relaxor based ferroelectric single-crystals PZN-PT and PMN-PT are practical examples of such systems.[1] In this case, the crystal symmetry belongs to rhombohedral $3m$ with dipoles formed in <111> of the cubic structure at the ferroelectric phase transition. When it is poled along [001] the effective symmetry of the multi-domain systems could be tetragonal $4mm$,[2] orthorhombic $mm2$, or monoclinic m.[3,4] It also depends on the relative volume ratio of the existing domains.[5]

For simplicity, we calculate a single twinband structure in which only two of the low temperature variants are present. The symmetry of such a twin structure of two domains with equal volume ratio is $mm2$.[5] We give here the general procedure to calculate the effective physical properties of such a twin structure. Such twin structures can be produced when the poling direction is different from the polarization directions, such as a rhombohedral 3m system poled in [001] or a tetragonal 4mm system poled in [111].

In a $m\overline{3}m \rightarrow 3m$ ferroelectric phase transition, such as in the PZN-PT and PMN-PT systems, the possible directions for dipole formation are along the cube diagonals, i.e., <111> in the cubic coordinate system. If the poling field is applied in the [001] direction rather than in one of the polar directions, four domain states remain degenerate after poling with dipoles in each domain forming a 55° angle with the poling field. Permissible domain walls[6] (DW's) among these four ferroelectric states are in <110> and <100>. Two perpendicular DW's always exist between any two given domain states, one is charged and the other is neutral.

For a $m\overline{3}m \rightarrow 4mm$ ferroelectric phase transition, e.g., $BaTiO_3$, the possible spontaneous polarization directions are [100], [010] and [001] (in the cubic coordinate system). In domain-engineered $BaTiO_3$ single-crystals, the poling field was applied in [111] rather than in one of the polarization directions. Three domain states remain degenerate after poling with the dipoles in each of the unit cells also form 55° angle with the poling field. Permissible DW's among these three remaining ferroelectric states are orientated in <110> family of orientations as shown in Table I.[5,6] There are also two permissible DWs for each pair of domains, one is a charged wall and the other is neutral.

Table I. Permissible domain walls in terms of lattice planes in a ferroelectric resulting from a $m\overline{3}m \rightarrow 4mm$ phase transition and poled in [111] direction.

Domains	$\mathbf{P^I} = Ps[100]$	$\mathbf{P^{II}} = Ps[010]$	$\mathbf{P^{III}} = Ps[001]$
$\mathbf{P^I} = Ps[100]$	N/A	(110) $(1\overline{1}0)$	(101) $(10\overline{1})$
$\mathbf{P^{II}} = Ps[010]$		N/A	(011) $(01\overline{1})$

[*] on leave from the Department of Physics, Technical University of Liberec, Liberec, Czech Republic

II. EFFECTIVE MATERIAL PROPERTIES OF TWINNED SINGLE CRYSTALS CONTAINING ONLY TWO VARIANTS

Experimental observations found that many domain engineered samples have only one type of twins, i.e., only two of the possible ferroelectric variants exist.[3] The effective symmetry of the twin is monoclinic m if the two domain volume ratios are different and orthorhombic $mm2$ if the volume ratios are the same. A common practice to calculate the effective material properties of a multidomain system is to use the volume ratio as the weighting factor.[7] We found that such treatment leads to some inconsistencies in boundary conditions.[4] A more direct calculation of using appropriate boundary conditions showed that one can use the following formula to calculate the effective material properties,[5]

$$\mathbf{M}^{eff} = [v^{(1)}\mathbf{M}^{(1)}(\mathbf{b}^{(1)})^{-1} + v^{(2)}\mathbf{M}^{(2)}(\mathbf{b}^{(2)})^{-1}][v^{(1)}(\mathbf{b}^{(1)})^{-1} + v^{(2)}(\mathbf{b}^{(2)})^{-1}]^{-1} \qquad (1)$$

where $v^{(1)} + v^{(2)} = 1$ are the volume ratios of the domains, matrices $\mathbf{M}$ and $\mathbf{b}$ are defined as

$$\mathbf{M}^{(i)} = \begin{pmatrix}
s_{11}^{(i)} & s_{12}^{(i)} & s_{13}^{(i)} & s_{14}^{(i)} & s_{14}^{(i)} & s_{15}^{(i)} & s_{16}^{(i)} & s_{16}^{(i)} & d_{11}^{(i)} & d_{21}^{(i)} & d_{31}^{(i)} \\
s_{12}^{(i)} & s_{22}^{(i)} & s_{23}^{(i)} & s_{24}^{(i)} & s_{24}^{(i)} & s_{25}^{(i)} & s_{26}^{(i)} & s_{26}^{(i)} & d_{12}^{(i)} & d_{22}^{(i)} & d_{32}^{(i)} \\
s_{13}^{(i)} & s_{23}^{(i)} & s_{33}^{(i)} & s_{34}^{(i)} & s_{34}^{(i)} & s_{35}^{(i)} & s_{36}^{(i)} & s_{36}^{(i)} & d_{13}^{(i)} & d_{23}^{(i)} & d_{33}^{(i)} \\
s_{14}^{(i)} & s_{24}^{(i)} & s_{34}^{(i)} & s_{44}^{(i)} & s_{44}^{(i)} & s_{45}^{(i)} & s_{46}^{(i)} & s_{46}^{(i)} & d_{14}^{(i)} & d_{24}^{(i)} & d_{34}^{(i)} \\
s_{14}^{(i)} & s_{24}^{(i)} & s_{34}^{(i)} & s_{44}^{(i)} & s_{44}^{(i)} & s_{45}^{(i)} & s_{46}^{(i)} & s_{46}^{(i)} & d_{14}^{(i)} & d_{24}^{(i)} & d_{34}^{(i)} \\
s_{15}^{(i)} & s_{25}^{(i)} & s_{35}^{(i)} & s_{45}^{(i)} & s_{45}^{(i)} & s_{55}^{(i)} & s_{56}^{(i)} & s_{56}^{(i)} & d_{15}^{(i)} & d_{25}^{(i)} & d_{35}^{(i)} \\
s_{16}^{(i)} & s_{26}^{(i)} & s_{36}^{(i)} & s_{46}^{(i)} & s_{46}^{(i)} & s_{56}^{(i)} & s_{66}^{(i)} & s_{66}^{(i)} & d_{16}^{(i)} & d_{26}^{(i)} & d_{36}^{(i)} \\
s_{16}^{(i)} & s_{26}^{(i)} & s_{36}^{(i)} & s_{46}^{(i)} & s_{46}^{(i)} & s_{56}^{(i)} & s_{66}^{(i)} & s_{66}^{(i)} & d_{16}^{(i)} & d_{26}^{(i)} & d_{36}^{(i)} \\
d_{11}^{(i)} & d_{12}^{(i)} & d_{13}^{(i)} & d_{14}^{(i)} & d_{14}^{(i)} & d_{15}^{(i)} & d_{16}^{(i)} & d_{16}^{(i)} & \varepsilon_{11}^{(i)} & \varepsilon_{12}^{(i)} & \varepsilon_{13}^{(i)} \\
d_{21}^{(i)} & d_{22}^{(i)} & d_{23}^{(i)} & d_{24}^{(i)} & d_{24}^{(i)} & d_{25}^{(i)} & d_{26}^{(i)} & d_{26}^{(i)} & \varepsilon_{12}^{(i)} & \varepsilon_{22}^{(i)} & \varepsilon_{23}^{(i)} \\
d_{31}^{(i)} & d_{32}^{(i)} & d_{33}^{(i)} & d_{34}^{(i)} & d_{34}^{(i)} & d_{35}^{(i)} & d_{36}^{(i)} & d_{36}^{(i)} & \varepsilon_{13}^{(i)} & \varepsilon_{23}^{(i)} & \varepsilon_{33}^{(i)}
\end{pmatrix}, \qquad (2)$$

$$\mathbf{b}^{(i)} = \begin{pmatrix}
s_{11}^{(i)} & s_{12}^{(i)} & s_{13}^{(i)} & s_{14}^{(i)} & s_{14}^{(i)} & s_{15}^{(i)} & s_{16}^{(i)} & s_{16}^{(i)} & d_{11}^{(i)} & d_{21}^{(i)} & d_{31}^{(i)} \\
0 & 1 & 0 & 0 & 0 & 0 & 0 & 0 & 0 & 0 & 0 \\
s_{13}^{(i)} & s_{23}^{(i)} & s_{33}^{(i)} & s_{34}^{(i)} & s_{34}^{(i)} & s_{35}^{(i)} & s_{36}^{(i)} & s_{36}^{(i)} & d_{13}^{(i)} & d_{23}^{(i)} & d_{33}^{(i)} \\
0 & 0 & 0 & 1 & 0 & 0 & 0 & 0 & 0 & 0 & 0 \\
s_{14}^{(i)} & s_{24}^{(i)} & s_{34}^{(i)} & s_{44}^{(i)} & s_{44}^{(i)} & s_{45}^{(i)} & s_{46}^{(i)} & s_{46}^{(i)} & d_{14}^{(i)} & d_{24}^{(i)} & d_{34}^{(i)} \\
s_{15}^{(i)} & s_{25}^{(i)} & s_{35}^{(i)} & s_{45}^{(i)} & s_{45}^{(i)} & s_{55}^{(i)} & s_{56}^{(i)} & s_{56}^{(i)} & d_{15}^{(i)} & d_{25}^{(i)} & d_{35}^{(i)} \\
s_{16}^{(i)} & s_{26}^{(i)} & s_{36}^{(i)} & s_{46}^{(i)} & s_{46}^{(i)} & s_{56}^{(i)} & s_{66}^{(i)} & s_{66}^{(i)} & d_{16}^{(i)} & d_{26}^{(i)} & d_{36}^{(i)} \\
0 & 0 & 0 & 0 & 0 & 0 & 0 & 1 & 0 & 0 & 0 \\
0 & 0 & 0 & 0 & 0 & 0 & 0 & 0 & 1 & 0 & 0 \\
d_{21}^{(i)} & d_{22}^{(i)} & d_{23}^{(i)} & d_{24}^{(i)} & d_{24}^{(i)} & d_{25}^{(i)} & d_{26}^{(i)} & d_{26}^{(i)} & \varepsilon_{12}^{(i)} & \varepsilon_{22}^{(i)} & \varepsilon_{23}^{(i)} \\
0 & 0 & 0 & 0 & 0 & 0 & 0 & 0 & 0 & 0 & 1
\end{pmatrix}, \quad (i = 1,2) \quad (3)$$

Superscripts *eff*, *(1)* and *(2)* in the above equations describe the physical properties of effective, domain 1 and domain 2, respectively. The matrix properties given in $\mathbf{M}$ and $\mathbf{b}$ for domain 1 and domain 2 must be transformed to the same cubic coordinate system before being put into the formula.

As a demonstration case, we show in Table II the calculated effective material properties of domain engineered tetragonal $BaTiO_3$ single crystal and study the property variation caused by the volume ratio change of the two domains involved. First of all, the properties of both domains were transformed to a unified coordinate system (i.e., the cubic coordinates), then these transformed properties were put into Eqs. (2) and (3) to find the $\mathbf{M}$ and $\mathbf{b}$. Finally, the effective properties were calculated using Eq. (1).

Table II. Effective material constants of a twinned tetragonal BaTiO$_3$ crystal with a charged DW. (Units: $S_{\alpha\beta}$ [10^{-12} m^{2}N^{-1}], $d_{i\alpha}$ [10^{-12} CN^{-1}], ε_{ij} [ε_0]). Polarization vector of the two domains are $\mathbf{P}^I = P_s$ [100] and $\mathbf{P}^{II} = P_s$ [010] and the DW is in (110).

$v^{(I)}$	1.00	0.00	0.50	0.55	0.60	0.65	0.70
Elastic Properties							
S_{11}	7.92	7.92	7.49	7.49	7.51	7.52	7.55
S_{12}	-1.28	-1.28	-1.71	-1.71	-1.69	-1.68	-1.65
S_{13}	-3.80	-3.80	-3.47	-3.47	-3.48	-3.50	-3.52
S_{14}	...	...	...	...	...	...	...
S_{15}	...	...	...	...	...	...	...
S_{16}	3.83	-3.83	...	0.34	0.69	1.04	1.39
S_{22}	7.92	7.92	7.49	7.49	7.51	7.52	7.55
S_{23}	-3.80	-3.80	-3.47	-3.47	-3.48	-3.50	-3.52
S_{24}	...	...	...	...	...	...	...
S_{25}	...	...	...	...	...	...	...
S_{26}	3.83	-3.83	...	0.34	0.69	1.04	1.39
S_{33}	8.05	8.05	7.81	7.81	7.81	7.83	7.84
S_{34}	...	...	...	...	...	...	...
S_{35}	...	...	...	...	...	...	...
S_{36}	-2.89	2.89	...	-0.26	-0.52	-0.78	-1.05
S_{44}	13.62	13.62	11.94	11.96	12.00	12.08	12.18
S_{45}	4.78	-4.78	...	0.42	0.84	1.27	1.71
S_{46}	...	...	...	...	...	...	...
S_{55}	13.62	13.62	11.94	11.96	12.00	12.08	12.18
S_{56}	...	...	...	...	...	...	...
S_{66}	34.23	34.23	30.63	30.66	30.76	30.92	31.16
Piezoelectric Properties							
d_{11}	-156.66	156.66	...	-16.14	-32.24	-48.30	-64.28
d_{12}	120.53	-120.53	...	11.58	23.19	34.85	46.59
d_{13}	24.40	-24.40	...	2.79	5.57	8.30	10.98
d_{14}	...	...	...	...	...	...	...
d_{15}	...	...	...	...	...	...	...
d_{16}	-84.92	-84.92	-127.29	-126.92	-125.77	-123.85	-121.12
d_{21}	120.53	120.53	130.02	129.93	129.68	129.44	128.63
d_{22}	-156.66	-156.66	-147.17	-147.26	-147.51	-147.94	-148.55
d_{23}	24.40	24.40	17.23	17.29	17.48	17.81	18.27
d_{24}	...	...	...	...	...	...	...
d_{25}	...	...	...	...	...	...	...
d_{26}	-84.92	84.92	...	-7.61	-15.26	-23.02	-30.92
d_{31}	...	...	...	...	...	...	...
d_{32}	...	...	...	...	...	...	...
d_{33}	...	...	...	...	...	...	...
d_{34}	-277.19	-277.19	-179.91	-180.76	-183.33	-187.67	-193.83
d_{35}	-277.19	277.19	...	-24.33	-48.85	-73.73	-99.17
d_{36}	...	...	...	...	...	...	...
Dielectric Properties							
ε_{11}	1530	1530	272	285	322	385	472
ε_{12}	-1362	1362	...	-135	-270	-405	-541
ε_{13}	...	...	...	...	...	...	...
ε_{22}	1530	1530	1506	1506	1507	1508	1509
ε_{23}	...	...	...	...	...	...	...
ε_{33}	2891	2891	2254	2260	2277	2305	2345

The twin structure calculated in Table II consists of two domains with polarization $\mathbf{P}^I = P_s[100]$ and $\mathbf{P}^{II} = P_s[010]$ and a DW oriented in (110). For equal volume ratio, the macroscopic symmetry of the twin is orthorhombic *mm2*, otherwise, it is monoclinic *m*. The dots in Table II represent that the corresponding components are zero. One must remember that the effective properties in Table II were given in the cubic coordinates. If a different coordinate system is chosen, these properties must be rotated to the new coordinate system in order to compare to experimental results.

From Table II we can see that the diagonal terms of the elastic compliance s_{11}, s_{22}, and s_{33} are insensitive to the volume ratio deviation while the shear components s_{16}, s_{26}, s_{36} and s_{45} are very sensitive to volume partition. The changes of piezoelectric coefficient due to the deviation of the volume ratio from 50% are more pronounced due to the fact that much more number of nonzero components can present for monoclinic symmetry than for orthorhombic symmetry, including d_{11}, d_{12}, d_{13}, d_{26} and d_{35}. As for the dielectric properties, major change caused by the volume ratio deviation is in ε_{12}, other components are not very sensitive to small deviation. Since the deviation of the volume ratio is often less than 5% for most of the twin structures, this effect is often ignored if one only at the diagonal terms. Experimentally, these slight deviations have already been detected.

We again emphasize that the macroscopic and microscopic symmetries are different in multidomain systems. The former refers to symmetry relations between different components of macroscopic properties while the latter refers to the crystal lattice structure. As analyzed above, the effective symmetry of a twin becomes lower if the domain volume ratio deviates from 50%. Although statistically the volume ratio of the two domains in a given twin structure should be equal, boundary conditions, geometric shape and external influence often produce slight deviation of the equal partition. Such deviation will lead to further reduction of the macroscopic symmetry of the twin structure.

III. SUMMARY AND CONCLUSIONS

The effective symmetry and material properties have been calculated theoretically for a twin crystal consists of two types of domain states. A general procedure and a formula are derived, which can be applied to domain engineered PZN-PT, PMN-PT and $BaTiO_3$ single crystal systems having only two variants.

In contrary to the conventional treatment of using statistical arguments, we showed that the macroscopic symmetry of a multi-domain system could be lower than the microscopic symmetry, particularly when the volume ratios of the two domains are different. The unequal partition of domain volumes leads to a symmetry reduction and is reflected in the macroscopic physical quantities that can be measured experimentally. Numerical calculation on $BaTiO_3$ showed that the changes of nonzero components of the elastic, dielectric and piezoelectric quantities are not significant if the deviation from equal partition is less than 5%. However, there are several more non-zero components being created by the volume ratio deviation. The change is particularly significant for piezoelectric properties.

REFERENCES
1. S.E.Park, T.R.Shrout, J.Appl.Phys. **82**, 4, 1804 (1997).
2. J.Yin, B. Jiang and W. Cao, Proc. SPIE, Medical Imaging (1999).
3. J. Yin, W. Cao, To be published (1999).
4. J.Erhart and W.Cao, J.Appl.Phys. **86**, 1073 (1999).
5. J.Erhart and W.Cao, J. Mat. Research, to be published (1999).
6. J.Fousek, V.Janovec, J.Appl.Phys. 40, 135 (1969).
7. E.Aksakaya, G.W.Farnell, J.Appl.Phys. **64**, 4469 (1988).

Fatigue Anisotropy in Pb(B1,B2)O$_3$ - PbTiO$_3$ Single Crystals and Epitaxial Films

Koichi Takemura*, Metin Ozgul, Veronique Bornand, Susan Trolier-McKinstry, and Clive A. Randall**

Materials Research Laboratory, The Pennsylvania State University, University Park, PA 16802-4800, U.S.A.
**Fax: 1-814-865-2326, e-mail: carl@psu.edu
* Present address: Functional Materials Research Laboratories, NEC Corporation, 4-1-1 Miyazaki, Miyamae-ku, Kawasaki 216-8555, Japan.
Fax: 81-44-856-2216, e-mail: takemura@fml.cl.nec.co.jp

Fatigue properties for rhombohedral Pb(Zn$_{1/3}$Nb$_{2/3}$)O$_3$ - PbTiO$_3$ single crystals have been studied. Fatigue depends on crystal orientation, and rhombohedral pseudocubic <001>-oriented crystals do not fatigue up to 10^5 cycles, whereas <111>- and <110>-oriented crystals fatigue. The orientation dependence appears to result from differences in the domain configuration and switching process. Epitaxially-grown rhombohedral <001>-oriented Pb(Yb$_{1/2}$Nb$_{1/2}$)O$_3$ - PbTiO$_3$ films on SrRuO$_3$/LaAlO$_3$ substrate with Pt top electrodes are also shown not to fatigue up to 10^{11} switching cycles. <111>-oriented films fatigue. Crystal anisotropy can be used to suppress the fatigue phenomena in non-volatile ferroelectric memories.

1. INTRODUCTION

Fatigue is the gradual decrease of remanent polarization with bipolar switching of a ferroelectric material. The mechanism of fatigue is not fully understood, but is generally regarded to be a systematic freezing out of switchable polarization through domain wall pinning with point defects and space charge.

Early studies of fatigue were mostly confined to single crystals, and fatigue was observed to be a general phenomenon in ferroelectrics [1,2]. More recent studies have focussed on thin film ferroelectrics, owing to the opportunity of memory devices. Non-volatile ferroelectric memories (FeRAM) have advantages over other memory schemes, such as Flash memories. However, there are two major problems with the FeRAM devices, namely fatigue and imprint. Imprint is the systematic off-set in the hysteresis loop that is developed by exposure to a unipolar field.

In the case of fatigue, there have been advances in the problem, through innovative utilization of top and bottom oxide electrodes, such as RuO$_2$ [3], SrRuO$_3$ [4], and (La,Sr)CoO$_3$ [5]. These electrodes appear to limit the reduction of ferroelectrics such as Pb(Zr,Ti)O$_3$ (PZT), and thus limit the increase of oxygen vacancies, that aid in the pinning of domain structures, and ultimately fatigue. Alternative ferroelectrics have also been explored such as SrBi$_2$Ta$_2$O$_9$ (SBT) and SrBi$_2$Nb$_2$O$_9$ (SBN) [6]. These materials have polarization lying in the a-b plane of the unit cell. In the SBT and SBN materials, there are relatively few allowed directions for the spontaneous polarization. Therefore, orientation has to be carefully controlled. Although it can be co-processed with Pt-electrodes, the high crystallization temperature and Bi-Pt reactions of the film limit performance [7].

This study returns to the utilization of single crystals to understand fatigue. However, unlike the earlier studies, we have examined the effect of anisotropy and domain engineering. The concept of domain engineering in ferroelectrics has gained popularity during the last few years in the periodic domain structures for second harmonic generation, and in high piezoelectric activity Pb(Zn$_{1/3}$Nb$_{2/3}$)O$_3$ - PbTiO$_3$ (PZN-PT) single crystals. The PZN-PT crystals demonstrate very high d_{33} coefficients for the rhombohedral phase when poled in the pseudocubic <001> direction. Coefficients as high as 2500 pC/N have been obtained [8].

This paper describes fatigue behavior in rhombohedral PZN-PT single crystals and rhombohedral Pb(Yb$_{1/2}$Nb$_{1/2}$)O$_3$ - PbTiO$_3$ (PYbN-PT) thin films. In both cases, it was observed that the pseudocubic <001>-oriented materials are fatigue-free.

2. EXPERIMENTAL PROCEDURE

PZN-PT crystals were grown by a high temperature flux technique [8]. The crystals were oriented along the pseudocubic <001>, <111>, or <110> axis by the back-reflection Laue method. Plate-shaped measurement samples were obtained by cutting off the oriented crystals, which were then polished with 3 μm alumina powder to obtain flat and parallel surfaces. 100-nm-thick Pt was sputtered as an electrode. The thickness of the samples ranged from 200 μm to 600 μm, and the electrode area ranged from 0.7 mm^2 to 7 mm^2.

Polarization and strain hysteresis loops were measured at room temperature using a modified Sawyer-Tower circuit and linear variable differential transducer.
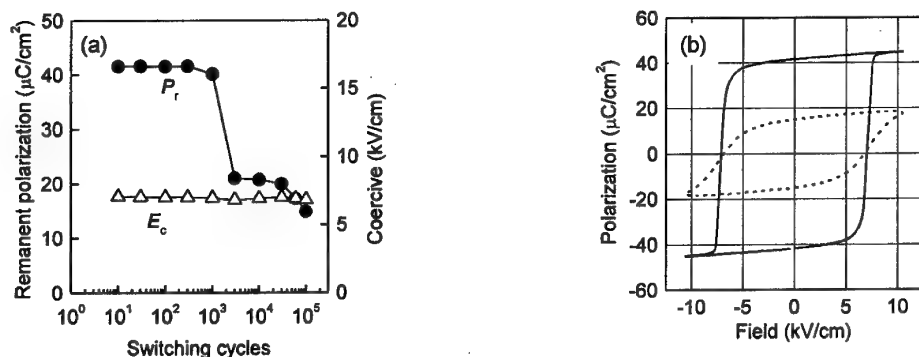
Fig. 1 Switching cycle dependence of P_r, E_c, and hysteresis loops for <111>-oriented PZN - 4.5 PT single crystals. In Fig. 1(b), the solid line is the hysteresis loop after 10 cycles, and the broken line is that after 1×10^5 cycles.
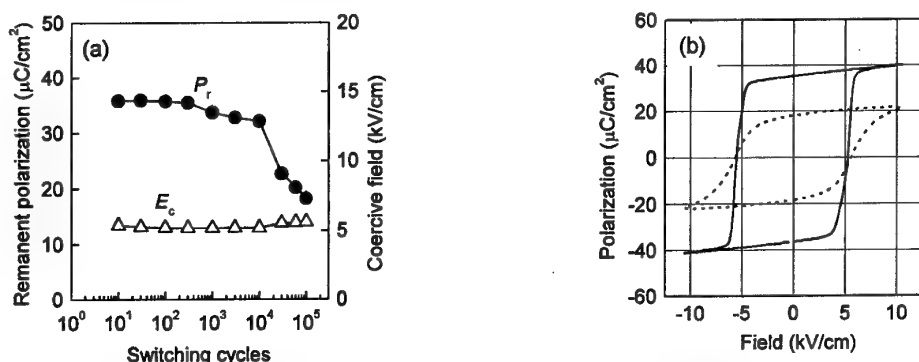
Fig. 2 Switching cycle dependence of P_r, E_c, and hysteresis loops for <110>-oriented PZN - 4.5 PT single crystals. In Fig. 2(b), the solid line is the hysteresis loop after 10 cycles, and the broken line is that after 1×10^5 cycles.

Electrical fields with a triangle bipolar waveform were applied using a high voltage dc amplifier (Trek Model 609C-6 or Kepco Model BOM 1000M). The frequency of the alternating field was 10 Hz for polarization measurement and switching in fatigue measurements, and 0.1 Hz for strain measurement. During measurement, the samples were immersed in Fluorinert to prevent arcing. The remanent polarization (P_r) and the coercive fields (E_c) were computed from the hysteresis loops obtained.

60 % PYbN - 40 % PT/SRO heterostructures were sequentially deposited by the pulsed laser deposition process onto pseudocubic <001>-oriented LaAlO$_3$ and <111>-oriented SrTiO$_3$ substrates. According to the substrate orientation, perovskite PYbN-PT films exhibit a strong <001>- or <111>-texture [9].

3. RESULTS AND DISCUSSION
3.1 PZN-PT Single Crystals

Figures 1 - 3 show P_r, E_c, and hysteresis loops for pseudocubic <111>-, <110>- and <001>-oriented 95.5 % PZN - 4.5 % PT (PZN - 4.5 PT) crystals depending on the number of switching cycles. The amplitude of the

alternating triangular electric field (E_{max}) is 10 kV/cm. Because <111> is the polar direction for rhombohedral ferroelectric crystals, the initial P_r value ($P_{r,<111>}$) is the highest of the three. The initial P_r values for <110>- and <001>-oriented crystals are consistent with $\sqrt{2}/\sqrt{3}$ and $1/\sqrt{3}$ of $P_{r,<111>}$, respectively.

As shown in Figs. 1 and 2, the P_r values for the <111>- and <110>-oriented crystals are almost constant up to 10^3 cycles and then decrease with switching cycles. The <110>- and <111>-oriented crystals obviously fatigue. The E_c values for these crystals are almost independent of the switching cycles.

In contrast, the P_r and E_c value for the <001>-oriented crystal are almost constant up to 10^5 switching cycles as shown in Fig. 3(a). The shape of the hysteresis loop does not change even after 10^5 cycles as shown in Fig. 3(b). The E_c value decreases slightly after 10 switching cycles. The same results for E_c are also observed in Fig. 5 for a switching study with a wide variation in field amplitude. It seems that some domain walls are weakly pinned in the initial state, causing some resistance to domain wall motion, but after a few cycles these domain walls are detached from the original defect
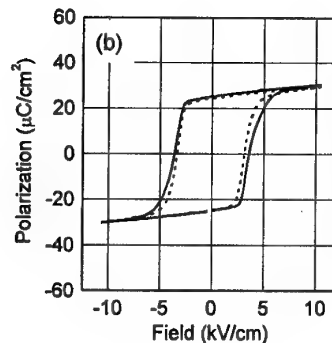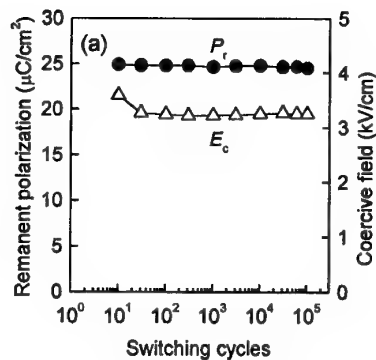
Fig. 3 Switching cycle dependence of P_r, E_c, and hysteresis loops for <001>-oriented PZN - 4.5 PT single crystals. In Fig. 3(b), the solid line is the hysteresis loop after 10 cycles, and the broken line is that after 1×10^5 cycles.
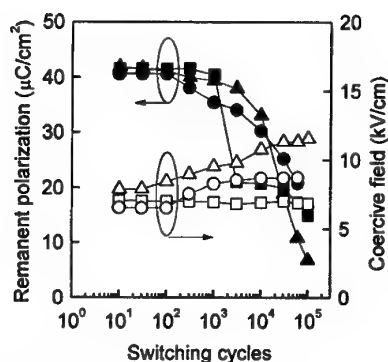
Fig. 4 Switching cycle dependence of P_r (solid symbols) and E_c (open symbols) for <111>-oriented PZN - 4.5 PT single crystals under various switching field strengths (■,□; 10 kV/cm, ●, ○; 20 kV/cm, ▲,△; 30 kV/cm).
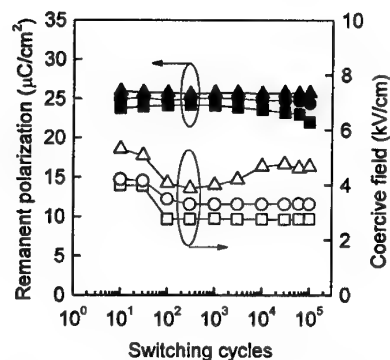
Fig. 5 Switching cycle dependence of P_r (solid symbols) and E_c (open symbols) for <001>-oriented PZN - 4.5 PT single crystals under various switching field strengths (■,□; 5 kV/cm, ●,○; 10 kV/cm, ▲,△; 20 kV/cm).

pinning sites. Possible origins for the pinning include such as impurities, oxygen or lead vacancies, or damage produced during crystal growth, polishing, or electroding.

In ferroelectric thin films, E_{max} often influences fatigue lifetime [10,11]. Figure 4 shows that the <111>-oriented crystals fatigue regardless of the E_{max} values. In contrast, the <001>-oriented crystals do not fatigue under various E_{max} as shown in Fig. 5. We therefore can conclude that the crystal orientation rather than E_{max} governs the fatigue behavior for these crystals. The E_{max} dependence of the fatigue lifetime for the <111>-oriented crystals is not clear. Increasing E_{max} often accelerates fatigue, as observed in thin film studies [10,11]. It is generally believed that carrier injection creates oxygen vacancies and then leads to the pinning of domain walls. In the present study, the applied field strength is one order smaller than that for thin films and the fatigue lifetime does not depend on E_{max}; therefore intrinsic defects rather than the oxygen vacancies

created by carrier injection play an important role in the domain wall pinning. After the onset of fatigue, the E_c values for the <111>-oriented crystals increase. The magnitude of E_c increases with E_{max}.

<111>-oriented PZN - 4.5 PT single crystals exhibit a strain change of 0.2 % in a switching cycle. Large strains sometimes result in microcracking, and microcracks have often been observed in fatigued bulk ceramics [12]. To check whether microcracking influenced the current results, fatigued samples were annealed at 250 °C and 450 °C, for 16 hr in air. Figure 6 shows that annealing improves the P_r value of the fatigued <111>-oriented PZN - 4.5 PT crystal. This crystal was fatigued by applying 30 kV/cm triangular switching fields prior to annealing. After 10^5 switching cycles, the fatigue P_r value had reduced to approximately 16 % of the initial value. P_r increases to more than 80 % of the initial P_r value after annealing. This result suggests that the fatigue observed in the present study on PZN-PT single crystals is recoverable,
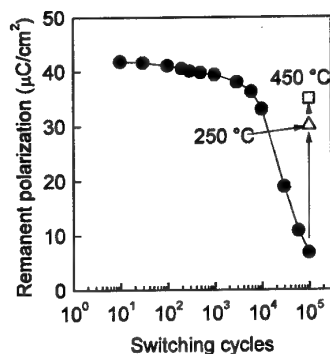
Fig. 6 Recovery of P_r for <111>-oriented PZN - 4.5 PT single crystals. After fatigue, the crystal was annealed at 250 °C, and then 450 °C for 16 h in air.

Fig. 7 Normalized switching charge of PYbN-PT thin films as a function of switching cycles. ● ; <001>-oriented heterostructure, △; <111>-oriented heterostructure.

and rules out fatigue by microcracking.

The same orientation dependence of fatigue is also observed in pure PZN single crystals. Therefore, fatigue in rhombohedral PZN-PT single crystals is surely dominated by the orientation of the crystals and not by the nature of the ferroelectricity, that is to say relaxor or normal [13,14].

3.2 PYbN-PT Epitaxial Films

Based on the single crystal observations, we expanded our investigation to epitaxial thin films with PYbN-PT. In good agreement with the single crystals, a significant orientation effect can be observed in the fatigue behavior of capacitors consisting of PYbN-PT heteroepitaxial thin films with conducting oxide $SrRuO_3$ bottom electrodes and Pt top electrodes.

The changes of net switching charge as a function of switching cycles for the two types of capacitors are compared in Fig. 7. Whereas the capacitor with the <001>-orientation does not fail up to nearly 10^{11} cycles, the <111>-oriented PYbN-PT/SRO layered structure presents a marked degradation after 10^9 cycles and shows more than 40 % decay after 10^{11} cycles. These results suggest that a significant impact on fatigue characteristics can be expected from the proper control of orientation in ferroelectric epitaxial thin films.

4. CONCLUSION

Fatigue properties for rhombohedral PZN-PT single crystals have been studied. Fatigue depends on the crystal orientation; pseudocubic <001>-oriented crystals do not fatigue up to 10^5 cycles, whereas <111>- and <110>-oriented crystals fatigue.

Epitaxially-grown <001>-oriented PYbN-PT films do not fatigue up to 10^{11} switching cycles even when Pt is used as the top electrode. The orientation dependence of fatigue is also observed in ferroelectric thin films.

REFERENCES

[1] F. Jona and G. Shirane, "Ferroelectric Crystals," Pergamon Press, Oxford (1962).

[2] E. Fatuzzo and W. J. Merz, "Ferroelectricity," John Wiley & Sons, Inc., New York (1967).

[3] H. N. Al-Shareef, B. A. Tuttle, T. J. Headley, D. Dimos, J. A. Voigt, and R. D. Nasby, *J. Appl. Phys.*, **79**, 1013 (1996).

[4] C. B. Eom, R. B. V. Dover, J. M. Phillips, R. M. Fliming, R. J. Cava, J. H. Marshall, D. J. Werder, C. H. Chen, and D. K. Fork, *Mater. Res. Soc. Symp. Proc.*, **310**, 145 (1993).

[5] H. N. Al-Shareef, B. A. Tuttle, W. L. Warren, D. Dimos, M. V. Raymond, and M. A. Rodriguez, *Appl. Phys. Lett.*, **68**, 272 (1996).

[6] C. A. Pas de Araujo, J. D. Cuchiaro, L. D. McMillan, M. C. Scott and J. F. Scott, *Nature*, **374**, 627 (1995).

[7] J. F. Scott, *Ferroelectrics*, **206-207**, 365 (1998).

[8] S.-E. Park and T. R. Shrout, *J. Appl. Phys.*, **82**, 1806 (1997).

[9] V. Bornand and S. Trolier-McKinstry, *submitted to J. Appl. Phys.*

[10] R. D. Nasby, J. R. Schwank, M. S. Rodgers, and S. L. Miller, *Proc. 3rd Int. Symp. Integr. Ferroelectr.*, Colorado Springs, p. 376 (1991).

[11] T. Mihara, H. Watanabe, H. Yoshimori, C. A. Araoujo, B. M. Melnick, and L. D. McMillan, *Proc. 3rd Int. Symp. Integr. Ferroelectr.*, Colorado Springs, p. 116 (1991).

[12] D. Wang, Y. Fotinich, and P. Carman, *J. Appl. Phys.*, **83**, 5342 (1998).

[13] L. E. Cross, *Ferroelectrics*, **76**, 241, (1987).

[14] C. A. Randall and A. S. Bhalla, *Jpn. J. Appl. Phys.*, **29**, 327 (1990).

Relaxor-Based Single Crystals by Seeded Polycrystal Conversion

Martin P. Harmer, Helen M. Chan, Ajmal Khan, Tao Li, Suxing Wu, and Adam Scotch

Materials Research Center, Lehigh University, Bethlehem, PA 18015

Fax: 1-610-758-3526, e-mail: mph2@lehigh.edu

Single crystals of relaxor-based ferroelectrics were grown using Seeded Polycrystal Conversion of polycrystalline precursors. This work reports the effect of controlled PbO additions on the growth kinetics of PMN-35PT single crystals. The hetero-epitaxial growth of PMN-PT single crystals from $SrTiO_3$ seeds is also described.

1. INTRODUCTION

Recent advances in the industry have demonstrated that single crystal ferroelectrics exhibit dramatic improvements in the electromechanical properties compared to their conventional polycrystalline ceramic counterparts. For example, single crystals of the relaxors $Pb(Mg_{1/3}Nb_{2/3})O_3$ (PMN) or $Pb(Zn_{1/3}Nb_{2/3})O_3$ (PZN) with $PbTiO_3$ (PT) near the morphotropic phase boundary possess electric-field induced strains > 0.7%,[1] longitudinal coupling coefficients k_{33} > 90%,[2] piezoelectric coefficients d_{33} > 1200 pC/N,[2] and dielectric constants from 1000 to 5000 with low dielectric loss.[2] Consequently, there exists great potential for these single crystal materials to be incorporated into existing devices such as ultrasonic transducers and actuators.

Conventional techniques for forming ferroelectric single crystals are based on high temperature solution growth from fluxes. Though suitable for growing bulk single crystals, these methods have relatively slow growth rates and are not readily transferable to large-scale manufacturing, especially for the fabrication of complex shapes. Furthermore, these methods often have difficulty in achieving chemically homogeneous crystals. Recently, the group at Lehigh University has pioneered the successful application of seeded polycrystal conversion (SPC) to ferroelectric materials. In the SPC technique, a seed crystal is brought into intimate contact with a polycrystalline ceramic matrix, and single crystal conversion takes place by coercing the crystal boundary to migrate at the expense of the smaller matrix grains. The driving forces for the single crystal boundary migration are differences in local boundary curvature, and minimization of overall boundary energy. This technique is directly compatible with current manufacturing of polycrystalline components, and as a result is potentially more cost-effective.

Initial work at Lehigh established the feasibility of using the SPC process to grow single crystals of the relaxor-based ferroelectric $Pb(Mg_{1/3}Nb_{2/3})O$-$35mol\%PbTiO_3$ (PMN-35PT) from seed crystals of the same composition.[3] A subsequent study showed that the <111> direction was a fast growth direction.[4] Further, this study demonstrated that a PbO-based liquid second phase at the single-crystal/polycrystal interface was a critical requirement for PMN-35PT single crystal growth. Although the grown single crystals contained trapped PbO-based inclusions, they nonetheless exhibited impressive strain vs. electric field properties, e.g., strain values up to 0.68% under an electric field of 30 kV/cm.[3,4]

2. EFFECT OF EXCESS PbO ON GROWTH

Recognizing the beneficial influence of excess PbO, the effect of controlled additions of PbO was investigated in a systematic study. Specifically, growth from a (111) PMN-35PT seed plate into a fully dense polycrystalline matrix of (A) PMN-35PT + 0 vol.% PbO, (B) PMN-35PT + 1 vol.% PbO, and (C) PMN-35PT + 5 vol.% PbO, was studied. Center-seeded specimens with similar matrix grain sizes, were formed by hot-pressing and then annealed at 1150°C for 10 h under conditions that ensured a constant PbO content in the specimen during the anneal, i.e., embedded in powder of the same composition in a double crucible arrangement. The annealing temperature was greater than the melting point of PbO, 886°C. No single crystal growth was observed in the PMN-35PT + 0 vol.% PbO matrix. In contrast, modest (~ 50 μm) and significant (~ 0.8 mm) single crystal growth occurred in the PMN-35PT + 1 vol.% PbO and PMN-35PT + 5 vol.% PbO matrix, respectively. These results, shown in Figure 2,

Polycrystal Precursor
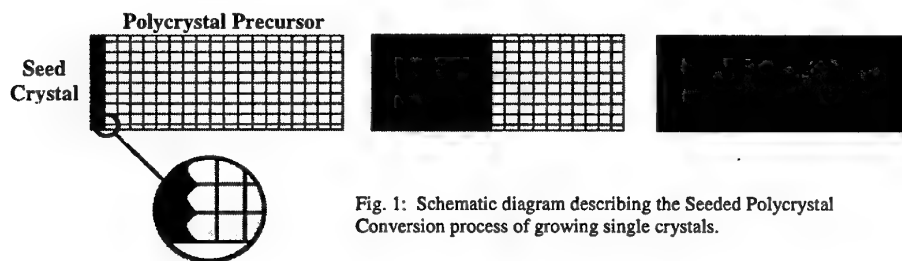
Seed Crystal

Fig. 1: Schematic diagram describing the Seeded Polycrystal Conversion process of growing single crystals.
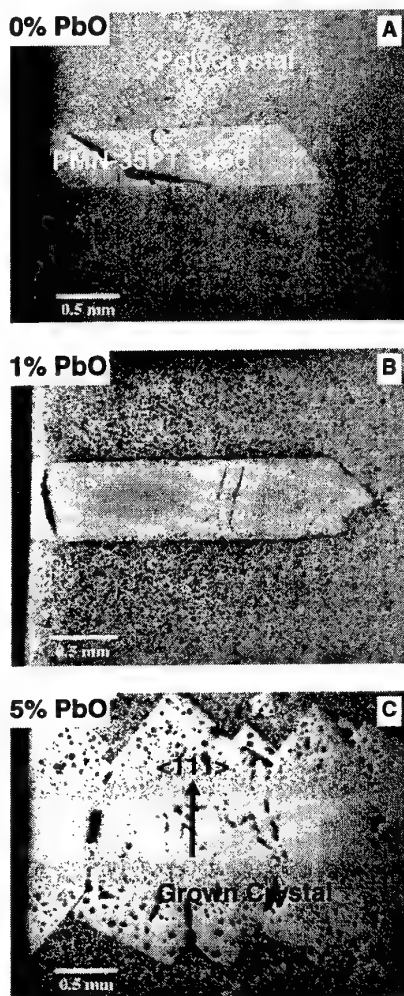
Fig. 2: Growth from (111) PMN-35PT seed plate into polycrystalline (A) PMN-35PT + 0 vol.% PbO, (B) PMN-35PT + 1 vol.% PbO, and (C) PMN-35PT + 5 vol.% PbO, after 1150°C/10h anneal.

Fig. 3: PMN-35PT matrix grain size vs. PbO content data reveals a peak in growth kinetics at an intermediate PbO content (peak is at 3vol.% for the PbO content step size studied).

clearly show that the single crystal boundary velocity is greatly enhanced by the presence of PbO liquid. Further, it demonstrates that boundary velocity depends on PbO vol.%, suggesting that an optimum volume content exists.

The effect of excess PbO content on the polycrystalline matrix growth kinetics was evaluated. Specifically, compositions containing 0, 1, 1.5, 3 and 5 vol.% excess PbO were hot-pressed to full density, and to the same grain size. These specimens were then annealed at 1150°C for 10 h, packed in powders of like composition to maintain constant PbO contents during the anneals. Final grain size was shown to exhibit a peak at 3 vol.% PbO, as indicated in Figures 3 and 4. This result implies that grain boundary mobility may have a maximum at an intermediate PbO content of ~3 vol.%. Further, it suggests that PbO contents significantly less than 5 vol.% should be effective in promoting single crystal growth, thus showing promise for grown crystals with minimum trapped PbO inclusions.

3. HETERO-EPITAXIAL GROWTH OF PMN-PT SINGLE CRYSTAL FROM SrTiO₃ SEED

Given the scarcity of high quality PMN-PT single crystals, it would be advantageous to explore the feasibility of alternative seed materials. Strontium titanate (SrTiO₃) was selected as a suitable candidate. Both SrTiO₃ (ST) and PMN-PT share the same crystal structure (i.e., perovskite), and their unit cell dimensions match closely (i.e., a=3.905 Å for ST[6] and a=4.0165 Å for PMN-35PT[7]). In addition, large ST crystals are widely available at relatively low cost.

In a recent study[8], fully dense PMN-32PT polycrystalline samples were seeded by bonding a polished (111) ST substrate onto the top surface using a PbO-based interlayer. After annealing at 1150°C for 10 hours, growth from the ST plate occurred, resulting in a pyramidal shaped single crystal of PMN-32PT (see Figure 5). The viability of other alternative seed materials is currently being examined.
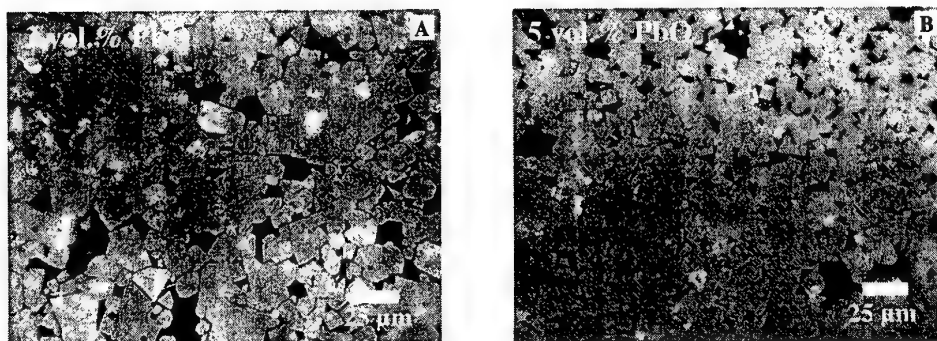
Fig. 4: Microstructure of polycrystalline PMN-35PT with (A) 3 vol.% PbO and (B) 5 vol.% PbO additions. Note the larger average grain size in 3 vol% PbO composition.
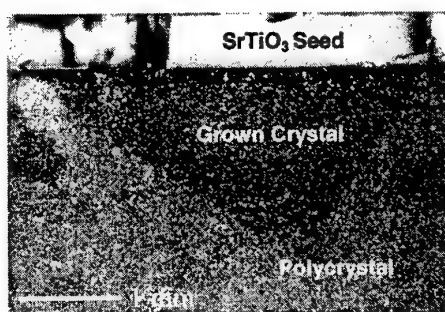
Fig. 5: Growth of a PMN-32PT single crystal from a (111) $SrTiO_3$ substrate after annealing at 1150°C for 10 hours.

4. ACKNOWLEDGMENTS

5. REFERENCES

1. S.-E. Park and T. R. Shrout, *Mater. Res. Innovations*, **1**, 20-25 (1997).
2. S.-E. Park and T. R. Park, *IEEE Transactions Ultrasonic, Ferroelectric Frequency Control*, **44** [5] 1140-47 (1997).
3. T. Li, A. M. Scotch, H. M. Chan, M. P. Harmer, S.-E. Park, T. R. Shrout and J. R. Michael, *J. Am. Ceram. Soc.*, **81** [1] 244-48 (1998).
4. A. Khan, F.A. Meschke, A.M. Scotch, T. Li, H.M. Chan, and M.P. Harmer, *J. Am. Ceram. Soc.*, in press.
5. A. Khan, E. P. Gorzkowski, A. M. Scotch, E. R. Leite, T. Li, H. M. Chan, and M. P. Harmer, in preparation for *J. Am. Ceram. Soc.*
6. H. Swanson, Natl. Bur. Stand. (U.S.), Circ. 539,3,44 (1954).
7. T. R. Shrout, Z. P. Chang, N. Kim, and S. Markgraf, *Ferroelectric Letters*, **12**, 63 (1990).
8. T. Li, S. Wu, A. Khan, A. M. Scotch, H. M. Chan, and M. P. Harmer, *J. Mat. Res.*, **14** [8], (1999).

The Growth of PMN-PT Single Crystals
by the Solid State Method

Hisao Yamada
Cerone, Inc.
2300 Overlook Road, #811
Cleveland Hts., OH 44106

Abstract

65PMN-35PT single crystals were grown by the solid state method at temperatures close to their critical temperature (T_c) for the onset of discontinuous grain growth. Only a very thin layer (~25 µm) of single crystal was grown at a temperature slightly less than T_c in high PbO activity. The boundary between the as-grown single crystal layer and ceramic preform was curved and conformed to the grain shapes of the ceramic preform. On the other hand, an approximately 200 µm thick single crystal layer was grown at a temperature slightly higher than T_c in high PbO activity. The boundaries between the as-grown single crystal layer and ceramic preform were much straighter than those found in the single crystals grown below T_c. Furthermore, the growth fronts along depth and lateral directions intersected with an angle very close to 90°. The as-grown single crystal layer contained voids and PMN-PT grains. A careful examination indicated that both number density and size of the voids increased with increasing thickness of the as-grown single crystal layer.

Experimental results obtained to date seem to suggest that dissolved nitrogen gas is playing a key role in single crystal growth. Its potential role on single crystal growth will be discussed along with the effects of impurities.

1. Introduction

Cerone, Inc. has been engaged in research and development to grow relaxor single crystals, especially PMN-PT single crystals, by the solid state method. By this method, PMN-PT ceramic preforms with a near theoretical density and uniform distribution of fine grains are mated with PMN-PT single crystal seeds. The preforms are then heat-treated at temperatures slightly less than the critical temperature for the onset of discontinuous grain growth.

The growth of PMN and PMN-PT single crystals by the solid state method has been demonstrated in DARPA SBIR and ONR contracts[1-3]. In this paper we will discuss our research and development results to date.

2. Experimental

PMN-PT powder was synthesized by the columbite precursor method[4]. Columbite($MgNb_2O_6$) was first synthesized from MgO and Nb_2O_5 powders by the mixed oxide method. Then, 65PMN-35PT powder was synthesized by thoroughly mixing columbite, PbO and TiO_2 powders and then firing the mixture at 700° C. A small amount of epoxy resin dissolved in acetone along with a few drops of a dispersant, Darvan-C (which was obtained from R. T. Vanderbilt Company), was added to the PMN-PT powder. The resultant slurries were milled overnight with high-density zirconia grinding media. After milling, the acetone was removed by ambient evaporation. The dried cake was ground gently by an agate mortar and pestle prior to uniaxial pressing of discs (2.54 cm in diameter and 0.35 cm in thickness) at 86 MPa (12.5 ksi) using a stainless steel die. The green ceramic discs were subsequently bisqued in air. After bisquing, the discs were completely covered with high-purity PMN powder and then pressureless-sintered in air. Finally the pressureless sintered ceramic discs with closed porosity were hipped (hot isostatically pressed).

The synthesized powders were examined by SEM and XRD prior to any further processing. The density of the sintered discs with closed porosity was determined by the liquid immersion method. For sintered discs with open porosity, the density was determined from their weights and dimensions. Uncertainties in density are estimated to be +/-0.005 g/cc for samples with closed porosity and +/-0.03 g/cc for samples with open porosity.

Discontinuous grain growth in 65PMN-35PT ceramics was investigated at high and low PbO activity environments. The ceramics were heat-treated in a high PbO activity environment by equilibrating a PMN-PT ceramic sample with a 1:1 weight ratio mixture of PMN and PbO in a sealed Pt capsule. In order to avoid a direct contact between the PMN-PT ceramic sample and PMN/PbO mixture, the PMN/PbO mixture was packed in a smaller Pt capsule and placed in a larger Pt capsule

along with a PMN-PT ceramic sample. Then the capsule was spot welded to obtain a gas-tight seal. On the other hand, the ceramics were heat-treated in a low PbO activity environment by self-equilibrating a PMN-PT ceramic sample in a sealed Pt capsule. Then the encapsulated PMN-PT ceramic samples were heat-treated at temperatures between 800° C and $1,250^{\circ}$ C for up to 200 hours. After heat treatment, the ceramic samples were grounded, polished and thermally etched prior to SEM examination.

The PMN-PT preforms were seeded, via PMN-PT single crystal grown by the flux method, as follows. First, surfaces of the preforms and single crystal seeds were ground and polished to a 1/4 µm diamond finish. After polishing, they were degreased in acetone, washed with soapy water, and rinsed thoroughly with DI water in an ultrasonic bath. Then the polished surfaces of the preforms and single crystal seeds were mated and placed with a small load. Subsequently, the seeded pairs were heat-treated at 800° C for 20 hours.

Three sets of single crystal growth runs were carried out to date. They are the following:

1) two runs heat-treated in a sealed Pt capsule with a 1:1 mixture of PMN and PbO (high PbO activity),
2) one run heat-treated in a MgO crucible packed with a large amount of PMN powder (intermediate PbO activity), and
3) three runs heat-treated without a controlled PbO environment (low PbO activity).

After the heat treatments, the pairs were ground and polished through the seed, the as-grown single crystal layer, and the unconverted ceramic preform and then examined by SEM.

3. Results and Discussion

The as-synthesized PMN-PT powder exhibited tetragonal perovskite symmetry. Furthermore, the powder had an average grain size of approximately 300 nm and were heavily agglomerated. After sintering the PMN-PT ceramics exhibited pseudocubic provskite symmetry and had a relative density higher than 96%. However, further densification was not possible because of discontinuous grain growth (Fig. 1).

In order to ascertain the causes of discontinuous grain growth, we have been conducting TEM examination of sintered PMN-PT ceramics. Preliminary results indicate the presence of submicron-sized MgO particles at some triple points. However, we have not been able to conclusively identify the presence of liquid phases along grain boundaries. We will report our TEM results in detail in the near future.
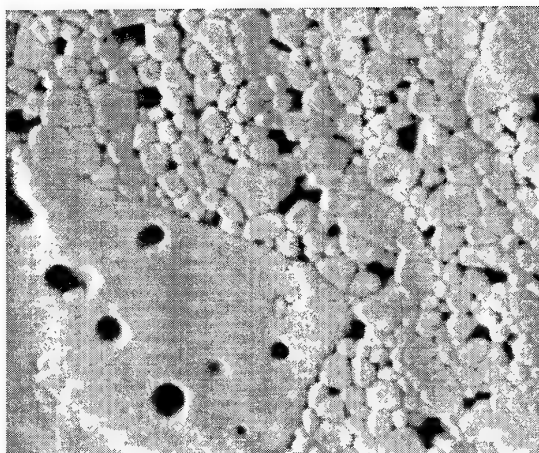
Fig. 1   SEM micrograph of the 65PMN-35PT ceramic preform sintered at 950° C for 10 hours showing discontinuously grown grains

Compared to sintering results published in the literature, our PMN-PT powders appear to be more sinterable. Our sintering temperature of 950° C is considerably lower than temperatures reported in the literature for powders synthesized by the columbite method and is comparable to those reported in the sintering of PMN powders synthesized by the alkoxide[5], sol-gel[6,7], and oxalate methods[8]. The high sinterability of our PMN-PT powder may be attributed to its weakly agglomerated particles with an average particle of 300 nm.

Although extra care was taken during the synthesis of columbite to make it as stoichiometric as possible, a small amount of unreacted MgO may be present in our columbite. This may explain the presence of submicron-sized particles of MgO in our ceramics compared to micron-sized particles in the PMN ceramics with excess MgO. However, it is not certain whether excess MgO has caused discontinuous grain growth or not. It is necessary to perform additional experiments to ascertain the causes of discontinuous grain growth.

Fig. 2 shows grain growth characteristics of the 65PMN-35PT ceramics heat-treated at the high PbO activity. The figure indicates that the PMN-PT ceramics exhibited normal grain growth at temperatures less than 825° C for up to 100 hours and discontinuous grain growth at temperatures higher than 875° C. At 850° C the ceramics did not exhibit discontinuous grain growth for up to 20 hours, but did exhibit discontinuous grain growth when soaked for more than 60 hours. Thus the results indicate that the PMN-PT ceramics heat-treated in the high PbO activity undergo a normal to discontinuous grain growth transition at a temperature between 825° C and 850° C. It is highly encouraging to observe a critical temperature lower than 900° C where the loss of PbO due to evaporation is minimal.
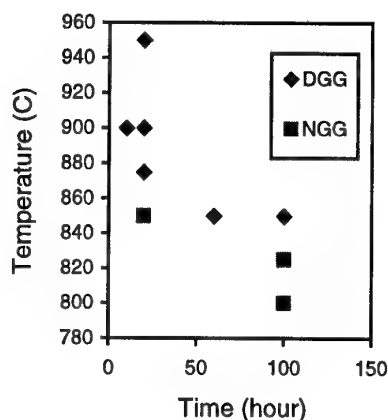
Fig. 2 Temperature-time-transition curve of the 65PMN-35PT ceramics

Because of extensive void formation when the hipped PMN-PT preforms were heat-treated at temperatures higher than 1,000° C, we did not extensively investigate discontinuous grain growth characteristics in the low PbO activity. However, preliminary results indicate that the critical temperature for the onset of discontinuous grain growth in the low PbO activity may be significantly higher than that found in the high PbO activity.

The PMN-PT ceramic preforms mated with a PMN-PT single crystal seed were heat-treated in the high PbO activity at 800° C and 900° C. Figs. 3 and 4 show cross-sectional SEM micrographs of the mated pairs heat-treated at 800° C and 900° C, respectively. An approximately 25 μm thick single crystal layer was grown when the mated pair was heat-treated at 800° C. The boundaries between the as-grown single crystal and ceramic preform were not straight and conformed to the shapes of grains in the ceramic preform. Furthermore, the as-grown single crystal layer contained secondary PMN-PT grains, as well as large (1 to 2 μm in diameter) and small (< .2 μm in diameter) voids.

An approximately 200 μm thick single crystal layer was grown when heat-treated at 900° C. The boundaries between the as-grown single crystal and ceramic preform were much straighter than those found in the mated pair heat-treated at 800° C. Furthermore, the growth fronts along the depth and lateral directions intersected with an angle very close to 90°, suggesting that the as-grown single crystal may have been grown along the [001] direction of a cubic crystal. The as-grown single crystal layer also contained voids and a few PMN-PT grains. A careful examination indicated that the density of the number of voids increased

with increasing thickness of the as-grown single crystal indicating that voids in the ceramic preform may be dragged along the direction of single crystal growth before they were isolated and left in the single crystal layer. Because 900° C > T_C, the unconverted ceramic preform contained many discontinuously grown grains along with numerous large voids. Some discontinuously grown grains exhibited a well-defined cubic symmetry.
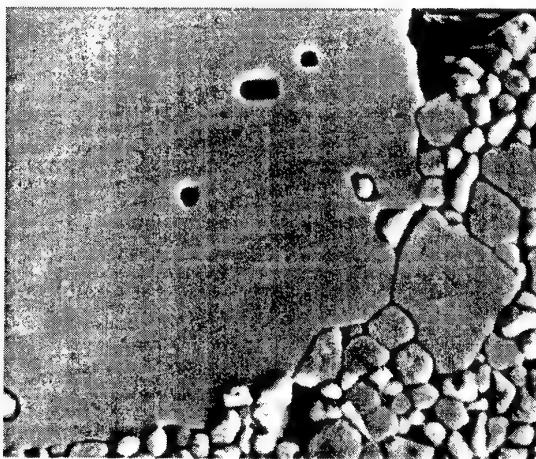
Fig. 3 Cross-sectional SEM micrograph of the seeded ceramic preform heat-treated at 800° C in the high PbO activity environment showing the growth of an approximately 25 μm thick single crystal layer
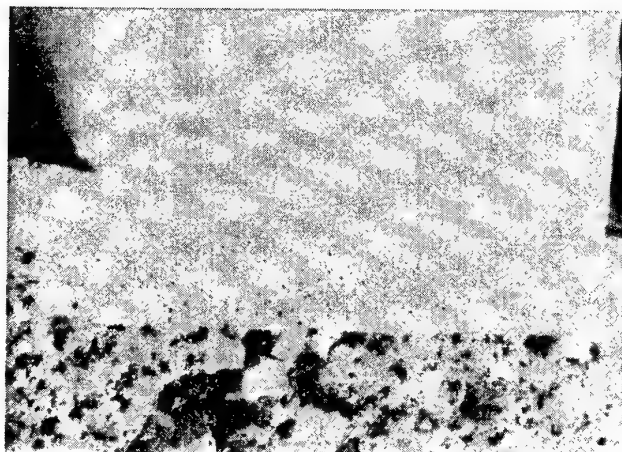
Fig. 4 Cross-sectional SEM micrograph of the seeded ceramic preform heat-treated at 900° C in the high PbO activity environment showing the growth of an approximately 200 μm thick single crystal layer

The seeded PMN-PT ceramic preforms were heat-treated in the low PbO activity environment at temperatures between 900° C and 1,200° C. Even after 100 hours at 900° C, the PMN-

PT ceramic preform did not undergo any single crystal growth and exhibited normal grain growth. However, when heat-treated at 1,100° C, the ceramic preform exhibited a small amount of single crystal growth, which can be identified by the presence of etch pits along the boundary between the single crystal seed and ceramic preform. When heated at 1,200° C, a thin outer layer of the ceramic preform decomposed into large discontinuously grown grains, which are most likely to be a pyrochlore phase, and MgO-rich porous grain boundary phase. The central portion of the ceramic preform maintained the original grain morphology without any hints of discontinuous grain growth.

The results discussed above indicate that PbO activity plays a key role in determining the critical temperature for the onset of discontinuous grain growth in PMN-PT ceramics. In order to ascertain this important effect, we conducted a series of additional single crystal growth runs in the intermediate PbO activity. In these runs, the PbO activities have been controlled by compacting the mated pairs with a large amount of stoichiometric PMN powder. When heat-treated at 1,000° C, an approximately 200 µm thick single crystal layer was grown along its thickness and along lateral directions of the ceramic preform. The as-grown single crystal layer contained a distribution of small voids near the original boundary between the single crystal seed and the ceramic preform. With increasing single crystal layer thickness, voids became larger and their number density decreased, which is similar to the mated pair heat-treated in the high PbO activity at 900° C. The unconverted portion of the ceramic preform exhibited extensive discontinuous grain growth. Furthermore, the presence of PbO-rich phase was observed along the boundaries between the as-grown single crystal layer and discontinuously grown grains.

4. Conclusions

We have demonstrated that it is possible to grow PMN-PT single crystals by the solid state method. However, our ceramic preforms have two major deficiencies. First, the ceramic preforms have been contaminated with Zr, which is most likely to have been introduced by milling with YSZ grinding media during powder synthesis. The Zr contamination has significantly lowered the critical temperature for the onset of discontinuous grain growth. This lowering of the critical temperature has prevented the growth of large single crystals without causing spontaneous discontinuous grain growth in the ceramic preforms during the single crystal growth runs. Second, pressureless sintering in air and subsequent hot isostatic pressing used to obtain fully dense ceramic preforms, have introduced a significant amount of nitrogen gas in the lattice matrix of the ceramic preforms. The dissolved nitrogen gas molecules coalesced and formed voids during the single crystal growth runs.

In our judgement, the formation of the voids has been most detrimental for single crystal growth. Our observations to date indicate that the process proceeded as follows. Initially the small voids were dragged along single crystal growth fronts. However, as they grew bigger, they were left as isolated voids in the as-grown single crystal layer. Eventually, the voids grew too big to completely suppress the single crystal growth.

4. Acknowledgements

5. References

1. H. Yamada, "Solid State Growth of Advanced Ceramic Single Crystals," Phase I SBIR Final Report submitted to DARPA by Cerone, Inc. (Jan. 1997)
2. H. Yamada, "Near-Net Shape Single Crystal Multilayer Electrostrictive Displacement Actuators," Phase I SBIR Final Report submitted to DARPA by Cerone, Inc. (Jan. 1998)
3. H. Yamada, "In-situ Seeding for PMN Single Crystal Growth by the Solid State Method," Final Report submitted to DARPA by Cerone, Inc. (June, 1999)
4. S. L. Swartz and T. R. Shrout, Mater. Res. Bull., **17**, 1245-50 (1982)
5. N. Kim, D. A. McHenry, S. J. Jang and T. R. Shrout, J. Amer. Ceram. Soc., **73**(4) 923-8 (1990)
6. P. Ravindranathan, S. Komarneni, A. S. Bhalla and R. Roy, J. Amer. Ceram. Soc., **74**(12) 2996-99 (1991)
7. F. Chaput, J.-P. Boilot, M. Lejeune, R. Papiernik, L. G. Hubert-Pfalzgraf, J. Amer. Ceram. Soc., **72**(8) 1,335-7 (1989)
8. D-Y Jeng, C-J Chen and S. R. Chaudhuri, p. 227-230, in Proceedings of The Eighth US-Japan Seminar on Dielectric & Piezoelectric Ceramics, in Plymouth, MA, October 15-18 (1997)

Crystal Growth and Characterization of New Langasite-type Compounds for Piezoelectric Applications

K.Shimamura, T.Kato, J.Sato and T.Fukuda

Institute for Materials Research, Tohoku University, 980-8577, Japan

Tel: +81-22-215-2103, Fax: +81-22-215-2104, E-mail: shimak@lexus.imr.tohoku.ac.jp

New material research for $La_3Ga_5SiO_{14}$-type crystals has been carried out by means of the solid state reaction and the micro pulling-down technique. Based on these results, we have successfully grown new piezoelectric single crystals, $La_{3-x}Sr_xTa_{0.5+x/2}Ga_{5.5-x/2}O_{14}$ and $Sr_3TaGa_3Si_2O_{14}$, by the Czochralski technique. These two kinds of crystals showed large electro-mechanical coupling factors comparable to those of $La_3Ga_5SiO_{14}$ and $La_3Ta_{0.5}Ga_{5.5}O_{14}$.

1. INTRODUCTION

Recent progress in electronic technology requires new piezoelectric crystals with high thermal stability of frequency and large electromechanical coupling factors. $La_3Ga_5SiO_{14}$ (langasite, LGS) has been reported as a leading candidate to satisfy those requirements [1]. We have developed and succeeded to grow 2 and 3 inch $La_3Nb_{0.5}Ga_{5.5}O_{14}$ (LNG) and $La_3Ta_{0.5}Ga_{5.5}O_{14}$ (LTG) single crystals, which showed superior piezoelectric properties to those of LGS [2-5]. However, these LGS-type single crystals have the potential to show much better piezoelectric properties by the substitution of constituent cations, as the LSG-type structure has 4 kinds of cation sites. Based on this concept, we have also been dealing with the development of new LGS-type single crystals. Recently, we have found that the electro-mechanical coupling factor, k, of LGS-type crystals increases almost in proportion to the lattice constant, a [6-8].

In this paper, we report research on new materials with LGS-type structure based on the almost linear relation between k and a. Bulk crystal growth and preliminary investigation of the piezoelectric properties have both been done.

New materials with better piezoelectric properties have been designed in the following two ways, with the aim of increasing the lattice constant, a. One is A-site substitution. LGS-type crystals can be expressed via the chemical formula, $A_3BC_3D_2O_{14}$, where A, B, C and D represent each cation site. Since we have found that A-site substituion was most effective to increase lattice constant, this substition was examined using Sr^{2+} and Ba^{2+}. These two cations have larger ionic radii (Sr^{2+}:1.26 Å, Ba^{2+}:1.38 Å) than that of La^{3+} (1.16 Å) [9]. Second way is all-site substition. Since substition of B-, C-, or D-sites alone is not effective [10], substitution of all sites at the same time was investigated. For this purpose, cations such as Ga^{3+}, Nb^{5+} and Ta^{5+} for B-site, and Ga^{3+}, Ge^{4+} and Si^{4+} for C-, and D-site have been examined.

2. EXPERIMENTAL

The langasite phase formation was studied in various mixtures by the solid state reaction technique. Single phase polycrystals were used as starting materials for the growth of fiber-form micro crystals by the micro pulling-down (μ-PD) method [11], which is convenient for determining whether single crystals of the material can be grown by the Czochralski (CZ) technique or not. Growth of micro crystals was performed at a pulling down rate of 1.2-6 mm/h in air, with use of Pt or Pt/Rh crucibles having a nozzle 0.8-1.0 mm in diameter.

Single crystals were then grown by a

conventional RF-heating CZ technique with a Pt crucible (50mm in diameter and height) under air atmosphere. Starting materials were prepared by mixing 99.99% purity oxide powders. Crystal pulling and rotation speeds were 0.4-1.5 mm/h and 10 rpm, respectively.

The phase identification, measurement of lattice constant, and the structure analysis of grown crystals was performed by the X-ray powder diffraction method. Chemical composition of the grown crystals was measured by quantitative X-ray fluorescence analysis.

3. RESULTS AND DISCUSSION

3.1 A-site substitution

In order to enlarge the lattice constant of LGS, the chemical formula $La_{3-x}AE_xGa_{5-x}Si_{1+x}O_{14}$ was employed. For LNG and LTG, the chemical formulae $La_{3-x}AE_xNb_{0.5+x/2}Ga_{5.5-x/2}O_{14}$ and $La_{3-x}AE_xTa_{0.5+x/2}Ga_{5.5-x/2}O_{14}$ were examined. Solid state reaction was carried out for Sr^{2+} as AE at x=0.25, 0.5, 0.75 and 1.0, and for Ba^{2+} as AE at 0.25, 0.5 and 1.0. Among these combinations, $La_{3-x}Sr_xGa_{5-x}Si_{1+x}O_{14}$ (x=0.25, 0.5 and 0.75), $La_{3-x}Ba_xGa_{5-x}Si_{1+x}O_{14}$ (x=0.25), $La_{3-x}Sr_xNb_{0.5+x/2}Ga_{5.5-x/2}O_{14}$ (x=0.25), $La_{3-x}Sr_xTa_{0.5+x/2}Ga_{5.5-x/2}O_{14}$ (x=0.25, 0.5 and 0.75), and $La_{3-x}Ba_xTa_{0.5+x/2}Ga_{5.5-x/2}O_{14}$ (x=0.25), showed LGS-type single phase.

Growth of micro crystals was performed using the compositions exhibiting a single phase mentioned above. Among them, a transparent micro crystal without cracks was obtained from the composition $La_{3-x}Sr_xTa_{0.5+x/2}Ga_{5.5-x/2}O_{14}$ (LSTG, x=0.25). Micro crystals with other compositions were opaque and/or had cracks. Fig.1 shows LSTG micro crystals with x=0.25 and 0.5. Although LSTG (x=0.5) had several cracks, LSTG (x=0.25) did not. The lattice constants a and c of LSTG (x=0.25) were 8.255 Å and 5.122 Å, respectively. Compared with LTG (a=8.235 Å), LSTG (x=0.25) had a larger lattice constant, as expected.

Single crystals of LSTG (x=0.25) were grown by the CZ technique. At a pulling speed of 1.5 mm/h,

Fig.1 $La_{3-x}Sr_xTa_{0.5+x/2}Ga_{5.5-x/2}O_{14}$ micro crystals, x=0.5 (a) and 0.25 (b).

the grown crystals had many cracks and inclusions. Inclusions were determined to be composed of $LaTaO_4$. $LaTaO_4$ is a material which has the highest melting temperature in the La-Sr-Ta-Ga system. This formation was also accelerated by the evaporation of gallium sub-oxide and the small distribution coefficient of Sr^{2+}. In order to grow LSTG single crystals with better quality, decrease of the pulling speed and the concentration of Sr^{2+} was examined. At the same pulling speed, decrease of Sr^{2+} concentration was not effective. Grown LSTG (x=0.1554) had cracks and $LaTaO_4$ as inclusions.

Fig.2 shows an as-grown LSTG (0.1554) single crystal pulled at a speed of 0.4 mm/h. Although crystals pulled at 0.75 mm/h contained cracks at the shoulder part and no inclusions, the crystal shown in Fig.2 was transparent without cracks. This crystal was 18 mm in diameter, and was large enough for the preliminary examination of piezoelectric properties.
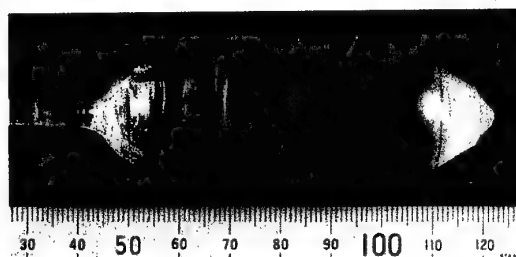
Fig.2 As-grown $La_{3-x}Sr_xTa_{0.5+x/2}Ga_{5.5-x/2}O_{14}$ single crystal (x=0.1554).

3.2 All-site substitution

$Sr_3NbGa_3Si_2O_{14}$ (SNGS), $Sr_3TaGa_3Si_2O_{14}$ (STGS) and $Sr_3TaGa_3Ge_2O_{14}$ (STGG) have shown single phase among possible combinations using Sr^{2+}, Ga^{3+}, Nb^{5+}, Ta^{5+}, Ge^{4+}, Si^{4+} based on the LGS-type structure.

Growth of SNGS, STGS and STGG micro crystals was done. Although SNGS and STGS showed better quality and a smaller number of cracks, STGG micro crystals were completely opaque with numerous cracks. Fig.3 shows as-grown STGS and STGG micro crystals. Lattice constants a and c of STGS were 8.266 Å and 5.081 Å, and those of SNGS were 8.257 Å and 5.088 Å, respectively. Both STGS and SNGS showed a lattice constant a larger than LTG, as expected.
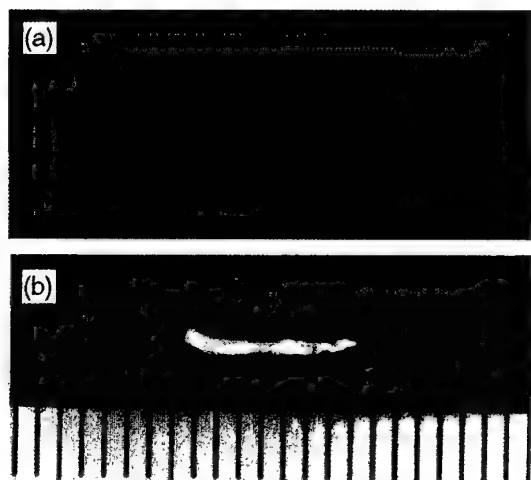
Fig.3 $Sr_3TaGa_3Si_2O_{14}$ (a) and
$Sr_3TaGa_3Ge_2O_{14}$ (b) micro crystals.

Single crystals of STGS and SNGS have been grown by the CZ technique. Growth of STGS single crystal was examined at a pulling speed of 1.0 mm/h, using LTG single crystal as seed. This crystal contained many cracks. For further experiments, STGS seed crystals were prepared using this crystal. Fig.4 shows an as-grown STGS single crystal pulled at a speed of 0.8 mm/h using an STGS seed crystal. This crystal was 18 mm in diameter and large enough for the preliminary examination of piezoelectric properties, although it contained a small number of cracks. Growth of SNGS single crystals by the CZ technique was started using an STGS single crystal seed. At a

Fig.4 As-grown $Sr_3TaGa_3Si_2O_{14}$ single crystal.

pulling speed of 1 mm/h, grown SNGS single crystals were full of cracks. For further growth experiments with SNGS single crystals, the seed crystals were prepared from this totally cracked crystal. Although transparent SNGS single crystals with small quantity of cracks could be obtained in this way, further improvement of growth conditions is required for growth of crystals with better quality.

3.3 Characterization of grown crystals

Structure analysis was done for the grown LSTG and STGS single crystals in order to understand the site occupation of each cation. Table 1 shows the result of structure analysis compared with LGS and LTG. In the case of LSTG, the A-site is partially occupied by Sr^{2+} as expected. In the case of STGS, the site occupation of each site is different from that of LGS and LTG. This also shows that each site was occupied by different cations, as expected. These results agree well with the increased lattice constants of LSTG and STGS.

Fig.5 shows the electro-mechanical coupling factor, k_{12}, of each crystal, along with the lattice constant, a. LSTG and STGS showed large k_{12} value comparable to LGS, LNG and LTG. Although k_{12} of LSTG and STGS was relatively smaller than the extrapolated value from the linear dependence between k_{12} and a, much larger k_{12} can be expected by improvement of crystal quality.

Table 1　Cation distribution in each site of $A_3BC_3D_2O_{14}$-type complex oxide.

	A site	B site	C site	D site
$La_3Ga_5SiO_{14}$	La	Ga	Ga 0.99(1), Si 0.01	Ga 0.51(1), Si 0.49
$La_3Ta_{0.5}Ga_{5.5}O_{14}$	La	Ga 0.46(1), Ta 0.54	Ga	Ga
$La_{3-x}Sr_xTa_{0.5+x/2}Ga_{5.5-x/2}O_{14}$ (x=0.25)	La 0.96(1), Sr 0.04	Ga 0.44, Ta 0.56(6)	Ga	Ga
$Sr_3TaGa_3Si_2O_{14}$	Sr	Ga 0.06, Ta 0.94(1)	Ga 0.94(1), Si 0.06	Ga 0.02(1), Si 0.98

NGS : $Nd_3Ga_5SiO_{14}$, PGS : $Pr_3Ga_5SiO_{14}$,
LGAS : $La_3Ga_{5-x}Al_xSiO_{14}$
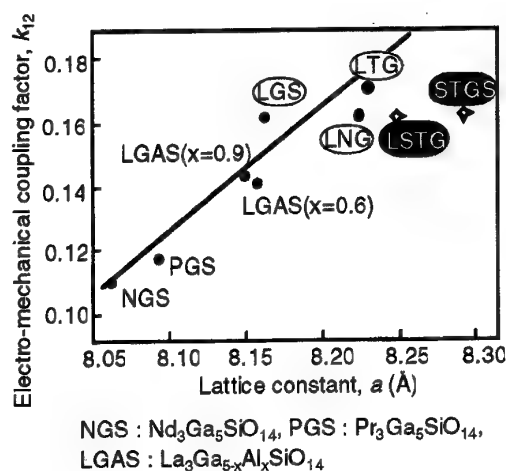
Fig.5　Electro-mechanical coupling
factor vs. lattice constant.

4. SUMMARY

Research on new materials with LGS-type structure has been done in order to develop crystals with better piezoelectric properties than LGS and LTG, using the solid state reaction and the μ-PD technique. Based on these investigations, LSTG and STGS single crystals 18 mm in diameter have been grown by the CZ technique. These crystals showed large k_{12} comparable to LGS, LNG and LTG. Much larger k_{12} of LSTG and STGS can be expected through improvement of crystal quality.

References

[1] K.Shimamura, H.Takeda, T.Kohno and T.Fukuda, J. Cryst. Growth 163(1996)388.

[2] H.Takeda, K.Shimamura, T.Kohno and T.Fukuda, J. Cryst. Growth 169(1996)503.

[3] H.Takeda, K.Sugiyama, K.Inaba, K.Shimamura and T.Fukuda, Jpn. J. Appl. Phys. 36(1997)L919.

[4] H.Kawanaka, H.Takeda, K.Shimamura and T.Fukuda, J. Cryst. Growth 183(1998)274.

[5] H.Takeda, K.Shimamura, V.I.Chani and T.Fukuda, J. Cryst. Growth 197(1999)204.

[6] V.V.Kochurikhin, M.Kumatoriya, K.Shimamura, H.Takagi and T.Fukuda, J. Cryst. Growth 181(1997)452.

[7] H.Takeda, R.Uecker, M.Kumatoriya, K.Shimamura, P.Reiche and T.Fukuda, Cryst. Res. Tech. 32(1997)939.

[8] H.Takeda, T.Kato, V.I.Chani, H.Morikoshi, K.Shimamura and T.Fukuda, J. Alloys Comp. (in press).

[9] R.D.Shannon, Acta Cryst. A32(1976)751.

[10] J.Sato, H.Takeda, H.Morikoshi, K.Shimamura, P.Rudolph and T.Fukuda, J. Cryst. Growth 191(1998)746.

[11] D-H.Yoon, I.Yonenaga, T.Fukuda and N.Ohnishi, J. Crystal Growth 142(1994)339.

Crystalline Structure and Piezoelectric Properties of Bi Layer Structured Compound $SrBi_2Nb_2O_9$

Akira Ando, Masahiko Kimura and Yukio Sakabe

Murata Manufacturing Company Limited, Japan

Fax: 81-77-586-8205, e-mail: a_ando@murata.co.jp

Abstract: Crystalline structure and dielectric properties of $SrBi_2Nb_2O_9$(SBN) material system were investigated with substitution of Ca, and Ba ions to Sr site in this study. X-ray diffraction analysis revealed that these substitutes formed solid solutions through out the composition. The Ca substitution heightens the ferroelectric transition temperature, and the Ba substitution lowers the transition temperatures. Moreover the $Sr_{1-x}Ba_xBi_2Nb_2O_9$ becomes a relaxor ferroelectrics in Ba rich compositional region, while $Sr_{1-x}Ca_xBi_2Nb_2O_9$ maintains a normal ferroelectric behavior at Ca rich compositions. This paper also describes an electronic structure for the ferroelectricity in the SBN by a simple discrete variational Hartree-Fock-Slater (DV-Xα) calculation.

1. INTRODUCTION

Many studies have been done around Bi layer structured materials for ferroelectric random access memory (FRAM) applications due to the low coercive field, large remanent polarization, and high resistance to fatigue exhibited for these materials [1, 2].

On the other hand, it has been reported that a randomly orientated $SrBi_2Nb_2O_9$ ceramic material (SBN) can be used in piezoelectric resonator applications with fine frequency tolerances at high frequencies, because of the low mechanical coupling coefficient, the high mechanical quality factor, and the relatively small temperature coefficients of the elastic constants presented in this material [3]. An energy-trapping phenomenon was successfully achieved for the second harmonic of the thickness extensional (TE2) mode of an electrode-buried-type resonator of SBN [3]. Moreover a highly stable resonator characteristics at high temperatures may be expected since the measured Curie temperature for the SBN was around 400°C [3].

Recently, piezoelectric properties in samples of $BaBi_4Nb_4O_{15}$ [4], $SrBi_2Ti_4O_{15}$ [5], and $CaBi_4Ti_4O_{15}$ [6] ceramic materials have also been studied, with very good values reported. In particular, the obtained values for the electromechanical coupling factor of randomly oriented ceramics were between 15% and 20%, and regarding to the mechanical quality factor, values higher than 2000 were measured [6]. These values make the Bi-layer structured materials very appropriate for practical applications, and present them as very strong candidates as high quality piezoelectric materials for the next decade.

However, relations between electric properties and material compositions in SBN system are not clear yet. Differences in ferroelectric properties between $SrBi_2Nb_2O_9$ and $SrBi_2Ta_2O_9$ were explained from the viewpoint of electronic states of ions by Miura et al. with the discrete variational Hartree-Fock-Slater(DV-Xα) calculation [7]. However there have been few studies on compositional modifications to Sr site, which is valuable in material designs for the practical applications, such as piezoelectric devices. Therefore, it is important to clarify the effect of substitute ion to the Sr site on the piezoelectric properties.

In this paper we describe experimental results such as lattice constants, ferroelectric transition temperatures, and dielectric and piezoelectric properties for SBN materials which were compositionally modified at Sr site. Ca and Ba ions were chosen as the substitute ion in the compositions.

Electronic states of $SrBi_2Nb_2O_9$, $CaBi_2Nb_2O_9$, $BaBi_2Nb_2O_9$ were also calculated by a simple DV-Xα method in order to clarify the effect of the substitute ions on the ferroelectric properties of SBN material system.

2. EXPERIMENTAL PROCEDURE

The ceramic specimens were prepared by the conventional powder processing. $SrCO_3$, $BaCO_3$, $CaCO_3$, Bi_2O_3, Nb_2O_5 were chosen as the starting materials. These materials were weighed and mixed with ball milling in water. The mixed materials were calcined at 900°C for 2h. The disc shaped bodies were prepared by the die pressing of the calcined powder and fired at 1150°C for 2h in air. Silver electrodes were formed on both surfaces of the specimens, and the samples were polarized at 5kV/mm during 10 minutes at 150°C.

Dielectric permittivity of each sample was measured with the impedance analyzer (HP4294A). Ferroelectric transition temperature of each specimen was determined by the temperature dependence of dielectric permitivity. The piezoelectric properties were also investigated. Piezoelectric d_{33} constant was measured with the d_{33}-meter (Channel Products Inc.) in the polarized specimens.

The Crystalline structure was investigated by the X ray diffraction (XRD) with the powder sample, which was obtained by crushing the sintered specimen.

3. RESULTS AND DISCUSSION

3-1. Crystalline Structure

All the prepared samples showed tetragonal or pseudo tetragonal XRD patterns except for $CaBi_2Nb_2O_9$ which showed an orthorhombic pattern.

Figure 1 (Fig.1) shows the lattice constant changes with the substitute amounts of Ca and Ba ions. The lattice constants decrease monotonically with the amount of the Ca substitution, while the Ba substitution increases those. The XRD analysis revealed that neither phase separation nor segregation phases were observed in the prepared samples. These results indicated that Ca and Ba ions exist on the lattice sites throughout the composition.
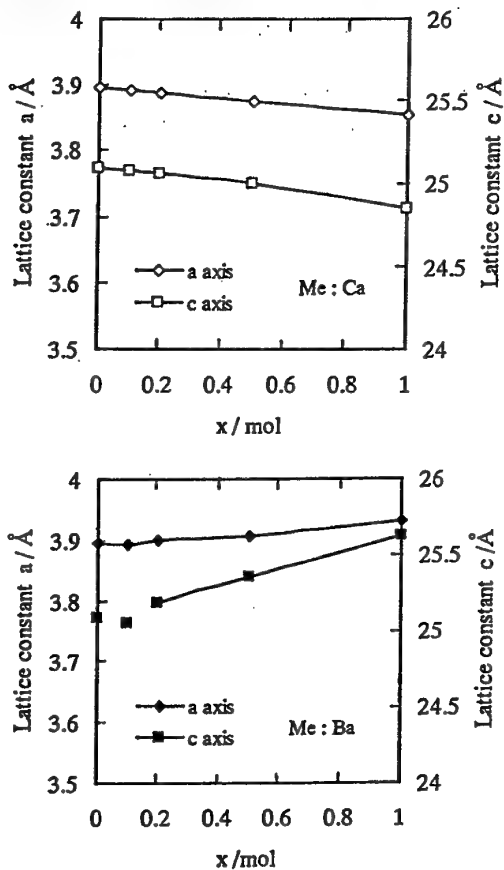
Fig.1. Lattice constant of $Sr_{1-x}Me_xBi_2Nb_2O_9$ ceramic sample (Me: Ca, Ba)

3-2 Dielectric Properties

Fig.2 shows dielectric permittivity as a function of temperature of SBN material system. The transition temperature was determined as the temperature where the dielectric permittivity has a peak value in Fig.2. Fig.3 shows the transition temperature as a function of the substitute amount. The ferroelectric transition temperature decreased by Ba substitution and the shape of the transition change became smoother in Ba rich composition. This result agrees well with the previous study of Subbarao [8]. On the other hand, Ca substitution heightens the transition temperature, and maintains the transition style normal even with a depressing of a peak value of the dielectric permittivity, in Ca rich region.
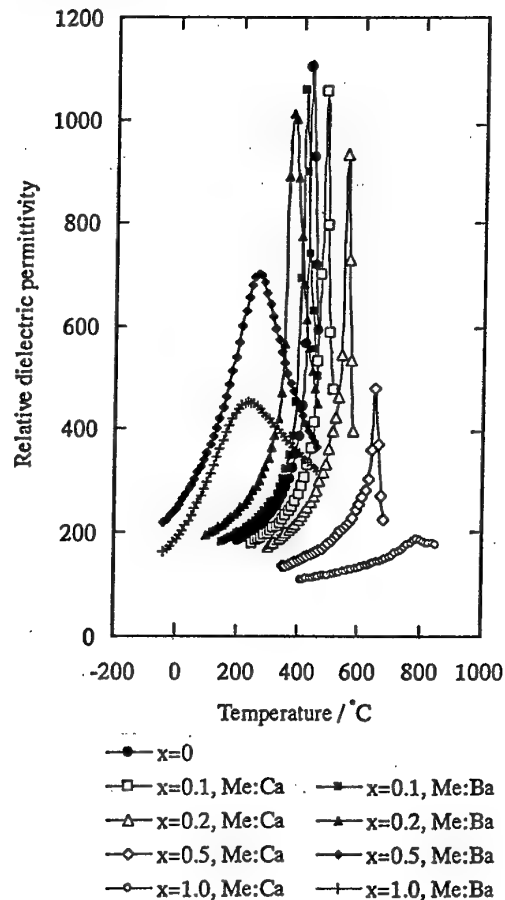
Fig.2. Temperature dependence of the dielectric permittivity of $Sr_{1-x}Me_xBi_2Nb_2O_9$ ceramic sample (Me: Ca, Ba)
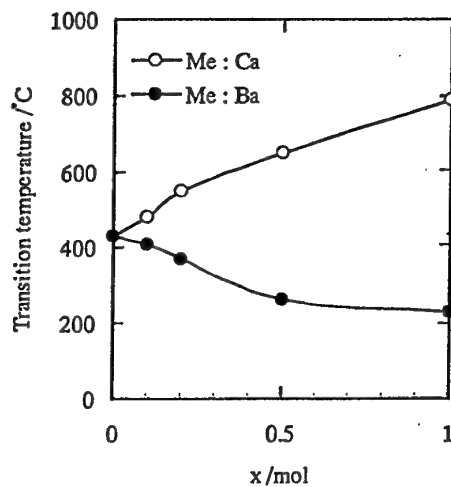
Fig.3. Transition temperature of $Sr_{1-x}Me_xBi_2Nb_2O_9$ ceramic sample (Me: Ca, Ba)

Fig. 4 shows a fit of the reciprocal dielectric susceptibility to a Curie-Weiss form for $Sr_{1-x}Ba_xBi_2Nb_2O_9$. It is clear that the Curie-Weiss law could not be applied to the Ba rich compositions.

On the other hand, dielectric permittivity for the Ba rich composition changes in manner of $A+B\ (T-T_0)^2$ above T_0, where A and B are constants, T is temperature, and T_0 is the transition temperature. This tendency has been observed in the typical relaxor materials such as $Pb(Mg_{1/3}Nb_{2/3})O_3(PMN)$ [9].
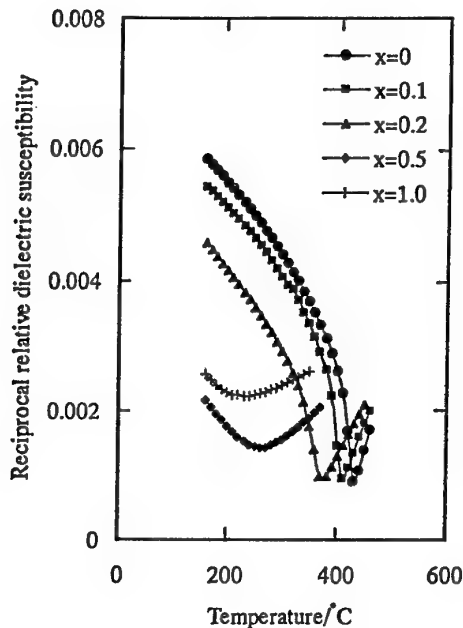
Fig.4. Reciprocal permittivity as a function of temperature for $Sr_{1-x}Ba_xBi_2Nb_2O_9$

The discrepancy in the temperature characteristics of the dielectric permittivity for different frequencies, as shown in Fig.5, also indicates that $(Sr,Ba)Bi_2Nb_2O_9$ becomes a relaxor-type ferroelectric at Ba rich compositions. Considering that the $(Sr,Ca)Bi_2Nb_2O_9$ system does not change its transition style, the nano scale compositional disorder of Ba might exist and cause the diffuse transition.

3-3. Piezoelectric Properties

The piezoelectric d_{33} constants of the SBN samples were measured with the d_{33}-meter and they are tabulated in Table I.

Table I. d_{33} constant of $Sr_{1-x}Me_xBi_2Nb_2O_9$ (pC/N)

Me \ x	0.0	0.1	0.2	0.5	1.0
Ba	17.0	17.0	17.0	11.5	----
Sr	17.0	16.5	16.0	9.5	6.5
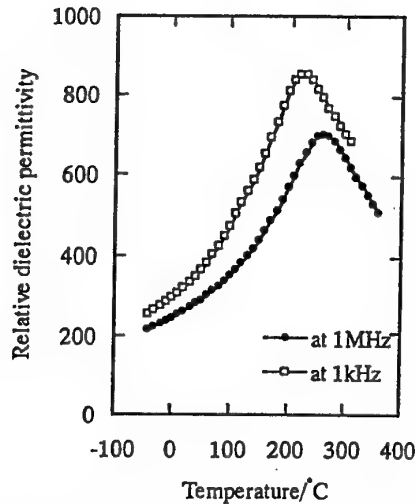
Fig.5. Temperature dependence of the dielectric permittivity of $Sr_{0.5}Ba_{0.5}Bi_2Nb_2O_9$ ceramic sample at different frequencies (1 kHz, 1MHz)

Statistically significant differences in the d_{33} value were not recognized between the samples of which the substitute amount x is within 0.2.

$BaBi_2Nb_2O_9$ ceramics showed no piezoelectricity depending on the relaxor characteristics, and Ca rich compositions were difficult to polarize because of their high transition temperatures.

4. DV-Xα CALCULATION

4.1 The models for the calculation

The DV-Xα Calculation[10] was applied to $SrBi_2Nb_2O_9$, $BaBi_2Nb_2O_9$, and $CaBi_2Nb_2O_9$. The cluster models of $SrBi_2Nb_8O_{36}^{24-}$, $BaBi_2Nb_8O_{36}^{24-}$, and $CaBi_2Nb_8O_{36}^{24-}$ were adapted for the calculations. Point charges were placed on the rest ion sites of the unit cell, and the unit cell was surrounded by point charges placed on each ion site of 11x11x11 unit cells to create the Madelung potential. The calculation was repeated until a consistency was obtained between the point charge values and electric charges of each ion in the cluster.

The lattice constants were assumed to be same in the three materials in order to clarify the difference originated from electronic structure of each substitute ion

4.2 The band structures

A couple of reports described the relations between material compositions and the ferroelectricity by the calculations of the electronic states in materials which possess oxygen octahedrons such as perovskite oxide materials or layered perovskite oxide materials [11, 12]. They described that the strong electronic coupling between the oxygens of the oxygen octahedrons and cations surrounded by them stabilizes the ferroelectric state [7,11].

The valence band is formed of 4d electrons of Nb and 2p electrons of oxygen. The influence from outer

oxygens of the model cluster was neglected. Table II shows the band expansion for the three materials.

Table II. Calculated band expansion of $MeBi_2Nb_2O_9$ (eV)

Me	Ca	Sr	Ba
	3.087	3.081	3.055

The band expansion is strongly related to the coupling between 4d electrons of Nb and 2p electrons of oxygen in these material systems. The electron coupling leads to a larger band expansion.

The expansion for $BaBi_2Nb_2O_9$ is the smallest of the three materials and $CaBi_2Nb_2O_9$ gives the largest. This calculation result agrees well with the experimental result that the ferroelectric transition temperature is the lowest for $BaBi_2Nb_2O_9$ and is the highest for $CaBi_2Nb_2O_9$ of the three materials, as shown in Fig.3. Even though the lattice constant for each material has not been taken into account here, an electronic state of the substituted ion seems to have some effect on stabilizing the ferroelectricity of the material.

4.3 The effect of the substitution on ferroelectricity

As shown in Fig.1 and Fig.3, the Ca substitution to the Sr site decreases the lattice constants of SBN, and heightens its ferroelectric transition temperature. On the contrary the Ba substitution increases the lattice constant and lowers the transition temperature. These experimental results indicate that the ferroelectric transition temperature is strongly influenced by the spacing between the ions in the composition.

The lattice deformation, such as a change in lattice constants, is considered to enhance the electronic coupling between ions in the materials, and leads to stabilizing the ferroelectricity in the SBN material system.

5. ACKNOWLEDGEMENT

References

[1] J. F. Scott, A. J. Hartmann, R. N. Lamb, F. M. Ross, A. De Vilbis, C. A. Paz De Araujo, M. C. Scott, and G.Derbenwick, "Ferroelectric thin films V" Ed. by S. B. Desu, R. Ramesh, B.A. Tuttle, R.E. Jones, I.K. Yoo, Mater. Res. Soc., Pittsburgh (1996) pp. 77-84.
[2] T. Hase, T. Noguchi, K. Takemura, and Y. Miyasaka, Jpn. J. Appl. Phys., vol. 37, pp. 5198-5202 (1998)
[3] A. Ando, M. Kimura, and Y. Sakabe, Proceedings of the 11th International Symposium on Applications of ferroelectrics IEEE-UFC, p.303 (1999)
[4] Y. Nakai and S. Fukuoka, to be published in Jpn. J. Appl. Phys., vol. 38, No.9B (1999)
[5] M. Hirose, T. Suzuki, H. Oka, K. Itakura, Y. Miyauchi, and T. Tsukada, to be published in Jpn. J. Appl. Phys., vol. 38, No.9B (1999)
[6] M. Kimura, A. Ando, and Y. Sakabe, to be published in Jpn. J. Appl. Phys., vol. 38, No.9B (1999)
[7] K. Miura and M. Tanaka, Jpn. J. Appl. Phys. vol. 37, pp. 606-607 (1998)
[8] E.C. Subbarao, J. Phys. Chem. Solids vol. 23, pp. 665-676 (1962)
[9] G. A. Smolensky, J. Phys. Soc. Jpn. vol. 28, supplement, Proceedings of the Second International Meeting on Ferroelectricity pp.26-37 (1970)
[10] H. Adachi, M. Tanaka, and C. Satoko, J. Phys. Soc. Jpn., 45 p. 875 (1978)
[11] R. E. Cohen and H. Krakauer, Ferroelectrics, vol. 136, pp. 65-83 (1992)

The thickness-extensional and thickness-shear vibration mode characteristics of bismuth layer-structure compounds

Hitoshi Oka, Masakazu Hirose, Takeo Tsukada, Keisuke Itakura, Yasuharu Miyauchi

Materials Research Center, TDK Corporation, 570-2 Minami-Hatori, Narita, Chiba 286-8588, Japan

Fax: 0476-37-1648, e-mail: hioka@mb1.tdk.co.jp

The thickness-extensional vibration mode and thickness-shear vibration mode have been investigated in bismuth layer-structure compounds $SrBi_2Nb_2O_9$ and $SrBi_4Ti_4O_{15}$. Also the effects of La substitution and Mn addition were investigated. The temperature dependence of resonant frequency of $SrBi_2Nb_2O_9$ (SBN) is more stable than that of $SrBi_4Ti_4O_{15}$ (SBT) in both thickness-extensional and thickness-shear vibration modes. On the other hand, self polarization of SBT is 9.4×10^{-2} C/m^2 and that of SBN is 4.5×10^{-2} C/m^2. For both compositions, La substitution reduced mechanical quality factor Qm, but 0.1mol substitution for SBT improved its density. Addition of Mn hardened both SBN and SBT piezoelectrically. Qm of SBT increased with Mn addition while Qm of SBN decreased.

1. INTRODUCTION

Recently, lead containing piezoceramics, such as lead titanate (PT) or lead zirconate titanate (PZT) have been used widely in electronic filters, resonators and actuators. These materials include PbO from 60 to 70 weight %. These devices would be subjected to exposure to the acid rain after disposal, causing environmental pollution. Due to this, the development of lead free electronic devices becomes more important.

As examples of lead free materials, perovskite-structure compounds, tungsten bronze-structure compounds and bismuth layer-structure compounds[1] are well known. Among these materials, we have studied bismuth layer-structure compounds because of its ease in achieving high density and high Q characteristics. Since many of the bismuth layer-structure compounds have higher Curie temperature compared to PT and PZT, they are thought to have higher thermal stability and smaller aging rate.

It is general that evaluation of piezoelectric ceramics are performed in radial vibration mode or thickness-extentional (TE) vibration mode, which are obtained by poling disc samples along their thickness direction. On the other hand, characteristics of thickness-shear (TS) vibration mode are obtained by poling rectangular samples along their longitudinal direction. As a result, poling voltage tends to be higher than that of TE mode. Therefore, in the past, characteristics of TS mode were less reported because of its difficulty in poling.

This paper describes the TS characteristics of bismuth layer-structure compounds, the comparison for TE characteristics and the results of some compositional modification.

2. EXPERIMENTAL

$SrCO_3$, Bi_2O_3, TiO_2, Nb_2O_5, $La(OH)_3$ and $MnCO_3$ were used as the starting materials. Ceramic powders were synthesized by the conventional oxide mixing method. These materials were mixed for 16h by ball-milling, they were calcined at temperatures between 800 and 1000 °C for 2h. The calcined powders were ball-milled again so that average particle sizes were 1 to 2 μm. These powders were pressed into square pellets, 30 x 30 x 7 mm in dimension, then sintered at temperatures between 1160 and 1290°C for 4h.

These sintered bodies were cut and electroded into following sizes. TE mode measurement: cut into 6 x 6mm and 0.42mm thickness, then 5 x 5mm silver electrodes were formed on both sides of the specimen by vacuum deposition. TS mode measurement: cut into 7 x 3mm and 0.33mm thickness after poling, then 1.5mm in diameter silver electrodes were formed in the same way as TE mode.

Coercive field strength (Ec) was obtained from hysteresis measurement.

Poling was carried out 150 to 200°C (SBN) and 250°C (SBT) in a silicone oil bath. Poling electric field was about three times of coercive field (TE) and from 1.5 to 2 times the coercive field (TS). Poling time was 1 to 10min.

Impedance characteristics of these samples were measured at 5MHz (TE) and at 4MHz (TS). Mechanical quality factor (Qm) was calculated by the resonance anti-resonance method.

Temperature dependence of resonant frequency (fr) was obtained as follows; fr deviations from -40 to 85°C versus fr at 20°C were fitted to a straight line using the least squares method. The temperature coefficient

(frTC) was defined as the slope of that line.

3. RESULTS AND DISCUSSION

3.1 TE and TS characteristics of SBN and SBT

TE and TS characteristics were evaluated in order to compare the basic properties of SBN and SBT, which have different numbers of pseudo-perovskite layers.

Table I shows the densities of SBN and SBT used in this study. The densities were measured by the Archimedean method. The theoretical densities were calculated from formula weights and the lattice constants[2].

Table I   Density of SBN and SBT

Compound	Sintering temperature	Density	Relative density
	(°C)	(10^3 kg/m³)	(%)
SBN	1190	7.18	98.0
SBT	1275	7.18	96.2

SBN has a higher relative density than SBT at lower temperature. The densities of both samples are more than 95% of theoretical value. Fig. 1 shows SEM micrographs of polished surfaces of the samples. Although less than 10μm diameter pores can be seen in both samples, larger pores which would affect piezoelectric properties are not observed. TE and TS characteristics of plain SBN and SBT are given in Table

(a)

10 μm

(b)

10 μm
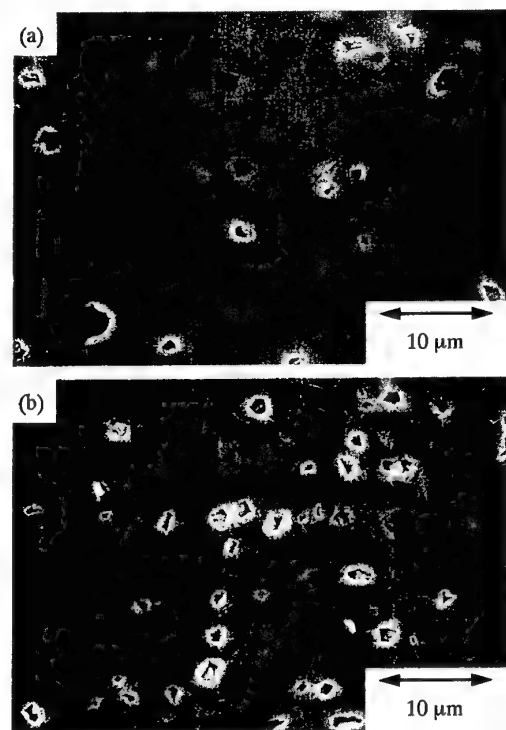
Fig. 1 SEM micrographs of polished surfaces of (a) SBN, (b) SBT.

II. The comparison of SBN and SBT indicates that temperature coefficient of resonance frequency (frTC) of SBN is as about half of that of SBT. This result is observed in both TE and TS mode.

Table II   Thickness-extensional and thickness-shear characteristics of SBN and SBT

	TE		TS	
	Qm	frTC (ppm/°C)	Qm	frTC (ppm/°C)
SBN	1670	-15	5450	-46
SBT	930	-43	6820	-80

Fig. 2 shows the result of hysteresis measurement. The hysteresis measurement indicates that the self polarization (Ps) of SBN is 4.5×10^{-2} C/m² and that Ps of SBT is 9.4×10^{-2} C/m². Thus the Ps of SBT is almost twice of that of SBN.
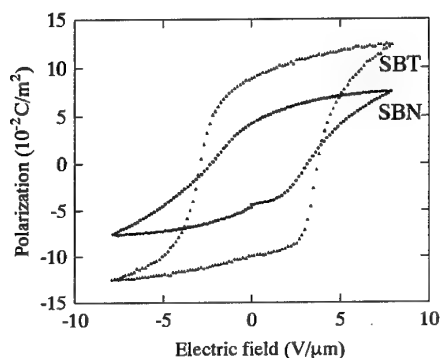
Fig.2 Electric hysteresis loops of SBN and SBT

In bismuth layer-structure compounds, pseudo-perovskite layers between $(Bi_2O_2)^{2-}$ layers are thought to reflect piezoelectricity. Therefore it is considered that SBT, which has more pseudo-perovskite layers, exhibits larger self polarization.

The comparison of TE and TS mode indicates that TE mode has smaller frTC than that of TS mode. On the other hand, Qm depends on the sample's shape. Qm of TE and TS mode cannot be compared directly.

3.2 Effect of La substitution

In the case of PT and PZT ceramics, lanthanide elements are used to shift the Curie temperature, so they are widely used in practical materials. In order to investigate the effect of lanthanide elements on SBN and SBT, La substitution for A site of pseude-perovskite layers was carried out.

Fig. 3 shows the relationship between TS mode Qm and the amount of La substitution, when Sr site of SBN and SBT are substituted by La. In the both cases of SBN and SBT, Qm decreases with the amount of La substitution. While the density of SBN did not change with La substitution, the sinterability of SBT improved only at 0.1 mol by La substitution.
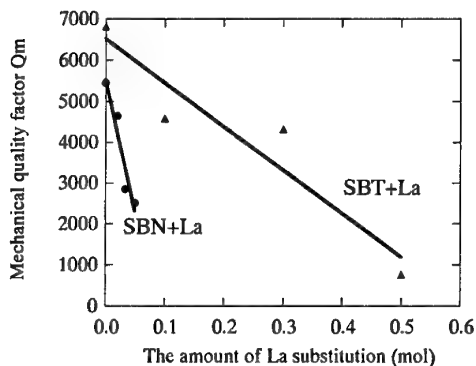
Fig.3 The effect of La substitution on SBN and SBT

3.3 Effect of Mn addition

It is well known that Mn is a typical "hardening" element for PT and PZT. Namely, addition of Mn increases Ec. On the other hand, the Ec of SBT also increased by Mn addition, hence improvement of Q characteristics in TE mode was observed. In the same way, the effect of Mn addition for SBN was examined.

Table III shows TS mode Qm of SBN with no addition and with 0.31wt% Mn addition.

Table III Effect of Mn addition to SBN

	Density (10^3kg/m^3)	Ec (V/μm)	Qm
SBN	7.18	3.1	5450
SBN+MnCO$_3$ 0.31wt%	7.14	4.1	3220

More than 0.5wt% Mn addition reduced the resistance of SBN. Therefore poling became more difficult. Considering this, 0.31wt% Mn addition was selected. In contrast with SBT, Mn addition reduces Qm of SBN. SEM mirograph of polished surface of Mn-doped SBN is given in Fig. 4.
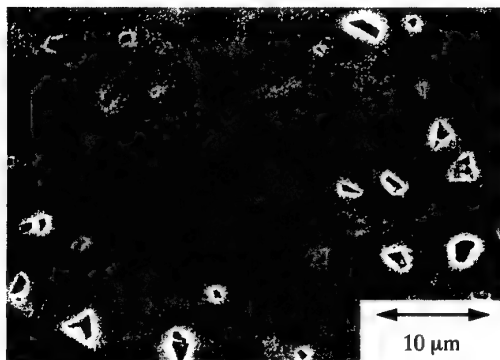
Fig.4 SEM micrograph of polished surface of Mn doped SBN

Mn doped SBN has the same microstructure as that of undoped SBN (Fig.1 (a)). Also the density remained almost the same.

Fig. 5(a) shows the hysteresis curves of SBN with and without Mn. In the case of SBN, the value of Ec at 150°C increases form 3.1V/μm to 4.1V/μm by Mn addition. This indicates that Mn acts as the hardening additive for SBN. Fig. 5(b) shows that the effect of Mn addition for SBT. Its density was improved by substituting 0.1mol La for Sr. In this case, both Ec and Ps are increased by Mn addition. Qm of TS mode improved from 4580 to 9930 by 0.5wt% Mn addition.
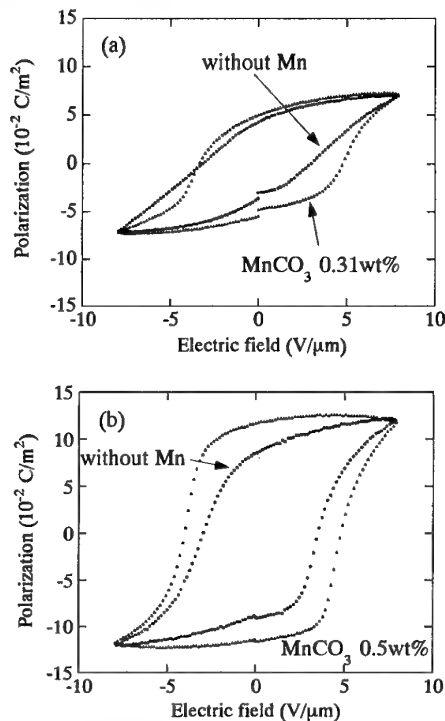
Fig.5 The effect of Mn addition on (a) SBN and (b) SBT substituted by 0.1mol La.

It is interesting that the effect of Mn addition is different for SBN and SBT. Ikegami and Ueda reported that Mn and Cr showed the opposite effects for SBT and Na$_{0.5}$Bi$_{4.5}$Ti$_4$O$_{15}$[3]. Lambeck and Jonker proposed that domain structure was stabilized by the defect dipole of Mn$_{Ti}$ and oxygen vacancy in perovskite type compounds[4]. Nb and Ti, which correspond the B site atoms in perovskite, have different valence in SBN and SBT respectively. This difference in valence would be thought to affect the result of Mn addition to SBN and SBT. More detailed study is required on the effect of Mn addition.

4. SUMMARY

TE and TS mode characteristics were investigated in the bismuth layer-structure compounds: SBN and SBT. Consequently, the following results were found:
(1) Temperature dependence of resonant frequency of SBN was more stable than that of SBT.

(2) Self polarization of SBT had higher value than that of SBN, hence SBT had larger piezoelectricity.

(3) Generally, La substitution in SBN and SBT reduced the value fo Qm, but in case of 0.1mol substitution, it actually improved sinterability of SBT.

(4) Both SBN and SBT were hardened with Mn addition. Though Qm of SBT increased while Qm of SBN decreased by Mn addition.

5. References

1. G. A. Smolenskii, V. A. Ispov, A. I. Agranovskaya, Sov. Phys.-Solid State, **3**, 3, 651-655 (1961)

2. E. C. Subbarao, J. Am. Ceram. Soc., **45**, 166-169 (1962)

3. S. Ikegami, I. Ueda, J. J. Appl. Phys., **13**, 10, 1572-1577 (1974)

4. P. V. Lambeck, G. H. Jonker, Ferroelectrics, **22**, 729 (1978)

Additive Effects on Piezoelectric Properties of $(Bi_{1/2}Na_{1/2})TiO_3$ Ceramics

H. Nagata, S. Morita, A. Itoh and T. Takenaka

Faculty of Science and Technology, Science University of Tokyo,
Yamazaki, Noda, Chiba 278-8510, Japan
Fax: 81-471-23-0856, e-mail: nagata@takenaka.ee.noda.sut.ac.jp

Dielectric, ferroelectric and piezoelectric properties of bismuth sodium titanate, $(Bi_{1/2}Na_{1/2})TiO_3$ (BNT) were studied on some additive dopants for a candidate as lead-free piezoelectric ceramics. Electromechanical coupling factors, k, of BNT ceramics depend on the purity of starting raw materials and additive dopants. The k_{33} in the longitudinal mode for high and normal purities are 0.38 and 0.43, respectively. It is considered that the difference in the k_{33} is caused by the impurities in the starting materials. In the case of Mn addition, the mechanical quality factor, Q_m, and resistivity, ρ, are enhanced to Q_m=380 and ρ=1×10^{14} (Ω cm)(at 40 $^\circ$C) for BNT+$MnCO_3$0.2wt%, respectively.

1. INTRODUCTION

Bismuth sodium titanate, $(Bi_{1/2}Na_{1/2})TiO_3$ (abbreviated as BNT),[1-4] is considered to be an excellent candidate as a key material of lead-free piezoelectric ceramics. The BNT shows strong ferroelectric properties of a large remanent polarization, P_r=38 $\mu C/cm^2$, and a large coercive field, E_c(=73kV/cm), and has a Curie temperature T_c=320°C and a phase transition T_p=200°C from ferroelectric to antiferroelectric. However, data on piezoelectric properties of the BNT ceramic are scarce because it is difficult to pole this ceramic due to the high E_c.

Some researchers investigated the effect of small amount of dopant such as Fe_2O_3, MnO_2 and NiO on dielectric and piezoelectric properties for perovskite materials.[5-7] T. Kamiya et al.[8] reported the effect of MnO_2 addition on piezoelectric properties of $Pb(Zr_{0.52}Ti_{0.48})O_3$ (PZT). They found that Mn-doped PZT possessed both piezoelectric properties of 'soft' and 'hard' simultaneously.

In this study, basic dielectric, ferroelectric and piezoelectric properties of the BNT ceramic were studied on some additive dopants. As a first step of this investigation, the BNT ceramic was prepared using two kinds of starting materials with defferent purities. Table I shows purities of starting materials. Two grades of normal and high purities were chosen as starting materials of Na_2CO_3, Bi_2O_3 and TiO_2. These starting materials of normal purity include some impurities such as Si, Al, Fe, Pb and Ca (=0.001~0.003wt%, respectively). These impurities correspond to additive dopants for the BNT ceramic. As the second step of this investigation, small amount of $MnCO_3$ were doped to BNT ceramic as the typical additive dopant. Some effects on dielectric, ferroelectric and piezoelectric properties were investigated for BNT+$MnCO_3$$x$wt%.

2. EXPERIMENTAL

The conventional ceramic fabrication technique was used to prepare doped and no doped BNT ceramics. Reagent-grade metal oxide or carbonate powders shown in Table I were used as starting raw materials. In the case of preparing BNT+$MnCO_3$ ceramics, the high purity of starting materials was chosen. These oxide or carbonate powders were mixed in acetone with zirconium balls by ball-milling for 10 h. After calcining, the ground and ball-milled ceramic powders

Table 1 Purities of starting materials for the BNT ceramic.

Starting material	Normal purity (%)	high purity (%)
Bi_2O_3	99.7 (Shin-Nihon Chemical CO. Ltd.)	99.95 (Soekawa Chemical CO. Ltd.)
Na_2CO_3	99.8 (Kanto Chemical CO. INC.)	99.98 (Soekawa Chemical CO. Ltd.)
TiO_2	99.9 (Toho Titanium CO. Ltd.)	99.99 (Toho Titanium CO. Ltd.)

Fig. 1 D-E hysteresis loops of BNT ceramic prepared by (a) normal purity and (b) high purity.

Fig. 2 Electromechanical coupling factor, k_{33}, versus poling field, E_p, on BNT ceramics prepared by using high and normal purity.

Fig. 3 X-ray diffraction patterns at room temperature for BNT+MnCO$_3$ $x$wt% (x=0, 0,01, 0,2, 0.5) and MnCO$_3$.

were pressed into discs and sintered at 1200 ℃ for 2 h in an air atmosphere. The crystal phase of sintered ceramics was checked using an X-ray diffractometer.

The specimens were thermally etched at 1100℃ 1 hour and for the microstructure were observed by scanning electron microscope (SEM). An average grain size was obtained using a line intercept method.

Fire-on silver paste was used as the electrode for electrical measurements such as dielectric and piezoelectric measurements. Temperature dependence on the dielectric constant, ε_s, and loss tangent, tanδ, were measured for the determination of the Curie temperature, T_c, at 1MHz by means of an automated dielectric measurement system with a multifrequency LCR meter (YHP 4275A). D-E hysteresis loops were observed by a standard Sawyer-Tower circuit at 50Hz. Specimens for piezoelectric measurements were poled in a stirred silicone oil. Piezoelectric properties were measured by means of a resonance-antiresonance method on the basis of IEEE standards using an impedance analyzer (YHP 4192A). The electromechanical coupling factor, k_{33}, were calculated from the resonance and antiresonance frequencies using Onoe's formula. Temperature dependence of resistivity was measured by using a high resistance meter (YHP 4329A).

3. RESULTS AND DISCUSSION

3.1 Effects of the purity of starting materials

Figure 1 shows D-E hysteresis loops of BNT ceramic prepared by (a) normal purity and (b) high purity. The remanent polarization, P_r, and the coercive field, E_c, of the high purity sample are higher than those of the normal purity sample. Especially, the E_c of the high purity sample is twice as large as that of the normal purity sample. Figure 2 shows the electromechanical coupling factor, k_{33}, as a function of a poling field, E_p, on BNT ceramics prepared by using the high and normal purity. The k_{33} of the high and normal purity are 0.38 and 0.43, respectively. The BNT ceramic of the normal purity is easily poled at a low applied poling filed. Therefore, the BNT ceramic which was prepared by normal purity seem to be easily poled and to have the relative high k_{33} because of the low E_c. It is considered that impurities in starting materials are influence for ferroelectric and piezoelectric properties.

3.2 Mn-doped BNT ceramics

It is not necessary with these ceramics to control the atmosphere during the sintering process, which is not the case with PZT ceramics. Figure 3 shows X-ray diffraction patterns at room temperature for BNT+MnCO$_3$$x$wt% ($x$=0, 0,01, 0,2, 0.5) and MnCO$_3$. These patterns show a single phase of perovskite structure
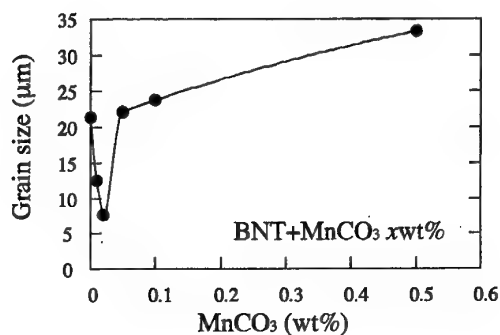
Fig. 4 Average grain size of Mn doped BNT as a function of the $MnCO_3$ content.
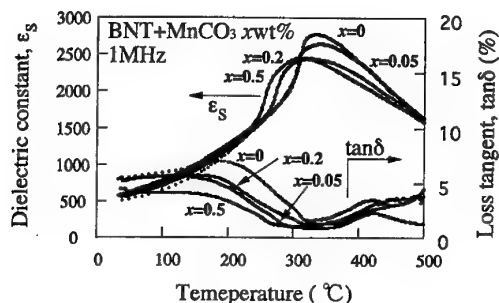
Fig. 5 Temperature dependence on dielectric constant, ε_s, and loss tangent, $\tan\delta$, for BNT+$MnCO_3$$x$wt% ($x$=0, 0,01, 0,2, 0.5) ceramics at 1MHz.

with a rhombohedral symmetry. These ceramics were very easy to sinter the ceramic body with a high measured density ratio more than 90% to the theoretical density. A color of pure BNT specimen is white, and those of BNT+MnCO ceramics become darker with increasing the amount of $MnCO_3$ content. These results indicate that BNT+$MnCO_3$ ceramics are reduced with increasing the $MnCO_3$ content.

Figure 4 shows an average grain size with of $MnCO_3$ content. The average grain size of BNT+$MnCO_3$$x$wt% ($x$=0.01 and 0.02) becomes smaller than that of pure BNT, and those of BNT+$MnCO_3$$x$wt% ($x$=0.05, 0.1 and 0.5) become larger than that of pure BNT. Therefore, a grain growth was suppressed for a little amount of Mn-doped BNT ceramics (x=0.01 and 0.02), and was promoted for much amount of Mn-doped BNT ceramics (x=0.05, 0.1 and 0.5).

Figure 5 shows the temperature dependencie on dielectric constant, ε_s, and loss tangent, $\tan\delta$, for BNT+ $MnCO_3$$x$wt% ($x$=0, 0,01, 0,2, 0.5) ceramics

Fig. 6 Curie temperature, T_c, of Mn doped BNT versus $MnCO_3$ content.
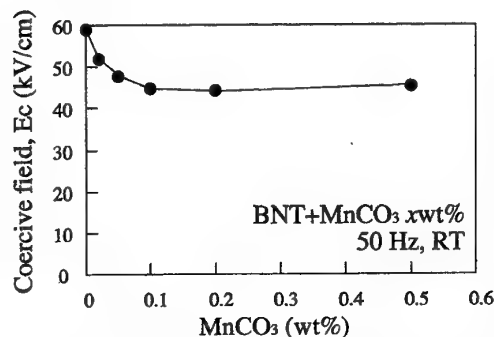
Fig. 7 Coercive field, E_c, of Mn doped BNT versus $MnCO_3$ content.

at 1MHz. The ε_s ($\fallingdotseq$500 at RT.) are smaller than those of conventional PZT or PZT-based ceramics. The ε_s -temperature curves display a broad shape near the Curie point, T_c. The value of $\varepsilon_{s\ MAX}$ at T_c and loss tangent, $\tan\delta$, at RT becomes lower with increasing the $MnCO_3$ content.

Figure 6 shows the T_c at 1MHz of BNT+ $MnCO_3$ ceramics versus $MnCO_3$ content. The T_c of BNT+ $MnCO_3$ $x$wt% are almost a constant in the range of x=0 to 0.05 and become lower with increasing the amount of $MnCO_3$ content in the range of x=0.1 to 0.5. Therefore, Mn ions seem to exist on the grain boundary in the range of x=0 to 0.05, and substitute on A- or B-site of perovskite structure in the range of x=0.1 to 0.5 wth lower lattice ditortion. However, it is unclear that which site of A or B in perovskite structure is substituted by the Mn ion.

Figure 7 shows the E_c as a function of $MnCO_3$ content. The E_c decreases with increasing $MnCO_3$ content. This tendency is the same as that of the T_c.

Figure 8 shows the mechanical quality factor, Q_m,
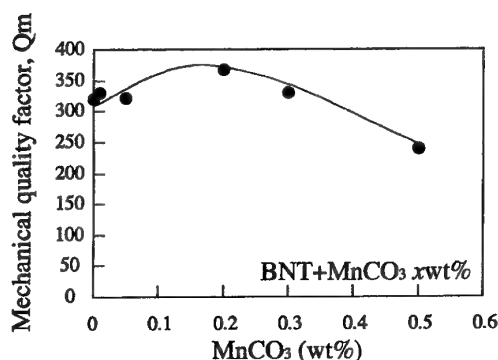
Fig. 8 Mechanical quality factor, Qm, versus MnCO₃ content.
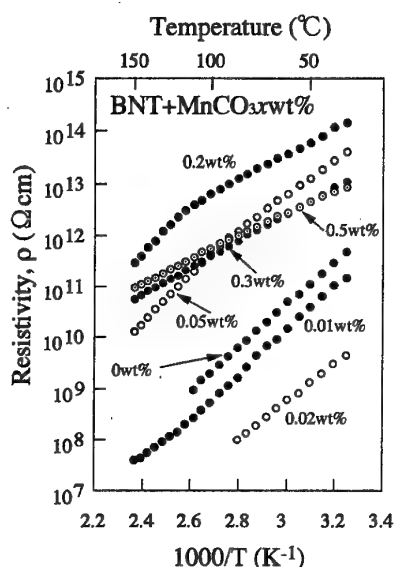
Fig. 9 Temperature dependence on resistivity, ρ, of BNT+MnCO$_3$$x$wt%.

Fig. 10 Resistivity, ρ, of Mn doped BNT at 40℃ versus MnCO$_3$ content.

as a function of MnCO$_3$ content. The maximum value of Q_m is 380 for BNT+MnCO$_3$0.2wt%. Generally, Q_m of Mn-doped PZT are much higher than that of pure PZT and this is called the 'hard' piezoelectrics. On the other hand, Q_m of Mn-doped BNT are almost same as that of pure BNT. The 'hard' behavior was not observed for Mn-doped BNT ceramics as results from E_c and Q_m.

Figures 9 and 10 show the temperature dependence on resistivity, ρ, and the ρ at 40℃ for BNT+MnCO$_3$. The maximum value of ρ is 1×10^{14} (Ωcm) for MnCO$_3$0.2wt% at 40 ℃. Mn ions compensate an electrical neutrality on the BNT+MnCO$_3$0.2wt% ceramic. However, the valence of Mn ions in the BNT ceramic is unclear in the present investigation.

4. CONCLUSIONS

Dielectric, ferroelectric and piezoelectric properties of bismuth sodium titanate, $(Bi_{1/2}Na_{1/2})TiO_3$ (BNT) are studied on some additive dopants for a candidate as lead-free piezoelectric ceramics. The BNT ceramic prepared by normal purity was easily poled because of the lower E_c. The k_{33} is relatively high comparing with that of the high purity sample. It is considered that impurities in starting materials are influence for ferroelectric and piezoelectric properties. In the case of BNT+MnCO$_3$ $x$wt%, Mn ions seem to exist on the grain boundary in the range of x=0 to 0.05, and substitute on A- or B-site of perovskite structure in the range of x=0.1 to 0.5. The resistivity, ρ, are enhanced to 1×10^{14} (Ωcm)(at 40 ℃) for BNT+ Mn0.2wt%. Mn ions compensate an electrical neutrality for the BNT+MnCO$_3$0.2wt% ceramic.

References
1) G. A. Smolensky, V. A. Isupov, A. I. Agranovskaya and N. N. ktainik, *Sov. Phys. Solid State* **2** (1961) 2651.
2) C. F. Buhrer, *J. Chem. Phys.* **36**, 798 (1962).
3) J. Suchanicz, K. Roleder, A. Kania and J. Handerek: *Ferroelectrics* **77**, 107 (1988).
4) K. Roleder, J. Suchanicz and A. Kania, *Ferroelectrics* **89**, 1 (1989).
5) K. H. Hardtl, *J. Amer.Ceram. Soc.* **64**, 283 (1981).
6) T. B. Westib, A. H. Wesber and V. M. McNamara, *J. Amer.Ceram. Soc.* **52**, 253 (1969).
7) J. S. Kim, K. H. Yoon, B. H. Choi, J. O. Park and J. M. Lee, *J. Korian Ceram Soc.* **27**, 1330 (1990).
8) T. Kamiya, T. Suzuki, T. Tsurumi and M. Daimon, *Jpn. J. Appl. Phys.* **31**, 3058 (1992).

Processing and Piezoelectric Properties of $Pb(Ni_{1/3}Nb_{2/3})O_3$-$PbTiO_3$-$PbZrO_3$ Solid Solutions from PbO-excess Compositions

Keiji Kusumoto and Tadashi Sekiya

National Industrial Research Institute of Nagoya
1 Hirate-cho, Kita-ku, Nagoya 462-8510, Japan
Fax: 81-52-916-2802, e-mail: kusumoto@nirin.go.jp

Perovskite solid solutions, $Pb(Ni_{1/3}Nb_{2/3})O_3$-$PbTiO_3$-$PbZrO_3$, were prepared without the formation of pyrochlore phase through the process of heat treatment and then acid treatment of oxide mixtures containing PbO in amount greater than in the perovskite composition. The perovskite phases obtained were characterized by discrete and cube-shaped particles of 0.5-2μm size. The relative density of the ceramics reached 94% or more after sintering the perovskite particles at 1220℃ for 3h in a PbO atmosphere. The ceramics showed a good electromechanical property near $0.5Pb(Ni_{1/3}Nb_{2/3})O_3 \cdot 0.35PbTiO_3 \cdot 0.15PbZrO_3$ compositions, as the longitudinal strain was about 0.17% under an electric field of 1500V/mm at room temperatures and the hysteresis was very little.

1. INTRODUCTION

Relaxor-type ferroelectric perovskites attract much attention as actuator materials for their electrostrictive property. The most well-known electrostrictive material is the solid solution of $Pb(Mg_{1/3}Nb_{2/3})O_3$ (PMN) with about 10 mol% $PbTiO_3$ (PT) [1]. The present authors have recently found that the electrostrictive performance in the PMN-PT ceramics is highly improved by adopting a synthesis method free from the formation of pyrochlore phase, which consists of processing scheme of heat treatment and then acid treatment of oxide mixture containing PbO in amount greater than in the perovskite composition [2]. Furthermore, this process lead to success in the formation of $Pb(Ni_{1/3}Nb_{2/3})O_3$ (PNN) in pure phase, which is also relaxor-type ferroelectric perovskite with the same structure, and as a result it was found that the solid solutions with PT show an electrostriction as good as that of PMN-PT solid solution [3].

On the other hand, it is known that PNN produces excellent piezoelectric materials in the combination with both $PbZrO_3$ (PZ) and PT perovskites. Banno et al. revealed that PNN-PT-PZ ceramics show high dielectric and piezoelectric properties near the morphotropic phase boundary (MPB) [4]. Kondo et al. observed that the electromechanical coupling factor is the highest near the composition $0.5PNN \cdot 0.35PT \cdot 0.15PZ$ [5]. Since their ceramics are made by solid state reaction, there is a question whether the contamination with pyrochlore phase is entirely avoided or not. It is of great interest to make clear how performance appears in the PNN-PT-PZ ceramics made by our process free from the formation of pyrochlore phase.

In this study, the (1-x-y)PNN·xPT·yPZ perovskite ceramics were prepared in the composition range of x=0.33-0.36 and y=0.14-0.17, in the vicinity of MPB, through process of heat treatment and then acid treatment of oxide mixture containing PbO in amount greater than in the perovskite composition. The ceramics were made from the perovskite particles obtained, and the dielectric and piezoelectric properties were examined.

2. EXPERIMENTS

The starting oxides used were reagent grade powders of PbO, NiO, Nb_2O_5, TiO_2, and ZrO_2. Figure 1 shows the processing scheme for preparing the perovskite phases and the ceramics. After heat treatment, the oxide mixtures were treated with 1N acetic acid solution to remove the unreacted oxides. The purified perovskite powders were pressed into disks by applying pressure of 200MPa and sintered at 1220°C for 3h in a PbO atmosphere. The relative density of ceramics ranged 94-97% in sample to sample. The samples were polished into 1 mm thickness and electrode-silver paste was

applied to both faces to measure the dielectric and piezoelectric properties. The dielectric constants and dielectric losses were measured at 1, 10 and 100kHz by an impedance analyzer. The electromechanical coupling factors (Kp) were measured by the resonant-antiresonant frequency method, after poling under an electric field of 2000V/mm at room temperature for 30 min in a silicone oil bath. This electric field was selected in order to make perfect the poled state. The electric field induced longitudinal strains were estimated under electric fields of 0-1500V/mm by a laser-type displacement meter.

```
┌──────────────────────────────┐
│       Raw materials          │
│ PbO, NiO, Nb₂O₅, TiO₂, ZrO₂  │
└──────────────────────────────┘
              ↓
┌──────────────────────────────┐
│          Mixing              │
└──────────────────────────────┘
              ↓
┌──────────────────────────────┐
│       Heat treatment         │
│          950℃, 1h            │
└──────────────────────────────┘
              ↓
┌──────────────────────────────┐
│       Acid treatment         │
│    1N acetic acid solution   │
└──────────────────────────────┘
              ↓
┌──────────────────────────────┐
│     Perovskite particles     │
└──────────────────────────────┘
              ↓
┌──────────────────────────────┐
│      Forming into disk       │
│           200MPa             │
└──────────────────────────────┘
              ↓
┌──────────────────────────────┐
│          Sintering           │
│   1220℃, in PbO atmosphere   │
└──────────────────────────────┘
              ↓
┌──────────────────────────────┐
│        Measurement           │
│    Dielectric properties     │
│   Piezoelectric properties   │
└──────────────────────────────┘
```

Fig.1. Processing scheme for obtaining PNN-PT-PZ ceramics.

3. RESULTS AND DISCUSSION

3.1 Preparation of Perovskite Phases

For the purpose of determining the starting composition adequate to produce perovskite phase in high yield, investigation was made through the formation of perovskite with the composition $0.5PNN \cdot 0.35PT \cdot 0.15PZ$. Table I compares the fractions of $0.5PNN \cdot 0.35PT \cdot 0.15PZ$ perovskite phase to pyrochlore phase formed in the mixtures with different PbO content, by heat treatment at 950°C for 1h and then acid treatment. The fraction of the perovskite was calculated as follows:

$$\text{Perovskite (\%)} = I_{pero} / (I_{pero} + I_{pyro}) \times 100$$

where, I_{pero} and I_{pyro} denote XRD intensities of (100) of perovskite and (222) of pyrochlore, respectively.

Table I. Fractions of $0.5PNN \cdot 0.35PT \cdot 0.15PZ$ perovskite phase to pyrochlore phase formed in the mixtures with different PbO content

Starting composition	Perovskite yield (%)
$3PbO+0.5NiO+0.5Nb_2O_5+1.05TiO_2+0.45ZrO_2$	73
$4PbO+0.5NiO+0.5Nb_2O_5+1.05TiO_2+0.45ZrO_2$	91
$5PbO+0.5NiO+0.5Nb_2O_5+1.05TiO_2+0.45ZrO_2$	100

The stoichiometric composition does not produce the perovskite phase in reasonable yield because of the predominance in the formation of pyrochlore phase. The yield of the perovskite phase is remarkably improved in the compositions containing excess PbO. Eventually, the composition, $5PbO+0.5NiO+0.5Nb_2O_5+1.05TiO_2+0.45ZrO_2$ (2PbO+perovskite), produced perovskite phase in almost 100% yield. The solid solutions with the other compositions could be also obtained in single phase by adding 2 mol excess of PbO.

In order to confirm the formation mechanism of the perovskite phase, the starting mixtures were subjected to DTA. As shown in Fig.2, it is found that the excess addition of PbO causes a sharp endothermic peak on the DTA curves at around 850°C, which corresponds to the formation of liquid phase. From the fact that the perovskite yield was considerably increased beyond this temperature, no doubt the existence of liquid phase contributes to promote the perovskite formation.

Fig.2. DTA curves of the mixtures.
(a) $3PbO+0.5NiO+0.5Nb_2O_5+1.05TiO_2+0.45ZrO_2$,
(b) $4PbO+0.5NiO+0.5Nb_2O_5+1.05TiO_2+0.45ZrO_2$,
(c) $5PbO+0.5NiO+0.5Nb_2O_5+1.05TiO_2+0.45ZrO_2$.

As can be seen from SEM photograph in Fig.3, the perovskite phases are crystallized in discrete and cube-shaped particles of 0.5 to 2μm size. High dispersed state of the particles seems to be because they are formed in the matrix in plenty without disturbance from each other.

Fig.3. SEM photograph of the 0.5PNN·0.35PT·0.15PZ perovskite particles obtained from the mixture $5PbO+0.5NiO+0.5Nb_2O_5+1.05TiO_2+0.45ZrO_2$ after heating at 950°C for 1h and acid treatment.

3.2 Dielectric Properties

As an example, Figure 4 shows the temperature dependence of dielectric constants and dielectric losses for 0.5PNN·0.35PT·0.15PZ perovskite ceramic. The relaxor behavior still remains as the dielectric constant varies drawing a broad peak and the peak position of dielectric constant is dependent on the measuring frequency. The other samples investigated also exhibited similar dielectric constant curve.

Figure 5 plots the dielectric constants at Curie temperature (Tc) and isotherms of Tc against the composition. The dielectric constants are similar to those already reported [5]. In these Tc values, it seems that additivity is valid, because the measured values coincide with those calculated according to the following equation:

$$Tc = (1-x-y)T_{PNN} + xT_{PT} + yT_{PZ}$$
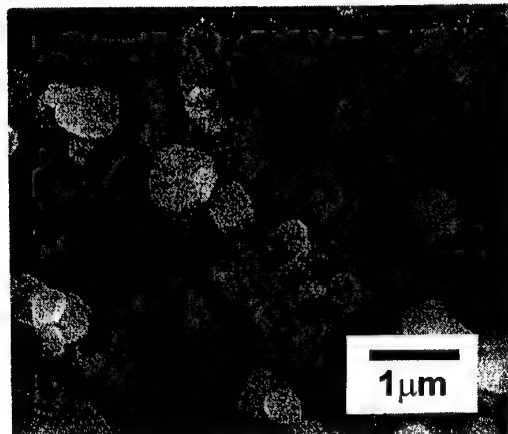
where, T_{PNN}, T_{PT} and T_{PZ} are the Curie points of PNN, PT and PZ, respectively. Therefore, it is considered that the perovskite particles are crystallized in desirable composition.

3.3 Piezoelectric Properties

Table II summarizes the electromechanical coupling factors (Kp) and electric field induced strains under 1500V/mm. Both the values of Kp and longitudinal strains vary more or less with the composition. It is very difficult to argue quantitatively this behavior, since these values are merely obtained at room temperature. Further high performance should be expected in the vicinity of
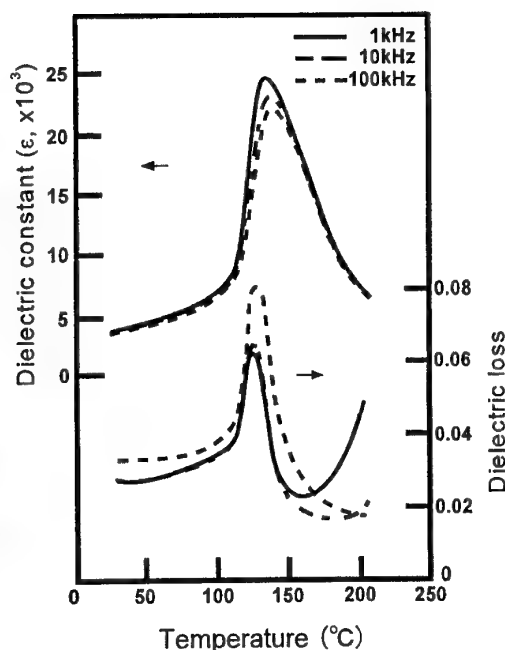
Fig.4. Temperature dependence of dielectric constants and dielectric losses measured at 1, 10, and 100kHz for 0.5PNN·0.35PT·0.15PZ ceramic.
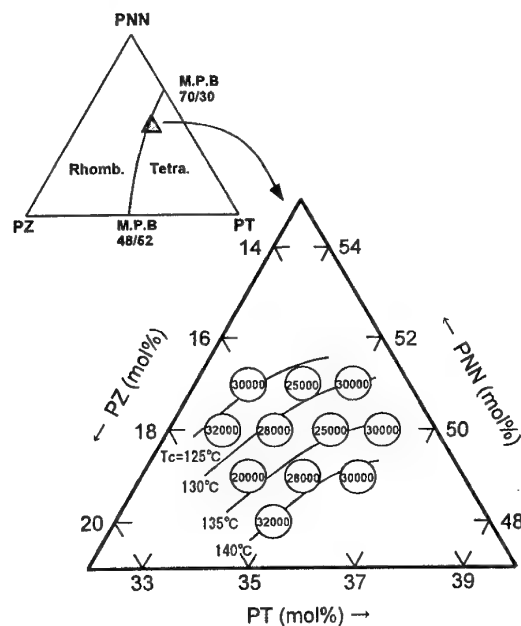
Fig.5. Plots of the dielectric constants at Curie temperature (Tc) and isotherms of Tc against the composition in the PNN-PT-PZ ceramics.

Tc, however, these compositions lead to Tc much higher than room temperature, as can be seen from Fig.5. Anyhow, the Kp values ranging from 0.55 to 0.7 are much improved compared to those reported by Banno et al. [4]. This may be because the absence of pyrochlore phase is favorable for these performances. It seems likely that the composition closer to MPB line leads to higher Kp, and this is consistent with the fact that Kondo et al. observed higher value of Kp near the $0.5PNN \cdot 0.34PT \cdot 0.16PZ$ composition [5]. In this work, the $0.51PNN \cdot 0.34PT \cdot 0.15PZ$ composition leads to surprisingly high strain, 0.24%, though exhibited a hysteresis with a small residual strain on the strain response curve against electric field, which is relatively large compared to the others observed, but not so extraordinary as those of the popular PZT ceramics.

Table II. Electromechanical properties of the PNN-PT-PZ ceramics at room temperature

Composition	Kp	Longitudinal Strain (%)
$0.51PNN \cdot 0.35PT \cdot 0.14PZ$	0.61	0.18
$0.51PNN \cdot 0.34PT \cdot 0.15PZ$	0.65	0.24
$0.51PNN \cdot 0.33PT \cdot 0.16PZ$	0.64	0.12
$0.5PNN \cdot 0.36PT \cdot 0.14PZ$	0.55	0.14
$0.5PNN \cdot 0.35PT \cdot 0.15PZ$	0.62	0.17
$0.5PNN \cdot 0.34PT \cdot 0.16PZ$	0.70	0.17
$0.5PNN \cdot 0.33PT \cdot 0.17PZ$	0.65	0.16
$0.49PNN \cdot 0.36PT \cdot 0.15PZ$	0.58	0.18
$0.49PNN \cdot 0.35PT \cdot 0.16PZ$	0.62	0.16
$0.49PNN \cdot 0.34PT \cdot 0.17PZ$	0.66	0.08

For the discussion of the relation between hysteresis and composition, Figure 6 demonstrates the longitudinal response curves acquired by the electric field of 0 to 1500V/mm for the ceramics with PNN content held constant at 0.5 mol. It can be seen at least from this figure that the hysteresis becomes larger with increase of PZ content. This phenomenon seems quite reasonable taking consideration that the PZT ceramics show always large hysteresis.

In the practical use of ceramic actuators, of course large displacement is a very fine thing, but little hysteresis is also very important matter. Anyhow, the scale of the hysteresis seen in this composition series is out of the question compared to those of the PZT ceramics. Through this work, thus, we could find a way of making ceramic actuator materials with the natures of high displacement and little hysteresis in the combination of electrostrictive perovskite and piezoelectric perovskite.
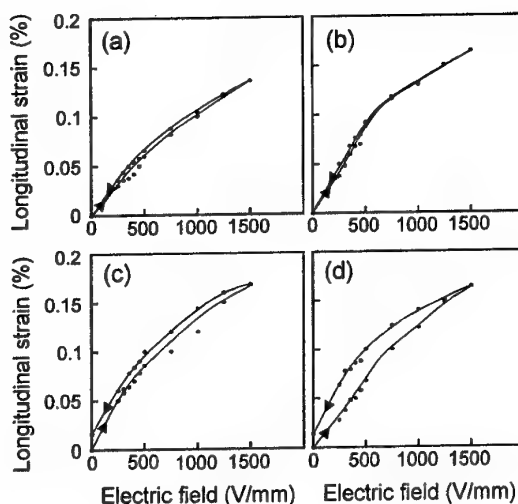
Fig.6. Plots of longitudinal strain vs. applied electric field at room temperature for the PNN-PT-PZ ceramics. (a) $0.5PNN \cdot 0.36PT \cdot 0.14PZ$, (b) $0.5PNN \cdot 0.35PT \cdot 0.15PZ$, (c) $0.5PNN \cdot 0.34PT \cdot 0.16PZ$, (d) $0.5PNN \cdot 0.33PT \cdot 0.17PZ$.

4. CONCLUSIONS

The relaxor-based ferroelectric perovskites, $Pb(Ni_{1/3}Nb_{2/3})O_3$-$PbTiO_3$-$PbZrO_3$ solid solutions could be obtained without the formation of pyrochlore phase by heat treatment and then acid treatment of oxide mixtures containing PbO in amount greater than in the perovskite composition. The ceramics showed reasonable piezoelectric properties in all samples. Among investigated, it was found that the ceramics near the $0.5PNN \cdot 0.35PT \cdot 0.15PZ$ composition are suitable for ceramic actuator materials because of both the performances of high strain and little hysteresis.

REFERENCES

[1] J.Zhao, Q.M.Zhang, N.Kim and T.Shrout, Jpn. J. Appl. Phys., **34**, 5658-5663 (1995).
[2] K.Kusumoto and T.Sekiya, Mat. Res. Bull., **33**, 1367-1375 (1998).
[3] K.Kusumoto and T.Sekiya, Electroceramics in Japan, Trans Tech Publications, Switzerland (1999) pp.45-48.
[4] H.Banno, T.Tsunooka and I.Shimano, Pro. 1st Meet. Ferroelectric Materials and Their Applications, Keihin Printing, Kyoto (1977) pp.339-344.
[5] M.Kondo, M.Hida, M.Tsukada, K.Kurihara and N.Kamehara, Jpn. J. Appl. Phys., **36**, 6043-6045 (1997).

PROPERTIES OF PMN AND PZT IN COMPRESSION

Lynn Ewart, Elizabeth McLaughlin and Kim Gittings
Naval Undersea Warfare Center
Attn: Code 2132, 1176 Howell Street
Newport, RI 02841-1708
Fax: (401) 832-6401, e-mail: ewartlm@npt.nuwc.navy.mil

Most active ceramics used in Navy sonar transducers are mechanically loaded in compression during fabrication to ensure that the ceramic does not experience deleterious tensile forces during operation. This research investigates the effect of compressive stresses on the properties of five electroactive ceramics; 1) poled lead zirconate titanate (PZT), 2) unpoled PZT, 3) piezoelectric lead magnesium niobate (PMN), 4) barium doped electrostrictive PMN, and 5) lanthanum doped electrostrictive PMN. Failure strength, Young's modulus and the Poisson's ratio were measured at three load rates. Failure strength increased with increasing load rate in all five materials. While the electrostrictive PMNs are weaker in compression than either of the PZTs, the piezoelectric PMN was by far the strongest material. The piezoelectric PMN is at least 48% stronger than the electrostrictive PMNs and at least 23% stronger that the PZTs. Interrupted tests were also performed in which the specimens were not loaded to failure. Microstructural analysis performed on lanthanum doped PMN specimens from interrupted tests indicates that damage occurs in the ceramics at stress levels significantly below the failure strength. Damage occurs initially as intergranular cracking with intragranular cracking observed at higher stress levels. Crack densities rise steeply with increasing stress until failure.

1. INTRODUCTION

Sonar transducer stacks have traditionally been made from piezoelectric ceramics and more recently from electrostrictive ceramics. During transducer operation these ceramics are subject to dynamic cyclic stresses. Since ceramics lack ductility and have poor tensile strength at sonar operating temperatures transducers are designed to apply a compressive stress to the ceramic stack. This ensures that the ceramic elements remain in compression during active driving.

As the requirements on sonar systems change due to a shift from blue water to littoral arenas, performance gains need to be realized in the electroactive ceramics. Performance gains in PZT can be realized by increasing the magnitude of the electrical field used to drive transducers. Larger electric fields will necessitate the application of larger compressive stresses on the stack of PZT ceramic elements during transducer fabrication and use. To support the use of PZT under these more severe mechanical conditions and to aid the transition of developmental materials such as lead magnesium niobate (PMN) into Fleet transducers, the mechanical properties of these materials, especially in compression, need to be elucidated.

The application of compressive mechanical stress on electroactive ceramics has received some attention [1-4], but the focus has been the effect on dielectric and electromechanical properties. Even when the focus shifts more heavily toward mechanical properties [5], not all the relevant testing issues are addressed.

The structural ceramics community has laid an extensive groundwork for the accurate mechanical testing of brittle materials. Much research has been dedicated to the development of test methodologies for the study of compressive properties [6-8]. Proper design of the test specimen and of the loading fixture is paramount for ensuring both the desired stress state in the sample and the repeatability and accuracy of the test technique.

Research on the mechanical properties of structural ceramics in compression has revealed behavior of interest to the sonar community. Lankford [9] studied high purity alumina under a monotonically increasing compressive stress and discovered that a stress threshold exists above which grain boundary microcracking occurs. In the Lankford study [9] the stress at which the damage threshold occurred was approximately half of the compressive strength of the material. Acoustic emission results indicated that increasing the stress beyond the damage threshold led to increasing microstructural damage.

The existence of a damage threshold at stresses significantly below the compression strength of the material has not been explored in electroactive ceramics. As compressive stresses on the ceramic stacks are increased to improve electromechanical performance the possibility of exceeding the damage threshold increases. Operating transducers at stresses above the damage threshold could negatively impact the material properties and thus transducer performance and lifetime.

The work reported herein utilizes a compression test technique that was developed by the structural ceramics community and is the foundation of a proposed American Society for Testing and Materials (ASTM) standard to study the behavior of electroactive ceramics under a uniform compressive stress state. The research focuses on commercially available PZTs and PMNs that are in use or under investigation for future use by the U.S. Navy. The compressive strength, Young's modulus and Poisson's ratio at several load rates are measured on specimens having a reduced gage section geometry optimized to minimize variations in the stress state through the gage section. Microstructural analysis of lanthanum doped PMN specimens subjected to peak loads below failure (interrupted tests) are employed to examine microstructural damage at stress levels below the compression strength.

2. EXPERIMENTAL PROCEDURE

The compressive properties of five electroactive ceramics were investigated; a poled and unpoled Navy Type III PZT from EDO Corporation, an unpoled piezoelectric PMN (PMN-unpoled) from EDO Corporation, and barium and lanthanum doped electrostrictive PMNs (PMNw/Ba and PMNw/La, respectively) from TRS Ceramics.

Bulk materials were machined into reduced gage section dumbbell shaped specimens as described by Tracy [6] and Dunlay et al. [7]. The two electrostrictive PMNs were machined into large dumbbells (3.6 cm tall x 1.3 cm outer diameter) and the other three ceramics were machined into small dumbbells (3 cm tall x 1 cm outer diameter). In the case of the poled PZT the specimens were machined with the poling direction perpendicular to the long axis of the specimen. Thus, during testing the poling direction was perpendicular to the axis of compression. The current research verified through finite element analysis that the variation in the compressive stresses through the gage section of the specimens is less than 7%. To minimize misalignment a double ball joint fixture was used to load the load train and the specimens.

On all specimens the end faces, where the compressive loads were applied, were electroded. Specimens were tested under short circuit conditions. The application of three biaxial strain gages spaced 120° apart in the same cross sectional plane in the middle of the reduced gage section allowed the measurement of both the Young's modulus and the Poisson's ratio. The gaged specimens were encapsulated to help retain the broken pieces of the test specimens for further analysis. The encapsulation procedure entailed priming the specimens with Dow Corning Z 6020 silane and then potting them with Composite Polymer Design 9130 polyurethane.

The specimens were tested in a servohydraulic test machine (Instron load frame model 1332 and control system 8500). The standard testing rate was 6 kN/min. To examine the effect of load rate on the mechanical properties specimens were also tested at 0.6 kN/min and 60 kN/min. However, the presented results represent specimens tested at 6 kN/min unless otherwise specified. At least three specimens per load rate were tested to failure.

Microstructural studies were performed on PMNw/La. Four PMNw/La specimens were loaded in compression to a specific peak stress and unloaded. The four peak stresses were 92, 253, 568 and 726 MPa. Along with an untested PMNw/La specimen, these specimens were cut at 45° to the loading axis, polished, chemically etched and examined in the scanning electron microscope for microstructural defects and damage.

3. RESULTS

The five electroactive ceramics exhibited a large range of strengths. The electrostrictive PMNs have the lowest compressive strengths of the five materials tested (Table I). Despite the difference in dopant composition and quantity the two electrostrictive PMNs have essentially the same strength ($\approx$ 874 MPa). In comparison, however, the process of poling has a significant effect on the strength of PZT. When the poling direction is oriented perpendicular to the applied compressive stress the strength drops 10% from 1045 MPa for the unpoled ceramic to 944 MPa for the poled PZT. The PMN-unpoled, at a compressive strength of 1309 MPa, is 25 to 39 percent stronger than the PZTs, depending upon electrical history, and 48% stronger than the electrostrictive PMNs.

Table I: Materials and Compressive Mechanical Properties

Material	Failure Strength at 6 kN/min (MPa)	Young's Modulus (GPa)	Poisson's Ratio
PMNw/Ba	877 ± 117	131 ±4	0.30 ± 0.02
PMNw/La	871 ± 43	132 ± 4	0.30 ± 0.02
PMN	1309 ± 41	111 ± 4	0.46 ± 0.02
PZT Unpoled	1045 ± 45	76 ± 1	0.43 ± 0.02
PZT Poled ⊥	944 ± 50	83 ± 4	0.44 ± 0.06

The stress-strain behavior of the materials varied greatly as did their Young's modulus and Poisson's ratio (Table I). Both of the electrostrictive PMNs responded linearly to the compressive loading up to failure. Their Young's modulus and Poisson's ratio values, 131 GPa and 0.30 respectively, were essentially the same. The PMN-unpoled appears to have two linear regions (Fig.1). The initial part of the stress-strain curve is linear to approximately 200 MPa. Beyond this stress the stress-strain curve deviates to a slope higher than the Young's modulus of 111 GPa. The PMN-unpoled had the largest Poisson's ratio of 0.46.

The initial linear region of the PZTs was very small (Fig. 1). The poled PZT was linear up to approximately 150 MPa giving a Young's modulus of 83 GPa and a Poisson's ratio of 0.44 (see Table I). The unpoled PZT was linear only up to approximately 60 MPa. The
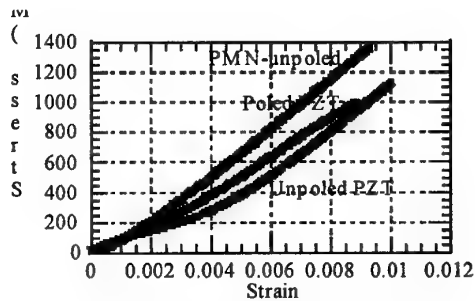
Fig. 1 Stress-Strain Curves at 6 kN/min

resulting Young's modulus was 76 GPa with a Poisson's ratio of 0.43.

The effect of load rate on the compressive strength of the ceramics was investigated. For all five materials the compression strength increased with increasing load rate. The PMN-unpoled showed the strongest response to a change in load rate.

Microstructural analysis of PMNw/La specimens from the interrupted tests revealed that grain boundary microcracking can occur at loads as low as 92 MPa. The density of microcracks increased with increasing peak stress. At 726 MPa intragranular cracking was also observed.

4. DISCUSSION

The two electrostrictive PMNs had the lowest compressive strengths of all five ceramics (Table I). In flexural strength studies [10, 11] comparing electrostrictive PMNw/Ba and PMNw/La to PZT (all materials from the same manufacturers as in this study), the PMNs also had similar strengths and were weak compared to the PZTs. Fractographic analysis identifying the native flaw at each fracture origin was able to guide processing changes that reduced flaw sizes and significantly raised the PMN strengths. Failure in compression leads to pulverization of the test specimen. Thus, there is essentially no specimen left for post-mortem examinations to allow identification of the flaw that led to final fracture, its size or its orientation.

Interestingly, the PMN-unpoled is, by far, the strongest of the five ceramics in compression. One possible reason for the high compressive strength is that the PMN-unpoled has the largest fracture toughness value(s) (K_{IC} in tension and/or K_{IIC} in shear) of all five materials. Both K_{IC} and K_{IIC} are considered because a fracture criterion for failure in compression has not been established. Cracks do not grow in compression. Under far-field compressive loads local tensile and shear stresses govern crack initiation and propagation. It is not known whether K_{IC} and/or K_{IIC} dominates the local fracture process. The local fracture process is stable because the bulk of the material is in compression. Failure occurs when K_{IC} and/or K_{IIC} for the material is exceeded locally *and* conditions for unstable propagation are achieved in · the bulk.

A comparison of numerous studies in the literature reveals that various compositions of PMN have a lower

K_{IC} than PZT regardless of its electrical state [10, 12-15]. Studies of PMN have focused on electrostrictive compositions so a definitive statement on the K_{IC} of the PMN-unpoled relative to PZT cannot be made. Measurements of K_{IIC} for these materials have not been made. However, the same vendor manufactured the PMN-unpoled and the two PZTs. Thus, it is reasonable to assume that the native flaw population introduced during processing is similar, especially in size, for the PMN-unpoled and the PZTs. This would imply that the PMN-unpoled does indeed have the largest fracture toughness value(s). This possibility is further supported by the idea, suggested in the literature, that the fracture process in compression is not dominated by the native flaw population but rather by the initiation and coalescence of microcracks. The process of microcrack coalescence and final fracture would then be governed by the fracture toughness value(s) of the material.

A comparison of the PZTs reveals that the unpoled material is stronger. Since these PZTs are from the same batch of material, processing variations cannot explain the difference. The strength difference between the unpoled and poled PZTs can be explained based upon the effect of electrical history on the fracture toughness of PZT. Studies have shown that poling affects the K_{IC} of PZT as does the relationship of poling direction to the direction of crack propagation [10, 12-15]. The literature indicates that the K_{IC} is highest when cracks propagate parallel to the poling direction and lowest when cracks grow perpendicular to the poling direction. The K_{IC} value of unpoled PZT falls between the two poled cases. Since local tensile and shear forces drive crack propagation, crack orientation is expected to be parallel to and 45° to the compression axis. For the poled PZT this means that crack growth occurs perpendicular to and at 45° to the poling direction (since the poling direction is perpendicular to the compression axis). Thus, the poled PZT is expected to have a K_{IC} value smaller than the unpoled PZT. Assuming either that the PZTs have a similar native flaw sizes or that the native flaw population does not dominate failure, a smaller fracture toughness value equates to a lower strength.

All five of the materials have strengths that exceed the expected stress levels in naval transducers in use. For most devices the static compressive stress applied to the ceramic elements during fabrication does not exceed 82 MPa, although in a few designs the ceramic elements may be subjected to stresses as high as 345 MPa. The static stress is sufficiently large in magnitude to avoid the development of tensile stresses during excitation with an oscillating signal. Thus, the largest oscillating signal would cause stresses to vary from zero to twice the static compressive stress, or 164 to 690 MPa, depending upon transducer type. While the compressive strength of all five materials exceeded 690 MPa, the wide range of strengths in the PMNw/Ba, 877 ± 177 MPa, is of concern.

All five materials were sensitive to changes in the strain rate. In alumina [16] microstructural evidence suggests that the strain rate sensitivity is due to the role of

microplasticity, in the form of twinning and slip, in initiating microcracks. In electroactive ceramics detailed mirostructural analysis of as tested specimens is needed to determine the cause of the strain rate sensitivity.

Microstructural analysis of tested PMNw/La specimens that were polished and etched revealed microcracking at stress levels well below the compression strength. Occasional grain boundary microcracks were observed at loads as low as 10% of the compression strength. While these microcracks occurred at stress levels experienced by U.S. Navy transducers, the density of microcracks was very low. The first observations of intragranular cracking occurred at stress levels 83% of the compression strength. The observation of mechanical damage at these stress levels warrants the exploration of the combined effect of mechanical stress and electric field on the initiation of microcracks in electroactive ceramics.

5. SUMMARY

The five electroactive ceramics studied had a spectrum of strengths. The electrostrictive PMNs were the weakest with average strengths in the 870 MPa (126 ksi) range. They were followed in order of increasing strength by PZT poled perpendicular to the loading axis, unpoled PZT, and piezoelectric PMN. There is a 48% increase in strength from the electrostrictive PMNs to the piezoelectric PMN. It is argued that the differences in strength between all 5 materials are due mainly to differences in the fracture toughness value(s).

In each of the five electroactive ceramics, the compressive strength is a function of load rate similar to behavior seen in structural ceramics. The specific relationship is one in which strength increases with increasing load rate.

In PMNw/La microstructural damage, in the form of microcracking, was observed. Intergranular microcracking occurred at low loads with intragranular cracking also observed at loads close to the failure strength. Further studies examining the effect of electric field on the initiation of microcracking in electroactive ceramics is needed.

6. ACKNOWLEDGEMENTS

7. REFERENCES

1. H.H.A. Krueger, "Stress Sensitivity of Piezoelectric Ceramics: Part 1. Sensitivity to Compressive Stress Parallel to the Polar Axis," *Journal of the Acoustical Society of America*, vol.42, no. 3, p.636 (1968).
2. H.H.A. Krueger, "Stress Sensitivity of Piezoelectric Ceramics: Part 3. Sensitivity to Compressive Stress Perpendicular to the Polar Axis," *Journal of the Acoustical Society of America*, vol. 43, no. 3, p.583 (1968).
3. W.P. Mason, ed., *Physical Acoustics*, Academic Press, New York (1964).
4. D. Berlincourt, "Piezoelectric Ceramics: Characteristics and Applications," *Journal of the Acoustical Society of America*, vol. 70, no. 6, p.1586 (1981).
5. H. Cao and A.G. Evans, "Nonlinear Deformation of Ferroelectric Ceramics," *Journal of the American Ceramic Society*, vol. 76, no. 4, p.890 (1993).
6. C.A. Tracy, "A Compression Test for High Strength Ceramics," *Journal of Testing & Evaluation*, vol. 15, no. 1, p.14 (1987).
7. W.A. Dunlay, C.A. Tracy and P.J. Perrone, "A Proposed Uniaxial Compression Test for High Strength Ceramics" (U), MTL Technical Report 89-89, U.S. Army Materials Technology Laboratory, Watertown, MA, September 1989 (UNCLASSIFIED).
8. J.M.Birch, B. Wilshire, D.J.R. Owen, D.Shantaram, "The Influence of Stress Distribution on the Deformation and Fracture Behavior of Ceramic Materials Under Compression Creep Conditions," *Journal of Materials Science*, vol. 11, p.1817 (1976).
9. J. Lankford, "compressive Microfracture and Indentation Damage in Al_2O_3", in Fracture Mechanics of Ceramics, ed. R.C. Bradt, D.P.H. Hasselman and F.F. Lange, Plenum Press, NY, p.245 (1974).
10. L. Ewart, "Flexural Failure of Navy Type III PZT," Extended abstracts of the Eighth US-Japan Seminar on Dielectric & Piezoelectric Ceramic" (1997).
11. K. Okazaki, "Mechanical Behavior of Ferroelectric Ceramics," *Ceramic Bulletin*, vol. 63, p.1150 (1984).
12. L. Ewart, "Analysis of Flexural Strength and Failure in PMN-PT," *Ceramic Transactions-Advances in Dielectric Ceramic Materials*, American Ceramic Society (1998).
13. K. Mehta and A.V. Virkar, "Fracture Mechanisms in Ferroelectric-Ferroelastic Lead Zirconate Titanate (Zr:Ti=0.54:0.46) Ceramics," *Journal of the American Ceramic Society*, vol. 73, p.567 (1990).
14. T. Tanimoto, K. Yamamoto, and T. Morii, "Nonlinear Stress-Strain Behavior of Piezoelectric Ceramics Under Tensile Loading," *Proceedings of the 9th International Symposium on Application of Ferroelectrics*, p.394 (1994).
15. G. G. Pisarenko, V. M. Chushko, and S. P. Kovalev, "Anisotropy of Fracture Toughness of Piezoelectric Ceramics," *Journal of the American.Ceramic Society*, vol. 68, p.259 (1985).
16. J.Lankford, "Compressive Strength and Microplasticity in Polycrystalline Alumina," *Journal of Materials Science*, vol. 12, p.791 (1977).

High Frequency Piezoelectric Properties of
Lead Titanate Ceramics

Koichi HAYASHI, Akira ANDO, Seigo HAYASHI and Yukio SAKABE

Murata Manufacturing Co., Ltd. Yasu-gun, Siga 520-2393, Japan

Fax: 81-77-586-8515, e-mail: kohaya @ murata. co. jp

Abstract

Four-layered piezoelectric plates of $PbTiO_3$ and $Pb(Zr,Ti)O_3$ ceramics were prepared to evaluate the piezoelectric characteristics in high frequency region. These monolithic plates prepared with co-fired with inner electrodes generate the fourth harmonic thickness extensional vibration. A single resonance was obtained around 60MHz without spurious between the resonance and antiresonance frequency. Especially, high electromechanical coupling factor and low-loss characteristics were shown in the $PbTiO_3$ ceramics. We proposed that the high frequency resonators are possible by using high order harmonic vibration.

1. Introduction

Piezoelectric materials have been widely used for the various electronic devices such as filters, resonators, sensors and so on. Piezoelectric ceramics have many advantages over single crystals: they have high piezoelectricity and are easy to machine into desired shapes. Especially, lead titanate ($PbTiO_3$, PT) and lead zirconate titanate ($Pb(Zr,Ti)O_3$, PZT) are useful piezoelectric ceramics because they are able to have various properties due to minor chemical modifications.[1-7]

Recent developments in applications of the microprocessors and mobile appliances working at high speed require high frequency piezoelectric ceramics oscillators. The driving frequency of the piezoelectric oscillators depends on the materials, the vibration mode and the effective length. In the frequency range of MHz ceramics oscillators the thickness extension or shear vibration modes are normally used. When PZT ceramics are used as the 10 MHz oscillator by the thickness extensional mode, the thickness of the ceramics plate is about 200 μm. In order to develop the higher frequency oscillators the thickness of the ceramics bodies have to decrease to less than 100 μm. In these thin ceramics body the mechanical strength decreases, therefore it is difficult to machine the desired thickness accurately. It is well known that the other method to develop the higher frequency oscillators is the use of the surface acoustic wave (SAW). However, the miniaturization of the SAW devices is difficult because of they need the reflectors.

Two of the authors (A.A. and Y. S.) in the present study have already reported the new piezoelectric oscillators using the second harmonic thickness extensional vibration in a two-layered monolithic piezoelectric ceramics plate.[8] This has an inner electrode placed at the middle of the ceramic plate. There are several advantages in the oscillator we proposed against the thickness mode resonators of the single plate and the SAW devices. Firstly, this two-layered type has twice the thickness of the single type for the same resonant frequency. Therefore, the ceramics body has sufficient

mechanical strength for machining. Secondly, the various piezoelectric ceramics can be adopted in this mode because the energy trapping occurs even in the materials with the effective Poisson's ratio smaller than 1/3. Finally, this is easy to minimize, compared to the SAW oscillators.

The two-layered type piezoelectric oscillator mentioned above has the characteristics promising the high frequency applications. In addition, it is expected that the same characteristics of the two-layered type can be performed when the number of layer is increased. The multilayered oscillator with increased number of layers can be used as the oscillators at the higher frequencies because the thickness of an individual layer determining the resonance frequency can be decreased without the decreasing the total thickness of the ceramic plate by increasing the number of layers.

In the present study, four-layered monolithic piezoelectric plates of the PT and PZT ceramics were prepared to investigate the characteristics of the fourth harmonic thickness extensional vibration at high frequencies.

2. Experimental Procedure

PT and PZT ceramics specimens were prepared with the conventional powder processing. The composition of the PT ceramics is modified with small quantities La and Mn ions. The composition is based on assumption that the La ions substitute Pb ions, and the Mn ions are incorporation on the Ti ion sites. It has been well known as the useful material with the high electromechanical coupling factor (kt) of the thickness extensional vibration and high mechanical quality factor (Qm).[3,4] The PZT specimens having the composition of the $0.5PbTiO_3$-$0.4PbZrO_3$-$0.1Pb(Mn_{1/3}Nb_{2/3})O_3$ were prepared. The PZT ceramics has high Qm and a tetragonal structure with its effective Poisson's ratio less than 1/3 as same as the PT.

High purity PbO, TiO_2, ZrO_2, MnO_2, La_2O_3, Nb_2O_5 were used as the starting raw materials. These raw materials were weighed to the desired composition and

milled for 20 hours in a ball mill with the pulverizing media. After drying, the mixed powder was calcined at 900°C for 2 hours.

The obtained powder was milled in water and mixed with organic binder by ball-milling to prepare a slurry, the slurry was cast into green sheets about 50μm thick by the conventional doctor blade method. The green sheets were stripped from the carrier film and the inner electrode patterns were screen-printed on them with platina paste. The sheets laminated into plates under a pressure of 2ton/cm^2. After the binder burning out, the PT and the PZT were sintered at 1200°C and 1150°C, respectively in sealed alumina crucibles for 2 hours.

Cu and Ag was evaporated as the electrodes on the both surfaces of the sintered plates and Ag paste was applied on the edges to obtain the electrical connection between the surface and inner electrodes. The poling of the PT and PZT plates were performed in an insulator oil bath for 30 min. The poling condition was an under electric field of 5000kV/m at 100°C in the case of the PT and under 3000kV/m at 80°C in PZT for 30 min. In order to generate the fourth harmonic thickness extensional vibration, the poling direction was opposite between the nearest layers. The plates were cut into the square plates with 4×4mm after removing the Ag paste on the edges. Configuration of these prepared oscillators with four-layered monolithic structure is shown in Figure 1.
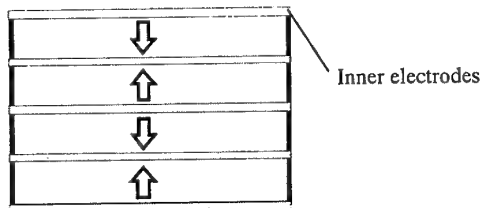
Figure 1 Configuration of four-layered monolithic piezoelectric plate. Arrows indicate the poling direction.

The characterizations of the vibration were evaluated from the impedance frequency characteristics of resonators around their resonance frequency. The impedance was measured in a frequency range between 100 Hz and 100MHz by HP 4194A impedance analyzer with an impedance probe.

3. Results and Discussion

Material constants of the PT and PZT measured in single layered plate with the same composition in this study are shown in Table I. The frequency constant of the PT is higher than that of the PZT. The resonance frequency of piezoelectric oscillators is determined from the frequency constant. Therefore, the PT with the higher value is expediency for the high frequency oscillator applications. Both specimens with the effective Poisson's smaller than 1/3 were not able to obtain the energy-trapping oscillators in the single plate of the thickness extensional mode. The Poisson's ratio of the PT is much small for its large piezoelectric anisotropy.

Table I
Material constants of the single plate.

	(Pb,La)TiO$_3$+Mn	Pb(Zr,Ti)O$_3$-Pb(Mn$_{1/3}$Nb$_{2/3}$)O$_3$
$\varepsilon_{33}/\varepsilon_0$	180	510
kt(%)	49.5	38.8
Frequency constant (Hz•m)	2320	1830
Effective Poisson's ratio	0.24	0.31

Table II shows the thickness of the obtained four-layered specimens after the sintering without lapping. The thickness of the layers was determined by the observation with SEM of the polished cross section. The whole and one layer thickness of the sintered PT specimens were thinner than that of the PZT.

Table II
The whole and one layer thickness of
the monolithic plates.

	(Pb,La)TiO$_3$+Mn	Pb(Zr,Ti)O$_3$-Pb(Mn$_{1/3}$Nb$_{2/3}$)O$_3$
The whole thickness (μm)	144	153
The mean thickness of one layer (μm)	36	38

Figure 2(a) and (b) show SEM photographs of the fracture surfaces. The mean grin size is about 1μm in the PT and a few μm in the PZT.
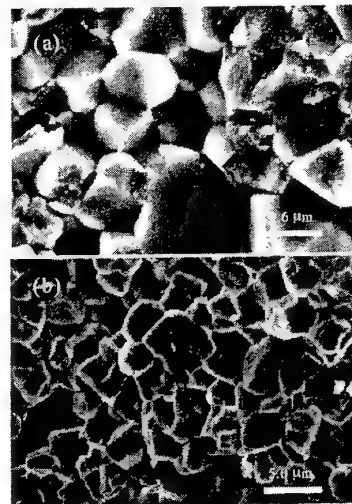
Figure 2 SEM photographs of the fracture surface in the
(a) (Pb,La)TiO$_3$+Mn and
(b) Pb(Zr,Ti)O$_3$-Pb(Mn$_{1/3}$Nb$_{2/3}$)O$_3$

The impedance characteristics of the four layered monolithic PT plates are shown in Figure 3 (a) and (b) in the different frequency range. A single mode resonance is observed around 60MHz in (a) and there is no spurious or ripples between resonance and antiresonance frequencies. The antiresonance frequency appears at 63.8MHz which corresponds to 4 times of what can be obtained with single plate resonator with same thickness as entire four layered type. These indicate obviously that the fourth harmonic thickness extensional vibration is generated in the resonator.
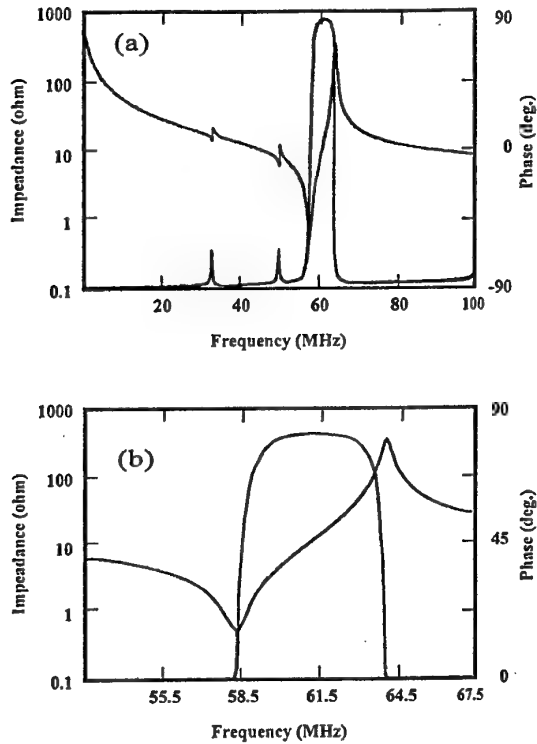
Figure 3 Impedance characteristic of the (Pb,La)TiO₃+Mn in the frequency of (a) 1MHz − 100MHz and (b) 52.5MHz -67.5MHz

Figure 4(a) and (b) show the impedance obtained from the PZT four layered plates. A resonance signal is observed around 55MHz which matches that expected from the frequency constant and the thickness of one layer. However, the impedance at resonance frequency seems to be high value compared to that of single plate and the PT.
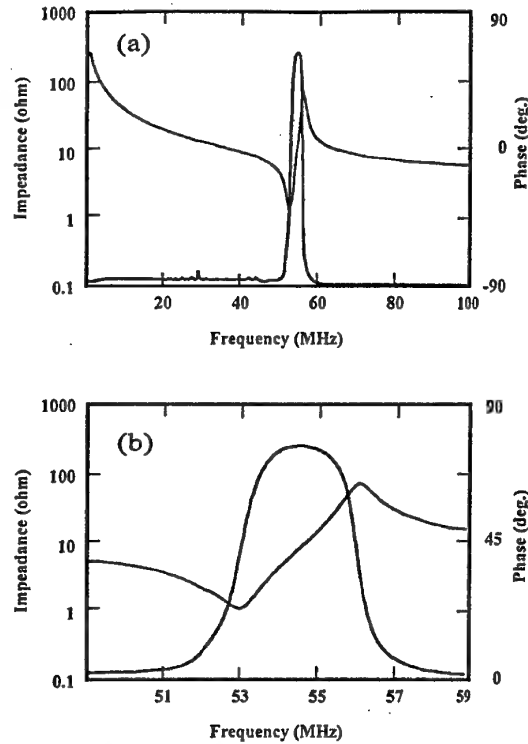
Figure 4 Impedance characteristic of the Pb(Zr,Ti)O$_3$-Pb(Mn$_{1/3}$Nb$_{2/3}$)O$_3$in the frequency of
(a) 1MHz – 100MHz and (b) 50MHz -59MHz.

The obtained piezoelectric properties of the layered plates are shown in Table III. The impedance ratio in the table is defined as 20log(Za/Zr), where Zr and Za is impedance at the resonance and antiresonance frequencies, respectively. This value has been used to evaluate the quality of oscillators.

Table III
Piezoelectric properties of four-layered plates.

	(Pb,La)TiO$_3$+Mn	Pb(Zr,Ti)O$_3$-Pb(Mn$_{1/3}$Nb$_{2/3}$)O$_3$
Resonance frequency (MHz)	57.93	52.98
Antiresonance frequency (MHz)	64.11	56.19
Effective electro-mechanical coupling factor (%)	49.0	37.6
Impedance ratio (dB)	60.7	37.7

The effective electromechanical coupling factor of four-layered plates in the PT and PZT is almost equal to kt of the single plates with same composition as shown in Table I. Additionally, the impedance characteristics in both specimens show a single resonance and this means that it enables us a high frequency piezoelectric resonator application with a simple structure and a thermally stable material such a PT or tetragonal PZT. The fourth-harmonic thickness extensional oscillators as the PT ceramics show a high impedance ratio and low-loss. On the contrary, an impedance ratio of the PZT has about 40dB that is much smaller than the value expected from single plates (60dB). The reason of increasing the loss in the layered PZT plates has not been clarified yet. However, it can be thought that the PT ceramics are very promising materials for the high frequency applications because of the low dielectric constant, large piezoelectric anisotropy and fine grain. Furthermore, differences in domain structure might lead to the difference in the high frequency resonant properties. They are under investigation.

The four-layered oscillator with the PT ceramics prepared in this study shows excellent performance as the high frequency device. Further, the realization of higher frequency oscillators is expected by using high order harmonic vibration and decreasing the thickness of one layer.

4. Conclusion

High frequency oscillators of four-layer PT and PZT ceramics have been studied. These showed a single resonance without spurious around 60MHz. In the case of PT, these have had a high electromechanical coupling factor and low-loss. It is thought that the oscillator can be used as the commercial high frequency resonators. Furthermore studies to realize higher frequency oscillators than that of this will be needed.

References

1) D. Berlincourt: J. Acoust. Soc. Am. **70** (1981) 1586.
2) L. E. Cross: *Ferroelectric Ceramics*, eds. N. Setter and E. L. Colla (Brinkhäser Verlag Basel 1993)
3) I. Ueda and S. Ikegami: Jpn. J. Appl. Phys. **7** (1968) 236.
4) I. Ueda: Jpn. J. Appl. Phys. **11** (1972) 450.
5) S. Takahashi and M. Takahashi: Jpn. J. Appl. Phys. **11** (1972) 31.
6) S. Takahashi: Ferroelectrics **41** (1982) 143.
7) K. Hase, M. Saitoh, T. Kittaka and K. Tomono: Jpn. J. Appl. Phys. **32** (1993) 4227.
8) A. Ando, T. Kittaka, T. Okada, Y. Sakabe and K. Wakino: Ferroelectrics **112** (1990) 141.

Composites and Medical Imaging Arrays for Frequencies Above 20 MHz

T. Ritter, K.K. Shung, R.L. Tutwiler, and T.R. Shrout

NIH Resource Center for Medical Ultrasonic Transducer Technology
Bioengineering Program, Penn State University
205 Hallowell Building
University Park, PA 16802
Fax: 814 863 0490, e-mail: tar145@psu.edu

Abstract – Methods for designing and fabricating high frequency 2-2 composites and arrays are presented. The composites were found to be suitable not only for arrays but also for small aperture, single element devices. Coupling coefficients of 0.60 and lateral mode frequencies above 70 MHz were achieved. Prototype 30 MHz linear arrays were designed and built using this composite. Backing and matching layers were fabricated and characterized while coaxial cable was used to impedance match the elements to a 50-ohm imaging system. The measured properties of passive and active components were used to analyze the design in both an equivalent circuit model and a time-domain finite element analysis program. Bandwidths of 70% and crosstalk levels less than -30dB were achieved.

1. INTRODUCTION

Ultrasonic imaging at frequencies from 20 to 100 MHz can provide high spatial resolution for dermatological, opthalmological, articular, and intravascular applications [1]. In addition, it has found use in the evaluation and manipulation of small animal models in biological research [2, 3]. Current high frequency imaging systems rely on single element transducer technology. For enhanced performance imaging arrays are desired [1]. In response to this need, the focus of this research is the design and fabrication of high frequency arrays.

Previous array achievements in this frequency range include a pair of 20 MHz PZT arrays [4][5], a 100 MHz array incorporating a sapphire lens and thin film ZnO [6], and a polymer array with built-in transmit and receive circuitry [7]. O'Donnel et al, in cooperation with Endosonics Corporation, describes the operation of a 20 MHz phased array imaging system for catheter use [8][9]. In addition, novel sol-gel composite PZT has been used in combination with laser dicing to produce array elements at frequencies above 50 MHz [10].

The focus of this paper is the design, fabrication, and testing of 30 MHz arrays incorporating 2-2 composite elements. The 2-2 composite is manufactured using a new technique and incorporates fine grain PZT-5H equivalent ceramic. Matching, backing, electrical impedance matching, and elevation focusing are used to provide optimum performance. Prototypes of the 30 MHz design have shown bandwidths of 71% and crosstalk levels of less than 30dB. A 48-element array is currently under construction and will be discussed in this paper. In addition to this device a 50 MHz array is also being developed.

2. DESIGN AND FABRICATION

The 30 MHz array incorporates 2-2 composite piezoelectric elements, a conductive backing, two matching layers, and a lens for elevation focusing. Table I lists the performance specifications for this array. Both one-dimensional models and finite element analysis were used to optimize the design. High impedance coax was used to provide both electrical impedance matching and interconnect to each element through a custom flex circuit.

Table I   Performance specifications for the 30 MHz array.

Center Frequency	30 MHz
Element Pitch	0.100 mm
Number of Elements	48
Elevation Aperture	1.5mm
Elevation Focus	7.5mm
Bandwidth	>50%
-20dB Pulse Length	<150 nsec
Crosstalk	<-30dB

Array elements with widths more than half the height suffer from degraded performance due to

coupling to the width resonance [11]. In order to avoid this dilemma a 2-2 composite can be utilized. The design of the composite involves choosing a polymer filler with the proper elastic properties and selecting the spatial scale of each constituent to avoid lamb waves within the passband of the device [12]. Traditional dice-and-fill technology cannot achieve the spatial scale required for operation above 20 MHz, so a novel fabrication technique was developed. Fine grain PZT-5H equivalent material (TRS 600, TRS Ceramics, State College, PA) was lapped to a thickness equal to the desired element width in the composite. For the 48-element array this was 25 microns. Plates of this material were stacked and bonded, with the plate-to-plate spacing controlled by incorporating polystyrene spheres into the bonding epoxy. Thin sections were then diced from the stack to form a 2-2 composite with the element width determined by the thickness of the individual plates. These composites were then lapped to a thickness of 0.100mm, electroded with 2000A° of Au over a thin Cr layer, and poled at 2000V/mm and 50°C.

The next step in the fabrication was the addition of an electrically conductive backing material with high acoustic attenuation and an impedance of 6.0 MRayls. A silver epoxy (E-3022, Von Rolla Isola, New Haven CT, USA) was centrifuged to achieve the desired properties. After adding the backing, a low dielectric ceramic was used to provide a rigid frame around the backed composite. Brass posts (50 microns square) were bonded into the frame to provide interconnect to the elements. The face was then lapped flat to achieve a composite thickness of 53 microns. Figure 1 shows the backed composite with the rigid ceramic frame and the brass posts.

Preliminary acoustic matching was selected using the Redwood equivalent circuit [13]. In order to investigate the impact of complex vibrations a time-domain finite element package was used (PZFLEX, Weidlinger Associates, Los Altos, CA, USA). Based on these studies a two-layer acoustic matching scheme was adopted and materials were developed and characterized to meet design specifications. The first matching layer was cast onto the surface of the array and lapped to the proper thickness (14 microns). This layer was electrically conductive and provided enhanced interconnect across each element of the array. A dicing saw was then used to cut a 16 micron kerf through the first matching layer and the composite, and into the backing to define the individual elements of the array. The kerfs were diced to different depths in order to reduce the impact of inter-element resonances through the backing [14]. The positions of the kerfs are shown (before dicing) as dashed lines in Figure 1.
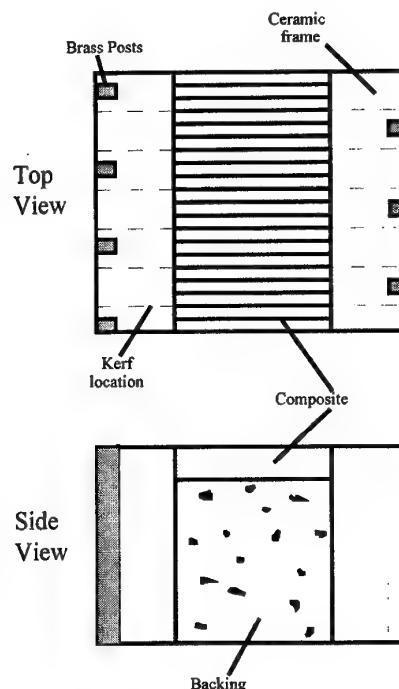
Figure 1 Top and side views of the array under construction.

The second matching layer was bonded to the array after the kerfs were diced, and this necessitated special care in selecting a kerf filler. Air was used for prototype devices with good results, but special high attenuation and low impedance materials are currently being researched for improved reliability. Once the second matching layer (20 microns thick) was in place, a 0.250mm TPX layer was bonded to the face. A precision milling process was used to machine a cylindrical concave surface of 2.38mm radius into the lens for elevation focusing. This surface was then lapped using a custom lapping fixture to provide a 1 micron finish and a 20 micron thickness at the lens center. Figure 2 shows a cut-away view of the device.

Electrical impedance matching was provided by high impedance micro-coax. Low capacitance 42 gauge coax from Precision Interconnect (Portland, OR, USA) was tested and found to have an electrical impedance of 85 -5j ohms. Transmission line equations were used to determine the optimum length of coax to impedance match the 200 ohm array elements to a 50 ohm imaging system.
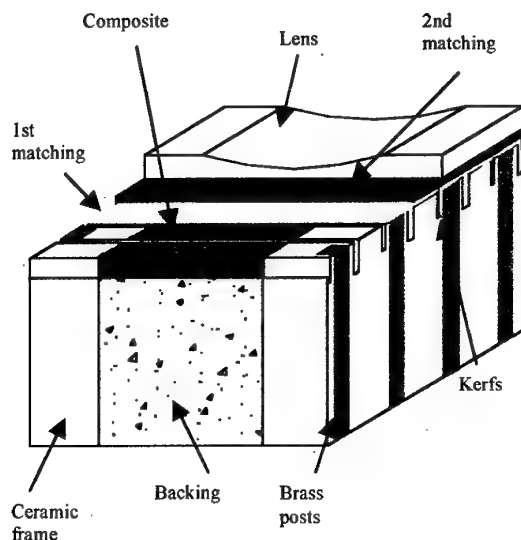
Figure 2   A cut-away view of the array.

recorded for adjacent elements and -32 dB for next nearest elements.

Table II   Representative 2-2 composite properties.

Volume Fraction	80%
Kerf width	6.5μm
Ceramic width	26.0μm
Dielectric constant, $\epsilon_{33}^S/\epsilon_o$	1100
Thickness velocity at F_p*	4000 m/s
1st lateral mode frequency	>70 MHz
Coupling coefficient k_t	0.60

*Fp is the parallel resonance frequency
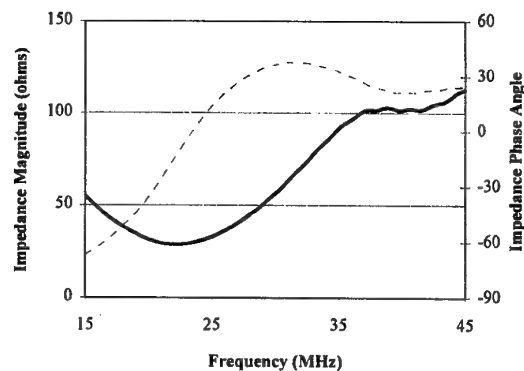
Figure 3   Electrical impedance magnitude (solid line) and phase angle (dashed line) for a typical array element.
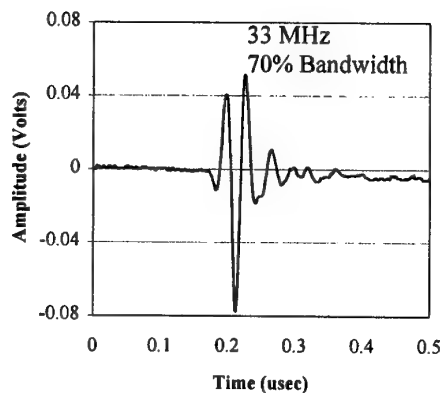
Figure 4   Pulse-echo impulse response for a typical array element.

The coaxial cables were soldered to the brass posts using an intermediate flex circuit and a low temperature solder process.   The finished array assembly was housed in a cylindrical case with a length of 88mm, a diameter of 15mm, and an integral RF shield.

3. RESULTS

Composite materials were designed and fabricated with a variety of polymer and ceramic dimensions. Resonance techniques were used to characterize the electromechanical properties. Typical test results are displayed in Table II.

Several four-element prototype arrays were constructed and tested.   Pulse-echo testing was performed using a polished flat plate target placed at the focal point of the elevation lens.   A Panametrics pulser, model 5900, on the 2 uJ energy setting was used to excite the device.   Electrical and acoustic crosstalk was characterized over the passband using tonebursts from a Wavetek model 81 function generator.   Electrical impedance was measured using an HP 4194 impedance analyzer.

Figure 3 shows the electrical impedance of a typical element, and Figure 4 shows the pulse-echo impulse response.   Both of these devices incorporated an air kerf.   Maximum crosstalk levels of -31dB were

4. DISCUSSSION AND CONCLUSIONS

Table II demonstrates that high electromechanical coupling and fine spatial scale can be achieved in a 2-2 composite structure. In addition, a highly uniform structure resulted, with the kerf and ceramic widths displaying standard deviations of 0.3 microns and 0.5 microns, respectively. The 1st lateral mode frequencies in excess of 70 MHz indicate that arrays and single element devices with center frequencies above 30 MHz can easily be constructed [15].

The present array design displays short impulse responses and acceptable levels of crosstalk. An improved interconnect method may reduce crosstalk even further and is currently being investigated. The broad bandwidth will not only increase axial resolution but will serve to ameliorate problems with grating lobes[16]. A 48-element array based on this design is under construction. Testing of this array will reveal information on acceptance angle, grating lobe amplitude, and element-to-element uniformity.

5. ACKNOWLEDGEMENTS

6. REFERENCES

[1] G.R. Lockwood, D.H. Turnbull, D.A. Christopher, and F.S. Foster, "Beyond 30 MHz," *IEEE Eng. in Med. and Biol*, vol. 15, pp. 60-71, 1996.

[2] C.J. Hartley, G.E.Taffet, L.H. Michael, T.T. Pham, and M.L. Entman, "Noninvasive determination of pulse-wave velocity in mice," *American Journal of Physiology*, 273(1 pt 2), pp. 494-500, 1997.

[3] D.H. Turnbull, "In utero ultrasound backscatter microscopy of early stage mouse embryos," *Computerized Medical Imaging and Graphics*, vol. 23, no. 1, pp. 25-31, 1999.

[4] M. Lethiecq, et al.., "Miniature High Frequency Array Transducers Based on New Fine Grain Ceramics," *1994 Ultrasonics Symposium*, 1994, pp.1009-1013.

[5] A. Nguyen-Dinh et al., "High Frequency Piezo-Composite Transducer Array Designed for Ultrasound Scanning Applications," *1996 IEEE Ultrasonics Symposium*, 1996, pp. 943-947.

[6] Y. Ito et al., "A 100 MHz Ultrasonic Transducer Array Using ZnO Thin Films," *IEEE Transactions on UFFC*, vol. 42, no. 2, pp. 316-324, March 1995.

[7] P. A. Payne. et al., "Integrated Ultrasound Tranducers," *1994 Ultrasonics Symposium*, 1994, pp.1523-1526.

[8] M. O'Donnel and L.J. Thomas, "Efficient Synthetic Aperture Imaging from a Circular Aperture with Possible Applications to Catheter Based Imaging," *IEEE Transactions on UFFC*, vol. 39, no. 3, pp. 366-380, May 1992.

[9] Endosonics Corporation Web Site (http://www.endosonics.com)

[10] M. Lukacs, M. Sayer, and F.S. Foster, "Single element and linear array transducer design for ultrasound biomicroscopy," *Proceedings of Medical Imaging 1998: Ultrasonic Transducer Engineering*, vol. 3341, pp. 272-282, 1998.

[11] C.S. DeSilets, *Transducer Arrays Suitable for Acoustic Imaging*. G. L. Report no. 2833, Edward L Ginzton Laboratory, Stanford, CA, 1978.

[12] C,G, Oakley, *Analysis and Development of Piezoelectric Composites for Medical Ultrasound Transducer Applications*, PhD thesis in Acoustics, Penn State University, December, 1991.

[13] A. Puttmer, P. Hauptmann, R. Lucklum, O. Krause, and B. Henning, "SPICE Model for Lossy Piezoceramic Transducers," ," *IEEE Trans. Ultrason., Ferroelect., and Freq. Control*, vol. 44, no. 1, pp. 60-66, 1997.

[14] J.F. Dias, "An experimental investigation of the cross coupling between elements of an acoustic imaging array transducer," *Ultrasonic Imaging*, vol. 4, pp.44-55, 1982.

[15] W.A. Smith, and B.A. Auld, "Modeling 1-3 composite piezoelectrics: thickness mode oscillations.,"*IEEE Trans. Ultrason., Ferroelect., and Freq. Control*, vol. 38, no. 1, pp. 40-47, 1991.

[16] A. Macovski, *Medical Imaging Systems*, N.J., Prentice Hall Inc., 1983.

Single Crystal Transducers for Medical Imaging Applications

R.K. Panda, J. Chen, H. Beck and T. R. Gururaja

Imaging Systems, Hewlett-Packard Company
3000 Minuteman Road, Andover, MA 01810

Abstract – Many researchers have focused on growing large relaxor single crystals, fabricating compositions with high electromechanical properties, and optimizing the crystal cuts for best properties. In this work PMN-PT and PZN-PT single crystals with different compositions were studied. One of the important characteristics studied was the composition variation from lot to lot and within different regions of a single crystal. The compositional inhomogeneity and its impact on electrical properties were correlated. The presence of inclusions and defects, and their effect on dicing capability of the crystals was also looked into. The temperature stability of polarization and electromechanical properties were studied to identify the impact on device applications. The single crystal acoustic parameters were determined for transducer modeling. The agreement between the measured and the theoretical prediction was excellent. When single crystals replace the traditional PZT ceramics in a transducer, a 20-25% bandwidth improvement can be obtained. The expanded frequency range allows the single crystal transducers to cover the frequencies of two traditional PZT-type transducers. An experimental phased array transducer has been built and used for imaging to demonstrate the performance of single crystal transducers.

1. INTRODUCTION

The development of relaxor-type single crystals including PZN-PT, PMN-PT, and PSN-PT materials has generated a lot of interest in the last few years. These single crystals exhibit very high coupling coefficients (k_{33} > 90%) and provide better sensitivity and bandwidth for medical imaging applications [1-3]. They offer the possibility of dramatic improvements in ultrasonic transducer performance.

It would be impossible to make transducers with consistent properties if the single crystal properties varied from lot to lot and sample to sample. Therefore, tests were conducted to study the chemical composition of single crystals from various lots. It is important to study the mechanical integrity of the single crystals to ensure high manufacturing yields. Also, the effect of any microcracking, chipping and breakage on the electrical properties needs to be studied. The ultrasound transducers would be used in the field under varying temperature conditions, hence, it is crucial to understand the stability of the electrical properties as a function of temperature. Finally, before building an ultrasonic transducer for medical imaging, it is important to develop a few models and study them to determine the advantages and disadvantages of the design and chosen components such as the piezoelectric material matching and backing layer, etc. The finite element models and the images obtained from a single crystal transducer fabricated are also described.

2. RESULTS AND DISCUSSION

2.1 Uniformity of Single Crystals:

The properties of PZT-5H ceramic, and PMN-32% PT and PZN-4.5% PT single crystal sliver (length >>> thickness > width) specimens are shown in Table I. It can be seen that the thickness coupling factor k_t' of single crystals is much larger than traditionally used PZT-5H type ceramics. Also, the single crystal samples (especially PZN-PT) have a lower longitudinal velocity and acoustic impedance compared to PZT-5H ceramic. This makes it easy for the acoustic impedance matching of the piezoelectric crystal to the body. However, the Curie temperature of the PMN-PT single crystals is only 155°C making it more prone to depoling under environmental cycling.

Table I: Properties of ceramic and single crystal materials.

Parameters	Ceramic (PZT-5H)	Single Crystal (PMN-PT)	Single Crystal (PZN-PT)
Acoustic Impedance 'Z' [sliver] (MRayl)	31	26	22
Longitudinal Velocity [sliver] (m/s)	3750	3200	2480
Coupling Factor [sliver] (k_t')	0.66	0.82	0.83
Curie Temp. (°C)	190	155	174

The values shown in Table I were taken from sliver specimens that showed good properties. However, one of the concerns working with single crystal materials is the property variation within a plate, between different plates from the same batch and between plates from different growth runs. In many instances single crystal plates received from different growth runs showed large composition variations. Also, in some of the plates obtained recently, wide variations were seen within the same plate. Slivers cut from different ends (10 mm apart) of the same plate showed completely different coupling constants. On a closer examination it was observed that the slivers that showed a high coupling k_t' (~0.82) had a very uniform elemental distribution across the length (Figure 1(a)). On the other hand as shown in figure 1(b), slivers with low coupling and spurious modes had a wide fluctuation in the chemical composition within a region as small as 3 mm. The chemical homogeneity and consistency of properties for single crystals have to be improved significantly to be able to put them in devices that are reliable for medical imaging applications.

(a)

(b)
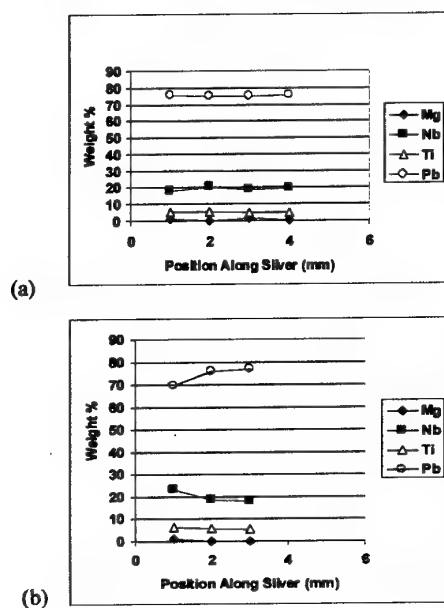
Figure 1: Distribution of elements along the length of PMN-PT single crystal slivers with (a) high k_t' and (b) low k_t'.

2.2 Processability of Single Crystals:

For achieving a high manufacturing yield of transducers the single crystals should resist damage during the dicing process. The crystals are diced into fine slivers when making phased arrays. Before building actual transducers it was necessary to conduct a few experiments to observe the effect of dicing speed and

crystal chipping, etc. on the electrical properties. The crystals were diced at different speeds to find the ease of diceability. It was observed that with the traditional dicing speeds used for PZT ceramic plates, the single crystal samples got heavily damaged. Because of the short supply of samples and to make sure that most of the sliver samples were available for electrical property measurement, the plates were diced using much lower speeds (five to six times slower). Also, care was taken to minimize blade vibrations during dicing to avoid any damage to the slivers.

Some of the crystal plates shattered into a large number of pieces even on dicing at low speeds. This was attributed to the presence of inhomogeneties in the sample including inclusions and microcracks. High quality single crystals with no defects were relatively easy to dice, producing sliver samples with minimal or no cracking and chipping. Figure 2(a) shows slivers of width 120 μm and 90 μm diced from a single crystal plate. For these crystals even higher speeds up to 50% of the value used for ceramic plates were also tried. Samples of the same width shown in Figure 2(a), survived without any problems. For crystals of moderately good quality there was heavy chipping damage observed at the edges at low dicing speeds. Figure 3(a) shows the effect of edge chipping in a sliver samples with widths of 170 μm. The problem became worse for slivers of lower widths.

(a)

(b)
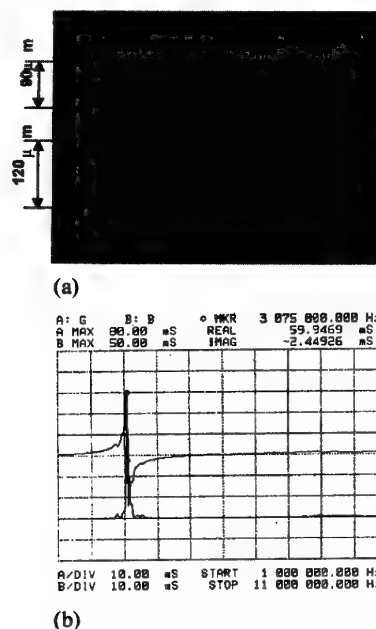
Figure 2: (a) Slivers of PMN-PT single crystal showing no chipping or edge damage, and (b) G-B resonance plot for one of the above slivers.

Apart from the mechanical integrity it is also important to understand the effect of chipping on the

electrical properties of the slivers. Hence, an experiment was performed taking three kinds of slivers – defect free, moderately chipped and heavily damaged slivers. On measuring the impedance plots of all these materials the biggest difference was observed in the nature of the G-B plots. For slivers that had no observable chipping defects (Figure 2(a)), the resonance peak was very clean and sharp as shown in figure 2(b). For slivers with heavy chipping damage, as shown in figure 3(a), the G-B resonance peak was very noisy with multiple peaks (Figure 3(b)). For moderately chipped slivers the number of spurious modes decreased, but overall the peak was still slightly noisy. Any spurious resonances in the passband could lead to notches in the spectrum. Hence, to avoid that the single crystal plate should have enough mechanical strength to avoid chipping.

(a)

(b)
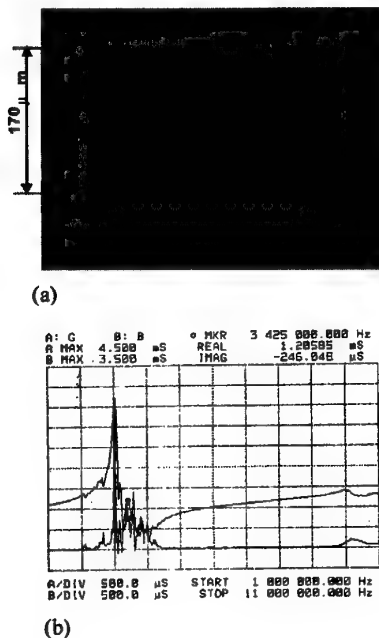
Figure 3: Sliver of PMN-PT single crystal showing extensive edge damage, and (b) G-B resonance plot for the above sliver.

The ultrasonic medical imaging transducers are transported and used in the field under a variety of temperature conditions. The Curie temperature of the PZN-PT and PMN-PT materials is lower than that of conventional PZT-5H type materials (Table I). Hence, theoretically they have a higher tendency of depoling at elevated temperatures, thus lowering their electrical properties. A set of experiments was designed to find the effect of elevated temperatures on the k_t' of slivers of single crystal material. In this experiment slivers of PZT-5H ceramic, PMN-PT and PZN-PT single crystals were kept in an environmental chamber at 80°C for 6 hours.

The coupling constants (k_t') were measured before and after putting the samples in the chamber. It was seen that the coupling of all the ceramic and single crystal materials did not change much (< 1% decrease) after exposure to the high temperature environment. Hence, it is expected that the single crystals will be able to withstand usage under rugged environmental conditions without depoling.

2.4 Design and building of an ultrasound transducer

One of the goals of this work is to test the feasibility of building phased array ultrasonic transducers using relaxor single crystals and to compare the image quality with that obtained from transducers with PZT-5H. Before actually fabricating the transducers it was important to choose a proper design and make models to predict and compare the performance boost obtained by inserting single crystals in transducers. As a step in that direction, finite element models were designed for phased array transducers with single crystal relaxors and PZT-5H ceramic as the active driving elements. The number and type of matching layers was varied to obtain the final design with the highest sensitivity and bandwidth.

The data shown in Table I was used as input for the software models. The property values shown are for sliver samples very similar in size compared to element size of the phased array design. From the table it can be seen that the PZN-PT single crystals have much lower acoustic impedance compared to the PMN-PT crystals. The difference in the acoustic impedance (Z) of the ceramic PZT and single crystal PMN-PT and PZN-PT materials made it necessary to look at many different matching layer materials for the transducer designs.

A phased array transducer with a center frequency of 5 MHz was chosen for comparing the properties of the single crystal to the ceramic PZT-5H. The matching layer, backing layer and lens materials and their thickness were optimized for the ceramic and single crystal transducers for maximizing the acoustic output.

Figure 4(a) shows the modeled spectrum for a PZT-5H transducer at a center frequency of 5 MHz. It can be seen that the transducer has a –6 dB bandwidth of ~66 %. Figure 4(b) shows the corresponding spectrum for an optimized PMN-PT single crystal transducer. It can be seen that the –6 dB bandwidth jumped from 66% to > 90% by substituting the PZT-5H with a single crystal. The spectrum sensitivity was also 3-5 dB higher than the PZT-5H transducer. This is a significant improvement over the ceramic transducer.

The PZN-PT single crystal transducer design also projected bandwidth and sensitivity very similar to the PMN-PT based transducer designs. However, because of the low velocity of sound in the PZN-PT material, the crystal thickness was lower than PMN-PT crystal for the same resonant frequency. This is advantageous as it leads to a higher capacitance of the elements, thus increasing the sensitivity.

A phased array transducer was built using a single crystal PMN-PT as the piezoelectric material. The

short axis and apical four chamber views of the human heart are shown in figure 5 and figure 6 respectively. These images obtained with the single crystal transducer show an excellent image quality.

(a)

(b)
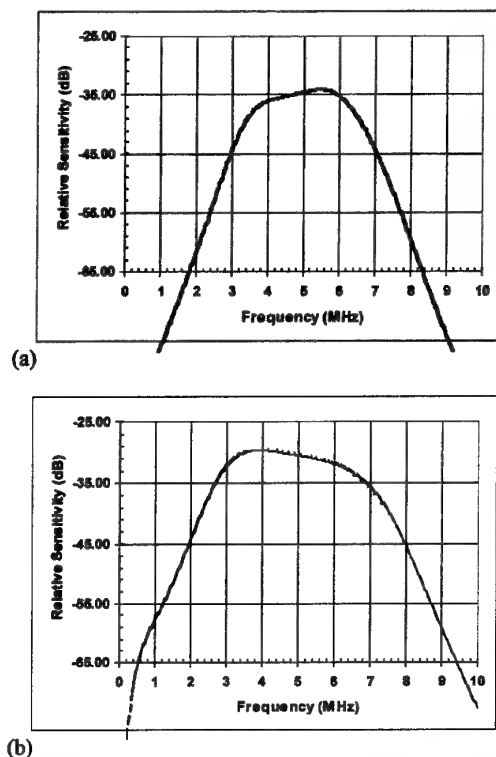
Figure 4: Modeled spectrum of ultrasonic transducers with (a) PZT-5H and (b) PMN-PT single crystal piezoelectric material.
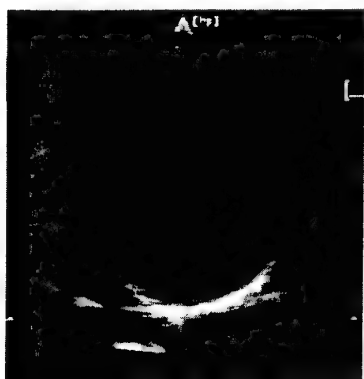
Figure 5: Image of an adult human heart showing the short axis view obtained using a PMN-PT single crystal phased array transducer.

Figure 6: Image of an adult human heart showing the apical four chamber view obtained using a PMN-PT single crystal phased array transducer.

3. CONCLUSIONS

The piezoelectric single crystals of PMN-PT and PZN-PT with high coupling constants show a great deal of promise for medical imaging applications. The elimination of lot to lot variation in the chemical composition and good mechanical integrity of the single crystals is necessary to obtain consistent electrical properties. The modeled spectrum for a single crystal transducer was shown to exhibit a bandwidth >90% and a sensitivity 3-5 dB higher than a comparable PZT-5H based transducer. Because of a higher bandwidth and sensitivity, high quality images of the heart were obtained using a single crystal based transducer.

4. ACKNOWLEDGMENTS

5. REFERENCES

1. J. Kuwata, K. Uchino, and S. Nomura, "Dielectric and Piezoelectric Properties of 0.91PZN-0.09PT Single Crystals," *Jap. J. Appl. Phys.*, **9**: 1298, 1982
2. S. E. Park, and T. R. Shrout, "Characteristics of Relaxor based Piezoelectric Single Crystals for Ultrasonic Transducers," *IEEE Trans. Ultrason, Ferro. Freq. Control*, **44**: 1140, 1997.
3. S. Saitoh, T. Takeuchi, T. Kobayashi, K. Harada, S. Shimanuki and Y. Yamashita, " A 3.7 MHz Phased Array Probe Using PZN-PT Single Crystal", *IEEE Trans. Ultrason, Ferro. Freq. Control*, **46**: 414, 1999

Piezoelectric ultrasonic motor using flextensional amplification of a disc radial mode with elastic fin drive.

P.J. Rayner, R.W. Whatmore*

*Dept. of Nanotechnology, School of Industrial and Manufacturing Science, Cranfield University, Beds, UK.
Fax:+44 1234 751346, email: r.w.whatmore@cranfield.ac.uk

Piezoelectric motors, which exploit the ultrasonic vibrations of a component, usually stationary, to force the motion of a rotor or slider, have been made in a wide variety of forms. Most current piezomotors have significant complexity in their construction, and many require multi-phase electrical drives to make them work. There has been little published to date on piezoelectric motors, which use the piezoelectric vibration of a simple radial mode of a thin flat disc, which (for many of the PZT family of piezoelectric ceramics) possesses excellent coupling efficiency. This paper will describe the use of such a vibration mode which, in association with flextensional amplifier and simple inclined elastic fin mode converters, can be used to make an excellent unidirectional motor which is both simple and low-cost in construction and its electrical drive requirements. The design, construction and operational characteristics of a prototype of such a motor will be discussed.

INTRODUCTION

In general, piezomotors have high fabrication cost, being due in part to the motors being made in small volumes at present. Nevertheless the precision and machine time required in fabricating stators with teeth and bonding the piezoceramic elements to the stator introduce considerable costs. However, the flextensional motor has been envisaged as a low cost design, possible to construct from pressed metal structures and not requiring tolerances less than approximately 0.1mm. Furthermore, the use of radial excitation of a piezoelectric disc, which has a high coupling factor, gives a high effective coupling factor of the vibrating transducer, especially when compared to travelling wave motors.

The flextensional motor, shown in Figure 1, incorporates two independent methods of mode conversion of vibrations that have been developed previously in piezoelectric actuator research; the flextensional [i] and the elastic fin driven rotor. These two stages of mode conversion convert radial vibrations of an electro-active ceramic into unidirectional rotating motion of a component. The first stage uses the radial vibrations of a piezoelectric ceramic disc, which are amplified by the two flextensional displacement amplifiers, and converted into vertical oscillations of the diaphragm top surfaces. Sonar transducers have been developed to utilise flextensional transducers to match the acoustic impedance of the transducer to that of water, predating the use of piezoelectric materials with electromagnetic and magnetostricitve excitation [ii,iii].

The vibrations of the flextensional diaphragm surface are then converted by oblique elastic fins into unidirectional rotary motion of a rotor, which is pressed in frictional contact with the diaphragms by a force imposed by a spring or magnetic attraction. The elastic fin ultrasonic motor arose in piezomotor development

before 1985 by Vishnevsky et al [iv] and Sashida [v]. Published elastic fin piezomotors include those of Uchiki et al [vi] and the Muralt et al micromotor [vii].

Figure 1: Prototype flextensional motor.
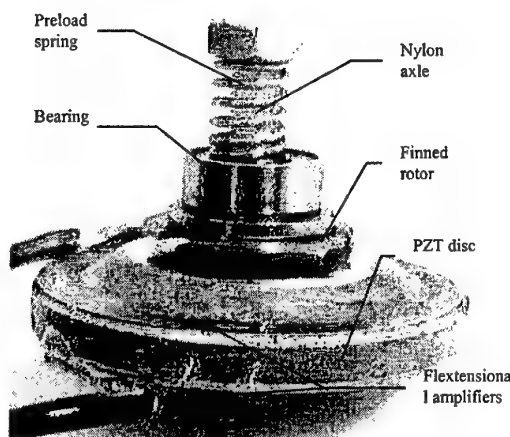
The rotor, pressed into frictional contact with one of the diaphragms, is propelled along 1 to 10μm per diaphragm oscillation by the mechanism shown schematically in Figure 2. The oblique elastic fins bend on the upstroke of the vibrator and, since slippage does not occur, the fin imparts a side thrust to the rotor. On the downward return stroke the fin tip does slip, allowing the fin to relax into its original position. The fin bends as a cantilever, although is shown for simplicity in Figure 2 as though bending at the fin root, where most of the bending rotation occurs.

This ratchet type movement can only drive the rotor in one direction, the speed of the movement depending largely on the fin's contact angle, θ, with the perpendicular of the vibrating surface. Previous elastic

fin motors [vi] have set θ as 15° and Eusemann et al [viii] proposed that the most efficient fin angle is defined by the static friction, μ, by:

$$\theta = \tan^{-1}\mu \tag{1}$$

The ratio of rotor velocity, v_r to vibration velocity, v_v, is strongly dependent on the contact angle, and to a first approximation is (from [vi]):

$$v_r = v_v/\tan\theta \tag{2}$$

This type of motion can also be generated by fins which are bent in an L or curved shaped, possibly giving lower wear at the interface.

Figure 2: Unidirectional driving mechanism of elastic fins
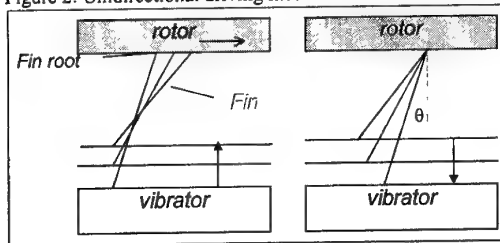
The flextensional design can be modified greatly to give larger displacement amplification or greater vibrational energy of the diaphragm. Furthermore, the diaphragms can be modified so that they contain the elastic fins, which will then act on a simple disc rotor.

MOTOR CONSTRUCTION

Figure 3: CAD drawing of cross-section of flextensional motor.
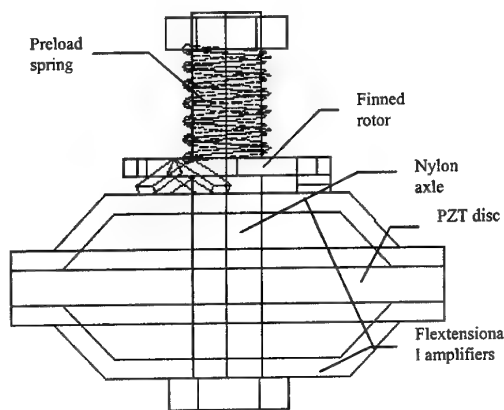
The prototype motor has been constructed in its present format such that the vibrating PZT disc and flextensional assembly is held stationary, thus defining the stator of the motor. Figure 1 and Figure 3, consists of a stator excited by a 25mm diameter, 2mm thick ring of PC8 (Morgan Matroc [ix]) low loss PZT, which were supplied poled through-thickness and electroded with 7μm of fused silver, then drilled centrally giving a 4mm hole. The flextensional displacement amplifiers were fabricated from 25mm OD, 4mm ID and 0.5mm thick

2% beryllium copper washers, which were pressed into the shapes seen in Figure 3 with a two-piece punch. These were attached to the electrodes on each side with silver loaded epoxy. The rotor was formed from a similar beryllium copper disc 12mm OD 4mm ID which had 3 L shaped tabs cut out which were bent out of the plane of the disc to form the elastic fins, at θ≈15°. A nylon bolt was passed through the stator and attached the lower diaphragm, to act as an axle. A bearing was attached to the finned rotor, and the rotor was slid over the axle with a preload spring, which is compressed via a nut on the nylon bolt.

This configuration is used to allow both diaphragms to contribute to the rotor/stator relative movement. Other twin rotor designs are also envisaged.

STATOR EVALUATION.

Figure 4: Admittance magnitude and phase variation of free flextensional stator with frequency.
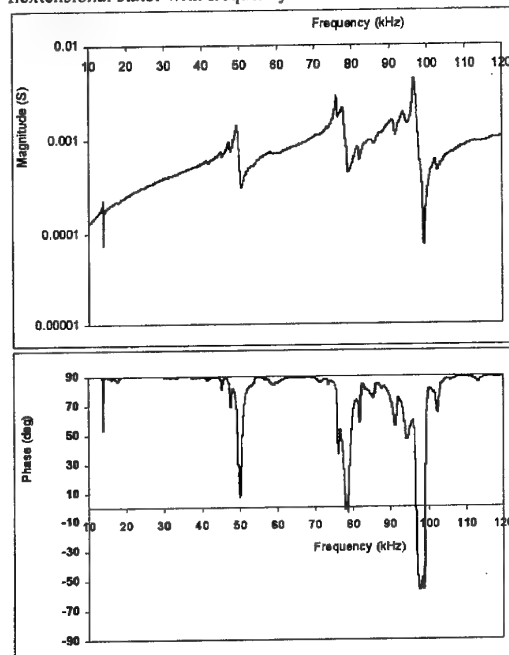
The stator admittance, with no rotor, was evaluated as a function of frequency across the resonance with an HP4192 impedance analyser, as shown in Figure 4. This was performed after the motoring tests described later

To visualise the modes of vibration of the flextensional vibrator a finite element analysis (FEA) using ATILA [x], was carried out with an axi-symmetric representation similar to that used by Tressler et al [xi], further simplified by using the plane of symmetry at the mid-thickness of the PZT disc. The model included materials and structural properties of the PZT, brass diaphragms and a 50μm epoxy layer. The fundamental, 2nd, 3rd and 4th modal shapes of the flextensional vibrator are shown in Figure 5.

Resonant frequency and coupling factors of the experimental admittance are compared with the FEA results in Table I. The experimental results agree very closely with the FE model. There are differences in the coupling of the 3rd and 4th modes, which may arise from minor differences between FE model and prototype. The 2nd and 3rd modes gave motoring with the current rotor configuration; the 2nd mode giving the best output, since the radial fin placement was correct for this mode. Both modes exhibited quality factor, Q_m, of approximately 240 at original construction, which decreased to 60 (Figure 4), after 30 minutes of use at varying duty and power levels. Furthermore, the large amount of displacement amplification can be seen in the FE models. The 4th mode has highest coupling factor and is substantially the PZT disc radial mode. The radial coupling factor of a 25mm disc of PC8 was also tested and found to be 45.8% at Fr=97.6kHz.

Table I: Comparison of FEA and experimental coupling and resonant frequency.

	Fund	2nd	3rd	4th
Exp. Fr (kHz)	13.9	50.2	78.7	96.6
Exp. Keff (%)	10.0	22.5	22.0	23.6
FEA Fr (kHz)	14.5	47.0	78.9	90.6
FEA Keff(%)	10.8	21.7	14.6	27.6

Figure 5: FEA Vibration modes of axi-symmetrical model of flextensional vibrator.

Mode	K_{eff}%	Fr (kHz)
Fund	10.8	14.5
2nd	21.7	47.0
3rd	14.6	78.9
4th	27.6	90.6
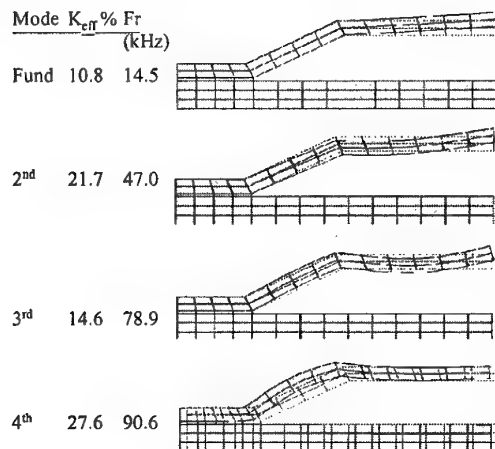
MOTOR PERFORMANCE.

Initial performance characteristics of the prototype were found for optimised preloads to $70V_{rms}$ and $95V_{rms}$ input voltages. The spring constant of the preload spring was found to be 1.6N/mm allowing conversion of spring compression into preload force. The three tests performed on the motor quantified the electrical input power and stall torque and no-load rotor speed. Stall torque, T_{st}, was measured by the angular displacement given as the motor acted against an angular spring. No-load speed, N_{nl}, was measured with a timed strobe lamp. Peak power output was estimated to occur at half the no-load speed and half the stall torque, i.e. $P_{out} = N_{nl}.T_{st}/4$.

The first test (10N preload) was performed with no lubrication, however, wear and surface damage of the fin tips and diaphragm surface was very rapid at these high drive levels, causing 70-80% degradation of performance within 1 to 2mins of operation. Polishing the diaphragm surface with 1200 and 4000grit SiC paper repaired this damage. However, it is believed that the vibrator performance had degraded after this test due to elevated temperature. A small amount of WD40 lubricating agent was added, which decreased torque output, but allowed for up to 10 minutes of operation by reducing the surface wear damage, and gave more stable operation without the fins becoming stuck on the wear damage.

Table II: Motor testing of flextensional prototype.

Preload	V_r ms	P_{in}, W	T_{st},mN m	N_{nl},rpm	P_{out},W	Eff,%
10N	70	3.2	2	1080	.06	1.7
7N	95	3	1.1	1050	.03	1.0
6N	70	2.7	1	450	.01	0.4

At these higher power levels shown the temperature rise of the flextensional amplifier stator and rotor was extremely rapid, due to the high input power and low efficiency for the motor's mass. After 2 minutes use the diaphragm and rotor temperature rose 30°C. High temperature operation above 70°C significantly reduced Q_m of the vibrator irreversibly, rendering the motor much more inefficient.

Lower power tests were also carried out to find the voltage level to give onset of rotor motion for a 2.5N preload. Surface roughness conditions proved to be far more important here, with wear damage often causing fin sticking. Starting with a 1200grit polished surface, at voltages less than $25V_{rms}$ no rotation was observed. As the voltage increased the rotation speed increased in an approximately linear manner with voltage until at $55V_{rms}$ the speed saturated at 300rpm. Any further increase of drive voltage gave more contact noise and wear particle emission. This behaviour closely matches that found in [vi]. These low power tests gave far less heating, however surface damage from wear continued to occur.

DISCUSSION

Motor Performance

The performance of this prototype motor is currently low due to low efficiency. Peak efficiency was estimate to be 1.7% in the first tests of the motor, decreasing by a factor of 3 to 4 for the same drive input during tests. The probable sources of energy loss are thought to occur from slip of the fin tips at the contact interface and losses in the bonding layer between the PZT and diaphragms and internal losses in the PZT and beryllium copper.

Reduction of the fin tip losses can be achieved by appropriate matching of the compliance of the elastic fins and flextensional vibrator. For the elastic fins the fin length and thickness will change the compliance, whilst not apparently affecting the rotor speed. This

motor, in particular, also allows the adjustment of the vibrator geometry and materials to assist in compliance matching. Additionally, the use of a complaint friction layer, curved or L shaped fins and increasing the number of fins to reduce contact pressure may give benefits. In a motor of this small size, bearing friction and damping losses in the nylon bolt will also be significant. Such optimisations will be greatly assisted by FE modelling.

Degradation Issues

The motor exhibited rapid heating and wear, both causing degradations to the performance with time. These factors also make it difficult to characterise the motor performance due to its changing behaviour.

A corollary of the slip at the friction interface is wear damage to the surfaces of the diaphragm and fin tips, which reduced the performance over time due to the surface roughness becoming comparable to the amplitude of vibrations. The process is especially rapid with the similar materials used at the contact interface, which cause welding microscopically, but can be overcome by using a dissimilar material combination, e.g. a ceramic (alumina) and metal (steel) [viii], or the use of a polishing friction layer such as SiC paper.

The effects of stator heating are more serious, since they irreversibly reduce the Q_m of the vibrator and thus motor performance. The sources of the heat generation were considered to be the sources of power loss described previously. A large temperature increase of the rotor was evidence that heat was generated at the fin tips, since the thermal path for transfer of heat from the stator is very small. Measures taken to increase motor performance will also reduce this heat generation. The main mechanism for this thermal degradation is alteration of the vibrator bonding-layer, since the temperatures encountered are greatly below those required to depole the PZT ceramic.

CONCLUSIONS

We have presented a new type of ultrasonic motor, developed from a combination of technologies from different fields of piezoelectric actuators. The use of flextensional amplifiers and a radial piezoelectric mode give very high coupling efficiency and the elastic fin rotor drive gives simplicity and cheap manufacture. The motor has high performance for its mass and high speed, whilst having a construction that is tolerant of imprecise manufacture, can be constructed very cheaply from pressed metal discs and has a single-phase drive. These factors also encourage the miniaturisation of this design and the alteration of its design to fit high volume applications for small motors, where it could compete effectively with electro-magnetic motors in cost.

Efficiency of the prototype motor is currently low, but should benefit greatly from a reduction in wear, achievable by careful choice of interface materials and optimising the rotor and stator compliance relatively. This will also reduce the wear and the dramatic increase in temperature of the motor during high power driving.

REFERENCES

i G. A. Bingham & B. Glass. J. Acoust. Soc. Am., 68, 4, pp.1046-52, 1980.

ii W. J. Toulis. US Patent 3,277,433, 1966.

iii S. W. Meeks & R. W. Timme. J. Acoust. Soc. Am., 49, pp.1609-20, 1971.

iv V. Vishnevsky et al. US Patent 4,453,103, 1984.

v T. Sashida. US Patent 4,548,090, 1985.

vi T. Uchiki, T. Nakazawa, K. Nakamura, M. Kurosawa, S. Ueha. Jpn. J. Appl. Phys., Vol 30, No. 9b, pp.2289-2291, 1991.

vii P. Muralt, M. Kohli, T. Maeder, A. Kholkon, K.G. Brooks, N.Setter & R. Luthier. Sens. Actuators A, Vol.48, pp.157-165, 1995.

viii Eusemann et al. US Patent 4,884,002, 1989.

ix Morgan Matroc Unilator, Ruabon, Wrexham, North Wales, UK.

x ATILAv5,Cedrat, 10, Chemin de Pré Carré - ZIRST 38246 Meylan, FRANCE.

xi J. Tressler, W. Cao, K. Uchino, R. Newham. IEEE Trans. on Ultrason., Ferroelec. and Freq. Contr., Vol 45, No. 5, 1998.

Travelling Wave Ultrasonic Motor using the B_{08} Flexural Mode of a Circular Membrane

P.J. Rayner, R.W. Whatmore*

*Dept. of Nanotechnology, School of Industrial and Manufacturing Science, Cranfield University, Beds, UK.

Fax:+44 1234 751346, email: r.w.whatmore@cranfield.ac.uk

Ultrasonic motors are increasing in use for positioning applications and in microengineering. They have a high stall torque and slow speed rotation and hence there is no need for a gearbox. They also can have low inertia and high torque density with a large holding torque with power off. This paper describes the design, construction and performance of a piezoelectric motor that uses a travelling B_{08} mode of a circular membrane to drive a rotor by frictional contact. Investigations of the free stator with a vibration pattern imager and impedance analyser gave the resonant frequency, mode and electromechanical coupling of the stator. Motor speed as a function of frequency for a constant voltage and performance charts of speed, output power and efficiency against torque are presented for a particular input voltage and rotor preload. The motor has been designed for miniaturisation to a silicon micromotor of 2mm in diameter, constructed using lithographic techniques. The performance predictions for this micromotor are discussed.

INTRODUCTION

Travelling wave ultrasonic motors (TWUM) were first developed by Sashida in 1982 [i] and have been developed commercially by companies including Shinsei (Japan), Canon (Japan) and Physik Instrumente(PI, Germany). TWUM designs have a large frictional rotor to stator interface with continuous contact, and thus have low contact pressure and wear. This paper describes and evaluates a motor that uses a travelling B_{08} resonant mode excited in a circular membrane of 80mm diameter by piezoelectric elements. This membrane motor possesses a planar construction, suitable for building with lithography techniques into a 2mm diameter piezoelectric micromotor.

Figure 1: B_{08} membrane motor stator and rotor without preloading assembly.
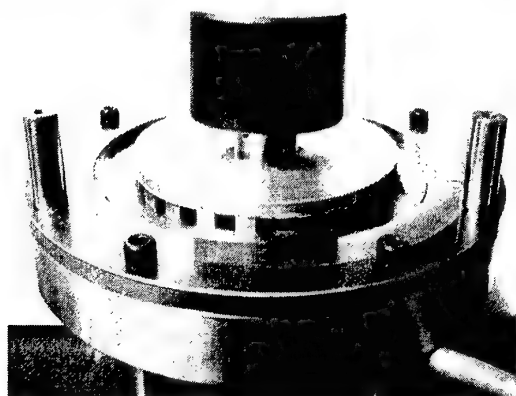
TWUMs generate two resonant standing waves of the same mode, shifted in space by ¼ of a wavelength and $\pi/2$ in electrical time, which superpose to generate a travelling wave. The standing waves are excited by piezoelectric elements, poled perpendicularly to the stator bonding surface, which pull the stator into bending when driven by an ac signal at the mode's resonant frequency. The travelling wave causes points on the surface of the membrane to follow an elliptical trajectory, which is amplified horizontally by teeth acting as levers. The rotor is pressed into frictional contact with the tops of these teeth and is propelled along 1 to 5µm per wave passing. The excitation is above 20kHz for silent operation, allowing rotor to stator interface speeds of 0.1 to 0.5m/s.

Figure 2: Showing the B_{08} mode of the membrane obtained by FEA.
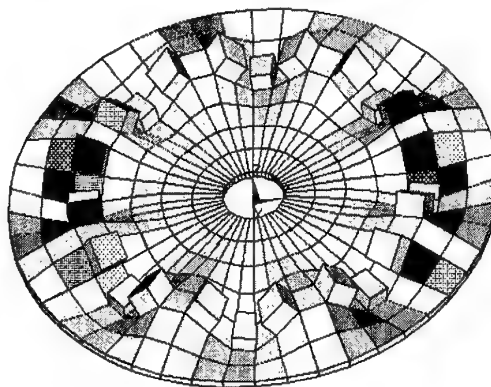
CONSTRUCTION OF THE MOTOR

The motor, as shown in Figure 1, consists of a stator membrane with 80mm outside diameter, 10mm inside diameter and 1mm thickness made from 520Type (S143D) martensitic stainless steel: Young's Modulus=2.06GPa, Poisson's ratio=0.29, Density=7830kgm^{-3}. Protruding from this membrane are teeth 2.5mm high, arranged in a circular pattern at the locus of maximum vibration. Bonded to the other side of the membrane is a 0.5mm thick ring of PC8 (Morgan Matroc [ii]) low loss PZT, which is segmented into a four phase drive; the segments being driven in a repeating pattern: sin, cos, -sin, -cos, thus requiring 32 segments for the 8 wavelengths. The membrane equates to a disc clamped at the circumference. Teeth were placed at the radius of maximum vibration, found using finite element analysis (ATILA), shown in Figure 2, also estimating the resonant frequency and electromechanical coupling, k_{eff}. The rotor consists of an aluminium disc, with a thin friction layer bonded to the face. For best performance the compliance of the rotor system and friction layer has to be optimised [iii,iv].

STATOR EVALUATION.

Figure 3: Admittance magnitude and phase variation with frequency.
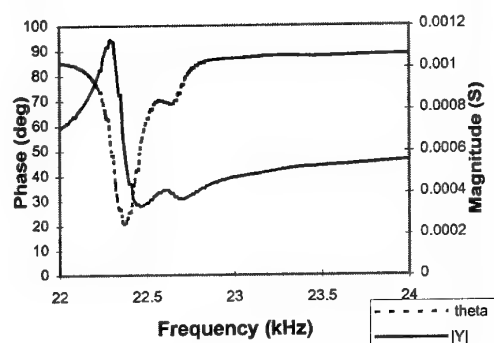
The stator admittance, as a function of frequency, as evaluated across the resonance with an HP4192 impedance analyser is shown in Figure 3. Resonant frequency and coupling factors were calculated and are compared with the FEA results in Table I. The differences between the FEA model and experimental results, of the order of 20%, require further investigation. The quality factor, Q_m, of the free stator was found to be a little low at 65, showing significant damping of the vibration and contrasting with the high effective coupling of 17.1%. The low quality factor has some advantages in allowing a simple open-loop electronic drive system.

Table I: Comparison of FEA and experimental coupling and resonant frequency.

	Res. Freq. (kHz)	Coupling K_{eff} %
FEA ATILA)	28.1	17.2
Experimental	22.4	22.1

A vibration pattern imager, Ometron VPI 8000, was used to observe the mode of vibration of the stator. This scans the object surface with a He-Ne laser, measuring the Doppler shift of the reflected light at each point, filtered to the drive frequency, to give the velocity of the out of plane vibration. Figure 4 clearly shows the B08 mode generated by the +/-sin phase, the white circle signifying the membrane circumference. White and black areas are receding and approaching, respectively. Vibration peak velocity was found to be 40mm/s equating to 0.28μm peak displacement at 10Vrms.

Figure 4: Doppler scan of stator at 22.4kHz, 10Vrms per phase.
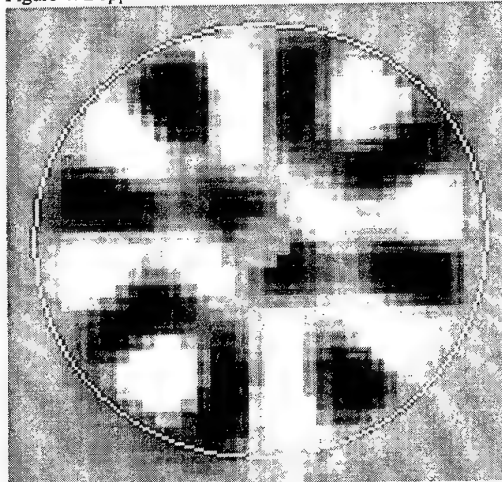
MOTOR PERFORMANCE.

Firstly, the motor was investigated for variation of zero load speed over a frequency range for several voltage and rotor preload settings. An example of such is shown in Figure 5. The rotor preload affects the drive behaviour at the rotor/stator friction interface and must be optimised for a given input voltage to give best motor performance in efficiency and power output.

Figure 5: Variation of rotor speed, N, and input power, P_{in}, with frequency for zero load at 40Vrms /phase, 20N preload.
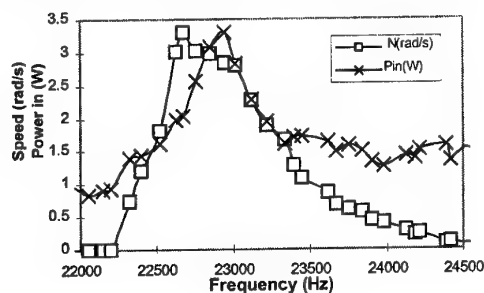
Performance characteristics under a torque load were then found for an optimised preload to an 80Vrms voltage per phase input voltage. The maximum torque

and efficiency, shown in Figure 6, were 0.33Nm and 4.9% respectively.

Figure 6: Motor performance at 23.1kHz, 80Vrms per phase drive, 70N preload.
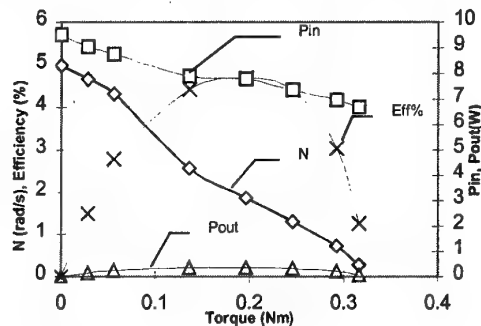
DISCUSSION

Performance Issues

Although this prototype motor has large overall dimensions, when including the preload assembly, the total rotor and stator dimensions are 5mm thick with 80mm diameter, giving high torque density. This is calculated below as the maximum torque per volume ratio, D_v, or maximum torque per mass ratio, D_m, and compared to a commercially available Shinsei USR45 travelling wave motor. The figures for D_v are comparable but the D_m for the prototype motor is less due to the mass of the large clamping ring. By improving the motor efficiency and design mass both factors can be improved.

Table II: Comparison of Torque density.

	Shinsei USR45 (man. data)	Membrane motor
D_v=Torque/Vol. (N/m^3)	est.1.4x10^4	1.3x10^4
D_m=Torque/Mass (Nm/kg)	4.0	1.6

Moreover, the predominant sources of power loss causing the relatively low efficiency of this motor are now discussed.

The motor showed significant vibration of the interior of the membrane in Figure 4 and also of the mounting frame of approximately 18% of the B_{08} peak displacement. The vibration of the frame is especially significant since it has a large cross-section and thus vibrational energy, which does not contribute to rotor motion. The membrane structure has high radial stresses in vibration due to the clamping constraints at the edges, thus it is believed that use of low internal damping material, such as beryllium copper, would further benefit the resonance quality, Q_m, of the stator, and thus the motor performance.

The effect on motor performance with teeth height is modelled by Hagood and McFarland [v], and predicts that there is an optimum length of teeth height for maximum efficiency for a given preload on a piezomotor. A teeth height less than this value will have

tangential vibration energy much less than the normal vibration energy, thus the total energy input is not efficiently driving the rotor. Increasing to the optimum teeth height gives higher rotor speeds and the tangential and normal vibration energies become comparable. After this point rotor speed continues to increase, but efficiency does not increase further, and will eventually decline, as the stall torque declines

Piezoelectric micromotor predictions

The membrane design was developed primarily to evaluate the performance and design issues in the development of a B_{02} membrane micromotor of 1 to 2mm in design. A CAD drawing of the stator, with a 1.3mm diameter rotor disc, is shown in Figure 7.

Figure 7: CAD drawing of 2mm piezoelectric micromotor.
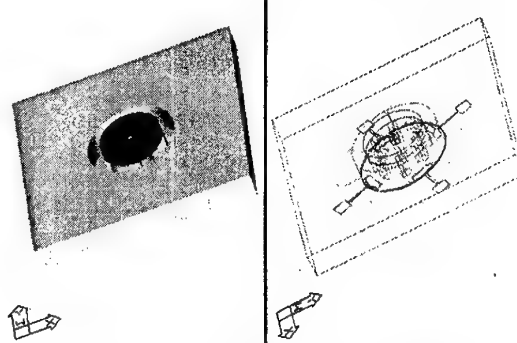
With the use of a simple scaling exercise, as in Table III, the output performance of the micromotor can be estimated from the 80mm diameter motor. When performing a scaled reduction in size by a ratio s, where s= original length/new length, then motor torque decreases by a ratio s^3 and rotor speed by s^{-1}.

Table III: Predictions of micromotor performance via scaling.

Dimension	B_{08} 80mm	B_{08} 2mm	S
Membrane thickness	1mm	25µm	1
Preload	70N	44mN	2
Speed	50rpm	2000rpm	-1
Torque	0.33Nm	7.5µNm	3
Frequency	23kHz	1000kHz	-1

There are numerous factors that this simple analysis does not include. Primarily, there is a predicted large decrease in rotor speed from the use of the B_{02} mode since the resonant frequency is lower, although this may be counteracted by an increase in amplitude due to lower vibrational stresses and the planned use of longer teeth. Other elements which may decrease performance are the use of thick PZT sol-gel films (with lower piezoelectric coefficients) and full clamping at the membrane edge. Factors which may increase performance are the low internal damping of Silicon and the possibility of using much larger electric fields which can be sustained without electrical breakdown in the micro-size domain.

CONCLUSIONS

We have described and evaluated a travelling wave ultrasonic motor based on 4 phase piezoelectric excitation of a flexural mode of a membrane. The design is a thin planar design suitable for miniaturisation and has a high electromechanical coupling factor in comparison with other TWUMs, with a substantial torque output for its volume, which is compared with a Shinsei USR45 TWUM. Sources of power loss have also been discussed and scaling predictions of performance for a micromotor have been presented.

ACKNOWLEDGEMENTS

REFERENCES

I T. Sashida. US Patent 4,562,374, US, 1983.

ii Morgan Matroc Unilator, Ruabon, Wrexham, North Wales, UK.

iii Y. Kawai, K. Asai, S. Nato, T. Fukui, Y. Adachi, N. Handa, K. Ikeda, K. Tsuda. Jpn. J. Appl. Phys, Vol 34, pp.2711-2714, 1995.

iv P. Minotti, P. Cusin, P. LeMoal A. Ferreira. Jpn. J. Appl. Phys. Vol. 36, pp.7009-7018, 1997.

v N. Hagood, A. McFarland. IEEE Trans. on Ultrason., Ferroelec., and Freq. Contr., Vol 42, No 2, pp.210-223, 1995.

Piezoelectric Actuators and Dampers Using Interdigital Electrodes

Shoko Yoshikawa, Michael Farrell, David Warkentin, Robert Jacques, Erik Saarmaa

Active Control eXperts, Inc. (ACX), 215 First Street, Cambridge, MA 02142

Fax: 81-617-577-0656, e-mail: shoko@acx.com

A quantitative performance assessment of interdigital electrode (IDE) actuators and dampers constructed using ACX QuickPack® packaging technology is provided in this paper. IDE device concept, device design, experimental plan and results, and subsequent analysis are presented. Electromechanical coupling coefficients calculated using two different methods demonstrate values of 0.45 to 0.71 were obtained for IDE devices, as compared to 0.29 to 0.35 for conventional d_{31} devices. Resistively shunted IDE damper devices achieved greater than a factor of two in improvement in added damping over conventional PZT damper devices. In addition, the high field generative strain of IDE actuators was shown to be 70% greater than that produced by d_{31} actuators.

1. INTRODUCTION

Fine line interdigital electrodes (IDE) have been used extensively in the fabrication of electronics devices such as electronic filters, oscillators, and sensors since the late 1960's.[1] These devices function using the principles of surface acoustic wave (SAW) propagation through solids and are sometimes referred to as interdigital transducers (IDT). A majority of the IDT's presently in use are operated using low electric field, high frequency propagation waves instead of high field, low frequency waves. The latter conditions are necessary for actuation and damping applications. The principles behind IDE permit the device to make use of the more efficient "33" properties for in-plane actuation or damping instead of the more commonly used "31" properties. This is accomplished by arranging the electrodes so that the poling and excitation fields run largely parallel to the plane of actuation. The electromechanical properties in the 33 direction are generally more than twice the properties in the 31 direction. The line IDE concept for the actuator applications appeared in a Japanese patent in 1991[2] followed by additional work performed at Tokin Corporation.[3] In both cases, the line IDE concept also makes use of co-fired multilayer processes for device fabrication.

Line IDE devices have been successful for some low field applications. However, when large fields are applied during poling or excitation, internal cracks or electrical shorts sometimes result. These failures are due to internal stresses caused by the non-uniform electrical field in the material near the ends of the electrodes. It is also apparent that the bus line connecting the interdigital lines creates additional stress concentrations.

Line IDE patterns have also been used in the construction of piezoelectric fiber composite devices[4] where stress concentrations are reduced. Piezoelectric fibers may have some advantages over unpackaged monolithic ceramic plates, such as their ability to conform to highly curved surfaces and their ability to resist crack propagation. However, the total piezoceramic volume is limited to a maximum of 78.5% solid volume due to packing density of the fibers. In addition, the device cost is still relatively high and prohibitive for commercial use.

To overcome these limitations, a interdigital electrode monolithic thin plate piezoelectric device (QP10Ni) was developed at ACX utilizing QuickPack packaging technology. This paper describes the QP10Ni construction, experimental procedures, test results, and analyses of the devices used as dampers and strain actuators. The results are compared to an ACX product QP10N device that uses a conventional d_{31} piezoceramic plate with solid electrodes on both surfaces of the plate. These conventional devices have been used extensively as actuators and dampers in various commercial products.[5] Electrical and mechanical energy calculations and experimental results of resonance measurements were used to quantify and compare the electromechanical coupling coefficients and damping capabilities of these devices.

2. EXPERIMENTAL SETUP

2.1 QuickPack Device Configurations

Figure 1 shows the electrode pattern and electric field lines for the piezoceramic material in both the QP10Ni and QP10N devices, as well as photographs of the completed devices themselves. Both types of devices were fabricated using a PZT-5A type material with dimensions 46.05 mm x 20.65 mm x 0.254mm. Research has been performed elsewhere to determine optimum values for the dimensions of the piezoceramic thickness and electrodes of an IDE device.[6,7] The ratios of these parameters are important, but the determination of optimum values depends on application-specific requirements including displacement, generative strain, force, and available drive voltage. For this work a representative design was selected in which the

QP10Ni electrode pattern consisted of 0.38 mm line widths on a 1.52 mm pitch. The piezoceramic material and electrodes were packaged in a protective polymer skin with pre-attached electrical leads.
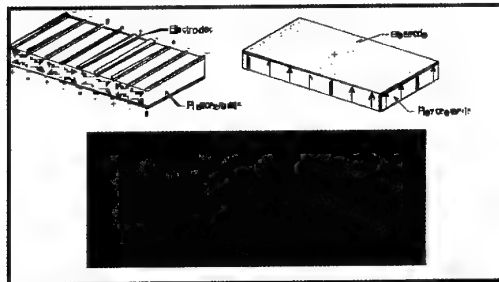
Figure 1. Top - IDE pattern (left) and conventional electrode pattern (right). Bottom - QP10Ni device (left) and QP10N device (right).

2.2 Vibration Damper Experiment

Damping experiments were constructed using the QP10Ni and QP10N devices bonded to aluminum beams with optimum resistive shunt circuit based on the piezopasssive damping research described in references [8,9]. The beams were 229.0 mm x 31.8 mm x 2.3 mm with a clamped free length of 133.0 mm. The devices were bonded to one surface of the aluminum beam 6.35 mm away from the clamp edge. The tip motion due to an initial displacement was measured with a laser displacement sensor. Damping was computed from the ring down of tip displacement using the logarithmic decrement method. Damping measurements were taken for the following configurations: bare beam, beams with resistively shunted QP10Ni and QP10N devices, and beams with un-shunted QP10Ni and QP10N devices

2.3 Field Induced Strain Measurement

The free strain of the devices was measured at room temperature by averaging the signals from strain gages applied to both surfaces of the devices. The applied drive signal was a 1 Hz sine wave; the maximum voltage was +/- 600 Volts (1200 Vp-p) for the QP10Ni device and +/- 100 Volts (200 Vp-p) for the QP10N device.

2.4 Electromechanical Coupling Factor

The electromechanical coupling coefficient is one of the single best properties for quantifying the performance of a piezoelectric device. It is a non-dimensional parameter calculated from the electrical and mechanical energy of the system. It can be found from

$$k^2 = \frac{W_M}{W_E} = \frac{\frac{1}{2}(modulus)(volume)(strain)^2}{\frac{1}{2}(capacitance)(voltage)^2} \tag{1}$$

where the mechanical energy output of a device is represented by W_M and the electrical energy input to the system is represented by W_E. Alternatively, electromechanical coupling coefficient can be computed from the antiresonance and resonance frequencies measured with and impedance analyzer.[10] However, the resonance method is only strictly accurate if the samples are bar shaped and satisfy the condition: $(length/width)^2 > 10$, in addition to the no mechanical loading condition. Since QuickPack devices are piezoceramic packaged with conductor and insulator, the results can only be used for comparing devices of similar shape and type.

3. RESULTS AND DISCUSSION

3.1 Vibration Damper Results

Figure 2 illustrates the percentage of critical damping measured in the response of the beams as a function of the average strain on the surface of the devices bonded to the aluminum beams. A fairly large scatter in the data is observed due to the difficulty associated with consistently exciting the beams at their first resonant mode. A large number of data points were taken to provide a better indication of the damper performance and least squares straight line fits were computed to illustrate the nominal performance of the dampers on the beams. The shunted QP10Ni damper is shown to provide more than twice the added damping achieved by the shunted QP10N damper when compared to either unshunted device bonded to a beam.
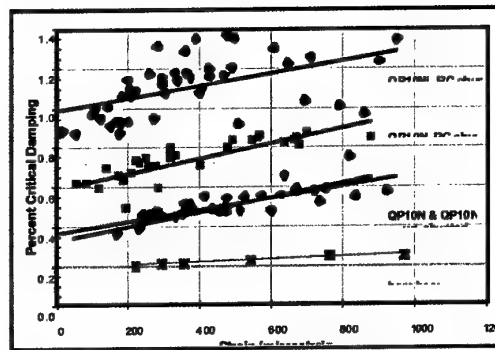
Figure 2. Percentage of critical damping as a function of average strain on the surface of the damper.

3.2. Free Strain Actuation Results

The results of the free field induced strain measurements are shown in Figure 3. The applied electric field was calculated based on the 0.25 mm spacing between the electrode planes for the QP10N device, and the 1.52 mm between the electrode lines for the QP10Ni device. Because the field in the QP10Ni device is non-uniform, the value calculated in this way should be considered an average or nominal value. The induced strain of QP10Ni device is approximately 70% higher than that of the QP10N device at the same field strength.
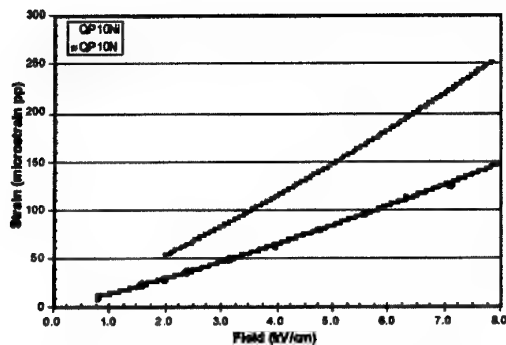
Figure 3. Free strain of QP10Ni and QP10N as a function of excitation and field

3.4 Electromechanical Coupling Factor

Table I contains calculated values for the effective electromechanical coupling coefficients, k_{eff}, determined using both methods described in section 2.4. The estimate based on equation 1 yields a coupling coefficient of 0.71 for the QP10Ni device and 0.32 for the QP10N device at an applied field of 8kV/cm. The estimate based on resonance method indicates that the coupling coefficient of the QP10Ni device is approximately 65% higher than that of the QP10N device.

Table I: Calculated k_{eff} using energy method and resonance method.

	QP10N	QP10Ni
Energy Method		
4 kV/cm	0.29	0.65
8 kV/cm	0.32	0.71
Resonance Method		
Low field	0.29	0.49

4. SUMMARY

Thin plate interdigital electrode (IDE) devices have been successfully prepared using QuickPack packaging technology. The experimental results of piezopassive damping showed resistively shunted IDE damper devices achieved greater than a factor of two in improvement in added damping over conventional PZT dampers. Furthermore, the high field generative strain of IDE actuators was shown to be 70% greater than that produced by a d_{31} actuator. Electromechanical coupling coefficients calculated using two different methods showed that values of 0.45 to 0.71 were achieved for IDE devices as compared to 0.29 to 0.35 for conventional d_{31} devices.

REFERENCES

1. R.M. White, F.W. Voltmer, "Interdigital electrode transducers," *Appl. Phys. Lett.*, 7, 314-316, 1965.
2. S. Suekichi, "Piezoelectric Actuator," Hei3-94487 Japan, 1991. (in Japanese)
3. Y. Fuda, T. Yoshida, T. Ohno, and S. Yoshikawa, "Ceramic Actuator with Three-Dimensional Electrode Structure," *IEEE International Symposium on Applications of Ferroelectrics, Proceeding*, pp. 573-576, 1992.
4. N.W. Hagood, A.A. Bent "Development of Piezoelectric Fiber Composites for Structural Actuation.", *Proceedings of the 34th AIAA Structures, Structural Dynamics, and Materials Conference*, AIAA Paper No. 93-1717., 1993.
5. Active Control eXperts, Inc. Product Information.
6. S. Hirose, H. Nakamura, H. Shimizu, "Analysis of Piezoelectric Ceramic Length-Expansion-Mode Resonators Using Interdigital Electrodes for Both Poling Treatment and AC Excitation," *Electronics and Communications in Japan*, Part 1, Vol 71 No.5, pp. 41-49, 1988.
7. N.W. Hagood, R. Kindel, R. Ghandi, P. Gaudenzi, "Improving Transverse Actuation of Piezoelectrics Using Interdigitated Surface Electrodes,", *Proceedings of the 1993 North American Conference on Smart Structures and Materials*, SPIE Paper No. 1917-25.
8. A. R. Ramachandran, Q.C. Xu, L.E. Cross and R.E. Newnham "Passive Vibration Damping" *Proceeding of the First Joint US/Japan Conference on Adaptive Structures*, B.Wada, J.L. Fanson and K.Miura eds., pp 523-528, 1990.
9. N. Hagood and A. von Flotow, "Damping of Structural Vibrations with Piezoelectric Materials and Passive Electrical Networks" *Journal of Sounds and Vibration*, Vol 146 [2] pp. 243-268, 1991.
10. Standard Definitions and Methods of Measurement for Piezoelectric Vibrators, IEEE No. 177, May 1966.

Dielectric Studies of K(Ta$_x$Nb$_{1-x}$)O$_3$ and Pb(Fe$_{2/3}$W$_{1/3}$)O$_3$ for Use as Ferroic Materials at Cryogenic Temperatures

C.B. DiAntonio and S.M. Pilgrim
New York State College of Ceramics at Alfred University
Diantocb@auvax.alfred.edu and pilgrim@auvax.alfred.edu
Fax: 607-871-2354

Abstract--Renewed interest in space exploration and continuing development of superconducting applications have highlighted the need for electronic components with performance at cryogenic temperatures (15 to 77K). Several of these needed components, e.g., capacitors and electromechanical actuators, will likely depend on an enabling ferroic response. In this examination of dielectric properties, high-density ceramic samples from two families have been examined. The specific families are: KTaO$_3$-KNbO$_3$ and Pb(Fe$_{2/3}$W$_{1/3}$)O$_3$. Variations in diffuseness, frequency dispersion, and dielectric transition are discussed with reference to composition. All materials show a dielectric maximum and frequency dispersion characteristic of ferroelectric relaxors.

1. INTRODUCTION

Although a number of compositions [1] have been previously investigated, little recent and integrated work has been completed. Some of the candidate compositions are listed in Table I.

Table I. Candidate cryogenic ferroelectrics.

Composition	Curie or Transition Temperature (@ 1 kHz)
Pb (Mg$_{1/3}$Ta$_{2/3}$) O$_3$ - PMT	175 K (average)
Pb (Mg$_{1/3}$Nb$_{2/3}$) O$_3$	265 K (average)
Pb (Ni$_{1/3}$Ta$_{2/3}$) O$_3$	113 K - 93 K
Pb (Ni$_{1/3}$Nb$_{2/3}$)O$_3$	163 K - 133 K
Pb (Co$_{1/2}$W$_{1/2}$)O$_3$	83 K - 103 K
(Ba$_{1-x}$Sr$_x$) TiO$_3$	1 K - 400 K
Sr$_4$Na$_2$Ta$_{10}$O$_{30}$ (tungsten bronze)	123 K
Sr$_2$Ta$_2$O$_7$	161 K
(Sr$_{1-x}$Ca$_x$)(Ni$_{1/3}$Ta$_{2/3}$)O$_3$ – SCNT	?
Pb(Fe$_{2/3}$W$_{1/3}$)O$_3$	≈150K
KTaO$_3$ - KNbO$_3$ system (KTN)	*KTaO$_3$ - 1.5 K KNbO$_3$ - 691 K

*(Debate exists as to the nature and temperature of the ferroelectric transition.)

2. KTN CERAMICS

The ferroelectric properties of the compound, KTaO$_3$ were discovered by Matthias [2] around 1949. The symmetry of the room temperature phase is cubic and the lattice parameter is almost identical to that of KNbO$_3$ in its centrosymmetric phase, i.e., above 691K. In spite of its similarity, the Curie temperature of KTaO$_3$ is <13 K, one of the two lowest ferroelectric transition temperatures known to date (the other is that of lithium thallium tartrate monohydrate, LiTlC$_4$H$_4$O$_6$ * H$_2$O, 10 K). The temperature dependence of the dielectric constant has been measured down to 1.3 K by Hulm et al. [3]. The results show that the dielectric constant obeys the Curie-Weiss law only down to 52 K, below which it still increases, but less rapidly than required by that law. A flat maximum is reached at the Curie point, below which the curve levels off in a smooth fashion. No conclusive information is available, to date, about the symmetry of the polar phase. The deviation from the Curie-Weiss law at low temperatures is a phenomenon characteristic of ferroelectrics with very low Curie points. It was shown by Barrett [4] that quantum effects play an important role in these low temperature regions and that these effects can explain the deviation from the Curie-Weiss law observed experimentally.

The KTN (KTa$_x$Nb$_{1-x}$O$_3$) system is a ferroelectric material for x=0.05 and exhibits the same three ferroelectric phases as BaTiO$_3$ and KNbO$_3$. In the case of KTN, the diffuseness and frequency dispersion decrease with increasing levels of Ta. The Curie temperature of the solid solution varies smoothly between the end members (see Figure 1). The system of solid solutions KTa$_x$Nb$_{1-x}$O$_3$ was first investigated by Reisman et al. [5] with thermal and X-ray measurements. Subsequently, a detailed study of this system was completed by Triebwasser [6], with particular attention to its dielectric properties. The measurements were made on single crystals of solid solutions with different compositions. The results show that the Curie temperature varies almost linearly between the two end-members of the system with a cubic-tetragonal transition in the region of room temperature when x≈0.37 (see Figure 1).
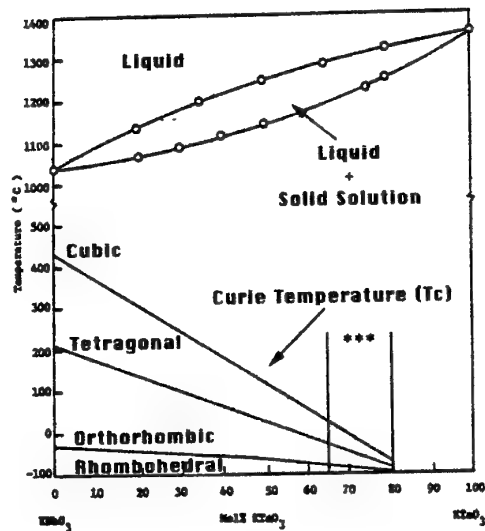
Fig. 1. Phase diagram of system KNbO₃ –KTaO₃. [6]

The permittivity and dielectric loss response of KTN at 65 mol% and 35 mol% Ta_2O_5 as a function of frequency and temperature are shown in Figures 2, 3, 4, and 5. An interesting feature revealed by the dielectric study is that the ferroelectric transition (paraelectric-tetragonal), which is of the first order in $KNbO_3$, becomes of second order when the tantalum concentration exceeds 55 mol%. Note that significant relaxation effects appear to be present for x=0.65. The summary dielectric data for $KT_xN_{1-x}O3$ is listed in Table II.

Table II. Summary dielectric data for $KT_xN_{1-x}O_3$.

Composition	δ [°C]	T_{max} [°C] (@1KHz)	Average Permittivity @ T_{max}
x=0.65	55.6 ±1.5	-31 ± 3.0	2850±19.0
x=0.80	23.3 ±2.0	-152±1.0	4260±2.5

Fig. 2. Weak field permittivity measurements of KTN (x=0.65) as a function of frequency and temperature.
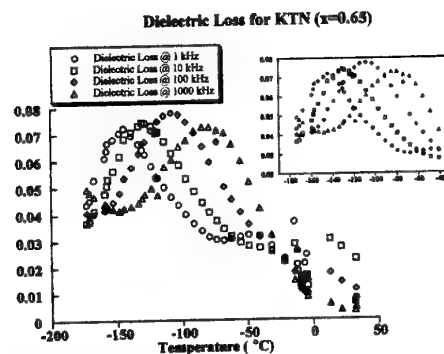
Fig. 3. Dielectric loss for KTN (x=0.65) as a function of temperature and frequency.

Fig. 4. Weak field permittivity measurements of KTN (x=0.80) as a function of frequency and temperature.

Fig. 5. Dielectric loss for KTN (x=0.80) as a function of temperature and frequency.

3. PFW CERAMICS

Lead iron tungstate (Pb(Fe$_{2/3}$W$_{1/3}$)O$_3$) is considered to be a relaxor ferroelectric material. Traditionally, PFW is processed using the conventional mixed oxide route with the possible use of the columbite precursor route. Typical starting raw materials used in processing of PFW have been; PbO, Fe$_2$O$_3$, and WO$_3$. The PbO and Fe$_2$O$_3$ have relatively small particle size distributions and are highly reactive (large specific surface areas). These characteristics make them ideal for powder preparation. However, WO$_3$ is a very hard material that is difficult to comminute to prepare a mixed oxide material. Recent research has revealed that tungstic acid (H$_2$WO$_4$) is a suitable replacement for WO$_3$ [7] H$_2$WO$_4$ has a small particle size distribution that is much more favorable for comminution and mixing with other starting raw materials. The substitution of H$_2$WO$_4$ for WO$_3$ in the batch provides for a more homogeneous precursor powder of Fe$_2$WO$_6$. Tungstic acid has been fully characterized in terms of, phase purity and verification of the full transformation from H$_2$WO$_4$ to WO$_3$ (powder x-ray diffraction), particle morphology, particle size and distribution (scanning electron microscopy, specific surface area, and laser scattering). Thermal analysis (DTA) and thermogravimetric analysis (TGA) quantitatively show the volatilization of bound H$_2$O as ≈7.20wt% [7].

PFW is synthesized by the conventional mixed oxide method, although it is difficult to prepare as a monophasic compound. A lead tungstate oxide second phase (PbWO$_4$, Pb$_2$FeWO$_{6.5}$, and/or Pb$_2$WO$_5$) has been reported to always be present, in relatively large quantities [8]. The columbite / wolframite precursor method, using the reaction between a prereacted columbite - type structure compound B'B"$_2$O$_6$ (in the systems Pb(B'$_{1/3}$B"$_{2/3}$)O$_3$) or the wolframite - type structure compound B'B"O$_4$ (in the systems Pb(B'$_{1/2}$B"$_{1/2}$)O$_3$) and lead oxide, has proven to be successful in preparing compounds such as PMN, PNN and PFN, almost free of A$_2$B$_2$O$_7$ pyrochlore phases [8].

In this work, the columbite precursor method, developed by Swartz and Shrout [9], was used to prepare PFW, with Fe$_2$WO$_6$ as the precursor phase Although differently arranged in space, the Fe$_2$WO$_6$ (PDF card #42-0492) and PFW (PDF card #40-0374) structures have the same basic WO$_6$ octahedra units. It is possible then to expect the formation of the perovskite PFW structure from the columbite iron tungstate (FW) to be relatively easy. The final PFW powder has been fully characterized and dry pressed into disc shaped samples for dielectric measurements [7]. These measurements include, the permittivity and dielectric loss of the material as a function of temperature (-180°C to 50°C) and frequency (100 Hz to 1000 kHz) as shown in Figures 6 and 7.

More recent research has found evidence for higher values of permittivity and a slightly lower curie temperature, work is underway to confirm the variation and study the polarization and strain response of the material.

Weak Field Permittivity Measurements of PFW
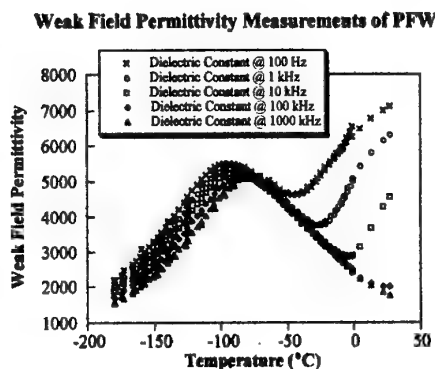
Fig. 6. Weak field permittivity measurements as a function of temperature and frequency for PFW.

Dielectric Loss for PFW
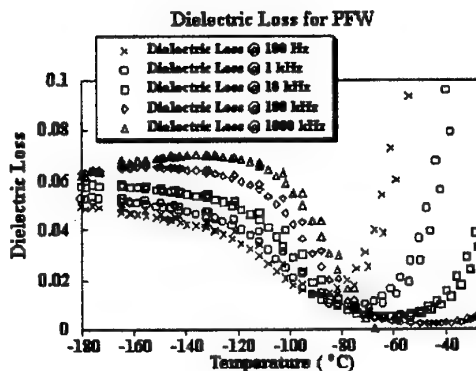
Fig. 7. Dielectric Loss data for PFW.

Note that the diffuseness parameter (δ) given in Table III is strongly affected by the increasing loss at elevated temperatures.

Table III. Summary dielectric data for PFW.

Composition	δ [°C]	T$_{max}$ [°C] (@1 kHz)	Average Permittivity @ T$_{max}$
PFW	74.1± 1.0	-76 ± 1.5	5207±25.0

3. CONCLUSIONS

Both systems show potential for use at cryogenic temperatures. They display typical relaxor behavior; however, the loss characteristics are not ideal. The indefinite character of relaxations in the $K(Ta_{0.65}Nb_{0.35})O_3$ system and the onset of significant loss in the PFW system require additional investigation.

Compositional modification of the systems to reduce the dielectric loss and further decrease the transition temperature is indicated. Direct measurement of electromecnanical properties is necessary to fully access potential performance and is currently being examined.

4. REFERENCES

[1] K. Toyoda, Ferroelectrics. Landolt-Bornstein, New Series, Group III, Volume 3. Springer-Verlag, Berlin, 1970.

[2] B.T. Matthias, "New Ferroelectric Crystals," Phys. Rev., 75 [11] 1771 (1949).

[3] J. K Hulm, B. T. Matthias and E. A. Long, "A Ferromagnetic Curie Point in $KTaO_3$ at Very Low Temperatures," Phys. Rev., 79 [5] 885 (1950).

[4] J. H. Barrett, "Dielectric Constant in Perovskite Type Crystals," Phys. Rev., 86 [1] 118 (1952).

[5] A. Reisman and E. Banks, "Reactions of the Group VB Pentoxides. VIII. Thermal, Density and X-Ray Studies of the Systems $KNbO_3$-$NaNbO_3$ and $KTaO_3$-$KNbO_3$," J. Am. Chem. Soc., 80 [8] 1877 (1958).

[6] S. Triebwasser, "Study of Ferroelectric Transitions of Solid-Solution Single Crystals of $KNbO_3$-$KTaO_3$," Phys. Rev., 114 [1] 63 (1959).

[7] C.B. DiAntonio, "Processing, Characterization, and Dielectric Studies on $K(Ta_{1-x}Nb_x)O_3$ and $Pb(Fe_{2/3}W_{1/3})O_3$ for use as Smart Materials at Cryogenic Temperatures," MS Thesis Alfred University (1998).

[8] L. Zhou and P.M. Vilarinho, "Synthesis and Characterization of Lead Iron TungstateCeramics Obtained by Two Preparation Methods," Mater. Res. Bull., 29, [11] 1193-1201 (1994).

[9] S. L. Swartz and T. R. Shrout, "Fabrication of Perovskite Lead Magnesium Niobate," Mater. Res. Bull., 17 [10] 1245-1250 (1982).

Development of Piezoelectric Ceramic Torsional Actuators Based on Shear Piezoelectric Response and Their Potential Applications

Chulho Kim[a], Alexandre Glazounov[b] and Qiming Zhang[c]

[a]Naval Research Laboratory, 4555 Overlook Avenue, Washington, DC 20375, USA
Fax: 202-404-7176, e-mail: kim@anvil.nrl.navy.mil

[b]Universität Karlsruhe, IKM, Zentrallaboratorium, Haid-und-Neu-Str. 7, D-76131 Karlsruhe, Germany
Fax:+49 / (0)721-608 8891, e-mail: Alexandre.Glazounov@mach.uni-karlsruhe.de

[c]187 Materials Research Laboratory, Pennsylvania State University, University Park, PA 16802, USA
Fax: 814-863-7846, e-mail: QXZ1@PSU.EDU

Novel piezoelectric cylindrical ceramic actuators have been developed utilizing the d_{15} piezoelectric shear coefficient that is higher than the d_{33} for commercially available lead zirconate titanate ceramics. These solid state actuators are segmented piezoelectric tubes that generate high torque and angular displacement. The torque output is directly proportional to the cross sectional area of the actuator tube. The stroke amplitude is amplified by increasing the aspect ratio of the tube without significant loss of dynamic torque output. At the resonance frequency of the actuator, the amplitude of the torsional angle is amplified by the mechanical quality factor of the device. Since the torsional actuator design features are simple and provide direct electromechanical energy conversion, a high efficiency piezoelectric motor has been built. The piezoelectric motor utilizes a direct coupling mechanism between the rotor and the stator where a specially designed clutch transmits force for a stepwise continuous or finite rotation. Another potential application of the torsional actuator is in helicopter rotor blade trailing edge flap actuation to reduce noise and vibration and to provide real time active blade tuning. The design principles, fabrication techniques, and performance tests and results are presented for the prototype piezoelectric torsional actuators.

1. INTRODUCTION

In the last half century that has elapsed since the discovery of piezoelectricity,[1] piezoelectric ceramic materials, such as lead zirconate titanate (PZT), have been widely used in applications for sensors, transducers, actuators and other electromechanical devices.[2] For some smart materials and structures applications of recent interest, a large rotational motion with a large torque output is demanded, as for example in helicopter rotor blade vibration and noise control.[3,4] In other applications of interest, piezoelectric ultrasonic motors[5,6] have been developed for higher torque density than electromagnetic motors. However most piezoelectric motors developed have either lower power density or efficiency than the latter because the force converting mechanism into rotary motion is not direct.

In this paper, we report on a novel tubular torsional actuator in which the shear piezoelectric effect of the monolithic PZT segments is directly transformed to generate the desired angular displacement and torque. Its simple and direct energy conversion mechanism provides high authority actuation and angular displacement without complex actuator designs and linkages. This solid state tubular actuator produces a direct rotational displacement utilizing the shear piezoelectric coefficient, d_{15}, which is typically the highest among piezoelectric coefficients in most PZT materials. Design principles, fabrication techniques and experimentally measured characteristics of the prototype torsional actuator and its applications in piezoelectric motors and in helicopter rotor blade/trailing edge flap are reported here.

2. ACTUATOR DESIGN

A torsional actuator[7,8] that can produce a large angular displacement and high torque has been designed, as shown in Fig. 1. This solid state, tubular actuator consists of an even number of piezoelectric ceramic segments, poled along their length in such a way that the polarity alternates between adjacent segments. The segments are then joined with a conductive adhesive and assembled into a tubular actuator. Application of an electric field, E, perpendicular to the polarization direction of the segments results in a twisting deformation of the tube due to the coherent piezoelectric shear response of the individual segments and the cylindrical symmetry of the actuator. The shear strain, S_5, induced in each segment is directly transformed into the angular displacement, β, of one end of the tube with respect to the other, as described by the equation:

$$\beta = S_5 L / R \qquad (1)$$
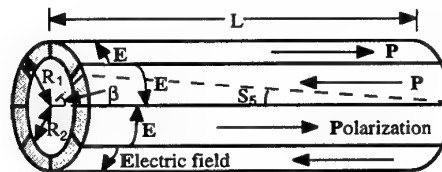
Fig.1. Even number of PZT segments are poled along the length and assembled alternately and then bonded together with a conductive adhesive. Application of E field normal to polarization direction results in shear strain, S_5, and hence twist the tube due to the d_{15} shear effect.

where $S_5 = d_{15}E$ and $R = (R_1+R_2)/2$, and where R_2 and R_1 are the inner and outer radii of the tube. If $L > R$, then $\beta > S_5$, and angular displacement amplification is easily achieved. The torque, T, developed by this tubular actuator is given by:

$$T = \frac{d_{15}nV(R_1 - R_2)}{s_{44}}R \qquad (2)$$

Here, the torque is a function of the voltage, V, shear elastic compliance, s_{44}, number of segments, n, and d_{15}. The field, E, in Eq. (1) is related to the voltage, V, in Eq. (2) by $E \approx nV/\pi(R_1+R_2) = nV/2\pi R$. Eq. (2) shows that the torque, T, is independent of the length of the tube, L, even though the angular deformation, β, increases linearly with L.

3. PROTOTYPE ACTUATOR FABRICATION

The material for the torsional actuator was selected based on its ability to have the highest shear response under the limiting electric field (the field limit before depoling occurs) as well as a high d_{15} under operating conditions. The material should also have a low elastic shear compliance and a high depoling shear stress. Commercially available soft and hard PZT materials were examined with respect to these parameters.[7] The results showed that PZT-5A (obtained from EDO Inc.) had a high maximum shear piezoelectric response (>1,200 micro-strain). Thus, this PZT-5A was selected to produce a prototype actuator. All the materials investigated exhibited significant nonlinear behavior with respect to the field. The d_{15} coefficient of PZT-5A at high fields (4.8 kV/cm), for example, is 2,500 pC/N, as compared to 700 pC/N at low fields (<200 V/cm). There is, however, no marked change of d_{15} and s_{44} with respect to the shear load applied up to stresses of 10 MPa.

Piezoelectric ceramic segments for the assembly of the tubular actuator were prepared by cutting PZT-5A tubes longitudinally to produce eight equal segments.[7] Trapezoidal segments were also used to prepare polygonal cylindrical actuators. In order to pole these slender actuator segments, a continuous poling fixture was developed.[7] This was required by the trade-off between the minimum electric field strength necessary to approach full uniform spontaneous polarization and the maximum field strength to avoid material breakdown. The continuous poling was accomplished by moving the long PZT-5A segments between two conductive rubber electrodes separated by a distance of 1.4 cm with 20 kV between electrodes while the entire system was immersed in a dielectric oil bath heated to 80-100 °C. These continuously poled segments exhibited more than 95% (>460 pC/N) of the d_{33} value (~480 pC/N) of short samples poled fully using the conventional method.

The poled segments were assembled into a tubular actuator, with a high shear strength conductive epoxy which serves as both joint and electrode, and cured using a vacuum bagging process. Consolidation of the joints by vacuum bagging leads to joints typically 25 μm in thickness and very uniform along the length of the joints. Two individual actuator assemblies thus fabricated can be connected to make a longer tubular actuator, as shown in Fig. 2.

Fig. 2. Torsional actuator tube (13 cm long) assembly. Conductive joint acts as electrodes and neighboring electrodes are electrically connected in parallel.

4. EVALUATION OF ACTUATORS

In all experiments, the twist angle, β, of the actuator tube was measured[9] using an MTI-2000 photonic sensor by attaching a small mirror on the top of the actuator (bottom clamped) and measuring the changes in distance between the mirror and an optical fiber probe. The twist angle, β, is plotted as a function of ac driving field at 10 Hz, as shown in Fig.3. For both tubes (#3 & #7), the actuation behavior is almost identical and angular displacement is doubled when the length of the actuator is increased by joining these two tubes as indicated in Eq. (1). The values of the d_{15} derived from the angular displacement data using Eq. (1) for all the torsional actuators, including 6.35 and 12.7 cm long tubes, are nearly the same as those measured on the individual parallelepiped sample in the ac field range investigated. In Fig. 4, it is shown the induced shear strain calculated from the data on torsional angle as a function of external torque and dc driving voltage. The data for single tube and lengthened tube coincide with each other indicating that the torque output produced by torsional actuator is independent of the length, as predicted by Eq. (2). Therefore, the results presented in Figs. 3 & 4 support the concept of the proposed torsional actuator, Eqs. (1) and (2).

The enhanced shear coefficient, d_{15}, with increased driving electric field, E, combined with the geometric amplification factor, L/R, generates a large angular displacement, β, and torque, T. The clear advantage of the present design is that the torque generated by this actuator is independent of the length of the actuator as opposed to the actuators based on piezoelectric bimorphs.[10] In the bimorph system, both the produced torsional angle and the force output depend upon the length of the bimorph. Even though, the increase in the
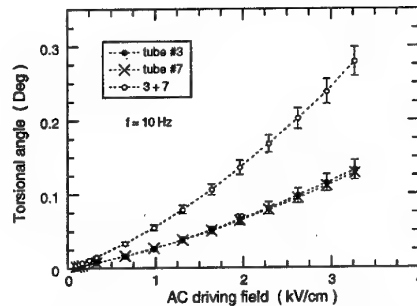
Fig. 3. The torsional angle, β, measured at 10 Hz is plotted as a function of the ac driving voltage. The plot shows that the joining of two identical tubes (#3, #7) results in the doubling of induced torsional angle, as predicted by Eq. (1).
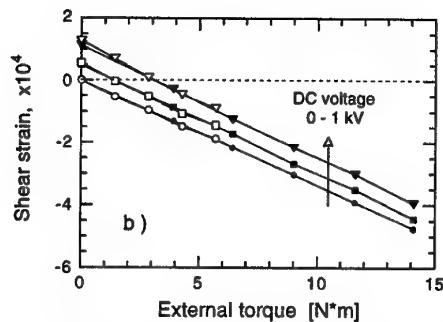
Fig. 4. Induced shear strain calculated from the data on torsional angle as a function of external static torque and dc driving voltage.

Fig. 5. Frequency dependence of the torsional angle normalized over its static value. Different clamping conditions are compared for the same actuator.

length will result in larger values of the torsional angle, it will simultaneously reduce the force output, because the force is inversely proportional to the length of the bimorph.

5. APPLICATIONS

5.1. Piezoelectric Motors

Pieoelectric motors[11] operate at resonant frequency, at which the rotational displacement amplitude of the piezoelectric actuator can be magnified substantially. Even larger rotational angles can be generated by attaching a torsional resonator bar to the torsional actuator where the natural resonance frequency of the resonator is matched with that of the piezoelectric torsional actuator.[12]

An application of the torsional actuator is in the ultrasonic piezoelectric motors. In this study, for a small electric field, E=50 V/cm, the frequency dependence of β was measured over a broad frequency range. The frequency dependence of torsional angle of the cylindrical torsional actuator tube (13 cm long) is shown in Fig. 5. The plot shows the frequency dependence of the ratio $\beta(f)/\beta(0)$, where $\beta(0)$ corresponds to the low-frequency value of the torsional angle, given by Eq. (1). Also it shows different clamping conditions of the tube resulted in different resonance frequencies. The torsional angle shows sharp peaks at around 6 kHz for bottom clamped and 13 kHz for midsection clamped and free stand (unclamped) conditions. The analysis showed that the peaks correspond to the first resonant frequency of the fundamental shear mode propagating along the length of the actuator. Using an equivalent circuit model around the resonant frequency, one can show that at resonant frequency, f_r, dependence of the torsional angle is given by:

$$\beta(f_r) = d_{15} E_m (L/R_1) Q_m \qquad (3)$$

where Q_m is the mechanical quality factor of the actuator. This additional torsional angle amplification term, Q_m, at f_r can be utilized in piezoelectric ultrasonic motor development.

In this case the piezoelectric ceramic tube was made from hard PZT ceramic (APC-841) because of its high Q_m. The tube generates high frequency torsional
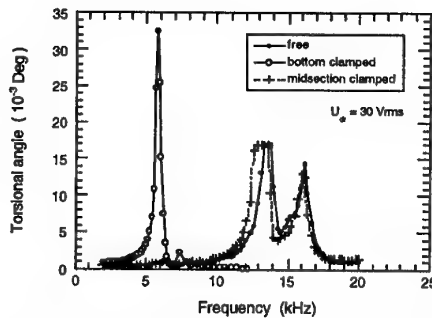
vibrations at the free ends. The vibrating tube can be used as a stator for the rotary inchworm or the motor.[11] One-way clutches commercially available from Torrington were connected to the piezoelectric tube so that it could move together with the tube and were used to accumulate the angular displacement of the rotor in one direction as shown in Fig. 6. In this figure, one end of the stator transmits the displacement to the rotor only if it moves in the counterclockwise direction, when the rollers are wedged between the tilted slope of the cam and the surface of the rotor. In the clockwise direction, the rollers disengage and do not transmit the displacement. The other end of the stator operates exactly in the opposite fashion such that the stator transmits the displacement continuously to the rotor. The mid-section of the ceramic tube stator is anchored to the outer housing body such that the whole structure is symmetric. When activating the tube at resonance frequency, the center of the tube will be a nodal point (stationary) and both ends of the tube oscillate in opposite twist directions.[13]
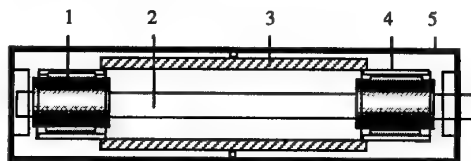
Fig. 6. Schematic of piezoelectric motor based on the torsional actuator stator (3), rotor (2), roller clutches (1 & 4) and housing (5).

5.2. Other Potential Applications

Another potential application of the torsional actuator is in helicopter rotor blade trailing edge flap actuation to reduce noise and vibration and to provide real time active blade tuning. Calculations[14] for the PZT-5A torsional actuator applied to helicopter rotor blade (with appropriate size constraints) estimate a 2° angular displacement and 47 N-m blocking torque. These outputs are between the required values[15] for trailing edge flap (±4°, 5±3.5 N-m) and blade twist (±2°, ±54 N-m) in the rotor blade actuation for an eight seat commercial helicopter. Increased twist angle can be

achieved simply by lengthening the actuator, or trading off some of the excess torque of the actuator with mechanical displacement amplification. The specific values of torsional angle and torque can be tailored for each particular application. In Table I, the comparison is made between the required values for the helicopter rotor blade control and the projected data from torsional actuator tubes. The torque output of the actuator tube is proportional to its cross-sectional area, and the rotational angle to its aspect ratio (length/diameter). The geometry of the actuator is ideal for some cases where the shape of the actuator uses the space available efficiently, e.g., a helicopter rotor spar[14] as shown in Fig. 7.

Table I. Comparison of the projected results of the torsional actuator and helicopter rotor blade control requirments

	Trailing Edge Flap		Blade Twist	
	cylinder	required	cylinder	required
Torque,Ncm	±587.5	486±362	±4,689	±5,423
Angle, deg.	± 4	± 4	± 2	± 2
ODmax, cm	1.27	0.787	2.54	1.905
Length, cm	50.8	< 61	50.8	< 61
Weight, gr	218	454	862	< 1,814
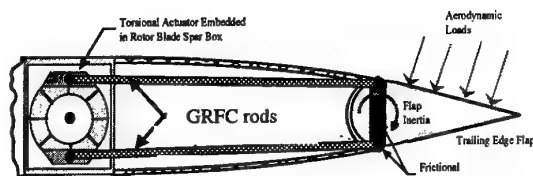
Fig. 7. Schematic of helicopter rotor blade/trailing edge flap. The torsional actuator is embedded in the spar and linked to the TEF with dual graphite fiber reinforced composite rods.

6. SUMMARY

A novel, solid state, torsional actuator has been developed based on the use of the piezoelectric shear coupling coefficient, and experiments demonstrate that the conceptual actuator operates as predicted by analytical and numerical models. The actuator is capable of producing both large torque and large angular displacement in a compact package, sufficient to meet many smart structure requirements, and can be tailored for a variety of performance specifications. Here, the following modes of piezoelectric torsional actuators were used: a) low frequency, high voltage, non-resonance mode where the twist angle per cycle is proportional to the L/R ratio,, and the torque is independent of length; b) high frequency, low voltage resonance mode where the twist angle is increased by the mechanical quality factor

of the device, c) cummulative mode where the b) mode was modified to increase the angle indefinitely by using a cumulative unidirectional force transfer clutch mechanism resulting in motor and/or rotary inchworm devices.

REFERENCES

1) Roberts, S., *Physical Review*, **71**, 890 (1947)
2) Cross, L. E., *Ceramic Trans.*, **65**, 15 (1996).
3) Chopra, I., "Status of application of smart structures technology to rotorcraft system", Presented at the innovation in rotorcraft technology, Royal Aeronautical Society, London, June 1997.
4) Straub, F.K., Ngo, H.T., Anand, V., and Domzalski, D.B., *SPIE Proc.*, **3668**, 104, Mar. (1999).
5) Uchino, K., "Piezoelectric Devices and Ultrasonic Motors", Kluwar Academic Publishers, 1997.
6) Ueha, K. and Tomikawa, Y., "Ultrasonic Motors; Theory and Applications", Oxford University Press, 1993.
7) Kim, C., Jesson, T., DeGiorgi, V., Bender, B., Wu,. C.C.M., Flippen, D., Lewis, D., Zhang, Q.M., Mueller, V., Kahn, M., Silberglit, R. and Len, L.K., NRL/MR/6380--97-7997 (1997).
8) Glazounov, A.E., Zhang, Q.M. and Kim, C., *Appl. Phys. Lett.*, **72**, 2526 (1998).
9) Glazounov, A.E., Zhang, Q.M. and Kim, C., *SPIE Proc.*, **3324**, 82, Mar (1998).
10) Kugel, V.D., Chadran, S. and Cross. L.E., *Appl. Phys. Lett.*, **69**, 2021 (1996).
11) Glazounov, A.E., Kim, C. and Zhang, Q.M., *Appl. Phys. Lett.*, **75**, 862 (1999).
12) Kim, J. and Chi, H., *SPIE Proc.*, **3241**, 354 (1997).
13) Kim, C., Glazounov, A.E. and Zhang, Q.M., *SPIE Proc.*, to be published.
14) Kim, C., Glazounov, A.E., Flippen, F.D., Pattnaik, A., Zhang, Q.M. and Lewis, D., *SPIE Proc.*, **3675**, 53, Mar (1999).
15) Private communication, Straub, F.K., McDonald Douglas Helicopter Systems, Oct. 1995.
16) Lewis, D., Kim, C., Wu, C.C.M., Jessen, T.L., Kahn, M. and Chase, M., "Thirty Years of NRL Research in Functional Ceramics: From Failure Analysis to Novel Ceramic Devices", *1999 NRL Review*, pp.55-67, April (1999)

Development of Pb(Zr,Ti)O$_3$-based Ceramics for Photostrictors

Kazuhiro Nonaka, Morito Akiyama, Tsuyoshi Hagio and Akira Takase
Kyushu National Industrial Research Institute, Agency of Industrial Science and Technology,
Ministry of International Trade and Industry, 807-1 Shuku-machi, Tosu, Saga 841-0052, Japan
Fax: 81-942-83-9858, e-mail: nonaka@kniri.go.jp

Photostriction materials convert light directly to physical movement. The mechanism of photostriction is explained by superposition of the photovoltaic effect and piezoelectricity. In certain ferroelectrics, photovoltage is of the order of kilovolts to megavolts per centimeter to induce a mechanical strain along particular directions by means of the piezoelectric effect. This property enables the ferroelectrics to be used as photo-driven actuators, capable of wireless remote control and hence suitable for application in devices such as microactuators and microsensors. Considering the practical applications of those devices, however, some problems remain, such as slow response speed resulting from relatively small photovoltaic current. It has been confirmed that the strain rate of photostrictors by illumination depends strongly on the photovoltaic current and that the maximum strain is dependent on the photovoltage. In this study, samples of Pb(Zr$_x$,Ti$_{1-x}$)O$_3$-based ceramics doped with 1 mol% of Ta^{5+} were prepared by sintering at 1100 °C for 2h to investigate photovoltaic responses such as photovoltaic current and photovoltage and piezoelectric and ferroelectric properties such as strain constant and remanent polarization. Results confirmed that maximum photovoltaic power was obtained from the sample with x=0.54, whereas the strain constant became maximum in the sample with x=0.52. From this result, it is expected that high efficient photostrictors can be fabricated by combining materials of the two different compositions.

1. INTRODUCTION

It was recently found that a very high voltage (kilovolt to megavolt per centimeter) is generated upon illumination of homogeneous noncentrosymmetric materials, which include ferroelectrics and piezoelectrics,[1] and that this voltage can be utilized for realizing photodriven actuators (photostrictors).[2] The phenomenon of photostrictor movement is explained by the convolution effect upon the photovoltaic and piezoelectric effects. Focusing on the capability of noncontact energy supply by light, photostrictors are believed to be promising candidates for device elements in microsized systems, such as microelectromechanical systems and microoptoelectromechanical systems. Although the miniaturization of device size is favorable to enhance response speeds and to reduce the power of the light source, the performance of the photostrictor materials needs to be further improved to suit various demands more flexibly. To date, a large amount of research has been carried out on photostrictors, in regard to material composition, microstructures, preparation method, impurity doping, and nonstoichiometry.[3-7] From this research, we have confirmed that the formation of Pb vacancies is essential for inducing the photovoltaic effect in lead zirconate-titanate (PZT) ceramics.[8] As a result, advances in the performance of photostrictor materials have been made. However, most research has been conducted on homogeneous and monolithic materials which have led to the compromised levels of photostrictors.

Considering photostrictors from the standpoint of elemental functions, they can be divided into two components such as a photovoltaic generator near the surface and a piezostrictor as the bulk. Hence, to fabricate highly efficient photostrictors, the hybridization of the two components each of which is optimized is considered to be a very useful technique. We have already begun investigating the hybridization of the photostrictor material elements using PZT ceramics. The preliminary experiment revealed that the optimum compositions which gave the maximum responses differed in regards to photovoltaic and piezoelectric properties.[9] The photovoltaic power and the piezoelectric strain constant, respectively, became maximum at compositions with Zr/Ti molar ratios of 54/46 and 52/48.

In this paper, we report the detailed basic data for the hybridization of photostrictor material elements, as the first step. Photovoltaic properties as well as the piezoelectric and ferroelectric properties were investigated in PZT ceramics having various compositions and introduced with Pb vacancies by doping of Ta^{5+}.

2. EXPERIMENTAL PROCEDURE

2.1 Sample Preparation

Samples of Pb(Zr$_x$, Ti$_{1-x}$)O$_3$ (x=0.48-0.6) ceramics doped with 1 mol% of Ta^{5+} were prepared by the conventional solid-state reaction process. The detailed preparation technique has been described in a previous paper.[8] The sintering of samples was performed at 1100 °C for 2 h in magnesia crucibles. The sintered bodies were then cut and polished to fabricate samples. Fired-on silver paste was applied to adequate surfaces of the samples as electrodes.

The poling of the samples was carried out in silicone oil at 70 °C by applying a dc field of 3 kV/mm for 30 min.

2.2 Measurements

Bar-shaped samples of $3\times3\times8$ mm^3 were used for the photovoltaic and piezoelectric measurements. An ultrahigh-pressure mercury lamp (500 W) was used as the light source. Using optical glass filters, light with wavelengths ranging from 300 to 400 nm with a maximum intensity of around 365 nm was obtained and illuminated on the optically polished 3×8 mm^2 face of the sample which was electroded on the 3×8 mm^2 faces. The photoinduced current and voltage were measured under short- and open-circuit conditions, respectively, using an electrometer (Keithley 617). The piezoelectric constants were determined using a vector impedance analyzer (HP-4194A) for the samples electroded on the 3×3 mm^2 faces. The ferroelectric hysteresis loops were measured using an RT6000HVS (Radiant Technologies) for disk-shaped samples of 15 mm diameter and 0.5 mm thickness.

The crystalline phases formed were identified using a powder X-ray diffraction (XRD) technique using monochromated Cu K α radiation.

3. RESULTS AND DISCUSSION

3.1 Photovoltaic Responses

Figure 1 shows the photovoltaic responses for the $Pb(Zr_x,Ti_{1-x})O_3$-based ceramics (x=0.48-0.6) doped with 1 mol% of Ta^{5+}. The photovoltaic current tends to decrease with increasing x, but peaks at x=0.54. In this composition, the photovoltage also reaches a maximum and consequently, the output power becomes maximum. Accordingly, the optimized composition for a photovoltaic generator is determined to be x=0.54.

Figure 2 shows the dark conductivity in the various samples. The dark conductivity decreases with increasing x. This leads to the tendency of decrease of the photovoltaic current and of increase of the photovoltage with increasing x, as shown in Fig. 1 (a) and Fig. 1 (b), respectively, although this change has no significant consequences in terms of the photovoltaics. On the basis of the result in Fig. 1 (c), however, the peaks of the photovoltaic current and photovoltage observed around x=0.54 can be ascribed to the net enhancement in the photovoltaic response.

In the microstructures of the samples, no significant difference was observed by scanning electron microscopy in regard to the composition changes and the average grain sizes were measured to be approximately 2 μm.

3.2 Piezoelectric Properties

Figure 3 shows the piezoelectric strain constant, d_{33}, for the various samples. As is well known, values of d_{33} become maximum at x=0.52; this composition is near the morphotropic phase boundary as mentioned below.[10]

It is hence confirmed that the optimum compositions for a photovoltaic generator and for a piezostrictor differ from one another in the photostrictor. We believe that highly efficient photostrictors can be fabricated by hybridizing the materials of two different compositions optimized as a photovoltaic generator at x=0.54 and a piezostrictor at x=0.52.
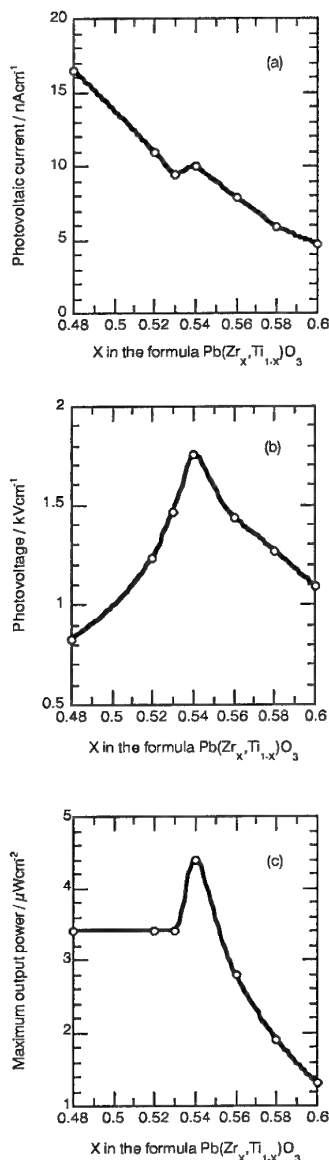
Fig. 1 Photovoltaic current (a), photovoltage (b), and maximum output power (c), as a function of composition. (Illumination intensity: 20 mWcm^{-2})

3.3 Effects of Polarization and Crystal Structure

Figure 4 shows the remanent polarization derived from the hysteresis loops for the various samples. The maximum polarization is obtained in the sample with x=0.54. Based on this result and that in Fig. 1, it is confirmed that the photovoltaic response is strongly dependent on the degree of remanent polarization in the samples. Comparing this result with that in Fig. 3, the photovoltaic properties are found to exhibit a stronger correlation with the remanent polarization than the piezoelectric properties. However, in the samples with
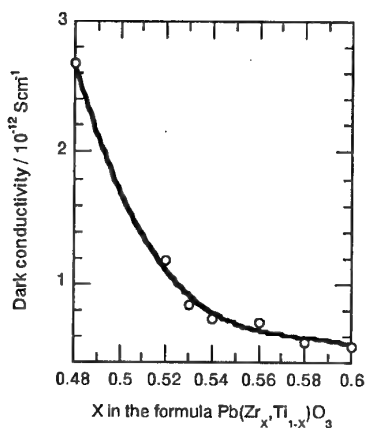
Fig. 2 Dark conductivity as a function of composition.
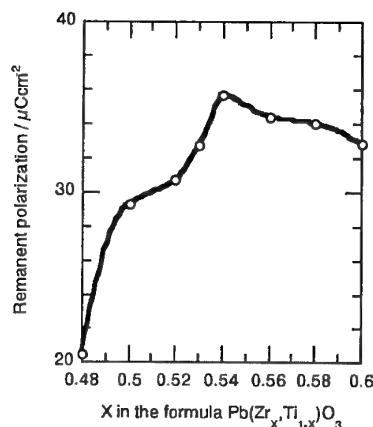
Fig. 4 Remanent polarization as a function of composition.
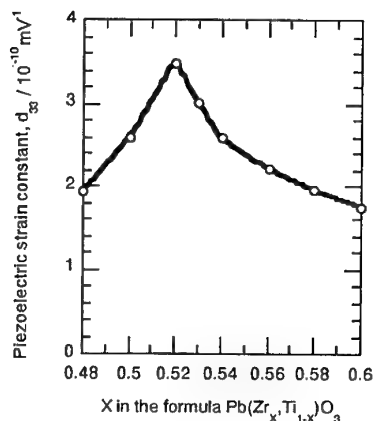
Fig. 3 Piezoelectric strain constant as a function of composition.
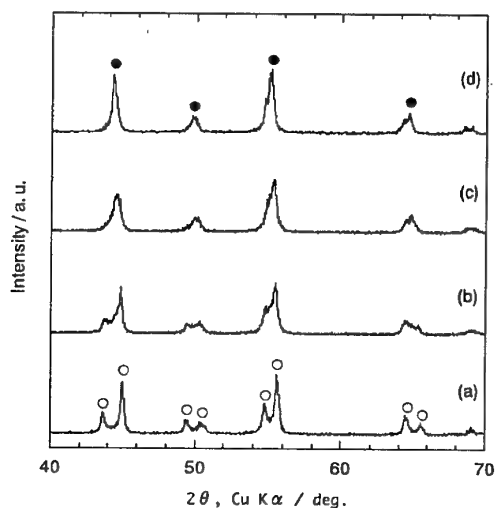
Fig. 5 XRD patterns as a function of composition: x=0.48 (a), 0.52 (b), 0.54 (c), 0.6 (d); tetragonal (○), rhombohedral (●)

x<0.52, the degree of remanent polarization decreases with decreasing x, but the photovoltaic power remains almost constant level of relatively high, as can be seen in Fig. 1 (c). The reason of this can be ascribed to the effect of crystal structures in the samples.

For the effects of crystal structures on the photovoltaic responses, it was reported in PLZT ceramics that the degree of polarization capable of producing a certain magnitude of photovoltaic current is larger in the rhombohedral structure group than in the tetragonal group.[11] To discuss the net changes of photovoltaic responses, however, we must consider the changes of the photovoltaic power because the values of photovoltaic current are dependent on second factors, such as the dark conductivity. In general, when the dark conductivity increases, the photovoltaic current also increases, but the photovoltage decreases, resulting in the almost constant values of the photovoltaic power.[12]

Figure 5 shows the XRD patterns for the various samples. The resultant crystalline phase is identified to be of tetragonal structure for the samples with x=0.48-0.5. The sample with x=0.52 is determined to have two phases of tetragonal and rhombohedral structures; it is near the morphotropic phase boundary.[10] For x>0.53, a rhombohedral structure is identified in the samples.

The values of the dark conductivity in the samples of tetragonal structure were higher than those in the samples of rhombohedral structure [Fig. 2 and 5]. Accordingly, relatively high values of photovoltaic current and relatively low photovoltage were measured in the former sample [Fig. 1 (a) and 1 (b)]. It should be noted, however, that the sample of tetragonal structure with x=0.48 showed the relatively high photovoltaic

power in spite of its small remanent polarization [Fig. 1 (c) and 4]. For PZT ceramics, it can thus be said that samples of tetragonal structure potentially have the high photovoltaic responsibility compared with those of rhombohedral structure.

4. CONCLUSIONS

(1) Maximum photovoltaic power was obtained from the sample with $x=0.54$, whereas the strain constant became maximum in the sample with $x=0.52$.

(2) Photovoltaic properties exhibit a stronger correlation with the remanent polarization than the piezoelectric properties.

(3) Highly efficient photostrictors are expected to be fabricated by hybridizing the materials of two different compositions of $x=0.54$ as a photovoltaic generator and $x=0.52$ as a piezostrictor.

(4) Samples of tetragonal structure potentially have the high photovoltaic responsibility compared with those of rhombohedral structure.

Acknowledgement

References

1. V. M. Fridkin, "Photoferroelectrics", Solid State Sciences, Vol. 9, Ed. by M. Cardona, P. Fulde and H.-J. Queisser, Springer-Verlag, New York (1979) pp. 85-113.

2. P. S. Brody, Ferroelectrics, **50**, 27-32 (1983).

3. T. Sada, M. Inoue and K. Uchino, Yogyo-Kyokai-Shi, **95**, 545 -50 (1987).

4. K. Nonaka, M. Akiyama, T. Hagio and A. Takase, Ferroelectrics, **223**, 357-64 (1999).

5. P. Poosanaas, A. Dogan, A.V. Prasadarao, S. Komarneni and K. Uchino, J. Electroceramics, **1**, 105-11 (1997).

6. M. Tanimura and K. Uchino, Sens. & Mater., **1**, 47-56 (1988).

7. K. Nonaka, M. Akiyama, T. Hagio, A. Takase, T. Baba, K. Yamamoto and H. Ito, J. Mater. Sci. Lett., **15**, 2096-98 (1996).

8. K. Nonaka, M. Akiyama, T. Hagio and A. Takase, J. Euro. Ceram. Soc., **19**, 1143-48 (1999).

9. K. Nonaka, M. Akiyama, T. Hagio and A. Takase, Proceedings of Annual Meeting of the Ceramic Society of Japan, 1999, Tokyo (1999) pp. 529.

10. Y. Xu, "Ferroelectric Materials and Their Applications", North-Holland, New York (1991) pp. 104-12.

11. K. Uchino, Y. Miyazawa and S. Nomura, Jpn. J. Appl. Phys., **22** (1983) Suppl. **22-2**, pp.102-5.

12. K. Nonaka, M. Akiyama, A. Takase, T. Baba, K. Yamamoto, M. Hiraoka and H. Ito, "Mass and Charge Transport in Ceramics", Ceram. Trans., Vol. 71, Ed. by K. Koumoto, L. M. Sheppard and H. Matsubara, American Ceramic Society, Westerville (1996) pp. 563-73.

The Dynamic Analysis of Kyser-type Ink-Jet Head

Yujiro Kitaide

Fuji Electric Corporate R&D ,Ltd

2-2-1,Nagasaka,Yokosuka-city,Kanagawa,240-0194,Japan

Fax:81-468-57-6732,e-mail:kitaide-yujiro@fujielectric.co.jp

Abstract: This paper deals with a mathematical model for describing the dynamic characteristics of Kyser type ink-jet head.The ink-jet head mainly consists of an ink reservior,a supply orifice,a chamber and a nozzle.We analyze the mathematical model of the system taking the dynamic characteristics of the piezo-electric actuator into consideration,as well as the flexibility of the chamber wall.In the experiment,we observed the motion of the ink meniscus.The experimental result agreed well with the simulated result and thus the validity of the mathematical model was confirmed.

*Keywords:*Transient response, Modeling, Meniscus, Surface tension

1.Introduction

Demands for hi-quality and low-cost printers are increasing. In this paper, we study the behavior of the ink ejection of the Kyser-type ink-jet head, in which the ejection of the ink occured with the deformation of the piezo-electric actuator. Printing is achieved with the firing to the piezo-electric actuator in the Kyser-type ink-jet head Several studies have been done about the head [1][2],but few studies pay attention to the behavior of ink stream in a high velocity.

We analyze the behavior of the ink stream growing in the nozzle and derive the mathematical model which describes the ink ejection process The simulation results agreed well with the experimental results. We confirmed the validity of our mathematical model.

2.Principal of the ink jet head

Figure1(a)-(c) shows the principal of the Kyser type ink-jet head. Before the ejection, the drive voltage applied to the piezo-electric element Fig.1(a). In the inhalation process, the piezo-electric element is released, the ink meniscus is drawn back and the ink refill the chamber Fig.(b). After that, the piezo-electric element is fired again ,then the ink stream comes out through the nozzle.

Figure2 shows the Head-chip of our ink-jet print head. The specification of the head is shown in Table1

(a)Initial state

(b)Ink inhalation

(c)Ink drop ejection
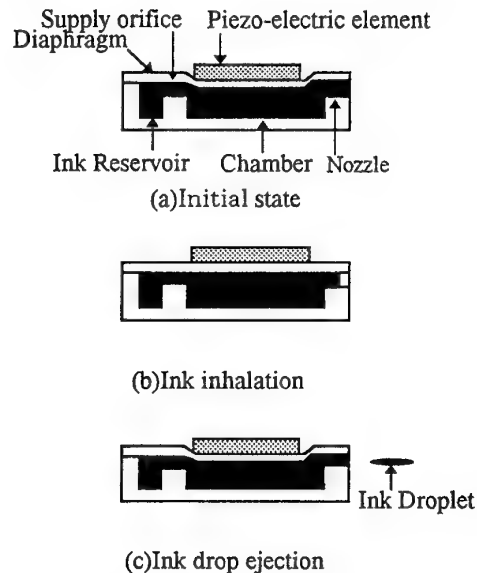
Fig.1 Principal of the ink ejection
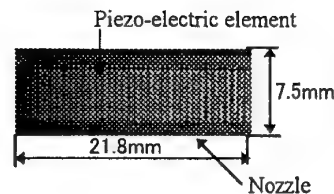
Fig.2 Ink-Jet Head

Table1.Specifications of the Ink-Jet Head

Item	Specification
Print density	300dot/inch
Print frequency	6kHz
Number of nozzles	60nozzles

3.Mathematical model

To analyze the behavior of the ink ejection, we simulate the condition of the ink separation with a consideration of a surface tension of the ink.

But, the separation of the ink is a complex behavior, thus to analyze the separation of the ink stream becomes a difficult problem.

In this paper, we deal with ink ejection system consists of three major components as a chamber, a nozzle and a supply orifice. The piezo actuator fixed on the wall upper side of the chamber wall. Then, piezo-electric actuator is modeled as the simple 2nd order spring-mass system.

Figure3 shows the physical model of our simulation.
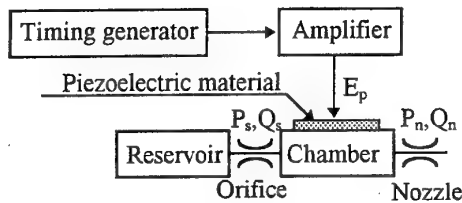
Fig.3 Physical model

To build the mathematical model, we assume conditions as follows.

(1)The pressure of the outlet of the nozzle and the orifice P_n is 1atm.
(2)the nozzle, the orifice and the chamber are the pipelines.

Table2 shows the dimensions of the nozzle, the chamber, the supply orifice, the actuator and the characteristics of the ink.

Table.2 Specifications of the actuator

Item	Specification
Thickness of the PZT element	35×10^{-6}m
Thickness of the diaphragm	20×10^{-6}m
Dimension of the actuator and the chamber	W0.5$\times 10^{-6}$m D3.7$\times 10^{-6}$m
Depth of the chamber	70×10^{-6}m
Length of the nozzle	1.7×10^{-6}m
Diameter of the nozzle	46×10^{-6}m
Length of the supply orifice	2.4×10^{-6}m
Diameter of the supply orifice	55×10^{-6}m
Viscosity	2.0cps
Surface tension of the Ink	50×10^{-3} N/m

(1)Actuator

We calculate the actuator force each time from the drive voltage applied to the piezo-electric element, and the deformation of the actuator.

To analyze the actuator force, we calculate the deformation and the natural frequency of the actuator at the reference voltage with the finite element method. Figure4 is one of the simulation results which shows the deformation of the piezo-electric actuator.
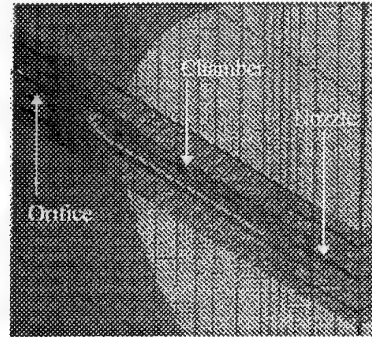
Fig.4 Deformation of the actuator

With this result, we calculate the actuator force from the equation(1).

$$F = (\frac{E}{E_0} F_0 - kx) + c\dot{x} + m_e \ddot{x} \qquad (1)$$

where
F: Actuator force(N)
E_0: Reference voltage(V)
F_0: Force at the reference voltage(N)
k: Rigidity of the actuator(N/m)
c: Dumping coefficient of the actuator (Ns/m)

(2) The pressure in the chamber

We assume that the actuator deforms uniformly when the piezoelectric-element is fired then, the deformation of the actuator can be represented by equation(2).

$$q_c = a_p \frac{dx}{dt} \qquad (2)$$

where
q_c: The deformed volume of the chamber(m³/s)
a_p: Area of the chamber(m²)

We calculate the pressure in the chamber with the equation(3).

$$\frac{dp_c}{dt} = \frac{K_c}{v_{init} - v_c}(q_s - q_n - q_c) \quad (3)$$

where

K_c: Rigidity of the ink (N/m^2)
v_{init}: Initial volume of the chamber (m^3)
v_c: Deforme volume of the chamber (m^3)
q_s: Flow rate through the supply orifice (m^3/s)
q_c: Flow rate through the nozzle (m^3/s)

(3) Flow rate through the supply orifice

We calculate the flow rate across the supply orifice with the equation(4).[3]

$$\Delta p_s = \frac{\rho V_s^2}{2} + \frac{32\eta l_s V_s}{d_s^2} \quad (4)$$

where

Δp_s: Pressure drop at the orifice (N/m^2)
ρ: Density of the ink (m^3/s)
V_s: Velocity of the ink (m/s)
η: Viscosity of the ink (Ns/m)
l_s: Length of the supply orifice (m)
d_s: Diameter of the supply orifice (m)

(4) Flow rate through the nozzle

To analyze the flow rate across the nozzle, we calculate the pressure with the equation(5) shown below

$$\Delta p_n = \frac{\rho V_n^2}{2} + \frac{32\eta l_n V_n}{d_n^2} \quad (5)$$

where

Δp_n: Pressure drop at the nozzle (N/m^2)
V_n: Velocity of the ink (m/s)
l_n: Length of the nozzle (m)
d_n: Diameter of the nozzle (m)

(5)Ink surface tension

In this section, we consider about the surface tension of the ink where the force acts on. We calculate an energy loss at the ink surface with equation(6)

$$E_{loss} = \pi d_n \sigma_d x_m \quad (6)$$

where

σ_d: Surface tension of the ink (N/m^2)
x_m: Position of the ink meniscus

We can calculate the length of the ink stream using the motion energy and the energy of the surface tension of the ink. The behavior of the stream can be modeled by a mechanical mass-spring system shown in Figure4.
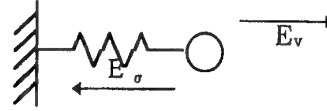
Fig.4 Ink stream model

5.Experiment
(1)Measurement system

Figure5 shows a measurement system for the meniscus of the ink. The system is composed of a microscope, a strobe light , a television camera and an image processor.

Fig.5 Measurement system

(2)Experimental results

Figure6 is the simulation and the experimental results showing the velocity of the ink stream. Figure7 shows the volume of the ink droplet.

Figure8 shows the experimental results of the ink ejection. To measure the meniscus of the ink, we applied three kind of voltage,20V,30V and 40V to the piezo-electric actuator. The dotted line shows the simulation results at each case. The simulation results agreed well to the experimental results. When the piezo-electric actuator is drived by 20V,the meniscus is not agreed well. Main reason for the disagreement is that the surface tension of the ink reduces the length of the ink stream at the case.
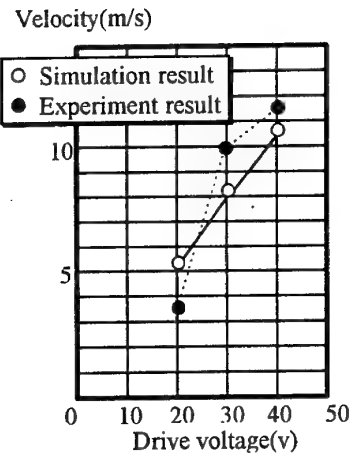
Velocity(m/s)

Fig.6 Velocity of the ink droplet

Volume of the droplet($\times 10^{-15} m^3$)
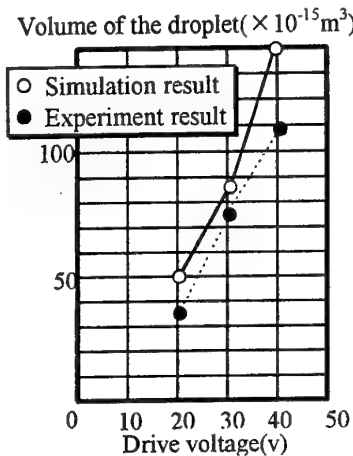
Fig.7Volume of the ink droplet

Ink meniscus($\times 10^{-6} m$)
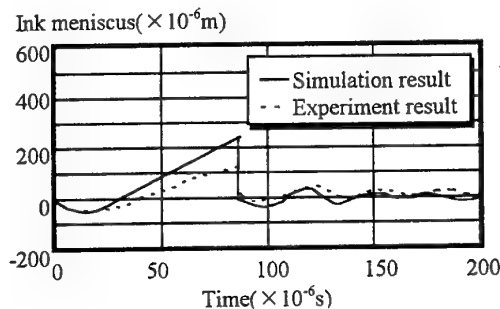
(a)Applied voltage:20V

Ink meniscus($\times 10^{-6} m$)
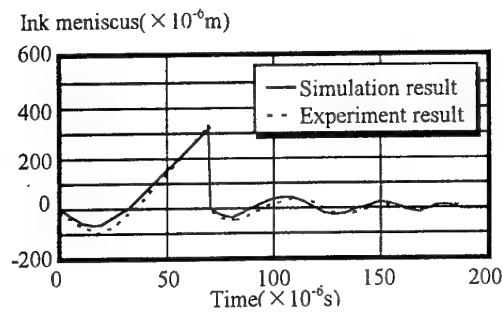
(b) Applied voltage:30V

Ink meniscus($\times 10^{-6} m$)
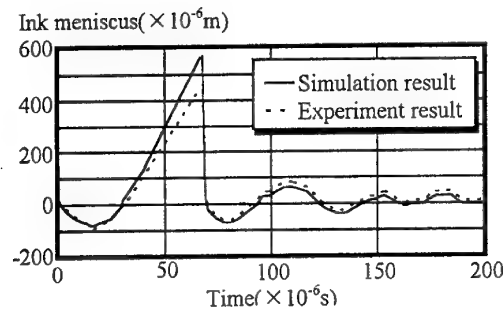
(c) Applied voltage:40V

Fig.8Meniscus of the ink ejection

6.Conclusions

In this paper, we have built a mathematical model of Kyser-type ink-jet head. With the mathematical model, we explained the effects of the dimension of the nozzle, chamber, supply orifice and the actuator. The simulation results agreed well with the experiment results, thus, we confirmed the validity of the model.

Adding to this research, we will analyze the multi-channel model and a behavior of the ink droplet which flies in the air.

References

1.Kyser, et al., "Design of an Impulse Ink Jet .J. Applied Photographic Eng.,7-3(1981),73-79.

2.Yoichiro Shimizu, Hironao Yamada, Takayoshi Mutou, Yujiro Kitaide,.
"Analysis of the ejection of Kyser type Ink Jet Head"
The 9th Symposium on Electromagnetics and Dynamics,(1997),313-316

3. C.A.BRUCE "Dependence of Ink Jet Dynamics on fluid Characteristics"
IBM J.RES.DEVELOP

Study of Electric-Field-Induced Strain in PLZT

Yoshikazu Akiyama

Fax: 81-45-590-1894, e-mail: aaki@rdc.ricoh.co.jp
Research and Development Group, RICOH Co., Ltd., 16-1 Shinei-cho, Tuzuki-ku, Yokohama 224-0035, Japan

Abstract

The strains induced by a large electric field were measured for the (Pb La) (Zr Ti)O_3 solid solution system. Three types of strains which were involved with an inverse piezoelectric effect, an electrostriction and a forced phase transition, were measured. A strain of 0.24%, large enough for high performance actuators, was observed under 40kV/cm for the 8.4/70/30 composition near the rhombohedral - cubic phase boundary.

1. Introduction

The lead zirconate titanate ceramics family causes strain under an applied electric field. There are three types of strains: first is an inverse piezoelectric effect which is defined as a primary electromechanical coupling effect, i.e. the strain is proportional to the electric field (hereafter simply described as piezoelectric effect). Second is the electrostriction which is a secondary coupling, and the strain is proportional to the square of the electric field. Third is a forced phase transition that can be observed in an antiferroelectric or paraelectric phase material. [1,2] The PLZT (lead lanthanum zirconate titanate) solid solution system has four kinds of crystal structures, as reported by Haertling and Land[3] which correspond to antiferroelectric (AFE), ferroelectric (FE_{Rh}, and FE_{Tet}), and paraelectric (PE_{Cubic}) phases at room temperature. Therefore, it is easy to obtain samples of each phase by changing the composition and systematically studying the electric field-induced strains.

In this study, the compositions near the morphotropic phase boundary (MPB) between the AFE and the rhombohedral FE (FE_{Rh}), and between the FE_{Rh} and the cubic PE (PE_{Cubic}) phases are selected, as listed in Table 1. The strain behavior will be discussed with respect to the strain / electric field relationship for PLZT with the above phase and anticipated actuator performance.

2. Experimental Procedures

Compositions were prepared according to the following formula : $(Pb_{1-x} \ La_x) \ (Zr_y \ Ti_z)_{1-x/4}O_3$, as PLZT (100x/100y/100z). Here, the compositions were adjusted to be close to the MPB by varying the amount of La with a constant ratio of Zr / Ti. Specimens were prepared essentially by a conventional sintering process. The starting materials used were PbO, La_2O_3, ZrO_2, and TiO_2 powders. The chemical purity of each material was greater than 99.9% (excluding the Hf element). The 5 wt% excess PbO was used. These oxides were mixed, ball-milled, dried, and then calcined at 850°C and 950°C. The calcined powder was formed into discs and sintered. A two-stage sintering process was used to promote grain growth, because the strain properties depend upon the size of the grain. During the first stage, the specimens were heated at 1250°C for 8h in a MgO crucible, and during the second stage, they were sintered at 1150°C for 16 - 24h in a platinum crucible. The relative density of the sintered bodies was 99%, and the average grain size, measured using scanning electron microscopy, was greater than 4μm. The disc samples were polished to approximately 0.5 mm thickness for the electric measurement. Fired-on silver paste was applied on both surfaces of the specimen as electrodes. The crystal structure of the sintered body was determined from X-ray diffraction patterns.

The dielectric properties were measured at 1 kHz using an impedance analyzer (YHP 4194A) for 2.5 mm square-shaped specimens. P-E hysteresis loop measurements were carried out at 22-23°C, and the applied electric field frequency was 0.1 Hz. The induced charge was detected using a charge amplifier.[7] The field induced strains were determined using a contact-type displacement sensor (Millitron: Model 1240) at 0.1 Hz and same temperature. Silicon oil was employed to prevent arcing under high electric field during the measurement.

3. Results and Discussion

3.1 Crystal structures

The crystal structures were examined by XRD. When the observed patterns are assumed to correspond to a cubic perovskite-type structure, the peaks at the lower and higher angles correspond to (111) and (200) plane diffractions, respectively. The diffraction pattern of PLZT (7.0/80/20) consisted of two crystal systems, i.e. tetragonal and rhombohedral structure. It was observed during a strict analysis that the 7.5/75/25 sample was a rhombohedral, the 8.6/70/30 was a pseudo cubic, and the 9/65/35 was a cubic structure. The volume of the unit cell did not depend upon the lanthanum concentration and the value increased with an increase in the zirconium / titanium ratio.

3.2 Electric permittivity

Temperature dependence of electric permittivity in the x/70/30 compositions were measured. The Curie temperature decreased with an increase in the amount of lanthanum and the maximum value of the electric permittivity decreased with an increase in the amount of lanthanum. A similar tendency was observed in

compositions with x/80/20. These phenomena can be explained by the composition change approaching the phase boundary.

3.3 Polarization and strain in PLZT (x/80/20)

P-E hysteresis loops of x/80/20 compositions are shown in Fig. 1, where a square-shaped loop changed to a slim and double-like loop with an increase in the amount of lanthanum. The 7/80/20 composition gave a double-loop with the value of remanent polarization close to zero. Figure 2 shows the strain behavior of these samples. The 6/80/20 composition gave a butterfly-shaped loop which is a typical shape of piezoelectric materials, and it had a clear coercive field (Ec), and a remanent strain at zero of the electric field. Increase in the amount of lanthanum changed the shape of the strain loop. The 7/80/20 sample did not exhibit Ec and any remanent strain. In the phase diagram of PLZT, this composition corresponds to the AEF phase. The transverse strain is toward the positive direction, if the phase is antiferroelectric, and the strain of the antiferroelectric material is not in the same direction as the transverse strain of piezoelectric and electrostriction materials. The transverse strain behavior of the 7/80/20 sample was measured. The data includes a shift of the base line and a noisy signal, because the amount of the displacement is very small. However, a slightly positive strain appears in the same electric field intensity at which the longitudinal strain occurred. Furthermore, by increasing the electric field intensity, the strain changed to a negative direction. The direction change was attributed to the piezoelectric effect of the ferroelectric phase that was derived from phase switching. The strain behavior is loose, as compared with an antiferroelectric stanate modified PZT,[2, 8, 9] Therefore, this composition is not considered to be a single phase of antiferroelectric type. The series of PLZT (x/75/25) samples exhibited only square-shaped (P-E) and butterfly-shaped (S-E) loops.

3.4 Polarization and strain in PLZT (x/70/30)

P-E hysteresis loops of x/70/30 compositions are shown in Fig. 3. A square-shaped loop changed to a slim-loop with an increase in the amount of lanthanum. The 8.6/70/30 composition gave a distorted slim shape. This shape is similar to that of the 7/80/20 sample which involves the AFE phase. However the X-ray diffraction pattern and the transverse measurement did not exhibit antiferroelectric appearances. Figure 4 shows the strain behavior under unipolar driving of the electric field from 0 to 40 kV/cm. Unipolar driving is critical for actuator devices. It is easy to understand that the 7.6/70/30 composition has undesirable properties for actuator devices, as it has remanent strain. The piezoelectric coefficient (d_{33}) was calculated directly from the slope of the strain versus the electric field in the high field region (between 30 and 40 kV/cm in Fig. 4). The values of d_{33} for the 7.6/7./30, 8.2/70/30, 8.6/70/30 samples are 245, 249 and 248 pm/V, respectively. These approximately similar

values imply that a strain derived under a large electric field comes from a common origin. We introduce the concept of the "micro polar domain" for the explanation of these phenomena. The FE_{Rh} phase changes to a PE_{Cubic} phase with an increase in the amount of lanthanum. The 8.6/70/30 sample has a small amount of remanent polarization. Therefore, this composition is not a paraelectric phase at the P-E hysteresis measurement temperature. It is just called "quasi ferroelectric phase".[10] Randomly oriented micro polar domains will be arranged by electrostriction effect, and become a ferroelectric domain. At this point, the materials involve displacement, and the derived ferroelectric domain is the same as another ferroelectric one, and finally the resulting value of the piezoelectric coefficient coincides with another value of ferroelectric. Namely, the electric field-induced strain takes place by multiple steps involving micro polar domain transformation and domain reorientation. Decreasing the spontaneous polarization with a decreased lanthanum ratio (shown in Fig. 3) because of an arrangement of the micro polar domain, it has been necessary for some free energies. A definition of micro polar domain is not easy because the micro polar domain has a specific volume which depends upon the composition or an effective volume which is associated with the harmonic space which will be changeable for the composition. This problem will be solved in the near future.

3.5 Virgin strain effects

Figure 5 shows the strain behavior of the virgin samples. The samples (a), (b) and (c) have the 7/80/20, 7.5/75/25, 8.6/70/30 compositions, respectively. The samples (a) and (b) have a virgin strain, which comes from an antiferroelectric and ferroelectric domain arrangement, whereas sample (c) does not has it. In Fig. 5, the bar indicates an effective strain at the actuator driving. Sample (c) does not have the virgin and remanent strains. The generated maximum strain was approximately 0.24 % at 40 kV/cm.

4. Conclusion

We have elucidated a complete set of dielectric properties, and the polarization and the electric field induced strain data for a series of PLZT ceramic compositions. Three types of strains: an inverse piezoelectric effect, an electrostriction and a forced phase transition were measured. In the high electric field intensity, the strain behavior is associated with both the structural switching and domain reorientation. The quasi ferroelectric phase of PLZT does not have the virgin and the remanent strains. A strain of 0.24% was observed under 40 kV/cm for the 8.4/70/30 composition. This material is a promising candidate for high performance actuators.

Table I. Physical, dielectric, ferroelectric and strain properties for various compositions in the PLZT system.

La	Zr	Ti	d	D	Cryst.	a	c	a'	ε_r(RT)	tanδ	Tc	ε_r(max)	Pind	Pr	Ec	Phase	Strain1	Strain2	d(1)
6.00	80.0	20.0	7.71	-	p-T+R	4.122	4.106	4.117	2120	2.5	129.3	6760	34.1	28.9	7.9	F	0.171	0.106	221
6.25	80.0	20.0	7.72	-	p-T+R	-	-	-	2200	2.1	123.2	6200	34.1	27.8	7.4	F	0.160	0.115	259
6.50	80.0	20.0	7.72	-	pseudo-T	4.121	4.102	4.115	2020	2.1	121.4	5370	33.3	-	-	F-AF	0.166	0.114	204
6.75	80.0	20.0	7.68	-	pseudo-T	-	-	-	2180	1.9	116.7	5250	32.4	-	-	F-AF	0.154	0.149	210
7.00	80.0	20.0	7.67	4.5	pseudo-T	4.118	4.102	4.113	1940	1.5	114.9	4210	29.5	-	-	AF	0.137	0.135	283
6.70	75.0	25.0	7.67	-	pseudo-C	4.099	-	4.099	2660	3.2	114.9	10350	32.2	26.9	6.1	F	0.234	0.128	228
7.10	75.0	25.0	7.61	-	pseudo-C	-	-	-	3390	3.1	98.1	8920	32.9	27.2	5.9	F	0.248	0.135	258
7.25	75.0	25.0	7.60	-	pseudo-C	-	-	-	3390	3.2	97.7	9340	32.9	27.3	6.1	F	0.232	0.132	240
7.50	75.0	25.0	7.62	-	pseudo-C	4.100	-	4.100	3490	2.9	93.5	12500	32.5	25.4	5.9	F	0.180	0.127	223
7.60	70.0	30.0	7.59	4.5	pseudo-C	4.096	-	4.096	3970	3.2	93.5	11850	33.6	27.5	5.3	F	0.287	0.142	245
8.00	70.0	30.0	7.57	-	pseudo-C	-	-	-	4130	2.9	83.5	9570	31.5	-	-	P-F	0.255	0.224	215
8.20	70.0	30.0	7.60	-	Cubic	4.094	-	4.094	4060	2.9	81.9	9390	31.8	-	-	P-F	0.245	0.234	249
8.40	70.0	30.0	7.56	-	Cubic	-	-	-	4130	2.9	80.1	8610	31.4	-	-	P-F	0.246	0.244	248
8.60	70.0	30.0	7.52	7.7	Cubic	4.096	-	4.096	4260	2.9	75.9	8550	30.9	-	-	P-F	0.243	0.237	272
9.00	65.0	35.0	7.62	9.0	Cubic	4.083	-	4.083	4720	3.2	80.9	10370	31.3	-	-	P-F	0.260	-	290

d: density (g/cm³), D: grain size (μ m), Cryst.: crystal phase, a and c: unit cell parameter, a': cubic root of cell volume, ε_r(RT): permittivity at room temperature, tanδ: dielectric loss (%), Tc: Curie point (℃), ε_r(max): maximum permittivity, Pind: induced polarization at 40 kV/cm, Pr: remanent polarization (μ C/cm²), Ec: coercive field (kV/cm), Phase: ferroelectric phases, Strain 1: maximum strain under bipolar driving, Strain 2: maximum strain under unipolar driving, d(1): piezoelectric coefficient derived at strain (E-field region between 30 and 40 kV/cm).
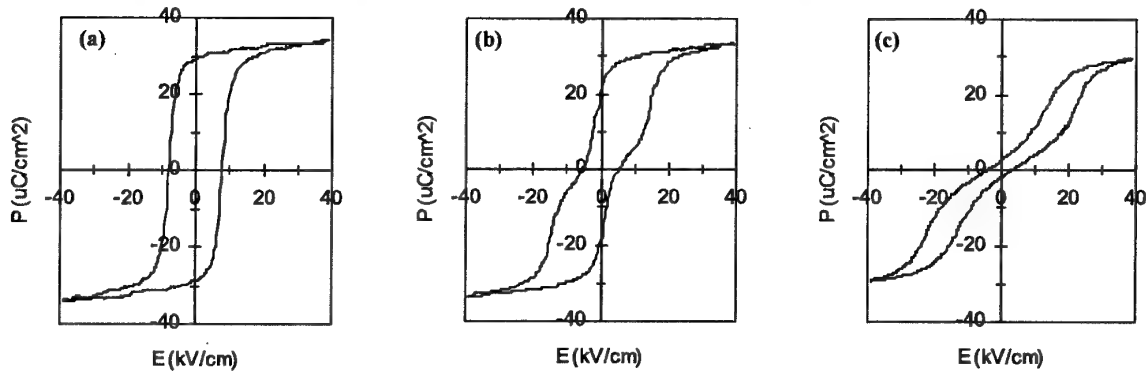
Fig. 1. P-E hysteresis loops for (a) PLZT 6/80/20, (b) PLZT 6.5/80/20, (c) PLZT 7.0/80/20.
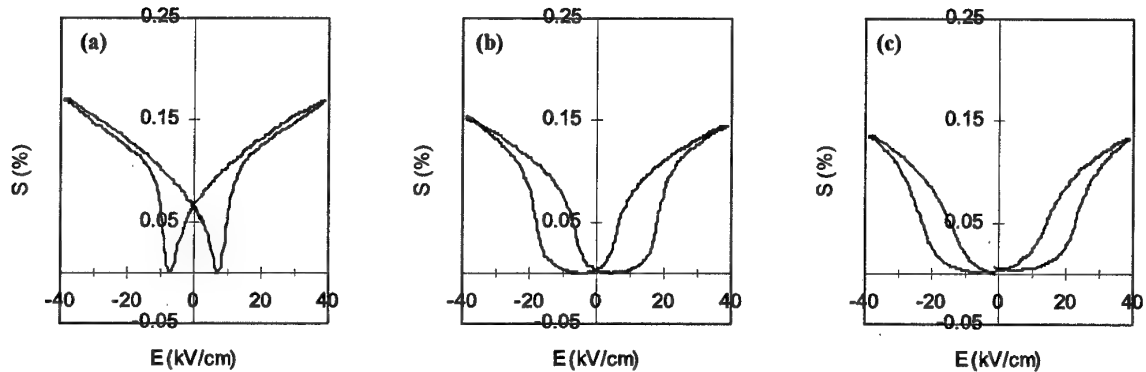
Fig. 2. Lougitudinal strain loops for (a) PLZT 6/80/20, (b) PLZT 6.75/80/20, (c) PLZT 7.0/80/20.
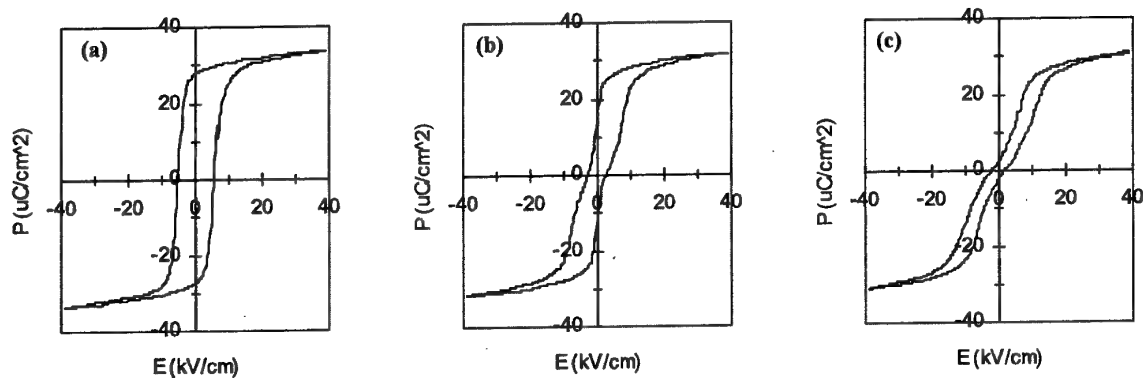
Fig. 3. P-E hysteresis loops for (a) PLZT 7.6/70/30, (b) PLZT 8.2/70/30, (c) PLZT 8.6/70/30.
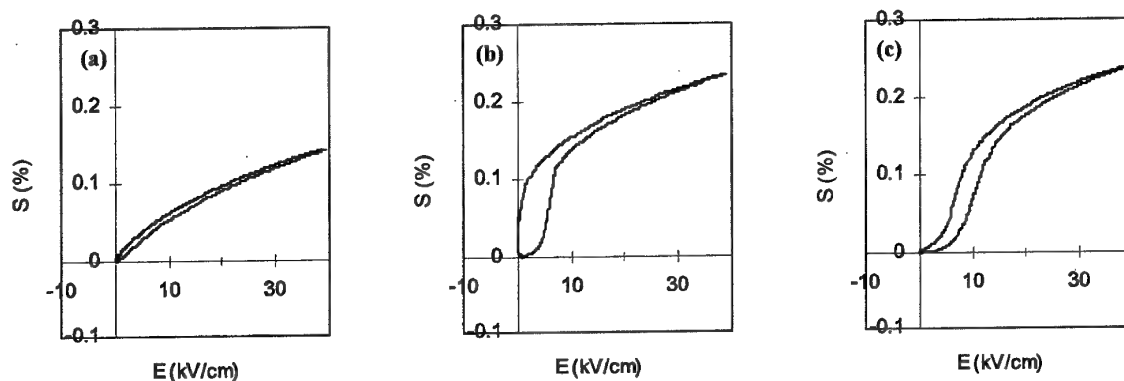
Fig. 4. Lougitudinal strain loops for (a) PLZT 7.6/70/30, (b) PLZT 8.2/70/30, (c) PLZT 8.6/70/30.
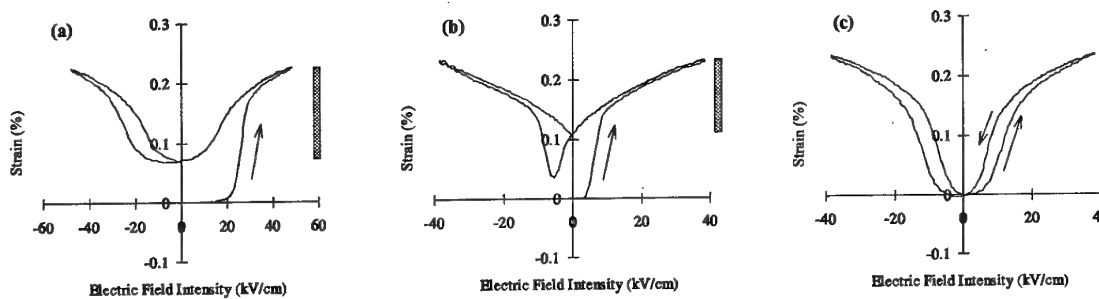
Fig. 5. Strain behavior of virgin samples for (a) PLZT 7/80/20, (b) PLZT 7.5/75/25, (c) PLZT 8.6/70/30.

References
1) L. E. Cross, S. J. Jang, R. E. Newnham, S. Nomura and K. Uchino: Ferroelectrics 23 (1980) 187
2) Y. Akiyama and E. Fujisawa: Jpn. J. Appl. Phys. 36 (1997) 5997
3) G. H. Haertling and C. E. Land: J. Am. Ceram. Soc. 54 (1971) 1
4) Landolt-Bornstein III 16/a Ferroelectrics and Related Substances, ed. K. H. Hellwege (Springer-Verlag Berlin-Heidelberg, 1981)
5) D. Luff, R. Lane, K. R. Brown and H. J. Marshallsay: Trans. J. Br. Ceram. Soc. 73 (1974) 251
6) K. Furuta and K. Uchino: Adv. Ceram. Mater. 1 (1986) 61
7) M. Date, T. Furukawa and E. Fukada: J. Appl. Phys. 51 (1980) 3830
8) Y. Akiyama, S. Kimura and I. Fujimura: Jpn. J. Appl. Phys. 32 (1993) 4154
9) S. E. Park, M. J. Pan, K. Markowski, S. Yoshikawa and L. E. Cross: J. Appl. Phys. 82 (1997) 1798
10) K. Carl and K. Geisen : Proc. IEEE 61 (1973) 967

The Electrical Properties of Thin Barium Strontium Titanate Films and their Impact on the Performance of Capacitors for DRAM Memories

T.M Shaw*, J.D. Baniecki[+], R.B. Laibowitz*, E.Liniger*,Z. Suo[++], M. Huang[+], D.E. Kotecki**, J. Lian[++], H. Shen[++].

*IBM Research Division, T.J. Watson Research Center, Yorktown Heights, New York 10598,
**IBM Microelectronics Division, Hopewell Junction, New York 12533,
[+]Columbia University, New York, New York 10027
[++] Princeton University, Princeton NJ 08544
[++]Siemens Microelctronics Incorporated Hopewell Junction, New York 12533.

ABSTRACT
The factors that influence the performance of Barium Strontium Titanate as a dielectric for DRAM capacitors are examined. The studies indicate that the dielectric properties of the thin films can be understood in terms of simple model in which the interior of the films have dielectric properties similar to that of bulk material whereas a layer of lower pemitivity material forms at each electrode interface. The effect of stress on capacitance is also quantified. Charge retention in the capacitors is shown to depend strongly on the annealing conditions the dielectric is subjected to during integration. Possible models of the influence of annealing on leakage and dielectric relaxation are discussed.

INTRODUCTION
The historical trend for the density of DRAM memories has been for the density to increase by a factor of 4X every three years. However, as cell size and hence the corresponding chip area occupied by capacitor has decreased the required capacitance per unit area has remained nearly constant at 25-30 fF/cell. The fixed capacitance is set by the need to store sufficient charge to trigger sense amplifiers, overcome the parasitic capacitance of the bit line, and overcome noise introduced by events such as alpha particles. This trend has lead to the need for dielectrics that have a high charge storage density[1].

Figure (1) shows an example of the charge storage density required for 30 fF stacked capacitors of different heights as a function of minimum capacitor dimension
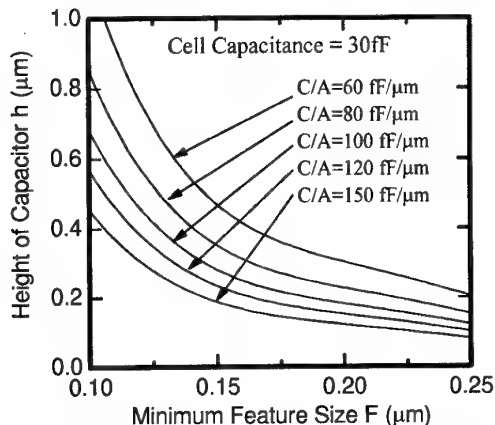
Figure (1) The variation of stacked-capacitor height with minimum feature size for dielectrics with different specific capcitances.

. As can be seen, if the stack height is limited to 0.5µm, a specific capacitance on the order of 150 fF/µm² will be required as the dimension of the minimum feature size approaches 0.1µm. In addition to charge storage, charge loss from the capacitor must also be limited to about 1 fA per capacitor to enable reliable reading of the DRAM cell after a memory refresh cycle.

The high charge storage densities attainable using the parraelectric phase of ferroelectric materials make them attractive as dielectrics for DRAM capacitors. For example charge storage densities as high as 140 fF/µm² have been achieved in barium strontium titanate BSTO films making it a leading candidate for use is stacked DRAM capacitor structures [1,2]. Evaluation of the properties of BSTO dielectrics shows that films in the thickness range 10-30nm will be required to meet the requirements of future generations of DRAM memories. The electrical properties BSTO films in this thickness range differ significantly from those of the more conventional silicon oxynitride dielectrics currently in use. In particular the measured permitivity of BSTO films is found to vary significantly with stress, temperature, film thickness, electric field and frequency[1,3-5]. In addition to understanding the basic properties BSTO films, the impact of annealing and etching processes on the electrical properties is required to integrate capacitors into DRAM device structures.

This paper presents the results of studies we have made of the leakage, dielectric relaxation and stress and temperature dependence of the dielectric properties of different thickness MOCVD grown BSTO films.

EXPERIMENTAL
The films for the present study were prepared by MOCVD deposition using a liquid delivery system[6] . Ba(thd)2(4-glyme), Sr(thd)2(4-glyme), and Ti(i-OPr)2 (thd)2 were used as the liquid metal organic sources.

Silicon substrates with a 400nm thick coating of SiO₂ followed by a blanket 100nm thick Pt electrode were used as substrates. BSTO Films were deposited with a Ba/Sr ratio of 70/30 in the temperature range of 600-700°C. The electrical properties of the films were measured on 100μm diameter Pt dots deposited on the film by e-beam evaporation through a shadow mask. An HP 4274A LCR meter was used for capacitance measurements. Leakage and dielectric relaxation measurements were made using an HP 4140B pico ameter.

CAPACITANCE OF THIN BSTO FILMS

Figure(2)a shows a comparison between the temperature dependence of a 100nm thick BSTO film prepared by MOCVD and a capacitor prepared from bulk ceramic material of the same composition . It is immediately apparent that, in contrast to the sharp ferroelectric transition observed in the ceramic, the thin film has only a broad maximum in capacitance and much reduced dielectric constant. Suprisingly however, reploting of the same data as $1/\varepsilon$ vs temperature reveals that over a temperature range above the maximum in capacitance the

film follows a Curie-Weiss law with a Curie constant close to that observed in the bulk ceramic. The curve for the thin film, however is displaced up from that of the ceramic in the Curie Weiss plot. We find that several factors contribute to this displacement.

The first factor is the large biaxial tensile stress (600-700 Mpa) that is present in the thin film after deposition. To quantify this effect, the variation in the capacitance of a thin film BSTO capacitor with applied stress was monitored during biaxial loading on a wafer bending jig. A plot of reciprocal of the effective dielectric constant of the film shown in Figure (3) shows a linear relationship with applied stress as expected from the electrostrictive behaviour of a paraelectric phase. The slope of the curve gives an estimate of the electrostrictive coefficient Q_{12} . The estimated value for Q_{12} of $2.26 \times 10^{-2} m^4/C^2$ is close to that observed in bulk Barium Titanate[7]. Using this value we estimate that the stresses in the as deposited film are responsible for a 20-25% reduction in film capacitance. A plot of a stress shifted line on the Curie-Weiss plot in figure (2)b shows that stress alone cannot account for that difference in capacitance of the thin film. (See also Ref 4)

Figure(2) A comparison of the temperature dependence of the dielectric properties of ceramic and thin film BSTO.
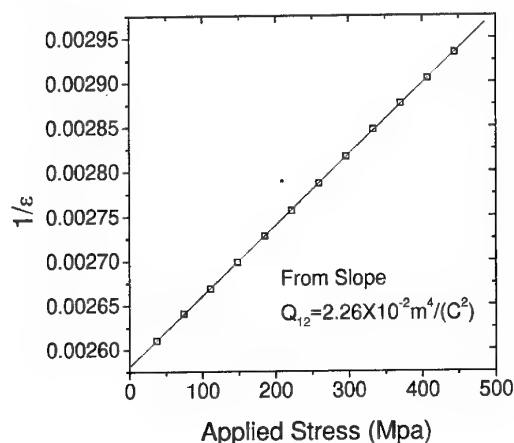
Figure(3) The effect of an applied stress on the capacitance of a 100nm thick BSTO film.

A second factor that is known to contribute to a reduction in capacitance in thin BSTO films is the presence of an apparent interfacial layer at the electrode dielectric interface. This is most clearly revealed in a plot of 1/capacitance vs film thickness, as has been shown by numerous other authors[1,3]. A simple series capacitance model predicts a linear relationship with an intercept equal the value of the interfacial capacitance. Experimentally we observe that this linear relationship holds down to the thinnest films measured (8nm) implying that any interfacial layer present is less than 4nm thick. Under optimized conditions we have obtained films with an apparent interfacial capacitance of 200fF/μm² allowing us to produce films with a specific capacitance as high as 140fF/μm². For the processing conditions used to prepare the film in figure(2)

asomewhat lower interfacial capacitance of $80fF/\mu m^2$ was obtained.

Several possible explanations for the presence of an interfacial capacitance have been ruled out. Transmission electron microscopy studies have failed to detect the presence of a second phase at the electrode interface that could account for the capacitance. It is also known that films in the thickness range studied are fully depleted of free charge[8]. Thus variations in the width of depletion regions at the electrode interfaces cannot contribute to the film capacitance. Zhou and Newns[9] have proposed on the basis of the Thomas theory of ferrolectricity that an intrinsic layer in which ferrolectricity is suppressed may be present at the surface of a ferroelectric materials. This so called "dead layer" would be expected to have a dielectric constant corresponding to that of the material in the absence of ferrolecroicity and a thickness of a few unit cells.

Based on the current observations we propose the following phenomenological model to describe the temperature and thickness dependence of the capacitance of BSTO films. It is proposed that the center of the film has dielectric properties identical to those of bulk material including a Curie Weiss temperature dependence for its dielectric constant. The effect of film stress is compensated for by shifting the Curie Weiss law by the appropriate factor. A similar correction for Ti eccess in the film can also be made[4]. The dielectric constant of an interfacial layer of thickness t_i is assumed to have a reduced dielectric constant that is temperature independent as observed by Basceri et al[3]. Using this model the effective dielectric constant for the film is described by the following equations.

$$\varepsilon_{eff} = \frac{t}{\varepsilon_0}\frac{C}{A}$$

$$\frac{A}{C} = \frac{A}{C_b} + \frac{2A}{C_i}$$

$$\frac{1}{\varepsilon_{eff}} = \frac{t-2t_i}{t}\gamma(T - T_0) + \frac{2t_i}{t\varepsilon_i}$$

Where A is the area of the capacitor, C_b and C_i are the capacitance of the bulk and interfacial regions of the film, t is the total film thickness and γ is the reciprocal Curie constant. T_0 is the bulk ferroelectric transition temperature. This functional form is the same as that predicted by the model of Zhou and Newns[9].

It is apparent from this relationship that the effect of the interfacial capacitance is to shift the Curie Weiss curve for the thin films vertically on a Curie Weiss plot as is experimentally observed. A comparison data from several different thickness films with the prediction based on the bulk ceramic data is shown in figure(4). The observed trend of upward displacement of Curie Weiss curves in thin films is in substantial agreement with the prediction of this simple model. A less obvious feature of the model is that it predicts that the slope of the Curie Weiss curve is also thickness dependent as can be seen from inspection of the above equations. Indeed theprediction is that the slope should depend only on the thickness of

the film, the reciprocal Curie constant γ for the bulk material, both of which are known, and the thickness of the interfacial layer. Thus by examining the thickness dependence of the apparent Curie constant an estimate of the thickness of the interfacial layer can be made. A plot of the apparent reciprocal Curie constant γ' vs film thickness is shown in figure (5). The predicted decrease in γ' in the thinner films and an asymptotic rise of γ' to the bulk value with increasing film thickness are both observed. A fit to the experimental data gives an estimate of 3.7nm +/- 1nm for the thickness of the interfacial layer. This value combined with the interfacial capacitance obtained from the plot of 1/C vs film thickness gives an estimated value for the dielectric constant of the interfacial layer of 50-70.
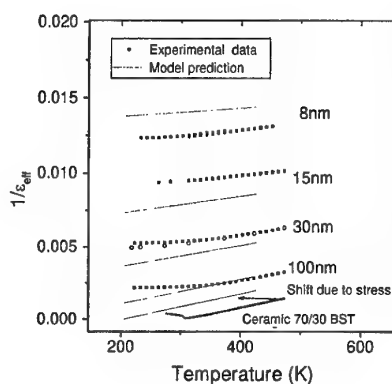
Figure(4) Comparison of the temperature dependence of the dielectric constant of different thickness BSTO films with the model descibed in the text.
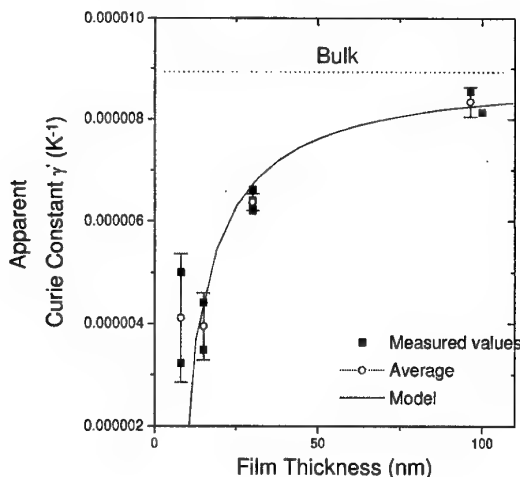
Figure(5). Variation in the apparent curie constant for BSTO thin films with film thickness.

The dielectric constant of 70%Ba/30%Sr BSTO in the absence of a ferroelectric contribution can be estimated from the atomic polarizabilities of the individual atom using the procedure described by Shannon[10]. The exact value calculated depends sensitively on the volume of the unit cell but for a cell volume of 0.064nm^3 we obtain a value of 68 which lies in the range for the estimated dielectric constant of the dead layer. Our experimental observations are therefore in responsible agreement with the predictions of dead layer model of Zhou and Newns. However, basic theory is unable to account for the variations interfacial capacitance that are seen with changes in processing. Also recent observations suggest that use of oxide electrodes can completely remove the interfacial capacitance[11,12]. As the original model only considered the free surface of a ferroelectric it is possible that a more complete model in which the presence of the electrode is consider could account for these difficulties.

CHARGE LOSS MECHANISMS

In conventional oxynitride dielectrics used for DRAM capacitors charge retention is influenced only by the leakage current of the dielectric. In BSTO the response of the material to an applied field is more complex. At short times there is the high frequency dielectric response of the material. At intermediate times, however, there is a slower dielectric relaxation that results in a continuous polarization of the material over a very broad time range (nSecs-1000) secs[13,14]. This results in a dielectric relaxation current that follows an inverse power law with an exponent close to unity. At long times a steady state current corresponding to the leakage of the film is reached. Both the dielectric relaxation current and the steady state leakage current can contribute to loss of the available charge to activate the sense amplifier in a DRAM circuit. Both these contributions to charge loss are considered below.

Steady State Leakage currents

Several authors have shown that the steady state leakage currents in BSTO at intermediate fields is controlled by the barrier height lowering caused by the Schottky effect at the electrode dielectric interface[15,16]. Both the electric field and temperature dependence of the leakage fit well to the standard expression for thermionic emission over a reverse biased Schottky barrier. It has also been shown for strontium titanate there is a strong work function dependence to the leakage current as expected for an ideal Schottky barrier[16]. One complication, however, that has been noted is that the value obtained for the Richardson constant is unphysically small implying a greatly reduce carrier mobility in the films[15,17]. Another difficulty is that the leakage is very sensitive to annealing conditions. Figure(6) shows the effect of various annealing treatments on the voltage dependence of the leakage in a 30nm thick BSTO film[18]. As deposited the film has a unacceptably large leakage current. On annealing in oxygen this is reduced by several orders of magnitude. Forming gas annealing, a commonly used process in semiconductor manufacture, also has a big impact on the leakage currents observed.
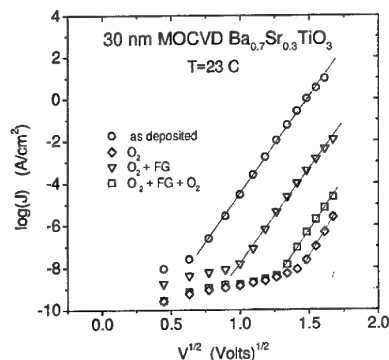
Figure(6) The effect of annealing conditions on the voltage dependence of the leakage current.

Annealing at 400°C for 20 mins increases the leakage current significantly. The effect however can be reversed by reannealing in oxygen. Barrier heights extracted from the voltage a temperature dependence of the leakage current are shown in Table I. It can be seen that the observed changes in leakage correlate well with the measured changes in barrier height. It is difficult to reconcile these observations with the fully deleted nature of the films if an ideal Schottky barrier model is adopted. It seems likely that one of the effects of the annealing treatments is modulate the density of mid gap states that are present at electrode/dielectric interface and hence the extent to which Fermi level pinning controls the barrier height. Further experimentation is need to understand these effects in detail.

Table I The effect of annealing conditions on the Schottky barrier height measured for thin BSTO films.

Annealing Condition	Barrier Height eV	Applied voltage Volts
as deposited	0.67	1.4
550 C 15 min O2	1.29	2.2
550C 15 min O2 + 400 C 20 min FG	0.92	1.6
550 C 15 min O2 +400 C 20 min FG + 400 C 20 min O2	1.22	2.2

Dielectric relaxation

The dielectric relaxation currents observed in BSTO have also been the subject of several investigations. The voltage, time and temperature dependence of these currents have all been studied[14,19-21]. The temperature dependence of the relaxation currents is particularly striking. As shown for our films in figure (7) the magnitude of the relaxation currents are also essentially independent of temperature below room temperature but
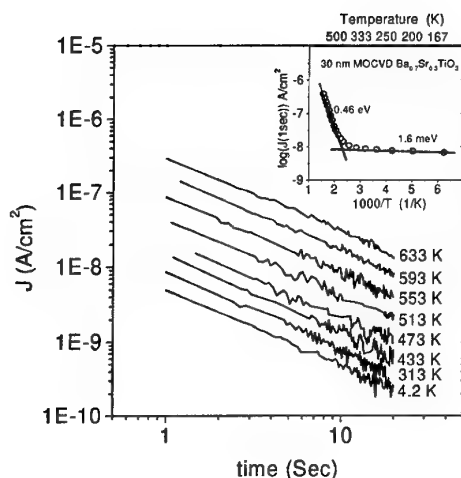
Figure(7) Temperature dependence of the relaxation currents observed in a 30nm thick BSTO film

rise steeply with an activation energy of 0.46eV at higher temperatures. Similar behavior has been reported by Schumacher et al[18] . They have proposed that hoping between localized impurity defect states near the fermi level leads to the weak temperature dependence at low temperatures., whereas thermal excitation of carriers into the conduction band occurs at higher temperatures. A similar temperature dependence can also arise from a polaron hoping model[22,23,24]

As with the steady state leakage currents annealing in different atmospheres has a strong influence on the magnitude of the relaxation currents[18,20]. The effect forming gas annealing is shown in figure(8). An initial anneal in oxygen has little effect on the relaxation currents but annealing in forming gas for 20 mins at 400°C causes them to increase by more that an order of magnitude.
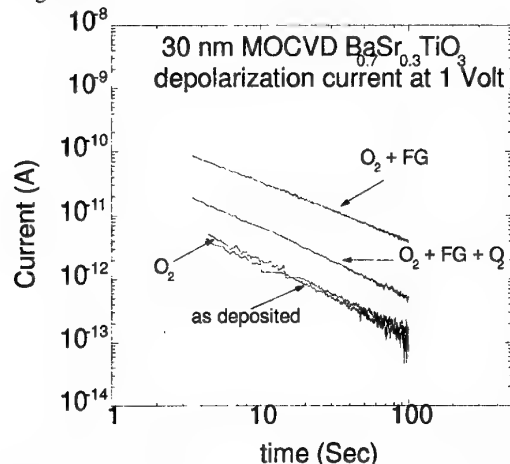
Figure(8) The effect of annealing conditions on the relaxation currents observed in thin BSTO films.

This effect can only be partially reversed by reannealing in oxygen. A similar increase in relaxation currents is observed if a film is vacuum annealed in the absence of hydrogen, only in this case the effect is completely reversible. These observations suggest both reduction, creating oxygen vacancies, and the dissolution of hydrogen in the film may contribute to the increased relaxation currents. At present there is no detailed understanding of the types of defects that are responsible for relaxation currents.
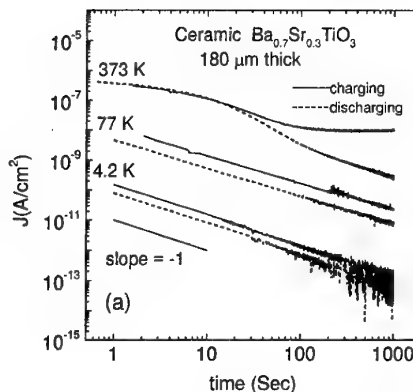
Figure(9) Dielectric relaxation currents observed in ceramic BSTO capacitors.

Some indication that the relaxation currents are not simply associated with the high density of grain boundaries in thin MOCVD films is provided by the study of bulk ceramic materials. Figure (9) shows the response of a capacitor made from a thin disk of BSTO (grain size 10μm) to a step voltage of 10 volts. At 373K a typical Debye like response is seen . This , however is suppressed at lower temperatures revealing a power law relaxation current that persists to 4.2K. The magnitude of the observed relaxation currents is comparable to those observed in thin films. Similar behavior can also be seen in single crystal strontium titanate. These observations strongly support the idea the relaxation currents are associated with point defects in the bulk of the film.

CONCLUSIONS

The dielectric properties of BSTO thin films can be understood in terms of simple model in which the interior of the films have dielectric properties similar to that of bulk material whereas a layer of lower pemitivity material forms at each electrode interface. Stress also affects the capacitance of the films causing a 20-30% reduction in the charge storage density in the films studied in this paper. Charge loss from BSTO capacitors as strongly affected by the annealing treatments used during device integration. Both leakage currents and dielectric relaxation contributions to charge loss are increased by annealing in forming gas. A better understanding of the mechanisms that lead to this degradation is needed.

REFERENCES:

[1] D.E. Kotecki, J.D. Banieck, H. Shen, R. Laibowitz, K.L. Saenger, J. Lian, T.M. Shaw, S. Athavale, C. Cabral Jr., P. Duncombe, M. Gutsche, G. Kunkel, Y.J. Park, Y. Wang, and R. Wise, IBM J Res. Dev 43(3), 36 (1999).

[2]A.I. Kingon, S.K. Streiffer, C. Basceri and S.R. Summerfelt, MRS Bull. 21, 46 (1996).

[3]C. Basceri, S.K. Streiffer, A. I. Kingon, R.Waser, J. Appl. Phys. 82 (5), 2497 (1997).

[4]S.K. Streifer, C. Basceri, C.B. Parker, S.E. Lash, J. Christman, H. Maiwa, and A.I. Kingon, Proc. Int. Symp. On the Applic. Of Ferroelectrics, in press (1999). S.K. Streiffer, C. Basceri, C.B. Parker, S.E. Lash, and A.I. Kingon Submitted J. Appl. Phys.

[5]S. Hoffmann and Rainer Waser, 2nd European Meeting on Integrated Ferroelectrics EMIF2, Sept. 29-30, (1997)

[6]H. Shen, D.E. Kotecki, R.J. Murphy, M. Zaitz, R.B. Laibowitz, T.M. Shaw, K.L. Saenger, J. Baniecki, G. Beitel, V. Kueppel and H. Cerva, Mater. Res. Soc. Symp. Proc. 493, 33 (1997).

[7]M.E. Lines and A.M. Glass, "Principles and Applications of Ferroelectrics and Related Materails",Clarendon, Oxford, (1977).

[8]. Copel, P.R. Duncombe, D.A. Neumayer, T.M Shaw, and R.M. Tromp, Appl. Phys. Lett. 70, 3227 (1997).

[9]C. Zhou and D. M. Newns, J. Appl. Phys. 82 (6), 3081 (1997).

[10]R.D. Shanon J. Appl. Phys. 73(1), 348, (1993).

[11]C.S. Hwamg, B.T. Lee, C.S. Kamg, K.H. Lee, H.J. Cho, H. Hideki, W. D. Kim, S.I. Leeand M. Y. Lee, J. Appl. Phys. 85, 287, (1999).

[12] K, Hieda, K. Eguchi, N. Fukushima, T. Aoyama, K. Natori, M. Kiyotoshi, S. Yamazaki, M. Izuha, S. Niwa, Y. Fukuzimi, Y. Ishibashi, Y. Kohyama, T. Arikado, and K. Okumura, Proceedings of the International Electron Devices Meeting (IEEE, New York, 1998), p. 807.

[13]S.K. Streiffer, C. Basceri, A.I. Kingon, S. Lipa, S Bilodeau, R. Carl, and P.C. van Buskirk, Mater. Res. Soc. Symp. Proc. 415, 219 (1996)

[14]J.D. Baniecki, R.B. Laibowitz, T.M. Shaw, P.R. Duncombe, D.A. Neumayer, D.E. Kotecki, H. Shen, Q.Y. Ma, Appl. Phys. Lett., 72 (4), 26 Jan., 498 (1998).

[15]W. Dietz, M. Schumacher, R. Waser, S.K. Streiffer, C. Basceri, and A. I. Kingon, J. Appl. Phys. 82 (5), 1 Sept., 2359 (1997).

[16]G.W. Dietz and R. Waser, "Charge Injection into SrTiO3 Thin Films", Thin Solid Films, Vol. 299 No. 1-2, May 15, pp 53-58 (1997).

[17]S. Zafar, R.E. Jones, B. Jiang, B. White, V. Kaushik, and S. Gillespie Appl. Phys. Lett. 73(24), 3533, (1998).

[18] J.D. Banieck,R. B. Laibowitz , T.M. Shaw, K.L. Saenger, P. Duncombe, C. Cabral Jr., D. E. Kotecki, H. Shen, J. Lian and Q.Y. Ma, J. European Ceram. Soc 19, 1457 (1999)

[19]M. Schumacher and R. Waser, Vol. 22, pp 109-121 (1998).

[20] Y. Fukuda, H. Haneda, I. Sakaguchi, K. Numata, K. Aoki, and A Nishimura, Jpn. J. Appl. Phys. 36, Part2, 11B, L1514 (1997).

[21]S. Zafar, R. E. Jones, P. Chu, B. White, B. Jiang, D. Taylor, P. Zurcher, and S. Gillespie, Appl. Phys . Lett. 72(22), 2820, (1998).

[22] A.P. Schmid, J. Appl. Phys., Vol 40, No. 10. pp 4128, (1969)

[23]K. Shimakawa, Phil. Mag. B, Vol. 46, No2., pp 123 (1982),

[24]D. Emin, Phys. Rev. B, Vol. 46, No. 15 pp 9419, (1992)

The Ferroelectric Memories and It's Applications

Hidemi TAKASU

Semiconductor Research and Development Headquarters, ROHM CO., LTD. 21, Saiin Mizosaki-cho,
Ukyo-ku, Kyoto 615-8585, Japan

Abstract

The ferroelectric memory is not an ideal memory with it the clear advantages such as non-volatility, low power consumption, high endurance and high speed writing, but also the most suitable device for memory embedded applications. Its manufacturing process makes it more compatible with the standard CMOS process than the traditional non-volatile memory process, due to the device does not require and high voltage operations, and the ferroelectric process does not influence to the characteristics of CMOS devices used in logic cells, analog cells and core cells. In the spreading of IP (Intellectual Property) application for LSI Industry, this embedded application takes more important position.

In the near future, the ferroelectric memory technology will be taken into reconfigurable devices as programmable interconnect switches besides using as embedded memories. These ferroelectric memory based reconfigurable devices can be used as DPGA (Dynamic Programmable Gate Array), which is able to be reconfigured their original logic in a system under a operation mode.

New logic circuits will take the position for lower power consumption or a resume function by introducing ferroelectric gated transistors or ferroelectric capacitors.

Even the ferroelectric memory technology has many advantages, it is not popular yet. Because, the conventional semiconductor process degrade the ferroelectric layer easily. How to prevent from this degradation of ferroelectric film in the silicon wafer process will be discussed also.

1. INTRODUCTION

The needs for lower power and non-volatility on memory devices are increasing by the magnifying demand for portable electronic apparatuses such as mobile phones.

PDA requires not only higher speed access but also higher speed writing. The conventional non-volatile memories have limited endurance up to 1 million cycles, which is not enough for the variety of applications using non-volatile memories.

Battery back up SRAMs should be replaced to non-volatile memories from the viewpoint of the ecology problems.

The development work of ferroelectric memories has been around since the 1960's[1], but the works have not spread as fast as other silicon technology, because the introduction of a new material such as PZT ($PbZr_xTi_{1-x}O_3$) to the silicon process is not welcome.

In 1988, a 1T1C (1 transistor and 1 capacitor) nonvolatile ferroelectric memory [2] was presented, and showed us the potential to be a practical memory. The further progress of thin film technology of PZT and $BiSr_2Ta_2O_9$, and strong demands on nonvolatile memories for portable system applications have been promoting the development works for ferroelectric memories.

Today serial 4k-64k FRAMs and FRAM embedded RF-ID chips are available at the market.

2. FEATURES OF FERROELECTRIC MEMORIES

Conventional non-volatile memories are ROM type only, and are used for limited application area. On the other hand, ferroelectric memories are non-volatile RAM, and will provide wider application field than existing conventional memories.

There are 2 types of memory operation principals for ferroelectric memories as shown in Fig. 1. One type is a detecting the charge of stored electric charges (the differential between the polarization switching charge current and the polarization none-switching charge current), another type is a detecting the difference of FET channel conductance. This channel conductance is modified by the polarization direction of
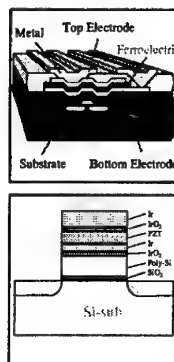
• Ferroelectric Process adapts
   to CMOS Process WELL.

• Ferroelectric Process influences
   LESS in CMOS Device charactristics.

Fig. 1. Ferroelectric Process Adaptability

	Nonvolatile Memory		Read Only Memory				Random Access Memory	
	FFRAM	FRAM	FLASH	EEPROM	EPROM	MaskROM	DRAM	SRAM
Access Time	60ns	200ns	120ns	150ns	120ns	120ns	70ns	70ns
Programming Time	100ns	400ns	10μs	10ms	10ms	N/A	70ns	70ns
Programming Voltage	5V	5V	12V	12.5V	12.5V	N/A	5V	5V
Erase Time	—	0ns	10ms	0ms	(15Wmolus²)	N/A	0ns	0ns
Endurance	10^{12}	10^{18}	10^5	10^6	10^2	N/A	∞	∞
Retention	10Year	10Year	10Year	10Year	10Year	∞	0	0
Operation Current	1mA	5mA	10mA	80mA	10mA	35mA	70mA	10mA
Standby Current	50μA	200μA	50μA	300μA	1μA	100μA	100μA	2μA
Cell Area	0.8~1	1~2	0.8	1	0.8	0.5	1	3~4
(Condition)	(16MHz)	(5MHz)	(6MHz)	(6MHz)	(1MHz)	(8MHz)	(14MHz)	(14MHz)
Product	Nontitle	FM1208	I28F010	AT28C010	MXDC101AG-12	LH5308OOA	ac8a01012SA-70	M462812RRL-7

Fig. 2. Comparison of Memory IC

ferroelectric film on the FET channel region. The former type of ferroelectric memories are practically used, the later type enables none destructive read out, but is not exist for practical use yet, only the memory cell operation has been demonstrated. [3-4]

The ferroelectric memory has the feature as a non-volatile RAM as shown in Fig. 2. Writing endurance cycle has been reached up to 10^{10}-10^{13} cycles. The recent works of $BiSr_2Ta_2O_9$ [5] ferroelectric material or IrO_2 electrode [6] have improved the fatigue of switching charge amount, and indicate even more than 10^{12}-10^{13} cycles can be achievable. 100nsec writing speed of FRAM is almost same level as SRAM and DRAM, it is much faster than the writing speed of conventional non-volatile memory.

Even 2V single power supply is applied externally, as FLASH and EEPROM are using F-N tunnel or hot electron for the electron injection or erasing, so that a charge pump to generate high voltage (12-15V) is required internally.

The other hand, the ferroelectric memory is operated at 3V now, it will be operated at 1.5V in the near future. Because 1.5V saturation on P-E hysteresis curve has been reported. [7]

At the present time, the cell size of ferroelectric memory is not small enough ($6.2 \times 5.6 \mu m^2$/cell)[8], because the ferroelectric process technology is not well established yet for a half micron level patterning.

But, once fine process technology becomes available,
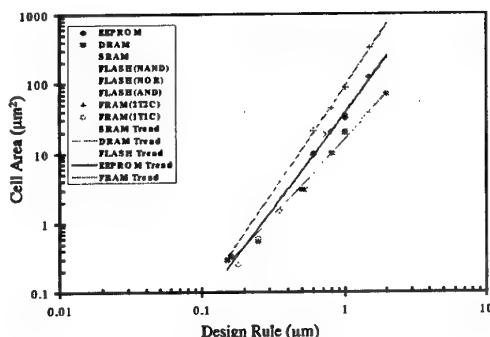
ferroelectric memories will have potential to achieve a cell size compatible to a DRAM cell size with 1T1C cell in comparison with the same design rule as shown in Fig. 3. When 1T (1 transistor) cell become available, the size will be close to a cell size of a flash memory.

3. PROCESS TECHNOLOGY AND DEVICE RELIABILITY

Ferroelectric memory technology brings many features to us, even FRAMs and FRAM embedded RF-ID chips are available in the market now, but still many of the process technology problems should be solved before making FRAM as universal memory.

The first problem is a fine pattern technology. A ferroelectric film such as PZT and Pt, Ir or IrO_2 electrodes are very difficult to form an anisotropic etching profile without creating a side wall fence.

The inherent non-volatility of etch products of the materials used in FRAM such as Ir/ IrO_2, Pt and PZT forces the abandonment of regular etching processes.

The etching profile of the ferroelectric capacitor is shown on Fig. 4. 50 degree of slope etch is required to prevent from forming sidewall deposition and minimize the damage to the PZT film during or after the etching of Ir/IrO_2 top electrode. This slope etch brings the difficulty to minimize the layout rule of the FRAM device.

Also, the inherently non-volatile etching materials cause the

Top Electrode

PZT

Bottom Electrode
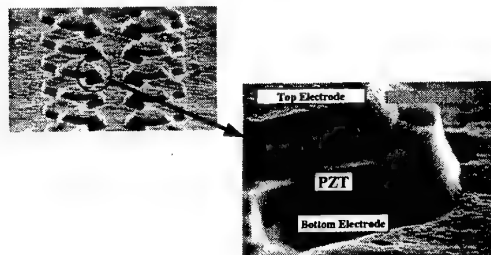
Fig. 4. Etching Profile of Ferroelectric Capacitors

many particles in the etching chamber.

Future process development for the ferroelectric film etching and electrode films etching is required to proceed to $0.35 \mu m$ layout devices.

The second problem is the ferroelectric film deposition. In general, a sputtering method and a sol-gel method have been applied for a ferroelectric film formation. But the quality of the film formed by these methods is not good enough at this time. Further development works on other film deposition methods such as MOCVD (metal organic chemical vapor deposition) are
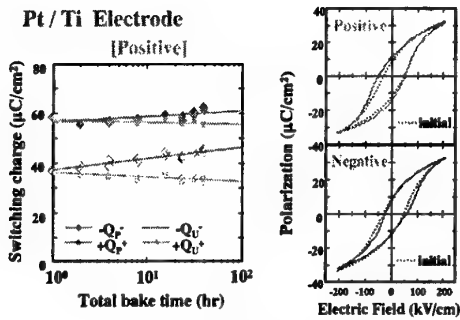
Fig. 3. Memory Design Trend

Fig. 5. Retention Characteristics of PZT Films

Fig. 7. Fatigue Properties of PZT Thin Films with Various Electrodes

Fig. 6. Retention Characteristics of PZT Films

Fig. 8. Electrode Induced Degradation[10]
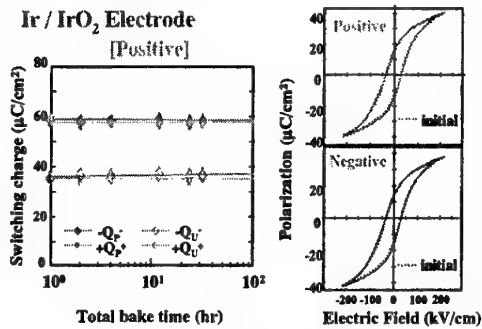
strongly required for a higher density memory. The bottom electrode film should also be improved to grow a good crystal of ferroelectric film on top of it.

The third problem is the retention problem, this problem has became less issue by introducing IrO_2 electrode, especially under high temperature. This problem seems to be related to the second problem, the formation of oxygen vacancies and/or Pb vacancies cause the poor retention problem. The imprint effect of PZT film causes opposite data retention problems occasionally. This problem happens, when one site of data has been kept a long time under a high temperature, and then writing the opposite site of data on the same bit, sometimes the data retention the bit is not long enough. This problem is caused by the decreasing margin between $+Qp^+$ and $-Qu^-$ as shown in Fig. 5. But, this opposite data retention problem is improved, if the opposite site of data is written more than two times on the bit. The recent studies of ferroelectric film such as $BiSr_2Ta_2O_9$ and IrO_2 electrodes shows us good results on this problem as well as on the fatigue problem of switching charge of a ferroelectric capacitor as shown in Figs. 6 and 7. Hydrogen content atmosphere such as passivation process affects polarization characteristics of Pt/PZT/Pt structured ferroelectric thin film capacitors. The PZT film itself is not degraded when annealed in a hydrogen atmosphere even at 400℃ as shown in Fig. 8 [9]. The catalytic effect of platinum for hydrogen reaction enhances this problem [10].

To minimize this hydrogen induced degradation, IrO_2 top electrode ferroelectric capacitors have been studied. As shown on Fig. 9, the electrode induced process degradation on ferroelectric polarization characteristics depends on the top electrode material. IrO_2 top electrode PZT capacitors have less affection of hydrogen
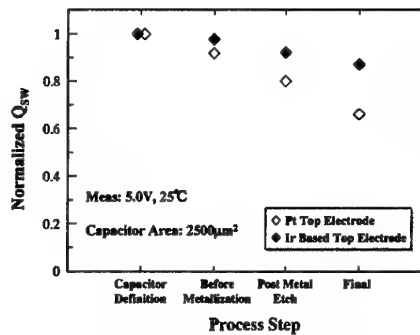
Fig. 9. PZT Capacitors Process Degradation

Test Item		LOT A P NG/N	LOT B P NG/N	LOT C P NG/N	LOT B' P NG/N	LOT C' P NG/N
B/IN (125℃)	240h	0/30	0/30	0/30	-	-
	500h	0/30	0/30	0/30	-	-
	1000h	0/30	0/30	0/30	-	-
PCT (121℃,100%)	300h	0/30	0/30	0/30	-	-
	500h	0/30	0/30	0/30	-	-
TCY (150℃/-65℃)	300cyc	0/30	0/30	0/30	-	-
	500cyc	0/30	0/30	0/30	-	-
HBT (150℃)	240h	0/30	0/30	0/30	-	-
	500h	0/30	0/30	0/30	-	-
	1000h	0/30	0/30	0/30	-	-
HAST (130℃/85%)	200h	0/30	0/30	0/30	-	-
	300h	0/30	0/30	0/30	-	-
Retention (150℃)	240h	0/100	0/100	0/100	0/99	0/100
	500h	0/100	0/100	0/100	0/99	0/100
	1000h	0/100	0/100	0/100	0/99	0/100
Fatigue	1E+09cyc	0/100	0/100	0/100	-	-
Ret after Fatigue	1E9&1000h	0/100	0/100	0/100	-	-

Fig. 10. Reliability Test Results

induced process degradation compare to Pt top electrode PZT capacitors.

The reliability of ferroelectric memory devices is confirmed as same level as regular LSI devices. Several unique tests are carried out to evaluate the ferroelectric film besides on regular reliability /life tests of semiconductors, such as fatigue, imprint, retention and etc. The results are shown in Fig. 10.

4. PROCESS COMPATIVILITY

The ferroelectric process takes the place after CMOS device formation, before contact operating process. The ferroelectric process does not change CMOS devices formed under ferroelectric Film, because of the process does not have high temperature treatment, and does not change the source and drain diffusion depth. However, as ferroelectric film is so sensitive to the hydrogen ambient which is widely used in semiconductor manufacturing process, and so modified process is required to minimize the hydrogen degradation.

Conventional non-volatile memories such as EEPROM and FLASH require high voltage transistors for writing and erasing, and high voltage transistors formation process changes the original CMOS devices, which are, used non-high voltage circuit region. From this effect, when EEPROM or FLASH memory is embedded to the CMOS logic/analog device, original CMOS designed cell libraries are not applicable to embedded to a chip without modification. Ferroelectric memory embedded approach is most suitable from the process viewpoint and CMOS cell libraries are able to used without any modification.

5. FRAM EMBEDDED APPLICATION

The features of ferroelectric memories are not only replacing the existing memory market, but also creating new application fields, and are impacting the society.

As the importance of ecology is increasing, ferroelectric memories will be getting more important position between the memories. For example, battery back SRAM will be replaced by ferroelectric memories, because of the disposition of used batteries. A ferroelectric memory has more advantages as a memory embedded product than other conventional memories, because of its non-volatile, high speed writing / programming, low power supply voltage, high endurance and good CMOS process adaptability. Ferroelectric memory embedded RF-ID tag / contactless smart IC cards are one of the most adequate examples.

They require power as low as possible, because they get power from RF without having back up battery as shown in Figs. 11 and 12.

RF-ID tags / contactless smart IC cards will change our life style in various fields. Some trials or investigations are being carried out in the following applications; logistics control, medical

Smart Tag

Merit	
- High speed operation	- High Endurance
- Low power consumption	- Battery free
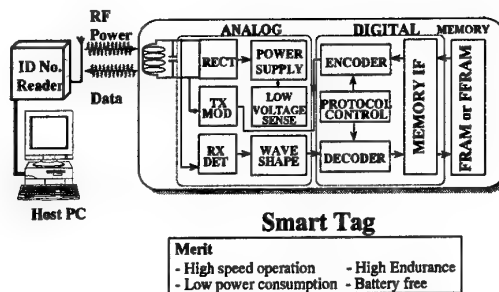
Fig. 11. FRAM Embedded Product - RF-ID Tag -

[FRAM® Embedded RF-ID Chip]   [RF-ID Bagtag and Tunnel Reader/Writer]
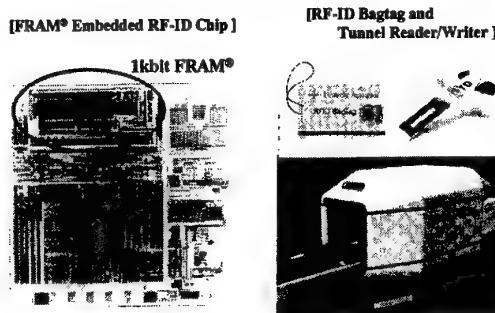
Fig. 12. RF-ID card application

care, bank card / electronic purse, airline bag tags, pre-paid cards, courier, postage, passport, license cards and ID cards etc..

A courier system is under progress to be combined with a logistics system, both systems have a strong demand to use RF-ID tags or contactless IC cards in their system for automatic sorting, and logistic data transmissions between an ID card and a read/program terminal keeping some remote distance.

RF-ID cards are not only used for identification but for data storage and data transmission, and enable the connection of a courier information and logistic information in the same network. 1.9 billion of parcels were handled including 0.5 billion of postal parcels in 1995 in Japan, this volume is growing 10% at annual base. The demand for RF-ID cards becomes more important with the increase of the customer's variety of requirements such as many kinds of parcels with a small volume of each type, shorten a delivery time, frequent delivery with a small lot, reducing mistakes and cost reduction.

The demand of RF-ID card is expected up to 10-20 billion cards per year.

Recently, flash memory embedded system LSI chips are getting popular, especially flash memory embedded CPUs is used to many electronic systems. A simultaneous multi-process implementation for a fine electronic control is required in a recent system. As a performance of software algorithm gives more influence to a system, a development work of algorithm takes more time. Under these circumstances, conventional mask ROM embedded type CPUs have more difficult situation for a short

development cycle, because of a revised LSI have to be made again to change ROM when a software has a bug.

If mask ROM is replaced to flash memory, a LSI is able to be manufactured without waiting a completion of software development. An algorithm installation to a CPU shall be done just before fab out a final product set by writing the program to the flash memory embedded to a LSI chip.

In additional, flash embedded architecture enables to upgrade software without changing the LSI chip.

In further, if FRAM is applied as embedded ROM and RAM for CPU, in system programming becomes reality, because of using the features of FRAM such as high speed/low power programming.

It is not far away to change software or to have learning function and takes the learning results in the system to change a configuration of a system.

6.   A NEW DEVICE ARCHITECTURE

The ferroelectric memory is not an ideal memory with it the clear advantages such as non–volatility, low power consumption, high endurance and high speed writing, but also the most suitable device for memory embedded applications. Its manufacturing process makes it more compatible with the standard CMOS process than the traditional non–volatile memory process, due to the device does not require and high voltage operations, and the ferroelectric process does not influence to the characteristics of CMOS devices used in logic cells, analog cells and core cells. In the spreading of IP (Intellectual Property) application for LSI Industry, this embedded application takes more important position.

In the near future, the ferroelectric memory technology will be taken into reconfigurable devices as programmable interconnect switches besides using as embedded memories. These ferroelectric memory based reconfigurable devices can be used as DPGA (Dynamic Programmable Gate Array), which is able to be reconfigured their original logic in a system under a operation mode.

Memory in logic circuits will take the position for lower power consumption by introducing ferroelectric gated transistors or ferroelectric capacitors as shown in Fig. 13. This memory in logic technology will open the new semiconductor technology for reconfigurable devices.

Ferroelectric memories have a good matching process to the conventional CMOS device. It has been confirmed the technologies of ferroelectric memories can be applied for low voltage (less than 3V) operation and multi level metallization, therefore system LSIs with lower power and
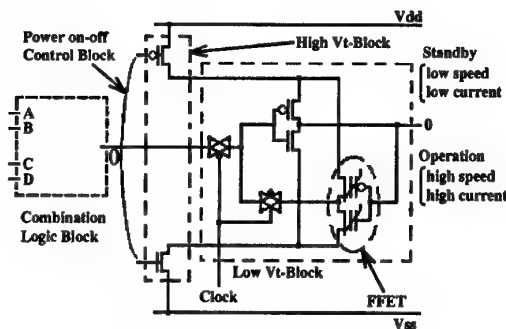
Fig. 13. Lach block with ferroelectric gate transistors

Single Chip Solution
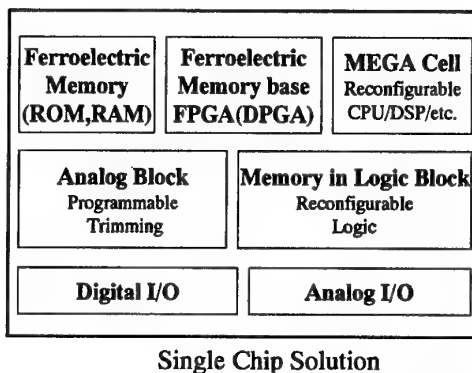
Fig. 14. Ferroelecric memory embedded devices

higher performance (reconfigurable multi function) by using the ferroelectric devices. The existing cell library portfolio can be utilized in ferroelectric memories embedded products as shown in Fig. 14.

The ferroelectric memory technology will lead to new semiconductor device architecture, including a neuron device using ferroelectric memories as analog memory, and will take the major place in the coming multi- media era.

7.   CONCLUSION

The ferroelectric memory technology will give a big impact to the existing semiconductor memories, and open new application fields, which will change our life style. Also, the technology will enable new device architectures for the 21st century.

References

1) J. L.Moll and Tarui, Trans. Electron Devices (Solid State Res. Conf. Abs), ED-10,338 (1963)

2) S.S.Eaton, D.B.Butler, M.Parris, D.Wilson, H.McNeillie, Proc. of IEEE International Solid-State Circuits Conference (1988)

3) T. Nakamura, Y, Nakao, A. Kamisawa and H. Takasu:, Dig.

Tech. Pap. IEEE Int. Solid-State Circuit Conf., 68 (1995)

4) Y. Fujimori, N. Izumi, T. Nakamura and A.Kamisawa, Integrated Ferroelectrics, 21(1-4), 73 (1996)

5) T. Mihara, et al, Proc. of Int. Symp. Integrated Ferroelectric 1992, 137 (1994)

6) T.Nakamura, Y.Nakao, A.Kamisawa and H.Takasu, Appl. Phys. Lett.,65, 1522, (1994)

7) D. J. Wouters, G. J. Norga, F. Beckers, L. Bogaerts, and H. E. Maes, abst. of 9th Int. Symp. on Integr. Ferroelectrics, 19c (1997)

8) H. Koike, et. al. Proc. of IEEE Int. Solid-State Circuits Conf. (1996)

9) K.Kushida-Abdelghafar, et al, Appl. Phys. Lett., 69(21), (1996)

10) Y. Shimamoto, et al, Appl. Phys. Lett., 70(23), (1997)

Orientation Mechanism and Electrical properties of Low-Temperature Processed Sol-Gel Derived PZT Thin Film

Hisao Suzuki*, Yasuhiro Kondo*, Shoji Kaneko* and Takashi Hayashi**

*Shizuoka University, 3-5-1 Johoku, Hamamatsu, Shizuoka 432-8561, Japan
Fax : 81-53-478-1157, e-mail : hisao.suzuki@eng.shizuoka.ac.jp
**Shonan Institute of Technology, 1-1-25 Tsujido-Nishikaigan, Fujisawa 251, Japan
Fax : 81-466-36-1594, e-mail : hayashi@mate.shonan-it.ac.jp

Ferroelectric $Pb(Zr_{0.53}Ti_{0.47})O_3$ (PZT) thin film was successfully deposited on the $Pt/Ti/SiO_2/Si$ wafer at low temperature of 525 °C by the sol-gel method from molecular-designed precusor solution with 20 mol % excess lead than stoichiometric composition. The composition of the resultant PZT film showed slightly lead excess than a stoichiometric composition. Zr/Ti ratio of the film was slightly shifted toward the Zr rich composition. Therefore, the resultant PZT film had rhombohedral symmetry. In addition, orientation of the resultant PZT thin film could be controlled by changing the pre-annealing temperature, which affected the interfacial state between Pt electrode and PZT thin film. The electrical properties of the resultant PZT thin film were also affected by the orientation of the film. As a result, low-temperature processed PZT thin film exhibited enough potential for the FE-RAM.

1. INTRODUCTION

$Pb(Zr, Ti)O_3$ thin films have been attracting wide interest due to their high potential for various applications such as in optical modulator, non-volatile semiconductor memories and in high-frequency surface acoustic wave (SAW) devices[1)-3)]. PZT thin films are deposited by several techniques such as chemical vapor deposition, sputtering and chemical solution deposition (CSD). Among them, an alkoxide process is one of the most promising techniques for processing high-performance thin films because it offers precise control of compositions on a molecular scale as well as a low processing temperature. However, a sophisticated alkoxide process is very hard to realize. In this paper, ferroelectric PZT thin films were successfully deposited on a $Pt/Ti/SiO_2/Si$ substrate at low temperature though alkoxide route.

Ferroelectric PZT has a perovskite structure and therefore, PZT thin films with good ferroelectricity have a polarization axis, showing the different electrical properties depending on the crystal orientations of the resultant films. Consequently, orientation control is essential for the PZT films to apply various electronic devises. In some papers, preferred orientation and the orientation mechanism for the PZT thin films on Pt electrode were investigated. Brooks et al. explained film orientation with a view point of phase transition rate of pyrochlore phase into perovskite phase which occurred during pre-annealing stage[4), 5)]. Chen et al. explained that film orientation was determined by the phases formed at the interface between film and substrate[6)]. Namely, PZT showed (111)- and (100)- orientation if the $Pt_{5-7}Pb$ intermetallic compound and PbO were formed at the interface, respectively. Tani et al. also demonstrated that PLZT showed (111) orientation when the Pt_3Ti intermetallic compound exsisted on the substrate[7)]. Liu et al. suggested that PZT thin film had (111)

orientation if the film was grown epitaxially, whereas the PZT film showed (100) orientation with a minimum surface energy when the homogeneous nucleation occurred[8)]. Actually, Aoki et al. prepared (111) or (100) oriented PZT films by a sol-gel method, which showed different electrical properties depending on the crystal orientation. However, these orientation control could be possible only for the films annealed at high temperature above 600 °C. For the PZT thin films, a low-temperature processing is very important because PZT thin films are used in a semiconductor process. High temperature processing will degrade a transistor on a silicon wafer due to the migration of some elements during processing. In addition, various substrates with low-melting points can be available if the PZT films are deposited at lower temperatures, leading to the wide application of the ferroelectric PZT thin films. In the previous paper, PZT thin film with a relatively good dielectric property was prepared from the molecular-designed alkoxide precursor solution as well as by controlling the nucleation using seeding layers[9), 10)]. There are some papers on the low-temperature processing of PZT thin films[11), 12), 13)]. However, these PZT films required relatively high-temperature annealing above 600 °C to obtain good electrical properties.

This paper focuses on the low-temperature processing as well as the orientation mechanism of the PZT thin films for the excellent electrical properties. In addition, effect of molecular structure of precursors on the crystallization and orientation control of the resultant PZT films was described. Crystal orientation of the resultant films was successfully controlled by the pre-annealing temperature and the addition of an excess lead oxide for the alkoxide-derived precursor. Excess lead oxide is also expected to play an important role for the low-temperature processing.

2. EXPERIMENTAL PROCEDURE

Preparation method for precursor solution and sol were described eleswahere[14), 15)]. Precursor films were dip-coated on the Pt/Ti/SiO$_2$/Si substrate. The thickness of film for one coating was about 40 nm. The total film thickness was in the range from 300 to 400 nm. After dip-coating, precursor films were dried at 115 °C and pre-annealed for 10 minutes. Pre-annealing temperature was in the range from 300 to 450 °C. Annealing was carried out in the range from 450 to 600 °C for 2 hours. Crystalline phases in the annealed films were identified by the X-ray diffraction using Cu-Kα radiation. Dielectric properties of the resultant films were measured by LCR meter (YHP-4284 A). Ferroelectric properties were measured by Radiant RT-6600 S.

3. RESULTS AND DISCUSSION

3.1 Effect of precursor structure

Figure 1 shows the crystallization behavior of the PZT precursor powders. Both precursors crystallizaed into single phase perovskite at 600 °C. However at low temperature, perovskite ratio of the precursor powder derived from molecular-designed solution was higher than that of the precursor powder derived from stable precursor sol. In addition, perovskite lead titanate was identified at 500 °C for the film derived from stable sol.

Figure 2 shows the size distribution of the colloidal particles in the stable precursor sol with a stoichiometric composition, showing the average particle size of about 12 nm. For the molecular-designed precursor solution, particle size could not be measured. These results exhibits that the chemical homogeneity of the precursor solution is higher than that of the stable precursor sol. Therefore, PZT films were deposited from the molecular designed precursor solutions for the further experiments.
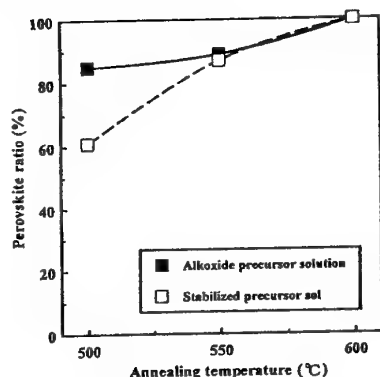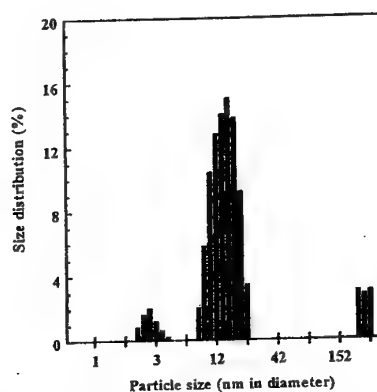
Fig. 2 Size distribution of colloid for the stable precursor PZT(100/53/47) sol.

3.2 Effect of pre-annealing temperature and addition of excess lead oxide

Figure 3 shows the relation between crystal orientation and the pre-annealing temperatures for the PZT(100/53/47) films pre-annealed at 350 °C or 420 °C followed by the annealing at 600 °C. At 600 °C, only a perovskite phase was identified. However, the crystal orientation of the resultant films depended on the pre-annealing temperature. PZT(100/53/47) film with a pre-annealing temperature of 350 °C showed (111)-orientation. On the other hand, pre-annealing at 420 °C resulted in the partial crystallization, leading to the (100) orientation of the PZT(100/53/47) film at 600 °C. This suggests that the orientation of the resultant PZT(100/53/47) film could be successfully controlled by the pre-annealing temperature.

The factors that affect the crystal orientation of the thin film are the nucleation and the crystal growth. In this study, we assumed that the nucleation had large effect on the crystal orientation. The crystalline phases for the PZT(100/53/47) films annealed at 350 °C or 420 °C for 10 minutes were identified. As a result, intermetallic compound of Pt$_{5.7}$Pb(111) was identified clealy in the XRD pattern for the film pre-annealed at 350 °C . In this case, the lattice spacing for (111) plane of Pt, Pt$_{5.7}$Pb, and PZT is 2.774 Å, 2.864 Å and 2.854~2.893 Å, respectively. It shows that each atom locates within 4 % lattice mismatching. Therefore, it was concluded that intermetallic Pt$_{5.7}$Pb compound formed during pre-annealing at 350 °C would reduce the interfacial energy between substrate and PZT(100/53/47) film, leading to the (111) orientation. On the other hand, weak Pt$_{5.7}$Pb (111) peak was identified in XRD pattern of PZT(100/53/47) film pre-annealed at 420 °C. In this case, orientation mechanism is not clear. However, the heterogeneous nucleation would lead to the self-oriented growth of the (100) orientation that had minimum surface energy.

As described above, orientation control of the PZT(100/53/47) film is attained at above 600 °C. However in this case, low-temperature processing is

Fig. 1 Change in perovskite ratio for the PZT(100/53/47) powders from different precursors with temperature.

not possible because the pyrochlore phase with low dielectric property is still remained below 600 °C. Therefore, the crystallization beahvior of the PZT(120/53/47) film was investigated.

As shown in the figure 4, single phase perovskite films with different orientation were successfully deposited at 525 °C by changing the pre-annealing temperature for the PZT system with 20 mol % excess lead oxide addition. This shows that the excess addition of lead oxide lowers the conversion temperature of pyrochlore into perovskite phase. In addition, orientation of the low-temperature processed PZT (120/53/47) film was successfully controlled by the pre-annealing temperature. This also confirmed the orientation mechanism for the PZT film described above.
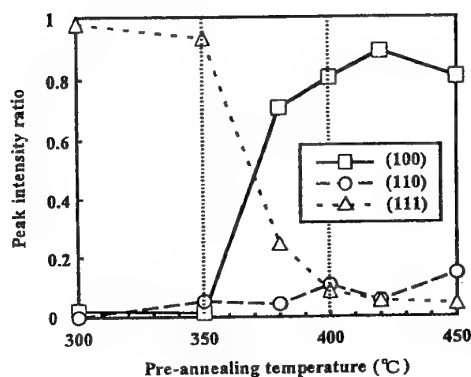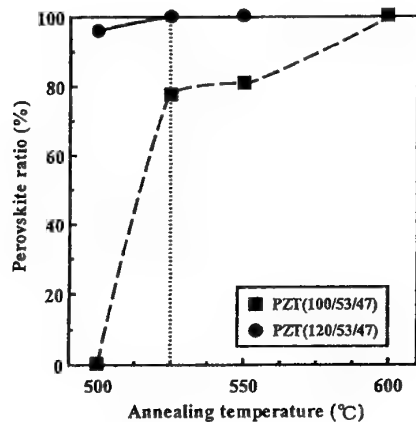
3.3 Ferroelectric property

The electrical properties of the PZT films are significantly affected by the residual pyrochlore phase and the crystal orientation of the resultant films. Figure 5 shows the P-E hysteresis loops for the PZT(100/53/47) and PZT(120/53/47) films with different annealing temperatures. As a result, remanent polarization (Pr) of (111)-oriented and (100)-oriented films were 46.1 and 21.7 (μC/cm^2), respectively. Figure 6 shows the good ferroelectricity of the resultant PZT(120/53/47) films. The difference of Pr for the resultant films was ascribed to the crystal symmetry of the resultant films.
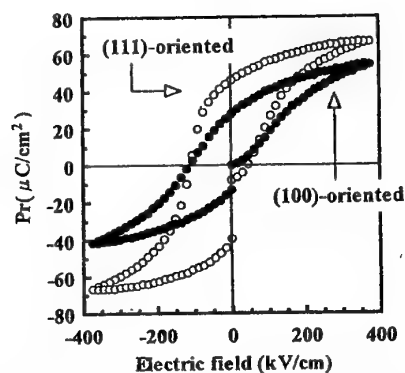
Fig.5 P-E hysteresis loops for the PZT(120/53/47) thin films annealed at 525 °C.

3.4 Orientation control

As already mentioned in section 3.2, orientation of the PZT(100/53/47) and PZT(120/53/47) films was successfully controlled by changing the pre-annealing temperature, which affected the electrical properties of the resulting PZT thin films. Namely, intermetallic compound of Pt$_{5.7}$Pb(111) has the large effect on the orientation mechanism for the case of (111)-oriented PZT films. On the other hand, the orientation mechanism for the (100)-oriented PZT films was not obvious. Figure 6 shows the XRD patterns for the PZT films with different compositions and pre-annealing temperatures. Intermetallic compound of Pt$_{5.7}$Pb(111) was identified in all XRD pattern. The peak intensity for the intermetallic compound of Pt$_{5.7}$Pb(111) was lower if the films were pre-annealed at 420 °C. In addition, the peak intensity was higher for the PZT films with excess lead (PZT(120/53/47)). This indicates that the different in-situ seeding layer was formed during pre-annealing at 420°C. Considering the lattice matching, the in-situ seeding layer for the films pre-annealed at 420 °C should be a lead oxide. Lattice parameter of the PbO (001) plane (0.3973 nm) is very similar to that of the PZT (100) plane (0.4036 nm). Therefore, hetero-epitaxial growth of (100)-oriented PZT is expected for the films pre-annealed at 420 °C. To confirm this hypothesis, PbO precursor layer was dip-coated between substrate and PZT(120/53/47) precursor film followed by the pre-

Fig. 3 Change in orientation of the PZT(100/53/47) film annealed at 600 °C with pre-annealing temperature.

Fig. 4 Relation between annealing temperature and perovskite ratio for the films from precursor solution.

annealing at 350 °C and 420 °C. The final annealing was carried out at 550 °C. As a result, (100)-oriented PZT films were deposited independent of the pre-annealing temperatures (fig. 7). Accordingly, the orientation of the PZT film could be successfully controlled by changing the pre-annealing temperature and/or the insertion of the PbO layer between electrode and PZT precursor film.
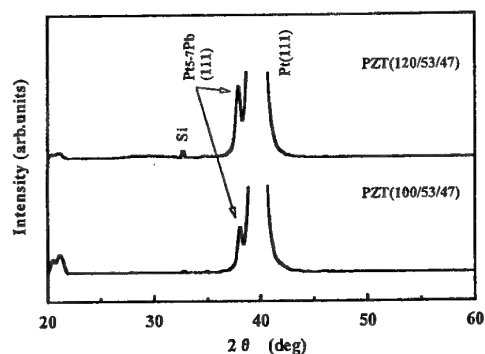
(a) pre-annealed at 350℃
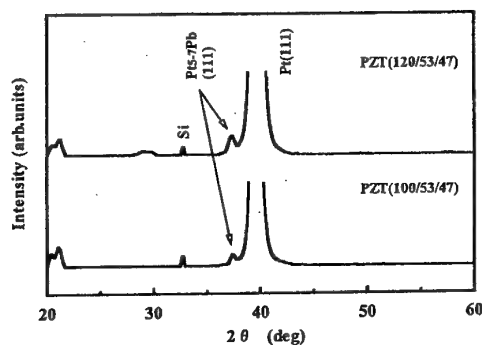
(b) pre-annealed at 420℃

Fig.6 XRD patterns for the PZT films pre-annealed at different temperatures.
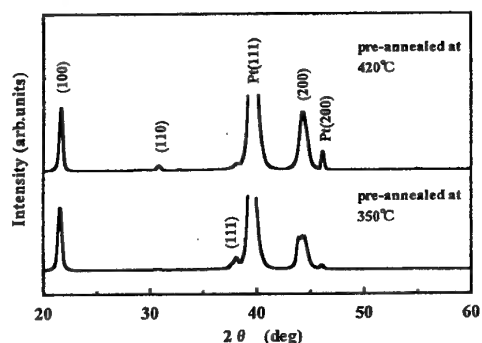
Fig. 7 XRD patterns for the PZT films with PbO seeding layer pre-annealed at 350 °C or 420 °C and annealed at 550 °C.

4. CONCLUSIONS

This paper focused on the precursor structure and the orientation mechanism for the low-temperature processed PZT thin films. Some parameters of pre-annealing temperature, annealing temperature and the addition of excess lead oxide in the precursor solution were changed to investigate the effects on the crystallization behavior and ferroelectric properties of the resultant films. As a result, followings are concluded;

(1) For the low-temperature processing, molecular designed precursor solution is essential.
(2) The orientation of alkoxide-derived PZT thin films on Pt/Ti/SiO$_2$/Si substrate is significantly affected by the pre-annealing temperature. ·
(3) Excess addition of lead oxide is very effective for a low-temperature processing of PZT thin films.
(4) Highly oriented PZT thin films with good ferroelectricity were deposited as low as 525 °C.

REFERENCES

1) J.F.Scott, L.Kammerdiner, M.Parris, S.Traynor, V.Ottenbacher, A.Shawabkeh and W.F.Oliver, *J.Appl.Phys.*, **64,** 787 (1989)
2) S.G.Varnado and W.E.Smith, *IEEE J.Quantum Electron.*, **8,** 88 (1972)
3) R.N.Castellane and L.G.Feinstein, *J.Appl.Physs.*, **50,** 4406 (1979)
4) K.G.Brooks, I.M.Reaney, R.Klissurska, Y.Huang, L.Bursill, and N.Setter, *J.Mater.Res.*, **9** [10], 2540 (1993)
5) I.M.Reaney, K.G.Brooks, R.Klissurska, C.Pawlaczyk, and N.Setter, *J.Am.Ceram.Soc.*, **77** [5], 1209 (1994)
6) S.Y.Chen and I.W.Chen, *J.Am.Ceram.Soc.*, **77** [9], 2332 (1994)
7) S.Y.Chen and I.W.Chen, *J.Am.Ceram.Soc.*, **77** [9], 2337 (1994)
8) T.Tani, Z.XU, and D.A.Payne, *Mat.Res.Soc.Symp. Proc.*, **310**, 269 (1993)
9) Y.Liu and P.P.Phule, *J.Am.Ceram.Soc.*, **79** [2], 495 (1996)
10) K.Aoki, Y.Fukuda, K.Numata, and A.Nishimura, *Jpn.J Appl.Phys.*, **33**, 5155 (1994)
11) H.Suzuki, M.B.Othman, K.Murakami, S.Kaneko, and T.Hayasi, *Jpn.J Appl.Phys.*, **35**, 4896 (1996)
12) H.Suzuki, M.B.Othman, K.Murakami, S.Kaneko, and T.Hayasi, *Jpn.J.Appl.Phys.*, **36**, 5803 (1997)
13) T.Takusazawa, N.Yamada, T.Kato, H.Hattori, and T.Matsui, *Jpn.J.Appl.Phys.*, **33**, 5151 (1994)
14) G.Yi, Z.Wu, and M.Sayer, *J.Appl.Phys.*, **64**, 2717 (1988)
15) S.Hirano, T.Yogo, K.Kikuta, Y.Araki, M.Saitoh, and S.Ogasahara, *J.Am.Ceram.Soc.*, **75** [10], 2785 (1992)

A Wet-Oxidation Process for Sputter-deposited Pb(Zr, Ti)O$_3$ Films

Song-Min Nam, Hiroyuki Kimura, Naoki Ohashi and Takaaki Tsurumi
Department of Inorganic Materials, Graduate School of Science and Engineering, Tokyo Institute of Technology
2-12-1, Ookayama, Meguro-ku, Tokyo 152-8552, Japan
Fax: 81-03-5734-2514, e-mail: smnam@crystal.ceram.titech.ac.jp

A wet-oxidation process was proposed to improve the quality and electrical properties of Pb(Zr, Ti)O$_3$ (PZT) thin films prepared by the RF-magnetron sputtering technique. For the oxidation of metallic Pb in as-deposited PZT films, the wet-oxidation process was carried out using hydrogen peroxide solutions prior to postannealing for crystallization. In the case of PZT films on Pt/Ti/SiO$_2$/Si substrates, the density of defects observed using an optical microscope was drastically decreased by means of the wet-oxidation process, and the shape of polarization vs voltage hysteresis loops of PZT films was also improved. In the case of PZT films on Pt/IrO$_2$/SiO$_2$/Si substrates, microvoids were diminished by means of the wet-oxidation process. For 70 nm-thick PZT films on Pt/IrO$_2$/SiO$_2$/Si substrates, hysteresis loops could not be measured without the wet-oxidation process. However, the films with the wet-oxidation process exhibited the slim-type hysteresis loop with a remanent polarization of over 23 μC/cm^2 even at 2 V and a coercive voltage of about 0.7 V.
Keywords: ferroelectrics, thin films, PZT, sputtering, hydrogen peroxide solution, oxidation

1. INTRODUCTION

Ferroelectric thin films, such as Pb(Zr, Ti)O$_3$ and SrBi$_2$Ta$_2$O$_9$, have been intensively studied in order to apply them in the ferroelectric nonvolatile memories. Many problems in practical applications have been overcome by improving process technology and employing Ir-based or conducting-oxide fatigue-free electrodes. PZT films have been one of the most promising materials for application in the ferroelectric nonvolatile memories because of their high remanent polarization. It was recently reported that mass production of PZT films has become possible, using the sol-gel technique and Ir-based electrodes[1]. PZT films prepared by the sol-gel technique usually exhibit better electrical properties than those prepared by other techniques such as chemical vapor deposition and sputtering[2-5]. The sputtering method has advantages over other methods from the viewpoint of industrialization and suitability for semiconductor process lines.

This study started with the question of how PZT films with electrical properties as good as those of sol-gel PZT films can be prepared using the sputtering technique. It has been reported that a part of Pb in an amorphous PZT film sputtered at room temperature is unstable and metallic due to broken Pb-O bonds formed by sputtering[6]. Desu and Kwok[7] demonstrated using X-ray photoelectron spectroscopy that metallic Pb was formed by sputtering. It was also reported that dimple-like defects or microvoids were formed on the surfaces of PZT films by evaporation and diffusion of Pb during the postannealing of these sputtered PbTiO$_3$ and PZT films[8-10]. These types of defects are believed to cause the degradation of electrical properties. We considered that the metallic Pb in the amorphous PZT films was possibly oxidized to form Pb-O bonds by a wet-oxidation process using oxidizing chemicals. The wet-oxidation process prior to crystallization may suppress the evaporation and the diffusion of Pb and therefore reduce the defect density. In this study, a hydrogen peroxide solution was used as the chemical for the wet-oxidation process. The effects of the wet-oxidation process on the microstructure and the electrical properties of sputtered PZT films were investigated.

2. EXPERIMENTAL

Amorphous PZT thin films were deposited on Pt(175 nm)/Ti(20 nm)/SiO$_2$/Si(100) substrates and Pt(150 nm)/IrO$_2$(50 nm)/SiO$_2$/Si(100) substrates at room temperature using a typical sputter-up type RF-magnetron sputtering system (Seed Lab. Co.). Sintered PZT ceramics, 50 mm in diameter and 4 mm thick, were used as sputtering targets. The molar ratio of Zr and Ti of the targets was 0.52 and 0.48, respectively, and excess PbO was added by 10 mol%. The deposition chamber was evacuated to 5 × 10^{-6} Torr using a diffusion pumping system before the deposition. The deposition of PZT films was carried out at 20 mTorr using Ar/O$_2$ (8/2) as a sputtering gas. The RF input power was 50 W. The thickness of PZT films was 110 nm and 70 nm for Pt/Ti/SiO$_2$/Si(100) substrates, and 140 nm and 70 nm for Pt/Ir/SiO$_2$/Si(100) substrates.

The wet-oxidation process was carried out using hydrogen peroxide (Mitsubishi Gas Chemical Comp. Inc., M.W.=34.02). Hydrogen peroxide solutions, namely 1/10, 1/5, 1/3, 1/2 (vol% of H$_2$O$_2$/ vol% of H$_2$O) solutions and undiluted hydrogen peroxide, were prepared by diluting with deionized water. Deionized water was also used for comparison. In the wet-oxidation process, as-deposited amorphous PZT films were spun at 100 rpm using a spinner and 50 μl of hydrogen peroxide solution was dropped onto the surface of the films. Then the rotation speed was immediately increased to 500 rpm. After drying, films were crystallized by postannealing at 650°C for 5~15 min in air using a tube furnace. To analyze the electrical properties of the films, Pt top-electrodes of 100 μm in diameter were deposited at room temperature using the same RF-sputtering system. After the Pt top-electrodes were deposited, they were annealed at 550°C for 5 min.

Phase identification of the deposited films was performed using an X-ray diffractometer (XRD). The film thickness was measured using a stylus method (DEKTAK). The chemical composition of the films was analyzed by X-ray fluorescence spectroscopy (XRF), and the surface morphology of the films was observed using a reflective optical microscope and a field emission scanning electron microscope (FE-SEM). The ferroelectricity of the PZT films (P-V hysteresis loop) was measured using a ferroelectric test system (Radiant Tech., RT-66A) at virtual ground mode.

3. RESULTS AND DISCUSSION

3.1 Chemical composition and structure of PZT films

The chemical composition of PZT films on $Pt/Ti/SiO_2/Si(100)$ could not be analyzed by XRF because of the presence of a Ti buffer layer. The chemical composition of as-deposited PZT films on $Pt/Ir/SiO_2/Si(100)$ substrates was $1.07PbO \cdot 0.56ZrO_2 \cdot 0.44TiO_2$. This indicates that the Ti content in PZT films was less than that of the PZT ceramic targets. Similar results were reported in a previous study[11]. There were no apparent changes in the chemical composition after the postannealing, indicating that the amount of PbO evaporation was negligible. Kugimiya et al.[12] reported that PbO diffusion rather than evaporation was dominant in the postannealing process.

Figures 1 and 2 show XRD profiles of PZT films on $Pt/Ti/SiO_2/Si(100)$ substrates and $Pt/IrO_2/SiO_2/Si(100)$ substrates. The as-deposited films were amorphous and had no PbO or pyrochlore phases, as shown in Figs. 1(a) and 2(a). PZT films with a single perovskite phase were formed by annealing amorphous films at 650°C regardless of substrates used. No notable differences were observed in the XRD profiles between untreated films and those treated with hydrogen peroxide solution. It was worth noting that PZT films on $Pt/Ti/SiO_2/Si$ substrates had a 100 orientation, while those on $Pt/IrO_2/SiO_2/Si$ substrates had a strong 111 orientation (Figs. 1(b) and 2(b)).

3.2 Surface morphology

As shown in Fig. 3(a), many defects of 5~10 μm in diameter were observed using a reflecting optical microscope on the surface of crystallized PZT films which were prepared on $Pt/Ti/SiO_2/Si$ substrates without the wet-oxidation process. These defects could not be observed by SEM. This indicates that the defects were observable as a difference in the refractive index of the optical microscope. These defects seem to form at the interface between PZT films and bottom electrodes. Lee et al.[13]reported that the Ti-buffer layer in $Pt/Ti/SiO_2/Si$ substrates was oxidized during the annealing so that an erupted region was formed on the surface of $Pt/Ti/SiO_2/Si$ substrates. It is thought that the diffusion of Pb through the deteriorated regions enhances the defect formation. The optical micrographs in Fig. 3 also show the changes in defect density. It increased when the wet-oxidation process was carried out with deionized water but it was reduced drastically by choosing a suitable concentration of hydrogen peroxide solution. It was found that the wet-oxidation process is effective in reducing the defect density observed using an optical microscope. This effect is possibly due to the

suppression of Pb diffusion into the electrodes on the substrates.
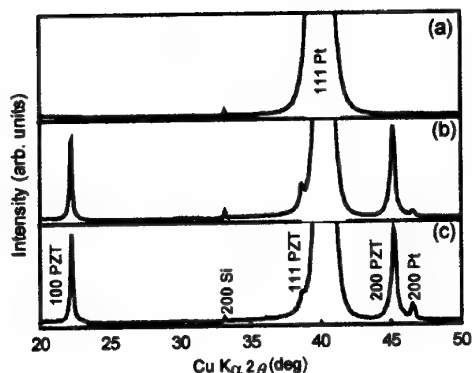
Fig. 1. XRD profiles of PZT films on $Pt/Ti/SiO_2/Si$ substrates. (a) as-deposited, (b) after postannealing without wet-oxidation process and (c) after postannealing with wet-oxidation process.
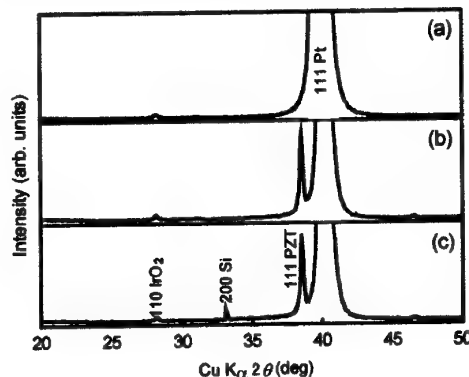
Fig. 2. XRD profiles of PZT films on $Pt/IrO_2/SiO_2/Si$ substrates. (a) as-deposited, (b) after postannealing without wet-oxidation process and (c) after postannealing with wet-oxidation process.
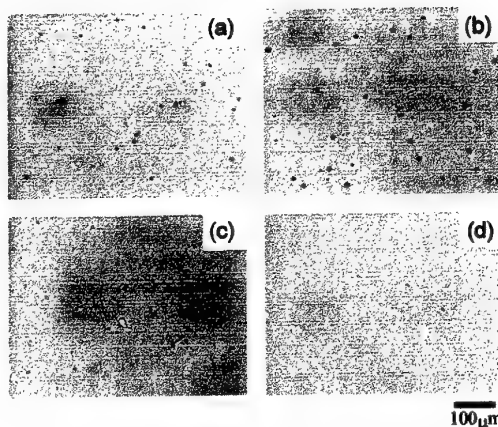
Fig. 3. Optical micrographs of crystallized PZT films. (a) without wet-oxidation process, (b) with wet-oxidation process using deionized water, (c) with the process using 1/10 diluted hydrogen peroxide solution, and (d) with the process using 1/5 diluted hydrogen peroxide solution.

Figure 4 shows the defect density at various hydrogen peroxide concentrations for PZT films 110 nm and 70 nm thick prepared on Pt/Ti/SiO$_2$/Si substrates. The defect density initially increases with increasing concentration and then steeply decreases from 1/10 to 1/5 diluted solution. We found that there was an optimum concentration of hydrogen peroxide solution for the wet-oxidation process, but this changed depending on other conditions, such as process time, sputtering condition of PZT films, temperature during the process and the spinner speed. The increase in the defect density after the process using deionized water and that using 1/10 diluted solution is probably due to the formation of Pb(OH)$_2$ in the films. We attempted one experiment in which as-deposited films were postannealed in H$_2$O vapor. The result showed that the defect density in the obtained films increased markedly. The reaction of water with sputter-deposited amorphous PZT film caused the degradation of the quality and properties of PZT films after crystallization. In this sense, the reaction with water and the oxidation of metallic Pb are competing processes.
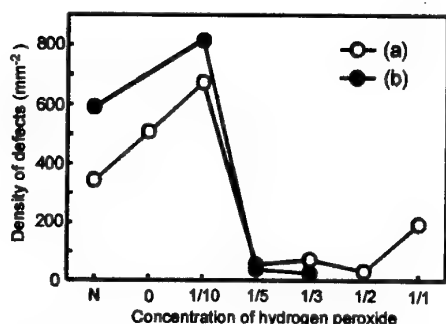
Fig. 4. Defect density of PZT films (a) 110 nm thick and (b) 70 nm thick on Pt/Ti/SiO$_2$/Si substrates observed using an optical microscope as a function of the concentration of hydrogen peroxide solution. In the concentration of hydrogen peroxide solution, N indicates without wet-oxidation process, 0 indicates with process using deionized water, and 1/m means with the process using m-times diluted hydrogen peroxide solution.

In the case of PZT films on Pt/IrO$_2$/SiO$_2$/Si substrates, the defect concentration decreased to 20–40 mm^{-2} even in the films prepared without the wet-oxidation process. The defects were hardly observed using an optical microscope after the wet-oxidation process was carried out using 1/10 to 1/2 diluted solutions. Figure 5 shows the surface morphology of the PZT films observed by FE-SEM. The surface of the as-deposited films was uniform without any defects. After the postannealing, a rosette structure[14] was observed for films both with and without the wet-oxidation process (Figs. 5(a) and 5(b)). It has been reported that sol-gel derived PZT films with Zr-rich compositions exhibit the same rosette structure[15]. At higher magnifications of FE-SEM, a notable difference could be observed between films with and without the oxidation process. In Fig. 5(c) and 5(d), the white area is the rosette and the dark area is the matrix. For PZT films without the wet-oxidation process, there were countless microvoids, which are indicated by circles in Fig. 5(c). On the contrary, the number of

microvoids was diminished by the wet-oxidation process, as shown in Fig. 5(d). The origin of microvoids is still unclear at present, but the evaporation of Pb seems to be one of the important origins. Since the wet-oxidation process forms chemical bonds between metallic Pb and oxygen, the evaporation of Pb should be suppressed by this process. From the experimental results mentioned above, it is confirmed that the wet-oxidation process is effective in suppressing the evaporation and the diffusion of Pb in the PZT films during the postannealing.
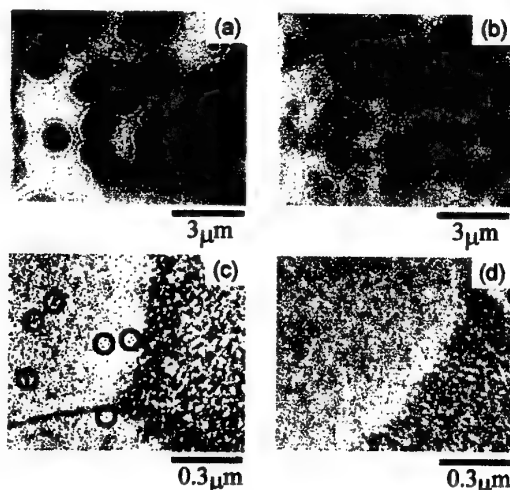
Fig. 5. FE-SEM micrographs of 70 nm-thick PZT films on Pt/IrO$_2$/SiO$_2$/Si substrates prepared without wet-oxidation process ((a) and(c)) and with wet-oxidation process using 1/5 diluted hydrogen peroxide solution ((b) and (d)).

3.3 Electrical properties

Figure 6 shows P-V hysteresis loops of 110 nm-PZT films prepared on Pt/Ti/SiO$_2$/Si substrates. The PZT films without the wet-oxidation process exhibit a hysteresis loop with a rounded shape, indicating that the leakage current is not negligible. On the other hand, the PZT films with the wet-oxidation process exhibit a hysteresis loop with a suitable shape for ferroelectrics. Thus, it is confirmed that the wet-oxidation process is also effective in improving electrical properties of PZT films. However, the high coercive voltage implies that an interfacial layer with a low dielectric constant was formed between PZT films and substrates.
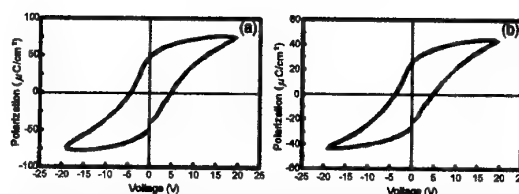
Fig. 6. Hysteresis loops of 110 nm-thick PZT films on Pt/Ti/SiO$_2$/Si substrates prepared (a) without and (b) with wet-oxidation process.

Hysteresis loops of 70 nm-PZT films formed on

Pt/Ti/SiO$_2$/Si substrates are shown in Fig. 7. Despite the reduction of the defect density by the wet-oxidation process as shown in Fig. 4, the hysteresis loop of films with the wet-oxidation was not closed, indicating that the polarization was not maintained. This indicates that the wet-oxidation process is not sufficiently effective to exhibit a proper hysteresis loop if thinner PZT films are formed on Pt/Ti/SiO$_2$/Si substrates.
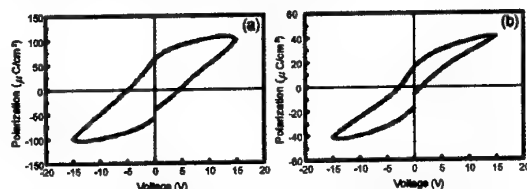
Fig. 7. Hysteresis loops of 70 nm-thick PZT films on Pt/Ti/SiO$_2$/Si substrates prepared (a) without and (b) with wet-oxidation process.

In the case of 140 nm-PZT films prepared on Pt/IrO$_2$/SiO$_2$/Si substrates, a suitable hysteresis loop could be obtained even without the wet-oxidation process and the effect of the wet-oxidation was not observed, which is in contrast with the results of films prepared on Pt/Ti/SiO$_2$/Si substrates. This is because the IrO$_2$ buffer layer suppressed the diffusion of Pb through the electrodes and the PZT thickness was great enough to exhibit the ferroelectricity although microvoids existed. The effect of the wet-oxidization process appeared when the thickness of PZT films on Pt/IrO$_2$/SiO$_2$/Si substrates was decreased to 70 nm. As shown in Fig. 8, a P-V hysteresis loop of the films prepared without the wet-oxidation process exhibited a round shape, which indicates that the films were very leaky. On the other hand, the films with the wet-oxidation process exhibited an excellent ferroelectricity with a slim-type hysteresis loop. The remanent polarization was over 23 μC/cm^2 even at 2 V and the coercive voltage was as low as about 0.7 V. These properties were obtained by combining the wet-oxidation process with the use of Ir-based electrodes.
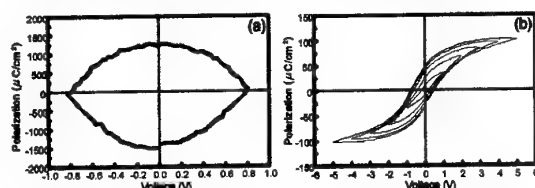
Fig. 8. Hysteresis loops of 70 nm-thick PZT films on Pt/IrO$_2$/SiO$_2$/Si substrates prepared (a) without and (b) with wet-oxidation process.

The sputtering method is thought to be most suitable for application in semiconductor process lines. For commercial application of this method in the preparation of PZT films, the films should be formed by room temperature sputtering followed by a postannealing process. However, the electrical properties of such films were usually not sufficient because of defects formed by the diffusion and the evaporation of metallic Pb during postannealing. In this study, we have demonstrated that the wet-oxidation process using a hydrogen peroxide solution is very effective in improving the quality and electrical properties of the sputter-deposited PZT films.

By combining this process with the use of Ir-based electrodes, it was possible to fabricate PZT films with excellent ferroelectric properties by the sputtering process.

4. CONCLUSION

The effects of the wet-oxidation process using hydrogen peroxide solutions on the microstructure and the electrical properties of sputter-deposited PZT films have been demonstrated. The results are summarized as follows.

(1) A single perovskite phase was formed from as-deposited amorphous films by postannealing at 650°C in a tube furnace.

(2) In the PZT films deposited on Pt/Ti/SiO$_2$/Si substrates, the defect density observed using an optical microscope was drastically decreased by the wet-oxidation process with an optimum concentration of hydrogen peroxide solution.

(3) In the PZT films deposited on Pt/IrO$_2$/SiO$_2$/Si substrates, the number of microvoids formed during postannealing was diminished by the wet-oxidation process.

(4) The 70 nm-thick PZT films on Pt/IrO$_2$/SiO$_2$/Si substrates exhibited the slim-type hysteresis loop with a remanent polarization of over 23 μC/cm^2 even at 2 V and a coercive voltage of about 0.7 V.

REFERENCES

[1] T. Nakamura, *Oyo Buturi*, **67**, 1263–69 (1998) [in Japanese].

[2] Y. Fukuda and K. Aoki, *Jpn. J. Appl. Phys.*, **36**, 5793-98 (1997).

[3] L. L. Boyer, N. Velasquez and J. T. Evans, Jr., *Jpn. J. Appl. Phys.*, **36**, 5799-02 (1997) 5799.

[4] K. Aoki, T. Sakoda and Y. Fukuda, *Jpn. J. Appl. Phys.*, **37** L522-24 (1998).

[5] H. Miki and Y. Ohji, *Jpn. J. Appl. Phys.*, **33**, 5143-46 (1994).

[6] K. Torii, Ph. D. Thesis, Tokyo Institute of Technology, Tokyo, (1998).

[7] S. B. Desu and C. K. Kwok, *Mater. Res. Symp. Proc.*, **200**, 267-74 (1990).

[8] D. K. Choi, S. M. Nam and D. W. Seo, *Ferroelectrics*, **195**, 317-20 (1997).

[9] T. S. Kalkur, G. Argos and L. Kammerdiner, *Mater. Res. Soc. Symp. Proc.*, **200**, 313-18 (1990).

[10] J. P. Goral, M. Huffman and M. M. Al-Jassim, *Mater. Res. Soc. Symp. Proc.*, **200**, 225-30 (1990).

[11] S. M. Nam, H. Kimura, N. Ohashi and T. Tsurumi, *Trans. Mater. Res. Soc. Jpn.*, **24**, 35-8 (1999).

[12] K. Kugimiya, I. Ueda and K. Iizima, *Mater. Res. Soc. Symp. Proc.*, **243**, 179-84 (1992).

[13] J. S. Lee, H. J. Kwon, Y. W. Jeong, H. H. Kim, K. H. Park and C. Y. Kim, *Mater. Res. Soc. Symp. Proc.*, **433**, 175-80 (1996).

[14] L. N. Chapin and S. A. Mayers, *Mater. Res. Soc. Symp. Proc.*, **200**, 153-58 (1990).

[15] T. Atsuki, N. Soyama, G. Sakaki, T. Yonezawa, K. Ogi, K. Sameshima, K. Hoshiba, Y. Nakao and A. Kamisawa, *Jpn. J. Appl. Phys.*, **33**, 5196-00 (1994).

Electric Conduction Characteristics of Pb(Zr, Ti)O$_3$ Thin Films Measured with Interdigitated Electrodes

Hirotake Okino, Toshihisa Horiuchi, Hirofumi Yamada and Kazumi Matsushige

Department of Electronic Science and Engineering, Graduate School of Engineering, Kyoto University, Yoshida Honmachi, Sakyo-ku, Kyoto 606-8501, Japan
Fax: +81-75-753-5749, E-mail: hokino@kuee.kyoto-u.ac.jp

The electric conduction characteristics of as-deposited and H$_2$ annealed Pb(Zr, Ti)O$_3$ (PZT) thin films capacitors were investigated using Pt interdigitated electrodes (IDTs). The *I-V* characteristics of these capacitors were interpreted by a simple conduction model which consisted of series connections of Schottky barriers and an ohmic resistance. It was found that the *I-V* characteristics of as-deposited PZT capacitors almost obeyed the Ohm's law due to the high resistivity of the bulk PZT. Besides, the *I-V* characteristics of H$_2$ annealed capacitors were dominated both by the interface Schottky emission and by the bulk ohmic resistance. It was revealed that both electrons from oxygen vacancies ($E_a \simeq 0.3$ eV) and holes from lead vacancies ($E_a \simeq 0.8$ eV) contributed to the bulk PZT conduction. It was also suggested that the barrier height of the Pt/H$_2$-annealed-PZT Schottky junction was reduced to be 0.28 eV due to the Fermi level pinning derived from the oxygen vacancies.

1 Introduction

There has been great interest in applying ferroelectric thin films to high-density dynamic random access memories (DRAMs) and nonvolatile ferroelectric random access memories (NV-FeRAMs). Pb(Zr, Ti)O$_3$ (PZT) ferroelectric thin films are promising candidates for these applications. In order to achieve highly reliable devices, an understanding of the conduction mechanism of ferroelectric PZT thin films is required. Therefore, there have been many published papers focused on the electric conduction characteristics of PZT films. In these studies, different physical models describing the conduction characteristics have been proposed. These can be grouped into two general classes: interface-controlled and bulk-controlled mechanisms.

Moazzami *et al.* reported on a single-carrier conduction mechanism at high electric field based on a bulk-limited hopping model with an activation energy of about 0.35 eV. The possibility of a Schottky and Frenkel-Poole emission current was discussed by Scott *et al.*[1] Sudlhama *et al.* proposed a two-carrier injection metal-semiconductor-metal model incorporating blocking Schottky contacts with a barrier height of 0.6 eV [2]. Mihara and Watanabe proposed that the conduction mechanism of leakage current at high electric fields was a combination of Schottky and Frenkel-Poole emissions considering the extracted dynamic dielectric constant [3]. Most of articles showed that the electric conduction characteristics (particularly *I-V* characteristics) of PZT films were complicated and it was difficult to distinguish bulk-controlled conduction from interface-controlled conduction.

Therefore, It is necessary to investigate the conduction properties of PZT capacitors which have long distance ($> 1\mu$m) between electrodes so as to discuss bulk-controlled conduction characteristics. Nevertheless, thick and uniform ferroelectric films are hardly prepared using thin film deposition technique such as metalorganic chemical vapor deposition (MOCVD), sputtering and sol-gel. Thus, we adopted interdigitated electrodes (IDTs). Using IDTs, PZT capacitors which have several microns distance between electrodes are able to be obtained. Furthermore, electrical properties of IDT capacitors are intrinsically symmetric in terms of applied electric field direction. This makes it easier to discuss the electrical properties.

In this paper, the electric conduction characteristics of as-deposited and H$_2$ annealed PZT thin films capacitors were investigated. Interface-controlled conduction and bulk-controlled conduction were successfully discussed separately.
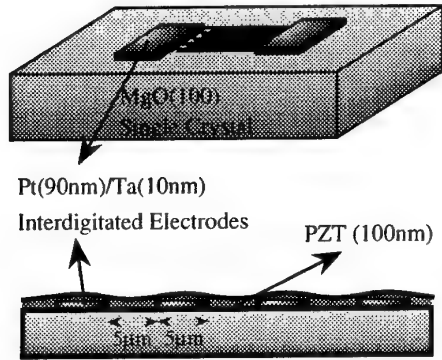
Figure 1: Schematic drawing of the PZT capacitor with IDTs.

Figure 2: Cross-sectional equipotential lines around IDT/PZT surface calculated with a conventional finite-element method.

2   Experimental

The Pt IDTs were fabricated on (100)-cut MgO single crystals (10 mm × 10 mm × 1 mm) by a photolithographic liftoff technique. The 90 nm Pt thin films and the 10 nm Ta adhesion layers were formed using RF planar magnetron sputtering equipment at room temperature. The pattern of the interdigitated electrodes consisted of 100 fingers with a finger width and spacing of 5 μm and a finger length of 2 mm. PZT thin films were deposited on IDT/MgO substrates by MOCVD. The metalorganic precursors used were $Pb(C_2H_5)_4$, $Zr(O\text{-}t\text{-}C_4H_9)_4$ and $Ti(O\text{-}i\text{-}C_3H_7)_4$, and O_2 was used as an oxidizing gas. The substrate temperature was fixed at 550 °C and the reactor pressure was maintained at 5 Torr. The thicknesses of the PZT films were 100 nm. The PZT films were epitaxially grown on the MgO(100) substrates, confirmed using the in-plane energy-dispersive total reflection X-ray diffraction (ED-TXRD) method [4]. The final sample structure is shown in Fig. 1.

The I-V characteristics were measured using a HP4140B programmable electrometer with a built-in voltage source in an air-tight chamber. For I-V measurements, the DC bias takes the form of a staircase and a leakage current is measured at each step. The height of each step (ΔV) and the period between the edge of a step and a moment of current measurement (t_d) were 2 V(4 kV/cm) and 20 s, respectively.

3   Results and Discussions

First, we calculated the distribution of the applied electric field for our sample geometry. Figure 2 shows a cross-sectional equipotential lines around IDT/PZT surface calculated with a conventional finite-element method. The relative dielectric constant of PZT and MgO adopted for this calculation is 500 and 10, respectively. As shown in Fig. 2, the applied electric fields in the PZT films are uniform and parallel to the substrate surface. Thus, the applied electric field E and the electrode contact area S can be approximated by $E = V/d$ and $S = nlh$, respectively. Here, n is the number of periods of electrodes, h is the thickness of the PZT films, and l and d are the length and spacing of the fingers of electrodes, respectively.

Figure 3 shows I-V characteristics of the as-deposited and H_2 annealed PZT capacitor with IDTs measured at 360 K. As shown in Fig. 3 (a), the I-V characteristic of the as-deposited capacitor obeyed the Ohm's law and estimated resistivity of PZT was $\approx 10^{12}$ $\Omega \cdot$m. Nevertheless, after the capacitor was annealed at 620 K for 1 hour in a reduction atmosphere (H_2:N_2 = 0.5:99.5, 1 atm), current was increased remarkably and the I-V curve did not obey either the Ohm's law or the Schottky emission equation. In order to interpret these $I - V$ curves, a simple conduction model which consists of series connections of interface Schottky barriers and an ohmic resistance was conducted.(see Fig. 4) Here, the ohmic current J_{oh} is expressed as
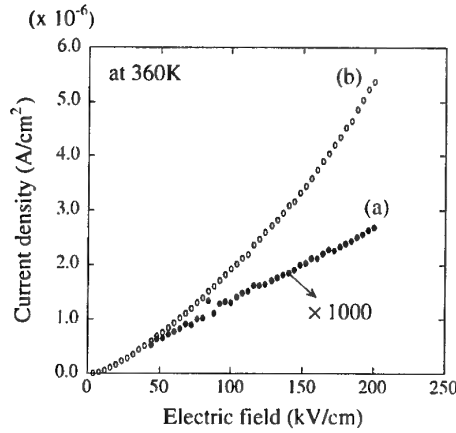
Figure 3: I-V characteristics of (a) the as-deposited and (b) H$_2$ annealed PZT capacitor with IDT measured at 360K
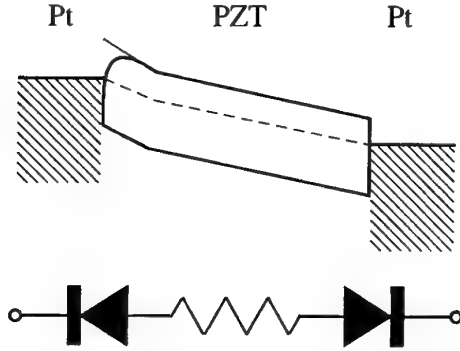
Figure 4: Series connection model which consists of interface Schottky barriers and a bulk ohmic resistance.

$$J_{oh} = \sigma_0 E exp \left(-\frac{qE_a}{k_B T} \right) \quad (1)$$

where σ_0: a constant; E: external electric field; E_a: activation energy; T: temperature; q: unit charge; k_B: Boltzmann's constant. And the Schottky emission current J_{Sch} is written as

$$J_{Sch} = A^* T^2 exp \left[\frac{-q(\phi_B - \sqrt{\frac{qE}{4\pi\epsilon_i\epsilon_0}})}{k_B T} \right] \quad (2)$$

where A^*: the Richardson constant; ϕ_B: potential barrier height; ϵ_0: the permittivity of free space; ϵ_i: dynamic dielectric constant in ferroelectric material in the infrared region.
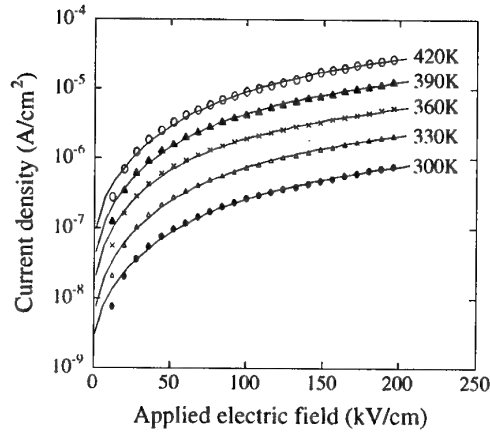
Figure 5: Temperature dependence of the I-V characteristics of H$_2$ annealed PZT capacitors (dots) and fitting curves (lines) by eq. (3).

From eq. (1) and eq. (2), the relationship between applied electric field E and current density J of the series circuit shown in Fig. 4 is given as the following equation.

$$
\begin{aligned}
E &= E_{oh} + E_{Sch} \\
&= \frac{J}{\sigma_0} exp \left(\frac{qE_a}{k_B T} \right) + \\
&\quad \frac{4\pi\epsilon_i\epsilon_0}{q} \left[\frac{k_B T}{q} ln \left(\frac{J}{A^* T^2} \right) + \phi_B \right]^2 (3)
\end{aligned}
$$

Figure 5 shows the temperature dependence of the I-V characteristics of H$_2$ annealed PZT capacitors and fitting curves by eq. (3). There was good agreement with measured I-V curves and the fitting curves ranging over all applied electric field, while in most of publications the only high-field conduction regime was considered and was fitted with different conduction laws. Thus, the proposed model is enough valid to interpret the I-V characteristics of PZT capacitors with IDTs.

From the fitting results, the activation energy E_a of the bulk PZT conduction and the Schottky barrier height ϕ_B were estimated. Figure 6 shows the Arrhenius plot of the calculated electric conductivity of the H$_2$ annealed bulk PZT resistance ranging from 300 K to 420 K. The estimated activation energy E_a was 0.32 eV. Since electrons detrapped from oxygen vacancies were majority carriers after H$_2$ annealing, this value was ascribable to the activation energy of trapped electrons in an oxygen vacancies. The activation energy E_a of the bulk
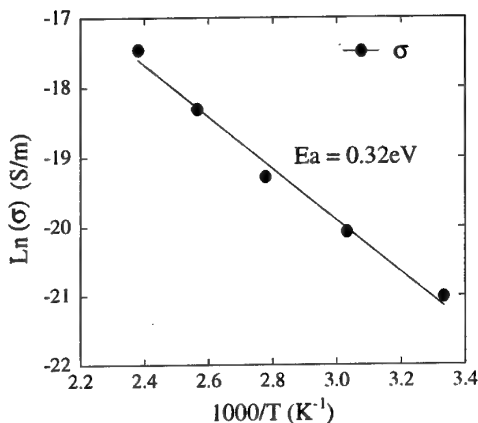
Figure 6: Arrhenius plot of calculated electric conductivity of bulk PZT resistance after H_2 annealing.

Figure 7: Plot of $ln(J_{Sch}/T^2)$ vs $1000/T$ for the H_2 annealed PZT capacitor with IDT.

as-deposited PZT conduction were also calculated using eq. (3) and the estimated value was 0.85 eV. This evaluation agreed with the reported value on the activation energy of hole conduction of ceramic PZT [5], showing that the majority carriers of the as-deposited PZT were holes detrapped from lead vacancies.

The estimated Schottky barrier height ϕ_B on the Pt/H_2-annealed-PZT surface was 0.28 eV as shown in Fig. 7. This value was less than the widely reported values (0.5–0.9 eV) of the Schottky barrier height with Pt/PZT/Pt thin film capacitors. Because this estimated value 0.28 eV was almost the same as the value of the activation energy of trapped electrons, it was suggested that the Fermi level on the Pt/H_2-annealed-PZT surface was pinned by the surface state derived from the oxygen vacancies.

4   Conclusions

The I-V characteristics of the PZT capacitors with IDTs were successfully interpreted by the conduction model which consisted of series connections of interface Schottky barriers and an ohmic resistance ascribable to bulk PZT. Applying this model to the conduction behavior of the PZT capacitors with IDTs, interface-controlled conduction and bulk-controlled conduction were investigated separately. The bulk PZT conduction was found to be dominated both by electrons from oxygen vacancies ($E_a \simeq$ 0.3 eV) and by holes from lead vacancies ($E_a \simeq$ 0.8 eV). The estimated barrier height of the

Pt/H_2-annealed-PZT Schottky junction was 0.28 eV because of the Fermi level pinning derived from the oxygen vacancies.

References

[1] J. F. Scott, M. Azuma, C. A. Araujo, L. D. McMillan, M. Scott and T. Roberts: *Proceedings of the Fifth International Symposium on Integrated Ferroelectrics, Colorad Springs, 1993,*

[2] C. Sudhama, A. C. Campbell, P. D. Maniar, R. E. Jones, R. Moazzami, C. J. Mogab and J. C. Lee: J. Appl. Phys. **75** (1994) 1014

[3] T. Mihara and H. Watanabe Jpn. J. Appl. Phys. **34** (1995) 5664

[4] T. Horiuchi, K. Fukao and K. Matsushige: Jpn. J. Appl. Phys. **26** (1987) L1839.

[5] M. V. Raymond, and D. M. Smyth: Integrated Ferroelectrics **4** (1994) 145

Microstructures of Sol-Gel Derived PZT Thin Films

Kazunari Maki, Nobuyuki Soyama, Satoru Mori, Kensuke Kageyama*, Masaya Matsuura*, and Katsumi Ogi*

Sanda Plant Development Section, Mitsubishi Materials Corporation, 12-6, Technopark, Sanda, Hyogo 669-1339, Japan
Fax: 81-795-68-2325, e-mail: k-maki@mmc.co.jp
*Central Research Institute, Mitsubishi Materials Corporation, 1-297, Kitabukuro-cho, Omiya, Saitama 330-8508, Japan

We have studied the pyrolysis temperature dependence of the microstructure, orientation, and electric properties for $PbZr_{0.52}Ti_{0.48}O_3$ thin films prepared from two-type of sol-gel solutions. One was a conventional standard solution (STD), the other was a modified solution prepared by optimization of the hydrolysis and condensation condition. The results clearly showed that (111)-oriented films comprised of fine columnar grains with perovskite single-phase had the better ferroelectric properties (higher remanent polarization and lower leakage current) than films with the nanocrystalline pyrochlore grains. One of the methods to get PZT films with good properties mentioned above is to pyrolyze gel films at low temperature. Another method is to use the modified solution that enables us to get the dense heterogeneous nucleation at a wide range of the pyrolysis temperature.

1. INTRODUCTION

PZT and La-doped PZT (PLZT) films are attractive for application to nonvolatile memories, infrared sensors, electro-optic devices, and microactuators. The microstructure, orientation, and electric properties of chemical-solution derived P(L)ZT thin films on Pt(111) electrode have been modified by optimization of the composition of films (Zr/Ti ratio[1,2] and excess Pb content[1,3]), the seeding method (PbTiO$_3$[4], TiO$_x$[1] and so on), preparing process of films (heating rate of crystallization[1,3,5], pyrolysis temperature[6-10] and pyrolysis atmosphere[11] and so on), and the chemical solution (sol-gel[12], MOD[9], the preparing condition[13,14] and so on). Most experiment mentioned above was conducted by using Pt(111)/Ti/SiO$_2$/Si.[1,3-11,15,16] However, it is known that diffusion of Ti through Pt layer from Ti adhesion layer and oxidation of Ti on Pt layer occur at the processing temperature for the preparation of PZT film.[6] This TiO$_x$ becomes nucleation site of perovskite and has an effect on nucleation density of perovskite. We used Pt(111)/SiO$_2$/Si substrate to ignore the influence of Ti adhesion layer. We have studied the pyrolysis temperature dependence of the microstructure, orientation, and electric properties for the films prepared from two-type of sol-gel solutions. One of the solutions is a conventional standard solution (STD), the other is a modified solution. This pyrolysis dependence is applicable to the substrate without Ti layer (Pt/Ta, Pt/IrO$_2$, Pt/Ir and so on). And we have discussed the mechanism of nucleation and crystal growth of PZT film.

2. EXPERIMENTAL PROCEDURE

PZT films were fabricated from two-type of sol-gel solutions (Mitsubishi Materials Corp.). The starting materials for the solutions were lead acetate trihydrate, titanium tetra-iso-propoxide, zirconium tetra-n-butoxide, 2-methoxyethanol (solvent), acetylacetone, and water.[1] The modified solutions were prepared by optimizing the hydrolysis and condensation condition of STD. The concentration and composition of the solution were 10wt% $Pb_{1+x}(Zr_{0.52}Ti_{0.48})O_{3+x}$ (x=0.1 or 0.15). Pt(200nm) or Pt(200nm)/Ti(10nm) bottom electrodes were deposited on the SiO$_2$(500nm)/Si(100) wafers by dc magnetron sputtering. The solutions were spin-coated onto Pt/(Ti)/SiO$_2$/Si substrate at 500rpm for 3s and continuously at 3000rpm for 15s. Then the films were pyrolyzed in air at various temperatures (200-400℃) for 10min on a hot plate. This process was repeated 5 times. Then the films were crystallized in O$_2$ at 700℃ for 1min by rapid thermal annealing (RTA). The thickness of resultant PZT films was 200nm. The microstructure of the film was observed by SEM. Crystallinity was analyzed by θ-2θ X-ray diffraction (XRD), and depth profile of PZT film was measured by Auger electron spectroscopy (AES). For electrical measurements, Pt(200nm) top electrodes (the size was $6.5 \times 10^{-4}cm^2$) were deposited by dc magnetron sputtering and the films were again annealed in O$_2$ at 700℃ for 1min by RTA as the recovery annealing. The hysteresis loops and leakage current density were measured by Radiant Technologies RT66A and Keithley 236 source measurement respectively.

3. RESULTS AND DISCUSSION

3.1 Substrate dependence of films

Fig.1 shows the substrate dependence of surface morphology for $Pb_{1.1}(Zr_{0.52}Ti_{0.48})O_{3.1}$ [PZT(110/52/48)] annealed films. The films were prepared from STD and processed at the pyrolysis temperature 400℃. PZT film on Pt(111)/SiO$_2$/Si substrate had "rosette" structure[2,5]. The rosette size was 2-7μm. On the other hand, PZT film on Pt(111)/Ti/SiO$_2$/Si substrate had fine perovskite grains (the grain size was 150nm) with the nanocrystalline pyrochlore grains at the surface. It is clear that Ti species diffuse onto Pt layer from Ti layer and become nucleation sites of perovskite. Hereafter, we used Pt(111)/SiO$_2$/Si substrate to ignore the influence of Ti layer.

3.2 Pyrolysis temperature dependence of films

Fig.2 shows the pyrolysis temperature dependence of surface morphology for PZT(115/52/48) annealed films. In the case of STD, the films processed at the low pyrolysis temperature (200-250℃) formed fine perovskite single-phase. The film tends to form larger perovskite grains and has the nanocrystalline pyrochlore, as the pyrolysis temperature increases. Especially, the films processed at the pyrolysis temperature 350-400℃ had the same rosette structure that we mentioned above. On the other hand, films prepared from modified solution formed the fine perovskite single-phase irrespective of the pyrolysis temperature. The film slightly tends to form finer grains,

as the pyrolysis temperature decreases. The grain sizes in the films processed at the pyrolysis temperature 200-250°C, 300°C, and 350-400°C were 50-100nm, about 100nm, and 100-150nm. It was found that modified solution made nucleation density increase at a wide range of the pyrolysis temperature. Fig.3 shows the cross-sectional SEM image of PZT(115/52/48) annealed films, which is one of the representatives of fine columnar grains with perovskite single-phase. The film was processed at the pyrolysis temperature 200°C from modified solution (refer to Fig.2(b)). Films prepared from modified solution or films processed at the low pyrolysis temperature from STD had the columnar grains.

Fig.4 shows XRD patterns of PZT(115/52/48) as-pyrolyzed films. The broad amorphous humps centered at about 29° were observed from all as-pyrolyzed films. These XRD patterns resemble the results of Brooks et al.[6]. The height of the broad hump slightly increases, as the pyrolysis temperature increases. $Pt_{5-7}Pb$ peak reported by others[9,10,16] was not observed at a whole range of the pyrolysis temperature. The broad peaks at about 20° are confirmed to originate from the substrates. Significant difference between XRD patterns of films from STD and those from modified solution was not observed.

Fig.5 shows the pyrolysis temperature dependence of XRD patterns for PZT(115/52/48) annealed films. XRD patterns of the films prepared from modified solution had a strong (111) peak and weak peaks of (110) and (211), irrespective of pyrolysis temperature. It is considered that the strong (111) peak is due to the majority of perovskite

grains nucleated on Pt(111) surface, the weak peaks of (110) and (211) are due to the minority of perovskite grains nucleated in the bulk of PZT films. In the case of STD, XRD patterns of films processed at the low pyrolysis temperature (200-250°C) had the same peaks as those from modified solution. The film processed at the pyrolysis temperature 300°C had the strongest (111) orientation. The film has the lower nucleation density than films processed at the low pyrolysis temperature (200-250°C) and seems to have hardly any perovskite grains nucleated in the bulk of PZT film. The films processed at the pyrolysis temperature 350-400°C were randomly oriented. It is considered that the perovskite grains which form radial lamellae of rosettes are no preferred oriented, as previously reported.[2,5] This random orientation of films on Pt substrate is different from other results on Pt/Ti substrate. PZT film processed at the high pyrolysis temperature is (100)-oriented on $Pt/Ti/SiO_2/Si$.[5-7,9,10,16] The difference of the orientation may be due to Ti layer. In the case of Pt/Ti substrate, TiO_x on Pt layer reacts with Pb and forms $PbTiO_3$ or Ti-rich PZT.[1,6] It is quite likely to have an effect on nucleation mechanism and orientation of the nucleus.

Fig.6 shows AES depth profiles of PZT(110/52/48) annealed films. The films were pyrolyzed at 400°C. In the case of STD, the results clearly shows that Ti concentration is nearly constant throughout PZT film, Pb concentration tends to decrease from PZT/Pt interface to PZT surface. It is known that nanocrystalline pyrochlore matrix surrounding rosettes is Pb-deficient compared to

Fig.1 Substrate dependence of surface morphology for PZT(110/52/48) films, which were prepared from STD.

Fig.2 Pyrolysis temperature dependence of surface morphology for PZT(115/52/48) annealed films, which were prepared from (a) STD and (b) modified solution.

the perovskite rosette.[1,7] The nanocrystalline pyrochlore exists more near PZT surface than PZT/Pt interface, because perovskite crystal growth develops from PZT/Pt interface to PZT surface.[6] It is considered that Pb-deficiency near PZT surface is due to more pyrochlore matrix. In the case of modified solution, it was found that Ti concentration tended to decrease from PZT/Pt interface to PZT surface, Pb concentration was nearly constant throughout PZT film. Nucleation and crystal growth of the film from modified solution are inferred from these results in the following way. (refer to Fig.7)

(a) Nucleation: It is known that PZT is (111)-oriented on Pt/Ti/SiO$_2$/Si substrate, when films are processed at the low pyrolysis temperature.[6,7,10,16] It is supposed that TiO$_x$ on Pt/Ti/SiO$_2$/Si is the source of the enhanced Ti concentration, facilitates nucleation of Ti-rich PZT(111) that reduces the lattice mismatch between Pt(111) and PZT(111).[1,6] From our results, we suppose that PbTiO$_3$(111) or Ti-rich PZT(111) nucleates epitaxially on Pt(111) to reduce the lattice mismatching between Pt(111) and PZT(111), even if the source of the enhanced Ti concentration (PbTiO$_3$ and TiO$_x$ and so on) does not exist

Fig.3 Cross-sectional SEM image of PZT(115/52/48) annealed film, which was prepared from modified solution and pyrolyzed at 200℃.
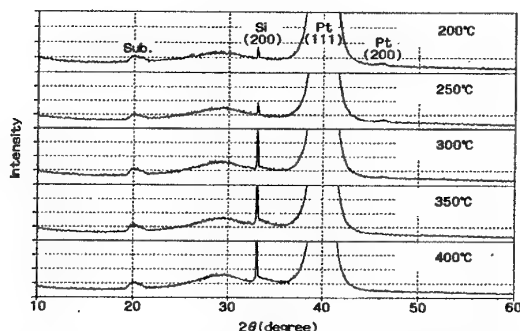
on Pt(111). d$_{111}$ of Pt, PbTiO$_3$, and Pb(Zr$_{0.52}$Ti$_{0.48}$)O$_3$ is 2.265 Å, 2.297 Å, and 2.351 Å.[17] The mismatch of d$_{111}$ between Pt and PbTiO$_3$ (1.4%) is smaller than that between Pt and Pb(Zr$_{0.52}$Ti$_{0.48}$)O$_3$ (3.8%).

(b) Crystal growth: Following nucleation, crystal growth of PZT(111) develops increasing Zr concentration toward film surface. Consequently the resultant film becomes (111)-oriented film comprised of fine columnar grains with perovskite single-phase. It is considered that nucleation and crystal growth of films processed at the low pyrolysis temperature from STD are the same.

Fig.8 shows the pyrolysis temperature dependence of hysteresis loops for PZT(115/52/48) films. The ferroelectric properties of films processed at the pyrolysis temperature 250℃ are summarized in Table I. Hysteresis loops of the films prepared from modified solution were independent of pyrolysis temperature in accordance with the microstructure and orientation. In the case of STD, hysteresis loops of films processed at the pyrolysis temperature 250-300℃ were larger than those processed at the high temperature, the difference of (111)-orientation seems to be the main cause. Remanent polarization (P$_r$) of films from modified solution was higher than that from STD at a whole range of the pyrolysis temperature. Quantity of perovskite and/or (111)-orientation seems to be the cause of difference between P$_r$ of the film from STD and that from modified solution, when the pyrolysis temperature is 300-400℃. Fig.9 shows leakage current density of PZT(115/52/48) annealed films. Leakage current density of films from modified solution was lower than that from STD, when the pyrolysis temperature was 300℃. There was no significant difference between STD and modified solution, when the pyrolysis temperature

(a) STD

(b) modified

Fig.4 Pyrolysis temperature dependence of XRD patterns for PZT (115/52/48) as-pyrolyzed films, which were prepared from (a) STD and (b) modified solution.
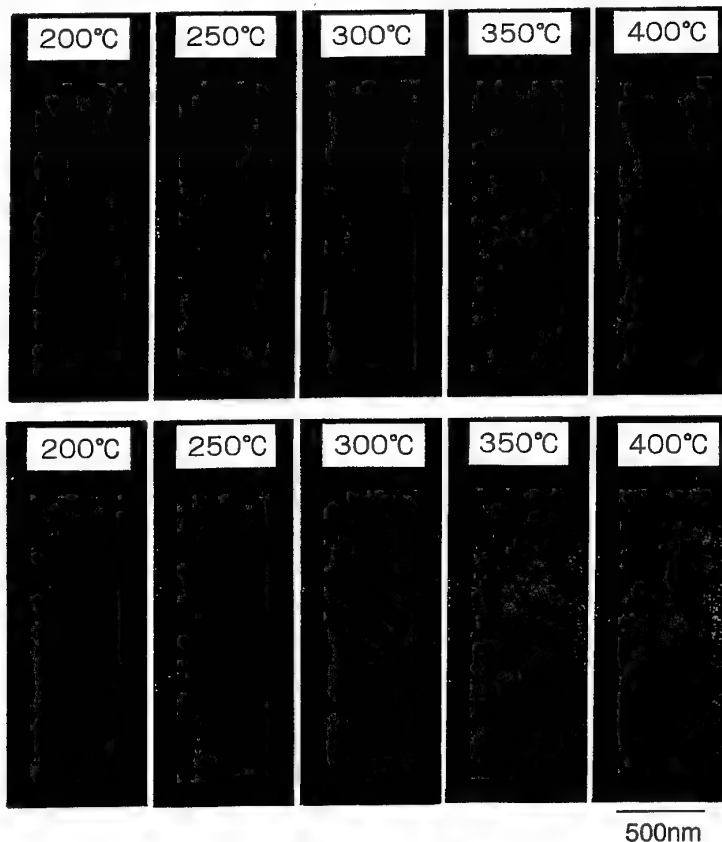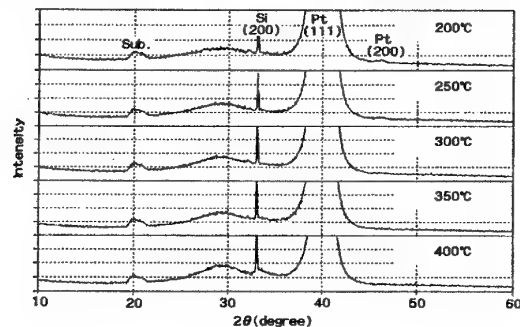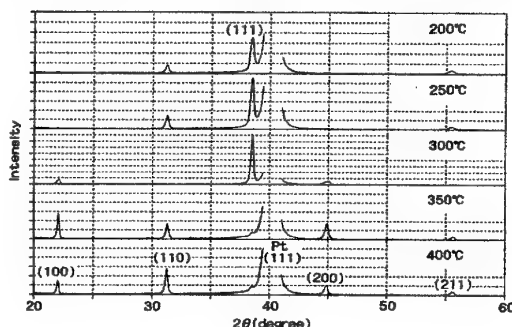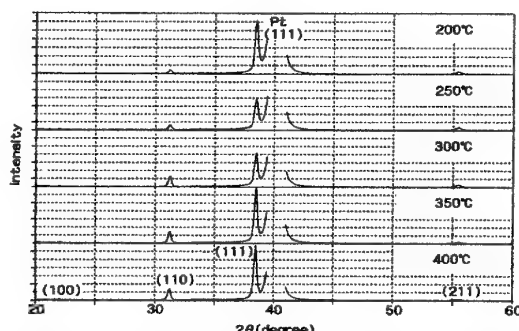

(a) STD

(b) modified

Fig.5 Pyrolysis temperature dependence of XRD patterns for PZT (115/52/48) annealed films, which were prepared from (a) STD and (b) modified solution.

(a)
STD

(b)
modified
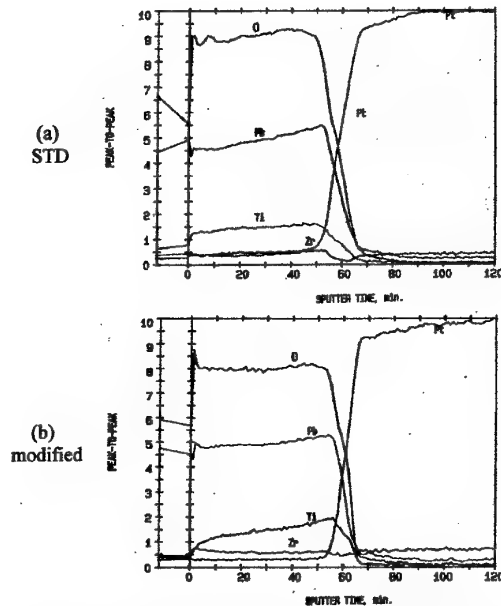
Fig.6 AES depth profiles of PZT(115/52/48) annealed films, which were prepared from (a) STD and (b) modified solution.

(a) nucleation   (b) crystal growth
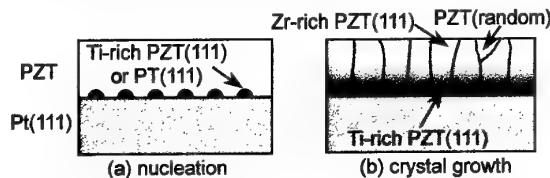
Fig.7 Schematic representations of nucleation and crystal growth of films comprised of fine columnar perovskite grains.

Fig.8 Pyrolysis temperature dependence of hysteresis loops for PZT(115/52/48) annealed films.

Fig.9 Pyrolysis temperature dependence of leakage current density for PZT(115/52/48) annealed films

was 250°C. The leakage current density depends on the microstructure of the film, and the films comprised of fine grains with perovskite single-phase have lower leakage current density, as Doi et al.[4] reported.

Table I. Ferroelectric properties of 200nm PZT(115/52/48) annealed films. The pyrolysis temperature was 250°C.

solution	$P_r(\mu C/cm^2)$ at 150kV/cm	$E_c(kV/cm)$ at 150kV/cm	$P_r(\mu C/cm^2)$ at 250kV/cm	$E_c(kV/cm)$ at 250kV/cm
modified	18.0	36	20.6	41
STD	15.4	35	18.7	41

4. CONCLUSIONS

We have studied the pyrolysis temperature dependence (200-400°C) of the microstructure, orientation, and electric properties for PZT films prepared from two-type of sol-gel solutions on Pt(111)/SiO$_2$/Si substrate.

(1) The films prepared from modified solution were (111)-oriented and comprised of fine columnar grains with perovskite single-phase irrespective of the pyrolysis temperature. In the case of conventional standard solution (STD), the films processed at the low pyrolysis temperature formed the same structure as films from modified solution. The film tends to form randomly oriented film comprised of larger perovskite grains and nanocrystalline pyrochlore, as the pyrolysis temperature increases.

(2) P$_r$ of film prepared from modified solution was higher than that from STD at a whole range of the pyrolysis temperature. Leakage current density of films processed at the pyrolysis temperature 300 °C from

modified solution was lower than that from STD. (111)-oriented films comprised of fine columnar grains with perovskite single-phase had the better ferroelectric properties than films with nanocrystalline pyrochlore.

(3) Mechanism of nucleation and crystal growth of films comprised of fine columnar perovskite grains was inferred.

5. REFERENCES

[1]T.Atsuki, N.Soyama, G.Sasaki, T.Yonezawa, K.Ogi, K.Sameshima, K.Hoshiba, Y.Nakao, and A.Kamisawa, Jpn. J. Appl. Phys., 33, 5196-200 (1994)

[2]S.A.Myers and L.N.Chapin, Mater. Res. Soc. Symp. Proc., 200, 231-36 (1990)

[3]B.A.Tuttle, R.W.Schwartz, D.H.Doughty, J.A.Voigt, and A.H.Garim, Mater. Res. Soc. Symp. Proc., 200, 159-65 (1990)

[4]H.Doi, T.Atsuki, N.Soyama, G.Sasaki, T.Yonezawa, and K.Ogi, Jpn. J. Appl. Phys., 33, 5159-66 (1994)

[5]S.Y.Chen and I.W.Chen, J. Am. Ceram. Soc., 81, 97-105 (1998)

[6]K.G.Brooks, I.M.Reaney, R.Klissurska, Y.Huang. L.Bursill, and N.Setter, J. Mater. Res., 9, 2540-53 (1994)

[7]I.M.Reaney, K.Brooks, R.Klissurska, C.Pawlaczyk, and N.Setter, J. Am. Ceram. Soc., 77, 1209-16 (1994)

[8]Y.Liu and P.P.Phule, J. Am. Ceram. Soc., 79, 495-98 (1996)

[9]S.Y.Chen and I.W.Chen, J. Am. Ceram. Soc., 77, 2332-36 (1994)

[10]S.Y.Chen and I.W.Chen, J. Am. Ceram. Soc., 77, 2337-44 (1994)

[11]S.Hirano, T.Yogo, K.Kikuta, Y.Araki, M.Saitoh, and S.Ogasahara, J. Am. Ceram. Soc., 75, 2785-89 (1992)

[12]K.D.Budd, S.K.Dey, and D.A.Payne, Br. Ceram. Proc., 36, 107-21 (1985)

[13]R.W.Schwartz, B.C.Bunker, D.B.Dimos, R.A.Assink, B.A.Tuttle, D.R.Tallant, and I.A.Weinstock, Proceedings of the 3rd International Symposium on Integrated Ferroelectrics, 535-46 (1991)

[14]C.D.E.Lakeman and D.A.Payne, J. Am. Ceram. Soc., 75, 3091-96 (1992)

[15]T.Tani, Z.Xu, and D.A.Payne, Mater. Res. Soc. Symp. Proc., 310, 269-74 (1993)

[16]H.Suzuki, Y.Kondo, S.Kaneko, and T.Hayashi, "Orientation Control of Low-Temperature Processed Pb(Zr,Ti)O$_3$ Thin Films", Mater. Res. Soc. Symp. Proc., in press

[17]JCPDS card, 4-802, 6-452, 33-784

Effects of Stacking Structure on Crystallization and Electrical Properties of $Pb(Zr_{0.53}Ti_{0.47})O_3$ Thin Films from Stable Precursor Sol

Hisao Suzuki*, Takahiro Koizumi*

*Department of Materials Science Shizuoka University, 3-5-1 Johoku, Hamamatsu, Shizuoka 432-8561, Japan
Fax : 81-53-478-1157, e-mail : hisuzuki@eng.shizuoka.ac.jp

A stable sol was prepared from a lead acetate trihydrate, zirconium and titanium alkoxides for a low-temperature processing of a lead zirconate titanate ($Pb(Zr_{0.53}Ti_{0.47})O_3$;PZT) thin film. The process involves the addition of an excess lead oxide and the insertion of seeding layer of a perovskite lead titanate (PT) between PZT precursor layer and substrate. A perovskite ratio in the thin films increased with increasing amount of excess lead oxide and a single phase perovskite film was deposited at 550℃. As a result, ferroelectric PZT thin films were successfully deposited at above 550℃. The crystallization behavior was also affected by the amount of excessive lead. The PZT films deposited on the ITO/glass substrate has random orientation whereas the PZT thin films on the Pt/Ti/SiO$_2$/Si substrate exhibited (111) orientation at above 550℃. The low-temperature processed PZT thin films with thickness about 500nm exhibited relatively good dielectric and ferroelectric properties (ε_r: 550 - 840, P_r:39 - 63 μC/cm^2).

1. INTRODUCTION

Ferroelectric thin films with a perovskite structure have been attracting attention to apply nonvolatile memories, an infrared sensor, micro actuators and electrooptic devices. Especially, lead zirconate titanate (PZT) thin films with different compositions have been widely studied because of their high dielectric constant and remanent polarization as well as the superior pyroelectric and piezoelectric properties.

A physical method such as sputtering and laser ablation, chemical vapor deposition and wet chemical processing such as a sol-gel process have been used for the formation of ferroelectric PZT thin films[1)-3)]. Among them, a sol-gel process is one of the most promising method because it offers precise control of a composition at molecule level as well as the lower processing temperature, production of large film area with homogeneous composition. However, an alkoxide precursor solution reacts sensitively with the water in the atmosphere.

On the other hand, low-temperature processing is very important for the PZT thin films because high temperature annealing above 700 ℃ degrades the silicon transistor. In addition, interdiffusion of the atoms between a PZT film and a substrate causes a serious problem, leading to the fatigue of the resultant films. Therefore, low-temperature processing of the PZT films is indispensable for the memory application with high density integration. Moreover, various substrates with low-melting temperatures such as glass and aluminum could be available, leading to the wide application areas. In the previous paper[4),5),6)], low-temperature processing of PZT thin films have been successfully attained through single- or multi-seeding process from alkoxide precursor solution, in which a lead titanate (PT) seeding layers are inserted between PZT layers.

In this paper, effects of the excess lead oxide addition and substrates on the crystallization and electrical properties of the PZT thin films deposited from stable precursor sols were investigated, as well as the effect of the stacking structure of the precursor films including seeding layer. In this process, acetic acid was used as a chelating agent to stabilize the sols. In this study, single seeding process was used. Excess addition of lead oxide will compensate the depletion of a lead oxide by the evaporation and diffusion during annealing, leading to the low-temperature processing. This paper described the optimum conditions of these parameters for low-temperature processing of PZT thin film from stable precursor sol.

2. EXPERIMENTAL PROCEDURE

PZT (Zr/Ti=53/47) precursor sol of 0.3M was prepared from lead acetate trihydrate ($Pb(OCOCH_3)_2 \cdot 3H_2O$), titanium iso-propoxide ($Ti[(CH_3)_2CHO]_4$), zirconium n- propoxide ($Zr(C_3H_7)_4$) acetic acid, water and ethanol. At first, lead acetate trihydrated was dehydrated and then dissolved in acetic acid at 80℃. On the other hand, titanium iso-propoxide or zirconium n- propoxide was mixed and reacted with an acetic acid in ethanol, respectively. Ti-precursor solution was mixed and reacted with Pb solution and then reacted with the Zr-precursor solution to prepare the PZT precursor solution. PZT precursor solution was hydrolyzed with stoichiometric amount of water to form a stable sol. Finally, acetylacetone was added to the sol as a stabilizing agent.

A PZT precursor film was deposited by dip-coating method on a Pt(111)/Ti/SiO$_2$/Si or ITO/glass substrates, in this study. The film thickness was about 500nm with 9 and 11times of coatings for silicon wafer and ITO/glass, respectively. After each precursor layers were deposited, precursor films were pre-annealed at 350 ℃ for 1 hour in an ambient atmosphere to pyrolyze the residual organic compound. Finally, these amorphous precursor films were annealed in the range

from 450℃ to 600℃ for 2 hours in an ambient atmosphere using muffle furnace.

Crystalline phases in the PZT thin films were identified by X-ray diffraction (XRD). For electrical measurement, Au top electrodes with a diameter of 0.2 mm were sputtered. Dielectric property of the thin film was measured by LCR meter (HP-4284A). P-E hysteresis loops of the resultant thin films were measured by RT6600S (Radiant Technology Inc.).

3. RESULTS AND DISCUSSION

3.1 Crystallization behavior

PZT precursor sol or films with a stoichiometric composition, 30 and 50 mol % of excess lead oxide were abbreviated as PZT(100/53/47), PZT(130/53/47) and PZT(150/53/47), respectively. Lead titanate layer with a stoichiometric composition (PT(100)) or 50 mol % of excess lead oxide (PT(150)) was used as a seeding layer. Figure 1 shows three types of the stacking structures for the PZT thin films.
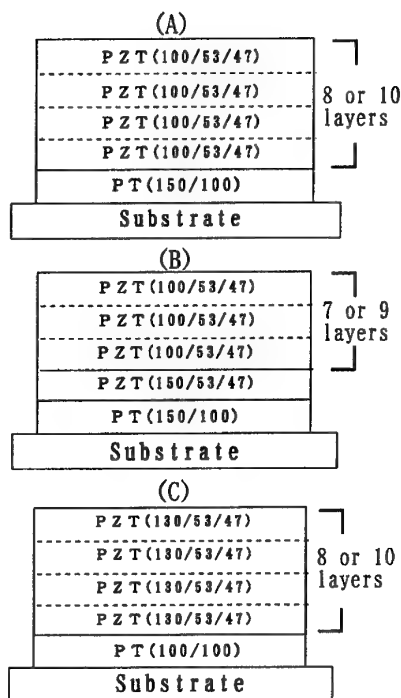
Fig. 1 Stacking structures of PZT thin films.

Figure 2 shows the XRD patterns for the PZT films deposited on a Pt/Ti/SiO₂/Si substrate, annealed at 550 ℃ to investigate the effect of the stacking structure on the crystallization behavior. The difference between stacking (A) and (B) is the composition of a PZT layer just above the seeding layer. (A) structure promoted the crystallization of a perovskite phase but still exhibited residual pyrochlore

phase in the film. On the other hand, PZT films with stacking structures of (B) and (C) showed the single-phase perovskite structure. These results indicates that the lead element diffused into substrate during annealing and at least two layers (about 100 nm thick) with excess lead were indispensable for low-temperature processing of PZT thin films on a Pt/Ti/SiO₂/Si substrate through this process. As a result, single-phase perovskite PZT thin films with different stacking structures were successfully deposited on a Pt/Ti/SiO₂/Si substrate at low temperature of 550℃ by the insertion of PT seeding layer and the addition of excess lead oxide. In this case, PZT films showed (111) orientation.
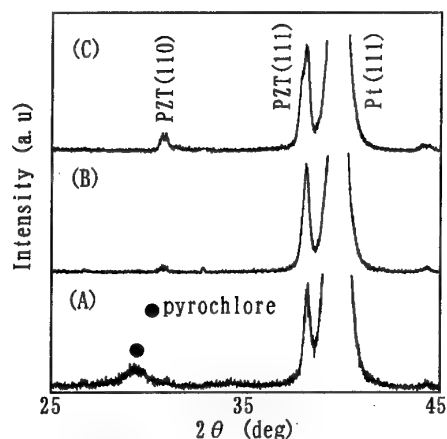
Fig. 2 XRD patterns for PZT thin films on Pt/Ti/SiO₂/Si substrates annealed at 550℃.
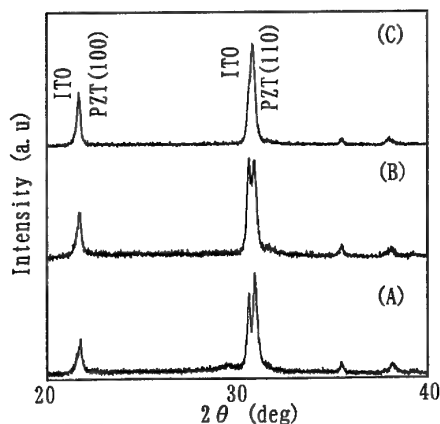
Fig. 3 XRD patterns for PZT thin films on ITO/glass substrates annealed at 550℃.

Figure 3 shows the XRD patterns for the PZT films on ITO/glass substrate annealed at 550℃. Only the single-phase perovskite with random orientation was identified for the films on ITO/glass substrate. However, the main peak shifted toward the lower

angle by the 0.06° for the case of the PZT film with excess amount of a lead oxide (Fig. 3(C)). The reason was not clear. Figures 2 and 3 exhibited that the substrates had large effect on the crystallization behavior of the PZT thin film. This difference is ascribed to the columnar structure of the Pt electrode on Si, which leads to the diffusion of lead through boundary at higher temperatures.

3.2 Electrical properties

Figure 4 exhibits the change in the relative permittivity of the resultant film on ITO/glass and Pt/Ti/SiO$_2$/Si substrate with the amount of excess lead oxide in the PZT precursor film. The amount of the excess lead oxide was calculated from the stacking structures. This figure shows that the PZT films on a Pt/Ti/SiO$_2$/Si substrate had superior dielectric property than those on the ITO/glass substrate. Furthermore, relative permittivity of the resultant PZT films tends to be leveled off at above 30 mol % excess addition of a lead oxide. In addition, high temperature annealing improved the dielectric property of the resultant films, especially for the films on a Pt/Ti/SiO$_2$/Si substrate. For the PZT film with a (C) stacking structure annealed at 600 ℃, highest permittivity of about 840 was obtained.
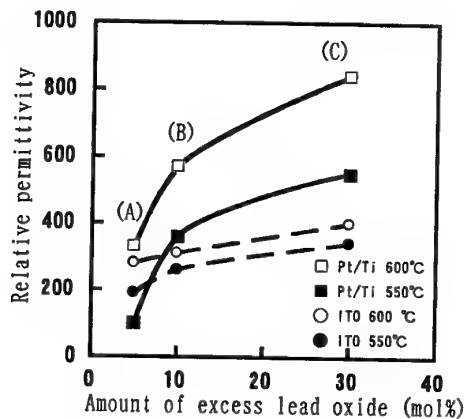
Fig. 4 A relation between relative permittivity and amount of excess lead oxide.

As already described, relatively good PZT films were deposited both on the Pt/Ti/SiO$_2$/Si and ITO/glass substrates at low temperature of 550℃. Therefore, ferroelectric property of the PZT films on Pt/Ti/SiO$_2$/Si and ITO/glass substrates was estimated and shown in figure 5. From this figure, it is concluded that the PZT films with a single-phase perovskite structure and different stacking structures of (B) and (C) on a Pt/Ti/SiO$_2$/Si substrate exhibited relatively high remanent polarization of 36 and 39 μ C/cm^2, respectively. Coercive field of these films exhibited similar values (Fig. 5 (a)). On the other hand, PZT thin films with stacking structures of (A), (B) and

(C) on ITO/glass substrate, annealed at 550 ℃, exhibited the remanent polarization of 19, 42 and 50 μ C/cm^2, respectively. The PZT films on ITO/glass substrate showed relatively good ferroelectricity although the relative permittivity of these films was not so good. This suggests the formation of the amorphous reaction phase with low relative permittivity for the films on ITO/glass substrate. In addition, PZT films with larger amount of excess lead oxide tends to have higher remanent polarization and lower coercive field independent of the substrates.
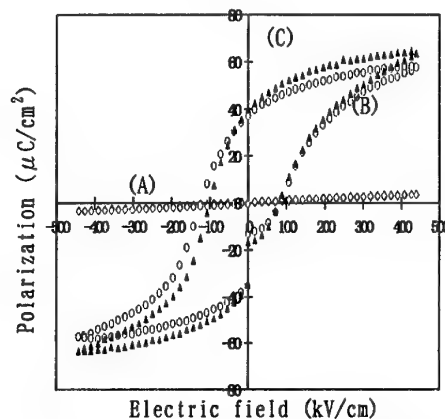
Fig. 5 (a) P-E Hysteresis loops of PZT thin films on Pt/Ti/SiO₂/Si substrates with different stacking structures of (A), (B) and (C) in Fig. 1 annealed at 550℃.
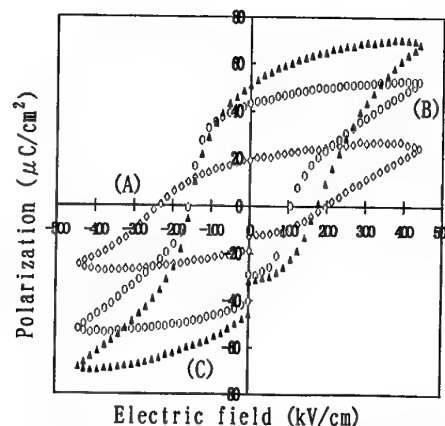
Fig. 5 (b) P-E Hysteresis loops of PZT thin films on ITO/glass substrates with different stacking structures of (A), (B) and (C) in Fig. 1 annealed at 550℃.

Figure 6 exhibited the change in the leakage current density for the PZT films on the different substrates with applied voltage. PZT/Pt capacitors on a Si substrate have a leakage current of (A) 1.4×10^{-7}, (B)

8.7×10^{-6} and (C) 7.5×10^{-5} (A/cm²) at 2.5 V respectively, depending upon the stacking structures. On the other hand, PZT/ITO capacitors on a soda-lime glass have a leakage current density of (A) 1.4×10^{-7}, (B) 1.9×10^{-6} and (C) 2.3×10^{-6} (A/cm²) at 2.5 V, respectively. Therefore, a leakage current density abruptly increased with increasing applied voltage for the PZT/Pt capacitors, showing the large effect of the columnar electrode structure. In addition, it is obvious that excess addition of a lead oxide increased the leakage current density especially for the case of PZT/Pt capacitor. These results indicate the importance of the electrode.
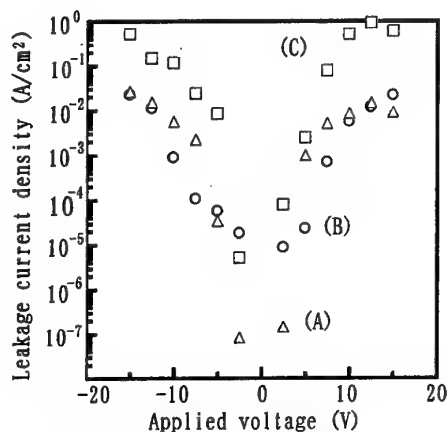
Fig. 6 (a) Leakage current density for the PZT films on Pt/Ti/SiO₂/Si substrates with different stacking structures annealed at 550℃.
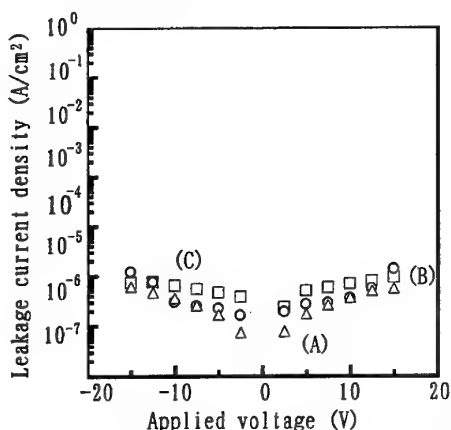
Fig. 6 (b) Leakage current density for the PZT films on ITO/glass substrates with different stacking structures annealed at 550℃.

4. CONCLUSIONS

In this paper, effects of the excess lead oxide

addition and the substrate on the crystallization and electrical properties of the resultant PZT thin films were investigated in details. As a result, followings are concluded:

(1) Crystallization behavior of the PZT thin film was significantly affected by the amount of the excess lead oxide addition. Insertion of two layers with excess lead addition of 50 mol % was sufficient to obtain single-phase perovskite PZT thin film at relatively low temperature of 550℃, independent of the substrate.

(2) Dielectric property of the resultant PZT film was affected by the amount of the excess lead oxide addition and substrate. Addition of 30 mol % excess lead oxide was estimated to be enough to obtain the saturated dielectric property. In addition, a Pt/Ti/SiO₂/Si substrate was better to obtain a PZT film with a good dielectric property at low temperature.

(3) PZT thin films with relatively good ferroelectricity were successfully deposited at low temperature of 550 ℃, independent of the substrate by the insertion of PT seeding layer with excess lead oxide addition of 50 mol % or 30 mol % of excess addition for the PZT films.

(4) Bottom electrode and the amount of the excess lead oxide had large effect on the leakage current density of the resulting PZT thin films. The PZT films on a ITO/glass substrate exhibited relatively low leakage current density of the order of 10^{-7} (A/cm²) at 2.5 V and did not increase abruptly with increasing applied voltage, independent of the amount of excess lead oxide.

REFERENCES

1) H.Fujisawa, M.Yoshida, M.Shimizu and H.Niu, Jpn.J.Appl.Phys.,**37**, 5132 (1998)
2) Yi.G and M.Sayer, J.Sol-Gel Sci. and Tech., **6**, 65 (1996)
3) Yi.G and M.Sayer, J.Sol-Gel Sci. and Tech., **6**, 75 (1996)
4) H.Suzuki, M.B.Othman, K.Murakami, S.Kaneko and T.Hayashi, Jpn.J.Appl.Phys.,**35**, 4896 (1996)
5) H.Suzuki, M.B.Othman, K.Murakami, S.Kaneko and T.Hayashi, Jpn.J.Appl.Phys.,**36**, 5803 (1997)
6) H.Suzuki, T.Koizumi, Y.Kondo and S.Kaneko, J.Eur.Ceram.Soc.,**19**,1397 (1999)

Effects of B-site Substitution in Ferroelectric PbTiO$_3$ Thin Films on Crystal Structure and Electrical Properties

Masato MIYAKE, Akihisa INOUE, Ryo TERAURA, Takashi NISHIDA,

Soichiro OKAMURA and Tadashi SHIOSAKI

Graduate School of Materials Science, Nara Institute of Science and Technology (*NAIST*)

8916-5 Takayama-cho, Ikoma, Nara 630-0101, Japan

Fax: +81-743-72-6069, e-mail: m-masato@ms.aist-nara.ac.jp

Effects of B-site substitution by Nb atoms on the crystal structure and the electrical properties of ferroelectric PbTiO$_3$ thin films were investigated. PbTiO$_3$ and Pb(Ti, Nb)O$_3$ thin films were deposited on Ir/SiO$_2$/Si substrates by reactive rf-magnetron sputtering with a flattened multi-component target consisted of a Ti plate, a Ti cover disk, a Nb disk and four PbO pellets. The Pb/Ti ratio of the films was controlled to be 1.0 by adjusting the diameter of the Ti cover disk. An amount of doped Nb atoms in the films were changed by changing the diameter of the Nb disk. The Lattice constants of a-axis increased and grain size was to be smaller and more uniform with increasing of the amount of doped Nb atoms. The dielectric constants increased and the dielectric losses decreased by doping an appropriate amount of Nb atoms. Leakage current decreased by Nb-doping. The remanent polarization and the coercive field of the Nb-doped films were estimated to be 20 μC/cm^2 and 120 kV/cm, respectively.

1.INTRODUCTION

Lead titanate, PbTiO$_3$, is a well-known ferroelectric material having remarked ferroelectric, pyroelectric and piezoelectric properties. Its large remanent polarization and low crystallization temperature are suitable for a capacitor material of high-density ferroelectric random access memories (FeRAM). It is, however, difficult to reverse the spontaneous polarization of PbTiO$_3$ thin films by low driving voltage because of their high coercive field. Furthermore, usually, non-doped PbTiO$_3$ thin films fabricated by conventional methods exhibit large leakage current. The substitution of B-site atoms by niobium or aluminium was studied to prevent the leakage current[1-3]. It is expected that Nb atoms in the PbTiO$_3$ thin films act as donors and compensate the hole carriers caused by lead vacancies. In this paper, we describe the effects of B-site substitution in PbTiO$_3$ thin films by Nb atoms on the crystal structure and the electrical properties.

2.EXPERIMENTAL

PbTiO$_3$ and Pb(Ti, Nb)O$_3$ thin films were deposited on silicon wafers with metal electrodes by reactive rf-magnetron sputtering. A flattened multi-component target as shown in Fig. 1 was used. This target consisted of a Ti plate with four holes, a Ti cover disk, a Nb disk and four lead oxide (PbO) pellets which were set in the four holes. Purity of all materials was 99.9%. The surface of the PbO pellets and the Ti plate were aligned at same height. Expo-

sure area of PbO pellets was adjusted by changing the diameter of the Ti cover disk. For the accurate positioning of the Ti cover disk and the Nb disk, they had holes with a diameter of 1 mm at the center while the Ti plate had a projection at the center. This flattened multi-component target drastically improved the reproductivity of experiments. Pt/SiO$_2$/Si substrates were used in the preparatory experiments to determine the diameter of the Ti cover disk for the deposition of stoichiometric PbTiO$_3$ thin films. Ir/SiO$_2$/Si substrates were used in the evaluation of electrical propeties of non-doped and Nb-doped PbTiO$_3$ thin films. The amount of doped Nb atoms was adjusted by changing the diameter of the Nb disk. We used Nb disks
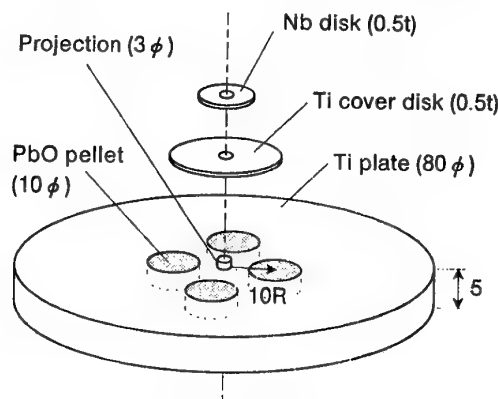
Fig.1 A flattened multi-component target for the depositon of Pb(Ti, Nb)O$_3$ thin films.

with diameters of 5, 7 and 9 mm. The sputtering power was 50W, the sputtering gas was O_2 mixed Ar gas at Ar:O_2 ratio of 9:1 and the sputtering pressure was 0.8 Pa. Substrates were heated to 580℃ during the deposition. The deposition time was two to four hours. The deposition rate was about 1.2 nm/min.

The crystal structure of obtained films was confirmed by X-ray diffraction (XRD). The Pb:Ti ratio in the non-doped PbTiO$_3$ thin films was determined by X-ray fluorescence (XRF) analysis. To evaluate electrical properties, circular Pt top electrodes with a diameter of 0.15 mm were deposited on the film surface by rf-magnetron sputtering. The films were annealed at 400℃ for 20 min in air after the top electrode deposition. The D-E hysteresis loops of the films were measured using a Sawyer-Tower circuit at 10 kHz with a triangle waveform. The C-V characteristics, dielectric constants and lossess were evaluated using an impedance analyzer (HP4194A) at 100 kHz.

3.RESULTS AND DISCUSSION

3.1 Determation of the diameter of a Ti cover disk

Figure 2 shows XRD patterns of the PbTiO$_3$ thin films fabricated using Ti cover disks with various diameters.
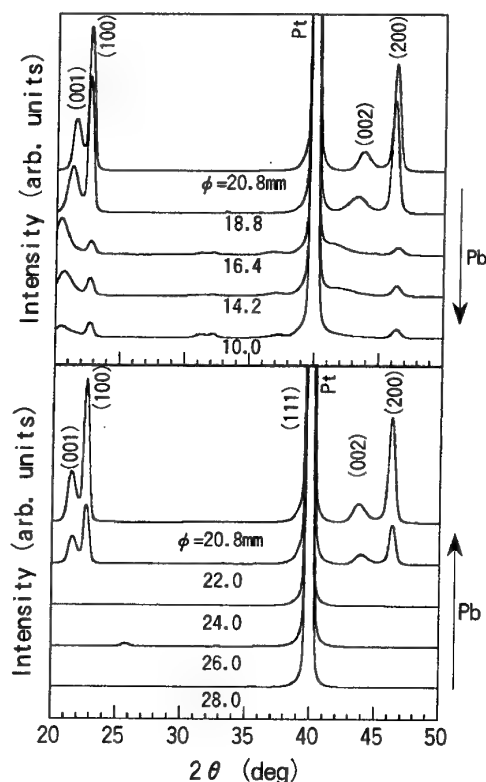
Fig.2 XRD patterns of PbTiO$_3$ thin films deposited on Pt/SiO$_2$/Si substrates using Ti cover disks with various diameter.

Single phase PbTiO$_3$ thin films were obtained by using Ti cover disks with the diameters ranging from 18.8 to 22.0 mm. In these films, only peaks of (00*l*) and (*h*00) were observed. It seems that all grains had either *a*- or *c*-axis orientation perpendicular to substrates. When the diameters of Ti cover disks were higher than 24.0 mm, no diffraction peak was observed. These films were not crystallized into perovskite PbTiO$_3$ phase because of the lack of lead atoms. On the other hand, in case of the diameters less than 16.4mm, the peaks of (00*l*) shifted towards lower angle while the peaks of (*h*00) were still in the same position. It seems that excess lead atoms deformed the crystal structure of PbTiO$_3$. Figure 3 shows Pb/Ti ratio in the PbTiO$_3$ thin films estimated by XRF analysis. The Pb/Ti
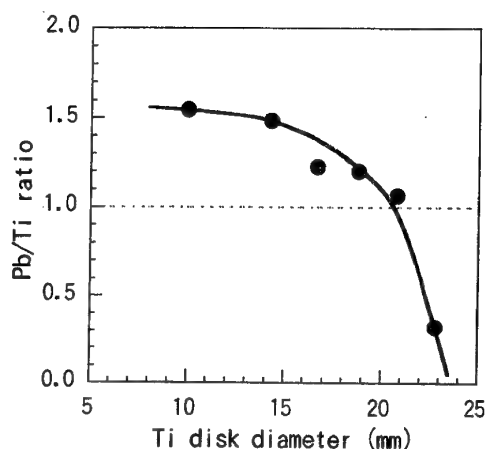
Fig.3 Pb/Ti ratio in the PbTiO$_3$ thin films deposited on Pt/SiO$_2$/Si substrates using Ti cover disks with various diameter.
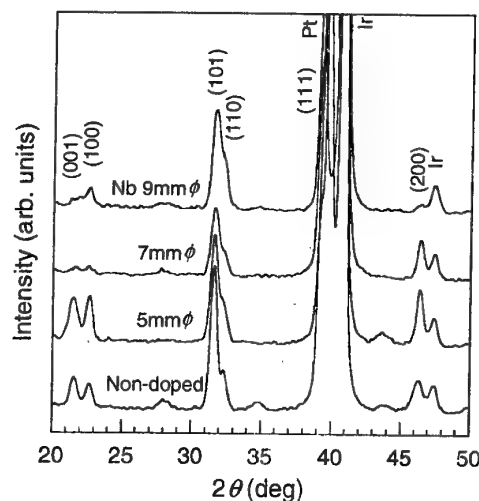
Fig.4 XRD patterns of Pb(Ti, Nb)O$_3$ thin films deposited on Ir/SiO$_2$/Si substrates using Nb disks with various diameter.

ratio in the films monotonously decreased with increasing of the Ti disk diameter, that is, decreasing of PbO exposure area. The ratio was equal to 1.0 at the diameter of about 21.0 mm. From these results, we have decided that we will use a Ti cover disk with a diameter of 20.8 mm in the experiments after this.

3.2 Effects of Nb doping on the crystallinity of PbTiO₃ thin films

Figure 4 shows XRD patterns of the Nb-doped PbTiO$_3$ thin films fabricated on Ir/SiO$_2$/Si substrates using Nb disks with the diameters of 5, 7 and 9 mm. It was difficult to estimate the exact amount of doped-Nb atoms because their XRF intensities were very weak. In this figure, (111) peaks of Pt and Ir were observed because the measurement were carried out after top Pt electrode deposition. All the films were crystallized into single phase PbTiO$_3$ with random orientation. Two peaks caused by (101) and (110) planes were relatively separated in the non-doped film. However, the (110) peaks made the schoulders in the (101) peaks in case of the Nb-doped films. The shoulders were to be smaller with increasing of Nb disk diameter because the (110) peaks shifted toward lower angle. It seems that the crystal structure of Nb-doped PbTiO$_3$ thin films were deformed and the lattice constant of a-axis was expanded by the Nb-doping because Ti atoms at B-site were substituted by Nb atoms which had larger ionic radius than that of Ti. Figure 5 shows surface morphology of Nb-doped PbTiO$_3$ thin films. In the non-doped film (Fig. 5(a)) and in case of 5 mm (Fig. 5(b)), grain size was ununiform. In case of 7 mm (Fig. 5(c)), the film consisted of small and uniform grains. In case of 9 mm (Fig. 5(d)), grain size was slightly larger than that in case of 7 mm. From these results, it is found that microstructure of PbTiO$_3$ thin films was controlled by Nb-doping.

3.3 Effects of Nb doping on the electrical properties of PbTiO₃ thin films

Figure 6 shows D-E hysteresis loops of the Nb-doped PbTiO$_3$ thin films fabricated on Ir/SiO$_2$/Si substrates. Thickness of the films was 300 nm. In case of non-doped PbTiO$_3$ thin films, leakage current was relatively high al-

500 nm
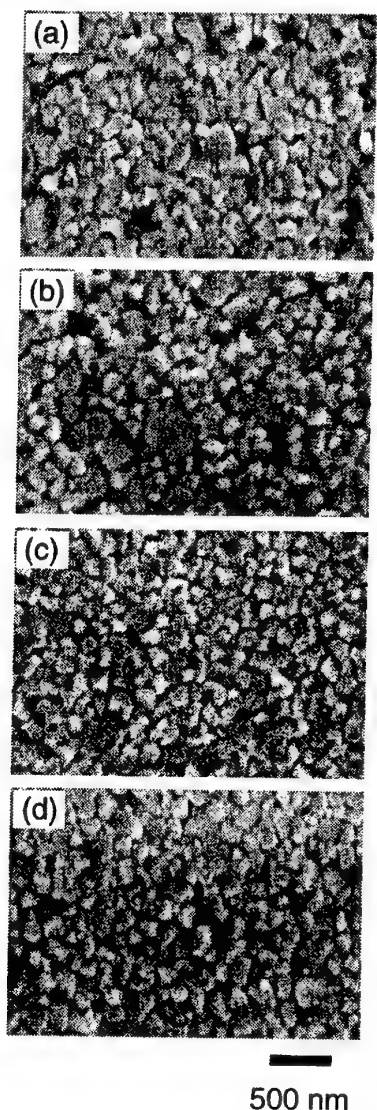
Fig.5 Surface morphology of Pb(Ti, Nb)O$_3$ thin films deposited on Ir/SiO$_2$/Si substrates using Nb disks with diameters of (a) 0 mm (non-doped), (b) 5 mm, (c) 7 mm and (d) 9 mm.
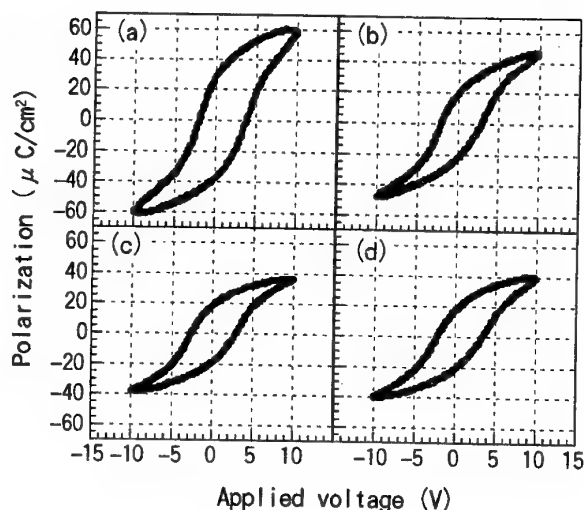
Fig.6 D-E hysteresis loops of Pb(Ti, Nb)O$_3$ thin films deposited on Ir/SiO$_2$/Si substrates using Nb disks with diameters of (a) 0 mm (non-doped), (b) 5 mm, (c) 7 mm and (d) 9 mm.
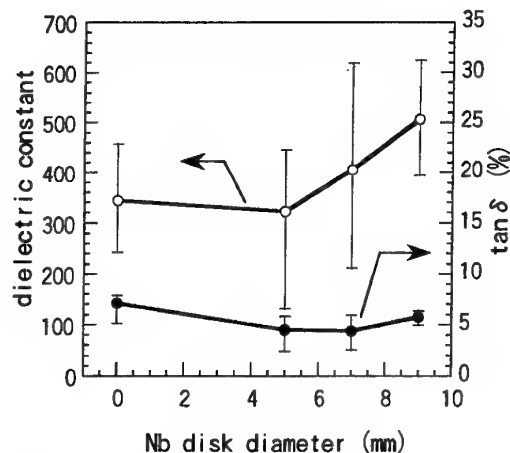
Fig.7 Dielectric constants and losses of Pb(Ti, Nb)O$_3$ thin films deposited using Nb disks with various diameter.

Fig.8 C-V characteristics of the Pb(Ti,Nb)O$_3$ thin film deposited using the Nb disk with a diameter of 7 mm.

though a ferroelectric hysteresis loop was observed. On the other hand, Nb-doped films exhibited well saturated hysteresis loops. The remanent polarization and the coercive field of the films were estimated to be 20 μC/cm^2 and 120 kV/cm, respectively. In this time, no obvious change in the remanent polarization and the coercive filed caused by increasing of the amount of doped Nb atoms was observed. Figure 7 shows the dielectric constants and losses of Nb-doped PbTiO$_3$ thin films fabricated by changing the diameter of Nb disks. Average, maximum and minimum values of 20 measurement points in each film are indicated in this figure. The dielectric constants decreased at 5 mm and increased with increasing of Nb disk diameter after that point. The dielectric losses had minimum value at 5 and 7 mm. It can be concluded that Nb-doping is effective on the improvement of ferroelectric and dielectric properties of PbTiO$_3$ thin films. It is not yet clear as to why the dielectric constants of these thin films (300 ∼ 500) was much higher than that of bulks (∼200). The C-V characteristics of the Nb-doped film fabricated using the 7 mm ϕ Nb disk exhibited the shift towards the negative-bias field as shown in Fig.8. Other films also exhibited same shifts. It seems that these shifts were caused by the difference of top and bottom electrode materials. Capacitance at zero-bias field was changed due to their polarization states. This is the reason why dielectric constants had large deviations in Fig.7.

4.CONCLUSIONS

PbTiO$_3$ and Nb-doped PbTiO$_3$, Pb(Ti, Nb)O$_3$, thin films were fabricated by reactive rf-magnetron sputtering with the flattened multi-component target consisted of a Ti plate, a Ti cover disk, a Nb disk and four PbO pellets. Pb content in the films monotoneously decreased with increasing of
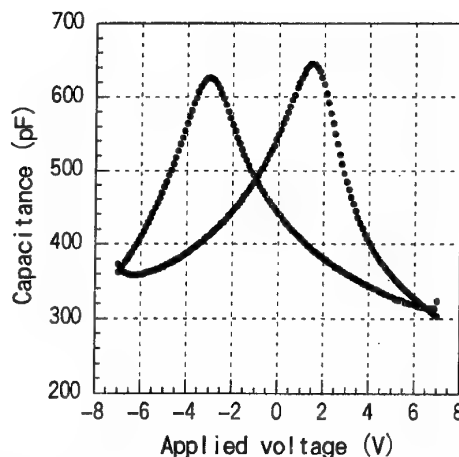
the diameter of the Ti cover disk which hid PbO pellets in part. We have decided optimum diameter for PbTiO$_3$ deposition from the results of XRD and XRF analysis. The amount of doped Nb atoms was controlled by changing the diameter of Nb disks. Lattice constant of a-axis increased and grain size was to be smaller and more uniform with increasing of the amount of doped Nb atoms. Generally, Nb doping improved the shape of D-E hysteresis loops. The remanent polarization and the coercive field of Nb-doped PbTiO$_3$ thin films with a thickness of 300 nm were 20 μC/cm^2 and 120 kV/cm, respectively. The dielectric constants increased and the dielectric losses decreased by doping of an appropriate amount of Nb atoms. It has been concluded that Nb-doping is effective on the improvement of ferroelectric and dielectric properties of PbTiO$_3$ thin films.

REFERENCES

1) R. C. Ibraham, T. Sakai, T. Nishida, T. Horiuchi, T. Shiosaki and K. Matushige, Jpn. J. Appl. Phys., **35**, 4995-4998 (1996). ·

2) T. Iijima, S. Kudo and N. Sanada, Jpn. J. Appl. Phys., **36**, 5829-5833 (1997).

3) T. Matuzaki, N. Okuda and H. Funakubo, Trans. Mater. Res. Soc. Jpn., in press (1999).

Texture control of Sol-Gel Derived PZT Thin Films

Takashi Iijima, Toshihiko Abe and Norio Sanada
Tohoku national Industrial Research Institute
4-2-1 Nigatake, Miyagino-ku, Sendai 983, JAPAN
Fax: 81-22-237-5211, e-mail: iijima@tniri.go.jp

Texture control of $Pb(Zr_xTi_{1-x})O_3$ thin films, x= 0.45, 0.53 and 0.6, were investigated to increase the ferroelectric and piezoelectric properties using a sol-gel method. In pyrolysis process, precursor films heat-treated less than 450°C indicated the (100) dominant orientation, whereas the precursor films heat-treated above 450°C showed (111) dominant orientation. It is clear that (111) oriented bottom Pt layer is related to the texture orientation of PZT, but crystal structure and Zr content did not affect it. The P-E hysteresis curves of tetragonal and rhombohedral texture oriented films were measured. In the case of tetragonal, x= 0.45, Pr for the (100) and (111) preferred thin films were $23\mu C/cm^2$ and $27\mu C/cm^2$, respectively. And in the case of rhombohedral, x= 0.6, Pr for the (100) and (111) preferred thin films of were $10\mu C/cm^2$ and $24\mu C/cm^2$, respectively. Furthermore, the displacement property of 2-μm-thick PZT film deposited onto Pt (111)/Pt foil substrate was examined. Assuming the bend motion is explained by a mono-morph structure, d_{31} could be calculated, and it was estimated to be 124×10^{-12} m/V. This value was consistent with that of bulk PZT ceramics.

1. INTRODUCTION

Ferroelectric thin films including PZT is demanded for applying for many fields like sensor, memory and actuator. One of the effective techniques to increase the ferroelectric and piezoelectric properties is supposed to be arrangement of the polarization direction using a texture control process. Various possibilities of the texture control of PZT thin film were investigated for a sol-gel,[1-4] sputtering [5-6] and MOCVD process.[7-8] In a sol-gel method, an importance of heat treatment process had been pointed out, and a TTT diagram of PZT precursor films was proposed.[9] In this work, we revealed the condition of the texture control process of PZT thin films using a sol-gel method, and succeeded to fabricate the tetragonal and rhombohedral $Pb(Zr_xTi_{1-x})O_3$, x= 0.45, 0.53 and 0.6, thin films with the (100) and (111) preferred orientation. The ferroelectric properties of the predominantly (100) and (111) oriented tetragonal and rhombohedral PZT thin films were measured. Furthermore, to investigate the possibility of PZT film actuator, displacement property of the texture oriented PZT film was examined, and the piezoelectric constant was calculated.

2. EXPERIMENTAL PROCEDURE

To prepare the sol-gel precursor solution, we used trihydrated lead acetate, titanium iso-propoxide and zirconium iso-propoxide as starting materials, and 2-methoxyethanol as the solvent. The nominal compositions of the solutions were equivalent to those of $Pb(Zr_xTi_{1-x})O_3$, x= 0.45, 0.53 and 0.6 that corresponded to rhombohedral, morphotropic phase boundary and tetragonal phase. The precursor preparation process was described in detail in elsewhere.[10]

A 0.5M precursor solution, which was not hydrolyzed, was deposited onto (111) oriented Pt on $Ti/SiO_2/Si$ substrate and (111) oriented Pt on 50μm-thick-Pt foil substrate using a spin coater operated at 3000rpm. The (111) oriented Pt layer was fabricated using a sputtering method. The sequence of spin coating, drying at room temperature or 120°C and pyrolysis treatment between 400°C and 520°C for 3-5min was performed five times, and the samples were fired at 650°C or 700°C for 1min by RTA treatment in oxygen flow atmosphere. This process was repeated several times to increase the film thickness and to examine the piezoelectric property. The fired film thickness determined from SEM micrographs ranged from 280nm to 350nm. A flow diagram of coating process is shown in Fig. 1.

The crystal structure of the thin films was examined with an X-ray diffractometer. 0.5-mm-diameter gold or platinum electrodes were deposited onto the surface of PZT thin films. The P-E hysteresis curves of the thin films were measured by RT66A (Radiant Technology), and displacement property of the thin film was examined by photonic sensor (MIT200, MIT corp.) or heterodyne type laser interferometer (MLD-102, Nihonkagaku Engineering) connected with RT6000HVS system, respectively.
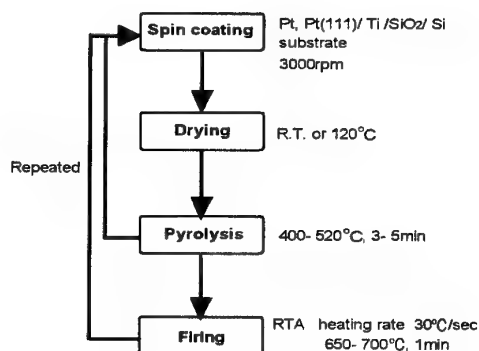
Fig. 1 Flow diagram for thin film fabrication.
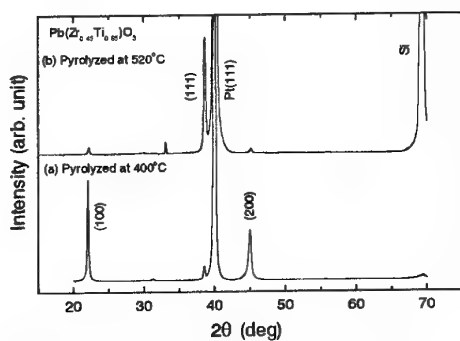
Fig. 2 X-ray diffraction patterns of PZT thin films
for x= 0.45.
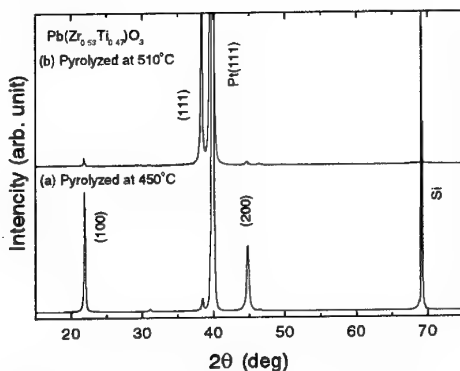
Fig. 3 X-ray diffraction patterns of PZT thin films
for x= 0.53.
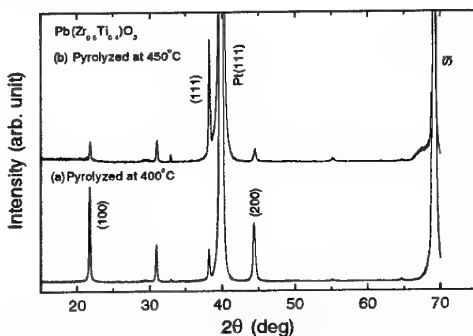
Fig. 5 X-ray diffraction patterns of PZT thin films
for x= 0.6.

3. RESULT AND DISCUSSION

3.1 Texture control of PZT thin film

Fig. 2 shows the result of XRD analysis of the PZT thin film for x= 0.45 deposited onto Pt/Ti/SiO$_2$/Si substrate. The thin film that was pyrolyzed at 400°C and then fired at 650°C indicated a (100) dominant oriented texture as shown in Fig. 2 (a). On the other hand, when the pyrolysis temperature increased to 520°C, the thin film after firing at 650°C showed a (111) dominant orientated texture as shown in Fig. 2 (b). Therefore, it can be seen that the texture orientation changed abruptly from (100) to (111) with increasing pyrolysis temperature from 400 °C to 520°C. Fig. 3 shows the result of XRD analysis of the PZT thin film for x= 0.53 deposited onto Pt/Ti/SiO$_2$/Si substrate and fired at 700°C. When the pyrolysis process was performed at 450°C,
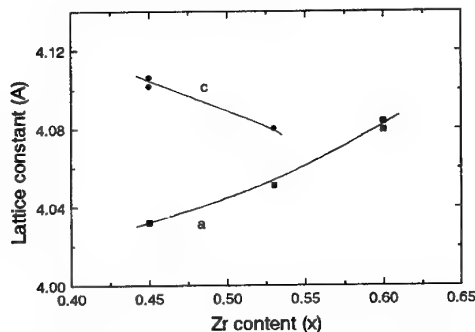
Fig. 5 Lattice constant of Pb(Zr$_x$Ti$_{1-x}$)O$_3$ thin films

texture of the thin film showed the (100) preferred orientation. However, the thin film pyrolyzed at 510°C showed the (111) dominant orientated texture. The result of XRD analysis of the PZT thin film for x= 0.6 deposited onto Pt/ Ti/ SiO$_2$/ Si substrate and then fired at 650°C is shown in Fig. 4. It can be seen that the (100) preferred orientation was formed for 400°C and the (111) preferred orientation formed for 450°C. These results suggest that the (100) texture predominates lower than 450 °C and the (111) texture predominates higher than 450°C in the pyrolysis process. On the other hand, we could not identify an intermetallic phase described in other paper,[4, 9] and PZT thin films deposited onto Pt foil did not show remarkable texture orientation like Fig. 2-4. Detail of this phenomenon is described later. Therefore, a nucleation mode of PZT on a surface of the (111) oriented Pt layer seems to be related to the texture orientation of PZT.

From these X-ray diffraction patterns, a lattice constant of PZT thin films was calculated using a (100), (111) and (200) peak. Fig. 5 shows the relationship between the lattice constant and Zr content of Pb(Zr$_x$Ti$_{1-x}$)O$_3$ thin films. The crystal structure of the thin films was determined tetragonal for x= 0.45 and 0.53, and rhombohedral for x= 0.6. With increasing Zr content, value of c axis decreased and that of a axis increased. This tendency of the lattice constant for PZT thin film was consistent to the reported data.[7, 11] Therefore, it appears that Zr/Ti rate and crystal structure do not affect the texture orientation of the PZT thin films. This suggests that pyrolysis temperature is an important factor to control the PZT thin film texture using a sol-gel method.

The P-E hysteresis curves of the predominantly (100) and (111) oriented PZT thin films for tetragonal and rhombohedral phase are indicated in Fig. 6 and 7. In the case of x= 0.45 which is tetragonal phase (Fig. 6), the thin film with the (111) dominant orientation showed high value of the spontaneous polarization, Ps, compared to the (100) dominant oriented film. However, the remanent polarization, Pr, did not show remarkable difference between the (100) and (111) orientation. A polarization axis of the tetragonal PZT is [001] direction and an angle between [001] and [111] direction is smaller than that between [001] and [100], so that the Pr of the (111) preferred film appears to be higher than that of the (100) preferred film. These values for the (100) and (111) preferred thin films of x= 0.45 were Ps= 38μC/cm^2, Pr= 23μC/cm^2 and Ps= 61μC/cm^2 Pr=
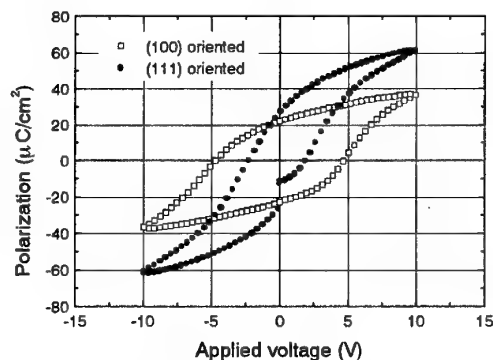
Fig. 6 P-E hysteresis curve of tetragonal phase $Pb(Zr_{45}Ti_{55})O_3$ thin.
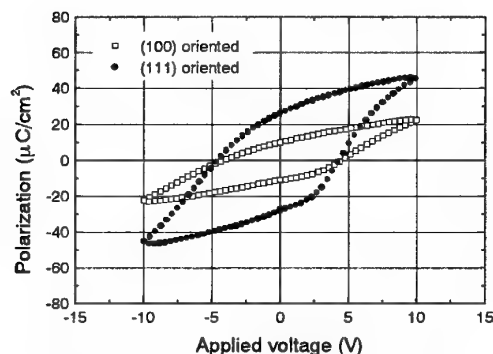
Fig. 7 P-E hysteresis curve of rhombohedral phase $Pb(Zr_{60}Ti_{40})O_3$ thin.

Fig. 8 X-ray diffraction patterns of $Pb(Zr_{53}Ti_{47})O_3$ thin films.
(a) deposited on Pt foil substrate,
(b) deposited on Pt (111)/Pt foil substrate.
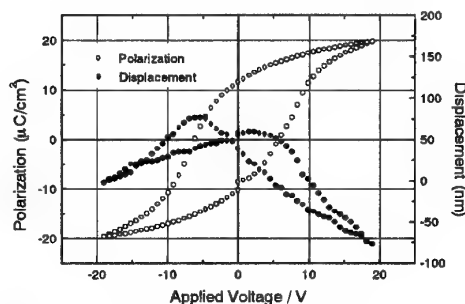
Fig. 9 P-E hysteresis curve and displacement property of 2-μm-thick $Pb(Zr_{53}Ti_{47})O_3$ film deposited on Pt (111)/Pt foil substrate

$27\mu C/cm^2$, respectively. In the case of x=0.6 which is rhombohedral phase as indicated in Fig.7, the (111) predominantly oriented thin film showed large hysteresis compared to the (100) preferred thin film because the polarization direction of rhombohedral phase is equivalent to [111] direction. These values of the (100) and (111) preferred thin films for x= 0.6 were Ps= $22\mu C/cm^2$, Pr= $10\mu C/cm^2$ and Ps= $42\mu C/cm^2$ Pr= $24\mu C/cm^2$, respectively. The coercive field, Ec, of all texture oriented PZT films ranged from 80 to $160kVcm^2$ was considerably larger than PZT bulk ceramics. The high Ec observed on the film is probably due to the small grain size.

3.2 Displacement property of PZT thin films

The result of XRD analysis suggests that the (111) oriented bottom Pt layer remarkably affect the texture orientation of PZT thin films. Fig. 8 shows X- ray diffraction patterns of the PZT thin films for x= 0.53 deposited on a Pt foil substrate with and without the (111) oriented bottom Pt layer. When PZT thin film was deposited on the Pt foil substrate directly and pyrolyzed at 520°C as shown in Fig. 8 (a), the diffraction pattern was not similar to that in Fig. 3 (b), but comparable to that of the PZT powder. Therefore the thin film texture seems to be random orientation. XRD diffraction pattern of the PZT thin film deposited onto the (111) preferred Pt/ Pt foil substrate and then pyrolyzed at 400°C is

shown in Fig. 8 (b). Intensity of (110) peak was relatively high, but the diffraction pattern was nearly equivalent to that in Fig. 3 (a). Therefore, in the case of the PZT thin film deposited onto the Pt (111)/ Pt foil substrate, it could be possible to control the texture orientation of the PZT thin films. To measure the displacement property and achieve the sufficient piezoelectric property, it is necessary to increase a film thickness by means of repeating the coating process. The thin film indicated in Fig. 8 (b) was prepared using this repeated process and the thickness reached to 2μm.

Fig. 9 shows the P-E hysteresis curve and the displacement property of the 2-μm-thick PZT film. These properties were measured simultaneously using bipolar drive at ±20V. The P-E hysteresis curve was not fully saturated, but the ferroelectric property appeared to be good. Furthermore, the film exhibited the butterfly like displacement curve. This shape is equivalent to that of typical piezoelectric bulk PZT, so that the film seems to show piezoelectricity. However, this displacement property indicates bend motion in the vertical direction on the film surface and does not reflect the genuine piezoelectric property. Assuming the bend motion is explained by a mono-morph structure, the piezoelectric constant, d_{31}, of the film can be calculated. When the (100) preferred PZT film which was deposited on the Pt (111)/ Pt foil substrate was driven at 20V, d_{31} was
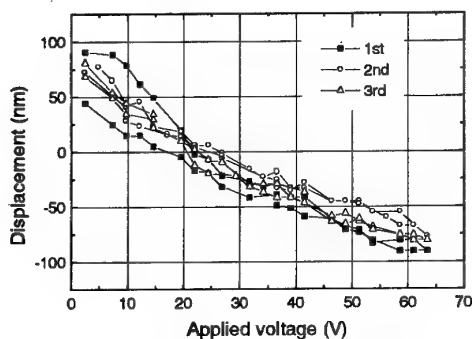
Fig. 10 Displacement property of 2-μm-thick
$Pb(Zr_{53}Ti_{47})O_3$ film driven at 65V.

estimated to be 124×10^{-12} m/V. This value was consistent with that of bulk PZT ceramics. Fig. 10 shows the displacement property of 2-μm-thick $Pb(Zr_{53}Ti_{47})O_3$ film which was driven three times using unipolar drive at 65V. At first drive motion, the displacement property showed hysteresis, and the origin moved. However, for second and third drive motion, it can not be seen remarkable hysteresis, and origin was nearly equal. Therefore, it is thought that the fabrication process using (111) oriented Pt bottom layer to control the texture of PZT film is applicable to the film actuator deposited on various substrates.

4. CONCLUSION

Texture control of $Pb(Zr_xTi_{1-x})O_3$, x= 0.45, 0.53 and 0.6, thin film was attempted to fabricate. When the thin films were deposited onto Pt $(111)/Ti/SiO_2/Si$ substrate or Pt (111)/Pt foil substrate and were pyrolyzed between 400°C and 520°C, (100) or (111) dominant texture could be formed. However, crystal structure and Zr content of PZT did not affect the texture orientation, and PZT thin film directly deposited on Pt foil substrate did not show the texture orientation, too. Therefore, we suppose that a nucleation mode of PZT on a surface of the (111) oriented Pt layer seems to be related to the texture orientation. The P-E hysteresis curves of tetragonal and rhombohedral texture oriented films were measured. In the case of (111) oriented tetragonal, x= 0.45, and rhombohedral, x= 0.6, PZT thin films, Pr was $27\mu C/cm^2$ and $24\mu C/cm^2$, respectively. Moreover, the displacement property of 2-μm-thick (100) oriented PZT film deposited onto Pt (111)/Pt foil substrate was examined. The piezoelectric constant, d_{31}, was estimated to be 124×10^{-12} m/V. This texture control process is applicable to the (111) Pt layered various substrate.

AKNOWRILEDGEMENTS

REFERANCE

1. B. A. Tuttle, J. A. Voigt, D. C. Goodnow, D. L. Lamppa, T. J. Headley, M. O. Eatough, G. Zender, R. D. Nasby and S. M. Rodgers, *J. Am. Ceram. Soc.*, 76, 1537-1544 (1993).
2. Y. Liu and P. P. Phule, *J. Am. Ceram. Soc.*, 79, 495-498 (1996).
3. K. Aoki, Y. Fukuda, K. Numata and A. Nishimura, *Jpn. J. Appl. Phys.*, 33, Part1, No. 9B, 5155-5158 (1994).
4. K. G. Brooks, I. M. Reaney, R. Klissurska, Y. Huang, L. Bursill and N. Setter, J. Mater. Res., 9, 2540-2553 (1994)
5. M. Adachi, T. Matsuzaki, T. Yamada, T. Shiosaki and A. Kawabata, *Jpn. J. Appl. Phys.*, 26, 550-553 (1987).
6. R. Takayama and Y. Tomita, *J. Appl. Phys.*, 65, 1666-1670 (1989)
7. Y. Sakashita, T. Ono, H. Segawa, K. Tominaga and M. Okada, *J. Appl. Phys.*, 69, 8352-8357(1991)
8. D. Kim, T. Y. Kim, J. K. Lee, W. Tao and S. B. Desu, *Mat. Res. Soc. Symp. Proc.*, 433, 213-224 (1996)
9. S. Y. Chen and I. W. Chen, *J. Am. Ceram. Soc.*, 77, 2332-2336 (1994).
10. T. Iijima and N. Sanada, *Proc. 2nd Int. Meet. Pac. Rim. Ceram. Soc.*, Cairns (1996)
11. N. Tohge, S. Takahashi and T. Minami, *J. Am. Ceram. Soc.*, 74, 67-71 (1991).

Optimization of Buffer Layers and Device Structures in Ferroelectric-Gate FETs

Hiroshi Ishiwara, Eisuke Tokumitsu*, and Gen Fujii

Frontier Collaborative Research Center, Tokyo Institute of Technology
4259 Nagatsuda, Midoriku, Yokohama 226-8503
Fax ; 81-45-924-5961, e-mail ; ishiwara@pi.titech.ac.jp
*Precision and Intelligence Laboratory, Tokyo Institute of Technology

Data retention characteristics of ferroelectric-gate FETs with MFIS (M ; metal, F ; ferroelectric, I ; insulator (buffer layer), S; semiconductor) and MFMIS structures are discussed. It has been shown that the important factors to improve the retention characteristics are (1) increase of the buffer layer capacitance, (2) decrease of the leakage current of both a ferroelectric film and a buffer layer, and (3) optimization of the area ratio between the MFM and MIS parts in the MFMIS structure. Based on these considerations, MFMIS-FETs were fabricated and a current on/off ratio larger than 10^3 was obtained at a retention time of 10 hours, in which a stacked buffer layer of $SrTa_2O_6$/SiON was used and the area ratio between the MIS and MFM parts was optimized to 5.9.

1. INTRODUCTION

A key device in the FET-type ferroelectric memories is a ferroelectric-gate FET or an MFSFET (metal-ferroelectric-semiconductor FET), in which the gate insulator is composed of a ferroelectric material. In this FET, the polarization direction of the ferroelectric film can nondestructively be read-out using drain current. The NDRO (nondestructive read-out) characteristic is one of the most important features of the FET-type FeRAM (ferroelectric random access memory). The ferroelectric-gate FET can also be used as a nonvolatile analog memory, if the polarization of the ferroelectric film is continuously controlled by applying pulse signals shorter than the polarization reversal time.

The original idea of ferroelectric-gate FET was proposed from Bell Laboratory in 1955 [1] and many experimental studies were conducted in 1960's and 70's. However, since it was very difficult to form the ferroelectric-semiconductor interface with good electrical properties, the studies were almost stopped in late 70's. Then, after invention of the present capacitor-type FeRAM, importance of the ferroelectric-gate FET was again recognized and the studies are now getting popular. In this presentation, current status of the experimental studies on MF(MI)S (I : insulator) capacitors and FETs is first presented and then prospects of FET-type ferroelectric memory are discussed.

2. STATUS OF FERROELECTRIC-GATE FETS

A typical sheet carrier density in the channel region of a MOSFET is about 2×10^{12} cm^{-2}, assuming that t_{OX} = 30 nm and V_G - V_T = 3 V, where t_{OX} is the oxide thickness, V_G is gate voltage, and V_T is the threshold voltage. This value corresponds to a charge density of 0.32μ m/cm^2, and thus in the application of ferroelectric-gate FETs, the remnant polarization value of a ferroelectric film is not necessary to be large, if it is effectively used to induce carriers on the semiconductor surface.

However, if a ferroelectric film is directly deposited on a Si surface, it is generally difficult to form a good interface between them, since constituent elements in both materials easily diffuse each other, and since a transition layer is formed at the interface. In order to avoid these phenomena, a buffer layer is usually inserted between a ferroelectric film and Si substrate, which is composed of either a dielectric material (MFIS structure) or a stacked structure of conductive and dielectric materials (MFMIS structure).

Typical dielectric buffer layers are CeO_2 [2], $SrTiO_3$ [3], Si_3N_4 [4], and Y_2O_3 [5]. They are used as buffer layers for both $PbZr_{1-x}Ti_xO_3$ (PZT) and $SrBi_2Ta_2O_9$ (SBT). Figure 1 shows a typical I_D - V_G characteristic of an MFISFET with PLZT (L;La)/ $SrTiO_3$/ Si structure [3]. A hysteresis loop was obtained with a counterclockwise trace as indicated by arrows. Since no hysteresis was observed in the I_D - V_G characteristic of a $SrTiO_3$/ Si MISFET, this hysteresis is considered to be due to the ferroelectric nature of PLZT film. A memory window, i.e. threshold voltage shift, of the fabricated device was 0.9 V for a V_G sweep from -7 V to +2 V.

Concerning the MFMIS structure, an Ir/IrO$_2$/PZT/Ir /IrO$_2$/poly-Si/SiO$_2$/Si structure [6] seems to be most promising, in which the underlying Ir/IrO$_2$ layers act as the diffusion barrier for Pb atoms, as well as they act as a fatigue-free electrode for PZT. In a p-channel FET with the gate length of 1.2 μm, the memory window width of 3.3 V and the current on/off ratio of 6 orders-of-magnitude have been obtained for a bias sweep of $\pm$15 V. In these structures, however, the retention time of stored data is reported to be the order of 1 hour, except for a few recent reports [7,8]. Thus, it can be said that improvement of the data retention characteristics is most important in the future studies on ferroelectric-gate FETs.

3. IMPROVEMENT OF DATA RETENTION CHARAC-TERISTICS

The short retention time in MFIS and MFMIS structures originates from a fact that a dielectric capacitor is equivalently connected in series to the ferroelectric capacitor, as explained in the following. When power supply is turned off and the gate terminal of the FET is grounded, the top and bottom electrodes of the two capacitors are short-circuited. At the same time, electric charges $\pm$Q appear on the electrodes of the both capacitors due to the remnant polarization of the ferroelectric film and due to the charge neutrality condition at a node between the two capacitors (the FI interface in the MFIS structure or the floating gate M in the MFMIS structure).

The Q - V relation for the buffer layer capacitor is Q = CV, and thus the relation in the ferroelectric capacitor becomes Q = - CV under the short-circuited condition, where C is capacitance of the buffer layer. That is, the direction of the electric field in the ferroelectric capacitor is opposite to that of polarization of the film. This field is known as a depolarization field and it reduces the data retention time greatly, particular when C is small. Thus, the buffer layer capacitance C must be as large as possible, so that the depolarization field becomes small. This condition means that a thin buffer layer with a high dielectric constant is preferable.

Another point to be considered is the leakage current of both the ferroelectric film and the buffer layer. If the charge neutrality at a node between the two capacitors is destroyed by the leakage current, electric charges on the electrodes of the buffer layer capacitor disappear, which means that carriers on the semiconductor surface disappear and the stored data can not be read-out by drain current of the FET, even if the polarization of the ferroelectric film is retained. Thus, it is very important to reduce the leakage current of both a ferroelectric film and a buffer layer.

Next, improvement of data retention characteristics is discussed from a device structure viewpoint. It is well known that dielectric constants of ferroelectric films are generally much higher than those of dielectric buffer layers. Thus, if both the ferroelectric and buffer layer capacitors are formed in the same size, most external voltage is applied to the buffer layer and only a little is to the ferroelectric film. In order to solve this mismatch problem on the dielectric constant, it is necessary to make the ferroelectric capacitor area small and also to make the film thickness thick. However, if a too thick ferroelectric film is used, the operation voltage of the FET becomes high. Thus, there is a limitation in the film thickness to be used.

The other problem is mismatch of the induced charge. The remnant polarization values of PZT and SBT are about 40 μC/cm^2 and 10 μC/cm^2, respectively and they can induce the same density of positive and negative charges to the electrodes of a capacitor. These values are generally much larger than the maximum induced charge density by a dielectric film. For example, the maximum induced charge density of SiO$_2$ is about 3.5 μC/cm^2 for an electric field of 10 MV/cm and the film breaks down for the higher electric field.

Thus, if a ferroelectric capacitor with a large remnant polarization is connected in series to a SiO$_2$ capacitor with the same area, and if a sufficiently high voltage is applied across the both capacitors, the SiO$_2$ film breaks down before the saturation polarization of the ferroelectric film is achieved. This situation is illustrated in Fig.2(a) for a combination of SBT and SiO$_2$. As shown in the figure, only a small hysteresis loop of SBT can be used under the condition that the SiO$_2$ buffer layer does not break down. It should be noted that this condition is independent of the film thickness of both capacitors.

In order to solve the mismatch problem on induced charge, it is necessary to form an MFMIS structure and to optimize the area ratio between the ferroelectric capacitor and the buffer layer capacitor. That is, in order to use the saturation polarization of the ferroelectric film effectively, it is important to make the ferroelectric capacitor area small. If the area of an SBT capacitor is reduced to 1/5 of an SiO$_2$ capacitor, the vertical scale of the P - V (polarization vs. voltage) characteristic equivalently becomes 1/5, as shown in

Fig.2(b), and the saturation polarization curve can be drawn in the region where the polarization value does not exceed the maximum induced charge density of SiO_2 ($\pm$ 3.5 μ C/cm^2).

These results suggest that combination of planar capacitors (MFM parts) and three-dimensional FETs (MIS parts) is important to integrate MFMIS-FETs with optimized area ratio in high density. It is interesting to note that this design concept is opposite to that of DRAM.

4. CHARACTERISTICS OF FETS WITH $SrTa_2O_6$/SiON BUFFER LAYERS

Based on these considerations, optimization of MFMIS-FETs was conducted [9]. First, Si (100) wafers were thermally nitridized at 1050℃ for 5 sec in NH_3 atmosphere. The SiO_2-equivalent thickness of the surface dielectric layer was about 2 nm and this value did not change by subsequent annealing at 850℃ for 1 hour in O_2 atmosphere. Then, a dielectric $SrTa_2O_6$ film was deposited using sol-gel spin-coating technique, in which crystallization annealing was conducted at 900℃ for 3 min in O_2 atmosphere. Total film thickness of the buffer layer ranged from 30 to 60 nm.

The dielectric constant of $SrTa_2O_6$ was calculated to be about 110 by measuring the difference of accumulation capacitances among the samples with different film thicknesses. The SiO_2-equivalent film thickness of a 30-nm-thick $SrTa_2O_6$ film was about 3.7 nm and the leakage current density of the film was about 3×10^{-8} A/cm^2, which is about 2 orders-of-magunitude smaller than the theoretically predicted tunneling current of an SiO_2 film with the same thickness.

Using the buffer layer described above, p-channel FETs with MFIS and MFMIS structures were fabricated, in which SBT was used as a ferroelectric film and the area ratio between the MFM part and MIS part was optimized in the MFMIS structure. The gate SBT film was formed using sol-gel spin-coating technique with crystallization annealing at 800℃ for 1 hour in O_2 atmosphere. Figure 3 (a) and (b) show I_D-V_G characteristics of FETs with (a) the MFIS structure (the area ratio is 1) and (b) the MFMIS structure (the area ratio is 1/5.9). As can be seen from the figure, the obtained memory window is much wider in the MFMIS structure, even if the gate material and film thickness are the same for the both structures.

Typical retention characteristics for these devices are shown in Fig.4 [10], in which variation of drain currents of on- and off-state is plotted. In this figure,

the dotted lines show the result for an FET with the Pt/SBT/Si gate structure. Since there exists a transition layer with poor electrical properties between SBT and Si, the retention time is the order of 1 hour. When the gate structure is changed to Pt/SBT/$SrTa_2O_6$/SiON/Si, the retention characteristics are improved, as shown in dashed lines. The solid lines show the characteristic for an FET with the gate structure of Pt/SBT/Pt/$SrTa_2O_6$/SiON/Si, and in this case the area ratio between the MIS and MFM parts is optimized to be 5.9. This figure clearly shows that the retention characteristics are much improved by optimizing the area ratio. The current on/off ratio at a retention time of 10 h is larger than 10^3 in this case.

5. SUMMARY

Current status of ferroelectric-gate FETs is summarized as follows. (1) Good hysteretic characteristics have been obtained in many MF(MI)S devices, particularly when dielectric buffer layers are properly inserted between the ferroelectric film and Si substrate and (2) the retention characteristics can be improved by optimizing the device structure as well as optimizing ferroelectric and buffer-layer materials.

References
1) I.M.Ross ; US Patent 2791760 (1957)
2) T.Hirai, K.Teramoto, K.Nagashima, H.Koike and Y.Tarui ; *Jpn. J. Appl. Phys.*, **34**, 4163-66 (1995)
3) E.Tokumitsu, R.Nakamura and H.Ishiwara; *IEEE Electron Device Lett.*, **1 8**, 160-62 (1997)
4) J-P.Han, X.Guo and T-P.Ma; *Integrated Ferroelectrics*, **2 2**, 213-21 (1998)
5) B-E.Park, E.Tokumitsu and H.Ishiwara; *Jpn. J. Appl. Phys.*, **3 7**, 5145-48 (1998)
6) T.Nakamura, Y.Nakao, A.Kamisawa, and H. Takasu; *Integrated Ferroelectrics*, **9**, 179-87 (1995)
7) T.Kijima and H.Matsunaga; *Jpn. J. Appl. Phys.*, **3 8**, 2281-84 (1999)
8) Y.Fujimori, T.Nakamura and A.Kamisawa; *Jpn. J. Appl. Phys.* **3 8**, 2285-88 (1999)
9) E.Tokumitsu, G.Fujii and H.Ishiwara; *Appl. Phys. Lett.* **7 5** (1999) in press
10) H.Ishiwara; 57th Device Research Conf. Digest, p.6, Santa Babara, 1999
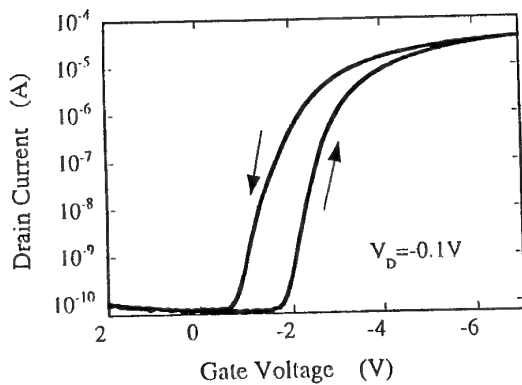
Fig.1 I_D-V_G characteristics of an MFIS-FET with PLZT/SrTiO$_3$/Si structure.
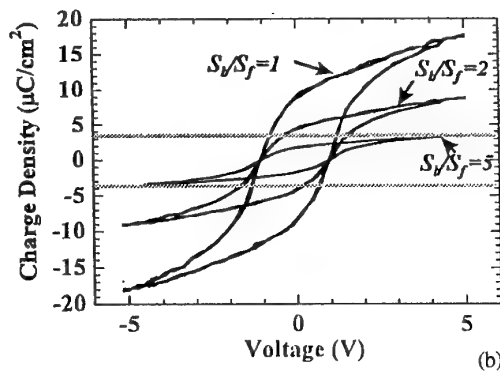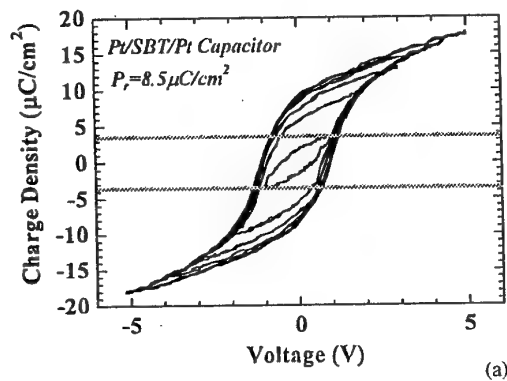
Fig.2 The induced charge density mismatch between SBT and SiO$_2$ (a) and variation of the hysteresis loop by optimization of capacitor area (b).
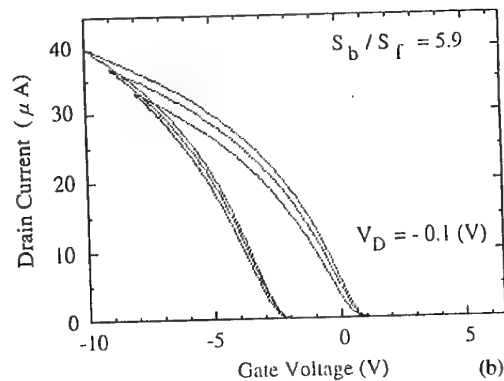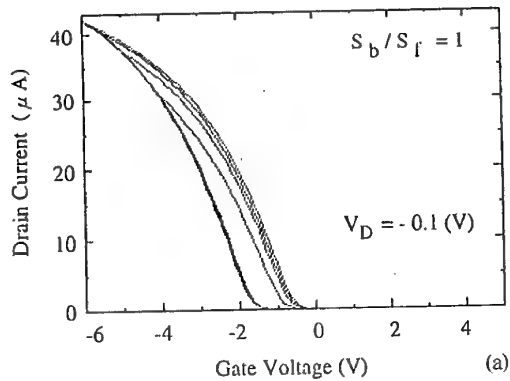
Fig.3 I_D - V_G characteristics of FETs with (a) Pt/SrBi$_2$Ta$_2$O$_9$/SrTa$_2$O$_6$/SiON/Si structure and (b) Pt/SrBi$_2$Ta$_2$O$_9$/Pt/SrTa$_2$O$_6$/SiON/Si structure.
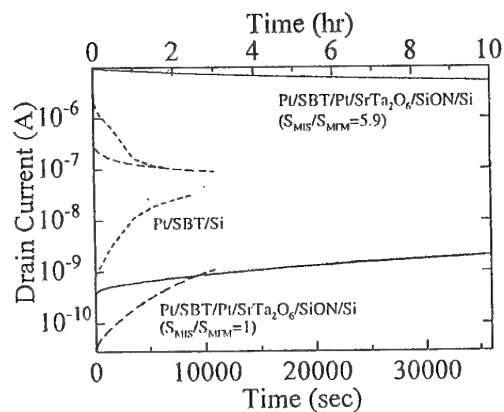
Fig.4 Time dependence of drain currents of various ferroelectric-gate FETs.

Pb(Mg$_{1/3}$Nb$_{2/3}$)O$_3$-PbTiO$_3$ Thin Films Synthesized by Metalorganic Chemical Vapor Deposition

S.K. Streiffer[*], G. R. Bai[*], S. Stemmer[§], O. Auciello[*], P.K. Baumann[*], K. Ghosh[*],
A. Munkholm[†], C. Thompson[*‡], R.A. Rao[††], and C.-B. Eom[††]

[*]Materials Science Division, Argonne National Laboratory, Argonne, IL 60439-4838
fax: 011-630-252-4289, email: streiffer@anl.gov
[§]Department of Physics, University of Illinois at Chicago, Chicago, IL 60607-7059
fax: 011-312-996-4451, email: stemmer@uic.edu
[†] Chemistry Division, Argonne National Laboratory, Argonne, IL. 60439
fax: 011-630-252-0365, email: munkholm@anl.gov
[‡] Dept. of Physics, Northern Illinois University, DeKalb, IL
fax: 011-630-252-7777, email: c_thompson@anl.gov
[††]Department of Mechanical Engineering and Materials Science, Duke University, Durham, NC 27708-0300
fax: 011-919-660-5164, email: eom@acpub.duke.edu

Metalorganic chemical vapor deposition was used to synthesize epitaxial Pb(Mg$_{1/3}$Nb$_{2/3}$)O$_3$-PbTiO$_3$ films on SrTiO$_3$ and SrRuO$_3$/SrTiO$_3$ substrates, using solid Mg(DPM)$_2$ as the Mg precursor. Deposition conditions have been identified under which phase-pure perovskite PMN-PT may be grown. In contrast, in lead-poor environments, an additional second phases of a disordered magnesium-niobium oxide has tentatively been identified. X-ray diffraction and selected area electron diffraction indicate a cube-on-cube orientation relationship between film and substrate, with a (001) rocking curve width of 0.1°, and in-plane mosaic of 0.8°. The rms surface roughness of a 200nm thick PMN film on SrTiO$_3$ was 2 to 3 nm as measured by scanned probe microscopy. The zero-bias dielectric constant and loss measured at room temperature and 10 kHz for a 350 nm thick pure PMN film on SrRuO$_3$/SrTiO$_3$ were 1100 and 2%, respectively. Small-signal permittivity ranged from 900 to 1400 depending on deposition conditions and Ti content; low values for the dielectric loss between 1 and 3% were determined for all specimens. Here we report on growth conditions and the initial structural and dielectric characterization of these samples.

1. INTRODUCTION

The relaxor ferroelectric Pb(Mg$_{1/3}$Nb$_{2/3}$)O$_3$ (PMN) and its solid solution with PbTiO$_3$ (PT) have attracted much attention recently because of excellent dielectric and electromechanical properties [1]. For many applications benefiting from integrated devices, deposition of thin film PMN-PT would be required. It is, however, difficult to synthesize phase pure perovskite PMN films because of the relatively poor stability of the perovskite phase relative to, for example, the pyrochlore phase. Despite this difficulty, a variety of thin film synthesis techniques have been used to fabricate PMN-PT films, including sol-gel [2], sputtering [3], pulsed laser ablation [4], and metalorganic chemical vapor deposition (MOCVD) [5]. Among these methods, and particularly among the vapor-phase techniques, MOCVD offers significant advantages for composition selection and control, film uniformity, high deposition rate, conformality, and scalability to large deposition areas. However, only very limited effort has been directed at obtaining PMN-PT using MOCVD [5]: thin films were grown with perovskite as the main phase only for compositions with Ti/(Mg+Nb+Ti) > 25 mol%, and little information on microstructure was reported. For many applications, it is desirable to obtain not only phase pure but also highly oriented or single-crystal PMN-PT thin films in order to fully utilize the anisotropic piezoelectric properties. Additionally, epitaxial films are essential as model systems so as to better understand properties.

Our goal is to prepare epitaxial (1-x)Pb(Mg$_{1/3}$Nb$_{2/3}$)O$_3$-xPbTiO$_3$ thin films with the perovskite structure by MOCVD. Careful control of deposition conditions was used to eliminate impurity phases formed in the preparation of PMN thin films, before PMN-PT films were deposited. Here we report the growth of phase pure, epitaxial PMN and PMN-PT films on (100) SrTiO$_3$ and SrRuO$_3$/SrTiO$_3$ substrates, using solid Mg(DPM)$_2$ as the Mg precursor. Results from initial structural and electrical characterization are described.

2. FILM GROWTH AND MICROSTRUCTURE

Thin films were grown in a cold-wall, horizontal, low-pressure MOCVD reactor with a resistive substrate heater. Tetraethyl lead, Pb(C$_2$H$_5$)$_4$, niobium pentaethoxide, Nb(OC$_2$H$_5$)$_5$, solid magnesium β-diketonate, Mg(C$_{11}$H$_{19}$O$_2$)$_2$, and titanium isopropoxide, Ti(C$_3$H$_7$O)$_4$, were chosen as the metal ion

precursors. A mixture of the metalorganic precursor vapor was introduced into the reactor via high purity nitrogen carrier gas. The temperatures, pressures, and carrier gas flow rates for each of the precursor chambers were controlled individually, and these parameters were used to adjust the film composition. Pure oxygen was used as the oxidant and introduced into the reactor via a separate delivery line. The precursor delivery lines, as well as the inlet flange, were heated to a temperature higher than the highest source temperature in order to avoid condensation of the vapor phase precursors. Single-side polished, single crystal (001) $SrTiO_3$ was chosen as the substrate for samples used for growth optimization and structural characterization, while (001) $SrRuO_3/SrTiO_3$ substrates were used for PMN-PT samples which were characterized electrically. Immediately prior to deposition, substrates were cleaned with acetone and methanol; no further surface treatments were performed. The typical growth conditions are given in Table I.

Table I: Growth conditions for PMN-PT films

Substrate Temperature:	700°C
Reactor Pressure:	6 Torr
Precursor Temperatures:	Pb: 28 - 30°C
	Mg: 120 - 140°C
	Nb: 78 - 84°C
	Ti: 36°C
Precursor Chamber Pressure:	Pb: 600 Torr
	Mg: 18 Torr
	Nb: 18 Torr
	Ti: 200 Torr
Carrier Gas Flow Rate:	Pb: 20 - 25 SCCM
	Mg: 36 - 42 SCCM
	Nb: 55 - 62 SCCM
	Ti: 18 - 26 SCCM
Oxygen Flow Rate:	400 SCCM
Background N_2 Flow Rate:	100 SCCM
Deposition Rate:	4 - 6 nm/min

The evaporation/sublimation temperatures of the Mg and Nb precursors in our case are somewhat reduced compared to those used by others. Because of this, the MOCVD process reproducibility and controllability were improved significantly.

Film phase content and crystallography were characterized by x-ray diffraction both on a laboratory source and on Beamline 12-ID-D of the Advanced Photon Source. Cu Kα symmetric theta – two theta diffraction spectra are shown in Figures 1 and 2 for a pure PMN film and a PMN-PT film with approximately 20% PT (based on precursor flow rates), respectively, deposited on (001) $SrTiO_3$ substrates. Both films were approximately 300 nm in thickness. Only (00l) peaks are observed, with an out-of-plane lattice parameter of 0.406 nm for the PMN sample and 0.402 nm for the PMN-PT sample.

Four circle x-ray diffraction using synchrotron radiation indicated a cube-on-cube orientation relationship between a second 200 nm PMN film and its $SrTiO_3$ substrate, with a (001) rocking curve width of
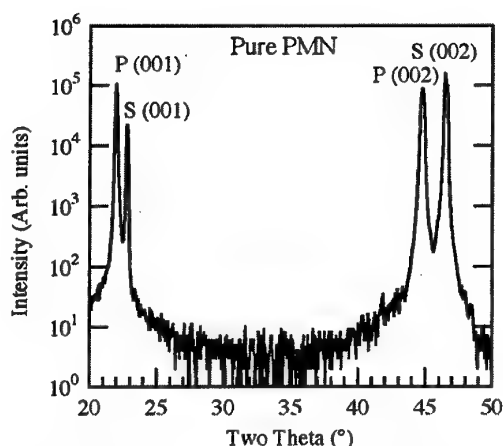
Figure 1: XRD spectrum of a PMN/$SrTiO_3$ sample, showing pure (00l) orientation. PMN peaks are indicated by "P", substrate peaks by "S".
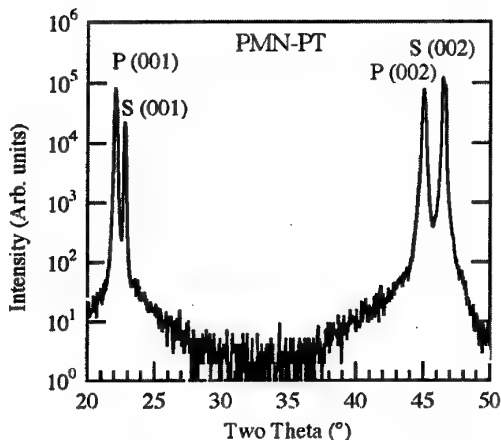
Figure 2: XRD spectrum of a PMN-PT/$SrTiO_3$ sample, showing pure (00l) orientation. PMN-PT peaks are indicated by "P", substrate peaks by "S".

0.1° and an in-plane mosaic spread of 0.8°. A tetragonal structure was found for the PMN film, with out-of-plane and in-plane lattice parameters of 0.406 and 0.404 nm, respectively. This tetragonal distortion is most likely the result of the temperature-dependent misfit strain present in the film because of epitaxy with the substrate, and which has only been partially relieved. Additionally, it appears that the unit cell volume of the PMN is slightly expanded relative to the bulk, perhaps because of point defects and/or slight nonstoichiometry in the film. Extremely weak, broad superlattice reflections were found at the (1/2,1/2,1/2) reciprocal lattice positions of the PMN, indicating a very small degree of B-site ordering [6]. The degree of ordering is less than has been observed in, for instance, PMN films prepared by chemical solution deposition [7], and which have experienced higher temperatures of 800 – 850°C.

A scanned probe microscope image of the surface of this sample is shown in Figure 3. The rms roughness of a 2 μm x 2 μm region was 2 nm, with a

maximum peak to valley height of approximately 12 nm. Despite the fact that there is a strong three-dimensional orientation relationship between the PMN and the $SrTiO_3$, the surface microstructure appears granular with a length scale slightly less than 100 nm. This suggests a growth mode with a relatively high nucleation density followed by columnar growth. This is not unexpected given the relatively large lattice mismatch between $SrTiO_3$ and PMN (3.5% at room temperature), and the relatively low growth temperature. These observations are also consistent with the 0.8° in-plane mosaic.
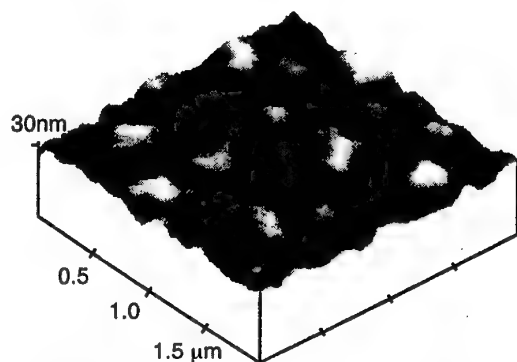
Figure 3: Scanned probe microscope image of the surface of a 200 nm PMN film on $SrTiO_3$. The rms roughness is approximately 2 nm over the 2 μm x 2 μm region.

The samples discussed so far were deposited under optimized conditions, and no impurity phases were detected. In contrast, under non-optimized, lead poor conditions, an impurity peak was found at $2\theta \sim$ 43.3°, corresponding to a d-spacing of ~0.21 nm. Furthermore, the impurity peak could be eliminated in the diffraction spectra by increasing the Pb flux and decreasing the Mg flux flowing into the reactor. Depending on the relative amounts of Mg and Nb in the deposited flux, this peak may correspond to $MgNb_2O_6$, (columbite), $Mg_4Nb_2O_9$, which is isostructural with α-Al_2O_3, or possibly to a disordered niobium-magnesium oxide.

To distinguish between these possibilities, cross-sectional transmission electron microscopy was performed, Figure 4. Coherent second phases were observed, as evidenced by stripes of Moiré fringes in the image running in the film thickness direction. The in-plane morphology of the second phase has yet to be determined; it is not clear from the cross-sectional micrographs whether the impurity phase has a planar or perhaps cylindrical microstructure.

Energy dispersive x-ray spectroscopy was performed on the inclusions to determine their composition, yielding a Mg:Nb ratio of 1.4 to 1.9, as compared to 0.5 to 0.6 measured in the film bulk. The out-of-plane lattice parameter and Mg:Nb ratio would appear to be consistent with a (114) or (106) oriented $Mg_4Nb_2O_9$ phase. However, electron diffraction and high-resolution imaging indicate that the impurity phase has a slightly distorted pseudocubic structure, rather than the hexagonal symmetry of bulk $Mg_4Nb_2O_9$.
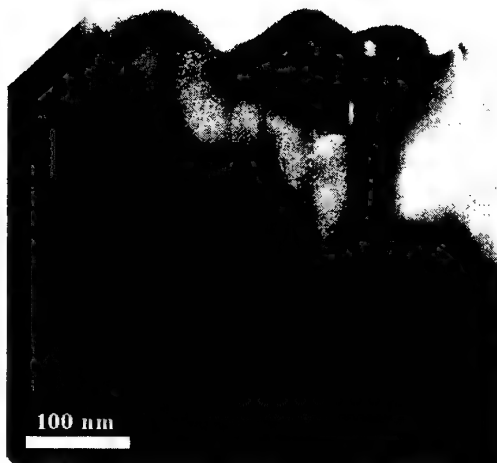
Figure 4: [100] cross-sectional transmission electron microscope image of a PMN film containing the impurity phase

Thus we postulate that the second phase is most likely a disordered magnesium – niobium oxide. More work is need to unambiguously determine the phase's identity. It also should be noted that Figure 4 confirms that these films are comprised of columnar grains separated by low-angle boundaries.

3. DIELECTRIC PROPERTIES

The relative permittivity and dielectric loss as a function of electric field at 10 kHz and 0.2 V oscillation level are given in Figure 5 for a 350 nm pure PMN film on $SrRuO_3/SrTiO_3$, with Pt top electrodes. Hysteresis in the forward and reverse sweeps indicates slim loop, relaxor-like behavior, which is also observed in polarization measurements (not shown).
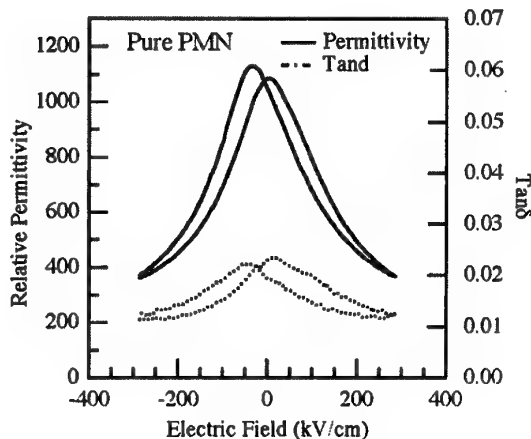
Figure 5: Forward and reverse permittivity – electric field curves taken at 10 kHz for a pure PMN film.

Permittivity as a function of frequency at zero bias is given in Figure 6 for this sample. Dielectric loss is approximately 2% and almost frequency independent over the range that it could be accurately measured, from 1 - 100 kHz, consistent with the modest level of dispersion observed for the permittivity.
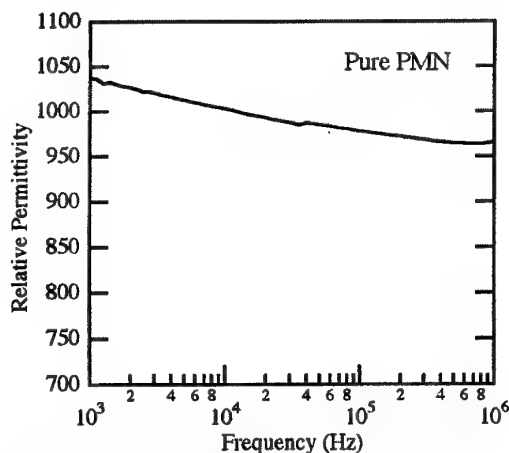
Figure 6: Permittivity vs. frequency at zero bias for a pure PMN film.

Similar results were obtained for PMN-PT films, again with approximately 20% PT. Dielectric constant was found to increase for all samples containing titanium relative to what was measured for pure PMN films, while losses were comparable or slightly higher. Representative forward and reverse permittivity and loss vs. electric field curves are shown in Figure 7. More hysteresis is found for PT-containing samples; however, polarization hysteresis measurements still showed slim loops for these films at room temperature.
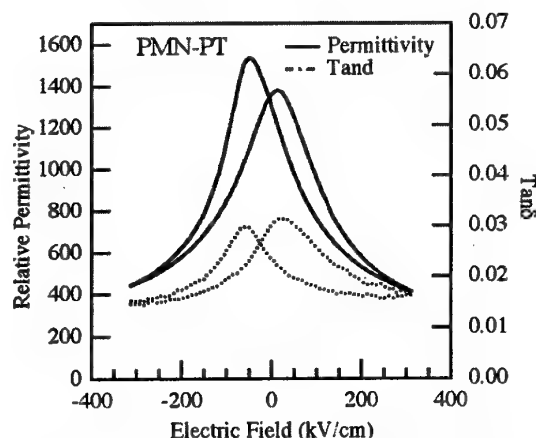
Figure 7: Forward and reverse permittivity – electric field curves taken at 10 kHz for a PMN-PT film.

4. CONCLUSIONS

An MOCVD process was developed for the growth of PMN-PT films, and initial structural and dielectric characterizations have been performed. Although film structural quality is quite high and dielectric losses are low, more work is required to obtain good ferroelectric behavior and square polarization hysteresis loops for these MOCVD samples. Future efforts will center on investigating a wider range of PT contents, and on optimizing the piezoelectric properties of these films.

ACKNOWLEDGMENTS

REFERENCES

1. Seung-Eek Park and Thomas R. Shrout, *J. Appl. Phys.* **82**, 1804-1811 (1997).
2. K. R. Udayakumar, J. Chen, P.J. Schuele, L.E. Cross, V. Kumar, and S.B. Krupanishi, *Appl. Phys. Lett.* **60**, 1187-1189 (1992). L.E. Francis, and D.A. Payne, *MRS Symp. Proc.* **200**, 173-178 (1990).
3. M.C. Jiang, T.J. Hong, and T.B. Wu, *Jpn. J. Appl. Phys.* **33**, 6301 (1994).
4. K.L Saenger, R.A. Roy, D.B. Beach, and K.F. Etzold, *MRS Symp. Proc.* **285**, 421-426 (1993). Dan Lavric, Rajesh A. Rao, Qing Gan, J.J. Krajewski, and Chang-Beom Eom, *Integrated Ferroelectrics* **21**, 499-509 (1998). J.-P. Maria, W. Hackenberger, and S. Trolier-McKinstry, *J. Appl. Phys.* **84**, 5147-5154 (1998).
5. Yutaka Takeshima, Kosuke Shiratsuyu, Hiroshi Takagi, and Kunisaburo Tomono, *Jpn. J. Appl. Phys.* **34** Pt 1, 5083-5085 (1995).
6. J. Chen, H.M. Chan, and M. Harmer, *J. Am. Cer. Soc.* **72**, 593-598 (1989). Mehmet A. Akbas and Peter K. Davies, *J. Am. Cer. Soc.* **80**, 2933-2936 (1997). Y. Yan, S.J. Pennycook, Z. Xu, and D. Viehland, *Appl. Phys. Lett.* **72**, 3145-3147 (1998).
7. Z. Kighelman, D. Damjanovic, A. Seifert, L. Sagalowicz, and N. Setter, *Appl. Phys. Lett.* **73**, 2281-2283 (1998).

Dielectric Behavior of multilayered $Pb(Mg_{1/3}Nb_{2/3})O_3$-$PbTiO_3$ Thin Film by Chemical Solution Deposition

Hisao Suzuki, Hiroyuki Kamei, Masami Kishi*, Junichi Takahashi**, Kohei Kodaira**

Department of Materials Science, Shizuoka University, 3-5-1 Johoku, Hamamatsu, 432-8561, Japan

Fax : 81-53-478-1157, e-mail : hisuzuki@mat.eng.shizuoka.ac.jp

*Hokkaido Institute of Technology, **Hokkaido University

Ferroelectric relaxor $Pb(Mg_{1/3}Nb_{2/3})O_3$ (hereafter abbreviated as PMN) thin films were prepared by the chemical solution deposition from molecular-designed alkoxides precursor solutions with $PbTiO_3$ (hereafter abbreviated as PT) multi-seeding layers. Alkoxide-derived PT seeding layer crystallized into a perovskite phase at low-temperatures above 450°C which offers the in-situ nucleation sites for PMN. In this study, crystallization behavior was controlled by using the seeding process as well as the stacking structures of precursor thin films. As a result, multilayered perovskite PMN-PT thin films with preferable dielectric behavior could be successfully prepared at 800°C. Relative permittivity of the resultant films was in the range from 1000 to 3500 at room temperature, depending upon the film thickness, annealing process and the stacking structure of multilayered thin films. The curie temperatures of the resultant films also changed by the deposition process and the stacking structure of multilayered films to form the compositional gradient.

1. Introduction

Ferroelectric thin films with perovskite structure are of renewed for microelectronics application, including ferroelecric random access memory (FRAM), dynamic random access memory (DRAM), and thin-layer capacitors integrated onto a silicon wafer [1]. In addition, resent advancement in micromachine requires a high performance microactuator. A perovskite type relaxor of $Pb(Mg_{1/3}Nb_{2/3})O_3$ is one of the promising materials for high performance capacitor and microactuator because of their high permittivity and electrostrictive coefficient. However, chemical solution deposition of perovskite type PMN thin film is very difficult because of the formation of stable intermediate pyrochlore phases, especially in the case of the thin film. In this study, a novel method for preparing perovskite type PMN thin films with PT seeding layers which offer the nucleation sites to lower the crystallization temperature and to form solid solution during annealing, leading to the control of the curie temperature of the resultant thin films. Only a few papers have been reported to deposit thin films of single phase perovskite type PMN or PMN-PT solid solutions [2-4]. In this paper, it is demonstrated that multi-layered PMN-PT films have the high dielectric constant and exhibits small dependence on the temperature, showing the potential for a high quality device such as the ceramic capacitors and DRAM by changing the stacking structure of the films and annealing process.

2. Experimental Procedure

2.1 Preparation of precursor solution

Flow chart for preparation of PMN and PT precursor solutions are shown in Figure 1. Lead acetate trihydrate, Nb- and Mg-alkoxide were used for raw materials. At first, Nb-ethoxide was mixed with Mg-ethoxide and then refluxed for 12 hours to form double alkoxide. On the other hand, lead acetate tryhidrate was dried at 150°C and then dissolved into ethanol with ammonia gas flow to form Pb-precursor solution. These two precursor solutions were mixed and refluxed for 12 hours. Monoethanolamine (MEA) was mixed to stabilize the solution. PT precursor solution was prepared in the same manner with PMN precursor solution. Acetylacetone was added as a stabilizing agent for PT precursor solution.
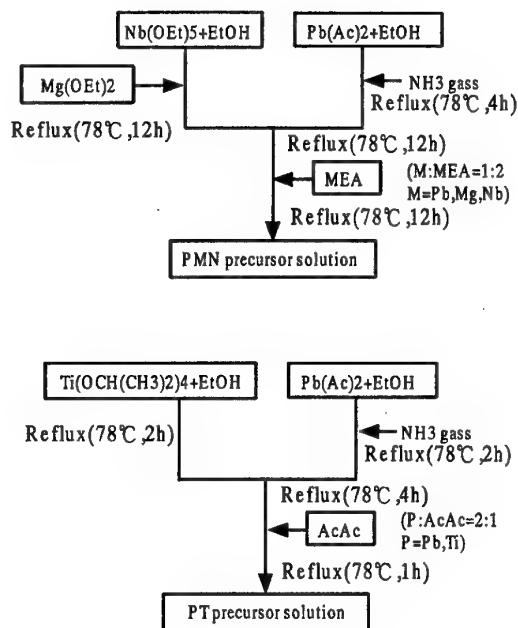
Fig. 1. Flow chart for preparation of PMN and PT precursor solutions.

2.2 Film Deposition

The PMN-PT thin films were deposited by the dip-coating method. Silicon wafer with Ti and SiO_2 buffer layers and Pt electrode were used as a substrate. Each coating layer was dried at 110°C for 5 minutes followed by the pre-annealing at 400°C up to 60 min to remove organics in the layers. The final annealing was carried out at 800°C for 30 seconds. Some films were annealed at 800°C up to 14 minutes. Gold was used as an upper electrode. Dielectric behavior of the resultant film was measured by the LCR meter (HP-4284A). P-E hysteresis loop of the resultant film was measured by RT6600S (Radiant Technology Inc.). Crystalline phase in the resultant films was identified by X-ray diffraction (XRD). Microstructure of the film was observed by field emission type scanning electron microscope (SEM).

3. Results and Discussion

3.1 Phase Development and Microstructure

Perovskite ratio in the films was calculated from the peak height of XRD diffraction for the perovskite and pyrochlore phases. Figure 2 shows the effect of pre-annealing time for the pyrolysis of the residual organic compound at 400°C on the perovskite ratio after annealing at 800°C. Perovskite ratio slightly increased with increasing pre-annealing time up to 60 minutes and reached at 97%. It is considered that densification by the removal of the organic compound influenced the crystallization of PMN-PT thin films. Because the pre-annealing time which is too long exerts the influence of diffusion of the lead in films and forms the pyrochlore phase, it is considered that suitable pre-annealing time is necessary.
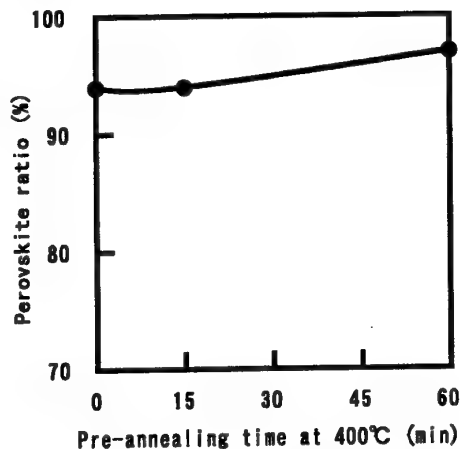
Fig.2. Change in the perovskite ratio with pre-annealing time at 400°C.

Figure 3 shows the microstructure of the resultant PMN-PT multi-layered films pre-annealed at 400°C for different time and annealed at 800°C. It is obvious that the longer pre-annealing resulted in the dense microstructure of the resultant films, leading to the superior electrical properties. This suggested that viscous sintering occurred at very low temperatures. In addition, perovskite PMN-PT films grew enough to form large grains ranging from 100 to 300 nm in diameter at 800°C. From this result, it is concluded that enough pre-annealing is essential for the dense PMN-PT multi-layered films.

(a)

(b)
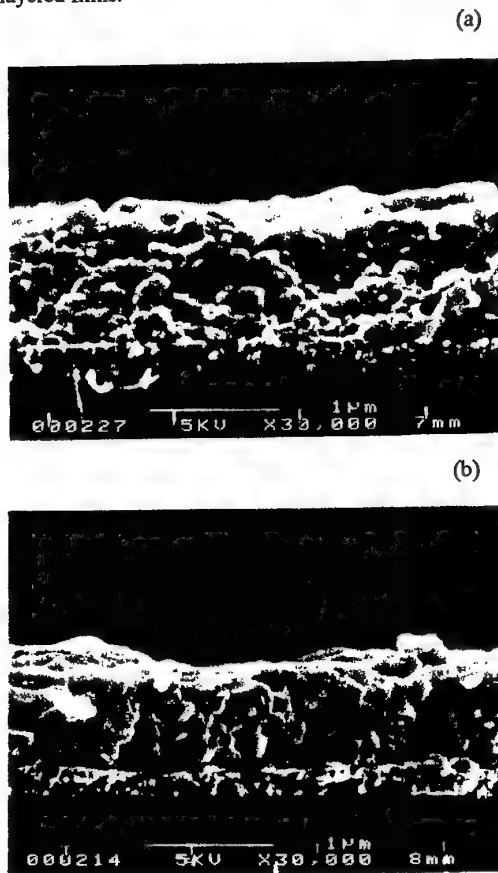
Fig.3. FE-SEM images of the PMN-PT multilayered films with different pre-annealing time.
(a) Pre-annealed at 400°C for 15 min. (cross section)
(b) Pre-annealed at 400°C for 60 min. (cross section)

3.2 Dielectric Behavior of PMN-PT multi-layered films

Figure 4 shows the temperature dependence of the dielectric constant for the resultant films with different pre-annealing time at 400°C. These results clearly showed that the resultant films had the ferroelectricity with the different curie temperatures and made solid solution between PMN and PT layers. As already described above, perovskite ratio changed with pre-annealing time at 400°C. Consequently, dielectric behavior changed with pre-annealing time and dielectric constant increased with prolonged pre-annealing time. The curie temperature of the resulting films depended on pre-annealing time, and existed in the range from below 0°C to around 15°C. This suggests that enough pre-annealing results in the improved dielectric properties
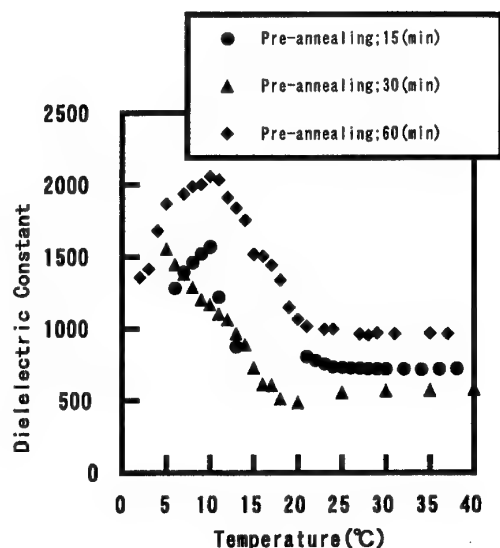
with higher curie temperatures.

Fig.4. Temperature dependence of dielectric constant for the PMN-PT multilayered films with different pre-annealing time.

3.3 Effect of Stacking Structure on Dielectric Behavior

To prepare the solid solution of PMN-PT thin film, we changed the stacking structure of the precursor films and annealing process. From the results of the multilayered films with layer by layer structure, precursor films were pre-annealed at 400°C for 60 minutes to remove the residual organics and to increase the film density, and were annealed at 800°C for about 10 minutes to promote the diffusion of the elements for the formation of solid solution. The difference of the stacking structure was illustrated below.
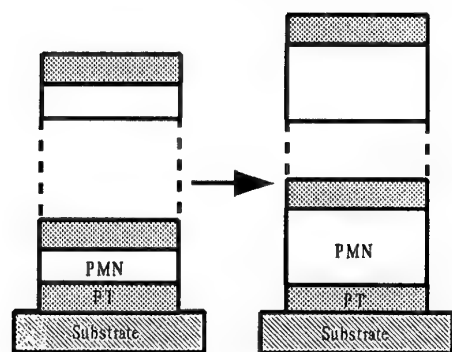
Original Stacking Structure   New Stacking Structure

The difference of the stacking structures

The new stacking structure was consisted of alternative stacking of one PT precursor and three PMN

precursor layers. One dipping process resulted in the film thickness of about 30~40 nm for both PT and PMN precursor layers. Therefore, the new stacking structure and annealing process would lead to the higher content of PMN-PT solid solution in the film, leading to the improved dielectric properties with higher curie temperatures. In addition, compositional gradient would be expected to form micro-domains with different curie temperatures in the resultant films. Figure 5 shows the dielectric properties for the resultant PMN-PT solid solution films as the function of temperature.
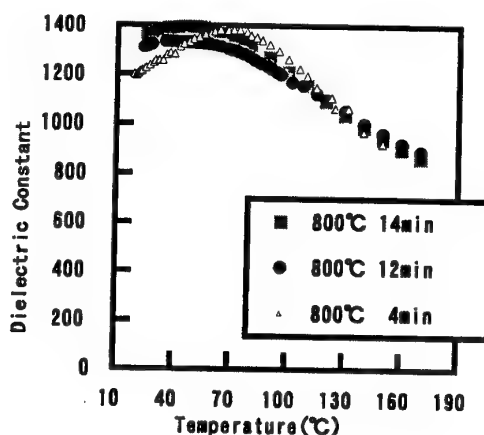
Fig.5. Temperature dependence of dielectric constant for the PMN-PT multilayered solid solution films annealed at 800°C for different times. Thickness of the films is about 450 nm.

As will be expected, the dielectric constant for the resultant solid solution films exhibited broad carve in the wide temperature range, suggesting the formation of the solid solution with PMN rich composition or compositional gradient to form micro-domains with different curie temperatures. However, the dielectric constant for the resultant films was relatively lower because thickness of these films were about 450 nm, including the very thin interfacial pyrochlore phase. In addition, the maximum value of the dielectric constant increased when the annealing time increased and curie temperature moved to the lower temperature side. This may be ascribed to the improved crystallinity and promoted formation of solid solution of PMN rich phases by the prolonged annealing.

Figure 6 shows the hysteresis loop measured at room temperature for the resultant PMN-PT solid solution film annealed for 12 minutes. Well-saturated hysteresis loop was observed, showing the ferroelectricity. This indicated that the curie temperature of the multi-layered PMN-PT film existed at above room temperature.
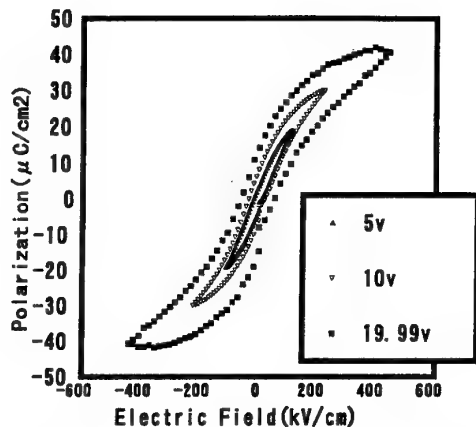
Fig.6. P-E hysteresis loops for the PMN-PT multilayered solid solution film annealed at 800°C for 12 min.

3.4 Effect of Film Thickness on Dielectric Constant

Figure 7 shows the dielectric property of the resultant PMN-PT solid solution film of about 800 nm thick as the function of temperature. Film thickness had large effect on the dielectric constant of the resultant PMN-PT multi-layered film through chemical solution deposition, showing the existence of the interfacial pyrochlore phase. The formation of pyrochlore phase may be suppressed by the selection of electrode as for the PZT thin film. Further investigation is essential for the thin PMN-PT films with good dielectric properties. In addition, the dielectric behavior for this thick film exhibited broad carve in the wide temperature range as well as for the thin films. This suggested the formation of the solid solution to form the compositional gradient with PMN rich composition, leading to the formation of micro-domains with different curie temperatures even in the thick multi-layered film.

4. Conclusions

This paper described the processing for the PMN-PT multi-layered films with superior dielectric behavior for thin layer capacitors and DRAM. As a result, followings were concluded;

(1) Pre-annealing process promote the densification of the amorphous precursor films to improve the dielectric property of the resultant multi-layered films.

(2) Stacking structure of the multi-layered precursor films had large effect on the dielectric behavior for the multi-layered PMN-PT films. Insertion of thick PMN layers improved the dielectric behavior of the resultant multi-layered films.

(3) Film thickness also had large effect on the dielectric constant of the resultant PMN-PT multi-layered films. The multi-layered film with about 800 nm thickness exhibited relatively high dielectric constant of about 3000, together with the good dielectric behavior.

References

[1] A. I. Kingon and E. R. Myers, Materials Research Society Symposium Proceedings, Vol. 200, Ferroelectric Thin Films, Pittburgh, PA: Materials Research Society, 1990

[2] L. F. Francis and D. Payne, "Thin-Layer Dielectrics in the $Pb[(Mg_{1/3}Nb_{2/3})_{1-x}Ti_x]O_3$ System", J. Am. Ceram. Soc., vol. 74, pp. 3000-3010, December, 1991

[3] S. Nagakari, K. Kamigaki and S. Nambu, "Dielectric Properties of Sol-Gel Derived $Pb(Mg_{1/3}Nb_{2/3})O_3$-$PbTiO_3$ Thin Films" , Jpn. J. Appl. Phys., vol. 35 Part 1, No. 9B, pp4933-4935, September 1996

[4] H. Suzuki, K. Suzuki, and S. Kaneko, "Preparation and Properties of Alkoxide-Derived $Pb(Mg_{1/3}Nb_{2/3})O_3$ Thin Films with $PbTiO_3$ Multi-Seeding Layers", J. Korean. Phys. Soc., vol.32, pp.S1494-S1496,February 1998

Fig.7. Temperature dependence of dielectric constant for the PMN-PT multilayered solid solution film annealed at 800°C. Thickness of the films is about 800 nm.

Piezoelectric Measurement of Thin Films Ferroelectric using AFM with an RT6000

Kenji   Shibata, Yasunori Yamaguchi   YA-MAN Ltd.

2-4-2Toyo,Koto-ku,Tokyo

Fax. 81-3-5635-1866   E-mail: info@ya-man.com

Joe T. Evans, Jr.   Radiant Technologies, Inc.

Dr. Seigen Otani   Fujitsu Laboratory Ltd.

Dr. Masatoshi Yasutake   Seiko Instruments Inc. Technical machine section

1.Introduction

As the study of Ferroelectric thin film application for semiconductor memory system is progressed, it is said that the thin film Piezo phenomena (which film becomes elastic with electric voltage loaded) has something to do with the deterioration of the element.

On the other hand, the study of thin film actuator and micro machine etc utilizing the thin film Piezo phenomena is getting active.

In both cases, it is important to measure Ferroelectric hysterisis and Displacement with the same voltage waveform simultaneously; thus, this result will allow researcher to understand and evaluate the characteristic of ferroelectric sample. However, obtaining this kind of measurement with precision and speed has been difficult task.

This report shall provide you with the fact that an integration of RT6000 (known as standard Hysteresis measurement system) and SPI-3800N (AFM: Atomic Force Microscope) is the solution for such ferroelectric characteristic evaluation.

2.Overview

AFM (Atomic Force Microscope) has been developed with scanning tunneling micro-scope technology to measure the sample surface roughness and other surface condition in atomic size level. AFM uses a small cantilever with an approximately 20 nm diameter tip as its sensor probe. It measures surface topology by placing the tip close to or in contact with the sample surface. By monitoring the displacement of the cantilever with laser light source, atomic size level measurement becomes available.

With AFM's accurate measurement function, the displacement of `Z direction (thickness)` which shows elasticity of thin film and of `X & Y direction` becomes possible. For the measurement control mechanism of AFM, the control of Z direction has been modified from Analog Feedback to Digital Feedback which enable a better interface with extermal instrument.

As a result, the displacement measurement of very thin Ferroelectric film like a few angstrom in z direction can be acheived. In this report, we used AFM SPI3800N fabricated with Seiko Instruments Inc. Displacement signal out-put circuit .

3.Connection of RT6000 and AFM

This system is integrated with RT6000 (known as standard Hysteresis measurement system in the industry which is supplied by Radiant Technology Inc.)and pre-mentioned AFM.

RT6000 drive channel is connected to AFM cantilever with coax cable. Cantilever contacts to the top electrode of the sample for AFM contact mode measurement. Thus,

now the condition for AFT to measure z displacement in AFM contact mode is filled; Simultaneously, RT6000 drive signal receives electrical attachment to the top electrode of the sample through cantilever to load Hysteresis measurement signal.

Currently, the sample's bottom electrode is directly attached to the AFM metal sample stage with silver past. RT6000 RETURN channel is connected to the metal stage for the loading and measurement of Hysteresis measurement signal. (see Figure 1)
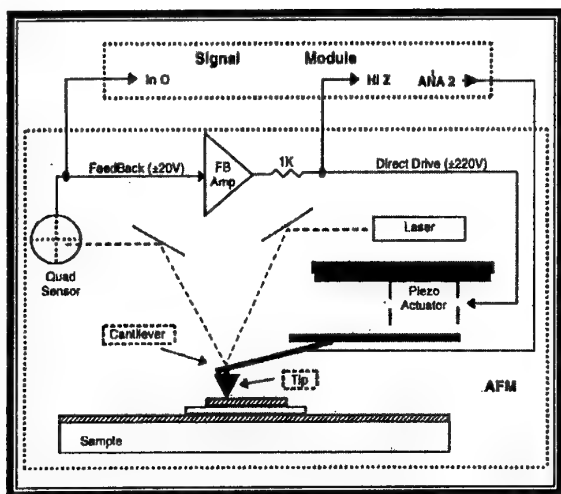
Fig.1 RT6000 conect to SPI3800N

4.Sample Description

The sample used in this experiment is a PLZT film fabricated by Radiant Technologies Inc. The film is 1 micron thick with the top electrode of $100\,\mu$ m x $100\,\mu$ m. Substrate size is 2cm x 2cm due to the AFM stage function.

5.Measurements Result

PZMANUAL software which can simultaneously measure Hysteresis and Displacement is used with the above integrated system to achieve the following results. A experiment time per test was a few second. Figure 2 is the Hysteresis measurement result.
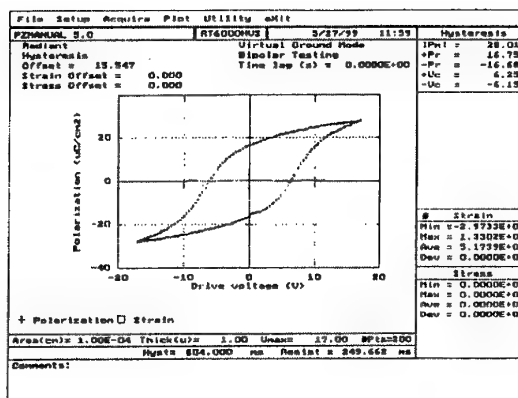
Fig.2 Hysteresis Loop

At Vmax : 17V, Pm = 28 μ c / cm2 Hysteresis characteristic is measured. Figure 3 shown is its Displacement measurement result which simultaneously is measured during the Hysteresis measurement. It shows a beautiful butterfly loop. Peak to peak is approximately 15 angstrom.
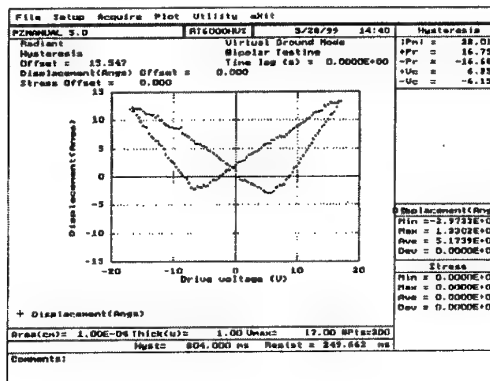
Fig.3 Displacement Loop

Figure 4 shows overlap of Hysteresis measurement and Displacement measurement.
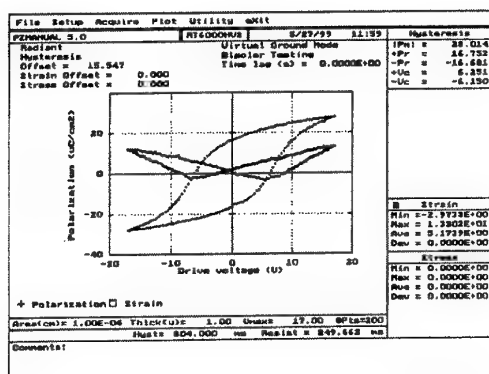
Fig.4 The same time measurement

A Cross-point of Hysteresis curve and horizontal axis (voltage axis)is almost same as bottom hollow point of butterfly loop.

6.Conclusion

We achieved simultaneous Hysteresis character and Displacement of thin Ferroelectric film with high speed and accuracy.

7.Future object

For the improvement of the system, we aim following items for the future.

- High speed Hysteresis measurement signal and High speed AFM.
- Simplify sample attachment. Wafer evaluation.
- Durability improvement of cantilever.
- Correspond to thick film sample (High voltage achievement)

References
* RT6000 manual
* RT6000 Piezo measurement manual
* SPI-3800N manual

Measurement and Calculation of PZT Thin Film Longitudinal Piezoelectric Coefficients

Hiroshi Maiwa, Jon-Paul Maria*, James A. Christman**, Seung-Hyun Kim*, Stephen K. Streiffer***, and Angus I. Kingon*

Department of materials Science and Ceramic Technology, Shonan Institute of Technology, Fujisawa, Kanagawa 251-8511, Japan

Fax: 81-466-36-1594, e-mail: maiwa@mate.shonan-it.ac.jp

*Department of Materials Science and Engineering and **Department of Physics, North Carolina State University, Raleigh, NC 27695, U.S.A.

***Materials Science Division, Argonne National Laboratory, Argonne, IL 60439, U.S.A.

The ferroelectric and piezoelectric properties of 2000 Å thick chemical solution deposited $Pb(Zr_xTi_{1-x})O_3$ (PZT)thin films were investigated. Several Zr/Ti ratios were studied: 30/70, 50/50 and 65/35, which correspond to tetragonal, near-morphotropic, and rhombohedral symmetries. In all samples, a {111}-texture is predominant. Longitudinal piezoelectric coefficients and their dc field dependence were measured using the contact AFM method. The expected trend of a maximum piezoelectric coefficient at or near to the MPB was not observed. The composition dependence was small, with the maximum d_{33} occurring in the tetragonal material. To explain the results, crystallographic texture and film thickness effects are suggested. Using a modified phenomenological approach, derived electrostrictive coefficients, and experimental data, d_{33} values were calculated. Qualitative agreement was observed between the measured and calculated coefficients. Justifications of modifications to the calculations are discussed.

1. INTRODUCTION

When the piezoelectric coefficients of thin film PZTs are reliably measured, values 30 to 75% smaller than those expected in the same bulk compositions are commonly observed. [1 - 4] Understanding this property difference is important with regards to the following issues; (i)incorporation of PZT thin films into reliable electromechanical devices, and (ii) understanding the fundamentals of domain walls by studying their behavior under the influences of boundary conditions associated with the thin film geometry.

Although the compositional dependence of d_{33} across the PZT phase diagram has been reported by several authors, simultaneous assessment of the results does not lead to a consistent conclusion regarding the importance or influence of the morphotropic composition. [5 – 8] A consistent difficulty, especially in sub micron films, is encountered when attempting to guarantee that the film stoichiometry, (i.e., A/B ratio), orientation, and microstructure are of sufficient consistency that meaningful comparisons can be drawn.

We present here the initial results of our investigations of PZT thin films directed towards understanding these issues. PZT thin films were deposited by chemical solution deposition with compositions providing tetragonal, near morphotropic, and rhombohedral symmetries. Insofar as possible, efforts were made to insure electrical and structural properties of consistent quality and character such that conclusions and relationships could be known. All films are consistently {111} oriented and have dense microstructures with ~ 0.1 μm grain diameters.

Structural characteristics were measured by x-ray diffraction and topographic scanning probe microscopy. Electrical properties including polarization hysteresis and the field dependence of the permittivity and loss were measured using an RT66A and an HP 4192A. Finally, the longitudinal piezoelectric coefficients were measured using a Park Scientific Scanning Probe Microscope. Recent modifications to the SPM based technique were performed such that previously encountered difficulties including capacitive coupling between the sample and tip, and unambiguous field application (as caused by insufficient supply of switching current to the capacitor) were overcome. Detailed discussions of these modifications are available in the references. [9] It is noted, however, that full qualifications of this SPM based method has not been completed. Influences from surface microstructure gradients, tip sample interaction, and wafer bending are still being investigated. In general, however, data comparison between the samples in this study, and the voltage dependence of individual samples appear reliable.

2. RESULTS AND DISCUSSION

Standard structural and electrical characterization was performed to make an initial assessment of the electrical properties. Interpretation of this data is straight forward , thus useful for the purpose of establishing a base line by which the film quality and characteristics are initially judged . Fig 1 shows the polarization hysteresis traces for the three film types used in this report.

As shown in the figures, the tetragonal material exhibits the largest polarization hysteresis values and the most rectangular shapes . As is commonly observed, when compositions tend towards rhombohedral symmetry, the loop shape becomes more slanted, remanent polarization and coercive field values are reduced, and

classically saturating loops are more difficult obtain. Figure 2 gives the dependence of the permittivity for the same set of film composition, while Fig. 3 shows the dielectric loss.
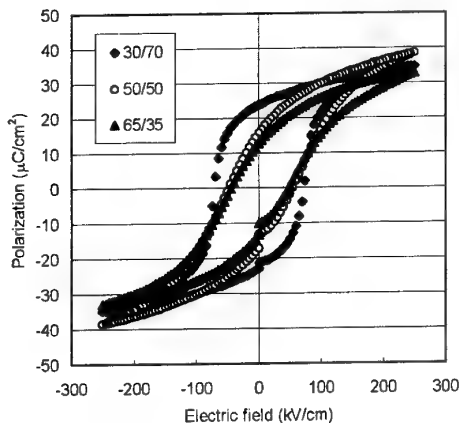
Fig. 1: Polarization hysteresis plots for the three film compositions used in this study.
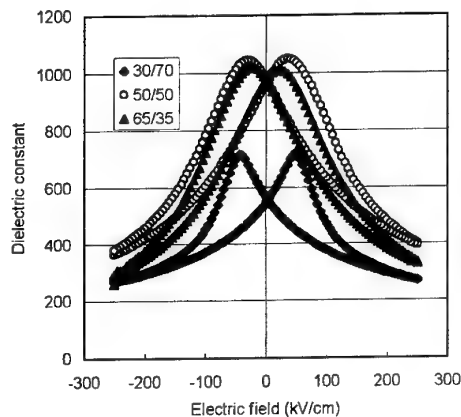
Fig. 2: Small-signal permittivity field dependence (1KHz) for the three film compositions.

The smaller permittivity values are consistent with expectations of the tetragonal films, as well as the more distinct saturation and larger coercive field values.

The loss tangent values for all compositions are similar, however, the peak breadth for the tetragonal composition is most narrow. This suggests that the tetragonal symmetry, in combination with the {111} orientation, provide for the most abrupt domain switching. Working with the assumption that for the films this thickness (i.e., 2000 Å) non-180° domain wall motion is strongly limited, it is reasonable to assume that the strong loss tangent field dependence results primarily from 180° domain wall motion. An important implication is that the small-signal permittivity measurements must contain an appreciable

extrinsic component. Furthermore, it is important to remember that the contribution of this component to the piezoelectric response is negligibly small. [10,11]
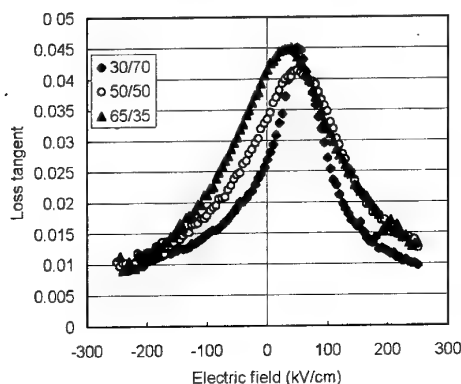
Fig. 3: Field dependence of the loss tangent (1KHz) for the three compositions studied. The measurements were taken for one field sweep direction only.

Finally, the SPM-technique was applied to characterize the longitudinal piezoelectric coefficient and its electric field dependence. Fig. 4 gives the piezoelectric data plotted in the form of a hysteresis loop.
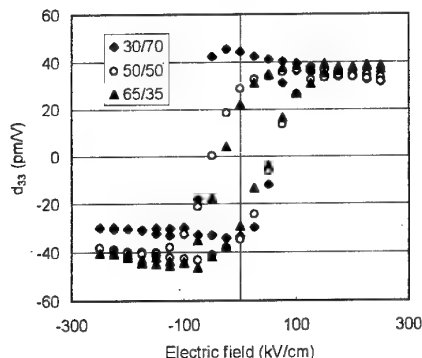
Fig. 4: d_{33} "hysteresis loops" measured for the three compositions studied.

As expected, the d_{33} loop bear a strong resemblance to the polarization hysteresis in loop shape, coercive field value, and magnitude. The coercive field found by the piezoelectric measurements are slightly different than the results from polarization hysrteresis. It is likely that this difference results from difference in the specific measurements parameters. Polarization hysteresis is a large ac signal excitation at ~ 1 Hz, while this piezoelectric measurement involves a small signal ac excitation at 1KHz superimposed upon a quasi-static dc bias.

The remanent values for the tetragonal composition are largest, while those for the rhombohedral composition are the smallest. This is in sharp contrast to ceramic materials in which a maximum is expected for the morphotropic composition. It is well known that the reason for the maxima at the MPB is the number of domain variants. Fourteen possible polar vector orientations are available, thus efficient poling and domain switching is possible. [11] In the case of thin films where the ability to switch non-180° domains may be limited, [1, 3, 12, 13] and the microstructure is highly textured, a maxima should not be expected at this composition. Therefore, without access to the extrinsic contribution of the electromechanical response present in ceramics, a different compositional dependence to the properties is likely. To further explore this possibility, the piezoelectric coefficients of the samples were estimated using a modified phenomenological equation:

$$d_{ij} = 2Q_{ijkl}\varepsilon_0\varepsilon_{ij}P_s$$

As written, this equation only applies to the case of a single-domain single crystal, however, several modifications can be made making application to other more practical situations possible. These include (i) calculation of an effective electrostrictive coefficient for a textured thin film under the influence of a residual biaxial strain [14] (see Table 1), and (ii) Substitution of the measured polarization for the spontaneous polarization. The importance of a corrected electrostrictive coefficient is clear, while the substitution of the measured polarization for the spontaneous polarization is required to reflect that real samples do not switch within an arbitrarily small voltage range, or to absolute completion at a well defined electric field. This substitution effectively considers the material as a series of discrete crystals with a "field–variable" spontaneous polarization equivalent to the component of the polarization vector in the direction of the applied field at a given field value. A final issue regarding this treatment is the extrinsic contribution of 180° domain wall motion to the measured permittivity, which must not be introduced into the calculated piezoelectric coefficients. Ideally, only the dielectric constant associated with the lattice polarizability would be included, however, determination of this quantity is particularly difficult. One possibility uses the dielectric constant measured at large electric field values, where the film is ideally approaching a single domain state. Since these films do not switch completely at a wel-defined electric field, choosing this permittivity value can be somewhat arbitrary. For this calculation, the "intrinsic" dielectric constants were estimated by constructing a linear fit to the highest-field dielectric constant (from the 200 kV/cm to 250kV/cm range) and extrapolating to zero field. The results are given in Fig. 5. A second possibility would be to use dP/dE values from the saturation portion of the polarization hysteresis curves. Derivatives of these curves however, yield unreasonably large permittivities. Our hysteresis curves are

obtained at very low frequencies, thus may contain contributions from several sources such as, all of which may not be associated to the switchable ferroelectric polarization (especially at the high field portions of most interest). As such these dielectric constant calculations appear unreasonably inflated. Figs 5 a and b give the calculated results for "intrinsic" dielectric constant and piezoelectric coefficients.

Table 1: Calculated effective electrostrictive coefficients

composition	30/70	50/50	65/35
Q_{33}^{eff}<111> m^4/cm^2	3.1	2.6	2.5
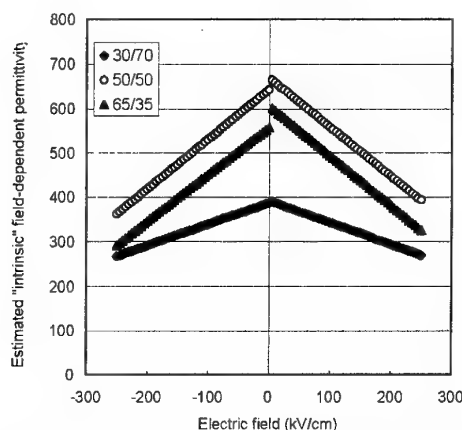
Fig. 5a: Estimated "intrinsic" permittivities for the three PZT compositions studied.
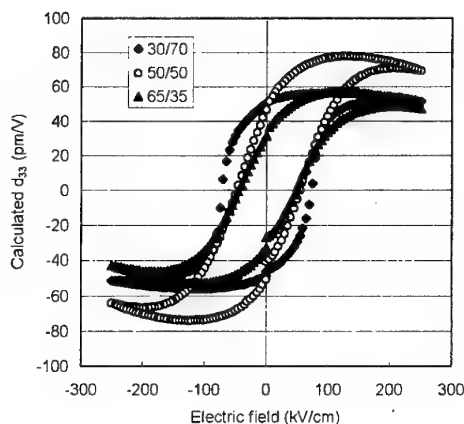
Fig. 5b: Estimated field-dependent longitudinal piezoelectric coefficients.

Comparison of the calculated results and the measured values reveals reasonable quantitative agreement- the functional forms are consistent for all three compositions. Additional efforts are , however, required for a good quantitative fit. We expect that corrections to the absolute values will necessitate a

more rigorous determination of the field-dependent intrinsic dielectric constant and additional corrections to the SPM-based piezoelectric measurement. The high-field polarization values also appear to contain a conduction component, which may be in part responsible for the differences. Measurements of polarization hysteresis at higher frequencies may provide the ability to separate the measured polarization components.

3. CONCLUSIONS

The dielectric and piezoelectric coefficients of PZT thin films having tetragonal, near-morphotropic, and rhombohedral symmetrics were measured. Using a modified phenomenological approach, the "predicted" piezoelectric coefficients were estimated from measured field-dependent permittivity and polarization data. Effective electrostrictive coefficients, which took crystallographic texture and a residual biaxial tensile strain into account, were used in this calculation. Reasonable qualitative agreement was observed between the measured and calculated results.

The expected maxima for piezoelectric coefficients of bulk ceramics was not observed in these thin films; tetragonal composition showed the largest remanent piezoelectric response. When the high-field values were measured, all compositions showed very similar behavior. The remanent calculated values revealed the same trend however the high-field values for the near-morphotroic composition were largest. We believe these values are artificially inflated by field-induced conduction loss. The importance of loop shape is also demonstrated by this study. Clearly, the slanted loop shape of the morphotropic and rhombohedral samples results in a smaller zero-field response, although the structures can potentially supply much stronger actuation. This indicates that oriented thin film samples intended for use as actuators should be optimized for square polarization hysteresis.

These results suggest that the optimal thin film PZT piezoelectric composition may not occur at the morphotropic phase boundary. In very thin films, if the intrinsic piezoelectric response predominates, and a strong {111} crystallographic texture is present, tetragonal material may provide the most desirable electromechanical properties.

Finally, the agreement between measured and calculated piezoelectric coefficients suggests that the derived effective electrostrictive coefficients are reasonable, and potentially useful for further assessment and modeling of PZT thin films.

REFERENCES

[1] S. Trolier-Mckinstry, J. F. S. Jr., T. Su, G. Zavala, and J. Fendler, Ferroelectrics **206-207**, 381-392 (1997)

[2] A. L. Kholkine, C. Wuetchrich, D. V. Taylor, and N. Setter, Rev. Sci. Instrum. **67**, 1935-1941 (1996).

[3] B.A. Tuttle, T. J. Garino, J. A. Voidt, T. J. Headley, D. Dimos, and M. O. Eatough, *Science and Technology of Electroceramic Thin Films* (Kluwer Academic Publishers, Netherlands, 1995).

[4] S. Watanabe, T. Fujiu. and T. Fujii, Appl. Phys. Lett., **66**, 1481-1483 (1995).

[5] F. Xu, F.Chu, J. F. S. Jr., and S. Trolier-Mckinstry, Proc. Symp. Mater. Res. Soc. **493**, 47-52 (1998)

[6] H. D.Chen, K. R. Udayakumar, C. J.Gaskey, and L. E. Cross, Appl. Phys. Lett., **67**, 3411-3413 (1995).

[7] X. Du, J. Zheng, U. Belegundu, and K.Uchino, Appl. Phys. Lett., **72**, 2421-2423 (1997).

[8] K. Lefki and Dormans, J. Appl. Phys., **76**, 1764-1767 (1994).

[9] J. A. Christman, R. R. Woolcott, A. I. Kingon, and R. J. Nemanich, Appl. Phys. Lett., **73**, 3851-3853 (1998).

[10] F. Jona and G. Shirane, *Ferroelectric Crystals* (Dover publications Inc., Mineola, NY, 1962).

[11] B. Jaffe, W. R. Cook, and H. Jaffe, *Piezoelectric Ceramics* (R. A. N. Publications Inc., Mineola, NY, 1962).

[12] A. Kholkin, Ferroelectrics, in press.

[13] D. Damjanovic, M. Demartin, F. Chu, and N.Setter, Proc. IEEE Ultrasonic Symposium, 251-257 (1996).

[14] S. K. Streiffer, to be published.

Application of Piezoelectric Microsystems in Structural Health Monitoring and Biomedical Engineering

Dennis L. Polla and William P. Robbins

Department of Biomedical Engineering
and
Microtechnology Laboratory
University of Minnesota
420 Delaware Street S.E.
Minneapolis, Minnesota USA 55455
TEL: 1-612-626-2753; FAX: 1-612-625-5012; polla@lenti.med.umn.edu

Introduction

Microelectromechanical systems (sometimes called MEMS or microsystems) represents an exciting new technology derived from the same manufacturing processes used to make integrated circuits. There are many diverse applications of MEMS for sensing and actuation, which are being aggressively pursued throughout the world. Piezoelectric MEMS offer distinct advantages in high signal-to-noise ratio and low power consumption in sensing applications and high output force in actuation applications.

Our work has used both piezoelectric bulk PZT integrated with MEMS-based mechanical structures and thin films of sol-gel PZT deposited directly on MEMS structures containing a Ti/Pt electrode surface. Some representative applications carried out in our laboratory are described for structural health-monitoring and medical applications.

Structural Health Monitoring: Acoustic Emission Microsensors

The real-time detection of the precursor signatures leading to material failure is critical to a variety of structures including aircraft, rotating machinery, and bridges. This is particularly relevant to helicopters were fatigue related crack formation can lead to catastrophic component failure. Real-time detection of crack formation is also important in routine maintenance of aircraft components and ship machinery where materials are often unnecessarily replaced or serviced even though they are structurally healthy.

Recent efforts in our laboratory have concentrated on developing the integrated AE microsensors for structural health monitoring applications. A monitoring coupon has been designed and fabricated based on the hybrid integration of piezoelectric acoustic emission (AE) microsensors with a CMOS charge amplifier. Successful operation with a bandwidth of 1 kHz to 1 MHz, gains of 40 db, and a dc power requirement (brought in on the same two interconnect leads that the amplified signal to the external world) of less than 1 mW has been demonstrated. A system level diagram of the IC chip is shown in Fig. 1. The overall size of the chip is 2.2 mm square and 0.5 mm thick. The overall package size is 6 mm by 6-mm lateral footprint and 6 mm tall.

Real diagnostic monitoring applications of the AE sensor system are currently underway. Fig. 2 shows the amplified voltage output versus time of the PZT sensor during a crack event. This waveform is monitored, filtered, and processed. The FFT of the waveform shows particular frequencies of monitoring interest around 170 kHz associated with the high frequency microcracking. Further efforts are directed toward fault-detection algorithm development.
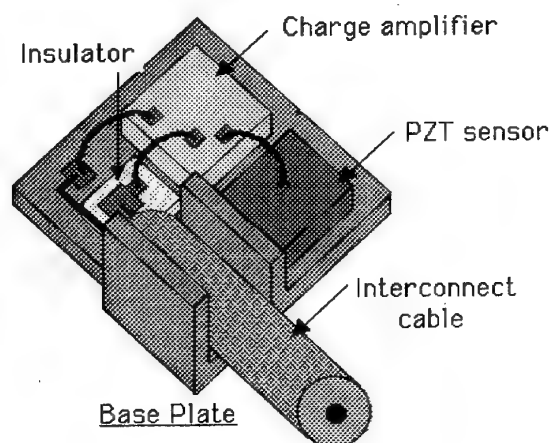
Fig. 1. AE structural health monitoring coupon.
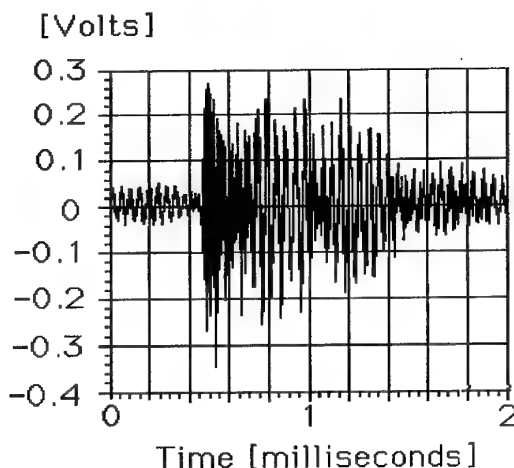
Fig. 2. Detected waveform during crack growth and propagation.

Structural Health Monitoring: Vibration Microsensors

One of the goals of structural health monitoring is to detect the onset of unusual vibration characteristics prior to component or bearing failure. This is desirable for reasons of both preventing major systems damage and providing timely information in regularly scheduled maintenance. Most mechanical vibrations present on either helicopters or ships have fundamental movements at frequencies below 10 kHz. This presents a challenge for both silicon microsensors and signal processing due to the high 1/f electrical noise and parasitic signal losses.

Our approach to vibration monitoring is based on the used on PZT-on-silicon nitride microcantilevers beams. These composite structures are realized by the deposition of lead-zirconate-titanate (PZT) thin films of approximately 0.5 μm-thickness on top of a silicon nitride support structure. A scanning electron micrograph of a representative finished device is shown in Fig. 3. The overall device dimensions are approximately 4.5 μm-thick, 300-μm wide, and 1000 μm long.

The electrical and mechanical responses of the microcantilever beams were tested using conventional impedance analyzers, spectrum analyzers, atomic force microscopes, and a mechanical shake table. The impedance versus frequency spectrum for the microcantilever is shown in Fig. 4. The frequency response of the PZT microcantilever under variable mechanical shake frequency was used to determine its acceleration responsivity to vibrations. The measured unamplified value at 1 kHz is approximately 0.11 pC/g based on the spectral data. The response of the device was found to decrease significantly at lower frequencies (less than 1 kHz) presumably due to charge leakage effects (dc charges do not persist across piezoelectric capacitors). This has been identified to be one of the limitations of this type of vibration sensor, particularly for the detection of very low frequencies in systems such as mechanical pumps.

Due to the microcantilever roll-off at low frequencies and the high interest in usable devices at frequencies below 200 Hz, a piezoelectric CMOS signal conditioning process is currently under development. Successful development of a piezoelectric CMOS process could potentially 1)

reduce parasitic interconnection losses, 2) provide signal amplification, and 3) implement filtering to both reject noise and linearize responsivity.
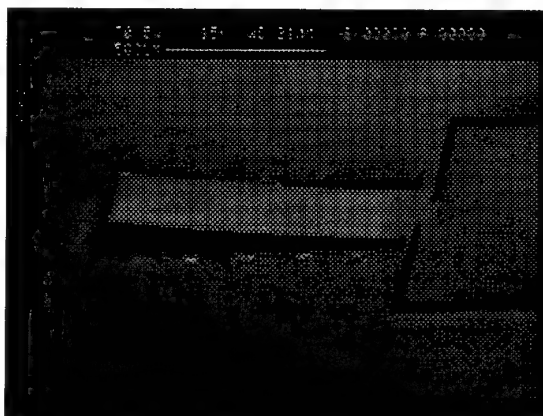
Fig. 3. PZT-on silicon nitride vibration Monitoring device.
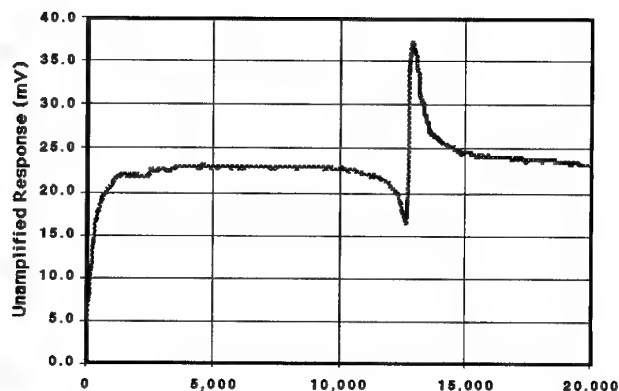
Fig. 4. Impedance spectrum for a PZT micro-cantilever beam.

Surgical Microsystems

Surgical microsensors represent a relatively new application for MEMS technology. The approach described in this work uses piezoelectric materials to monitor the impressed tissue loading on a surgical cutting tools. The real-time response (charge versus time or voltage versus time) provides information to the surgeon during procedures requiring delicate cutting.

Cataract removal by an ultrasonic cutting technique called phacoemulsification represents one of the most surgical procedure practiced throughout the world. Approximately 1.6 million are performed yearly. In this technique the hard, opaque, human lens is fragmented by a sharp ultrasonically-driven cutting needle. Because the ophthalmologist cannot see directly under the cutting needle as the lens is fragmented and aspirated, the underlying and much softer posterior capsule is sometimes unintentionally ruptured by the cutting needle. This tear usually required considerable time to repair and invariably leads to complications such as glaucoma, infection, and sometimes blindness. The complication rate of this procedure is highly dependent on the skill and experience of the surgeon.

A piezoelectric microsensor (force transducer) has therefore been designed and inserted directly behind the cutting needle to actively warn the surgeon when hard-to soft material transitions characteristic of the lens-to-posterior capsule transition are taking place. A diagram of a surgical cutting tool with a piezoelectric force monitoring device is shown in Fig. 5.

The electrical impedance versus frequency characteristic of the coupled microsensor plus surgical tool is analyzed in real-time as the surgical tool comes in contact with the lens tissue. A sharp fundamental resonance is observed at 39.3 kHz. As a mechanical load (hard material) is placed in contact with the cutting tool, the resonant characteristic sensed by the piezoelectric transducer is modified and detected by amplitude and phase sensitive electronics. Fig. 6 shows the detected waveform during an actual surgical procedure involving a live human. Fig. 7 shows an expanded view of the piezoelectric sensor waveform at a selected hard-to-soft material signature. The associated signal processing method developed to correlate hard-to soft material transitions with the

measured electrical waveform is used to present a warning light in the surgeon's microscope during a critical point in the surgery.
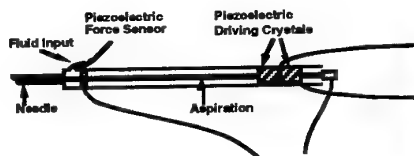
Fig. 5. Sketch of a surgical handpiece with a piezoelectric force transducer.
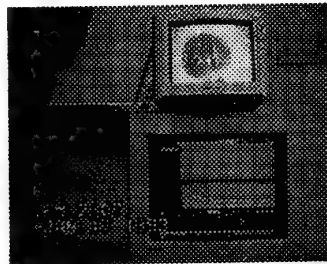
Fig. 6. Human clinical trial of force transducer in cataract removal (phacoemulsification).
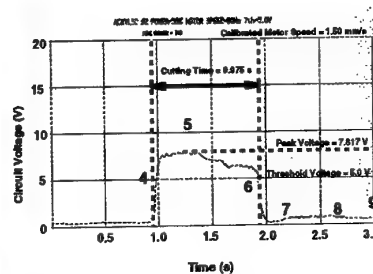
Fig. 7. Piezoelectric sensor waveform during a hard-to-soft material transition.

Precision Surgical Actuators

Microelectromechanical systems (MEMS) are presently the basis of several commercial products (accelerometers, pressure sensors, and computer display projectors). MEMs have many more potential applications including micro-robots, micro-manipulation tools for uses ranging from micro-surgery to industrial production, optical systems and devices, complete systems for fluid, thermal, biological, and chemical processing, and diverse sensors such as atomic force and scanning tunneling microscopes. Many of these applications will require a source of mechanical power, i.e. microscale actuators or microactuators.

Recent work has developed piezoelectric linear inchworm stepper motors (Fig. 8) and piezoelectric peristaltic micropumps (Fig. 9) for the manipulation of liquids on a microchip. The linear stepper motor is currently being evaluated for precision surgical applications (micro-invasive smart surgery) and the micropumps are being evaluated for possible DNA processing on a microchip as well as implantable drug delivery applications.
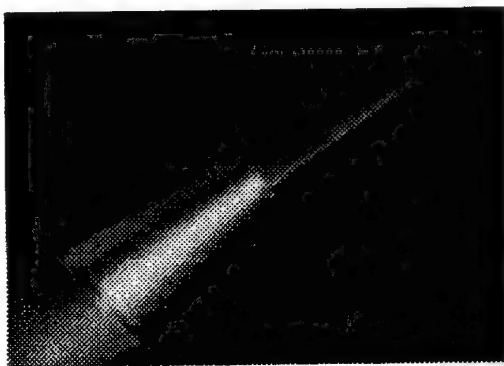
Fig. 8. Surgical cutting tool containing a piezoelectric liner micromotor.
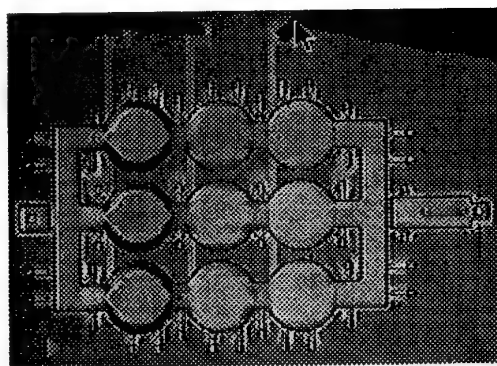
Fig. 9. Peristaltic micropump for precision Fluid manipulation on a microchip.

Growth of Epitaxial Bi-layered Ferroelectric Thin Films by MOCVD and Their Electrical Properties

Hiroshi Funakubo, Katsuyuki Ishikawa, Takayuki Watanabe and Norimasa Nukaga
Department of Innovative and Engineered Materials, Tokyo Institute of Technology
4259, Nagatsuta-cho, Midori-ku, Yokohama, 226-8502
Fax: +81-45-924-5446, e-mail: funakubo@iem.titech.ac.jp

Epitaxial Bi layered-structured ferroelectric, $Bi_4Ti_3O_{12}$ and $SrBi_2Ta_2O_9$ thin films were grown on various kinds of single crystals by MOCVD. (001)-oriented SBT films were deposited on (100)MgO, (100)LaAlO₃, (100)NdGaO₃, (100)SrTiO₃ and (100)LaAlO₃ substrates. Lower mismatch between a-axis of $SrBi_2Ta_2O_9$ and substrate, lower the deposition temperature of epitaxial growth of (001)-oriented $SrBi_2Ta_2O_9$ film. On the other hand, (001)-oriented $Bi_4Ti_3O_{12}$ films were deposited on (100)LaAlO₃ substrate at 500°C. This temperature was lower than the lowest temperature to grow epitaxial $SrBi_2Ta_2O_9$ film. Ferroerectricity of (001)- and (116)-oriented $SrBi_2Ta_2O_9$ films deposited on (100)SrRuO₃//(100)SrTiO₃ and (110)SrRuO₃//(110)SrTiO₃ substrates, respectively were investigated. Felloerectricity was observed for (116)-oriented films but was not observed for (001)-oriented one. The estimated remnant polarization along a-axis was about 22 $\mu C/cm^2$.

1. INTRODUCTION

Thin films of bismuth layer-structured ferroelectric (BLSF) , including $SrBi_2Ta_2O_9$(SBT) and $Bi_4Ti_3O_{12}$(BIT), have been studied for its potential application to nonvolatile ferroelectric memories(NV-FRAM). The ferroelectric anisotropy along crystal axis has been pointed out from the crystal-viewpoint[1]. However, it has been hardly reported in the case of the film form. This is because that the polycrystalline film has been mainly studied for the practical application to NV-FRAM. However, the epitaxially grown or highly oriented film is essential because of the uniformity of the property when the cell-size becomes small.

In the present study, we prepared epitaxially grown BIT and SBT films by MOCVD. MOCVD is one of the most promising methods for the practical application because of its high composition and film thickness uniformity over wide area. Moreover, the ferroelectric anisotropy of SBT was firstly investigated using epitaxially grown films with two orientations.

2. EXPERIMENTAL[1)-4)]

BIT and SBT films were prepared by MOCVD from $Bi(CH_3)_3 - Ti(O \cdot i-C_3H_7)_4 -O_2$ and $Bi(CH_3)_3 - Sr[Ta(O \cdot C_2H_5)_6]_2 -O_2$ systems, respectively. Various kinds of single crystals were used for the growth of the epitaxial films. (100)SrRuO₃ //(100)SrTiO₃ and (110)SrRuO₃//(110)SrTiO₃ were also used as substrates. About 200 nm-thick epitaxial (100)- and (110)- oriented SrRuO₃ films were grown on (100) and (110) SrTiO₃ substrates by MOCVD from $Sr(C_{11}H_{19}O_2)_2(C_8H_{23}N_5) - Ru(C_{11}H_{19}O_2)_3 - O_2$ systems[5),6)]. The resistivity of SrRuO₃ film was about 260 $\mu\Omega \cdot cm$.

Crystal structure of the film was measured by XRD. Electrical property of these film was measured by preparing 100 $\mu m\phi$ Pt top electrodes.

3. RESULTS AND DISCUSSION

3.1 Epitaxial growth of $SrBi_2Ta_2O_9$ Thin Film[7)-11)]

Table I summarize the constituent phase of the film deposited on various kinds of substrates at 620, 750 and 850 °C. The film composition was about $Sr_{0.7}Bi_{2.4}Ta_2O_9$. (001)-oriented SBT films were grown on (100)NdGaO₃, (100)SrTiO₃, (100)LaAlO₃ and (100)MgO substrates. Deposition temperature region of (001)-oriented SBT film was found to depend on the kinds of substrate. Epitaxially grown (001)-oriented SBT film was deposited even at 620 °C on (100)SrTiO₃ substrate. On the other hand, (100)-oriented fluorite phase was mainly deposited at 620 °C and the single

Table I Constituent phase of the film deposited on various kinds of substrates at various temperature.

Substrate	Deposition temperture / °C		
	620	750	820
(100)YSZ	(100)Fluorite	(100)Fluorite	(100)Fluorite
(100)LaAlO₃	(100)Fluorite + (001)SBT	(100)Fluorite + (001)SBT	(001)SBT
(100)NdGaO₃	(100)Fluorite	(001)SBT	(001)SBT
(100)SrTiO₃	(001)SBT	(001)SBT	(001)SBT
(100)MgO	—	—	(001)SBT
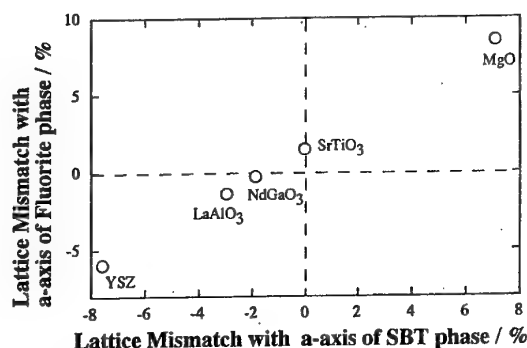
Fig.1 Lattice mismatch of a-axis of fluorite and SBT with various substrates.

Cu , K_α / degree

Fig.2 XRD pattern of BIT film on (100)LaAlO$_3$ substrate at 500 °C

phase of (001)-oriented SBT film was deposited at 820°C when the film was deposited on (100)LaAlO$_3$ substrate. In the case of (100)YSZ substrate, epitaxial (100)-oriented fluorite phase was grown from 620 to 850 °C.

Fig.1 shows the lattice mismatch of the a-axis of fluorite phase with various substrates as a function of that of a-axis of SBT phase with various substrates. Lattice mismatch was estimated from the lattice parameter data at room temperature because of the lack of the thermal expansion coefficient data of SBT and fluorite phases. In the case of (100)SrTiO$_3$ substrate, the lattice mismatch with a-axis of SBT phase was below 0.1 %. This low mismatch is the reason that (001)-oriented epitaxiual film was grown on (100)SrTiO$_3$ substrate even at lowest temperature, 620 °C. On the other hand, the lattice mismatch of a-axis of LaAlO$_3$ with a-axis of fluorite phase was 1.4% and was smaller that that with a-axis of SBT phase. This is the reason that (100)-oriented epitaxial fluorite phase was grown at lower deposition temperature and (001)-oriented SBT film was deposited at higher deposition temperature, 820°C. Lattice mismatch of a-axis of YSZ film with both of a-axis of SBT phase and fluorite phase was larger than those with other substrates. YSZ has fluorite structure, which was different from other kinds of substrate, perovskite structure. Therefore, the same crystal structure of YSZ with fluorite phase is the reason that fluorite phase is deposited at wide deposition temperature region.

(116)-oriented epitaxial SBT film was grown on (110)SrTiO$_3$ substrate. The atomic arrangement of (110) plane of SrTiO$_3$ was almost the same as that of (116) plane of (SrTaO$_7^{2-}$) octahedron in crystal structure of SBT. Table II summarizes the lattice parameter data

of (001)- and (116)-oriented epitaxial films grown on (001) and (110) SrTiO$_3$ substrates with two kinds of Sr/Ta ratio. Sr/Ta ratio was changed by CVD parameter and Bi/Ta ratio was about 1.2. Lattice parameters were obtained from the reciprocal mapping of XRD. Lattice parameters were almost equal to the reported values for the SBT powder and were independent of the Sr/Ta ratio and the crystal orientation of the film. This suggests that the strain hardly remained in the film. This strain free character is considered to be important for the fatigue free character of SBT film.

3.2 Epitaxial growth of Bi$_4$Ti$_3$O$_{12}$ Thin Film[4]

Fig.2 shows the XRD patterns of BIT films deposited on (100)LaAlO$_3$ substrate at 500 °C. Only (00*l*) diffraction peaks of BIT phase were observed together with those of substrate. Epitaxially growth of BIT film on (100)LaAlO$_3$ substrate was ascertained from the X-ray pole figure measurement. This result represents that epitaxial BIT film was grown on (100)LaAlO$_3$ substrate at lower deposition temperature than that of SBT film, even though the units cell volume of BIT is larger than that of SBT and its crystal structure is more complicated comparing with SBT.

3.3 Electrical property of epitaxially grown SrBi$_2$Ta$_2$O$_9$ film[8,12]

Fig.3 shows the XRD patterns of SBT films deposited on (100) SrTiO$_3$ substrate at 750°C and (110)SrTiO$_3$ substrates at 820°C, respectively. (001)-

Table II Lattice parameters of (001)- and (116)- oriented epitaxially grown SrBi$_2$Ta$_2$O$_9$ films deposited on (100) and (110)SrTiO$_3$ substrates, respectively.

Orientation	Sr/Ta ratio	Substrate	Dep.temp. / °C	a / nm	b / nm	c / nm	Volume / nm³
(001)	0.35	(100)SrTiO$_3$	750	0.5546	0.5538	2.4998	0.7633
	0.5			0.5516	0.5515	2.5014	0.7611
(116)	0.35	(110)SrTiO$_3$	820	0.5544	0.5512	2.4951	0.7625
	0.5			0.56	0.5543	2.5142	0.7803
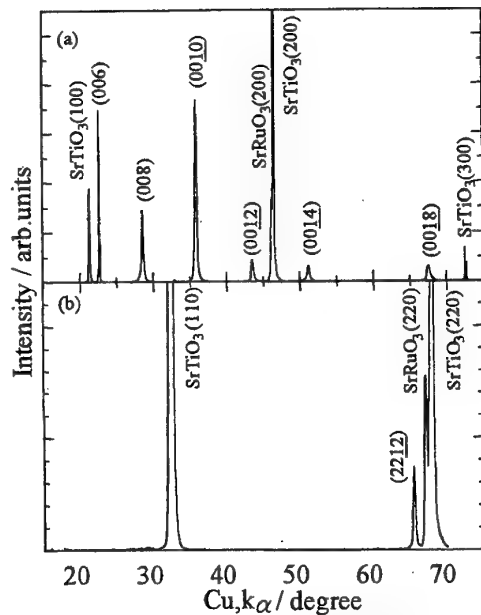
Fig.3 XRD patterns of SBT films deposited on (a) (100)SrRuO$_3$//(100)SrTiO$_3$ substrate at 750°C and (b) (110)SrRuO$_3$//(110)SrTiO$_3$ substrate at 820°C.

and (110)- oriented epitaxial SBT films were grown on (100)SrRuO$_3$//(100)SrTiO$_3$ and (110)SrRuO$_3$//(110)SrTiO$_3$ substrates, respectively. The full width of half maximum of the rocking curves of (200)SBT and (22$\underline{12}$)SBT of (001)- and (116) oriented SBT films were 0.288° and 0.397°, respectively. This result suggests that this film have high quality, so that
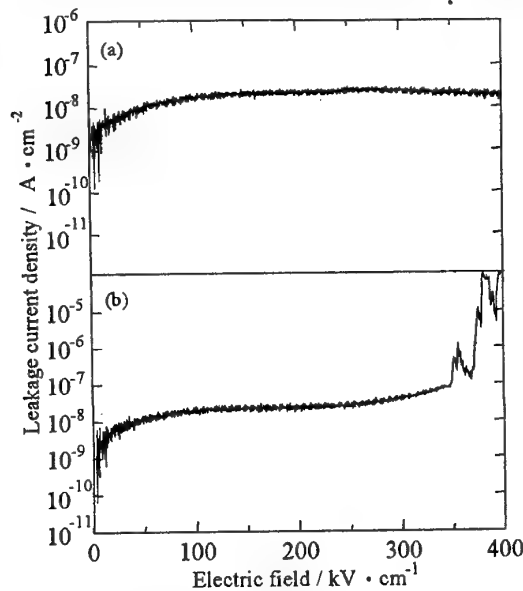
we can estimate the anisotropy of the ferroelectric properties of SBT film.

Fig.4 shows the leakage characters of the same films shown in Fig.3. There is any heat-treatment after the film deposition. The leakage current density of (001)-oriented SBT film with 200 nm in thickness was in the order of 10^{-8} A/cm^2 up to the applied electric field of 400 kV/cm. On the other hand, that of (116)-oriented film was almost the same order up to 350 kV/cm but was abruptly increased above this value. These values were good comparing with the reported values for polycrystalline SBT films[13]. We firstly measured the leakage characters of epitaxially grown SBT films with different orientation and found that SBT film had low leakage current. Low leakage current density of epitaxial film is originated to the decrease of the leakage pass such as grain boundaries in the film.

Fig.5 shows the hysteresis loops of the same films as Fig.4. No hysteresis loop was observed even at electric field of 500 kV/cm for (001)-oriented film as shown in Fig.5(a). Ferroelectric property of c-axis oriented film has been reported by some researchers[14],[15]. However, we did not observe ferroelectric properties in good agreement with the prediction from crystal symmetry[1]. On the other hand, (116)-oriented film shows ferroelectricity as shown in Fig.5(b). Remnant polarization(Pr) and coercive field(Ec) of this films were 11.4 µC/cm^2 and 80 kV/cm, respectively. This shows the large ferroelectric property along a- and b- axes. As a result, we firstly observed the ferroelctric anisotropy of SBT film. Moreover, Pr along a- and c-axes can be estimated to be about 22 µC/cm^2.

4. CONCLUSION

(001)- and (116)- oriented SBT and (001)-oriented BIT films were epitaxially grown by MOCVD. (001)-oriented BIT film was deposited on (100)LaAlO$_3$

Fig. 4 J-V characters of (a) (001)- and (b) (116)-oriented epitaxially grown SBT films.
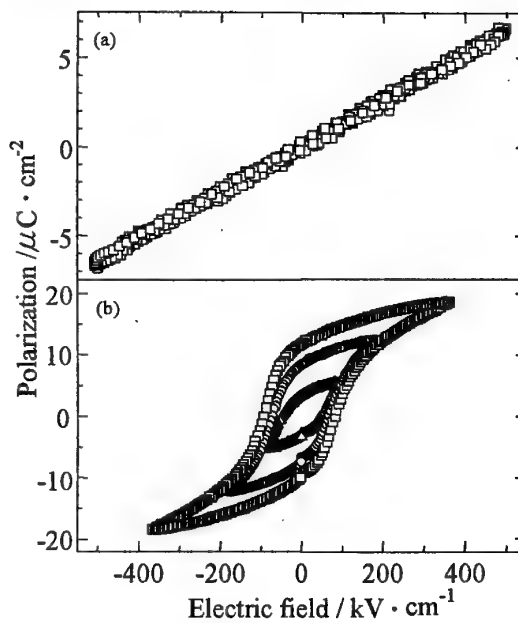
Fig. 5 P-E characters of (a) (001)- and (b) (116)-oriented epitaxially grown SBT films.

substrate at 500°C. On the other hand, (001)-oriented SBT film was epitaxially grown above 620 °C and lower lattice mismatch of SBT with substrate decrease the deposition temperature of the epitaxial SBT film. Ferrorlrctric properties of epitaxially grown (001)- and (116) -oriented SBT films were investigated. Leakage current densities of these epitaxial films without any heat treatment were good, in the order of 10^{-8} A/cm^2 up to 350 kV/cm. This shows that epitaxial film diminish the leakage of the film. Large ferroelectricity was observed for (116)-oriented film, but was not observed for (001)-oriented film. As a result, we firstly observed the anisotropy of the ferroelectricity of SBT.

References

1) A.D.Rae, J.G.Thomson and P.L.Withers, Acta Crystal., **B48**, 418(1992).
2) N.Nukaga, K.Isikawa, K.Shinozaki, N.Mizutani and H.Funakubo, Key.Eng.Mater., **169-170**, 145(1998).
3) H.Funakubo, N.Nukaga, K.Ishikawa and T. Watanabe, Jpn.J.Appl.Phys., **38**, L199(1999).
4) H.Funakubo, N.Nukaga, K.Ishikawa, H.Kokubun, H. Matchida, K.Shinozaki and N.Mizutani, Ferroelectrics,in, press(1999).
5) N.Okuda, T.Matsuzaki, K.Shinozaki, N.Mizutani and H.Funakubo, Trans. Mater.Res.Soc.Jpn., **24**, 51(1999).
6) N.Okuda and H.Funakubo, Jpn.J.Appl.Pys., submitted for publicatuion.
7) K.Ishikawa, N.Nukaga and H.Funakubo, Jpn.J.Appl.Phys., **38**, L258(1999)
8) K.Ishikawa and H.Funakubo, Appl.Phys.Lett. in press(1999).
9) N.Nukaga, K.Ishikawa and H.Funakubo, Jpn.J.Appl.Phys.,in press (1999).
10) T.Suzuki, Y.Nishi, M.Fujimoto, K.Ishikawa and H. Funakubo, Jpn.J.Appl.Phys., submitted for publication.
11) T.Suzuki, Y.Nishi, M.Fujimoto, K.Ishikawa and H. Funakubo, Jpn.J.Appl.Phys., submitted for publication,.
12) K.Ishikawa and H.Funakubo, J.Appl.Phsys, under preparation..
13) I.Koiwa, T.Kanehara, J.Mita, T.Iwabuchi, T.Osaka, S.Ono and M.Maeda, Jpn.J.Appl.Phys, **35**, 4946(1996).
14) S.B.Desu, D.P.Vijay, X.Zhang and B.P.He, Appl.Phys.Lett., **69**, 1719(1996).
15) T.K.Song, J.K.Lee and H.J.Jung, Appl.Phys.Lett., **69** 3839(1996).

Low-Temperature Processing Using Complex Alkoxides for

Ferroelectric SrBi$_2$Ta$_2$O$_9$ Thin Films

Kazumi Kato

National Industrial Research Institute of Nagoya, 1 Hirate-cho, Kita-ku, Nagoya 462-8510, Japan
Fax: 81-52-916-6992, e-mail: kzmkato@nirin.go.jp
Frontier Collaborative Research Center, Tokyo Institute of Technology,
4259 Nagatuta-cho, Midori-ku, Yokohama 226-8503, Japan

A complex alkoxide, which had a same arrangement of metals and oxygen as a sublattice of layer-structured perovskite, SrBi$_2$Ta$_2$O$_9$ (SBT), has been found to be an excellent precursor for the thin film. The alkoxy-derived gel films deposited on Pt-passivated Si substrates were exposed to saturate water vapor and followed by calcination and crystallization in oxygen flow. The films initiated crystallization at lower temperatures as below 500°C. The exposure to water vapor at various temperatures affected the crystallinity. The extended heat-treatment at 500°C for 1.5 h in oxygen was essential for acceleration of the nucleation and growth of SBT. The 650°C-post-annealed films showed improved ferroelectric hysteresis properties.

1. INTRODUCTION

SrBi$_2$Ta$_2$O$_9$ (SBT) thin film is one of reliable candidates for non-volatile ferroelectric random access memory (NV-FeRAM) applications, since it shows good performances for fatigue and imprint with Pt electrodes [1, 2]. One of serious drawbacks of the SBT thin film is that its processing temperature is too high such as 750-800°C. For NV-FeRAM applications, the processing of the SBT thin film must be compatible with complementary metal oxide semiconductor (CMOS) technology. The processing temperature of the SBT thin film should be lowered to below 650°C.

SBT has an unique crystal structure which consist of a stack of alternating layers of Bi$_2$O$_3{}^{2+}$ and two pseudoperovskite layers of oxygen octahedra, (SrTa$_2$O$_7$)$^{2-}$ in the c-direction [3, 4]. The spontaneous polarization is pararell to the plane of the layers, i.e., in the a- and b- directions, because this plane contains the O-Ta-O chain that is known to have high polarizibilities, as in the perovskite ferroelectrics. For thin film application of SBT such as NV-FeRAM, the crystallographic orientation should be controlled on simple electrodes such as Pt.

In our previous works [5-13], a triple alkoxide, Sr[BiTa(OR)$_9$]$_2$ (R: C$_2$H$_5$ or C$_2$H$_4$OCH$_3$), has been found to be a good precursor for SBT thin films through chemical solution deposition. The triple alkoxide had the same arrangement of metals and oxygen as a sublattice of SBT. By controlled hydrolysis of the triple alkoxide, the arrangement was considered to preserve in the alkoxy-derived gel films. The activation energies for the amorphous-gel to crystalline phase transformation were expected to be low. Actually, the film crystallized at lower temperatures below 500°C. The crystallization temperature, crystallinity and the degree of the c-axis orientation of the SBT thin films depended on the organic functional group of the triple alkoxide, which determined the hydrolysis and polycondensation reactions. Also, a mixture of water vapor and oxygen flow during calcination at 250°C was found to enhance the aforementioned crystallographic properties and microstructure development. However, the drastic enhancement of the degree of the c-axis orientation was not desirable for FeRAM applications. In this paper, effects of the hydrolysis, exposure to water vapor without oxygen flow, and extended heat-treatment at initiation temperature of crystallization on the crystallinity and orientation of the SBT thin films were investigated. Additionally, the ferroelectric hysteresis properties were examined.

2. EXPERIMENTAL PROCEDURE

The following procedure was conducted in a dry nitrogen atmosphere. Strontium metal was dissolved in anhydrous ethanol by reaction at 78°C. Bismuth triethoxide ($Bi(OC_2H_5)_3$) was added to the strontium ethoxide solution in the molar ratio of 2:1 and then heated at 78°C for 2 h. Tantalum pentaethoxide ($Ta(OC_2H_5)_5$) in the molar ratio of 2:1 with respect to the strontium ethoxide, was added to the strontium-bismuth double ethoxide. Diethanolamine ($NH(C_2H_4OH)_2$) was also added. The solution then was heated at 78°C for 2 h. Next, deionized and distilled water, diluted in ethanol in the volume ratio of 1:9 ($H_2O:C_2H_5OH$), was added to the strontium-bismuth-tantalum triple ethoxide $Sr[BiTa(OC_2H_5)_9]_2$ solution in the molar ratio of 1:6. The triple ethoxide solution was stirred at room temperature for 1 h after hydrolysis. The concentration of the hydrolyzed, triple ethoxide solution was 0.05 M.

Thin films were deposited on Pt-passivated silicon ($Pt/TiO_x/SiO_2/Si(100)$) substrates by spin-coating. Each layer was deposited at 3000 rpm for 30 s in air. The as-deposited layer was dried at 150°C for 5 min in air, and calcined at 250°C for 10 min and 350°C for 10 min in oxygen flow (Fig. 1(a)). Some of the layers were exposed to water vapor at 150°C for 30 min or at 250°C for 10 min on the way of the aforementioned steps (Fig. 1(b) and 1(c)), or were additionally heat-treated at 500°C for 1.5 h in oxygen. Then finally, the layer was subjected to heat treatment at 650°C for 10 min by rapid thermal annealing in oxygen. Film thickness increased to about 200 nm by repeating the aforementioned treatments 3 times.

The crystal phase and the crystallinity of the thin films were determined X-ray diffraction (XRD) measurements with Cu Kα radiation. The acceleration voltage and current were 35 kV and 20 mA, respectively. The ferroelectric hysteresis properties were measured at applied voltage of 5 V by using a Radiant RT6000S instrument. Before electrical measurements, Pt top electrodes were deposited by r. f. sputtering and the Pt-deposited films were annealed at 650°C for 1 h in oxygen.

3. RESULTS AND DISCUSSION

3.1. Crystallization and Crystallinity of SBT Thin Films

Figures 2(a) and 2(b) show XRD profiles for thin films, which were calcined and annealed at 650°C and 500°C for 10 min in oxygen, respectively. In the profile of 500°C-annealed film, a broad band at 28-29° (2Θ) appeared. It intends that crystallization initiated below 500°C. The 650°C-annealed film showed improved crystallinity and (115) diffraction line with a high intensity. Compared with our previous results on SBT thin films which prepared from the $Sr[BiTa(OC_2H_5)_9]_2$ solution hydrolized with smaller amount of water in the molar ratio of 1:18 [9, 10], the crystallinity was relatively enhanced with respect to the present film. Figures 3 (a) and 3(b) show XRD profiles for 650°C-annealed thin films, which underwent the exposure to water vapor at 150°C for 30 min and at 250°C for 10min, respectively. The 650°C-annealed film, which underwent the exposure to water vapor at 150°C for 30 min, showed (006), (008) and (0010) diffraction lines with high intensities. However, the 650°C-annealed film which underwent the exposure to water vapor at 250°C for 10min showed good crystallinity with high (115) diffraction line. It is considered that the O-M-O (M:Sr, Bi, Ta) network, which contained the same arrangement of SBT sublattice, was evolved in the amorphous gel film on the surface of Pt(111) by the exposure to water vapor at
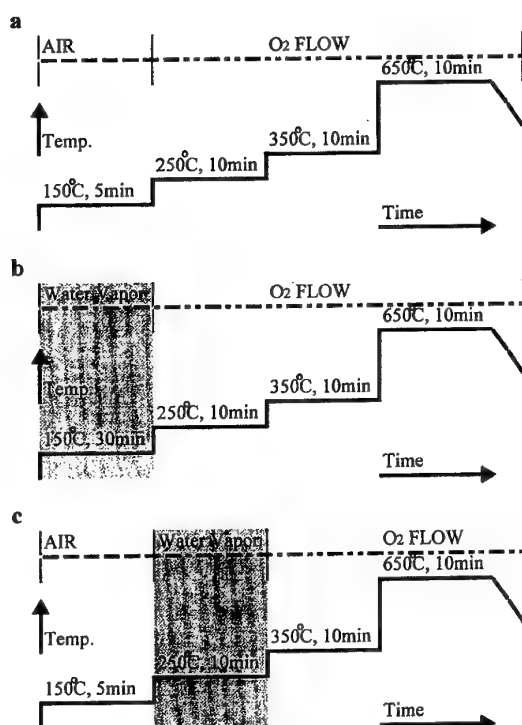
Fig. 1 Typical heating schedules for SBT thin films.
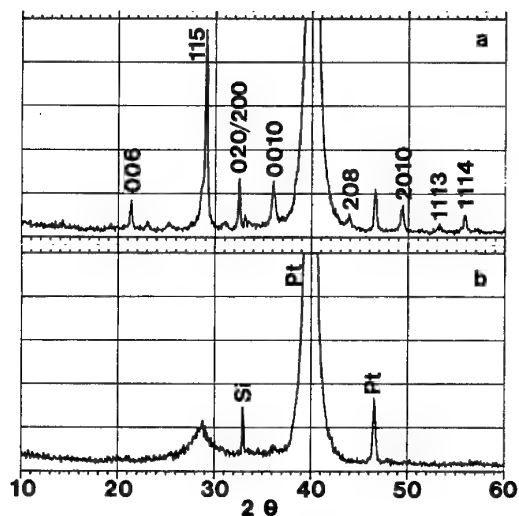
Fig. 2   XRD profiles for 650°C- and 500°C-annealed thin films.
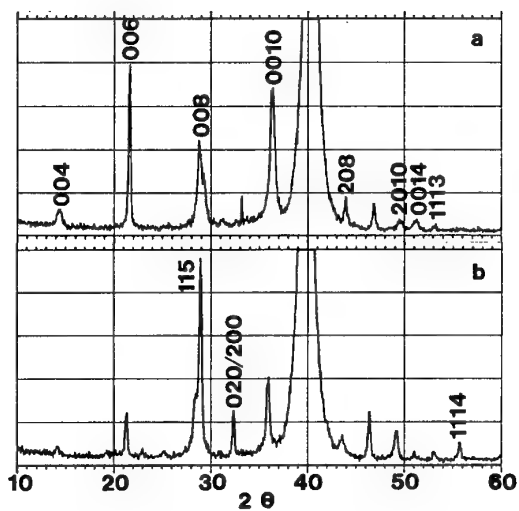
Fig. 3   XRD profiles for 650°C-annealed SBT thin films which underwent the exposure to water vapor at 150°C (a) and at 250°C (b).

Fig. 4   XRD profiles for 650°C-annealed SBT thin films, which were not exposed to water vapor (a) and were exposed to water vapor at 250°C (b), and then underwent extended heat-treatment at 500°C for 1.5h.

150°C, and therefore the crystallization may proceed preferentially in the direction perpendicular to the c-axis. Contrastively, the exposure to water vapor at 250°C seems to contribute to decomposition of organic groups remained in the gel film rather than the network formation.   Compared with the previous results on the effect of a mixture of water vapor and oxygen flow during calcination at 250°C [10], the enhancement of the degree of the c-axis orientation was significantly suppressed with respect to the exposure to water vapor

at 250°C.   Figures 4(a) and 4(b) show XRD profiles for 650°C-annealed thin films, which underwent extended heat-treatment at 500°C for 1.5 h.   Compared with the 650°C-annealed thin film without the extended heat-treatment (Fig. 2(a)), intensity of (115) diffraction line increased with respect to the 650°C-annealed thin film which was calcined in oxygen and then underwent the extended heat-treatment (Fig. 4(a)).   The improvement of the crystallinity is considered to be due to that the enough nucleation would be attained by the extended heat-treatment, which is the initiation temperature of crystallization, and the nuclei would grow through the following annealing at 650°C.   The 650°C-annealed thin film, which underwent the exposure to water vapor at 250°C and then the extended heat-treatment (Fig. 4(b)), exhibited a tendency to increase the degree of the c-axis orientation.

3.2. Ferroelectric Properties of the Thin Films

Ferroelectric hysteresis loops for 650°C-annealed thin films were evaluated.   The loops were saturated except for the thin film which underwent the exposure to water vapor at 150°C for 30 min.   It may mainly stem from the crystallographic orientation of the thin films. The 650°C-annealed thin film, which was calcined in oxygen and underwent the extended heat-treatment at 500°C for 1.5h, exhibited switching polarization ($2P_r$) of

2.6 $\mu C/cm^2$ and coercive electric field (E_c) of 25 kV/cm (Fig. 5(a)). Compared with the film which did not undergo the extended heat-treatment, the $2P_r$ and E_c were almost same. Although the crystallinity seems to be improved as mentioned before, the grain growth may not occur enough in the direction of (115) with respect to the film which was calcined in oxygen and underwent the extended heat-treatment. The 650°C-annealed thin film, which underwent the exposure to water vapor at 250°C and the extended heat- treatment at 500°C for 1.5 h, exhibited $2P_r$ of 10.0 $\mu C/cm^2$ and E_c of 38 kV/cm (Fig. 5(b)). The enhancement of $2P_r$ and E_c may be due to that microstructure development has more significant effect on than the enhancement of the degree of the c-axis orientation. The similar results have been obtained previously [10].

saturate water vapor and followed by calcination and crystallization in oxygen flow, initiated crystallization to SBT at lower temperatures as below 500°C. The 650°C-annealed film which underwent the exposure to water vapor at 150°C for 30 min exhibited preferred orientation along c-axis, however, the 650°C-annealed film which underwent the exposure to water vapor at 250°C for 10 min showed high (115) diffraction. The extended heat-treatment at 500°C for 1.5 h in oxygen was essential for acceleration of the nucleation and growth of SBT and enhancement of the crystallinity. The 650°C-post-annealed films, which underwent the exposure to water vapor at 250°C and the extended heat-treatment at 500°C for 1.5 h, exhibited improved ferroelectric hysteresis properties.

Fig. 5 P-E hysteresis loops for the 650°C-annealed SBT thin films, which were not exposed to water vapor (a) and exposed to water vapor at 250°C (b), and then underwent extended heat-treatment at 500°C for 1.5 h.

4. CONCLUSION

The triple-alkoxy-derived gel films, which were deposited on Pt-passivated Si substrates, exposed to

REFERENCES

[1] C. A-Paz de Araujo, J. D. Cuchiaro, L. D. McMillan, M. C. Scott and J. F. Scott, Nature, 374, 627, (1995).

[2] J. F. Scott, F. M. Ross, C. A-Paz de Araujo, M. C. Scott and M. Huffman, Mater. Res. Soc. Bull., July, 33 (1996).

[3] R. E. Newnham, R. W. Wolfe, R. S. Horsey, F. A. Diaz-Colon and M. I. Kay, Mater. Res. Bull., 8, 1183 (1973).

[4] A. D. Rae, J. G. Thompson and R. L. Withers, Acta Crystallogr., Sect B Struct. Sci., 48, 418 (1992).

[5] K. Kato, C. Zheng. S. K. Dey and Y. Torii, Integr. Ferroelectr., 18, 225 (1997).

[6] K. Kato, J. M. Finder, S. K. Dey and Y. Torii, Integr. Ferroelectr., 18, 237 (1997).

[7] K. Kato, C. Zheng, J. M. Finder, S. K. Dey and Y. Torii, J. Am. Ceram. Soc., 81, 1869 (1998).

[8] K. Kato, Y. Torii, C. Zheng, J. M. Finder, R. H. Barz and S. K. Dey, Key. Eng. Mater., 157-158, 189 (1998).

[9] K. Kato, Integr. Ferroelectr., 22, 13 (1998).

[10] K. Kato, Jpn. J. Appl. Phys., 37, 5178 (1998).

[11] K. Kato, Integr. Ferroelectr., in printing.

[12] K. Kato, Jpn. J. Appl. Phys., in printing.

Ferroelectric Properties of Bismuth Layer-Structured $Sr_{m-3+x}Bi_{4-x}Ti_{m-x}Ta_xO_{3m+3}$ ($m=2$, $x=1\sim2$; $m=3$, $x=0\sim2$)

Tadashi Takenaka, Hajime Nagata, Naohito Chikushi and Takeshi Takahashi

Faculty of Science and Technology, Science University of Tokyo,
Noda, Chiba-ken, 278-8510 Japan
e-mail: tadashi@takenaka.ee.noda.sut.ac.jp

The general formula, $Sr_{m-3+x}Bi_{4-x}Ti_{m-x}Ta_xO_{3m+3}$ ($m=2$ and 3) [$SBTTm(x)$] is a phase relation between well-known bismuth layer-structured ferroelectrics (BLSF) such as $Bi_4Ti_3O_{12}$ and $SrBi_2Ta_2O_9$ including a perovskite compound $SrTiO_3$. The BLSF series were discussed to form the layer structure with the layer numbers $m=2$ and 3, where x is the number of Ta ions in the layer structure and $1\leq x \leq 2$ for $m=2$ and $0\leq x \leq 2$ for $m=3$. Ferroelectric and fatigue properties were also studied. The Curie temperature, Tc, of SBTT2 ($m=2$) ceramics increases as the Sr concentration decreases and shows the highest (785 °C) in above BLSF series. D-E hysteresis loops measured by using a standard Sawyer-Tower circuit show that the remanent polarization, $2Pr$, of SBTT3($m=3$) ceramics reaches maximum (24.6 $\mu C/cm^2$) at $x=0.3$. Fatigue properties of SBTT2(2) [SBT], SBTT3(0) [$Bi_4Ti_3O_{12}$, BIT] and SBTT3(0.3) ceramics display that the fatigue-free behavior up to about 10^{10} cycles for SBT and SBTT-0.3 and fatigue in about 10^6 cycles for BIT. These results seem to be caused by substituted Ta and Sr ions.

1. INTRODUCTION

In recent years, bismuth layer-structured ferroelectrics (abbreviated to BLSF) have been extensively studied in the form of thin films because BLSF seem to be an excellent candidate material for nonvolatile FRAM (ferroelectric random access memory) [1-2] in various commercial applications. For example, one BLSF, $SrBi_2Ta_2O_9$ shows very high quality characteristics with fatigue-free property for FRAM [3].

A family of BLSF is also attractive from applicational viewpoints for electronic materials such as dielectrics, piezoelectrics and pyroelectrics because BLSF are characterized [4-7] by their low dielectric constant ε_s, high value of the Curie temperature Tc, and large anisotropy in electromechanical coupling factors kt/kp or $k33/k31$. Therefore, the BLSF ceramics are seen as superior candidates for piezoelectric sensor materials with high-Tc and anisotropic characteristics, or for pyroelectric sensor materials with a large figure of merit.

Bismuth layer-structured oxides (BLSO) are generally represented by the following formula:

$$(Bi_2O_2)^{2+}(A_{m-1}B_mO_{3m+1})^{2-}$$

where A is a combination of one or more mono-, di- and trivalent ions and B is a combination of tetra-, penta- and hexavalent ions, and the integer m takes any of the values from 1 to 5. BLSO have BO_6 octahedra like perovskite, pyrochlore and tungsten-bronze structures and many of them seem to be ferroelectrics. The condition of electrical neutrality gives the formula ($m-$1)$N(A)+mN(B)=6m$, where $N(A)=\Sigma N(A)/(m-1)$ and $N(B)=\Sigma N(B)/m$ indicate the mean valences of the A and the B ions. However, BLSO have a great variety of available combinations of A and B ions, respectively.

In this paper, as a part of study on characterization of a series [8-9] of BLSF compounds containing of various combinations of A- and B-site ions, the effects of partial substitution of Bi^{3+} by Sr^{2+} as A-site ions or Ti^{4+} by Ta^{5+} as B-site ions on their dielectric, ferroelectric and fatigue properties are investigated.

Figure 1 shows a phase relation between well-known BLSF such as Bi_3TiTaO_9 ($m=2$), $SrBi_2Ta_2O_9$ ($m=2$) and $Bi_4Ti_3O_{12}$ ($m=3$) including a perovskite compound $SrTiO_3$. The general formula of the phase relation in Fig. 1 is as follows:

$$Sr_{m-3+x}Bi_{4-x}Ti_{m-x}Ta_xO_{3m+3} ,$$

where m is a layer number and x is the content of Ta ions in the layer structure and $1\leq x\leq 2$ for $m=2$ and $0\leq x\leq 2$ for $m=3$. Hereafter the formula is abbreviated to $SBTTm(x)$.

2. EXPERIMENTAL

SBTT ceramic samples are prepared by a conventional sintering technique. Reagent-grade oxide or carbonate powders of $SrCO_3$, Bi_2O_3, TiO_2 and Ta_2O_5 with 99+% purity were used as the starting materials. These materials mixed by ball milling were calcined at 800 °C for 2 h. After calcining, the ground and ball-milled powders were pressed into disks of 20 mm in diameter and about 1 mm in thickness. These disks were sintered at $1100\sim1200$ °C for 2 h in air.
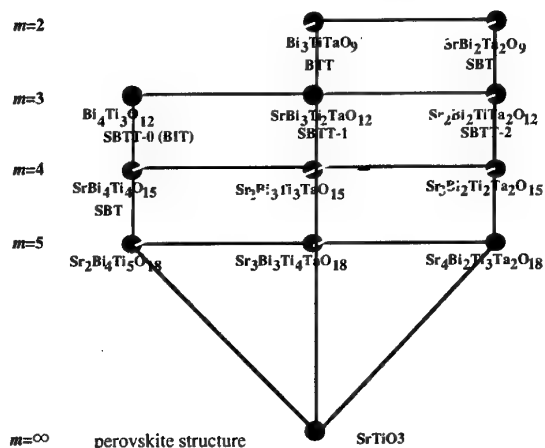
Fig. 1 Phase relation between well-known bismuth layer-structured ferroelectrics such as Bi3TiTaO9 (BTT, m=2), SrBi2Ta2O9 (SBT, m=2), and Bi4Ti3O12 (BIT, m=3).

The crystalline structure was confirmed by X-ray diffraction analysis using CuKα radiation through a Ni filter at a scanning speed of 1 deg/min. Electrodes were made with fired-on Ag-Pd paste for electrical measurements such as dielectric and ferroelectric properties, and sputtered Au for fatigue properties. The temperature dependence of the dielectric constant ε_s, and dielectric loss tangent, tanδ, was measured at 1 MHz using an automatic dielectric measurement system with a multifrequency LCR meter (YHP 4275A) in the temperature range of from RT to 800 °C. The D-E hysteresis loop was observed at RT using a standard Sawyer-Tower circuit at 50Hz. Fatigue properties were measured by using a standard RT6000 tester (Radiant Technologies, Inc) operating in a virtual ground mode. Square wave at 1 MHz was applied with driving corresponding to two or three times as large as the coercive field in fatigue measurements.

3. RESULTS AND DISCUSSION
3.1 Sr_{x-1}Bi4_{-x}Ti2_{-x}Ta$_x$O9
[SBTT2(x)] (m=2, 1≤x≤2)

Figure 2 shows the X-ray powder diffraction patterns of SBTT2(x) ceramics. These patterns show the single phase of bismuth layer-structured compounds with an orthorhombic symmetry. However, it was difficult for SBTT2(1) to obtain the high density sample. On the other hand, the other compositions except x=1 were very easily sintered with a high measured density ratio more than 95 % to the theoretical density.

Figure 3 shows the temperature dependence of the dielectric constant, ε_s in SBTT2(x) ceramics at 1 MHz.

The ε_s at Curie temperature, Tc, of SBTT2(2) [SBT] ceramic displays the maximum value in SBTT2(x) system. A peak of the ε_s-T curve on SBT shows the most sharp, on the other hand, those of the another compositions show relatively broad. These series have a relatively high Tc and SBTT2(1.2) ceramic has the highest Tc (=785 °C) in the prepared samples. The Tc as a function of the Ta amount (x) for SBTT2(x) becomes lower with increasing of x value. The reason why the Tc becomes lower temperature can be explained as the increase of the amount of modified SrTiO3, which has paraelectric phase at room temperature, for the perovskite-like unit in BLSF.
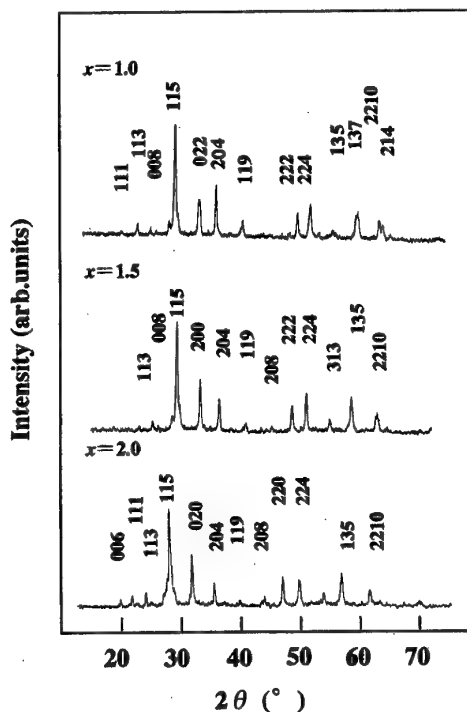
Fig. 2 X-ray diffraction patterns of SBTT2(x).
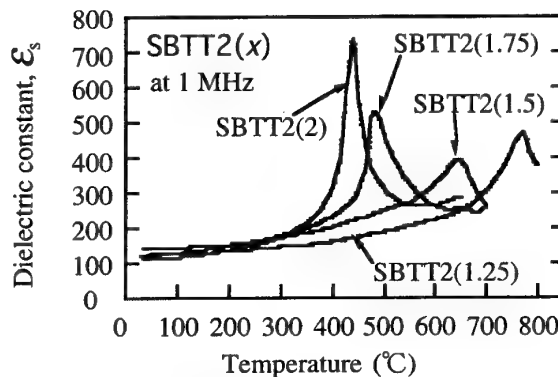
Fig. 3 Temperature dependence of the dielectric constant, ε_s, for SBTT2(x).
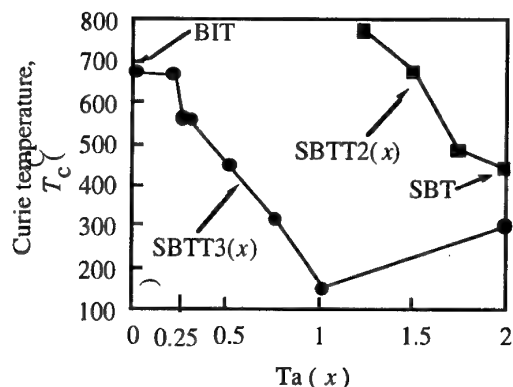
Fig. 4   Curie temperature, T_c, of SBTT2 and SBTT3 as a function of the Ta content (x).
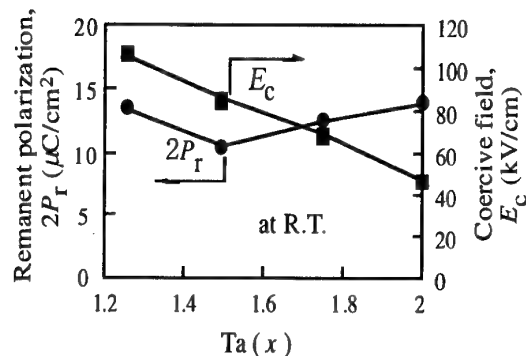
Fig. 5   Remanent polarization, $2Pr$ and coercive field, Ec, of the SBTT2(x).

Figure 4 shows the T_c of SBTT2 and SBTT3 as a function of the Ta content (x). Figure 5 shows the remanent polarization, $2Pr$, and the coercive field, Ec, of SBTT2(x) at RT. The values of $2Pr$ and Ec decrease sharply with increasing of Sr concentration (x). This tendency almost corresponds to the compositional dependence on T_c. SBTT2(1.2) may a candidate material for high temperature piezoelectric sensor devices.

3.2   SrxBi4-xTi3-xTaxO12
[SBTT3(x)] (($m=3$, $0 \leqq x \leqq 2$)

Figure 6 shows compositional dependence of remanent polarization, $2Pr$ of SBTT3(x) at RT measured by using a standard Sawyer-Tower circuit at 50 Hz. The $2Pr$ increases as x increases from 0 to 0.5 and reaches to maximum at $x=0.3$. The ferroelectric properties of SBTT3(0.3) show the largest value of $2Pr$ $(=24.6 \ \mu C/cm^2)$ and the coercive field $Ec=70.9$ kV/cm, respectively. On the other hand, the $2Pr$ decreases with increasing of x higher than 0.5. The new composition, SBTT3(0.3) seems to be a superior candidate for some

FRAM applications.

Figures 7 shows fatigue properties for SBTT2(2) [SBT], SBTT3(0) [BIT], SBTT3(0.25) and SBTT3(0.3) ceramics.   Table I shows the ferroelectric and fatigue properties under various measurement conditions for SBT, BIT, SBTT3(0.25) and SBTT3(0.3) ceramics. The applied field chosen was two or three times as large as the Ec obtained from the saturated D-E hysteresis loop by the Sawyer-Tower circuit (50 Hz).   As shown   in Fig. 7, SBTT3(0.25) and SBTT3(0.3) ceramics as well as SBT show the fatigue-free behavior up to about 10^{11} cycles under the applied field of three times as large as the Ec. On the other hand, BIT ceramic shows fatigue when the applied field is about three times as large as the Ec. However, BIT ceramic shows fatigue-free property up to about 10^{11} cycles under the applied field of two times as large as the Ec, Therefore, the applied field in fatigue measurements for bulk ceramics should be three times higher than the Ec. Usually it is very difficult to measure fatigue properties under this condition due to the electrical breakdown.
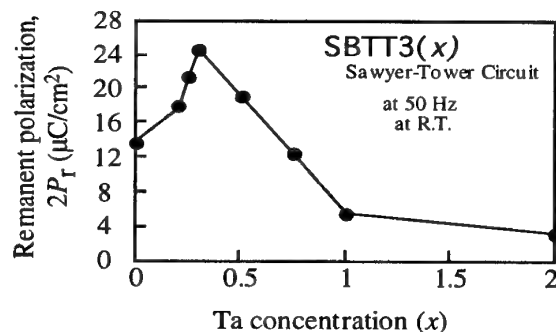
Fig. 6   Remanent polarization, $2Pr$, of the SBTT3(x).

The saturated D-E hysteresis loop of SBTT3(0.25) and SBTT3(0.3) ceramics can be obtained when the applied field is more than two times as large as the Ec, as shown in Fig. 6 and Table I. From the measurement of fatigue properties under the condition of the saturated D-E hysteresis loops, SBTT3(0.25) and SBTT3(0.3) ceramics seem to be the fatigue-free ferroelectrics in spite of the fatigue behavior in BIT ceramic with the same layer number (m=3). The reason for the difference of fatigue properties between SBTT3(0.25) or SBTT3(0.3) and BIT seems that the unstable Ti^{3+} or Ti^{4+} ion in BIT is substituted by the stable Ta^{5+} ion.

4. CONCLUSIONS

Bismuth layer-structured ferroelectrics (BLSF), Srm-3+xBi4-xTim-xTaxO3m+3 ($1 \leqq x \leqq 2$ for $m=2$ and $0 \leqq x \leqq 2$ for $m=3$) [SBTTm(x)] are studied for their dielectric, ferroelectric and fatigue properties. It is clear

that SBTT2(1.25) (m=2) ceramic has high Curie temperature (=785℃) and is seen as a superior candidate for high temperature piezoelectric sensor materials.

SBTT3(0.25) and SBTT3(0.3) (m=3) ceramics show the relatively large $2Pr$ (21.4 and 24.6 $\mu C/cm^2$ for x=0.25 and 0.3), comparing with SBT and BIT, and further, demonstrate the fatigue-free behavior up to 10^{11} switching cycles under the applied field of three times as large as the Ec. Therefore SBTT3(0.25) and SBTT3(0.3) are excellent candidate materials for future FRAM applications with a relatively large $2Pr$ and a fatigue-free characteristic.

References

[1] J. F. Scott and C.A. Araujo: *Science* **246**, 1400 (1989).

[2] S. K. Dey and R. Zuleeg: *Ferroelectrics* **108**, 37 (1990).

[3] T. Mihara, H. Watanabe, C. A. Araujo, J. Cuchiao, M. Scott and L. D. McMilan: Proc. 4th Inter. Symp. Integrated Ferroelectrics, p. 137 (1992).

[4] E. C. Subbarao: *J. Phys. & Chem. Solids* **23**, 665 (1962).

[5] E. C. Subbarao: *J. Amer. Ceram. Soc.* **45**, 166 (1962).

[6] S. Ikegami and I. Ueda: *Jpn. J. Appl. Phys.* **13**, 1572 (1974).

[7] T. Takenaka and K. Sakata: *J. Appl. Phys.* **55**, 1092 (1984).

[8] T. Takenaka, T. Gotoh, S. Mutoh and T Sasaki: *Jpn. J. Appl. Phys.* **3 4**, 5384 (1995).

[9] T. Takenaka and T. Sasaki: *Ferroelectrics* **2 0 1**, 117 (1997).
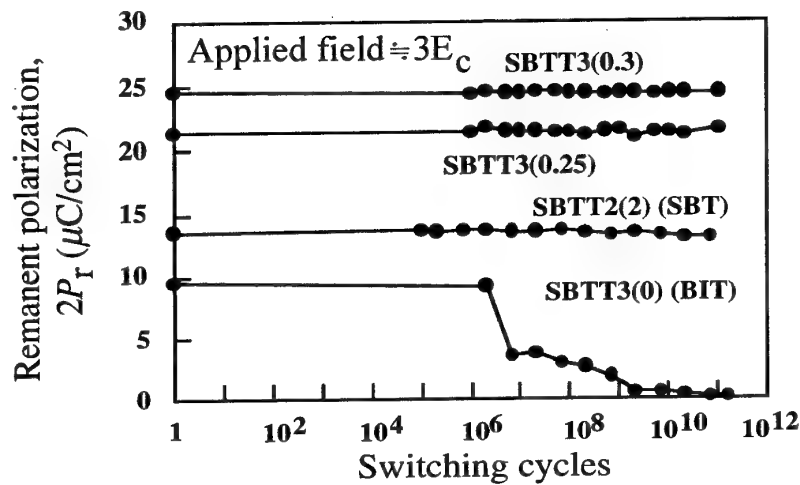
Fig. 7   Fatigue properties of SBT, BIT, SBTT3(0.25) and SBTT3(0.3) ceramics under the applied field of 3 times higher than the Ec..

Table I   Ferroelectric and fatigue properties of SBT, BIT, SBTT3(0.25) and SBTT3(0.3) ceramics.

	Ferroelectricity from Saturated loop by Sawer-Tower circuit		Drive field, E_d for fatigue measurement (kV/cm)	E_d/E_c (times)	$2P_r$ at intial state by RT6000 ($\mu C/cm^2$)	$2P_r$ after 10^{10} cycles by RT6000 ($\mu C/cm^2$)	Fatigue rate up to 10^{10} cycles(%)
	$2P_r$ ($\mu C/cm^2$)	E_c (kV/cm)					
SBTT3(0.3)	24.6	70.9	142	2.0	22.44	22.26	99.2
			212	3.0	24.60	24.49	99.6
SBTT3(0.25)	21.4	64.9	195	3.0	21.66	21.44	99.0
SBTT3(0) [BIT]	13.6	29.6	97.1	3.28	9.54	0.265	2.77
SBTT2(0) SBT	13.4	28.7	96.6	3.37	13.9	13.6	97.8

Structural Analyses of Ferroelectric SrBi$_2$Ta$_2$O$_9$ Thin Films Prepared by Sol-Gel   Method

Ichiro Koiwa, Hiroyo Kobayashi, Keiji Tatani, Kazuya Sano,*
Akira Hashimoto,** Yoshihiro Sawada,** and Tetsuya Osaka***
Semiconductor Technology Laboratories, Oki Electrid Industry Co., Ltd.,   550-5 Higashiasakawa-cho,
Hachioji-shi Tokyo 193-8550, Fax:+81-426-67-0545, e-mail: koiwa544@oki.co.jp
*Yokohama Plant, The Japan Steel Works, Ltd., 2-1-1 Fukuura, Knazawa-ku Yokohama-city,
Kanagawa 236-0004, Fax: +81-45-787-7215, e-mail: kazuya_sano@jsw.co.jp
** Research & Development, Tokyo Ohka Kogyo Co., Led., 1590 Tabata, Samukawa-cho, Koza-gun,
Kanagawa 253-0114, Fax: +81-467-75-3281, e-mail: a-hashimoto@tok.co.jp
*** Department of Applied Chemistry, Waseda University
3-4-1 Okubo, Shinjuku-ku, Tokyo 169-8555, Fax: +81-3-3205-2074, e-mail: osakatet@mn.waseda.ac.jp

Ferroelectric SrBi$_2$Ta$_2$O$_9$ thin films (SBT films) are actively investigated because they do not suffer from fatigue when polarization switching occurs.   Moreover, SBT films have one more main advantage of low voltage operation.   We have prepared SBT films by an originally-developed sol-gel method.   Thinner SBT films with lower leakage current and better ferroelectric properties are desired for higher density (finer capacitors) and lower-voltage operation.   We have developed excimer laser annealing (ELA) system and investigated combination with the SBT thin films prepared by originally developed sol-gel method.   Annealing process is necessary for sol-gel method, and SBT films were annealed by various method, such as furnace annealing (FA), rapid thermal annealing (RTA).   Only by the ELA, we have got 60nm-thick SBT films with good ferroelectric properties composed of fine grains.   The SBT films showed lower leakage current than those by the other annealing methods.   It is concluded that excimer laser annealing method is effective for preparation of ferroelectric thiner SBT films with lower leakage current than those by the other annealing method.   The structure of SBT films annealed by the ELA have been investigated mainly by transmission electron microscopy (TEM).   The ELA method enhances nucleation of SBT films.

1.INTRODUCTION

Ferroelectric thin film has been proposed as next generation nonvolatile memory, and related research has been active.[1]   Ferroelectric SrBi$_2$Ta$_2$O$_9$ (SBT) thin films do not suffer from fatigue in polarization switching.[2]   SBT films may be operated at voltages as low such as 1.5V.[3]   We previously prepared SBT films using an originally   developed sol-gel method.[4]   In general, SBT films were crystallized by annealing to improve ferroelectric properties[5].   With sol-gel preparation SBT films crystallized using rapid thermal annealing (RTA) show the same electrical properties as SBT films crystallized by furnace annealing (FA).[6]   Thinner SBT films are desirable for lower voltage operation, but show higher leakage current.   Since low leakage current is required for ferroelectric thin films, reducing the leakage current is an important problem.   Excimer laser annealing (ELA) has been actively investigated as low-temperature processes poly-Si film for thin film transistor (TFT).[7,8]   We report low-voltage operation in SBT thin films by excimer laser.

2.EXPERIMENTAL METHOD

SBT film was deposited in an originally developed alkoxide-based solution.[4]   We formed a 200-nm-thick SiO$_2$ oxidized film on a 6-inch Si wafer, then sputtered a 60 nm Pt lower electrode.   This solution was coated onto the substrate using a spin coater operating at 2,000 rpm.   Coated film was dried for 30 minutes at 150°C and prebaked for 60 minutes at 450°C – a cycle repeated once, twice, three times, and five times.   After coating and prebaking, film was annealed by three different methode, FA, RTA and ELA(Lambda 4308, The Japan Steel Works, Ltd.) at different power settings from 75 to 300 mJ/cm^2.   Temperature rise rate of FA is 10°C/min, and that of RTA is 125°C /sec.   ELA is thought that it show highest than all.   This system used pulse line beam of Xe-Cl whose wavelength is 308 nm and whose size is 200mm x 0.5mm.   A 200-nm-diameter upper Pt electrode was formed by RF sputtering through a metal mask.   Samples were second annealed for 30 minutes with a temperature rise rate of 10°C/min.   Hysteresis loops were measured using an RT6000S (Radiant Co. Ltd.).

3.RESULTS AND DISCUSSION
3.1.Effect of annealing method on leakage current

Figure 1 shows effect of applied voltage on leakage current density of 60nm-thick SBT films annealed by different annealing method, FA, RTA and excimer laser annealing. Only the SBT film annealed by excimer laser shows low leakage current density. The other two SBT films show very high leakage current density which are too high to evaluate ferroelectric properties. In general, a thinner film shows higher leakage current and lower breakdown voltage. These two problems, higher leakage current and low breakdown voltage, prevent the SBT film from using thinner film application. As is seen Fig.1, the SBT film annealed excimer laser have solved these two problems. Therefore ferroelectric properties of the film annealed by excimer laser has been evaluated.

Figure 2 shows hysteresis loops of the SBT films annealed by excimer laser. The hysteresis loops were measured by changing applied voltage. Good-shape hysteresis loops is clearly observed and the film is ferroelectric. Moreover, hysteresis loops are suturated by applied voltage less than 1V and this film has high potential for low-voltage operation.

Therefor, the excimer laser annealing method is effective for suppressing leakage current and increasing breakdown voltage.

3.2.Effect of annealing method on scanning electron microscope (SEM) micrographs.

Figure 3 shows surface and cross-sectional SEM micrographs of the SBT films annealed by different method. Grain size and surface morphology of the SBT film annealed by excimer laser is similar to the other two films. The film by excimer laser shows somewhat smoother surface than the other.

3.3.Effect of excimer laser annealing on cross-sectional transmission electron microscopy (TEM) micrographs.

The SBT films after excimer laser annealing shows the same amorphous patterns as that before laser irradiation. However, excimer laser irradiation exceeding 125 mJ/cm^2 changed the color of SBT films.

Moreoever, as shown in Figs.1 and 2, the excimer laser annealing affects electric properties after second annealing which is annealing after upper electrode formation. Therefore, effect of excimer laser annealing maintained even after second annealing. We used TEM to clarify effect of excimer laser annealing of SBT film structre. Figure 4shows high resolution TEM micrographs of the cross-sectional SBT films before and after excimer laser irradiation. 0.11μm-thick SBT films are used in this section, and these TEM micrographs is surface-side sections. TEM micrographs before irradiation shows amorphous-like structure, no lattice image is observed. However, lattice images are clearly observed for the film after laser irradiation. In Fig.4, white line indicate the region in which lattice images are clearly observed. Nucleation is occurred by excimer laser annealing.

4.CONCLUSION

Excimer laser annealing of SBT films was studied, with the following results:

1)Excimer laser irradiation exceeding 125 mJ/cm^2 changed the color of SBT films.
2)Excimer laser annealing did not affect XRD patterns.
3)SBT film annealed by excimer laser annealing show much lower leakage current than those annealed conventional methods, FA and RTA.
4)SBT film annealed by excimer laser annealing show much higher breakdown voltage than those annealed other methods.
5)SBT films annealed by excimer laser shows good ferroelectric properties after the second annealing at 800 °C. SBT films annealed other methods showed too high leakage current and too low breakdown voltage to evaluate ferroelectric properties.
6)Excimer laser annealing makes it possible to operate SBT film by low applied voltage such as 1V.
7)Grain size and surface morphology of the SBT film annealed by excimer laser is similar to the films annealed other methods. The film by excimer laser shows somewhat smoother surface than the other..
8) Since lattice images are clearly observed for the film after excimer laser irradiation, nucleation is occurred.
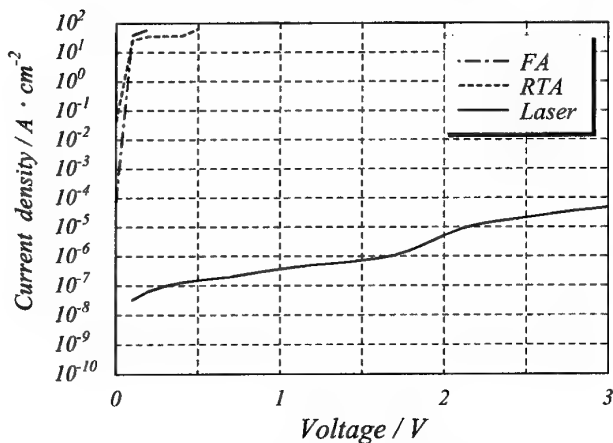
Fig.1 I-V curves of 60nm-thick SBT films annealed by different methods.
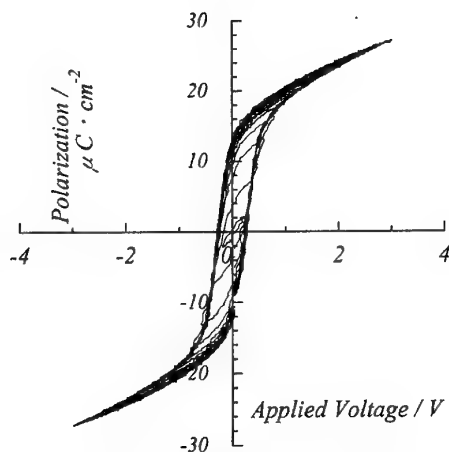
Fig.2 Hysteresis loops of 60nm-thick SBT films annealed by excimer laser.

REFERENCES
1)T.Sumi:*IEICE Trans. Electron.*, **E79-C**, 812-818 (1994).
2) C.A.Paz de Araujo, J.D.Cuchiaro L.D.McMillan, M.C.Scott and J.F.Scott: *Nature*, **374,** 627-629(1989).
3) E.Fujii, Y.Shimada, Y.Judai, T.Otsuki, N.Solayappan, L.D.McMillan and C.A.Paz de Araujo: *Extended Abstracts of the 45th Spring Meeting of Jpn. Appl. Phys. Soc.*, **No.1**, p.162. (1998, March)
4) T.Kanehara, I.Koiwa, Y.Okada, K.Ashikaga, H.Katoh and K.Kaifu: *Proc. of IEDM 97*, pp.601-604 (1997).
5) I.Koiwa, K.Tani, J.Mita and T.Iwabuchi: *Jpn. J. Appl.*

Phys., **37,** No.1, 192(1998).
6) I.Koiwa, Y.Okada, J.Mita, A.Hashimoto and Y.Sawada: *Proc. of 192nd meeting of the Electrochemical Society*, p.635 (1997, Sept.).
7) N.Matsuo, Y.Aya, T.Kanamori, T.Nouda, H.Hamada and T.Miyoshi: *Digest of 1998 International Workshop on Active-Matrix Liquid-Crystal Display*, .145 (1998).
8) M.Nishitani, M.Sakai, M.Terauchi, H.Nishitani, M.Yamamoto, H.Tsutsu, S.Ishikawa, K.Mizoguchi and S.Nakashima: *Digest of 1998 International Workshop on Active-Matrix Liquid-Crystal Display*, 149 (1998).
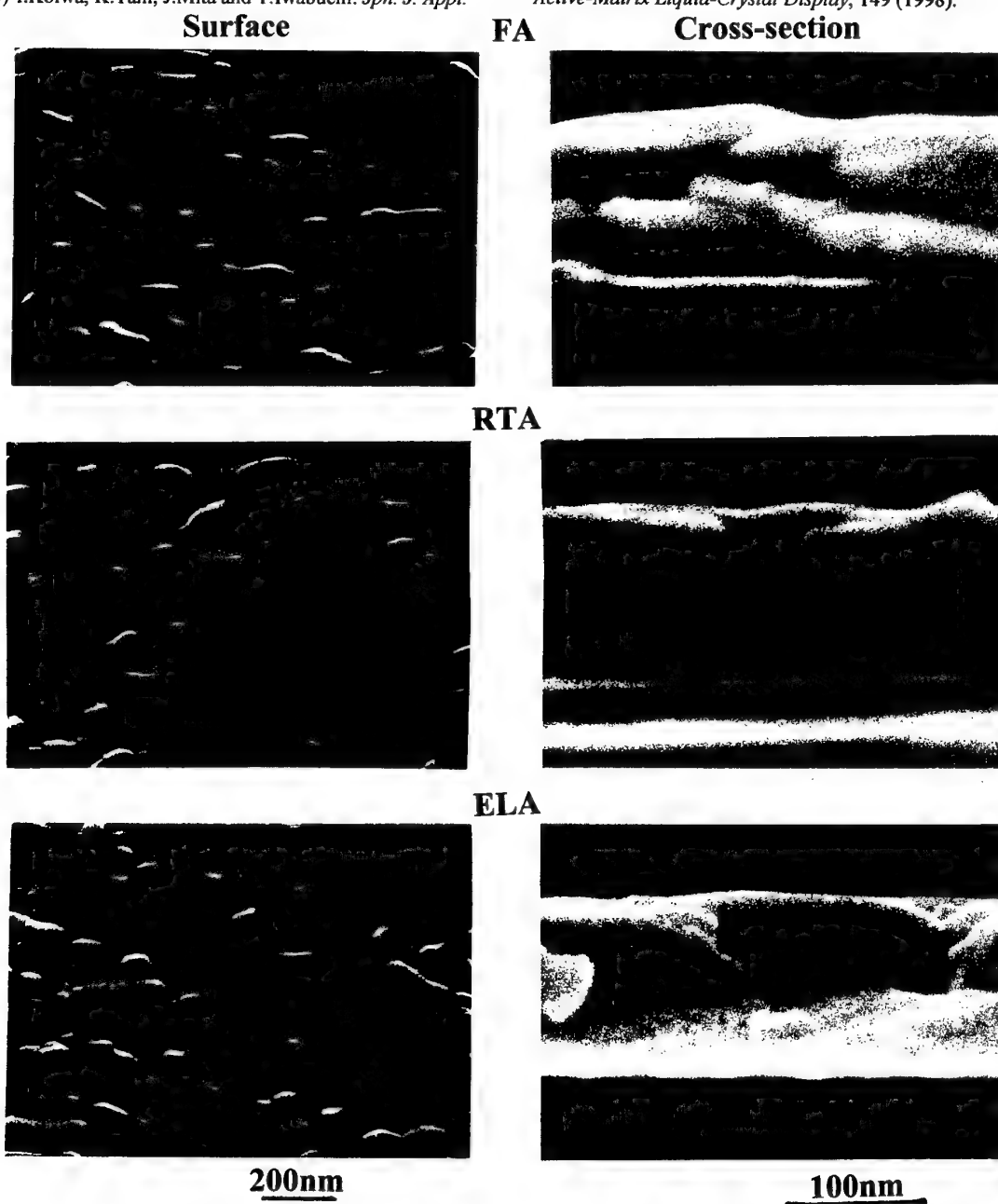
Fig. 3   Effect of annealing method, FA,RTA and ELA, on surface and cross-sectional SEM micrographs of SBT films prepared by sol-gel method.

Before annealing

After annealing

10nm

Fig.4   Effect of ELA on cross-sectional TEM micrographs of SBT film surface parts.

Orientation Control of $Bi_4Ti_3O_{12}$ Thin Films by MOCVD

Takeshi Kijima, Yutaka Nagasawa and Kaoru Suzuki
Ecological Technology Development Center, SHARP Corporation
273-1 Kashiwa, Kashiwa-shi, Chiba 277-0005, Japan
Fax: 81-471-34-6119, e-mail: kijima@kasiwa.sharp.co.jp

$Pt/Bi_2SiO_5/Si$ (MIS) and $Pt/200nm\text{-}Bi_4Ti_3O_{12}/Pt/30nm\text{-}Bi_2SiO_5/Si$ (Metal/Ferroelectric/Metal/Insulator /Semiconductor) structures were prepared by MOCVD method. An Oxygen concentration and a Bi/Ti composition ratio decide the $Bi_4Ti_3O_{12}$ orientation and the $Bi_4Ti_3O_{12}$ volume into the film, respectively. When the oxygen concentration and the Bi/Ti formation ratio was 33% and 0.65, we obtained the (001) $Bi_4Ti_3O_{12}$ film with the dielectric constant of 40.

On the other hand, when the capacitance-vs-voltage (C-V) characteristics of the $Pt/Bi_2SiO_5/Si$ structure, the inversion layer caused by minority carrier (electron) was observed. Moreover the C-V characteristics of $Pt/Bi_4Ti_3O_{12}/Pt/Bi_2SiO_5/Si$ structure have ferroelectric switching properties with memory window of about 2.0V, and the capacitance at zero-bias shows almost constant for 24 h.

1. INTRODUCTION

Recently, a nonvolatile ferroelectric memory (NVFRAM) with nondestructive readout operation has been extensively investigated[1-4]. A metal/ferroelectirc/ semiconductor field effect transitor (MFS-FET) is expected as one of its applications in the next generation. The most difficult problem of MFS structure is that the ferroelectric thin film must be directly deposited on a Si substrate. As a result, Si oxidization at ferroelectirc/Si interface and diffusion of ferroelectric components cause a increase of operation bias voltage and trap energy levels. We examined a metal/ferroelectirc/metal/ insulator/semiconductor (MFMIS) structure with a Pt floating gate and a intermediate buffer layer to avoid such problems.

In the experiments, we investigated a ferrroelectiric capacitor (MFM) and a diode (MIS) separately to establish techniques of thin film formation and then fabricated a MFMIS structure to confirm the electrical properties. The ferroelectic thin film was obtained by a MOCVD method using $Bi_4Ti_3O_{12}$. MOCVD allows easy composition and crystallinity control, excellent step coverage and a wide deposition area, which are compatible with large-scale processing and mass production. $Bi_4Ti_3O_{12}$ is one of the most interesting ferroelectric materials with Bi layered structure in recent years[5-7]. In this paper, we demonstrate that we could control the orientation and crystallinity of the $Bi_4Ti_3O_{12}$ thin film based on a new process and obtain good diode characteristics of MFMIS structure when using Bi_2SiO_5 [8] as a intermediate buffer layer.

Table 1. Deposition conditions of $Bi_4Ti_3O_{12}$ films

Precursors	$Bi(o\text{-}C\text{-}H_7)_3$	$Ti(i\text{-}OC_3H_7)_3$
Precursors temp.	160°C	50°C
Gas flow rate		
Ar carrier gas	50-350sccm	50sccm
O_2 gas	800-1000sccm	
Pressure	2-10Torr	
Substrate	Pt(111)/Ta/SiO$_2$/Si,p-Si(100),n-Si(100)	

Constant temperature box

Nozzle

O_2

Ar

Bi source

Ar

Ti source

Ar

Ribbon heater

Wafer   Heater

Mass flow controller

Reaction chamber   Source supplying part
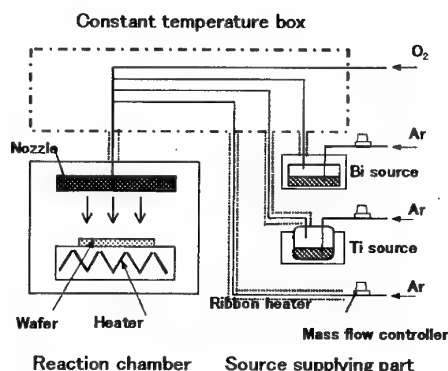
2. EXPERIMENTAL

$Bi_4Ti_3O_{12}$ and Bi_2SiO_5 thin films were deposited under the conditions in Table I using a vertical cold-wall type MOCVD system, as shown in Fig. 1. This MOCVD system consists of bubblers for source gases, a constant-temperature box and a reaction chamber. Bi and Ti source gases are transported by Ar carrier gas through the pipes kept at 160°C in the constant-temperature box. The reaction chamber has the nozzle which carries the mixture of the source and O_2 gases to a substrate warmed by heater. $Bi(o\text{-}C_7H_7)_3$ (purity:99.99%) and $Ti(i\text{-}OC_3H_7)_3$ (purity:99.999%) were used as source materials, where the Bi source are solid and that of Ti liquid at room temperature. They are vaporized by bubblers at 160°C and 50°C respectively. $Bi_4Ti_3O_{12}$ was deposited on a Pt-coated silicon substrate at 2 Torr. Ti and total gas flow rates were fixed at 50sccm and 2500sccm while those of Ti and O_2 were varied in the range of Table I. On the other hand, Bi_2SiO_5 was deposited on either p-type or n-type Si substrate at 10 Torr. Only Bi source was supplied to the substrate at 500°C. At that time Bi and O_2 gas flow rates were 250sccm and 1000sccm.

The crystal structure, the composition and the surface

morphology of the $Bi_4Ti_3O_{12}$ and Bi_2SiO_5 thin films were examined by X-ray diffraction (XRD), electron probe microanalysis (EPMA) and scanning electron microscopy (SEM). *D-E* hysteresis loops were measured using RT66A ferroelectric test system (Radiant Technologies, Inc.) with a frequency of 1kHz. The capacitor-vs-voltage, *C-V* characteristics were obtained with a LCR meter (4275A, Yokogawa Hewlett-Packard) in the range of 100Hz-1MHz.

(1) Film structure   (2) Temperature profile
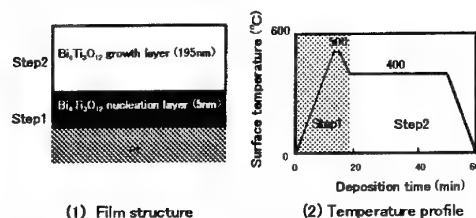
Fig. 2. Film structure and temperature profile for $Bi_4Ti_3O_{12}$ deposition process

3. RESULT AND DISCUSSION

3.1 Techniques of $Bi_4Ti_3O_{12}$ felloelectric capacitor formation by 2 step method

It is not easy to process a smooth-surface $Bi_4Ti_3O_{12}$ thin film on a Pt-coated substrate because of its complicated structure[5]. Hence, we examined a new process, the 2 step method (Fig. 2); a 5nm-$Bi_4Ti_3O_{12}$ nucleation layer is deposited on a Pt substrate at 500℃ for good crystallinity, in step 1 and a 195nm-$Bi_4Ti_3O_{12}$ growth layer at 400℃ for a flat and smooth surface, in step 2. In addition, since $Bi_4Ti_3O_{12}$ has strong ferroelectirc anisotropy, it is necessary to establish orientation control techniques of $Bi_4Ti_3O_{12}$ in order to obtain its good ferreoelectric properties efficiently. We also investigated the effect which the change of the Bi/Ti composition ratio and the oxygen gas concentration had on the orientation and the electric properties of the $Bi_4Ti_3O_{12}$ film processed by this method.

It is known that $Bi_4Ti_3O_{12}$ prefers a c-axis-oriented crystalline consisting of large plate like grains due to its anisotropic growth speed. The obtained nucleation layer in step 1, however, was a (001) and (117) random-oriented film; the XRD peak intensity ratio was approximately 1:4 similar to that of the spontaneous orientation (1:5). On the nucleation layer deposition, Bi, Ti and O_2 gas flows were 250sccm, 50sccm and 1000sccm in common throughout this experiments.

While changing Bi and O_2 gas flows within the range of Table I, we deposited the growth layer on the nucleation layer. According to the relationship between a Bi/Ti composition ratio and Bi gas flow of the 200nm-$Bi_4Ti_3O_{12}$ thin film, it is confirmed that the Bi/Ti composition ratio increases linearly with the Bi gas flow below the stoichiometry point(Bi/Ti=1.33) and saturates at about Bi/Ti=1.4 above it in all oxygen concentration. Fig. 3 shows the XRD patterns and peak intensities of the $Bi_4Ti_3O_{12}$, where the peak intensities tends to saturate at about Bi/Ti=1.4 in spite of the oxygen concentration as well. All the films show only the layered structure perovskit $Bi_4Ti_3O_{12}$ phase; a (001) single oriented film was obtained at the oxygen gas concentration of 33% , (117) single oriented one at 80%, and random-oriented
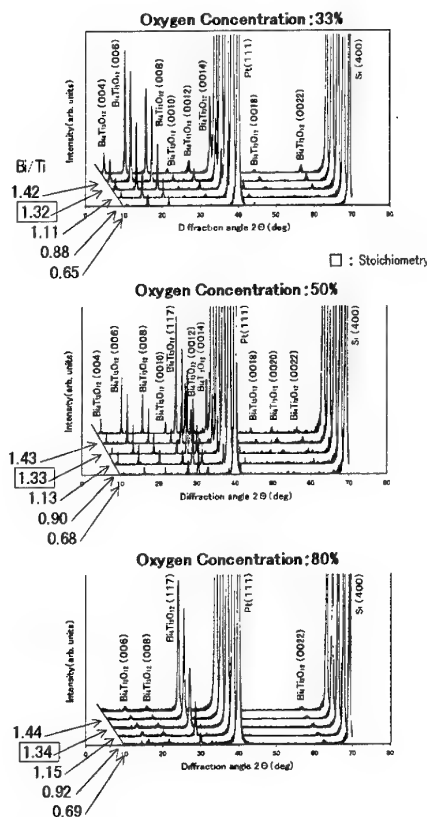
Fig. 3. Relationships between deposition conditions and film orientation

one at 50%. This result suggests that the orientation of the $Bi_4Ti_3O_{12}$ thin film strongly depends on the oxygen concentration. Namely, the (001) component dominantly grows if the oxygen concentration is high; on the contrary, that of (117) grows if it is low. Additionaly, the $Bi_4Ti_3O_{12}$ crystal volume into the film can be controlled by changing the Bi/Ti composition ratio.

The electrical properties of the $Bi_4Ti_3O_{12}$ film were examined after Pt top electrodes had been evaporated. Good *D-E* hysteresis loops were confirmed with the films at all the Bi/Ti composition ratios between 0.65 and 1.45 (Fig. 4). In the case of the fixed oxygen concentration, we could change the amount of the remnant polarization arbitrarily, keeping the hysteresis of good shape and the coercive field constant. Thus, we could obtain the electric properties controlled by the orientation and crystallinity with changing the oxygen concentration and the Bi/Ti composition ratio.

We can propose a film structure model when we consider the reason why we could obtain the films with such good electrical properties in spite that the film composition was different from the stoichiometry. Since nothing other than $Bi_4Ti_3O_{12}$ peaks was seen in the XRD patterns, we think that the film is the mixture of the $Bi_4Ti_3O_{12}$ crystal and the amorphous containing the component surplus from the stoichiometry. On the assumption that the ferroelectic and the amorphous exist in series

(1) O_2 : 33%

(2) O_2 : 50%

(3) O_2 : 80%

Polarization ($\mu C/cm^2$)

Applied voltage (V)

(a) Film structure   (b)D-E hysteresis loop

Fig. 5. Model of $Bi_4Ti_3O_{12}$ growth [張り替え]

3.2 Characteristics of Pt/Bi₂SiO₅/Si MIS structure

A Bi_2SiO_5 thin film is effective as a intermediate buffer layer due to relatively high dielectric constant and small lattice mismatching with respect to Si crystal. Bi_2SiO_5 is one of the Bi silicate families and easy to be formed on a Si substrate . The lattice mismatch is as small as –0.5% attributed to the lattice constant of both Bi_2SiO_5 and Si a-axis-planes[9].

A Bi_2SiO_5 thin film was deposited by MOCVD method on either p-Si(100) or n-Si(100) substrate, whose spontaneous oxidized film had been removed in advance. Bi source gas was supplied to the substrate at 500°C with O_2 gas. A flat and smooth (100) oriented 30nm-Bi_2SiO_5 thin film was confirmed from its morphology

Fig. 6. Capacitance-voltage characteristics of Pt/Bi₂SiO₅/Si MIS structure

between the electrodes, the voltage applied to the ferroelectric should be very low and the D-E hysteresis loop hardly opens. We cannot, therefore, explain the case. On the other hand, we can consider the model that the ferroelectric and the amorphous exist in parallel as shown in Fig. 5a. Provided that the $Bi_4Ti_3O_{12}$ crystal grows pillar like and perpendicular to the substrate around the nucleon, it is reasonable that a good D-E hsyteresis loop (Fig. 5b) could be seen because the applied voltage concentrated to the $Bi_4Ti_3O_{12}$ crystal (pillar). Moreover, the ratio occupied by the $Bi_4Ti_3O_{12}$ crystal pillar in the film and its orientation are considered to be strongly dependent on the Bi/Ti composition ratio and the oxygen concentration respectively.

The above experiments suggests that the ferroelectirc pillar penetrating between the top and bottom electrodes, whether partially or not, is indispensable in order to explain such good ferroelectric properties. The 2 step method is very effective to provide the $Bi_4Ti_3O_{12}$ thin films with the arbitrary electrical properties. In other words, the ferroelectric area can be controlled arbitrarily without any additional processes to the film. Especially, it is considered to be the important technique to the applications of the NVFRAMs with non-destructive readout operation with a intermediate buffer layer between ferroelectric and a silicon substrate.

and XRD patterns. The Bi_2SiO_5 layer was considered to be formed by the reaction between Si in the substrate and Bi and O elements supplied outside. The similar method was reported by Kim et al.[10]. After Pt top electrodes had been deposited on the surface by vacuum evaporation, the C-V characteristics of the MIS structure was evaluated in the frequency range of 10Hz-1MHz; well defined MIS diode characteristics and a inversion layer caused by minor carrier (electron) were confirmed (Fig. 6). This shows a good Bi_2SiO_5/Si interface was obtained. The C-V curve at frequency of 1 MHz indicates the dielectric constant is about 30. This relatively high value demonstrates that this film is effective to a intermediate buffer layer of the NVFRAMs with non-destructive readout operation.
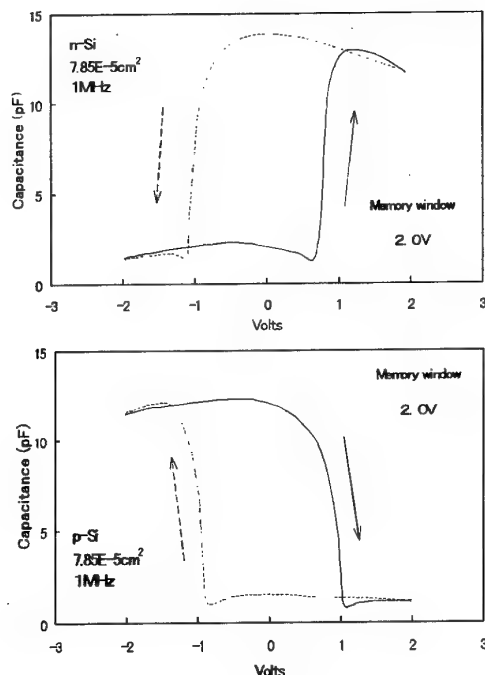
Fig. 7. Capacitance-voltage characteristics of
Pt/Bi$_4$Ti$_3$O$_{12}$/Pt/Bi$_2$SiO$_5$/Si MFMIS structure

3.3 Electrical properties of MFMIS structure

A new metal/ferroelctric/metal/insulator/ semicon-
ductor (MFMIS) structure was fabricated; 150nm-Pt
floating gates were formed by vacuum evaporation
where a 30nm-Bi$_2$SiO$_5$ buffer layer had been deposited
on either p-Si or n-Si substrate in advance; moreover a
(001) oriented 200nm-Bi$_4$Ti$_3$O$_{12}$ film was deposited by 2
step method at oxygen consentration of 30% and com-
position ratio Bi/Ti=0.65, where the electric properties
were estimated to Pr$\fallingdotseq$0.8μC/cm^2 and Ec$\fallingdotseq$40kV/cm;
at last Pt top electrodes were evaporated. Thus
Pt/200nm-Bi$_4$Ti$_3$O$_{12}$/Pt/30nm-Bi$_2$SiO$_5$/Si MFMIS struc-
ture was processed.

Fig. 7 shows the C-V curves of the MFMIS diode; the
dielectric constant was determined to about 40, which
is approximately 1/4 of the bulk (165). Consequently,
the voltage applied to the Bi$_4$Ti$_3$O$_{12}$ thin film was proved
to become higher enough for a good C-V hysteresis loop.
Though the applied voltage was as low as +2V or –2V,
the memory window was about 2V as expected from the
electric properties obtained before. These diode char-
acteristics also demonstrate that the 2 step method has
the potential that a ferroelectic thin film could be pre-
pared in accordance with the memory specification.
When the write bias voltage of +2V or -2V was applied
to the sample, the time dependence of the capacitance
was measured at zero bias. Fig. 8 indicates the capaci-
tance change was negligible over 24 h. Thus the good
retention properties were confirmed.
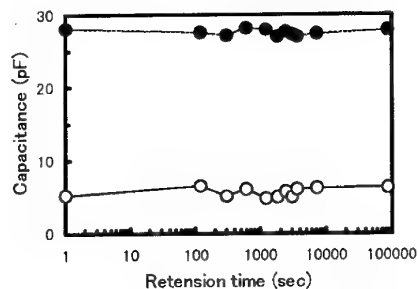
Fig. 8. Retention time dependence of the capacitance of
Pt/Bi$_4$Ti$_3$O$_{12}$/Pt/Bi$_2$SiO$_5$/Si MFMIS structure

4. CONCLUSIONS

Bi$_4$Ti$_3$O$_{12}$ thin films were fabricated on Pt deposited
substrate by MOCVD method using 2 step method. The
orientation and the crystal volume into the films were
controlled by mean of changing an oxygen concentration
and a Bi/Ti composition ratio, and their ferroelectric
properties were confiremed in accordance with them.

The Pt/Bi$_4$Ti$_3$O$_{12}$/Pt/Bi$_2$SiO$_5$/Si MFMIS structure
using the above Bi$_4$Ti$_3$O$_{12}$ film and the Bi$_2$SiO$_5$ films as
intermediate buffer layer had the C-V hysteresis attribut-
ed to the ferroelecticity of the both films. The memory
window was about 2V after the write bias voltage of
+2V or –2V and the estimated retention time was almost
constant for more than 24 hours.

References
1) J.L.Moll and Y.Tarui: *IEEE Trans. Electron. Device.*
ED-10 (1963) 338.
2) Sung-Min Yoon, E.Tokumitsu and H.Ishiwara,: Jpn. J.
Appl. Phys. **37** (1998) 936.
3) Y.Matsui, M.Okuyama, M.Noda and Y.Hamakawa,:
Appl. Phys. A **28** (1982) 161.
4)Y.Fujimori, N.Izumi, T.Nakamura and A.Kamisawa:
Jpn. J. Appl. Phys. **37** (1998) 5207.
5) T.Kijima, S.Satoh, H.Matsunaga and M.Koba: Jpn. J.
Appl. Phys. **35** (1996) 1246.
6) T.Nakamura, R.Muhammet, M.Shimizu and
T.Shiosaki: Jpn. J. Appl. Phys. **32** (1993) 4086.
7) A.Kakimi, S.Okamura, S.Ando and T.Tsukamoto: Jpn.
J. Appl. Phys. **34** (1995) 5193.
8) T.Kijima and H.Matsunaga: Jpn. J. Appl. Phys. **37**
(1998) 5171.
9) B.Aurivillius: Acta. Chem. Scand. **18** (1964) 1555.
10) J.H.Kim, T.Tsurumi, T.Kamiya and M.Daimon: J.
Appl. Phys. **75** (1994) 2924.

Bismuth Pyrochlore Films for Dielectric Applications

W. Ren, R. Thayer, C. A. Randall, and S. Trolier-McKinstry

Center for Dielectric Studies, Materials Research Laboratory
Pennsylvania State University. University Park, PA 16802
Fax: 1-814-865-2326, email: STMcKinstry@mrl.psu.edu

Abstract – Bismuth pyrochlore ceramics have modest temperature coefficients of capacitance, good microwave properties, and can be prepared at relatively modest temperatures (~900 – 1100°C). This work focuses on the preparation and characterization of thin films in this family for the first time. A sol-gel procedure using bismuth acetate in acetic acid and pyridine, in combination with zinc acetate dihydrate and niobium ethoxide in 2-methoxyethanol was developed. The solution chemistry was adjusted to prepare $(Bi_{1.5}Zn_{0.5})(Zn_{0.5}Nb_{1.5})O_7$ and $Bi_2(Zn_{1/3}Nb_{2/3})_2O_7$ films. Solutions were spin-coated onto platinized Si substrates and crystallized by rapid thermal annealing. In both cases, crystallization occurred by 550°C into the cubic pyrochlore structure. $(Bi_{1.5}Zn_{0.5})(Zn_{0.5}Nb_{1.5})O_7$ films remained in the cubic phase up to crystallization temperatures of 750°C, while the structure of the $Bi_2(Zn_{1/3}Nb_{2/3})_2O_7$ thin films is dependent of the firing temperature: cubic below 650°C and orthorhombic above 750°C. A mixture of cubic and orthorhombic structures is found at 700°C. The resulting BZN films are dense, uniform, and smooth (rms roughness of < 5 nm). Cubic bismuth zinc niobate films show dielectric constants up to 150, a negative temperature coefficient of capacitance, TCC, (≤ - 400 ppm/°C), tan δ < 0.01, and a field tunable dielectric constant. Orthorhombic films showed smaller dielectric constants (~80), low tan δ (≤ 1%), positive TCC, and field independent dielectric constants. TCC could be adjusted to new 0 ppm/°C using a mixture of orthorhombic and cubic material.

1. INTRODUCTION

The rapid development of communication technologies, especially mobile communication systems, is facilitated by miniaturization of devices. Dielectric materials for these applications must possess a large dielectric constant, low loss tangent (tan δ), high dielectric quality factor Q, and a small temperature coefficient of resonator frequency for resonators. The Bi_2O_3-ZnO-Nb_2O_5 (BZN) pyrochlore ceramic system with medium dielectric constants and high Q values has been developed for low firing multilayer capacitors [1-4]. Recent studies showed that some members of the BZN system also exhibit excellent microwave properties [5, 6]. BZN ceramics with dielectric constants >100, temperature coefficient of resonant frequency $|T_f|$ < 10 ppm/°C and Q·f > 5000 GHz have been reported [6]. The good dielectric properties shown by the BZN system suggest that thin films of this composition are potential materials for integrated microwave resonators and decoupling capacitors. Thin films may have the advantage of lower crystallization temperatures and smaller device size than bulk ceramics and can be integrated in microelectronic devices. To our knowledge, no BZN thin films have been reported previously.

In this study, we report on the fabrication and properties of BZN thin films prepared by a sol-gel process. The sol-gel process has been widely used to deposit dielectric and ferroelectric thin films due to low processing temperatures, precise composition control, uniform deposition over large area substrate and low cost.

2. EXPERIMENTAL PROCEDURE

Two compositions of BZN thin films were investigated in this study: $(Bi_{1.5}Zn_{0.5})(Zn_{0.5}Nb_{1.5})O_7$ and $Bi_2(Zn_{1/3}Nb_{2/3})_2O_7$. These two compositions are members of the general family $(Bi_{3x}Zn_{2-3x})(Zn_xNb_{2-x})O_7$.

The starting materials in the sol-gel process were bismuth acetate, zinc acetate dihydrate and niobium ethoxide (Aldrich). 2-methoxyethonal, pyridine and acetic acid (Aldrich) were selected as solvents. Zinc acetate dihydrate was first mixed with 2-methoxyethonal and vacuum distilled at 110°C to expel the water of hydration and to prevent niobium ethoxide from hydrolyzing. Niobium ethoxide was then added into the solution and refluxed at 120°C for 1 h to form a (Zn, Nb) complex precursor, followed by vacuum distillation of by-products. The solution was cooled down below 80°C. In a separate flask, bismuth acetate was mixed with pyridine and stirred for 0.5 h. 30 vol% of acetic acid was added into the solution and stirred for 1 h until the solution became totally clear. The bismuth acetate solution was then added to the (Zn, Nb) precursor and the solution was refluxed at 120°C for 0.5 h. After vacuum distilling off by-products, the final precursor solution was diluted using 2-methoxyethonal to a concentration of 0.3M.

To prepare films, the precursor solution was spin coated on platinum-coated Si wafers Pt/Ti/SiO₂/Si (Nova Electronic Materials, Inc., Richardson, TX) at a speed of 3000 rpm for 30 s. The as-deposited films were pyrolyzed on a hot plate at a temperature of 350°C for 1 min to remove the organics. The

coating-pyrolysis procedure was repeated until the desired thickness was reached. The film was then crystallized in air either using a preheated tube furnace for 5 min. or a rapid thermal annealer with a heating rate of 100 °C/s and a soak time of 60 s. The thickness of the films prepared was 0.4 to 0.5 μm.

The crystallinity of the BZN thin films was characterized with a Scintag DMC-105 X-ray diffractometer using Cu K_α radiation. A Digital Instruments Dimension 3100 atomic force microscope was used to investigate the surface morphology and roughness of the thin films. Tapping mode was adopted in this work. To examine the electrical properties, platinum dots of 0.5 mm or 1.5 mm in diameter were sputtered onto the films as top electrodes to form a Pt/BZN/Pt sandwich configuration. The dielectric properties of the BZN films were measured with a Hewlett Packard 4284A multi-frequency LCR meter with a test signal of 0.03 V rms. Two temperature measurement systems were employed to measure the temperature dependence of the dielectric properties. For the temperature range between 200 and –175 °C, a computer-controlled Delta 9023 temperature oven with a temperature cooling ramp of 2°C/min was used. For temperatures between 300 and 4 K, a second set-up was employed (again with a ramp rate of 2°C/min). The measurement frequencies were between 20 Hz and 1 MHz. The field dependence of the dielectric properties were measured using a DC bias voltage from a HP4284A LCR meter.

3. RESULTS AND DISCUSSION

Bulk $(Bi_{1.5}Zn_{0.5})(Zn_{0.5}Nb_{1.5})O_7$ ceramics have a cubic pyrochlore structure with a = 1.056 nm [2, 4]. The recent study by Wang et al. suggests that $Bi_2(Zn_{1/3}Nb_{2/3})_2O_7$ has a distorted pyrochlore phase with an orthorhombic structure with a = 0.7202 nm, b = 0.7603 nm and c = 1.064 nm [4]. The structure of $Bi_2(Zn_{1/3}Nb_{2/3})_2O_7$ ceramics is firing temperature dependent and the material converts to a cubic phase at a higher firing temperature (~ 1100°C) [7].

The XRD patterns of $(Bi_{1.5}Zn_{0.5})(Zn_{0.5}Nb_{1.5})O_7$ films fired at different temperatures are shown in Fig. 1. The films were amorphous at temperatures of 500°C and below: no sharp diffraction peaks were observed in the film. Films fired at 550°C were crystalline and showed a cubic pyrochlore structure. With increasing firing temperature, the intensities of the diffraction peaks strengthened, but the films maintained the cubic pyrochlore structure. No preferred orientation was found in the films. The lattice constant calculated from films fired at 750°C is 1.055 nm, which is close to the bulk value.

For $Bi_2(Zn_{1/3}Nb_{2/3})_2O_7$ solutions, after the 500°C anneal, the film was amorphous. Between 550°C and 650°C, the films appeared to have a cubic structure with a main peak (222) at 2θ = 29.3°. For the film
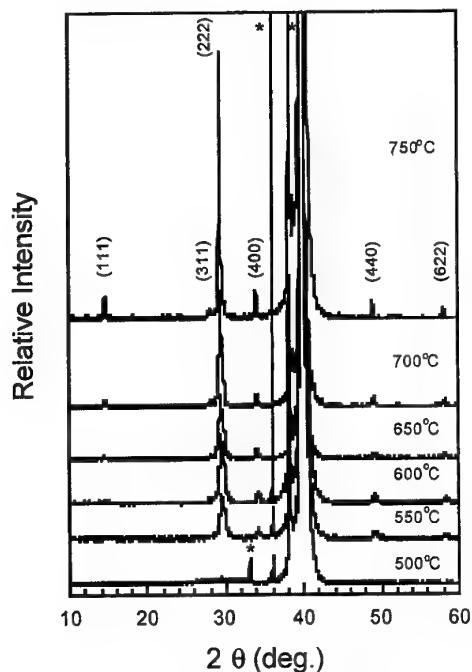
Fig. 1: X-ray diffraction patterns of $(Bi_{1.5}Zn_{0.5})(Zn_{0.5}Nb_{1.5})O_7$ films as a function of crystallization temperature

fired at 750°C, the diffraction pattern found was indexed to an orthorhombic phase with lattice constants of a = 0.718 nm, b = 0.759 nm, and c = 1.058 nm. A mixture of cubic and orthorhombic structures was observed in films fired at 700°C. $Bi_2(Zn_{1/3}Nb_{2/3})_2O_7$ films fired at 800 °C still maintained an orthorhombic structure and no cubic phase was detected from XRD analysis. All films were polycrystalline.

AFM was used to measure the surface morphologies of the BZN thin films as a function of firing temperature. Featureless AFM scans were found in the BZN films fired at 500°C, which were X-ray amorphous. When the temperature was increased to 550°C, very fine grains with a surface grain size of about 30 nm were observed in the films. The surface grain size increased with firing temperature. At temperatures of 750 °C, the grain size was ~100 nm. The BZN films exhibited a dense microstructure with no cracks or defects. RMS values of the surface roughness for $Bi_2(Zn_{1/3}Nb_{2/3})_2O_7$ films were very small. At firing temperature of 550°C, the average roughness was 0.4 nm. The roughness increased with temperature and was 4.2 nm at 750°C. AFM data for $(Bi_{1.5}Zn_{0.5})(Zn_{0.5}Nb_{1.5})O_7$ films showed similar features.

Table I gives the dielectric properties of $(Bi_{1.5}Zn_{0.5})(Zn_{0.5}Nb_{1.5})O_7$ films as a function of firing temperature. The dielectric constants of the films increased monotonically with crystallization

temperature and reached 150 at 750°C, which was comparable to the values of bulk ceramics with the same composition (140 – 170).[2, 4] All films exhibited very low dielectric losses (tanδ < 0.01). The dielectric constants changed linearly with temperature between -50 and 100 °C. The results are shown in Table II. The TCC of the $(Bi_{1.5}Zn_{0.5})(Zn_{0.5}Nb_{1.5})O_7$ films fired at 750°C was comparable to the reported values of bulk ceramics.[2, 4]

Table I: Dielectric constant for (BZN1) $(Bi_{1.5}Zn_{0.5})(Zn_{0.5}Nb_{1.5})O_7$ and $Bi_2(Zn_{1/3}Nb_{2/3})_2O_7$ (BZN2) films as a function of crystallization temperature

Crystallization Temperature (°C)	BZN1	BZN2
550	90	80
600	105	95
650	110	100
700	130	85
750	150	80

Table II: Temperature coefficient of capacitance for $(Bi_{1.5}Zn_{0.5})(Zn_{0.5}Nb_{1.5})O_7$ (BZN1) and $Bi_2(Zn_{1/3}Nb_{2/3})_2O_7$ (BZN2) films

Crystallization Temperature (°C)	BZN1 (ppm/°C)	BZN2 (ppm/°C)
550	0.1	75
600	-70	-0.1
650	-150	-60
700	-350	20
750	-400	150

The dielectric properties of $Bi_2(Zn_{1/3}Nb_{2/3})_2O_7$ films versus firing temperature are given in Table I. The dielectric constant of the $Bi_2(Zn_{1/3}Nb_{2/3})_2O_7$ films was a function of firing temperature and had a maximum at 650°C. The dielectric constant at 750°C was 80, which was comparable to the bulk value [2, 4]. XRD indicated that $Bi_2(Zn_{1/3}Nb_{2/3})_2O_7$ films had an orthorhombic phase at firing temperatures of 750°C. Based on the above results, we can conclude that dielectric constant of orthorhombic BZN was smaller than cubic films. Because of the cubic phase formed in $Bi_2(Zn_{1/3}Nb_{2/3})_2O_7$ films at the lower firing temperatures range of 650 – 700°C, the dielectric constant increased with decreasing firing temperature. Further lowering the firing temperature lead to a decrease in the dielectric constant due to weak crystallization of the films. The loss tangent of the films was lower than 0.01. The temperature dependence of dielectric constant of the $Bi_2(Zn_{1/3}Nb_{2/3})_2O_7$ films is shown in Table II. TCC of the films at 750 °C was 150 ppm/°C, which was

also comparable to the bulk values [2, 4]. Cubic BZN films had a negative TCC (-400 ppm/°C), while orthorhombic films had a positive TCC (150 ppm/°C). As the firing temperature decreased from 750 to 650°C, the TCC of $Bi_2(Zn_{1/3}Nb_{2/3})_2O_7$ films decreased due to the cubic phase which formed at low temperatures. A mixture of cubic and orthorhombic of $Bi_2(Zn_{1/3}Nb_{2/3})_2O_7$ films fired at 700°C give a very small TCC (~20 ppm/°C).

The dielectric constant and loss measured down to 4K of the $(Bi_{1.5}Zn_{0.5})(Zn_{0.5}Nb_{1.5})O_7$ films fired at 750°C are given in Fig. 2. A frequency dispersion in the dielectric properties was observed at low temperature. The dielectric constant maxima decreased and shifted to higher temperatures with increasing measuring frequency. The corresponding maxima in the loss tangent increased and shifted to higher temperature with increasing frequency. The
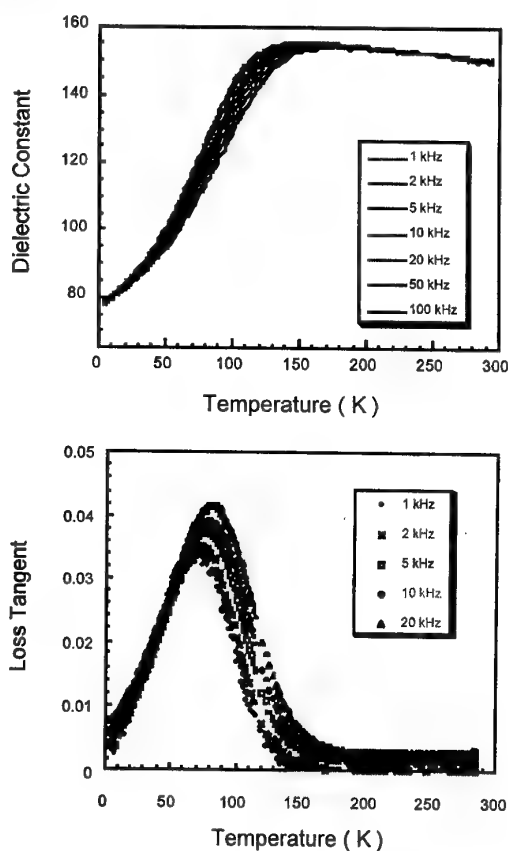
Fig. 2: Low temperature relaxation in cubic BZN films For the dielectric constant, the lowest frequencies have the highest permittivities

frequency dispersion of $(Bi_{1.5}Zn_{0.5})(Zn_{0.5}Nb_{1.5})O_7$ films are similar to those of dipole glasses [8-10].

An Arrhenius equation was used to fit the dispersion data of $(Bi_{1.5}Zn_{0.5})(Zn_{0.5}Nb_{1.5})O_7$ films:

$$1/\tau_c = \nu_0 exp[-E_a/k_BT] \qquad (1)$$

where τ_c is the characteristic relaxation time, ν_0 is the attempt jump frequency, E_a is the activation energy and k_B is Boltzmann constant. ν_0 and E_a are temperature independent. The logarithmic measuring frequency had a linear relationship with the reciprocal of the temperature at which the loss tangent was maximum. ν_0 and E_a were 0.13 eV and 2×10^{13} Hz respectively. The jump frequency ν_0 of $(Bi_{1.5}Zn_{0.5})(Zn_{0.5}Nb_{1.5})O_7$ films had the same order as typical ionic vibrations of the lattice ($\sim 10^{13}$ Hz), and was comparable to that of the K(Br, CN) system[10]. Attempts to fit to a Vogel-Fulcher equation were unsuccessful.

The electric field dependence of dielectric properties of the BZN films was investigated by applying DC bias voltage ($\pm$ 40 V max.) during dielectric property measurements. Fig. 3 gives the dielectric constant and loss for $(Bi_{1.5}Zn_{0.5})(Zn_{0.5}Nb_{1.5})O_7$ films fired at 750 °C as a function of the bias electric field at the measuring frequency of 10 kHz. It can be seen that dielectric constant of the cubic BZN films changed with the bias field, while the loss tangent was constant. The dielectric constant decreased with increasing bias field and changed by 10% with a bias of 830 kV/cm. The curve was symmetric with respect to zero-bias and had no hysteresis. The voltage variable dielectric constant makes cubic BZN thin films candidates for
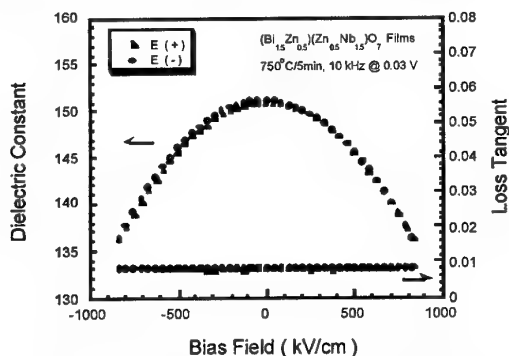
Fig. 3: Tunability of $(Bi_{1.5}Zn_{0.5})(Zn_{0.5}Nb_{1.5})O_7$ film

tunable microwave device applications.

The tunability of $(Bi_{1.5}Zn_{0.5})(Zn_{0.5}Nb_{1.5})O_7$ films was investigated at the different measuring temperatures. Fig. 4 shows the normalized tunability of the films fired at 750 °C at measuring temperatures of 25°C, -100°C, -130°C and -170 °C. It can be seen that all films demonstrated the same amount of relative tunability.

The bias electric field dependence of the dielectric constant and loss for $Bi_2(Zn_{1/3}Nb_{2/3})_2O_7$ films fired at 750°C is small. For the $Bi_2(Zn_{1/3}Nb_{2/3})_2O_7$ films fired at 650 °C and 700°C, their dielectric constants can be tuned by a bias field. This tunability is attributed to the cubic phase existing in the $Bi_2(Zn_{1/3}Nb_{2/3})_2O_7$ films fired at lower temperatures.
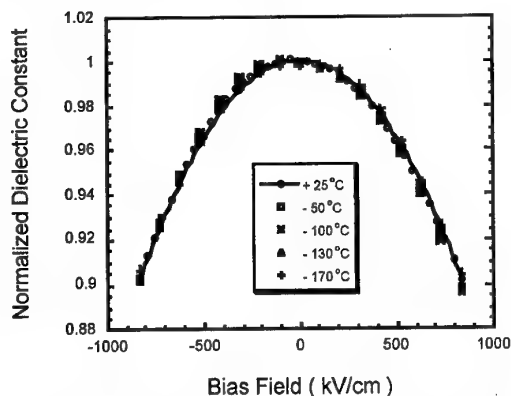
Fig. 4: Dependence of dielectric constant on dc bias field for cubic BZN films as a function of temperature

The dielectric measurements demonstrate that the dielectric constants, TCC and tunability of the BZN films depended not only on their composition, but also on the firing temperature and phase content. BZN films with the cubic phase have larger dielectric constants, negative TCC values and larger tunability. Films with the orthorhombic phase have smaller dielectric constants, positive TCC and low tunability. The above results suggest that the dielectric properties of the BZN films can be tailored to a given application by adjusting composition, phase and firing temperature.

4. CONCLUSIONS

$(Bi_{1.5}Zn_{0.5})(Zn_{0.5}Nb_{1.5})O_7$ and $Bi_2(Zn_{1/3}Nb_{2/3})_2O_7$ thin films were successfully prepared by the sol-gel process. $(Bi_{1.5}Zn_{0.5})(Zn_{0.5}Nb_{1.5})O_7$ films showed the cubic pyrochlore structure, while the structure of $Bi_2(Zn_{1/3}Nb_{2/3})_2O_7$ thin films depended on the firing temperature. Such films were cubic in the temperature range of 550-650°C and orthorhombic when crystallized at 750°C. A mixture of cubic and orthorhombic pyrochlore structures was formed at 700°C. The $(Bi_{1.5}Zn_{0.5})(Zn_{0.5}Nb_{1.5})O_7$ films fired at 750°C have a dielectric constant of ~150 and a negative TCC. $Bi_2(Zn_{1/3}Nb_{2/3})_2O_7$ thin films fired at 750°C had a smaller dielectric constant of ~80 and a positive TCC. Loss tangents of both types of BZN films are below 0.01 at 10 kHz. The cubic $(Bi_{1.5}Zn_{0.5})(Zn_{0.5}Nb_{1.5})O_7$ films fired at 750°C had a

large tunability and the orthorhombic $Bi_2(Zn_{1/3}Nb_{2/3})_2O_7$ films had a low tunability.

5. ACKNOWLEDGMENTS

6. REFERENCES

1. M. F. Yan, H. C. Ling, and W. W. Rhodes, *J. Am. Ceram. Soc.*, **73**, 1106 (1990).
2. D. Liu, Y. Liu, S. Huang, and X. Yao, *J. Am. Ceram. Soc.*, **76**, 2129 (1993).
3. D. P. Cann, C. A. Randall, and T. R. Shrout, *Solid State Comm.*, **100**, 529 (1996).
4. X. Wang, H. Wang, and X. Yao, *J. Am. Ceram. Soc.*, **80**, 2745 (1997).
5. H. Kagata, T. Inoue, J. Kato, and I. Kameyama, *Jpn. J. Appl. Phys.*, **31**, 3152 (1992).
6. S. L. Swartz, and T. R. Shrout, "Ceramic compositions for BZN dielectric resonators," U. S. Patent, No. 5449652 (1995).
7. D. P. Cann, "Bismuth pyrochlores for high frequency dielectric applications," MS Thesis, The Pennsylvania State University (1993).
8. E. Courtens, *Phys. Rev. Lett*, **52**, 69 (1984).
9. U. T. Höchli, *Phys. Rev. Lett.*, **48**, 1494 (1982).
10. S. Bhattacharya, S. R. Nagel, L. Fleishman and S. Susman, *Phys. Rev. Lett.*, **18**, 1267 (1982).
11. D. Huser, L.E. Wenger, A. J. van Duyneveldt, and J. A. Mydosh, *Phys. Rev.* **B 27**, 3100 (1983).

Microwave Properties of High-Tc Superconducting Thick Films on Ba(Sn,Mg,Ta)O₃ Dielectric Resonator and Silver Plate

Hiroshi Tamura, Tsutomu Tatekawa, Yuji Kintaka and Akio Oota*

Murata Manufacturing Co., Ltd., Yokaichi-shi, Shiga 527-8558, Japan
Fax: 81-748-23-1761, e-mail: tamura@murata.co.jp

*Toyohashi University of Technology, Tempaku-cho, Toyohashi, Aichi 441-8580, Japan
Fax: 81-532-44-6732, e-mail: oota@eee.tut.ac.jp

The microwave properties of $(Bi,Pb)_2Sr_2Ca_2Cu_3O_x$ (Bi2223) high-temperature superconducting thick film were investigated. The superconductor films were screen-printed on three substrates: silver plate, MgO and $Ba(Sn,Mg,Ta)O_3$ ceramic substrate, then sintered at 850℃. The Surface resistance R_s was measured at 10.7 GHz in the temperature range between 20 and 130 K using a dielectric resonator method. The resultant R_s's at 10.7 GHz were 1.3, 5.6 and 7.1 mΩ at 70K for the Bi2223 films on Ag plate, MgO and BSMT substrate. These values are lower than the R_s of 10.2 mΩ at 70K for Cu metal. For the practical usage, The TM_{010} mode $Ba(Sn,Mg,Ta)O_3$ dielectric resonator was fabricated using with Bi2223 superconductor on both end of the resonator. Its unloaded Q at 2.1 GHz was 30,000 at 70K, which is 7 times higher than the resonator with silver electrodes. The microstructure of the obtained Bi2223 films is also reported.

1. INTRODUCTION

Microwave filter for mobile telecommunication base stations is one of the promising applications for the high-temperature superconductors (HTS). For the realization of this devices, great efforts has been paid to improve the microwave properties of $YBa_2Cu_3O_{7-\delta}$ (YBCO) thin films, but little to those of $(Bi,Pb)_2Sr_2Ca_2Cu_3O_x$ (Bi2223) thick films. This is due to the difficulty in controlling the surface morphology and homogeneity of Bi2223 thick films.

This paper reports the microstructure and surface resistance R_s of Bi2223 thick films formed on silver plate, MgO and $Ba(Sn,Mg,Ta)O_3$ (BSMT) ceramic substrate. The unloaded quality factor Q_u of the TM_{010} mode BSMT dielectric resonator with Bi2223 thick films is also presented.

2. EXPERIMENTAL PROCEDURES

2.1 Sample Preparation

The Bi2223 superconducting paste was made of calcined $(Bi,Pb)_2Sr_2Ca_2Cu_3O_x$ powder and organic vehicles. This paste was screen-printed by 10 μm thick on the one side of Ag plate, MgO and BSMT substrates in a disk shape with the diameter of 30 mm and thickness of 1 mm.

After drying at 130℃, the samples were heat-treated at 400℃ in air to evaporate organic binders. Then, the Bi2223 films on MgO and BSMT ceramic substrates were subjected to cold isostatic pressing at 0.2 GPa. In the case of films on silver substrate, two surfaces of printed films were sandwiched face to face so as to contact each other and pressed uniaxially at 1.4 GPa [1].

The samples were then sintered at temperatures from 840 to 850℃ for 50 hours in air. This pressing and sintering were repeated a few times. The sandwiched films between silver substrates can be easily separated at the center of the Bi2223 film by splitting the two silver substrates.

2.2 Measurement of Surface Resistance

Surface resistance of Bi2223 thick films was measured by the dielectric resonator method [2]. Figure 1 shows the configuration of measurement system.

A BSMT dielectric resonator with relative permittivity ε_r=24 and dimensions of 8.5 mm in diameter and 3.8 mm in height was used as a standard

dielectric resonator. This TE_{011} mode resonator, which has the resonance frequency of 10.7 GHz, is short-circuited at both ends by a HTS thick film and by an oxygen-free copper plate. As the value R_s of this copper plate was previously measured, the R_s of a HTS thick film can be obtained from the measured resonance frequency and unloaded quality factor Qu.

Using a cryogenic refrigerator, measurement temperature was changed from 20 to 130 K and kept within ±0.2 K during a measurement run. The value of R_s was calculated from the measured f_0 and Q_u values.

3. EXPERIMENTAL RESULTS

Figure 2 shows the temperature dependence of R_s at 10.7 GHz for Bi2223 thick films on Ag plate, MgO and BSMT substrates. Previously measured Rs of the oxygen-free Cu plate is also shown in the figure.

The Bi2223 thick film on Ag substrate has superior surface resistance at microwave frequency. It cross the R_s of copper plates at 100K and finally reaches 0.3 mΩ at around 30 K. This value is nearly comparable to high-quality YBCO thin films [3].

The R_s's of Bi2223 thick films on the MgO and BSMT substrates are higher than the one on silver plates. This reason was investigated using a scanning electron microscope (SEM) and X-ray diffraction (XRD).

Figure 3 shows SEM images of fractured surfaces of Bi2223 thick films on Ag and MgO substrates. It can be seen that the Bi2223 film on the Ag substrate has higher degree of c-axis-alignment in microstructures compared with that on the MgO substrate.

Figure 4 shows the XRD patterns of Bi2223 thick films on Ag, MgO and BSMT substrates. This shows that the film on Ag substrate has the single phase of Bi2223 structure, while, the films on MgO and BSMT

substrates are made of the Bi2223 phase and a amount of the Bi2212 ($Bi_2Sr_2CaCu_2O_x$) phase. The degree of c-axis-alignment for the films on MgO or BSMT are also lower than that for the film on Ag substrate, which were determined from the (00n) peaks of the Bi2223 phase.

Accordingly, the R_s values of the HTS film on the MgO and BSMT substrates are higher than the one on the Ag substrate.
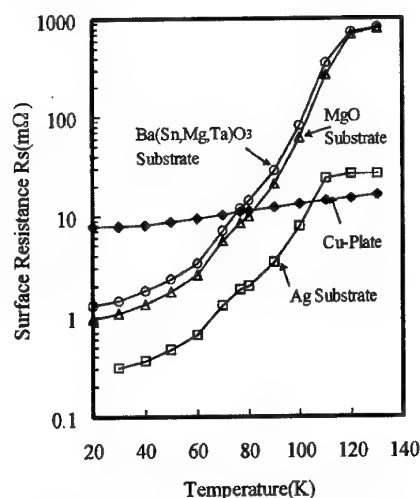
Fig.2. Surface resistance of Bi2223 thick films on Ag plate, MgO and BSMT substrates at 10.7 GHz.

Fig.3. SEM images of fractured surface of Bi2223 thick films on (A) Ag and (B) MgO substrates.

Fig.1. Configuration of measurement system for Rs of HTS thin films.

4. APPLICATION

Although the Bi2223 thick film on BSMT films has not so superior characteristics at 10.7 GHz compared with the one on Ag substrate, it still has the lower R_s than copper at 70K.

Moreover, it is known that the R_s of HTS film increases in proportion to the square of frequency, while, the R_s of metal conductor in proportion to the square root of frequency. Thus, the HTS film has the advantage for the applications at lower frequencies compared with metal conductors.

Figure 5 shows the TM_{010} mode dielectric resonator made of a BSMT disk (35 mm in diameter and 3 mm in thickness) and the Bi2223 thick films on both sides of the dielectric. This resonator with resonant frequency of 2.1 GHz was made for the filters of cellular base station.

4.1 Selection of Dielectric Resonator Material

Several papers report the temperature dependence of dielectric loss tangent at microwave frequency, which is in proportional to temperature under the condition that the effect of the phase transition is negligible. Figure 6 shows the temperature dependence tan δ and resonant frequency for three resonator materials: $(Zr,Sn)TiO_4$ $(\varepsilon_r=38)$, $Ba(Mg,Ta)O_3$ $(\varepsilon_r=24)$ and BSMT $(\varepsilon_r=24)$ [4].
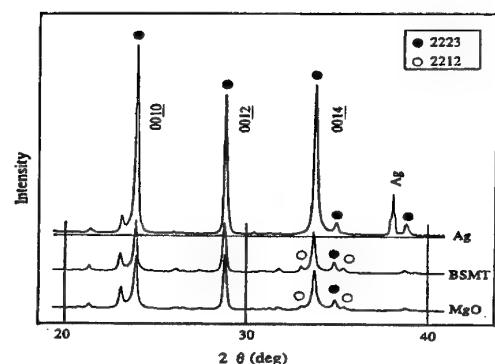
Fig.4. X-ray diffraction patterns of Bi2223 thick films on Ag, MgO and BSMT substrates.
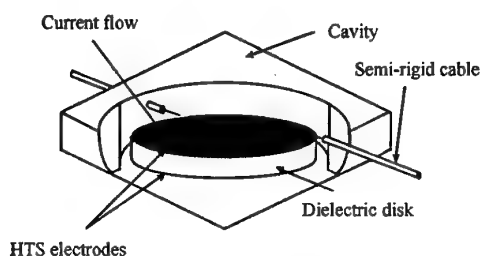
Fig. 5. Configuration of HTS dielectric resonator. The current direction is shown by thick solid line on the electrodes.

(a) tan δ

(b) Resonant frequency
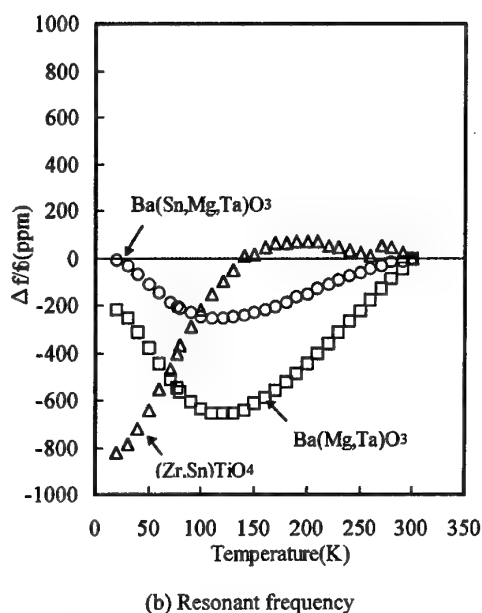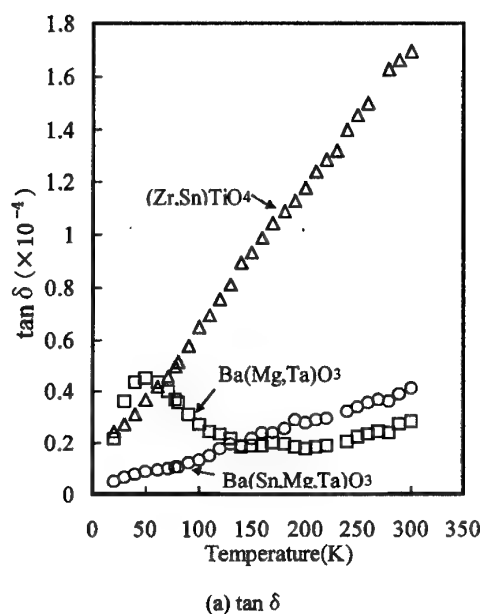
Fig.6. Temperature dependence of (a) tanδ and (B) resonant frequency for three dielectric resonator materials at 10 GHz.

As the tan δ of BSMT and (Zr,Sn)TiO$_4$ decreases monotonically with decreasing temperature, these materials are hopeful for low temperature applications. However, it became clear in the experiment that the Ti ions in (Zr,Sn)TiO$_4$ causes serious interface reaction with Bi2223 films, and the obtained HTS films do not work as superconductors. Thus, the Ti-free BSMT resonator was selected as a promising candidate for low-temperature microwave dielectrics.

4.2 Unloaded Q of TM$_{010}$ mode resonator

Figure 7 shows the temperature dependence of the unloaded Q, Q$_u$, of this TM$_{010}$ mode resonator at 2.1 GHz. The R$_s$ of the Bi2223 films can be calculated from the Q$_u$ value.

The unloaded Q of this resonator measured at incident power 5 mW is 30,000 at 70 K, which corresponds to R$_s$ of 0.8 mΩ. These values are much superior compared with the unloaded Q of 4,500 and Rs of 5.9 mΩ for the same size TM$_{010}$ mode resonator with silver electrode (Fig. 7).

The obtained property of this Bi2223 thick film, however, is not sufficiently high for the application of cellular base stations. When incident power increases from 5 mW to 100 mW, the unloaded Q of this resonator decreases from 30,000 to 18,000 at 70 K, which corresponds to the increase of Rs from 0.8 mΩ to 1.4 mΩ.

This fault is attributed to the microstructure of the Bi2223 thick film on the BSMT substrate. Higher degree of c-axis-alignment and the phase purity equal to the Bi2223 films on the Ag substrate is needed for this application.

5. CONCLUSIONS

Bi2223 thick films were formed on the three substrates made of silver metal, MgO and Ba(Sn,Mg,Ta)O$_3$ ceramics. Their surface resistances at 10.7 GHz were measured to be 1.5, 5.6 and 7.1 mΩ at 70K, respectively. The formation of Bi2223 single phase and the high degree c-axis-alignment is needed to obtain the lower surface resistance.

The TM$_{010}$ mode dielectric resonator with 2.1 GHz was fabricated for the filters of cellular base station. The BSMT resonator with Bi2223 thick films on both side of the dielectric disc had very high unloaded Q compared with the one for the resonator with silver electrode: 7 times higher at 70 K and 10 times higher at 30 K. But, further improvement is needed on the c-axis-alignment and the phase purity of HTS films for the filters of cellular base station.

Fig.7. Temperature dependence of unloaded Q and R$_s$ at 2.1 GHz for TM$_{010}$ mode dielectric resonator with Bi2223 thick films and silver conductors.

REFERENCES

[1] A.Oota, H.Matsui, M.Funakura, J.Iwaya, and K.Mitsuyama, "Fabrication, microstructure and critical current density of screen-printed Ag-(Bi,Pb)$_2$Sr$_2$Ca$_2$Cu$_3$O$_X$ superconducting tapes, "Physica C, vol.210, pp.489-501, June 1993.

[2] Y.Kobayashi, T.Imai, and H.Kayano, "Microwave Measurement of Temperature and Current Dependences of Surface Impedance for High-Tc Superconductors, "IEEE Trans. MTT, vol.39, pp.1530-1538, September 1991.

[3] Y.Ueno, N.Sakakibara, M.Okazaki, and M.Aoki, "High-Tc Superconducting Filters for Receiver Front-end of Mobile Telecommunication Base Station, "MWE'96 Microwave Workshop Digest, pp.150-155, December 1996.

[4] H.Tamura, H.Matsumoto, and K.Wakino, "Low Temperature Properties of Microwave Dielectrics, "Jpn J.Appl.Phys.,vol.28, Supplement 28-2, pp.21-23, 1989.

Synthesis of New Pyrochlore Compounds for Transparent Conductor Applications

Ravindran Mohanavelu, Alan P. Constant, and David P. Cann

Microelectronics Research Center
Material Science and Engineering Department
Iowa State University
Ames, IA 50011 USA

ABSTRACT: Transparent conducting oxides (TCOs) are finding increasing application due to their unique properties. Indium tin oxide systems have so far been the industry standard but it's low corrosion resistance and limited transmittance in the UV region has prompted the search for new materials. Other systems being studied include pyrochlores, spinels, delafossites, and amorphous materials. It is believed that a large band gap combined with a high-mobility BO_6 octahedral network is an important factor in potential TCO materials. Compounds based on the pyrochlore structure could satisfy the above requirements. Furthermore its unique tolerance to defects makes it suitable for thin film applications. This article discusses the identification of such compounds and the phase pure synthesis of the same.

1. INTRODUCTION AND BACKGROUND

Transparent conducting oxides (TCOs) have found extensive applications in areas such as photovoltaics, flat-panel displays and energy efficient windows. Compounds in the indium tin oxide system (ITO) are currently the most widely used TCOs owing to their large transmittance and excellent conductivity ($1 \times 10^{-3} \Omega cm$)[1]. These compounds however have low corrosion resistance and limited transmittance in the UV region. The increasing demand and rising cost for indium is another reason for the search for alternate systems.

Other systems that have been investigated include $SnO_2(SnO_2:Sb)$[2], zinc oxide (ZnO:Al)[3] and various compounds in the In_2O_3-Ga_2O_3-SnO_2 system [4]. Hosono and others have studied various spinel structures such as $MgIn_2O_4$, $CdGa_2O_4$, and $ZnGa_2O_4$ [5]. The criterion for the choosing of the above spinels was that these structures have MO_6 octahedra running along the [110] direction. This facilitates greater interaction among the metal (M) cation molecular orbitals due to their proximity in the absence of oxygen ions. These interactions result in a large dispersion of the conduction band leading to high mobility of the conduction electrons. The MO_6 octahedra is considered one of the determining factors for the dispersion of the conduction band. In addition, the above materials have band-gaps greater than the 3.1 eV minimum generally accepted to be the transparency limit.

The pyrochlore structure is a derivative of the fluorite structure with a 3-dimensional network of MO_6 octahedra similar to the perovskite structure. Pyrochlore oxides could be represented as:

$$A_2B_2O_6O'$$
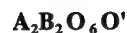
The B_2O_6 sublattice is made up of an interconnected BO_6 octahedral network with cage-like holes which contain an A_2O' sublattice. The special oxygen O' is located at the centers of the cages and may be partially or totally absent. Electrical properties have been well investigated and the 3-dimensional network of BO_6 octahedra is a believed to play a role in the enhanced conductivity of these systems.[6,7]

Recent work on the dielectric properties of thin film pyrochlore oxides has shown dielectric loss values similar to those shown in the bulk. This is in contrast to most dielectric materials, which generally

show higher loss values in thin films compared to the bulk. The mechanisms behind this phenomenon may be related to the relatively high defect densities prevalent in the thin films. Pyrochlores however have a built-in structural tolerance to defects. For example, the A-site can accommodate as much as 25% vacancies while maintaining the cubic pyrochlore structure . Alternately anion deficiency is tolerated by the special O' lattice.

Since the microscopic origins of dielectric loss and electrical mobility are not dissimilar, thin film pyrochlores could be expected to retain their high mobilities and large degree of conductivity in thin films.
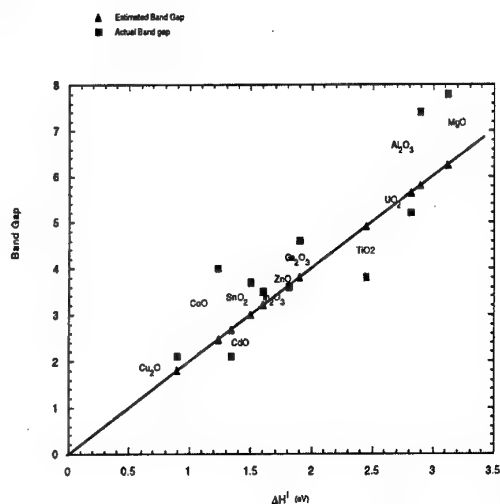
Fig1.Graph showing actual and estimated band gaps (from Vijh's model) of numerous oxides.

The optical transmissivity is to a large degree dependent upon the magnitude of the band gap. Unfortunately the literature on the band gaps of pyrochlores is sparse. Therefore in order to select pyrochlore compounds for TCO application Vijh's method of estimating band gaps from thermodynamic data was utilized [9]. In this method the thermodynamic heat of formation of the oxide is converted from kJ per mole to electron volts per bonding electron. The electronic band gap was then estimated as follows :

$$E_g \approx 2 \, \Delta H_f(oxide)$$

where ΔH_f is the heat of formation per equivalent (in eV). Figure 1 shows the band-gap of a number of oxides calculated by this method along with their actual values [9]. Discrepancies seen in Vijh's method could be due to the fact that the model assumes the compounds are completely ionic while all oxides have a certain degree of covalency.

Using known values for the thermodynamic heats of formation of binary oxides, the estimated band gap was calculated for a number of pyrochlore compounds. Some of the compounds shown in the graph above (Fig. 2) were selected from a variety of references [11] Other compounds were chosen with consideration of the geometric tolerance factor for the pyrochlore structure published by Isupov [11,12]. As can be seen, a wide range of band gaps are possible within the pyrochlore structure.

Using the graph the following four compositions were chosen for this study. These compounds have an appropriate band gap and a highly reducible ion which can generate a high density of charge carriers.

Table1 Pyrochlore compounds suitable for TCO application.

Pyrochlore composition	Estimated band gap
$Y_2Ti_2O_7$	5.6 eV
$La_2Sn_2O_7$	4.4
$La_2Zr_2O_7$	6.0
$Bi_2(Ni_{2/3} Nb_{4/3})O_7$	3.0
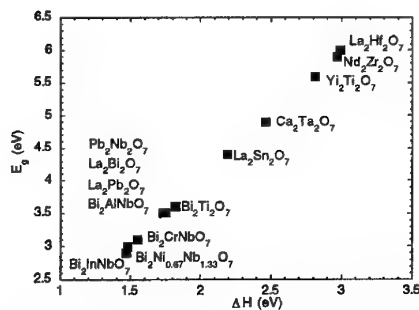
Fig2 .Band gap of known and proposed pyrochlore compounds calculated by Vijh's method.

2. EXPERIMENTAL.

A solid reaction route was used to prepare the compositions. Stoichiometric amounts of the oxides were weighed out and mixed in Nalgene bottles. The powders were milled in ethanol with zirconia media.

The milled powders were dried and ground. They were then calcined at different temperatures and x-ray diffraction analysis was used to identify the phases present.

In the case of bismuth nickel niobate, it is known that the usual $A_2B_2O_7$ does not yield a pyrochlore structure. The Ni cations can reside on both the B-sites and the A-sites. Thus, the pyrochlore composition is altered to $(Bi_{1.6}Ni_{0.3})(Ni_{0.5}Nb_{1.5})O_7$. Stoichiometric amounts of NiO and Nb_2O_5 powders were pre-reacted at 1300°C before milling with Bi_2O_3.

$Y_2Ti_2O_7$ was calcined at 950°C and 1300°C, $La_2Sn_2O_7$ at 1200°C and 1400°C, $La_2Zr_2O_7$ at 1200°C and 1450°C, and $(Bi_{1.6}Ni_{0.3})(Ni_{0.5}Nb_{1.5})O_7$ at 850°C and 950°C. All the powders were calcined for four hours at the mentioned temperatures. A Cu-α x-ray at 1.414 Å was used to perform x-ray analyses.

Preliminary optical measurements were conducted to verify the transparency of the powders in the visible spectrum. A fine coating of the powder was imbedded into a transparent polyethylene film and percentage transmittance noted with a Perkin Elmer Lamda-19 UV/VIS/NIR spectrometer.

3 RESULTS AND DISCUSSION
3.1 X-Ray Diffraction Analysis

$Y_2Ti_2O_7$, $Bi_2Ni_{.67}Nb_{1.33}O_7$ and $La_2Sn_2O_7$ showed pure pyrochlore phase after calcining at 1300°C, 1400°C and 950°C respectively. From the Figs. 2 to 5 we can observe the pyrochlore phase in the respective compositions.

$Y_2Ti_2O_7$ and $(Bi_{1.6}Ni_{0.3})(Ni_{0.5}Nb_{1.5})O_7$ showed a conspicuous [111] peak, which was, absent in the $La_2Sn_2O_7$ pattern. This has been attributed to the higher AB ordering in the $Y_2Ti_2O_7$ and $(Bi_{1.6}Ni_{0.3})(Ni_{0.5}Nb_{1.5})O_7$ structures over $La_2Sn_2O_7$. From the four

major peaks of the pure phases the lattice parameter of the pyrochlore oxides was estimated .

We were unable to create phase pure lanthanum zirconate with calcining temperatures up to 1450°C.
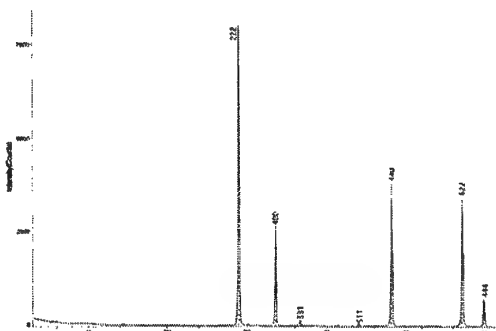
Fig 3. $La_2Sn_2O_7$ calcined at 1400°C .
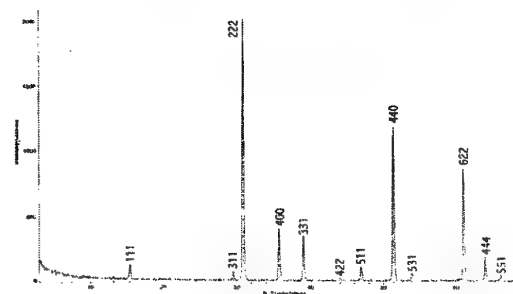
Fig 4 . $Y_2Ti_2O_7$ calcined at 1300°C.
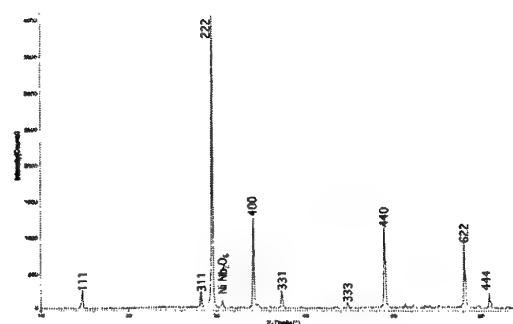
Fig5 . $Bi_2Ni_{.67}Nb_{1.33}O_7$ calcined at 950°C

Table II showing the lattice parameter of pyrochlores.

Pyrochlore Oxide	Lattice parameter
$Y_2Ti_2O_7$	10.0 A°
$Bi_2Ni_{.67}Nb_{1.33}O_7$	10.5 A°
$La_2Sn_2O_7$	10.7 A°

3.2 Optical Measurements

Preliminary transmissivity experiments of the $La_2Sn_2O_7$, $Y_2Ti_2O_7$ and $(Bi_{1.6}Ni_{0.3})(Ni_{0.5}Nb_{1.5})O_7$ showed no significant absorption in the visible spectrum verifying the transparent properties of these compounds. The transmission spectra did show a linear decrease in transmittance with decreasing wavelength which is attributed to the scattering by the powder particles. A more detailed optical analysis is pending.

4 CONCLUSIONS

Large band gap and defect structure are essential for better transparent conducting oxide thin films. These properties may be found in pyrochlores in this study. The compositions can be identified using simple thermodynamic calculations and processed by solid state reactions. Optical measurements confirm the transparent nature of these compositions. In future work thin films of these compounds will be deposited by pulsed laser deposition(PLD) from sintered targets of these powders.

REFERENCES

[1] Radhouane Bel Hadj, Takayuki Ban, Yutaka Ohya and Yastaka Takahashi, "Tin doped indium oxide thin films: Electrical Properties" *J. Appl. Phys.* Vol 83 No 5 pp 2631-2645

[2] J.L.Vossen: Physics of Thin Films, eds G.Hass, M.H.Francombe and R.W.Hoffman (Academic, New York, 1977)

[3] K.L.Chopra, S.Major and D.K.Pandra, *Thin Solid Films* 102 (1983) 1.

[4] D.D.Edwards, T.O.Mason, F.Goutenoire and K.R.Poeppelmeier, "A new transparent conducting oxide in the Ga_2O_3-In_2O_3-SnO_2 system" *Appl. Phys. Lett.* 70(13),March 1997.

[5] Kazuhiko Yanagawa,Yoshimichi Ohki,Takashisa Omata,Hideo Hosono,Naoyuki Ueda and Hiroshi Kawazoe "New Oxide Phase $Cd_{2(1-x)}Y_{2x}Sb_2O_7$ Pyrochlore with a Wide Band Gap and High Electrical Conductivity *Jap. J. Appl.. Phys.*, Vol33(1994) pp L238-L240

[6] J.E.Greedan, M.Sato, Naushad Ali and W.R.Datars, "Electrical Resistivity of Pyrochlore Compounds $R_2Mo_2O_7$ (R=Nd,Sm,Gd,Tb,Y)" *J Solid State Chem* 68, 300-306 (1987)

[7] R.A.Beyerlein,H.S.Horowitz and J.M.Longo "The Electrical Properties of A2[Ru2-xAx]O7-x (A=Pb or Bi) Pyrochlores as a Function of Composition and Temperature" *J Solid State Chem* 72, 2-13(1988)

[8] A.K.Vijh, "A Thermochemical Approach to the Bandgaps of Semiconducting and Insulating Materials" *J Mat Sci* 5 (1970) 379-382

[9] O.Kubaschewski,C.B.Alcock and P.J.Spencer "Materials Thermochemistry" 6th Edition, Pergamon Press 1993

[10] Walter A. Harrison, "Electronic Structure and Properties of Solids" Dover Publications Inc New York 1989

[11] Eugene Aleshin and Rustum Roy, "Crystal Chemistry of Pyrochlore" *J. Amer. Ceram. Soc.*, Vol 45 No1 Jan 1962pp19-2

[12] V.A.Isupov, "Geometrical Criteria of the Pyrochlore Structure Type" *Soviet Physics-Solid State*, Vol 7 1958 pp 98-99

Ferroelectric domain pinning in PZT thin film deposited on Pt and oxide buffer electrodes

Yoichiro Masuda, Shigetaka Fujita and Takashi Nishida*

Departments of Electric and Electronics Engineering, Faculty of Engineering,

Hachinohe Institute of Technology, 88-1 Oobiraki, Myo, Hachinohe, Aomori 031-8501, Japan

Fax: 81-178-30-1088 , e-mail: ymasuda@hi-tech.ac.jp

*Nara Institute of Science and Technology, Graduate School of Material Science,

8961-5 Takayama, Ikoma, Nara 630-0101, Japan

Fax: 81-743-72-6069 , e-mail: tnishida@ms.aist-naist.ac.jp

Ferroelectric thin films of $Pb(Zr,Ti)O_3$ (PZT) were prepared on platinum (Pt) and $SrRuO_3$ (SRO) thin film electrodes by laser ablation technique. Temperature, and voltage dependence, and ferroelectric degradation of the PZT thin film capacitors are investigated. As the results, it is confirmed that the distribution of remanent polarization (Pr) and coercive field (Ec) is strongly affected by homogeneity of the grain size of PZT thin film and is estimated by differentiating Pr(E) curves with respect to an applied electric field (dP(E)/dE). The remanent polarization value of PZT films deposited on an SRO electrode as a buffer layer is remained constantly more than 10^{11} switching cycles. It is confirmed that polarization switching degradation is improved by using an SRO thin film electrode as a buffer layer.

INTRODUCTION

Ferroelectric thin films have recently attracted great interest as new dielectric materials for Gbit-scale ferroelectric random access memories (FeRAMs) [1]. Many studies on synthesis of ferroelectric thin films have been made by using a laser ablation technique so far [2].

Degradation properties of the ferroelectric thin film have also been investigated. They have been explained by pinning and in-print effects associated with electronic-charge trapping and oxygen vacancies [3]. The ferroelectric degradation restricts lifetime and reliability of the devices. In order to overcome these problems, ferroelectric thin films have been grown on the oxide electrode, such as RuO_2, IrO_2 [4], $SrRuO_3$(SRO) [5] and cubic LSCO as the buffer layer. The degradation properties of the ferroelecric thin films can be improved by using oxide buffer electrodes. However, the effect of the crystalinity of the buffer layer on the ferroelectricity of the ferroelectric films is not fully understood.

In this study, PZT thin film capacitors are fabricated using Pt//Si and SRO/MgO substrates by laser ablation. The temperature and voltage dependence and ferroelectric degradation in the PZT thin film capacitors are investigated to discuss the effects of the buffer layer on the ferroelectric properties of the PZT thin film.

EXPERIMENTAL

A pulsed YAG laser (λ=1064 nm, SL805: Spectron Laser System) was used as a light source of the laser ablation, and the fourth harmonic wave (λ=266 nm) was generated using a nonlinear optical crystal (KDP: KH_2PO_4). In this study, we utilized a Pt/Si and SRO/MgO substrate as the bottom electrode substrate. The crystallinity and electric properties were presented in our previous paper [5]. Then an Au top electrode (0.3mm in diameter) were deposited on the PZT film. Characterization of ferroelectric properties of the PZT capacitors was performed by using RT-6000 (Radiant Co.). Surface morphologies of the PZT thin films were observed using Atomic Force Microscope (Digital Instruments: Nano Scope III).

RESULTS AND DISCUSSION

Figures 1(a) and (b) show surface morphologies of the PZT thin films deposited on both substrates, respectively. From these figures, it is confirmed that the PZT film deposited on the Pt/Si substrate has a rough surface which includes large grains and small sub-grains, while relatively large grains uniformly distribute in the PZT thin film deposited on SRO/MgO substrate. In our previous paper [5], dielectric constants, leakage current properties and polarization fatigue performances of PZT thin films have already been reported, and it has been confirmed that the PZT thin films deposited on the SRO/MgO show good crystallinity.

Next, we investigate the voltage dependence of the remanent polarization and coercive field in the PZT thin films. Figure 2 shows the D-E hysteresis loops for the Au/PZT/SRO/MgO thin film capacitor with varying the applied voltage. The hysteresis loops are not fully saturated even though the applied voltage is

(a) Au/PZT/Pt   (b) Au/PZT/SRO/MgO
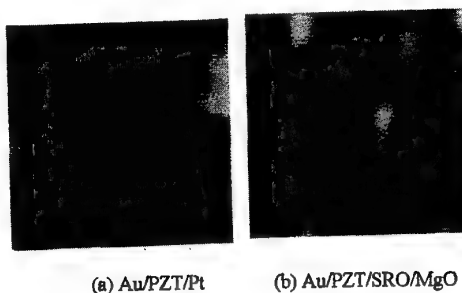
Fig. 1(a) and (b) show surface morphologies of the PZT thin films.

increased. This is because the PZT thin films consist of various sizes of grains and its composition is inhomogeneous, and the PZT thin films consist of crystallite with different coercive field and remanent polarization. Then, we measured the voltage dependence of the remanent polarization and coercive field in the PZT thin films and are shown in Fig. 3 and 4. From these results, distribution of the remanent polarization and coercive field is confirmed. The curve immediately increases up to around 200 kV/cm, then slightly increases. Therefore, we estimate the remanent polarization (Pr) and coercive field (Ec) at the inflection point as a typical value. Pr and Ec are calculated to be Pr=13.7 $\mu C/cm^2$ and Ec=69.2 kV/cm at 140 kV/cm for Au/PZT/SRO/MgO capacitor, and Pr=5.1 $\mu C/cm^2$ and Ec=94.7 kV/cm at 180 kV/cm for the Au/PZT/Pt capacitor, respectively. The PZT thin
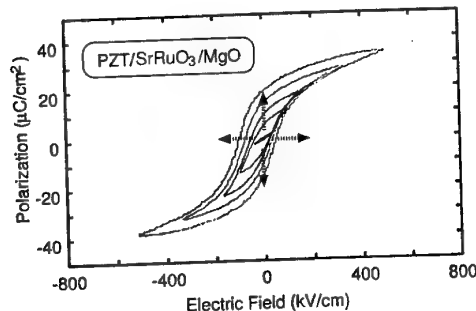
Fig.2 The applied electric field dependence of D-E hysteresis curve for the Au/PZT/SRO/MgO.

Fig.3 The applied electric field dependance of Pr.

grain size of the PZT thin film deposited on Pt thin film in coercive field can arise from the grain size of the

Fig.6 The temperature dependence of D-E hysteresis curves for the PZT film.
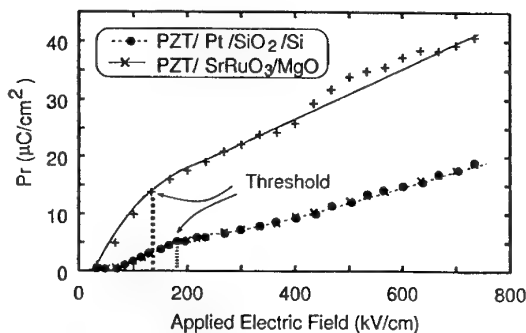
film capacitor deposited on SRO/MgO substrate is useful for device application, since it has large Pr and
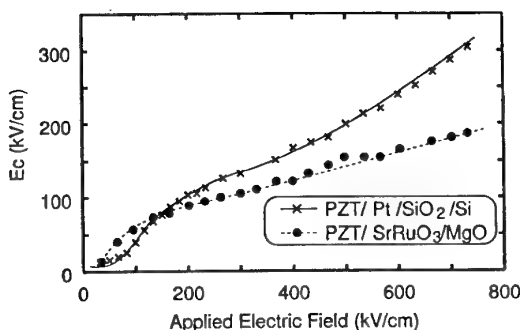
Fig.4 The applied electric field dependence of Ec.

small Ec properties. The difference in the remanent polarization seems to be caused by the preferential ordering and crystallinity of the PZT thin films deposited on the SRO and Pt electrode. The difference
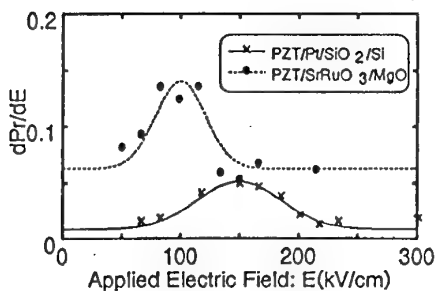
Fig.5 The applied voltage dependence of dPr/dE.

PZT films deposited on the SRO and Pt electrode. From AFM observations, as shown in Fig. 1(a), the becomes smaller than that deposited on the SRO film. Therefore, the coercive field of the PZT film deposited on Pt electrode becomes higher than that deposited on the SRO electrode. Furthermore, to discuss distribution of the remanent polarization of the PZT thin film capacitors, we differentiate Pr(E) with respect to an applied electric field, and is shown in Fig. 5. As it can be in the figure, the peak of dPr(E)/dE curve exists at 160 kV/cm and 100 kV/cm for the Au/PZT/Pt and Au/PZT/SRO/MgO capacitor, respectively. The FWHM (full width at half maximum) of the dPr/dE curves are 90 kV/cm (Au/PZT/SRO/MgO) and 150 kV/cm (Au/PZT/Pt). These results can also be explained by uniformity of the gain size of the PZT thin films from AFM observations.

From these results, it is clarified that the remanent polarization and coercive field are widely varied by the applied electric fields. In order to compare the remanent polarization and coercive field of different films, it seems to be useful to determine from dPr/dE curves.

Figure 6 shows the temperature dependence of the D-

polarization and coercive field of PZT deposited on Pt electrode are increased by the leakage current due to poor crystallinity of the film. As the temperature increases, grains of which polarization reversed also increases. As a result, distribution of the remenent polarization and coercive field move toward lower electric filed in Fig. 3 and 4.

On the other hand, the temperature dependence shows contrary properties for the case of PZT deposited on SRO/MgO substrate; that is the remanent polarization decreases with increasing the temperature. In order to explain this effect, we consider the residual stress of the PZT films. Since a thermal expansion coefficient (α) of the MgO thin film is relatively large ($\alpha_{MgO}=14ppm$ /K), the large residual stress should lie on the surface of PZT thin film at room temperature. There is a preferred orientation along the c-axis, since the a-axis is shorter than the c-axis. Under this condition, as the temperature increases, the stress can be relieved. As the result, the domains with a-axis orientation may increase compared to that with c-axis orientation. Therefore the Pr decreased with increasing the temperature. Furthermore, the remanent polarization value of PZT films deposited on an SRO electrode as a buffer layer is remained constant by more than 10^{11} switching cycles. It is confirmed that polarization switching degradation is improved by using an SRO thin film electrode as a buffer layer.

CONCLUSIONS

In conclusion, we have fabricated PZT thin films using Pt and SRO thin films as a buffer electrodes layer by fourth harmonic wave ($\lambda=266$ nm) of a pulsed Nd$^+$:YAG laser ablation technique. From XRD measurements and AFM observations, it is confirmed that crystallinity of the PZT thin films deposited on the SRO thin film electrode was improved. The temperature dependence of ferroelctric properties in PZT film capacitors are strongly affected by the buffer electrodes. The hysterisis properties are caused by various grains with different remanent polarization and coercive filed. Homogeneity of the grain size also affects on the distribution of the remanent polarization and coercive field. Furthermore, temperature dependence properties of the PZT films shows contrary properties in Pt and SRO buffer electrodes and they seems to be able to explained by the residual stress of the buffer films.

References

[1] J. F. Scott, F. M. Ross, C. A. Pa de Araujo, M. C. Scott and M. Huffman, Mat. Res. Bull., **21**, 33-39 (1996).

[2] Y. Masuda, S. Fujita, A.Baba, H. Masumoto and T. Hirai, Jpn. J. Appl. Phys., **36**, 5834-5839 (1997).

[3] M. Kohli, P. Muralt and N. Setter, Appl. Phys. Lett., **72**, 3217-3219 (1998).

[4] T. Nakamura, Y. Nakao, A. Kamisawa and H. Takasu, Appl. Phys. Lett., **63**, 1522-1524 (1994).

[5] Y. Masuda, S. Fujita, T. Nishida, H. Masumoto and T. Hirai, Proc. of ISAF98 (to be published).

Advances in "Low-Fire" Dielectric Technology for the Manufacture of MLCC and Comparison with Base Metal Electrode Technology

L.A. Mann
KEMET Electronics Corporation
P.O. Box 849
201 Fairview Street Extension
Fountain Inn, SC 29644-0849 USA

INTRODUCTION

The number of multilayer ceramic capacitors (MLCC) used each year in the manufacture of electronic products has grown at a phenomenal rate in the past decade. According to data collected by the EIA, sales of MLCC increased by an astonishing 400% in just six years, from 90 billion units in 1992 per year to 360 billion units in 1998.

In addition to rapid growth, the MLCC industry has been the subject of several other driving factors. These include demand for higher volumetric efficiencies, improved reliability, and reduced costs. Additionally, there has been growing demand for high capacitance value MLCC (1-10 uF) for use in high frequency digital circuits. This is due to the low equivalent series resistance (ESR) of MLCC as compared to tantalum capacitors, which have been the dominant technology for these capacitance values in the past.

The key to improving volumetric efficiency in MLCC is achieving larger numbers of ever thinner dielectric layers without compromising product quality or reliability. This, of course, also means using more and more layers of internal electrodes. Successfully producing MLCC with high volumetric efficiencies requires careful selection of dielectric and electrode materials and meticulous attention to the details of MLCC manufacture.

Traditionally, electrodes for MLCC have been made from precious metals, especially palladium (Pd) and palladium-silver alloys (Pd-Ag). MLCC made with these electrode materials can be fired in air as long as the firing temperature is kept below the electrode melting temperature. So-called "High-Fire" MLCC use 100% Pd electrodes and ceramic dielectrics that fire at 1300-1350 °C, typical of the firing temperature for

barium titanate (BT), the most common ceramic dielectric material. "Low-Fire" MLCC, on the other hand, are made from BT that has been doped with fluxes and/or sintering aids that reduce the firing temperature to less than 1150 °C, allowing Pd-Ag alloys with no more than 30% Pd to be used as electrode materials, thereby reducing electrode related costs. The use of "High-Fire" MLCC technology has predominated in Japan, while "Low-Fire" MLCC technology has prospered in the United States.

The increasing price of Pd over the past two years, from $100-$150 per T. oz. to over $300 per T. oz in recent months, has intensified efforts to either reduce Pd usage or replace Pd containing electrodes with nickel (Ni) and in some cases copper (Cu). Pd usage can be reduced by either converting to more silver rich Pd-Ag alloys (via reduction of the firing temperature of the associated dielectrics) or reducing the thickness of the electrodes (which results in other benefits as well, described later). The technology for using either Ni or Cu electrodes in MLCC is commonly referred to as Base Metal Electrode, or BME, technology. BME technology has received much attention in recent years, and significant advances have been made in overcoming the key challenges it presents. The most important of these is the ability to fire MLCC in the reducing atmospheres required for Ni or Cu electrodes without severely degrading their performance and reliability as result of the formation of oxygen vacancies and other defects in the dielectric. (1)

In this paper, the results of efforts to enhance the performance and reduce the cost of MLCC manufactured using "Advanced Low-Fire" technology are discussed. MLCC with X7R characteristics manufactured using state of the art "Low-Fire"

technology are compared to similar MLCC made with BME technology. Factors discussed include physical characteristics, electrical performance, reliability, and cost.

"LOW-FIRE" MLCC TECHNOLOGY

BT compositions with X7R and Y5V characteristics that fire at about 1100- 1150 °C have been used to manufacture high quality MLCC for many years. This "Low-Fire" MLCC technology is made possible by sintering aids which are added to BT based dielectric formulations, lowering their optimum firing temperature to 1150 °C or less. Common sintering aids include fluxes such as bismuth oxide or glasses such as lead-boro-silcate or lead-zinc-borate. "Low-Fire" dielectric systems typically have slightly lower dielectric constants, and larger and less uniform grain sizes than "High-Fire" systems, but at the same time can possess higher mechanical strength. (2) For dielectrics thinner than about 5 microns, the larger grains in MLCC made with traditional "Low-Fire" technology can lead to reduced breakdown voltages and degraded life performance.

Traditional "Low-Fire" materials consist of mixtures of BT and dopant powders, along with particles comprising the sintering aids. The grain structure of "Low-Fire" dielectric systems has been greatly improved by advances in powder preparation techniques which yield fine, uniform particles of BT that are coated with dopants and sintering aids. The surface chemistries of the coated dielectric systems can be tailored to make them compatible with water based binder systems, eliminating the need for organic solvents in the manufacture of the dielectric layers. High quality dielectric films as thin as 2 microns have been manufactured with these materials using water based binder systems.

The fine, uniform grain structure that can be achieved is evident in the photos in Figure 1, which show the grain structure of dielectric layers produced from commercial "Advanced Low-Fire" X7R compositions from Degussa and Cabot, respectively. (3,4)

As dielectric thickness is decreased, it is also desirable to reduce electrode thickness. Thin electrodes minimize stresses in the MLCC that can result from the differences in the thermal expansion coefficient and thermalconductivity of the metal electrode and ceramic dielectric layers. Thinner electrodes also make processing of the multilayer structure less difficult, as
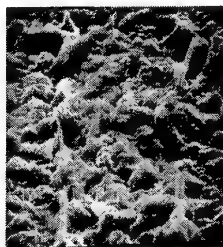
Figure 1a. 5 micron X7R dielectric from Degussa powder.
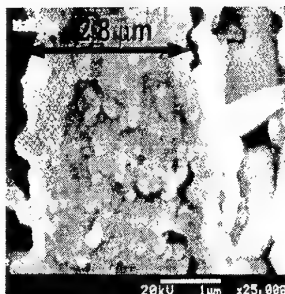
Figure 1B. 2.8 micron dielectric layer from Cabot powder.

the difference between the accumulated height in the active and margin areas of the structure is reduced as the electrodes are made thinner. In the case of "Low-Fire" MLCC with Pd-Ag electrodes, using thinner electrodes is also of primary importance in reducing manufacturing cost.

MLCC electrodes must possess sufficiently high conductivity in order to provide low dissipation factor (Df), low ESR, and high capacitance. The graph in Figure 2 shows a plot of capacitance verses electrode thickness, using arbitrary units, for incrementally thinner electrodes in a traditional "Low-Fire" dielectric and electrode system.
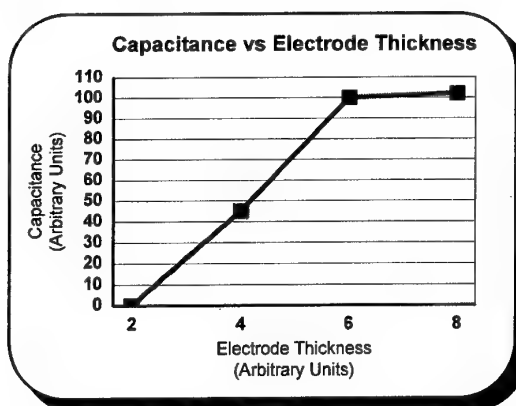
Figure 2. Capacitance vs Electrode Thickness Using Standard Pd-Ag Technology (25% Pd, 75% Ag)

The behavior exhibited in Figure 2 is typical for all electrode and dielectric systems ("Low-Fire", "High-Fire", and BME). Below a critical electrode thickness, the capacitance is lower, the Df and the ESR are higher. These undesirable characteristics are a result of the electrodes becoming discontinuous during the firing process. During the firing of the MLCC, the metal particles that make up the electrode sinter together. Following classic sintering behavior, smaller particles are consumed by larger particles. Above the critical electrode thickness, the resulting electrode maintains sufficient conductivity over the entire electrode area, but below the critical thickness, the electrode becomes discontinuous, and effective electrode area (that which remains electrically continuous) is diminished. The critical electrode thickness is a function of the chemical and physical nature of both the electrode and dielectric systems used, and the process conditions during firing-primarily the time and temperature profiles, but also the atmosphere. The interfacial energies at the metal-ceramic interfaces must certainly play a key role in determining the electrode structure and critical electrode thickness as well.

By studying Pd-Ag metal powders with many different characteristics (including particle size distribution, morphology, and degree of crystallinity), in conjunction with many different ceramic additives (again with varying composition, particle size and crystallinity), it has been found that the critical electrode thickness can be significantly decreased. The graph in Figure 3 shows the dramatic reduction in electrode thickness that has been achieved using advanced 25% Pd/75% Ag electrode technology.
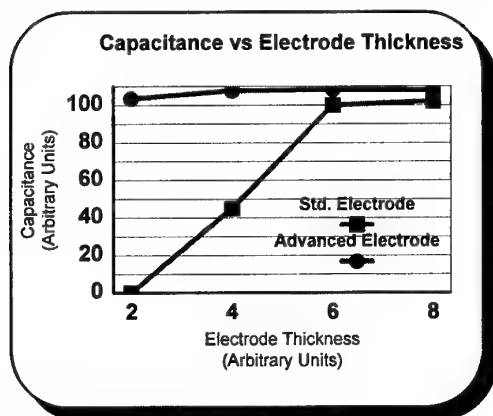
Figure 3. Capacitance vs Electrode Thickness Using Advanced Pd-Ag Technology (25% Pd, 75% Ag)

Combining the "Advanced Low-Fire" dielectric and electrode technologies described above results in MLCC with surprisingly high volumetric efficiencies and outstanding performance, at lower than expected costs. Photos showing X7R 1206 (EIA) size 1.0 uF and 1206 (EIA) size 4.7 uF MLCC made with "Advanced Low-Fire" technology are shown in Figure 4.

Figure 4a.

Figure 4b.

Figure 4. (a) 1206 1.0 uF 16v X7R chip made with Degussa dielectric (b) 1206 4.7 uF 10v X7R chip made with Cabot dielectric

BASE METAL ELECTRODE (BME) MLCC TECHNOLOGY

Detailed discussions of dielectric and electrode materials for BME MLCC can be found elsewhere, as can discussions of the effects of processing on BME MLCC performance and reliability (1, 5, 6, 7). Before comparing BME MLCC to their "Low-Fire" counterparts, however, it is worth noting some of the differences between the two.

BME dielectric materials must generally be of higher purity than their "Low-Fire" counterparts, because of the importance of maintaining precise stoichiometry in order to prevent the formation of oxygen vacancies and other defects when fired in a reducing atmosphere. Rare-earth dopants, such as yttrium, dysprosium, and holmium, are commonly added to BME dielectric formulations in order to improve their long term reliability.

Electrodes for BME MLCC are typically thicker than for "Low-Fire" MLCC. Nickel electrodes inevitably have nickel oxide layers at both dielectric interfaces, thus diminishing the thickness of the conductive nickel layer. Therefore, thicker layers of Ni must be deposited in order to maintain the conductivity of the electrodes in the multilayer structure. A review of BME product currently available failed to reveal any Ni electrodes as thin as 1 micron. This is three to four times the thickness of state of the art Pd-Ag electrodes.

A key difference between BME and "Low-Fire" MLCC is that BME MLCC must be fired in a reducing atmosphere in order to prevent complete oxidation of the Ni electrodes, where as "Low-Fire" MLCC are fired in air. Typical firing conditions are 1250-1350 °C, in a nitrogen-hydrogen-water vapor atmosphere with oxygen partial pressures of 10^{-10} atmospheres or less. These conditions require expensive kilns with sophisticated process control. A re-oxidation step is also required for BME MLCC in order to replenish some the oxygen lost during the firing step. These added capital equipment expenses and the costs of operating the kilns with a reducing atmosphere offset some of the potential cost savings of the nickel electrodes. Differences in performance and reliability will be discussed later.

COMPARISON OF PERFORMANCE

The performance of X7R 1206 1.0 uF 16v MLCC made with an "Advanced Low-Fire" technology has been studied extensively and compared to the performance of similar MLCC made with BME technology. One of the BME products used for comparison was manufactured in-house, the other two samples were manufactured by other suppliers. Typical fired dielectric thickness for these products ranged from 8-9 microns, and the products contained from 95-115 dielectric layers dielectric layers. Photos of each are shown in Figure 5 below.
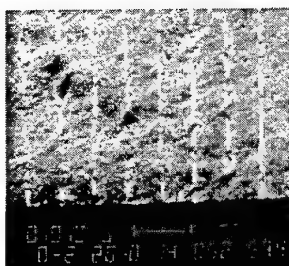
Figure 5a. Sample A- "Advanced Low-Fire"
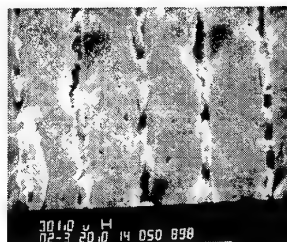
Figure 5b. Sample B- In-house BME
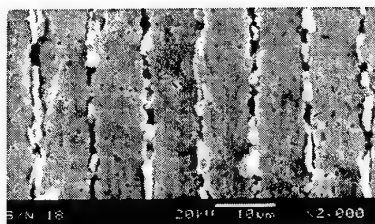
Figure 5c. Sample C- BME from Supplier C
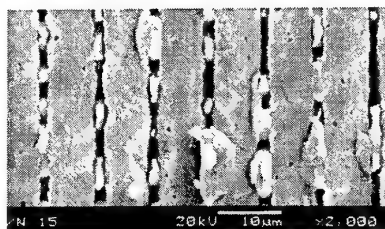
Figure 5d. Sample D- BME from Supplier D

Performance characteristics that have been studied include:

• Dielectric Breakdown Voltage
• Mechanical Strength
• Life Tests
• HALT (Highly Accelerated Life Test)

Dielectric Breakdown

The average breakdown strength for the "Advanced Low-Fire" MLCC (A) was 750 volts, or about 90 volts/micron. The three BME products (B, C, and D) had average breakdown strengths of 600, 530, and 700 volts or 75, 60, and 100 volts/micron, respectively. The normalized dielectric breakdown strength for the "Advanced Low-Fire" MLCC was higher than for all but one of the BME MLCC. Subjectively, the samples

with higher breakdown strength appeared to have less porosity in the dielectric.

Mechanical Strength

Modulus of Rupture (MOR) is one useful measure of mechanical strength (8), and was used to compare the four samples studied. The MOR of the "Low-Fire" MLCC (A) was about 320 MPa, while the MOR of the BME samples (B, C, and D) was determined to be 375, 420, and 290 MPa, respectively. This places the "Low-Fire" product in the lower range of observed mechanical strength.

It is interesting to note that there appears to be an inverse relationship between mechanical strength and normalized dielectric breakdown strength in these four samples. Product from manufacturer D had the highest normalized breakdown strength, but the lowest mechanical strength. Product from manufacturer C had the lowest normalized breakdown strength, but the highest mechanical strength.

Life Tests

Standard life test conditions for X7R product include

- 125 °C at rated twice rated voltage for 1000 hours
- 85 °C/85 % RH at rated voltage for 1000 hours
- 85 °C/85% RH at 1.5 v for 240 hours

Samples consisting of 100 MLCC from each of the four product groups were tested under each condition, with no failures observed.

HALT

One of the key concerns with MLCC made with BME technology is long term life performance. (Ref) It has been shown that oxygen vacancies created during firing in a reduced atmosphere can degrade the long term performance of MLCC. In order to study this phenomena, a common method is to use highly accelerated life tests (HALT). The HALT conditions used in this study were 140 °C, 224 volts (14 time rated voltage), for 92 hours. Multiple fifty (50) piece samples from each product type were tested, and the leakage current to each component was monitored continuously during the test. If the leakage current of an individual device reached 100 micro-amps, it was considered to have failed and the device was automatically disconnected from the test circuit.

MLCC produced using the "Advanced Low-Fire" technology (A) typically had from zero to 3 failures on this test, with the failures occurring at random times. The failures appeared to be due to dielectric breakdown. The behavior of the BME products from each of the three manufacturers studied were dramatically different. Product from group B typically had from 20-30 failures by the end of the test, and product from group D typically had from 40-50 failures by the end of the test. The failures were distributed in time and the behavior appears to be consistent with a failure mode associated with migration and accumulation of oxygen vacancies at the cathodic electrodes, as proposed by Ikeda et al. (9) Product from group C could not be tested at these conditions, because the leakage current at 224 volts and 140 C for these MLCC exceeded the test limit.

The graph in Figure 6 shows the cumulative failure rates for typical samples from product groups B and D.

HALT Performance (224v/140C/92 hrs)
1206 1.0 uF 16v rated MLCC
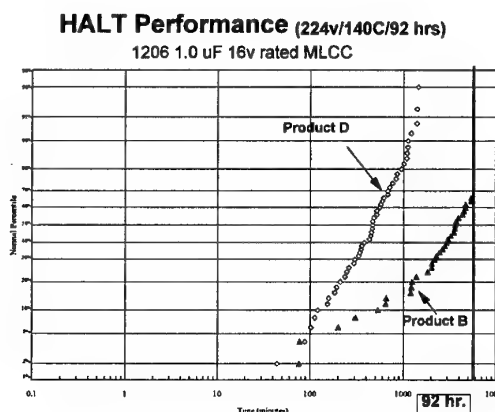
Figure 6. HALT Performance of Two BME MLCC Products

In summary, the most significant difference between the performance of product made using "Low-Fire" and BME technology was found to be their behavior on HALT. Many other MLCC products made with Pd-Ag electrodes have been studied using these same HALT conditions, with only small numbers of random failures observed. For MLCC made with BME technology, a wide range of performance has been observed. It is believed that the differences in performance of BME MLCC on HALT are a result of differences in dielectric chemistry and the conditions in which they are fired and re-oxidized. No industry standard for HALT

performance has been adopted, and each manufacturer has apparently established their own standard of acceptable performance. How HALT performance at these extreme conditions relates to product reliability under actual conditions of use remains an important and largely unanswered question.

COMPARISON OF COST

Cost is the key driver for the development and use of BME technology. High capacitance MLCC with large numbers of electrodes can be especially expensive to manufacture with Pd-Ag or Pd electrodes, due to the large amount of electrode material required. For low capacitance value products containing few electrodes, the cost of the electrode material is a small portion of the overall cost of production. The cost for these products are predominantly influenced by the cost of the other materials (dielectric, termination) and the costs of labor, capital, and expense.

Dielectric materials for BME are typically more expensive than for traditional "Low-Fire" materials. The main reason for this is that BME technology requires higher purity raw materials and more stringent control of dielectric chemistry in order to maintain consistent performance and reliability. Dielectric materials for "Advanced Low-Fire" materials, however, are also expensive relative to traditional "Low-Fire" dielectric materials. In this case, the higher cost is associated with the tight compositional and particle morphology control that is required to maintain the fine, uniform grain structure that sets the advanced materials apart from their traditional "Low-Fire" counterparts.

The general picture that emerges is that traditional "Low-Fire" technology is the lowest cost route for MLCC with only a few electrodes. For these products, the low cost of the ceramic material and low capital equipment and operational costs for traditional "Low-Fire" technology are the key factors. As the number of electrodes in the MLCC increases, at some point the advantages of higher breakdown strength and ability to produce thinner dielectric layers for a given voltage rating make the "Advanced Low-Fire" materials the technology of choice. In this category, the low cost of capital (relative to BME technology) and reduced requirements for electrode materials (relative to traditional "Low-Fire" technology) are the key factors. For MLCC products with very large numbers of electrodes, BME technology becomes the lowest cost alternative. For these products, the reduced electrode costs more than offset the additional capital and

operational costs associated with BME technology, as compared to "Advanced Low-Fire" technology. The economic break points for each transition depends on many factors, but the primary factors are the cost of palladium, the cost of the dielectric materials, and the cost of capital equipment for each process.

The breakpoint between traditional and advanced "Low-Fire" systems is not of major importance, but the breakpoint between "Advanced Low-Fire" and BME technologies is a subject of much discussion. If one assumes that the dielectric costs are essentially the same, then the three dominant factors that must be considered are:

1. Amount of Palladium Required to Produce Electrodes
2. Price of Palladium
3. Capital and Operational Costs

An analysis comparing "Advanced Low-Fire" and BME technologies using what are believed to be "state of the art" capabilities for each technology has been conducted, with the following conclusions. With palladium at $350/T.oz, the breakeven point between the two technologies is at about the 0.1 uF value for X7R MLCC. The breakpoint is only a weak function of chip size, and will be at slightly higher capacitance values for Y5V MLCC than for X7R. This is an interesting result because of the large popularity and high industry usage rate of 0.1 uF MLCC. Higher prices for palladium shift the breakpoint to lower capacitance values, and lower prices shift the breakpoint to higher capacitance values.. If one considers palladium at a price of $130/T.oz, which is near its long term value, the breakpoint shifts to about 1.0 uF for X7R MLCC.

CONCLUSIONS

1. High capacitance MLCC with excellent performance characteristics can be manufactured using either "Advanced Low-Fire" or BME technology.

2. Recent developments have significantly reduced the amount of palladium required to produce MLCC using "Low-Fire" dielectric technology, enhancing its cost competitiveness relative to BME Technology.

3. "Advanced Low-Fire" technology can be used to produce MLCC with 5-9 micron thick dielectric layers that have better performance under highly accelerated

conditions than similar MLCC made with BME technology.

4. The performance of MLCC made with BME technology under highly accelerated conditions varies widely from manufacturer to manufacturer. These differences are believed to be primarily due to the differences in dielectric chemistries and firing conditions employed in their manufacture.

5. Given the high cost of palladium, BME technology offers the lower cost route for manufacture of high capacitance value MLCC.

6. For applications in which long term reliability is a critical concern, the relationship between performance of BME MLCC on HALT and under actual conditions of use must be better understood.

REFERENCES

1. T. Nomura, T. Arashi, A. Sato, Y. Nakano, S. Sato, Proceedings of 8th US-JAPAN Seminar on Dielectric and Piezoelectric Ceramics, Plymouth, MA (1997) 148.

2. J. Bergenthal, "Mechanical Strength Characteristics of Multilayer Ceramic Capacitors", CARTS 1991.

3. D.K. Swanson, S.A. Bruno, I. Burn, K. Sasaki, and H.E. Bergna, Proceedings of the Center for Dielectric Studies Symposium on Improvement of Multilayer Ceramic Reliability, State College, PA (1991) 68.

4. J.J. Beeson, L.A. Mann, S. Venigalla, and S.A. Costantino, Proceedings of 8th US-JAPAN Seminar on Dielectric and Piezoelectric Ceramics, Plymouth, MA (1997) 180.

5. A. Hitomi, X. Liu, T.R. Shrout, and C.A. Randal, Proceedings of 8th US-JAPAN Seminar on Dielectric and Piezoelectric Ceramics, Plymouth, MA (1997) 44.

6. S. Sato, Y. Nakano, A. Sato, and T. Nomura, Proceedings of 8th US-JAPAN Seminar on Dielectric and Piezoelectric Ceramics, Plymouth, MA (1997) 161.

7. H. Shoki, H. Matsushita, Y. Nakano, H. Ogawa, A. Onoe, Y. Yamashita, and H. Kanai, Proceedings of 8th US-JAPAN Seminar on Dielectric and Piezoelectric Ceramics, Plymouth, MA (1997) 176.

8. C.R. Koripella, Proceedings of Electronic Components and Technology Conference (ECTC 1991) 457.

9. M. Ikeda, Y. Izumi, M. Yoshida, Y. Nakano, K. Nishiyama, S. Sumita, and T. Namura, Proceedings of the Center for Dielectric Studies Symposium on Improvement of Multilayer Ceramic Reliability, State College, PA (1991) 87.

Research Trends of Relaxor Ferroelectric Materials in Japan

Noboru Ichinose

Waseda University, 3-4-1 Ohkubo Shinguku-ku Tokyo, 169-8555, Japan

Fax: 81-3-3200-2567, E-mail: ichinose@mn.waseda.ac.jp

Research trends of relaxor ferroelectric materials in Japan are reviewed. Among the relaxor $-PbTiO_3$ materials, $Pb(Sc_{1/2}Nb_{1/2})O_3 - Pb(Mg_{1/3}Nb_{2/3})O_3 - PbTiO_3$ ($PSN - PMN - PT$) ceramic material exhibits excellent piezoelectric properties near the MPB, such as $k_p > 70\%$, $k_t > 54\%$, $k_{33} > 77\%$, $d_{33} > 500pC/N$ and $T_c = 160 - 260°C$. The ceramic has superior piezoelectric properties as compared with conventional PZT ceramics, which so far have been thought to be the best binary piezoelectric ceramic materials. One of the big advantage relaxor $-PT$ systems compared with PZT is the case with which single crystals of the MPB composition can be grown. These single crystals generally have superior properties compared with the ceramics if appropriate axis is utilized. The advantage and disadvantage of relaxor $-PT$ systems are compared with PZT.

1. INTRODUCTION

Many published works have already shown that the complex perovskites such as lead scandium niobate $Pb(Sc_{1/2}Nb_{1/2})O_3$ (PZN), lead magnesium niobate $Pb(Mg_{1/3}Nb_{2/3})O_3$ (PMN), lead nickel niobate $Pb(Ni_{1/3}Nb_{2/3})O_3$ (PNN), and lead zinc niobate $Pb(Zn_{1/3}Nb_{2/3})O_3$ (PZN) exhibit interesting ferroelectric properties. These are typical relaxor ferroelectric materials and show diffuse phase transitions at $90°C$, $-10°C$, $-120°C$, and $140°C$, respectively. In solid solution with the simple tetragonal perovskite $PbTiO_3$ (PT), which has a nomal ferroelectric transition at $490°C$, the existence of a morphotropic phase boundary (MPB) in the $PSN-PT$, $PMN-PT$ and $PZN-PT$ binary systems has been reported. The MPB separating the rhombohedral (pseudo cubic) and tetragonal phases, which is similar to $PbTiO_3 - PbZrO_3$ (PZT), has been reported to occur at $42mol\%$, $32mol\%$ and $9mol\%$ PT content, respectively. Attractive dielectric and piezoelectric properties have been reported in the vicinity of the MPB in $PSN-PT$, $PMN-PT$ and $PZN-PT$ binary systems in ceramic and single crystal forms.

Especially in the single srystal form, $PMN-PT$ and $PZN-PT$ binary systems have been found to exhibit longitudinal coupling coefficients $k_{33} > 90\%$, thickness coupling $k_t > 63\%$, dielectric constants ranging from 1000 to 5000 with low dielectric loss $< 1\%$ and exceptional piezoelectric coefficients $d_{33} > 2000pC/N$, which are promising properties for ultrasonic transducers.[1] Recently,

Yamashita et.al.[2] have successfully prepared single crystal of the $(1-x)Pb(Sc_{1/2}Nb_{1/2})O_3 - xPbTiO_3$ (PSNT) binary systems by a flux method using $75mol\%$ $PbO - 25mol\%$ B_2O_3 flux. Chemical analysis and X-ray studies revealed that the crystals are of perovskite structure with x = 0.33, making them slightly different from the charged MPB composition of x = 0.42. The (001) single crystal has a dielectric constant peak of 60,000 at 206°C and an electrcomechanical coupling factor k_{33}=72%.

Although there are many attractive dielectric and piezoelectric data for the binary systems, the physical and electrical properties of the $Pb(Sb_{1/2}Nb_{1/2})O_3$ based ternary system such as $PSN-PMN-PT$ and $PSN-PZN-PT$ have not been elucidated so far. The purpose of this paper is to review the dielectric and piezoelectric properties of the $PSN-PMN-PT$ and $PSN-PZN-PT$ ternary ceramic system in vicinity of the MPB in detail. Furthermore, the advantages and disadvantages of these systems compared with PZT system are also discussed. For single crystal piezoelectrics such as $PMN-PT$, $PZN-PT$ and $PSN-PT$ systems which will be the next generation materials of transducers, crystal growth device fabrication and testing are also discussed.

2. EXPERIMENTAL

Details of the procedure used to prepare the ceramic samples are described in the elsewhere[3]. Calcination was performed in two steps. In first step, scandium niobate ($ScNbO_4$),

magnesium niobate (MgNb$_2$O$_6$), zinc niobate (ZnNb$_2$O$_6$) and nickel niobate (NiNb$_2$O$_6$) were prepared using columbite process.[4] After wet-mixing the starting materials using a plastic ball mill with 5 mm ZrO$_2$ balls, the slurry was dried. In second step, the mixture was calcined at 800°C for 2 h in air. The calcined cake was then ball-milled in the same mill for 24 h. Pellets 18 mm in diameter and 1.5~3 mm in thickness were pressed at 1000kg/cm^2. After burnout the binder, the samples were sintered at a temperature of 1050~1275°C for 3~4 h in the MgO crucible. Usually the suitable sintering temperature for the PSZNT system is lower temperature (150~200°C) than that of the PSMNT and PSNNT system which is due to PbO liquid sintering. Single crystals of the relaxor – PT binary system were prepared by the flux method. In the case of PSNT, 75 mol% PbO – 25 mol% B$_2$O$_3$ flux was effective for growing relatively large crystals.

For the ceramic materials, the fired density was measured using the Archimedes method. Grain size was determined by the linear intercept method on the fired surface as observed by a scanning electron microscope (SEM). The crystallografic study was performed by X–ray diffraction (monochromatized CuKα radiation). Capacitance was measured using same impedance analyzer at room temperature. The dielectric constant was calculated from the capacitance at a frequency of 1 kHz.

For the electrical and piezoelectric measurements, disk specimens 18 mm in diameter and 1.0 in thickness were formed from the sintered ceramics and Au–coated at 700°C for 5 min. The specimens were immersed in silicone oil and poled in a 3 kV/mm field. The electric field was applied at a temperature of 125°C for 15 min, and the specimens were cooled to 30°C in the field. After 24 hours of aging at room temperature, electromechanical coupling factors were measured using an impedance analyzer (HIP – 4192A) by the resonance – antiresonance frequency method. The standards of the Electronic Materials – Association of Japan (EMAS – 6100) were adapted in these measurements[5].

3. RESULTS AND DISCUSSION

3.1 Pb(Sc$_{1/2}$Nb$_{1/2}$)O$_3$ – Pb(Mg$_{1/3}$Nb$_{2/3}$)O$_3$ – PbTiO$_3$ Ceramic System[6]

In the PSMNT ternary system, the MPB locates

almost linear region between PSMNT 58/00/42 (PSNT 58/42) and PSMNT 00/68/32 (PMNT 68/32) compositions in each binary system. Among the MPB, an amount 100% perovskite phase is obtained except at PSMNT 00/68/32 where the perovskite phase is 98%. The densities, ranging from 7.6 to 7.8 are better than 97% of theoretical values a calculated from the lattice constants. Fired grain sizes 3~5 micron.

Fired PSMNT 28/33/38 indicates a rhombohedral (R) phase, while PSMNT 29/30/41 has a tetragonal (T) phase. However, compositions from PSMNT 29/36/35 to 29/33/38 exhibit three different peaks, representing a mixture of the rhombohedral and the tetragonal phases.
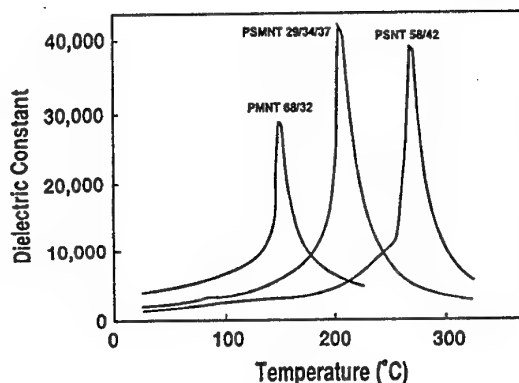
Fig. 1   Dielectric properties of PSMNT ceramic system

Dielectric properties of the PSMNT ceramics are shown in Fig. 1. The composition PSMNT 29/34/37 shows a large dielectric constant of 42,000. It is found from these data that the Curie temperature varies from 150°C to 260°C as a function of the PSNT composition. Figure 2 indicates the remanent polarization, Pr and coercive field, Ec of PSMNT ceramics. Pr values are more than 35 μC/cm^2 which are slightly larger than for PZT ceramics. The electromechanical coupling factor, kp for PSMNT ceramics are given in Fig.3. The largest electromechanical coupling factors (kp =72%, k_{31}=45% and k_{33}=77%) was observed in the PSMNT 29/34/37 composition, where $\varepsilon^T_{33}/\varepsilon_0$=3,000, d_{33}=640pC/N and Tc =205°C were obtained. The maximum piezoelectric constant, d_{33}=680pC/N, was found at PSMNT 29/33/38, where $\varepsilon^T_{33}/\varepsilon_0$=3,800, and electro-
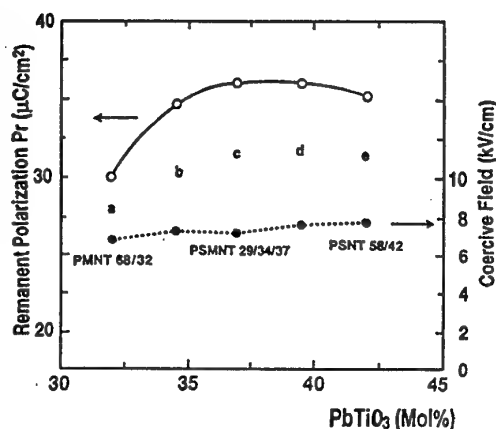
Fig. 2   Remanent polarization, *Ps* and
coercive field, *Ec*   of the PSMNT
ceramics

Fig. 4   Distribution of dielectric constant
at room temperature in the PSZNT
system

Fig. 3   Electromechanical coupling factor
kp in the PSMNT ceramics
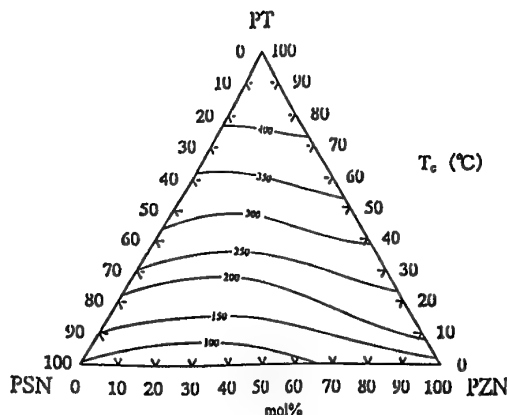
Fig. 5   Distribution of Curie temperature
in the PSZNT system

mechanical coupling factors (kp=70%, k_{31}=43%
and k_{33}=76%) and Tc=270℃ were obtained.
One mol% composition difference of the peak
value of dielectric constant and kp is observed.
These characteristics are similar to those of
PZT.[7]

The PSMNT 29/35/36 composition, near the
MPB has the lowest Poisson's ratio of 0.18.
This is lower than that of a modified PT
ceramic. The lower Poisson's value is reported
for the PSNT system[8] and may be due to
higher coupling factors.

3.2 $Pb(Sc_{1/2}Nb_{1/2})O_3 - Pb(Zn_{1/3}Nb_{1/3})O_3 - PbTiO_3$
Ceramic System[9]

For the percentage of the perovskite phase as
determined from X−ray study of the PSZNT
system,   a   complete   perovskite   phase   is

obtained where the PZN content is less than 20
mol%. However, larger PT contents, of more than
50mol%, cause the perovskite phase to be more
stable. The grain size of the PSZNT 31/40/29 fired
at 1,200℃ is 3.3 μm, which is almost the same as
that of PSMNT 29/34/37.

The dielectric constants of the PSZNT system
at room temperature are given in Fig.4. The
maximum value of the dielectric constant, 2,000
at room temperature, is obtained at the PSZNT
30/30/40 composition which is near the MPB
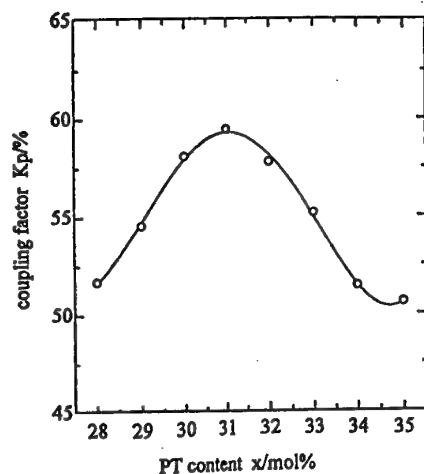
Fig. 6 Electromechanical coupling factor
kp for xPSN$-$0.4PZN$-$(0.6$-$x)PT
system
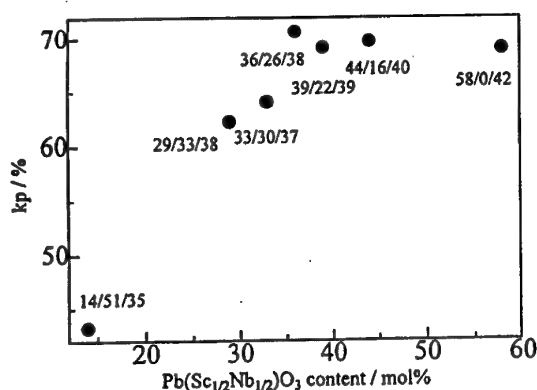
Fig. 7 Electromechanical coupling factor
kp for the xPSN$-$0.26PNN$-$(0.74$-$
x)PT system

region. However, they are decreasing monotonously as a function of PZN content. This may be due to the presence of a small amount of pyrochlore, which has a lower dielectric constant than the perovskite.

The distribution of Tc in the PSZNT system is indicated in Fig. 5. Figure 6 shows the coupling factor kp in the xPSN$-$0.4PZN$-$(0.6$-$x)PT composition. A maximum kp (60%) is found at the PSZNT 31/40/29 composition. This value is considerably lower than that of the PSMNT 29/34/37 (72%).

3.3 Pb(Sb$_{1/2}$Nb$_{1/2}$)O$_3$$-$Pb(Ni$_{1/3}Nb_{2/3}$)O$_3$$-$PbTiO$_3$ Ceramic System[10]

In the PSNNT ternary system, a complete perovskite phsse is obtained in the whole range. The kp has the maximum value (kp=70.7%) at the composition of PSNNT 36/26/38 as found in Fig.7, where $\varepsilon^T_{33}/\varepsilon_0$=3,019 and Tc=210°C. The kp and mechanical quality factor were slightly improved by doping NiO and Nb$_2$O$_5$.

3.4 Pb(Sc$_{1/2}$Nb$_{1/2}$)O$_3$$-$PbTiO$_3$ Single Crystals

Table 1 is a summary of the crystal growth process data.[2] Weight losses of 2% to 8% due to PbO evaporation were observed for the PbO flux batches. The PbO flux batches caused considerable damage to the Pt crucible. The flux batch with a PSNT ratio of 85:15 completely tore the Pt crucible apart due to expansion of the contents during cooling. In addition, the PbO flux batches did not create any crystals more than 0.5 mm in size. In contrast, PbO$-$B$_2$O$_3$ flux batches caused little damage to the Pt crucible and the weight loss was less than 1.5% under the same condition. Crystals were visible to the unaided eye in all PbO$-$B$_2$O$_3$ flux batches except the 65PbO$-$B$_2$O$_3$: 35PSNT batch.

A high PSNT content, more than 35mol%, in the PbO$-$B$_2$O$_3$ flux makes it difficult to involve all the powder, even at 1,200 °C. Chemical analysis and X$-$ray studies revealed that the
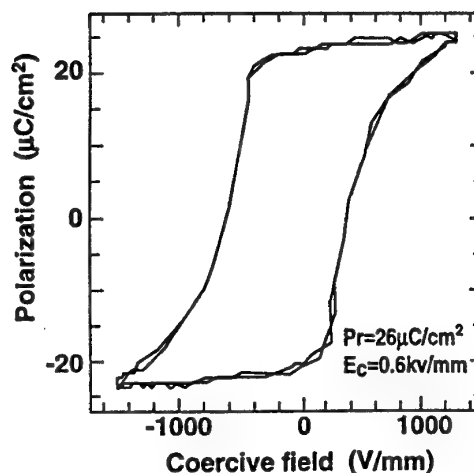
Fig. 8 P$-$E hysteresis curve of PSNT 67/33 single crystal.

TABLE I Crystal growth results by flux type and concentration of the solution

Flux type (mol%)	Flux:PSNT (mol%)	Wt. loss (wt%)	Pt crucible	Crystal size (mm)
100PbO	85:5	8.1	Somewhat deformed by the content	< 0.5
100PbO	85:15	2.3	Destroyed by content expansion	< 0.5
$82PbO-18B_2O_3$	95:5	1.1	Slightly contaminated by PbO	< 1-3
$82PbO-18B_2O_3$	85:15	1.5	No trace of contamination by PbO	< 2-6
$82PbO-18B_2O_3$	75:25	1.3	No trace of contamination by PbO	< 3-7
$82PbO-18B_2O_3$	65:35	0.9	No trace of contamination by PbO	< 0.5

Table 2 Piezoelectric properties of various relaxor—PT ceramic materials

Materials	Firing Temp. (°C)	MPB composition and abbreviation	Curie Temp. (°C)	E/M Coupling factor k_p (%)
$Pb[(Yb_{1/2}Nb_{1/2})_{1-x}Ti_x]O_3$	1,000	PYbNT 50/50	360	53
$Pb[(In_{1/2}Nb_{1/2})_{1-x}Ti_x]O_3$	1,200	PInNT 63/37	320	58
$Pb[(Sc_{1/2}Nb_{1/2})_{1-x}Ti_x]O_3$	1,250	PSNT 58/42	260	70
$Pb[(Ga_{1/2}Nb_{1/2})_{1-x}Ti_x]O_3$	1,100	PGaNT 50/50	—	—
$Pb[(Sc_{1/2}Ta_{1/2})_{1-x}Ti_x]O_3$	1,300	PSTT 55/45	205	60
$Pb[(Mg_{1/3}Nb_{2/3})_{1-x}Ti_x]O_3$	1,250	PMNT 68/32	155	64
$Pb[(Sc_{1/2}Nb_{1/2})_{1-x-y}(Mg_{1/3}Nb_{2/3})_yTi_x]O_3$	1,250	PSMNT 29/34/37	205	.72
$Pb[(Sc_{1/2}Nb_{1/2})_{1-x-y}(Zn_{1/3}Nb_{2/3})_yTi_x]O_3$	1,200	PSZNT 31/40/29	222	60
$Pb[(Sc_{1/2}Nb_{1/2})_{1-x-y}(Ni_{1/3}Nb_{2/3})_yTi_x]O_3$	1,160	PSNNT 36/26/38	202	71

crystals are of perovskite structure with x=0.33, making them slightly different from the charged MPB composition of x=0.42. The (001) single crystal has a dielectric constant peake of 60,000 at 206 ℃ and an electromechanical coupling factor k_{33}=72%. P—E hysteresis curve was shown in Figure 8. It is found from this figure that remanent polarization and coercive field were $26\mu C/cm^1$ and 4—6kV/cm, respectively.

Among relaxor—PT single crystals, higher values of electromechanical coupling factors and piezoelectric constants were obtained in the $Pb(Zn_{1/3}Nb_{2/3})O_3 - PbTiO_3$ (PZNT) system and $Pb(Mg_{1/3}Nb_{2/3})O_3 - PbTiO_3$ (PMNT) system. In the case of the PZNT system, single crystals 40 mm in diameter were successfully grown from solution by the Bridgman method with a PbO flux[11]. The crystals were grown in a platinum crucible heated to 1,130℃. Growth rate was 0.35 mm/h. The obtained crystals were ~40 mm in diameter x 20 mm in length were a rust — brown color. The Curie temperature, Tc, ranged from 175 to 185℃, and the dielectric constant before poling at room temperature was 2,000—8,900 within a wafer. After electrical poling, specimens had electromechanical coupling coefficients in rectangular bar mode, k_{33}, of 79—88%, which were larger than for PZT ceramics (k_{33}< 70%). These single crystals have great potentiality for use as transducer materials.

4 CONCLUSION

This review has focused on some of the piezoelectric properties of various relaxor—PT systems compared to PZT. Two ceramic compositions PSMNT 29/34/38 and PSNNT 36/26/38 as shown in Table 2[10] offer larger electromechanical coupling factors than PZT. Single crystals of relaxor — PT system have superior properties compared with ceramics if appropriate axis utilized. Concerning the single crystal growth processing, further study is required to determine the best way to make commercially usable sizes.

References
1) S. E. Park and T.R. Shrout; IEEE Ultasonic Sympo. (1996) 935
2) Y. Yamashita and K. Harada; Jpn. J. Appl. Phys. 36 (1997) 6039
3) N. Ichinose and Y. Yamashita; Ferroelectrics 217 (1998) 263
4) S. L Swartz and T. R. Shrout; Mat. Res. Bull. 17 (1982) 1245
5) Electrical Measurement Method for Piezoelectric Ceramic Elements (Standards of Electronic Materials Manufactures Association of Japan) April (1993) EMAS — 6100 (in Japanese)
6) Y. Yamashita, K. Harada, T. Tao and N. Ichinose; Integrated Ferroelectrics 123 (1996) 17
7) B. Jaffe, R. S. Roth and S. Marzullo; J. Res. Natl. Bull. Stand. 55 (1955) 239
8) Y. Yamashita; Jpn. J. Appl. Phys. 33 (1994) 4652
9) Y. Yamashita, Y. Hosono and N. Ichinose; Jpn. J. Appl. Phys. 36 (1997) 1141
10) Y. Yamashita, K. Harada, Y. Hosono, S. Natume and N. Ichinose; Jpn. J. Appl. Phys.37 (1998) 5288
11) K. Harada, S. Shimanuki, T. Kobayashi, S. Saitoh and Y. Yamashita; J. Am. Ceram. Soc. 81 (1998) 2785

Binder Burn-Out Process for Highly Reliable MLCCs with Ni Electrodes

Takeshi NOMURA, Tamami KATO, and Yukie NAKANO

Materials Research Center, TDK Corporation

570-2,Matsugashita, Minami-Hatori, Narita-shi, Chiba, 286-8088

FAX: 81-476-1637, e-mail : tnomura@mb1.tdk.co.jp

Abstract - Binder burn-out step is one of the most important process for achieving perfect MLCCs. Ni-electrode MLCCs should be fired under reducing atmosphere in order to prevent the oxidation of Ni-electrodes. The binder burn-out step, however, requires great amount of oxygen, so that Ni electrode easily oxidizes during binder burn-out step. In this study, effect of the binder burn-out conditions on the mechanical and electrical properties of Ni-electrode MLCCs. It is shown that the binder burn-out process is a key step for obtaining highly reliable MLCCs. Not only faults such as delaminations and cracks but also mechanical strength of MLCCs are strongly affected by the binder burn-out conditions. This is well explained by the residual carbon of MLCCs.

1. INTRODUCTION

Surface mount technology is the biggest theme for the world's electronic engineers of the 1990's. Particularly in Japan, the awareness of the need to vigorously promote higher density mounting on printe circuit boards, the nucleus of the electronic assembly, and the rationalization of assembly processes is given a high priority because the NIES are making much effort to catch up with Japan over the ten years, and because of the excessive competition among the electronic companies. This increases the demand for surface mount even more. Recent trend of electronic equipments or facilities is down sizing, which accelerates the miniaturization of chip components. Chip components show a rapid growth despite the gloomy economic circumstances. Among them, especially MLCCs market expands on a large scale overcoming the economic situation. The price of MLCCs has yet to be reduced because of the strong demand of low price. It is known that MLCCs is composed of alternately layers of dielectrics and internal electrode such as Pd or Ni. Since Pd is a precious metal, the cost is another major problem. Ni-electrode MLCCs are a promising way of reducing the cost. In the initial stage of the R&D, Ni-electrode MLCCs had a serious problem about reliability. However, since the authors had succeeded in achieving highly reliable MLCCs with Ni-electrodes, it show a remarkable expansion in both quantity and extent of application.

Multiplication and thinning of dielectrics and Ni-electrode layers are strongly requested for attaining larger capacitance. Recently, MLCCs with 300 layers of 3 μ m dielectrics in 3216 (mm) type have been developed. Multiplication and thinning of dielectrics, however, may cause some faults such as delaminations and cracks.

These faults causes inferior IR properties, so that these faults should be avoided. It is well known that delamination and crack are caused by the insufficient removal of binder during binder burn-out process in case of MLCCs with Pd-electrodes.

In the present paper, the effect of binder burn-out condition on the mechanically related failures of MLCCs with Ni-electrodes, in order to overcome the barrier for larger capacitances by multiplication and thinning of dielectrics.

2. EXPERIMENTAL PROCEDURE

The dielectric compositions employed in this study were $BaTiO_3+aMgO+bBa_{0.4}Ca_{0.6}SiO_3+cMnO+dY_2O_3+eV_2O_5$ for X7R characteristics, $[(Ba_{1-x}Ca_x)O]_m\{Ti_{1-y}Zr_y)O_2]+aSiO_2+bMnO+cY_2O_3+dV_2O_5+eWO_3$ for Y5V characteristics, and $(Ca_{1-x}Sr_x)m(Ti_{1-x}Zr_x)$ system for C0G characteristis. $BaTiO_3$, $[(Ba_{1-x}Ca_x)O]_m\{Ti_{1-y}Zr_y)O_2]$, and $(Ca_{1-x}Sr_x)_m(Ti_{1-x}Zr_x)$ were emloyed highly pure oxalate derived powders. Average particle sizes of these powders were 0.3-1.0 μ m. Multilayer ceramic capacitors (MLCCs) were formed by so-called sheet methods using pastes of the dielectric

materials and nickel powder. Green sheet thickness was controlled to 5-10 μ m. After printing nickel electrodes, green sheets were laminated and pressed to form 4-280 dielectric layers. Then, they were cut into green chips. These chips were heated at certain temperature under certain atmosphere to remove the acrylic resin used as an binder, followed by firing at elevated temperatures between 1200 and 1340 ℃. Oxygen partial pressure of the ambient atmosphere during firing was controlled to 10^{-8}-10^{-13}MPa by adjusting the amounts of H_2 and H_2O gas mixture. Fired chips were then heat treated at temperatures between 900 and 1100 ℃ in N_2-H_2O gas mixture in order to compensate the oxygen vacancies which might be formed during firing in a reducing atmosphere.

Techniques used are dilatometry, TG, SEM, VSM, and TEM.

3. RESULTS AND DISCUSSION

Binders such as ethylcellulose and acrylic resin generally burn at around 250℃ in air. Rapid burn out of binders may cause the delamination because a large amount of exhaust gas generates in an instance. Accordingly, binder should be slowly burned out without any combustion. Even if the binder burn-out is slowly performed, it is not perfect for Ni-electrode MLCCs, because Ni easily oxidize in air and it generates O_2 gas during firing under reducing atmosphere. Moreover, the discrepancy of shrinkage between dielectrics and Ni electrode will be stressed by the multiplication. This is remarkable for the case of fine powders as dielectrics and nickel. Typical photographs of delaminetion and crack are shown in Figs.1 & 2. The main causes of these faults are considered as the expansion by the oxidation of Ni or the gas generation caused by the reduction of NiO. Figure 3 shows the effect of temperature for binder burn-out process on the residual carbon of the de-bindered chips. Higher temperatures than 300 ℃ in air is effective to remove the binder of chips. Nickel, however, easily oxidize so that high temperature in air can not be adopted. On the contrary, even if in a reducing atmosphere, binder can be effectively removed in the case of higher
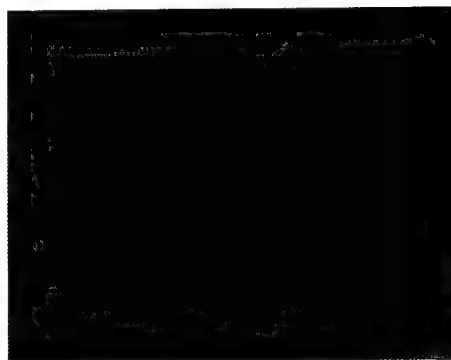
Fig.1　Typical delamination observed in large capacitance Ni electrode MLCC.

Fig.2　Typical cracks observed in large capacitance Ni electrode MLCC.
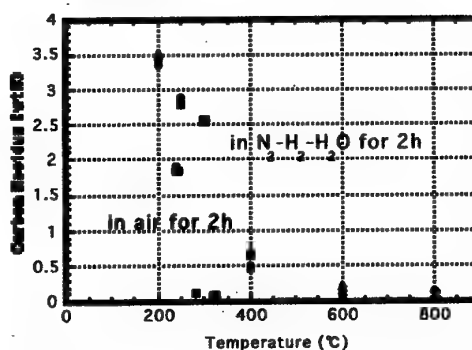
Fig.3　Effect of binder burn-out temperature on the carbon residue.

temperatures than 600 ℃ . The effect of temperature for binder burn-out process on the fraction oxidized of Ni is shown in Fig.4. Even if it is at lower temperatures than 200 ℃, few percent of Ni oxidized in air. Of course, this can be strongly affected by the particle size and
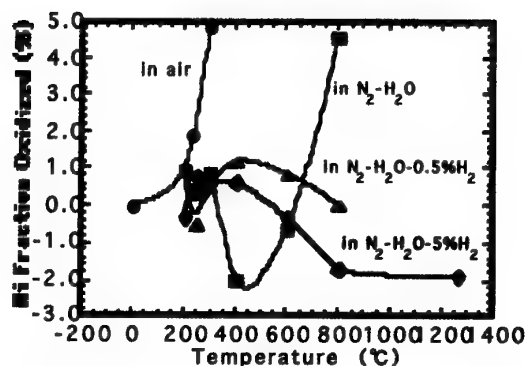
Fig.4　Effect of binder burn-out temperature on the Ni fraction oxidized.

Fig.6　Effect of binder burn-out temperature on the fraction of cracks.

crystallinity of Ni oxidized in air. Of course,this can be strongly affected by the particle size and crystallinity of Ni powder. This is not preferable for supressing the expansion during de-binder process and degassing during firing of electrode layers. Figure 5 shows the relationship between residual carbon content and fraction oxidized of Ni. Binder burn-out in N_2-H_2-H_2O is so effective way to remove the binder without any oxidation of Ni, so that it is perfect to restrain the delaminations or cracks as is shown in Fig. 6.

As a conclusion, binder burn-out in air, which is widely used in an industry scale, is not adequate for multiplication and thinning of dielectrics and Ni electrodes. Contrarily, binder burn-out under reducing atmosphere such as H_2-H_2O-N_2 effectively reduces residual carbon without any oxidation of Ni electrodes.

In general, MLCCs are automatically mounted and soldered on printed circuit board, then higher mechanical and thermal strength is required. From this poit of view, delaminations and cracks are so serious because they are the decisive factors for strength. The authors have been paid much effort to ensure higher mechanical and thermal strength, and discovered that the residual carbon content is an important factor for deciding mechanical and thermal strength. Figure 7 shows the effect of residual carbon after firing on the bending strength of MLCCs with Ni electrodes. Lower content of carbon residue is preferable for achieving higher mechanical strength. In any case, delamination or crack is not detected. Residual carbon content is affected not only by the conditions of binder burn-out process but also by the firing conditions.

Fig.5　Relationship between carbon residue and the Ni fraction oxidized.
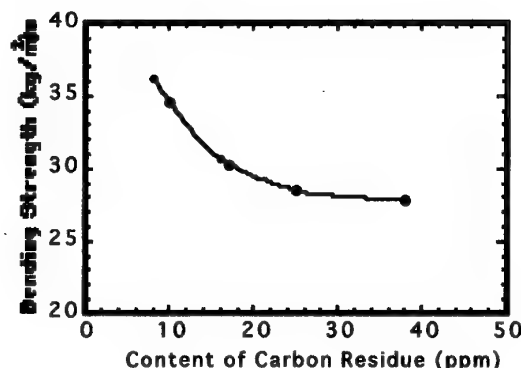
Fig.7　Effect of carbon residue after firing on the bending strength of MLCCs.

Unfortunately, the state of carbon residue is not clarified up to the present. Residual carbon is not detected by TEM observation, because its content is very low level by gas analysis.

4. CONCLUSIONS

In this study, binder burn-out process has been studied from the view point of residual carbon and oxidation of Ni. This work can be summarized as follows:

(1) Binder burn-out in air is not adequate for multiplication and thinning of dielectrics and Ni electrodes, because

Ni could be oxidized.

(2) Reducing atmosphere such as N_2-H_2-H_2O is so effective to remove the binder withou any oxidation of Ni

electrodes.

(3) Residual carbon after firing is an important factor for the mechanical strength of MLCCs.

5. REFERENCES

(1) J.M.Herbert, Trans.Br.Ceram.Soc., 62 (1963) 645.

(2) I.Burn, and G.H.Maher, J.Mater.Sci., 10 (1975)633.

(3) Y.Sakabe, K.Minai and K.Wakino, Jpn. J.Appl.Phys., 20 (1981)Suppl. 20-4 147.

(4) T.Nomura, A.Sato and Y.Nakano, J.Soc. Mater.Eng.Resour.Jpn., 5 (1992) 44.

(5) T.Nomura, S.Sumita, Y.Nakano and K.Nishiyama, Proc.5th US-Jpn. Seminar Dielectric Piezoelectric Ceramics,Kyoto, Japan, (1990) 29.

(6) S.Sumita, M.Ikeda, Y.Nakano, K.Nishiyama and T.Nomura, J.Am.Ceram. Soc., 74 (1991)2739.

(7) T.Nomura and Y.Nakano, Denshi Tokyo, 31 (1993) 168.

(8) Y.Nakano, A.Sato, J.Hitomi and T.Nomura, Ceram.Trans., 32 (1993) 119.

(9) J.Yamamatsu, N.Kawano, T.Arashi, A.Sato, Y.Nakano and T.Nomura, J.Power Sources, 60 (1996)1996.

(10) T.Nomura, N.Kawano, J.Yamamatsu, T.Arashi, Y.Nakano, and A.Sato, Jpn. J.Appl.Phys., 34 (1-9B) (1995) 5389.

Ni COMPATIBLE X7R AND Y5V DIELECTRICS:
THE EVOLUTION IN TECHNOLOGY

I. Burn, D. Lee , D. Spang and D. Swanson
Degussa-Hüls, Electronic Materials America
South Plainfield, New Jersey, USA
Fax: 01-908-757-0411

W. Derks, J. Roelofsma and S. Santoro
Degussa-Hüls, Electronic Materials BV
Uden, The Netherlands
Fax: 31-413-250-524

1. INTRODUCTION

In the last few years the technology for making multilayer ceramic capacitors (MLC's) has been driven by the need to reduce or eliminate the use of costly Pd in the inner electrodes, and by the need to decrease the dielectric layer thickness for higher volumetric efficiency. Several dielectric powder manufacturers have developed proprietary Ni compatible dielectrics to bypass the use of Pd and have been manufacturing product for some time. In this paper, we will review state of the art commercial Ni-compatible dielectrics made using high purity barium titanate and the latest milling and mixing techniques. In addition, we will describe new X7R and Y5V dielectrics based on chemical technology that are being developed to meet the requirements for next generation MLC's with ultra thin dielectric layers.

2. X7R COMPOSITIONS

2.1 Background

Philips (Centralab), in the early seventies, was the first company in the MLC industry to make a serious attempt to introduce X7R capacitors with nickel internal electrodes. However, in spite of some excellent theoretical work on dielectric degradation at the Philips research laboratories in Europe, these capacitors suffered from poor reliability and serious failures occurred in the field. At that time it was debated whether or not MLC's with Ni electrodes could ever be made with adequate reliability. Eventually, it was realized that the use of very high purity barium titanate was a prerequisite for high reliability in BME X7R capacitors because of the core-shell structure of the grains. This has recently been demonstrated very nicely by

Kobyashi and coworkers at TDK (1). Consequently, high purity chemically prepared barium titanate is now used universally for this application whether it be made by the oxalate, hydrothermal, or other chemical precipitation process.

2.2 Current Technology

Commercial Ni compatible X7R dielectric powder is currently made by Degussa using oxalate derived barium titanate, to which a finely milled proprietary dopant mix is added. Average particle size (D_{50}) of the barium titanate is typically 0.7 μm, whereas the dopant mix has a particle size of about 0.4 μm, with 90% of the particles less than 0.8 μm. This combination of powders (AD352N) provides a fired dielectric with high dielectric constant, low loss, outstanding fired density and excellent reliability. A micrograph of a fractured section is shown in Fig. 1. Typical electrical properties are summarized in Table 1.
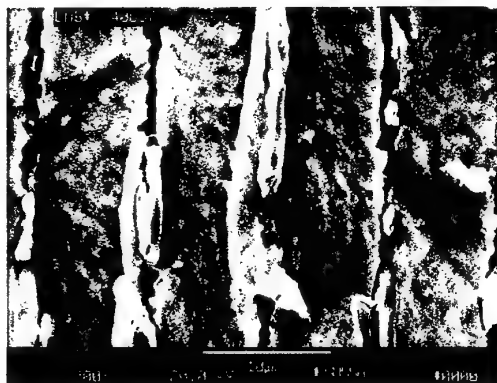
Fig. 1. Fracture Section of AD352N

Table I. AD352N Properties
(51 layers at 7.5 μm)

Capacitance (μF)	0.103
K	3800
DF (1.0 V)	2.73
TCC (%)	
@ -55 °C	-6.5
@ 125 °C	-12.4
IR (100 V)	600 Ω.F

Table II. RD252N Properties

Surface Area	$5.7 M^2/g$
D_{50}	0.39 μm
D_{90}	0.61 μm
K	2300
DF (0.32 V/ μm)	5.0 %
TCC (%)	
@-55 °C	-15.9
@ 125 °C	+1.6
IR	3200 Ω.F

The dielectric has been reported by customers to perform well for fired dielectric thicknesses as low as 3-5 μm. This is probably because of the excellent fired density and proprietary formulation, which is designed for high HALT (highly accelerated life test) performance.

2.3 Next Generation Technology

For applications requiring a fired dielectric thickness ≤ 3 μm, the particle size of the barium titanate must be reduced to < 0.5 μm and the homogeneity of the barium titanate/dopant mix must be optimized. Particle size of oxalate derived barium titanate can be reduced to about 0.4 μm by adjusting the processing conditions, and hydrothermal or alkoxide derived powders are also options. Sakabe (2), for example, has demonstrated the feasibility of using alkoxide derived barium titanate for a fired dielectric layer thickness as low as 1 μm. At Degussa we have developed fine oxalate derived barium titanate as well as alkoxide derived powder, both with similar particle size.

In addition to fine particle size, the particles must be chemically coated with dopant solution for optimum compositional uniformity. Coating technology for dielectric powders has been pioneered by Degussa and has been well proven in the industry for dielectrics compatible with Ag-Pd electrodes (3). Coating technology is now being applied to Ni compatible compositions. For example, tests on laboratory MLC's containing Degussa alkoxide derived barium titanate (ADHPBT) have shown dielectric constant of about 2300. Excellent HALT performance has been reported, even at a fired layer thickness as low as 2 μm. Initial properties are given in Table II. Fig. 2 illustrates the excellent small grain microstructure obtained after firing. Work on the fine oxalate powder is in progress.

Fig. 2. Microstructure of Fired BME X7R made with Alkoxide-derived $BaTiO_3$

3. Y5V COMPOSITIONS
3.1 $BaTiO_3/CaZrO_3$ Mixtures

Early Ni compatible high K (Z5U/Y5V) compositions were based on mixtures of pre-made barium titanate and calcium zirconate. Reduction of the dielectric during firing was inhibited with a small amount of added manganese oxide powder, and good reliability was maintained by adding a small amount of niobium oxide powder (4). While the electrical performance of capacitors made by this technique was quite good, the electrical properties and grain size were very sensitive to the oxygen partial pressure during firing (Figs. 3, 4). It was realized that this effect was due to Ni diffusing from the electrodes into the dielectric during firing and interfering with the solid solution of the calcium zirconate into the barium titanate (5). Complete solid solution was
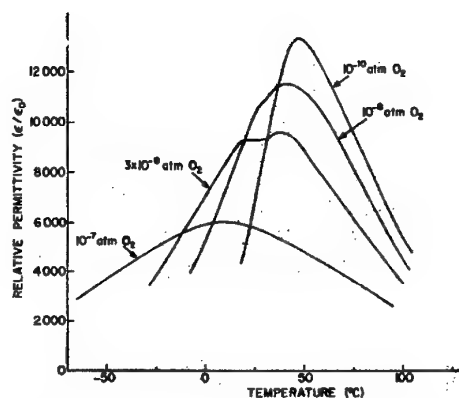
Fig. 3 Dependence of K on Firing Atmosphere
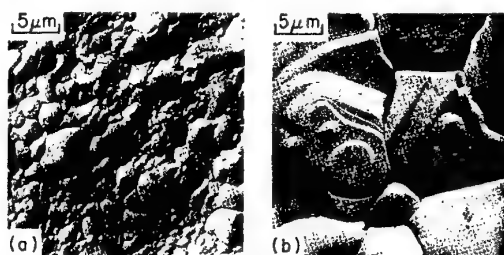
Fig. 4. Dependence of Grain Size on Firing Atmosphere: (a) 10^{-7}, (b) 10^{-10} atm. O_2

achieved only for very large grain sizes (low oxygen partial pressures).

3.2 BaTiO$_3$/CaZrO$_3$ Solid Solutions

Solid solutions of CaO and ZrO$_2$ with barium titanate (such as Ba$_{0.96}$Ca$_{0.04}$Ti$_{0.82}$Zr$_{0.18}$O$_3$) are now available commercially from several powder suppliers. Dopant oxides are generally added during slip preparation when the powder is being processed into MLC's by the customer. MLC manufacturers can then use their own mix of additives to inhibit reduction, adjust TCC, optimize HALT, etc. This approach reduces the influence of firing atmosphere on Zr solid solution but incorporation of B site ions from the dopant mix is difficult unless appreciable grain growth occurs during firing. This is because of the slow diffusivity of B site ions in the perovskite crystal structure.

3.3 Current Technology

The technology used by Degussa overcomes the issues described above. Very fine powders of high purity, BaCO$_3$, CaCO$_3$, TiO$_2$, ZrO$_2$ and

dopants are pre-milled together using the latest bead-milling technology and then calcined to produce a solid solution. The powder is bead-milled again after calcination to provide a very uniform material with average particle size (D$_{50}$) of 0.8 μm. Typical properties are summarized in Table III. A fracture section of a commercial MLC is shown in Fig. 5. As is the case for the X7R dielectric, outstanding fired density can be obtained. The TCC indicated by laboratory samples (5 layers) is adjusted to allow for the shift in Curie point, which normally occurs with high

Table III. AD143N Properties
(79 layers at 9.4 μm)

Capacitance (μF)	1.3
K	19,000
DF (1.0 V)	6.7
TCC (%)	
@-30 C	-35.7
@ 85 C	-82.0
IR (25 V)	>100,000 Ω.F
HALT @80V, 140 °C	No degradation

Fig. 5. Fracture Section of AD143N
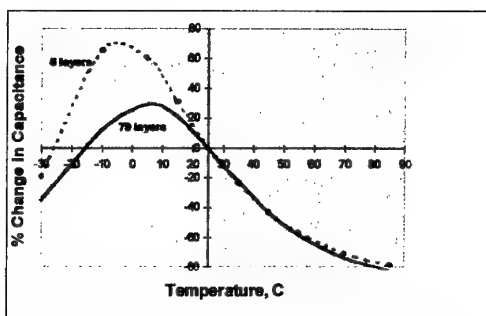
Fig. 6. Influence of Number of Layers on TCC

layer MLC's (Fig. 6). This shift is thought to be due to internal stresses in the MLC caused by thermal expansion difference between the Ni electrodes and the dielectric.

3.4 Next Generation Technology

While very high performance can be obtained with the current Y5V technology described above, the ultimate in chemical uniformity, which is required for the smallest grain sizes, is obtained by mixing the components in a liquid chemical process. The alkoxide process, for example, allows for intimate mixing of the dielectric components on an atomic scale. Current work indicates that high dielectric constant with very fine grain size can be obtained using alkoxide derived powder. Typical properties (RD193N) are given in Table IV for firing conditions of 1275 °C and 10^{-10} atm. O_2. Fig. 7 illustrates the small grain size that can be obtained in the fired dielectric. Initial feedback from customers who are evaluating this material is very favorable. Development work is continuing, so that a dielectric constant $\geq 15,000$ can be achieved with a grain size $\approx 1 \mu m$.

Table IV. RD193N Properties

Surface Area	7.9 M^2/g
D_{50}	0.37 μm
D_{90}	0.46 μm
K	13,800
DF (0.05 V/ μm)	1.5 %
TCC (%)	
@-35 °C	-39.7
@ 85 °C	-76.5
IR	50,000 Ω.F

4. SUMMARY

The evolutionary development of Ni compatible X7R and Y5V dielectrics has been described. This review contains a report on the high performance products currently available from Degussa and includes a summary of current efforts aimed at providing next generation products that can be used for fired dielectric thickness $\leq 3 \mu m$.
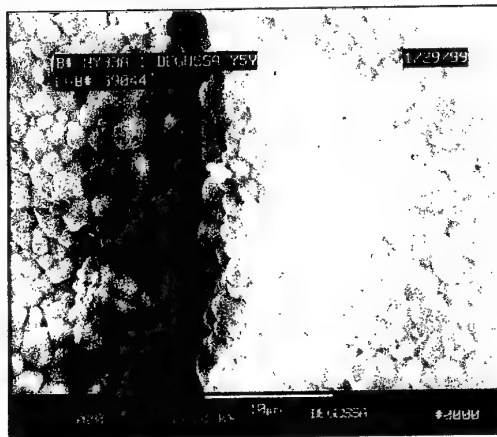
Fig.7. Fracture Section of MLC made with Alkoxide derived Powder.

5. REFERENCES

1. R. Kobayashi, T. Ishigaki, M. Fujimoto, O. Otani and W. Takahara, "Multilayer Ceramic Capacitors Incorporating Nickel Internal Electrodes and Ultra Thin Dielectric Layers", IEMT/IMC Proceedings, 372-374, (1997).

2. Y. Sakabe, N. Wada and Y. Hamaji, "Grain Size Effects on Dielectric Properties and Crystal Structure of Fine Grained BaTiO₃ Ceramics", J. Korean Phys. Soc., **32**, S260-S264, (1998).

3. I. Burn, D. Goia, M. Mehta, and S. Santoro, "Dielectric and Electrode Systems for Multilayer Ceramic Capacitors with Layer Thickness Below 10 μm", Proc. 7th US-Japan Seminar on Dielectric and Piezoelectric Ceramics, 277-280 (1995).

4. N.G. Error, I. Burn and G.H. Maher, "Method for Forming a Dielectric Body (with BME)", US Patent 3,920,781 (1975).

5. I.Burn and G.H. Maher, "High Resistivity BaTiO₃ Ceramics Sintered in CO-CO₂ Atmospheres", J. Mater. Sci., **10**, 633-640, (1975).

Influence of the Microstructure on the Redox Behavior in BTZ Based Material

Hirokazu Chazono, Yasuyuki Inomata, Noriyuki Kohzu, and Hiroshi Kishi

Material Development Department, General R&D Laboratories, Taiyo Yuden Co. Ltd.,

5607-2 Nakamuroda, Haruna-machi, Gunma-gun, Gunma 370-3347, Japan

Fax: 81-027-360-8307, e-mail: hchazono@jty.yuden.co.jp

The influence of the microstructure on the redox behavior in barium zirconium titanate (BTZ) based material was investigated. The mean grain size and the dielectric constant (ϵ) was larger for the chips fired at 1230°C than those for the chips fired at 1200°C. Comparison of the temperature characteristics (TC) of ϵ between the chips fired in a reducing atmosphere and those treated in a weakly oxidizing atmosphere revealed that the increase of ϵ accmpanied by the reoxidation treatment was larger for the chip fired at 1230°C than for the chip fired at 1200°C. Moreover, the hysteresis of ϵ against direct current (dc) bias was larger for the chips as fired in a reducing atmosphere than for the chips with reoxidation treatment. The electrical properties including the redox behavior and a response to dc-bias were discussed in the viewpoint of the amount of oxygen vacancies.

INTRODUCTION

Currently, nickel (Ni) has been preferentially used for the internal electrode of multi-layer ceramic capacitor (Ni-MLCC) performing a large capacitance. It is well known that the rate of grain growth was large and that the higher dielectric constant (ϵ) was attained by the grain growth in $(Ba,Ca)(Ti,Zr)O_3$ ceramics as indicated by Hansen et al [1]. In fact, when the active layer thickness becomes below 3μm, there can exist only one grain in each active layer of the MLCC with the material conforming to such as Y5V specification of EIA since grain grows easily in this kind of material. Shizuno et al reported that the addition of Ho_2O_3 increased the rate of restoration of the resistivity on cooling stage and that they developed Ni-MLCC conforming to Y5V specification of EIA; 4.7μF with 6.8μm active layer thickness in 3.2mm by 1.6mm size (1206 type) [2]. It is noteworthy that the rare earth addition played an important role for the wide use of Ni-MLCC since the life time of Ni-MLCC with the material containing Ho was significantly improved to the equal one of MLCC with Pd internal electrode. Nowadays, the 22μF Ni-MLCC (1206 type) conforming to Y5V with about 4.6μm active layer thickness is under mass-production.

Chazono et al. reported the influence of the strength of the electrical field for Ni-MLCC in BTZ based material containing Ho oxide using MLCCs with various active layer thickness [3]. They reported that the dielectric constant of the chips fired in a reducing atmosphere was raised by the reoxidation treatment in a weakly oxidizing atmosphere and that the weight change of the sample before and after reoxidation treatment was about 50~80ppm irrespective of the active layer thickness. In addition, Pike et al. reported that positively charged oxygen vacancy and trapped electron were responsible for the voltage offsets in PLZT thin films [4]. The objective of this work is, therefore, to investigate the influence of the microstructure on the redox behavior in BTZ-based material using the chips fired at various temperatures.

EXPERIMENTAL PROCEDURE

Precalcined $Ba(Ti_{0.86}Zr_{0.14})O_3$ powder, Ho_2O_3, and some sintering aid were weighed, ball-milled, dried, and then calcined at 1150°C for 2hr. The obtained powder was mixed with organic binder into a slurry. They were cast into a green sheet. 20 green sheets, on which printed Ni paste for internal electrodes, as well as the protective sheets at the upper and lower sides were stacked and pressed into a bar and then cut into pieces. Terminal Ni electrodes were formed on both sides of the chips. Two kinds of firing cycle were used as illustrated in Fig.1: the firing cycle with a reducing atmosphere, which was controlled by H_2, N_2, O_2 and H_2O (PO_2 of approximately $10^{-11} \sim 10^{-13}$Pa), wholly and the firing cycle with the same reducing atmosphere and a cooling stage below 1000°C with PO_2 of 30Pa. The sample fired in the former and the latter cycle will be abbreviated as the as-reduced sample and as-reoxed sample, respectively, hereafter. The chips were fired at desired temperatures for 2hr in both firing cycles. The microstructure for the grounded and thermally etched cross section and the surface of chips was observed with a field emission scanning electron microscope (FE-SEM; Hitachi). The grain diameter was measured by a micrometer with SEM photographs of the chip surface. For the investigation of temperature characteristics (TC) of dielectric constant (ε), the chips were placed into a container, in which temperature could be controlled in the range of ± 1°C over the temperature range from -55° to 125°C. Capacitance was measured with an impedance analyzer (HP-4284A; YHP) at 1kHz with 1Vrms and desired direct current bias.
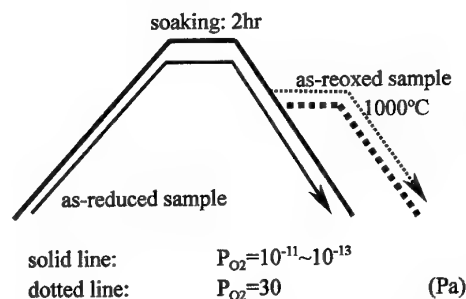
Fig.1 Schematic illustration of the firing condition.

RESULTS AND DISCUSSIONS

Figure 2 shows TCs for the as-reduced and as-reoxed samples having 2.8 and 6.4μm active layer thickness. For the as-reduced samples, ε decreased and TC became flatter as the active layer thickness decreased. The increase of ε from the as-reduced sample to the as-reoxed one was about 60% for the sample of 2.8μm active layer thickness, whereas it was about 15% for that
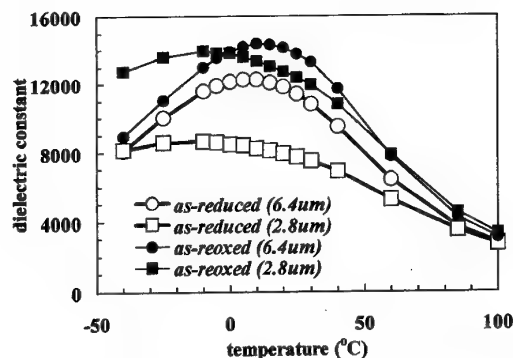
Fig.2 TCs for the as-reduced and as-reoxed sample having 2.8 and 6.4μm active layer thickness.

of 6.4μm thickness. The broadening and the shift of TC for as-reoxed sample with 2.8μm thickness compared with those for one with 6.4μm thickness was well explained from the measurement of TCs as a parameter of the applying electric field strength [3]. In addition, the influence of the electrical field on the TC was also confirmed by Tsurumi et al. [5]. The microstructure of the chips with various active layer thickness was almost the same. Therefore, the chip with about 5.5μm active layer thickness was fired at various temperatures for the investigation of the influence of the microstructure on
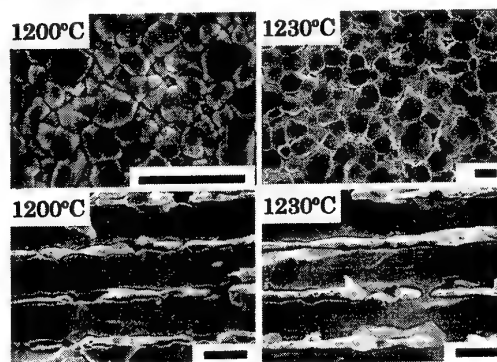
Fig.3 SEM micrographs of the chips fired at 1200° and 1230°C for 2hr (bar = 6μm).

the electrical properties.

FE-SEM images for the surface and the cross-section of chips fired at 1200° and 1230°C for 2hr are shown in Fig.3. Both samples were fully dense and the active layer thickness was about 5.5μm for both samples. The continuity of the internal Ni electrode was decreased for the chips fired above 1240°C. The mean grain size was determined with these micrographs by counting over 300 grains.
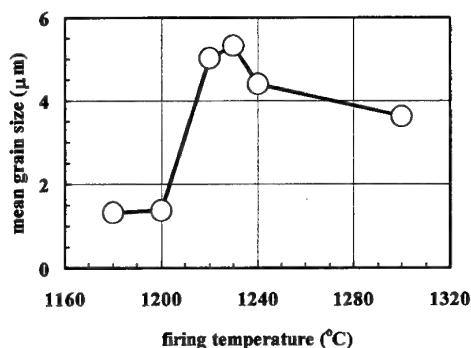
Fig.4 Influence of the firing temperature on the mean grain size of the chip surface.

Figure 4 shows the influence of the firing temperature on the mean grain size of the chip surface. The mean grain size was as four times as the starting particle size when fired below 1200°C. However, the rate of grain growth was largest at around 1230°C. The mean grain size decreased above 1240°C.

The typical TC curves of as-reduced and as-reoxed chips fired at 1200° and 1230°C for 2hr were shown in Fig.5. The peak of ε was at about 0°C for all samples. It was found that ε of the as-reoxed sample was larger than for the chip fired at 1230°C than that for the chip fired at 1200°C. This fact was consistent with the result of Hansen et al. [1]. It was evident that ε was small and the TC curve was flat for as-reduced samples compared with those of as-reoxed samples irrespective of the firing temperature. The increase of ε was larger for the chip fired at 1200°C than for one fired at 1230°C. The increase of ε was ascribed to the decrease of the amount of the oxygen vacancy suggested from the frequency response of the imaginary part of permittivity [3]. The large amount of oxygen vacancy is suspected to reduce ε

due to pin the ferroelectric domain walls [6].
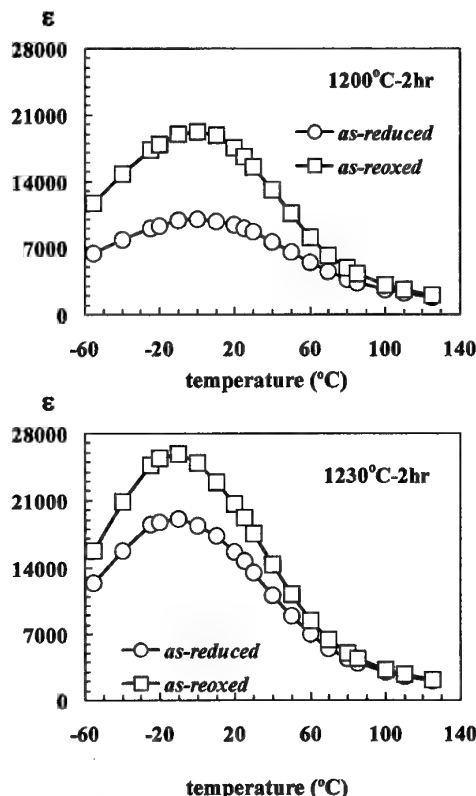
Fig.5 Temperature characteristics of the dielectric constant for as-fired and as-reoxed samples fired at 1200° and 1230°C for 2hr.

For further investigation of the redox behavior in this system, ε under the direct current bias was measured. Figure 6 shows the influence of the dc-bias on ε at room temperature for as-reduced and as-reoxed samples fired at 1200° and 1230°C. It was found that ε decreased as the applying dc-bias increased for both as-reduced and as-reoxed samples. The response of ε against the dc-bias was small for the chip fired at 1200°C, which was composed of smaller grains than the chip fired at 1230°C. However, ε was not restored after the dc-bias removal. In addition, the decrease of ε after removal of dc-bias was larger for as-reduced sample (20%) than for as-reoxed sample (6%). For the chips fired at 1200°C, the decrease of ε after removal of dc-bias was about 20% for as-reduced sample and 2% for as-reoxed sample.

Figure 7 shows the TCs under dc-bias applying for the chip fired at 1230C. When the dc-bias applied, TCs became diffused compared with those seen in Fig.5.

Under dc-bias applying condition, ε for as-reoxed sample was almost the same as that for as-reduced sample in the whole measuring temperature range.
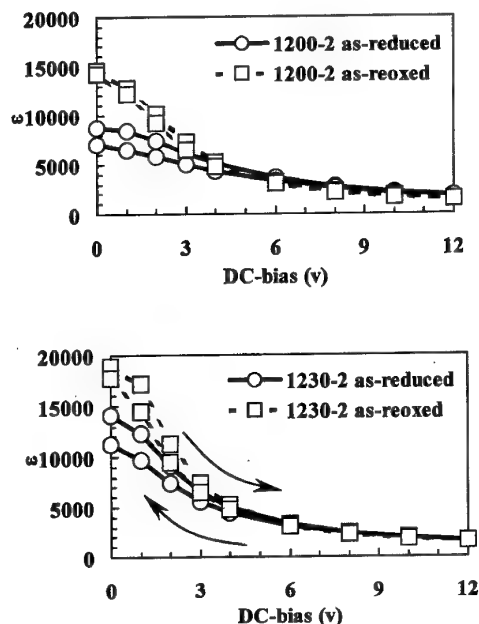
Fig.6　Influence of dc-bias on ε for the sample fired at 1200° and 1230°C.
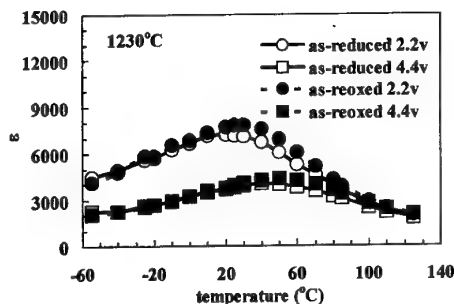
Fig.7　TCs for as-reduced and as-reoxed sample fired at 1230°C for 2hr.

Moreover, ε was almost the same value above 100°C for all samples irrespective of applying dc-bias (Figs.5 and 6). This was also confirmed for the chips fired at 1200°C, which was not shown here. BTZ- or BCTZ-based dielectric material behaved like relaxor [1, 3]. In addition, it was well explained that the shift of TC peak was attributed to the amount of the micro polar region which could be oscillated by the applying electric field [3, 5]. Therefore, it was suggested that the micro polar

region was arranged to the direction of the applying dc-bias. This means the increase of the frozen micro polar region under dc-bias and resulted in the decrease of ε. The same degree of ε decrease after dc-bias removal shown in Fig.6 suggested that the amount of oxygen vacancy was the same order. However, since the chip fired at 1200°C was composed of the small grains, the rate of the elimination of the oxygen vacancy must be larger than that for the chip fired at 1230°C.

REFERENCES

1. P.Hansen, D. Hennings and H. Schreinemacher, *J. Am. Ceram. Soc.*, **81** [5] (1998) 1369.

2. H. Shizuno, S. Kusumi, H. Saito and H. Kishi, *Jpn. J. Appl. Phys.*, **32** [Part 1, No. 9B] (1993) 4380.

3. H. Chazono, Y. Inomata, N. Kohzu and H. Kishi, "Electroceramics in Japan II", Ed. by N. Mizutani, K. Shinozaki, N. Kamehara and T. Kimura, Trans Thech Publications, Switzerland, (1998) 31.

4. G. E. Pike, W. L. Warren, D. Dimos, B. A. Tuttle, R. Ramesh, J.Lee, V. G. Keramidas, and J. T. Evans,Jr., *Appl. Phys. Lett.*, **66** [4] (1995) 484.

5. T. Tsurumi, Y. Yamamoto and N. Ohashi, (in Japanese) *Proc. Annual Meeting of The Ceramic Society of Japan* (1999) 187.

6. B. Jaffe, W. R. Cook and H. Jaffe, "Piezoelectric Ceramics", Ed. by J. P. Roberts and P. Popper, Academic Press, London (1971) 237.

A New $BaTiO_3$ For Low Fire Y5V & BME Y5V Dielectrics

S. Butcher, M. Chu, V. Ganine, D. Rose, and T. Stone

Ferro Electronic Materials, 4511 Hyde park Blvd., Niagara Falls, NY 14305-0067

Tel. (716) 278 9400, Fax (716) 285 3026

Abstract :

The market for Multilayer Ceramic Capacitors (MLCCs) continues to demand smaller size components for a given capacitance or increased capacitance within a given part design. There is also an ongoing demand to reduce its manufacturing cost. One of the approaches to meeting these demands is to decrease the dielectric layer thickness to increase capacitance per unit volume. Another approach is to use base metal electrodes. Barium titanate is the most widely used dielectric material but to meet the demand for thinner layers smaller particle size powders are required. The properties and performance of a new barium titanate powder developed for thin layers are described in the following. This powder consists of submicron particles and ceramic discs can be sintered to high density at 1240°C with uniform microstructures. The powder densifies at lower temperatures than commercially available hydrothermal powders. Using this new powder technology a submicron low fire Y5V powder and a BME Y5V powder were formulated. Work is underway to demonstrate these dielectrics in thin layer MLCCs with fired layers < 4 μm thick.

1. Introduction :

The capacitance per unit volume for an MLCC can be derived as:

$$C_v = n\, K_o\, K\, /\, t^2$$

where C_v is capacitance per unit volume of the active part of the capacitor, n is the number of active layers, K_o is the permittivity of free space (a constant), K is the dielectric constant of the ceramic and t is the thickness separating the active layers. In a given MLCC design with a fixed active volume C_v has to be increased by:

(1) Using a ceramic with higher K
(2) Making thinner ceramic layers, t
(3) Putting more layers, n, in the component
(4) A combination of the above

It is important to note that because of the reciprocal relationship with the square of the thickness, (2) is an effective way to increase C_v and thinner layers, of both ceramic and electrode are required to realize the benefits of more layers (3).

Furthermore, manufacturing cost of MLCCs can be further reduced if base metal electrodes such as Ni or Cu are used to replace conventionally used precious metal electrodes such as Pd and Pd/Ag.

In order to form thin layers of ceramic it is important to avoid agglomerates in the slips used to fabricate the MLCCs[1] and the fired layers should have at least 5 grains between electrodes to make reliable parts. In order to apply base metal electrodes it is important to control precisely the Ba to Ti ratio of the $BaTiO_3$ since MLCCs with base metal electrodes are sintered in low oxygen partial pressure to prevent Ni or Cu from oxidation and Ba to Ti ratio plays a major role in preventing $BaTiO_3$ from reducing to semiconductor.

In order to meet these requirements for layers < 4μm and for BME application submicron barium titanate powders have been made by a variety of chemical processes. The method, which has received most attention in this respect, is hydrothermal processing. In this case barium titanate is produced in an aqueous medium usually from the hydroxides or oxides of barium and titanium according to the equation:

$$Ba(OH)_2 + Ti(OH)_4 = BaTiO_3 + 3H_2O$$
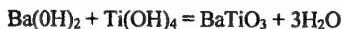
The reactants are subjected to high temperatures and pressures under strongly alkaline conditions to complete the reaction to

barium titanate. In this way a submicron powders with the perovskite structure (including barium titanate) can be formed and several patents have been filed around the world by various companies with respect to this process. In addition to the benefits already mentioned further merits claimed for using fine barium titanate powders in MLCCs are[2]:

1. increased mechanical strength
2. improved voltage dependency
3. flatter temperature characteristic
4. higher voltage breakdown

In the following section we will present data on the properties of a new $BaTiO_3$ powder (TICON F) produced by FERRO using a chemical route and compare this to commercially available hydrothermal powders. Electrical data on the properties of a low fire Y5V and a BME Y5V formulation made with this new powder will be presented.

2. Experimental Results :
Following extensive laboratory trials at FERRO a new process for the manufacture of barium titanate was identified with respect to producing a submicron powder. Barium titanate produced on a large scale (> 5000 kg) using this process was shown to be submicron by laser particle size analysis using a Microtrak - X100 instrument.

The SEM picture of this barium titanate indicates that the primary particles are round fragments with an average size around 0.3µm. The surface area of this powder was measured as 6.5 m^2/g by the BET method. An X-ray powder diffraction spectrum of the powder confirmed that this was a totally reacted cubic barium titanate and no other phases were detected.

The ratio of Ba/Ti was determined by an X-ray fluorescence method
as 1.000 ± 0.002. Selected trace elements were analyzed by an ICP method.
All of them are less than 200 ppm.

To test the sinter activity of this powder disks were pressed and sintered for dwell times of 2 hours at temperatures from 1160°C to 1320°C at 20°C intervals and their densities were measured. In addition to this TICON F powder, this experiment was carried out with 2 commercial sources of hydrothermal barium

titanate powder and HPB-S, another standard Ferro high purity barium titanate. This experiment shows that TICON F densifies at lower temperaptures than the hydrothermal or standard high purity barium titanate discs. Furthermore the TICON F reaches a density of > 5.80 g/cc at 1240°C which is > 96% theoretical. The grains are relatively well developed and uniform even at this low firing temperature; For this reason we decided to develop from this barium titanate Y5V formulations compatible with 70Ag/30Pd electrodes which has to be fired at < 1150°C and also Y5V formulations compatible with Ni electrodes which has to be fired in low oxygen partial pressure.

Typical electrical properties of MLCCs made from a low fire Y5V dielectric powder developed from Ticon-F $BaTiO_3$, using 70Ag/30Pd electrodes and fired at 1130°C for 3 hours can achieve a dielectric constant, K, of above 17,000 with DF of about 3.0 %. TC meets EIA Y5V specification. IR, DF, BDV also meet EIA specifications. Fired grain size is about 2 to 3 microns.

Typical electrical properties of MLCCs made from a BME Y5V dielectric powder developed from Ticon-F $BaTiO_3$, using Ni electrodes and fired at 13000°C for 2 hours in N_2/H_2/H_2O gas with PO_2 of 10^{-8} can achieve a dielectric constant, K, of above 15,000 with DF of about 3.5 %. TC meets EIA Y5V specification. IR, DF, BDV also meet EIA specifications. Fired grain size is about 3 to 4 microns.

It was demonstrated that this dielectric powder offers high K, low DF, Y5V TC, high IR, high BDV, and small fired grain size. It is suitable for manufacturing MLCCs with thin layers and with Ni electrodes.

3. Conclusions :
A new route to submicron barium titanate, TICON F, has been demonstrated on a large scale. This powder densifies at lower temperatures than commercially available submicron barium titanate powders made by hydrothermal processing. Work to-date indicates that the TICON F can be formulated into low fire Y5V and BME Y5V type dielectrics for manufacturing of thin layer and metal electrode MLCCs.

Reference

1. R. Kobayashi, T. Ishigaki, M. Fujimoto, O. Otani and W. Takahara, " Multilayer Ceramic Capacitors Incorporating Nickel Internal Electrodes and Ultra Thin Dielectric Layers ", IEMT/IMC Proceedings, 1997, p372-377.
2. M. Aoki, " Barium Titanate Powders '", Ceramics (Japan), 29, No.8, p1-5

Occupational Sites of Rare-Earth Elements in BaTiO$_3$

Hiroshi Kishi*, Noriyuki Kohzu, Youichi Mizuno, Yoshiaki Iguchi
Junichi Sugino[1], Hitoshi Ohsato[1] **and Takashi Okuda[1]

Taiyo Yuden Co., Ltd., 5607-2 Nakamuroda, Haruna-machi, Gunma-gun, Gunma 370-3347, Japan
*Fax: 81-027-360-8315, e-mail: hkishi@jty.yuden.co.jp
[1]Nagoya Institute of Technology, Gokiso-cho, Showaku, Nagoya 466-8555, Japan
**Fax: 81-052-735-5294, e-mail: ohsato@mse.nitech.ac.jp

The effect of occupational sites of rare-earth elements such as La, Sm, Dy, Ho, Er and Yb on the microstructure in BaTiO$_3$ (ABO_3) with various Ba/Ti ratios was studied. The grain size changed markedly depending on the Ba/Ti ratio in the case of larger ion (La, Sm)- and smaller ion Yb-doped BaTiO$_3$. On the other hand, in the case of intermediate ionic radius rare-earth element (Dy, Ho, Er)-doped BaTiO$_3$, the grain size changed gradually in a wide range of Ba/Ti ratio. It is considered that the intermediate ionic radius rare-earth ions occupy both A- and B-sites, depending on the Ba/Ti ratio, while the larger rare-earth ions and the smaller rare-earth ions occupy A- and B-sites, respectively. The solubility, the microstructure and the resistivity of rare-earth elements and Mg-substituted BaTiO$_3$ were also investigated. It was also confirmed that larger ion (La, Sm) occupied A-sites, smaller ion Yb occupied B-sites and intermediate ionic size (Dy, Ho, Er) ions occupied both A- and B-sites. It was found that the drastic change of the resistivity of the intermediate ionic size rare-earth- and Mg-substituted BaTiO$_3$ was due to the change in the predominant occupational site of rare-earth ions.

1. Introduction

In recent years, multilayer capacitors (MLCs) with Ni electrodes have been widely used in electronic components to meet requirements for high volumetric efficiency and reduced manufacturing costs. In nonreducible dielectrics based on BaTiO$_3$ (ABO_3), it is well known that the resistance degradation of dielectrics strongly depends on the A/B molar ratio and the ratio of donor dopant to acceptor dopant.[1, 2] Okino et al. reported that highly reliable Ni-MLCs conforming to X7R specification were obtained by the addition of a intermediate ionic size rare-earth oxide (R_2O_3) such as Dy, Ho and Er into the BaTiO$_3$-MgO-R_2O_3 based system.[3] Furthermore, the authors reported the relationship between the microstructure and the solubility of rare-earth elements in the BaTiO$_3$-MgO-R_2O_3 based system.[4, 5] It was suggested that the substitution of rare-earth elements into the shell phase of the BaTiO$_3$-MgO-R_2O_3 based system changed from A-site to B-site occupation as the ionic radius decreased. On the other hand, Takada et al. reported that rare-earth elements with intermediate ionic size in BaTiO$_3$ occupied both A- and B-sites depending on the Ba/Ti ratio.[6] These studies suggest that both the electrical properties and the microstructure of rare-earth doped BaTiO$_3$ are strongly affected by the change in occupational sites of rare-earth elements in perovskite.

The increase in capacitance per volume of MLCs is mainly due to a reduction in thickness of the dielectric layers. During the past decade, the dielectric layer thickness has been reduced to 3 μm. Further investigation of the relationship between the microstructure and the occupational site of doped rare-earth elements in the shell region is necessary to improve

the electrical properties of thin dielectric layer Ni-MLCs. However, the relationship between the microstructure and the change in occupational sites of rare-earth elements in BaTiO$_3$ have not been reported so far.

Therefore, in the present study, using various rare-earth elements having different ionic radii, we examined the effect of occupational sites of the rare-earth elements on the microstructure in BaTiO$_3$. The ionic radii of Ba, Ti, and rare-earth elements are summarized as follows: A-site (12 coordinate): Ba^{2+}=1.610 Å, La^{3+}=1.360 Å, Sm^{3+}=1.240 Å Dy^{3+}=1.253 Å, Ho^{3+}=1.234 Å, Er^{3+}=1.234 Å Yb^{3+}=1.217 Å; and B-site (6 coordinate): Ti^{4+}=0.605 Å, La^{3+}=1.032 Å, Sm^{3+}=0.958 Å Dy^{3+}=0.912 Å, Ho^{3+}=0.901 Å, Er^{3+}=0.890 Å, Yb^{3+}=0.868 Å. The ionic radii of Dy, Ho, Er and Yb ions in a 12-coordinate system are based on the relationship between coordination number and effective ionic radii according to Shannon's table.[7] We investigated the effect of rare-earth elements on the microstructures and the substitution in BaTiO$_3$ with different Ba/Ti ratios, and also investigated the microstructures and the solubility of rare-earth elements and Mg-substituted BaTiO$_3$ solid solutions, assuming the shell phase of a BaTiO$_3$-MgO-R_2O_3 based system.

2. Experimental

In order to examine the effect of rare-earth elements on the microstructure in BaTiO$_3$ with different Ba/Ti ratios, samples were prepared by the conventional method as follows. Hydrothermally synthesized BaTiO$_3$ with a mean particle size of about 0.4 μm (Sakai Chemical Industry Co., Ltd.), reagent-grade BaCO$_3$ and TiO$_2$, and fine grained rare-earth oxides were

used as raw materials. The Ba/Ti ratio of $BaTiO_3$ was determined by X-ray fluorescence analysis to be Ba/Ti=0.997. Along with 1.5 atomic% rare-earth oxide (La_2O_3, Sm_2O_3, Dy_2O_3, Ho_2O_3, Er_2O_3, Yb_2O_3), $BaCO_3$ or TiO_2 was added into $BaTiO_3$ to modify the Ba/Ti ratio of samples in the range 0.985 to 1.015. Additives and $BaTiO_3$ were weighed, mixed by ball milling for 15 h and then dried. The powder mixture containing an organic binder was pressed into disks, and then the disks were fired at 1400°C in a low oxygen atmosphere controlled by H_2, N_2, O_2 and H_2O after the binder was burned out. The microstructures of the sintered samples were observed by scanning electron microscopy (SEM). The ceramics were crushed and ground into powder, and then the sample was characterized by powder X-ray diffraction (XRD).

To analyze the influence of rare-earth elements on the microstructure and the solubility in the shell phase of the $BaTiO_3$-MgO-R_2O_3 based system, other samples were prepared according to the formula $(Ba_{1-2x}R_{2x})(Ti_{1-x}Mg_x)O_3$; where x=0–0.15. This formula is based on a model substituting R and Mg ion for Ba and Ti, respectively. The raw materials, $BaCO_3$, $MgCO_3$, TiO_2, La_2O_3, Sm_2O_3, Dy_2O_3, Ho_2O_3, Er_2O_3 and Yb_2O_3 were mixed and then calcined at 1250°C. Identification of crystalline phases was performed by powder XRD analysis. The occupational site of the rare-earth element was determined by the behavior of the lattice parameters as a function of the amount doped x. In order to avoid the influence on the lattice parameters by phase transition, high-temperature powder XRD analysis was carried out at 300°C much higher than the Curie point. The lattice parameters were determined precisely using the whole-powder-pattern decomposition method (WPPD[8]) program as described in a previous paper.[9] The disk samples were also prepared using the calcined powders by the same method as the former samples. The disks were sintered at 1380°C in a low oxygen atmosphere. The electrical resistivity of the samples was measured by the two-probe dc technique. The microstructure of the samples was also observed by SEM.

3. Results and Discussion
3.1 Rare-earth doped $BaTiO_3$ with various Ba/Ti ratios

Figure 1 shows the change in grain size of 1.5 atomic% various rare-earth oxides doped $BaTiO_3$ as a function of the Ba/Ti ratio. The Ba/Ti ratio showed a significant effect on the grain size. However, the grain growth behavior strongly depended on the type of rare-earth elements. In the case of larger ion (La, Sm)- and smaller ion Yb-doped $BaTiO_3$, the grain size changed drastically depending on the Ba/Ti ratio. Grain growth occurred at Ba/Ti ratios smaller than 0.995 for La- and Sm-doped $BaTiO_3$ and 1.010 for Yb-doped $BaTiO_3$. On the other hand, in the case of intermediate ionic size (Dy, Ho, Er)-doped $BaTiO_3$, the grain size changed gradually in a wide range of Ba/Ti ratio.

In perovskite materials such as $SrTiO_3$ and $BaTiO_3$, it is well known that the microstructures are strongly affected by A/B ratio. Many authors have reported that abnormal grain growth occurred when the composition had excess B-sites, and

that the inhibition of grain growth was observed when the composition had excess A-sites.[10, 11] Therefore, to analyze the site occupancy of R ions in the $BaTiO_3$ lattice, we examined the crystalline phases in the sintered samples by powder XRD. Figure 2 shows XRD profiles of 1.5 atomic% various rare-earth-doped $BaTiO_3$ with Ba/Ti ratio=1.000 sintered at 1400°C. The peak of R_2O_3 was not observed for all samples. The $BaCO_3$ peaks were observed as a secondary phase for La- and Sm-doped $BaTiO_3$. The unknown peak was observed for Sm-doped $BaTiO_3$ with Ba/Ti ratio above 1.000. It is considered that the slight grain growth for Sm-doped $BaTiO_3$ in a range Ba/Ti ratio between 1.000 to 1.010 is related to the existence of the unknown phase. The intensity of $BaCO_3$ peak increased with increasing Ba/Ti ratio. This suggests that La and Sm ions occupy A-sites and generate excess BaO. In the case of Yb-doped $BaTiO_3$, pyrochlore ($Yb_2Ti_2O_7$) peaks were observed. The intensity of the pyrochlore peak increased with decreasing Ba/Ti ratio. It is considered that a portion of Yb ions substitute for Ti ions and residual Yb_2O_3 reacts with excess TiO_2. On the other hand, in the case of Dy-, Ho-and Er-doped $BaTiO_3$, no secondary phase appeared in all those samples with various
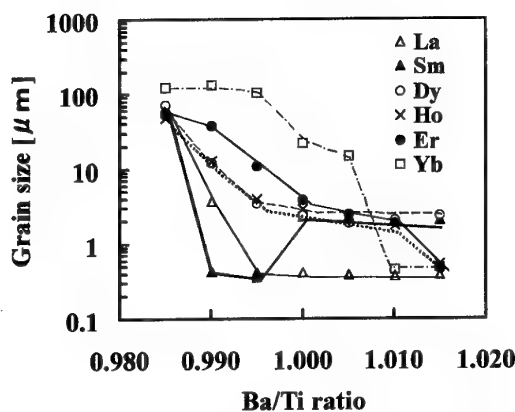
Fig.1 Grain size of La-,Sm-,Dy-,Ho-,Er- and Yb-doped $BaTiO_3$ with various Ba/Ti ratios sintered at 1400°C .
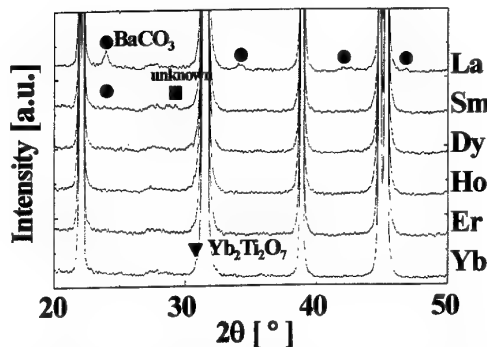
Fig.2 XRD profile of La-, Sm-, Dy-, Ho-, Er- and Yb-doped $BaTiO_3$ with Ba/Ti ratio = 1.000 sintered at 1400°C.

Ba/Ti ratios. This suggests that Dy, Ho and Er ions occupy both A- and B-sites depending on the Ba/Ti ratio.

Taking into consideration the grain growth behavior and the total A/B ratio including the substitution of rare-earth ions into the BaTiO₃ lattice, the present results can be explained as follows. The larger ionic radius (La, Sm) ions predominantly occupy A-sites, while the smaller ionic radius Yb ions predominantly occupy B-sites irrespective of the Ba/Ti ratio. On the other hand, the intermediate ionic radius (Dy, Ho, Er) ions can occupy both A- and B-sites, depending on the Ba/Ti ratio and keep the balance of site occupation.

3.2 Rare-earth- and Mg-substituted BaTiO₃

In a previous study[5], it was suggested that the formation of a core-shell structure in the BaTiO₃-MgO-R_2O_3 based system is dependent on the substitution ratio of rare-earth ions into the A-site. To promote further understanding of the solubility behavior of rare-earth ions in the shell phase, we also investigated the substitution site, the microstructure and the resistivity of the $(Ba_{1-2x}R_{2x})(Ti_{1-x}Mg_x)O_3$ solid solutions. Here, Mg is considered to occupy the B-site, since the radius of Mg ion (0.720 Å) is similar to that of Ti ion.

Figure 3 shows the lattice parameters of the samples measured at 300°C, as determined by WPPD. The solubility behavior strongly depended on the ionic radius of the rare-earth element. The crystalline phases of the samples were as follows. A single phase of BaTiO₃ solid solution was obtained in wide range for larger ion (La, Sm)- and Mg- substituted samples. No secondary phase appeared in the range up to x=0.150 for La-Mg-substituted samples and x=0.050 for Sm-Mg-substituted samples. On the other hand, in the case of (Dy, Ho, Er, Yb)- and Mg-substituted samples, a single phase of BaTiO₃ solid solution was obtained only up to x=0.005. As secondary phases, pyrochlore ($R_2Ti_2O_7$), R_2O_3, R_2MgTiO_6, etc., were observed. The substitution sites were determined based on the change of the lattice parameter as follows. The increase in lattice parameter is based on B-site replacement with cations (Mg, rare-earth) larger than Ti ion. The decrease in lattice parameter is based on A-site replacement with cations (rare-earth) smaller than Ba ion. As a result, in the case of $(Ba_{1-2x}R_{2x})(Ti_{1-x}Mg_x)O_3$ solid solutions, it was also confirmed that larger ion (La, Sm) predominantly occupied A-sites, smaller ion Yb predominantly occupied B-sites and ions of intermediate size (Dy, Ho, Er) occupied both A- and B-sites, as described in the following. In the case of La-Mg- and Sm-Mg-substituted samples, the lattice parameter decreased, dividing into two stages. The lattice parameter decreased gradually up to x=0.050 for La-Mg-substituted samples, x=0.030 for Sm-Mg-substituted samples in the first stage, and then they decreased steeply in the second stage. As the second slopes of both samples were steeper than those of the first slopes, the substitution ratio of A-sites in the second stage is larger than those in the first stage. Thus, this shows that the substitution in the second stage is ideal and obeys the substitution formula $(Ba_{1-2x}R_{2x})(Ti_{1-x}Mg_x)O_3$. In the case of Dy-Mg-, Ho-Mg-, Er-Mg-substituted samples, both the

decrease and the increase in lattice parameters were observed. Initially, the lattice parameter decreased gradually up to x=0.050 for Dy-Mg-substituted samples, x=0.010 for Ho-Mg-substituted samples and x=0.005 for Er-Mg-substituted samples. In the second stage, they showed little change up to x=0.100 for Dy-Mg-substituted samples, x=0.025 for Ho-Mg-substituted samples and x=0.010 for Er-Mg-substituted samples. In the third stage, the increase in the lattice parameter was observed up to x=0.150 for Dy-Mg-substituted samples, x=0.050 for Ho-Mg-substituted samples and x=0.030 for Er-Mg-substituted samples. The lattice parameter showed little change above x=0.050 for Ho-Mg-substituted samples and x=0.030 for Er-
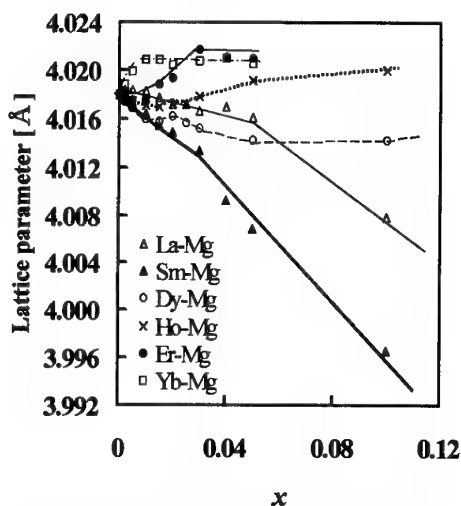
Fig.3 Lattice parameter of $Ba_{1-2x}R_{2x}Ti_{1-x}Mg_xO_3$ solid solutions measured at 300°C as a function of x (R=La, Sm, Dy, Ho, Er, Yb).
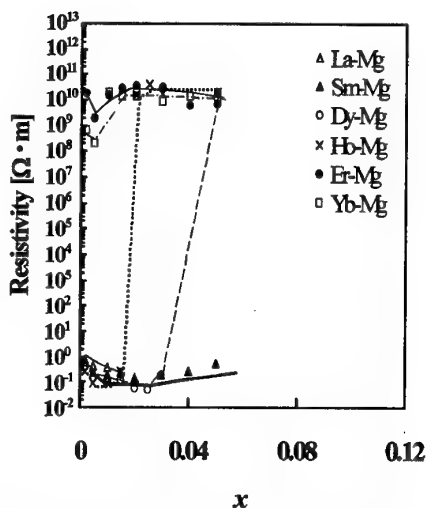
Fig.4 Resistivity of $Ba_{1-2x}R_{2x}Ti_{1-x}Mg_xO_3$ solid solutions sintered at 1380°C as a function of x (R=La, Sm, Dy, Ho, Er, Yb).

Mg-substituted samples. This shows the limit of solid solutions. Thus, Dy, Ho and Yb ion is considered to occupy both A- and B-sites depending on the composition. It appeared that the substitution ratio of rare-earth (Dy, Ho, Er) into A-site decreased as ionic radius decreased. On the other hand, in the case of the Yb-Mg-substituted samples, the lattice parameter increased up to $x=0.010$ and showed no change above $x=0.010$. Therefore, Yb ion is considered to predominantly occupy the B-site up to $x=0.010$. It also appeared that the limit of solid solution of rare-earth ions into the $BaTiO_3$ lattice decreased as ionic radius decreased. These results suggest that larger ion (La, Sm) predominantly acts as a donor dopant, smaller ion Yb predominantly acts as an acceptor dopant and intermediate ionic radius (Dy, Ho, Er) ions act as both donor and acceptor dopants. It is also considered that the ions of intermediate size behave more likely as acceptor dopants as ionic radius decreases.

The electrical resistivity of $(Ba_{1-2x}R_{2x})(Ti_{1-x}Mg_x)O_3$ solid solutions measured at room temperature is shown in Fig. 4. As can be seen in Figs. 3 and 4, the change in resistivity almost corresponds to the change of the lattice parameter for each sample. The resistivities of the La-Mg- and Sm-Mg-substituted samples were quite low. In the case of Dy-Mg- and Ho-Mg-substituted samples, the resistivity was quite low up to $x=0.030$ and $x=0.015$, respectively and then increased abruptly thereafter. In the case of Er-Mg- and Yb-Mg-substituted samples, all samples showed high resistivities. It is well known that a donor dopant can effectively reduce the resistivity of $BaTiO_3$, and that an acceptor dopant can effectively prevent the reduction of $BaTiO_3$ sintered in a reducing atmosphere. These results showed good agreement with the result of lattice parameters.

To clarify the relationship between the resistivity and the microstructure of intermediate ionic radius (Dy, Ho, Er) and Mg substituted samples, the grain size of the samples was examined. For the donor-doped $BaTiO_3$ sintered in air, it is well known that the grain size decreases rapidly with increasing donor concentration when the ceramic transits from a semiconductor to an insulator.[12] However, in the case of Dy-Mg- and Ho-Mg-substituted sample, the grain size changed little even when the resistivity increased abruptly. Thus, this result is also evidence that the increase in the resistivity of intermediate ionic radius (Dy, Ho, Er)- and Mg-substituted samples is due to the change of the predominant substitution site of rare-earth ion, from the A-site (act as a donor) to the B-site (act as an acceptor). Consequently, it was confirmed that intermediate ionic radius (Dy, Ho, Er) ions were very effective for controlling both the A/B ratio and the donor/acceptor dopant ratio in $BaTiO_3$. Thus, it is considered that the high reliability of Ni-MLCs using the intermediate ionic radius rare-earth doped $BaTiO_3$ is due to the balance of the site occupation of rare-earth ions in the $BaTiO_3$ lattice.

4. Conclusion

The effect of occupational sites of rare-earth element on the microstructure in $BaTiO_3$ with various Ba/Ti ratios was investigated. The grain growth behavior strongly depended on the kind of rare-earth element used. The grain size changed drastically depending on the Ba/Ti ratio, for larger ion (La, Sm)- and smaller ion Yb-doped $BaTiO_3$. It is considered that La and Sm ions occupy A-sites, while Yb ions occupy B-sites irrespective of the Ba/Ti ratio. On the other hand, in the case of intermediate ionic radius (Dy, Ho, Er)-doped $BaTiO_3$, the grain size changed gradually in a wide range of Ba/Ti ratio. It is considered that Dy, Ho and Er ions occupy both sites, depending on the Ba/Ti ratio.

The substitution, the microstructures and the electrical resistivity of $(Ba_{1-2x}R_{2x})(Ti_{1-x}Mg_x)O_3$ solid solutions, as a model of the shell phase of the $BaTiO_3$-MgO-R_2O_3 based system, were also investigated. By high-temperature powder XRD analysis, it was also confirmed that the larger rare-earth ions occupy A-sites, the smaller rare-earth ions occupy B-sites and the intermediate ionic radius rare-earth ions occupy both A- and B-sites. The grain size of Dy-Mg- and Ho-Mg-substituted samples gradually decreased with increasing dopant content. It is obvious that the drastic increase in the resistivity of these samples is due to the change of the predominant occupational site of rare-earth ions. It was found that intermediate ionic size (Dy, Ho, Er) ions were effective for controlling both the microstructure and the electrical properties of $BaTiO_3$.

References

1. Y. Sakabe, K. Minai and K. Wakino: *Proc. 3rd Meeting on Ferroelectric Materials and their Applications*, Jpn. J. Appl. Phys. **20** (1981) Suppl. 20-4 , p.147.
2. Y. Nakano, A. Satoh, A. Hitomi and T. Nomura: Ceram. Trans. **32** (1993) 119.
3. Y. Okino, H. Shizuno, S. Kusumi and H. Kishi: Jpn. J. Appl. Phys. **33** (1994) 5393.
4. H. Kishi, Y. Okino, M. Honda, Y. Iguchi, M. Imaeda, Y. Takahashi, H. Ohsato and T. Okuda: Jpn. J. Appl. Phys. **36** (1997) 5954.
5. H. Kishi, N. Kohzu, J. Sugino, H. Ohsato, Y. Iguchi and T. Okuda: J. Euro. Ceram. Soc. **19** (1999) 1043.
6. K. Takada, E. Chang and D. M. Smith: *Advanced in Ceramics*, eds. J. B. Blum, W. R. Cannon (Amer. Ceram. Soc.) 2nd ed., Vol. 1, p. 147.
7. R. D. Shannon: Acta. Crystallogr. **A32** (1976) 751.
8. H. Toraya: J. Appl. Crystallogr. **16** (1986) 440.
9. H. Ohsato, M. Imaeda, Y. Okino, H. Kishi and T. Okuda: Adv. X-ray Anal. **40** (1997) (CD-ROM: International Centre for Diffraction Data).
10. C. Kawashima and N. Setaka: Yougyou Kyoukaisi **70** (1962) 225 [in Japanese].
11. N. Kohzu, S. Hayashi, N. Mabuchi, K. Tanaka, Y. Iguchi and H. Kishi: J. Jpn. Powder & Powder Metall. **42** (1995) 1441 [in Japanese].
12. S. B. Desu and D. A. Payne: J. Am. Ceram. Soc. **73** (1990) 3407.

Effect of Rare-Earth Doping on the Temperature-Capacitance Characteristics for MLCCs with Ni electrodes

Shigeki Sato, Yoshinori Fujikawa, Akiko Nagai, Yoshihiro Terada, and Takeshi Nomura

Materials Research Center, TDK Corporation,
570-2 Aza-Matsugashita, Minamihatori, Narita-shi, Chiba-ken, 286-8588 Japan.
Tel :051-476-37-1637 E-mail:Shigekis@MB1.TDK.CO.JP

Abstract   Doping effect of rare-earths on the temperature-capacitance characteristics of MLCCs with Ni electrodes has been investigated for $BaTiO_3$-MgO-Rare-earth system.   Temperature dependence of capacitance became smaller with smaller radii ions such as Ho, Er, Tm, Yb, and Lu.   Especially, Tm,Yb, and Lu were effective dopants to depress the temperature dependence of capacitance.   The Curie temperature also shifted toward higher temperatures by the doping of smaller ionic radii rare-earth elements.   On the other hand, temperature dependence of capacitance became larger and the insulation resistance became lower by the doping of larger ionic radii rare earth elements such as Tb and Gd.   It is clear that ionic radius of rare-earth dopants is an important factor to control the temperature-capacitance characteristics as well as improving the reliability.   Ni electrode MLCCs with X8R characteristics specification for automotive use have been newly developed using rare-earth dopant having smaller ionic radii such as Tm, Yb, Lu.

INTRODUCTION

The requirement for higher capacitance and further miniaturization in multilayer ceramic capacitors (MLCCs) is driven by the downsizing trend in electronics. Structurally this has meant reduction of layer thickness and an increase in the number of layers. The internal electrode of choice has shifted from Pd to Ni in order to realize low cost production.

These requirements also have demanded in automotive uses with the introduction of electronic controls, such as ECU(Engine Control Unit), PGM-FI(Programmed Fuel Injection), ABS(Anti-Lock Brake System), and so on.   Recently, since the weight reduction of automobile in order to improve the fuel consumption, elimination of wire harness and the control module to be mounted in engine room is desirable. Hence, electronic parts in the control module for the automotive applications must keep their performance under higher temperatures.   The Bi_2O_3-PbO-TiO_2 composition has been commonly used for the X8R-MLCCs.   However, the Bi_2O_3-PbO-TiO_2 type MLCCs could not be realized with thinner layers, and has to use Pd, or Ag-Pd as inner electrode.   Therefore, the demand

of X8R MLCCs with Ni electrodes for automotive application become stronger with the trend of miniaturization, cost reduction and environmental protection (Pb-Free).   In order to realize above, the authors have been studying dielectric formulation and microstructure, especially focusing on the temperature characteristics of capacitance of $BaTiO_3$ based materials, and then successfully developed the X8R-MLCCs with Ni electrodes.   In this paper, we report the relationship between temperature-capacitance characteristic and rare earths doping in Ni-X7R material.

EXPERIMENTAL PROCEDURE

The dielectric compositions were $BaTiO_3$ +R_2O_3 (R=Gd,Dy,Ho,E,Tm,Yb,Lu)+ MgO + MnO + V_2O_5+ $(Ba_{0.4}Ca_{0.6})SiO_3$.   Highly pure oxalate or hydrothermal $BaTiO_3$ powders were employed here. The additives were reagent grade oxides or carbonates.   MLCCs were prepared by the so-called sheet methods.   Green sheets were formed by doctor-blade casting and the thickness was controlled between 5 and 10 microns.   After casting, the sheets were dried and Ni electrodes were printed on to them using screen-printing system.   Next,

4 to 100 layers of the sheets were stacked, laminated, and cut into green chips. Binder burn-out was followed by sintering between 1260 and 1340 ℃. During sintering, the oxygen partial pressure was controlled between 10^{-8} and 10^{-13} MPa by adjusting the amounts of H_2 and H_2O in the N_2-H_2-H_2O gas mixture. The chips were then annealed between 700 and 1100℃ in a N_2-H_2O gas mixture in order to re-oxidize the dielectrics.

The permittivity, dissipation factor and their temperature dependencies were measured using an HP-4284A LCR meter (Hewlett-Packard) at 1 kHz with 1.0 V_{rms}. The microstructure were analyzed by the EPMA, TEM, and XRD. The Curie temperature was determined using DSC.

RESULTS AND DISCUSSION

Figure1 shows the temperature-capacitance characteristics of dielectric doped with rare earths. The temperature coefficient of capacitance became smaller with the smaller ionic radii such as Y, Dy, Ho, Er, Tm, Yb, and Lu and satisfied the X7R specification. Especially, it should be noted that Tm,Yb,Lu doped samples satisfy the X8R specification. On the other hand, temperature coefficient of capacitance became larger by the doping of the larger ionic radii rare-earth such as Tb and Gd. In addition the insulation resistance was became lower.

The Curie temperature of various rare earth doped BaTiO$_3$ were measured using DSC and the results are shown in Fig.2. An endothermic peak due to tetragonal-cubic phase transition was observed at a temperature between 110°C to 135°C. The peak shifted toward higher temperatures and the peak width was broadened by the doping of smaller ionic radii rare-earth. The peak shift toward higher temperatures indicated that the tetragonal phase became stable. The broadening of peak width suggest that the tetragonal-cubic phase transition became dispersive. It is considered that increase of Curie temperature and dispersion of phase transition improve the temperature-capacitance characteristics at high temperatures.
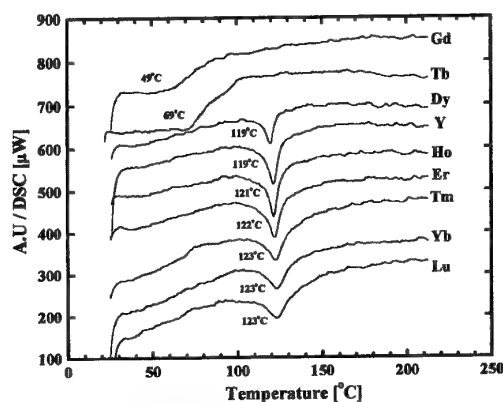
Fig.2 DSC profiles of BaTiO$_3$ doped with various rare-earth elements.

Fig.1 Temperature dependence of capacitance change for various rare-earth doped BaTiO$_3$
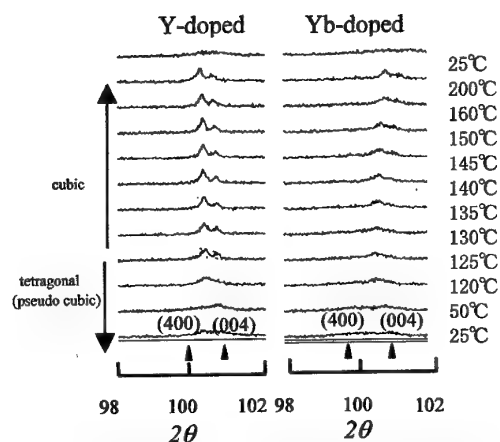
Fig.3 Phase transition of Y-doped X7R material and Yb-doped X8R material measured by hot stage XRD

The (004), (400) peaks for the Y-doped X7R-material and Yb-doped X8R-material were measured between 25°C to 200°C using the hot stage XRD, in order to investigate the effect of the rare earth doping on phase transition of BaTiO$_3$, as shown in Fig.3. XRD peak width of Y-doped X7R-mateial decreased at a temperature above 125°C, along with the tetragonal-cubic phase transition. On the other hand, for the Yb-doped X8R-material, phase transition was not observed clearly by XRD. This phenomenon corresponds to DSC results.

Next, the effect of rare earth doping on microstructure was investigated. Fig.4 shows the XRD profiles around (002), (200) peaks for the rare-earths doped BaTiO$_3$. The distance between (002) and (200) peaks tended to increase by the doping of smaller ionic rare-earth elements. It is assumed that tetragonality become stronger by the smaller ionic radii rare-earth doping. On the other hand, crystal structure of BaTiO$_3$ doped with larger ionic radii rare-earth such as Gd and Tb was considered as cubic.
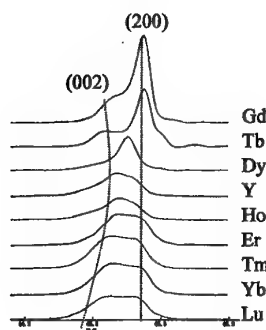
Fig.4   XRD profiles for various rare-earth doped BaTiO$_3$ around (002),(200).

The distribution of rare earth dopant observed by EPMA is shown in Fig.5. The segregation of Y, Ho, Yb, Lu were observed. It is found that segregation increases with the decrease of ionic radii. In the case of larger ionic radii such as Dy,Gd and Tb, no segregation was observed. It is considered that solubility of rare-earth ions into BaTiO$_3$ decreases with the decrease of the ionic radii .

The site occupancy of rare earth ions for the BaTiO$_3$ was investigated using the XRD minor phase analysis[1].

It is found that rare-earths of smaller ionic radii such as Tm, Yb and Lu substitute into the perovskite B site and site occupancy did not depend on A/B ratio as shown in Table 1. Thus, it is assumed that smaller ionic radii rare-earths substitute into perovskite B site and act as depressor for BaTiO$_3$, like MgO. It is thought that the Curie temperature shift toward higher temperatures and the dispersal phase transition are related to stress in the BaTiO$_3$ lattice caused by ionic radius difference between Mg^{2+} and Yb^{3+}.

38*42μm
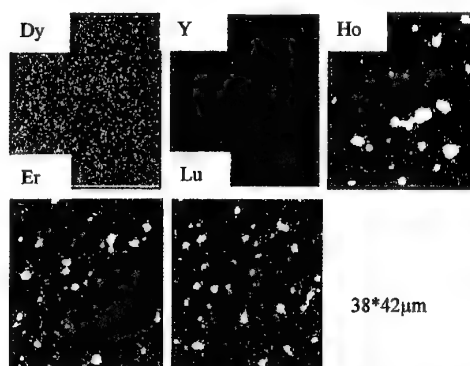
Fig.5 Distribution of rare-earth ions for BaTiO$_3$ observed by EPMA.

Table 1   Minor phase analysis for BaTiO$_3$ Rare-earth system.

		A/B=1.01	A/B=1.00	A/B=0.99
	BaTiO$_3$	Ba$_2$TiO$_5$		Ba$_6$Ti$_{17}$O$_{40}$
Dy	0.5at%			Ba$_6$Ti$_{17}$O$_{40}$
	1.0at%			Ba$_6$Ti$_{17}$O$_{40}$
	1.5at%			Ba$_6$Ti$_{17}$O$_{40}$
		B-site	A,B-site	A,B-site
Y	0.5at%			
	1.0at%		BaO	
	1.5at%		BaO	BaO
		B-site	A-site	A-site
Ho	0.5at%			Ba$_6$Ti$_{17}$O$_{40}$
	1.0at%			Ba$_6$Ti$_{17}$O$_{40}$
	1.5at%			Ba$_6$Ti$_{17}$O$_{40}$ Ho$_2$Ti$_2$O$_7$
		B-site	A,B-site	A,B-site
Yb	0.5at%			Ba$_6$Ti$_{17}$O$_{40}$
	1.0at%		Ba$_6$Ti$_{17}$O$_{40}$	Ba$_6$Ti$_{17}$O$_{40}$ Yb$_2$Ti$_2$O$_7$
	1.5at%		Ba$_6$Ti$_{17}$O$_{40}$ Yb$_2$Ti$_2$O$_7$	Ba$_6$Ti$_{17}$O$_{40}$ Yb$_2$Ti$_2$O$_7$
		B-site	B-site	B-site

Fig.5 shows a TEM micrograph for the Y-doped X7R-material and Yb-doped X8R materials. Their

microstructures have a mixture of largely homogeneous (non-diffused grain) and inhomogeneous grains (partially diffused grain). Especially, many interference fringes probably due to stress, were observed for Yb-doped X8R material. TEM-EDS observation indicated that Yb existed at partial diffused areas and grain boundaries. Therefore, the stress might be originated from substitution of Yb into $BaTiO_3$. These diffused and non-diffused phases were not like the so-called core-shell structure, which is commonly observed in X7R type dielectric materials. However, a very small number of core-shell like grains were also observed. Therefore, it has been demonstrated that the core-shell structure was not necessary in order to satisfy X7R and X8R characteristics.

Fig.6 TEM micrograph of Y-doped X7R material and Yb-doped X8R material.

Finally, the electrical properties for new X8R-MLCCs
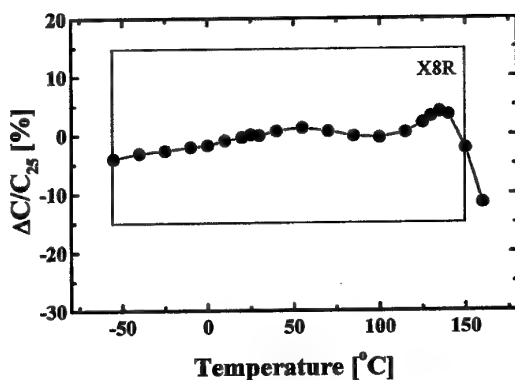
Fig.7 Temperature dependence of newly developed Ni electrode MLCCs with X8R characteristics.

Table 2 Electrical properties of newly developed Ni electrode MLCCs with X8R

1206-0.1μF	16μm -45Layers	W.V=50V
0804-0.1μF	8μm -91Layers	W.V=50V
Internal electrode is Ni.		
Temperature-capacitance specification is X8R		
$\Delta C \leq \pm 15\%$ (T= -55°C~150°C)		
Permittivity	εr=1900	
tanδ	tan δ ≦1%	
Insulation resistance	IR≧1.4*10^{10}	
CR-product	CR=1600MΩμF	
DC Break down voltage	V_{BD}=120V /μm	
HALT	~30hr	at 200°C-15V/μm

1mm
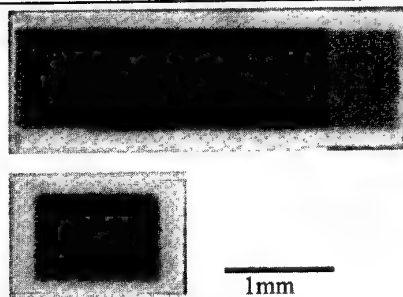
Fig.8 Cross-section of newly developed Ni electrode MLCCs with X8R characteristics.

CONCLUSIONS

(1) It is found that temperature-capacitance characteristics for $BaTiO_3$-MgO-Rare-earth system could be controlled using various ionic radii rare-earths. Especially, smaller ionic radii rare-earthsx such as Tm, Yb and Lu were effective dopants to realize the X8R characteristics.

(2) Curie temperature shift toward higher temperature and the dispersal phase transition were observed by DSC and hot stage XRD in the case of smaller ionic radii rare-earth doping.

(3) It is thought that smaller ionic radii rare-earths substitute into the B-site for $BaTiO_3$ and cause the stress in the lattice.

(4) We have newly developed X8R-MLCCs with Ni electrodes for automotive application through the investigation of suitable formulation and microstructure for Yb-doped $BaTiO_3$ system.

REFERENCES

(1) S.Sato, Y. Nakano, A Sato and T. Nomura, J Eur. Ceram Soc 1 9 (1999) 1061-1065.

AQUEOUS-BASED, Ni-ELECTRODE COMPATIBLE DIELECTRICS FOR ADVANCED MLCC APPLICATIONS

Sridhar Venigalla, David V. Miller, Jeffrey A. Kerchner, Donald J. Clancy, Kathleen A. Thrush, and Stephen A. Costantino, *Cabot Corporation, Boyertown PA 19512*

Multilayer ceramic capacitors (MLCCs) offer unique combination of characteristics such as low equivalent series resistance (ESR), high insulation resistance and breakdown voltage. This makes them attractive in digital and high frequency circuit applications including DC-DC converters, switching power supplies, and power supply bypass capacitors in liquid crystal modules. High capacitance MLCCs also offer an attractive replacement to tantalum and aluminum electrolytic capacitors due to their higher permissible ripple current values, smaller case sizes relative to rated voltage, improved reliability, and lower cost. Recent strides in microelectronic and communication technologies have propelled the miniaturization of multilayer ceramic capacitors (MLCCs), while the performance requirements have tremendously increased: higher capacitance in smaller case sizes (high volumetric efficiency), higher mechanical strength and reliability. In order to meet these advanced performance features, the manufacturers need to fabricate MLCCs possessing 200-400 uniform, ultra-thin ceramic active layers (<3 μm fired thickness), with dense, defect-free microstructure and controlled grain size. In addition, recent increases in Pd price has made the MLCCs containing precious metal electrodes (Pd, Ag-Pd) cost prohibitive. While reducing the manufacturing cost, use of nickel as the electrode material also enhances solderability and thermal shock resistance of MLCCs, improving the overall reliability of the device. Therefore, most MLCC manufacturers have an immediate need to develop high volumetric efficiency MLCCs with base metal (Ni) internal electrodes.

Dielectric Capabilities

Several characteristics of the dielectric material are important for the manufacture of MLCCs with ultra-thin active layers. Fine, uniform, sub-micron particle size and good dispersibility of the dielectric are essential to be able to fabricate good quality thin (<5 μm) green sheets of ceramic. These features also improve surface quality of the green sheet, which is critical to minimize processing-related defects during electrode printing and multilayer

(several hundred alternating layers of dielectric and electrode) lamination. A variety of dopants are added to the dielectric to obtain temperature stability of capacitance as well as reduction resistance (to withstand the reducing atmospheric conditions of sintering employed in Ni electrode MLCC fabrication). Uniform distribution of these dopants among the sub-micron dielectric particles is critical for the optimal control of grain size and microstructure to maintain high reliability. To provide these dielectric material capabilities for the manufacture of advanced MLCCs, Cabot Corporation has developed high purity, sub-micron hydrothermal barium titanate-based ceramic formulations. Through unique coating and dispersion techniques, these formulated particles are provided in highly stable, sub-micron aqueous suspensions suitable for preparation of good quality green ceramic sheets of 5 μm or less in thickness. Compared to conventional dry powder-based dielectrics, Cabot dielectric slurries reduce several processing steps and the manufacturing cost, while providing substantial benefits in green sheet fabrication.

Hydrothermal Barium Titanate Precursors

Cabot's patented hydrothermal process produces spherical, uniform nano-sized particles of $BaTiO_3$ using a low temperature, aqueous reaction between hydrous TiO_2 and $Ba(OH)_2$. Similar particles of perovskite solid solutions having a general formula: $Ba_{1-x-x'}Sr_xCa_{x'}Ti_{1-y-y'}Zr_yHf_{y'}O_3$ can also be synthesized using this process. Pure $BaTiO_3$ is primarily used in the manufacture of MLCCs with X7R specifications to obtain relatively stable temperature characteristics, while the solid solutions are commonly used in Y5V type MLCCs to obtain very high capacitance. The reaction conditions in the hydrothermal process are maintained such that the formation of crystalline, stoichiometric perovskite (ABO_3) compound is thermodynamically favored, thereby eliminating the need for drying, calcination or any other post synthesis adjustments to achieve crystallinity and phase purity. In addition, the kinetics of hydrothermal reaction (nucleation and growth rates)

are precisely controlled to vary the primary particle size in the range 50-400 nm, yielding a wide variety
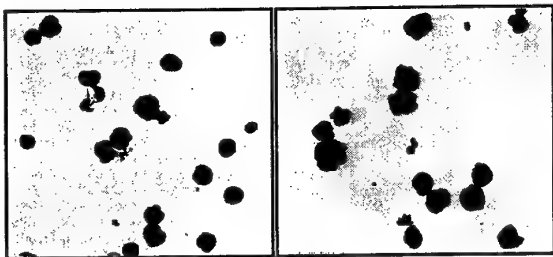
Figure 1: TEM micrographs of two particle size grades of Cabot hydrothermal barium titanate: (left) BT-6 with 250 nm average particle size, and (right) BT-4 with 400 nm average particle size.

of particle size grades to suit specific dielectric applications. Two different grades of particle size suitable for Ni-electrode compatible dielectric formulations (250 nm and 400 nm) are shown in Figure 1. At the end of hydrothermal reaction, the particles are washed while carefully maintaining the stability and chemical homogeneity of the dielectric particles. The aqueous medium in which the particles are synthesized and washed enables further processing (formulation and dispersion) of the material with ease and economy. Since the total aqueous process developed by Cabot does not include a drying or calcination step, hard agglomeration of particles is avoided while the spherical morphology and high dispersibility are maintained.

Surface Coatings of Reduction Resistant Dopants

As mentioned earlier, uniform distribution of dopants is critical to control the sintered microstructure of the dielectric layers (average grain size, grain size distribution, porosity and average pore size) as well as the consistency of electrical characteristics. Achieving uniform distribution of various dopants using conventional formulation methods such as ad-mixing and calcination becomes even more challenging as the primary particle size of dielectric gets smaller. To overcome this hurdle, Cabot has developed a unique aqueous coating process to incorporate a variety of dopants onto the surface of the ceramic particles, providing a uniform layer of dopant compounds. Each dopant is individually coated and varied in sequence to provide optimal performance. Typical Ni electrode compatible dopant elements that can be incorporated

using this technique include Y, Ce, Mn, Ca, Mg, Co, Ho, Dy, Sm, Yb, W, and Mo. Various combinations of dopant elements in a wide range of concentrations can be applied to match customer-specific dielectric formulations. Sophisticated multi-variant statistical methods are applied via experimental design and mathematical modeling to rapidly optimize the formulation and achieve desired MLCC characteristics. Since the formulation coatings are applied to the particles that were never removed from water, the formation of dopant layers is uniform due to the non-agglomerated and dispersible nature of the dielectric particles. Figure 2 shows the transmission electron micrograph of a group of barium titanate particles coated with dopants.
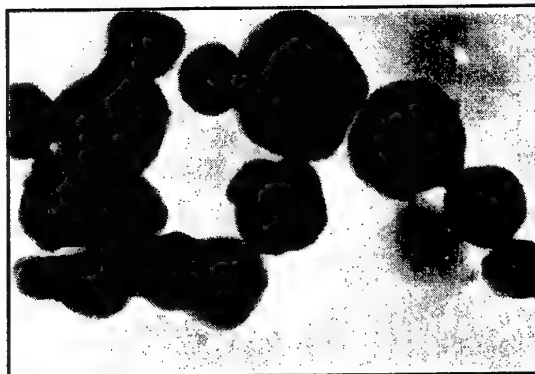
Figure 2: TEM micrograph of surface coated (with dopants) barium titanate particles. The 'mottled' contrast on the surface indicates the adherence of the coated dopants.

The 'mottled' contrast on the surface of each particle indicates the dopant coatings adhering to the surface. Formulated particles are washed in aqueous medium to control ionic strength, while maintaining the stability of the dopants.

Synthesis of Glass Frit Compositions

Most Ni electrode-compatible dielectric formulations include a silicate-based glass forming additive (frit) to reduce sintering temperature. While pure, colloidal SiO_2 is commonly added to serve as the sintering aid, a compound silicate is preferred in some cases to maintain optimum grain boundary composition. Depending on the particular set of atmospheric conditions and desired sintering temperature, these frits typically consist of a binary or ternary silicate composition derived from BaO-SrO-CaO-Li_2O-SiO_2 system. Conventionally, these

frits are manufactured using melt techniques, where individual oxides are mixed together and heated to a molten state and solidified into a single glass phase. The solid glass is subsequently crushed and milled extensively to obtain a small particle sized powder. However, it is extremely difficult to achieve

Figure 3: Particle size comparison of (left) solution derived Cabot frit particles of 50-100 nm range and (right) melt derived, commercially available frit particles of 0.5 - 10 μm range.

uniform particle sizes significantly less than 1 micron using this approach, rendering conventional frit powders less than optimal for use with advanced dielectrics. To provide uniform distribution of the glass phase and achieve superior grain size control, Cabot Corporation has developed a solution synthesis process to obtain 50-100 nanometer sized particles of compound silicates that can be used as dielectric additives. Figure 3 shows a comparison of particle sizes of Cabot synthesized (1-x)BaO•xCaO•SiO$_2$ frit and a commercially available frit with similar composition. Aqueous dielectric slurries were prepared with identical loading of both Cabot and commercial frits to compare particle size distribution and shrinkage behavior. As shown in Figure 4, the final particle size distribution of the
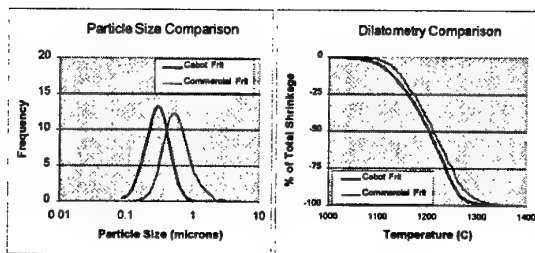
Figure 4: Particle size and dilatometric analysis of dielectric slurries with Cabot frit and commercially available frit.

dielectric slurry was comparatively finer with Cabot frit addition. Additionally, the dielectric sintered to a

similar density at approximately 25°C lower sintering temperature, compared to the commercial frit added dielectric.

Stable Aqueous Dispersions

Hydrothermal barium titanate-based formulated dielectrics produced as described earlier are spontaneously dispersible into stable, sub-micron suspensions. A high solid content aqueous slurry or wetcake (obtained at the end of formulation process) is typically mixed with a small amount of dispersant (actual dosage is based on primary particle size of the dielectric) to produce a stable dispersion. Since the particles were never allowed to form hard agglomerates (which typically occurs during drying and calcination processes), only a short, high shear homogenization step is required to obtain a slurry with no particles larger than 1 μm, as shown in Figure 4. The dispersed slurries exhibit shear thinning rheological behavior (Figure 5) with very low viscosity (10-15 cP) at high shear rates. In slurries that are allowed to stand for extended time, gravitational settling occurs, resulting in a gradual
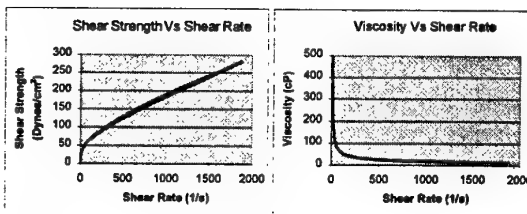
Figure 5: Rheological data of Cabot dielectric slurries: (left) Shear Strength Vs Shear Rate and (right) Viscosity Vs Shear Rate.

stratification of solids from top to bottom. The rate of settling and the hardness of sediment at the bottom vary, depending on primary particle size and slurry viscosity. However, the sediment is easily redispersible, and the slurry can be restored to original viscosity and particle size by either rolling or agitation for a short time. An aging study indicated that slurries undergo minimal change in particle size and viscosity (Figure 6) over a period of six months. The solids content of the formulated slurries typically ranges between 70 and 76 % by weight, depending on primary particle size and dielectric formulation. It can be accurately adjusted and maintained at a specific level, as required by the customer application. Cabot's patented aqueous dielectric slurries are found compatible with many

binders and surfactants used in the preparation of ceramic slip for coating thin green sheets on various polymeric substrates. Green ceramic sheets with
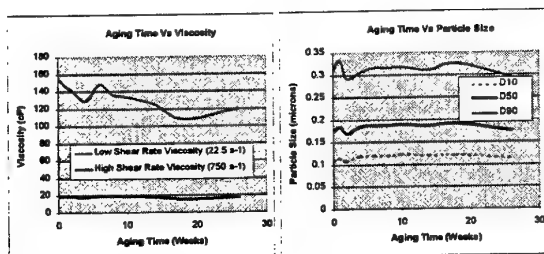
Figure 6: Stability of dielectric slurry viscosity (left) and particle size (right) with time. Individual samples were allowed to stand, and rolled for 24h prior to weekly analysis. Similar results were obtained in a sample that was rolled continuously all through out the period of study.

excellent surface quality and microstructure have been fabricated in 3-5 micron thickness range. Suspension stability and fine, dispersed particle size allow the use of extremely fine slip filtration systems to remove foreign contaminants and minimize defect density in the green sheet, which are critical to meet stringent MLCC reliability requirements.

Microstructure and Electrical Characteristics

Use of nickel as internal electrode requires that the green MLCCs are sintered in a reducing atmosphere (pO_2 between 10^{-7} and 10^{-11} atm) to prevent the oxidation of nickel. However, the dielectric has to be formulated with reduction-resistant dopants to prevent loss of insulation characteristics. As listed
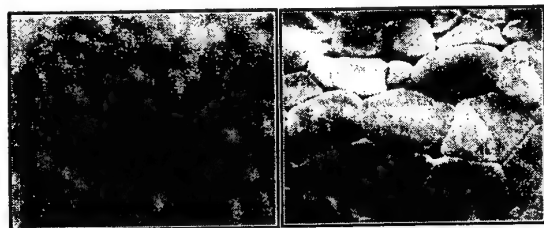
Figure 7: SEM micrographs of typical grain structures of Ni electrode compatible Cabot dielectrics (left) X7R with 0.15 - 0.25 μm grain size and (right) Y5V with 0.5 - 2.0 μm grain size.

earlier, several dopants in various patented combinations and concentrations have been

successfully used by MLCC manufacturers to impart reduction resistance to the dielectric. However, these formulations are very specific to the type of gas mixtures used in creating reducing atmosphere, the sintering profile, the pO_2 level, the post-sinter annealing and several other processing conditions. To meet these specific formulation requirements, Cabot Corporation has begun offering custom formulated dielectric slurries for direct use in fabricating the green sheet. Typical sintered microstructures for X7R and Y5V dielectrics are shown in Figure 7, where the advantage of uniform distribution of dopants at microscopic levels is manifested via the uniform, controlled grain structure. Typical electrical characteristics are
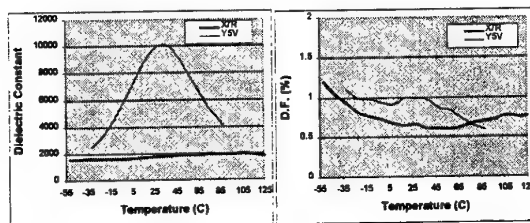
Figure 8: Typical dielectric constant (left) and dissipation factor (right) data for Ni elecrode compatible X7R and Y5V dielectrics. The data is obtained on 10 mm dia X 2 mm thick sintered discs.

shown in Figure 8. Very often, the custom dielectric formulations need optimization to attain the desired electrical characteristics. This can be performed very rapidly and effectively by using experimental design and mathematical modeling.

Summary

Cabot Corporation has developed hydrothermal barium titanate - based dielectric slurries that are custom formulated for manufacturing high volumetric efficiency X7R and Y5V MLCCs with Ni internal electrodes. Manufactured by a total aqueous process where no drying step is involved, these stable, sub-micron suspensions provide significant benefits in the fabrication of thin green sheets with good surface quality and low defect density. Controlled grain structure resulting from the uniform primary particle size and the surface coating of dopants promotes higher part yields and device reliability.

Acknowledgments

Effect of Multiplication on Residual Stress and Reliability of MLCCs with Ni-electrode

Yukie Nakano, Takeshi Masuda   and   Takeshi Nomura

Materials Research Center, TDK Corporation,

570-2,Matsugashita, Minami-Hatori, Narita-shi, Chiba-ken, 286-8088

FAX:81-476-37-1637, e-mail: yukien@mb1.tdk.co.jp

With increase of the number of the dielectric layer of multilayer ceramic capacitors (MLCCs) for high capacitance, internal stress in the capacitors where the stress was estimated by the micro-indentation method. It is supposed that the difference of the shrinkage of the dielectrics and the Ni's oxidation and expansion of the Ni internal electrode caused the stress. The stress made the reliability worse. However the stress was decreased by the improvement of the internal electrode and the firing conditions.

1 INTRODUCTION

On demand of down sizing, high efficient and low cost of the electric parts for down sizing of the electronics, multiplication and thinning of dielectrics and base-metal electrode are highly requested for MLCCs. Now, MLCCs with 300 layers of 3μ m dielectrics have been developed, although MLCCs having under 100 layers of over 10μ m dielectrics were generally manufactured ten years ago. The limit of the thinning of dielectric layers has been discussed many times, but owing to the advanced technology of the sheet casting method and the improvement of the dielectrics, the limit had been broken. Now, the 1000 numbers of 1μ m layers' MLCCs are expected in the near future.

In the background of the rapid progresses of thinning and multiplication processes, Pd was replaced with base-metal Ni as an internal electrode material. In the case of Pd electrode, it cost high with the thinning and the multiplication, therefore it is inferior to other kinds of capacitor, for example aluminum-electrolytic capacitors, tantalum-electrolytic capacitors, and film capacitors. In the case of Ni is very cheap, so it has a cost merit with high capacitance. Since 1990's the production of Ni-MLCCs has expanded rapidly, because of their success in the high reliability. Now the market of the Ni-MLCCs is becoming wider owing to their cost advantage with high capacitance. Ni-MLCCs have much more merit than electrolytic capacitors such as no polarity, high capacitance value, low ESR(equivalent series resistance), miniaturization, and so on. However different materials i.e. dielectrics and internal electrode must be cofired, the difficulty of thinning and multiplication of layers have been exposed. The delamination and cracks are easily occur during firing. In the case of Pd internal electrode, firing process is carried out in air so the structural defects easily occur due to oxidation and reduction of Pd. However the Ni-MLCCs are fired in the reducing atmosphere, so the structural defects do not exist in general. But for high capacitance e.g. 100μ F, because of the multiplication and thinning of dielectrics, the defects appear because of the difference in the density of internal electrodes and dielectrics and other physical differences. Even if the defects were not generated, it is expected that the residual stress remained in them. Therefore it is a critical point for very high capacitance to solve this problem in the future.

Many studies have been carried out for the reliability of Ni-MLCCs,[1-5] but very few for the residual stress.[6,7] Therefore in this paper, from this point of view, the effect of multiplication of MLCCs on the residual stress has been studied with focusing on the electric characteristics in MLCCs.

2 EXPERIMENTAL PROCEDURE

In this study $BaTiO_3$-based general Ni-MLCCs were used for the experiments. The dielectric sheets with printed Ni internal electrodes were laminated and pressed, followed by firing in the reducing atmosphere. After firing, In-Ga alloy was applied as external electrode. The microstructure was observed by using SEM and TEM. X-ray diffraction was used in order to identify the crystal structure.

The residual stress was estimated by using Vickers hardness tester.[8] MLCCs were lapped from the external electrode to the center and then polished. After these processes, a diamond shape indenter was struck on the margin area of the lapped MLCCs by using Vickers hardness tester. The residual stress was estimated from the impression size and the crack length (Fig.1) by using IF method (equation 1,2).

$$K_{IC}=0.026(E^{1/2}P^{1/2}a)/c^{3/2} \qquad (eq.1)$$
$$K_{IC}= K_{IC}{}^0=+2(c/\pi)^{1/2} \sigma_1 \qquad (eq.2)$$

E: elastic   modulus (Pa)

P: load(N)

σ_1: internal   stress (Pa)

Fig.1 Schematic model of the indentation cracks.
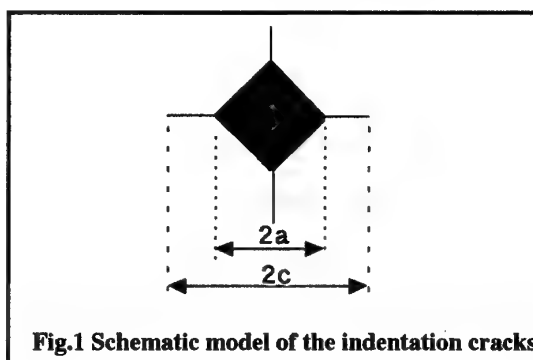
The capacitance aging was measured to evaluate the reliability. After annealing at 150℃ for 1hour and subsequent keeping at room temperature for 24 hours, the initial capacitance value was measured. After applying voltage at a certain temperature for certain hours, the capacitance aging was measured.
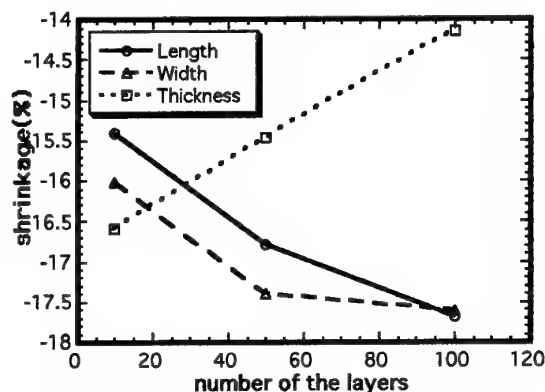
Fig.2 Shrinkage Vs. number of the layers

Fig.3 Shrinkage curves in the reducing atmosphere.

3   RESULTS and DISCUSSION

3.1 Effect of the multiplication on the shrinkage.

Effect of the number of dielectric layers in MLCCs on the shrinkage was investigated. The shrinkage of the MLCCs were measured in the three directions, consequently different values were obtained for the different directions (Fig.2). Namely with the multiplication, the rate of shrinkage in the thickness direction decreases, different direction gives different values of shrinkage. From this result, it is supposed that Ni internal electrodes shrink in plane direction and expand in thickness direction during firing. Fig.3 shows the shrinkage behavior of internal Ni electrode and that of dielectrics respectively in the firing conditions. It is supposed that this difference of the shrinkage behavior caused stress. The cross sections of the MLCCs with the various layer numbers are shown in Fig.4. The expansion in the thickness direction can be seen in this figure. This anisotropy of shrinkage is attributed to the origin of the stress.

3.2 Crack behavior evaluated by Micro-indentation method

An indenter was struck on the margin area of the lapped MLCCs by using Vickers hardness tester. As the result, the crack length occurring from the corners of the impression were so different. At the top or bottom margin, the cracks were long in the width direction and short in the thickness direction (Fig.5). At the side margin, the cracks were long in the thickness direction, and short in the width direction. Accordingly it is expected that the tensile stress was perpendicular to the longer cracks. On the estimation of the residual stress, the cracks were classified into two types on account of the anisotropy of the crack length by direction. Consequently the signs of the estimated stress were opposite (Fig.6). This means that the magnitude and the direction of the stress are different depending on the position in MLCCs.
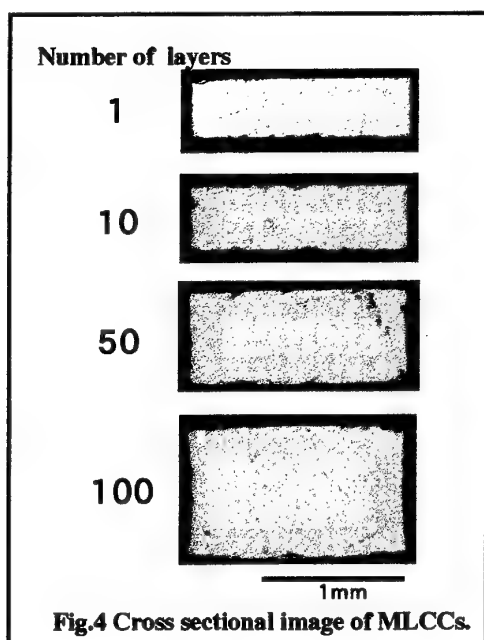
Fig.4 Cross sectional image of MLCCs.
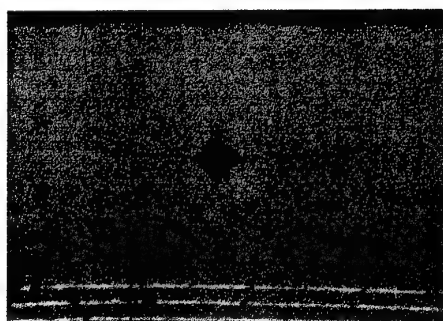
Fig.5 Anisotropy of the crack length at the top margin on MLCCs.
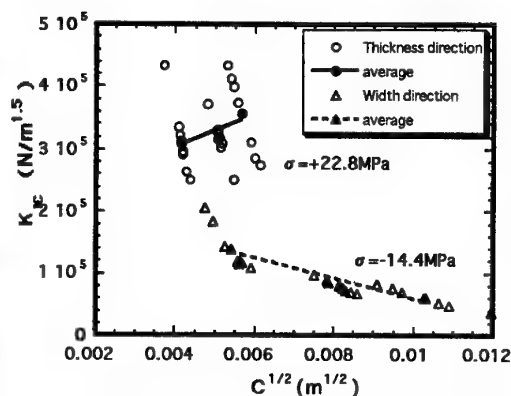
Fig.6. Estimation of the internal stress.
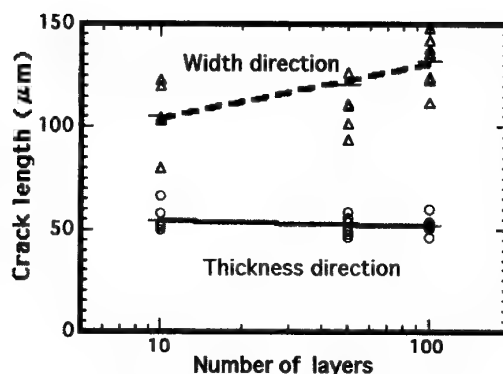
Fig.7 Length of cracks Vs.
number of layers on MLCCs.

3.3. Effect of the multiplication of MLCCs on the internal stress

The anisotropy of the crack length by the impression at the top margin was investigated for MLCCs with different number of dielectric layers. As a result, the anisotropy increased with number of the dielectric layers increasing. Therefore it is regarded that the stress enlarged with increase of the number of dielectric layers (Fig.7).

Fig.8 shows the X-ray diffraction profile of the surface of Ni-MLCCs. With increase of the number of the dielectric layers, (002) peak of BaTiO$_3$ sifted to low angle side and (200) peak decreased its intensity without shifting the peak angle. This means that the ratio of C-axis to A-axis increased and crystallographic anisotropy enlarged. In order to compare with this result, the dependence of the layer number was also studied for Ni-MLCCs in which 0.1wt% of NiO was added to the dielectrics. This experiment was carried out in order to confirm the effect of the diffusion of the internal electrode Ni to the dielectrics. As a result the same dependence behavior was observed(Fig.9). So the dependence of the number of the

dielectric layers on the X-ray peak's shift and size change are not attributed to the number of the Ni internal electrodes. Accordingly this change shows the residual stress.

3.4 Effect of the stress on the reliability

The capacitance aging was measured under an application of a dc voltage at 40℃ for MLCCs with various numbers of the dielectric layers. The result depends on the numbers. Consequently, it was found that the aging depends on the layer numbers(Fig.10). In the case that the margin area was eliminated by lapping after firing, the aging deterioration was small(Fig.11). Depending on the amount of the eliminated margin, the capacitance change decreased. From the fact described above, the stress was caused during firing. On the other hand, this stress was reversely proportional to the margin area of green chips before firing. To say that the dependence on the margin area of green chips, the deterioration tended to be soften. In the sintered body, the stress was released by eliminating the margin area by lapping. The dependence on this stress, capacitance aging deterioration increased.
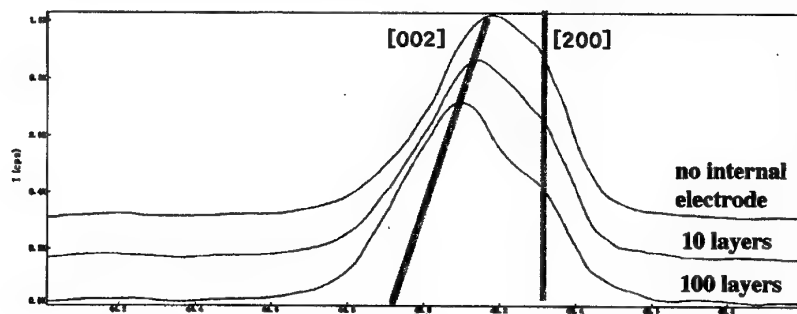
Fig.8 Effect of multiplication on the X-ray diffraction profile.
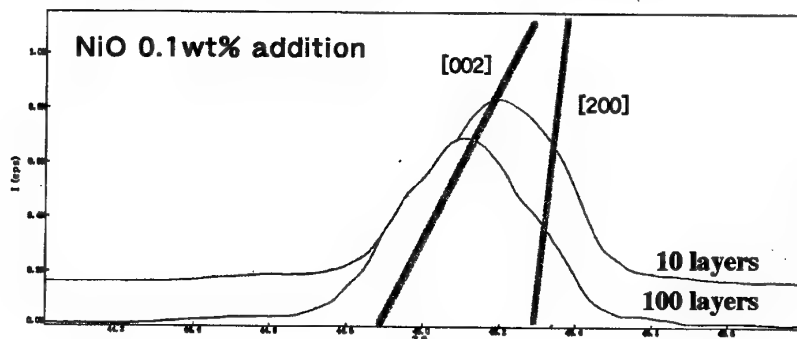
Fig.9 X-ray profiles of Ni- MLCCs with NiO addition.

— 325 —

3.5 Improvement of the MLCCs with high capacitance

Using the improved Ni-paste, 100 layers MLCCs were produced to investigate of the effect on the stress. The cross section images are shown(Fig.12). Without improvement of the Ni electrodes, MLCCs had big distortion. The stress estimated by the micro-indentation method was bigger than that of improved Ni used MLCCs. Then in which the new Ni-paste was used, the internal electrode thinned and the covering ratio of Ni were increased.

4. CONCLUSIONS

1) The estimating method of the internal stress in MLCCs has been proposed, which was based on the anisotropy of the impression cracks by Vickers hardness tester.
2) The internal stress in MLCCs tend to be increased by the multiplication of layers and resulting the acceleration of capacitance degradation.
3) The internal stress was improved by the reform of the internal electrode.
4) Removing the margin area of MLCCs after firing, the stress was released.

5. REFERENCES

1) T.Nomura,S.Sumita,Y.Nakano,K.Nishiyama, *Proc.5thUS-japan Seminar on Dielectric and Piezoelectric Ceramics*, (1990) 29-32.
2) Y.Yamamatsu et al.,*Jounal of power source*, 60 (1996)199-203.
3) R.Waser,T.Baiatu and K.Hardtl, *J.Am.Ceram.Soc.*, 3 (1990) 1645-1653.
4) Y.Takagi,Y.Kawaguchi,Y.Ueno,Y.Yoneda, *CARTS98:18th Capacitor and resistor Technology Syposium*,(1998)197-202.
5) N.Fujikawa, *NipponCeramiics Kykai Denshizairyou-bukai*, (1990) 86
6) H.Kabasawa,H.Saitoh,S.Tosaka,NEEDS&SEEDS,10(1994) 15-18
7) W.Carlson,T.Rutt,M.Wild,Ferroelectric Letters,21(1996)1-9
8) K.Okazaki, *Ceramic Bulletin*, 63,9 (1984)1150-1152.
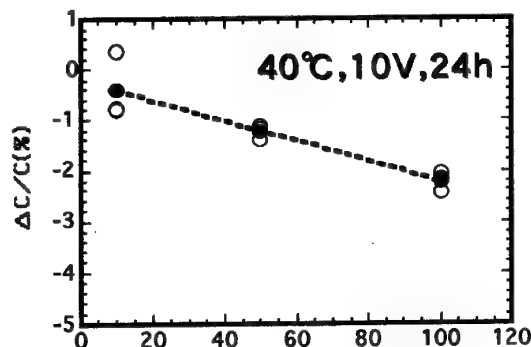
Fig.10 Effect of the number of layers on the capacitance aging
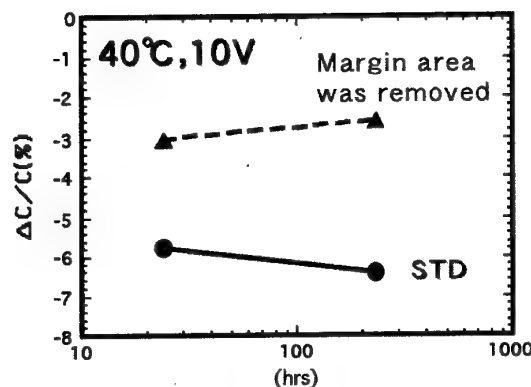
Fig.11 Capacitance aging before and after the removal of the margin area.
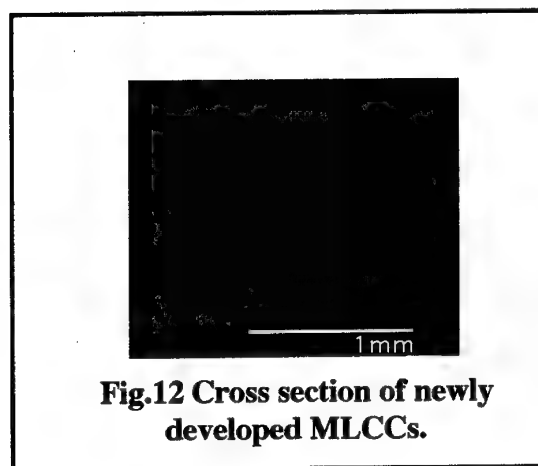
Fig.12 Cross section of newly developed MLCCs.

A Low Dielectric Aging X7R BaTiO3 Ceramic for BME MLC

Y. Yamashita, Y. Nakano*, H. Syoji*, K. Handa* and H. Ogawa*

Power Supply Materials & Devices Laboratory, Research & Development Center, Toshiba Corp.,
1 Komukai Toshiba-cho, Saiwai-ku, Kawasaki 210-8582, Japan,
Fax:81-44-520-1286, e-mail:yohachi.yamashita@toshiba.co.jp
*Engineering Div., Nippon Chemi-Con Co. Ltd., 1-167-1 Higashioume, Oume, Tokyo 198-0042, Japan
Fax:81-428-24-1062

Abstract:

The effect of various donor (Ta2O5 and Y2O3), acceptor (MnO, CoO, MgO and CaO), and glass (SiO2 and Al2O3) dopants on the sintering and dielectric properties of barium titanate ceramics fired at reducing atmosphere has been investigated. Dielectric materials have been developed high dielectric constant (2,500-3,000), low DF (<0.6%), and high capacitance times resistance value (CR>3,000 ohm F) at 125℃. In addition, the MLC using the dielectric material and Ni internal electrode shows very low dielectric aging rate, which is defined as a capacitance decrease as a function of time, less than 0.4%/decade with the X7R specification of the EIA standard.

1. Introduction

Ferroelectric ceramic materials more or less undergo a spontaneous and gradual change in dielectric constant and loss factors. This is called dielectric aging and takes place even under isothermal and stress-free conditions. The aging of the dielectric constant is approximately a linear function of logarithmic time(1); that is, capacitance decrease by a specific percentage each decade increase in time, by as much as 0.5-7% according to the dielectric materials used. At an aging rate of 2% per decade, the capacitor would then be expected to lose in 1.5 years about 10% of the initial capacitance measured at 10 min. after the last heat treatment above its Curie temperature (Tc). In addition, the aging rate is enhanced by DC voltage (2-3). Base metal electrode (BME) multilayer ceramic capacitors (MLCs) have been developed to last 10 years, and the amount of consumption has increased drastically in the last 3 years due to a sharp increase in the price of Pd metal which has been used for the precious metal electrode (PME) MLC. The X7R specification of the EIA standard requires a capacitance change within 15% from −55 to +125℃. The core-shell structure of the barium titanate dielectric has been used for this MLC specification. Several factors, such as grain size, number of layers and internal stress,

affect the aging rate of MLCs. However, the composition of dielectric materials has a fairly large effect on aging rate. Many acceptor dopants, such as MnO, CoO, CaO and MgO are added to base barium titanate to prevent a reduction of the dielectric material during a reducing atmosphere firing in N2/H2/H2O with Ni internal electrode. However, these dopants considerably increase the aging rate of BME MLCs. In this report, the effect of various donor (Ta2O5, Y2O3 et al.), acceptor (MnO, CoO, MgO, CaO et al.), and glass (SiO2 and, Al2O3) dopants on the sintering and dielectric properties of barium titanate ceramics fired in a reducing atmosphere has been investigated.

2. Experimental procedure

Reagent grades of donor (Ta2O5, Y2O3), acceptor (MnO, CoO, MgO, CaTiO3), and glass (SiO2 and Al2O3) dopant were added to hydrothermally prepared barium titanate (0.5 micron). These samples were prepared by a conventional solid solution process. Additives and base barium titanate were weighted and mixed with a mortal and pestle, and 8wt% of PVA binder was added. Powders with organic binder were pressed into disks and after the binder was burn-out at 500℃

in air, these disks were fired at 1,200-1,350℃ in a reducing atmosphere controlled by N2/H2/H2O. MLCs were prepared by the so-called green sheet method. Green sheets were formed by doctor-blade casting, and the thickness was controlled to 15 micron. After casting the tapes, the sheet was dried and the Ni electrode paste was printed using a screen printer. Next, 20 active layers of the sheets were stacked, laminated and cut into green chips. Binder burn-out followed, performed at 300 ℃ in air. Sintering was done between 1200-1250℃ for 2 hours with an oxygen partial pressure of 10^{-9}atm. The chips were annealed at 750℃ for 4 hours in air in order to re-oxidize the dielectrics. After the annealing, Cu paste was applied on both ends of the chips, and fired at 850℃ for 10 min. in a N2 atmosphere to evaluate their electrical properties. In order to measure the aging rate, samples were de-aged at 150℃ for 1 hour and transferred to a temperature controlled chamber at 25 ℃+-0.2℃. Capacitance was measured after 2 hours and 20 hours in the chamber. Aging rate was calculated by the following equation.

Aging rate(%/decade)=(Cap.2h-Cap.20h)/Cap.2h

The dielectric constant, dissipation factor and the temperature dependence of the capacitors were measured using an HP-4284A precision LCR meter at 1 kHz with 1.0 vrms. The insulation resistance (IR) was measured by applying a 2v/micron DC voltage after 1 minute. Then, the capacitance time resistivity product (CR) value was calculated.
The microstructure of the MLC was observed by scanning electron microscopy (SEM).

3. Experimental Results

Table I shows the aging rate of disk samples with different dopants. Acceptor dopant, except CaTiO3 increases aging rate. In contrast, donor dopants, such as Ta2O5 and Y2O3 decreases aging rate. Glass dopant, SiO2 and Al2O3 only slightly changes aging rate. In order to control the temperature coefficients of capacitance (TCC), insulation resistance and low-firing temperature, a mixture dopant of BaO-MgO-Y2O3-Ta2O5-SiO2-Al2O3 was mixed and calcined at 1150 ℃. The

calcined mixture dopant was then wet milled to sub-micron level by using a ball mill with 3-5 mm PSZ balls. The dried mixture was weighted and added to base barium titanate. Figure 1 shows aging rate as function of the BaO-MgO-Y2O3-Ta2O5-SiO2-Al2O3 mixture. Aging rates are decreased as a function of dopant level. When 4-5 wt% of mixture dopant was added to barium titanate, all electrical properties are optimized. Then, the MLC was manufactured by using dielectric material which was added to 5 wt% of BaO-MgO-Y2O3-Ta2O5-SiO2-Al2O3 mixture dopant to base barium titanate powder

Table I   Aging rate of disk samples with different dopant.

Dopant type	Dopant level (mol%)	Aging rate (%/decade)
None		1.7
CaTiO3	5.0	1.5
MgO	1.0	3.5
MnO	1.0	2.5
CoO	0.2	2.0
Ta2O5	2.0	0.3
Y2O3	2.0	0.5
SiO2	1.0	1.2
Ba-Mg-Y-Ta-Si-Al oxide mixture	0.5-8 wt%	2.2-0.3

Figure 2 shows the microstructure of MLC fired at 1250℃ for 2 hours. A very dense microstructure was obtained. The active dielectric thickness was 10 micron and 20 layers. Figure 3 shows the TCC of the MLC. The TCC meets both of the X7R and JB specifications. The dissipation factor is 1.5%, which is low for a BME MLC in this thickness range. The CR value of 1.0 mm thick disk and 10 micron MLC as a function of temperature are shown in Fig. 4. The disk sample shows a quite large CR value (>3,000 ohm farad) up to 125℃. However, that of the MLC is lower than the disk which is uncommon. This implies that the dielectric was affected by the Ni electrode presence, or re-oxidizing was not sufficient. Figure 5 shows the capacitance change as a function of time of the present MLC in comparison to conventional PME (Pd electrode) and BME (Ni) MLCs of X7R specification. Conventional BME MLCs have 1.2%/decade aging rate. The present MLC shows a

very low aging rate of 0.4%/decade which is lower than that of the PME MLC. When 1.0 v and 2.0 v/micron DC voltages applied to the MLC at room temperature for 24 h, the aging rates were 0.4%/decade and 1.5%/decade, respectively. These values are quite low compared to those of conventional BME MLCs(4-5).

Table II summarizes the physical and electrical properties of BME MLC.

Table II Physical and electrical properties of BME MLC.

Dopant: composition: 20BaO-20MgO-16Y2O3-4Ta2O5-32SiO2-8Al2O3, (mol%)
Dopant quantity: 3-8 wt% to base BaTiO3
Firing Condition: 1,200-1,250℃ x 2h,   2x10⁻⁹ atm
Microstructure: GS=0.7 μ m, Density= 5.80 cm³
K value: 2,400-2,700 @ 1mm disk, 2,600-3,000 @ 10 μ m BME MLC
DF: 1.6%@10 micron x 20 layers MLC @ 1 kHz 1.0 vrms
CR: 3,000-5,000 Ω F@25 ℃ ,   2,000-3,000 Ω F@125℃ @ 1mm disk @ 1.0 v/micron after 1 minute
CR: 3,000 Ω F@25℃, 700 Ω F@125℃ @ 10 μ m BME MLC @ 2.0 v/micron after 1 minute
TCC: X7P and JB(Cap. change +/- <10%) @ 10 μ m MLC
AR without dc bias of disk (1.0 mm) : 0.3%/decade
AR without dc bias of MLC (10 μ m x 20 layers): 0.3%/decade
AR with 1.0 v/ μ m dc bias of MLC : 0.4%/decade
AR with 2.0 v/ μ m dc bias of MLC : 1.5%/decade

4. Conclusion

Dielectric material for a BME (Ni) X7R MLC having a low aging rate (0.3-0.4%/decade) and high CR value was realized by adding BaO-MgO-Y2O3-Ta2O5-SiO2 Al2O3 dopant to base barium titanate. The BME MLC, employing the dielectric material, has 10 micron in active thickness layer meets the X7R and JB specifications.

Reference

(1) B. M. Marks, Ceramic dielectric materials, Electronics, 21(8),116-120(1948).

(2) J. R. Partington, G.V.Planer and I. Bosewell, "Voltage Effects in Titanate Polycrystals",Nature,162,pp.151-152(1948).

(3) M. C. McQuarrie and W. R. Buessem, "The aging effect in barium titanate", Bull. Am. Ceram. Soc., 34(12),402-406(1955).

(4) T. Nomura, N. Kawano, J. Yamamatsu, T. Arashi, Y. Nakano and A. Sato, "Aging behavior of Ni-Electrode Multilayer Ceramic Capacitors with X7R Characteristics", Jpn. J. Appl. Phys., 34 (9B) 5389-5395 (1995).

(5) Y. Nakano, and T. Nomura "Internal Stress in High Capacitance Multilayer Ceramic Capacitors" To be Published in Jpn. J. Appl. Phys., 38 (9B) (1999).

Fig. 1   Aging rate as function of the BaO-MgO-Y2O3-Ta2O5-SiO2-Al2O3 additive content

Fig. 2   Microstructure of BME MLC fired at 1250Cx2h with 10⁻⁹atm
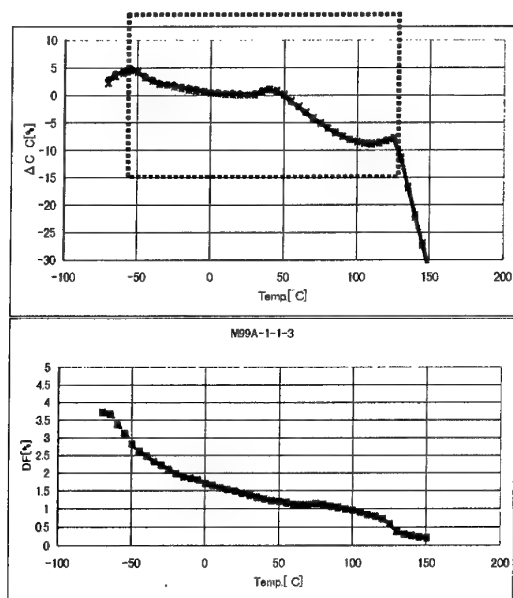
Fig. 3   TCC and DF of BME MLC
10 micron x 20 layers
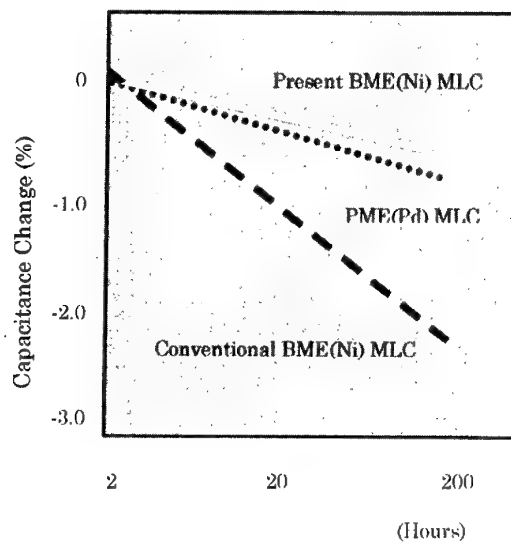
Fig.5   Capacitance change of presence BME
MLC, conventional BME MLC and PME
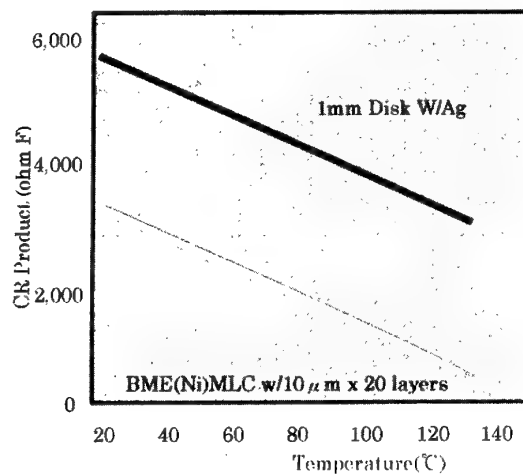
Fig. 4   CR versus temperature of disk and
BME MLC

Use of Chemically Prepared BaTiO₃ in the Manufacture of Multilayer Ceramic Capacitors

S.P. Gupta, Tom Poole, and Jeff Franklin
KEMET Electronics Corporation
P.O. Box 849
201 Fairview Street Extension
Fountain Inn, SC 29644-0849 USA

ABSTRACT

Selection of the proper type of BaTiO₃ plays a critical role in manufacturing multilayer ceramic capacitors (MLCCs). Prior to the development of chemically-prepared BaTiO₃, solid state BaTiO₃ material had been extensively used in manufacturing low and high fire MLCCs. Market pressure for more capacitance in smaller case sizes has increased the need for thinner ceramic layers while maintaining the highest quality standards. Chemically prepared BaTiO₃ material satisfies this need with a median particle size of approximately 0.3 microns, smaller sintered grain sizes, higher mechanical strength, denser microstructure, and improved reliability.

High capacitance Y5V multilayer ceramic capacitors have been developed and manufactured using chemically prepared BaTiO₃. The proper types and quantities of shifters, depressors, and reactive sintering aids are used to formulate the low fire dielectric system, which utilizes a low cost silver/palladium electrode system. Electrical and reliability properties of several MLCC part sizes made using this low fire Y5V dielectric formulation are discussed.

I. INTRODUCTION

The continuing drive for miniaturization of electronic circuitry is driving manufacturers of discrete capacitors to increase the volumetric efficiency of their products. This can be accomplished by using materials with higher dielectric constants and thinner dielectric layers. Higher dielectric constants can be achieved by using dielectrics having larger temperature coefficients of capacitance, such as Y5V. Cost is also reduced by utilizing electrodes containing a higher percentage of silver. Important characteristics of materials used in the manufacture of surface mount ceramic capacitors are reliability and mechanical strength. Therefore, the selection of proper types of barium titanate, shifters, depressors, and sintering aids play a critical role in achieving high mechanical strength and excellent reliability. The use of conventional solid-state barium titanate is typically limited for these applications due to its larger particle size and larger, non-uniform fired grain size. The use of chemically prepared barium titanate with high purity and finer particle size and other high purity raw materials provides smaller fired grain size, denser microstructure, and improved reliability.

In this paper, a comparison of solid-state and chemically prepared barium titanates and their impact on performance and reliability in surface mount applications are discussed.

II. BACKGROUND

Historically, barium titanate prepared through solid state reaction of barium carbonate and titanium oxide at high temperatures has been used to formulate ceramic dielectrics for use in MLCCs.[1] Over the past several years, however, many manufacturers of barium titanate have developed processes to manufacture barium titanate through wet chemical processes. The materials produced in this manner typically have tighter barium : titanium ratio control, higher purity, and more reactivity than barium titanates prepared through solid state processes.[2,3] Typical properties of solid state and chemically prepared barium titanates are shown in Table 1 and Figure 1.

Table 1
Physical and Chemical Properties of Solid State and
Chemically Prepared Barium Titanate

	Solid State BaTiO₃	Chemically Prepared BaTiO₃
Median Particle Size	1.06 μm	0.29 μm
Surface Area	2.61 m²/g	6.99 m²/g
Loss on Ignition	0.118%	0.995%
Ba:Ti Ratio	0.9960 ± 0.0105	1.0007 ± 0.0035
Soluble Ba⁺⁺	1670 ppm	1605 ppm
Al₂O₃	68 ppm	< 74 ppm
SiO₂	25 ppm	< 69 ppm
Fe₂O₃	124 ppm	< 72 ppm
Na₂O	148 ppm	N/A
SO₃	285 ppm	N/A

Figure 1

Particle Size Distribution
of Solid State and Chemically Prepared BaTiO₃

Solid State
Chemically Prepared
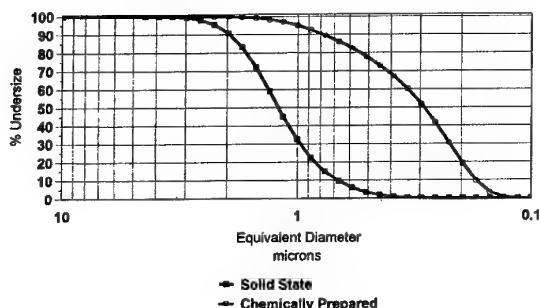
As a result of the finer particle size and higher specific surface area, lower firing temperatures are needed to sinter dielectric compositions containing chemically prepared barium titanates. Typical firing temperatures for high-fire dielectric compositions containing solid-state barium titanate are approximately 1400°C, while high-fire compositions containing chemically prepared barium titanate fire at approximately 1250°C to 1300°C. Through the use of properly selected reactive sintering aids, the firing temperatures of low-fire compositions containing chemically prepared barium titanate can be less than 1100°C. This low firing temperature enables the use of electrode metal systems containing less than 30% palladium by weight.

III. EXPERIMENTAL

Y5V dielectric formulations consisting of either solid state or chemically prepared barium titanate along with various shifters, depressors, and sintering aids were prepared. Other than the type of barium titanate used, both dielectric formulations were equivalent. Slurry composed of the dielectric powders, water, and a dispersing agent was milled in a vibratory mill containing stabilized ZrO_2 media for a total of 8 to 12 hours to deagglomerate the slurry. Following milling, the aqueous slurry was mixed with a binder system and coated onto a polymer carrier film. Green chips were manufactured by screen printing electrode patterns onto the green tape using an electrode ink containing a 73% silver, 27% palladium metal powder. The printed layers were then stacked, laminated, and diced into individual chips. All dielectric formulation, tape formation, and green chip manufacturing processes were conducted in class 10,000 or better clean room facilities in order to ensure high reliability in the finished parts. Following green chip processing, the binder system was removed through a binder burnout process with a maximum temperature of 600°C. The chips were then fired in a batch kiln at a temperature of 1060°C to

1080°C with a 6 hour soak at peak temperature. During firing the parts were bedded in ZrO_2 sand inside covered dense Al_2O_3 crucibles. Fired parts were corner rounded, silver terminated, and then plated with nickel and tin. Figure 2 summarizes the processing steps in the manufacture of the MLCCs. The capacitance, DF, TCC, IR, and breakdown voltage of the finished chips were measured. Modulus of rupture testing was conducted on a sample size of 30 chips using a three point bend test. The reliability of the parts was assessed using several standardized tests, including load life, load humidity, and HALT.

Figure 2
Ceramic Capacitor Manufacturing Process
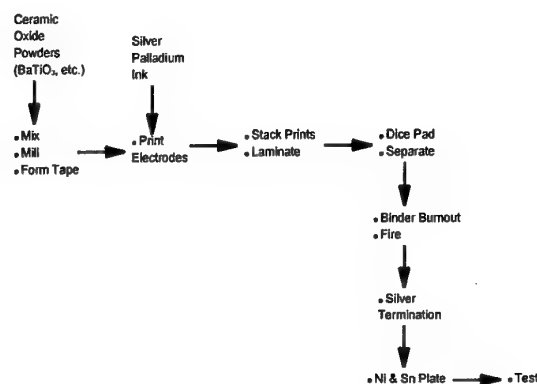
IV. RESULTS AND DISCUSSION

Electrical testing and reliability data for 4.7 μF 1206 parts is shown in Table 2 and Figures 3 and 4.

Table 2
Comparison of 1206 4.7 μF Parts Produced with
Solid State and Chemically Prepared BaTiO₃

	Solid State BaTiO₃	Chemically Prepared BaTiO₃
Capacitance	4.667 μF	4.537 μF
DF (@ 1 Volt)	4.561%	4.982%
TCC	+33.2%, -70.3%	+13.8%, -65.8%
Breakdown Voltage	35 V/μm	50 V/μm
Insulation Resistance @ 25°C	24000 Ω*F	26000 Ω*F
Dielectric Thickness	7.2 μm	6.5 μm
HALT 4 hr @ 128 V, 125°C	7/150	0/150
HAST 21 hr @ 16V,121°C, 85% R.H. & 2 Atm	58/300	0/300
Three Point Bend MOR[4]	299 MPa	408 MPa

Figure 3
Dielectric Breakdown Voltage Data

Solid State Barium Titanate

Figure 4
Dielectric Breakdown Voltage Data

Chemically Prepared Barium Titanate
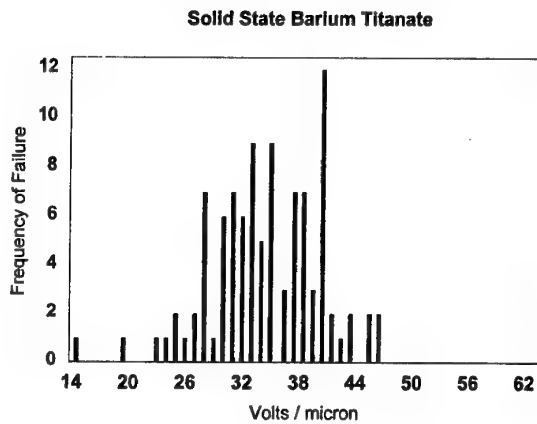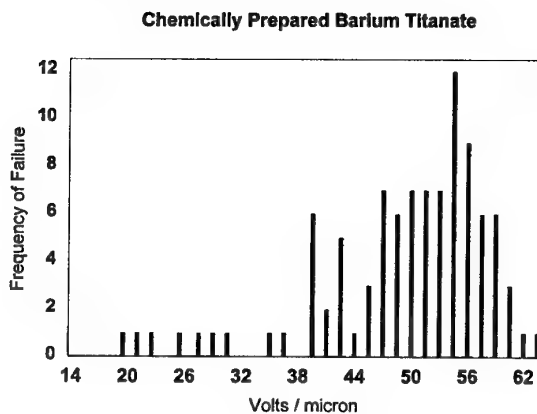
Figure 5
Microstructure of Dielectric Containing
Solid State BaTiO$_3$
(Chemically Etched)
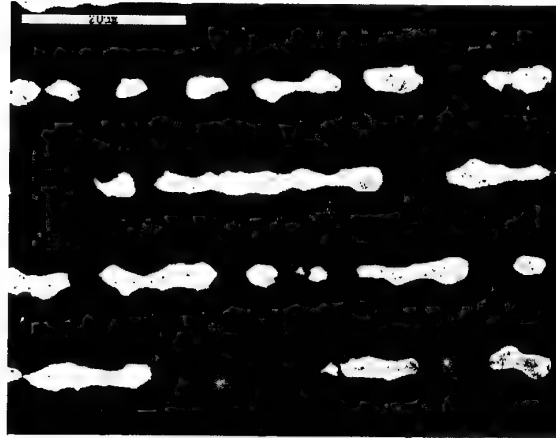
Figure 6
Microstructure of Dielectric Containing
Chemically Prepared BaTiO$_3$
(Chemically Etched)
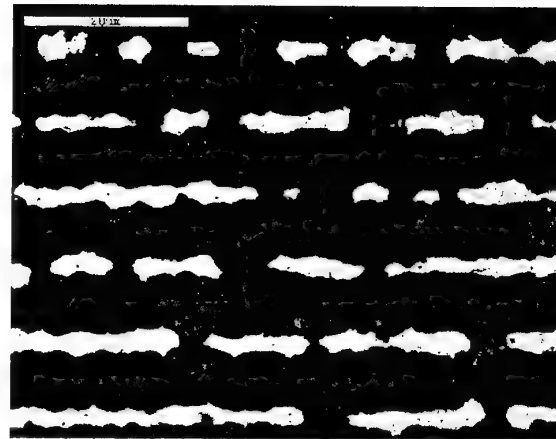
As illustrated in Table 2, the fired dielectric thickness of the parts containing chemically prepared barium titanate is 10% thinner, without negatively affecting electrical properties or mechanical robustness or reliability. The reason for this improvement is the denser, finer grained microstructure produced by the chemically prepared barium titanate formulation. Figures 5 and 6 show the difference in microstructure between the dielectrics produced using solid state and chemically prepared barium titanate. The typical grain size in the dielectric containing solid state barium titanate is from 3 to 4 µm, while the grain size in the formulation containing chemically prepared barium titanate is 2 to 3 µm. The smaller grain size in the body containing chemically prepared barium titanate contributes to the improved breakdown voltage, HALT, and insulation resistance noted in Table 2.

Initial attempts to extend the Y5V capacitance offering with the dielectric containing solid state barium titanate failed due to high levels of porosity between fired layers of the dielectric within the MLCC structure. This porosity, shown in Figure 7, was caused by poor particle packing and sintering due to the properties of the solid state barium titanate. Voltage and humidity testing of parts containing solid state barium titanate revealed low post-test insulation resistance and cracking between layers in the MLCC structure. As shown in Figure 8, MLCCs made with the dielectric containing chemically prepared barium titanate do not exhibit porosity between layers.

Figure 7
MLCC Containing Solid State BaTiO₃

Solid State Barium Titanate   50 X
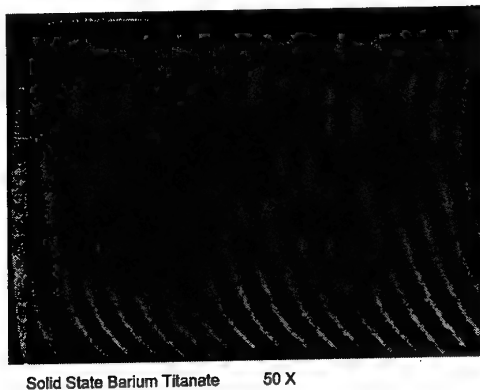
Figure 8
MLCC Containing Chemically Prepared BaTiO₃

Chemically Prepared Barium Titanate   50 X
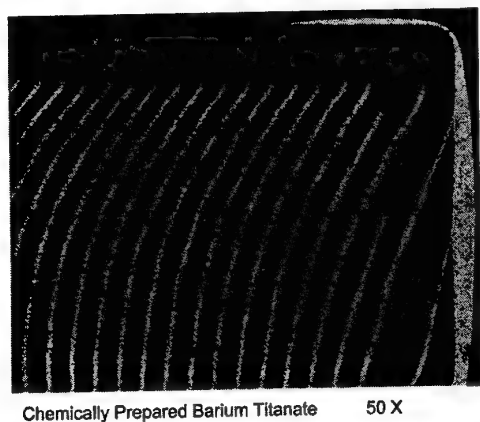
The micrographs in Figures 7 and 8 were obtained by mounting MLCCs in cold mount epoxy, then polishing at a 10° angle to the electrode plane to expose the interface between dielectric layers.

Table 3 summarizes important properties and characteristics of the 0402 0.1 μF, 0805 2.2 μF, and 1206 4.7 μF MLCC part types made using chemically prepared barium titanate.

Table 3
Typical Properties of Y5V MLCCs Made Using Chemically Prepared BaTiO₃

Part Type	0402 0.1 μF	0805 2.2 μF	1206 4.7 μF
DF (1.0 V)	< 5%	< 5%	≤ 5%
TCC	Y5V		
25°C IR	> 36000 Ω*F	> 33000 Ω*F	> 26000 Ω*F
85°C IR	> 29000 Ω*F	> 25000 Ω*F	> 20000 Ω*F
HALT @ 128 V & 125°C	0/150	1/150	0/150
Aging Rate	3.5% per decade		
Voltage Rating	16 V	16 V	16 V
Dielectric Thickness	6.0 μm	6.5 μm	6.5 μm

V. CONCLUSIONS

A high dielectric constant, low fire Y5V dielectric has been developed using chemically prepared barium titanate in the dielectric composition. The fired grain size of this dielectric is significantly smaller than was achieved using solid state barium titanate in the formulation. The finished MLCCs made from this material have excellent reliability, electrical properties, and robustness.

VI. REFERENCES

1. "1999 Materials Handbook - Barium Titanate," Ceramic Industry, Vol. 1, Issue No. 1, p. 82, 1999.

2. M. Nishido and K. Harada, "Manufacturing of Barium Titanium Powder by Oxalate Process," The Eighth US - Japan Seminar on Dielectric and Piezoelectric Ceramics, pp. 197-200 (1997).

3. J. Beeson, L. Mann, S. Venigalla, and S. Constantino, "Electrical and Physical Characteristics of Low-Fire X7R MLCCs with ≤ 3 μm Active Layers and 70 Ag - 30 Pd Electrodes," The Eighth US - Japan Seminar on Dielectric and Piezoelectric Ceramics, pp. 180-183 (1997).

4. C.R. Koripella, "Mechanical Behavior of Ceramic Capacitors," KEMET Engineering Bulletin), F-2107, June 1991, presented at the 41st Electronic Components and Technology Conference (ECTC) May 1991.

Development of Nanosize Metal Platelets for Thin Layer Dielectrics

D.O. Yener (doy100@psu.edu), J. Sindel (jxs95@psu.edu), N. Ogata (nxo4@email.psu.edu),
C.A. Randall (car4@psu.edu) and J.H. Adair (JAdair@mrl.psu.edu)
Center for Dielectric Studies
Fax: (814) 863-9704
Materials Research Laboratory
The Pennsylvania State University
University Park, PA 16802

Introduction

The ceramic layers used in the multilayer capacitors are between 2 to 3 μm thick. If the metal layers that are in the 0.1 to 0.2 μm range could be produced, substantial cost savings could accrue from the use of thinner layers of metal. While the submicron, spherical metal particles can produce thin layers, more efficient use of the relatively expensive metal is expected based on the lay down ability of the metal platelets relative to the spherical particles.

Adair and co-workers[1] have developed chemical synthesis techniques for powders composed of nanometer thick platelet particles that have potential for the metallic layers in multilayer devices. The particles are near agglomerate-free, if carefully processed, almost monosized, and can be single crystal. Adequate quantities of the powders can be synthesized to permit comprehensive studies on the processing characteristics and final properties of these uniquely shaped and sized particles. Particles have been synthesized in sizes as small as 30 nm in diameter without compromising the ability to control shape. This study is focused on the use of self-assembly (SA) systems in which to grow anisotropically-shaped particles.

Background

Particle shape control is a complex process requiring a fundamental understanding of the interactions between solid state chemistry, interfacial reactions and kinetics, and solution (or vapor) chemistry. During synthesis of other than a large single crystal the parameters controlling crystal growth must be balanced with the requirements for anisotropic powder nucleation and growth. Although there has been considerable progress in large single crystal growth and the synthesis of powders composed of monodispersed, spherical particles, these efforts have not been transferred to the synthesis of anisotropic nanoparticles. A primary objective of this study is to learn how to control anisotropic crystal growth within the constraints of particle precipitation.

There are two ways that anisotropically shaped particles have been produced from solution. The first is crystallographically controlled growth producing particle shapes dictated by the relative growth rate among the various habit planes. Growth rates are often controlled by the inclusion of adsorbates or "poisons" that selectively restrict the growth of certain faces. A second approach is to control nucleation and growth by the synthesis of materials in the presence of molecular templates (Figure 1). While this method has been successfully used to restrict the size of particles, there have been few attempts to control particle shape. The current work proposes to apply principles from both of these approaches to achieve particle shape control by employing amphiphilic molecules assembled into specific lyotropic micellular structures as templates for the formation of anisotropic inorganic particles. An important aspect of our approach will be to include careful analysis of the chemical nature of the particle/template interface, as this interaction can play an equally important role in determining the shape and orientation. Our hypothesis is that uniform dispersions of anisotropic inorganic particles can be produced with templating methods if the chemical interaction between the organic template and the particle is carefully controlled.

The major objective of the current program is to develop a fundamental understanding of the growth of anisotropic particles at organic templates, with emphasis on the chemical and structural aspects of layered organic assemblies that contribute to the formation of anisotropic inorganic particles. Target systems include both metal particles important to conductive pathways in microelectronics such as Ag/Pd alloys and Pt, and II-IV semiconductors such as CdSe and CdS.

Experimental

Silver nitrate as $Ag(NO_3)$, octylamine, amylamine, hydrazine hydrate and methyl ethyl ketone (MEK) were obtained from Aldrich Chemicals, Milwaukee, WI, USA. A 0.04 M of $Ag(NO_3)$ aqueous solution was prepared. The silver particles were made based on the flow chart below (Figure 2). During the synthesis steps, the amounts of the ingredient chemicals were arranged due to the phase diagram below (Figure 3). The gray region is the place where laminar bilayers form. The particles were characterized by HRTEM, atomic force microscopy for thickness, and XRD to verify phase.
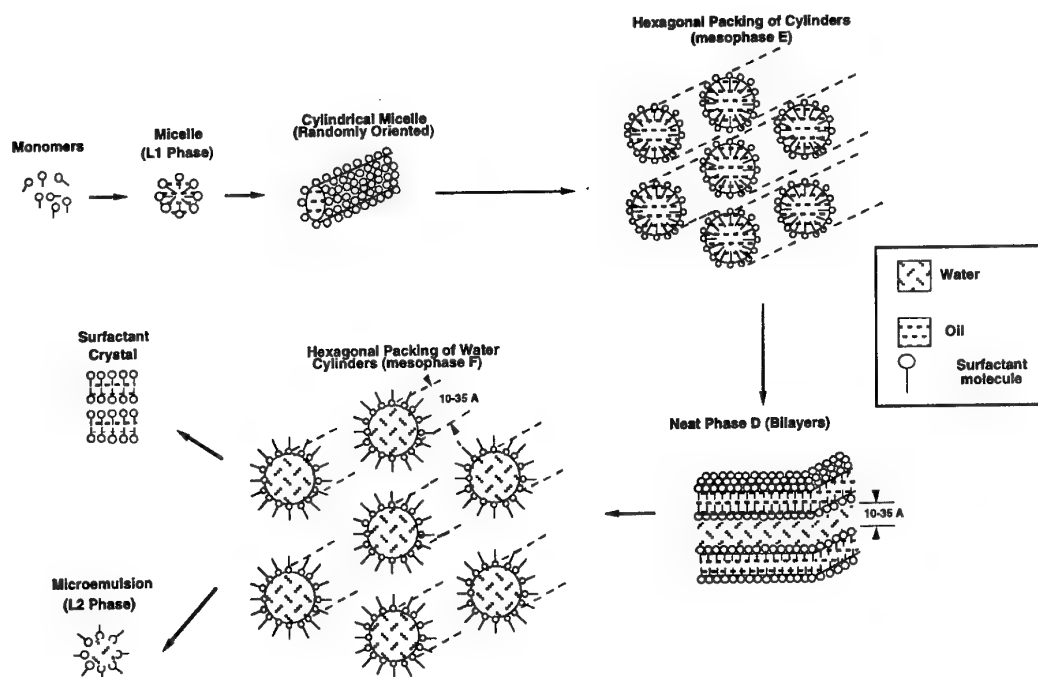
Figure 1. Phase structures for an ideal self-assembly system.

Results and Discussion

The platelet dimensions varied linearly over the nanometer range as a function of the [Ag$^+$] and the water to surfactant ratio. (Table 1). At the largest particle size of ~250nm for the particle face there is an exponential deviation from the linear regime found over the particle face range from ~1nm to 30nm. The particles formed are uniformly shaped

The face of the silver particles is in the {111} plane with an average d-spacing estimated from the HRTEM shown in Figure 4 of 2.5±0.3Å. The particles are uniformly shaped platelets as expected from the use of the bilayer self-assembly system and the prior studies.[3] The aspect ratio of the particles over the range of synthesis conditions investigated is 39.5±0.2. Based on modeling studies to better understand how the nature of the bilayer and local environment controls sizes of the platelet particles, a nucleation/deposition model has been proposed that reconciles the experimental date obtained to date.
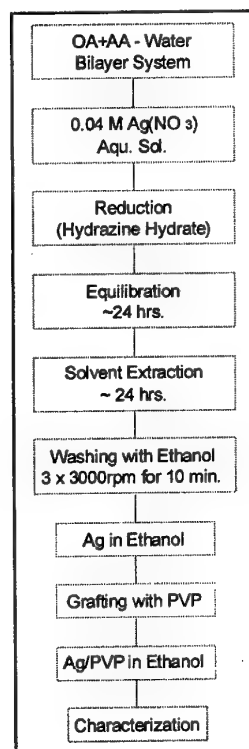
Figure 2. Ag synthesis flow chart.
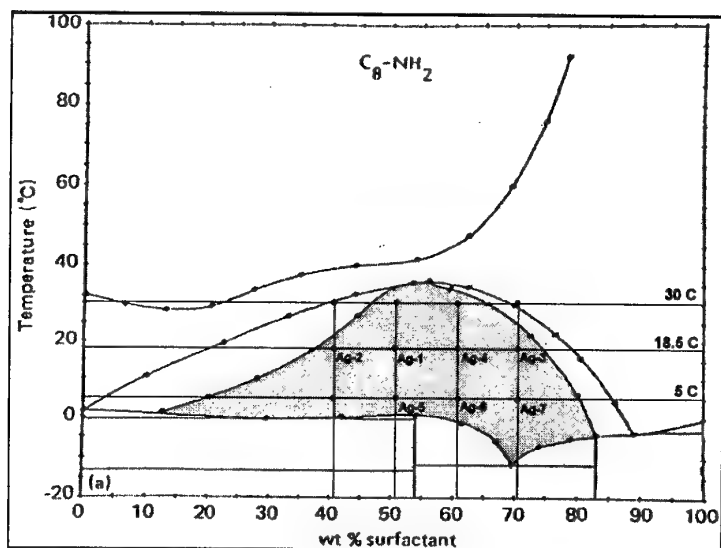
Figure 3. Octylamine water binary phase diagram with composition points indicated.[2]

Table 1. Selected composition points for the experiments. R= molar ratio of [Water]/[Octylamine], W= Water (wt.%)/Octylamine (wt.%). Octylamine to Amylamine weight ratio is 25:1. d_1 = Aqueous layer thickness, d_2 = Amphipilic molecular layer thickness

Sample No.	Octylamine (wt%)	Amylamine (wt%)	R	W	(d_1) (nm)	(d_2) (nm)	$[Ag^+]$ $(Mx10^{-3})$
Ag-Oct-1	81	3.2	1.7	0.5	3.2	9.8	0.94
Ag-Oct-2	71	2.8	2.9	0.7	8.2	9.9	1.64
Ag-Oct-3	61	2.4	4.6	1.0	10.2	10.1	2.56
Ag-Oct-4	51	2.0	6.8	1.6	16.6	10.1	3.81
Ag-Oct-5	41	1.6	10.3	2.5	27.4	10.3	5.76
Ag-Oct-6	31	1.2	15.9	4.3	556.8	10.7	8.89
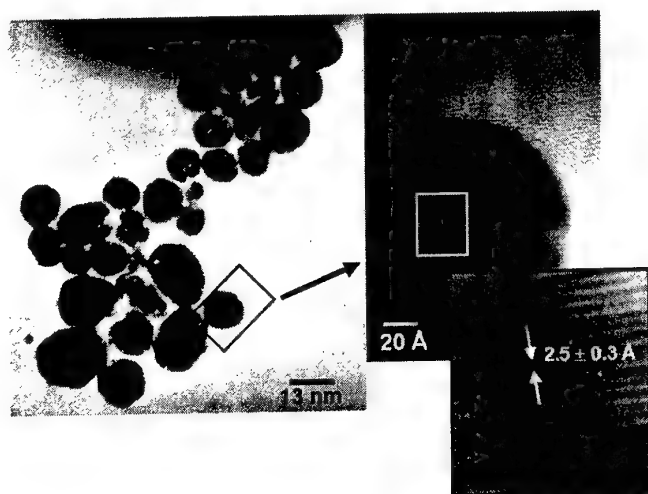
Figure 4. HRTEM micrographs of silver platelets through the [111] pole direction. Lattice spacing shown in the insert of the right hand photomicrograph. The 95% confidence interval is 2.5±0.3 Å

References
1. J.H. Adair, T. Li, T. Kido, K. Havey, J. Moon, J. Mecholsky, A. Morrone, D.R. Talham, M.H. Ludwig, and L. Wang, <u>Materials Science and Engineering Reports</u>, *R23*, Nos. 4-5, 1998, pp. 139-242.
2. J. Sjoblom and P. Stenius, Surfactant Science Series, Vol. 23, 398, Marcel Dekker, NY, 1987.
3. D. Yener, J. Sindel, and J.H. Adair, "Synthesis of Nanosized Platelets in Octylamine-Water Bilayer Systems," submitted to *Langmuir*.

Nanostructured Barium Titanate Prepared in Microemulsions

Herbert Giesche

NYSCC at Alfred University, 2 Pine street, Alfred, NY 14802 USA

Fax: +1 607 871 2317, Phone: +1 607 871 2677, e-mail: giesche@bigvax.alfred.edu

The present project studies the synthesis of well-defined nanometer sized BaTiO$_3$ particles by a microemulsion synthesis method. The overall project includes synthesis, processing, and sintering of a multilayer device. However, at this point only synthesis-related results will be presented.

1. INTRODUCTION

Nanostructured materials exhibit a tremendous potential for novel electronic applications and a few publications have addressed the formation of nanometer-sized barium titanate particles by various techniques.[1-4] One very interesting approach is the use of microemulsions. The latter synthesis technique allows for a very precise control of the particle size. By a particular choice of the surfactant/solvent combination even the chemical structure within the individual particles can be influenced. The particles are also extremely well dispersed, since the surfactant layer surrounds them. This latter fact is tremendously important in order to achieve high green densities. The layer acts as a steric repulsion between the particles and allows them to slide against each other. Particles then find their ideal position and higher green density results.

2. BACKGROUND

During the past decade substantial progress has been made in the area of microemulsions. A microemulsion system is essentially a water-oil-surfactant mixture. Depending on temperature and the concentration of each constituent various microstructures can be formed, e.g. micelles, reverse micelles, lamellar liquid crystal or hexagonal rod like structures. Fig. 1 shows a typical phase diagram for the H$_2$O / pentanol / sodium dodecyl sulfate (SDS) system. Numerous other surfactant
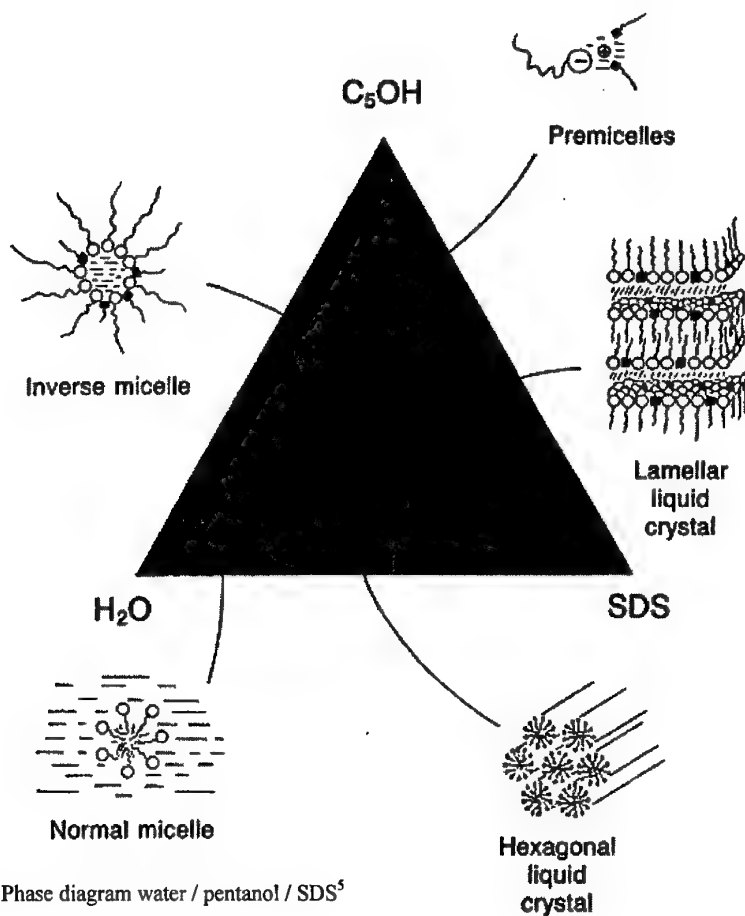
Fig. 1 Phase diagram water / pentanol / SDS[5]

combinations have been tested and similar phase diagrams will be shown. It is interesting to notice that nanometer sized microemulsion droplets or micelles are thermodynamically stable and that they will form spontaneously, in contrast to macroscopic emulsions, which are thermodynamically unstable. Micro-emulsions also form a narrow droplet size distribution, since the interaction between polar head-groups of the surfactant molecule and the interaction between the non-polar tails will favor only aggregates of a very specific size and molecular configuration. The latter droplet uniformity is important since this will have a direct effect on the resulting particle size during the precipitation reaction. For the present work microemulsions are used as miniature reaction vehicles for the formation of nanometer sized particles. Within a certain range the size of the reverse micelles can be varied by changing the water/surfactant ratio or the temperature of the reaction system. Larger droplets can also be achieved by using different surfactant molecules (with a different chemical structure).

3. EXPERIMENTAL PROCEDURES

Microemulsions were prepared at room temperature by mixing the various chemical constituents in cleaned glass flasks or sample vials. All liquids and solutions were filtered through 0.45 µm Teflon filter cartridges beforehand. Two different methods were employed in the actual precipitation process. First, a dual microemulsion method was used, which had barium and titanium salts as precursors in one microemulsion and precipitation was introduced by adding a second microemulsion, which contained oxalate or carbonate ions. The second method, which utilized only one microemulsion, was applicable to barium or titanium alkoxides. Here an initial microemulsion was formed from water, oil and surfactant. A second solution of the alkoxides in the oil phase was then slowly added to the initial microemulsion and precipitation occurred within the water droplets by diffusion of the alkoxides towards the droplet interface. The alkoxides are extremely reactive and especially the barium alkoxide had to be handled and stored absolutely water-free in a glove-box environment.

The particle size was confirmed by transmission electron microscopy and with a photo correlation spectroscopy instrument, Brookhaven 90 Plus.

4. RESULTS and DISCUSSION

Results of the concentrations of the various chemical constituents and the reaction temperature between 0°C and 50°C have been studied. The range within each phase diagram, which formed a reverse microemulsion changed at different temperatures and depending on the chosen reaction temperature different compositions had to be used. In general, lower temperatures favored a surfactant rich composition whereas a more oil-rich composition was needed at higher temperatures. The droplet size also changed with temperature and larger droplets formed at the higher temperatures. An increase of up to a factor of 2 was noticed in some of the systems. The barium or titanium salt concentrations also decreased the compositional range where a microemulsion formed due to the interaction of the ionic species with the polar head-group of the surfactant molecules.

In another approach truly nanosized titania particles were precipitated first and in a second step barium was precipitated onto the existing titania seeds. A major problem in this approach was the formation of aggregates during or prior to the coating step. Lower concentrations of all reactive species as well as a slow addition process of the barium precursor component were critical for a successful coating process.

In both processes barium titanate particles could be produced with typical particle sizes of 10 to 30 nm. The samples are well dispersed as could be seen in transmission electron micrographs. However, the chemical composition was not perfect. The barium precursor did not react completely and as a result slightly titanium rich materials resulted after calcination of the powders at 800°C. The effect will be corrected in the next couple of experiments either by increasing the concentration of the barium precursor or by an increase of the reaction efficiency either by longer reaction times or more drastic chemical conditions, e.g. higher pH or higher oxalate/carbonate concentrations.

Some of the systems showed crystallinity already after the precipitation at room temperature, whereas others needed an additional calcination step.

5. CONCLUSIONS

Nanosized barium titanate particles have been produced and in part the materials were already crystalline after the room temperature synthesis. However, a very critical step in terms of control of the overall chemical composition and/or the incorporation of dopants has to be further developed. The work is to be seen as an initial step and many further improvements have to be made within the reaction system. Including the development of a specific recycling process for all constituents. However, microemulsion synthesis provides the means to produce nanosized barium titanate in a very economic way. The second major advantage of this specific synthesis process is the agglomerate free dispersion state of the powder after the synthesis.

6. REFERENCES

1. Horst Herrig, Rolf Hempelmann; "*A colloidal approach to nanometre-sized mixed oxide ceramic powders*"; Materials Letters, **27**, 287-92 (1996)
2. P. Nanni, M. Leoni, V. Buscaglia, G. Aliprandi; "*Low-temperature aqueous preparation of barium metatitanate powders*"; J. Europ. Ceram. Soc., **14**, 85-90 (1994)
3. A. Kaiser, A. Berger, D. Sporn, H. Bertagnolli; "*Lyothermal synthesis of nanocrystalline BaTiO₃ and TiO₂-powders*"; Ceram. Transactions, **51**, 51-5 (1995)
4. Marco Alvazzi, Delfrate, Jaques Lemaitre, Vincenzo Buscaglia, Marcello Leoni, Paolo Nanni; "*Slip casting of submicron BaTiO₃ produced by low-temperature aqueous synthesis*"; J. Europ. Ceram. Soc., **16**, 975-84 (1996)
5. Sonia K. Ellis, Edward P McNamara Jr.; "*Powder synthesis research at CAMP*"; Ceramic Bulletin, **68[5]**, 988-94 (1989)

Development of Ultra-Low Fire COG and X7R Dielectric Compositions for Integrated Passive Component Applications

Brian C. Foster, Walter J. Symes, Everette A. Davis, and Dr. Matthew J. Creedon

Ferro Electronic Materials
1789 Transelco Drive
Penn Yan, New York, USA 14527
Tele: 001-315-536-3357
Fax: 001-315-536-0376
Email: FOSTERB@Ferro.com

ABSTRACT

A series of multilayer ceramic composites were produced to evaluate the feasibility of incorporating multiple dielectric constant materials within the same monolithic structure. A key feature of this investigation was the use of ultra-low firing ceramic materials which sinter at temperatures < 1000 °C and are compatible with 90% Ag internal conductors. Two and three dielectric composition composites ranging from ϵ' = 10 to 70 were produced in a parallel plate multilayer capacitor geometry with and without a barrier conductor separating dissimilar dielectric materials. Characterization of the internal microstructure and electrical property performance showed no adverse interaction between the dielectric compositions. The capacitance densities achieved were 7.3 to 18.6 pF/mm^2. The temperature stability of the composite structures remained within +/- 30 ppm/ °C limits between −55 and +125 °C. The frequency stability of the composite structures did not change from the individual dielectric performance behavior.

INTRODUCTION

A family of ultra-low firing temperature COG dielectric compositions have been developed which densify at temperatures below 1000 °C. This characteristic combined with their compatibility with low resistivity, high Ag content metal systems make them very attractive candidates for integration in integrated circuit packaging or discrete, multi-function passive component applications. The ability to incorporate multiple dielectric constant materials within the same functional block allows for increased miniaturization, lower assembly cost, reduced parasitic coupling, improved impedance matching, and reduced losses at higher operating frequencies. Previous authors have described various dielectric material systems designed for these applications [1-9]. In general chemical and physical property incompatibility problems have prevented the successful incorporation of multiple dielectric constant materials within the same co-fired structure. The ultra-low firing compositions in this work are not ceramic filled glass or recrystallizing glass materials but rather polycrystalline ceramics with < 15 wt% glass forming constituents to promote densification by liquid phase sintering.

RESULTS AND DISCUSSION

Prototype Fabrication

To evaluate the feasibility of using the ultra-low firing COG dielectric materials in a co-fired integrated passive component application a series of multilayer composites were produced. Structures using dielectric constants of 10, 28, and 70 were fabricated in 2 and 3 component composite variations with a 90:10 AgPd internal electrode. The K10 dielectric is a CaMgZr silicate composition. The K28 material is a substituted $BaTi_4O_9$ modified with ZrO_2, ZnO and SiO_2. The third composition is a BaNdBiPb titanate material.

A tape transfer prototype manufacturing process was used to fabricate the test structures. Dielectric tape was cast on a PET carrier film using a floating doctor blade, and internal conductors were deposited using a vision aligned screen printer. A PVB binder system, Ferro B74001 was used with binder solids loading adjusted for each dielectric composition to match green and fired shrinkage characteristics. Ferro EL44-002 90:10 AgPd internal conductor and Ferro TM63-120 100% Ag low stress platable termination were used as the compatible metal systems.

Physical and Electrical Property Characterization

The powder physical property characteristics for the three dielectric compositions are given in Table I. To achieve the ultra-low firing behavior desired the particle size distributions are very fine and the corresponding surface areas are higher than typical dielectric compositions. These materials are produced as deagglomerated powders that do not require extensive mechanical milling prior to incorporation in an organic binder system. Adjustments to compensate for the higher powder surface area effect on tape casting slip rheology are accomplished by the correct selection of dispersant chemistry, order and method of addition and volume concentration. For this study Ferro M1135 wetting agent was used.

Figure 1 shows a TMA comparison of the densification behavior of the three dielectric compositions. The TMA samples were prepared as tape cast laminates with geometry of 6.35 x 5.1 x 0.8 mm. An organic removal step of 250 °C for 6 hours in a mechanical convection oven preceded each TMA run. The heating rate was a linear 4 °C/min. The onset of shrinkage occurs between 500 and 600 °C while the

Table I. Powder physical property measurements							
Material	Particle Size			S.A.	Spec. Gr.	Tap Dens	LOI
	D10	D50	D90	m2/g	g/cm3	g/cm3	wt.%
K10	0.4	0.7	1.3	15.0	3.0	0.6	1.6
K28	0.7	1.1	1.8	4.8	4.5	1.1	1.0
K70	0.4	0.8	1.3	7.7	5.4	0.8	1.3

Table II. High frequency bulk electrical property summary						
Material	Firing Temp (deg C)	Fired Density (g/cc)	ε'	$\tan \delta$	Q*f (GHz)	τ_f (ppm/C) +25 to +60
K10	960	3.32	8.29	0.941*e-3	11,595@10.9 GHz	
K28	940	4.46	28.73	0.664*e-3	10,397@4.8 GHz	-3.45
K70	960	5.47	66.49	1.404*e-3	2,279@3.2 GHz	9.52

Table III. Electrical data summary for individual dielectric composition capacitors							
Material	Firing Temp (°C)	Cap. (pF)	Dielectric ε'	MHz DF (%)	MHz Q	TCC (ppm/deg C) -55°C	85°C 125°C
K10	940	12.17	10	0.017	5792	P132	P120 P121
	960	11.66	9	0.015	6536	P129	P117 P119
	980	10.59	8	0.030	3333	P132	P116 P117
K28	940	111.00	31	0.014	6974	P003	N003 N003
	960	110.85	31	0.015	6897	N003	N001 P003
	980	113.42	31	0.018	5435	N002	NPO P004
K70	940	276.11	69	0.013	7296	P019	P011 P008
	960	276.79	69	0.020	5000	P016	P008 P006
	980	272.04	71	0.022	4758	P013	P005 P003

Table IV. Electrical data summary for multiple dielectric constant composite capacitors									
Composite Configuration	Firing Temp (°C)	K10 Active (Yes or No)	Cap. (nF)	Dielectric ε'	MHz DF (%)	MHz Q	TCC (ppm/deg C) -55°C	85°C	125°C
K10/K28/K10	940	Yes	0.091	18	0.014	7380	46	12	28
	940	No	0.071	28	0.020	5000	1	-6	-4
	960	Yes	0.094	19	0.017	5763	32	32	33
	960	No	0.075	30	0.022	4498	2	0	1
	980	Yes	0.097	19	0.019	5219	32	32	34
	980	No	0.077	30	0.025	4000	2	1	1
K10/K70/K10	940	Yes	0.217	41	0.013	8433	54	-22	-9
	940	No	0.185	73	0.025	4000	46	-15	-13
	960	Yes	0.228	45	0.016	5924	46	-33	-18
	960	No	0.186	70	0.021	4760	23	-2	1
	980	Yes	0.232	46	0.014	7088	26	-6	-1
	980	No	0.176	64	0.015	6667	11	-10	-9
K10/K28/K70/K10	940	Yes	0.158	30	0.046	2255	148	-170	-99
	960	Yes	0.160	32	0.034	2905	106	-123	-73
	980	Yes	0.166	32	0.051	1921	123	-174	-109

Table V. Coaxial tuned line measurements									
sample configuration	Cap value (pF)	$\tan \delta$	140MHz ESR	380 MHz ESR	630 MHz ESR	880 MHz ESR	1360 MHz ESR	2265 MHz ESR	3170 MHz ESR
K28	112	5*e-5	0.0654	0.0991	0.1311	0.1524	0.1980	0.3197	1.1693
K70	270	2*e-4	0.0788	0.1422	0.1845	0.2231	0.2934	0.8315	0.6196
K10/28/10	75	1*e-4	0.0861	0.1415	0.1782	0.2110	0.2143	0.2787	0.3372
K10/70/10	200	2*e-4	0.1174	0.1854	0.2437	0.2974	0.3789	0.5754	1.8104

most rapid densification takes place between 750 and 900 °C. Electrical property measurements were performed on each dielectric material using both bulk ceramic and multilayer capacitor sample configurations. Dielectric constant, dissipation factor and transmission coefficient were characterized on bulk specimens using a Kent resonant mode dielectrometer. One port and 2-port cavity perturbation methods were used to measure Q*f and T_f values. Table II provides a summary of the high frequency bulk property test data.

Multilayer ceramic capacitor designs using each individual dielectric composition were fabricated as a control group for comparison with multiple dielectric constant material composites. The multilayer composite configurations evaluated utilized the K10 dielectric for
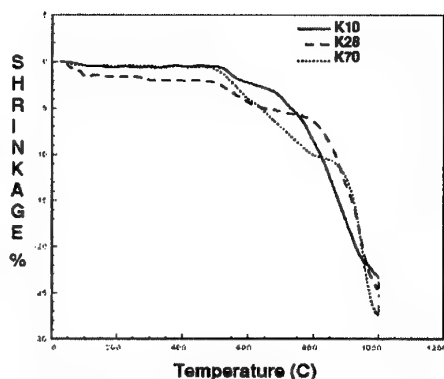
Figure -1 TMA Comparison of Compositions

the top and bottom layers with the higher dielectric constant K28 and K70 materials being used in the middle of the monolithic block. The dielectric layer thickness of the K10, K28 and K70 materials was approximately 35 microns. The external dimensions of the test capacitor structures were 3.1 x 1.5 x 0.5 mm. To investigate the effect of dielectric material interaction
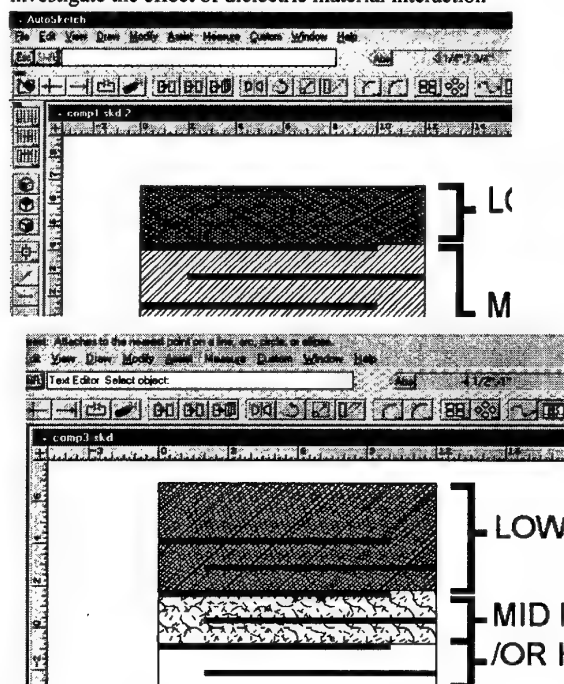
Figure 2 - Composite Construction Detail

each composite configuration was tested with and without a barrier conductor between dissimilar dielectric layers. This barrier design resulted in (4) higher dielectric constant layers being inserted between (4) lower dielectric constant layers, (2) on either side. Figure 2 outlines the construction detail for each multilayer capacitor design evaluated. Organic binder removal and sintering profiles are provided in Figure 3. The binder removal step was accomplished in a Blue M model MP-206C mechanical convection oven. The

sintering step utilized a Sierra Therm model 2K14-117C73-9AN (9) zone controlled atmosphere conveyor furnace. All of the samples were supported on zirconia setters during thermal processing.
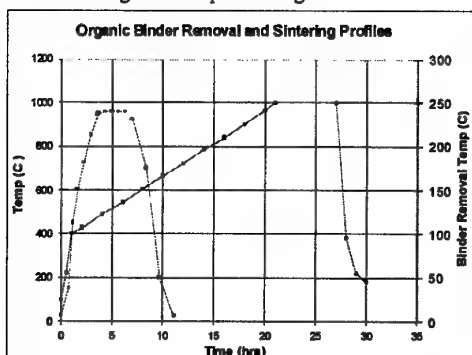
Figure 3 - Binder Removal and Sintering Profiles

Tables III and IV provide a summary of the electrical property data measured for the individual dielectric control capacitors and the multiple dielectric constant composite capacitors. All of the data summarized was generated at 1 MHz using a HP 4278A capacitance meter and a HP 16034E test fixture. The temperature coefficient measurements were performed using an Ingalls Engineering model IE-TCM-80 temperature chamber and capacitance test system.

A comparison of the composite electrical property data with the single dielectric control electrical property data shows there is no significant degradation in dielectric performance when two or more of the ultra-low fire dielectric compositions are integrated within the same discrete monolithic structure. Predictably the configurations where active layers of low dielectric constant and high dielectric constant are mixed the composite dielectric constant and temperature coefficient of capacitance values are intermediate between the single dielectric control values and those designs where low dielectric constant active layers are not incorporated. The capacitance densities achieved in the composite designs were 7.3 pF/mm^2 for the K10/K28 configuration and 18.6 pF/mm^2 for the K10/K70 configuration.

To evaluate the performance of the mixed dielectric constant composites at higher frequencies coaxial tuned line measurements were taken covering the frequency range from 140 MHz to 3.2 GHz. Two coaxial tuned lines, one 60 cm in length and one 15 cm in length manufactured by Ingalls Engineering were used to perform the measurements. Table 4 shows ESR behavior as a function of frequency for the single dielectric material control capacitor and the K10/K28 and K10/K70 composite capacitor structures. No appreciable differences were seen between the single dielectric and composite configurations after taking into account the difference in capacitance values.

To understand the interactions taking place between dielectric materials and the 90:10 AgPd conductor during co-firing a detailed microstructure analysis was conducted using a JEOL scanning electron microscope

(SEM) in both secondary and backscatter detection modes with a PGT energy dispersive x-ray analyzer (EDAX). Cross section samples were polished and thermally etched prior to the analysis.

In the K10/K28 composite a diffusion band is observed at the interface of the two materials that is approximately 30 microns in width. Silica is depleted from the interface and is replaced by Zr, Ca and Zn in a high aspect ratio, needle type grain structure. The presence of a barrier conductor between the dissimilar dielectric materials eliminates the formation of this intermediate microstructure. The K70/K10 composite also shows a diffusion zone between the two dissimilar dielectric materials, which is approximately 30 microns in width. In this case the diffusion of elements across the interface is not accompanied by the development of a large grain phase. EDAX analysis shows a preferential concentration of Zr in a thin 5 micron band at the interface with Ca diffusing across the interface the entire width of the diffusion zone. There is no evidence of Si mobility as seen in the K10/K28 composite microstructure. As with the K10/K28 composite the presence of a barrier conductor between the dissimilar dielectric materials eliminates the formation of this intermediate microstructure.

CONCLUSIONS

A series of composites using multiple ultra-low fire ceramic compositions having dielectric constants ranging from 10 to 70 were fabricated and tested. The test configurations evaluated utilized a standard parallel plate multilayer capacitor design with and without a barrier conductor between dissimilar dielectric materials. Both low and high frequency electrical characterization of the composites showed no evidence of degradation in the dielectric performance of the K28 or K70 compositions when they were integrated within the K10 composition. The capacitance density achievable with an integrated K28 dielectric in a K10 matrix is 7.3 pF/mm^2. By integrating the K70 dielectric the capacitance density increases to 18.6 pF/ mm^2. The dielectric loss measured as dissipation factor and Q remain comparable to the individual dielectric control capacitors. Dissipation factor measured a 1 MHz was <$/$= 0.025 % for both composite configurations. Q factor at 1 MHz with an optimized peak firing temperature was >21,000 for the K10/K28 composite and >10,000 for the K10/K70 composite.

In addition to the (2) dielectric composites a (3) dielectric composite was fabricated to assess the compatibility of the K28 and K70 compositions when they were both integrated within the K10 composition. The microstructure development and electrical property characterization results demonstrate that integrating a high and mid ε' material for maximum capacitance density and tuning capability within a low ε' material matrix is achievable.

In summary the present work with ultra-low fire ceramic compositions has shown that these material systems are capable of producing multiple dielectric constant integrated structures which are useful for discrete chip component or multilayer packaging architectures. Future work will evaluate these materials in a multilayer chip resonator, LC filter, and buried

microstrip geometry. In addition reliability testing including HALT and temp/humidity/bias will be performed to confirm that no degradation in useful life occurs when dissimilar dielectric constant materials are co-fired.

REFERENCES

[1] R.L. Brown et al., "The Integration of Passive Components Into MCM's Using Advanced Low-Temperature Co-fired Ceramics," *The International Journal of Microcircuits and Electronic Packaging,* Vol. 16, No. 4, pp. 328-337, Fourth Quarter 1993.

[2] T.K. Gupta, "In Search of Low Dielectric Constant Ceramic Materials for Electronic Packages," *The International Journal of Microcircuits and Electronic Packaging,* Vol. 17, No. 1, pp. 80-97, First Quarter 1994.

[3] G. Kniajer et al., "Low Loss, Low Temperature Co-fired Ceramics with Medium Dielectric Constants," *The International Journal of Microcircuits and Electronic Packaging,* Vol. 20, No. 3, pp. 246-253, Third Quarter 1997.

[4] D.L. Wilcox et al., "The Multilayer Ceramic Integrated Circuit (MCIC) Technology: Opportunities and Challenges," *Proceedings of the 1997 International Symposium on Microelectronics,* Philadelphia, PA, pp. 16-23.

[5] P. Danner, "Integrating Multiple Dielectric Constants in Ceramic Modules," *Proceedings of the 1997 International Symposium on Microelectronics,* Philadelphia, PA, pp. 37-41.

[6] P.J. Bolton, "Construction, Characterization, and Reliability of BaTiO$_3$ – Based Buried Thick Film Capacitor Materials Sets, 1200 < K, 1600," *Proceedings of the 1998 International Conference on Multichip Modules and High Density Packaging,* Denver, CO, pp. 484-489.

[7] T. Kubo et al., "Functional Multilayer Ceramic Substrate For Power Amplifier Module," *IMAPS 3rd Advanced Technology Workshop on Integrated Passives Technology,* Denver, CO, April 17-18, 1998.

[8] W. Wersing, "Integrated Passive Components Using Low Temperature Co-fired Ceramics," *Proceedings of the 1998 International Symposium on Microelectronics,* Sn Diego, CA, pp. 193-199.

[9] S. Scrantom et al., "Manufacture of Embedded Integrated Passive Components into Low Temperature Co-Fired Ceramic Systems," *Proceedings of the 1998 International Symposium on Microelectronics,* Sn Diego, CA, pp. 459-466.

Dielectric Property of $BaTiO_3$-$BaZrO_3$ Solid Solution under High Electric Field

Takaaki Tsurumi, Yuichi Yamamoto, Naoki Ohashi, Hirokazu Chazono*,
Yasuyuki Inomata* and Hiroshi Kishi*

Department of Metallurgy and Ceramics Science, Graduate School of Science and Engineering,
Tokyo Institute of Technology,
Fax: +81-3-5734-2514, e-mail: ttsurumi@ceram.titech.ac.jp
* R&D Materials dept., General R&D Laboratories, Taiyo Yuden Co., Ltd.
Fax:+81-27-360-8315, e-mail:hchazono@jty.yuden.co.jp

Dielectric constants of $BaTiO_3$-$BaZrO_3$ (BTZ) solid solution was measured for BTZ dielectric-layers in multilayer ceramic capacitors (MLCC) with Ni internal electrodes and BTZ ceramic disks. The dielectric constant vs. temperature (ε vs. T) variation of the BTZ-layers in MLCC was changed with the thickness of the BTZ layers. This behavior was almost completely reproduced in the electric field (AC-field) dependence of dielectric constant of BTZ ceramics. The AC-field dependence of dielectric constant was markedly observed below the temperature of a broad maximum in the ε vs. T curve. The dielectric property of BTZ ceramics under high AC-field could be explained by the model of relaxors which explained the property of relaxors in terms of the formation of polar micro regions (PMR) and the freezing of fluctuating dipoles in PMR

1. INTRODUCTION

The solid solutions of $BaTiO_3$-$BaZrO_3$ (BTZ) have been used for the dielectric materials in multilayer ceramics capacitors (MLCC) with Ni internal electrodes. The MLCC of BTZ has Y5V specification in EIA. The thickness of the BTZ dielectric-layers in MLCC is becoming thinner year by year to increase the capacitance. Recently, MLCC with the dielectric-layer thickness of 2.8μm have been developed, however, it has been realized that the dielectric properties of MLCC with very thin dielectric-layers is somewhat different from those with relatively thick dielectric-layers. The reason of this phenomenon is attributable to the increase in the electric field (AC-field) applied on the dielectric-layers. However, the dielectric properties under high AC-fields have not been studied in detail.

Relaxor materials are characterized mainly by a frequency dispersion and broad peak in the dielectric constant vs. temperature (ε vs.T) variation [1]. They appear most often in lead based perovskite compounds such as lead magnesium niobate (PMN), lead scandium tantalate (PST) and so on. Some lead-free, environmental-friendly, $BaTiO_3$ (BT)-based ceramics show the relaxor behavior and one of the simplest composition of them is BTZ with higher content of $BaZrO_3$ (BZ) than about 27% [2]. In the composition range of between 10 to 27% BZ, a broadened peak is observed in the ε vs.T curve, whose temperature does not depend on the frequency [2]. This region may be called as diffuse phase transition and actually used for dielectric materials in MLCC with Y5V specification.

The dielectric constant of PMN under high AC-field was measured by Tsurumi et al.[3]. They found that the maximum in ε vs. T curve disappeared under high AC-fields. It seems to be important to study AC-field dependence of dielectric property for lead-free relaxors

to utilize and design the these materials for MLCC with very thin dielectric-layers.

In this study, we have demonstrated that the variation of dielectric properties with the thickness of dielectric-layers in MLCC is reproduced by the change in the AC-field, and the dielectric properties under high AC-fields was explained by the model of relaxors.

2. EXPERIMENTAL PROCEDURE

2.1 Sample Preparation

(a) MLCC

Precalcined BTZ (BT:BZ=85:15) powder added with Ho_2O_3 and some sintering agents were weighed, ball-milled, dried and then calcined at 1150℃ for 2h. The obtained powder was mixed with organic binder into slurries. They were cast into green sheets with various thickness. 20 green sheets on which Ni paste was printed for internal electrodes were stacked with protective sheets at the upper and lower sides, and pressed into a bar and cut into pieces. After formation of terminal Ni electrodes on both sides of the pieces, they are fired at 1200℃ for 2h in reducing atmosphere followed by cooling in the same atmosphere to 1000℃ and in oxygen partial pressure of 30Pa below 1000℃. Four kinds of MLCC with different thickness of dielectric-layers (6.4, 5.6, 4.4, and 2.8μm) were prepared. The microstructure of grounded and thermally etched cross section of MLCC was observed by a field emission scanning microscope (FE-SEM, Hitachi).

(b) Ceramic Disks

Ceramic disks of BTZ were prepared by conventional ceramics process. Powder of BTZ (BT:BZ=79:21) was calcined at 1000℃ for 2h, isostatically pressed into disks, and fired at 1430℃ for 1h. The obtained ceramics with 99.1% of the theoretical density were cut into thin

disks of 100µm thick and annealed to remove the residual strains. Electrodes were made by Pt sputtering.

2.2 Measurements of Dielectric Property

The capacitance of MLCC was measured with an impedance analyzer (HP-4284A) from -40 to 100℃. The oscillation level of signal was 2.8V (peak to peak) and the frequency was 1kHz. Dielectric constants of the dielectric-layer in MLCC were calculated from the capacitance and sample geometry.

For measurements of dielectric property of the ceramic disks under high AC-field, equipment shown in Fig.1 was constructed. Sinusoidal signal at 10kHz from a function generator was amplified and applied to the specimens. The displacement-current through the specimen was converted to voltage signal with an operation amplifier in a virtual ground circuit. The signal of the operation amplifier was stored on a digital oscilloscope. The current was integrated in a computer to calculate polarization (P). Dielectric constant was calculated from electric displacement (D) divided by electric field (E), which is the slope of a line connecting a point (D,E) and the origin in D vs. E curve. The electric field (peak to peak) of singles applied to the specimens was changed from 48V/mm to 1.0kV/mm.

3. RESULTS AND DISCUSSION

3.1 Microstructure and Dielectric Property of MLCC

Figure 2 shows the FE-SEM images of the cross sectional view of MLCC with various dielectric-layer thickness. All specimens were dense and consisted of

grains of 1 - 3µm in size. There are at least 3 grains in the dielectric-layer of 6.4µm thick but some portion in the 2.8µm thick dielectric-layers consists of only one grain. The grain growth of dielectrics is a characteristic feature of MLCC of Y5V specification. High dielectric constants are attained by the grain growth as pointed out by Hansen et al. [4]. In the case of MLCC of X7R specification, there are many grains in one dielectric-layer and it is known that the grain growth degrades the temperature stability of dielectric constant [5-6].

Figure 3 shows the dielectric constant of MLCC calculated from the capacitance and sample geometry. It was confirmed that the dielectric constant vs. temperature relation changes with the thickness of dielectric-layer, i.e.: the dielectric constant at room

Fig.3 Dielectric constant of dielectric-layers with various thickness in MLCC as a function of temperature.

Fig.4 (A) Dielectric constant of BZT ceramics at room temperature and at 10kHz as a function of AC-field.

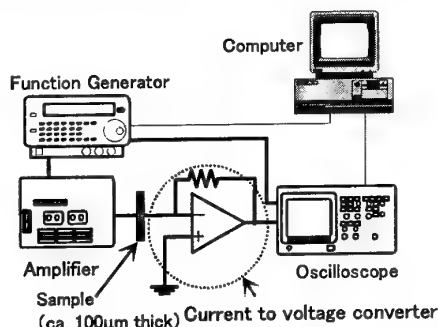(B) A typical D-E curve measured at room temperature and at 10 kHz.

Fig.1 Schematic diagram of measuring system.

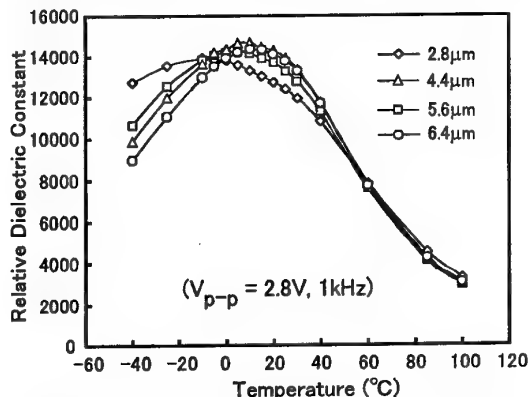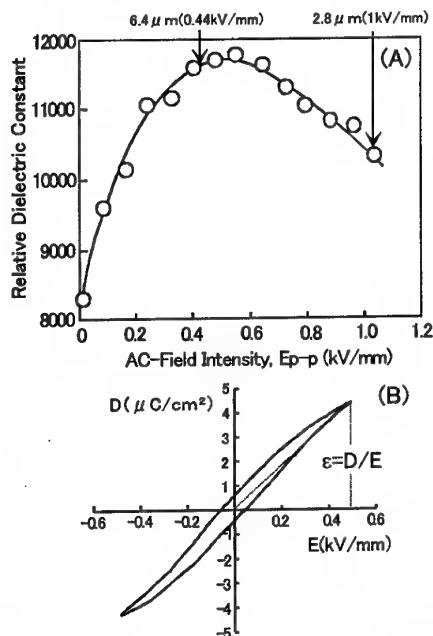
Fig.2 FE-SEM images of the cross sectional view of MLCC with various dielectric-layer thickness.

temperature decreases with decreasing dielectric-layer thickness, and the temperature showing maximum dielectric constant (T_m) also decreases with the thickness. These changes in the dielectric property is becoming a problem to use MLCC with very thin dielectric-layers.

3.2 Dielectric Property of Ceramic Disks

Dielectric constant of the BTZ ceramics is shown in Fig.4 (A) as a function of AC-field intensity. Dielectric constant first increases with increasing AC-field, and decreases after showing a maximum at $E_{p-p} = 0.5$kV/mm. Figure 4(B) shows a typical D-E curve measured with the equipment in Fig.1. A slim hysteresis loop, which is commonly observed in relaxors, indicates the existence of the non-linearity in dielectric properties of BTZ ceramics. Arrows in Fig.4 (B) are the electric fields corresponding to the fields applied to the dielectric-layers (6.4 and 2.8μm) in the MLCC. The decrease in the dielectric constant at room temperature observed in MLCC with thickness of dielectric-layers (Fig.3) is reproduced by the increase of AC-field intensity. The decrease of dielectric constant at high AC-fields can be explained by the non-linearity of D-E curve. On the other hand, the increase in the dielectric constant at low AC-fields (Fig.4 (A)) is due to the excitation of dipole fluctuations in the polar micro regions (PMR) in relaxors, which will be discussed in later.

Figure 5 indicates dielectric constant (ε) vs. temperature (T) relations of the BTZ ceramics measured under various AC-fields. It was found that the ε vs. T curve markedly depended on the AC-field intensity used
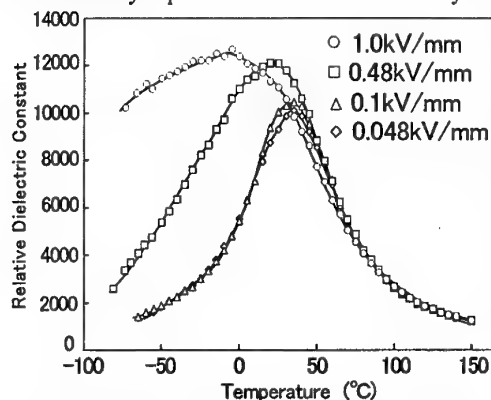

Fig.5 Dielectric constant vs. temperature relations of BTZ ceramics measured at various AC-fields.

in the measurements. Characteristic features seen in Fig.5 are summarized as follows: 1) the temperature of maximum dielectric constant (T_m) shifted to the low temperature side under high AC-fields, 2) the effect of high AC-fields is small on the high temperature side of the peak, 3) dielectric constants below T_m increases under high AC-fields and 4) the peak of dielectric constant becomes broad under high AC-fields. The AC-fields of 0.48kV/mm and 1.0kV/mm correspond to those applied to the dielectric-layers of 6.4μm and 2.8μm thick, respectively. By comparing the results in Fig.3 and Fig.5, it is confirmed that the change of dielectric property due to the thickness of dielectric-layers in MLCC is almost completely reproduced by the change of AC-field intensity.

3.3 Relaxor Behavior under High AC-Field

The experimental results in the previous sections are explained by the model of relaxors. Cross [1] has proposed a concept of polar micro regions (PMR), in which randomly oriented dipoles are fluctuating, and the fundamental mechanism of diffuse phase transition in relaxors. The mechanism of diffuse phase transition is possibly summarized in Fig.6. The ε vs. T curve of relaxors is tentatively divided into 3 regions (region I, II and III).

In the region I, PMR is formed in the matrix of paraelectric phase. The frequency of dipole fluctuation in PMR in this region is much higher than the frequencies normally used for dielectric measurements. The formation of PMR is therefore detected as a change in refractive index [7].

The total volume of PMR increases with decreasing temperature in the region II. In PMR, dipoles are fluctuating at a certain frequency and the external field changes their directions, which contributes to the electrically induced polarization. Therefore, dielectric constant increases with increasing volume of PMR. PMR can be regarded as nuclei of ferroelectric phase. In normal ferroelectrics, the phase transformation into ferroelectric phase occurs in the region II if the size of nuclei exceeds a critical value. However, relaxors do not transform into ferroelectric phase because the size of nuclei, in which soft phonons is vibrating in phase, may be restricted by macroscopic or microscopic imperfections in crystals, such as chemically ordered domains. The frequency of dipole fluctuation in PMR decreases with decreasing temperature without the phase transformation.
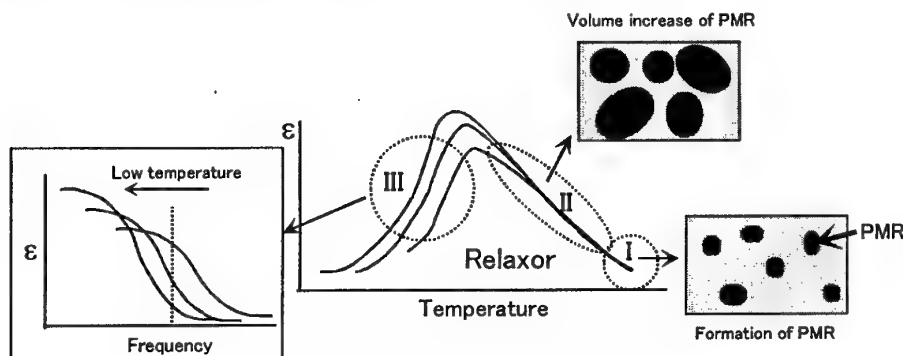

Fig.6 Mechanism of diffuse phase transition in relaxors

The region III is the freezing process of the fluctuation of dipoles. In this region, the frequency of the dipole fluctuation becomes comparable to the frequency used in the measurements and dielectric relaxation is normally observed. The dielectric constant decreases steeply if the relaxation frequency of dipoles becomes lower than the frequency used in measurements as shown in the ϵ vs. frequency curves in Fig.6 (the dotted line shows a tentative frequency used in measurements). The relaxation frequency approximately obeys the Arrhenius' relation and decreases with decreasing temperature. The dielectric constant in the region III is mainly determined by the comparison between the relaxation frequency and the frequency used in the measurements. If the measurement is done at a low frequency, the dielectric constant keeps high value to lower temperatures and vice versa. The dielectric dispersion and the shift the peak temperature (T_m) with frequency in Fig.6 is explained in this way.

The explanation of relaxor behaviors mentioned above is valid when the external AC-field is relatively low. Under high AC-fields, the situation changes especially in the region III. The AC-field dependence of dielectric constant cannot be expected in both region I and the high temperature side of region II because the response to the electric field in these regions is mainly determined by the paraelectric matrix. Figure 7 shows D-E curves of BTZ ceramics. At 100℃, the non-linearity of D-E curve is not observed, showing that the dielectric constant is independent of the AC-field intensity.

In the low temperature side of region II, e.g. room temperature in the BTZ ceramics, the contribution of dipoles in PMR to the polarization is observable as the AC-field dependence of dielectric constant. The field-induced change in the directions of fluctuating dipoles is enhanced by high AC-fields, which increases the dielectric constant, but simultaneously the non-linearity appearing in the D-E curve decreases the dielectric constant. The AC-field dependence of dielectric constant measured for BTZ ceramics in Fig.2 is explained in this way.
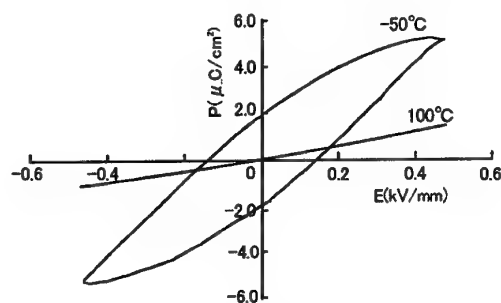

Fig.7 D-E curves of BTZ ceramics measured at -50℃ and 110℃ at 10kHz.

In the region III, high AC-fields force to move the freezing dipoles to change their directions. This gives rise to the increase in dielectric constant and the shift of the peak temperature (T_m) to the low temperature side. Under the very high AC-fields which does not allow the freezing of dipoles, the peak of dielectric constant disappears in the ϵ vs. T curve and the dielectric constant is expected to increase monotonously with decreasing temperature. The indication of this behavior is seen in the results of 1.0kV/mm in Fig.5. The forced oscillation of freezing dipoles enhance the non-linearity in D-E curve and induced ferroelectric response in it, which is clearly seen in the D-E curve at -50℃ in Fig.7.

The dielectric property of BTZ under high AC-field is consistently explained by the concept of PMR and the fundamental mechanism of diffuse phase transition proposed by Cross [1] as mentioned above. We think that the results obtained in this study strongly supports the validity of the model which explains the dielectric property of relaxors in terms of the formation of PMR and the freezing of fluctuating dipoles in PMR.

4. SUMMARY

Dielectric constant of BTZ-layers in MLCC changed with the layer thickness. To understand the mechanism of this phenomenon, dielectric constant of BTZ ceramics was measured as a function of AC-field intensity using equipment with a displacement-current to voltage converter. The dependence of dielectric constants on the layer thickness was almost completely reproduced by changing AC-field intensity in the measurements of BTZ ceramics. A broad peak was observed in ϵ vs. T curve of BTZ ceramics and AC-field dependence of dielectric constant was markedly observed in the low temperature side of the peak. Dielectric property of BZT under high AC-field was consistently explained by the model of relaxors. At low temperatures, high AC-field forced to move the freezing dipoles in PMR to change their directions, which gave rise to the increase in the dielectric constant and the shift of the peak temperature to low temperature side.

References
[1] L.E.Cross, Ferroelectrics, 151, 305 (1994).
[2] R.Farhi, M.El Marssi, A.Simon and J.Ravez, Eur.Phys.J. B9, 599 (1999).
[3] T.Tsurumi, K.Soejima, T.Kamiya and M.Daimon, Jpn.J.Appl.Phys., 33, 1959-64 (1994).
[4] P.Hansen, D.Hennings and H.Schreinemacher, J.Am.Ceram.Soc., 81, 1369 (1998).
[5] H.Chazono and M.Fujimoto, J.Appl.Phys., 34, 5354 (1995).
[6] R.Wernicke, Phys.Stat.Sol., 47, 139 (1978).
[7] G.Burns and F.H.Dacol, Phys.Rev., B28, 2527 (1983).

Dielectric Development for High Voltage Filter Capacitor Applications

T. Jessen[1], M. Chase[2], L. Kurihara[2], and M. Kahn[2]

[1]US Naval Research Laboratory, Washington, DC
[2]Potomac Research Incorporated, Fairfax, VA

The Power Electronic Building Block (PEBB) initiative of the US Navy has a requirement for high voltage filter capacitors, which are not available commercially. A formulation and processing study was conducted to determine the feasibility of developing an 'industrially-friendly' capacitor composition to address this need. Compositions in the family $(Pb_xBa_{1-x})(Zr_yTi_{1-y})O_3$ as well as processing variables were investigated. One formulation was identified which appears to meet the PEBB requirements of high dielectric breakdown strength and stable capacitance as a function of field and temperature. The processing and property studies conducted in this effort are described in this paper.

INTRODUCTION

The US Navy (USN) has begun development of a single package, high power, multi-function controller to address all its future shipboard power requirements [1]. The Power Electronic Building Block (PEBB) design is a device that incorporates integrated circuits, sensors, and passive components. The objectives of PEBB are two-fold: (1) simplify the design of large electric power systems and (2) reduce design/development costs for complex power circuits. When deployed, the PEBB will be able to service a variety of power requirements (either ac or dc) via simple software modifications and minimize fleet deployment inventories, generating further cost savings.

PEBB is envisioned in a variety of applications beyond providing a zonal distributed electrical system for shipboard machinery. Other US military applications include: fly by light, power by wire systems being developed by both the Air Force and NASA, as well as the electric tank effort of the Army. The Department of Energy is working on a range of commercial, low power applications including the hybrid-electric vehicle and generic power supplies for household appliances.

Two examples [2] of the design impact of PEBB on next generation USN platforms include: (1) shipboard power supply density and (2) submarine actuation systems. In the 1960's, shipboard power density was typically 1.4 kW/ft^3 at a cost of \$2.27/watt operating at a switching frequency of 60 Hz. Currently, power density is approximately 5 kW/ft^3 costing \$0.50/watt at a switching frequency of 20 kHz. PEBB devices will deliver 50 kW/ft^3 at 70 kHz in the next generation of surface ships at a cost of \$0.06/watt. In addition the PEBB 'footprint' will be only 1% of its 1960's era predecessor.

At present, US submarines have a centralized hydraulic system harnessed to the propulsion plant, which is maintenance intensive. In future generations of submarines, a distributed actuation system will be incorporated utilizing PEBB as discrete power supplies. It is estimated that this approach will save 70 tons in displaced weight, reduce the platform's radiated signature (i.e. noise), as well as improve combat survivability through the use of a distributed power grid.

While significant progress has been made in developing the integrated circuitry for PEBB, little effort has been directed toward the passive components (i.e. capacitors and inductors) [3]. PEBB will require both input and output passive filter devices. In current prototypes, 1920's-era oil and paper capacitors have been used because of the high voltage requirements of PEBB (500 V). These capacitors, while adequate for proof-of-concept demonstrations, are far too large for shipboard implementation. Commercially available multilayer ceramic capacitors, while volumetrically more efficient, do not meet the operating parameters for PEBB. This paper describes a preliminary dielectric formulation study conducted to identify compositions for PEBB capacitor applications.

EXPERIMENTAL PROCEDURE

In addition to operational parameters of volumetric efficiency (i.e. high dielectric constant) and stable capacitance as a function of both temperature and field; an off-the-shelf, near term production solution was desired. This requirement restricted formulation/processing development to 'industrially-friendly' approaches to improve the likelihood of technology transfer to a commercial manufacturer for capacitor fabrication. For this reason, the primary focus of this study was solid-state compositional processing. Furukawa et. al. [4] had previously identified the base composition used in this study $(Pb_xBa_{1-x}) (Zr_yTi_{1-y}) O_3$. as having a high dielectric constant and the potential for high voltage application.

Compositional variations (altering the Pb/Ba ratio) and processing variables such as milling time and both calcination and sintering temperature profiles were

investigated using commercially available powders. The Ba and Sr precursor powders were carbonate-based, while the Pb, Zr, and Ti powders were all oxides. 100 - 200 gm batches of the precursors in appropriate ratios were mixed by ball milling for 20 h as an alcohol-based slurry, with a solids content of 65%. The slurry was then flash dried and the mixed powder attrition milled for particle size reduction. The dried, milled powder was then calcined in flowing air on an open sagger to remove organics. Following a light grinding to break up agglomerates, the powders were uni-axially dry pressed at 5500 psi into disks. The disks were then fired in closed crucibles in a lead-rich setter powder in a box furnace with an ambient air atmosphere.

Following sintering, the disks, typically three to four per test condition, were measured for shrinkage and bulk density (via the Archimedes method). Sputtered noble metal electrodes were then applied to the top and bottom surfaces of the disks. The capacitance and dissipation factor were measured as a function of field, frequency, and temperature. Leakage resistance was also measured. Selected disks were broken and the microstructure observed using scanning electron microscopy (SEM).

RESULTS AND DISCUSSION

Table I compares the properties of selected compositions fabricated by the methods described above. Specific compositional information will be withheld at this time pending patent position determinations. Compositions 1-3 had increasing Pb content and decreasing Ba, while compositions 3-6 had a constant Pb/Ba ratio and variable calcination and sintering temperatures. The Zr to Ti ratio was fixed for all compositions. The density increases with increasing Pb content, as would be expected. A similar trend of increasing density with sintering temperature was not observed for compositions 4-6. Varying the calcination temperature (compositions 3 vs. 4) had little effect on density.

For the electrical properties an increase in the Pb/Ba ratio is seen to increase both the dielectric constant and the leakage resistance. A minimum dissipation factor, for all compositions, was observed with the lowest Pb/Ba ratio (Composition 1). Lowering the calcination temperature for a fixed composition (3 vs. 4) resulted in a decrease in dielectric constant and increase in dissipation factor, an indication that organic material remained after the lower temperature calcination. For compositions 4-6, with similar Pb/Ba ratios and calcination temperatures, a decrease in the sintering temperature resulted in an increase in both the dielectric constant and leakage resistance while decreasing the dissipation factor. The significant increase in both dielectric constant (3X) and leakage resistance (3X) with decreased sintering temperature suggests that increasing lead loss with higher firing temperatures occurs despite the use of closed crucibles and lead-rich setter powder. The dissipation factor is more significantly impacted (10X) by calcination than sintering temperature, suggesting that organic removal is more critical than control of lead loss for improving this property.

The best combination of electrical properties was obtained with Composition 6, therefore this material will be the focus of the remainder of this paper. The grain size, as determined by SEM examination, was typically 3 μm, a size shown to be near optimal for the electrical properties of lead-based ceramics. The triple points and grain boundaries appear to be free of impurities, an important factor for producing high dielectric constant materials. The lack of impurities should also aid the breakdown strength of the material. Fracture appeared to be a combination of inter- and intragranular; while itself not significant for this study, it allowed both the interior and surfaces of grains to be observed. The faceted structure of the 1280°C sintering differs from that of the higher temperature firings. At the elevated temperatures, the fracture surface has an increasingly 'glassy' appearance, evidence to support lead-loss as the mechanism for the lower electrical properties.

Figure 1 shows the dielectric constant (K) for Composition 6 as a function of temperature for both 0 and 3kV applied dc bias. For both plots there is some dispersion of K below 50°C as a function of frequency. There is also a shift in maximum dielectric constant with the application of voltage; with no bias the K typically peaks at room temperature while at 3kV bias the maximum values are obtained at 0°C.

The dissipation factor (tan δ) was typically unaffected by dc bias. Tan δ displayed a trend of increasing loss with measurement frequency but the dispersion was not large. The biggest impact on dissipation factor was temperature; at room temperature and above (25 to 125°C) the loss was typically 0.0001 to 0.002. However, below room temperature (0 to –65°C) the loss increased rapidly up to values approaching 0.10. The disk capacitors used in this study were unencapsulated so a likely explanation for the large change in tan δ is the presence of water (condensation in the form of ice). Earlier measurements made on disks with air-dried Ag electrodes showed even larger losses at low temperature, which corroborates this explanation.

Table I. Properties (@ 25°C, 1 kHz) as a Function of Composition and Processing Condition

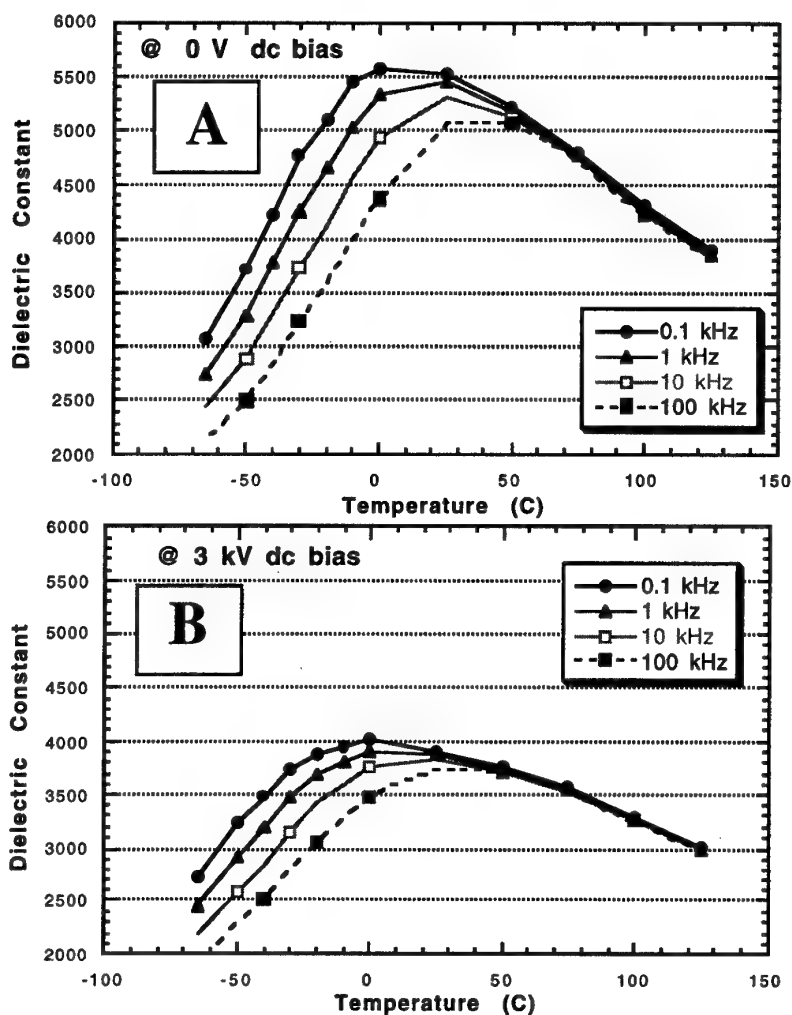| Comp.	Temperature (C) Calcine	Sinter	Density (g/cc)	Dielectric Constant	Dissipation Factor	Leakage Resistance (T ohms)
1	1050	1350	5.77	450	0.001	3.50
2	1050	1350	5.93	1440	0.003	0.58
3	1050	1350	7.14	2970	0.003	0.30
4	850	1350	7.17	1600	0.038	0.35
5	850	1330	7.50	3410	0.032	0.80
6	850	1280	7.02	5450	0.027	0.90

Figure 1. Dielectric constant as a function of temperature at 0 (A) and 3kV (B) dc bias.

Figure 2 shows the dielectric constant as a function of bias voltage at room temperature and the PEBB operating-envelope temperatures (-65 and 125°C). The trend with these and intermediate temperature measurements was decreasing K with applied voltage. The maximum bias (3 kV/mm) was limited by the test equipment rather than the material. None of the samples tested had electrical breakdown at this voltage. At all temperatures a large change in K was observed between 0 and 3 kV bias (22% @ 125°C, 29% @ 25°C, and 10% @ -65°C). However, within the operating envelope anticipated for PEBB devices (0 to 1

kV) the change was < 4%, well within the target tolerance of 10%. Similar trends and property variation in K versus bias was observed as a function of frequency.

The dissipation factor for Composition 6 samples was independent of frequency (100 Hz to 100 kHz) at temperatures above 25°C. At room temperature and below there was up to a 2X increase in tan δ across the test frequencies. The dissipation factor was independent of dc bias at all test temperatures.

SUMMARY

A dielectric formulation in the family $(Pb_xBa_{1-x})(Zr_yTi_{1-y})O_3$ has been developed which exhibits a dielectric constant in excess of 5400 at room temperature and excellent capacitance stability as a function of both temperature (-65°C to +125°C) and applied dc voltage (up to 3 kV/mm).

Processing variables were found to impact the electrical performance. Maximum dielectric constant was obtained at a sintering temperature of 1280°C. Increasing the sintering temperature was observed to lower the dielectric constant, which is likely a result of lead loss. Significant improvements in dissipation factor (10X) were obtained with a 1050°C rather than 850°C calcination treatment. It is probable that unreacted organic material was the cause of the degradation in dissipation factor.

Increased variability in electrical properties following voltage cycling was observed at the -65°C test condition. This result may be an artifact of the termination electrodes. Similar voltage cycling will be conducted with fired-on electrodes to investigate this hypothesis
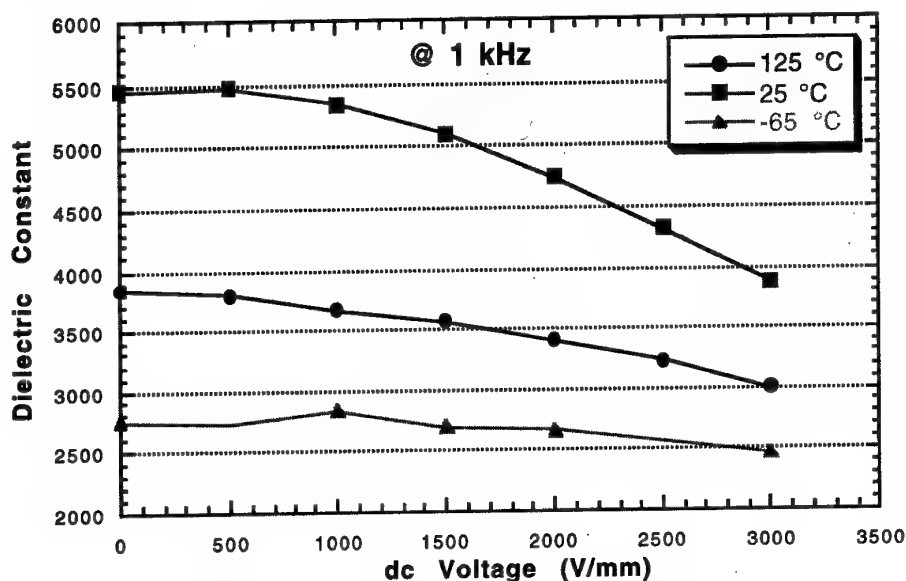

Figure 2. Dielectric constant as a function of bias voltage at three distinct test temperatures. The trends exhibited in this plot were similar for both intermediate temperatures and other measurement frequencies.

REFERENCES
1. T. Ericsen, A. Tucker, D. Hamilton, G. Campisi, C. Whitcomb, J. Borraccini, and W. Jacobsen, "Standardized Power Switch System Modules (Power Electronic Building Blocks)", Chap. 5.2, Proceedings of Power Systems World '97 (1997).
2. F.C. Lee, D. Borojevic, A. Elshabin-Riad, D.J. Nelson, T.A. Lipo, D.M. Divan, A.W. Kelley, and B.J. Baliga, "Power Electronics Building Block (PEBB)
Project Report," Virginia Polytechnical Institute & State University, pp. 3-35 to 3-69, (1996).
3. F. Kub, "Power Electronics S & T Proposal," private communication, (1998).
4. O. Furukawa, H. Kanai, and Y. Yamashita, "A New Relaxor Dielectric for High Voltage Multilayer Ceramic Capacitors with Large Capacitance," Jpn. J. Appl. Phys., [32] pp. 1708-11 (1993).

Dielectric Properties of MnO-Doped BaTiO$_3$ for Ni Electrode MLCCs

Takeshi Masuda, Akira Yamamoto and Takeshi Nomura
Materials Research Center, TDK Corporation, Narita-shi, Chiba286-8858, Japan
Fax: 81-476-37-1648, e-mail: masuken@mb1.tdk.co.jp

In this study, the relationship between the dielectric properties and the microstructure in MnO-doped BaTiO$_3$ for Ni electrode MLCCs has been investigated. In case of using BaTiO$_3$(Ba/Ti=1.005) and Ba$_{1.005}$(Ti$_{1.000}$Mn$_{0.005}$)O$_3$ as the starting materials, it was found that the dc bias property was different in spite of the same compositions. The domain walls were observed in both samples and the ratio of the domain areas was slightly different by transmission electron microscopy(TEM). Very few traces of MnO were observed in the domain for BaTiO$_3$(Ba/Ti=1.005). On the other hand, it was mainly found in the domain for the dielectric synthesized from Ba$_{1.005}$(Ti$_{1.000}$Mn$_{0.005}$)O$_3$ solid solution. It was confirmed that the difference of dielectric properties depended not only on the ratio of the domain areas but also on the microstructure of the domains.

1. INTRODUCTION

MnO-doped BaTiO$_3$ dielectrics are being studied for a long time. For example, Herbert showed the possibility of Base Metal Electrode(BME) capacitors in BaTiO$_3$ containing MnO.[1] Burn et al. reported that high permittivity and high insulation resistance dielectric in the system BaTiO$_3$-CaZrO$_3$ doped with MnO was obtained by sintering in reducing atmosphere.[2] MnO is one of the effective elements for BaTiO$_3$ for BME MLCCs based on the above facts. In this study, we investigated the relationship between the dielectric properties and the microstructure in MnO-doped BaTiO$_3$ for Ni electrode MLCCs.

2. EXPERIMENTAL PROCEDURE

The starting materials were BaTiO$_3$(Ba/Ti=1.005) and Ba$_{1.005}$(Ti$_{1.000}$Mn$_{0.005}$)O$_3$. These were highly pure powders, in which each average particle size was 0.3μm~0.5μm. BaTiO$_3$ was mixed with Y$_2$O$_3$, (Ba, Ca)SiO$_3$ and MnCO$_3$. On the other hand, Ba$_{1.005}$(Ti$_{1.000}$Mn$_{0.005}$)O$_3$ was mixed with Y$_2$O$_3$, (Ba, Ca)SiO$_3$. The total amount of MnO is equal in both mixtures.

Multilayer ceramic capacitors were formed by sheet method. Green sheets were made from the mixtures, the organic solvents and binders. The green sheets after printing Ni paste were laminated, pressed, and cut. These were fired at 1250℃ for 2 hrs in a reducing atmosphere. During firing, oxygen partial pressure was controlled between 10^{-8} and 10^{-13}MPa by adjusting the amounts of H$_2$ and H$_2$O in the N$_2$-H$_2$-H$_2$O gas mixtures, and end-terminated for electrical connections. Finally, the samples(A) and (B) which had 10μm dielectric thickness and 4 dielectric layers were obtained.

3. RESULTS AND DISCUSSION

Table I shows the compositions of the sample(A), (B).

Table I The compositions of samples

	Starting Materials	Additives[mol %]		
		MnCO$_3$	Y$_2$O$_3$	(Ba,Ca)SiO$_3$
Sample(A)	BaTiO$_3$(Ba/Ti=1.005)	0.005	0.5	3
Sample(B)	Ba$_{1.005}$(Ti$_{1.000}$Mn$_{0.005}$)O$_3$	0	0.5	3

Fig. 1 shows SEM photographs of polished and acid-etched samples. The average grain sizes were 0.4~0.5 μm in both samples. Fig. 2 shows the temperature dependence of capacitance change for both samples. The peaks of ferroelectric transition temperature(125℃) caused by pure BaTiO$_3$ were observed. However, the peak of the sample(B) is smaller than that of the sample(A). It can be said that the dielectric temperature characteristics of BaTiO$_3$-based ceramics were related to the ratio of the chemical inhomogeneity.[3]

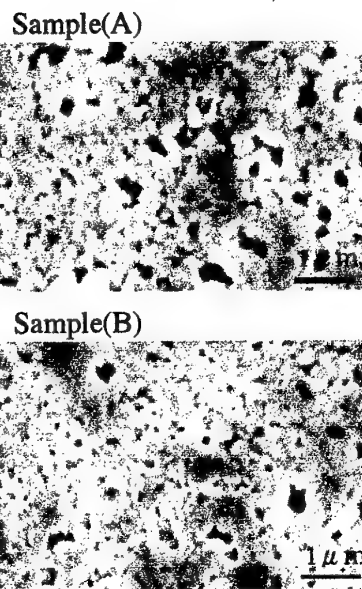### Sample(A)

Sample(B)

Fig.1 SEM photographs of sample(A) and (B)

For further investigation in this study, we observed the microstructure of these samples by TEM. Fig. 3 shows the TEM images of both samples. The domain walls were observed in both samples. The diameter of domain areas was about 0.25~0.3μm in the sample(A). On the other hand, it was 0.2~0.25μm in the sample(B). Since the

grain sizes are equal in both samples, the ratio of the domain in the grain for the sample(A) is slightly larger than that of the
sample(B). It was considered that the ratio of the domain areas was one of the factors for determining the temperature dependence of the change in capacitance. The D-E loops was measured next.
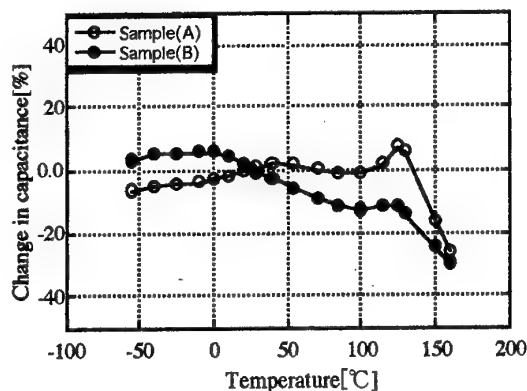
Fig. 4 shows the D-E loops of both samples. They were measured at 25℃ after heat treatment at 150℃ for 2 hrs. A large hysteresis loop was observed in the sample(A). On the other hand, the hysteresis loop of the sample(B) is not as large as that of the sample(A). It is said that the change of the slope in the hysteresis loop represents the dc bias property of the dielectrics. Therefore, the change in capacitance of sample(B) is smaller than that of the sample(A) under high dc field. Further investigation was required to explain dc bias property. It was expected that the microstructure of the domain was changed very much between the samples and EDS analysis was made to investigate the grain compositions in detail. According to the results, although there were equal amounts of additives in both samples, it was found that the microstructure was different. Therefore, very little MnO was observed in the domain for the sample(A). On the other hand, it was found satisfactorily in the domain of the sample(B), Since the starting material was $Ba_{1.005}(Ti_{1.000}Mn_{0.005})O_3$ solid solution for sample(B), it is natural that MnO existed in the domain area. It is assumed that the difference of dielectric properties in both samples depends not only on the ratio of the domain areas but also on the microstructure of the domains.

Fig.2 Temperature dependence of the change in capacitance of sample(A) and (B)

Sample(A)
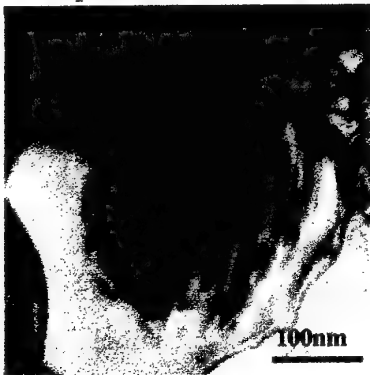
Sample(B)

Fig.3 TEM images of Sample(A) and (B)
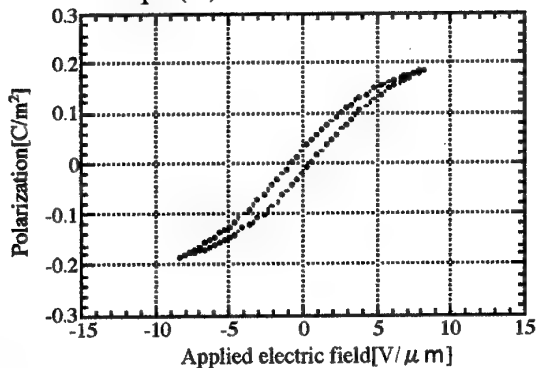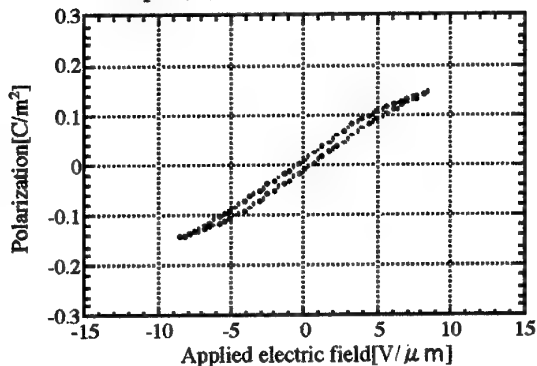
Sample(A)

Sample(B)

Fig.4 D-E loops of sample(A) and (B)

4. CONCLUSIONS

(1)In case of using $BaTiO_3(Ba/Ti=1.005)$ and $Ba_{1.005}(Ti_{1.000}Mn_{0.005})O_3$ as the starting materials, it was found that the dielectric properties were different, in spite of the same compositions.

(2)The domain walls were observed in both samples using TEM. MnO was mainly found in the domain for the dielectric synthesized from $Ba_{1.005}(Ti_{1.000}Mn_{0.005})O_3$ solid solution.

(3)It is confirmed that the difference of dielectric properties depends not only on the ratio of the domain areas but also on the microstructure of the domain.

5. REFERENCES

1) J. M. Herbert, Trans. Brit. Ceram. Soc., 62, 645-658 (1963)
2) I. Burn and G. H. Maher, J. Mater. Sci., 10, 633-640 (1975)
3) Y. Park and Y. Kim, J. Mater. Res., 10, 2770-2776 (1995)

Highly Accelerated Life Testing (HALT) of K-4500 Low Fired X7R Dielectric

By
Galeb H. Maher
MRA Laboratories
North Adams, MA U.S.A.

Abstract

Highly accelerated life test was performed on an 0805 – 100 nF X7R multilayer chips with 12 microns active layer thickness. The material is a low fired commercial product (SF-422) produced by MRA Laboratories, with a dielectric constant of about 4500.

The test conditions consisted of 125, 140, 155, and 175°C, and voltages ranging between 250 and 600 volts. The preliminary data showed a temperature dependence of an activation energy of 1.21 electron volt, nearly similar to that reported by other researchers on an X7R – BaTiO$_3$ system. However, the voltage dependence of acceleration factor (n) was found to be in the range of 5.4 to 7.1, almost twice as large as those reported in the literature. The experimental data showed a good fit with the Weibull statistical distribution. These observations suggest that this dielectric should be useful for high voltage and high temperature applications.

For this type of MLC chip, tested at twice rated voltage (100V, 125°C), the mean life time was predicted to be in excess of one million hours.

INTRODUCTION

We recently reported[1] on the physical and electrical properties of a high K (4500), low fired, barium titanate base X7R dielectric. This material is commercialized as product SF-422.

The shift in market demands for higher voltage (>200V) and higher temperature (>125°C) X7R applications have prompted us to examine the intrinsic capability of this dielectric for these applications. As a first phase of this study, we performed a highly accelerated life testing (HALT) in the temperature range of 125 to 175°C and voltage range of 250 to 600 volts on 0805-100nF chips with fired layer thickness of about 12 microns.

Accordingly, the objective of this paper is to report the HALT results on this dielectric.

Prokopowicz and Vaskas were the first to use an empirical relationship to predict the mean time to failure of multilayer ceramic capacitor, based on accelerated life testing at higher voltage and temperature.

$$\frac{t_1}{t_2} = \left(\frac{V_2}{V_1}\right)^n \exp\frac{E_a}{K}\left[\frac{1}{T_1} - \frac{1}{T_2}\right] \qquad (1)$$

Where:
t_1 = the mean time to failure at V_1 and T_1
t_2 = the mean time to failure at V_1 and T_2
V_1, V_2 = test voltages of the MLC, in Volts
T_1, T_2 = test temperatures of the MLC in °K
n = voltage stress exponent

E_a = activation energy (electron-volt)
K = Boltzman constant = 0.86×10^{-4} ev/°K

Based on the results observed by many researchers, this equation appeared to fairly predict the life expectancy of the capacitor and is widely used in the industry to assess the properties of the MLC capacitors.

For BaTiO$_3$ based MLC chips, Prokopowicz[2] reported a value of 2.7 for n and 0.9 ev for activation energy E_a.

Other researchers have reported slightly different values. The Table I below summarizes their findings.

Table I

Dielectric System	n	E_a (ev)	Reference
BaTiO$_3$-X7R	2.7	0.9	Prokopowicz (2)
BaTiO$_3$-X7R, Z5U	3.0	1.0	Munkon (3)
BaTiO$_3$-Z5U	2.46	1.19	Munford (4)
High K	2.5	1.0	Kurtz (5)
BaTiO$_3$-X7R	3.0	1.15	Coefer (6)
Y-doped BaTiO$_3$ with Ni electrode	3.0	1.4	Sano (7)
BaTiO$_3$-Y5V with Ni electrode	3.6	1.2	Pan and Rawal (8)
PMN	5.5 to 5.9	1.1 to 1.2	Pan and Rawal (8)

The Values generally used in the industries are: n=3 and E_a=1.1 ev.

During our research, we were surprised to find that the voltage acceleration exponent n, was greater than 5, however the average activation energy E_a was 1.21 ev and it is within the reported range shown in Table I.

EXPERIMENTAL SAMPLE

MLC capacitors of 0805 size with 30 layers of about 12 microns fired thickness were manufactured by the "wet" deposition process in our laboratories. The internal electrode was 70 Ag/30 Pd composition. The sample used for this study was taken from a single firing representing about 20,000 chips. After silver termination, the chips were measured for capacitance and dissipation factor, and all showed 100 nF ± 5%. No other testing was done prior to the HALT study. The pertinent physical and electrical properties of this sample are shown in Table II. The temperature coefficient of capacitance (TCC) and SEM image of a polished cross section are shown in figures 1 and 2, respectively.

Table II

- Sintering Temperature: 1130°C/3 hour
- Fired Density Ceramic only 5.85 g/cm^3
                                (97.5% of theoretical)
- Size: 0805 (2.0 x 1.25mm)
- Number of Layers: 30
- Fired Layer Thickness: 12 microns
- Average Capacitance at 1 KHz, 1 Vrms, 24 hours: 101 nF
- Average Dissipation Factor: 1.8%
- Calculated Dielectric Constant "K": 4600

HALT SETUP

A test fixture was assembled to accommodate 24 individual chips held in place by a spring loaded strip. The temperature chamber is a Blue-M oven Model OV-490A-1. The test temperature was held to ± 2°C from the set value. A 1000 Ω resistor and a relay were connected in series with each capacitor. The leakage current of each capacitor was monitored during the test. The test circuit was interphased with a PC which recorded the exact time of failure on each chip. When the leakage current exceeded 10^{-5} ampere, the relay opened up, thus removing the failure from the test and the time was recorded by the PC. The power supply is a KepCo Model 2000M where the voltage was held to ±1 volt from the set value.

TEST RESULTS

Although many researchers have used lognormal and Weilbull statistics to analyze the HALT data, in this study we used the Weilbull to determine the mean time to failure at 63% failure level of the test samples. Table III below shows the different test conditions that were used. 22 chips were tested at each condition until more than 90% of the sample had failed.

Table III
Life Test Conditions

Temperature °C	125	140	155	175
Voltages (Volt)	500	450	350	250
	550	500	400	300
	600	550	450	350

Figures 3, 4, 5 and 6 show the Weibull plot curves for 175, 155, 140 and 125°C for three different voltages, respectively. The early failures (below 30%) were considered to be caused by manufacturing defects such as thin spots in the active layers. The mean time to failure at 63% failure level for each test condition was determined from the graphs with the help of a MathCad program and curve fit linear regression statistic.

Using equation (1), the voltage acceleration factor n, and the activation energy E_a were determined for the various test conditions as shown in Figures 7 and 8, respectively.

It is interesting to note that a higher n (>6) was observed for test temperatures at 155 and 175, while for 125 and 140°C conditions, n was between 5.4 and 5.7.

Similarly the activation energy of failures was higher (E_a = 1.35 ev), for higher stress voltage 550V than for 300V, with an E_a = 1.1 ev.

PREDICTED VERSUS ACTUAL TIME TO FAILURE

Using an average voltage stress, n = 6.17, and an average activation energy, E_a = 1.21 ev, the predicted time to failure at 63% failure level was compared to the actual time observed in this study. The time to failure, t_2 at T_2 = 175°C, and V_2 = 350, were used to generate the data shown in Table IV.

As can be seen from the results, the predicted TTF at 125 and 140°C are somewhat lower than the actual values while for 155 and 175°C, the actual TTF values, are slightly lower than the predicted one. These differences can, perhaps, be explained by slight variation in test temperature.

Assuming we can further predict the TTF of these chips at 100V and 125°C, which corresponds to twice rated voltage, the life time will be greater than 10^6 hours (114 years).

Table IV
Examples of Time to Fail (TTF) Predictions
Based on the data for 175°C, 350 Volt case:
n = 6.17 (Average), Activation energy = 1.21 ev. (Average)
P = predicted TTF, A=actual TTF (at 63% Failed)

Oven temperature has a strong effect on the predictions. For example, the 125°C, 550 volt

case would be 133 hours at 123°, and 93 hours at 127°, instead of 111 hours at 125°

Predicted TTF vs Actual TTF (Hours)								
Temp	125		140		155		175	
Volts	P	A	P	A	P	A	P	A
50	$3*10^8$							
100	$4*10^6$							
250							279	299
300					393	365	91	86
350					152	156	xxx	35
400					67	45		
450			106	148				
500	200	270	55	74				
550	111	185	31	45				
600	65	90						

ULTIMATE DIELECTRIC BREAKDOWN VOLTAGE

To gain further insight into the capability of this dielectric, we have also performed a voltage breakdown analysis on a 22 chip size sample at 25, 125, 140, 155 and 175°C. The HALT fixture was used for this test. The voltage was raised slowly (about one minute) on each chip, until failure (relay opened). The failures distribution are shown in Table V.

Table V
Ultimate Dielectric Breakdown at Different Temperatures

Temperature °C	25	125	140	155	175
Minimum Voltage (Volts)	735	603	855	782	555
Maximum Voltage (Volts)	1120	990	1074	1140	1137
Average Voltage (Volts)	939	857	980	965	989

It is interesting to note that the ultimate dielectric breakdown remained relatively high even to 175°C. Further work will be performed with increase in temperature to 300°C.

SUMMARY
- A HALT analysis was performed on 0805, 100 nF chips, of a low fired K-4500 X7R dielectric, between 125 and 175°C, and voltage stress ranging from 250 to 600 volts, on 12 microns layer thickness.
- The voltage acceleration exponent, n, ranged between 5.4 to 7.1, while the activation energy, E_a, ranged between 1.1 and 1.35 electron-volts.
- The insulation resistance on test was monitored and remained relatively high $>10^8$ ohms and constant until breakdown (thermal runaway).
- The ultimate dielectric breakdown voltage remained relatively high, >75V/micron even to 175°C.
- Using the time to failure value generated at 175°C and 350V, and averages n = 6.17, and E_a = 1.21 ev, the predicted life time was in close agreement with actual values at the lower test temperatures and higher voltage.

- Assuming that the average n and E_a generated in this study to be valid, the predicted life time of the 0805, 100 nF chip will be:
at 100V, 125°C : 4×10^6 hours
and at 50 V, 125°C: 3×10^8 hours

REFERENCES:
1. Maher, G.M., et al., "Recent Developments in Low Fired X7R Dielectrics" Ceramic Transactions, Vol. 97, P17, 1999.
2. Prokopowicz, T., et al., "Research and Development Intrinsic Reliability, Subminiature Ceramic Capacitors" Final Report ECOM-9075-F, NTIS AO-864068, 69.
3. Munikoti, R., "Highly Accelerated Life Testing (HALT) for Multilayer Ceramic Capacitor Qualification" IEEE Transactions on Components, Hybrids, and Manufacturing Technology, Vol. 11, No.4, 1988.
4. Minford, W., "Accelerated Life Testing and Reliability of High K Multilayer Ceramic Capacitors". IEEE Transaction and Components, Hybrids, and Manufacturing Technology, Vol. CHMT-5, No.3, 1982.
5. Kurtz, S., et al., "Infant Mortality, Freaks and Wear Out:.." Proceeding of the Center for Dielectric Studies Symposium on Improvement of Multilayer Capacitor Reliability". Penn State University 1989.
6. Confer, R., et al., "Use of Highly Accelerated Life Test (HALT) to Determine Reliability of Multilayer Ceramic Capacitors". Proceeding of Electronic Component conference 1991.
7. Sato, S., et al., "Effect of Y-Doping on Resistance Degradation of Multilayer Ceramic Capacitors with Ni Electrode under Highly Accelerated Life Test". J.J. Appl. Phys., Vol. 36 (1997), pp 6016-6020.
8. Pak, H., et al., "Reliability Prediction of Multilayer Ceramic Capacitors Using an Improved Accelerated Life Testing and Weibull Analysis Technique". 1997 International Symposium on Microelectronic, pp 362-367.
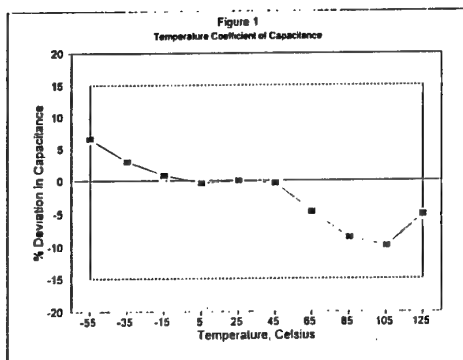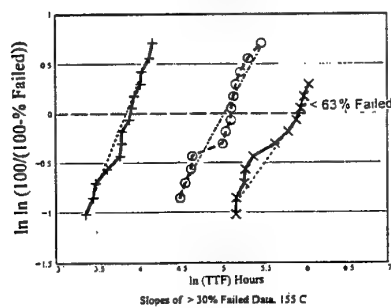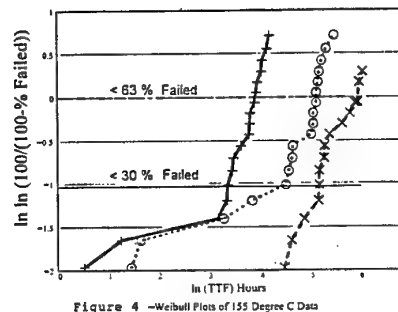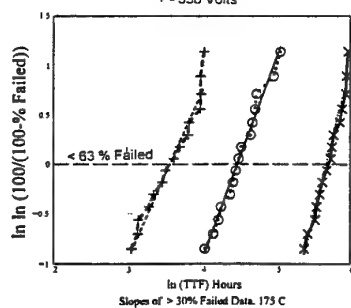
Figure 1
Temperature Coefficient of Capacitance

Figure 2
Polished Cross-section

⊢⊣ Bar Marker = 10 Micro Meters
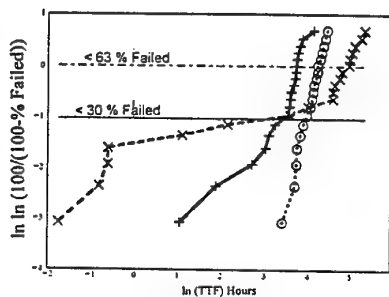

Figure 3 — Weibull Plots of 175 Degree C Data
X - 250 Volts
O - 300 Volts
+ - 350 Volts

Figure 4 — Weibull Plots of 155 Degree C Data
X - 300 Volts
O - 350 Volts
+ - 400 Volts

Slopes of > 30% Failed Data. 175 C

Slopes of > 30% Failed Data. 155 C
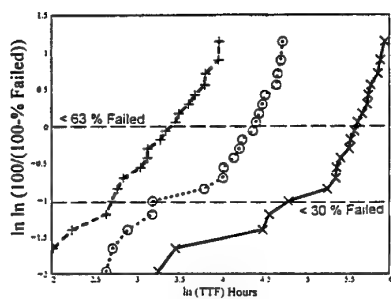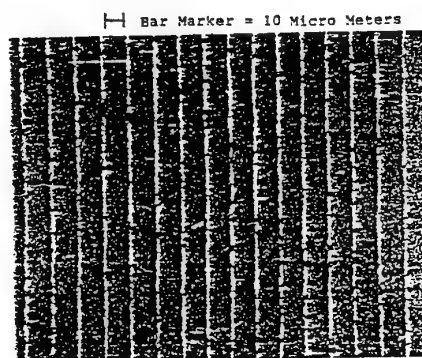
Figure 5 – Weibull Plots of 140 Degree C Data

X - 450 Volts
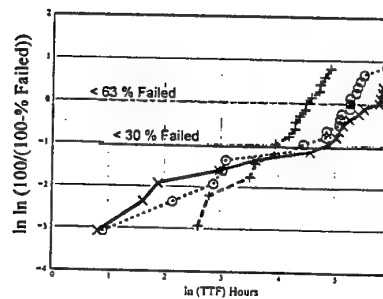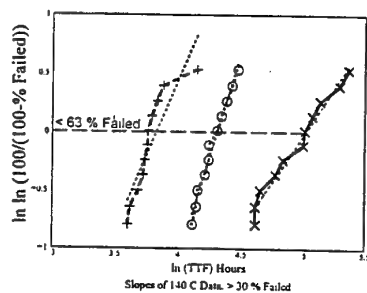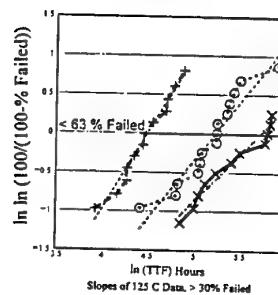O - 500 Volts
+ - 550 Volts

Figure 6 – Weibull Plots of 125 Degree C Data

X - 500 Volts
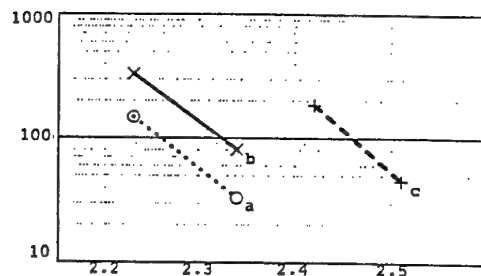O - 550 Volts
+ - 600 Volts

Slopes of 140 C Data. > 30 % Failed

Slopes of 125 C Data. > 30% Failed

Figure 7 - Voltage Acceleration Factor, n
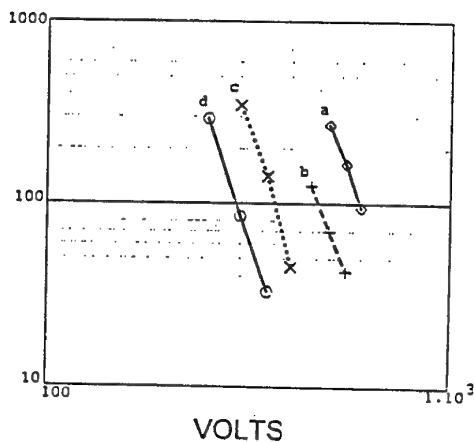
Figure 8 - ACTIVATION ENERGY, E_a

$1/T_i$ per degree K * 10^3

O - 300 Volts, 1.1 ev a

X - 350 Volts. 1.17 e; b

+ - 550 Volts, 1.35 ev c

VOLTS

125° C, n = -5.7 a
140° C, n = -5.4 b
155° C, n = -7.1 c
175° C, n = -6.5 d

— 361 —

Crystal Structure and Dielectric Properties of Perovskite Oxides A(Sc$_{1/2}$M$_{1/2}$)O$_3$ (A=Ca,Sr, M=Nb,Ta)

Ayuko Ozeki, Yue Jin Shan, Tetsuro Nakamura and Mitsuru Itoh*
Department of Applied Chemistry, Faculty of Engineering, Utsunomiya University,
7-1-2 Yoto, Utsunomiya 321 - 8585, Japan
Fax: 81-28-689-6009, e-mail: shan@cc.utsunomiya-u.ac.jp
*Materials and Structure Laboratory, Tokyo Institute of Technology 4259 Nagatsuta, Yokohama 226 - 8503, Japan
Fax: 81-45-924-5354, e-mail: itoh1@rlem.titech.ac.jp

Novel perovskite compounds Ca(Sc$_{1/2}$Nb$_{1/2}$)O$_3$, Ca(Sc$_{1/2}$Ta$_{1/2}$)O$_3$ and Sr(Sc$_{1/2}$Ta$_{1/2}$)O$_3$, together with the known Sr(Sc$_{1/2}$Nb$_{1/2}$)O$_3$ were obtained by high temperature synthesis in air. Their crystal structures were determined by X-ray powder diffraction analyses, combined with Rietveld refinements. The dielectric properties of sintered samples whose pore fractions are less than 5% were measured by LCZ meter. Crystal systems of both compounds were monoclinic. Ca-compounds could be refined by space group P2/n(No.14-2), while Sr-compounds could be refined by space group C2/c(No.15-1). Values of relative dielectric constants of these compounds are included within the range $\varepsilon = 20 \sim 40$, and increase gradually with an increasing temperature. These compounds show a low dielectric loss (tan$\delta = 10^{-4}$), and a small frequency dependence.

1. INTRODUCTION

The compounds having the general formula A(Sc$_{1/2}$M$_{1/2}$)O$_3$ (A = Sr, Ba, Pb, M = Nb, Ta), have been reported from the latter half of the 1950's to 1970's. According to those reports Pb(Sc$_{1/2}$M$_{1/2}$)O$_3$ (M = Nb, Ta) have tetragonal perovskite structures with ferroelectric properties[1], Ba(Sc$_{1/2}$M$_{1/2}$)O$_3$ (M = Nb, Ta) have cubic perovskite structures with paraelectric properties having rather small dielectric constants [2, 3]. Sr(Sc$_{1/2}$Nb$_{1/2}$)O$_3$ was also reported to have a cubic perovskite structure[4], however, the Sr(Sc$_{1/2}$Ta$_{1/2}$)O$_3$ compound is not known. Dielectric properties of Sr-compounds are not found. Moreover, also no reports are found for Ca(Sc$_{1/2}$M$_{1/2}$)O$_3$ (M = Nb, Ta) compounds.

In recent years, our group focuses on the synthesis and characterization of the new perovskite oxides, especially for dielectric materials. We are also interested in the relationships between the electric characters and the detailed crystal structural deformations caused by ordered B-site ions and smaller A-site ion. The system of A(Sc$_{1/2}$M$_{1/2}$)O$_3$ (A = Ca, Sr, M = Nb, Ta) is just suited for our aims. Therefore, we tried to synthesize new compounds, Ca(Sc$_{1/2}$M$_{1/2}$)O$_3$ (M = Nb, Ta), and Sr(Sc$_{1/2}$M$_{1/2}$)O$_3$ (M = Nb, Ta) to analyze their crystal structures and characterize their dielectric properties, then investigate their interrelationships. Furthermore, these results will be used to compare and discuss with those of the known Pb-compounds and Ba-compounds.

2. EXPERIMENTAL

A(Sc$_{1/2}$M$_{1/2}$)O$_3$ (A = Ca, Sr, M = Nb, Ta) samples were synthesized by the conventional solid state reaction method. CaCO$_3$(4N), SrCO$_3$(3N), Sc$_2$O$_3$(98.5), Nb$_2$O$_5$(3N), and Ta$_2$O$_5$(99.95) were used as the starting materials. The starting materials were mixed in their stoichiometric radio in an agate mortar. The mixed powder was pressed into a pellet with a dimension of 10 mm in diameter and 6 mm in thick at a pressure of 0.95 ton/cm^2. The pellets of Ca(Sc$_{1/2}$M$_{1/2}$)O$_3$ (M = Nb, Ta) were calcined at 1373 K for 10 hours, at 1523 K for 48 hours in air with intermediate pulverization and pelletization processes. The calcination process of

Sr(Sc$_{1/2}$M$_{1/2}$)O$_3$ (M = Nb, Ta) is similar to that of Ca(Sc$_{1/2}$M$_{1/2}$)O$_3$ (M = Nb, Ta). The process was carried out at 1373 K for 10 hours, and at 1723 K for 144 hours in air. The calcined pellets were pulverized, ground, pelletized, then sealed in a rubber tube with a depression and pressed isostatically at 1.8 ton/cm^2. The sinterings of Ca(Sc$_{1/2}$Nb$_{1/2}$)O$_3$ and Ca(Sc$_{1/2}$Ta$_{1/2}$)O$_3$ were carried out at 1673 K in air for 6 hours and 46 hours, respectively. The Sr(Sc$_{1/2}$M$_{1/2}$)O$_3$ (M = Nb, Ta) were sintered at 1973 K for 10 hours in air. The identification of the phases and the determination of the lattice parameters were carried out by powder X-ray diffraction analysis using CuK$_\alpha$ radiation by a Rigaku RINT-2100 diffractometer. The lattice parameters were determined using silicon powder (5N) as an internal standard. The crystal structures of the samples were analyzed using the Rietveld analysis program, RIETAN94. The data was collected with CuK$_\alpha$ radiation by accumulating counts for 5 seconds at 0.02 intervals in the range 2θ = 10$\sim$ 120° . The dielectric constants of the Ca-compounds and Sr-compounds were measured by a Hewlett Packard 4284A precision LCR meter from 12 to 300 K over the frequency range 10 Hz$\sim$1 MHz.

3. RESULT AND DISCUSSION

3.1 Synthesis of A(Sc$_{1/2}$M$_{1/2}$)O$_3$(A = Ca, Sr; M = Nb, Ta) by careful calcination

The titled compounds need fundamentally high temperature to react them in air. In the case of Sr-compounds, the final calcination temperature had to be set at 1723 K for getting a single phase compounds, in order to avoid the formation and stabilization of admixing oxides of Sr-Nb-O or Sr-Ta-O in the range of 1273$\sim$1473 K. For Ca-compounds, the calcination temperature of 1523 K was satisfied their reactions. In addition, it was found that the reaction temperature of the Nb-containing compounds is lower than that of the Ta-containing compounds. Through careful handling for keeping the reactivity of raw materials Sc$_2$O$_3$, the four compounds were synthesized as single phase perovskite structure with the above calcination temperature, although almost no sintering. Table I summarizes the

Table. I The details of synthesizing conditions of $A(Sc_{1/2}M_{1/2})O_3$(A=Ca,Sr, M=Nb,Ta)

Compounds	A = Ca, M = Nb	A = Ca, M = Ta	A = Sr, M = Nb	A = Sr, M = Ta
Calcining temperature /K	1523	1523	1723	1723
Calcining times / h	12×4	12×4	24×6	24×14
Sintering temperature /K	1873	1873	1973	1973
Sintering times / h	6	46	10	10
Degree of sintering (%)	95.9	97.0	76.1	68.9

detailed conditions of synthesis for $A(Sc_{1/2}M_{1/2})O_3$ (A = Ca, Sr; M = Nb, Ta).

3.2 Structure determination via X-ray diffraction analysis with Rietveld refinements

Figure 1 shows the powder X-ray diffraction patterns of $Ca(Sc_{1/2}M_{1/2})O_3$ (M = Nb, Ta). Both patterns resemble each other except for some difference in intensity radios. From the tendency of extinction in the diffraction lines and the presence of superlattice lines concerned with the rock-salt type ordering (1:1) of the Sc and M ions in the octahedral sites, these Ca-compounds were found to crystallize in the perovskite structure, whose possible space groups are P2/n(No.14-2), P2/c(No.13-5), C2/c(No.15-1), I2/m(No.12-3) etc. Rietverd refinements of the powder diffraction data of the Ca-compounds determined that the optimum space group is P2/n(No.14-2) with the reliability factors $R_{wp} \doteq$ 10%, S<4, R_I<4. Table II shows the results of Rietverd analysis, involving lattice parameters, coordinates of each ion and their thermal fluctuation parameters. It is found that the octahedral cations are almost ordered in 1:1 manner and the shifts in the coordinates of each ion are quite smaller for Nb-containing and Ta-containing compounds. This evidence of similarity is considered as Nb and Ta have the same ionic valence and the similar ionic radius. The patterns of Rietveld analysis for $Ca(Sc_{1/2}Ta_{1/2})O_3$ are shown in Fig. 2.
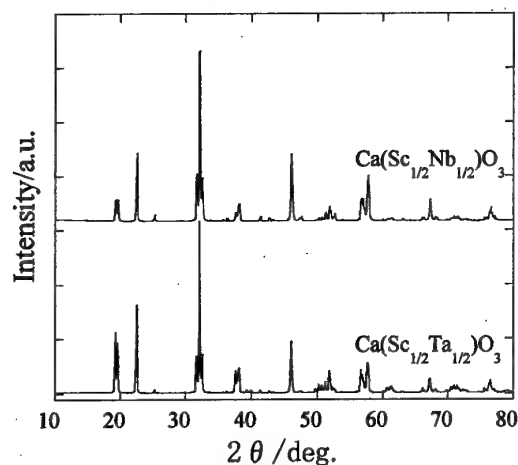

Fig.1 Powder X-ray diffraction patterns for $Ca(Sc_{1/2}M_{1/2})O_3$(M=Nb,Ta)
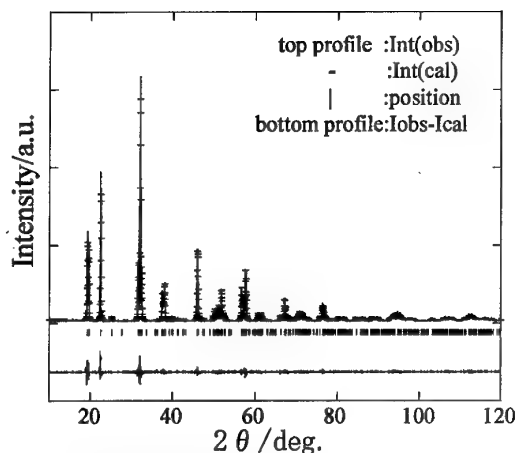
Fig.2 profile fit with space group P12/n1 to the powder X-ray diffraction data of $Ca(Sc_{1/2}Ta_{1/2})O_3$

Table. II Results of refinements for $Ca(Sc_{1/2}M_{1/2})O_3$ (M=Nb,Ta) at room temperature with space group P 1 2/n 1

	$Ca(Sc_{1/2}Nb_{1/2})O_3$	$Ca(Sc_{1/2}Ta_{1/2})O_3$
Space group	P12/n1	P12/n1
a /Å	5.5028(1)	5.50521(8)
b /Å	5.6473(1)	5.64610(8)
c /Å	7.8650(1)	7.8679(1)
β /deg.	90.009(4)	89.989(4)
Ca:x	0.018(1)	-0.011(3)
Ca:y	-0.0472(5)	0.0466(8)
Ca:z	0.2495(7)	0.2492(7)
B/Å²	0.47(8)	0.6(1)
Sc:g	0.952(1)	0.974(4)
Sc:x	0.0	0.0
Sc:y	0.5	0.5
Sc:z	0.0	0.0
B/Å²	0.2(1)	0.3(1)
M:g	0.952(1)	0.974(4)
M:x	0.5	0.5
M:y	0.0	0.0
M:z	0.0	0.0
B/Å²	0.27(6)	0.22(4)
O1:x	0.283(2)	0.213(3)
O1:y	0.268(2)	0.193(3)
O1:z	-0.051(3)	-0.047(4)
B/Å²	0.1(5)	0.29
O2:x	0.311(3)	0.205(3)
O2:y	0.295(3)	0.218(3)
O2:z	0.550(3)	0.555(4)
B/Å²	1.9(6)	0.31
O3:x	0.581(3)	0.406(3)
O3:y	0.026(2)	-0.029(3)
O3:z	0.242(3)	0.247(2)
B/Å²	3.0(5)	0.4(4)
Rwp	11.28	6.87
S	2.7828	2.5339
RI	3.34	1.31

$Sr(Sc_{1/2}Nb_{1/2})O_3$ was first synthesized by Penn. State University's McIlvried and McCarthy in 1972, and reported that it has a cubic perovskite structure and belongs to the space group Fm3m(No.225)[6]. Figure 3 shows the XRD patterns of $Sr(Sc_{1/2}M_{1/2})O_3$(M = Nb, Ta) synthesized by the present authors. The XRD patterns seemed as if they are cubic at the first glance, however,

Fig.3 Powder X-ray diffraction patterns for
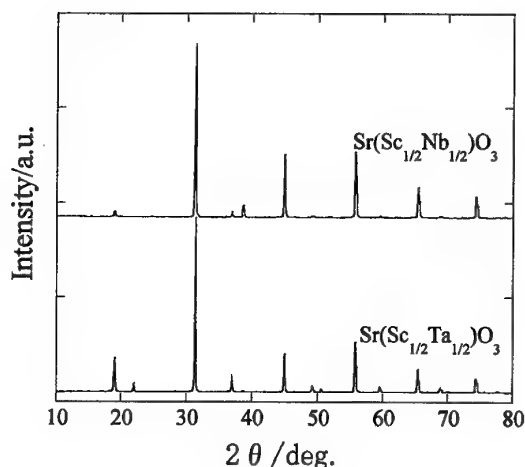Sr(Sc$_{1/2}$M$_{1/2}$)O$_3$(M=Nb,Ta)

Table. III Results of refinements for Sr(Sc$_{1/2}$M$_{1/2}$)O$_3$ (M=Nb,Ta)

	Sr(Sc$_{1/2}$Nb$_{1/2}$)O$_3$	Sr(Sc$_{1/2}$Ta$_{1/2}$)O$_3$
Space group	C 2/c	C 2/c
a /Å	8.0616(2)	8.0603(2)
b /Å	8.0504(1)	8.0528(1)
c /Å	8.0572(2)	8.0645(2)
β /deg.	90.065(1)	90.067(1)
Sr1:x	0.0	0.0
Sr1:y	-0.010(2)	-0.013(2)
Sr1:z	0.25	0.25
B/Å²	0.7(3)	0.29
Sr2:x	0.0	0.0
Sr2:y	0.493(2)	0.496(2)
Sr2:z	0.25	0.25
B/Å²	0.8(3)	0.34
Sc:g	0.85(1)	0.904(4)
Sc:x	0.25	0.25
Sc:y	0.25	0.25
Sc:z	0.0	0.0
B/Å²	0.2(1)	0.76
M:g	0.85(1)	0.904(4)
M:x	0.25	0.25
M:y	0.25	0.25
M:z	0.5	0.5
B/Å²	0.2(1)	0.032
O1:x	0.228(7)	0.269(7)
O1:y	-0.014(8)	-0.010(4)
O1:z	0.002	-0.007
B/Å²	2(1)	-2.0(6)
O2:x	-0.005(7)	0.025(8)
O2:y	0.273(7)	0.221(7)
O2:z	-0.036(9)	0.050(8)
B/Å²	1(1)	1(1)
O3:x	0.218(7)	0.308(6)
O3:y	0.252(2)	0.249(3)
O3:z	0.249(8)	0.248(5)
B/Å²	1(1)	-2.7(7)
Rwp	12.16	9.19
S	3.4662	3.4177
Rl	2.76	3.31

we could find several weak diffraction lines with the intensity radio less than 1%. Therefore, it is expected

that the symmetry of the Sr-compounds is lower than the cubic one. Possible space group were limited to Pn3(No.201-1), P4$_2$/nnm(No.134-1), P4$_2$/n(No.86-2) and C2/c(No.15-1) via examinations of weak superlattice lines. Rietveld refinements of the powder diffraction data of the Sr-compounds determined that the optimum space group is monoclinic C2/c(No.15-1) with at room temperature with space group C 2/c the reliability factors R$_{wp}$≒10%, S<4, R$_l$<4. The detailed results of Rietveld analysis and patterns for Sr(Sc$_{1/2}$Nb$_{1/2}$)O$_3$ are summarized in Table III and shown in Fig. 4, respectively. In this refinements, we found the 1:1 cation ordering in the octahedral sites for Sr-compounds is not complete but contains some disorder more than 10%. We do not think this disorder is the cause of the slight monoclinic lattice distortion. If the 1:1 ordering is completed, the monoclinic distortion in Sr-compounds will be much emphasized.
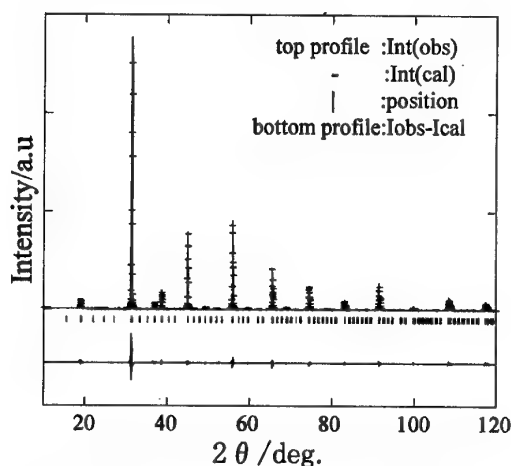

Fig.4 Profile fit with space group C2/c to the powder X-ray diffraction data for Sr(Sc$_{1/2}$Nb$_{1/2}$)O$_3$

3.3 Dielectric properties of sintered A(Sc$_{1/2}$M$_{1/2}$)O$_3$(A = Ca, Sr, M = Nb, Ta)

In order to obtain the reliable dielectric data for the titled compounds, final sintering were carried out at 1873 K for Ca-compounds and at 1973 K for Sr-compounds after isostatic pressings at 1.8 ton/cm². Higher density materials with porosity less than 5% were obtained by prolonged sintering. Figure 5 shows the temperature dependence of the dielectric properties for Ca-compounds and Sr-compounds. Dielectric constants of these compounds show very small temperature dependence with positive coefficient and a small frequency dependence. ε of every compounds increases gradually as the temperature increases from 12 K up to 300 K. The order of the absolute values of ε is ε[Ca(Sc$_{1/2}$Ta$_{1/2}$)O$_3$] < ε[Ca(Sc$_{1/2}$Nb$_{1/2}$)O$_3$] < ε[Sr(Sc$_{1/2}$Nb$_{1/2}$)O$_3$]. Thus, the synthesized Ca-compounds and Sr-compounds with the 1:1 cation ordering in the octahedral sites show relatively small dielectric constant ranging ε = 20 ~ 40, compared to those of perovskite titanates, with a dielectric loss(tan δ ~10⁻⁴) and a small frequency dependence.
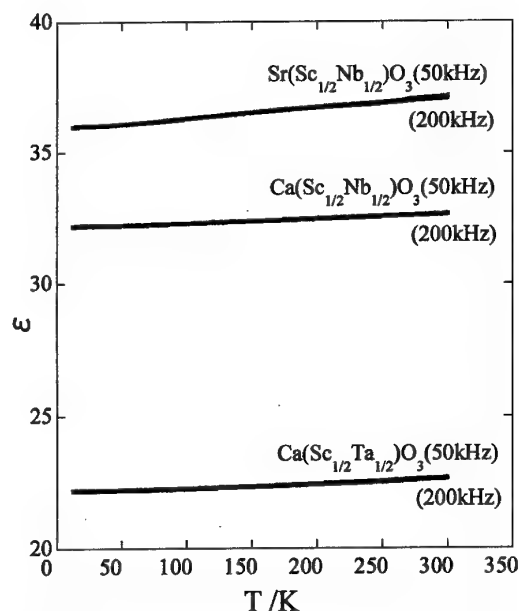
In Table IV compares the tolerance factor, the

Fig.5 Temperature dependence of the relative dielectric constants of $A(Sc_{1/2}M_{1/2})O_3$ (A=Ca,Sr, M=Nb,Ta)

Table.IV The comparison of $A(Sc_{1/2}Nb_{1/2})O_3$ (A=Ca,Sr,Ba,Pb, M=Nb,Ta)

Compounds	Tolerance factor	$V^{1/3}$	Crystal system
$Ba(Sc_{1/2}Nb_{1/2})O_3$	1.0169	4.121	Cubic[7]
$Ba(Sc_{1/2}Ta_{1/2})O_3$	1.0169	4.118	Cubic[8]
$Pb(Sc_{1/2}Nb_{1/2})O_3$	0.9764	4.073	Tetragonal
$Pb(Sc_{1/2}Ta_{1/2})O_3$	0.9764	4.076	Trigonal[5]
$Sr(Sc_{1/2}Nb_{1/2})O_3$	0.9595	4.025	Monoclimic
$Sr(Sc_{1/2}Ta_{1/2})O_3$	0.9595	4.03	Monoclimic
$Ca(Sc_{1/2}Nb_{1/2})O_3$	0.9257	3.942	Monoclimic
$Ca(Sc_{1/2}Ta_{1/2})O_3$	0.9257	3.948	Monoclimic

Compounds	Space group	Dielectric constant (293K)	Ferro electrics Tc(℃)
$Ba(Sc_{1/2}Nb_{1/2})O_3$	Pm3m[7]	27[4]	—
$Ba(Sc_{1/2}Ta_{1/2})O_3$	Fm3m[8]	8[4]	—
$Pb(Sc_{1/2}Nb_{1/2})O_3$	—	730[1]	90[1]
$Pb(Sc_{1/2}Ta_{1/2})O_3$	R3m[5]	1225[1]	26[1]
$Sr(Sc_{1/2}Nb_{1/2})O_3$	C2/n	37	—
$Sr(Sc_{1/2}Ta_{1/2})O_3$	C2/n	—	—
$Ca(Sc_{1/2}Nb_{1/2})O_3$	P1 2/n 1	32	—
$Ca(Sc_{1/2}Ta_{1/2})O_3$	P1 2/n 1	22	—

perovskite unit cell size, crystal system, space group, and dielectric properties of the $A(Sc_{1/2}M_{1/2})O_3$ (M = Nb, Ta) compounds including those A = Pb and Ba. It is noted for $A(Sc_{1/2}M_{1/2})O_3$ (M = Nb, Ta) compounds in Table IV that the smaller the unit cell size is, the greater the lattice distortion is. Such an evidence has been interpreted by the order of tolerance factors t(Ca-compounds) < t(Sr-compounds) < t(Pb-compounds) < t(Ba-compounds) relating to the order of A-ion radius r(Ca) < r(Sr) < r(Pb) < r(Ba) in the high temperature range.

In the low temperature range, however, Pb-compounds show marked lattice deformations caused by ferroelectric phase transitions. Those ferroelectric Pb-compounds are reported to have no 1:1 ordering between the Sc and M ions in the octahedral sites. On the other hand, the Ca-compounds, Sr-compounds and Ba-compounds involve the 1:1 ordering between the Sc and M ions, being accompanied by the center of symmetry. This evidence is consistent that those compounds are non-ferroelectric. The 1:1 cation ordering (rock-salt like ordering) in the octahedral sites are supposed to be harmful for the displacive type ferroelectricity. As for the cause of displacive type ferroelectricity in the perovskite ABO_3, it is still obscure. We are proposing that the driving factor of the ferroelectricity appearance in ABO_3 is the mass-inequality in the TO-modes. The electronic configuration of $6S^2$ for A ion (Pb^{2+} or Bi^{3+}) is supposed as a helpful factor, however, the 1:1 ordering of B ions in the octahedral sites is a harmful factor for the ferroelectricity.

4. Acknowledgements

5. References

1) G.A. Smolenskii, V.A. Isupov, and A.I. Agranovskaya, *Sov. Phys. Solid State*, **1**, 150-151 (1959).
2) L. Brixner, *J. Irong. Nucl. Chem.*, **15**, 352-355 (1960).
3) F.S. Galasso, G.K. Layden and D.E. Flinchbaugh, *J. Chem. Phys.*, **44**, 2703-2707 (1966).
4) A.I. Agranovskaya, *Bulletin of Acad. Sciences of USSR physics Series*, **24**, 1271-1277 (1960).
5) Baba-Kishi, *K.Z, Appl. Crystallogr.*, **17**, 333-337 (1998).
6) JCPDS card, 24-1124
7) JCPDS card, 24-1032
8) JCPDS card, 19-134

The quality factor of the $Ba_{6-3x}R_{8+2x}Ti_{18}O_{54}$ (R = rare earth) solid solutions depended on the ionic size difference between Ba and R

Hitoshi Ohsato, Masaki Imaeda, Hideyasu Sakashita and Susumu Nishigaki[*]

Nagoya Institute of Technology Gokiso-cho, Showa-ku, Nagoya 466-5888, Japan
Fax: +81-52-735-5294, e-mail: ohsato@mse.nitech.ac.jp
[*]Daiken Chemical Co., Ltd., Joto-ku, Osaka 536-0011, Japan

The tungstenbronze-type like $Ba_{6-3x}R_{8+2x}Ti_{18}O_{54}$ (R = rare earth) solid solutions have performed excellent microwave dielectric properties. The solid solution with $x=2/3$ composition shows the highest quality factor $Q \cdot f$ in each R-solid solution series because of low internal strain based on the ordering of Ba and R. On the other hand, the $Q \cdot f$ values of each R-compound with $x=2/3$ in the $Ba_{6-3x}R_{8+2x}Ti_{18}O_{54}$ solid solutions increase according to the lanthanoid contraction. Sm-compound has better $Q \cdot f$ than La-compound. This crystal structure is maintained by the size difference of large cations such as Ba and R. We measured internal strain using the extended Scherrer's equation for X-ray diffraction pattern in order to confirm the relationship between the quality factor and internal strain. It was revealed that the crystal structure with large difference size between Ba and R shows excellent quality factor, as it has low internal strain.

1. INTRODUCTION

The tungstenbronze-type like $Ba_{6-3x}R_{8+2x}Ti_{18}O_{54}$ (R = rare earth) solid solutions as shown in Fig.1 and 2 have excellent microwave dielectric properties [1-3] for dielectric resonator applications used in the microwave telecommunication such as mobile telephone systems and satellite broadcasting [4,5]. These properties are: high quality factor ($Q \cdot f$) near 10000 GHz, high dielectric constant (ε_r) around 80 and low temperature factor of resonant frequency (τ_f) near 0 ppm/℃ [6,7].

The $Q \cdot f$ values changes non-linearly as a function of the composition x in the $Ba_{6-3x}R_{8+2x}Ti_{18}O_{54}$ formula, though ε_r and τ_f are linearly [7,8]. It is considered that the non-linearity comes from the site occupancy of large cations such as Ba and R ions. The solid solutions with $x=2/3$ compositions have the highest $Q \cdot f$ values as shown in Fig.3. The internal strain of the Sm-solid

solution series was estimated by extended Scherrer's equation to be lowest at $x=2/3$ composition as shown in Fig.4 [8]. In the $x=2/3$ composition, Sm ions and Ba ions are occupied separately in $A1$-sites with medium size and $A2$-sites with the largest size, respectively. In the range of $0 \leqq x < 2/3$, Ba ions in perovskite block produce internal strain and reduce the $Q \cdot f$.

The tungstenbronze-type like structure [9-13] has three types of large cation sites: the largest ones are the pentagonal sites ($A2$), the medium one are the rhombic sties ($A1$) in 2 by 2 perovskite blocks and finally the trigonal sites (C). The trigonal C-sites are empty in this case. We presented structural formulae instead of the $Ba_{6-3x}R_{8+2x}Ti_{18}O_{54}$ compositional formula, which discriminate cations occupying $A1$ and $A2$-sites. The fundamental unit cell of tungstenbronze-type structure has ten $A1$-sites and four $A2$-sites. The basic structural formula is $[(R,Ba,V)_{10}]_{A1}[(Ba,V)_4]_{A2}Ti_{18}O_{54}$. In the range of $0 \leq x \leq 2/3$, the formula is $[R_{8+2x}Ba_{2-3x}V_x]_{A1}$
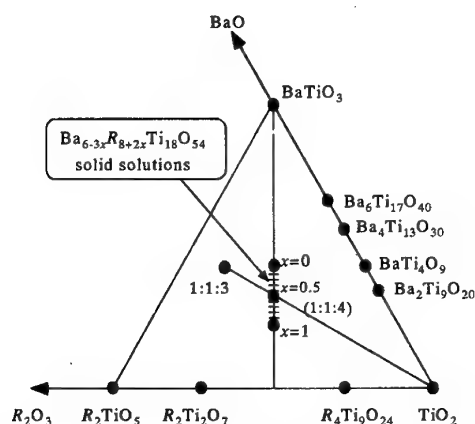
Fig.1: A part of the BaO-R_2O_3-TiO_2 ternary system.

2 × 2 perovskite block

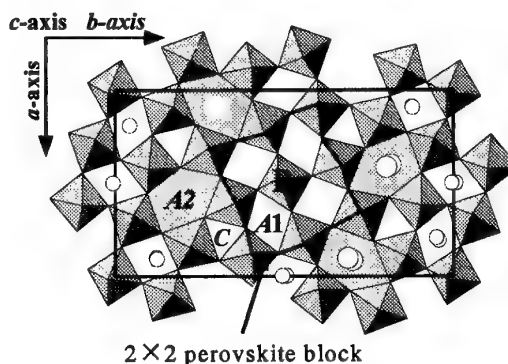Fig.2: Tungstenbronze-type like crystal structure of the $Ba_{6-3x}R_{8+2x}Ti_{18}O_{54}$ solid solutions, in which R and Ba ions occupy rhombic and pentagonal sites, respectively. $A1$: rhombic site, $A2$: pentagonal site and C: trigonal site
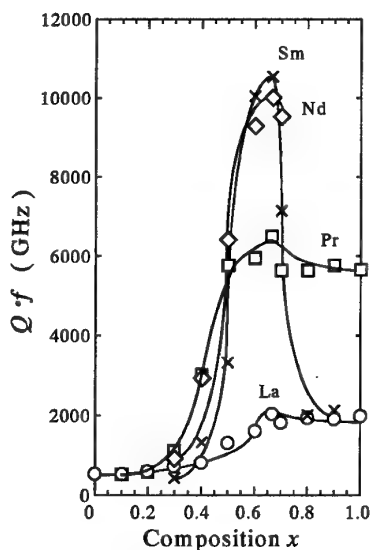
Fig.3: Quality factor of $Ba_{6-3x}R_{8+2x}Ti_{18}O_{54}$ solid solutions (R=La, Pr, Nd and Sm).

$[Ba_4]_{A2}Ti_{18}O_{54}$. Continuing the substitution, in the range of $2/3 \leq x \leq 1$, the formula is $[R_{9+1/3+2(x-2/3)}V_{2/3-2(x-2/3)}]_{A1}$ $[Ba_{4-3(x-2/3)}V_{3(x-2/3)}]_{A2}Ti_{18}O_{54}$. In the x=2/3 composition, the formula is $[R_{9+1/3}V_{2/3}]_{A1}[Ba_4]_{A2}Ti_{18}O_{54}$, in which R and Ba ions are occupied separately in A1-sites and A2-sites, respectively[14].

In this work, the dielectric properties of a series of specimens with x=2/3 in the each R-solid solutions system (R = La, Pr, Nd and Sm) are measured and compared with the ionic radii of rare earth. Moreover, the internal strains of the structure were obtained from full-width at half-maximum (FWHM) by fine X-ray diffraction patterns using synchrotron radiation, and the relationship between internal strain and dielectric properties is discussed.

2. EXPERIMENTAL PROCEDURE

We prepared sintered dielectric ceramics resonators with the desired composition for characterization. High purity (99.7%)$BaCO_3$, (99.9%)TiO_2, (99.9%)R_2O_3 (R = La, Nd and Sm) and Pr_5O_{11} powders were used as raw materials. The desired compositions for the resonators were as $Ba_{6-3x}R_{8+2x}Ti_{18}O_{54}$ (R = La, Pr, Nd and Sm). At first, both terminal compositions with x=0.0 and 1.0 of
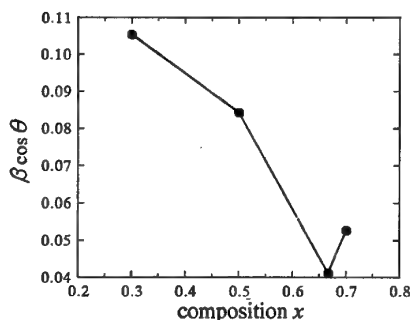
Fig.4: Internal strain of $Ba_{6-3x}Sm_{8+2x}Ti_{18}O_{54}$ solid solutions.
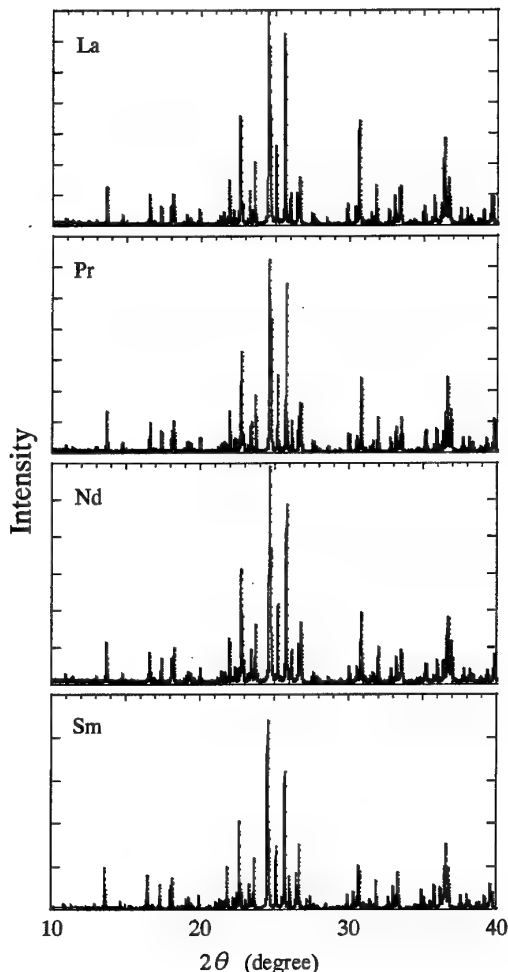
Fig.5: X-ray diffraction patterns of each R-compound with x=2/3. λ=1.21 Å for La-, Pr- and Nd-compound and λ=1.20 Å for Sm-compound.

each R-solid solutions series were prepared. Both mixtures were ground for 24h with ethanol using a ball mill, dried and calcined in air at 1000℃. The desired compositions prepared from these mixtures were ground again in ethanol and calcined in air at 1000℃ for 2h. The calcined powders added with organic binder were passed through a mesh and pressed into disks with 12mm in diameter and 6mm thick at a pressure of 98Mpa. The disks were sintered in air at 1460℃ for 2h.

The dielectric constants, unloaded quality factor (Q_u) and temperature coefficients of the resonant frequency (τ_f) between 20℃ and 80℃ were measured between a pair of parallel conducting Ag plates in the TE_{011} mode using the Hakki and Coleman method [15]. We selected the samples with optimum $Q \cdot f$ values for discussion.

X-ray diffraction powder patterns of the samples were obtained by the multiple-detector system (MDS) for rapid scanning of the entire powder pattern using synchrotron radiation at the BL-4B2 station in the "Photon Factory" of the National Laboratory for High Energy Physics in Tsukuba, Japan [16]. Wavelengths of 1.2 Å monochromated by a water-cooled double-crystal

Fig.6: Lattice parameters of each R-compound with x=2/3.

Si (111) were applied to each specimen. The MDS has five detector arms, which are attached radially at intervals of 25° on the 2θ axis of the goniometer. The step-scan technique in each scintillation counter with a flat Ge (111) plate crystal analyzer is performed at a step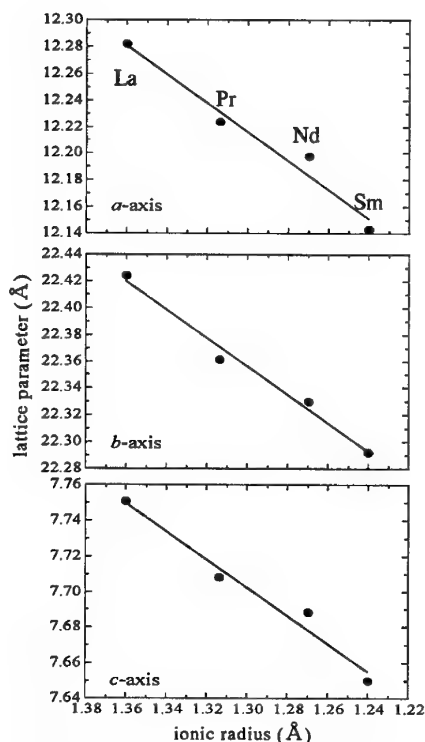 width of 0.005 in 2θ and fixed time of 5 sec. The lattice parameters of the solid solutions were determined using the whole-powder-pattern-decomposition method (WPPD) program [17] to refine the powder diffraction parameters.

The internal strain η is given as the slope of the drawing of the following equation in which $\beta \cos\theta$ is plotted as a function of $\sin\theta$.

$$\beta \cos\theta = \lambda/t + 2\,\eta \sin\theta \qquad (1)$$

Here β means FWHM, t: size of crystalline, λ: wave length of X-ray. The angle θ and β of the X-ray diffraction peaks are derived by using the computer program PRO-FIT for the individual profile fitting.

3. RESULT AND DISCUSSION

Fig.5 shows X-ray diffraction powder patterns of each R-compound (R = La, Pr, Nd and Sm) with the x=2/3 on the $Ba_{6-3x}R_{8+2x}Ti_{18}O_{54}$ solid solutions in the range of $10° < 2\theta < 40°$ using synchrotron radiation of which wavelength is 1.21Å or 1.20Å. Compared to using CuKα (1.5418 Å) filtered through Ni foil, all peaks shift to low angle. The diffraction patterns of each R-compound shift to high angle with decreasing of ionic radius of R but only that of Sm-compound used wavelength with 1.20Å shifts to low angle. This means that each sintered sample is a single phase of tungstenbronze-type like compound. Their lattice parameters refined by WPPD method are shown in Fig.6 as a function of ionic radii of R. According to the lanthanoid contraction, the lattice parameters of each R-compound are linearly decreased with larger scale than those of the $Ba_{6-3x}R_{8+2x}Ti_{18}O_{54}$ solid solutions series [3].

The dielectric properties of each R-compound with x=2/3 are shown in Fig.7. It should be noticed that the quality factors ($Q \cdot f$) increase according to the decreasing of the ionic radii of each R ion as described later. The $Q \cdot f$ values of Sm- and Nd-compound are excellent. The dielectric constants (ε_r) decrease linearly from 105 to 80 as a function of ionic radii, which are inversely proportional to the $Q \cdot f$ values as generally observed in dielectric properties. The ε_r of La-compound is the highest caused to decreasing tilt angle of TiO_6-octahedron according to the increase of lattice parameter. The temperature factors of resonant frequency (τ_f) decrease proportional to the ε_r. Especially, the τ_f of Sm-compound is close to 0 ppm/°C. Totally, the dielectric properties of Sm- and Nd-compounds are available for application on the microwave resonator.

The $Q \cdot f$ of Sm-compound is the highest based on the low internal strain in the atomic scale. The internal strain around the atoms will be determined using the modified Scherrer's equation as described in the previous paper [8]. According to the equation (1) for internal strain, $\beta \cos\theta$ is plotted against $\sin\theta$ for four diffraction peaks (002, 302, 103 and 222 indexed by superlattice constants) as shown in Fig.8(a). We could not separate and analyze more peaks in spite of the high angle resolution obtained by synchrotron radiation. In the profiles of the X-ray powder diffraction, there are too many Bragg diffraction peaks such as 1500 peaks in the range of $0° < 2\theta < 90°$, as the lattice parameters are large including the superlattice of doubled c-axis [10]. Internal
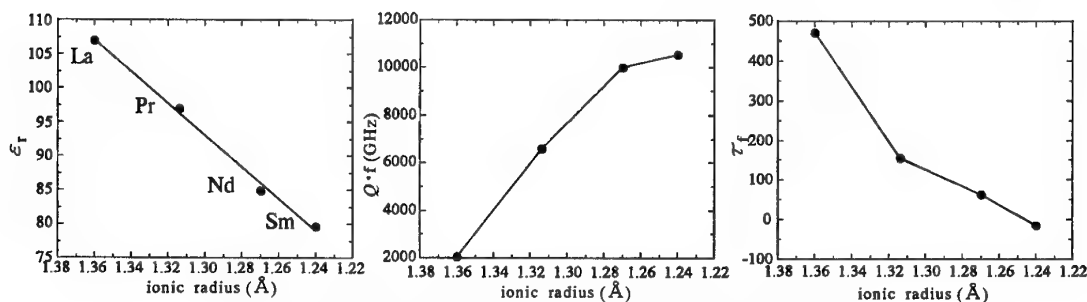

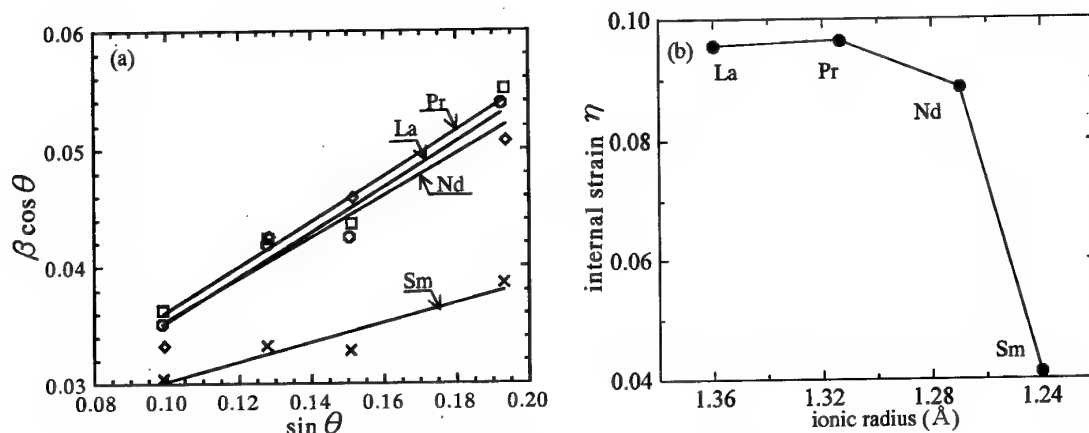Fig.7: Microwave dielectric properties of each R-compound with x=2/3.

Fig.8: Internal strain of each R-compound with x=2/3.

strain η values for each R-compound with x=2/3 are derived from the slopes of the equation (1) as shown in Fig.8(b). It should be noticed that the internal strain for Sm is the lowest. This low internal strain comes from the difference of ionic radii between R and Ba ions. In the case of $Ba_{6-3x}R_{8+2x}Ti_{18}O_{54}$ solid solution series, lower internal strain comes from the ordering R and Ba ions which occupy $A1$-sites and $A2$-sites, respectively. In this case of R-compounds with x=2/3, we are comparing R-compounds with different size of ionic radii. The tungstenbronze-type like structure is composed with two different parts. One is perovskite blocks including medium size ions such as R ions and the other is pentagonal columns including large size ions such as Ba. These two parts are produced by existence of different size in cations. So, the size of cations occupied the two sites should be different. Sm-compound with the smallest ionic radius in the R-compound series is the most stable for the rhombic sites in the perovskite blocks, which show the smallest internal strain. This stabilization of the crystal structure has improved $Q \cdot f$ values.

4. CONCLUSIONS

Sm-compound with x=2/3 in the $Ba_{6-3x}R_{8+2x}Ti_{18}O_{54}$ solid solutions has the highest values of the $Q \cdot f$ in the all R-compounds (R = La, Pr, Nd and Sm). The values of the $Q \cdot f$ are as follows: 10549 GHz in the Sm-compound, 10010 GHz in the Nd-compound, 6611 GHz in the Pr-compound and 2024 GHz in the La-compound.

The internal strain of each R-compound is obtained by the equation (1) using powder X-ray diffraction patterns of synchrotron radiation. Sm-compound is revealed to have the lowest internal strain. This low internal strain comes from stabilization of the crystal structure by difference of the ionic radii between Sm and Ba ions. The internal strain produces excellent $Q \cdot f$ value.

REFERENCES

[1] D. Kolar, Z. Stadler, S. Gaberscek and D. Suvorov: *Ber. Dtsch. Keram. Ges.* **55**, 346-347 (1978).
[2] M. B. Varfolomeev, A.S. Mironov, V.S. Kostomarov, L. A. Golubtova, and T. A. Zolotova: *Zh. Neorg. Khim.* **33**, 1070-1071 (1988), *Translation, Russ. J. Inorg. Chem.* **33**, 607-609 (1988).
[3] H. Ohsato, T. Ohhashi, S. Nishigaki, T. Okuda, K. Sumiya and S. Suzuki: *Jpn. J. Appl. Phys.* **32** 4323-4326 (1993).
[4] S. Nishigaki: *FC Rep.* **5**, 413-422 (1987). Translation, FC Annual Report for Overseas Readers 32-41(1988).
[5] S. Nishigaki: *New Ceramics.* **No.9**, 25-36 (1996).
[6] H. Ohsato, M. Mizuta, T. Ikoma, Z. Onogi, S. Nishigaki and T. Okuda: *J. Ceram. Soci. Japan*, **106(2)**, 178-182 (1998).
[7] H. Ohsato, M. Imaeda, A. Komura and Y. Takagi: *"Dielectric Ceramic Materials" Ceramic Transactions* **100**, 41-50 (1999).
[8] H. Ohsato, M. Imaeda, Y. Takagi, A. Komura and T. Okuda: *Proceeding of ISAF* XI'98 IEEE, (1998) in press.
[9] R. G. Matveeva, M. B. Varforomeev and L. S. ll'yuschenko: *Zh. Neorg. Khim.* **29**, 31-34 (1984). *Translation, Russ. J. Inorg. Chem.* **29**, 17-19 (1984).
[10] H. Ohsato, S. Nishigaki and T. Okuda: *Jpn. J. Appl. Phys.* **31**, 3136-3138 (1992).
[11] H. Ohsato, T. Ohhashi and T. Okuda: *Ext. Abstr. AsCA '92 Conf., Singapore, November*, **14U-50** (1992).
[12] H. Ohsato, H. Kato, M. Mizuta and T. Okuda: *Ext. Abstr. AsCA '95 Conf., Thailand, November*, **1P40** (1995).
[13] C. J. Rawn: *J. Mater. Res.*, **13**, No.1, 187-196 (1998).
[14] M. Imaeda, K. Ito, M. Mizuta, H. Ohsato, S. Nishigaki and T. Okuda: *Jpn. J. Appl. Phys.* **36**, 6012-6015 (1997).
[15] B. W. Hakki and P. D. Coleman: *IRE Trans. Microwave Theory & Tech.* **MTT-8** 402-410 (1960).
[16] H. Toraya, H. Hibino and K. Ohsumi,: *J. Synchrotron Rad.*, **3**, 75-83 (1996).
[17] H. Toraya: *J. Appl. Cryst.* **19**, 440-447 (1986).

Effects of Alkali Metal Oxide Addition on the Microwave Dielectric Properties of the $BaO-Sm_2O_3-TiO_2$ Ceramics

Motohiko Sato, Jun Otsuka, Hitoshi Yokoi and Kazushige Ohbayashi

R&D Center, NGK Spark Plug Co., Ltd.

2808, Iwasaki, Komaki, Aichi 485-8510, JAPAN

Fax : +81-568-76-5274

Abstract — In order to improve the microwave dielectric properties of the $BaO-Sm_2O_3-TiO_2$ ceramics, effects of addition of alkali metal oxides were investigated. All of a dielectric constant (ε_r), a quality factor (Q value) and a temperature coefficient of resonant frequency (τ_f) were very sensitive to the amount of K_2O, which was probably attributed to the proportion of $BaSm_2Ti_4O_{12}$, $BaTi_4O_9$ and TiO_2. The additive Na_2O and K_2O systems had positive and negative τ_f natures, respectively. Therefore, the τ_f value could be successfully adjusted to near zero by simultaneously adding the optimum amount of Na_2O and K_2O, maintaining high ε_r and Q·f value.

INTRODUCTION

Dielectric ceramics in the TiO_2-rich region of the $BaO-RE_2O_3-TiO_2$ system (RE=Nd,Sm) have been widely studied in the electronics industry due to their high dielectric constants and high quality factors.

In the case of RE=Nd [1], high ε_r and Q value are obtained in certain composition such as $BaNd_2Ti_5O_{14}$, but its τ_f is relatively high. Therefore, there is a demand to decrease it by compositional modifications. For example, the τ_f has been improved by partial replacement of Ba^{2+} with Pb^{2+} [2,3] and/or Nd^{3+} with Bi^{3+} [4].

In the case of RE=Sm, the good dielectric properties as well as RE=Nd have been reported [5]. Negative τ_f are characteristic of this system. Nishigaki et al. [5] improved the τ_f by substituting Sr^{2+} for a Ba^{2+} site. Ohsato et al. [6] adjusted the τ_f to zero by adding TiO_2.

Recently, the relations between dielectric properties and a crystal structure of the $Ba_{6-x}RE_{8+2/3x}Ti_{18}O_{54}$ solid solution [6,7] of which a molar ratio is $BaO:RE_2O_3:TiO_2=1:1:4$ have been mainly reported. The focal points of recent researches on this solid solution are the fabrication processes, the sintering agents and the chemical composition having excellent dielectric properties.

Although alkali metal oxides are generally avoided as impurities, we have found that the substitution of K^+ with the excess amount for Ba^{2+} in the $Ba(Zn_{1/3}Ta_{2/3})O_3$ ceramics results in the improvement of their dielectric properties, especially their Q values and the sinterability[8]. The purposes of the present study are to investigate effects of alkali metal oxide addition on the microwave dielectric properties of the $BaO-Sm_2O_3-TiO_2$ (BST) ceramics and to clarify the relations between dielectric properties and microstructures of the BST-A (A:alkali metal oxide) ceramics.

EXPERIMENTAL PROCEDURE

1. Sample Preparation

The commercially available powders of $BaCO_3$, $Sm(OH)_3$, TiO_2 and A_2CO_3 (A=Li, Na, K) were weighed and ball milled in ethanol for 15h. The typical composition selected in this study was in a $BaO:Sm_2O_3:TiO_2$ molar ratio of 12.5:15.0:72.5. The mixed slurry was dried and calcined at 1000°C for 2h. The calcined powder was re-milled with an organic binder and a dispersant in ethanol for 15h. After drying, the powder was pressed into disks with dimensions of 20mm in diameter and 12mm in thickness under a compaction pressure of 10MPa and CIPed under a pressure of 150MPa. These disks were sintered at 1300~1400°C for 2h in air. The both end surfaces of the disk specimens were ground with a #200 diamond wheel.

2. Characterization

The bulk densities of the sintered samples were determined by Alchimedes' method. The crystalline phases were identified by X-ray powder diffraction (XRD) using Cu-K α radiation. The microstructures were observed and analyzed by scanning electron microscopy (SEM) attached with analytical capability, energy dispersive X-ray spectroscopy (EDS). The ε_r and Q value in the microwave frequency range were measured in the TE_{011} resonant mode by means of Hakki-Colemans' dielectric resonator method[9]. The τ_f was measured in the temperature range of 30~80℃.

RESULTS AND DISCUSSION

1. Effects of Addition of the Alkali Metal Oxide on the Dielectric Properties of the BaO-Sm_2O_3-TiO_2 (BST) Ceramics

Fig.1 shows effects of addition of the alkali metal oxide ($\triangle$:Na_2O and ●:K_2O) to the BST ceramics on their dielectric properties. The x value represents the amount of alkali metal oxide for the BST in weight percent (wt%). Each specimen was sintered at 1350℃ for 2h. When x=0.0wt%, its Q value was too low to evaluate although a dense sintered body was obtained. However, the addition of small amounts of alkali oxides resulted in dramatic improvement of its dielectric properties. In the Na_2O system, the Q·f value increased over 6,000GHz at x=0.75wt%. Further excess of the addition led a decrease of the Q·f value. The ε_r and τ_f were approximately constant irrespective of its amount. On the other hand, when K_2O was added to the BST, all the dielectric properties were very sensitive to its amount. The Q·f value kept on increasing up to x=1.5wt% and exceeded 8,000GHz. With an

increase of K_2O, the ε_r decreased monotonously and the τ_f shifted to the negative away from 0ppm/℃.

As compared with the dielectric properties of the additive Na_2O system including the results of other BST compositions, when K_2O was added, they showed a) lower ε_r, b) higher Q·f values and c) smaller τ_f. As can be seen in this figure, the τ_f was not within $\pm$10ppm/℃ when an alkali metal oxide was added more than 1.0wt%, which was not favorable for the application of the electronic components. The addition of Li_2O was not very effective for improvement of the dielectric properties of the BST. Therefore, the results of its addition were not shown in Fig.1.

2. Relations between the Dielectric Properties and Morphology of the BST-A Ceramics

a) K_2O additive system (A=K)

Fig.2 shows XRD patterns of the BST-K ceramics. The main pattern coincided with $BaSm_2Ti_4O_{12}$ (BST_4), completely. In addition, TiO_2 and $BaTi_4O_9$ co-existed as secondary phases though it was difficult to identify them from the main phase peaks, because those peaks were likely hidden by the BST_4 pattern. With an increase of K_2O amount, the peak intensities of TiO_2 decreased while those of $BaTi_4O_9$ increased.

Fig.3 shows microstructures of the BST-K ceramics. When x=0.0wt%, microstructures consisted of the gray grains [A], black grains [B], and a little dark-gray grains [C]. The results of EDS analysis and the XRD measurement revealed that the phases of the grains [A], [B] and [C] were $BaSm_2Ti_4O_{12}$, TiO_2 and $BaTi_4O_9$, respectively. With an increase of K_2O amount in the range of x=0.5~1.0wt%, the number of
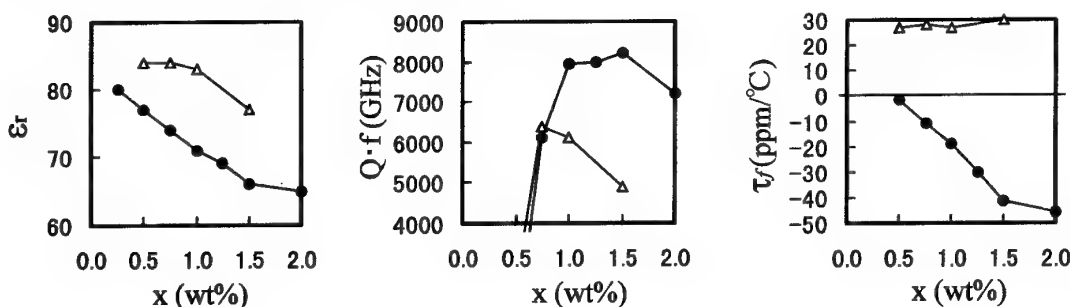
Fig.1 Effects of addition of the alkali metal oxide ($\triangle$; Na_2O , ●; K_2O) on the dielectric properties of the BST ceramics.
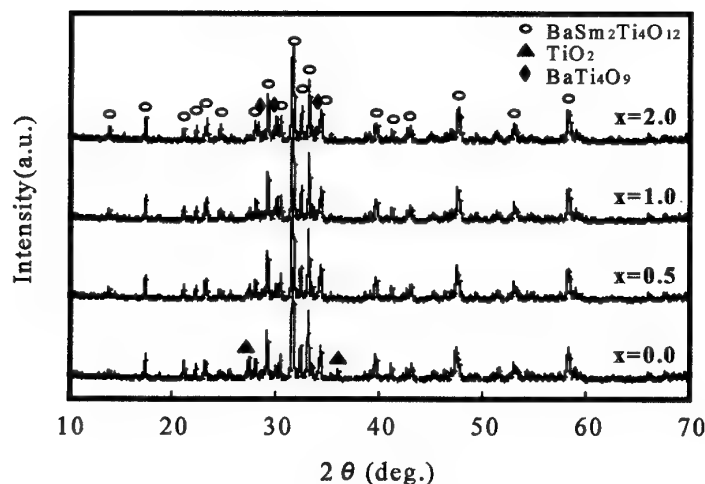
Fig.2 XRD patterns of the BST-K ceramics containing various
K$_2$O amounts (x wt%).

the TiO$_2$ grains (black grains [B]) decreased and that of the BaTi$_4$O$_9$ grains (dark-gray grains [C]) increased. This tendency is also confirmed in the XRD measurement. When 2.0wt% of K$_2$O was added (Fig.3 (4)), the BaTi$_4$O$_9$ grains (dark-gray grains) grew abnormally and the gray matrix consisted of very small grains. The TiO$_2$ grains (black grains) tended to disappear with an increase of the K$_2$O amount. This suggested that K$^+$ added was substituted for Ba^{2+} to form a compound expressed as (Ba,K)Sm$_2$Ti$_4$O$_{12}$ since the ionic radius of K$^+$ (1.38Å) is close to that of Ba^{2+} (1.36Å). Consequently, Ba^{2+} should exist in BaSm$_2$Ti$_4$O$_{12}$ reacted with TiO$_2$ existed as the secondary phase, leading to form BaTi$_4$O$_9$. The EPMA analysis proved that almost K$^+$ ions existed in the matrix phase, BaSm$_2$Ti$_4$O$_{12}$. From the

above results, it was clear that there was the close correlation between the dielectric properties and the microstructures of the BST-K ceramics.

b) Na$_2$O additive system (A=Na)

With an increase of Na$_2$O amount, the peak intensities of TiO$_2$ decreased in the same manner of K$_2$O additives. When x=1.5wt%, the excess Na$_2$O led to form a compound expressed as a complex perovskite, (Na$_{0.3125}$Sm$_{0.5625}$)TiO$_3$. As a consequence, BST$_4$ matrix should contain some Sm-poor compound to compensate the segregated small amount of (Na$_{0.3125}$Sm$_{0.5625}$)TiO$_3$. The perovskite seems to show lower ε$_r$ and Q value than TiO$_2$ as shown Fig.1, but the details have not yet been proven.
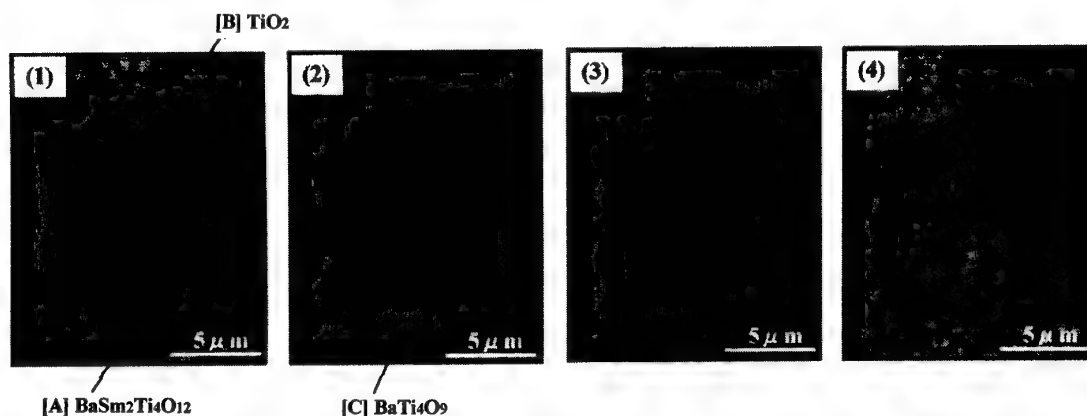

Fig.3 Microstructures of the BST-K(x wt%) ceramics ;
(1) x=0.0wt%, (2) x=0.5wt%, (3) x=1.0wt%, (4) x=2.0wt%.

3. Influence of the Simultaneous Addition of Na_2O and K_2O on the Dielectric Properties of the BST Ceramics

When either Na_2O or K_2O was added more than 1.0wt%, the τ_f could not be controlled within $\pm$ 10ppm/℃ as shown in Fig.1. Therefore, both Na_2O and K_2O were simultaneously added in order to cancel out their positive and negative τ_f, resulting in adjusting the τ_f to near zero. The results of the dielectric properties of the BST ceramics containing Na_2O and/or K_2O are depicted in Fig.4. The total amount of the additives was fixed at x=1.0wt%. The dielectric properties changed linearly with the ratio of two additives. There existed the optimum ratio to adjust the τ_f to near zero with maintaining high ε_r and Q·f value.
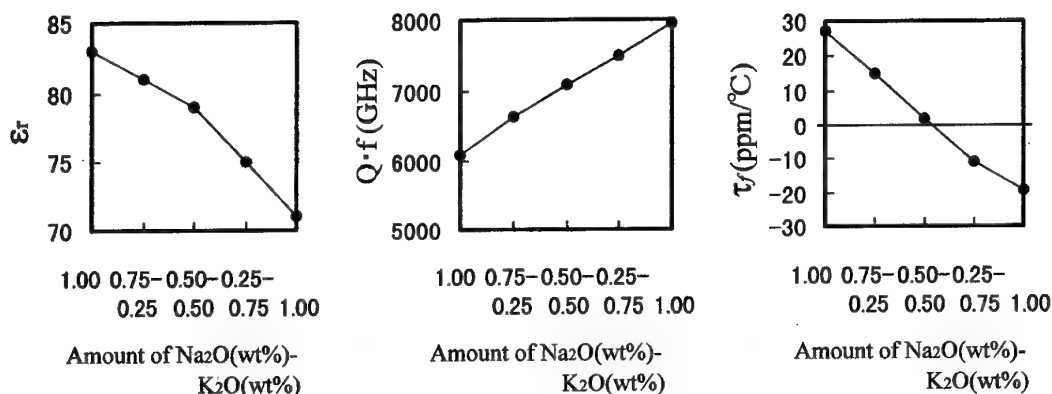
CONCLUSIONS

The addition of alkali metal oxide improved the dielectric properties of the BaO-Sm_2O_3-TiO_2 ceramics. All of the dielectric properties (ε_r, Q and τ_f) were sensitive to the amount of K_2O added. These results were attributed to the proportion of three phases in the BST-K ceramics. On the other hand, when Na_2O was added, the ε_r and τ_f were approximately constant irrespective of its amount. In addition, the dielectric properties changed linearly with the ratio of Na_2O and K_2O simultaneously added. It was concluded that the τ_f could be controlled within $\pm$ 10ppm/℃ with maintaining high ε_r and Q·f value by optimizing the ratio of Na_2O and K_2O.

Fig.4 Influence of the simultaneous addition of Na2O and K2O on the dielectric properties of the BST ceramics.

REFERENCES

[1]D.Kolar, Z.Stadler, S.Gaberscek and D.Suvorov, Ber. Dt. Keram. Ges., 55[7] 346-48 (1978).

[2]K.Wakino, K.Minami and H.Tamura, J. Am. Ceram. Soc., 67[4] 278-81 (1984).

[3]M.Podlipnik, M.Valant and D.Suvorov, Key Engineering Materials, 132-136, 1211-14 (1997).

[4]M.Valant, D.Suvorov and D.Kolar, J. Mater. Res., 11[4] 928-31 (1996).

[5]S.Nishigaki, H.Kato, S.Yano and R.Kamimura, Am. Ceram. Soc. Bull., 66[9] 1405-10 (1987).

[6]H.Ohsato, A.Komura, Y.Takagi, S.Nhisigaki and T.Okuda, Jpn. J. Appl. Phys., 37, 5357-59 (1998).

[7] H.Ohsato, H.Kato, M.Mizuta, S.Nishigaki and T.Okuda, Jpn. J. Appl. Phys., 34, 5413-17 (1995).

[8]H.Yokoi, A.Tosa and K.Ohbayashi, The 8th US-Japan Seminar on Dielectric & Piezoelectric Ceramics, 212-15 (1997).

[9]B.W.Hakki and P.D.Coleman, IRE Trans. Microwave Theory Tech., MTT-8, 402-10 (1960).

Microwave Dielectric Properties of Ceramics with Nominal Composition $(A_{1-x}A'_x)(BB')O_3$ (A, A'= Ba, Sr, Ca)

Hiroyuki Ikawa and Minoru Takemoto
Department of Applied Chemistry, Kanagawa Institute of Technology
1030 Shimo-ogino, Atsugi-shi, 243-0292 JAPAN
Fax: 81-46-242-8760, e-mail: ikawa@chem.kanagawa-it.ac.jp

Syntheses of five perovskite systems formulated as $(A_{1-x}A'_x)(B_{1/2}B'_{1/2})O_3$ (A, A'= Ba, Ca) were investigated. The smallest composition parameter x, XRD of which recorded diffraction(s) of a second phase for the first time, was roughly grouped into three. The first group had small x from 0.2 to 0.3, belonging member systems were $(Ba_{1-x}Ca_x)(Y_{1/2}Nb_{1/2})O_3$ and $(Ba_{1-x}Ca_x)(Y_{1/2}Ta_{1/2})O_3$. The second had middle x around 0.4, with $(Ba_{1-x}Ca_x)(Gd_{1/2}Ta_{1/2})O_3$ system as a member. The third group had large x around 0.8, of which's member systems were $(Ba_{1-x}Ca_x)(Nd_{1/2}Nb_{1/2})O_3$ and $(Ba_{1-x}Ca_x)(Nd_{1/2}Ta_{1/2})O_3$. The difference in ionic radii between Ca^{2+} ion and B^{3+} ion (B = Y, Gd, or Nd) was attributed to the results, because the difference in ionic radii controlled the possible occurrence of bimodal occupations at A- and B-sites of Ca^{2+} and B^{3+} ions. Dielectric properties of ceramics only belonging group one could be evaluated by means of a resonator method. Relative permittivities of them increased sharp to have peaks at x of 0.2, and further, decreased with x. The fQ values were larger at compositions with x's of 0.0 and 1.0. Those decreased sharply with x to have wide flat valleys at intermediate regions. Those dependences of dielectric properties on nominal compositions including the behaviors of temperature coefficient of resonance frequency were marked similar to those reported on $(Ba_{1-x}Ca_x)(Mg_{1/3}Ta_{2/3})O_3$ and others. However, the absolute values of the increase in relative permittivity were different significantly. That is to say, the reported increases were 40 to 49%, however, those of this study were 34% and 28%. Plausible two mechanisms to explain the deviation were discussed.

1. INTRODUCTION

Paraelectric properties of perovskite oxides change as a matter of course by partial substitutions of their A-site alkaline-earth ions by another ions. Are there rules for the substitutions, which are written by using primitive crystal chemical words, to predict the changes in paraelectric properties – relative permittivity, dielectric loss, and those changes with temperature? This inquiry has been the motivation of foregoing investigations [1-4] and this study by setting aside the physics of those absolute values of the terminal compounds. This is an interim report to discuss this scientific and engineering question by accumulating data on new systems expressed as $(A_{1-x}A'_x)(B_{1/2}B'_{1/2})O_3$ (A, A'= Ba, Ca). The foregoing published studies have been made on the systems $(A_{1-x}A'_x)ZrO_3$ and $(A_{1-x}A'_x)(B_{1/3}B'_{2/3})O_3$ (A, A'= Ba, Sr, Ca) including the pressure and temperature dependences of capacitances [1-3] and remarkable experimental relations among elastic parameters and dielectric properties [4].

2. EXPERIMENTALS

The nominal composition of the system studied was $(Ba_{1-x}Ca_x)(B_{1/2}B'_{1/2})O_3$, where B = Y, Nd, or Gd and B'=

Nb or Ta. Wide variety combinations of elements were studied by rough intervals of the x value typically 0.2.

Guaranteed grade reagents were used to prepare specimens according to a normal ceramic processing. Weighted reagents of oxide or carbonate were mixed in an agate mortal with ethanol before calcining at 1200°C for 5 h or 12 h. A micro pulverizer (Fritsch, P-5), fixing 80 ml pots made of partially stabilized zirconia, was used with ethanol after the first and second calcinations. The shaped pulverized powder was CIPed under 1 GPa. Disks about 8 mm in diameter with a length 1 mm or 4 mm were made by sintering in air at 1500°C or 1600°C for 5 h followed by cooling at 270 °C/h rate. Specimens were characterized by XRD (Rigaku, RINT2500VHF) with a CuKα radiation, SEM, and densities of powders and ceramics by a He densimeter (Micromeritrics, AccuPyc 1330). Silicon was added as an internal standard to correct from 15 to 20 diffraction angles, which were used to calculate lattice constants.

The two faces of a disk were carefully polished to be parallel by using a cylindrical brass tool and abrasive paper of #500, #1000 and #2000. The microwave dielectric properties were measured by means of the Hakki-Coleman [5] and Kobayashi [6] method on the

TE_{011} mode at about 10 GHz. A network analyzer (HP, 8722C) system was used to calculate by a program SU2-RODTE01 Ver.2 [6]. More than three disks with a length of 4 mm were measured at temperatures from 0 to 80°C. When the dielectric loss of a ceramic was too large to measure by the resonator method mentioned above, a disk, 1 mm in thickness, with two electrode faces by Pt-sputtering was connected to a capacitance bridge (Andeen-Hagerling, 2500A), which operated at 1 kHz.

3. RESULTS AND DISCUSSION

3.1 Solid Solution

In the cases of $(Ba_{1-x}Ca_x)(Y_{1/2}Nb_{1/2})O_3$ and $(Ba_{1-x}Ca_x)(Y_{1/2}Ta_{1/2})O_3$ systems, weak but clear X-ray diffraction peaks of respective second phases are recorded for compositions with x of 0.2. These results show that x=0.2 is almost the compositional limits of the BCYN and BCYT (abbreviation of the former and latter, respectively) solid solutions.

The cases of the two systems above mentioned are not those of the latter three systems. That is, in the $(Ba_{1-x}Ca_x)(Nd_{1/2}Nb_{1/2})O_3$ and $(Ba_{1-x}Ca_x)(Nd_{1/2}Ta_{1/2})O_3$ systems, the X-ray diffraction angles of peaks shift continuously with x, as though there are wide ranges of solid solutions from 0.0 to 0.8. The XRD's of the $(Ba_{1-x}Ca_x)(Gd_{1/2}Ta_{1/2})O_3$ system show that the range of x for making a solid solution of this system may be in middle of the narrower former two systems and the wider latter two systems.

More detailed studies are necessary to make it clear the phases and/or solubility limits of those systems. However, a plausible discussion is possible by referring following ionic radius in unit of pm [7]; Ba^{2+}(XII): 175, Ca^{2+}(XII): 148, Ca^{2+}: 114, Mg^{2+}: 86.0, Zn^{2+}: 88.0, Y^{3+}: 104, Nd^{3+}(XII): 141, Nd^{3+}: 112, Gd^{3+}: 108, Zr^{4+}: 86, Nb^{5+}: 78, Ta^{5+}: 78 (XII or VI coordination as written or not written, respectively).

The composition parameter x in $(Ba_{1-x}Ca_x)BO_3$ is discussed here, that is, the range of $BaBO_3$-type perovskite solid solution in which Ba^{2+} ions are partially substituted by Ca^{2+} ions. Those x values, although most of them are very rough estimations, are sorted in the

parentheses next of their formulas; $(Ba_{1-x}Ca_x)ZrO_3$ (0.2 < x < 0.3) [1], $(Ba_{1-x}Ca_x)(Mg_{1/3}Ta_{2/3})O_3$ ($x \sim 0.24$) [2, 3], $(Ba_{1-x}Ca_x)(Zn_{1/3}Ta_{2/3})O_3$ (0.2 < x < 0.3) [3], $(Ba_{1-x}Ca_x)(Y_{1/2}Ta_{1/2})O_3$ ($x \sim 0.2$), $(Ba_{1-x}Ca_x)(Y_{1/2}Nb_{1/2})O_3$ (0.2 < x < 0.4), $(Ba_{1-x}Ca_x)(Gd_{1/2}Ta_{1/2})O_3$ ($x \sim 0.4$, not clear yet), $(Ba_{1-x}Ca_x)(Nd_{1/2}Nb_{1/2})O_3$ ($x \sim 0.8$, not clear yet) and $(Ba_{1-x}Ca_x)(Nd_{1/2}Ta_{1/2})O_3$ ($x \sim 0.8$, not clear yet). Larger x values of the latter two compounds are explained by almost identical ionic radii of Ca^{2+} and Nd^{3+} ions. That is to say, the replacements of ions are not restricted in A-site ions as expressed by the formulas but are mixed up to include B-site ions. Accordingly, Ca^{2+} and Nd^{3+} ions can be located at A-site and B-site also. This A- and B-sites double occupations must be restricted by an increase of the difference in ionic radii between Ca^{2+} ion and B-site ions of the formulas. Hence, the value of x becomes smaller in the order with the formula containing B-site ions Gd^{3+}, Y^{3+}, and Zn^{2+} or Mg^{2+} or Zr^{4+}. Further, the observed smallest solubility, 0.2 - 0.24 of x, can be regarded as the solid solution limit for Ba^{2+} ions are replaced by Ca^{2+} ions in $BaBO_3$ perovskite, under an estimated condition that the occupation of Ca^{2+} ions at B-site are insignificant.

3.2 Dielectric Property

Relative permittivities (ε_r) and fQ values of the $(Ba_{1-x}Ca_x)(Y_{1/2}Ta_{1/2})O_3$ and $(Ba_{1-x}Ca_x)(Y_{1/2}Nb_{1/2})O_3$ systems are compared with the reported [1-3] in Fig.1 and Fig.2, respectively. It is noted again that composition is that of nominal, and it is the composition of the compound only when x is smaller than about 0.25, or larger than about 0.9. ε_r's at $x = 0.0$ in Fig.1 are compared well with 33 for BYN or 30 for BYT [8]. Moreover, ε_r's increase with x to have respective peak values at around solubility limits 0.2 in this experiment, and decrease afterwards with x. These features are almost identical to those cited in the figure.

The four connection lines in Fig.2 are also very similar each other. That is, the fQ values of terminal compounds are rather large, however, they decrease sharp to have flat valleys during intermediate x. The sharp decrease of fQ, namely the sharp increase of dielectric loss is common for systems of these studies

[1-3]. Furthermore, the sharp increase in dielectric loss is understandable by the discussion in a review [9], which predicts broadenings of the lowest and/or near the lowest frequency phonon modes [3]. Broadenings of the phonon modes must be inevitable to solid solutions of these kinds because of random modulations of mass of a fixed crystallographic site and bonding strength/length of a fixed bond.

The increase in ε_r is normalized to compare in Fig.3 by referring data [1-3]. The two ε_r's at $x = 0.0$ and $x = 1.0$ are connected by a line, and a deviation of the observed ε_r from the point on the tie line at each x is normalized by $\Delta\varepsilon_r\varepsilon_r^{-1}$. The increases in ε_r's owing to the A-site substitutions are different considerably to the combinations of alkaline-earth ions in the order of $(Ba_{1-x}Ca_x) \gg (Ba_{1-x}Sr_x) \gg (Sr_{1-x}Ca_x)$ [3]. Further, those differences are discussed on the basis of a simple rattling model, which has its origin in the difference in sizes at A-site ions [2,3].

It is notable that softening of the lattice is estimated in additional discussion [1,3] and verified latter [4]. Namely, softening of the lattices is one of the estimated mechanisms for the increases in ε_r's owing to the replacements of Ba^{2+} by Ca^{2+} ions [1,3]. Elastic moduli

of those BCMT ceramics of all compositions are evaluated by acoustic velocities to find that the decrease in Young's modulus – one-dimensional mechanical softening – is correlated well with the increase in ε_r –

Fig.2 fQ value of the ceramic disk vs. nominal composition parameter x for A-site substitution perovskite system. Solid mark: this study, open mark: cited from references [1, 3].
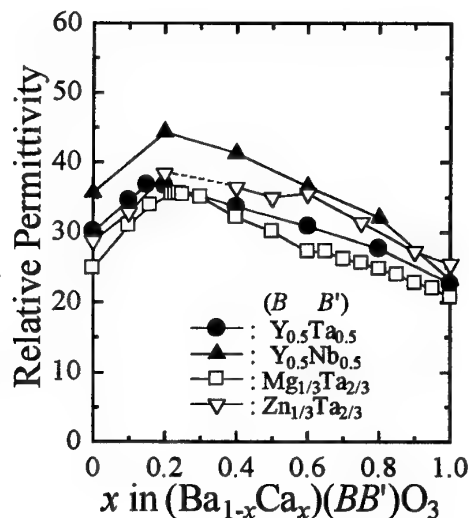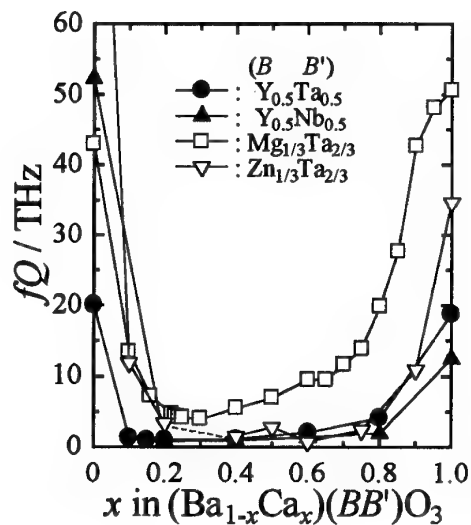

Fig.1 Relative permittivity of the ceramic disk vs. nominal composition parameter x for A-site substitution perovskite system. Solid mark: this study, open mark: cited from references [1, 3].
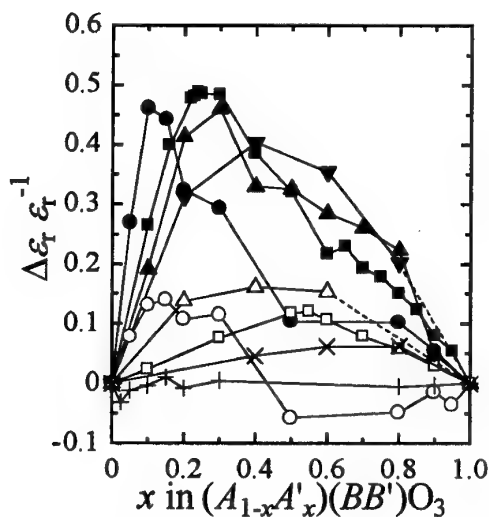

Fig.3 Rate of the increase in relative permittivity vs. nominal composition parameter x. Data are cited from the references [1-3]. A-site; solid marks: $(Ba_{1-x}Ca_x)$, open marks: $(Ba_{1-x}Sr_x)$, cross marks: $(Sr_{1-x}Ca_x)$. B-site; ● and ○: Zr, ■ and □: $Mg_{1/3}Ta_{2/3}$, ▲ and △: $Mg_{0.3}Ta_{0.6}Zr_{0.1}$, ▼ and ▽: $Zn_{0.3}Ta_{0.6}Zr_{0.1}$, +: Zr, ×: $Mg_{1/3}Ta_{2/3}$.

dielectric softening (one dimensional) [4]. Further, this correlation fits better than the relation between bulk modulus and ε_r of BCMT.

Fig.4 compares the increases in ε_r's of three systems, two of which with solid marks are those of this study. The increases in Fig.3 of the $(Ba_{1-x}Ca_x)$-systems are from 40 to 49%, one of them is cited in Fig.4, are lager significantly than the other two systems. Two terms are discussed on these results:

(1) It is roughly estimated that the maximum increase in ε_r is around 45% for the $(Ba_{1-x}Ca_x)$-system, if the situation is negligible of mixed occupations between A- and B-site ions. Accordingly, double occupations of Ca^{2+} and Y^{3+} ions at A- and B-sites are the reason of making those increases dispersed – depression of increases to those of Fig.4. The small difference in radii between Ca^{2+} and Y^{3+} ions makes the situation possible.

(2) The increase in ε_r of the $(Ba_{1-x}Ca_x)$-system is surely larger than the other two systems $(Ba_{1-x}Sr_x)$- and $(Sr_{1-x}Ca_x)$-systems as mentioned above. However, the value of the increase is characteristic to B-site ion(s).

The temperature coefficient of resonance frequency (TCf) of $Ba(Y_{1/2}Nb_{1/2})O_3$ is 154×10^{-6} K^{-1}. The TCf values decrease with x and that of $(Ba_{0.8}Ca_{0.2})(Y_{1/2}Nb_{1/2})O_3$ is 44.0×10^{-6} K^{-1}. Further, the value of $Ca(Y_{1/2}Nb_{1/2})O_3$ is -5.70×10^{-6} K^{-1}. Accordingly, a composition having TCf of 0.0 ppm can be made at x around 0.99. A similar change of TCf with x is also measured for BCYT. It is referred that the general trend of change in TCf with composition is also similar to that of BCMT, however, for the latter TCf is 0.0 ppm at x of around 0.76 [3].
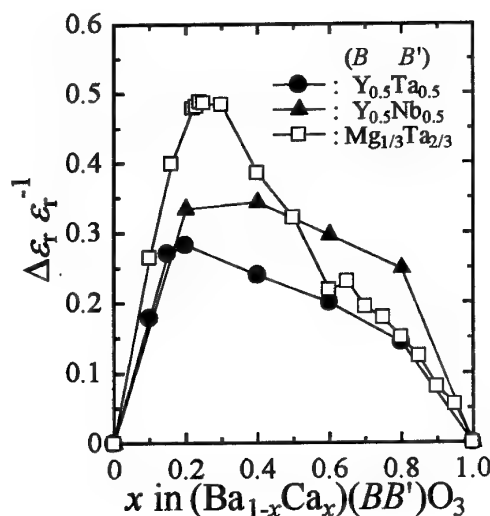
Fig.4 Rate of the increase in relative permittivity vs. nominal composition parameter x.

REFERENCES

[1] H. Ikawa, M. Touma, T. Shirakami, and O. Fukunaga, in Proceeds. of "*ELECTROCERAMICS 4*" vol.1, (1994) pp. 41-46.

[2] H. Ikawa, M. Yamashiro, T. Niwa, T. Omata, and K. Urabe, *Transactions of Mater. Res. Soc. Jpn.*, Vol.20, (1996) pp. 682-85.

[3] H. Ikawa, M. Yamashiro, T. Niwa, T. Omata, and M. Takemoto, in Proceeds. of "*ELECTROCERAMICS 5*" Book 1, (1996) pp. 41-44.

[4] H. Ikawa, M. Yamashiro, M. Fukuhara, and M. Takemoto, in Proceeds. of 11th *IEEE ISAF* (1998) pp. 529-32.

[5] B. W. Hakki and P. D. Coleman, IRE *Trans. Microwave Theory & Tech. MTT-8* (1960) pp. 402-10.

[6] Y. Kobayashi and M. Katoh, *IEEE Trans. on MTT*, MTT-33 (1985) pp. 586-92.

[7] R. D. Shannon, *Acta Cryst.* A32, 751-67 (1976).

[8] R. Zurmuhlen, J. Petzelt, S. Kamba, G. Kozlov, A. Volkov, B. Gorshunov, D. Dube, A. Tagantsev, and N. Setter, *J. Appl. Phys.*, 77, 5351-64 (1995).

[9] H. Ikawa, *Bull. Ceram. Soc. Jpn.*, 30, 313-17 (1995).

Influence of rare earth-ions on microwave dielectric property of R_2BaCuO_5 (R = Gd, Dy, Ho, Er, Tm, Yb) solid solutions

Akinori Kan, Hirotaka Ogawa and Hitoshi Ohsato*

Faculty of Science and Engineering, Meijo University, 1-501 Shiogamaguchi, Tenpaku-ku, Nagoya 468-8502, Japan

Fax: +81 - 52 - 832-1253, e-mail: c3993014@meijo-u.ac.jp

*Department of Material Science and Engineering, Nagoya Institute of Technology, Gokiso-cho, Showa-ku, Nagoya 466-8555, Japan   Fax: +81 - 52 - 735-7294, e-mail: ohsato@mse.niech.ac.jp

Abstract

R_2BaCuO_5 (R = rare-earth) solid solutions were investigated for the application as a microwave resonator. The experimental results show that the dielectric constant (ε_r) varies from 12 to 16, whereas the temperature coefficients of the resonant frequency (τ_f) and the quality factors ($Q \cdot f$) are renging from -43 to -6 ppm/°C and from 3.0×10^3 to 6.3×10^4 GHz, respectively. Moreover, in order to reveal the relationship between the microwave dielectric property and the variation in the atomic distances of the crystal structure with the increase in the temperature, the crystal structure of the solid solutions at room temperature (20°C) and 80°C are refined, using Rietveld method. From these results, it is clarified that the variation in the atomic distances of the R_2O_{11} polyhedron and the strain of that in the direction of b-axis influence closely on the temperature coefficient of dielectric constant (τ_r) and $Q \cdot f$ value, respectively.

1.Introduction

Recently, the frequency used for the area of mobile communications has been increased from 800 MHz to 1.9GHz. In this case, it is difficult to miniaturize the size of the microwave resonator when the materials with the high dielectric constant (ε) is utilized to a high resonant frequency. Therefore, the new materials with a low ε_r which can be used in the high microwave frequency range are expected. The microwave dielectric properties such as the high quality factor ($Q \cdot f$), and the temperature coefficient of the resonant frequency (τ_f) which is near 0 ppm/°C, are also especially required. Then, the dielectric properties of $Y_2Ba(Cu_{1-x}Zn_x)O_5$ (x = 0 to 1) solid solutions were investigated in our previous work[1]. It was clarified that the ε_r values range from 13 to 15, and τ_f and $Q \cdot f$ values range from -38 to -43 ppm/°C and from 2×10^4 to 1.1×10^5 GHz, respectively.

In this work, we investigate the microwave dielectric

properties of R_2BaCuO_5 (R = Gd, Dy, Ho, Er, Tm, Yb) solid solutions. In addition, the crystal structures of the solid solution used are refined to elucidate the relationship between the temperature coefficient of the resonant frequency and the variation in the crystal structures with the increase in the temperature, using the Rietveld method[2].

2.Experimental

R_2BaCuO_5 solid solutions were prepared by the solid-state reaction method, using R_2O_3, $BaCO_3$ and CuO powders of 99.9% purity. The powders were mixed with acetone and calcined in an alumina crucible at the temperature of 950°C for 20 h in the air. The powders added with an organic binder were passed through a screen mesh and pressed into a pellet of 12 mm in diameter and 7 mm in thickness under a pressure of 300 MPa, using the cold isotropic pressure (CIP). The pellets were sintered at

the appropriate sintering temperatures for 2 h in air, which were determined by the differential thermal analysis (DTA) and the thermogravimetry (TG). The sintered pellets were polished and then annealed to remove any strain at 900℃. The crystalline phases of the sintered pellets were identified by X-ray powder diffraction (XRD), using CuKα filtered through Ni foil. In addition, the lattice parameters were determined by the least squares method, using Si of 99.9% purity as an internal standard. The crystal structures of R_2BaCuO_5 (R = Dy, Tm and Er) solid solutions at room temperature (20℃) and 80℃ were refined in order to make clear the relationships between the τ_f and the variation in the crystal structure obtained by means of the Rietveld analysis program "RIETAN[3]". The microwave dielectric properties of the solid solutions were measured, by means of Hakki and Coleman's method[4].

3.Results and Discussion

All R_2BaCuO_5 compounds used in this study have recognized to have the same crystal structure from x-ray diffraction patterns. The lattice parameters of the solid solutions as a function of ionic radii are shown in Fig.1. The lattice parameters, a, b and c, increase linearly as the ionic radii of rare-earth element are increased. Thus, the variations in the lattice parameters are considered to be caused by the difference of the ionic radii on rare-earth ions. Therefore, the lattice parameters of R_2BaCuO_5 solid solutions obey the Vegard's law, which conforms the formation of the solid solutions.

The crystal structure of the R_2BaCuO_5 solid solution is shown in Fig.2. R^{3+} ions are surrounded by seven oxygen atoms, and then these atoms are composed of the $R(1)O7$ and $R(2)O7$ capped prisms. In addition, the two

prisms are linked by the common faces and make the R_2O_{11} polyhedron, and the R_2O_{11} polyhedron structure is shown in Fig.3. Here, O'(1)-O'(1) and O'(2)-O'(2) represent the atomic distances between the CuO_5 pyramids, whereas O(1)-O(1) and O(2)-O(2) do the atomic distances inside the CuO_5 pyramid. On the other hand, Cu^{2+} ions are positioned inside the isolated CuO_5 pyramid, which is shown in Fig.4, and Ba^{2+} ions are positioned in the Ba_2O_{11} polyhedron.
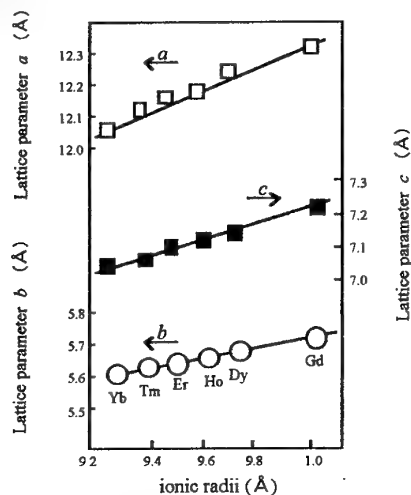

Fig.1 Lattice parameters of R_2BaCuO_5 solid solutions as a function of ionic radii.
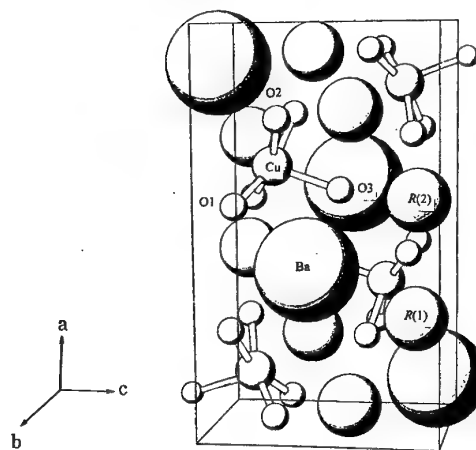
Fig.2 Crystal structure of R_2BaCuO_5 solid solutions.

Table I Reliability factors of the R_2BaCuO_5 (R=Dy, Er and Tm) solid solutions.

Reliability Factors (%)*	Dy		Er		Tm	
	20℃	80℃	20℃	80℃	20℃	80℃
R_{wp}	11.22	15.43	8.49	16.60	10.54	16.94
R_p	8.83	7.53	5.39	8.32	5.30	8.32
S	2.11	2.03	1.57	1.80	1.98	2.03

* R_{wp} is reliability factor for the weighted pattern, R_p is reliability factor for the pattern and S is goodness of fit indicator.

Fig.3 R_2O_{11} polyhedron structure.

Fig.4 CuO_5 pyramid structure.

Table II Atomic distacnces and angles of CuO_5 pyramid.

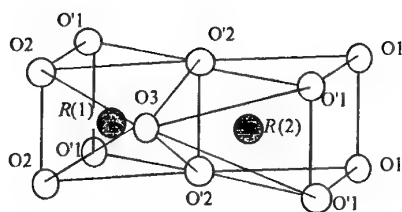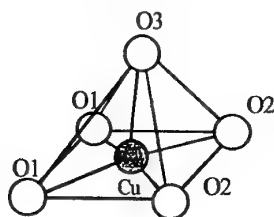| R	Atomic distances (Å) and angles (deg)	R.T.	80°C
Tm	Cu - O(1)	1.835(1)	1.853(3)
	Cu - O(2)	2.068(1)	2.103(2)
	Cu - O(3)	2.187(2)	2.199(5)
	∠O(1)CuO(1)	104.16	102.45
	∠O(2)CuO(2)	80.75	83.07
	∠O(1)CuO(3)	107.54	106.06
	∠O(2)CuO(3)	89.95	90.60
Er	Cu - O(1)	1.855(3)	1.903(1)
	Cu - O(2)	1.908(1)	1.902(4)
	Cu - O(3)	2.136(5)	2.134(1)
	∠O(1)CuO(1)	102.14	99.09
	∠O(2)CuO(2)	87.69	85.77
	∠O(1)CuO(3)	101.45	102.21
	∠O(2)CuO(3)	92.61	95.98
Dy	Cu - O(1)	1.954(6)	2.051(3)
	Cu - O(2)	1.940(1)	1.946(2)
	Cu - O(3)	2.155(1)	2.156(1)
	∠O(1)CuO(1)	95.34	89.59
	∠O(2)CuO(2)	92.27	91.92
	∠O(1)CuO(3)	101.62	102.01
	∠O(2)CuO(3)	92.69	93.07

Table III Atomic distacnces of R_2O_{11} polyhedron.

R	Atomic distance (Å)	R.T.	80°C
Tm	Tm(1) - O'(1)	2.005(2)	2.036(3)
	Tm(1) - O'(2)	2.376(1)	2.338(1)
	Tm(1) - O(2)	2.310(2)	2.349(1)
	Tm(1) - O(3)	2.301(1)	2.326(5)
	Tm(2) - O'(1)	2.480(2)	2.459(4)
	Tm(2) - O(1)	2.404(5)	2.403(1)
	Tm(2) - O'(2)	2.322(2)	2.277(2)
	Tm(2) - O(3)	2.283(2)	2.279(5)
Er	Er(1) - O'(1)	2.107(2)	2.108(2)
	Er(1) - O'(2)	2.366(3)	2.437(2)
	Er(1) - O(2)	2.302(1)	2.273(4)
	Er(1) - O(3)	2.426(2)	2.426(1)
	Er(2) - O'(1)	2.408(2)	2.392(2)
	Er(2) - O(1)	2.471(4)	2.414(3)
	Er(2) - O'(2)	2.502(1)	2.315(3)
	Er(2) - O(3)	2.380(3)	2.403(1)
Dy	Dy(1) - O'(1)	2.214(1)	2.298(2)
	Dy(1) - O'(2)	2.224(2)	2.236(1)
	Dy(1) - O(2)	2.473(3)	2.467(3)
	Dy(1) - O(3)	2.362(4)	2.341(2)
	Dy(2) - O'(1)	2.321(2)	2.234(3)
	Dy(2) - O(1)	2.430(1)	2.397(3)
	Dy(2) - O'(2)	2.492(3)	2.467(1)
	Dy(2) - O(3)	2.394(2)	2.367(1)

The reliability factors of these analysis are listed in Table I . The thermal expansion coefficient (α) which is determined by the variation in the lattice parameters with the increase in the temperature at R = Dy, Er and Tm are 29.4, 31.6 and 28.9 ppm/°C, respectively. Table II shows the atomic distances and the angles of CuO_5 pyramid at room temperature and 80°C. The bond length of Cu and O(3), which is located at the top of the pyramid, and those of Cu-O(1) and Cu-O(2) at 80°C are long in comparison with those at room temperature, whereas the bond angles in the CuO_5 pyramid do not show the large variations as shown in Table II . Therefore, it is suggested that the increment of the volume in the CuO_5 pyramid is consistent with the increase in the temperature. On the other hand, the atomic distances of the R_2O_{11} polyhedron obtained at 80°C are short in comparison with those at room temperature as shown in Table III . Hence, it is considered that the expansions of the lattice parameters changed with the increase in the temperature are induced by the increment of the atomic distances in the CuO_5 pyramid.

The microwave dielectric properties of the R_2BaCuO_5 solid solutions are listed in TableIV. From these dielectric properties, it is recognized that the dielectric constants increase as the ionic radii of rare-earth element are increased and these values vary from 12 to 16. The highest dielectric constant is obtained at R = Gd and the value is 15.96. Thus, the increase in the dielectric constant is caused by means of the increase in the polarization with the increase in the unit cell volume, as the rare-earth elements change in the ionic radii. The temperature coefficients of the resonant frequency (τ_f)are ranging from -41.7 to -6.4. The good τ_f value is obtained at R = Dy and the value is - 6.4 ppm/°C. In addition, the temperature coefficient of dielectric constant (τ_ε) is determined by the following equation: $\tau_f = -(\tau_\varepsilon/2 + \alpha)$. Here, the τ_ε on R = Dy, Er and Tm are -46.0, -10.8, -28.2 ppm/°C, respectively.

Since the values of these τ_ε are negative, it is suggested that these dielectric constants decrease as the temperature increases. Therefore, it may be account for the

Table IV Dielectric properties of R_2BaCuO_5 solid solutions.

R	Dr (%)	d (mm)	h (mm)	f (GHz)	ε_r	$Q \cdot f$ (GHz)	τ_f (ppm/°C)
Yb	89.5	10.046	5.098	11.051	13.8	62741	-42.8
Tm	84.1	10.766	4.989	11.363	12.8	14409	-14.8
Er	87.1	10.416	5.089	11.056	13.5	12564	-26.1
Ho	93.4	10.214	4.994	10.561	15.3	9360	-19.3
Dy	90.2	10.225	5.179	10.486	14.9	31617	-6.4
Gd	83.9	10.076	5.168	10.203	16.0	3324	-27.7

* Defined as follows: R—rare-earth element; Dr—relative density; d, h—dimension of the samples; f—resonant frequency; ε_r—dielectric constant; $Q \cdot f$—quality factor; τ_f—temperature coefficient of the resonant frequency.

variation in the polyhedron with the increase in the temperature of the unit cell, so the variation in volume of the polyhedron and the τ_f are interrelated in the usual way. In CuO_5 pyramid, since the atomic distances in the pyramid are increased as mentioned above, the variation in the volume of the CuO_5 pyramid does not coincide with the results of τ_f. However, the variations in the volume of R_2O_{11} polyhedron with the increase in the temperature are consistent with the results of τ_f, so that the atomic distances of the polyhedron at 80 °C are small in comparison with those at room temperature as described above. Therefore, in this case the τ_f is considered to be influenced on the variation in the volume of R_2O_{11} polyhedron with increasing the temperature. The $Q \cdot f$ value of the solid solutions are ranging from 3000 to 63000 GHz, and the highest $Q f$ is 62741 GHz in Yb_2BaCuO_5. The $Q \cdot f$ value closely relate to the internal strain of the crystal structure. Thus, it is shown that the $Q \cdot f$ value of Dy is higher than those of Tm and Er, because O1-O1, O'1-O'1, O2-O2 and O'2-O'2 distances, or the internal strain, in the direction of b-axis in R = Dy at room temperature are smaller than those in R = Er and Tm.

4. Conclusion

The R_2BaCuO_5 solid solutions were synthesized by the solid state reaction method and all the samples conform the solid solution. The dielectric constants of the solid solutions are changed from 12 to 16, and it is recognized that the dielectric constants increase as the ionic radii of rare-earth element are increased. Therefore, the variations in the dielectric constant are considered to be caused by the ionic size, the ionic radii, of rare-earth elements. The τ_f is ranging from -43 to -6.4 ppm/°C, and the suitable value is -6.4 ppm/°C obtained in Dy_2BaCuO_5 solid solution. Moreover, it is shown that the variations in the volume of R_2O_{11} polyhedron influence on the τ_f with an increase in temperature. The $Q \cdot f$ value varies from 3000 to 63000 GHz and the highest one obtained in this study is 62741GHz in Yb_2BaCuO_5 solid solution. Moreover, it is suggested that the quality factors of the solid solutions relate to the strain of the R_2O_{11} polyhedron in the direction of b-axis.

References

1) M.Watanabe, H. Ogawa, H.Ohsato and C. Humphreys: Jpn. J. Appl. Phys. 37 (1998) 5360.

2) H. M. Rietveld: J. Appl. Crystallogr. **2** 65 (1969).

3) F. Izumi: "Rietveld Method", ed. by R. A. Young (Oxford University Press, Oxford 1993) Chap. 13.

4) B. W. Hakki & P. D. Coleman: IRE Trans: Microwave Theory & Tech. **MTT-8** (1960) 402.

The Rapid Progress of Organic Package
for Semiconductor Integrated Circuit

Masami TERASAWA and Takuji SERI

Organic Material Components Division,
KYOCERA CORPORATION
6 Takeda-Tobadono-cho, Fushimi-ku, Kyoto, 612-8501, Japan
Fax: 81-075-674-3411, e-mail: masami-terasawa@kyocera.co.jp

ABSTRACT

Organic package technology is one of the most desired styles which meet the market needs. The major advantage of the organic packages is electrical performance. The use of the less expensive epoxy resin offers a cost advantage, while the low dielectric constant epoxy coupled with the high electrical conductivity copper offers higher electrical performance over ceramics.

The organic packages are classified under two structures. Packages with single layer structure have difficulty in controlling the impedance and reducing the inductance especially in high clock frequency area. On the other hand, packages with a multilayer structure are easier to control electrical performance. As electronic devices become faster, further improvements of the assembly area for ICs with higher pin counts and of electrical performance are required. The high-density printed circuit board package such as build-up printed circuit board package is available as a desired solution.

Further increase of pin counts on a semiconductor and higher performance require significant changes. Meeting the requirements necessitated a radical change in the conventional technology. Packages and ICs are recognized to be more and more inseparable from each other.

1. INTRODUCTION

Organic package technology is one of the most desired styles that meet the market needs. The clear winners will be those that understand the electrical, thermal and mechanical requirements to interconnect electronic devices and are able to standardize them to meet the needs of the market. The explosive growth of optimized high-density packaging has created a great impact on the electronics assembly and manufacturing industry. The purpose of this paper is to review the rapid progress of organic package technology for semiconductor integrated circuit.

The advantages of the organic packages are electrical characteristics, as well as the similar coefficient of thermal expansion of the printed circuit boards. The use of the less expensive epoxy resin offers the cost advantage, while the low dielectric constant epoxy coupled with the high electrical conductivity copper offers higher electrical performance over ceramics. Gradually, the organic packages come to be the main stream due to the development of the resin capacities.

The first dual in-line package (DIP) was constructed of ceramics. The requirement for cost-effectiveness led to the design of a molded plastic DIP (P-DIP). For industry applications a plastic pin grid array (P-PGA) package was developed in order to reduce the cost of a ceramic pin grid array (C-PGA) package as pin insertion type packages. A small outline package (SOP) and a quad flat package (QFP) have emerged in accordance with the needs for the surface mount technology (SMT), as well as ball grid array (BGA) and tape carrier packages (TCP). For further optimization of the assembly technology, a chip scale package (CSP) technology was introduced. For packages requiring a flip chip mount, a build-up printed circuit board package have been widely adopted in advanced applications.

Increasing pin counts on a semiconductor device to the level for the next generations of packaging requires significant changes in circuit design, pad layout, methods of interconnection and multilayer routing. Meeting the requirements of improved reliability, lower costs, higher density and high speed circuitry in smaller packaging space necessitated a radical change from conventional technology.

In this paper, we shall review the rapid progress of organic packaging for semiconductor integrated circuits. This paper is organized as follows: In section 2, a brief overview of products and ICs trends is summarized. Then, the progress of organic packages is presented in section 3. In section 4, one of the Kyocera's organic package technologies, High Density Build Up (HDBU(TM)) technology, is introduced and described. Lastly, a brief summary and perspectives are given in section 5.

2. PRODUCT AND IC TRENDS

There is an accelerating trend in the electronics industry towards portable products. It is estimated that more than 20 percent of all computers produced today are portable. Many of these products are relatively low cost, such as portable phones, laptop computers, personal digital assistants (PDAs) and digital camcorders.

One of the highest volume applications is the portable phone. An example of a portable phone is shown in figure 1. With an increasing drive for less weight and small size, the portable phone makers have been able to achieve their miniaturization targets.

Fig. 1 An example of a portable phone. It is one of the Kyocera's cellular phones. It is about 59g in weight, 40mm in width, 125mm in height and 17mm in depth.

As electrical applications become light and small, electronic devices are required to have higher performance and pin counts because many functions are being integrated into one chip. This industry trend of increased integration and reduced device size leads to rapid packaging development. The challenges are changes in circuit design, bond pad layout, a method of the interconnection and package routing density. Many leading electronic companies are now faced with developing, emerging and advanced technologies quite rapidly.
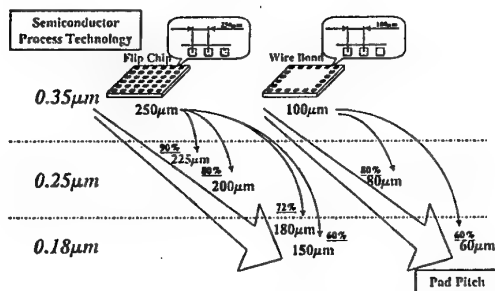

Fig. 2 The road map of MPUs and ASICs die pad pitch.

There is another trend of high performance towards higher frequency products. As the pin counts on a semiconductor integrated circuit increase, the pad pitch becomes gradually narrower. Figure 2 shows the road map of MPUs and ASICs die pad pitch. Since the semiconductor fine pitch technology has been developed, the die pad pitch becomes narrower from 0.35um to 0.18um, which requires high density and fine geometry package development due to the die pad pitch shrinkage.

The microprocessor is the brain of a computing system. Some well-known ones are Intel's microprocessor family and AMD's based on complex instruction set computing (CISC). Other well-known ones are IBM and Motorola's microprocessor family based on reduced instruction set computing (RISC). Both CISC and RISC microprocessors are expected to require more than 1,000 pin counts in devices and to perform over 400MHz clock frequency.

In the ASIC field, the package pin count is growing up to more than 3,000 and the means of interconnection between a device and a board fall into difficulties.

3. PROGRESS OF ORGANIC PACKAGE
3.1 OVERVIEW

As the chip and its embedded circuitry are delicate, the package is required to both carry and protect the IC chip. The major functions of the package are to:

1) supply the electrical power on the IC chip
2) distribute signals on and off the IC chip
3) remove the heat generated by the IC chip
4) support and protect the IC chip from hostile environments
5) transform the input/output (I/O) pitch
6) standardize the assembly

For consumer applications, low cost is most important. Since the major factor driving the cost is the area of a package, the smaller the area is, the lower the cost becomes. A package with fine pitch is required.

On the other hand, the performance is important for industry applications. Because of the requirements of high clock frequency, a package will often have more layers and the circuit will often be carefully routed. Also a package will often become minimized in order to improve the electrical performance. Fine design rules and multilayer routing are required due to the increase of higher pin counts. The downsizing of an engineering work station (EWS) and a personal computer (PC) requires a package with higher performance and lower cost.
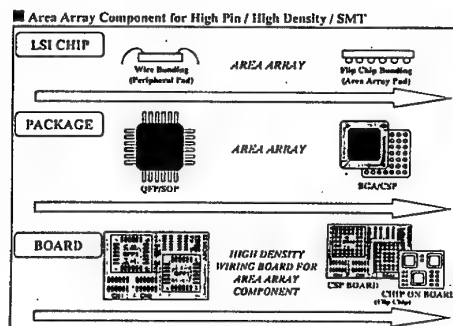
Fig. 3 The trend of organic packages.

Different applications and ICs require different packaging technologies. Figure 3 shows the trend of organic packages. IC packaging trends are classified under three application categories. According to pin pitch and pin counts, the use of package changes. Methods of chip connection, the chip direction and the material change also.
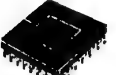
For high-end ASIC and MPU, a plastic BGA (P-BGA) package is applied. A P-BGA is a surface mount package and mounted on the assembly boards with use of solder balls. A P-BGA is a small thin package with high pin counts. Electrical performance is much better because the multilayer structure of a P-BGA makes it possible to control the impedance and to reduce the inductance. This is the reason why a P-BGA is adopted in high-end packaging area.

For ASIC and chipset, a plastic QFP (P-QFP) is applied in low pin counts and a P-BGA in high pin counts. A P-

QFP has a limitation of the lead pitch because assembly handling gets tougher and yield gets lower as the lead pitch becomes narrower. Though a P-QFP is cost-effective, a P-BGA is used for high pin count requirements. For memory it is the same trend.

The market requires excellent electrical performance and improvements in the assembly yields with high pin counts. The advantage of organic packages is electrical characteristics, as well as the similar coefficient of thermal expansion of the printed circuit boards. The low dielectric constant epoxy coupled with the high electrical conductivity copper offers higher electrical performance over ceramics, and the reliability for the second level assembly on boards is better for organic packages as compared to ceramic packages.

Table I The changes of typical organic packages.

Through Hole Mounting Technology	Surface Mounting Technology	
	Peripheral Type	Area Array Type
-DIP	-SOP	
-PGA	-QFP	-BGA	-CSP
1970	1980	1990	2000

The organic packages are classified under two structures. Changes of typical organic packages are given in table I. While P-DIP, SOP and P-QFP have single layer structure, P-PGA and BGA have multilayer structure. Packages with a single layer structure have difficulty in controlling the impedance and reducing the inductance especially in high clock frequency. On the other hand, packages with a multilayer structure are easier to control electrical performance and to meet the market needs. As an electronic device becomes faster, better electrical performance is required. The high density printed circuit board package such as a build-up printed circuit board package is expected for one of the solution.

3.2 EARLY ORGANIC PACKAGE

The first DIP was constructed of ceramics, and had an internal cavity for chip mounting. But the semiconductor industry required considerable reduction of IC packaging cost. This requirement of cost-effectiveness led to the design of a molded P-DIP. The P-DIP design was simple, used inexpensive materials, and agreed with mass production. These attributes enabled the P-DIP to become the most popular IC package.

For industry applications a P-PGA has been developed in order to reduce the cost of a C-PGA. An example of a P-PGA is shown in figure 4. The advantages of a P-PGA are low cost, as well as better electrical performance. The use of the inexpensive epoxy resin ruinforced with glass

fiber offers the cost advantage, while the low dielectric constant epoxy coupled with the high electrical conductivity copper offers higher electrical performance over C-PGA.
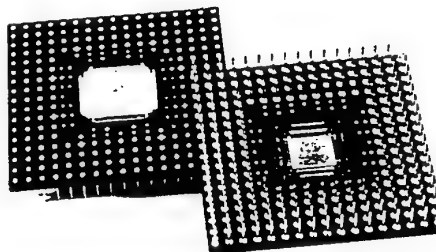
Fig. 4 An example of a P-PGA.

In spite of the low cost and the better electrical performance, reliability is a major concern in P-PGA applications. Thermal management in P-PGA was difficult because of the lower thermal conductivity of organic materials. A P-PGA in which the copper plates are embedded has been developed today.

An SOP because of its small-flat view, however, replaced the P-DIP dominance. An SOP is a very low profile plastic package which is specifically designed for SRAM, DRAM and flash memory devices for space limited applications.

For higher pin counts, the square package with leads on all sides was developed. This P-QFP has the similar molded construction with a P-DIP and an SOP. The P-QFP is one of the most cost-effective surface nount packages. An example of a P-QFP is shown in figure 5. They have been used extensively for ASICs, low performance microprocessors and memory devices. The lead frame of a P-QFP has been standardized for fanning the circuitry.
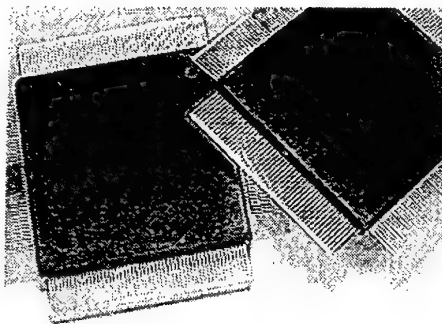
Fig. 5 An example of a P-QFP.

A P-QFP has a limitation of the lead pitch. As the pin counts of a P-QFP increase, the lead pitches required are narrower. As a P-QFP has leads on all sides, the higher pin counts create the difficulty in dealing with leads, which makes the assembly failure higher. In order to accomplish higher pin counts and to eliminate the leads, an area array surface mounted package was focused.

3.3 BALL GRID ARRAY (BGA) PACKAGE

Recently a BGA has been focused on as a surface mounted package solution. The market requires improvements in the assembly yield for ICs with high pin counts. Furthermore, the market requires excellent electrical performance, as well as the similar coefficient of thermal expansion with the printed circuit boards for advanced ICs such as ASICs and microprocessors. The multilayer structure of a BGA agrees well with the market needs. Motorola first developed a P-BGA for portable phone packaging. It was called an over molded pad-grid array carrier (OMPAC(TM)) package at that time. An example and schematic illustrations of the cross section of a BGA are given in figure 6 and figure 7, respectively. As the interconnection between a package and a board changed from a pin insertion type such as a P-PGA to a surface mounting type, the density of circuitry on a board was extremely improved.
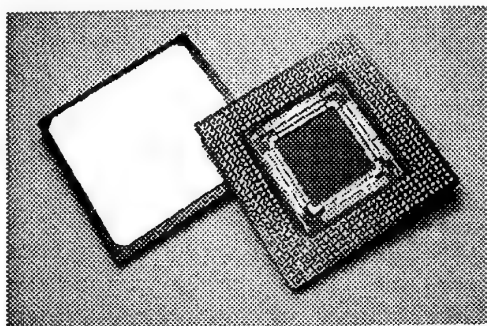
Fig. 6 An example of a BGA.
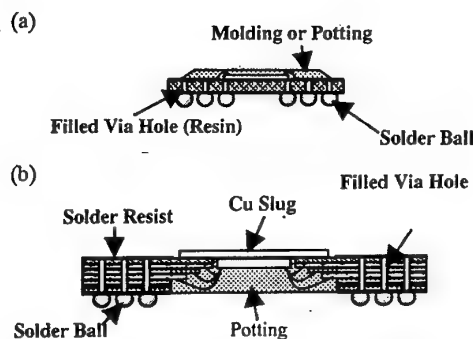
Fig. 7 Schematic illustrations of the cross section of a BGA, (a) 2-4 Layer W/B-PBGA, (b) Multi Layer with Heat Slug W/B-PBGA.

As a BGA is mounted on the assembly boards with use of solder balls, the assembly failure is quite low, which is caused by the surface tension force of the solder balls. This intriguing effect is called the self alignment effect of the solder balls. There is another excellence in assembly in contrast to a P-QFP. As the coplanarity between a package and a board can be relaxed in the solder ball reflow process, the assembly failure is lower also. Because of this excellence and the small area of assembly the total cost is lower, although a P-BGA is more expensive than a P-QFP.

In more than 300 pin count BGAs in particular, the electrical performance is much better than a P-QFP. The multilayer structure of a BGA makes it possible to control the impedance and to reduce the inductance. The merits of a BGA are summarized in table II.

Table II The merits of a BGA.

1. Excellence in Assembly 　(1) Self Alignment Effect of Solder Balls 　(2) No Transformation of Leads 　(3) Relaxation of Coplanarity 　　　between Package and Board
2. Excellence in Cost Reduction 　(1) Low Assembly Failure 　(2) Small Area of Assembly
3. Excellence in Electrical Performance 　(Especially in More Than 300 Pin Counts) 　(1) Easy Impedance Matching 　(2) Low Inductance

There are several types of BGAs, a ceramic BGA (C-BGA), a metal BGA (M-BGA), a tape automated bonding BGA (T-BGA) and a P-BGA. A C-BGA, an M-BGA and a T-BGA can meet the high pin counts, high power and high clock frequency requirements, but with higher costs. In an M-BGA, Cu alloys and aluminum are often used as base metal substrates. An M-BGA is excellent in lower thermal resistance. Table III shows the classifications of BGAs. A package type is classified from view points such as substrates, chip connection methods, chip directions and materials of solder balls. Several package types are proposed in combination with them.

Table III The classification of a BGA.

Substrate	Chip Connection	Chip Direction	Solder Ball
-Ceramic -Metal -Tape -Plastic	-Wire Bonding (WB) -Tape Automated Bonding (TAB) -Flip Chip	-Face up -Face down	-Eutectic -High Temperature Melting Point

Another BGA package type is a TCP. A TCP is one of the best excellent package styles for less thickness and high pin counts. A TCP offers smaller pin pitches, smaller footprints and thinner package profiles on the printed circuit board. A TCP mounts ICs on film resin with the tape automated bonding (TAB) technology. The film resin is often composed of polyimide, which is excellent in bending rigidity. An schematic illustration of the cross section of a TCP is described in figure 8. TCP can provide moderate performance solutions for applications such as ASICs, microprocessors and memory modules. Many microprocessor producers use a TCP to house microprocessors for portable computers.

A TCP have been successfully applied in drivers of liquid crystal displays because of its thin thickness, small size and fine pitch. As even further minimization of outer lead pitch is possible, a TCP has been applied more and more to ASICs, microprocessors and memory modules with higher pin counts.

Fig. 8 An schematic illustration of the cross section of a TCP (T-BGA type).

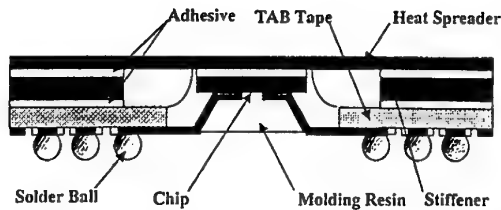We should note, however, that a TCP may not be cost-competitive due to the high development cost caused by an expensive resin tape such as film polyimide unless the TCP is produced in high volume. Also, a TCP suffers similar weakness to the P-QFP such as a peripheral chip carrier, long lead length, handling and yield loss.

Recently the BGA by use of TAB technology has been developed in order to meet the cost requirement. As this uses resin tape, it is called a T-BGA. A T-BGA is expected not to be so expensive while keeping its several advantages.

3.4 CHIP SCALE PACKAGE (CSP)

For further requirements to improve the assembly area for ICs with higher pin counts and to improve the electrical performance, a CSP has been gradually adopted for advanced applications. A CSP is often included as a BGA type package from the point of view of an area array mounting type packaging. A CSP is about 20 percent larger than the chip. An example of a CSP is shown in figure 9.
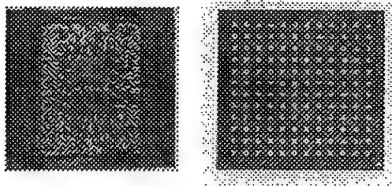
Fig. 9 An example of a CSP.

In order to meet the requirement for further electrical and thermal performance improvements as well as less weight, flip chip technology is now widely used. The flip chip technology is suitable for single chip modules with very high pin counts and performance requirements.

3.5 BUILD-UP PRINTED CIRCUIT BOARD PACKAGE

As electronic devices become faster, the package pin counts are increasing. For example, in the ASIC field in particular, the package pin counts are growing up to more than 3,000 and the means of interconnection between a device and a package are more important.

On the other hand, fine design rules and higher performance are also required for boards. IBM has performed this new approach first. The new high-density printed circuit boards, which are called build-up printed circuit boards, have been developed with photo imaging and laser drilling. They are manufactured by sequential fabrications of an insulation layer and a conduction layer.

This new technology and fabrication process are based on earlier development and production of the multilayer thin film copper and polyimide processes currently supplied in high volume with the semi-additive plating method.
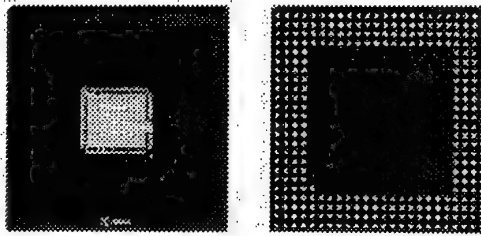
Fig. 10 An example of the build-up printed circuit board package.

For the last few years this board fabrication technology has been applied to a package which requires higher performance. This package also has several advantages of an organic multilayer one and meets recent severe requirements. This is the reason why the use of the build-up printed circuit board package is accelerating today. An example of the build-up printed circuit board package is shown in figure 10. Smaller vias, both blind and buried vias provide the solution. A further major advantage of these small blind and buried vias comes to be significant reductions in design time.

4. KYOCERA HIGH DENSITY BUILD UP (HDBU(TM)) PACKAGE

Recent requirements for electronic equipment with the higher performance have been accelerating the miniaturization of various electronic devices. For the needs in high-density surface mounting technology, Kyocera has achieved fine design rules where the via diameter is 50um and the line/space widths are 30um for build-up circuit board package using the dry film lamination/laser via fabrication method. Kyocera has developed the high-density build up (HDBU(TM)) package. A schematic illustration of the cross section of the HDBU package is described in figure 11.
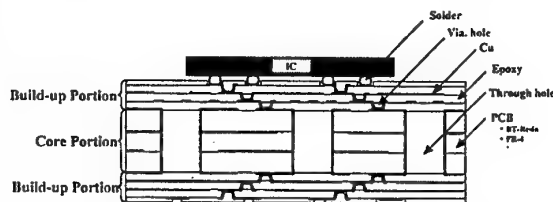
Fig. 11 A schematic illustration of the cross section of the HDBU package.

In HDBU, thermosetting epoxy resin is applied to form the build-up insulation layers. Kyocera uses it as dry film and the dry film lamination process has proved to be a simple process.

The HDBU package is developed with use of the laser techniques for via formation. As thermosetting epoxy resin is used to form the build-up insulation layers, high

energy and short pulse CO_2 laser has proved to be a high quality and cost-effective method of fabricating vias. An example of the HDBU package is shown in figure 12.
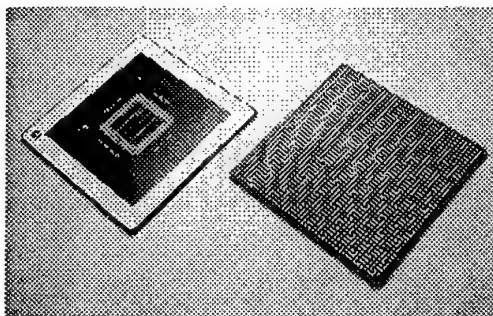
Fig. 12 An example of the HDBU package.

The increasing need for high density processing has resulted in the emergence of the build-up printed circuit board package. CO_2 lasers have enabled high quality, high speed and cost-effective processing of organic materials. Further fine geometry vias are expected to be fabricated easily.

As we have described above, this technology has made it possible to supply the most advanced packages with high pin counts and performance.

5. SUMMARY AND PERSPECTIVES

In this paper, we have reviewed the rapid progress of organic packages for semiconductor integrated circuits. Various organic packaging technologies, such as P-DIP, P-PGA, SOP, QFP, BGA, TCP and CSP have been described.

The organic packages are classified under two structures. While P-DIP, SOP and P-QFP have single layer structure, P-PGA and BGA have multilayer structure. Packages with single layer structure have difficulty in controlling the impedance and reducing the inductance especially in high clock frequency areas. On the other hand, packages with multilayer structures are easier to control electrical performance and meet the market needs. As electronic devices become faster, further improvements of the assembly area for ICs with higher pin counts and greater electrical performance are required. Understanding the market needs, the package profiles have changed and the packaging technologies have developed.

Further increase of pin counts on a semiconductor and higher performance for the next generation of packaging requires significant changes in circuit design, pad layout and methods of interconnection. Meeting the requirements of improved reliability, lower costs, higher density and high speed circuitry necessitated a radical change in the conventional technology. Packages and ICs are recognized to be more and more inseparable from each other.

ACKNOWLEDGMENTS

REFERENCES

[1] J.H.Law, Proc. IEMT/IMC, 32-36 (1997).
[2] P.V.Robock and L.T.Nguyen, "Microelectronics Packaging Handbook", Ed. by R.R.Tummala and E.J.Rymaszwski, van Nostrand Reinhold, New York (1989) pp.523-554.
[3] E.J.Vardaman and L. Matthew, Proc. 2nd Annual Semiconductor Packaging Symposium, 7-A (1999).
[4] M.Harazono, Y.Iwata and S.Takami, Proc. IEMT/IMC, 82-85 (1997).
[5] S.Ohwada, M.Harazono, H.Yugawa, S.Yoshiura and K.Kume, Proc. 2nd Annual Semiconductor Packaging Symposium, 6-B (1999).

Development of Novel Piezoelectric Actuators by Solid Freeform Fabrication Methods

A. SAFARI

Department of Ceramic and Materials Engineering, Rutgers University
607 Taylor Rd., Piscataway, NJ 08854, USA
Fax: 732-445-5577 / 3258   e-mail: safari@rci.rutgers.edu

Abstract- Novel piezoelectric ceramic, and ceramic /polymer composite structures were fabricated by solid freeform fabrication (SFF) techniques for sensor and actuator applications. SFF techniques including: Fused Deposition of Ceramics (FDC) and Sanders Prototyping (SP) were utilized to fabricate a variety of complex structures from computer aided design (CAD) files. Many novel and complex composite structures including volume fraction gradients (VFG) and radial tube composites, and actuator designs such as tubes array, spiral, and telescoping actuators were made using the flexibility provided by the above processes. Radial composites with various connectivities in the radial direction were made for towed array applications. VFG's were incorporated into some of these designs, with the ceramic content decreasing from the center towards the edges. Multi-material actuators are also being developed to manufacture high authority actuators utilizing the FDC technique. The design, fabrication, and electromechanical properties of these transducers for sensor and actuator structures are discussed in this paper.

1. INTRODUCTION

At present, piezoelectric ceramics and ceramic / polymer composites with novel designs are being widely studied for sensor and actuator applications [1,2]. This is because of their electromechanical properties, which can be tailored by changing the shape and spatial distribution of the ceramic material in the design. Traditional ceramic processing techniques such as dice and fill, and injection molding are either too restrictive in the types of designs that can be fabricated or are too costly and time consuming to fabricate novel ceramic skeleton structures. The advent of a new manufacturing / prototyping technique to fabricate polymer, ceramic, and metal components with very high design flexibility for novel structures and fast prototyping has generated a lot of interest among material scientists.

Solid Freeform Fabrication (SFF) is an emerging technology that provides an integrated way of manufacturing 3-D components, from computer aided design (CAD) files to finished parts, using primarily "additive processing". Additive processing implies that the structures are made by cumulative deposition of material, without using any hard tooling, dies, molds, or machining operations [3]. Over the last decade, several SFF methods have been developed as techniques to fabricate polymer, metal or ceramic structures on a fixtureless platform, directly from a CAD file. There are three general application areas of SFF – prototyping, high cost-low volume components, and mold and die fabrications. The parts that are made by conventional processing techniques are economically feasible only if large number of parts is produced. The cost per part is very high for small number of components. Hence, solid freeform fabrication can be used for rapid prototyping (RP) of a small lot of new research designs more economically than traditional processing techniques [3].

Traditionally, SFF techniques have been used to fabricate polymer parts for form and fit applications. However, in the past few years there have been rapid advancements in the technology for the manufacture of ceramics and metal components. At Rutgers University, Fused Deposition Modeling (FDM^{TM}), Fused Deposition of Ceramics (FDC), and Sanders Prototyping (SP) have been used to fabricate a variety of ceramics and metal parts, for applications in electroceramic, structural, bio-ceramic, and metal tooling [4,5]. In this paper, the SFF processing methods and some of the novel piezoelectric composite sensors and ceramic actuator designs with their electromechanical properties are discussed.

2. EXPERIMENTAL

For this work, the SFF techniques were used in two different ways: (a) direct route, by fused deposition of ceramics (FDC) and (b) indirect route or lost mold process, by FDM^{TM} or SP. In the direct processing route, FDC was used with a PZT powder loaded polymer filament as the feed material for the direct layered manufacturing of green ceramic structures. In the indirect route, Stratasys^{TM} ICW-06 wax filament or Sanders wax material was used to fabricate molds. A lost mold technique was then used to create the final structure. The details of the two processing routes and the steps in the electromechanical characterization of the sensors and actuator designs are described below.

In the direct method (FDC), filaments loaded with 55-vol.% PZT-5H powder were fabricated from the ECG-9 binder composition developed at Rutgers University [6]. The powders were pre-coated with stearic acid, and dried before compounding. Compounding was accomplished at 160°C using a

Haake System-9000 torque rheometer and a twin-roller blade mixing bowl operating at 100 rpm. Continuous spoolable filament, hundreds of meters long and 1.75 mm in diameter was extruded using the same torque rheometer with a single screw extrusion attachment. Fused deposition of these filaments was accomplished using a modified Stratasys 3D Modeler™ (Stratasys Inc., Eden Prairie, MN). The liquefier temperature was maintained at ~ 140°C while the temperature of the surrounding environment was in the range of 30-40°C. The structures were built using a 300-500 μm diameter nozzle. The road widths were also set at 300-500 μm, and the slice thickness was set at 250 μm. The parts were built layer-by-layer until the desired structure was completed.

In the indirect method, sacrificial polymer molds having the negative of the desired structures were fabricated via the FDM™ or SP processes. Commercially available investment casting wax (ICW-06, developed by Stratasys) was used by the 3D Modeler™, while the Sanders prototyping machine also utilized a wax based build material to make the molds. Water based ceramic slurry with 52 vol.% PZT loading was specifically developed for this process. After infiltrating with the slurry and drying, the thermoplastic polymer mold was evaporated using a specific thermal cycle during the early portion of the binder burnout step.

All the green parts made by the indirect and direct techniques were subjected to a careful heat treatment cycle of binder burnout to 550°C and sintering at 1285°C. The composite specimens were either poled conventionally or in a corona poling apparatus. The d_{33} coefficient of the composites was measured at 100 Hz using a piezo d_{33} meter. For the actuators, a fiber-optic photonic sensor (MTI-2000, Mechanical Technologies, Inc.) was utilized to measure the displacement as a function of the applied voltage. The effective d coefficient of the actuators was computed from these measurements based on $d_{eff} = t.\Delta l/l.\Delta V$. Where, t, ΔL, and L are the thickness, the displacement, and the length of spiral actuators and ΔV is the applied voltage.

2.1 Binder Development

Binder development is essential for the FDC process using ceramic materials like PZT. Therefore, a brief description of the binder processing and properties is given below. The binder formulations developed for the FDC process were comprised entirely of commercially available polymers, and exhibited properties adequate for usage in combination with PZT, calcium phosphate, alumina, stainless steel, and carbon powder filler. The binder consisted of a base binder, tackifier, wax, and plasticizer. The ECG-9 formulation has been shown to be superior to the other formulations based on mechanical, rheological, and thermal property requirements. The viscosity of the binder had to be adjusted in order to be used in the FDC process. As an example of rheological studies, Figure 1 compares the viscosity vs. shear rate for several formulations in the ECG series. ECG-9 consists of 100 parts of a poly-olefin base binder (by weight), along with 20 parts of a hydrocarbon resin tackifier, 15 parts of a polyethylene

wax, and 5 parts of a polybutylene plasticizer. The ECG-9 formulation was compounded in 50-60 vol.% powder-loaded systems, and extruded into filament with a nominal diameter of 1.75 mm. Figure 2 is a viscosity vs. shear rate plot for several PZT-loaded systems. The resulting filaments were used to fabricate various functional ceramic parts via FDC.

A study of the adsorption of several surfactants onto PZT powder was performed. The adsorption of oleyl alcohol, stearyl alcohol, oleic acid, and stearic acid onto PZT-5H powder (surface area = 2.58 m²/g) in a toluene medium was measured by thermogravimetric analysis. It was found that the stearic acid adsorbed onto the PZT-5H powder the most, to the extent of 8.1 mg/m². Trace amounts of stearyl alcohol adsorbed onto PZT, showing an adsorption of 0.8 mg/m². Once stearic acid was found to be a suitable surfactant for the PZT/ECG system, the coating process was studied to further optimize the amount adsorbed. A total of 6 solution concentrations, varying from 5 g/l to 70 g/l stearic acid in toluene, were tested. It was found that a solution concentration of 30 g/l stearic acid was sufficient to provide maximum coverage of the PZT surface.

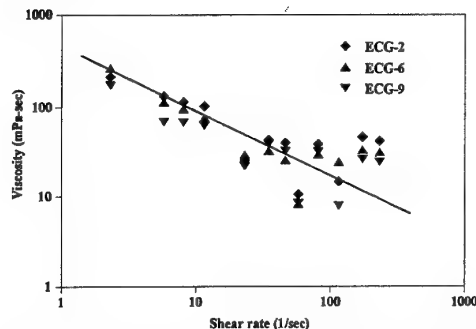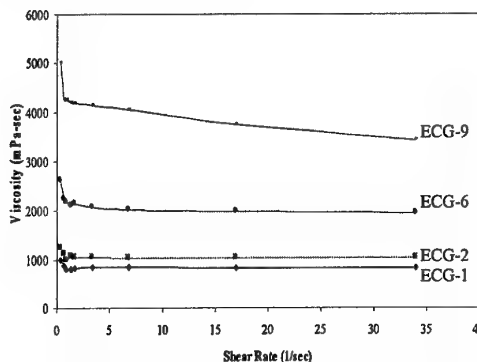Figure 1. Viscosity versus shear rate for several ECG-series binder formulations.

Figure 2. Viscosity versus shear rate for several 55 vol.% PZT loaded systems measured at 160°C.

3. RESULT AND DISCUSSION

3.1 Volume Fraction Gradient Composites

Volume fraction gradient (VFG) composites can be utilized to reduce the side and grating lobes in ultrasonic medical imaging transducers [7]. Many

— 390 —

different gradients including 2-2 Gaussian, linear, and exponential composites were fabricated by the indirect SFF route. The volume fraction of ceramic in all these composites was varied from 60-vol.% at the center to 20-vol.% at the edges. The ceramic wall width was kept constant at 115 μm, and the spacing between the walls was increased from the center to the edges. All the VFG structures had clean thickness mode resonance with high values of thickness coupling coefficient (>66%) and moderately low values of the k_p (<28%). The d_{33} of all these structures was also greater than 400 pC/N. The vibration profiles of the 2-2 composites with and without VFG's, as a function of the distance from the center, are shown in Figure 3. These measurements were taken by measuring the displacement of the composites using a photonic sensor.
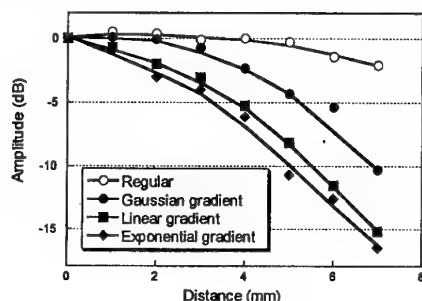

Figure 3. Vibration amplitude vs. distance Profiles for 2-2 regular and VFG composites.

The pressure outputs of the VFG designs were compared with a regular 2-2 composite, which was a diced PZT-5H ceramic structure having a wall width of 220 μm and a kerf of 440 μm. The regular design had ~ 33 vol.% total ceramic content with a d_{33} and k_t of 340 pC/N and 63% respectively. As expected, the amplitude of the vibration for the regular 2-2 composite did not vary much with the distance from the center to the edge. On the other hand, all the VFG distributions showed a decrease in the vibration amplitude with distance from the center to the edge of composite. The Gaussian VFG was designed to have the ceramic volume fraction fall very slowly with distance and hence, the vibration amplitude initially remained constant and later dropped by only –4 dB at a distance of 5 mm. Thus, this distribution was not very different from the regular 2-2 composite up to 5 mm from the center. The linear gradient showed a very smooth decline in the vibration amplitude with distance, falling linearly to about –8 dB at a distance of 5 mm. The exponential distribution had a vibration profile that was slightly lower in amplitude than the linear distribution.

PZFLEX (Weidlinger Associates, Los Altos, CA) finite element modeling studies were done to predict the effect of a volume fraction gradient on the acoustic beam pattern. Results for three different types of composites, including a regular, Gaussian, and a linear VFG distribution were modeled. The side lobe level was found to decrease significantly with the introduction of a VFG. The best results were obtained for a linear volume fraction gradient, with a reduction

in the level of the side lobe by -12 dB from the normal distribution. A model of the exponential distribution also showed a decrease in the side lobe intensity, but it was nearly equal or slightly higher than the linear distribution. Based on the vibration amplitude profile and PZFLEX modeling data, the linear distribution was expected to show the lowest off axis sensitivity.

3.2. Radial Composites

In current Naval undersea towed array systems, the hydrophone element consists of a monolithic ceramic tube poled in the radial direction. Like their planar counterparts, monolithic ceramic tubes suffer from similar deficiencies, such as high weight, low sensitivity, and low figure of merit $d_h g_h$. Until recently, the fabrication of functional piezoelectric composites with radially-oriented connectivity has been difficult or impossible using conventional processing. With the advent of Rapid Prototyping, these types of composites can be fabricated with relative ease. In this work, three different connectivities are being studied. These consist of 2-2, 3-1, and 3-2 type composites. For the purpose of simplicity, cylindrical coordinate systems are being used to designate the connectivity of each composite design. For 2-2 type composites, both the ceramic phase and the polymer phases are continuous in the radial (r) and z directions. In the case of 3-1 type composites, the ceramic phase is continuous in all three directions (r, θ, z), while the polymer is continuous in only the z direction. Finally, for the 3-2 type composites, the ceramic phase is continuous in all three directions, while the polymer phase is continuous in the z and θ directions. Radially oriented composites have been made using both direct and indirect methods. Figure 4 (a) shows the photograph of a tubular 2-2 PZT ceramic preform made using the FDC technique. In this structure, the inner and outer ceramic rings are approximately 1 mm in thickness, and the ceramic sheets connecting the inner and outer rings are approximately 1 mm thick by 3 mm wide. Figure 4 (b) is a picture of a 3-1 ceramic preform made using a Sanders Prototyping MM-6Pro rapid prototyping system. A wax mold is made using the Sanders Prototyping machine, and is then infiltrated with an aqueous-based PZT slurry. The mold is thermally removed, leaving the desired composite preform. Samples were embedded in epoxy, and machined to dimensions of 8 mm inside diameter, 14 mm outside diameter, and 10 mm in height. The composites were poled radially using the corona discharge method, and their hydrostatic piezoelectric response was measured using a hydrostatic acoustic chamber. Table 1 summarizes the preliminary electromechanical properties of the 3-2 tube composites only with the properties of solid tubes prepared by the FDC method.

3.3. Tube Actuators

The direct FDC method has successfully been employed in developing tubes and tube array actuators for broad band as well as resonant transducer and sensor applications. Several tubes with various outer diameter, wall thickness, and height have been

TABLE 1. Electromechanical properties of radial tube composite transducers.

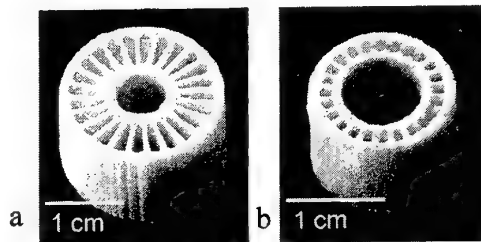| Sample	Dielectric Const.	Hyd. Ch. Coeff. (pC/N)	Vol. Fract. Ceramic (%)
3-2 Composite	1450±100	42.4	77
Solid tube	2064±100	26.0	100

a 1 cm   b 1 cm

Figure 4. Photograph showing (a) a sintered PZT-5H preform with a 2-2 connectivity processed by the direct FDC route and (b) a 3-1 structure made by the indirect route.

fabricated by FDC, and the deposition parameters were optimized to achieve defect-free tube arrays. Figure 5 shows sintered 2x2 and 4x4 as well as green 5x5 tube arrays. Single tubes with high densities (96% theoretical) were radially poled at 18 kV/cm electric field.

2 cm

1cm
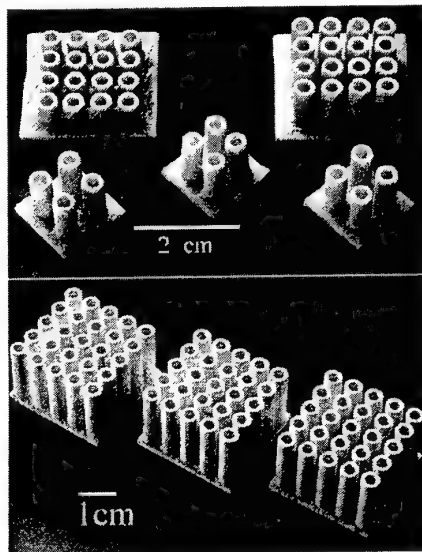
Figure 5. Photograph of sintered 2x2 and 4x4 tube arrays (top) and green 5x5 tube arrays fabricated by direct FDC method.

Electromechanical measurements were carried out in an applied bias of 200 V at 5 Hz (strain-voltage measurements) and also in applied AC voltage of 60

Volts from 10 Hz to 100 kHz (frequency measurements). Displacement versus voltage curves showed a small hysteresis and good linearity with applied voltage. Two resonance frequencies were observed for a tube at 1 kHz and 90 kHz, probably due to base vibration and tube axial extension mode. The quasi-static displacement curve indicated an effective axial d coefficient value of 170 pm/V up to 1kHz .(Figure 6).

In addition to tubes with straight walls, a new type of tube actuator, called bellows, was also investigated. Figure 7 shows an example of bellows tube. Fabrication of bellows has shown that deformation may take place since there is minimal support during deposition. In fact, low angle bellows (30° or lower) is hard to make since it either deforms during deposition or delaminates after deposition. On the other hand, higher angle bellows can be made by FDC without any difficulties.

Bellows and straight tubes of similar height, outer dimensions and wall thickness were fabricated by FDC technique. Figure 8-a shows the schematic of the straight and bellows (45 and 60° angle) tubes.
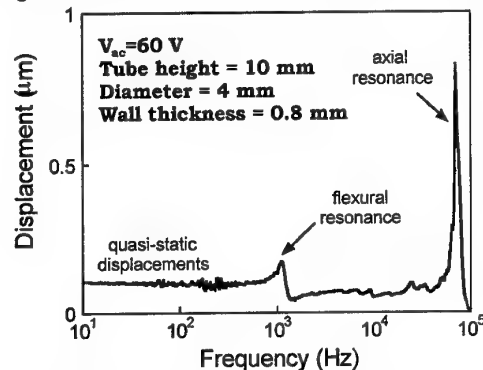
Figure 6. Vibrational spectrum of a single tube, indicating bending and axial resonance at about 1 and 90 kHz.

1 cm
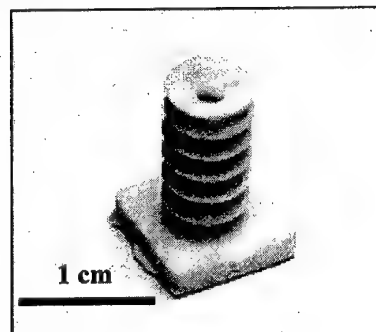
Figure 7. A sintered bellows tube made by the FDC technique.

The electromechanical properties of the straight and bellows tubes were measured and showed that the axial displacement of the radially-polled tubes is smaller for the bellows.. Figure 8-b shows the axial displacements as a function of inner to outer diameter ratio for three sets of tubes. Although it may seem that the larger effective length of the bellows, in comparison with

straight tubes, provides higher axial displacement, the results show the opposite where the straight tubes have higher axial displacement. The lower displacement of the bellows can be attributed to the particular structure that constrains displacement in the axial direction.
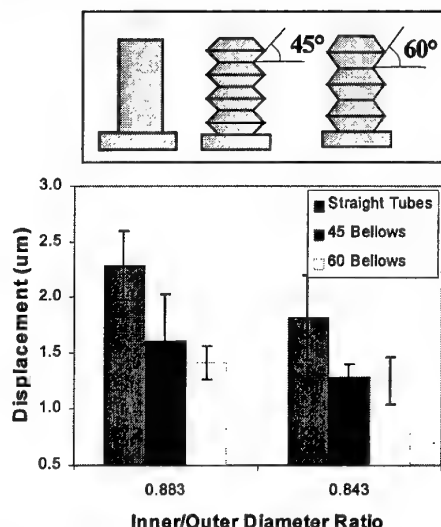
Figure 8. (a) Schematic of straight and bellows tubes. (b) Axial displacements of two sets of straight and bellows (45 and 60°) tubes, indicating lower displacement of bellows (Tube length 12 mm, outer diameter 2.6 mm, bipolar driving at 180 V, 5 Hz, peak to peak values).

3.4. Spiral Actuators

A new type of monolithic actuator with spiral geometry was developed and prototyped by FDC. The idea was to utilize the d_{31} displacement of high length-to-thickness ratio samples in spiral geometry (Figure 9). The spiral walls consisted of 1-4 roads deposited next to each other. The actuators were poled radially (in the wall thickness direction) and driven with an electric field applied in the poling direction. The spirals used for electromechanical measurements consisted of five turns with an outer diameter and wall width of 30 mm and 0.95 mm, respectively. The effective length of the spirals was 26 cm with a height (in the z direction) of 3.7 mm. The spiral actuators produced a large tangential (parallel to the spiral tip) displacement, Δl, of about 210 µm when a voltage (V_t) of 500 V was applied across the wall thickness. Theoretical calculations showed that a straight strip of PZT with the same length and thickness as the spirals would produce only 34 µm displacement at 500 volts (Figure 10). The effective piezoelectric coefficient of spiral actuators in the tangential direction was about 1,500 pm/V. By tailoring the geometry of the spiral actuators (effective length, number of turns, and wall thickness) this value is expected to further increase. The results demonstrate that the spiral actuators produced by FDC are promising for actuator applications.

Among other parameters investigated are the effect of wall width and effective length of the spiral actuator on

the tangential displacements and frequency of the fundamental resonance. Figure 11 shows the dependence of the above mentioned parameters on the effective length of the spiral. The effective length was changed by consecutive cutting off the ends of an actuator. As expected, the resonance frequency increases and displacement decreases on shortening the length of the spiral. The increase in the resonance frequency can be explained by both increasing the spring constant of the spiral and decreasing the spiral mass. Interestingly, the displacement exhibited an almost linear dependence on the spiral length (in the investigated length range) as it is expected for d_{31} response. This dependence, however, did not intersect the coordinate origin and, apparently, may slow down at small effective lengths. Therefore, it can be inferred that the inner parts of the spiral (having the largest curvature) produce relatively smaller displacement as compared to the outer parts. Earlier experiments on dome-like actuators have shown that the electric field-induced displacements of curved PZT ceramics decrease significantly on increasing curvature [8].
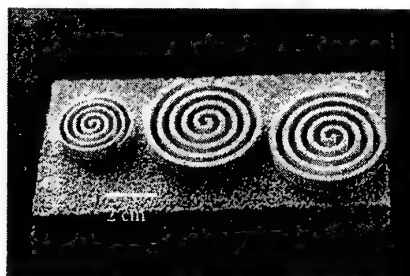
Figure 9. Photograph showing the various spiral actuators.
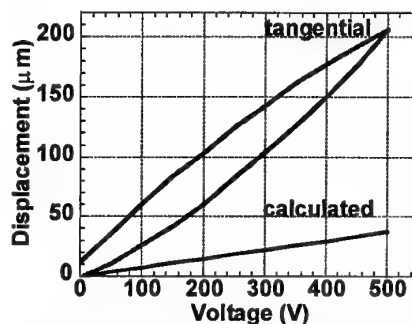
Figure 10. The tangential displacement of spiral actuators and the calculated displacement of PZT strip with similar dimensions.

In another experiment, the wall width of the spiral was changed, while maintaining the effective length and the number of turns constant (Figure 12). The driving voltage was also kept constant in this experiment. Obviously, greater wall thickness will increase the spring constant of the spiral and simultaneously will increase its mass. The first effect should shift the resonance to higher frequencies, while the second effect would decrease the resonance frequency. In the experiment, a gradual increase of the resonance
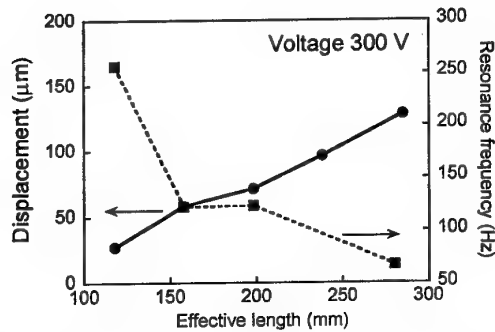
Figure 11. Variation of displacement and resonance frequency vs. effective length of the spiral actuator.

frequency was observed, suggesting that the spring constant effect dominates the width dependence. The tangential displacement dropped from 210 μm to about 70 μm when the width of the spiral was increased by 85%. If only the d_{31} actuation contributed to the displacement of the spiral tip, then the displacement would be inversely proportional to the wall width according to the equation:

$$\Delta L_t = d_{31} \frac{L}{d} V$$

where ΔL_t is the tangential displacement, L is the effective length of the spiral, d_{31} is the transverse piezoelectric coefficient, d is the wall width, and V is the applied voltage. The fast decrease of the displacement with the wall width suggests again that the total displacement consists mostly of the bending component, which is expected to be a highly non-linear function of the wall width. Thus, the actuator having a small width and a high effective length would possess very low resonance frequency of the order of several Hz and extremely high displacement of several mm. Tailoring both the width and the effective length of the spiral can tune the displacement and resonance frequency into the desired range. The advantage of the spiral actuator is in its compact design, which can be easily achieved by the FDC and other techniques.

Figure 12. Displacement and resonance frequency of the spiral actuator versus wall width at 500 volts.

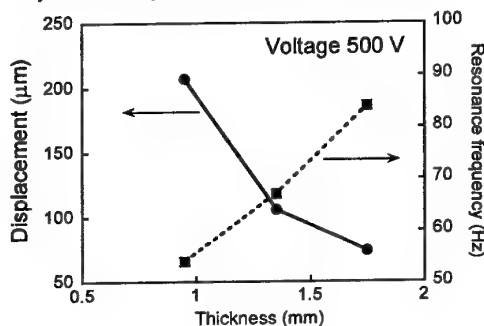The bending contribution to the displacement can be further enhanced by depositing a composite bi-layer spiral consisting of non-piezoelectric shim (internal part) together with piezoelectric material (external part of the spiral). This can be also accomplished with the FDC technique using a specially designed liquefier heads for the deposition of several materials.

Modeling of Spiral Actuator

The displacement and force developed by the actuators can be controlled to a large extent by the geometry (thickness, width, number of turns, effective length) and the mathematical form of the spiral. Theoretical analysis of spiral actuators turns out to be very difficult and hence finite element modeling techniques are used to study the effect of above mentioned parameters on the actuator response. Finite element method can also be used as an efficient design tool for designing spiral actuators. Finite element analysis was carried out using commercial FE package ANSYS5.4 on an IBM workstation. A representative finite element model of the spiral actuator is shown in Figure 13. The model consists of approximately 3200 eight-node 3D piezoelectric elements. Since the actuator was poled through the wall width, each element is individually assigned a local element coordinate system in which all the anisotropic material properties are interpreted. A typical spiral actuator with an effective length of 25 cm, wall width of 1.5 mm, height of 4 mm, spacing of 1.5 mm and 5 turns shows a tangential tip displacement of 175μm and generates a blocking force of 0.2 N under a field of 5 kV/cm. The displacement of a thin strip of PZT having the same thickness and length and driven with the same field produces a displacement of ~40 μm. Thus the spiral actuator shows an amplification of about 4-5 times higher while offering a much more compact structure. The non-uniform electric filed that exists across the width of spiral generates differential strain, leading to bending and large amplification in displacement.
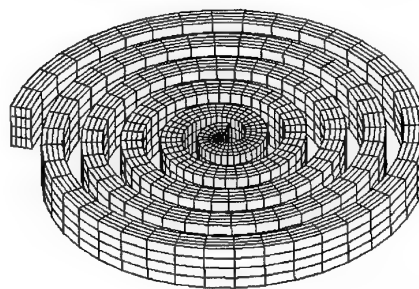

Figure 13. A representative finite element model of spiral actuator.

Parametric study carried out using FEM shows that the tip displacement decreases as the height of the spiral is increased (Figure 14). However the decrease is only about 10% as the height is increased from 1 mm to 10 mm. Blocking force developed by the actuator shows a linear increase with height (Figure 15).

3.6. Telescoping Actuators

Another monolithic ceramic actuator with telescoping actuation was also fabricated by the FDC method. The device consists of interconnected PZT ceramic tubes bearing a common center with internal
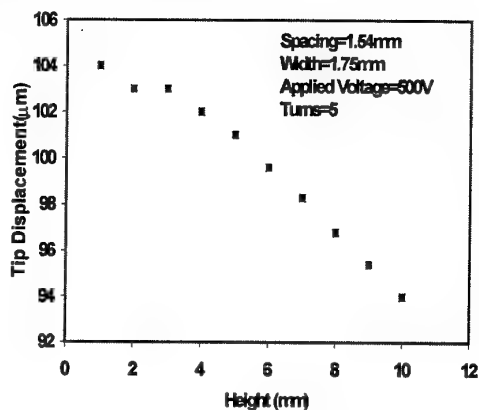

Figure 14. Modeling results for variation of tip displacement versus height of the actuator.
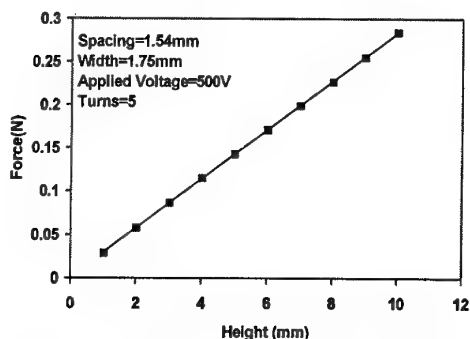
Figure 15. Modeling results for blocking force versus height of the actuator.

displacement amplification under electric field (Figure 16). Upon the application of an electric field, the tubes elongate and shrink alternatively in the z direction, yielding a net additive displacement in the z direction. The telescoping actuators used in the measurements consist of three interconnected PZT ceramic tubes with a common center. Under applied electric field, the inner and outer tubes elongate and the middle tube shrinks in the z direction. The telescoping actuation of the device is the summation of actuation of all individual tubes in the actuator (Figure 17). Therefore, increasing the number of the tubes, which are the driving component of the actuator, will further increase the displacement. Tailoring of the thickness, height, and the number of driving components of the actuator, the displacement and the exerted force of these actuators, can be altered. FDC is capable of making wall thicknesses of less than 250 μm with 125 μm wall

spacing. This can contribute significantly towards miniaturization and displacement amplification of these actuators.
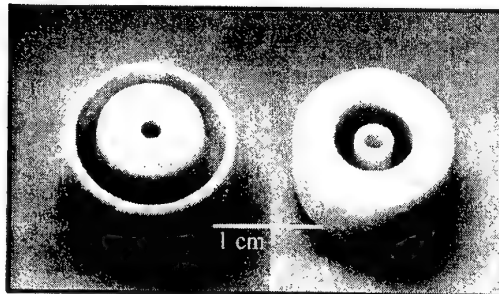
Figure 16. Photograph showing the top and bottom faces of a telescoping actuator structure.
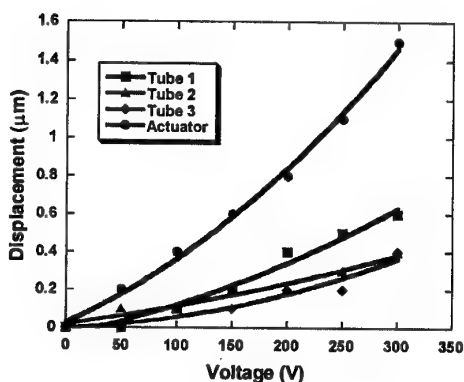
Figure 17. Field induced displacement of telescoping actuators.

3.7 Multi-material Actuators

Multilayer transducer structures offer potential for improved performance in terms of transmitting sensitivity, greater bandwidth, and enhanced reception characteristics [9]. At Rutgers University, several novel multi-material structures for transducer and actuator applications were developed and evaluated. Figure 18 (a) shows a multi-material multilayer design, which involves two different piezoelectrically active materials, deposited layer by layer, alternatively with a layer thickness of ~200 μm.

No delamination or defects were observed at the interface between hard and soft PZT. The structure consists of 50 vol.% soft PZT (5H) and 50 vol.% hard PZT (8). Another novel multi-material transducer design is multilayer ladder structure, which is shown in Figure 18 (b), can be poled in two different directions. The electrical properties of these structures will be discussed in future publications.
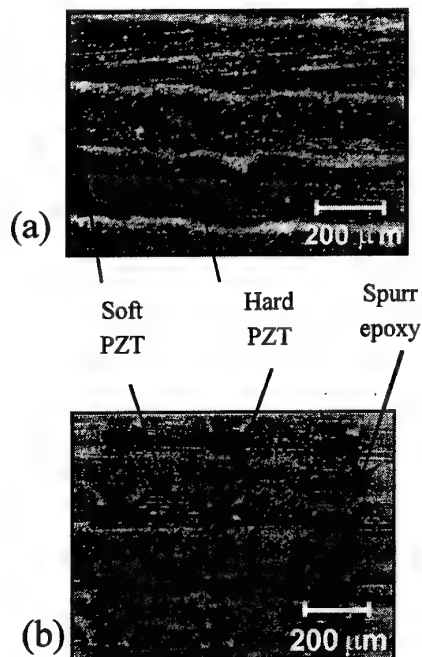
Figure 18. Optical micrographs from the cross section of multi-material: (a) multilayer, and ladder structures (b).

4. CONCLUSION

In this work, Solid Freeform Fabrication (SFF) techniques such as Fused Deposition of Ceramics (FDC) and Sanders Prototype (SP) were used to form a variety of novel piezoelectric ceramic/polymer composites and actuator structures. The indirect and direct routes were used for the development of these structures. The composites made by either the lost mold or the direct FDC technique, including a 2-2 volume fraction gradient, radial, and multi-material multilayer and ladder composites showed good electromechanical properties. A new type of monolithic actuators with spiral configuration was also developed with a displacement of above 200 μm at 5 kV/cm. Very complex architectures such as telescoping actuators were fabricated by this process. The design flexibility of the FDC process can be effectively used to enhance the total strain and force of piezoelectric actuators.

5. ACKNOWLEDGEMENT

6. REFERENCES

1. Safari, A. (1994) Development of piezoelectric composites for transducers, *J. Phys. III France* **4**, 1129.
2. Janas, V.F. and Safari, A. (1995) Overview of fine scale piezoelectric ceramic/polymer composite processing, *Journal of the American Ceramic Society* **78** (11), 2945.
3. Marcus, H.L. and Bourell, D L. (1993) Solid freeform fabrication finds new applications, *Advanced Materials & Processing* **9**, 28.
4. Danforth, S.C., Safari, A., Jafari, M., and Langrana, N. (1998) Solid Freeform Fabrication (SFF) of Functional advanced ceramic components, *Naval research Reviews* **L** (3), 27-38.
5. Danforth, S.C., Agarwala, M., Bandyopadghyay, A., Langrana, N., Jamalabad, V.R., Safari, A., and Weerner, R. (1998), Solid freeform fabrication methods, *United States patents*, 5,738,817.
6. McNulty, T.F., Mohammadi, F., Bandyopadghyay, A., Shanefield, D.F., Danforth, S.C., and Safari, A. (1998), Development of a binder formulation for fused deposition of ceramics, *Rapid Prototyping Journal* **4** (4), 144-150.
7. Panda, R.K., Kholkine, A., Danforth, S. C., and Safari, A. (1999) Volume fraction gradient composites for ultrasonic medical imaging transducers, to be published in the *J. Mater. Sci.: Mater. In Electronics*.
8. F. Mohammadi, A. L. Kholkine, B. Jadidian, S. C. Danforth, and A. Safari, Proc. of the Int. Symposium on Applications of Ferroelectrics, 273 (1998).
9. Powell, D.J. and Hayward, G. (1998) "Unidimensional Modeling of Multi-Layered Piezoelectric Transducer Structures", *IEEE Transactions on Ultrasonic, Ferroelectrics, and Frequency Control* **45** (3), 667-677.

Preparation and Semiconductive Properties of La-doped BaTiO₃ Films Fabricated by RF Magnetron Sputtering

Kazuo Shinozaki, Chih-Hsiu Yeh, Naoki Wakiya, Hiroshi Funakubo*
and Nobuyasu Mizutani

Department of Metallurgy and Ceramics Science, Tokyo Institute of Technology
Fax: 81-3-5734-3369, e-mail: ksino@ceram.titech.ac.jp
*Department of Innovative and Engineered Materials, Tokyo Institute of Technology
Fax: 81-45-924-5446, e-mail: funakubo@iem.titech.ac.jp

La doped BaTiO₃ epitaxial thin films were deposited on (100) MgO substrate by RF magnetron sputtering and annealed in air and reduced atmosphere at 800 and 1000°C. The Ba/Ti ratio and the La doping amount were controlled by the combination of the 0.25 at% La doped BaTiO₃ target (main target) and the small La-Ba-Ti-O pellets with various compositions which were placed on the main target. La was doped into BaTiO₃ epitaxial films up to 6 at%. At the range from 0.5 to 6 at% of La addition, the semiconductive films were obtained by annealing at 1000°C in 5%H₂+95%N₂ atmosphere. Semiconductive properties disappeared by heating at 400°C in air. The origin of the semiconductive nature was thought to be the formation of the oxygen vacancy by reduction. The existence of La seemed to assist the vacancy formation in reduced atmosphere, however controlled valency effects by doped La was not obtained.

1. INTRODUCTION

Semiconductive BaTiO₃ ceramics have attractive electrical properties such as PTCR. Many devices and products are developed using semiconductive BaTiO₃, i.e., PTC thermistor, self-temperature-control ceramic heater, boundary layer (BL) capacitor, etc. Semiconductive BaTiO₃ thin film has a potential to realize the future devices, such as on chip sensing devices or on chip PTC devices mounting with thin film circuits or on the Si circuits.

Large number of studies have been conducted concerning the formation of BaTiO₃ thin film using vacuum vapor deposition, sputtering, MOCVD, etc. Almost all studies, however, have been focused on the dielectric properties of BaTiO₃ thin films. Only few studies were conducted for making semiconductive BaTiO₃ films. S. R. Gillbert, et al.[1] succeeded to form the La doped semiconductive BaTiO₃ thin film on (100) Al₂O₃ substrate by MOCVD. The minimum resistivity of the film was 55 ohm·cm, but the La content was not reported. D. Nagano, et al.[2] also deposited the Nb doped semiconductive BaTiO₃ film on (100) MgO substrate. Nb doped BaTiO₃ film showed the lower electrical resistivity, 10^{-2}–10^3 ohm·cm with 1.2-7.8 at% of Nb contents. The minimum electrical resistivity was $2.8×10^{-2}$ ohm·cm at 5.7 at% Nb addition. The range and the upper limit of Nb doping with semiconductive nature were very wide and high compared with those of bulk ceramics. La doped BaTiO₃ bulk ceramics showed minimum electrical resistivity value at 0.2-0.3 at% of La addition. Increasing the La addition, electrical resistivity abruptly increased at 0.4-0.5 at%.[3] The controlled valency effects might be obtained in La or Nb doped BaTiO₃ thin film fabricated by MOCVD. However the amount of La or Nb addition for realizing semiconductive nature is much larger than that in bulk ceramics.

Many challenges have been done, but it might be very difficult to form semiconductive BaTiO₃ thin film by sputtering method. H. Igarashi, et al.[4] tried to introduce Y into BaTiO₃ by sputtering using two targets with different compositions. The electrical resistivity was 10^7 - 10^8 ohm·cm. H. Ardakani, et al.[5] fabricated the La doped BaTiO₃ thin film for sensing application by sputtering. But amount of dopant and electrical resistivity was not reported. In general, sputtering technique makes a thin film easier than other film making methods. Composition difference between targets and the thin film, however, becomes difficult problem in complex materials. Controlling the target composition enables to adjust the film composition. The other problem is how to control the amount of impurity-level dopant. Doping of different valence elements from Ba²⁺ such as La, Sm or Nb enables the BaTiO₃ semiconductive in the bulk ceramics. But it's difficult in the thin film case. One possible reason of this problem is that the optimum dopant amount in the thin film differs from that in ceramics for realizing semi-conductive nature.

In this paper, we tried to make clear the factors as follows, (1) making epitaxial BaTiO₃ thin film, (2) introducing the wide range of La dopant (0–6.5 at% of La/Ti), (3) clarifying the effect of post annealing. As a result, semiconductive thin film was obtained by the combination of La doping and the heat treatment in reduced atmosphere. It is still unclear that whether the doped La substituted the Ba site. The existence of La might assist the reduction process in reduced atmosphere.

2.EXPERIMENT

2.1 Basic sputtering procedure

RF magnetron sputtering apparatus (Nihon Seed Laboratory, Japan) was used. Two kinds of targets, i.e. main target and composition compensation targets (see

2.2), were used. Main targets were 0, 0.1 and 0.25 at% of La doped $BaTiO_3$ with the size 2 inches in diameter and 3 mm thickness. The actual composition of the 0.25 at% La doped target was Ba:La:Ti=1.005:0.002:1.000. Cleaved substrate with the size 10x10x0.5 mm³ from (100) MgO single crystal (Tateho Chemicals: MillaCrysta) was used. AFM measurement revealed the cleaved MgO surface had the atomic order steps in small area. Table 1 shows the sputtering condition. "Condition I" was for seeking the optimum condition to realize epitaxial film and the "Condition II" for the representative forming condition in this study.

Table 1. Sputtering condition

	Condition I	Condition II
Target diameter / mm	50.8	50.8
RF power density / Wcm⁻²	2.0-13.8	2.0
Target-substrate spacing / mm	50	50
Substrate temperature / °C	R.T. – 700	700
Ar / O_2 gas ratio	80/20	80/20
Working pressure / mTorr	5.0 – 50.0	5.0
Base pressure / mTorr	1x10⁻⁶	1.0x10⁻⁶
Deposition time / min	60-600	120

2.2 Composition control of Ba/Ti and La doping

Combinations of eight compensation targets with different compositions were placed on the main target at concentric circle position for controlling the thin film composition. The size of each target was 8.4 mm in diameter. Since the deposited film using main target had Ba/Ti<<1 composition, four kinds of compensation targets were made with Ba/Ti=1.1 to 1.6 at constant La/Ti ratio (0.25 at%) for increasing the Ba content. Seven kinds of targets with different La content, 1 to 15 at% of La/Ti at Ba/Ti=1 were also made for controlling the La composition.

2.3 Heat treatment

Thin films were heated at 800 and 1000 °C for 2 hours in the vertical type furnace. Dried air passed through P_2O_5 trap or 5%H_2-95%N_2 gas was introduced into furnace. After heating, the thin film was quenched by pulling up the sample holder.

2.4 Characterization

ICP spectrometry (Seiko instruments: SPS1500VR) and WDS X-ray Fluorescence Spectroscopy (Rigaku: RIX2000) were used to determine the composition. X-ray diffractometer (Philips: PW-1874) was used for determine the phases and the orientation of the film. Electrical resistivity at room temperature was measured by the four probe method[6] with 1mm distance between each needle. Van der Pauw apparatus (Keithley: 236 Source Measure Unit) was used for Hall coefficient measurement.

3. RESULT AND DISCUSSION

3.1 Growth condition of epitaxial thin film

We tried to form the stoichiometric $BaTiO_3$ film using the main targets under various conditions (Condition I in Table 1). It was very difficult to control Ba/Ti ratio when the main target was used, also the La composition. Condition II in Table 1 shows the optimum condition to achieve the epitaxial thin film using main target.

Deposition rate was 2.2 nm/min. The film had smooth and flat surface within 10 nm roughness by AFM observation. Cross section of the film showed homogeneous microstructure and no obvious grain boundaries and voids. Typical composition of the epitaxial film formed using 0.25 at% La doped main target was Ba:La:Ti=0.762:0.002:1.000. Ba/Ti ratio is 0.76. La amount was same as that of main target. X-ray diffraction data showed the film was $BaTiO_3$ single phase with c-axis orientation normal to the substrate. [001] projection of pole figure measurement (Fig.1) shows the thin film was epitaxially grown. Lattice parameter was as follows, a=4.048 A, c=4.062 A, c/a=1.004. Since c/a value in bulk $BaTiO_3$ is 1.011, unit cell in the thin film was more close to cubic. The lattice mismatch and the thermal expansion difference between $BaTiO_3$ film and substrate might cause the difference of c/a ratio. Thin film tends to have wider composition range having single phase compared with that of ceramic phase diagram.[2] The composition of the thin film shows extremely high deviation, 31% of excess Ti, shows the $BaTiO_3$ single phase.
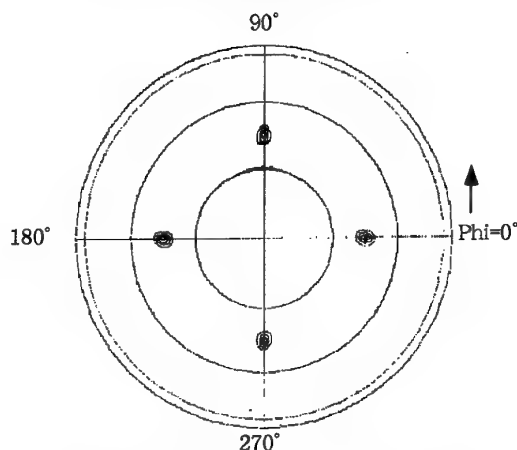
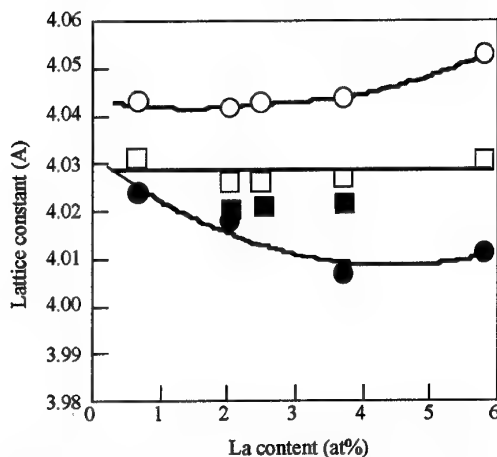

Fig. 1 [001] projection of pole figure measurement

Fig. 2 Change of c-axis lattice parameter with La/Ti ratio of the film with Ba/(Ba+Ti)=0.45-0.47
○: as-deposited film, □: annealed at 800°C in air,
■: annealed at 1000°C in air,
●: annealed at 1000°C in reduced atmosphere

3.2 Composition control by compensation targets

Combination of main target with 0.25 at% La doped BaTiO$_3$ and compensation targets enabled various La doped epitaxial BaTiO$_3$ films with single phase. The composition range of Ba/(Ba+Ti) was 0.42–0.52 at%. Amount of La addition was 0.2-6.5 at% (La/Ti). Series of the samples with various La contents and constant Ba/(Ba+Ti) ratio were obtained only at the film with the composition Ba/(Ba+Ti)=0.45-0.48. The samples with Ba/Ti=1 were only obtained at lower La concentration (La/Ti <0.5at%).

3.3 Effect of La addition and heat treatment

Fig. 2 shows the relation between c-axis lattice parameter and La/Ti ratio of the films with the composition Ba/(Ba+Ti)=0.45-0.47. Symbols show the sample conditions: as-deposited film (O), annealed in air at 800 (□) and 1000°C (■) and annealed at 1000°C in reduced atmosphere (●). Lattice parameters of the as-deposited films are almost constant with La addition up to 4 at%, then increasing gradually with La addition. By heat treatment in air at 800 and 1000°C, lattice parameters decrease about 0.01 to 0.02 A. With increasing the La, lattice parameters show the minimum at 2 at% of La addition. Since the change of lattice parameter with La addition is not so large and the heat treatment affects the lattice parameter value, the effect of La addition into film might be lower than that in the heat treatment. On the other hand, the lattice parameter of the films heated in reduced condition (5%H$_2$-95%N$_2$) decreases with increasing La addition up to 3.5 at%. In the region between 3.5 and 5.8 at% of La addition, lattice parameter is almost constant or slightly increasing. This tendency is agree with that of the bulk ceramics. This suggests the possibility of La occupying the Ba lattice site during reduction.

Fig. 3 shows effect of various heat treatments ((a)as-deposition, (b)800°C in air and (c)1000°C in reduced atmosphere) on (001) XRD peak profile of the 0.6 at% La doped film. With increasing the heating temperature, decreasing the unit cell volume and increasing the crystalinity. This means the residual strain and/or lattice defects might be removed by the heat treatment.

Fig. 4 shows the representative V-I characteristics of the film with the composition Ba/(Ba+Ti)=0.467 and La/Ti=4.0at% heated in reduced atmosphere. It is clear that there is ohmic relationship and no voltage barrier in the film plane of semiconductive BaTiO$_3$. Microstructure observation showed no obvious microstructure such as grain boundaries in the cross section of the film.

Fig. 5 shows the effect of La addition on the electrical resistivity of the films heat-treated at 1000°C in the reduced atmosphere. The resistivity of bulk ceramic data[3] is also plotted (O). Adding the La up to 0.5 at%, the resistivity decreases rapidly to 10^2 ohm cm. Increasing the La addition, resistivity somewhat decreases (up to 3.8 at%) and then increases again. The films heated at 1000 °C in air have no semiconductive nature.

Hall coefficient measurement revealed the carrier was electron. Fig. 6 shows the dependency of the carrier concentration and the mobility on the electrical conductivity of the films plotted in Fig.5. The mobility is almost constant with electrical conductivity. The

Fig. 3 Change of (001) peak profile of the films with 0.6 at% of La/Ti
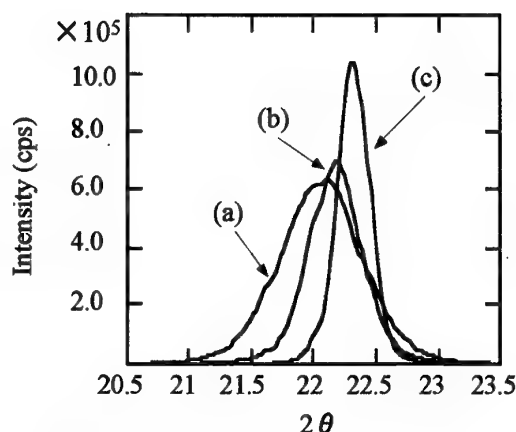 (a): as-deposition, (b): annealed at 800°C in air,
  (c): annealed at 1000°C in reduced atmosphere

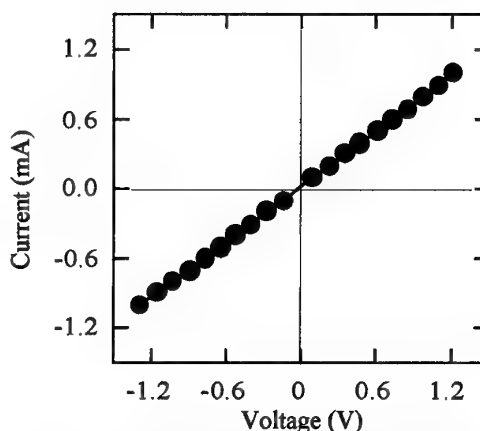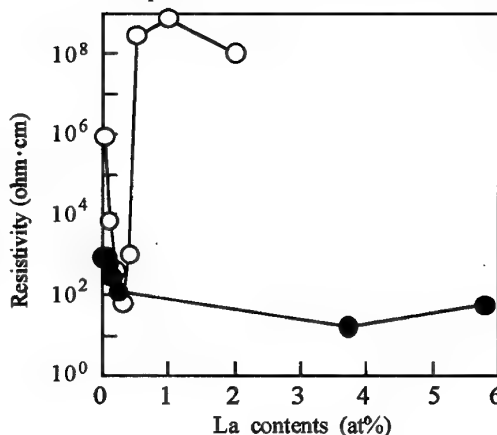Fig. 4 V-I characteristics of the film with Ba/(Ba+Ti) = 0.467 and La/Ti=4.0at% heated in reduced atmosphere

Fig. 5 Change of resistivity as a function of La addition
  ●: films heated at 1000°C in reduced atmosphere,
  O: reported value of bulk ceramic[3]

electrical conductivity is controlled by the change of carrier concentration in the La doped semiconductive BaTiO$_3$ film heated in reduced atmosphere. Both values of mobility 1–10cm^2·V^{-1}·s^{-1} and carrier concentration 10^{17}–10^{19}cm^{-3} of the semiconductive BaTiO$_3$ films correspond with the values of the sintered BaTiO$_3$ and the BaTiO$_3$ single crystal.[6]

3.4 Effect of re-oxidation

Fig. 7 shows the change of electrical resistivity of the semiconductive thin film under heating and cooling condition in air. Sample had the composition Ba/(Ba+Ti) =0.521 and La/Ti=0.2at%. With increasing the temperature, electrical resistivity decreases, and has minimum at 350°C. Continuing to heat the film, the resistivity increases gradually and abruptly increase at 700°C. The film turns to insulator at 700 °C, and keep high resistivity even decreasing the temperature (●).

3.5 Role of La in the semiconductive BaTiO$_3$ film

Fig. 8 shows the schematic diagram of the relationship between as-deposited epitaxial BaTiO$_3$ film and the heat treated films. The insulating film becomes semiconductor by the heat treatment in reduced atmosphere, but not in air. The main cause of realizing the semiconductivity seems to be existence of electrons supplied by the oxygen vacancies that are formed by the heat treatment in reduced atmosphere. The added La plays a role of assisting the vacancy formation and stabilizing the vacancy up to 400°C.

4. SUMARRY

La doped epitaxial BaTiO$_3$ thin films were formed by the RF magnetron sputtering using combination of main target and compensation targets with different composition. Heat treatment of the La doped thin film in H$_2$-N$_2$ atmosphere produced the semiconductive film. La might substitute to the Ba site lattice with vacancy formation under reduced condition. Semiconductive film formation seems to be reduction mechanism with assistance of vacancy formation by La.

REFERENCES
1) S.R.Gilbert et al., J.Appl.Phys., 80 [2] 969-977 (1996)
2) D.Nagano, et al., App.Phys.Lett., 72 [16] 2017-2019 (1998)
3) O.Saburi, J.Phys.Soc.Japan, 14 [9] 1159-1174 (1959)
4) H.Igarashi and M.Yuasa, "PTC effects in BaTiO$_3$ thin film", ElectronicCeramics, [9] 28-33 (1987) (in Japanese)
5) F.M.Smits, Bell.Sys.Tech.J., 37 [3] 711-718 (1958)
6) C.N.Berglund et al., Phys.Rev., 157 [2] 358-366 (1967)

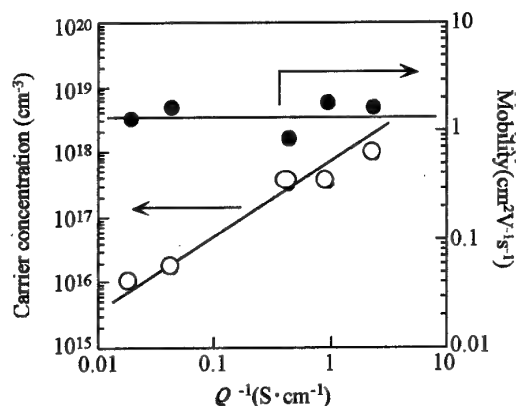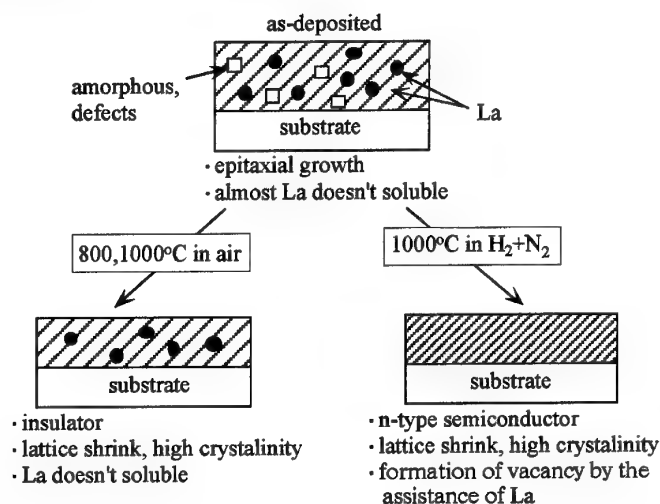Fig. 6 Change of carrier concentration and mobility as a function of electrical conductivity of various films plotted in Fig.5

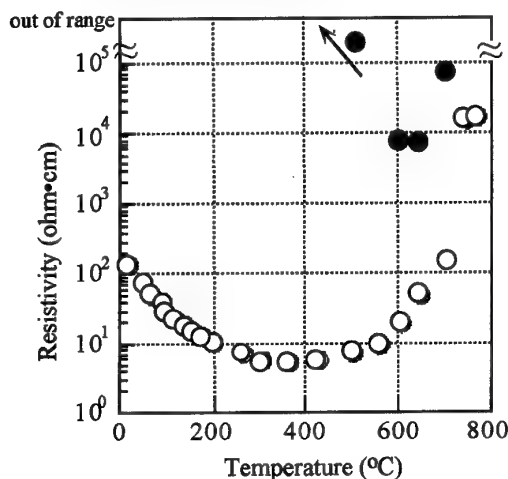

Fig. 7 Change of electrical resistivity of the semiconductive thin film under heating and cooling condition in air (○: heating, ●: cooling) Films: Ba/(Ba+Ti)=0.521 and La/Ti=0.2at%, heated in reduced atmosphere.

Fig. 8 Schematic diagram of the relation between as-deposited film and heat treated films.

Lead Zirconate Titanate thin films on base-metal foils: An approach for embedded high-K passive components

J-P. Maria, Kevin Cheek, S. K. Streiffer, S-H. Kim, G. Dunn[‡], and A. I. Kingon

North Carolina State University, Department of Materials Science and Engineering, Raleigh, NC 27695,
fax: 011-919-515-5055, emsil: jpmaria@unity.ncsu.edu
Materials Science Division, [†]Argonne National Laboratory, Argonne, IL 60439.
fax: 011-630-252-4289, email: streiffer@anl.gov
[‡]Motorola Advanced Technology Center, Shaumburg, IL 60196,
fax: 011-847-576-2111, email: AGD010@lmpsil02.comm.mot.com

ABSTRACT

An approach for embedding high-K dielectric thin films into polymer packages has been developed. $Pb_{0.85}La_{0.15}(Zr_{0.52}Ti_{0.48})_{0.96}O_3$ thin films were prepared by chemical solution deposition on 50 µm thick Ni-coated Cu foils. Sputter deposited Ni top electrodes completed the all base-metal capacitor stack. After high temperature N_2 crystallization anneals, the PLZT composition showed reduction resistance while the base-metal foils remained flexible. Capacitance density and Loss tangent values range between 300 and 400 nF/cm^2 and 0.01 and 0.02 from 1 to 1000 kHz respectively. These properties represent a 2 to 3 order of magnitude improvement over available embedded capacitor technologies for polymeric packages.[1]

INTRODUCTION

Embedding thin film high-permittivity dielectrics into low temperature processed polymer packages offers advantages in electronics miniaturization and manufacturing cost reduction. Miniaturization potential stems from replacement of surface mount components and the subsequent reduction of the required wiring board real estate. Cost reductions are associated with the ability to produce packaging substrates with capacitive layers pre-embedded. Such layers remove the need for pick-and-place assembly operations which can comprise an appreciable fraction of the manufacturing cost.[1] Photolithographic methods coupled with etching and metallization steps can conceivably be used synthesize the necessary combinations of capacitive elements and interconnects rapidly and in large quantity.

We present here a strategy to produce high permittivity capacitive layers compatible with low temperature processed polymer packages. To avoid traditional temperature limitations, all high temperature processing steps required by the oxide dielectric would be performed prior to the embedding process. This goal was achieved through film deposition onto metal foils which could be subsequently embedded using standard lamination methods. Unlike other commonly used substrates, metal foils are thin enough as not to add appreciable thickness to the subsequent package. Such metal foils are, however, thick enough to support the brittle as deposited oxides. In this study, composite base metal foils (comprised of 50 µm Cu coated with 4 µm of electroless Ni) were used as the carrier substrates to minimize cost. This work follows several previous investigations of high-K films on metal foils, and/or with base-metal electrodes.[2-7]

La-doped $Pb(Zr,Ti)O_3$ was used as the high permittivity dielectric. The La doping drives the Curie transition below room temperature leaving a large K and non-hysteritic electrical properties. This composition is tolerant of the non-stoichiometry expected after processing in the inert atmospheres required to preserve the base metal foil. Resulting oxygen vacancy populations can be ionically compensated by controlled Pb-deficiency.

EXPERIMENTAL PROCEDURE

50 μm thick Cu-foil substrates (0.5 oz. gage) were obtained from Motorola. 4 μm of autocatalytic (i.e., electroless) Ni (abbreviated as e-Ni) was deposited on each side of the metal foil by MacDermid Inc. from a $NiCl_2$ - $Na(H_2PO_2)^-$ solution bath. The foils were obtained in 12 " x 14" sheets. Sections of foil 2.5 cm x 5 cm were cut from the large sheets and used as the standard substrate size. Prior to depositions, the foils were cleaned by rinsing in acetone and isopropanol. AFM surface imaging of the as-received foils revealed ~ 2 μm rms roughness, with 1-3 μm diameter e-Ni clusters.

PLZT was prepared by chemical solution deposition. The precursor solution was methanol-based, incorporating lead acetate trihydrate, titanium isopropoxide, lanthanum isopropoxide, and zirconium N-butoxide chemical sources.[8] After spin-on deposition, the films were dried on a hot plate at 250 °C for 5 min, then pyrolyzed in air @ 450 °C (tube furnace) for 10 minutes. This procedure was repeated 6 times to achieve the desired thickness of ~ 6000 Å. After deposition, drying, and pyrolysis, the films were crystallized in an N_2 tube furnace at 600 °C for 30 minutes. Capacitor structures were completed by ion beam deposition of Pt or Ni top electrodes.

The film surface topography, crystallinity, and microstructure, were characterized using atomic force microscopy, X-ray diffraction, and transmission electron microscopy. Frequency and electric field dependent dielectric properties were measured using an HP 4192A impedance analyzer.

RESULTS AND DISCUSSION

Fig. 1 shows an θ-2θ x-ray diffraction pattern respective of thin film PLZT samples deposited on e-Ni substrates under the optimized processing conditions. As seen in the figure, peaks are present from Ni, Cu, Ni_3P, and PLZT. Under the optimal processing conditions, no evidence is found suggesting the presence of pyrochlore crystals. It is also apparent from the diffraction pattern that the reducing anneal conditions are effective in

preventing oxide formation in the composite base metal foil. The Ni_3P phase forms via a precipitation reaction in the as-deposited e-Ni which contains between 9 and 11% dissolved phosphorus.[9]
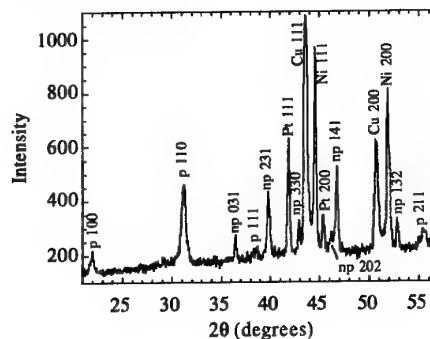
Fig. 1: θ-2θ x-ray diffraction pattern of 6 layer (~6000 Å thick) PLZT thin film deposited on an e-Ni coated foil substrate. In the figure, p = perovskite PLZT, np = Ni_3P, and Pt refers reflections from Pt top electrodes.

Of some concern was the large surface roughness of the as-received e-Ni surfaces (~ 10 x greater than the dielectric thickness). The large undulations could potentially lead to shorting or premature electrical breakdown. AFM analysis was performed on the final PLZT thin films, a typical result is given in Fig. 2.
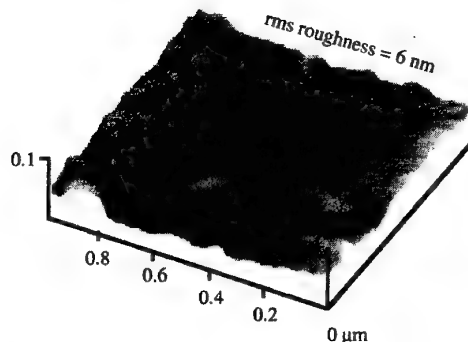
Fig. 2: Tapping mode AFM image of 6 layer (~6000 Å thick) PLZT thin film deposited on an e-Ni coated foil substrate.

Note that on the scale of this image, the surface appears quite smooth. If, however, an image is taken over a larger area (10 μm x 10 μm), the roughness is similar to that of the e-Ni substrate prior to deposition, i.e., ~ 2μm rms. This surface topography suggests a typical lateral grain size between 20 and 100 nm, and relatively conformal coverage.

In this report, electrical characterization is limited to room temperature measurements. Fig. 3 shows a capacitance-voltage curve typical of the PLZT: the non-hysteritic response indicates the effectiveness of La-doping to temperature-shift the ferroelectric transition below room temperature.
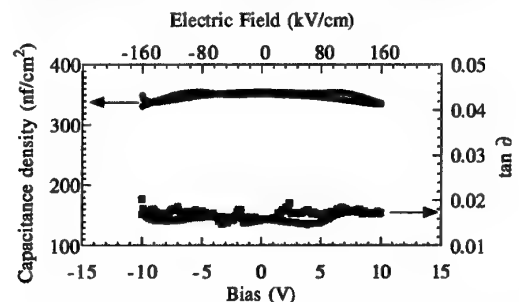
Fig. 3: Voltage dependence of the permittivity and dielectric loss tangent for a 6 layer (~6000 Å thick) PLZT thin film deposited on an e-Ni coated foil substrate.

Fig. 3 also demonstrates the limited dielectric tunability - the combination of a small grain size and relatively low-temperature processing likely contributes to this condition. (The lack of tunability is desired for the targeted applications.)
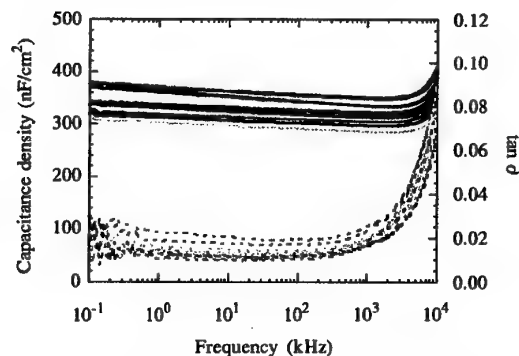

Fig. 4: Frequency dependence of the permittivity and dielectric loss tangent for a 6 layer (~6000 Å thick) PLZT thin film deposited on an e-Ni coated Cu foil substrate.

Fig. 4 gives the frequency dependence of the permittivity and loss tangent for a typical PLZT sample. In Fig. 4, 10 curves are given and indicate the `degree of variability among test capacitor structures. Typically, the yield of functional capacitors (500 μm diameter circles defined with a shadow mask) is ~80 %. This data is presented as capacitance/unit area since these units can be readily compared to other capacitor technologies. (The average dielectric constant at 10 kHz was 240.) The dielectric constant was found to drop approximately 1 % per decade.

One likely influence producing the relatively low dielectric constant of this PLZT (when compared to bulk values exceeding 10,000)[10] is the formation of a low-permittivity layer at the PLZT / e–Ni interface. Cross-sectional TEM images were taken to investigate this possibility, Fig. 5 gives the result. In this image an interfacial layer between 35 and 40 nm in thickness becomes apparent.

Fig. 5: Cross-sectional TEM image of a foil-based capacitor detailing the dielectric layers and interface formation between PLZT and e-Ni bottom electrode.

At this point it remains unclear as to the exact composition of this layer. However, the size of

the structural features is on the order of those found in the PLZT and peaks from CuO_2 or NiO were not seen in xrd scans. These results suggest that the region may be comprised of reacted or poorly crystallized PLZT. Though this layer is present in the as-deposited films, with the exception of a reduced total permittivity, it appears not to strongly influence the frequency dependent electrical properties. As such, structures containing these interface layers may be appropriate for a functional device application in the frequency range investigated. The influence of these interfaces may become more important if applications are geared towards microwave frequencies.

Foil samples were qualitatively tested after deposition to roughly determine handle-ability. In general, the foils could be repeatedly wrapped around 3 cm diameter mandrels without cracking or delamination. This type of resilience is important as it will facilitate handling and storage on rolls. Moreover, it suggests that these structures will survive the potentially aggressive conditions required for lamination into polymer packages.

CONCLUSIONS

A method has been developed which produces high-K capacitors on base-metal foil substrates suitable for embedding into polymer-based printed wiring boards. Depositing the dielectric on e-Ni coated Cu foils allows all high temperature processing steps necessary for structure and property development to be isolated from the temperature sensitive organic-based packages. The high-permittivity layers were produced by chemical solution deposition. The specific starting composition and firing temperatures were chosen such that high-quality material could be achieved despite the reducing N_2 atmospheres used during crystallization anneals. Shadow mask defined capacitors (Ni or Pt metal) typically exhibited permittivities and loss tangents of 240 and ≤ 0.017 in the frequency range between 0.1 and 100 kHz. Dispersion was limited to approximately 1% / decade in this range. Transmission electron microscopy revealed the presence of a ~ 35 nm interface layer between the PLZT and e-Ni substrate. This layer and its effects on film properties is under continued investigation. Even with the existence of this interface region, the electrical properties appear to be appropriate for capacitor applications.

REFERENCES

[1] Personal communication, Greg Dunn, Motorola Corporate Manufacturing Research Center (1999).

[2] K. B. Lee, B. R. Rhee, and S. K. Cho, Mat. Res. Soc. Symp. Proc. **433**, 181-186 (1996).

[3] S. A. Myers and E. R. Myers, Mat. Res. Soc. Symp. Proc., 107-112 (1992).

[4] T. Ogawa, S. Shindou, A. Senda, and T. Kasanami, Mat. Res. Soc. Symp. Proc., 93-99 (1992).

[5] T. Ogawa, S. Saitoh, O. Sugiyama, A. Kondoh, T. Mochizuka, and H. Masuda, Proc. 9th Int. Symp. Application of Ferroelectrics, 399-403 (1994).

[6] T. Ogawa, N. Ujie, and K. Hukuta, Proc. 10th Int. Symp. Application of Ferroelectrics, 459-462 (1996).

[7] K. Saegusa, Jpn. J. Appl. Phys. **30 Pt. 1 (11)**, 6888-6893 (1997).

[8] S.-H. Kim, D.-J. Kim, J. Hong, S. K. Streiffer, and A. I. Kingon, J. Mater. Res. **14 (4)**, 1371-1377 (1999).

[9] J. K. Dennis and T. E. Such, *Nickel and chromium plating*, Third ed. (ASM International, The Materials Information Society, Materials Park, OH, 1993).

[10] B. Jaffe, W. R. Cook, and H. Jaffe, *Piezoelectric Ceramics* (R. A. N. Publishers, Marietta, OH, 1971).

Preparation and Multifunction of Highly Oriented AlN Thin Films
-Ceramic Skin-

Morito Akiyama, Chao-Nan Xu, Kazuhiro Nonaka and Tadahiko Watanabe
Kyushu National Industrial Research Institute, Shuku, Tosu, Saga 841-0052 Japan
Fax: +81-942-83-9858, e-mail: akiyamam@kniri.go.jp

We have investigated the effects of sputtering control factors on the crystal orientation of AlN thin films by design of experiments and the analysis of variance. Consequently, it was proved statistically that the distance between the target and the substrate, the sputtering pressure and the substrate temperature were significant control factors in eight control factors. Furthermore, it is possible that highly oriented AlN thin films are prepared on polycrystalline ceramic substrates, such as SiC, Si_3N_4, Al_2O_3 and $MoSi_2$, by helicon plasma sputtering. The annealing of 800 °C in vacuum was effective to improve the crystal orientation of the AlN thin films. The highly oriented AlN thin films sensitively respond to mechanical impact, stress and temperature change, and have high corrosion-resistance to HF and HCl (10 %), and increase the thermal radiation of aluminum substrates from 0.48 to 0.60. These results suggest that the highly oriented AlN thin film is a promising material as artificial skin for a robot and a multi-function sensor.

1. INTRODUCTION

Human skin produces cutaneous sensations, such as sensations of touch, pressure, pain, hot and cool, against various outer stimuli to protect a body from danger. Diverse organs in the skin detect these sensations as shown in Fig. 1. Furthermore, the skin serves as both a protection film and a cooler. We believe that the low reliability of structural ceramics would be improved by preparing a multi functional ceramic film like human skin on them, because we could easily get information about structural ceramics and immediately react to various danger.

Since aluminum nitride (AlN) is a pyroelectric ceramic, an AlN thin film is expected to respond to various different stimuli as shown in Fig. 1. Attention was focused on obtaining highly oriented AlN thin films on polycrystalline substrates in an effort to make the films pyroelectric, because there is no very strong statement on AlN thin films deposited on polycrystalline substrates [1, 2]. In the present study, we report the preparation and the multifunction of the highly c-axis oriented AlN thin films deposited on glass, sintered SiC, Si_3N_4, Al_2O_3, and $MoSi_2$ substrates.

2. EXPERIMENTAL

AlN thin films were prepared by helicon plasma sputtering system shown in Fig.2. The sputtering conditions were optimized by design of experiments and the analysis of variance (ANOVA). The target was aluminum (99.999%) and the substrates were glass, sintered SiC, Si_3N_4, Al_2O_3, and $MoSi_2$. The crystal structures of the films were investigated by X-ray diffraction (XRD). To examine the ability of detecting mechanical impact, we used an iron ball drop system [3]. Stress was applied to the film surfaces by using weights or a autograph, the film capacitances were measured
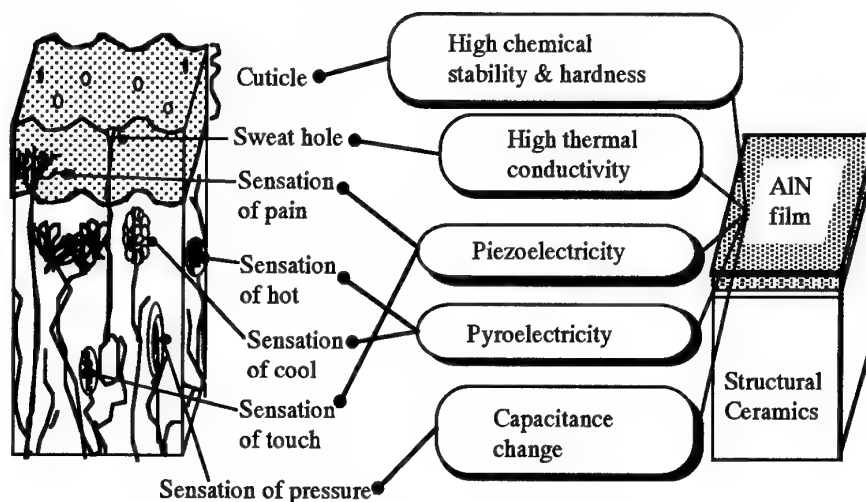

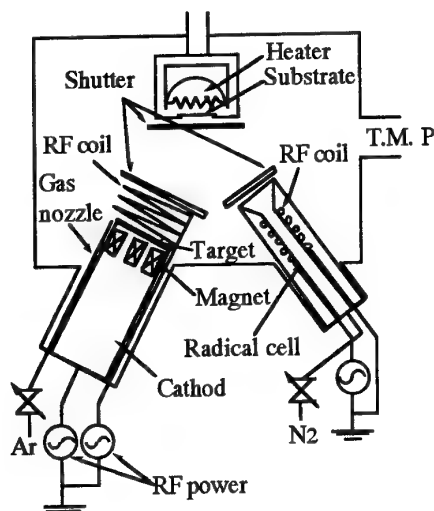Fig.1 Correspondence of human skin to AlN thin film.

Fig.2 Schematic diagram of helicon sputtering system with radical cell.

with a LCZ meter, and the produced voltage output was measured with a storage oscilloscope. The films were given temperature change by dipping into an oil bath of 84°C. Electric current produced by the films was measured with a electrometer.

3. RESULTS AND DISCUSSION
3.1 Preparation of AlN thin films

The eight control factors, the distance between the target and the substrate, the substrate temperature, the sputtering pressure, the cathode rf coil power, the radical cell rf coil power, the nitrogen concentration, the sputtering time and the cathode power, were selected as sputtering control factors. In this study, we utilized a L18 orthogonal array, because this orthogonal array is the most common one in process engineering [4]. Table I lists the sputtering control factors and their each level.

The result of the ANOVA on the AlN thin films deposited on glass substrates was shown in Table II. The distance between the substrate and the target, the pressure and the substrate temperature were statistically significant factors. The distance is the most important control factor in the examined range. On the other

Table I Sputtering control factors and levels

Factor	Level 1	Level 2	Level 3
A Distance (mm)	150	200	-
B Sub.temp. (°C)	150	300	450
C Pressure (Pa)	0.12	0.36	0.60
D Coil power (W)	0	50	100
E Rad. power (W)	0	50	100
F N2 conc. (%)	30	40	50
G Sputt. time (h)	4	6	8
H Cathode power (W)	120	160	200

Table II Analysis of variance table on orientation of AlN thin films

Factor	S	f	V	F
A Distance	51.5	1	51.5	13.0
B Sub. temp.	34.1	2	17.1	4.33
C Pressure	55.4	2	27.7	7.01
D Coil power	1.05	2	0.525	○
E Rad. power	9.86	2	4.93	○
F N2 conc.	2.29	2	1.15	○
G Sputter time	10.9	2	5.45	1.38
H Cathode power	16.4	2	8.20	2.08
Error	18.4	2	9.20	○
Error (○ mark pooled)	31.6	8	3.95	

hand, the effects of the cathode r.f. coil power, the radical cell power, the nitrogen concentration, the sputtering time and the cathode power are not statistically significant. Highly oriented AlN thin films were obtained on polycrystalline substrates by optimizing the three significant sputtering control factors [5]. Figure 3 shows the XRD pattern and Figure 4 shows the rocking curve of the films deposited under the optimized sputtering conditions. Only the two AlN (002) and AlN (004) peaks are observed. The peak positions are consistent with the ASTM card [6]; hence, the uniform stress in the film is not observed. The crystalline size of the film is 58.6 nm, suggesting that many c-axis oriented crystals compose the highly oriented AlN thin film, because the film thickness is about 1.0 μm. The FWHM of the rocking curve is 3.1°. The micro structure of the film is dense and the film consists of the array of poorly defined fibrous grains. Furthermore, the FWHM was decreased to 2.8° by the anneal of 800°C in vacuum.
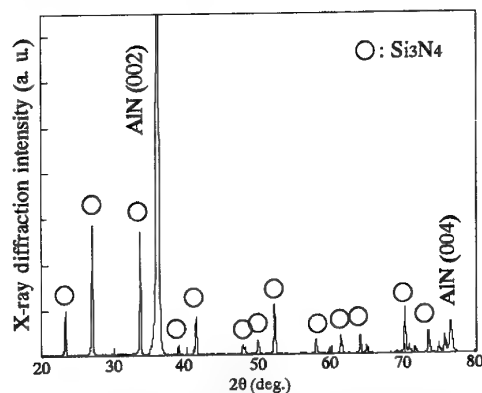

Fig. 3 X-ray diffraction pattern of AlN thin film deposited on Si3N4 substrate under optimized sputtering conditions:distance 150 mm, sputtering pressure 0.13 Pa, substrate temperature 450 °C.
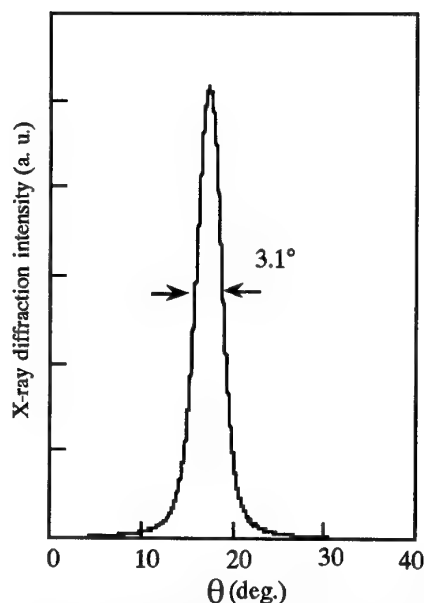
Fig. 4 X-ray rocking curve of AlN thin film deposited on Si₃N₄ substrate.

3.2 Multifunction of AlN thin films

We investigated the ability of detecting mechanical impact of the AlN thin films deposited on $MoSi_2$ substrates. Figure 5 shows the generation of voltage by the sample when a steel ball dropped from a height of 1.0 cm to the Ag electrode surface of the AlN thin film.
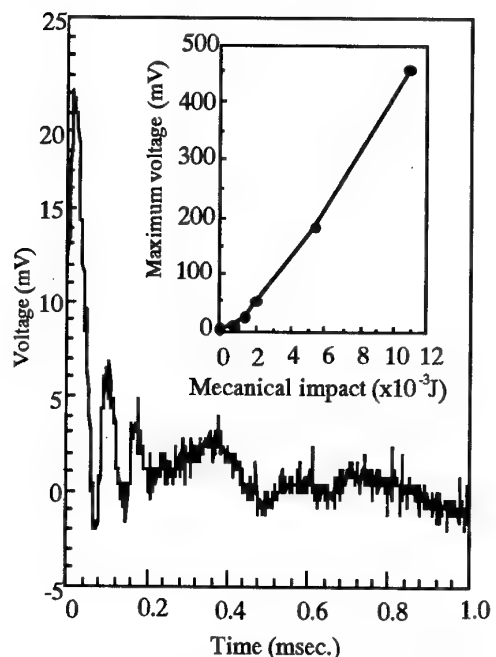

Fig. 5 Voltage signal produced by AlN thin film on mechanical impact ($1.37X10^3$ J). Inset shows the dependence of voltage signal on mechanical impact.

Voltage oscillation occurred with the maximum voltage of 21.2 mV and then was rapidly attenuated. When the ball dropped to the surface of a $MoSi_2$ substrate, the generation of voltage was not observed. Since the frequency of the voltage oscillation was very high (11.1 kHz), the oscillation was not due to the bound of the steel ball. Consequently, the oscillation was caused by the mechanical relaxation of the AlN thin film, so that the film functioned as a piezoelectric and responded to the mechanical impact.

To evaluate the detective property of the AlN thin films, the experiments were extended further to cover various mechanical impacts. The inset to Fig. 5 shows the results. The film produced 456 mV when mechanical impact of $11 X 10^{-3}$ J (a height of 8.0 cm) was given. The maximum voltage increased almost linearly with the mechanical impact intensity. These results indicate that the produced voltage depended on the impact intensity and we can know the intensity.

It is generally known that the spontaneous polarization of ferroelectric changes owing to pressure [7]. However, there is no information available on the dependence of AlN film capacitance on pressure, so that we investigated the response of AlN thin film capacitance to pressure. Figure 6 shows the results. The first capacitance of the film agreed with calculated value [8] and increased almost linearly with applied pressure. As shown in the inset to Fig. 6, the film responded to pressure-on and pressure-off by reversible changes in capacitance. The 90% response times to pressure-on was less than one second. The capacitance change was not due to the change of distance between electrodes, because AlN Young's modulus is very large (314 GPa) [9] and the distance between the Ag electrode and the
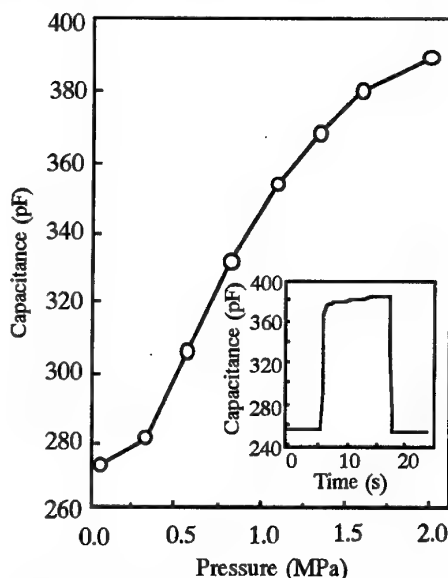

Fig. 6 Pressure dependence of capacitance of AlN thin film. Inset shows film response tran -sients to pressure of 2.0 MPa.
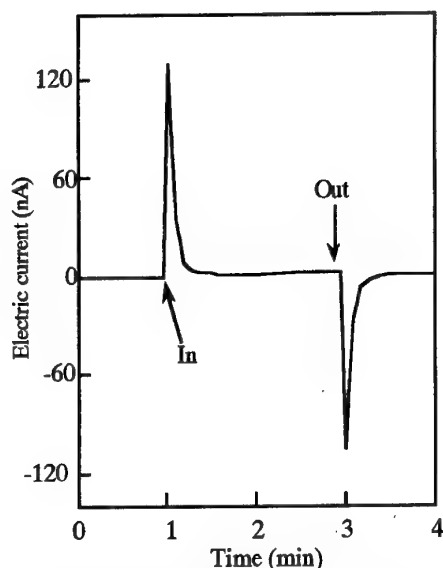
Fig. 7 Response transients of AlN thin film deposited on $MoSi_2$ to thermal shock of 60 °C (24 to 84 °C).

$MoSi_2$ surface hardly changes. Therefore, it was thought that the film capacitance change was due to the film permittivity change.

Figure 7 shows the response transient of the film to thermal shock. When a $MoSi_2$ substrate with an AlN thin film was dipped in an oil bath of 84 °C, the electric current of about 120 nA flowed suddenly and decreased immediately. When it was put out, electric current conversely flowed. These results indicate that the AlN thin film deposited on the $MoSi_2$ substrate had the ability to detect thermal shock and the film was pyroelectrics.

Further, fracture, wear and stress distribution also can be detected by devising the position of the films and the electrodes [10]. The thermal conductivity of AlN single crystal (320 W/mK) [11], which is as high as that of copper (385 W/mK), is rather higher than that of $MoSi_2$ (48.5 W/mK), AlN can nimbly emit inside heat. We confirmed that the thermal radiation of aluminum substrates increases from 0.48 to 0.60 by the deposition of the AlN thin films. Thus, the AlN thin film deposited on the $MoSi_2$ substrate would function as a cooler. Moreover, the film would function as a protection film, because the chemical stability of AlN is very high [12]. The AlN thin film was not corroded by HF and HCl (10%). AlN strength is greater than alumina [11].

4. CONCLUSIONS

We prepared highly c-axis oriented AlN thin films on structural ceramic substrates by helicon plasma sputtering with a radical cell, and investigated the effects of eight sputtering control factors on the crystal orientation of the films by design of experiments and the ANOVA. These statistical methods are effective to compare the importance of many sputtering control factors. For the used deposition arrangement and within the selected range of the investigated deposition parameters, it was proved statistically that the distance between the target and the substrate, the sputtering pressure and the substrate temperature were significant control factors. Especially, the distance was the most important control factor among the eight factors. On the other hand, the effects of the rf coil power, the radical cell power, the nitrogen concentration, the sputtering time and the cathode power were not statistically significant. The micro structure of the film deposited under the optimized sputtering conditions is dense and this film consists of the c-axis oriented small crystallites. The FWHM of the film is 3.1-3.5°. It is possible to synthesize highly oriented AlN thin films on polycrystalline substrates by the helicon plasma sputtering.

The AlN thin films deposited on polycrystalline substrates had multifunction and responded to various physical stimuli such as mechanical impact, pressure and thermal shock and so on. The oriented AlN thin films would be expected to have multifunction. We believe that the combination of a structural ceramic and a functional ceramic film is a promising method to improve the reliability of structural ceramics. Moreover, we think other application of the films to artificial skin for a robot and a multi-function sensor.

REFERENCES

1) M. Akiyama, K. Nonaka, K. Shobu and T. Watanabe, J. Ceram. Soc. Jpn., 103, 1093-96 (1995).
2) M. Akiyama, H. R. Kokabi, K. Nonaka, K. Shobu and T. Watanabe, J. Am. Ceram. Soc., 78, 3304-08 (1995).
3) M. Akiyama, K. Nonaka, K. Shobu and T. Watanabe, J. Ceram. Soc. Jpn., 103, 974-76 (1995).
4) I.Usui, F. Tamai, Y. Towata and T. Yamada, J. Ceram. Soc. Jpn., 105, 97-100 (1997).
5) M. Akiyama, T. Harada, C. N. Xu, K. Nonaka and T. Watanabe, Thin Solid Films (in press).
6) Nat. Bur. Stand. (US) Monogr. 25, 12 (1975).
7) S. Egusa and N. Iwasa, Ferroelectrics, 145, 45-60 (1994).
8) G. A. Samara, Phys. Rev., 151, 378-86 (1966).
9) K. Komeya, Bull. Ceram. Soc. Jpn., 20, 506-11 (1985).
10) M. Akiyama, C. N. Xu, K. Nonaka, T. Watanabe and I. Usui, J. Mater. Sci. Lett., 17, 2093-95 (1998).
11) L. M. Sheppard, Am. Ceram. Soc. Bull., 69, 1801-12 (1990).
12) M. Sternitzke and G. Muller, J. Am. Ceram. Soc., 77, 737-42 (1994).

Preparation of C-axis Oriented Zinc Oxide Polycrystalline and its Piezoelectric Application

Satoru Fujitsu, Haruo Sekiguchi and Takashi Kondoh
Department of Materials Science and Ceramic Technology,
Shonan Institute of Technology, 1-1-25 Tsujido-Nishikaigan,
Fujisawa, Kanagawa 251-8511, Japan
FAX: 81-466-34-4111 ext.376, e-mail: fuji@mate.shonan-it.ac.jp

Large transparent specimens of polycrystalline zinc oxide with c-axis orientation were prepared by the vapor transport method. The cut and polished specimen was transparent for recognizing the distant view. In the X-ray diffraction measurement on the vertical plane to the growing direction, it was not observed except for the reflection peak from ($00l$) plane. The obtained specimens were n-type semiconductor with resistivity below 50 Ωcm at room temperature. By doping of Li_2O, its resistivity increased remarkably to be >10 $G\Omega$cm and then the doped material showed the piezoelectric characteristics. The electromechanical coupling constant depended strongly on the crystal axis orientation. The optimum specimen showed the comparable values to the reported data of the single crystal. A couple of the obtained piezoelectric ZnO was joined directly using the hot press method. The piezoelectric filter property was observed in the sample with the junction type of a piezoelectric transformer but the acceleration of the voltage could not be observed in such a specimen.

1. INTRODUCTION

Zinc oxide with c-axis preferential orientation shows piezoelectric properties and its piezoelectricity is relatively large. Considering the harmfulness to the environment of the commercially applied piezoelectric materials ($BaTiO_3$, PZT, etc.), ZnO is the most profitable candidate of the piezoelectric material in the next generation. However, the preparation of large ZnO single crystal is very difficult. And then the application of ZnO has been restricted to thin film applications such as the surface acoustic wave (SAW) devices prepared by the sputtering method.[1] The authors reported that large transparent specimens of polycrystalline ZnO with c-axis orientation was prepared by applying the vapor transport method.[2] After insulating the sample by doping of Li_2O, the sample showed piezoelectric properties.[3] Under the optimum sample conditions of the insulating, the crystal axis orientation and the crystal cutting, the electromechanical coupling coefficient for the traverse mode (k_{31}) was around 18% which was comparable to that of ZnO single crystal reported.[1] Ando et al.[4] prepared preferentially oriented ZnO ceramics using the same process. They measured the characteristics of the prepared ZnO as the trapped-energy-type resonator of thickness extensional mode.

The authors consider that the joining the specimens with the various combinations of their crystal axis directions is useful to apply the preferentially oriented ZnO bulk ceramics to the various piezoelectric devices. In this work, a couple of the oriented ZnO specimens were joined directly by the hot press method and its piezoelectric characteristic was estimated.[5]

2. EXPERIMENTAL PROCEDURE

2.1 Sample Preparation

The apparatus used to obtain the transparent ZnO is shown schematically in Fig.1. Sintered rodlike ceramics of ZnO (powder from Sakai Chemical Industry Co., Ltd.) were placed as a vapor source in the hottest zone in the mullite tube. The central area of this furnace was heated with a SiC heater to produce a temperature gradient from the hot zone to both sides of the tube. The maximum temperature gradient in the reaction tube was 100°C to 200°C/cm, which was close to the hottest zone. Polished flat surface of ZnO ceramics were employed as a substrate, placed in the lower temperature zone and rotated at 0.3 rpm. The optimum temperatures of source and substrate used here were 1150°C and 930°C, respectively. Nitrogen gas with 6% hydrogen was employed to maintain a reducing atmosphere in the mullite tube. Columnar crystals approximately 0.1 to 1 μm in diameter were grown densely on the substrate at the rate of 0.3 mm/h. The sample was cut into rectangular bar by diamond saw.

To obtain the sample with high resistivity, Li_2O was doped by solid state diffusion process. Since the sample was obtained in the reducing atmosphere, the as-grown sample showed low resistivity (<50 Ωcm). The cut specimen was soaked in the 0.1 mol/l Li_2CO_3 aqueous solution and dried at 100°C. The sample coated by Li_2CO_3 was heated at 900°C for 300 h in air.
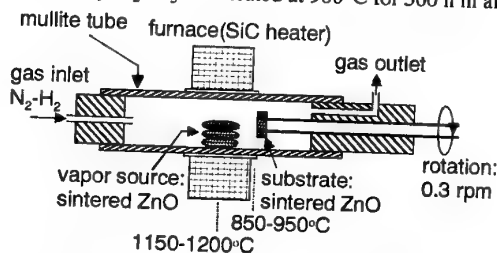

Fig.1 Schematic diagram of the apparatus for preparation of zinc oxide polycrystal.

The electrical resistivity was measured by the DC method in dry air. In-Ga alloy was painted as an ohmic electrode for this measurement.

2.2 Joining

The specimen prepared by this method was composed of columnar crystals growing perpendicular to the substrate. X-ray diffraction patterns indicated that the ZnO crystals were highly oriented with their c-axes aligned normal to the substrate. We call this aligning direction as "C-direction" and the plane normal to C-direction as "C-plane". The direction normal to the C-direction and the plane normal to the C-plane are called as "A-direction" and "A-plane", respectively. Two types of junction were prepared in this work. One is the joining of C-planes (C-C junction), the other is the joining of C-plane and A-plane(C-A junction).

The surface to join was mirror finished by a diamond paste (0.25 μm) and a couple of polished samples was assembled in the hot press instrument as shown in Fig.2. The couple was joined at 1200°C for 4 h in air under the uniaxial pressure of 30MPa.

2.3 Piezoelectric Characteristics

The electromechanical coupling coefficients (k_{31} and k_{33}) of the bulk ZnO were estimated from the results of the frequency dependence of the impedance (measured by HP-4195A). The plate (8.8 × 2.9 × 0.7 mm) was used for the k_{31} and the rod (3.4φ × 6.0 mm) was used for the k_{33} measurement as a normal sample. The temperature dependence of the k was measured at

20-500°C.

For the specimen with C-A junction, the transformation of the voltage by the piezoelectric effect was measured by using the circuit shown in Fig.3.

3. RESULTS AND DISCUSSION

3.1 Prepared Crystal and Li₂O Doping

Figure 4 shows photographs of (a) a cut and polished as-grown crystal and (b) a crystal annealed in air for 24 h. As-grown sample showed dark brown color: this might be due to oxygen vacancies introduced during the growth in the reducing atmosphere. By annealing this sample in air, the color changed into light yellow. This sample was transparent recognizing the distant view.

Figure 5 shows the X-ray diffraction patterns from ZnO powder, C-plane and A-plane. The strong reflections only from the ($00l$) (l = even number) planes were detected on the measurement of the C-plane. Since various X-ray diffraction peaks were detected from the A-plane (Fig.3(C)), it is judged that this prepared crystal is composed of polycrystalline with highly crystal axis orientation.

As-grown sample showed the metallic low resistivity. The enough high resistivity to measure the piezoelectric property (>10 GΩcm at room temperature) was achieved by doping with Li₂O as shown in Fig.6. The resistivity was homogeneous in the whole sample and the crystal became the colorlessness by this doping.

Fig.4 Photographs of (a) a cut and polished As-grown crystal and (b) a crystal annealed in air at 800°C for 24 h.
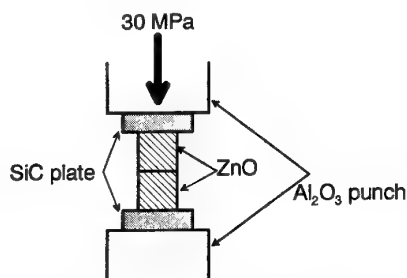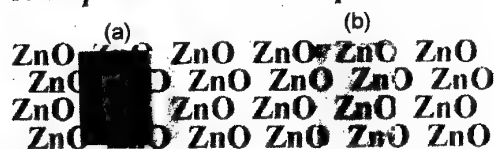

Fig.2 Schmatic diagrm for joining assembly in hot press instrument.

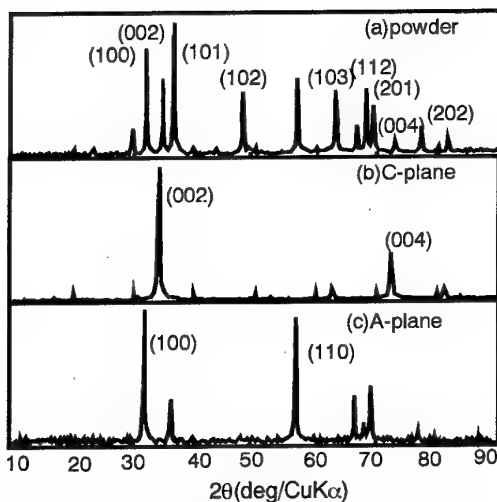Fig.3 Sample (A-C junction) and the voltage tranforming measurement.

Fig.5 X-ray diffraction patterns for ZnO (a) powder, (b) C-plane and (c) A-plane.
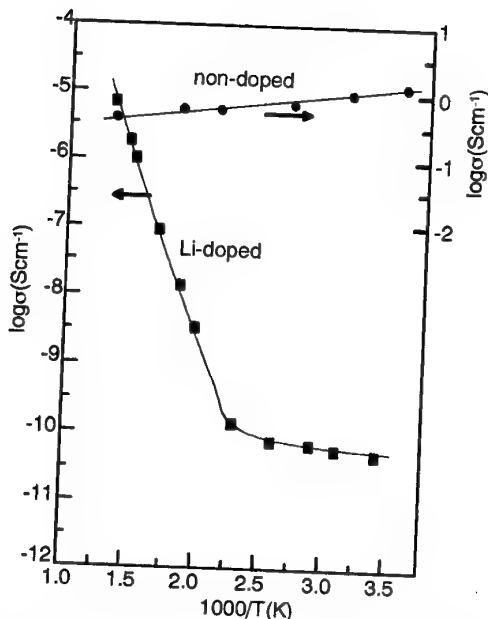
Fig.6 Temperature dependence for non-doped and Li doped sample. Resissitivity was over 10 GΩcm at room temperature and over 100 kΩcm at 500°C.

The increase in the resistivity of ZnO is explained by the following manner. In low temperature region (<1000°C), it is considered that the singly ionized oxygen vacancy or excess zinc ion in the interstitial site should be the electron donor of zinc oxide as

$$O_O^\times = V_O^\bullet + 1/2 O_2 \qquad (1)$$
$$V_O = V_O^\bullet + e' \qquad (2)$$
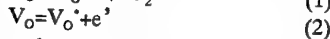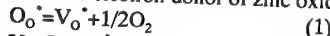
where the Kröger-Vink notation is employed. When Li_2O is doped into ZnO crystal, dissolved Li_2O consumes the conducting electron and forms the singly ionized oxygen vacancy as

$$Li_2O + e' = 2Li_{Zn}' + O_O + V_O^\bullet \qquad (3).$$
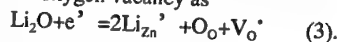
3.2 Piezoelectric Properties
3.2.1 Normal Specimen

It is well known that preferentially c-axis oriented ZnO shows the piezoelectric properties. Table I shows the electromechanical coupling coefficients (k_{31} and K_{33}) and the intensity ratio of the X-ray diffraction peaks from (103) and (004) planes. The small I_{103}/I_{004} means the high crystal orientation. The coupling coefficient depended on the crystal orientation. The similar result was reported in the ZnO thin film.[1] In the optimum specimen, the k_{31} was comparable to the data of ZnO single crystal, but the k_{33} was smaller than that of the single crystal. Since the thickness of the sample to measure the k_{31} is thin (0.7 mm), the plate with high crystal orientation can be obtained easily from the prepared ZnO block. While the sample to measure the k_{33} requires enough thickness (6.0 mm) and the sample contains the low orientation region in the vicinity of the substrate.

Since the crystal structure of ZnO does not change by changing in temperature, it is expected that ZnO is useful as a piezoelectric material for high temperature application. As shown in Fig.7, the temperature

Table I Electromechanical Coupling coefficients (k_{31} and k_{33}) and crystal axis orientation.

sample	k_{31}(%)	k_{33}(%)	I_{103}/I_{004}(T)	I_{103}/I_{004}(B)
1	12.1		3.81	
2	14.5		1.02	
3	18.1		0.03	
4		16.7	0.16	4.2
5		35.8	0.04	0.11
single cry.	18.4	41.9	0	0
powder			14.5	14.5

(T) and (B) indicate the planes cut from the top and bottom areas of grown crystal, respectively. The bottom area is close to the substrate.
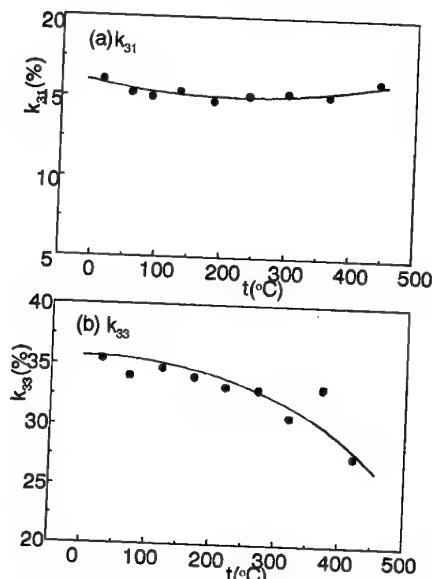
Fig.7 Temperature dependence of (a) k_{31} and (b) k_{33}.

dependence of the k_{31} was almost flat and the k_{33} decreased gradually with increasing the temperature. Since the change in the impedance at the resonant frequency decreased in both 31 and 33 modes, the mechanical quality factor (Q_m) decreased with increasing the temperature.

3.2.1 Joined ZnO Crystal

Even in the sample etched thermally (1000°C for 10 min after mirror finishing), the microstructure observation by SEM showed no joining interface of the C-C junction. No gap and no secondary phase was observed along this junction area as shown in Fig.8. It is judged that the excellent C-C junction was prepared by the process employed in this work. The k_{33} for the sample with this C-C junction was nearly equal to the value of each original specimen.

The joining interface was found in the sample with C-A junction. The microstructure for the cross section showed the gaps (0.1 to 0.5 μm in width and 0.5 to 5 μm in length) existing along the interface and the several cracks (10 to 100 μm in length) existing normal to the interface. The developing of the cracks is due to the mismatching of the thermal expansion between A- and
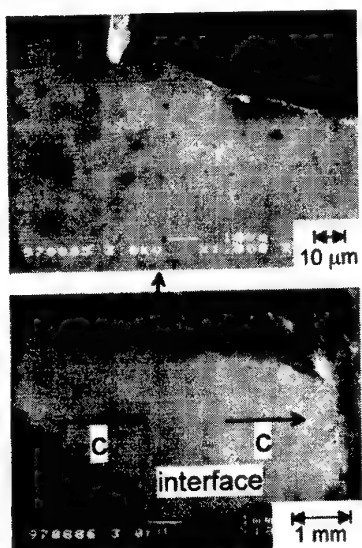
Fig.8 SEM observation for C-C joined specimen.
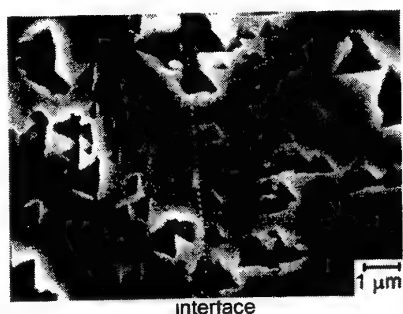
interface
Fig.9 SEM observation of etch-pits formed on the polished cross section. The dashed line indicates the interface of C-A junction.

C-plane. But the substantial region (over 90 %) of the interface area was joined smoothly by this process. The joining did not affect on the crystal axis orientation even in the region close to the interface. The etch-pits observed in the vicinity of the interface are shown in Fig.9. The polished sample was etched by soaking for 1 min into aqua. HNO_3 (0.01N). The etch-pits directed to left in the left side area of the interface of the C-A junction and those directed to top in the right side area of the interface. The direction of etch-pit indicates the C-direction.

The transformation of the voltage was measured by using the circuit shown in Fig.3 for the specimen with C-A junction. Since this specimen has the piezoelectric transformer type of configuration and the mechanical quality factor (Q_m) of this type of ZnO is relatively high, the acceleration of voltage was expected in this joining.[6] From the theoretical estimation, 30 times of gain in voltage was prospected. As a result, the acceleration was not observed in this measurement. The very small output of voltage was detected at the resonant frequency as shown in Fig.10, which characteristic is similar to the piezoelectric filter. But this output value is approximately same level to that from the sample used for k_{31} measurement with same
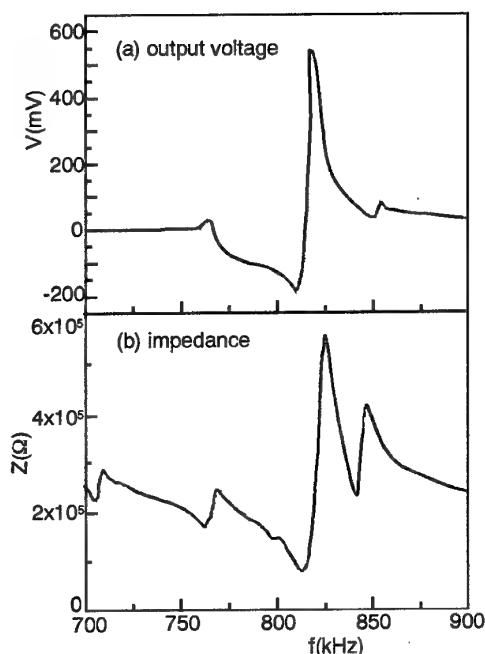
Fig.10 Frequency dependences of (a) output voltage and (b) impedance. The input voltage (10V) was applied on a-b electrodes and the output voltage from b-c was measured by the circuit shown in Fig.3.

electrode configuration and the peculiarity of C-A junction has not been revealed yet. Though it is considered as one possible reason that the input impedance of the oscilloscope is too low, the detail reason has not be clarified yet.

ACKNOWLEGEMENT

REFERENCES
[1] T. Shiozaki, "Piezoelectric ZnO Film and its Application", Electronics Ceramics, Edited by K. Okazaki, (CMC., Tokyo, 1981), pp. 301-40 (in Japanese).
[2] F. Noritake, N. Yamamoto, Y. Horiguchi, S. Fujitsu, K. Koumoto and H. Yanagida, J. Am. Ceram. Soc., 74 (1991), p.232.
[3] S. Fujitsu and F. Noritake, Proc. 4th Fall Meet. Ceram. Soc. Jpn., (1991), p.82 (in Japanese).
[4] A. Ando, T. Minamikawa, H. Takagi and K. Tomono, Jpn. J. Appl. Phys., 34 (1995) p.5320.
[5] S. Fujitsu, T. Kondoh and H. Sekiguchi, Key Engineering Materials 169-170 (1999) 61-64, (Electroceramics in Japan II, edited by N. Mizutani et al.)
[6] C. A. Rosen, Proc. Electr. Comp. Symp., (1957) p.205.

Sol-Gel Growth and Properties of Lead Scandium Tantalate Thin Films for Dielectric Bolometer Applications

T. Takeishi, A.P. de Kroon and R.W. Whatmore*

TDK Materials Research Center, 570-2, Matsugashita, Minamihatori, Narita-shi, Chiba 286-8588, Japan.

Fax: 81-476-37-1648, email: taku_takeishi@mb1.tdk.co.jp

*Dept. of Nanotechnology, School of Industrial and Manufacturing Science, Cranfield University, Beds., UK.

Fax: 44-1234-751346, email: r.w.whatmore@cranfield.ac.uk

Lead scandium tantalate (PST) ceramics have been shown to offer some of the most promising pyroelectric properties when operated under electrical bias, with demonstrated values of the figure-of-merit F_D in the order of 15×10^{-5} $Pa^{-1/2}$. There is thus a considerable drive to produce thin films of this material by growth onto silicon for use in uncooled thermal detector applications. This paper will discuss the growth of PST thin films by sol-gel techniques onto Pt/Ti-on-Si substrates and how the dielectric properties vary with the conditions of growth. PST-solutions were prepared by a modified sol-gel method and deposited according to two different techniques. Dielectric and pyroelectric properties were measured between -30 and 90 °C. Maximum figures of merit $F_V = 5.64 \times 10^{-2}$ m^2C^{-1} and $F_D = 1.44 \times 10^{-5}$ $Pa^{-1/2}$ were obtained after firing to 800 °C.

1. INTRODUCTION

The pyroelectric effect, like the piezoelectric effect, relies on the presence of permanent electrical dipoles in a crystal. Below the Curie-temperature these dipoles align to form a spontaneous electrical polarization P of the crystal. The pyroelectric effect is defined as:

$$\Delta P_i = p_i \cdot \Delta T \qquad (1)$$

where ΔP_i is the change of the crystal polarization in the direction i, under the influence of the temperature variation ΔT, and p_i the corresponding pyroelectric coefficient.

For sensor applications equation (1) can be rewritten in the more appropriate form [1]:

$$V = \frac{p}{(C_v \cdot \varepsilon_r)} \cdot \frac{W_0}{(\varepsilon_o \cdot A)} \qquad (2)$$

where C_v is the volume heat capacity, ε_r and ε_o the relative and absolute dielectric constant, respectively, A the area of the detector and W_o the input energy. Every energy flow can now be measured in the form of a voltage output.

For the development of a pyroelectric material figures of merit are indispensable. Examples are:

$$F_i = p/C_v \qquad (3)$$
$$F_V = p/(C_v \, \varepsilon_r \, \varepsilon_o) \qquad (4)$$
$$F_D = p/(C_v \sqrt{(\varepsilon_r \varepsilon_o \tan\delta)}) \qquad (5)$$

where F_i is the current responsivity, F_V the voltage responsivity, and F_D the detectivity [2].

High figures of merit can be achieved with ferroelectric materials operated in 'dielectric bolometer'

mode, i.e. near their Curie-temperature and under an applied electrical bias field. For further improvements a low dielectric constant together with a low dielectric loss is required. In the case of the complex perovskite PST this can be achieved by ordering the crystal (figure 1).

For integrated Si-manufacturing a low temperature of perovskite crystallization (typically <500 °C) is necessary. This can be done by sol-gel processing. The main advantages of the method are low-cost and good compositional control. The main disadvantage is the environmental aspects of its mainly toxic precursors.
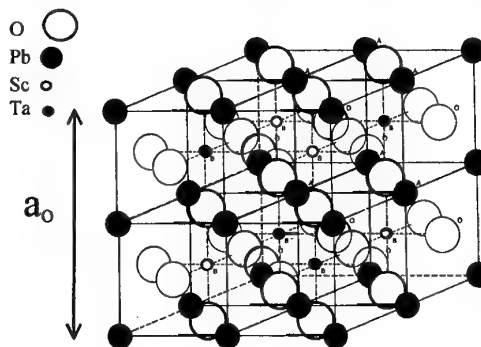

Fig. 1 Crystal structure of (1:1)-ordered perovskite PST

2. FILM PREPARATION

PST-solutions were prepared by a modified sol-gel process in two steps: $Sc(AcAc)_3$ was prepared in the first step following the work of Morgan and Moss [3], and in the second step $Pb(OAc)_2 \cdot 3H_2O$ was prereacted with $Sc(AcAc)_3$ in 2ME or $Sc(AcAc)_3$ with $Ta(OEt)_5$. The to-

tal concentration of the solutions was adjusted to 0.8 M. The lead content of the solutions was varied according to the formula $Pb_{1+x}(Sc_{0.5}Ta_{0.5})O_3$ with $0.05<x<0.20$.

Films were deposited onto cut 4 cm² fragments of 4" Pt/Ti/SiO₂/Si-wafers (GEC-Marconi Materials Technology Ltd., UK.) using a photoresist spinner (Headway Research Inc., Model 315) at 3000 rpm for 30 s. Two different deposition methods were employed. In deposition method 1 each individual layer was dried on a hot plate (J. Bibby Scientific Products Ltd., Model B212) at 300 °C for 5 min., and the finished film was fired once at 500 to 700 °C for 15 min. using either a hot plate (Model B212) or a tube furnace (Pyrotherm Furnaces). In deposition method 2 each individual layer was dried/fired on a hot plate (Brewer Scientific Inc., Model 1100, under 25 cm Hg vacuum suction) at 500 to 600 °C for 5 min, and the finished film was fired once at 600 to 900 °C using a rapid thermal annealer (AG Associates, Heatpulse 210T) under 40 ml/min flowing air. Films of up to 6 layers were thus prepared, with a typical thickness of 0.64 μm. All films were deposited under air atmosphere in a clean room of Class 10,000 (1,000 underneath the laminar flow hoods).

3. FILM CHARACTERIZATION

Figure 2 shows the phase assembly of fired PST thin films prepared by ST- or PS-method, respectively, following deposition method 1 using a tube furnace. The films consist of 3 individual layers each, employing 10% Pb-excess. The ST-method is characterized by low-temperature perovskite crystallization, with the complete transformation to perovskite PST occurring between 500 and 700 °C.
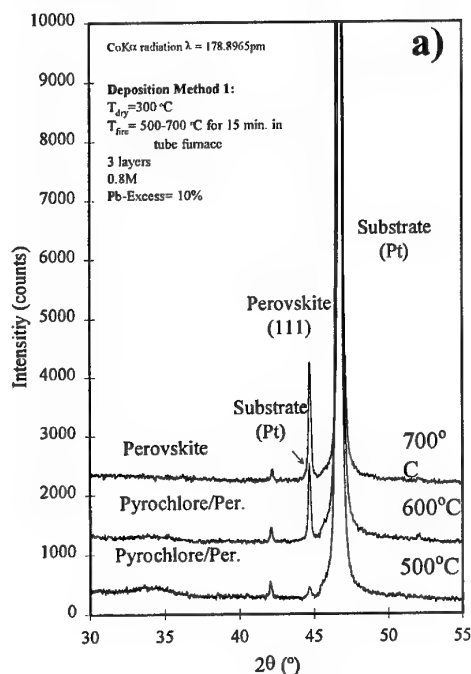
The PS-method exhibits complete transformation to perovskite PST between 600 and 700 °C, together with a much better crystallinity of the obtained perovskite phase. Due to the abrupt transition to perovskite PST at the higher temperature in the PS-method, the temperature range where pyrochlore and perosvkite phases coexist in the PS-method is smaller than in the ST-method.

Both the effect of the use of a small hot plate in deposition method 1, instead of a tube furnace, and the amount of lead excess in deposition method 2 on the phase development of perovskite PST was reported previously [4]. Hot plate firing in the PS-method lowered the complete transformation to perovskite PST to 520 °C, and the amount of lead excess decreased the amount of pyrochlore and increased the crystallinity of the perovskite phase.

Room temperature dielectric properties of PST thin films prepared by the PS-method using deposition method 1 with either a hot plate or a tube furnace and deposition method 2 with various amounts of Pb-excess are listed in table 1 and shown in figure 3. Upon increasing the measuring frequency from 100 Hz to 100 kHz, the Curie-Weiss temperature shifted to lower temperatures depending on the original firing temperature of the thin film. Films fired at 600 °C showed a decrease from 60 to 0 °C and films fired at 700 °C showed a decrease from 80 to 40 °C. Films fired at 800 °C were fully ordered and no longer showed any relaxor-type behaviour. These films exhibited a constant Curie-Weiss temperature at 40 °C between 100 Hz and 100 kHz.

By increasing the measuring temperature from −20 to 90 °C at a fixed frequency of 100 Hz the dielectric constant of the thin films fired at 600 and 700 °C could be observed to increase gradually until the Curie-Weiss

Fig. 2 X-ray diffraction patterns of fired PST thin films
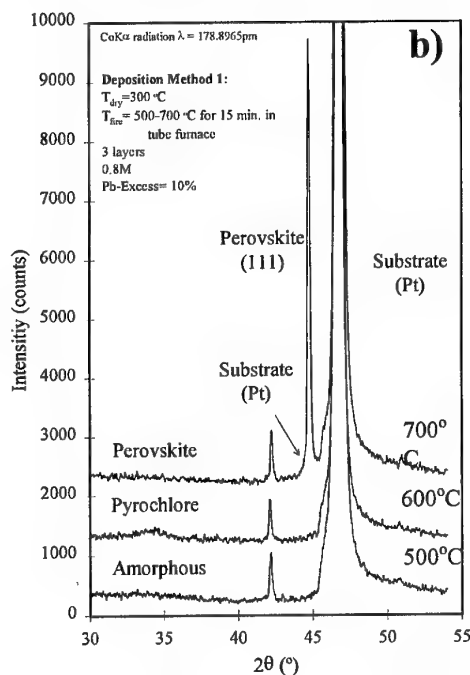(a) ST-prereaction method

Fig. 2 X-ray diffraction patterns of fired PST thin films
- Continued. (b) PS-prereaction method

temperature was reached, after which they decreased slightly. The dielectric constant of the film fired at 800 °C increased until 50 °C, after which it decreased sharply. This is interpreted as its ferroelectric to paraelectric phase transition occurring between 50 and 60 °C. All dielectric loss increased continuously with temperature.

Tab. I RT dielectric properties of selected PST thin films, 0V DC-bias.

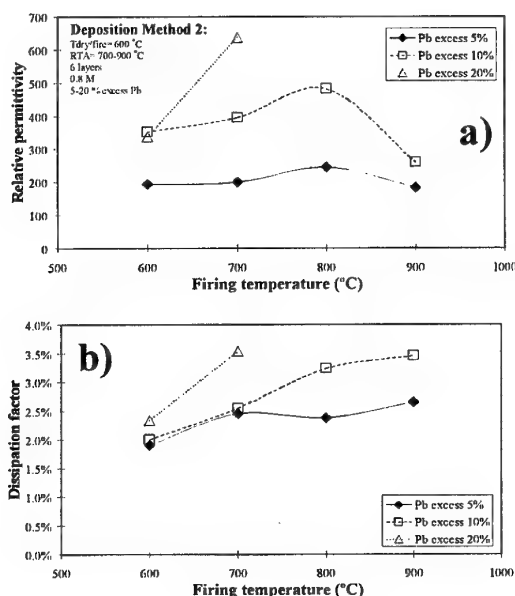| Film Name	ε_r			tan δ (%)		
	1 kHz	10 kHz	100 kHz	1 kHz	10 kHz	100 kHz
5%-600	319	311	305	1.85	1.57	2.08
-700	326	316	307	2.20	2.05	2.83
-800	459	460	420	2.39	2.23	2.38
-900	310	299	289	2.58	2.45	2.65
10%-600	548	533	525	1.61	1.64	2.19
-700	661	640	619	2.30	2.21	2.55
-800	796	768	740	2.97	2.62	3.54
-900	447	425	406	3.50	3.27	3.46
20%-600	616	601	588	1.76	3.96	2.54
-700	1061	1024	995	2.97	2.34	3.54

Fig. 3 RT dielectric properties of PST thin films at 100 kHz: (a) relative dielectric constant (b) loss factor

Figure 4 shows the pyroelectric current profile at –30 °C under an applied DC-bias field of 3 V/0.64 μm of a fired PST thin film prepared by deposition method 2. The thin film was dried/fired at 600 °C and annealed at 700 °C in the RTA. The saw tooth temperature profile was generated by a Peltier heater and the resulting current was measured by a Keithley Model 6517 Electrometer. The pyroelectric current is given by half the step size of the current density (top electrode diameter 0.75 mm) at the reversal of the heating rate (±1 °C/min). The average current density over the entire time interval is determined by the DC-resistivity of the sample at the mea-

suring time and temperature and under the applied DC-bias field. The pyroelectric current response increases linearly with the value of the DC-bias field at values below 5 MV/m. The application of a higher DC-bias field would improve the pyroelectric coefficient of the material but could lead to break down of the film.
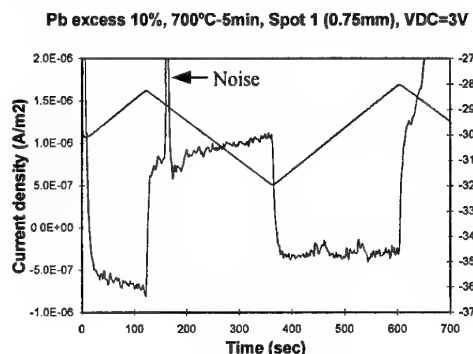
Pb excess 10%, 700°C-5min, Spot 1 (0.75mm), VDC=3V

Fig. 4 Pyroelectric current profile of a fired PST thin film at –30 °C: Pb-excess = 10%, DC-bias = 3V.

Figure 5a shows the pyroelectric coefficient of fired PST thin films prepared by deposition method 2 as a function of the firing temperature and the amount of excess Pb. A positive linear relationship exists between the pyroelectric coefficient and the firing temperature. At 800 °C and with 10% excess Pb the maximum pyroelectric coefficient is 4×10^{-4} Cm^{-2}K^{-1}. At 600 °C and with 5% excess Pb it is only 5×10^{-5} Cm^{-2}K^{-1}. The increase in the pyroelectric coefficient with the firing temperature can be explained by the increase in the crystallinity of the perovskite PST phase and the decrease of the parasitic pyrochlore phase. The degree of (111) film orientation is largely independent of the firing temperature, and increases only slightly with the amount of Pb-excess.

The fact that pyrochlore phase remains present between 600 and 800 °C is not apparent from the X-ray diffractograms of figure 2b on account of the nanocrystalline nature of the pyrochlore grains. Peak broadening analysis revealed that the grain size of the pyrochlore phase is on the order of 4 nm, and is independent of both the excess amount of Pb and the firing temperature used. Figure 5b, which shows the DC-resistivity data of the same PST thin films as a function of the firing temperature and the amount of Pb-excess does show the influence of the pyrochlore phase below 700 °C. At 900 °C partial decomposition occurs.

The pyroelectric properties including the calculated figures of merit F_V and F_D of selected PST thin films have been summarized in Table II.

Tab. II Pyroelectric properties of selected PST thin films

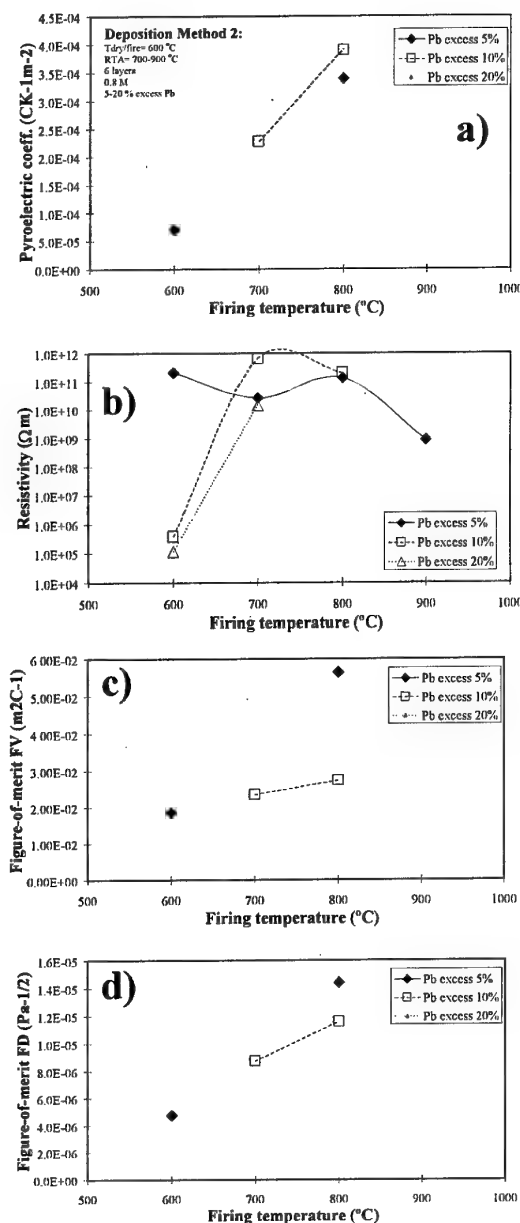| Film Name	Temp. (°C)	Bias Field (MV/m)	ε_r (100 kHz)	tan δ (%) (100 kHz)	p (x10^{-4}CK^{-1}m^{-2})	F_V (x10^{-2}m^{2}C^{-1})	F_D (x10^{-5}Pa$^{-1/2}$)	Ref
5%-800	28	5	249	2.14	74.4	5.64	1.44	-
10%-800	28	5	394	3.42	45.9	2.84	1.22	-
PST-525	30	5	-	-	4.2	-	2.40	[5]
PST-900	30	10	3100	1.70	38.0	-	5-11	[6]
PST-1200	30	5	750 (0.4 kHz)	2.70	13.6 (30 Hz)	7.18	11.50	[7]

Fig. 5 RT pyroelectric properties of fired PST thin films under 3V DC-bias: (a) pyroelectric coefficient, (b) DC-resistivity, (c) figure-of-merit F_V, (d) figure-of-merit F_D

The maximum value of F_V and F_D was obtained with the PST thin film fired at 800 °C, and containing 5% excess Pb. This is due to its relatively low dielectric constant. The figures of merit increase with the firing temperature similar to the pyroelectric coefficient. In order to obtain higher figures of merit F_V for PST thin films it is necessary to increase the pyroelectric coefficient. This can be done by increasing: (i) the firing temperature of the material, (ii) the order of the perovskite crystal, and (iii) the measuring temperature and/or DC-bias field. To increase

the value of F_D it is necessary to increase the pyroelectric coefficient and decrease the dielectric loss. The use of higher amounts of excess Pb may be advantageous, but this may increase the danger of film break down by the introduction of macroscopic defects. Similarly, the use of higher DC-bias fields may cause the PST thin films to break down earlier.

To prevent the presence of remanent pyrochlore in the fired PST thin films it is necessary to guarantee the homogeneity of the PST solutions and to fully complete the transformation to perovskite PST.

4. CONCLUSIONS

Thin films of lead scandium tantalate were successfully grown on $Pt/Ti/SiO_2/Si$-substrates at low temperatures by modified sol-gel processing. The films exhibit a high (111)-orientation together with a high crystallinity of the perovskite phase. Pre-reaction of the Sc- and Ta-precursors (ST-method) resulted in a lower temperature of perovskite PST formation, but the crystallinity of the phase was reduced. Dielectric and pyroelectric properties between −30 and 90 °C of the thin films prepared between 600 and 900 °C with a Pb-excess of 5 to 20% suffered from the presence of pyrochlore. Maximum pyroelectric figures of merit were obtained with PST thin films fired at high temperatures (800 °C), containing little excess amount of Pb (5%). The maximum values of F_V and F_D were 5.64×10^{-2} m^2C^{-1} and 1.44×10^{-5} $Pa^{-1/2}$, respectively. These values may seem low, as they are only about 10 and 20% of the values reported in the literature for PST bulk and thin films, respectively, but they can be expected to increase after further optimization of the processing and firing conditions.

5. ACKNOWLEDGEMENTS

6. REFERENCES

[1] Editor, *Physik in Unserer Zeit*, **19**, 109 (1988).
[2] R.W. Whatmore, *Ferroelectrics*, **118**, 241-259 (1991).
[3] G.T. Morgan and H.W. Moss, *J. Chem. Soc.*, 189-214 (1914).
[4] T. Takeishi and R.W. Whatmore, *J. Phys. IV France*, **8**, 57-60 (1998).
[5] R. Watton, P.A. Manning, M.C.J. Perkins, J.P. Gillham and M.A. Todd, Infrared Technology and Applications, XXII, April 1996, SPIE, vol. 2744.
[6] A. Patel, N. Shorrocks and R.W. Whatmore, *Ferroelectrics*, **134**, 343-348 (1992).
[7] N.M. Shorrocks, R.W.Whatmore and P.C. Osbond, *Ferroelectrics*, **106**, 387-392 (1990).

Fabrication and Characterization of PZT Thick Films by a New Sol-Gel Process Using an Interfacial Polymerization

Shuichi Ozawa, Naoki Ohashi, Masayuki Yamane, Takaaki Tsurumi

Department of Metallurgy and Ceramics Science, Graduate School of Science
and Engineering, Tokyo Institute of Technology, Japan
Fax:81-03-5734-2514, e-mail:ttsurumi@ceram.titech.ac.jp

$Pb(Zr_x,Ti_{1-x})O_3$ (PZT) films of 10-20μm in thickness have been fabricated by a new sol-gel process using an interfacial polymerization technique. Interfacial polymerization is that the alkoxide precursor solution is poured on the surface of water in a container and a gel film is formed at the interface between the two immiscible liquids. The precursor solution was prepared by adding PZT alkoxide solution, PZT powders coated with $Pb_5Ge_3O_{11}$ (PG), and a dispersion stabilizer into Hexane solvent. The precursor solution was poured on the water and the PZT gel film was formed at the interface. The gel film was gently placed on the Si substrate by draining the water from the container. After drying the film was sintered at 850℃ for 30 min. PZT films (thickness:14-15μm) could be fabricated by this process. The PG-coated powder was effective to reduce the sintering temperature. The films adhered on the Pt electrode on Si substrate showed remnant polarization (P_r) of 7.0μ/cm^2.

1. INTRODUCTION

In recent years, there has been an increasing interest in micro-electro-mechanical-system (MEMS). MEMS are fabricated to take advantage of Si electronic and mechanical properties. $Pb(Zr_x,Ti_{1-x})O_3$ (PZT) films are possibly used for many piezoelectric devices in MEMS such as micro actuators, sensors, ultrasonic motors and so on. PZT thick films ($\sim$10μm) are required for these applications, especially micro actuators, to produce a large piezoelectric displacement and a generative force.

Some methods have been reported to deposit PZT thick films on Si substrate, such as screen printing [1], sol-gel method [2], hydrothermal method [3], and electrophoresis method [4]. However, each process has peculiar problems, i.e.: Si substrates are corroded in the hydrothermal condition and high sintering temperatures required in the screen printing and the electrophoresis method enhance the volatility of PbO and the interdiffusion of the Si and Pb through the bottom electrode. A low temperature sintering of PZT films has been achieved in conventional sol-gel method but it requires repeating of the coating and drying processes for many times to make thick films without clacking [5-6]. Therefore, it seems to be necessary to develop a new process to make PZT thick films on Si substrates.

We have been trying to make PZT thick films by a sol-gel method with single coating process. A new sol-gel method using an interfacial polymerization was originally proposed by Yamane et al. [7-8] for silicate glasses. In this process, alkoxide solutions of raw materials were hydrolyze and polymerize on the water. The gel films formed at the interface between the organic solvent of alkoxide solution and water could be shrink without the restriction from the substrate. After completing polycondensation at the interface of the two immiscible liquids, the gel film was placed on a substrate by draining the water. The thickness of the film was controlled by the concentration of the alkoxide solution in the precursor solution. We thought this process could be useful to fabricate the PZT thick films. In this paper, the development of the PZT thick films by the sol-gel process using an interfacial polymerization is reported.

2. EXPERIMENTAL PROCEDURE

2.1 Film Preparation

A precursor solution was prepared by dissolving the PZT (53/47) alkoxide solution (800μl; High Purity Chemical Laboratory Co.Ltd.) into Hexane solvent (10ml). Acetyl acetone (25μl) was also added to control reaction of the precursor solution. To reduce the shrinkage of the gel film during hydrolysis and polycondensation, PZT powders (0.2μm; Sakai Chemical Co.) were added to the precursor solution. To reduce the sintering temperature, PZT powder coated with a sintering agent of $Pb_5Ge_3O_{11}$ (PG) was also used. The amount of PG to the PZT powder was 2wt%. The PG-coated powder was supplied from Dr.T.Hayashi in Shonan Inst. of Tech. A surface-active agent was dissolved in the precursor solution to disperse the powders. The amounts of these components were listed in Table I.

The reaction container is showed in Fig.1. A Pt/IrO$_2$/SiO$_2$/Si substrate was placed on the bottom of the container and distilled water was poured in the container. After stirring, the precursor solution was gently poured on the surface of the water. After the hydrolysis and polycondensation, a PZT gel film formed on the water was placed on the substrate by draining the water from bottom of the container. The PZT gel film on the substrate was dried at room temperature in humidity of 70% for 6 h and 35% for 6 h. After drying, the film added with the PG-coated powder was heated at the rate of 20℃/h to 400℃, 180℃/h to 850℃ and kept at 850℃ for 30 min. The sintering temperature of the film added

Table.I Components of precursor solution

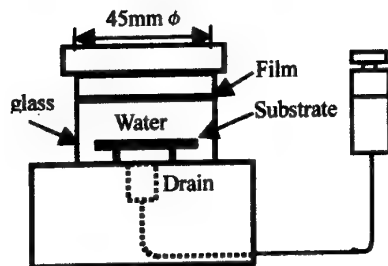|	
PZT (53/47) alkoxide	35μl
PZT–2wt%PG powder	0.1 g
Surface active agent	1.0×10^{-4} mol
Hexane	10 ml

Fig.1 Illustration of the reaction container

PZT powders without PG-coatng (non-coated powder) was 950℃.

2.2 Characterization of PZT thick films

The microstructure of the films was observed by SEM. The crystallization of the films was monitored by X-ray diffraction (XRD) method. Ferroelectric properties were measured using ferroelectric test system (Radiant Technologies, RT66A) after top Pt electrode was sputtered (diameter = 1mmϕ).

3. RESULTS AND DISCUSSION
3.1 Gel films

Figure 2(A) shows a photograph of a gel film without PZT powders after hydrolysis and polycondensation on the water in the container. The gel film broken into small pieces because of the large shrinkage during poly-condensation. Experimental conditions such as contents of alkoxide and acetyl acetone have been changed but it was impossible to avoid the cracking. Figure 2(B) is a photograph of the gel films containing the PG-coated PZT powders. The number of cracks markedly reduced by adding PZT powders because the addition of powders decreased the shrinkage of gel films. The gel film thus obtained was flexible and kept its shape on the water, showing that the PZT powders were connected to each other by PZT gel. The dispersion of PZT powder in the precursor solution was essentially important to make uniform and flexible gel films. The diameter of the gel film was restricted by the size of the container (40mmϕ in this case).

After hydrolysis and polycondensation on the water, the film was placed on the substrate by draining the water from the container.

(A)   (B)

Fig.2 Photographs of gel film after hydrolysis and poly-
condensation.
(A) gel film without PZT powder,
(B) gel film with PG-coated PZT powders.

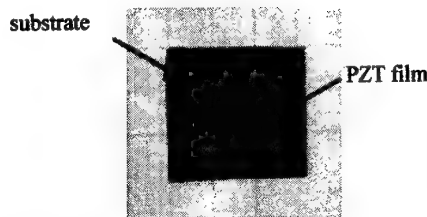Fig.3 Photograph of a PZT film sintered at 850℃ for
30 min. on Pt/IrO$_2$/SiO$_2$/Si substrate.

3.2 Formation of Crystalline Films

The gel films were dried in a humid atmosphere. The drying condition was important to avoid the cracking of films. Figure 3 shows the photograph of PZT films after sintering. The PZT films adhered on the Si substrate. Cracking and exfoliation of PZT films were not observed and the adhering force was relatively strong.

Figure 4 shows XRD profiles of PZT film after sintering and PZT powders added in the precursor solution. The XRD profiles of the PZT powders with and without PG-coating (B and D) indicated the mixture of tetragonal and rhombohedral phases because the chemical composition of PZT powders was near MPB. A peak observed at 30.4° in the profile of PZT film with the PG-coated powder (A) is due to the crystallized PG.. Profile (A) is approximately the same as the raw powder (B) except this peak and those from the substrate. This indicates the reaction between the film and substrate was negligible at the sintering temperature of 850℃. The separation of 101 and 110 peaks is observed in the profile of PZT films added with the non-coated powder (C), indicating the PZT phase in the film was
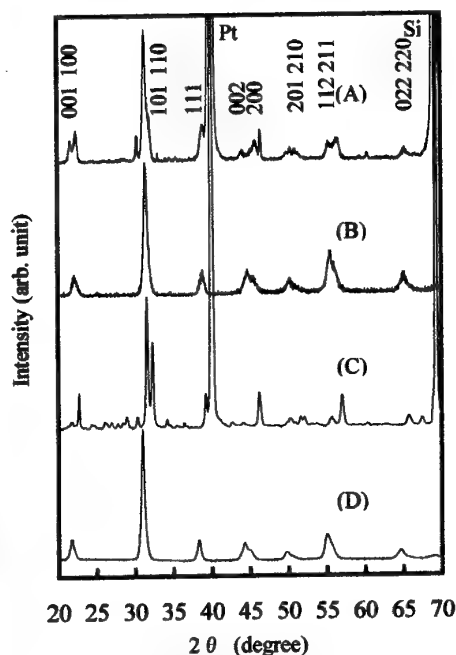

Fig.4 The XRD profiles of (A) PZT film with PG-
coated powder, (B) PG-coated powder,
(C) PZT film with non-coated commercial
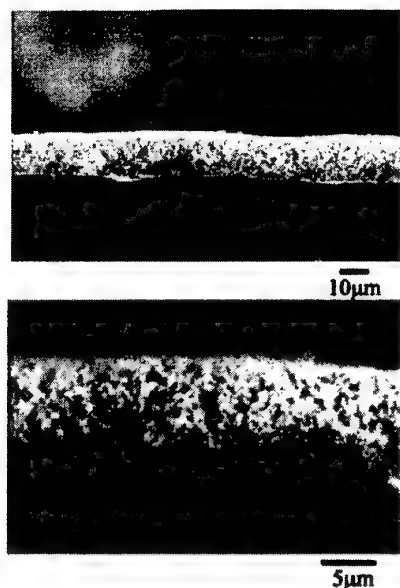PZT powder and (D) commercial PZT powder.

Fig.5 SEM photographs of cross section of PZT thick
film added with PG-coated powder

Fig.6 SEM photographs of cross section of PZT thick
film added with non-coated powder.

slightly shifted to the tetragonal phase. Furthermore,
many unknown peak are observable from 25 - 45°.
These peaks show that the chemical reaction occurred
between the PZT film and Si substrate at the sintering
temperature of 950℃.

3.3 Microstructure

SEM photographs of the cross section of a PZT film
added with the PG-coated powder and that with the non-
coated powder are shown in Fig.5 and Fig.6,
respectively. The both thick films were relatively flat
with good adhesion to the substrate. The thickness of the
PZT film with PG-coated powder was 14.6μm, and that
of PZT film with the non-coated powder was about
10μm. We have succeeded in making PZT thick films by
a sol-gel process using and interfacial polymerization.

Small pores are observed in the films and fully
densified films have not been obtained yet. However, the
necking between PZT powders were formed by the
sintering. It is noted that big differences could not be
observed in the microstructures of the two films in spite
of the difference in the sintering temperatures. The
sintering was not proceeded when the PZT film with the
non-coated powder was heated at the same temperature
of the film with the PG-coated powder. This means that
the PG-coating is very effective to reduce the sintering
temperature. In PZT film with PG-coated powder, fully
densified portion is observed near the substrate. We
think this portion is formed by that Si diffused through
the bottom electrode acts as a sintering agent. It is
expected that the density of the films is improved by
enlarging this portion through the films.

3.4 Ferroelectric Property

A P-E hysteresis curve of the PZT film added with the
non-coated powder is shown in Fig.8. The remnant
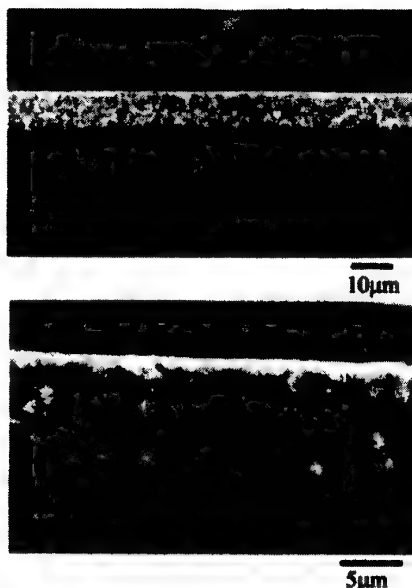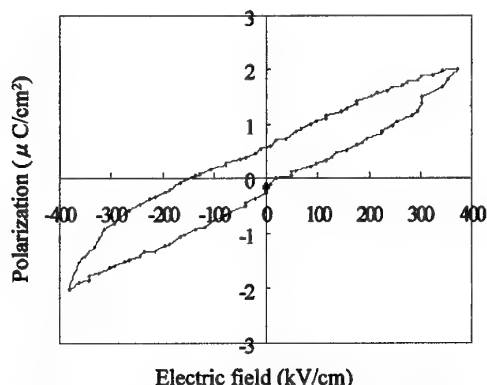polarization is very small. This seems to be due to the

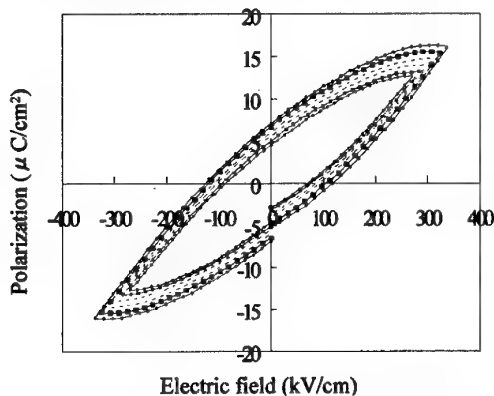Fig.8 P-E hysteresis curve of PZT thick film added with
the non-coated powder.

Fig.9 Ferroelectric hysteresis loop of the PZT thick film

reaction of PZT film with the substrate as shown in XRD profile (Fig.4(C).

A P-E hysteresis curve of the PZT film with the PG-coated powder is shown in Fig.9. Although the hysteresis loop was not saturated, the remnant polarization and coercive field were determined to be $7.0\mu C/cm^2$ and 117kV/cm, respectively. The shape of hysteresis curve was markedly improved by using the PG-coated powder to reduce the sintering temperature. However, the film still showed a large leak current when the electric field was increased above 40kV/cm. The small remnant polarization and leaky properties are due to the low quality of films. It is essential to improve the quality in the future study to obtain good ferroelectric properties.

4. SUMMARY

A new sol-gel process using an interfacial polymerization has made it possible to fabricate PZT thick films on Si substrate. The precursor solution was prepared by mixing the PZT alkoxide solution, PZT powders coated with 2wt% of PG and a surface active agent into hexane solvent. A PZT thick film (thickness = 14.6μ m) was successfully fabricated on Si substrates with single coating process. The thick film was flat and adheres to the substrate after sintering at 850℃. The addition of PZT powder was indispensable to avoid clacking of gel film. The PG-coated powder was effective to reduce the sintering temperature. A PZT-thick film prepared in this study showed a P-E hysteresis curve with a remnant polarization of $7.0\mu C/cm^2$.

References
[1] J.F.Fernandes, E.Nieto, C.Moure, P.Duran and R.E.Newnham, *J.Mater.Sci.*, **30**, 5399-404 (1995).
[2] D.A.Barrow, T.E.Petroff, R.P.Tandon and M.Sayer, *J.Appl.Phys.*, **81**, 876-82 (1997).
[3] K.Shinomura, T.Tsurumi, Y.Ohba and M. Daimon, *Jpn.J.Appl.Phys.*, **31**, 3090-93 (1992).
[4] T.Sweeney and R.W.Whatmore, *Proc.10th IEEE Int.Symp.Appl.Ferroelectrics*, 193-96 (1996).
[5] H.D.Chen, K.R.Udayakumar, C.J.Gaskey and L.E.Cross, *J.Am.Ceram. Soc.*, **79**, 2189-92 (1996).
[6] Y.L.Tu and S.L.Milne, *J.Mater.Res.*, **11**, 2556-64, (1996).
[7] M.Yamane, S.Shibata, A.Yasumori, T.Yano and S.Uchihiro, *J.Sol-Gel Science and Technology*, **2**, 457-60 (1994).
[8] H.Schulze-Bergkamen and M.Yamane, *J.Sol-Gel Science and Technology*, **5**, 185-91 (1995).

CHEMICAL PREPARATION AND PROPERTIES OF La DOPED

$K_{0.4}(Pb_{0.6}Ba_{0.4})_{0.8}Nb_2O_6$ THIN FILMS

Wataru Sakamoto, Kana Kosugi, Toshinobu Yogo and Shin-ichi Hirano
Department of Applied Chemistry, Graduate School of Engineering,
Nagoya University, Furo-cho, Chikusa-ku, Nagoya 464-8603, Japan
Fax: 81-52-789-3182, e-mail: sakamoto@apchem.nagoya-u.ac.jp

La doped $K_{0.4}(Pb_{0.6}Ba_{0.4})_{0.8}Nb_2O_6$ thin films have been synthesized by the chemical solution process. Tungsten bronze $K_{0.45}(Pb_{0.6}Ba_{0.4})_{0.7}La_{0.05}Nb_2O_6$ (KPBLN60/5) thin films were fabricated on fused silica, MgO(100) and Pt(100)/MgO(100) substrates at 700°C. Incorporation of La ions in KPBN60 was found to be effective in forming the tungsten bronze phase and improving the surface morphology of the films on the substrates. The propagation modes were observed for the KPBLN60/5 films on fused silica via the prism coupling method. The Curie temperature of the KPBLN60/5 thin film on a Pt/MgO(100) substrate was around 280°C. The KPBLN60/5 thin film on Pt/MgO(100) showed a typical ferroelectric P-E hysteresis loop.

1. Introduction

Lead barium niobate ($Pb_{1-x}Ba_xNb_2O_6$, PBN) is a ferroelectric solid solution of $PbNb_2O_6$ and $BaNb_2O_6$ with a tungsten bronze structure. PBN based materials are known to have excellent piezoelectric, pyroelectric and electro-optic properties. The chemical solution process which is one of the most common methods for film fabrication has characterized by advantages such as high purity, good homogeneity, lower processing temperature, feasibility of composition control.[1-3] Dielectric thin films with high transparency and high refractive index are expected for application in optical devices, including optical wave guides. The crystallization of ferroelectric tungsten bronze films at lower temperatures is indispensable for the fabrication of high-quality films. The substitution with alkali ion is found to be very effective in reducing the crystallization temperature of the tungsten bronze phase.[2,3] On the other hand, $K_{0.8}La_{0.4}Nb_2O_6$ has the filled-tungsten bronze structure, and its tungsten bronze phase is considered to exhibit high structural stability.[4] Further increase in the stability of the tungsten bronze phase in K-substituted PBN (KPBN) is expected by the formation of a solid solution with $K_{0.8}La_{0.4}Nb_2O_6$ (La doping).

This paper focuses on the chemical processing of La-doped $K_{0.4}(Pb_{0.6}Ba_{0.4})_{0.8}Nb_2O_6$ (KPBLN) thin films from metal-organic substances. The crystallization behavior and microstructure of tungsten bronze KPBLN films were investigated. The optical and electrical properties of the films were also evaluated.

2. Experimental Procedure

The precursor solution was prepared by the reaction of Ba metal, $Pb(CH_3COO)_2$, KOEt, $La(O^iPr)_3$ and $Nb(OEt)_5$ in 2-methoxyethanol.

Films were fabricated using the precursor solution by dip coating on fused silica, MgO(100) and Pt(100)/MgO(100) substrates.

The prepared films were analyzed by X-ray diffraction (XRD), UV-visible spectroscopy and scanning electron microscopy (SEM). The propagation modes in the films were measured via the prism coupling method. The electrical properties of the films were measured using Au as the top electrode and Pt(100) layer on MgO(100) as the bottom electrode. The dielectric and ferroelectric properties were measured using a LCZ meter and a ferroelectric test system, respectively.

3. Results and Discussion

A homogeneous precursor solution was prepared by controlling the reaction of metallo-organics in 2-methoxyethanol. Thin films were synthesized using the KPBLN precursor solution on various substrates. Figure 1 shows the XRD profile of $K_{0.45}(Pb_{0.6}Ba_{0.4})_{0.7}La_{0.05}Nb_2O_6$ (KPBLN60/5) thin film on fused silica substrate. It was quite difficult to prepare thin films of single-phase tungsten bronze on the silica substrate, because the pyrochlore phase crystallized easily before the crystallization of the tungsten bronze phase. KPBLN is the solid solution between $K_{0.8}La_{0.4}Nb_2O_6$ and $K_{0.4}(Pb_{0.6}Ba_{0.4})_{0.8}Nb_2O_6$ (KPBN60). $K_{0.8}La_{0.4}Nb_2O_6$ precursor synthesized by a similar chemical process was found to directly crystallize in the tungsten bronze phase at 650°C. The structural stability of the tungsten bronze phase was enhanced by the formation of solid solution with $K_{0.8}La_{0.4}Nb_2O_6$.

The propagation modes in the KPBLN films were measured for the potential application in optical wave-guides. Ferroelectric tungsten bronze niobate crystals are known to have a high refractive index (above 2.30) compared to SiO_2 glass (1.46). The synthesized KPBLN60/5 thin films were found to have high transparency over a wide wavelength region and the absorption edge of the film was about 340 nm. The interference fringes that are derived from the uniform thickness of the film are also observed. Since the optical propagation loss depends upon the transmittance of the film, the KPBLN film is required to be highly transparent. La doping was also found to be effective in suppressing the nonuniform grain growth, which results in the fabrication of a thin film with high transparency. Figure 2 shows the TE and TM modes via the prism coupling method for the KPBLN60/5 thin films prepared on fused silica substrates. Three modes, numbers (m) 0, 1 and 2, appear in both the TE and TM modes. The calculated refractive index and film thickness from the three mode angles in the TE mode

were about 2.1 and 0.8 µm, respectively. This value of refractive index is lower than that of the lead-based tungsten bronze niobate single crystals. The grain size of the film ranged from 50 to 100 nm and a slight porous microstructure was observed on the surface SEM image. The lower value of refractive index may be due to the lower density of the KPBLN film compared to that of single crystals.
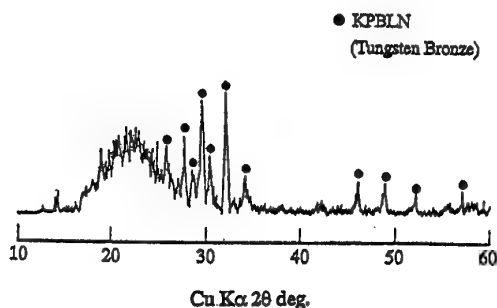

Fig.1 XRD profile of KPBLN60/5 thin film on a fused silica substrate crystallized at 700°C.
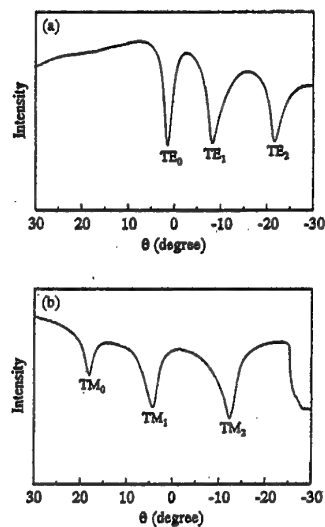

Fig.2 Optical propagation of KPBLN60/5 thin film on a fused silica substrate crystallized at 700°C (a) TE-mode observation and (b) TM-mode observation.

Figure 3 shows the XRD profiles of the KPBLN60/5 thin films on MgO(100) and Pt/MgO(100) substrates. The KPBLN60/5 films on both MgO(100) and Pt/MgO(100) substrates have only 001 and 002 reflections with high intensities, although KPBN60 on a Pt/MgO(100) substrate crystallized at 700°C showed a small amount of the pyrochlore phase.[2] This result indicates that the KPBLN60/5 thin films on MgO(100) and Pt/MgO(100) substrates crystallize to the tungsten bronze KPBLN single phase with a c-axis (direction of polarization)-preferred orientation. La doping was found to be an effective method to achieve crystallization to the tungsten bronze phase as well as for the improvement of the surface morphology.
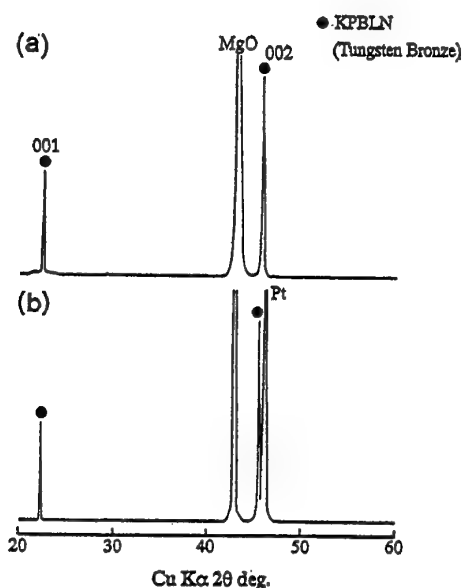

Fig.3 XRD profiles of KPBLN60/5 thin films on
(a) MgO(100) and (b) Pt(100)/MgO(100)
substrates crystallized at 700°C.

Figure 4 shows the temperature dependence of the dielectric constant (ϵ_r) and the loss tangent for the KPBLN60/5 thin film crystallized at 700°C on a Pt/MgO(100) substrate. The film had the dielectric maximum at around 280°C. The peak of ϵ_r-T curve is

broadened compared with that of the PBN single crystals.[5,6] This behavior might reflect the diffuse phase transition of the KPBLN60/5 thin film on Pt/MgO(100) substrates. The Curie temperature (T_c) of the KPBLN60/5 thin film was a little lower than that of PBN60 single crystal. The Curie temperature of lead based tungsten bronze materials generally shifts towards lower temperatures by substitution with potassium or lanthanum ions. Figure 5 shows the P-E hysteresis loop and the temperature dependence of the remnant polarization for the KPBLN60/5 thin film on a Pt/MgO(100) substrate. The typical ferroelectric P-E hysteresis loop was also observed at 20°C. The value of remnant polarization (P_r) gradually decreases with an increase in measurement temperature. The grain size of the KPBLN60/5 thin film was confirmed to be approximately 50-100 nm as observed by SEM. The gradual change of the P-E hysteresis loop and the broadening of the ϵ_r-T curve peak are attributed to the small grain size and the random distribution of K^+, Pb^{2+}, Ba^{2+} and La^{3+} ions in the tungsten bronze structure. Additional factors, such as the mechanical stresses imposed on the films by the substrates might be responsible for the observed dielectric and ferroelectric properties around and below the Curie temperature.
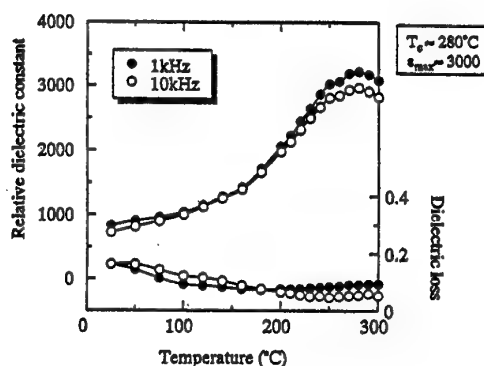

Fig.4 Temperature dependence of the dielectric
constant and loss tangent for KPBLN60/5
thin film on a Pt(100)/MgO(100) substrate
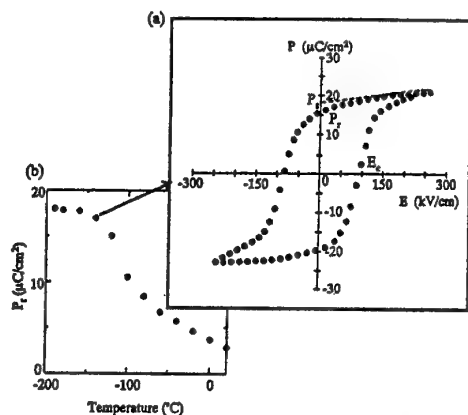crystallized at 700°C.

Fig.5 (a) P-E hysteresis loop for KPBLN60/5 thin film on a Pt(100)/MgO(100) substrate crystallized at 700°C, measured at −140°C and (b) temperature dependence of remnant polarization.

4. Conclusions

Crack-free $K_{0.45}(Pb_{0.6}Ba_{0.4})_{0.7}La_{0.05}Nb_2O_6$ (KPBLN60/5) films with the tungsten bronze phase were successfully prepared on fused silica, MgO(100) and Pt(100)/MgO(100) substrates using a metal-organic precursor solution. La doping was found to be a key for the improvement of the surface morphology of the synthesized films, as well as for the crystallization to the tungsten bronze phase at lower temperatures. This result is due to the formation of a solid solution with $K_{0.8}La_{0.4}Nb_2O_6$, which exhibits high stability of the tungsten bronze structure. KPBLN60/5 thin films on fused silica substrates showed high transparency, in which the laser light could propagate. The ferroelectric KPBLN phase was sufficiently stable around room temperature and underwent a gradual phase transition with increasing temperature.

References

1. W. Sakamoto, T. Yogo, K. Kikuta, T. Arimoto and S. Hirano, *J. Am. Ceram. Soc.*, **79**, 889-894 (1996).

2. W.Sakamoto, K.Kosugi, T.Yogo and S.Hirano, *Jpn. J. Appl. Phys.*, **37**, 5215-5219 (1998).

3. W.Sakamoto, K.Kosugi, T.Arimoto, T.Yogo and S.Hirano, *J. Sol-Gel Sci. Tech.*, **14**, 1-11 (1999).

4. B.A.Scott, E.A.Giess, G.Burns and D.F.O'Kane, *Mater. Res. Bull.*, **3**, 831-842 (1968).

5. R. Guo, A. S. Bhalla, C. A. Randall, Z. P. Chang and L. E. Cross, *J. Appl. Phys.*, **67**, 1453-1460 (1990).

6. J. R. Oliver, R. R. Neurgaonkar and L. E. Cross, *J. Am. Ceram. Soc.*, **72**, 202-211 (1989).

Preparation of Submicron Barium Titanate by Oxalate Process

Tsutomu Kajita and Morihito Nishido*

R&D Dept., Electronic Materials Division, Fuji Titanium Ind. Co., Ltd.

12-8 Sengen-cho, Hiratsuka-City, Kanagawa-Prf., Japan

FAX:0463-32-1270, e-mail:kajita@fuji-titan.co.jp

e-mail:nishido@fuji-titan.co.jp*

High purity stoichiometric barium titanate powders with fine particle and good crystallinity to be used for dielectric basic raw materials can be prepared by barium titanyl oxalate with higher specific surface area under controlled process conditions. Some behavior on calcined barium titanate from oxalate process was also investigated and discussed.

1.INTRODUCTION

Wet chemical methods for manufacturing process of barium titanate powders, such as oxalate process, sol-gel process, hydrothermal process, and alkoxide process, etc., have been developed to meet the requirements for high purity barium titanate with the fine particles. Among these, the oxalate process has several advantages in view of process economy, chemical purity and stoichiometry of the product. Since the barium titanates obtained by calcination of barium titanyl oxalate contain agglomerated particles, the calcined barium tianates need to be pulverized to eliminate such agglomerates.

Many researches on the synthesis methods and conditions of oxalate process [1),2)] and the thermal decomposition of barium titanyl oxalate [3),4)] have been reported. However, few studies have focused sufficiently on agglomeration of barium titanate powders from oxalate process.

In this paper, the calcination behavior and properties of barium titanate from barium titanyl oxalates with various specific surface areas are investigated and discussed.

2.EXPERIMENTAL PROCEDURE

Preparation process of barium titanate by oxalate process is shown in Fig 1.[5)]

The barium titanyl oxalates(BTO) with various specific surface areas(1.2～26.2 m^2/g) were obtained by adjusting process conditions, such as concentrations of aqueous solutions of Ba^{2+}-Ti^{4+} and oxalic acid ,mixing ratio of Ba:Ti, temperature of the solution and rate of mixing(reaction time). The BTO were calcined at 900℃ and 850℃ for 2 hours to form barium titante.

The BTO was thermoanalyzed to determine the decomposition temperature (TG8120, Rigaku, Japan). XRD (RINT2200, Rigaku, Japan) was used to observe the tetragonality of each calcined barium titanate. The specific surface area(SSA) of each calcined barium titanate and each BTO was determined by BET method(Flowsorb- Ⅱ 2300, Shimadzu).

The shapes and sizes of the particle in each sample were examined by SEM observation. The particle size distribution (Nikkiso : Microtrac9320), The Ba/Ti mol-ratio (F-Xray : type 3070S1, Rigaku, Japan) and the impurities (ICP : ICPS7500, Shimadzu) of each sample were carried out.

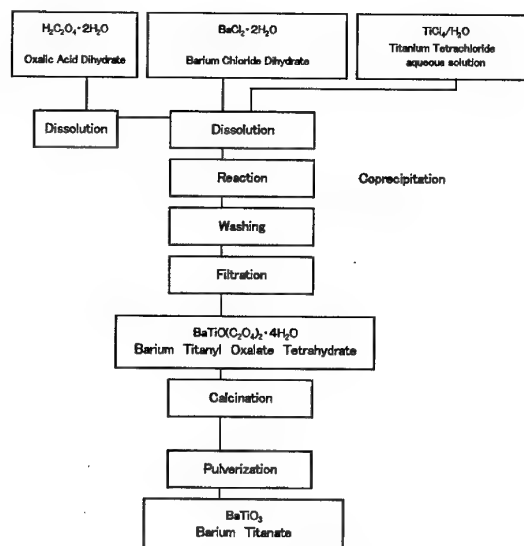Fig. 1   Flow chart for preparation process of barium titanate by oxalate process.

3.RESULTS AND DISCUSSION

The thermal decomposition temperatures of the oxalate in BTO determined by TG-DTA results of each BTO with various specific surface area (1.2～26.2 m^2/g), were plotted in Fig 2. The decomposition temperature decreases gradually with increasing the SSA of the BTO. This suggests that the temperature to form the barium

titanate from BTO decreases with increasing the SSA of BTO.

The X-ray diffraction patterns of calcined barium titanate samples from BTO with various SSAs are shown in Fig 3. It appears that the tetragonality of calcined barium titanate increases with higher SSA of BTO at the same calcination temperature.

Table. I shows the SSA of calcined barium titanate at 900℃ and 850℃ from BTO with various SSA. It is probably that the decrease((b)-(a), table. I) of SSA of calcined barium titanate with increasing calcining temperature from 850℃ to 900℃ is caused by the increase of agglomeration and grain growth.[6]

The more decrease of SSA in calcined barium titanate from BTO with lower SSA suggests that the agglomeration of barium titanate increases with decreasing the SSA of BTO. This trend of agglomeration confirms the XRD results shown in Fig 3. It seems that barium titanate with lower agglomerates and higher tetragonality can be obtained from BTO with higher SSA.

Fig.4, 5 and table. II show SEM observation, X-ray pattern and the properties of the typical barium titanate powder obtained from BTO with higher SSA.

Table I   SSA of BTO from oxalate process and barium titanate calcined oxalates.

Test No.	OX-1	OX-2	OX-3	OX-4	OX-5
SSA(m^2/g)	1.2	7.1	11.6	18.0	26.2
850℃ SSA(a)	8.14	6.30	5.38	5.61	6.45
900℃ SSA(b)	3.37	3.14	3.31	3.88	5.13
(b)-(a)	-4.77	-3.16	-2.07	-1.73	-1.32

1 μ m

Fig.4   SEM micrograph of typical barium titanate powder from oxalate process.

Table II   Typical barium titanate powder obtained from oxalate process.

Chemical Analysis

Ba/Ti Mol Ratio	0.997	
SrO	0.02	%
SiO_2	0.02	%
Al_2O_3	0.003	%
Na_2O	0.002	%
Fe_2O_3	0.002	%

Physical Analysis

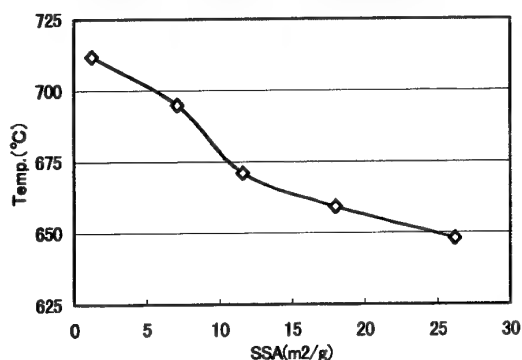|			
SSA		6.86	m^2/g
PS(BET)		0.15	μm
PSD	D10	0.434	μm
	D50	0.527	μm
	D90	0.661	μm

Fig.2   The relation between the thermal decomposition temperature of the oxalate in BTO and the specific surface area of BTO.
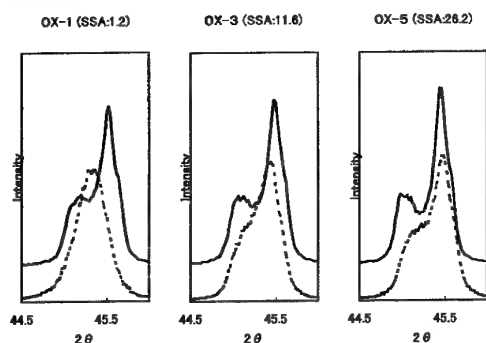

Fig.3   XRD patterns of the (002),(200)plane of calcined barium titanate at 850℃and 950℃.(OX-1,OX-3andOX-5)

Broken line:850℃,Solid line:900℃

Fig.5 XRD pattern of typical barium titanate powder by oxalate process.

4.CONCLUTION

Barium titanyl oxalates with various surface areas, precursor of barium titanate, can be prepared under optimized process conditions. Barium titanate powders with fine particle size and good crystalinity (tetragonality) and low agglomeration can be prepared from barium titanyl oxalate with higher specific surface area.
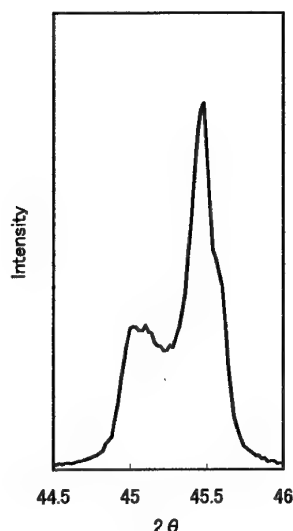
5.Reference

1) H.Yamamera , A.Watanabe , S.Shirasaki , Y.Moriyoshi and M.Tanada , "Preparation of Barium Titanate by Oxalate Method Ethanol Solution" Ceramics International Vol.11.n.1,17-22(1985)

2) Zee Hoon Park, Hyo Soon Shin, Byung Kyo Lee, and Sang Hee Cho, "Particle Size Control of Barium Titanate Prepared from Barium Titanyl Oxalate" J.Am.Ceram.Soc.80 [6] 1599-604(1997)

3) K. Iizumi, K. Sobata, K. Kudaka, "Thermal Decomposition of barium Titanium (IV) bis (Oxalate) Oxide and the Formation of Barium Titanate" Journal of the Ceramic Society of Japan 92[1](1984)

4) Jianfei XU, S.Tsutai, S. Hayashi, M. Sugai and Z.Nakagawa, "Thermal Decomposition Process of Barium Titanyl Oxalate Tetrahydrate" Journal of the Ceramic Society of Japan 107[1] 27-30(1999)

5) W.Stanley Clabaugh, Edward M. Swiggard, and Raleigh Gilchrist, "Preparation of Barium Titanyl Oxalate Tetrahydrate for Conversion to Barium Titanate of High Purity", Journal of research of National Bureau of Standards, Vol.56, No.5, May (1956)

6) K. Kudaka, K. Iizumi, Y. Tokugawa, S.Takeda, T. Okumura, H.Sasaki, M. Tamura, and H. Inagaki, "Some Observasion on the Aggregate Particles Produced during Pyrolisis of PTC Barium Titanate Precursor Synthesazed by the Oxalate Method", Journal of the Ceramic Society

Low-Temperature Sintering of PZT Powders

with Sintering Aids Using Chemical Process

Takashi Hayashi, Takayuki Inoue, Tetsuo Shibusawa and Yoshikazu Akiyama*

Shonan Institute of Technology, Fujisawa, Kanagawa, 251-8511, Japan

Fax: 81-466-36-1594, e-mail: hayashi@mate.shonan-it.ac.jp

*R&D Center, RICOH Co., Ltd., Shinei-cho, Tuzuki-ku, Yokohama 224-0035, Japan

ABSTRACT

Low-temperature sintering of PZT was investigated using $Pb_5Ge_3O_{11}$ (PGO), $Pb_5Ge_{2.4}Si_{0.6}O_{11}$ (PGSO) or Pb_2SiO_4 (PSO) as sintering aids. PZT powders were coated with PGO, PGSO and PSO which were prepared by chemical process using $Ge(O^iPr)_4$, $Si(OEt)_4$ and $Pb(NO_3)_2$ or $Pb(CH_3COO)_2 \cdot 3H_2O$. The sintering aids-added PZT powders could be densified at 750℃ for 2 h to sintered bodies with 95% relative density. An addition of sintering aids was effective for improving the sinterability of PZT powders and piezo & ferroelectric properties of PZT ceramics prepared at relatively low sintering temperatures below 900 ℃. Dielectric, piezoelectric and ferroelectric properties of PGO-added PZT ceramics were superior to those of PZT ceramics with PGSO or PSO. 2wt% PGO-added PZT bodies sintered at 850 − 900℃ exhibited an electro-mechanical coupling factor, kp of about 65%.

1. INTRODUCTION

Piezoelectric ceramics are currently used in applications such as stack-type actuators, ultrasonic motors and piezoelectric transformers. It is known that the sintering temperature of lead zirconate titanate(PZT) ceramics is above 1200℃. But, compared with sintering temperatures of lead-based relaxer ferroelectric materials, the sintering temperature of about 1200 ℃ is considerably high. This high-temperature processing brings about serious problems such as compositional change and environmental pollution due to the volatility of lead oxide. Thus, a low-temperature sintering process is required from the viewpoint of improvement in reproducibility, reduction in energy consumption and decrease in pollution. Also, low-temperature processing is required for fabrication of multilayer ceramic actuators and capacitors to suppress the reaction between ceramics and electrodes.

In general, the sintering temperature of ceramics can be reduced by utilizing low-melting point additives. However, some research results have indicated that electrical properties of sintered ceramics using sintering aids are degraded. Therefore, it is important to select a suitable sintering aid. Adachi et al.[1] and Ogawa et al.[2] reported that lead germanium oxide ($Pb_5Ge_3O_{11}$: PGO) powder, which is a ferroelectric material with a melting point as low as 738 ℃, was effective for low-temperature sintering of $BaTiO_3$ and PZT powders. It is very important to disperse homogeneously a small amount of sintering aids in the matrix and to control the microstructure of these materials in order to improve their electrical properties and reliability. Hayashi et al.[3]

demonstrated that PZT powders coated with PGO prepared from a precursor solution of $Ge(O^iPr)_4$ and $Pb(NO_3)_2$ by sol-gel method were densified at lower temperatures and 1wt% PGO-added PZT bodies sintered at 750℃ exhibited an electro-mechanical coupling factor, kp, of about 56%. Lead germanium silicon oxide ($Pb_5Ge_{2.4}Si_{0.6}O_{11}$: PGSO) and lead silicon oxide (Pb_2SiO_4: PSO) are also expected to be effective as sintering aids because they have lower melting point of 740 − 750℃. Although PGSO is a ferroelectric material, PSO is not a ferroelectric material.

This paper describes low-temperature sintering of PZT powders with sintering aids such as PGO, PGSO and PSO added using chemical process. The dielectric, ferroelectric and piezoelectric properties of these samples are also described.

2. EXPERIMENTAL PROCEDURES

PZT ($Pb(Zr_{0.52}Ti_{0.48})O_3$) powder with particle size of 150nm containing 0.3 mol% Nb_2O_5 was used.

Figure 1 shows the flow diagram for preparation of sintering aids-coated PZT composite powders. PZT powders were coated with of PGO, PGSO or PSO which was prepared from precursor solution by chemical process using $Ge(O^iPr)_4$, $Si(OEt)_4$ and $Pb(NO_3)_2$ or $Pb(CH_3COO)_2 \cdot 3H_2O$ as starting materials. They were mixed at a desired composition in ethyleneglycol or 2-methoxy-ethanol and heated at 80 ℃ for 1h, and then the resulting precursor solutions of sintering aids were added to PZT aqueous suspensions, followed by heating at 80℃ for 1 h to proceed hydrolysis reaction. Sintering aids-added PZT powders were ultrafiltered and washed with propanol, and then dried. The content of PGO, PGSO or PSO
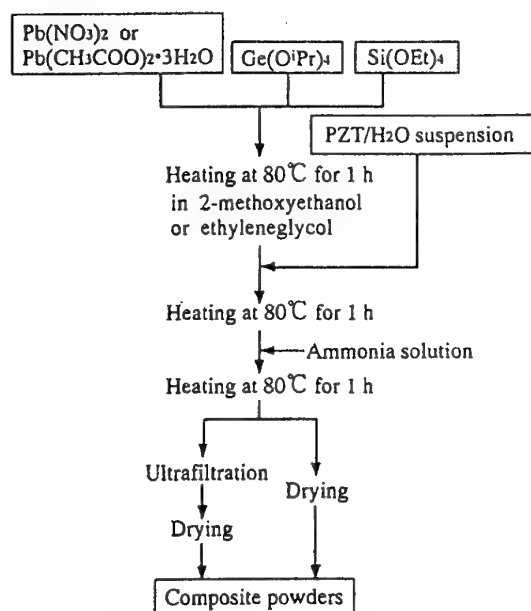
Fig. 1 Flow diagram for preparation of sintering aids-coated PZT composite powders.

additives was varied with 1 to 4wt%. These powders were pressed, and sintered at $700 - 1000°C$ for 2 h.

After the sintered disc samples were polished to approximately 0.5 mm thickness, fired-on silver paste was applied to both surfaces of the samples as electrodes. The samples were poled at 120°C for 1 h under an electric field of 20 kV/cm in silicone oil.

The microstructure and the chemical composition of the sintered bodies were observed using a field-emission scanning electron microscope (FE-SEM) and electron probe X-ray microanalyzer (EPMA). The dielectric constant was measured at 1 kHz and the electromechanical coupling factor, kp, was calculated by the resonant-antiresonance method using an impedance analyzer (HP4192A). The polarization-electric field (P-E) hysteresis loops were measured by a Sawyer-Tower circuit at 50 Hz at room temperature.

3. RESULTS AND DISCUSSION
3-1. Physical Properties and Microstructure

Figure 2 shows a typical FE-SEM micrograph of PGO-added PZT composite particles. PZT particles can be seen to be uniformly coated and modified with fine PGO particles.

Figure 3 shows the relative density of PZT sintered bodies with 2wt% PGO, 2wt% PGSO or 4wt% PSO additives as a function of sintering temperature. The optimal amount of sintering aids used in this work was determined to be 2wt% for PGO, 2wt% for PGSO and 4wt% for PSO from
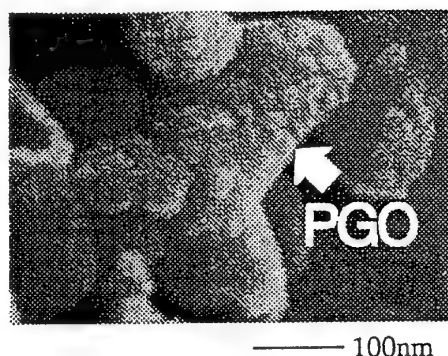

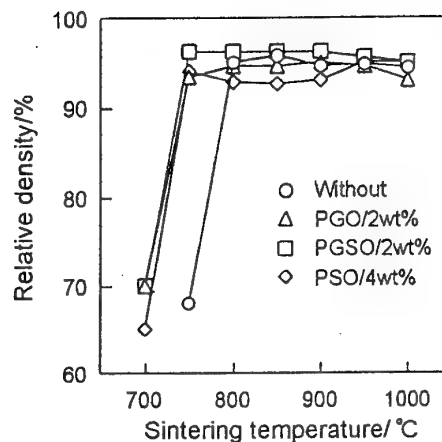Fig. 2 FE-SEM micrograph of PGO-coated PZT composite particles.

Fig. 3 Relative density of sintering aids-added PZT sintered bodies as a function of sintering temperature.

evaluating the piezoelectric properties of sintered bodies. An addition of sintering aids improved the sinterability of PZT powders with a reduction of sintering temperature by approximately 50°C.

Figure 4 shows the grain size of sintering aids-added PZT sintered bodies as a function of sintering temperature. An addition of PGO to PZT powders promoted considerable grain growth at sintering temperatures above 900°C. This may be due to the liquid phase sintering with addition of PGO. However, PGSO and PSO additives were not so effective for grain growth.

Figures 5 and 6 show FE-SEM micrographs and EPMA image of surfaces of PGO-added PZT bodies sintered at 950 °C and 1000 °C. Secondary phase existed along the grain boundaries of PZT sintered bodies at 950 °C, as shown in Fig. 4(a). From results of EPMA, it was confirmed that germanium was present at the grain boundaries of PZT bodies sintered at 950°C, as shown in Fig. 5. In contrast, the secondary phase could not be
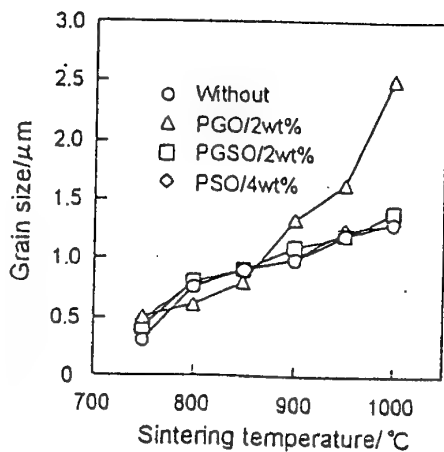
Fig. 4 Grain size of sintering aids-added PZT sintered bodies as a function of sintering temperature.
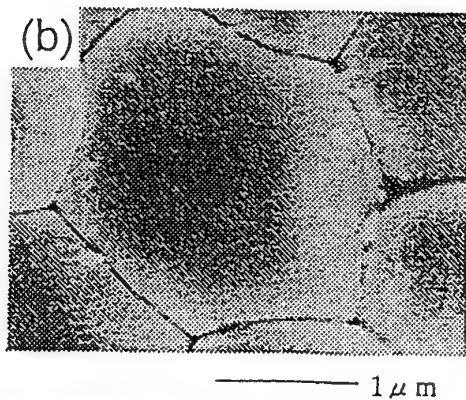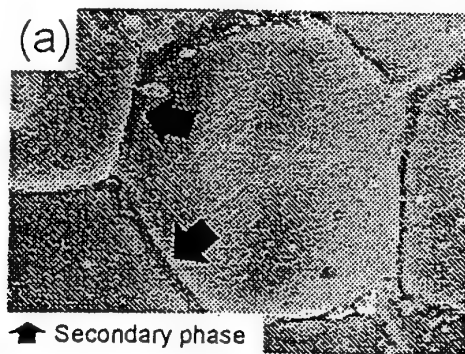

Fig. 5 FE-SEM micrographs of surfaces of PGO-added PZT bodies sintered at (a)950℃ ′ and (b)1000℃.
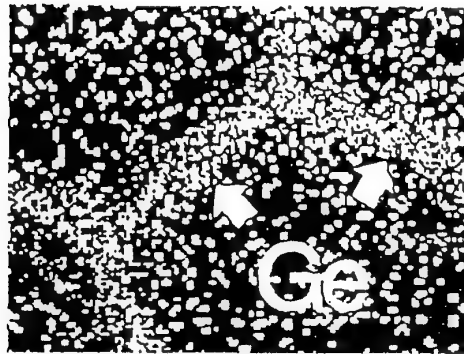
Fig. 6 EPMA image of PGO-added PZT bodies sintered at 950℃.
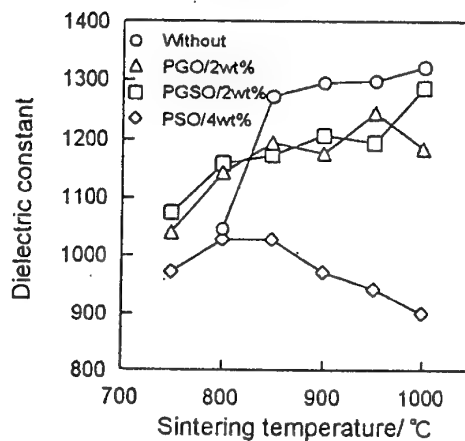
Fig. 7 Dielectric constant of sintering aids-added PZT sintered bodies as a function of sintering temperature.

observed at the grain boundaries of PZT bodies sintered at 1000℃, as shown in Fig. 4(b). This result suggests that the formation of solid solution between PZT matrix and PGO additive proceeded at an elevated sintering temperature.

3-2. Dielectric, Piezoelectric and Ferroelectric Properties

Figure 7 shows dielectric constants of PZT sintered bodies as a function of sintering temperature. The dielectric constants of sintering aids-added PZT sintered bodies were lower than that of PZT sintered bodies without sintering aids. The decrease of dielectric constant may be attributable to the addition of the materials with low dielectric constants.

Figure 8 shows the electromechanical coupling factor, k_p, of PZT sintered bodies as a function of sintering temperature. 2wt% PGO-added PZT bodies sintered at 850 and 900℃ showed the k_p of approximately 65%. However, the values of k_p of PZT sintered bodies with sintering aids decreased

Fig. 8 Electromechanical coupling factor, kp, of sintering aids-added PZT sintered bodies as a function of sintering temperature.

Fig. 10 XRD patterns of sintering aids-added PZT bodies sintered at 850 ℃.

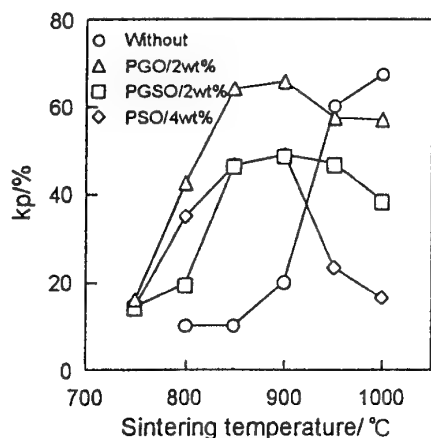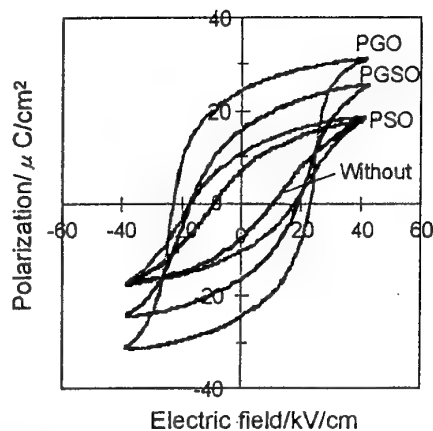PGO. Figure 10 shows XRD patterns of sintering aids-added PZT bodies sintered at 850℃. Secondary phase such as pyrochlore phase was not observed in every specimens. PGSO and PSO added-PZT sintered bodies exhibited a lower tetragonality than PZT with PGO additive.

4. CONCLUSION

Low-temperature sintering, microstructural development and piezoelectric & ferroelectric properties of PGO, PGSO and PSO-added PZT ceramics were investigated. The addition of sintering aids improved the sinterability of PZT powder. The PGO sintering aids existed along the grain boundaries of PGO-added PZT bodies sintered at $\leqq 950$ ℃. In addition, the addition of PGO improved dielectric, piezoelectric & ferroelectric properties of PZT ceramics at low sintering temperatures from 850℃ to 900℃. However, their properties were deteriorated at an elevated sintering temperature because of the easier formation of solid solution between PZT and sintering aids. The best piezoelectric properties were found for 2wt% PGO-added PZT bodies sintered at temperature range of 850 ℃ to 900 ℃ : The value of kp is approximately 65%. A low-sintering temperature was achieved for those ceramics to which PGO had been added.

Fig. 9 P-E histeresis loops of sintering aids-added PZT sintered bodies at 850 ℃.

rapidly with the increase of sintering temperatures of 950℃ to 1000℃. This may be related to the formation of solid solution between PZT and PGO involving with the disappearance of secondary phase, as shown in Fig. 5.

Figure 9 shows P-E hysteresis loops of PZT bodies sintered at 850 ℃. The well-saturated hysteresis loops were obtained for PGO-added PZT sintered bodies. The P-E hysteresis loop of PGO-added PZT ceramics was superior to those without these sintering aids. The values of remanent polarization, Pr, and coercive field, Ec, were 26(μ C/cm^2) and 22(kV/cm), respectively. However, the values of Pr of PGSO and PSO added-PZT sintered bodies were much lower, compared to those of the PZT bodies sintered with

REFERENCES

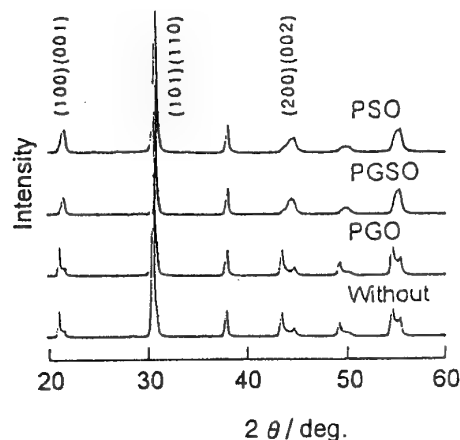1. M. Adachi, N.Nishibe, T. Shiosaki and A. Kawabata : Jpn. J. Appl. Phys. 22 (1983) Suppl. 2, 77.
2. T. Ogawa, A. Sano, A. Senda and K. Wakino: Jpn. J. Appl. Phys. 28 (1989) Suppl. 28-2, 91
3. T. Hayashi, T. Inoue and Y. Akiyama: J. Euro. Ceram. Soc. 19 (1999) 999.

Low-Temperature Processing of $Pb(Zr_{0.53},Ti_{0.47})O_3$ Thin Films By Sol-Gel-Casting

Hisao Suzuki*, Masahumi Kunieda*

*Department of Materials Science, Shizuoka University,3-5-1 Johoku, Hamamatsu, 432-8561 Japan
Fax : 81-53-478-1157, e-mail : hisuzuki@mat.eng.shizuoka.ac.jp

This paper focuses on a new class of processing for low-temperature deposition of thin films. In this study, ferroelectric $Pb(Zr_{0.53},Ti_{0.47})O_3$ (PZT) thin films were successfully prepared at low-temperature of 600℃. We proposed a new processing as a "Sol-Gel-Casting" which includes dispersion of fine crystalline particle in the solgel derived precursor solutions followed by the casting and annealing at relatively low-temperature. As a result, relatively dense ferroelectric PZT thin films with a few μm thickness were deposited. When the solid concentration was 30wt.%, this films showed a dielectric constant of 960 at room temperature. The dielectric properties of the resultant films depended on the solid concentration and the microstructure of the film. The microstructure of the film was affected by the agglomeration of the particles and the viscosity in the precursor slurry.

1. INTRODUCTION

Ferroelectric thin films are essential to the development of electronic devices such as capacitors, memories, sensors and actuators. For these applications, lead zirconate titanate (PZT) thin films are typical and a number of fabrication processes have been developed such as sol-gel, sputtering and chemical vapor deposition(CVD). On the other hand, recent advancement in micromachine requires a high performance microactuator. For this purpose, a new class of processing for low-temperature deposition of piezoelectric ceramic thin films with several micrometer thickness has been expected to be developed. As for such thick films, sol-gel method[1)2)], hydrothermal method[3)], and Jet Printing System (JPS)[4),5)] have been applied.

In this paper, a new class of processing for ceramic thin films with several micrometer thickness and low processing temperature is proposed. This method includes dispersion of fine particles in the alkoxide-derived precursor solutions followed by the casting on a substrate and annealing at relatively low-temperatures. We proposed to call this process as a "Sol-Gel-Casting" because this process is consisted of sol-gel process and "Gel-Casting". Gelcasting[6)] is a novel method for molding ceramic powder to form a dense green body, leading to the low-temperature sintering of ceramics. This new sol-gel based process has been developed by Sayer et al. to prepare thick PZT films with ferroelectric and piezoelectric properties[7)].

However in their process, relatively high annealing temperatures of above 650℃ were required to deposit piezoelectric PZT films.

We think that the key to prepare the ferroelectric thin film at relatively low temperatures by this process is how to control the agglomeration of the particles in the precursor slurry to prepare a well dispersed slurry with high solid content.

2. EXPERIMENTAL PROCEDURE

2.1 Deposition of PZT Film

The starting reagents for preparation of PZT precursor solution were lead acetate trihydrate, titanium i-propoxide and zirconium n-propoxide. Experimental details were described elsewhere. Previous paper have been demonstrated that the addition of excess Pb lowered the crystallization temperature and improved the electrical properties of the resultant thin films. Therefore, we prepared 20% Pb-excess precursor solution. Commercial PZT powders (Hayashi Chemical Co.Ltd.) were used as raw powders in this study. Precursor films were deposited by spin coating at 3000 rpm for 20 seconds onto $Pt/TiO_2/SiO_2/Si$ substrate. The spin-coated precursor films were pre-annealed at 350 ºC for 1.5 h to remove the residual organics in the films. Films are deposited 5 times to increase the film thickness. Final annealing was carried out up to 700 ºC for 2h.

2.2 Film Characterization

The microstructure of the resultant film was observed by the scanning electron microscope (SEM). Dielectric property of the film was mesured by the LCR meter.

3. RESULTS AND DISCUSSION

3.1 Characterization of Slurry

As already described, the agglomeration control of the particles in the precursor slurry with high solid content is essential for the low-temperature deposition of ferroelectric thin films by the sol-gel-casting. Therefore, size distribution of the particles in the slurry with or without dispersant were measured (Fig. 1). The 50% diameter of PZT powder was less than 0.4 μ m. However in the slurry, avarage particle size was about 0.5 μ m. It suggested that particles in the slurry slightly agglomerated with each other. Therefore, different types of dispersant were added to the slurry. As a result, average particle size of the particles increased by the addition of any kinds of dispersants used in this study. Therefore, we did not use the dispersant in this study.
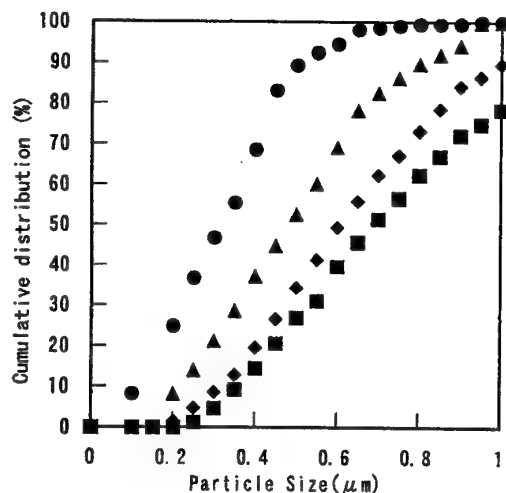

Fig.1 Size distribution of PZT particles of (a) Low PZT powders:● and (b) in slurry without dispersant:▲ and in slurry with different dispersant of (c) Stearic Acid:◆ and (d) Oleic Acid:■.

3.2 Effect of Solid Content on Electrical properties of the Films

For the sol-gel-casting, particles in the precursor slurry should be well dispersed to give the dense precursor film. Therefore, appropriate ratio of the powder to precursor solution should be determined. We defined "solid content" and "solid concentration" for the optimum ratio of the powder to precursor solution as follows;

Solid content (wt.%) = A/(A+B)
Solid concentration (g/ml) = (A+B)/C

where A is the weight of the raw particles, B is the powder weight of alkoxide-derived particles, and C is the volume of the precursor solution.

Figure 2 shows the relation between annealing temperature and relative permittivity for the sol-gel-casted PZT films deposited from slurry with 0.3M alkoxide concentration and 70wt.% of solid content. Relative permittivity was increased with increasing annealing temperature. Relative permittivity of the resultant film annealed at 500 ºC was 450 and was increased with temperature up to about 600 at 700 ºC. The increase in relative permittivity with temperature is ascribed to the increased film density and crystallinity. However, the microstructurefor the film surface did not show the significant change with temperature. This may be ascribed to the infiltration of precursor during sol-gel casting through large pores formed by the agglomeration. Therefore, good dispersant is essential for the further investigation.

Figure 2 also shows the relative permittivity of the resultant films with various solid content of the slurry.
The film with solid content of 30 wt.% and annealed at 600 ºC exhibited highest relative permittivity. Relative permittivity showed a tendency of decreasing as solid content increased from the 30wt.%.
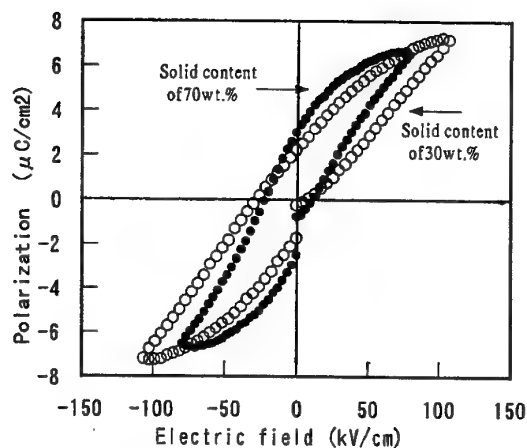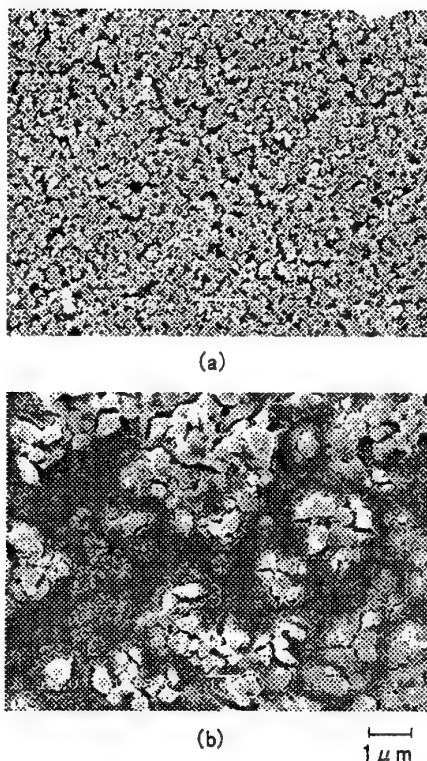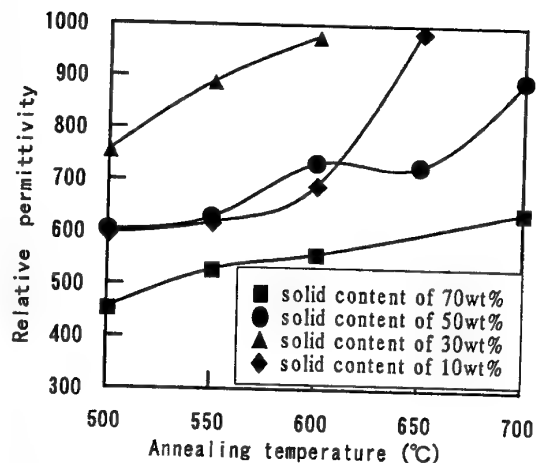
Fig.2 Relationship between annealing temperature and relative permittivity for the sol-gel-casted films deposited from slurry with 0.3M alkoxide concentration with different solid content of (a) 70wt.%: ■, (b) 50wt.%:●, (c) 30wt.%:▲ and (d) 10wt.%:◆.

(a)

(b)   1 μm

Fig.4 The microstructures of the PZT films with different solid content of (a) 70wt.% and (b) 30wt.%.

Figure 4 shows the microstructures of the resultant films with different solid content (30 and 70wt.%) annealed at 600℃. The surface of the films, when the low solid content, the microstructure of the film was different from the high soild content. So, it is considered the film which have low solid content was affected by the alkoxide-derive property. And, it was found that large cracks was into the film surfaces. In addition, film thickness for one coating operation decreased with increasing solid content, suggesting that agglomeration in the slurry resulted in the porous layer for one coating. From SEM observation of film crossections, the average thickness for one-coating was estimated to be about 0.2 to 0.8 μ m.

Fig.3 P-E hysteresis loops of PZT (120/53/47) films annealed at 600℃ with solid content of 30wt.% or 70wt.%.

The hysteresis loop for the films with solid content of 30 wt.% or 70 wt.% shown in figure 3 indicates that higher solid content is good for the ferroelectric property of the resultant film.

3.3 Effect of Solid Concentration on Dielectric property of Film

As already mentioned, solid content in the slurry have large effect on the electrical properties of the resulting films with sol-gel-casting. In this section, effect of solid concentration was discussed. For this purpose, slurries with different concentration of precursor solution were prepared. The solid content was fixed at 70 wt.% and the solid concentration was changed from 0.1M to 0.6M (solid concentration was changed from 0.08 to 0.46g/ml).
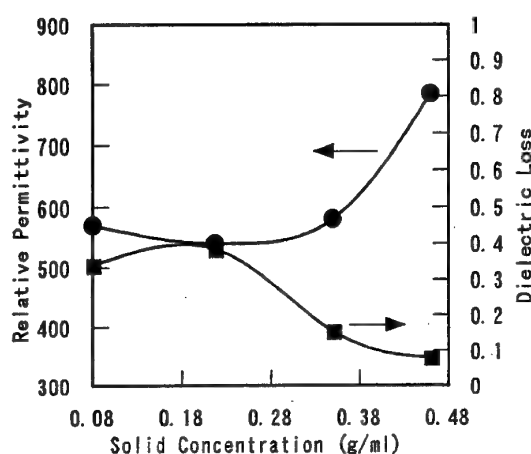

Fig.5 Relationship between solid concentration and relative permittivity for the PZT films annealed at 600℃ with 70wt.% solid content.

Figure 5 shows the relative permittivity of the resultant films with various solid concentration of the slurry. As a result, the highest relative permittivity was obtained when the precurour solution concentration was 0.6M at 600 ℃. This may be ascribed to the viscosity of the slurry which decreased with the decrease in solid concentration, corresponding to the films with lower solid content.

From these results, it is concluded that the electrical properties of the resultant films deposited with a sol-gel-casting were varied both with the solid content and the solid concentration.

4. SUMMARY

In this paper, a new class of processing for low-temperature deposition of PZT films was demonstrated. This process included dispersion of PZT fine particles in the alkoxide-derived precursor solutions followed by the casting on a substrate and annealing at relatively low-temperatures. Sol-gel derived precursors infiltrated in the pores of densely packed crystalline particles to form relatively dense films with ferroelectricity after the annealing at 600 ℃. The key to deposit the ferroelectric films at relatively low temperatures by the Sol-gel-casting is to prepare a well dispersed slurry with high solid content. Sol-gel-casting is very promising for a low-temperature processing of ceramic films with several micrometer. Properties of the resultant films were changed greatly by the solid content and viscosity of the slurry. Further investigations is essential for the dispersant to improve a film quality.

REFERENCES
1. Y. L. Tu and S. J. Milne , *J. Mater. Res., 11, (1996) 2556.*
2. K. Miyazawa and K. Ito , *J. Am. Ceram. Soc., 81[9] , (1998) 2333.*
3. K. Shimomura , T. Tsurumi and M. Daimon , *Jpn. J. Appl. Phys., 30, (1992) 153.*
4. H. Adachi, Y. Kuroda, T. Imahashi and K. Yanagisawa , *Jpn. J. Appl. Phys., 36, (1997) 1159.*
5. M. Ichiki, J. Akedo, A. Schroth, R. Maeda and Y. Ishikawa , *Jpn. J. Appl. Phys., 36, (1997) 5815.*
6. A. C. Young, O. O. Omatete, M. A. Janney and P. A. Menchhofer , *J. Am. Ceram. Soc., 74 [3], (1991) 612.*
7. D. A. Barrow, T. E. Petroff, Tandon and M. Sayer , *J. Appl. Phys., 81[2], (1997) 876*

Structural and Electrical Characterization of $Bi_5Ti_3Fe_{1-x}Mn_xO_{15}$ Solid Solutions

Sung-lak Ahn, Yuji Noguchi, Masaru Miyayama, and Tetsuichi Kudo
Department of Applied Chemistry, School of Engineering, The University of Tokyo,
7-3-1 Hongo, Bunkyo-ku, Tokyo 113-8656, Japan,
Fax:+81-3-3818-0284, e-mail:ahn@imat.chem.t.u-tokyo.ac.jp

Solid solutions in bismuth layer-structured $Bi_5Ti_3Fe_{1-x}Mn_xO_{15}$ (x = 0 ~ 1) system were prepared by solid state reaction technique using component oxides, and evaluations of crystal structure and electrical properties were performed. Their powder X-ray diffraction (XRD) patterns were analyzed by the Rietveld method using the RIETAN program. The $Bi_5Ti_3FeO_{15}$ structure was maintained in the region of $0 \leq x \leq 0.4$, but a structural change was suggested at $x \geq 0.5$. The substitution of Fe^{3+} site by Mn^{3+} ion in $Bi_5Ti_3FeO_{15}$ was found to shift the Curie-temperature T_c toward the low-temperature region and to decrease the dielectric permittivity at T_c in the region of $0 \leq x \leq 0.4$. The correlation between atomic displacement in the pseudo-perovskite block and the Curie-temperature was discussed.

1. INTRODUCTION

Since B. Aurivillius[1-2] discovered the bismuth layer-structured oxides (BLSO) in 1949, some 100 compounds belonging to so-called "Aurivillius phase" have been reported so far. The general formula of these phase is expressed by $(Bi_2O_2)^{2+}(A_{m-1}B_mO_{3m+1})^{2-}$, where A ion represents Bi^{3+}, Pb^{2+}, Sr^{2+}, Ca^{2+}, Ba^{2+}, etc., at the 12-coordinated site, B ion represents Fe^{3+}, Mn^{3+}, Ti^{4+}, V^{5+}, Nb^{5+}, Ta^{5+}, W^{6+}, etc., at the 6-coordinated site and m means an integer corresponding to the number of oxygen octahedron of the B ion, in the pseudo-perovskite block. $Bi_5Ti_3FeO_{15}$ ($m = 4$), represented with the formula of $(Bi_2O_2)^{2+}(Bi_3Ti_3FeO_{13})^{2-}$, is orthorhombic system with the space group $A2_1am$, and is known to show a relatively high electrical conductivity among BLSO.[3-8]

It is well known that ion substitution is very useful for modifying electrical properties. After Smolenskii[9] discovered the ferroelectricity in $PbBi_2Nb_2O_9$ belonging to the Aurivillius phase, Subarrao et al. investigated the modification of dielectric, ferroelectric property and crystal structure by using the solid solution system over this phase[10-12]. They experimentally evaluated the macroscopic influence of substitution of A site, B site, or simultaneously both the sites.

Most of bismuth layer-structured ferroelectrics is known to be displacive ferroelectrics[8] with relatively high Curie-temperature (T_c) more than 200 °C [11], and several features on the polarization property have been shown, such as : 1) the octahedral B-site ions contribute mainly to the spontaneous polarization[8], 2) the A-site ions, especially Bi^{3+}, are strongly displaced and exhibit high polarizability[13-14], 3) the perovskite layers contain excess oxygen ions[15], and 4) cations with lone pair electrons (Pb^{2+}, Bi^{3+}) may give rise to asymmetric distortion of ions [16].

In the present study, $Bi_5Ti_3Fe_{1-x}Mn_xO_{15}$ (x = 0 ~ 1) solid solution system was prepared, and evaluations of crystal structure and electrical properties were performed. Especially, the present study focused on the

relationship between transition temperature, T_c, and atomic displacement, which is most important property of the displacive ferroelectrics, with the change of B-site ion in $Bi_5Ti_3Fe_{1-x}Mn_xO_{15}$ system. The correlation between crystal structure and electrical properties will be also discussed.

2. EXPERIMENTAL

2.1 Sample preparation

Polycrystalline $Bi_5Ti_3Fe_{1-x}Mn_xO_{15}$ (x = 0 ~ 1) were prepared by a conventional solid state reaction. Constituent oxides of Bi_2O_3, TiO_2, Fe_2O_3, and Mn_2O_3 with the purity of 99.99% were calcined at 800 °C for 4 h. Samples with 10mm in diameter and 2-3mm in thickness were pressed uniaxially at about 90 MPa and sintered in air at 1000 °C for 4 h. Each sample was electroded with Pt by ion sputtering (SC-701, SANYU, Japan) onto the well-polished pellet and annealed at 600 °C for 30 min to improve mechanical and electrical properties of electrodes.

2.2 Measurements

Powder XRD patterns of the $Bi_5Ti_3Fe_{1-x}Mn_xO_{15}$ heat-treated at 1000 °C for 4h were taken by an X-ray diffratometer (RINT 2400, Rigaku, Japan) using Cu K_α radiation at room temperature. To investigate the variation of crystal structure and lattice parameters in $Bi_5Ti_3Fe_{1-x}Mn_xO_{15}$ (x= 0 ~ 1) system, the Rietveld analysis using the RIETAN program[17] was performed from the XRD powder patterns obtained above. Data were collected in the 2θ range of 5 ~ 80 ° in a step scanning mode, with a step length of 0.05 ° and a step-counting time of 4 sec.

Electrical conductivity was measured by the two-probe direct current method using a pA meter/DC voltage source (4140B, Hewlett-Packard, Japan) at an applied voltage of 0.5 ~ 1.0 V. Dielectric property was measured with an LCR meter (4284A, Hewlett-Packard, Japan) at the frequencies range of 1 kHz ~ 1 MHz.
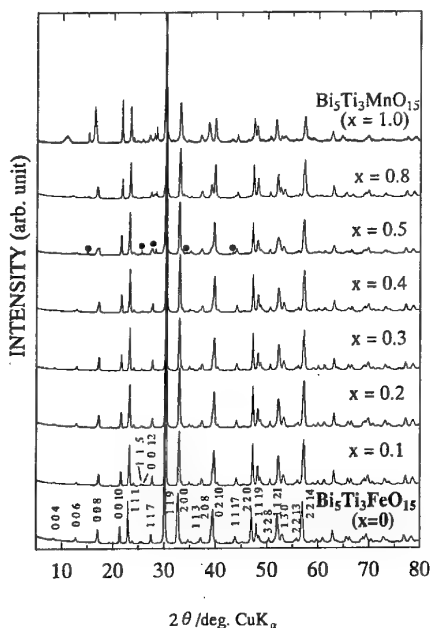
Fig.1. Powder XRD patterns of $Bi_5Ti_3Fe_{1-x}Mn_xO_{15}$ system. Peaks marked with ● are those observed at $x \geqq 0.5$.

3. RESULTS AND DISCUSSION
3.1 Characterization

Figure 1 shows the powder XRD patterns of $Bi_5Ti_3Fe_{1-x}Mn_xO_{15}$ ($x = 0 \sim 1$) ceramics obtained from the powder heat-treated at 1000 °C for 4h. The peak indices for $x = 0$ were cited from the JCPDS index NO. 38-1257, $Bi_5Ti_3FeO_{15}$. The XRD patterns of the $x = 0.1 \sim 0.4$ were coincided well with that of $x = 0$ ($Bi_5Ti_3FeO_{15}$) reported in literatures[3,6], indicating that the orthorhombic system is maintained in the range of $0 \leqq x \leqq 0.4$. With an increase in Mn substitution, some new peaks began to show up around 2θ of 15.0°, 25.6°, 27.7°, 34.2°, and 43.3° for samples of $x \geqq 0.5$, suggesting a structural change from $Bi_5Ti_3FeO_{15}$. New peaks (marked with ●) are at least not those of metal oxides, such as MnO, Mn_2O_3, MnO_2, Fe_2O_3 etc. from peak indexing.

The Rietveld analysis using RIETAN program gave a more information about the solid solution of $Bi_5Ti_3Fe_{1-x}Mn_xO_{15}$ ($x = 0 \sim 1$) system. The space group of $A2_1am$ (36)[8] was used as the starting structural model of $Bi_5Ti_3FeO_{15}$($a \doteqdot 0.546$ nm, $b \doteqdot 0.543$ nm, $c \doteqdot 4.12$ nm, Z=4) for analyzing, in which it was assumed that B-site ions of Ti, Fe and Mn , at the center of octahedron, are randomly distributed in the pseudo-perovskite block.

The observed and simulated XRD pattern for $x = 0.3$ is shown in Fig. 2. For $0.1 \leqq x \leqq 0.4$, the structure of $Bi_5Ti_3Fe_{1-x}Mn_xO_{15}$ system was refined in space group $A2_1am$ and the refinement converged to R_{wp} between 8.66 ~ 14.6% and goodness of fit, $S = R_{wp} / R_{exp}$ between 1.49 ~ 2.37. However, the values of S and R factors for x = 0.5 and 0.8 became so large that their structures are not in the starting structure of $Bi_5Ti_3FeO_{15}$ any more. In addition, to identify the unknown peaks for samples of x = 0.5 and x = 0.8, we analyzed the powder XRD patterns assuming that main phase of above samples have structure of $Bi_4Ti_3O_{12}$ with three octahedrons in pseudo-provskite block. However, satisfactory fitness between observed and simulated peaks as a single phase could not be obtained.

3.2 Dielectric properties

Figure 3-(a) shows the temperature dependence of dielectric permittivity of $Bi_5Ti_3Fe_{1-x}Mn_xO_{15}$ ($x = 0 \sim 1$) system measured at 1 MHz. For $Bi_5Ti_3FeO_{15}$, x = 0, the Curie temperature where the maximum dielectric permittivity is shown was observed at 752°C. Newnham et al. has suggested that many of bismuth layer structured ferroelectrics (BLSF) with even number of octahedron in the pseudo-perovskite block show two phase transitions (560 °C, 750 °C for $Bi_5Ti_3FeO_{15}$ with m=4 [6,8]). However, only one phase transition was observed in the present $Bi_5Ti_3Fe_{1-x}Mn_xO_{15}$ (x= 0 ~ 1) samples, although a shoulder is observed at about 600 °C in the line in Fig. 3-(a) for the $Bi_5Ti_3FeO_{15}$ (x = 0) sample. The Curie-temperature was shifted toward the low temperature region with increasing x. The change is a little at $x \leqq 0.4$ but drastic at $x \geqq 0.4$. In addition, within x = 0.4, Curie-temperature showed little dependence on measurement frequency and sharpness of the peak at Curie-temperature remained. However, at $x \geqq 0.5$, the low-frequency dispersive behavior was observed, which may be attributed to the increase in dielectric loss or
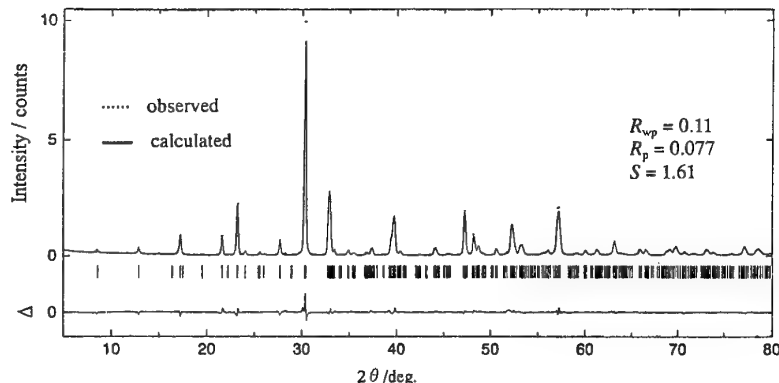

Fig.2. Rietveld analysis of powder X-ray diffraction pattern of $Bi_5Ti_3Fe_{0.7}Mn_{0.3}O_{15}$. The short vertical lines below the profiles represent the position of all possible Bragg's reflection.

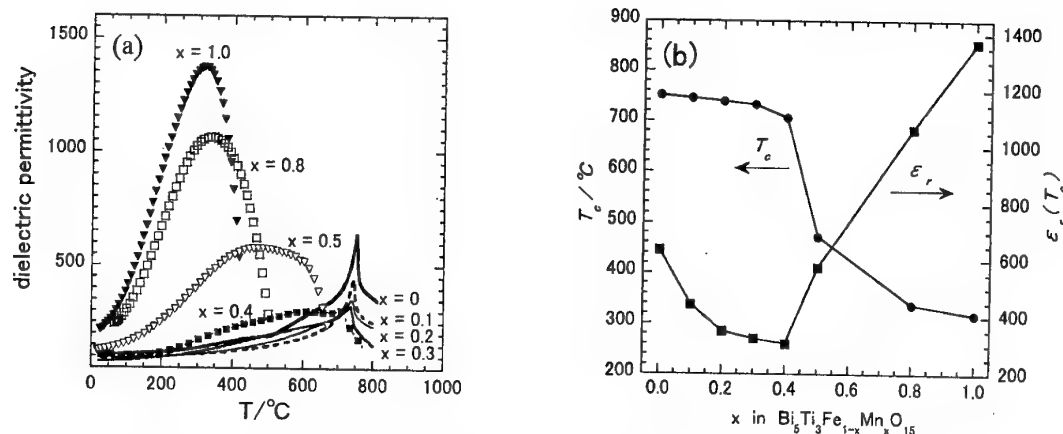Fig.3. (a) Temperature dependence of dielectric permittivity ε_r, and (b) composition dependence of T_c and ε_r at T_c.

compositional fluctuation.

Figure 3-(b) shows changes in Curie-temperature (T_c) and dielectric permttivity at the Curie-temperature ($\varepsilon_r(T_c)$) as a function of x. For $0.1 \leqq x \leqq 0.4$, $\varepsilon_r(T_c)$ has the tendency to exponentially decrease with an increase in x, whereas opposite behavior was observed at x above 0.4. From the result of XRD analysis utilizing the Rietveld method, the changes in $\varepsilon_r(T_c)$ and T_c at x above 0.4 are considered to be resulted from the structural variation in the $Bi_5Ti_3Fe_{1-x}Mn_xO_{15}$ system. It is, therefore, suggested that 40% of Mn^{3+} ion may be substitutable for Fe^{3+} ion (10% of the B-site ions) without a structural change of $Bi_5Ti_3FeO_{15}$.

3.3 Relative atomic displacement

It has been known that the structural deviation of displacive ferroelectrics away from underlying parent structure with a high symmetry is attributed to the origin of ferroelectricity, as in $BaTiO_3$ or $LiNbO_3$[18]. In Aurivillius phase, the deformation from the prototype structure has been also discussed with relation to its polarization mechanism. Newnham et al. has proposed that the evolution of ferroelectricity should be related to the atomic displacement of B-site ion, such as Ti^{4+}, Nb^{5+}, Ta^{5+}, and W^{6+} forming BO_6 octahedron in pseudo-perovskite block, which shifted along the a-axis away from the center of the octahedron.[8] On the contrary, recent refinement on the crystal structure of Aurivillius phase by Rae et al. has focused about the displacement of A-site ion in pseudo-perovskite block, such as Bi^{3+} in $Bi_4Ti_3O_{12}$, Bi_3TiNbO_9, and Bi_2WO_6[14]. They showed that the main structural cause of ferroelectricity is the a-axis displacement of Bi atoms in the perovskite A-site, which is opposite to the earlier report, above.

In this study, to discuss the influence with substitution of Mn^{3+} on variation of Curie-temperature, the relative atomic displacement in $Bi_5Ti_3Fe_{1-x}Mn_xO_{15}$ system was evaluated. Since 1) most of Aurivillius phase are orthorhombic and ferroelectric with polar axis parallel to the direction of a-axis, 2) the species of A-site ion Bi^{3+} is not varied by substitution, relative atomic displacement of B-site in the (100) direction was focused and estimated on the basis of the results of structural refinement using the Rietveld method. There are two different B-site ions with respect to four octahedrons in the pseudo-perovskite block, as shown in Fig. 4. Accordingly, relative atomic displacement of B-site ion is defined using the position of Bi(3) ion in the $(Bi_2O_2)^{2+}$ layer as the standard, as following ;

$$\Delta B_{site} = a \times \{2 \Delta_{Bsite(1)} + 2 \Delta_{Bsite(2)}\} / 4$$

where **a** is the lattice parameter of unit cell of $Bi_5Ti_3Fe_{1-x}Mn_xO_{15}$ in a-axis.

Figure 5 shows composition dependence of the Curie-temperature and atomic displacements. It is found that B-site atomic displacement and Curie-temperature decrease with an increase of x, Mn^{3+} content, in the region of $0.1 \leqq x \leqq 0.4$. The difference in $\Delta_{Bsite(1)}$ and $\Delta_{Bsite(2)}$ was not evident. It is suggested that the decrease in displacement of B-site ion by Mn^{3+} substitution leads to decrease in the degree of distortion of perovskite cell so that Curie-temperature, where ferroelectric-paraelectric transition occurs, is lowered. In similar way, we also estimated the relative atomic displacement of A-site ions using the position of Bi(3) ion in the $(Bi_2O_2)^{2+}$ layer as the standard, which is defined as $\Delta A_{site} = a \times \{\Delta_{Bi(1)} + 2 \Delta_{Bi(2)}\} / 3$. ΔA_{site} with the value in the range of 0.0029 ~ 0.0061 nm was found to be not so large as ΔB_{site} and to show little contribution to the variation of phase transition temperature in this study. It can be inferred from the above results that the displacement of B-site ion may be more correlated with the evolution of ferroeletricity than that of A-site ion in this $Bi_5Ti_3Fe_{1-x}Mn_xO_{15}$ system.

3.4 DC conductivity

Figure 6 shows the composition dependence of DC conductivity in polycrystalline $Bi_5Ti_3Fe_{1-x}Mn_xO_{15}$ (x = 0 ~ 1) system. For $Bi_5Ti_3FeO_{15}$, the conductivity below 50℃ was too unstable to measure due to very low conductivity. It was found that electrical conductivity in the $Bi_5Ti_3Fe_{1-x}Mn_xO_{15}$ (x = 0 ~ 1) system increases with x, Mn^{3+} content. Above x of 0.5, electrical conductivity converged toward that of $Bi_5Ti_3MnO_{15}$[19]. The conduction mechanism is not clear at present and is now under investigation.

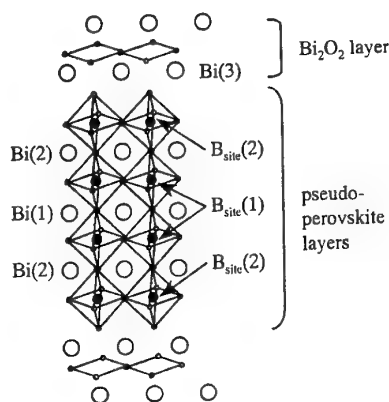Fig.4. A perspective drawing, approximately down <110>, of prototype structure of $Bi_5Ti_3Fe_{1-x}Mn_xO_{15}$.

Fig.5. Composition dependences of T_c and relative atomic displacement (Δ) for A- and B-site ions at $x \leqq 0.4$.

4. CONCLUSIONS

In the $Bi_5Ti_3Fe_{1-x}Mn_xO_{15}$ ($x = 0 \sim 1$) system, $Bi_5Ti_3FeO_{15}$ structure with orthorhombic system was found to be maintained in the range of $0 \leqq x \leqq 0.4$ and a structural change was suggested at samples of $x \geqq 0.5$ from the XRD analysis using Rietveld method. With increasing x, the Curie-temperature T_c was shifted toward the low temperature region, and dielectric permttivity at T_c decreased at $x \leqq 0.4$ but increased at x above 0.4.

Atomic displacement of B-site ions also decreased in $0 \leqq x \leqq 0.4$ and that of A-site ions was found to be not so large. This decrease of atomic displacement of B-site ions seems to be responsible for a decrease in distortion of perovskite cell, leading to the lowering of T_c.
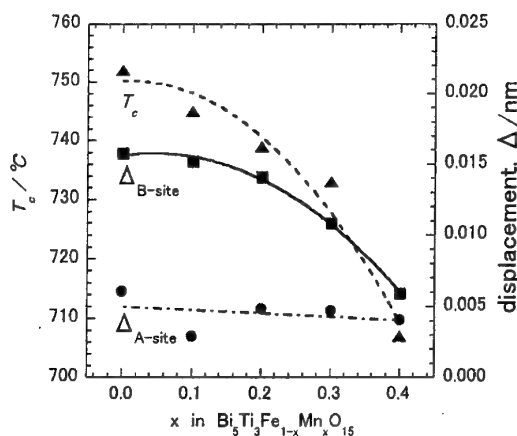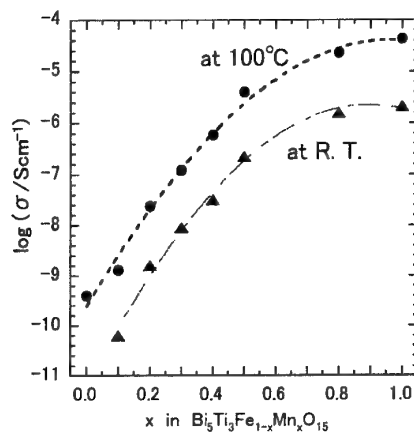

Fig.6. Composition dependences of conductivity at room temperature and 100°C in $Bi_5Ti_3Fe_{1-x}Mn_xO_{15}$ system.

REFERENCES

1. B. Aurivillius: *Arkiv Kemi*, **1**, 463 (1949).
2. B. Aurivillius: *Arkiv Kemi* , **1**, 499 (1949).
3. I. G. Ismailzade et al., *Sov. Phys. Crystallogr.*, **12**, 400 (1967).
4. S. A. Kizhaev et al., *Sov. Phys. Solid State*, **15**, 214 (1973).
5. Geys D. Sultanov et al., *Ferroelectrics*, **5**, 197 (1973).
6. F. Kubel and H. Schmid, *Ferroelectrics*, **129**, 101 (1992).
7. A. R. James et al., *Modern Phys. Lett.* **B 11**, 633 (1997).
8. R. E. Newnham et al., *Mater. Res. Bull.*, **6**, 1029 (1971).
9. G. Smolenskii, *Sov. Phys. Solid State*, **1**, 149 (1959).
10. E. C. Subbarao, *J. Chem. Phys.*, **34**, 695 (1961).
11. E. C. Subbarao, *J. Phys. Chem. Solids*, **23**, 665 (1962).
12. L. A. Shebanov et al., *Mater. Res. Bulll.*, **20**, 781 (1985).
13. R. L. Withers et al., *J. Solid State Chem.*, **94**, 404 (1991).
14. A. David Rae, *Acta. Cryst.*, **B 46**, 474 (1990).
15. L. A. Reznichenko et al., *Inorganic Materials*, **32**, 423 (1996).
16. Smolenskii et al., *Fiz. Tverd. Tela.*, **2**, 2982 (1960).
17. F. Izumi, *"Rietveld method"*, edited by R. A. Young, Oxford univ. press, Oxford, chap.13. (1993).
18. S. C. Abrahams, S. K. Kurtz and P. B. Jamison, *Phys. Rev.*, **172**, 551 (1968).
19. M. Mahesh. Kumar et al., *Solid State Commun.*, **104**, 741 (1997).

Piezoresistance in Thin $BaTiO_3$ Ceramic Bars and Their Applications

K. Hamamoto, H. Matsuda, K. Miyazawa, and M. Kuwabara

Department of Materials Science, School of Engineering, The University of Tokyo

7-3-1 Hongo, Bunkyo-ku, Tokyo 113-8656

Phone: 03-5841-7134 Fax: 03-5841-8653

hamamoto@ecl.mm.t.u-tokyo.ac.jp

We have prepared semiconducting $BaTiO_3$ ceramic fibers with a diameter of 10~20μm, whose microstructure consists of single grains sintered together in series. Measurements of piezoresistive effects using alternating stress (compression and tension) were carried out on single grain boundaries formed in these fibers. Large piezoresistive effects (gage factor $>10^5$) were observed for some of the single grain boundaries in the present samples at room temperature, but no distinct piezoresistance was observed in the bulk. Simultaneously, we observed motion of a 90° domain wall responding to a mechanical oscillation in a sample with a polarizing microscope. As a result, it has been found that the observed large piezoresistance is closely related to the morphological change of ferroelectric domain structures in the vicinity of grain boundaries in the sample. We intend to develop various types of sensors, such as thermal and mechanical ones, using the piezoresistance in single grain boundaries of semiconducting barium titanate. Development of high sensitive stress-sensors using these materials is now in progress.

1. Introduction

It is well known that donor-doped barium titanate ($BaTiO_3$) semiconducting ceramics show distinct piezoresistive effects (stress-sensitive resistivity) in a relatively narrow temperature range around the Curie point.[1-3] The mechanism of the piezoresistive effect has been explained in terms of the stress dependence of dielectric constant on the basis of the Heywang model[4], which has been widely accepted as the mechanism of the positive temperature coefficient of resistivity (PTCR) effect.[2-3] However, no comprehensive study on the piezoresistivity in $BaTiO_3$ ceramics in light of its structural dependence has been made, though the influence spontaneous polarization on the grain boundary resistance below the Curie point has been argued.[5] To clarify the mechanism of the piezoresistivity in $BaTiO_3$ ceramics, we have prepared semiconducting $BaTiO_3$ ceramic bars, with a diameter in the range of 10~20μm, whose microstructure consists of single grains sintered together in series.[6] And we have carried out measurements of piezoresistance for strictly single grain boundaries formed in the samples. It has been found that, some of the grain boundaries examined showed extremely large piezoresistance[7] given by a gage factor of $> 10^7$. When ferroelectric domain structures in the vicinity

of a grain boundary in the samples changed, distinct piezoresistance occurred. This was confirmed from observation using a polarizing microscope. In this study, measurements of piezoresistive effects and observation of ferroelectric domain structures are simultaneously carried out. As the result, it has been found that the occurrence of piezoresistance in $BaTiO_3$ ceramics is directly related to the morophological change of the domain structure at grain boundaries.

Fig. 1 SEM image of a thin semiconducting $BaTiO_3$ ceramic bar.

2. Experimental

Slurry of a mixed powder, with the composition of $Ba_{0.999}La_{0.001}TiO_3+0.4mol\%TiO_2$, was prepared from commercial high purity powders of $BaTiO_3$, La_2O_3, and TiO_2, using polyvinyl butyral (PVB) as a binder. Green fibers drawn from the slurry were fired at 1370°C in air

to yield thin ceramic bar samples with a microstructure consisting of single grains joined together in series, with a diameter in the range of 10~20μm. The piezoresistive effect for a single grain boundary formed in the samples was measured at room temperature by a two-probe method using In-Ga alloy electrodes put on two grains adjacent to the grain boundary, under varied mechanical stresses. Cyclic mechanical stresses in the frequency range of 10-100mHz were also used to investigate the dynamical change in the ferroelectric domain structure that characterizes the dynamic piezoresistance in the samples. The data obtained is expected to provide definite information on the mechanism of the piezoresistivity in the materials. The magnitude of strains given to a sample was evaluated by the equation $S=(L-L_0)/L_0$, where L and L_0 denote the length of the sample stressed and stress-free, respectively. This means, therefore, that a positive value of S ($S > 0$) corresponds to a tensile strain and a negative value of S ($S < 0$) a compressive strain. The change of ferroelectric domain structures and motion of 90° domain walls were observed using a polarizing microscope. The structure of grains of the ceramic bar samples was examined by a scanning electron microscope (SEM). Figure 1 shows a typical SEM image of thin BaTiO$_3$ ceramic bars produced in this study.

3. Results and Discussion

Figure 2 shows a current-time characteristic obtained for a single grain boundary in a BaTiO$_3$ ceramic bar at room temperature, where the current was measured at a bias voltage of 0.01V and the strain was changed to oscillate between $+1 \times 10^{-3}$ and -1×10^{-3} at a modulation frequency of 50mHz. It can be seen that the grain boundary showed current oscillating at exactly the same frequency as that of the stress applied, with its change by more than two orders of magnitude. Such a large piezoresistive effect at room temperature has never been observed in bulk ceramics until now. Thus thin BaTiO$_3$ ceramic bars with such large piezoresistance as this are expected to find novel device applications, such as high sensitive stress sensors.

Figure 3 shows a current-time characteristic obtained for another grain boundary under cyclic
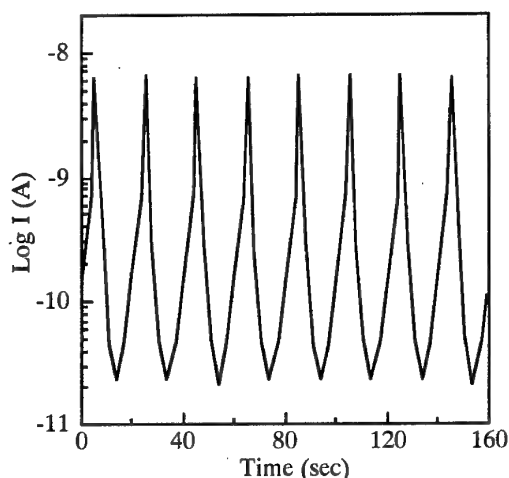

Fig. 2 Current-time characteristic obtained for a single grain boundary under cyclic mechnical stresses at room temperature. Modulation frequency = 50mHz and bias voltage = 0.01V.
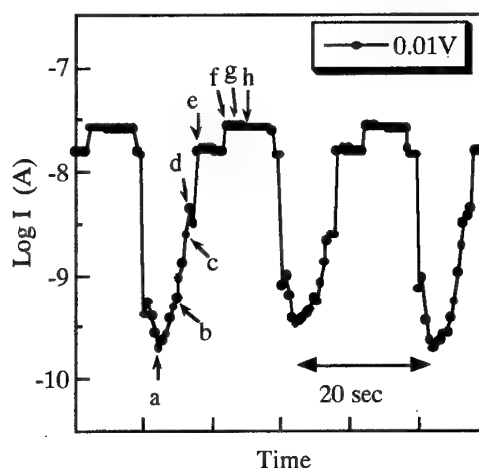

Fig 3 Current-time characteristic obtained for a single grain boundary under cyclic mechnical stresses at room temperature. Modulation frequency = 20mHz and bias voltage = 0.01V.

mechanical stresses. At the same time, polarizing microscope images of the sample were obtained, which are shown in Fig. 4. Images (a) to (h) of Fig. 4 were taken at the points a to h indicated on the curve of Fig. 3. Images (a) to (h) of Fig. 4 indicate consecutive change of the domain structure in the sample under cyclic mechanical stresses; (a) is the state under a compressive stress of $S = -1 \times 10^{-3}$, (d) the stress-free state and (h) is that under a tensile stress of $S = +1 \times 10^{-3}$. It can be seen that the domain structure changed
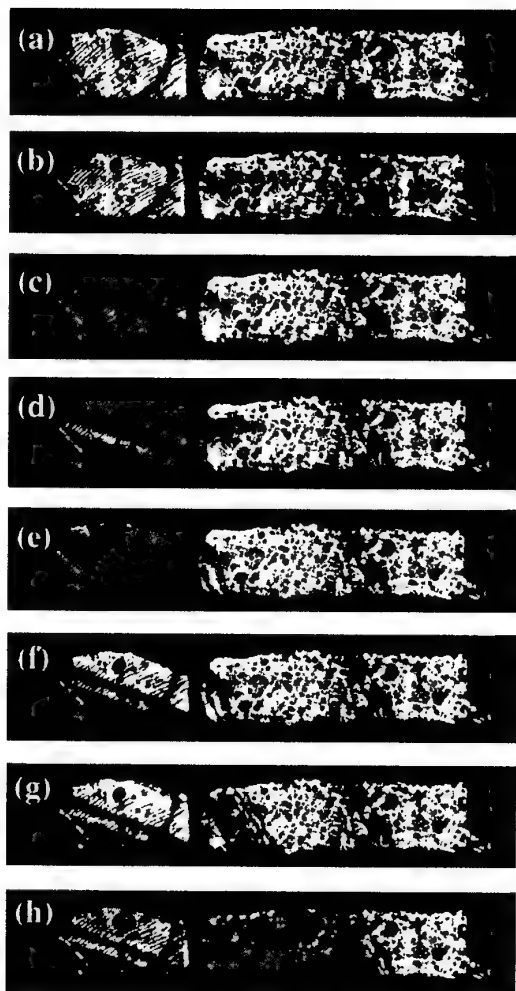
Fig. 4 Polarizing microscope images of BaTiO₃ ceramic bar under various cyclic mechanical stresses. Images (a) through (c) show the domain structures under compressive stresses, images (e) through (h) are those under tensile stresses. Image (d) shows the stress-free state of the sample.

Fig 5 Illustrations showing the domain structures in the sample in the defferent states (a), (d) and (h) shown in FIg. 4, respectively. The directions of 90° domain walls and c-axis were calculated by analyzing their interference color images.

Fig. 6 Configuration models of spontaneous polarization in two grains adjacent to a grain boundary giving three different values of C_N (0, 1 and a value between 0 and 1).

with strain. From the data of Fig. 3 and 4 it is obvious that, the current changed significantly when the domain structure in the vicinity of grain boundary changed. The domain structures in the sample in the states (a), (d) and (h) shown in Fig. 4, respectively, are schematically shown in Fig. 5. In this figure are shown the directions of spontaneous polarization (c-axis) in the grains (in illustration (a)) and also those of 90° domain walls (in illustrations (d) and (h)), which were determined by analyzing the respectiveinterference color images o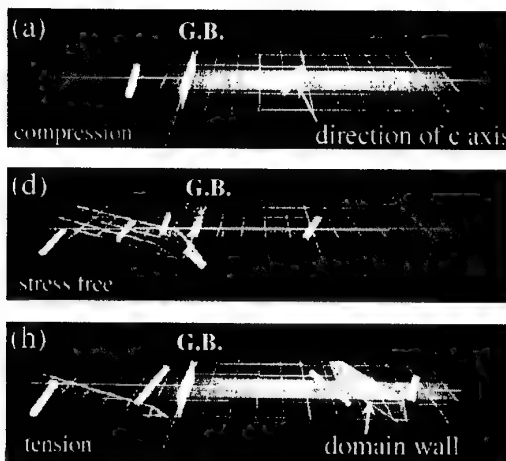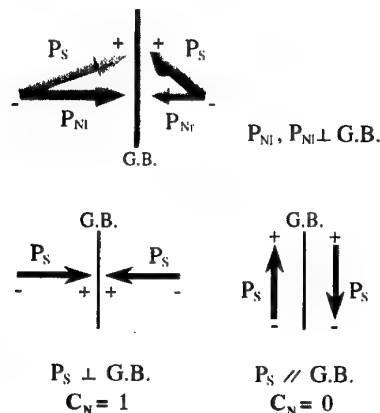f Fig. 4 using a simple vector analysis. On the basis of the illustration of Fig. 5 we can estimate the normal component of spontaneous polarization (P_S) to the grain boundary in the sample at respective states. Estimation of the magnitude of the normal component of P_S (taking its value to be a constant) to the grain boundary for three cases are shown in Fig. 6. P_{Nl} and P_{Nr} shown in this figure represent the normal components of PS to the grain boundary in the grains on the left and right, respectively. The negative charge of surface acceptor state (N_s) at a grain boundary is compensated by the net charge (P_N) of the normal component of P_S to the grain boundary, that is
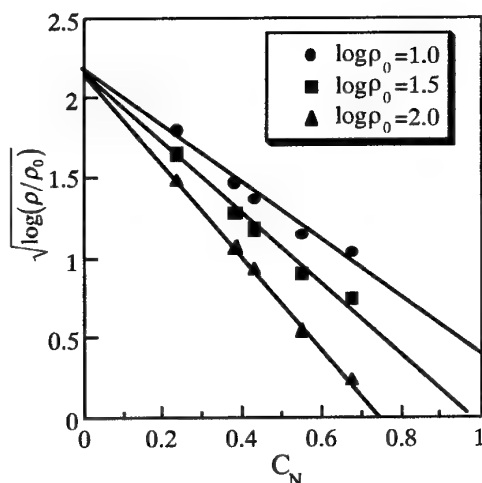
Fig. 7 $\sqrt{\log(\rho/\rho_0)}$ versus C_N plots obtained for the single boundary that exhibited the data of Fig. 3, taking the value of $\log\rho_0$ to be 1.0, 1.5 and 2.0.

$P_N = P_{Nl} + P_{Nr}$. Since we do not know the exact value of P_S, it is convenient to use the normalized polarization charge defined by $P_N/2P_S$ ($\equiv C_N$) for evaluation of the degree of compensation of N_S by spontaneous polarization. If we assume that the height (eϕ) of a potential barrier formed at a grain boundary is given by the equation

$$e\phi = \frac{(eN_S - P_S)^2}{2\varepsilon_r \varepsilon_0 N_d} \quad , \qquad (1)$$

bases on Jonker's model[5] and the grain boundary resistivity ρ is determines by the eϕ as;

$$\rho = \rho_0 \exp\left(\frac{e\phi}{kT}\right) \quad , \qquad (2)$$

then we obtain the following relationship by assuming the dielectric constant er to be cons

$$\sqrt{\ln\frac{\rho}{\rho_0}} \propto (eN_S - C_N) \quad , \qquad (4)$$

where ρ_0 is the bulk resistivity.

From the data of Fig. 3 and domain structure analysis we obtained the relationships between $\sqrt{\log(\rho/\rho_0)}$ and C_N assuming the value of ρ_0 to be $\log\rho_0$=1.0, 1.5 and 2.0. The results are shown in Fig. 7. Since all the plot of Fig. 7 show fairly a good liner relasionship, the validity of eq. (3) is obvious. From the data of Fig. 7 the grain boundary examined should be expected to exhibit a resistance change of more than four orders of magnitude at room temperature if mechanical stress

is applied to cause the change of the value of C_N from 1 to 0.

Based on the results obtained in this study we may conclude that the piezoresistive effect in semiconducting BaTiO$_3$ ceramics can be interpreted in terms of stress dependence of surface charge compensation by spontaneous polarization, not stress dependence of the dielectric constant of the materials according to the Heywang model.

4. Conclusion

We confirmed that there exist single grain boundaries which exhibit significantly large piezoresistive effects at room temperature in thin BaTiO$_3$ ceramic bars. Measurements of resistivity and observation of domain structures were simultaneously carried out for some samples under cyclic mechanical stresses. As a result, it is concluded that the piezoresistive effect in BaTiO$_3$ ceramics is attributed to the change in the degree of surface charge compensation by spontaneous polarization resulting from changes of the domain structure morphologies in the vicinity of grain boundaries under mechanical stresses.

5. References

[1]O. Saburi, *J. Phys. Soc. Jpn.*, **15**, 733-734 (1960).

[2]A. Amin, *J. Am. Ceram. Soc.*, **72** (3) 369-376 (1989).

[3]J. S. Capurso, et al. *J. Am. Ceram. Soc.*, **78** (9) 2476-2480 (1989).

[4]W. Heywang, *J. Am. Ceram. Soc.*, **47** (10) 484-490 (1964).

[5]G. H. Jonker, Solid State Electron., **7** 895-903 (1964).

[6]H. Matsuda, et al. *J. Am. Ceram. Soc.*, **81** (1) 229-232 (1998).

[7]M. Kuwabara, et al. J. Electroceramics, in press.

Growth of Potassium Lithium Niobate (KLN) Crystals by the Continue-Charged Czochralski Method

Masatoshi Adachi, Mayumi Nakatsuji and Tomoaki Karaki

Department of Electronics and Informatics, Faculty of Engineering, Toyama Prefectural University,
5180 Kurokawa, Kosugi-machi, Toyama 939-0398, Japan
Fax: 81-76-656-8023, e-mail: adachi@pu-toyama.ac.jp

To avoid the deviation of $K_3Li_2Nb_5O_{15}$ (KLN) crystal composition during the growth, an improved Czochralski technique, so called continue-charged Czochralski method, has been employed to offset the compositional change in melt during the growth by continually throwing calcined powder into the crucible. Using this method, the KLN crystal with composition of $0.3K_2O\text{-}0.18Li_2O\text{-}0.52Nb_2O_5$ has been grown from melt of $0.3K_2O\text{-}0.263Li_2O\text{-}0.437Nb_2O_5$. A 30-mm-long crystal was investigated for compositional deviation by measuring its Curie temperature T_c. Three samples were cut out from shoulder, center and bottom parts. The T_c of all samples were coincident with each other and determined to be 560°C, indicating that the crystal is compositional deviation free and its concentration of Nb is 51.8mol%.

1. INTRODUCTION

$K_3Li_2Nb_5O_{15}$ (KLN) single crystals with the tungsten-bronze type structure have recently been considered to be superior materials for blue second harmonic generation (SHG), because of their advantages such as high optical damage resistance, low optical losses with an absorption edge of 376nm, and wide phase matching characteristics. According to the phase equilibrium diagram of the $K_2O\text{-}Li_2O\text{-}Nb_2O_5$, ternary system[1], stoichiometric KLN could not be grown by Czochralski pulling method. Nb-rich pale-yellow KLN crystals up to about 100mm in length has been successfully obtained from potassium and lithium enriched incongruent melt using the usual Czochralski method[2-5].

However, the deviation of crystal composition during the growth can not be avoided essentially when using the Czochralski method even though one can attempt KLN crystal growth with less deviation from a big crucible, because of the incongruent nature[2]. Another problem that hinders the applications of the KLN crystal is the niobium concentration in the crystals. Usually the crystals with high Nb content (>54mol%) are easy to be grown from melt. But it has been pointed out that Nb should be less than 52% for 425nm-blue-beam SHG, according to the phase matching characteristics[2]. The KLN crystals with less Nb concentration or closer to the stoichiometric composition have larger birefringence and wide phase matching angle. But it is difficult to grow KLN with Nb less than 52mol%, because the critical point given by the phase equilibrium diagram is Nb 51mol%[1].

For solution of these serious problems, an improved Czochralski technique, so called continue-charged Czochralski method, was successfully employed to grow uniform crystal, which has been used for crystal growth of stoichiometrical $LiNbO_3$[6]. This method is effective to offset the compositional change in the melt during the growth by continually throwing calcined powder into the crucible. A skilled technician and a stable temperature condition around the crucible are requested for the growth. In this paper, the details of the crystal growth, compositional deviation and properties of the crystal will be reported.

2. CONTINUE-CHARGED CRYSTAL GROWTH

The starting materials used in this work were K_2CO_3 of 99% purity, Li_2CO_3 of 99.99% purity, and Nb_2O_5 of 99.99% purity. The oxide mixture, weighing about 340 g (about 300 g of KLN) with the composition of $0.3K_2O\text{-}0.263Li_2O\text{-}0.437Nb_2O_5$ was calcined at 900°C for 3h and then charged into a double-crucible, a $\phi50\times$ 50mm Zr-reinforced platinum crucible with a

φ35mm platinum cylinder inside. Figure 1 shows the structure of the double-crucible used in this work. Usually an inside cylinder of a double-crucible has same height as the outside crucible. In our case, the outside crucible is not large enough in diameter. For the purpose of quick homogenization of the melt after continue-charging, a short cylinder of 10 to 15 mm in height was designed to be laid on the outside crucible. An auto-charging system controlled by a computer was employed to continually throw calcined charge powder which composition was the same as the grown crystal, $0.3K_2O-0.18Li_2O-0.52Nb_2O_5$, so that the melt composition could be kept without variation, as shown in Fig. 2. The calcined charge powder should be a sintered dense grain with a diameter of 0.5 to 1 mm. A loose powder dropped to the melt would be floating on the surface and not be dissolved, because the melting point of the powder was higher than the surface temperature of the melt. A sintered dense-grain powder would sink to the melt and then dissolve.

Seeding temperature was about 980°C, and the growth was carried out in air. Pulling rate was 0.5mm/h, and seed-rotation speed was 30-40 rpm. The growth was along the <110> direction. Since the crystal was grown from the lithium enriched incongruent melt, and moreover the crystal composition was close to the critical point, Nb 51mol%, wide temperature change and fast growth would cause anomalous solidification leading to many cracks in the crystal or a loose polycrystalline lump.

A well grown crystal is shown in Fig. 3. The crystal is almost colorless and much paler than that of the Nb 53.5mol% crystal[2], because the crystal near to the stoichiometric composition has less vacancy. The crystals grown along <110> are generally prismatic with clearly defined faces such as (001) and (110). The longer lateral direction presents the <001> axis. The crystal was then X-ray-oriented and cut off. The samples were poled by the field-cooling method under a DC current of about 1-2mA/cm² from temperature of 550°C to 450°C along the <001> axis.

2. RESULTS AND DISCUSSION

The most important thing is to check the composition in the crystal. The chemical analysis is not easy to determine the concentration of Li and K. Since Curie temperature T_c decreases slightly with increasing Li/Nb at constant K_2O content,
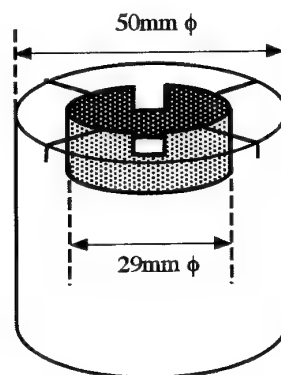

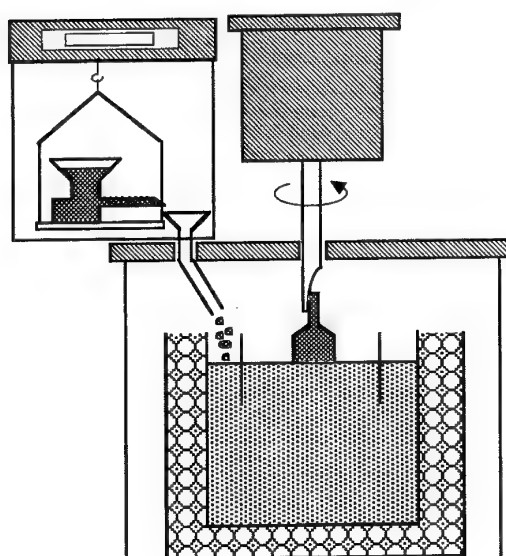Fig. 1. Structure of double-crucible.

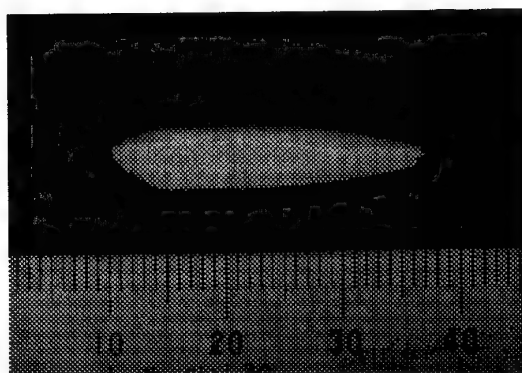Fig. 2. Schematic drawing of continue-charged Czochralski technique system.

Fig. 3. Photo of well grown KLN crystal by continue-charged method.

T_c is influenced somewhat by Li/Nb ratio in the crystal[1,7]. Therefore, the concentration could be approximately determined by measuring T_c of the samples. The temperature dependence of dielectric constants $\varepsilon_{33}/\varepsilon_0$ at 100 kHz is shown in Fig. 4. Three samples were cut from the shoulder, center and bottom of a 40-mm-long continue-charged-grown KLN crystal. The three samples show sharp peaks at the Curie temperature T_c around 560°C. The dielectric constants at room temperature and Curie temperature are 40 and 11000, respectively. The three samples show same T_c, indicating no compositional deviation in the crystal. The concentration of Nb is determined as 51.8mol% in accordance with the relationship[1]. The large $\varepsilon_{33}/\varepsilon_0$, 11000, at T_c indicates the crystal is highly anisotropic.

The KLN crystals have tetragonal 4mm symmetry and large electro-mechanical coupling factor k. Usually the coupling factors are similar to the electrooptic constants and nonlinear coefficients, showing larger volume with larger anisotropy c/a.

Large piezoelectric constants, coupling factors, k_t=0.66, $k_{33} \doteqdot 0.68$ and k_{31}=0.21 at room temperature were obtained by the resonant and antiresonant frequency method. These coupling factors are much larger than that of Nb 54.2mol% KLN crystal[3]. Therefore, large electrooptic constants and nonlinear optic coefficient are also expected in the crystal.

The optical transmittance of the crystal was measured using a c-cut plate with a thickness of 1.1 mm, as shown in Fig. 5. The crystal has the absorption edge at about 370nm, which little shifts to shorter wavelength than that of the Nb 53.5mol% crystal[2]. This transparent crystal also has very small optical absorption, less than $0.3cm^{-1}$ in 420-450nm region, less than $0.2cm^{-1}$ in 450-500nm region, and less than $0.1cm^{-1}$ in 500-800nm region.

The uniform composition and very low absorption make the KLN crystal possible to the applications of blue SHG.

4. CONCLUSIONS

The continue-charged Czochralski technique is very effective to grow uniform crystals from incongruent melt. The double-crucible must be devised to dissolve charged powder and homogenize the melt quickly with least temperature variation after continue-charging. The uniform KLN crystal with high anisotropy,

Nb 51.8mol%, was successfully grown by the continue-charged Czochralski method. However, the crystal with composition near 51mol% is very difficult to grow because several solid phases exist in a small temperature and composition rang. Rigorous temperature control and skillful hands are requested for the crystal growth. To grow a large size crystal for practical use will be a subject of our future work.

The measurement of refractive index dispersion, nonlinear optical coefficients, optical damage resistivity, electrooptic constants, phase matching characteristics and lattice constants are planed in this work.
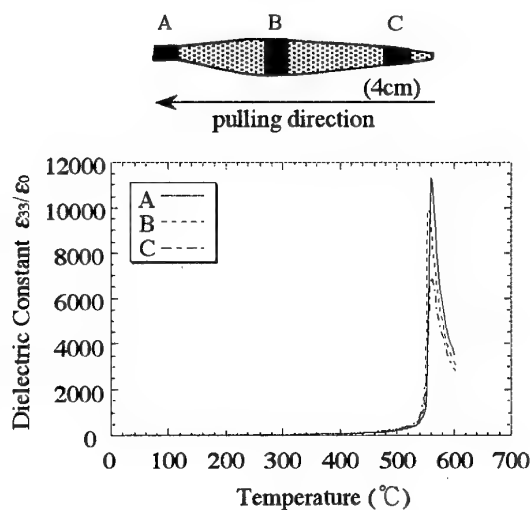

Fig. 4. Dielectric constant *vs.* temperature, a, b, and c represent the shoulder, center and bottom, respectively.
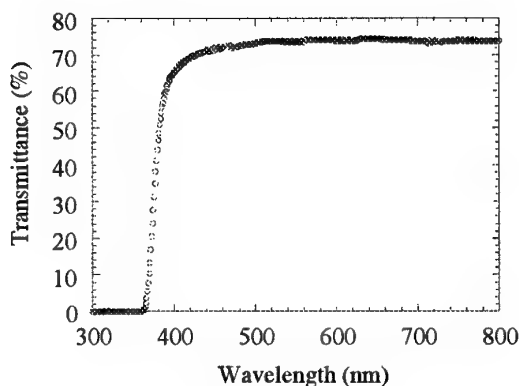

Fig. 5. Transmittance of a 1.1-mm-thick c-cut sample.

Since the uniform KLN crystal shows high electro-mechanical coupling factors, large electrooptic constants and nonlinear optic coefficients can be expected. Moreover the crystal has very low optical absorption at a wavelength from 420nm. These strong points will enable the applications of high-power SHG of blue light wave (*e.g.* λ=425nm).

REFERENCES

[1] B. A. Scott, E. A. Giess, B. L. Olson, G. Burns, A. W. Smith, and D. F. O'Kane, *Mat. Res. Bull.*, **5**, 47-56 (1970).

[2] T. Karaki, K. Miyashita, M. Nakatsuji and M. Adachi, *Jpn. J. Appl. Phys.*, **37**, 5277-5279 (1998).

[3] M. Adachi and A. Kawabata, *Jpn. J. Appl. Phys.*, **17**, 1969-1973 (1978).

[4] R. R. Neurgaonkar, W. K. Cory, J. R. Oliver, and L. E. Cross, *Mat. Res. Bull.*, **24**, 1025-1030 (1989).

[5] Z. Chen, M. Tago, M. Adachi, and A. Kawabata, *Ferroelectrics*, **196**, 265-268 (1997).

[6] K. Kitamura, J. K. Yamamoto, N. Iyi, S. Kimura and T. Hayashi, *J. Crystal Growth*, **116**, 327 (1992).

[7] T. Nagai and T. Ikeda, *Jpn. J. Appl. Phys.*, **12**, 199-204 (1973).

A Low Loss, Temperature Stable (T_f) LTCC RF Material System for Consumer Wireless Applications

Rong-Fong Huang, Steve X. Dai and David Wilcox Sr.

Ceramic Technology Research Laboratories, Motorola Labs
7700 S. River Parkway, Tempe, Arizona 85284, USA
Fax: 480-755-5350, e-mail: crh006@email.mot.com

The unique requirement of battery operated wireless products imposes significant challenges on the traditional low temperature cofired (LTCC) materials systems to achieve low electrical losses and frequency temperature stability for the RF signals employed in these applications. This paper reports on the progress related to the development of a material system with properties tailored to satisfy the applications in the 0.5 to 6 GHz range. The effect of reaction kinetics on the densification and dielectric loss of a Pb free, low fire (850-900°C) RF ceramic dielectric is presented. This material system is proposed to serve as a common host dielectric for consumer wireless applications, much like the FR4 has become a common material for the PCB industry.

1. INTRODUCTION

Low fired multilayer ceramic technology has shown great capability to integrate passive components effectively. The ability to co-fire low loss dielectric ceramic tapes with low loss metal systems such as Ag or Cu, and to integrate components in a 3 dimensional fashion uniquely enable this technology to integrate low loss circuit functions for wireless applications. This multilayer ceramic integrated circuit (MCIC) technology [1] has been used to integrate high frequency RF front-end functions such as the antenna, T/R switch[2], filters[3,4], VCO[5], and matching networks [6,7]into a single structure. The technology is aiding significantly in the drive to reduce the size and the number of components in wireless phones [8,9] while maintaining superior performance and reliability.

However, the unique requirement of high frequency circuits, operating in the 0.5 to 6 GHz range for most consumer wireless applications, imposes significant challenges on the traditional LTCC material systems. There are currently two types of LTCC material systems available on the market. One is based on the mixture of low melting glass with ceramic powder (such as alumina) as a filler for the dielectric used in the tape [10]. It generally has a dielectric constant (K) of 7-9, a loss factor of 0.01-0.002, and a temperature coefficient of frequency (T_f) of 50-100 ppm/°C. In this system, the glass acts as a bonding agent to hold the ceramic particles together and little reaction between the glass and ceramic filler occurs. The fired properties of these dielectrics display a reasonable process window and they have been widely used for multilayer interconnect modules for digital and automotive applications. The other type of tape compatible dielectric is made of re-crystallizeable glasses [11]. During firing, the glass, enabling a low firing temperature, crystallizes to produce a low dielectric loss ceramic body. Loss factors of < 0.0004 at high frequency are common. This type of dielectric tape is suitable for 20-30 GHz applications such as in military and aerospace where very low loss is required. The dielectric constant is in the range of 5-7 with a T_f similar to the glass bonding type. The processing window for this dielectric family is, in general, not as forgiving as the previous one, as the crystallization of the glass complicates the densification process of the ceramic. These two types of ceramic systems have been used to make integrated RF (radio frequency) devices for the consumer wireless applications.

2. PROPERTY REQUIREMENTS FOR an RF LTCC MATERIAL SYSTEM

As the trend toward higher frequency and tighter frequency specifications continues, there are needs to improve the material system to satisfy the property requirements for the consumer wireless market. The desired host dielectric material should exhibit low loss, low T_f and a K in the 8-10 range. If the K is too low (<6), the device dimension can not be effectively reduced. On the other hand, if the K is high (>10), the fluctuation on embedded component's value due to processing variation can be too large to achieve high yield manufacturing. Low dielectric loss is essential for hand held, battery powered applications. A loss factor of < 0.001 (Q > 1000) is sufficient for most applications to reduce power drain. Because many critical RF front-end functions require integrating filtering and resonating circuits, the required dielectric should have a T_f < 10ppm/°C to provide high quality filtering and frequency stability. To increase the volumetric efficiency of the embedded capacitors, co-firable dielectric pastes with a K higher than the host tapes are required as part of the material system. The material properties for these dielectric pastes should also be low loss (Q >200) with low T_f as well when components from these materials are inserted in the energy stream. In the high frequency circuits, the capacitance values tend to be low and materials with K ranging from 20 to 200 are adequate for most embedded

capacitor requirements. Co-firable resistor pastes with resistance values from 100 ohm/sq. to 10000 ohm/sq. are desired for most applications. Therefore, a complete LTCC material system for RF applications will consist of: (1) a dielectric material for green tapes to serve as a host for the embedded functions; (2) an array of high conductivity metal pastes for via, internal and external metallization; (3) dielectric pastes with dielectric constants higher than the host tapes to increase the volumetric efficiency of large embedded capacitors; and (4) resistive pastes that can effectively cover the requirement for the embedded resistors. It is also highly desirable to develop the complete material system avoiding environmentally unfriendly elements such as Pb and Cd. In the following section, progress on the development of such a material system is discussed.

3. SYTHESIS OF A RF LTCC MATERIAL SYSTEM
3.1. High Q, Temperature Stable (Low T_f) Host Dielectric Tape Development

The high Q dielectric for host tapes is based on a glass-ceramic material system. The system includes a specially formulated lead-free glass, a high Q ceramic filler (Al_2O_3) that will react with the glass to form high Q phases, and an appropriate oxide additive which also participates in the reaction to form phases that reduces the overall T_f. Most of the low melting glasses exhibit high losses at high frequencies that limiting the overall Q in the sintered dielectric. This dielectric composition is designed to have a minimum amount of glass left after sintering. Ingredients in the glass are B_2O_3, K_2O, SiO_2, CaO, SrO and BaO. The softening temperature and viscosity of the glass are mainly determined by the amounts of B_2O_3, K_2O and SiO_2.

Compositions with glass contents in the range of 40-60 wt % were examined. The glass/filler ratio was used to adjust the sintering behavior and the RF properties of the dielectric. During sintering the Al_2O_3 particles react with glass and form the high Q crystalline phases both at the Al_2O_3-glass interface and inside the glass matrix. Figure 1
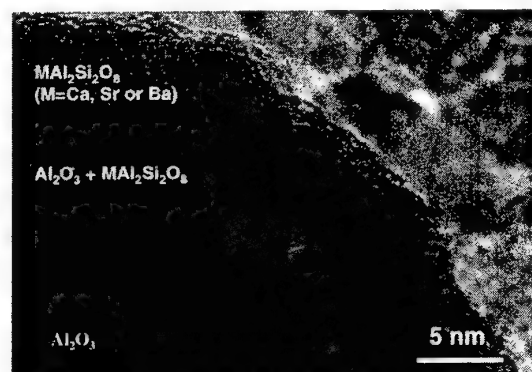

Figure 1. HRTEM of high Q samples showing reactive Al_2O_3 - glass interface

shows the high resolution TEM (HRTEM) picture for samples that exhibit high Q properties. The reaction zone between the glass and Al_2O_3 is clearly shown. The HRTEM image for samples with low Q is shown in Figure 2 - no reaction occurred between the glass and Al_2O_3. The comparison of these pictures suggests that the formation of the high Q anorthite type phases $MSi_2Al_2O_8$ (M=Ca, Sr or Ba) is responsible for the high Q behavior for this dielectric composition. The consumption of SiO_2, CaO, SrO and BaO greatly reduces the volume of glass in the final structure and results in a dielectric with Q >1000 at 1GHz.
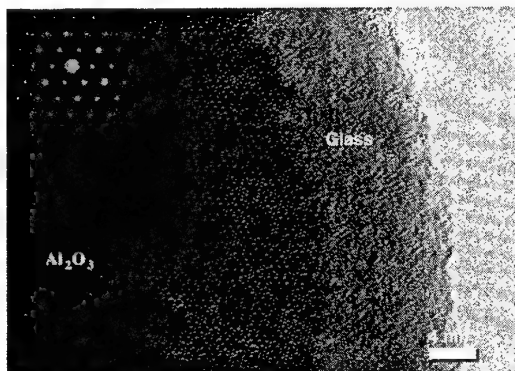

Figure 2. HRTEM of low Q samples without the reaction layer formation.

Since the reaction occurs at the interface between the glass and Al_2O_3, the size and surface area of these particles as well as the firing profiles should affect the kinetics of the reaction. To study the influence of particle size on the reaction kinetics, densification behavior and RF dielectric properties, a series of samples were prepared with different Al_2O_3 particle sizes and surface areas. Results show that formulations with fine Al_2O_3 powder cannot achieve high fired density but the dielectric Q is high. This is likely due to the fast reaction between the glass and chemically highly active fine Al_2O_3 particles, resulting in less free glass to aid the densification process. The Q of these samples is high attributed to the large amount of high Q anorthite type phases and the reduction in volume of the low Q glassy phase in the sample. On the other hand, formulations with large Al_2O_3 powder densified well, but did not achieve high dielectric Q. With limited reaction between the low surface area Al_2O_3 and the glass, very little high Q phases are formed. The increase in residual glass in these samples acts to promote the densification. The importance of reaction kinetic can also be seen from the effect of heating rate to the sintered properties of the dielectric. Figure 3 and 4 show the effect of heating rates on the fired density and Q for samples prepared with the same raw materials.
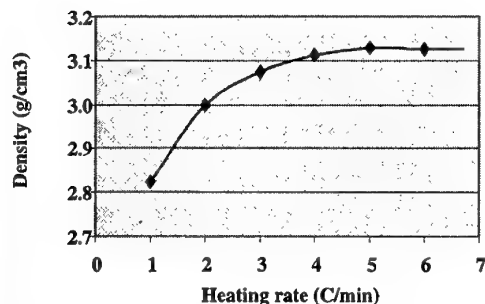
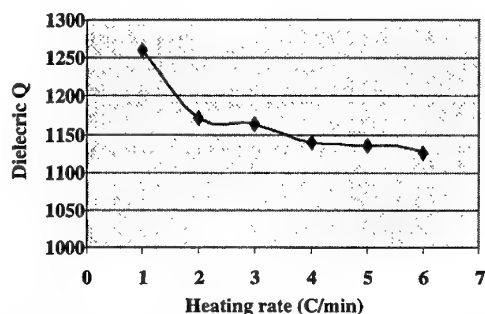Figure 3. Density as a function of heating rate in 450-875° C range

Figure 4. Dielectric Q vs heating rate from 450 to 875°C

Slow firing rates increase the time for the formation of the high Q phases but with low density because of less remaining glassy phase to aid the densification. The two paths for the densification process are depicted in Figure 5. To achieve high Q and high density simultaneously, the glass must first form the liquid phase to help densify the oxide filler and later must react with Al_2O_3 to form the high Q anorthite type phases, reducing the content of the low Q glassy phase. The reaction is a self-limiting process as the formation of these high Q phases consumes the anorthite forming ingredients in the glass and a diffusion barrier forms around the filler particles (see Figure 1).
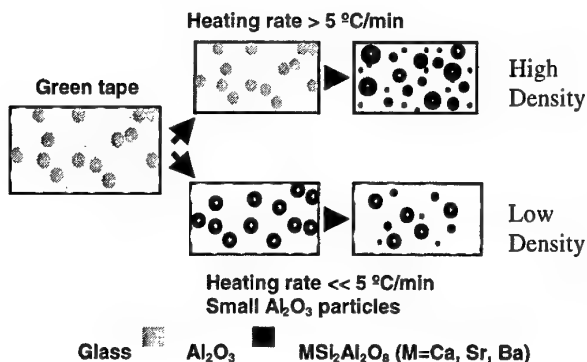

Figure 5. Densification paths for the dielectric tape.

Using a hot-stage X-ray diffractometer to examine the anorthite formation rates, these high Q crystalline phases are found to reach saturation after 20 minutes at 875°C. Hence, the reaction kinetics of this ceramic dielectric can be controlled by proper selection of the raw materials and suitable firing profiles. Excellent RF dielectric properties and microstructures have been achieved routinely through appropriate control of these parameters.

The formulated Al_2O_3- glass composition has a T_f of -78 ppm/°C. Thus, an additive is incorporated to reduce the T_f. It was found that the T_f could be reduced to less than 10 ppm/°C with the addition of fine particle size TiO_2 powders. Formulations from 3 to 15 wt% were examined. The fine grain TiO_2 particles react with the glass during sintering. No TiO_2 can be found after firing based on Field Emission SEM and X-ray Photo Spectroscopy examinations. It is believed that complex titanates with large positive T_f's are formed which effectively reduce the overall T_f. Figure 6 shows the frequency shift vs the temperature for this modified composition (T2000) as compared with other commercially available dielectric tapes.
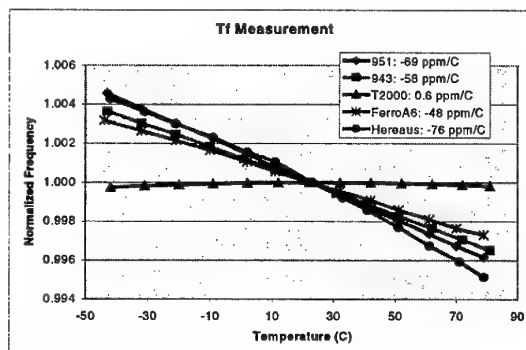

Figure 6. The frequency shift vs temperature for five different tape systems.

Further efforts are underway to examine the role of TiO_2 in the development of the final microstructure.

3.2. Co-firable metallization development

A family of silver pastes that are co-firable with the tape at 850-900°C has been established. Glass powders are typically incorporated into the paste formulation to provide adhesion between the silver and the dielectric. However, the existence of non-conductive bonding agents such as glass reduces the conductivity of the film. To ensure high conductivity (high metal Q), a paste was developed containing small amounts of non-glass type adhesion promoters [12]. This resulted in high conductivity and good adhesion to the ceramic. For ease of processing, it is desirable to have external metal systems that can be co-fired with the LTCC structure in one firing operation. The use of non-glass adhesion promoters avoids the tendency of glassy phase formation on the metal film surface often

observed in conventional pastes when fired on the surface of these devices. This improves solderability.

3.3. High Q dielectric paste with a K of 20

A dielectric paste formulation meeting the high Q requirement has been developed which is co-firable with the host tape. The paste consists of a high Q ceramic powder (Ca,Sr)TiO$_3$ [SCT] that has a K of 250 as a main ingredient and a glass that is capable of reacting with the SCT to form high Q phases. The reactive glass functions as an effective flux for reducing the densification temperature to the 850-900°C region needed for the total RF LTCC material system. The dielectric paste after co-firing with the tape exhibits a K in the range of 21 to 28, depending on the specific SCT to glass ratio. The Q is in the range of 500 to 1000 when measured at 1 MHz. The capacitance drift from -40°C to 80°C is ±3%, adequate for the RF by-pass and shunt capacitor applications.

4. PROPOSED COMMON LTCC MATERIAL SYSTEM FOR RF APPLICATIONS

Currently there are several commercially available LTCC material systems, each serving a portion of the market. These material systems are generally not cross-compatible, requiring different firing profiles and processes. None of them were developed to achieve properties specifically tailored to the consumer wireless applications. In order to increase the tape volume and thereby reduce costs and establish multiple sources of supply, there is a need to establish a common host dielectric material for these LTCC RF applications, much like the FR4 has become a common material for the printed circuit board industry. As the focus on a common FR4 material aided in the design, manufacture and growth of applications and infrastructure, for the reasons noted above, we believe a similar dynamic would develop should a common host material be identified for the LTCC RF wireless applications. The equipment suppliers can develop unique equipment that can efficiently process these common materials in high speed. All of these steps will speed up the wide spread adaptation of the LTCC technology for the RF application. The new LTCC host dielectric material reported here has properties suitable for these consumer wireless applications. It could serve as that common material system for these applications.

5. SUMMARY

This paper reports the development of a new low fire (850-900°C) material system that consists of a host ceramic dielectric specifically formulated to meet the Q and T$_f$ (temperature coefficient of frequency) requirements for the emerging consumer wireless applications. Metal inks and a dielectric paste tailored to achieve low electrical losses and the high frequency temperature stability properties required for this application are also discussed. The desired material properties for the LTCC material system for RF wireless applications are presented. The synthesis strategy and the influence of particle morphology and firing profile on the densification and dielectric loss characteristics of this Pb free LTCC host dielectric are discussed. Properties of specially formulated conductive and dielectric pastes with high Q co-firable with the tape system are also presented. The importance and rationale for establishing a common LTCC host dielectric for consumer wireless communication applications is discussed and the material system suitable for this purpose proposed.

REFERENCES

1. D. L. Wilcox, R.F. Huang, and D. Anderson, Proceedings of 1997 ISHM, Philadelphia (1997) 17.
2. R.F. Huang and R.S. Kommrusch, in "Materials and Processes for Wireless Communications" Eds. T. Negas and H. Ling, (1995) 169.
3. H. Hayashi, T. Ikeda, and S. Nishigaki, ISHM '91 Proceedings, Orlando, (1991) 508.
4. T. Ishizaki and T. Uwano, IEEE MTT-S Digest, WE1C-4 (1994) 617.
5. Y. Yasukawa, S.-Y. Nakai, K. Kawamura, and M. Kobayashi, IMC 1992 Proceedings, Yokohama (1992) 309.
6. D.J. Davis, Jr., and V. Insetta, Miniature Monolithic Ceramic Coupler for Electronic Circuits, U.S. Patent No. 5,162,970 (1992).
7. T.K.Kawasaki, S.Sakuragi, T. Ikeda, and T. Kuroda, Multilayered Ceramic Type Electromagnetic Coupler Apparatus, U.S. Patent No. 5,214,392 (1993).
8. E.L. Rich, III, Multi-layer Single Substrate Microwave Transmit/Receive Module, U.S. Patent No. 4,967,201 (1990).
9. J. Estes, R. Kommrusch, and R.F. Huang, Proceedings of the 1997 Wireless Communications Conference, Boulder, Co.,(1997).
10. A.L. Eustice, S.J. Horowitz, J.J. Stewart, A.R. Travis, and H.T. Sawhill, 36th Electronic Components Conference, Seattle, WA, (1986) pp37-67
11. J.H. Alexander, S.K. Muralidhar, G.J. Roberts, T.J. Vlach, in Proc. Int'l Sym. on Microelectronics, Orlando, FL, (1991) pp414-417.
12. J. Lombard and R.F. Huang, High Adhesion, Solderable, Metallization Materials, U.S. Patent No. 5431718 (1995).

NPO capacitors based on Bi-pyrochlore dielectric materials

Juan C. Nino, Tomohiro Sogabe, Michael Lanagan, Thomas Shrout, and Clive Randall

Center for Dielectric Studies, Materials Research Laboratory,
Pennsylvania State University, University Park, PA 16802, U.S.A.
FAX: (814) 865 8126   e-mail: CAR4@PSU.EDU

The Bi_2O_3–ZnO–Nb_2O_5 (BZN) pyrochlore system was studied as candidate for electronic devices in the microwave region such as NPO (negative or positive but almost zero temperature coefficient of capacitance) capacitors. The calcination, during the ceramic preparation process for this system was studied. A mathematical model for predicting the properties of sintered compositions is presented. Dielectric dispersion was detected at low temperatures (~150K) in one of the end-member phase. High frequency dielectric properties were measured, and one pyrochlore phase was determined to have excellent, high Q, characteristics.

I. INTRODUCTION

The crystal chemistry of pyrochlores has been studied by many researchers over the past several years. A comprehensive review of this family and its properties was done by Subbarao et al. [1]. The general formula unit of the oxide pyrochlores is $A_2B_2O_6O'$, which is a derivative structure of the fluorite structure AX_2 where the unit cell is doubled and the A sites are distinguished into A and B sites. The A cations (usually the larger ones) are eightfold,
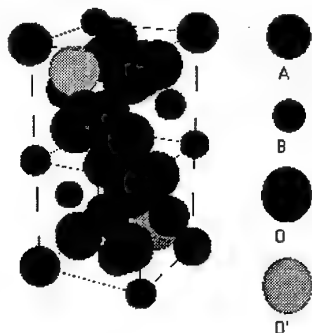

Figure 1. A quarter of a pyrochlore unit cell based on the $A_2B_2O_6O'$ formulation.

coordinated forming distorted cubes or scalenohedra that contain 6 bonds to O anions, and two shorter equally spaced bonds to the O' anions. The B cations (the smaller ones) are six coordinated, forming distorted octahedra or trigonal antiprisms [1]. One fourth of the crystal unit is presented in Figure 1. Due to the wide variety of elements soluble in the pyrochlore structure a wide spectrum of properties such as electrical, magnetic and dielectric behavior can be obtained. In this paper we consider the utilization of Bi-pyrochlores for capacitor applications, specially NPO dielectrics.

NPO stands for negative or positive but almost zero temperature coefficient of capacitance (TCC). Typical values for these NPOs are: $tan\delta \sim 10^{-3}$ to 10^{-4}, dielectric constants between 40 and 150, and less than 30 ppm/°C
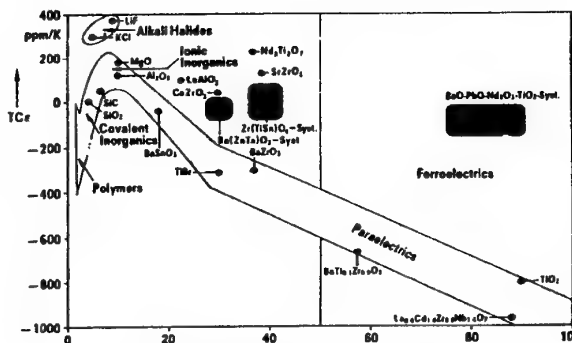

Figure 2. Classification of dielectric materials with respect to the TCε and the magnitude of the dielectric permittivity (after Harrop) [2].

variation in the dielectric permittivity over a temperature window between –55 and 125 °C. A summary of the TCε (temperature coefficient of permittivity) and the factors affecting it for various systems was presented by Harrop [2]. The plot of TCε vs. permittivity for these systems is presented in Figure 2. It can be seen from the picture that there are few candidate materials with large dielectric constants and low temperature coefficient of capacitance. Some systems suited for NPO dielectrics include mixed phases of the following: Mg_2TiO_4 / $MgTi_2O_5$ [3], TiO_2 / ZrO_2 [4], $CaSiTiO_5$ / $CaTiO_3$ [5], and $La_2Ti_2O_7$ / $La_2Sn_2O_7$ [6]. One of the major disadvantages of these systems is their sintering temperature, which is typically between 1300°C and 1500°C, thus requiring (Pt:Pd) or high Pd/low Ag electrode materials.

The need for a higher capacitance density and lower electrode cost has led to the research, study and development of new low sintering temperature formulations and/or base metal electrodes. Bismuth-containing compositions have recently been reported with sintering temperatures around 920°C [7]. Since the firing temperature is below the melting temperature of silver, pure silver electrode materials can potentially be used.

Consequently, there is an interest in the development of bismuth-based pyrochlores for NPO capacitors and integrated capacitors for LTCC (low temperature cofire-ceramics).

An early attempt to obtain a low sintering Bi-containing composition with NPO dielectric characteristics was presented by Ling and Rhodes [8]; the lowest TCC reported was ± 50 ppm/°C. Little is known about the thermodynamics and kinetics of the Bi-pyrochlore systems. Mergen and Lee [9] studied the Bi_2O_3–ZnO–Sb_2O_3 (BZS) system. Xi Yao's group [10]-[12], has reported studies on the Bi_2O_3–ZnO–Nb_2O_5 (BZN) system. Two main phases with the pyrochlore structure were identified and characterized: an orthorhombic pyrochlore phase with the chemical formula $Bi_2(Zn_{1/3}Nb_{2/3})_2O_7$, and a cubic pyrochlore phase with the chemical formula $(Bi_{1.5}Zn_{0.5})(Zn_{0.5}Nb_{1.5})O_7$.

The BZN system was chosen as a model to further understand the behavior of the pyrochlore systems, in terms of phase mixing, and observed properties.

II. EXPERIMENTAL PROCEDURE

Bulk specimens were prepared using conventional ceramic preparation techniques. High-purity (>99.9%) Bi_2O_3, ZnO and Nb_2O_5 powders were weighed and milled for 16h using stabilized ZrO_2 media in de-ionized water. As part of the investigation two different ways for calcination were studied. The powders were then pressed under a pressure of 1200 kg/cm^2 and sintered at 950°C for 4 h in air.

The dielectric properties of sintered samples were measured using a HP 4248A Precision LCR Meter and a Delta Design 9023 oven. Microstructures of the sintered specimens were examined via SEM (Model ISI DS-130). XRD data were collected using CuKα radiation typically in the 2θ range of 10° – 70° (Scintag PAD V).
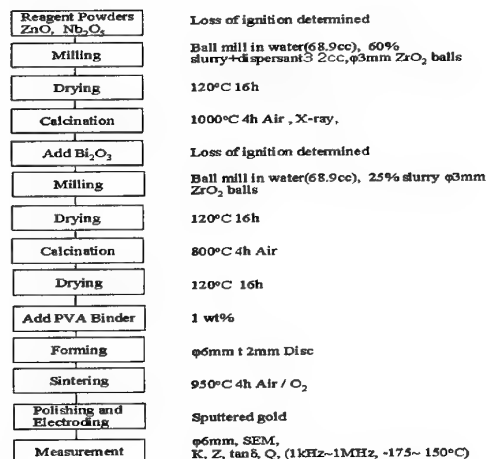
III. RESULTS AND DISCUSSION

Figure 3. Ceramic preparation process flowchart.

(1) Ceramic Preparation Process

Samples with compositions for the end-member phases i.e. cubic pyrochlore, orthorhombic pyrochlore, and mixed-phase compositions were prepared. Figure 3 shows the flowchart of the ceramic preparation process. It can be seen that two calcinations take place during the process. The first, to form columbite $ZnNbO_6$, was done at 1000°C for 4 h, and the second was performed at 800°C for 4 h after the addition of the bismuth oxide. This two-step calcination process was compared with a single calcination of the overall oxide mixture at 800°C in terms of final phase formation. The formation of the pure end-member phase was checked via XRD. It was found that two-step calcination process led to sharper phase peaks. It was also found that with a single calcination traces of unreacted oxides and intermediate compounds such as $Bi_5Nb_3O_{15}$ were present, both after calcination and after sintering of the different compositions. Even after two calcinations, when mixed-phase specimens were prepared, traces of $BiNbO_4$ phase were found through X-ray analysis.

Table I. Characterization of dielectric compositions.

Composition Name	Phases Present	B / Z / N mol ratio Batched	Exp. Dens. (g/cc)	Dielectric Constant	TCC (ppm/oC)
JM81001	Cubic + Ortho. + BiNbO4	1.2 / 1.0 / 1.0	6.48	69	-102
BN1	Bismuth Niobate	1.0 / 0.0 / 1.0	6.92	46	-125
JM81000	Cubic pyrochlore	0.75 / 1.0 / 0.75	6.65	118	202
JM81501	Orthorhombic pyrochlore	1.0 / 0.75 / 1.0	7.61	75	-394

(2) Phase characterization.

Characterization data for the end-members and mixed-phase specimens are presented in Table 1. Dielectric constant values correspond to 1MHz at room temperature. It is shown that the cubic pyrochlore phase has a high permittivity and a large negative TCC. On the other hand, the orthorhombic phase has a smaller dielectric constant and a positive TCC. This suggested that by having a mixture between these phases, a specimen with intermediate behavior (NPO characteristics), could be obtained. To verify the above assumption, mixed phase compositions such as JM81001 were prepared. Measured properties for this composition are presented in Table I above. $BiNbO_4$ was also detected in this sample. This can clearly be seen by comparison of the X-ray patterns of the end-members and mixed compositions in Figure 4.
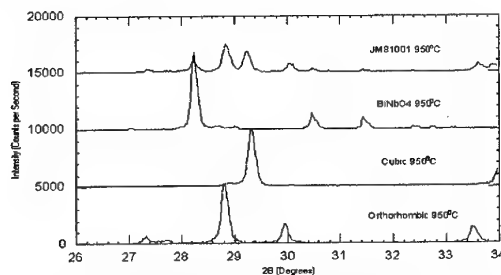

Figure 4. Detail of the XRD patterns for the phases present in the BZN pyrochlore phase.

Even though $BiNbO_4$ was found to help in flattening the composition's TCC, it has also been proven to be incompatible with silver electrodes by Cho et al. [13]. Nonetheless for study purposes, bismuth niobate was prepared as a single phase and characterized. As explained later it was treated as an end-member of the BZN system.

(3) Application of mixing rules

Under the assumption that there is no chemical interaction between phases, a mathematical method for predicting the properties of the mixed phase compositions was developed. It is well known that some properties such as density (ρ) scale according to the relative amount of each phase that is present. Lichtenecker [14] showed that a logarithmic mixing rule can be applied to the dielectric constant (K) and that differentiation of this relation yields the appropriate mixing rule for the TCC. The mixing rule relations for these three properties (i.e. density, permittivity and temperature coefficient of capacitance) are:

$$\rho_m = \sum \upsilon_i \rho_i \qquad (1)$$

$$\log K_m = \sum \upsilon_i \log K_i \qquad (2)$$

$$TCC_m = \sum \upsilon_i TCC_i \qquad (3)$$

where υ is the volume fraction of the *i-th* phase and the subscript m represents the overall mixed phase property. This set of equations can be arranged in a matrix form in which the volume fractions form the vector of unknowns ([v]), the characteristic matrix is formed by the end-member properties ([P]), and the mixed-phase composition properties forms the dependent vector ([M]). This arrangement leads to the equation (4), and using matrix operations, one can easily solve for the [v] vector as shown in equation (5).

$$[P] \cdot [\upsilon] = [M] \qquad (4)$$

$$[\upsilon] = [P]^{-1} \cdot [M] \qquad (5)$$

This was applied to a set of mixed phase specimens. Experimental property values were corrected for porosity before using them in the model. The dielectric constant values were corrected following the Maxwell equation [15]. The model was used to predict the volume fraction of phases present in the mixed phased compositions as shown in Table II.

Table II. Volume fraction comparison between predicted and X-ray determined values for three mixed-phase pyrochlore compositions.

Composition	CUBIC PHASE		ORTHORHOMBIC		Bismuth Niobate	
	Matrix	X-ray	Matrix	X-ray	Matrix	X-ray
1	39.1 %	38.9 %	38.2 %	41.7 %	22.6 %	19.3 %
2	55.8 %	50.8 %	30.3 %	28.9 %	13.8 %	20.1 %
3	76.4 %	74.9 %	0.3 %	0%	23.2 %	25.0 %

Volume fractions obtained from the model were compared with the values calculated from the strongest peak intensities for each phase in the XRD patterns. It was found that calculated results and the X-Ray values are in agreement within an overall 10% error. Refinement of the model for a better agreement is ongoing. Special detail is being stressed on the modeling around the vicinities of the end-members (property variations due to solubility).

(4) Dielectric anomalies

Relaxation character of the dielectric polarization for Bi-based pyrochlore structure was first reported by Isupov et al. [16]. Cann et al. [17] studied the dielectric properties of bismuth pyrochlores and reported a frequency dispersive decrease in the dielectric permittivity and a correlated peak in the dielectric loss at low temperatures.

In order to check the compositions for this phenomena dielectric measurements at low temperatures (up to 100K) and from 10kHz to 1MHz were performed on end-member and mixed phase specimens. Figure 5 shows the relaxation on the dielectric constant and the correlated peak in the dielectric loss for the cubic pyrochlore phase. Properties

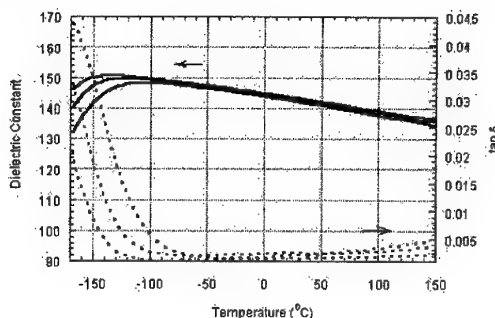**Figure 5 Dielectric constant and tanδ (dielectric loss) vs. temperature measured at 10, 100 and 1000 kHz (from left to right) for the cubic pyrochlore phase.**

were measured at 10kHz, 100kHz, and 1 MHz. Frequency dispersion was observed where the maxima in the dielectric loss is shifted to the right as the frequency is increased. As can be seen the relaxation process starts around $-125^\circ C$ (~ 150 K). Mixed-phase compositions showed similar relaxation behavior as the cubic phase but, interestingly enough, the orthorhombic pyrochlore phase did not show any anomalies in the dielectric behavior. Cann [17] analyzed this type of dispersion in bismuth-based pyrochlores using phenomenological models often used for dipolar glass systems. In order to better understand the nature of this phenomena dielectric measurements at cryogenic temperatures (up to 12K) are currently being done. Much more investigation has to be done to fully understand these relaxation phenomena.

(5) High frequency measurements

Dielectric properties at high frequencies were measured using the Hakki-Coleman post resonance method

[18]. The frequency response at the TE_{011} mode for the orthorhombic pyrochlore is presented in Figure 6. The frequency of the mode, as well as the peak width at 3dB below the maxima were measured. With this data and the sample geometry, a computer program was utilized to
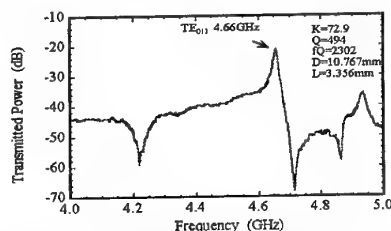

Figure 6. Frequency response at the TE_{011} mode for $Bi_2(ZnNb_2)_{2/3}O_7$ sintered at 950°C.

calculate the dielectric constant and the dielectric loss. Calculated values are included in Figure 6. It is interesting to notice the relatively high fQ (~2000) for this phase. No sharp resonance peaks were detected in the cubic pyrochlore phase sample. This is usually related to a higher dielectric loss (~0.01) of the specimen. The dielectric loss for the cubic phase is <0.002 at one MHz. As can be seen in Figure 5 the dielectric loss peak is expected to appear at higher temperatures when the frequency is increased. Cann [17] estimated that for mixed phase BZN compositions the maxima for the dielectric loss would be below 183K at 10GHz, so at room temperature the loss should not be as high as 0.01. Dielectric measurements at frequencies between 1MHz and 1 GHz are currently being done in order to understand the unexpected dielectric loss behavior between low and high frequency measurements.

IV. CONCLUSIONS

The BZN system was studied as a model for a potential use of Bi-based pyrochlores in electronic devices such as NPO capacitors. It was found that two-step calcination during the ceramic preparation process results in better phase formation after sintering. A mathematical model for predicting the properties of mixed phase compositions and/or the volume fractions of each phase out of the property of the sintered sample was presented. A relaxation phenomenon in the dielectric properties was found both in the cubic pyrochlore and mixed phase compositions. No anomalies of this kind were detected in the orthorhombic pyrochlore phase. High frequency characterization of the orthorhombic pyrochlore phase was done and the composition proved to be good enough for microwave devices. The cubic pyrochlore phase showed a high loss (~0.01) at microwave frequencies in a phenomenon that is currently under investigation.

References

[1]   M.A. Subramanian, G. Aravamudan, and G.V. Subbarao, "Oxide Pyrochlores – A review"; *Prog. Solid State Chem.,* **15**, 55-143 (1983).

[2]   Harrop, P.J. TCC of Solids, *J. Mater. Sci.,* 1969.

[3]   Von W. Rath, *Ber. Deut. Keram. Ges.* **28940**, 177-193 (1951).

[4]   H. Stetson and B. Schwarz, *J. Am. Ceram. Soc.* **44** (8), 420-421 (1961).

[5]   T. Yamaguchi, Y. Komatsu, T. Otobe, and Y. Murakami, *Ferroelectrics* **27**, 273-276 (1980).

[6]   J. Takahashi and K. Kageyama, in "Ceramic Dielectrics: Compositions, Processing and Properties," *Ceramic Transactions,* edited by H.C. Ling and M.F. Yan (Am. Ceram. Soc., 1990) Vol. 8, pp. 333-343.

[7]   S.L. Swartz and T.R. Shrout, Ceramic compositions for BZN dielectric resonators, US5449652.

[8]   H.C. Ling, M.F. Yan, and W.W. Rhodes, *J. Mater. Res.,* Vol. 5, No. 8, Aug 1990.

[9]   A. Mergen and W.E. Lee, *Materials Research Bulletin,* Vol. 32, No.2 pp.175-189, 1997.

[10]   D. Liu, Y. Liu, S. Huang and X. Yao, *J. Am. Ceram. Soc.,* **76** [8] 2129-32 (1993).

[11]   H. Wang , X. Wang, and X. Yao, , *J. Chin. Ceram. Soc.,* **23** [3] 241-47 (1995).

[12]   X. Wang , H. Wang, and X. Yao, , *J. Am. Ceram. Soc.,* **80** [10] 2745-48 (1997).

[13]   S. Cho, H.Youn, D. Kim, T. Kim and K. Hong, *J. Am. Ceram. Soc.,* **81** [11] 3038-40 (1998).

[14]   K. Lichtenecker. *Physikal Z.* **27**, 115-58, 1926.

[15]   A.J. Moulson and J.M. Herbert, Electroceramics, Chapman & Hall, London, 1995 pp.79-82.

[16]   G.I. Golovshchikova, V.A. Isupov, A.G. Tutov, I.E. Myl'nikova, P.A. Nikitina and O.I. Tulinova, *Sov. Phys. – Solid State,* **14** 2539-42, 1973.

[17]   D.P. Cann, C.A. Randall and T.R. Shrout. *Solid State Communications.* Vol. 100, No.7, pp529-534, 1996.

[18]   B.W. Hakki, and P.D. Coleman. *IRE Trans. On Microwave Theory and Tech.,* MTT-8 p.402, 1960.

Participant List (U.S.)

Joanne Aller
169 Materials Research Lab.
The Pennsylvania State University
University Park, PA 16802 USA
Phone: 1-814-865-2896
Fax: 1-814-865-8126
e-mail: joannealler@psu.edu

Ian Burn
Director Research & Applied
Technology
Degussa-Huls
3900 South Clinton Av., South
Plainfield NJ 07080 USA
Phone: 31-908-226-2161
Fax: 31-908-757-0411
e-mail: ian.burn@Degussa.com

David Cann
Materials Science and Technology
Iowa State University
3136 Gilman Ames, IA 50011
USA
Phone: 1-515-294-3202
Fax: 1-515-294-5444
e-mail: dcann@iastate.edu

Wenwu Cao
164 Materials Research Lab.
The Pennsylvania State University
University Park, PA 16802 USA
Phone: 1-814-865-4101
Fax: 1-814-865-2326
e-mail: cao@math.psu.edu

Jie Chen
Imaging Systems
Hewlett-Packard Company
3000 Minuteman Road, Andover,
MA 01810 USA
Phone: 1-978-659-2197
Fax: 1-978-687-7265
e-mail: chenj@an.hp.com

Yet-Ming Chiang
Room 13-4086, Dept. of
Materials Science & Eng.
Massachusetts Institute of
Technology
77 Massachusetts Avenue,
Cambridge, MA 02139 USA
Phone: 1-617-253-5471
Fax: 1-17-253-6201
e-mail: ychiang@mit.edu

Mike S.H. Chu
Ferro Electronics Materials
TAM Ceramics, Inc.
4511 Hyde Park Blvd., Niagara
Falls, NY 14305 USA
Phone: 1-716-278-9495
Fax: 1-716-278-9575
e-mail: mchu@tam.cookson.com

L. Eric Cross
187 Materials Research Lab
The Pennsylvania State University
University Park, PA 16802 USA
Phone: 1-814-865-1181
Fax: 1-814-865-7846
e-mail: LEC3@psu.edu

Lynn Ewart
Naval Undersea Warfare Center
Code 2132, Bldg. 1170, 1176
Howell Street, Newport RI 02841-
1708 USA
Phone: 1-401-832-5093
Fax: 1-401-832-6401
e-mail:
ewartlm@npt.nuwc.navy.mil

Brian C. Foster
Technical Manager
Ferro Corporation
1709 Transelco Drive, Penn Yan,
NY 14527 USA
Phone: 1-315-536-3357
Fax: 1-315-536-0376
e-mail: FosterB@Ferro.com

Herbert Geische
NYSCC at Alfred Univ.
2 Pine St., Alfred NY 14802 USA
Phone: 1-607-871-2677
Fax: 1-606-871-2317
e-mail: giesche@bigvax.alfred.edu

Martin P. Harmer
Materials Research Center
Lehigh University
Whitaker Lab, 5 East Packer
Avenue Bethlehem, PA 18015
USA
Phone: 1-610-758-4227
Fax: 1-610-758-3526
e-mail: mph2@lehigh.edu

Rong-Fong Huang
Electronic Material system
Technology
Motorola
7700 S. River Parkway, Tempe,
AZ 85284 USA
Phone: 1-480-755-6014
Fax: 1-480-755-5350
e-mail: CRH006@email.not.com

Kerchner A. Jeffrey
Cabot Corporation
Boyertown PA 19512 USA
Phone: 1-610-369-8268
Fax: 1-610-369-8552
e-mail: Jeff_Kerchner@cabot-
corp.com

Todd L Jessen
US Naval Research Laboratory
Code 6350, 4555 Overlook
avenue, SW Washington, DC
20375 USA
Phone: 1-202-404-1534
Fax: 1-202-404-7176
e-mail: jessen@anvil.nrl.navy.mil

Chulho Kim
Code 6354
US Naval Research Laboratory
4555 Overlook Ave., S.W.
Washington DC 20375-5320 USA
Phone: 1-202-767-2628
Fax: 1-202-404-7176
e-mail: kim@anvil.nrl.navy.mil

David V. Miller
Cabot Corporation
Boyertown PA 19512 USA
Phone: 1-610-369-8418
Fax: 1-610-369-8552
e-mail: David_Miller@cabot-corp.com

C.A.Randall
Materials Research Lab.
The Pennsylvania State University
University Park, PA 16802 USA
Phone: 1-814-863-1328
Fax: 1-814-865-2326
e-mail: car4@psu.edu

Angus I. Kington
Dept. of Mterials Science &
Engineering
NCSU
Raleigh, NC 27695-7919 USA
Phone: 1-919-515-8636
Fax: 1-919-515-3419
e-mail: Angus_Kingon@ncsu.edu

N. Ogata
262 Materials Research Lab.
The Pennsylvania State University
University Park, PA 16802 USA
Phone: 1-814-865-0648
Fax: 1-814-865-2326
e-mail: nxo4@psu.edu

Ahmad Safari
Rutgers University
607 Taylor Road, Piscataway, NJ
08854-8065
Phone: 1-732-445-4367
Fax: 1-732-445-5577
e-mail: safari@rci.rutgers.edu

Galeb H. Maher
96 Marshall Street
MRA Laboratories, Inc.
North Adams, MA 01247 USA
Phone: 1-413-664-4524
Fax: 1-413-663-5535
e-mail: mralabs@sover.net

S.M. Pilgrim
NYSCC at Alfred University
2 Pine St., Alfred NY 14802 USA
Phone: 1-607-871-2431
Fax: 1-607-871-3469
e-mail: pilgrim@alfred.edu

Steven G. Santoro
Degussa Electroic Materials
Front Street 2, 5405 PB Uden, The
Netherlands USA
Phone: 31-413-283-291
Fax: 31-413-250-524
e-mail:
steve_santoro@degussa.com

Larry A. Mann
Kemet Electronics
201 Fairview St Ext. P.O. Box 849
Fountain Inn, Sc 29644-0849 USA
Phone: 1-864-409-5746
Fax: 1-864-409-5665
e-mail: larrymann@kemet.com

Robert C. Pohanka
Office of Naval Research, ONR
332
800 North Quincy Street, Room
502, Arlington, Virginia 22217-5660 USA
Phone: 1-703-696-4309
Fax: 1-703-696-0934
e-mail: pohankr@onr.navy.mil

Thomas. M. Shaw
IBM T.J. Watson Research Center
IBM Research
P.O.Box 218, Yorktown Heights
NY 10598 USA
Phone: 1-914-945-3196
Fax: 1-914-945-3623
e-mail: tmshaw@vs.ibm.com

Jon-Paul Maria
North Carolina State University
223-D EGRC, Raleigh, NC 27695
USA
Phone: 1-919-513-2843
Fax: 1-919-515-5055
e-mail: jpmaria@unity.ncsu.edu

Dennis L. Polla
University of Minnesota
420 Delaware St. SE,
Minneapolis, Minnesota 55455
USA
Phone: 1-612-626-2753
Fax: 1-612-626-6583
e-mail: polla@ece.umn.edu

Thomas R. Shrout
150 Materials Research Lab
Penn State University
University Park, PA 16802 USA
Phone: 1-814-865-1645
Fax: 1-814-865-2326
e-mail: TShrout@psu.edu

Wallace Arden Smith
Office of Naval Research, ONR 332
800 North Quincy Street, Room 502, Arlington, Virginia 22217-5660 USA
Phone: 1-703-696-0284
Fax: 1-703-696-0934
e-mail: smithw@onr.navy.mil

Donald M. Smyth
Materials Research Center
Lehigh University
5 E. Packer Ave. Bethlehem PA18015 USA
Phone: 1-610-758-3852
Fax: 1-610-758-3526
e-mail: dms4@lehigh.edu

Tomohiro Sogabe
Visiting Res., 161 Materials Research Lab.
The Pennsylvania State University
University Park, PA 16802 USA
Phone: 1-814-863-3231
Fax: 1-814-865-2326
e-mail: txs35@psu.edu

Stephen K. Streiffer
MSD 212/C212, 9700 S. Cass Ave.
Argonne National Laboratory
Argonne, IL 60439-4838 USA
Phone: 1-630-252-5832
Fax: 1-630-252-4289
e-mail: streiffer@anl.gov

Koichi Takemura
Functional Materials Research Laboratories
NEC Corporation
4-1-1 Miyazaki, Miyamae-ku, Kawasaki 216-8555 Japan
Phone: 81-44-856-2187
Fax: 81-44-856-2216
e-mail: takemura@fml.cl.nec.co.jp

S. Trolier-McKinstsry
151 Mateirals Research Lab.
Penn State University
University Park, PA 16802 USA
Phone: 1-814-863-8348
Fax: 1-814-865-2326
e-mail: STMcKinstry@mrl.psu.edu

Dwight Viehland
Naval Undersea Warfare Center, Code 2131
Bldg 1170, 1176 Howell Street, Newport, RI 02841-1708 USA
Phone: 1-800669-6892(x25107)
Fax: 1-401-832-6401
e-mail: viehlandd@npt.nuwc.navy.mil

Koto White
Tokyo office
US Air Force Office of Scientific Research
7-23-17 Roppoingi, Minato-ku Tokyo 106-0032 Japan
Phone: 81-3-5410-4409
Fax: 81-3-5410-4407
e-mail: whiteko@aoard.af.mil

Hisao Yamada
President
Cerone, Inc.
2300 Overlook Road, #811, Cleveland Hts., OH #44106 USA
Phone: 1-216-421-2248
Fax:
e-mail: ceroneinc@yahoo.com

Shoko Yoshikawa
Director, Materials Research
Active Control eXperts. Inc
215 First St. Cambridge, MA 02142 USA
Phone: 1-617-577-0700
Fax: 1-617-577-0656
e-mail: shoko@acx.com

Participant List (Japan)

Masatoshi Adachi
Dept. of Electronics & Informatics
Toyama Prefectural University
5180 Kurokawa, Kosugi-machi,
Toyama, 939-0398 Japan
Phone: 81-76-656-7500 (ext.495)
Fax: 81-76-656-8023
e-mail: adachi@pu-toyama.ac.jp

Sung-lak Ahn
Kudo Lab. Dept. of Applied
Chemistry, School of Engineering
The University of Tokyo
7-3-1 Hongo, Bunkyo-ku, Tokyo,
113-8656 Japan
Phone: 81-3-5841-7199
Fax: 81-3-3818-0284
e-mail: ahn@imat.chem.t.u-
tokyo.ac.jp

Yuji Akimoto
SHOEI CHEMICAL INC.
5-3, Aza Wakazakura,
Fujinokimachi, Tosu-shi, 841-
0048 Japan
Phone: 81-942-82-6661
Fax: 81-942-82-6667

Morito Akiyama
Kyushu National Industrial
Research Institute
807-1 Shuku, Tosu, 841-0052
Japan
Phone: 81-942-82-5161
Fax: 81-942-83-9858
e-mail: akiyamam@kniri.go.jp

Yoshikazu Akiyama
RICOH Co., Ltd. R&D Center
16-1, Shinei-cho, Tsuzuki-ku
Yokohama, 224-0035 Japan
Phone: 81-45-590-1027
Fax: 81-45-590-1894
e-mail: aaki@rdc.ricoh.co.jp

Akira Ando
Murata Manufacturing Company
Limited
2288 Oshinohara Yasu-cho
Shiga, 520-2393 Japan
Phone: 81-77-586-8205
Fax: 81-77-587-1923
e-mail: a_ando@murata.co.jp

Hirokazu Chazono
General R&D laboratories
Taiyo Yuden Co., Ltd.
5607-2 Nakamuroda, Haruna-
machi, Gunma-gun, 370-3347
Japan
Phone: 81-27-360-8307
Fax: 81-27-360-8315
e-mail: hchazono@jty.yuden.co.jp

Kouji Fujishiro
Dept. of Physics, School of Sci.
and Eng.
Waseda University
3-4-1 Okubo, Shinjuku-ku, Tokyo,
169-8555 Japan
Phone: 81-3-5286-3096
Fax: 81-3-5272-5819
e-mail: wistevia@mn.waseda.ac.jp

Shigetaka Fujita
Hachinohe Institute of Technology
88-1, Myo Ohbiraki, Hachinohe,
031-8501 Japan
Phone: 81-178-25-8054
Fax: 81-178-25-1430
e-mail: sfujita@hi-tech.ac.jp

Satoru Fujitsu
Dept. of Materials Science and
Ceramic Technology
Shonan Institute of Technology
1-1-25 Tsujido-Nishikaigan,
Fujisawa, 251-8511 Japan
Phone: 81-466-34-4111(ext376)
Fax: 81-466-36-1594
e-mail: fuji@mate.shonan-it.ac.jp

Junya Fukazawa
Nippon Chemical Industrial Co.,
Ltd.
9-11-1, Kameido, Koto-ku,
Tokyo, Japan
Phone: 81-3-3636-8083
Fax: 81-3-3636-8193
e-mail: junya.fukaza@nippon-
chem.co.jp

Hiroshi Funakubo
Dept.Innov.Eng.Mater.
Tokyo Institute of Technology
4259 Nagatsuta-cho, Midori-ku,
Yokohama, 226-8502 Japan
Phone: 81-45-924-5446
Fax: 81-45-924-5446
e-mail: funakubo@iem.titech.ac.jp

Kouichi Hamamoto
Graduate School of Eng., Dept of
Mater. Sci.
The University of Tokyo
7-3-1 Hongo, Bunkyo-ku, Tokyo,
113-8656 Japan
Phone: 81-3-5841-7180
Fax: 81-3-5841-8653
e-mail: hamamoto@ecl. Mm.t.u-
tokyo.ac.jp

Hajime Haneda
National Institute for Research in
Inorganic Materials
1-1 Namiki Tsukuba, 305-0044
Japan
Phone: 81-298-51-3354 (ext.575)
Fax: 81-298-52-7449
e-mail: haneda@nirim.go.jp

Koichi Hayashi
Murata Manufacturing Company
Limited
2288 Oshinohara Yasu-cho Shiga,
520-2393 Japan
Phone: 81-77-586-8515
Fax: 81-77-587-1923
e-mail: kohaya@murata.co.jp

Takashi Hayashi
Dept. of Materials Science and
Ceramic Technology
Shonan Institute of Technology
1-1-25 Tsujido-Nishikaigan,
Fujisawa, 251-8511 Japan
Phone: 81-466-34-4111(ext.370)
Fax: 81-466-36-1594
e-mail: hayashi@mate.shonan-
it.ac.jp

Noboru Ichinose
Waseda University
3-4-1 Ohkubo Shinjuku-ku Tokyo,
169-8555 Japan
Phone: 81-3-5286-3307
Fax: 81-3-3200-2567
e-mail: ichinose@mn.waseda.ac.jp

Takashi Iijima
Tohoku National Industrial
Research Institute
4-2-1 Nigatake, Miyagino- ku,
Sendai, 983-8551 Japan
Phone: 81-22-237-5211
Fax: 81-22- 239-0629
e-mail: iijima@tniri.go.jp

Hiroyuki Ikawa
Dept of Applied Chemistry,
Kanagawa Institute of Technology
1030 Shimo-ogino, Atsugi-shi,
243-0292 Japan
Phone: 81-462-91-3162
Fax: 81-462-42-8760
e-mail: ikawa@cserver.chem.
kanagawa-it.ac.jp

Akira Inaba
Degussa Japan Co., Ltd
21 Kasuminosato, Ami-machi,
Inashiki-gun Ibaraki, Japan
Phone: 81-298-89-2801
Fax: 81-298-892804

Hiroshi Irie
Research Center for Advanced
Science and Technology
The University of Tokyo
4-6-1, Komaba, Meguro-ku,
Tokyo, 153-8904 Japan
Phone: 81-3-5452-5300
Fax: 81-3-5452-5300
e-mail: irie-hrs@imat.chem.t.u-
tokyo.ac.jp

Hiroshi Ishiwara
Frontier Collabosrative Research
Center
Tokyo Institute of Technology
4259 Nagatsuda, Midoriku,
Yokohama, 226-8503 Japan
Phone: 81-45-924-5040
Fax: 81-45-924-5961
e-mail: ishiwara@pi.titech.ac.jp

Toshiro Isoya
Fuji Titanium Ind. Co.,Ltd,.
12-8 Sengen-Cho, Hiratsuka-City,
254-0041 Japan
Phone: 81-463-32-1266
Fax: 81-463-32-1270
e-mail: isoya@fuji-titan.co.jp

Kenji Ito
Degussa Japan Co., Ltd
2-3-1, Nishi-Shinjuku, Shinjuku-
ku, Tokyo, 163-09 Japan
Phone: 81-3-5323-7312
Fax: 81-3-5323-7396

Tsutomu Kajita
R&D Dept.,Electric Material Div.
Fuji Titanium Ind. Co.,Ltd,.
12-8 Sengen-Cho, Hiratsuka-City,
254-0041 Japan
Phone: 81-463-32-1266
Fax: 81-463-32-1270
e-mail: kajita@fuji-titan.co.jp

Hiroyuki Kamei
Suzuki Lab., Dept of Materials
Science
Shizuoka University
3-5-1 Johoku, Hamamatsu, 432-
8561 Japan
Phone: 81-53-478-1157
Fax: 81-53-478-1157
e-mail:
hisuzuki@mat.eng.shizuoka.ac.jp

Akinori Kan
H. Ogawa Lab.
Meijio University
1-501 Shiogamaguchi, Tenpaku-
ku, Nagoya, 468-8502 Japan
Phone: 81-52-832-1151(ext.5160)
Fax: 81-52-832-1253
e-mail: c3993014@meijo-u.ac.jp

Kazumi Kato
National Industrial Research
Institute of Nagoya
1 Hirate-cho, Kita-ku, Nagoya,
462-8510 Japan
Phone: 81-52-911-2179
Fax: 81-52-916-6992
e-mail: kzmkato@nirin.go.jp

Takeshi Kijima
SHARP Corporation
273-1, Kashiwa, Kashiwa-shi, 277-
0005 Japan
Phone: 81-471-34-6116
Fax: 81-471-34-6119
e-mail: kijima@kasiwa.sharp.co.jp

Hiroshi Kishi
General R&D laboratories
Taiyo Yuden Co., Ltd.
5607-2 Nakamuroda, Haruna-
machi, Gunma-gun, 370-3347
Japan
Phone: 81-27-360-8307
Fax: 81-27-360-8315
e-mail: hkishi@jty.yuden.co.jp

Yujiro Kitaide
Fuji Electric corporated R&D, Ltd.
2-2-1, Nagasaka Yokosuka City,
240-0194 Japan
Phone: 81-468-57-6732
Fax: 81-468-57-6946
e-mail: kitaide-yujiro@
fujielectric.co.jp

Ichiro Koiwa
Semiconductor Technology
Laboratories
Oki Electric Industry Co.,Ltd.
550-5 Higashiasakawa-cho,
Hachiogi-shi, 193-8550 Japan
Phone: 81-426-62-6754
Fax: 81-426-67-0545
e-mail: koiwa544@oki.co.jp

Takahiro Koizumi
Suzuki Lab., Dept of Materials
Science
Shizuoka University
3-5-1 Johoku, Hamamatsu, 432-
8561 Japan
Phone: 81-53-478-1157
Fax: 81-53-478-1157
e-mail:
hisuzuki@mat.eng.shizuoka.ac.jp

Toshihiro Kojima
Faculty of Engineering
Tamagawa University
6-1-1-, Tamagawa-gakuen,
Machida, Tokyo, 194-8610 Japan
Phone: 81-42-739-8440
Fax: 81-42-739-8858
e-mail:
kojima@eng.tamagawa.ac.jp

Masahumi Kunieda
Suzuki Lab., Dept of Materials
Science
Shizuoka University
3-5-1 Johoku, Hamamatsu, 432-
8561 Japan
Phone: 81-53-478-1157
Fax: 81-53-478-1157
e-mail:
hisuzuki@mat.eng.shizuoka.ac.jp

Keiji Kusumoto
Ceramic Science Dep. Electronic
Ceramics Lab.
National Industrial Research
Institute of Nagoya
1 Hirate-cho, Kita-ku, Nagoya,
462-8510 Japan
Phone: 81-52-911-2111
Fax: 81-52-916-2802
e-mail: kusumoto@nirin.go.jp

Hiroshi Maiwa
Dept. Mat. Sci. & Ceram. Tech.
Shonan Institute of Technology
1-1-25 Tsujido-Nishikaigan,
Fujisawa, 251-8511 Japan
Phone: 81-466-34-4111
Fax: 81-466-36-1594
e-mail: maiwa@mate.shonan-
it.ac.jp

Kazunari Maki
Development section
Mitsubishi Materials Corporation
12-6, Technopark, Sanda-Shi, 669-
1339 Japan
Phone: 81-795-68-2320
Fax: 81-795-68-2325
e-mail: k-maki@mmc.co.jp

Takeshi Masuda
Materials Research Center
TDK Corp.
570-2 Matsugashita,
Minamihatori, Narita-shi, 286-
8588 Japan
Phone: 81-476-37-1637
Fax: 81-476-37-1648
e-mail: masuken@mb1.tdk.co.jp

Yoichiro Masuda
Dept. of Electric & Electronics
Hachinohe Institue of Technology
88-1, Myo, Obiraki, Hachinohe,
031-8501 Japan
Phone: 81-178-25-8047
Fax: 81-178-25-1430
e-mail: ymasuda@hi-tech.ac.jp

Takanobu Matsuda
Furuno Electric Co., Ltd.
Ashihara-cho 9-52, Nishinomiya,
Hyogo, 662-8580 Japan
Phone: 81-798-63-1171
Fax: 81-798-64-6302
e-mail:
matsuda@feclab.furuno.co.jp

Kazuo Miyabe
Materials Research Center
TDK Corp
570-2 Matsugashita,
Minamihatori, Narita-shi, 286-
8588 Japan
Phone: 81-476-37-1631
Fax: 81-476-37-1648
e-mail: kmiyabe@mb1.tdk.co.jp

Masato Miyake
Grad. School of Mat. Sci.
Nara Institute of Science and
Technology
8916-5 Takayama-cho, Ikoma,
Nara, 630-0101 Japan
Phone: 81-743-72-6061
Fax: 81-743-72-6069
e-mail: m-masato@ms.aist-
nara.ac.jp

Kazuro Nagashima
Shoei Chemical Inc.
5-3, Wakazakura, Fujinoki-machi,
Tosu-shi, 841-0048 Japan
Phone: 81-942-82-6661
Fax: 81-942-82-6667

Hajime Nagata
Takenaka Lab, Faculty of Science
and Technology
Science University of Tokyo
2641 Yamazaki, Noda, 278-8510
Japan
Phone: 81-471-24-1501(+3726)
Fax: 81-471-23-0856
e-mail:
nagata@takenaka.ee.noda.sut.ac.jp

Tetsuro Nakamura
Professor emeritus
Tokyo Institute of Technology
, Japan
Phone: 81-42-574-4631(home)

Yukie Nakano
Materials Research Center
TDK Corp.
570-2 Matsugashita,
Minamihatori, Narita-shi, 286-
8588 Japan
Phone: 81-476-37-1637
Fax: 81-476-37-1648
e-mail: yukien@mb1.tdk.co.jp

Song-Min Nam
Dept.Inorg.Mater. Tsurumi Lab.
Tokyo Institute of Technology
2-12-1 Ookayama, Meguro,
Tokyo, 152-8552 Japan
Phone: 81-3-5734-2829
Fax: 81-3-5734-2514
e-mail:
smnam@crystal.ceram.titech.ac.jp

Eiji Narita
TAM Ceramics Japan Co., Ltd
2-17-1 Hamamatsu-cho, Minato-
ku Tokyo, 105-0013 Japan
Phone: 81-3-5473-9561
Fax: 81-3-5473-9560
e-mail: enarita@po.globe.jp

Morihito Nishido
Fuji Titanium Ind. Co.,Ltd,.
12-8 Sengen-Cho, Hiratsuka-City,
254-0041 Japan
Phone: 81-463-32-1266
Fax: 81-463-32-1270
e-mail: nisido@fuji-titan.co.jp

Takeshi Nomura
Materials Research Center
TDK Corp.
570-2 Matsugashita,
Minamihatori, Narita-shi, 286-
8588 Japan
Phone: 81-476-37-1633
Fax: 81-476-37-1648
e-mail: tnomura@mb1.tdk.co.jp

Kazuhiro Nonaka
Kyushu National Industrial
Research Institute
807-1 Shuku-machi, Tosu, 841-
0052 Japan
Phone: 81-942-82-5161
Fax: 81-942-83-9858
e-mail: nonaka@kniri.go.jp

Toshio Ogawa
Shizuoka Institute of Science and
Technology
2200-2 Toyosawa, Fukuroi,
Shizuoka, 437-8555 Japan
Phone: 81-538-45-0149
Fax: 81-538-45-0154
e-mail: ogawa@ee.sist.ac.jp

Hitoshi Ohsato
Dept. of Materials Science and
Engineering
Nagoya Institute of Technology
Gokiso-cho, Showa-ku, Nagoya,
466-8555 Japan
Phone: 81-52-735-5284
Fax: 81-52-735-5294
e-mail: ohsato@mse.nitech.ac.jp

Hitoshi Oka
Materials Research Center
TDK Corporation
570-2 Minami-Hatori, Narita, 286-
8588 Japan
Phone: 81-476-37-1631
Fax: 81-476-37-1648
e-mail: hioka@mb1.tdk.co.jp

Hirotake Okino
Shigematsu Lab., Dept of Elec.
Sci. & Eng., Grad. School of Eng.
Kyoto University
Yoshida Honmachi, Sakyo-ku,
Kyoto, 606-8501 Japan
Phone: 81-75-753-5327
Fax: 81-75-753-5749
e-mail: hokino@kuee.kyoto-u.ac.jp

Isao Osada
Nippon Chemical Industrial Co.,
Ltd.
9-11-1, Kameido, Koto-ku,
Tokyo, Japan
Phone: 81-3-3636-8088
Fax: 81-3-3636-8193
e-mail: isao.osada@nippon-
chem.co.jp

Iwao Oyobe
Fuji Titanium Ind. Co.,Ltd,.
12-8 Sengen-Cho, Hiratsuka-City,
254-0041 Japan
Phone: 81-463-32-1266
Fax: 81-463-32-1270

Shuichi Ozawa
Dept.Inorg.Mater. Tsurumi Lab.
Tokyo Institute of Technology
2-12-1 Ookayama, Meguro,
Tokyo, 152-8552 Japan
Phone: 81-3-5734-2829
Fax: 81-3-5734-2514
e-mail:
ozawa@crystal.ceram.titech.ac.jp

Ayuko Ozeki
Shan Lab. Dept of applied Chem.
Utsunomiya University
7-1-2 Yoto Utsunomiya, 321-8585
Japan
Phone: 81-28-689-6174
Fax: 81-28-689-6009
e-mail: ozekia@cc.utsunomiya-
u.ac.jp

Radhika M.V. Rao
Munekata Lab., Imaging Sci. &
Eng. Lab.
Tokyo Institute of Technology
4259 Nagatsuta-cho, Midori-ku,
Yokohama, 226-8501 Japan
Phone: 81-45-924-5398
Fax: 81-45-924-5399
e-mail:
radhika@oxide.rlem.titech.ac.jp

Yukio Sakabe
Murata Manufucturing Co., Ltd.
2288 Ooshinohara, Yasu-machi,
Yasu-gun, 520-2393 Japan
Phone: 81-77-586-8275
Fax: 81-77-587-1923
e-mail: sakabe@murata.co.jp

Wataru Sakamoto
Dept. of Applied Chem.,
Graduated School of Engineering
Nagoya University
Furo-cho, Chikusa-ku, Nagoya,
464-8603 Japan
Phone: 81-52-789-3345
Fax: 81-52-789-3182
e-mail:
sakamoto@apchem.nagoya-u.ac.jp

Kyoichi Sasaki
Fuji Titanium Ind. Co.,Ltd,.
12-8 Sengen-Cho, Hiratsuka-City,
254-0041 Japan
Phone: 81-463-32-1266
Fax: 81-463-32-1270

Motohiko Sato
R&D Center
NGK Spark Plug Co., Ltd.
2808, Iwasaki, Komaki, 485-8510
Japan
Phone: 81-568-76-9704
Fax: 81-568-76-5274
e-mail: (y-okimura_rd@
mg.ngkntk.co.jp.)

Shigeki Sato
Materials Research Center
TDK Corporation
570-2 Matsugashita,
Minamihatori, Narita-shi, 286-
8588 Japan
Phone: 81-476-37-1637
Fax: 81-476-37-1648
e-mail: shigekis@mb1.tdk.co.jp

Tadashi Sekiya
National Industrial Research
Institute of Nagoya
Hirate-cho, Kita-ku, Nagoya, 462-
8510 Japan
Phone: 81-52-911-2111
Fax: 81-52-916-6992
e-mail: tdsekiya@nirin.go.jp

Takuji Seri
The Rapid Progress of Organic
Package Technology
Kyocera Corporation
6 Takeda-Tobadono-cho, Fushimi-
ku, Kyoto, 612-8501 Japan
Phone: 81-995-46-8635
Fax: 81-995-46-8597

Yue Jin Shan
Faculty of Engineering
Utsunomiya University
7-1-2 Yoto, Utsunomiya, 321-
8585 Japan
Phone: 81-28-689-6174
Fax: 81-28-689-6009
e-mail: shan@cc.utsunomiya-
u.ac.jp

Kenji Shibata
Ya-man Ltd.
Shingu Bldg. 4F, 2-4-2, Toyo
Koto-ku, Tokyo, 135-0016 Japan
Phone: 81-3-5635-1861
Fax: 81-3-5635-1866
e-mail: shibata@ya-man.com

Kiyoshi Shimamura
Institute for Materials Research
Tohoku University
2-1-1 Katahira, Aoba-ku, Sendai,
980-8577 Japan
Phone: 81-22-215-2103
Fax: 81-22-215-2104
e-mail:
shimak@lexus.imr.tohoku.ac.jp

Kazuo Shinozaki
Dept. of Metallurgy and Ceramic
Science
Tokyo Institute of Technology
2-12-1 Ookayama, Meguro-ku,
Tokyo, 152-8552 Japan
Phone: 81-3-5734-2518
Fax: 81-3-5734-3369
e-mail: ksino@ceram.titech.ac.jp

Tadashi Shiosaki
Nara Institute of Science and
Technology
8916-5 Takayama-cho, Ikoma,
Nara, 630-0101 Japan
Phone: 81-743-72-6063
Fax: 81-743-72-6069
e-mail: m-masato@ms.aist-
nara.ac.jp

Hisao Suzuki
Dept. of Materials Science
Shizuoka University
3-5-1 Johoku, Hamamatsu, 432-
8561 Japan
Phone: 81-53-478-1157
Fax: 81-53-478-1157
e-mail:
hisuzuki@mat.eng.shizuoka.ac.jp

Sadayuki Takahashi
R & D Group
NEC Corporation
4-1-1, Miyazaki Miyamae,
Kawasaki-shi, 216-8555 Japan
Phone: 81-44-856-2164
Fax: 81-44-856-2128
e-mail: takahasi@rdg.cl.nec.co.jp

Yukichi Takamatsu
Japan Pionics Co., Ltd
5181 Tamura, Hiratsuka-shi, 253-0013 Japan
Phone: 81-463-53-8318
Fax: 81-463-53-8334

Hidemi Takasu
ROHM CO.LTD
21 Saiin Mizosakicho, Ukyo-ku, Kyoto, 615-8585 Japan
Phone: 81-75-311-2121
Fax: 81-75-321-6256
e-mail: takasu@rohm.co.jp

Tadashi Takenaka
Faculty of Sci. and Tech.
Science University of Tokyo
2641 Yamazaki, Noda, 278-8510 Japan
Phone: 81-471-24-1501(+3716)
Fax: 81-471-23-0856
e-mail: tadashi@takenaka.ee.noda.sut.ac.jp

Hiroshi Tamura
Materials Production Dept.
Murata Manufacturing Co., Ltd.
Higashiokino, Yokaichi, Shiga, 527-8558 Japan
Phone: 81-748-22-5500
Fax: 81-748-23-8009
e-mail: tamura@murata.co.jp

Masami Terasawa
The Rapid Progress of Organic Package Technology
Kyocera Corporation
6 Takeda-Tobadono-cho, Fushimi-ku, Kyoto, 612-8501 Japan
Phone: 81-75-604-3500
Fax: 81-75-674-3411
e-mail: masami-terasawa@kyocera.co.jp

Takaaki Tsurumi
Dept. of Inorg. Mater.
Tokyo Institute of Technology
2-12-1 Ookayama, Meguro, Tokyo, 152-8552 Japan
Phone: 81-3-5734-2517
Fax: 81-3-5734-2514
e-mail: ttsurumi@ceram.titech.ac.jp

Yoshiaki Uesu
Dept. of Physics
Waseda University
3-4-1 Okubo, Shinjuku-ku, Tokyo, 169-8555 Japan
Phone: 81-3-5286-3446
Fax: 81-3-3202-4962
e-mail: uesu93@mn.waseda.ac.jp

Satoshi Wada
Dept. of Inorg. Mater.
Tokyo Institute of Technology
2-12-1 Ookayama, Meguro, Tokyo, 152-8552 Japan
Phone: 81-3-5734-2829
Fax: 81-3-5734-2514
e-mail: swada@ceram.titech.ac.jp

Kikuo Wakino
Honorary Corporate Advisor, Technology
Murata Manufacturing Co, Ltd.
26-10, Tenjin 2-chome, Nagaokakyo-shi, Kyoto, 617-8555 Japan
Phone: 81-75-955-6504
Fax: 81-75-958-2219
e-mail:

Ruiping Wang
Materials and Structure Lab.
Tokyo Institute of Tecnology
4259 Nagatsuta, Midori-ku, Yokohama, 226-8503 Japan
Phone: 81-45-924-5626
Fax: 81-45-924-5626
e-mail: wang1@rlem.titech.ac.jp

Roger W. Whatmore
TDK Nanotechnology Centere
Cranfield University
College Rd., Bedford, MK43 0AL, UK
Phone: 44-1234-754057
Fax: 44-1235-751346
e-mail: r.w.whatmore@cranfield.ac.uk

Yasunori Yamaguchi
Ya-man Ltd.
Shingu Bldg. 4F, 2-4-2, Toyo Koto-ku, Tokyo, 135-0016 Japan
Phone: 81-3-5635-1861
Fax: 81-3-5635-1866
e-mail: fwih6440@mb.infoweb.ne.jp

Takashi Yamamoto
Dept.Electrical Eng.
National Defense Academy
1-10-20 Hashirimizu, Yokosuka, 239-8686 Japan
Phone: 81-468-41-3810 (ext.2585)
Fax: 81-468-44-5903
e-mail: ytakashi@cc.nda.ac.jp

Yohachi Yamashita
Research & Development Center, [PML]
Toshiba Corp.
1 Komukai Toshiba-Cho, Kawasaki, 210-8585 Japan
Phone: 81-44-549-2118
Fax: 81-44-520-1286
e-mail: yohachi.yamashita@toshiba.co.jp

Author Index